RĒZEKNES TEHNOLOĢIJU AKADĒMIJA
Inženieru fakultāte

REZEKNE ACADEMY OF TECHNOLOGIES
Faculty of Engineering

VIDE. TEHNOLOĢIJA. RESURSI

XV starptautiskās zinātniski praktiskās konferences rakstu krājums
2024.gada 27.-28.jūnijs

3.SĒJUMS

ENVIRONMENT. TECHNOLOGY. RESOURCES

Proceedings of the 15th International Scientific and Practical Conference
June 27th – 28th, 2024

Volume III

Rēzekne
2024

15.starptautiskās zinātniski praktiskās konferences "Vide. Tehnoloģija. Resursi" materiālos četros sējumos ir pārstāvēti jaunākie pētījumi vides inženierzinātnē, vides un dabas aizsardzībā, ilgtspējīgā lauksaimniecībā, enerģētikā, materiālzinātnē, mehānikā, metālapstrādē, lāzeru tehnoloģijās, matemātiskajā modelēšanā, elektrotehnikā, vides ekonomikā un vadībā, informācijas tehnoloģijās un sociotehnisko sistēmu modelēšanā, vides izglītībā un ilgtspējīgas attīstības procesos, izglītība inženierzinātnēs, aizsardzības un drošības tehnoloģijās. Krājumā pārstāvēto pētījumu joma ir daudzpusīga un starpdisciplināra, balstīta uz starptautisko zinātnieku kolektīvu sasniegumu rezultātiem. Konferences materiālos iekļauti 303 zinātniskie raksti. Konferences dalībnieki pārstāv 23 valstis.
Šī konference un konferences materiālu krājums ir veltīti konferences "Vide. Tehnoloģija. Resursi" dibinātāja un konferences ilggadējā priekšsēdētāja profesora Dr.habil.geol. Gotfrīda Novika piemiņai.
15.starptautiskās zinātniski praktiskās konferences "Vide. Tehnoloģija. Resursi" norises vieta ir "Vasil Levski" Nacionālā Militārā universitāte, Veliko Tarnovo, Bulgārija.

Proceedings of the 15th International Scientific and Practical Conference "Environment. Technology. Resources" include recent research in fields of engineering, environmental and nature protection, sustainable agriculture, energy, material science, mechanics, metalworking, laser technologies, mathematical modelling, electrical engineering, environmental economics and management, information technologies and sociotechnical systems modelling, environmental education and sustainable development, education in engineering sciences, defense and security technologies. The research area presented in the proceedings is comprehensive and cross disciplinary-based, on advances of international researchers. The proceedings comprise 303 scientific papers. Conference participants represent 23 countries.
This conference and proceedings are dedicated to the conference "Environment. Technology. Resources" founder and long-time chairman of the conference, professor Dr.habil.geol. Gotfrīds Noviks memory.
15th International Scientific and Practical Conference "Environment. Technology. Resources." hosted by "Vasil Levski" National Military University, Veliko Tarnovo, Bulgaria
https://conferences.rta.lv/index.php/ETR/ETR2024
Link to conference proceedings: http://journals.rta.lv/index.php/ETR

PhD Gunars Strods, Rezekne Academy of Technologies, Latvia
Dr.sc.ing. Artis Teilāns, Rezekne Academy of Technologies, Latvia
Dr.sc.ing. Edmunds Teirumnieks, Rezekne Academy of Technologies, Latvia
PhD Ērika Teirumnieka, Rezekne Academy of Technologies, Latvia
PhD Plamen Teodosiev, University of Library Studies and Information Technologies, Bulgaria
Dr.-Ing. Josef Timmerberg, Jade University of Applied Sciences, Germany
Dr.biol. Rasma Tretjakova, Rezekne Academy of Technologies, Latvia
PhD Andra Ulme, Riga Technical University, Latvia
PhD Nikolay Urummov, "Vasil Levski" National Military University, Bulgaria
PhD Dragomir Vassilev, Technical University of Gabrovo, Bulgaria
PhD Valentin Vassilev, South-West University "Neofit Rilski", Bulgaria
PhD Emil Yankov, Rezekne Academy of Technologies, Latvia
PhD Tsanka Zlateva-Petkova, Technical University of Gabrovo, Bulgaria
PhD Anda Zvaigzne, Rezekne Academy of Technologies, Latvia

Organising Committee Chairman

PhD Nikolay Dolchinkov, "Vasil Levski" National Military University, Bulgaria

Organising Committee

Dr.agr. Aleksandrs Adamovičs, Latvia University of Life Sciences and Technologies, Latvia
MA Yanitsa Boyanova, "Vasil Levski" National Military University, Bulgaria
Dr.sc.ing. Aleksandrs Gorbunovs, Riga Technical University, Latvia
Dr.sc.ing. Pēteris Grabusts, Rezekne Academy of Technologies, Latvia
MA Georgi Hristov, "Vasil Levski" National Military University, Bulgaria
Dr.sc.ing. Ēriks Kronbergs, Latvia University of Life Sciences and Technologies, Latvia
Dr.sc.ing. Sergejs Kodors, Rezekne Academy of Technologies, Latvia
Dr.sc.ing. Lyubomir Lazov, Rezekne Academy of Technologies, Latvia
Dr.sc.ing. Andris Martinovs, Rezekne Academy of Technologies, Latvia
PhD Rumen Marinov, Vasil Levski National Military University, Bulgaria
PhD Magdalena Mitkova, Assen Zlatarov University Burgas, Bulgaria
PhD Valyo Nikolov, Technical University of Sofia, Bulgaria
PhD Nikolay Padarev, "Vasil Levski" National Military University, Bulgaria
MA Svetoslav Pashunov, "Vasil Levski" National Military University, Bulgaria
Dr.agr. Liena Poiša, Rezekne Academy of Technologies, Latvia
Vilnis Rantins, Member of the Council of the Association of Mechanical Engineering and Metalworking Industries of Latvia, Latvia
Dr.geol. Valdis Segliņš, University of Latvia, Latvia
Dr.sc.ing. Andris Skromulis, Rezekne Academy of Technologies, Latvia
Dr.biol. Artūrs Škute, Daugavpils University, Latvia
Dr.sc.ing. Artis Teilāns, Rezekne Academy of Technologies, Latvia
MA.sc.comp. Gundega Teilāne, Rezekne Academy of Technologies, Latvia
PhD Ērika Teirumnieka, Rezekne Academy of Technologies, Latvia
Dr.biol. Rasma Tretjakova, Rezekne Academy of Technologies, Latvia

Reviewers

Dr.agr. Aleksandrs Adamovičs, Latvia University of Life Sciences and Technologies, Latvia
PhD Nikolaj Angelov, Technical University of Gabrovo, Bulgaria
Dr. agr. Lidiia Antypova, Mykolayiv National Agrarian University, Ukraine
PhD Ekaterina Arabska, Higher School of Agribusiness and Regional Development, Bulgaria
PhD Iluta Arbidane, Rezekne Academy of Technologies, Latvia
PhD Svetlana Asmuss, University of Latvia, Latvia

PhD Nikolay Padarev, "Vasil Levski" National Military University, Bulgaria
PhD Jana Paidere, Daugavpils University, Latvia
PhD Hristian Panayotov, Technical University of Sofia, Bulgaria
PhD Stanimir Parvanov, "Vasil Levski" National Military University, Bulgaria
PhD Plamen Pavlov, School of Telecommunications and Posts, Bulgaria
Dr.sc.ing. Jeļena Pečerska, Riga Technical University, Latvia
PhD Penyo Penev, "Georgi Benkovski" Bulgarian Air Force Academy, Bulgaria
Dr.sc.ing. Desislava Petrova, Technical University of Gabrovo, Bulgaria
Dr.agr. Liena Poiša, Rezekne Academy of Technologies, Latvia
Dr. agr. Valentīna Pole, IK Tava zeme, Latvia
PhD Dimcho Pulov, Technical University of Gabrovo, Bulgaria
Dr. agr. Gundega Putniece, Latvia University of Life Sciences and Technologies, Latvia
PhD Todor Rachovski, Plovdiv University "Paisii Hilendarski", Bulgaria
Dr.phys. Gita Rēvalde, Riga Technical University, Latvia
PhD Jolanta Šadauskiene, Kaunas University of Technology, Lithuania
Dr.sc.math. Felikss Sadirbajevs, Daugavpils University, Latvia
PhD Andrejs Šiškins, Riga Technical University, Latvia
Dr.sc.ing. Andris Skromulis, Rezekne Academy of Technologies, Latvia
PhD Krasimir Slavyanov, "Vasil Levski" National Military University, Bulgaria
PhD Nikolay Stefanov, "Vasil Levski" National Military University, Bulgaria
PhD Julija Steinhart, BA school of banking and finance, Switzerland
PhD Stoyko Stoykov, "Vasil Levski" National Military University, Bulgaria
PhD Aina Strode, Rezekne Academy of Technologies, Latvia
PhD Gunars Strods, Rezekne Academy of Technologies, Latvia
Dr.sc.ing. Artis Teilāns, Rezekne Academy of Technologies, Latvia
Dr.sc.ing. Edmunds Teirumnieks, Rezekne Academy of Technologies, Latvia
PhD Plamen Teodosiev, University of Library Studies and Information Technologies, Bulgaria
Dr.-Ing. Josef Timmerberg, Jade University of Applied Sciences, Germany
Dr.biol. Rasma Tretjakova, Rezekne Academy of Technologies, Latvia
PhD Andra Ulme, Riga Technical University, Latvia
PhD Nikolay Urummov, "Vasil Levski" National Military University, Bulgaria
PhD Dragomir Vassilev, Technical University of Gabrovo, Bulgaria
PhD Valentin Vassilev, South-West University "Neofit Rilski", Bulgaria
Dr.habil.sc.ing Janis Viba, Riga Technical University, Latvia
PhD Emil Yankov, Rezekne Academy of Technologies, Latvia
Dr.sc.ing. Imants Zarembo, Rezekne Academy of Technologies, Latvia
PhD Tsanka Zlateva-Petkova, Technical University of Gabrovo, Bulgaria
PhD Anda Zvaigzne, Rezekne Academy of Technologies, Latvia

Secretariat Chairman

PhD Ērika Teirumnieka, Rezekne Academy of Technologies, Latvia

Secretariat Members

Dr.agr. Liena Poiša, Rezekne Academy of Technologies, Latvia
MA.sc.comp. Gundega Teilāne, Rezekne Academy of Technologies, Latvia

III

ENGINEERING SCIENCES AND PRODUCTION TECHNOLOGIES

SATURS
CONTENTS

Engineering Sciences and Production Technologies

Laser Technologies

A case study of simulating various number of gate positions and their impact through T-RTM technology

Blagovest Bankov
Department of „Armament and Technology for Design"
National Military University "Vasil Levski"
Shumen, Bulgaria
blagovest.bankov@gmail.com

Abstract. **The study presented aims to investigate the influence from different gate positioning on the final product in T-RTM technology. The research is done using the specialized Moldex3D software. The studies conducted found that the symmetrical arrangement of injection ports and the approach to progressive injection with reduced pressure on the secondary gates result in significantly better deformation outcomes, with values close to 95% better compared to the deformation results in the approach with simultaneously open ports.**

Keywords: Injection Molding, Moldex3D, Polymer, T-RTM

I. INTRODUCTION

With the development of the global market, composite materials have significantly penetrated the manufacturing strategies of many industries, such as automotive, rail transport, the space industry, aircraft construction, etc., with one of the main goals being the reduction of the overall weight and improvement of various characteristics of the products, which directly affect the life cycle of the final product [1], [2], [3], [4], [5], [6], [7].

In recent years, there has been significant discussion about the possibility of using materials that can be easily recycled after their use to protect the environment [8], [9], [10], [11], [12]. One of the technologies that facilitates this development is "Thermoplastic Resin Transfer Molding" (T-RTM), combining the advantages of the known "Resin Transfer Molding" (RTM) technology with those of the thermoplastic matrix (recyclability, processability, plasticity, durability, etc.) and the high-pressure injection from the "High-Pressure Resin Transfer Molding" (HP-RTM) technology [13], [14], [15], [16].

Manufacturers opting to use T-RTM technology face a number of questions, but thanks to advanced computer technologies and various specialized software products that allow the creation of virtual prototypes and their examination through different mathematical models, these questions can be significantly more easily addressed [15], [17], [18], [19], [20].

Properly determining the number and location of injection points is crucial [21], [22], [23], [24], [25], [26], in various polymer product creation technologies, as this can significantly affect the different characteristics of the final product [27], [28], [29], [30].

From the perspective of design, manufacturing, and commissioning of molding tools, it's important that these two issues are resolved early on due to the potential for exponential increase in tool correction costs, delays in manufacturing processes, and loss of potential profits.

Incorrect parameter determination leads to several consequences, such as:

- Change in processing pressure;
- Failure to fill the mold completely;
- Appearance of weld lines, contributing to reduced mechanical properties of the product;
- Uneven shrinkage of the polymer - deviations in dimensions and weight;
- Deformations, warping of the product;
- Prerequisites for the entrapment of air volumes.

Due to the tremendous impact on the process, it is extremely important to correctly determine the number, position, and operation of the injection points.

Further studies and improvements of the technologies have found various combinations to improve the filling process with control over the inflows, some of which are:

- Injecting polymer simultaneously from all gates;
- Injecting polymer with progressive opening and closing of individual filling points;
- Fixed filling pressure through all injection points;
- Variable pressure in different filling zones.

Fig. 1 visually shows the different variations of injection, as well as the change in melt speed in single-point and multi-point injection.
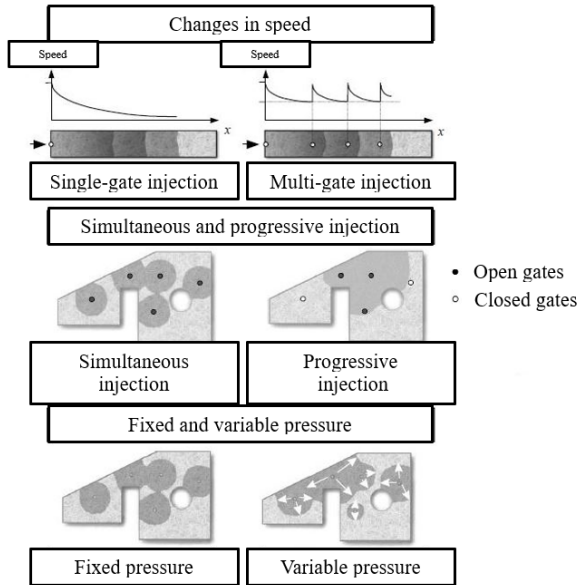
Fig. 1. Variations of injection [27].

This study examines the impact of the position and number of injection points in the T-RTM technology, with virtual prototypes of the analyzed object being created with different configurations of the placement of injection openings and their operation. The software tools used are:

- SolidWorks – for designing the virtual models;
- Rhinoceros – for creating mesh models;
- Moldex3D – for analyzing the filling process.

II. MATERIALS AND METHODS

To conduct the study, it is necessary to go through various stages (Fig. 2), which includes:
- Design of the basic geometry;
- Determining the number and location of injection points;
- Creating a finite element mesh model
- Setting material properties;
- Setting process parameters;
- Choosing an approach for managing the injection points.
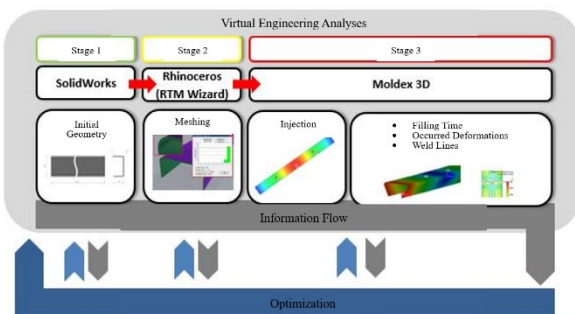
Fig. 2. Stages of creating the analysis.

A. Virtual models

To determine the optimal position of the injection points, a set of variations is considered (Fig. 3), through which the goal is to analyze the filling speed of the mold, the possibility of weld lines appearance, and the deformation values that occur in the detail.
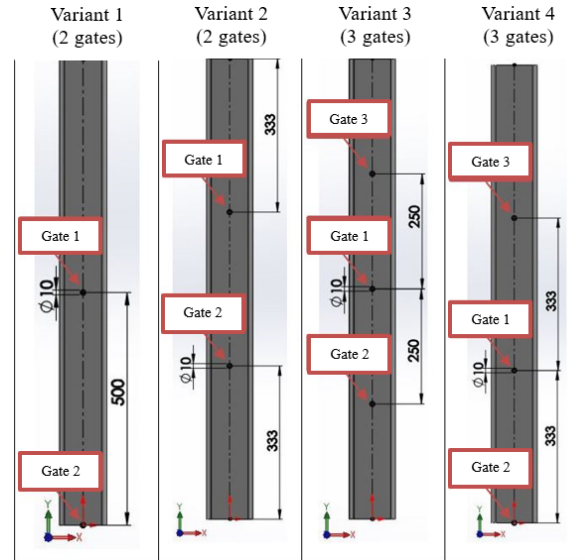
Fig. 3. Initial models for study.

B. Mesh model

The construction of the finite element mesh model was carried out using specialized software "Rhinoceros", and the available tools for this purpose, where the fiber orientation of the available preform was also determined. (Fig. 4).
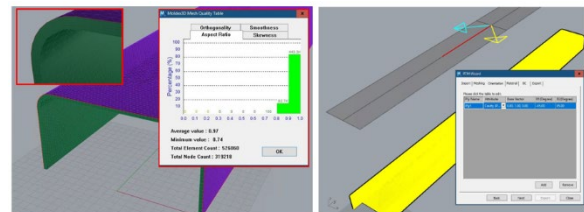
Fig. 4. Mesh model and fiber orientation.

C. Materials

The material characteristics used for the preform are shown in Table 1. For the matrix component of the composite, material characteristics of the thermoplastic polymer Polyamide 6 (PA6) were used.

TABLE 1 MATERIAL CHARACTERISTICS OF THE PREFORM

Variable	Aramid Fiber Kevlar 49		
	Designation of the variable	*Value*	*Dimension*
Permeability	K11	1.92e-08	m^3
	K22	1.92e-08	
	K33	1.00e-08	
Porosity	φ	0.33	-
Young's modulus	E1	57.89e+09	Pa
	E2	57.89e+09	
	E3	6.89e+08	
Poisson's ratio	v12	0.35	-
	v23	0.35	
	v13	0.3	

Variable	Aramid Fiber Kevlar 49		
	Designation of the variable	*Value*	*Dimension*
Shear modulus	G12	16.49e+09	Pa
	G23	16.49e+09	
	G13	1.81e+09	
Coefficient of linear thermal expansion	CLTE1	-2e-06	1/K
	CLTE2	-2e-06	
	CLTE3	1e-06	

All variants have been subjected to analyses with similar initial process parameters shown in Table 2.

TABLE 2 INITIAL PROCESS SETTINGS

Variable	*Value*	*Dimension*
Filling time	360	sec
Filling pressure	150	MPa
Resin temperature	140	°C
Mold temperature	90	°C
Curing time	5	Sec

Several injection variants have been studied:

- With identical pressure at the inlets;
- With different pressure at the inlets.

D. The approach for the gates controlling

The approach chosen involves the progressive opening and closing of the injection ports, with this action being controlled through the simulation of a pressure sensor that manages the flow gates.

To determine the exact position of the sensor, three models were made to study their behavior (Fig. 5).
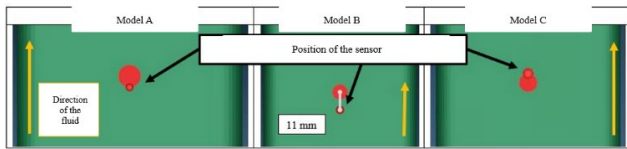
Fig. 5. Studied models for the position of the pressure sensor.

In Fig. 6, the initial moments after the injection ports are opened in the models are shown, and it can be observed that the most at-risk model for the appearance of weld lines is Model B, while the lowest risk is Model C. Table 3 shows the results after the molds are filled, indicating that Model A has the most balanced indicators in terms of time and chances for the appearance of weld lines.

Based on the results, Model A is chosen, with the position of the sensor immediately before the injection port, as the most balanced and low-risk for the occurrence of weld lines.
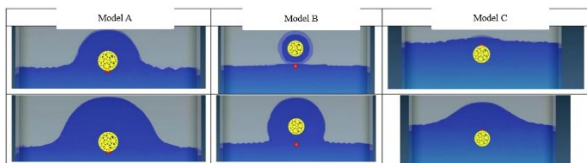
Fig. 6. Initial moments of filling.

TABLE 3 FINAL RESULTS OF THE FILLING

Model	*Filling of the mold (%)*	*Filling time (sec)*	*Maximum deformations (mm)*	*Presence of weld lines*
A	100	268.50	16.46	No
B	100	261.63	16.46	No
C	100	279.16	16.46	No

III. RESULTS AND DISCUSSION

In Table 4 and Table 5, the results of studies with two different pressures (150 and 100 MPa) are compared, including the sequence of opening the injection ports for polymer injection.

Due to the presence of two combinations of opening points, the results of both variations in models B5 and B6 are shown.

TABLE 4 RESULTS AT 150 MPA PRESSURE

Model	Sequence of opening			*Filling of the mold (%)*	*Filling time (sec)*	*Maximum deformations (mm)*	*Presence of weld lines*
V1	1	2	-	70,45	-	-	No
V2	1	2	-	100	268.50	16.46	No
V31	2	1	3	100	222.42	16.45	No
V32	1	2&3		100	153.25	16.45	No
V41	2	1	3	98,15	-	-	No
V42	1	2&3		100	265.46	16.44	No

TABLE 5 RESULTS AT 100 MPA PRESSURE

Model	Sequence of opening			*Filling of the mold (%)*	*Filling time (sec)*	*Maximum deformations (mm)*	*Presence of weld lines*
V1	1	2	-	63.35	-	-	No
V2	1	2	-	92.98	-	-	No
V31	2	1	3	100	358.18	6.90	No
V32	1	2&3		100	248.28	6.90	No
V41	2	1	3	62.32	-	-	No
V42	1	2&3		95.51	-	-	No

Fig. 7 shows a graph comparing the mean values of the deformations that occurred throughout the volume of the detail under different injection combinations in models V31 and V32.
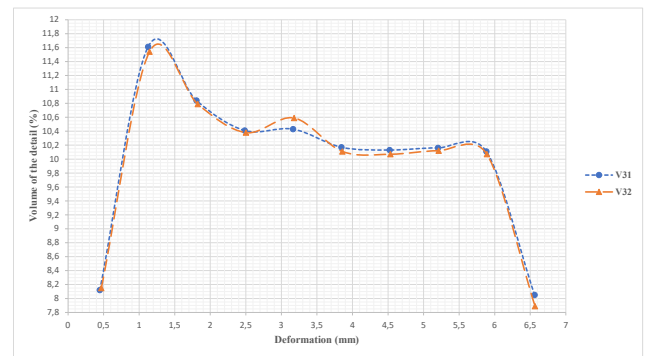
Fig. 7. Occurred deformations.

From the above figure, it is observed that the more balanced fluid flow, caused by symmetrically distributed inlets, shows better results in terms of deformations.

To compare the results of the study with variable pressure in the injection ports, model V32 was examined in more detail, with different variants of the distances between the initial injection point at intervals of 50 mm (Fig. 8) being designed.
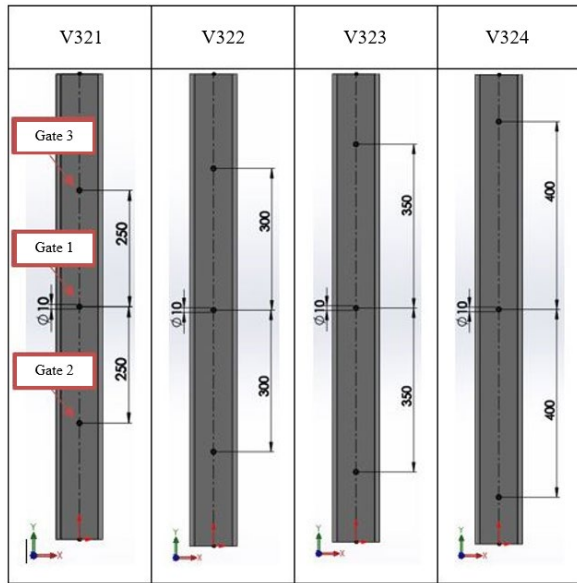
Fig. 8. Additional models for study.

The results of the study, with a pressure of 150 MPa in the first inlet and 100 MPa in the other two points, are shown in Table 6, from which it is determined that model V322 fills the fastest.

TABLE 6 RESULTS FROM THE VARIABLE PRESSURE (150/100 MPA)

Model	Filling of the mold (%)	Filling time (sec)	Maximum deformations (mm)	Presence of weld lines
V321	100	194.98	6.90	No
V322	100	190.47	6.90	No
V323	100	201.83	6.90	No
V324	100	230.96	6.91	No

In a further study, with the pressure reduced to 65 MPa in the secondary injections, it was found that the deformation fell below 0.500 mm in all models (Fig. 9), which represents a decrease of nearly 95% from the previous results (with 100 MPa in the secondary gates).
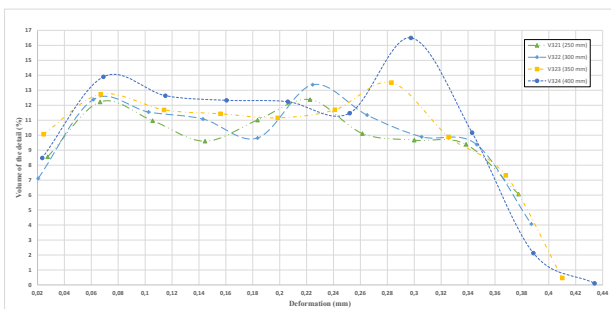
Fig. 9. Deformation.

The rate (Figure 12) and shear forces (Figure 13) obtained during filling, which are related to the flow rate and the drop in pressure, have been examined. Too high values can be a precondition for the occurrence of defects in the product, such as cracking [31].
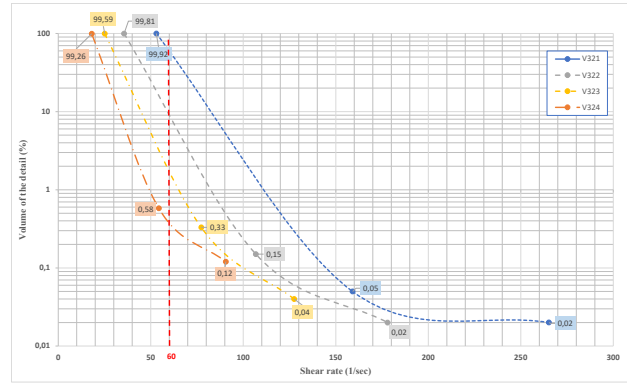
Fig. 10. Shear rate.
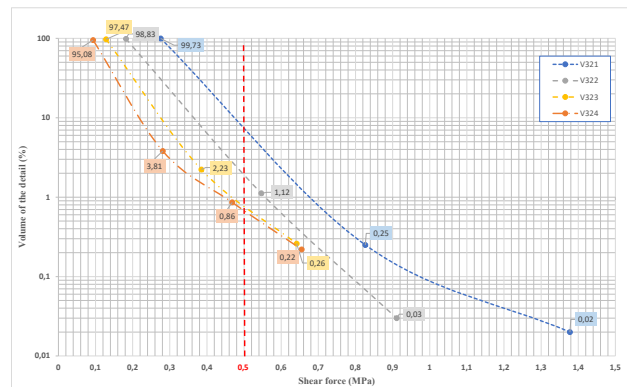
Fig. 11. Shear force.

Upon examining the forces and shear rates, their relationship with the occurred deformations is established, with the peak of lower values in the model with 400 mm (Model V324) being due to the lower values of forces and speed.

The secondary injection points closer to the primary one experience difficulties in filling the mold, and the shear forces increase, leading to an increase in the affected volumes of the detail between the values of 0.36 to 0.40 mm.

IV. CONCLUSION

By using a multi-step approach to analyze the impact of filling points in T-RTM technology, it has been established that the position and number of filling points significantly influence the complex fluid flow, the possibility of filling the mold, and the necessary time for this.

Using more injection points allows for the choice of a strategy for their progressive opening with specifically set pressure, which supports the balancing of the fluid flow in T-RTM technology and reduces the values of the occurred deformations.

A relationship has been noted between the deformations, forces, and shear rates, the set pressure, and the position of the inlets.

It has been established that, even in T-RTM technology, the correct positioning of injection ports reduces the deformations that occur in the product, with the best results observed when they are symmetrically arranged.

Progressive opening of the injection points helps to eliminate weld lines, thereby ensuring the uniform wetting of the reinforcing fibers.

18

REFERENCES

[1] M. Eugeni et al., 'An industry 4.0 approach to large scale production of satellite constellations. The case study of composite sandwich panel manufacturing', Acta Astronautica, vol. 192, pp. 276–290, Mar. 2022, doi: 10.1016/j.actaastro.2021.12.039.

[2] J. Goodsell, M. Bogdanor, and A. Favaloro, 'Design for manufacture', in Design and Manufacture of Structural Composites, Elsevier, 2023, pp. 349–372. doi: 10.1016/B978-0-12-819160-6.00012-3

[3] S. Hancock and L. Harper, 'Cost, rate, and robustness', in Design and Manufacture of Structural Composites, Elsevier, 2023, pp. 447–471. doi: 10.1016/B978-0-12-819160-6.00022-6

[4] D. Jayasekara, N. Y. G. Lai, K.-H. Wong, K. Pawar, and Y. Zhu, 'Level of automation (LOA) in aerospace composite manufacturing: Present status and future directions towards industry 4.0', Journal of Manufacturing Systems, vol. 62, pp. 44–61, Jan. 2022, doi: 10.1016/j.jmsy.2021.10.015

[5] M. R. Mansor, S. H. S. M. Fadzullah, and A. H. Nurfaizey, 'Life cycle assessment (LCA) analysis of composite products in automotive applications', in Biocomposite and Synthetic Composites for Automotive Applications, Elsevier, 2021, pp. 147–172. doi: 10.1016/B978-0-12-820559-4.00005-5

[6] J. Zhang, G. Lin, U. Vaidya, and H. Wang, 'Past, present and future prospective of global carbon fibre composite developments and applications', Composites Part B: Engineering, vol. 250, p. 110463, Feb. 2023, doi: 10.1016/j.compositesb.2022.110463

[7] T. Todorov, G. Todorov, B. Romanov. 'Design and simulation of mould tools with multi-material structure for plastaic injection moulding based on Additive Technology', 2019 International Conference on Creative Business for Smart and Sustainable Growth, CreBUS 2019

[8] N. H. Mohd Nasir, F. Usman, A. Saggaf, and Saloma, 'Development of composite material from Recycled Polyethylene Terephthalate and fly ash: Four decades progress review', Current Research in Green and Sustainable Chemistry, vol. 5, p. 100280, 2022, doi: 10.1016/j.crgsc.2022.100280

[9] B. Miranda Campos, S. Bourbigot, G. Fontaine, and F. Bonnet, 'Thermoplastic matrix‐based composites produced by resin transfer molding: A review', Polymer Composites, vol. 43, no. 5, pp. 2485–2506, May 2022, doi: 10.1002/pc.26575

[10] F. P. Martins, L. Santos, R. Torcato, P. S. Lima, and J. M. Oliveira, 'Reproducibility Study of the Thermoplastic Resin Transfer Molding Process for Glass Fiber Reinforced Polyamide 6 Composites', Materials, vol. 16, no. 13, p. 4652, Jun. 2023, doi: 10.3390/ma16134652

[11] G. Todorov, Y. Sofronov, B. Romanov, T. Gavrilov. 'New product development and production in extremely short terms – Safety goggles', 10th International Scientific Conference on Engineering, Technologies and Systems, TECHSYS 2021.

[12] M. Zagorski, G. Todorov, N. Nikolov, Y. Sofronov, M. Kandeva. 'Investigation on wear of biopolymer parts produced by 3D printing in lubricated sliding conditions', *Industrial Lubrication and Tribology*, Volume 74, Issue 3, Pages 360 – 366, 29 March 2022.

[13] C. Gomez et al., 'Resin Transfer molding of High-Fluidity Polyamide-6 with modified Glass-Fabric preforms', Composites Part A: Applied Science and Manufacturing, no. 147, 2021

[14] E. Poodts, G. Minak, L. Mazzocchetti, and L. Giorgini, 'Fabrication, process simulation and testing of a thick CFRP component using the RTM process', Composites Part B: Engineering, vol. 56, pp. 673–680, Jan. 2014, doi: 10.1016/j.compositesb.2013.08.088

[15] D. Heider, 'High-Pressure Resin Transfer Molding (HP-RTM)', University of Delaware, Mar. 2019. [Online]. Available: https://nwp.engr.udel.edu/ccm/tech-briefs/2019/hp-rtm-0301.pdf

[16] J. Sloan, 'Getting real: Thermoplastic resin transfer molding', CompositesWorld, Jun. 21, 2016. [Online]. Available: https://www.compositesworld.com/articles/getting-real-thermoplastic-resin-transfer-molding

[17] L. Kärger et al., 'Development and validation of a CAE chain for unidirectional fibre reinforced composite components', Composite Structures, vol. 132, pp. 350–358, Nov. 2015, doi: 10.1016/j.compstruct.2015.05.047

[18] T. Todorov, B. Romanov, and Y. Sofronov, 'Design and simulation of mould tools with conformal cooling system based on multi-shot moulding technology', presented at the 10th International Scientific Conference on Engineering, Technologies and Systems, TECHSYS 2021

[19] S. M. Afazov, A. A. Becker, and T. H. Hyde, 'Development of a Finite Element Data Exchange System for chain simulation of manufacturing processes', Advances in Engineering Software, vol. 47, no. 1, pp. 104–113, May 2012, doi: 10.1016/j.advengsoft.2011.12.011

[20] V. Ganev, Ya. Dimitrova, and S. Antonov, 'FAST PROTOTYPING IN THE MANUFACTURING OF COMPLEX ARMAMENT PARTS', presented at the INTERNATIONAL SCIENTIFIC JOURNAL 'SECURITY & FUTURE', 2018

[21] S. Jiang, C. Zhang, and B. Wang, 'Optimum arrangement of gate and vent locations for RTM process design using a mesh distance-based approach', Composites Part A: Applied Science and Manufacturing, vol. 33, no. 4, pp. 471–481, Apr. 2002, doi: 10.1016/S1359-835X(01)00146-4

[22] X. Ye, C. Zhang, Z. Liang, and B. Wang, 'Heuristic algorithm for determining optimal gate and vent locations for RTM process design', Journal of Manufacturing Systems, vol. 23, no. 4, pp. 267–277, Jan. 2004, doi: 10.1016/S0278-6125(04)80039-6

[23] M. Seyednourani, M. Yildiz, and H. S. Sas, 'A two-stage optimization methodology for gate and vent locations and distribution media layout for liquid composite molding process', Composites Part A: Applied Science and Manufacturing, vol. 149, p. 106522, Oct. 2021, doi: 10.1016/j.compositesa.2021.106522

[24] B. Liu, S. Bickerton, and S. G. Advani, 'Modelling and simulation of resin transfer moulding (RTM)—gate control, venting and dry spot prediction', Composites Part A: Applied Science and Manufacturing, vol. 27, no. 2, pp. 135–141, Jan. 1996, doi: 10.1016/1359-835X(95)00012-Q

[25] J. Wang, P. Simacek, and S. G. Advani, 'Use of Centroidal Voronoi Diagram to find optimal gate locations to minimize mold filling time in resin transfer molding', Composites Part A: Applied Science and Manufacturing, vol. 87, pp. 243–255, Aug. 2016, doi: 10.1016/j.compositesa.2016.04.026

[26] T., Todorov, G., Todorov, B., Romanov. Design Solution for an Extreme Concept of Specific Geometry in Complex Plastic Parts. 11th International Scientific Conference on Engineering, Technologies and Systems, TechSys 2022

[27] M. K. Kang, J. J. Jung, and W. I. Lee, 'Analysis of resin transfer moulding process with controlled multiple gates resin injection', Composites Part A: Applied Science and Manufacturing, vol. 31, no. 5, pp. 407–422, May 2000, doi: 10.1016/S1359-835X(99)00086-X

[28] J. M. Lawrence, P. Fried, and S. G. Advani, 'Automated manufacturing environment to address bulk permeability variations and race tracking in resin transfer molding by redirecting flow with auxiliary gates', Composites Part A: Applied Science and Manufacturing, vol. 36, no. 8, pp. 1128–1141, Aug. 2005, doi: 10.1016/j.compositesa.2005.01.024

[29] B. X. Chai et al., 'Simulation-based optimisation for injection configuration design of liquid composite moulding processes: A review', Composites Part A: Applied Science and Manufacturing, vol. 149, p. 106540, Oct. 2021, doi: 10.1016/j.compositesa.2021.106540

[30] S. Laurenzi, A. Casini, and D. Pocci, 'Design and fabrication of a helicopter unitized structure using resin transfer moulding', Composites Part A: Applied Science and Manufacturing, vol. 67, pp. 221–232, Dec. 2014, doi: 10.1016/j.compositesa.2014.09.007

[31] M. Betterlich, 'Thermoplastic Resin Transfer Molding (T-RTM): Tailored to Reactive Polyamide 6', Specialist Article. Accessed: Aug. 20, 2020. [Online]. Available: https://en.kunststoffe.de/a/specialistarticle/thermoplastic-resin-transfer-molding-t-r-264160

A multi-step approach for analyzing the number of polymer injection molding gate spots and their position in T-RTM technology

Blagovest Bankov
Department of „Armament and Technology for Design" National Military University "Vasil Levski"
Shumen, Bulgaria
blagovest.bankov@gmail.com

Todor Todorov
FIT, Laboratory "CAD/CAM/CAE in Industry", Technical University
Sofia, Bulgaria
todorttodorov@tu-sofia.bg

Yavor Sofronov
FIT, Laboratory "CAD/CAM/CAE in Industry", Technical University
Sofia, Bulgaria
ysofronov@tu-sofia.bg

Ivan Ivanov
FIT, Laboratory "CAD/CAM/CAE in Industry", Technical University
Sofia, Bulgaria
ivan.st.ivanov@abv.bg

Abstract. **The purpose of this study is to present a multi-step approach for building a virtual analysis supporting the determination of the number and position of the injection molding gate spots in Resin Transfer Molding (RTM) and the relatively new Thermoplastic Resin Transfer Molding (T-RTM) technologies. The methodology provides an opportunity to determine the behavior of the fluid flow based on the location of the inlets, as well as potential problems and defects.**

Keywords: Injection Molding, Moldex3D, Polymer, T-RTM

I. Introduction

Composite products are increasingly occupying a larger share of the market, being used in the aviation and automotive industries, the production of various sports facilities, and building elements, with the goal of reducing the overall weight and thereby enhancing various characteristics that directly affect the life cycle of the final product [1], [2], [3], [4], [5].

Strategies for using fewer raw materials and creating less environmental pollution are adopted for the creation of such composite products, which can be more easily processed after they are no longer in use. The relatively new technology "Thermoplastic Resin Transfer Molding" (T-RTM) is used for their creation, combining the advantages of "Resin Transfer Molding" (RTM) technology with those of the thermoplastic matrix (recyclability, workability, plasticity, durability, etc.) and the high-pressure injection from the "High-Pressure Resin Transfer Molding" (HP-RTM) technology [6], [7], [8].

Although RTM technology and its processes are well known to process engineers, there are still various difficulties in creating large parts. With the development of computer technologies and mathematical models, manufacturers have the opportunity to analyze and optimize processes in advance by creating virtual prototypes to be investigated with specialized software products [9], [10], [11], [12], [13], [14], [15], [16], [17], [18], [19], [20], thereby reducing the potential risks of defective products and financial losses.

One of the important steps in creating a quality product through RTM and T-RTM technologies is the initial determination of the number, type, geometry, and position of the filling point or points [21], [22], [23], [24], [25], known as the "gate," which directly affects various characteristics of the final product (geometric and mechanical), as well as the parameters during the polymer casting process into the mold-forming tool. The gate is part of the mold system of the mold-forming tool, which ensures the passage of the polymer from the mixing head (in "Liquid Composite Molding" (LCM) technologies) or the chamber with the melted material, in machines for standard high-temperature melt injection, into the molding cavities.

From the perspective of mold making, incorrect positioning or number of gates can lead to an exponential increase in tool correction costs, production process delays, and loss of potential profits.

Incorrect determination of parameters leads to several consequences, such as:

- Change in process pressure;
- Incomplete mold filling;
- Appearance of weld lines, contributing to reduced mechanical properties of the product;
- Different polymer shrinkage – deviations in dimensions and weight;
- Deformations, warping of the product;

- Preconditions for trapping air volumes.

In continuation, the study and improvement of technologies have found various combinations to improve the filling process with control over the gates, part of them being:

- Injection of polymer simultaneously from all gates;
- Injection of polymer with progressive opening and closing of individual filling gates;
- Fixed filling pressure through all injection gates;
- Variable pressure in different filling zones.

Fig. 1 visually shows the different variations of injection, as well as the change in the melt speed during single-gate and multi-gate injection
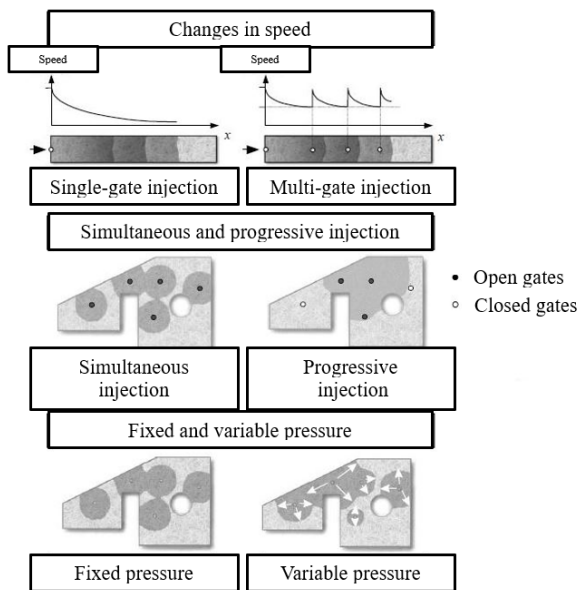
Fig. 1. Variations of injection [26].

Through the position of the injection ports and complex control over the process, it is possible to influence the direction and speed of the fluid, which affects the different characteristics of the final product [26], [27], [28], [29].

II. MATERIALS AND METHODS

To conduct the study, three key stages need to be passed (Fig. 2), through which the basic geometry for analysis is created, the finite element mesh model is generated, the number and locations of the filling points are determined, material characteristics and process parameters are set.
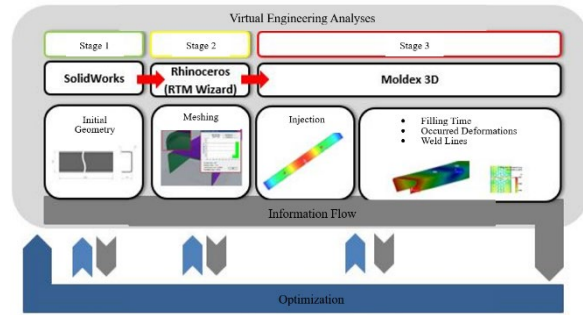
Fig. 2. Stages of creating the analysis.

A. Stage 1 – Design of the model

The design of the virtual object for the study was performed using the CAD software "SolidWorks", which detail was subsequently exported in a file format with the extension "STEP", to facilitate the preparation of a mesh model in the next stage (Fig. 3).
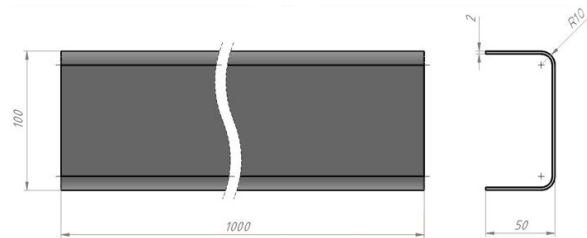
Fig. 3. CAD Model.

B. Stage 2 – Creating a mesh model and determining the number and location of the filling points

The construction of the finite element mesh model was carried out using the specialized software "Rhinoceros", and the available tools for this purpose, where the fiber orientation of the available preform was also determined. (Fig. 4).
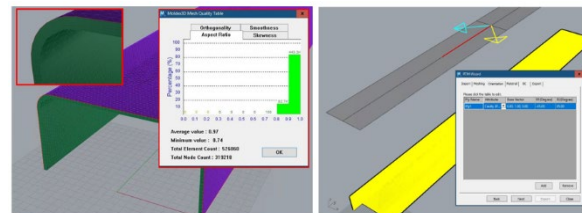
Fig. 4. Stages of building a finite element model.

The steps used in building the mesh model are:

- Importing the STEP file;
- Creating a shell mesh of finite elements;
- Merging all elements of the mesh into a unified model;
- Creating an offset of the mesh relative to the original, with a distance equal to the thickness of the designed detail;
- Building a volumetric mesh of finite elements through topological synchronization of the two surface meshes and determining the number of volumetric layers;
- Setting the fiber orientation and direction of the base vector, dividing the angle formed between the fibers into two equal halves, with the possibility to

introduce information about different fiber orientations in separate zones through the inclusion of an additional stage in the study, namely - analysis of the preform molding and the orientations created in the product;

- Positioning of the injection points in the models.

To determine the optimal position of the filling points, a set of variations is considered (Fig. 5), aiming to analyze the filling speed of the mold, the possibility of weld lines appearance, and the deformation values occurred in the detail
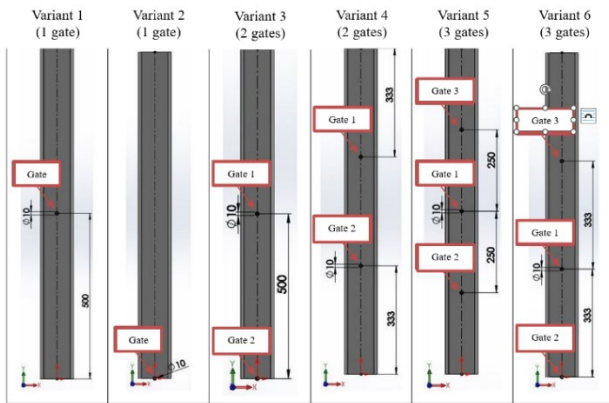
Fig. 5. Initial models for study.

C.   Stage 3 - Construction of a model to analyze the influence of the number and position of injection points on the fluid flow

The exported mesh of finite elements with the introduced characteristics for fiber orientation is imported into the next tool for engineering analysis (Moldex3D), introducing material properties for the individual structural components (reinforcing structure and polymer matrix) and process settings necessary for completing the analysis.
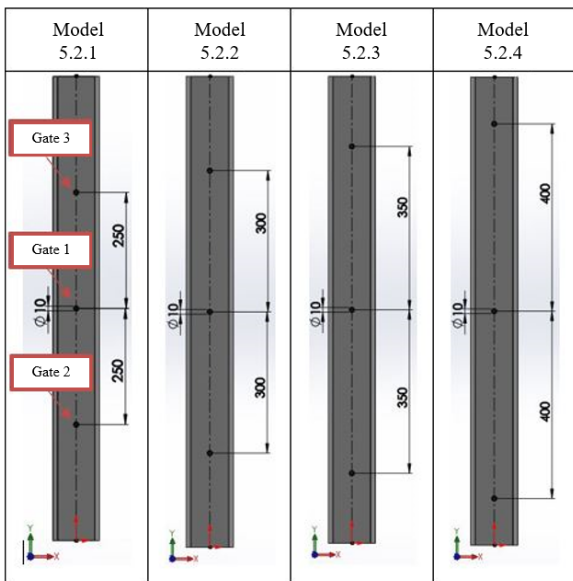
Fig. 6. Additional models for study.

After the preliminary analyses of the models and their comparison based on the selected control parameters, additional studies need to be conducted on the model

with the best results, aiming to examine further similar variations in the arrangement of the injection points (Fig. 6).

III. CONCLUSION

A multi-step approach for conducting a virtual analysis is presented to investigate the influence of the number and position of injection gates on the quality of the final product. By using three tools in separate stages, in the creation of products through Thermoplastic Resin Transfer Molding (T-RTM) and Resin Transfer Molding (RTM) technologies, it is possible to prevent potential problems such as underfilling of the mold, the appearance of weld lines, and other defects in the technological process directly related to the injection gates.

The method of using virtual engineering analysis at the stage of designing the mold-making tool provides extremely valuable information to designers for identifying potential issues and their preemptive resolution, thereby saving resources and time in the manufacturing of tooling equipment.

By including an additional stage, a preliminary analysis of the preform molding and thus the created fiber orientations, it is possible to enrich the information flow with combined data and more accurately track the behavior of the fluid flow, the consequences arising from the set input parameters, and to pinpoint problem areas.

REFERENCES

[1] S. Hancock and L. Harper, 'Cost, rate, and robustness', in Design and Manufacture of Structural Composites, Elsevier, 2023, pp. 447–471. doi: 10.1016/B978-0-12-819160-6.00022-6.

[2] M. R. Mansor, S. H. S. M. Fadzullah, and A. H. Nurfaizey, 'Life cycle assessment (LCA) analysis of composite products in automotive applications', in Biocomposite and Synthetic Composites for Automotive Applications, Elsevier, 2021, pp. 147–172. doi: 10.1016/B978-0-12-820559-4.00005-5

[3] J. Goodsell, M. Bogdanor, and A. Favaloro, 'Design for manufacture', in Design and Manufacture of Structural Composites, Elsevier, 2023, pp. 349–372. doi: 10.1016/B978-0-12-819160-6.00012-3

[4] X. Lim, 'The World Is Running Out of Elements, and Researchers Are Looking in Unlikely Places for Replacements', Discover, May 16, 2020. [Online]. Available: https://www.discovermagazine.com/planet-earth/the-world-is-running-out-of-elements-and-researchers-are-looking-in-unlikely

[5] S. H. Han, E. J. Cho, H. C. Lee, K. Jeong, and S. S. Kim, 'Study on high-speed RTM to reduce the impregnation time of carbon/epoxy composites', Composite Structures, vol. 119, pp. 50–58, Jan. 2015, doi: 10.1016/j.compstruct.2014.08.023

[6] C. Gomez, D. Salvatori, B. Caglar, R. Trigueira, G. Orange, V. Michaud, 'Resin Transfer molding of High-Fluidity Polyamide-6 with modified Glass-Fabric preforms', Composites Part A: Applied Science and Manufacturing, no. 147, 2021

[7] E. Poodts, G. Minak, L. Mazzocchetti, and L. Giorgini, 'Fabrication, process simulation and testing of a thick CFRP component using the RTM process', Composites Part B: Engineering, vol. 56, pp. 673–680, Jan. 2014, doi: 10.1016/j.compositesb.2013.08.088

[8] D. Heider, 'High-Pressure Resin Transfer Molding (HP-RTM)', University of Delaware, Mar. 2019. [Online]. Available: https://nwp.engr.udel.edu/ccm/tech-briefs/2019/hp-rtm-0301.pdf

[9] L. Kärger et al., 'Development and validation of a CAE chain for unidirectional fibre reinforced composite components', Composite Structures, vol. 132, pp. 350–358, Nov. 2015, doi: 10.1016/j.compstruct.2015.05.047

[10] G. Todorov, K. Kamberov, and T. Ivanov, 'Parametric optimisation of resistance temperature detector design using validated virtual prototyping approach', Case Studies in Thermal Engineering, vol. 28, p. 101302, Dec. 2021, doi: 10.1016/j.csite.2021.101302.

[11] S. M. Afazov, A. A. Becker, and T. H. Hyde, 'Development of a Finite Element Data Exchange System for chain simulation of manufacturing processes', Advances in Engineering Software, vol. 47, no. 1, pp. 104–113, May 2012, doi: 10.1016/j.advengsoft.2011.12.011

[12] S. Bickerton, P. Šimáček, S. E. Guglielmi, and S. G. Advani, 'Investigation of draping and its effects on the mold filling process during manufacturing of a compound curved composite part', Composites Part A: Applied Science and Manufacturing, vol. 28, no. 9–10, pp. 801–816, Jan. 1997, doi: 10.1016/S1359-835X(97)00033-X

[13] V. Ganev., Ya. Dimitrova, and S. Antonov, 'Fast prototyping in the manufacturing of complex armament parts', presented at the International scientific journal 'security & future', 2018

[14] F. Trochu, E. Ruiz, V. Achim, and S. Soukane, 'Advanced numerical simulation of liquid composite molding for process analysis and optimization', Composites Part A: Applied Science and Manufacturing, vol. 37, no. 6, pp. 890–902, Jun. 2006, doi: 10.1016/j.compositesa.2005.06.003

[15] S. Soukane and F. Trochu, 'Application of the level set method to the simulation of resin transfer molding', Composites Science and Technology, vol. 66, no. 7–8, pp. 1067–1080, Jun. 2006, doi: 10.1016/j.compscitech.2005.03.001

[16] M. Y. Lin, M. J. Murphy, and H. T. Hahn, 'Resin transfer molding process optimization', Composites Part A: Applied Science and Manufacturing, vol. 31, no. 4, pp. 361–371, Apr. 2000, doi: 10.1016/S1359-835X(99)00054-8

[17] L. Kroll, 'Modeling, integrative simulation, and optimization', in Multifunctional Lightweight Structures, L. Kroll, Ed., Berlin, Heidelberg: Springer Berlin Heidelberg, 2023, pp. 563–629. doi: 10.1007/978-3-662-62217-9_8

[18] G. Todorov, B. Zlatev, and K. Kamberov, 'Digital twin definition based on virtual prototype evolution of an UPS with kinetic battery accumulator', presented at the THERMOPHYSICAL BASIS OF ENERGY TECHNOLOGIES (TBET 2020), Tomsk, Russia, 2021, p. 110008. doi: 10.1063/5.0044792.

[19] G. Todorov, K. Kamberov, H. Vasilev, and T. Ivanov, 'Design Variants Assessment Of Street LED Device Based On Virtual Prototyping', in 2021 17th Conference on Electrical Machines, Drives and Power Systems (ELMA), Sofia, Bulgaria: IEEE, Jul. 2021, pp. 1–4. doi: 10.1109/ELMA52514.2021.9503086.

[20] G. Todorov, V. Obretenov, K. Kamberov, T. Ivanov, T. Tsalov, and B. Zlatev, 'Concept and Physical Prototyping of Micro Hydropower System Using Vertical Crossflow Turbine', in 2021 6th International Symposium on Environment-Friendly Energies and Applications (EFEA), Sofia, Bulgaria: IEEE, Mar. 2021, pp. 1–4. doi: 10.1109/EFEA49713.2021.9406242.

[21] S. Jiang, C. Zhang, and B. Wang, 'Optimum arrangement of gate and vent locations for RTM process design using a mesh distance-based approach', Composites Part A: Applied Science and Manufacturing, vol. 33, no. 4, pp. 471–481, Apr. 2002, doi: 10.1016/S1359-835X(01)00146-4

[22] X. Ye, C. Zhang, Z. Liang, and B. Wang, 'Heuristic algorithm for determining optimal gate and vent locations for RTM process design', Journal of Manufacturing Systems, vol. 23, no. 4, pp. 267–277, Jan. 2004, doi: 10.1016/S0278-6125(04)80039-6

[23] M. Seyednourani, M. Yildiz, and H. S. Sas, 'A two-stage optimization methodology for gate and vent locations and distribution media layout for liquid composite molding process', Composites Part A: Applied Science and Manufacturing, vol. 149, p. 106522, Oct. 2021, doi: 10.1016/j.compositesa.2021.106522

[24] B. Liu, S. Bickerton, and S. G. Advani, 'Modelling and simulation of resin transfer moulding (RTM)—gate control, venting and dry spot prediction', Composites Part A: Applied Science and Manufacturing, vol. 27, no. 2, pp. 135–141, Jan. 1996, doi: 10.1016/1359-835X(95)00012-Q

[25] J. Wang, P. Simacek, and S. G. Advani, 'Use of Centroidal Voronoi Diagram to find optimal gate locations to minimize mold filling time in resin transfer molding', Composites Part A: Applied Science and Manufacturing, vol. 87, pp. 243–255, Aug. 2016, doi: 10.1016/j.compositesa.2016.04.026

[26] M. K. Kang, J. J. Jung, and W. I. Lee, 'Analysis of resin transfer moulding process with controlled multiple gates resin injection', Composites Part A: Applied Science and Manufacturing, vol. 31, no. 5, pp. 407–422, May 2000, doi: 10.1016/S1359-835X(99)00086-X

[27] J. M. Lawrence, P. Fried, and S. G. Advani, 'Automated manufacturing environment to address bulk permeability variations and race tracking in resin transfer molding by redirecting flow with auxiliary gates', Composites Part A: Applied Science and Manufacturing, vol. 36, no. 8, pp. 1128–1141, Aug. 2005, doi: 10.1016/j.compositesa.2005.01.024

[28] B. X. Chai et al., 'Simulation-based optimisation for injection configuration design of liquid composite moulding processes: A review', Composites Part A: Applied Science and Manufacturing, vol. 149, p. 106540, Oct. 2021, doi: 10.1016/j.compositesa.2021.106540

[29] S. Laurenzi, A. Casini, and D. Pocci, 'Design and fabrication of a helicopter unitized structure using resin transfer moulding', Composites Part A: Applied Science and Manufacturing, vol. 67, pp. 221–232, Dec. 2014, doi: 10.1016/j.compositesa.2014.09.007

Two Generalizations of Skew-Symmetric Sequences With Odd Lengths

Borislav Bedzhev
Faculty "Atillery, AD and CIS"
"Vasil Levski" National Military University
Veliko Tarnovo, Bulgaria
bedzhev@abv.bg

Dilyan Dimitrov
Faculty "Atillery, AD and CIS"
"Vasil Levski" National Military University
Veliko Tarnovo, Bulgaria
dilyaniv@abv.bg

Abstract. **The signals, exploited by the radar sensor networks and remote control systems, have to provide simultaneously high range resolution and ability to work stable in a hostile radio electronic environment. An effective approach for satisfying of these requirements is the frequent change of many different signals, which autocorrelation functions have small sidelobes. Accounting this situation in the paper the generalizations of the skew-symmetric sequences with odd lengths, which are phase manipulated signals, possessing high autocorrelation merit factor, are explored. As a result, two methods for synthesis of infinite families of phase manipulated signals with good autocorrelation properties are substantiated.**

Keywords: skew-symmetric sequences, synthesis of signals with small autocorrelation.

I. INTRODUCTION

Today the so-called Internet of things (IoT) is one of the basic system of technologies, providing the rapid progress of the Fourth Industrial Revolution ("4IR", or "Industry 4.0"), which will improve radically the life-style of all people around the world [1]. The advancement of the IoT but essentially depend on the ability to provide the electromagnetic compatibility of a great amount of specialized small radar sensor networks and remote control systems, operating simultaneously, as well as their stable performance in a hostile radio electronic environment [2].

As known, an effective approach for satisfying of these requirements is the frequent change of many different signals, which autocorrelation functions have small sidelobes [3], [4]. Accounting this situation in the paper the generalizations of the so-called skew-symmetric sequences with odd lengths, which are phase manipulated (PM) signals, possessing high autocorrelation merit factor, are explored. As a result, two methods for synthesis of infinite families of PM signals with good autocorrelation properties are substantiated.

The paper is organized as follows. First, the basics of the signal processing in the receivers of the communication systems are recalled. After that the possibility the negative effects, caused by the multipath spread of the electromagnetic waves, to be minimized by the application of PM signals with good autocorrelation properties are investigated. On this base two methods for synthesis of infinite families of PM signals, which are skew-symmetric sequences with odd lengths, possessing high autocorrelation merit factor, are substantiated. At the end, the applications of the proposed PM signals are analysed.

II. METHODOLOGY OF THE STUDY

Most often, the digital signal processing in the receivers of radio-communication systems (RCSs) can be described by the following polynomial model [5]:

$$\left[\sum_{k=0}^{N-1} \mu(k)x^i\right]\left[\sum_{k=0}^{N-1} \mu^*(k)x^{-i}\right] = \\ = \sum_{r=-N+1}^{N-1} P_{\mu\mu}(r)x^r \ . \tag{1}$$

In (1) the following notations are used. First, the digital signal:

$$\{\mu(k)\}_{k=0}^{N-1} = \{\mu(0), \mu(1), \dots, \mu(N-1)\ \}, \tag{2}$$

consists of the samples of the digitalized received signal. As the sent signal passes a large distance between the transmitter and the receiver the received signal is a diminished copy of the signal, emitted by the transmitter [3], [4], [5]. Due to this reason, the samples (2) are complex numbers, presenting the complex envelopes of the consecutive elementary phase symbols (or chips) with duration τ_{ch}, forming the sent signal.

Analogously, the sequences of complex numbers:

$$\{\mu^*(k)\}_{k=0}^{N-1} = \{\mu^*(0), \mu^*(1), \dots, \mu^*(N-1)\ \}, \tag{3}$$

$$\{P_{\mu\mu}(r)\}_{r=-N+1}^{N-1} = \{P_{\mu\mu}(-N+1), \dots, \\ \dots, P_{\mu\mu}(-1), P_{\mu\mu}(0), \dots P_{\mu\mu}(N-1)\}, \tag{4}$$

are the transfer function's (TF) samples of the finite impulse response (FIR) matched filter (FIRMF), used in the receiver, and the autocorrelation function (ACF) of the digital signal (2) respectively.

In (3) the symbol "*" stands for "complex conjugation".

Second,

$$F_\mu(x) = \sum_{k=0}^{N-1} \mu(k)x^i, \tag{5}$$

is the so-called generating function or Hall polynomial, associated with the digital signal (2).

It should be pointed out that the powers of the variable x^{-k}, x^k denote "overtaking or delay at k time-clocks with duration τ_{ch} during the signal processing" respectively.

Analogously, the generating functions (Hall polynomials) of the digital signals (3) and (4) are

$$F_\mu^*(x^{-1}) = \sum_{k=0}^{N-1} \mu^*(k)x^{-i}, \tag{6}$$

$$F_{P_{\mu\mu}}(x) = \sum_{r=-N+1}^{N-1} P_{\mu\mu}(r)x^r. \tag{7}$$

From (1), (2), (3), (4), (5), (6) and (7) it is not hard to obtain the next well known formula for direct calculation of the ACF's samples:

$$P_{\mu\mu}(r) = \\ = \begin{cases} \sum_{k=0}^{N-1-\lceil r \rceil} \mu(k+\lceil r \rceil)\mu^*(k), & -(N-1) \le r \le 0, \\ \sum_{k=0}^{N-1-r} \mu(k)\mu^*(k+r), & 0 \le r \le N-1. \end{cases} \tag{8}$$

Now the following two facts should be taken in consideration.

First, in order to diminish the negative effects, caused by the multipath spread of the electromagnetic waves, the ACF of the sent signal have to resemble a delta pulse (i.e. to have thumbtack form) [3], [4], [5].

Second, the simplest type of phase manipulation, which is the most preferable for applications in the small (miniature) radio-electronic devices, is the binary phase shift keying (BPSK). When it is exploited the samples of the digital signal (2) can be considered as 1 and -1.

From the above facts it can be concluded that the ideal ACF of binary signals with crest factor equal to one has the form:

$$P_{\mu\mu}(r) = \begin{cases} N, & N - \lceil r \rceil = N, \\ \pm 1, & N - \lceil r \rceil = odd, \\ 0, & N - \lceil r \rceil = even. \end{cases} \tag{9}$$

The binary signals with crest factor equal to one, which ACFs satisfy (9), are called Barker codes or Barker sequences after their inventor Ronald Hugh Barker.

Accounting the ideal autocorrelation properties of the Barker codes (signals), they will be analyzed in more detail in the sequel in this chapter of the paper.

More specifically, ever the generating function (Hall polynomial), associated with the digital signal (2), can be presented as a sum of two polynomials, comprising only the even and odd powers of the variable x respectively:

$$F_\mu(x) = F_{e\mu}(x) + F_{o\mu}(x), \\ F_{e\mu}(x) = \sum_{k=0}^{L} \mu(2k)x^{2k}, \\ F_{o\mu}(x) = \sum_{k=1}^{L} \mu(2k-1)x^{2k-1}. \tag{10}$$

Obviously, analogous separation of the generating function (Hall polynomial) (6), associated with the TF of the FIRMF, exploited in the receiver, is possible:

$$F_\mu^*(x^{-1}) = F_{e\mu}^*(x^{-1}) + F_{o\mu}^*(x^{-1}), \\ F_{e\mu}^*(x^{-1}) = \sum_{k=0}^{L} \mu^*(2k)x^{-2k}, \\ F_{o\mu}^*(x^{-1}) = \sum_{k=1}^{L} \mu^*(2k-1)x^{-2k+1}. \tag{11}$$

After taking into consideration (10) and (11) in (1), the result is:

$$\sum_{r=-N+1}^{N-1} P_{\mu\mu}(r)x^r = \\ = [F_{e\mu}(x) + F_{o\mu}(x)][F_{e\mu}^*(x^{-1}) + F_{o\mu}^*(x^{-1})] = \\ = F_{e\mu}(x)F_{e\mu}^*(x^{-1}) + F_{e\mu}(x)F_{o\mu}^*(x^{-1}) + \\ + F_{o\mu}(x)F_{e\mu}^*(x^{-1}) + F_{o\mu}(x)F_{o\mu}^*(x^{-1}). \tag{12}$$

Here it should be especially noted that during the analysis of Barker signals with odd lengths

$$N = 2L + 1, \tag{13}$$

Marcel Golay has observed [6], [7], [8], [9], that they satisfy the condition:

$$\mu(L+k) = (-1)^k\mu(L-k), \quad k = 1, 2, \dots, L. \tag{14}$$

In order to reach the aim of this paper, the condition (14) will be generalized as follows:

$$\mu(L+k) = (-1)^k\mu^*(L-k), \quad k = 0, 1, 2, \dots, L. \tag{15}$$

Due to the alternate symmetry of (14), the PM signals, which satisfy the condition (14), are called skew-symmetric sequences (signals). Analogously, in this paper when the condition (15) takes place the respective PM signal will be called generalized skew-symmetric (GSS) sequence (signal).

Here it should be especially noted that M. Golay has pointed out the skew-symmetric sequences as signals with good autocorrelation properties as for them the ratio of the mean peak energy to the aggregated energy of all the sidelobes:

$$MF = \frac{N^2}{2\sum_{k=1}^{N-1} \mu(k)\mu^*(k)} \tag{16}$$

is great [6], [10]. The ratio (16) is called the Merit Factor (MF) and together with the so-called Peak-to-Sidelobe ratio (PSR)

$$PSR = \frac{N}{\max_k \{|\mu(k)|\}_{k=1}^{N-1}} \tag{17}$$

are the two basic parameters for estimating the autocorrelation properties of every concrete PM signal. More specifically, the bigger are the MF and PSR, the better is the resolution of signals, passed different ways among the transmitter and the receiver.

From all the above stated, the following conclusions ensue.

First, the condition (15) simplifies to the condition (14), when in the communication devices only BPSK is used.

Second, if a PM signal satisfies the condition (15), then its ACF has non-zero sidelobes only when time-shifts r are even integers. Indeed, when $N \equiv 1 mod 4$, then $L \equiv 0 mod 2$. As a result $F_{e\mu}(x)$ contains odd (namely $(L + 1)$) number of monomials and its reciprocal polynomial $\tilde{F}_{e\mu}(x)$ (i.e. the polynomial, which coefficients are arranged in the mirror reversal order $\{\mu(L - 2k)\}_{k=0}^{L}$) has the form

$$\tilde{F}_{e\mu}(x) = \sum_{k=0}^{L} \mu(L - 2k)x^{2k} = -F_{e\mu}^*(x). \quad (18)$$

Besides, $F_{o\mu}(x)$ contains even (namely (L)) number of monomials and its reciprocal polynomial $\tilde{F}_{o\mu}(x)$ is

$$\tilde{F}_{o\mu}(x) = \sum_{k=0}^{L} \mu(L - 2k)x^{2k} = F_{o\mu}^*(x). \quad (19)$$

When $N \equiv 3 mod 4$, then $L \equiv 1 mod 2$ and, at the one hand, $F_{e\mu}(x)$ contains even number (namely $(L + 1)$) of monomials and its reciprocal polynomial $\tilde{F}_{e\mu}(x)$ has the form

$$\tilde{F}_{e\mu}(x) = \sum_{k=0}^{L} \mu(L - 2k)x^{2k} = F_{e\mu}^*(x). \quad (20)$$

At the other hand, $F_{o\mu}(x)$ contains odd number (namely (L)) of monomials and its reciprocal polynomial $\tilde{F}_{o\mu}(x)$ has the form

$$\tilde{F}_{o\mu}(x) = \sum_{k=0}^{L} \mu(L - 2k)x^{2k} = -F_{o\mu}^*(x). \quad (21)$$

From (18) and (19) it ensues, that in the cases, when $N \equiv 1 mod 4$, the second polynomial product in (12) can be transformed as follows:

$$F_{e\mu}(x)F_{o\mu}^*(x^{-1}) = \tilde{F}_{e\mu}(x^{-1})\tilde{F}_{o\mu}^*(x) =$$
$$= \left[-F_{e\mu}(x^{-1})\right]^* F_{o\mu} = -F_{o\mu}(x)F_{e\mu}^*(x^{-1}). \quad (22)$$

Analogously, from (20) and (21) it ensues, that in the cases, when $N \equiv 3 mod 4$, the second polynomial product in (12) can be transformed as follows:

$$F_{e\mu}(x)F_{o\mu}^*(x^{-1}) = \tilde{F}_{e\mu}(x^{-1})\tilde{F}_{o\mu}^*(x) =$$
$$F_{e\mu}^*(x^{-1})\left[-F_{o\mu}^*(x)\right]^* = -F_{o\mu}(x)F_{e\mu}^*(x^{-1}). \quad (23)$$

After accounting (22) and (23) in (12), the result is:

$$\sum_{r=-N+1}^{N-1} P_{\mu\mu}(r)x^r =$$
$$= \left[F_{e\mu}(x) + F_{o\mu}(x)\right]\left[F_{e\mu}^*(x^{-1}) + F_{o\mu}^*(x^{-1})\right] = \quad (24)$$
$$= F_{e\mu}(x)F_{e\mu}^*(x^{-1}) + F_{o\mu}(x)F_{o\mu}^*(x^{-1}),$$

which has to be proven.

The above analysis demonstrates that the GSS signals could have ACFs, similar to the ideal ACF of binary signals (9), if the ACF sidelobes for even time-shifts are as small as possible. This problem will be studied in more detail in the next chapter of the paper.

III.   RESULTS AND DISCUSSION

As mentioned above, a very effective approach for providing electromagnetic compatibility of all working simultaneously electronic devices as well as their resistance in a hostile radio electronic environment is the pseudo random change the emitted signals, using all volume of a large signal family. Accounting this fact in sequel the method, substantiated in the previous chapter of the paper, will be elaborated. This will allow two infinite families of GSS signals with odd lengths and nearly ideal ACF to be synthesized.

Obviously, the law of phase modulation (15), exploited for PM signal generation (or simply the coding rule (15)), is a generalization of skew-symmetric sequences with odd lengths, as the classic coding rule (14) is its particular case.

The reasonability of including of such GSS signals in the signal family, exploited by the communication devices, will be demonstrated by the means of the GSS signal with length $N = 15$:

$$\{\mu(k)\}_{k=0}^{14} = \{-1, -1, -1, -i, -i, -1, i, \quad (25)$$
$$i, -i, 1, i, -i, 1, 1, -1\}, \quad i = \sqrt{-1}.$$

The ACF of the GSS signal (25) is presented on Fig. 1. As seen, the ACF of the GSS signal (25) has the form (9).
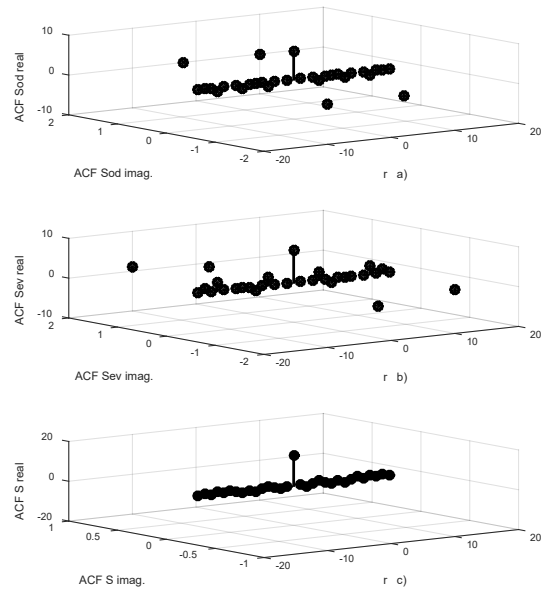
Fig. 1.   ACFs of the GSS signal (25) (c) and its odd (a) and even (b) components.

In fact, this signal (accounting the possible equivalence transformations of PM signals) is the longest signal in the

class of so-called complex Barker signals, which chips belong to the signal alphabet $\{-1, 1, i, -i\}$.

Another generalization of skew-symmetric sequences with odd lengths can be obtained, exploiting the following coding rule

$$\begin{aligned} \mu(L) &= 0 \ or \ \pm i, \\ \mu(L+k) &= (-1)^{k+1}\mu^*(L-k), \quad k = 1, 2, \ldots, L, \end{aligned} \quad (26)$$

Here it should be pointed out that the coding rule (26) changes the roles of the even and odd parts of the digital signal (2). Namely, in contrast with the coding rule (15), when $N \equiv 1 \bmod 4$, $L \equiv 0 \bmod 2$, the reciprocal polynomials $\tilde{F}_{e\mu}(x)$ and $\tilde{F}_{o\mu}(x)$ have the following forms:

$$\tilde{F}_{e\mu}(x) = \sum_{k=0}^{L} \mu(L-2k)x^{2k} = F_{e\mu}^*(x), \quad (27)$$

$$\tilde{F}_{o\mu}(x) = \sum_{k=0}^{L} \mu(L-2k)x^{2k} = -F_{o\mu}^*(x). \quad (28)$$

Analogously, when $N \equiv 3 \bmod 4$, $L \equiv 1 \bmod 2$, the reciprocal polynomials $\tilde{F}_{e\mu}(x)$ and $\tilde{F}_{o\mu}(x)$ have the following forms:

$$\tilde{F}_{e\mu}(x) = \sum_{k=0}^{L} \mu(L-2k)x^{2k} = -F_{e\mu}^*(x), \quad (29)$$

$$\tilde{F}_{o\mu}(x) = \sum_{k=0}^{L} \mu(L-2k)x^{2k} = F_{o\mu}^*(x). \quad (30)$$

The reasonability of including of GSS signals, synthesized by the coding rule (26) with $\mu(L) = 0$, in the signal family, exploited by the communication devices, will be demonstrated by the means of the GSS signal with length $N = 33$:

$$\begin{aligned} \{\mu(k)\}_{k=0}^{32} = \{&1,1,-1,-1,-1,-1,1,1,1,1,1,1, \\ &-1,1,1,1,0,1,-1,1,1,1,-1,1,-1,1,-1,-1, \quad (31) \\ &1,-1,1,1,-1\}. \end{aligned}$$
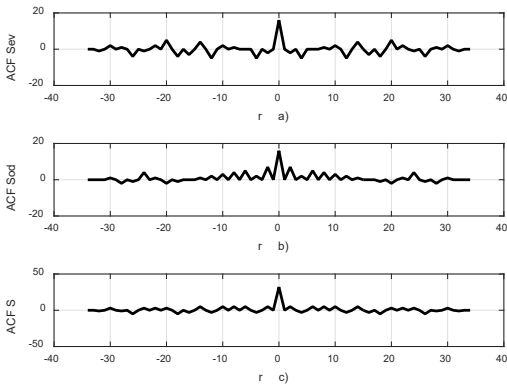
Fig. 2.   ACFs of the GSS signal (31) (c) and its odd (a) and even (b) components.

Analogously, the reasonability of including of GSS signals, synthesized by the coding rule (24) with $\mu(L) = i$, in the signal family, exploited by the communication devices, will be demonstrated by the means of the GSS signal with length $N = 33$:

$$\begin{aligned} \{\mu(k)\}_{k=0}^{32} = \{&1,-1,1,-1,1,1,-1,-1,1,-1, \\ &1,-1,-1,1,1,1,i,1,-1,1,1,-1,-1,-1, \quad (32) \\ &-1,-1,1,1,-1,-1,-1,-1,-1\}. \end{aligned}$$
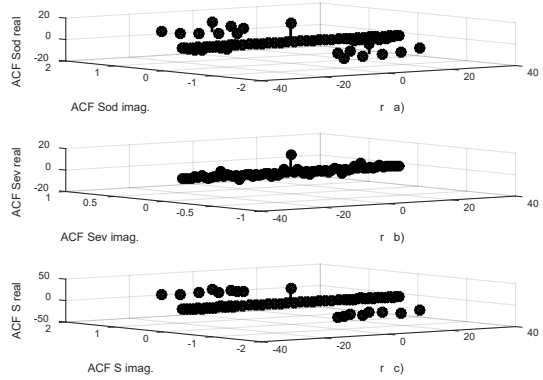
Fig. 3.   ACFs of the GSS signal (32) (c) and its odd (a) and even (b) components.

The ACFs of GSS signals, presented on Fig. 1, Fig. 2 and Fig. 3 demonstrate that GSS signals possess high MFs and PSRs, which make them suitable for application in the radar sensor networks and remote control systems.

The practical importance the study, presented in the paper, ensues from the following circumstances.

First, at the one hand, the GSS signals, presented above, possess complex inner structure and can have great lengths, which allow their energy to be spread in very large spectral bands. As a result, the GSS signals can have both very small spectral density and energy, sufficient for normal operation of the radar sensor networks and remote control systems. At the other hand, according to the analyses in [12], [13] the exploitation of such signals provides both electromagnetic compatibility of a great amount of users, operating simultaneously, and high resistance in a hostile radio electronic environment. Moreover, the fact that the GSS signals, developed in the paper, form a large signal family allows the pseudo-random choosing of GSS signals from it to be managed by artificial intelligence and adaptive self-learning computer systems.

Second, the family of GSS signals can be extra extended in several ways. For example, according to the exploration, presented in our previous paper [11], it is possible GSS signals together with complementary pairs (CPs) of binary signals to be used in the recursive procedures for synthesis of quasi CPs (QCPs) [4], [5], which aggregated ACFs have very small relative quantity of non-zero sidelobes. Another way for extension of the GSS signal family is the application of transformations, preserving the autocorrelation properties of the PM signals (i.e. using all negative, reflective and alternate derivatives of the PM signals in the initial GSS signal family).

Third, it should be noted that according to the analysis in [14], every GSS signal can be implemented practically by the means of a single frequency channel, divided into two subchannels by quadrature phase manipulation (QPSK) or by two different types of polarization.

IV. CONCLUSIONS

In the paper two methods for synthesis of infinite families of PM signals with high MFs and PSRs are substantiated. The usage of the methods allows the electromagnetic compatibility of all working simultaneously electronic devices as well as their resistance in a hostile radio electronic environment to be improved. The study, conducted in the paper, could be useful during the modernization of the extant or development of new radar sensor networks and remote control systems.

ACKNOWLEDGMENTS

REFERENCES

[1] M. Iliev and M. Bedzheva, "An approach for application of UAVs for observation of processes in agriculture," Proceedings of 7th International Conference on Energy Efficiency and Agricultural Engineering (EE&AE 2020), 12-14 November 2020, Ruse, Bulgaria.

[2] L. Nikolov and Kr. Slavyanov, "On the contemporary cybersecurity threats," Proceedings of the I st Int. conference CONFSEC 2017, 11-14.12.2017, Borovets, Bulgaria, ISSN Print: 2603-2945, ISSN Online: 2603-2953, pp. 142-144.

[3] T. Ignatova, M. Nedelchev, and M. Bedzheva, "Contemporary approaches for effective radio spectrum utilization," Proceedings of University of Ruse - 2022, volume 61, book 3.2., pp. 161-166 (in Bulgarian), ISSN 1311-3321 (print), ISSN 2535-1028 (CD-ROM), ISSN 2603-4123 (on-line).

[4] Kr. Slavyanov and L. Nikolov, "An algorithm for ISAR image classification procedure," International scientific journal "Industry 4.0," Vol. 2 (2017), Issue 2, web ISSN 2534-997X, print ISSN 2543-8582, pp. 76-79.

[5] M. Iliev, N. Nikolov, and M. Bedzheva, "A heuristic approach for synthesis of quasi complementary signals," Proceedings of University of Ruse - 2022, volume 61, book 3.2., pp. 167-173 (in Bulgarian), ISSN 1311-3321 (print), ISSN 2535-1028 (CD-ROM), ISSN 2603-4123 (on-line).

[6] M. Golay, "A class of finite binary sequences with alternate auto-correlation values equal to zero (corresp.)," IEEE Transactions on Information Theory, Vol. 18, Issue 3, pp. 449-450, 1972.

[7] M. J. Golay and D. B. Harris, "A new search for skew-symmetric binary sequences with optimal merit factors," IEEE Transactions on Information Theory, Vol. 36, Issue 5, pp. 1163–1166, 1990.

[8] M. Golay, "Hybrid low autocorrelation sequences (corresp.)," IEEE Transactions on Information Theory, Vol. 21, Issue 4, pp. 460–462, 1975.

[9] M. Dimitrov, "On the skew-symmetric binary sequences and the merit factor problem," arXiv preprint arXiv:2106.03377, 2021.

[10] M. Golay, "Sieves for low autocorrelation binary sequences," IEEE Transactions on information theory, Vol. 23, Issue 1, pp. 43–51, 1977.

[11] B. Bedzhev and D. Dimitrov, "Generalizations of the recursive methods for synthesis of Complementary pairs of phase manipulated signals," Proceedings of the 2023 IEEE International Conference on Information Technologies (InfoTech-2023), 20-21 September 2023, Bulgaria.

[12] R.C. Dixon, Spread Spectrum Systems. John Wiley & Sons, 1976.

[13] B. Bedzhev and D. Dimitrov, "A model of signal processing in software defined radio communication systems," Proceedings of the 2023 IEEE International Conference on Information Technologies (InfoTech-2023), 20-21 September 2023, Bulgaria.

[14] M. Iliev, B. Bedzhev, M. Bedzheva, and K. Kanchev, "Approaches for implementation of Golay's Complementary signals and Welti's Quaternary signals in radio-communication systems," Proceedings of the 2021 IEEE International Conference on Information Technologies (InfoTech-2021), 16-17 September 2021, St. St. Constantine and Elena, Bulgaria.

Mismatched Filters for Processing of Phase Manipulated Signals with Three-Valued Autocorrelation

Borislav Bedzhev
Faculty "Atillery, AD and CIS"
"Vasil Levski" National Military University
Veliko Tarnovo, Bulgaria
bedzhev@abv.bg

Dilyan Dimitrov
Faculty "Atillery, AD and CIS"
"Vasil Levski" National Military University
Veliko Tarnovo, Bulgaria
dilyaniv@abv.bg

***Abstract*. The phase manipulated signals, which autocorrelation functions resemble delta pulses, play a very important role for the radars, radio navigation networks and remote control systems as they provide the highest possible resolution of the received signals. Unfortunately, today known classes of such signals have small volumes, which often cannot ensure the necessary electromagnetic compatibility as well as high resistance in a hostile radio electronic environment. Accounting this situation in the paper a method for synthesis of mismatched filters, which effectively suppress the sidelobes of three-valued autocorrelations of phase manipulated signals, is substantiated.**

Keywords: signal with three-valued autocorrelation, synthesis of mismatched filter.

I. Introduction

Today a tremendous amount of autonomous devices is used practically in all spheres of industry, science, medicine, transportation, education and so on. As a result, the problems of ensuring: precise positioning, secure remote control and guidance, as well as electromagnetic compatibility of these devices, became a great importance [1], [2].

As known, a universal approach for solving of the above listed problems, is the exploitation of phase manipulated (PM) signals, which autocorrelation functions (ACFs) resemble delta pulses, as they provide the highest possible resolution of the received signals [3], [4]. Unfortunately, today known classes of such signals have small volumes, which often cannot ensure the necessary electromagnetic compatibility as well as high resistance in a hostile radio electronic environment. An effective approach for solving of this problem is the processing of received signals with mismatched filters (MMFs), which substitute the signals' ACFs with cross-correlation functions (CCFs), resembling delta pulses.

Accounting this situation in the paper a method for synthesis of MMFs, which process the PM signals with nearly uniform autocorrelation with small losses in the signal-to-noise ratio, is substantiated.

The paper is organized as follows. First, the basics of the signal processing in the receivers of the communication systems are recalled. After that the possibility the negative effects, caused by the multipath spread of the electromagnetic waves, to be minimized by simple transformations of PM signals' ACFs is substantiated. On this base infinite classes of PM signals, which can be processed effectively by the developed MMFs, are systematized. At the end, the applications of the proposed MMFs are analysed.

II. Methodology of the Study

Methodology of the study will be explained by the means of the so-called Barker codes (sequences, signals). Namely, the Barker signals can be presented mathematically by the following number sequence with length N:

$$\{\mu(k)\}_{k=0}^{N-1} = \{\mu(0), \mu(1), \dots, \mu(N-1)\}. \tag{1}$$

The samples in the right side of (1) are integers $+1$ or -1, presenting the envelopes of the consecutive elementary phase pulses (or chips) with duration τ_{ch}, forming the Barker signal. Besides, N is the quantity of the chips. Due to this reason, the generation and the processing of the Barker signals can be realized by simple, reliable and cost-effective radio-electronic components. As a result, the Barker signals are widely used for positioning, sensing and remote control of small (miniature) autonomous devices.

Here it should be recalled that the most often, the receivers in the communication systems are built as matched filters (MFs). They are digital filters with finite impulse response (FIR), which transfer functions (TFs) are a conjugate and mirror-reversed copy of the sent (expected) signal:

$$\{\mu^*(k)\}_{k=0}^{N-1} = \{\mu^*(0), \mu^*(1), \ldots, \mu^*(N-1)\}. \quad (2)$$

In (2) the symbol "*" stands for "complex conjugation". In cases of Barker signals, the complex conjugation does not change the samples in the both sides of (2).

As known, the result of signal processing by the respective MF is the ACF of the sent (received) signal:

$$P_{\mu\mu}(r) =$$
$$= \begin{cases} \sum_{k=0}^{N-1-\lceil r \rceil} \mu(k + \lceil r \rceil)\mu^*(k), & -(N-1) \le r \le 0, \\ \sum_{k=0}^{N-1-r} \mu(k)\mu^*(k+r), & 0 \le r \le N-1. \end{cases} \quad (3)$$

In (3) $P_{\mu\mu}(r)$ is the r-th sample of the ACF of the digital signal (1).

The wide exploitation of MFs can be explained by the fact that this type of signal processing maximizes the signal-to-noise ratio (SNR) in the presence of the so-called additive white Gaussian noise (AWGN), which meets most often in the practice.

In order to minimize the negative effects, caused by the multipath spread of the electromagnetic waves, the ACF of the sent signal have to resemble a delta pulse (i.e. to have a thumbtack form) [5], [6], [7]:

$$P_{\mu\mu}(r) = \begin{cases} E_s, & r = 0, \\ 0, & r \ne 0. \end{cases} \quad (4)$$

In (4) E_s is the main peak (lobe) of the signal ACF:

$$E_s = \sum_{k=0}^{N-1} |\mu(k)|^2 = \sum_{k=0}^{N-1} \mu(k)\mu^*(k), \quad (5)$$

which is the result of the coherent accumulation of the energies of all the chips (elementary phase pulses), forming the signal (1).

Here it should be noted that the Barker signals' ACFs are very similar to delta pulses as the lobes (samples) of their ACFs satisfy the conditions:

$$P_{\mu\mu}(r) = \begin{cases} N, & r = 0, \\ 0, & r \equiv 1 \bmod 2, \\ = \begin{cases} -1, & N \equiv 3 \bmod 4, r \equiv 0 \bmod 2, \\ 1, & N \equiv 1 \bmod 4, r \equiv 0 \bmod 2. \end{cases} \end{cases} \quad (6)$$

The conditions (6) give reason the Barker signals' ACFs to be classified as three-valued autocorrelations as ACF lobes can take only three different values - $\{N, 0, -1\}$ or $\{N, 0, 1\}$.

Despite of the very small level of the sidelobes of the Barker signals' ACFs too often it is possible an ACF sidelobe of a powerful signal to mask the ACF main lobe of a weak signal, which could be much more important. It is accepted such situations to be called self-interferences

(SIs). Due to this reason the methods for synthesis of MMFs, whish suppress (diminish) the sidelobes of the Barker signals' ACFs, have been intensively researched during the past fifty years. In fact, in Internet can be found many research articles as well as patents which present approaches for synthesis of such MMFs, but their inner structure is very complex [8], [9]. Due to this reason, the probability of their application for positioning, sensing and remote control in the sphere of miniature autonomous devices is small.

Accounting this situation, in the rest part of this section the possibility the ACF sidelobes of Barker signals to be suppressed effectively by simple (from implementation point of view) MMFs will be substantiated. More specifically, conditions (6) show that the Barker signals' ACFs have a very regular form, as their sidelobes are sequences, consisting of $N-1$ repeating patterns $\{1,0\}$ or $\{-1,0\}$. As a result, the non-zero sidelobes of each concrete ACF can be eliminated by subtraction of the ACF and its copy, shifted (delayed) at $r = 2$ time-clocks with duration τ_{ch}. This fact is explained on Fig. 1 by the means of the Barker signal with length $N = 11$:

$$\{\mu(k)\}_{k=0}^{10} = \{1,1,1,-1,-1,-1,1,-1,-1,1,-1\}. \quad (7)$$

Here it should be pointed out the following facts.

First, the above processing of the Barker signals' ACFs can be easily realized by a digital filter with FIR, which TF is:

$$\{\xi(k)\}_{k=0}^{2} = \{-1,0,1\}. \quad (8)$$

Second, the positive effect of usage of above MMF is the eliminating of all the ACF sidelobes with exception of the first and the last sidelobes. The negative effect is the significant increasing of the sidelobe at the position $r = 2$.

Third, if the processing of the Barker signals' ACFs is performed by two consecutively connected MMF with TFs (8), the peak-to-sidelobe ratio (PSR) increases two times. This approach is explained on Fig. 2, where Difference1 (D1) corresponds to Fig. 1c.
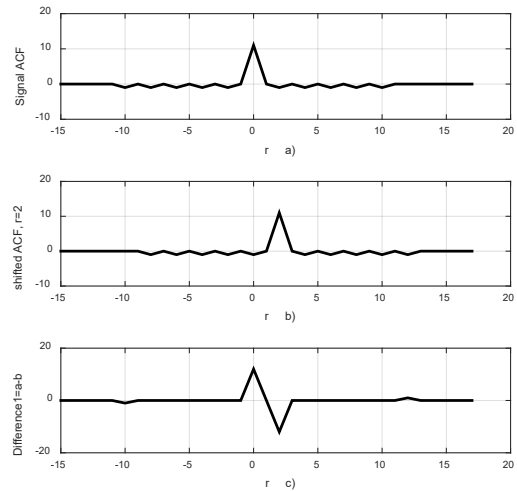
Fig. 1. ACF of the Barker signal (7) (a), its copy, shifted at $r = 2$ time-clocks (b) and the result of their subtraction (Difference1) (c).
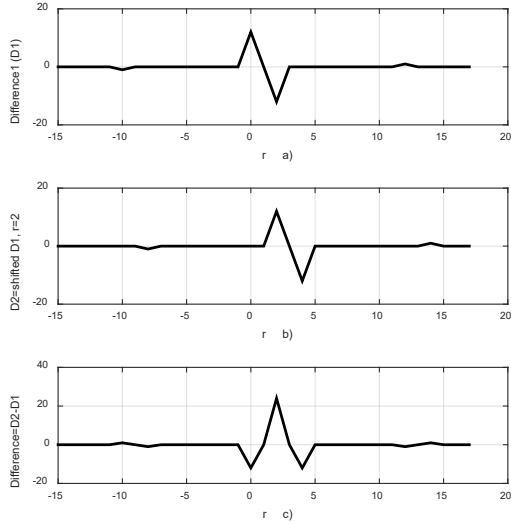
Fig. 2.   The result of processing the ACF of the Barker signal (7) by two consecutively connected MMFs with TF (8).

Obviously, the last approach for processing the Barker signals' ACFs can be realized by one digital filter, which TF is the result of the convolution of TF (8) by itself:

$$\{\xi(k)\}_{k=0}^{4} = \{-1,0,2,0,-1 \}. \tag{9}$$

From all the above stated, the following conclusions ensue.

First, the MMFs with TFs (8) and (9) can be applied for processing of every three-valued ACF, which sidelobes are sequences, consisting of $N-1$ repeating patterns $\{a, b\}$, where a and b are arbitrary numbers.

Second, the only shortcoming (the significant increasing of the sidelobe at the position $r = 2$)) of the performance of the MMFs with TFs (8) and (9) could be easily avoided in communication systems, using many receivers at different positions (i.e. communication systems with spatial diversity). Due to this reason, the main obstacle for the practical implementation of the above MMFs is the small volume of the Barker signals' class. This problem will be studied in more detail in the next chapter of the paper.

III.   RESULTS AND DISCUSSION

As known, a very effective approach for providing electromagnetic compatibility of all working simultaneously electronic devices as well as their resistance in a hostile radio electronic environment is the pseudo random change the emitted signals, using all volume of a large signal family. Accounting this fact as well as the small volume of the Barker signals' class, in sequel it will be substantiated the possibility the ACFs of two other classes of binary signals to be processed by simple MMFs, applying the method, developed in the previous chapter of the paper.

The first candidate in this way is the very large class of binary signals, which ACFs consist mostly of repeating patterns $\{1,0,-3,0\}$ or $\{-1,0,3,0\}$. In the sequel these PM signals will be called quasi Barker (QB) signals.

Obviously, the TFs of MMFs for processing the QB signals' ACFs, should be:

$$\{\xi(k)\}_{k=0}^{4} = \{-1,0,0,0,1 \}, \tag{10}$$

$$\{\xi(k)\}_{k=0}^{8} = \{-1,0,0,0,2,0,0,0,-1 \}. \tag{11}$$

The reasonability of including the QB signals in the signal family, exploited by the communication devices, will be demonstrated by the means of the QB signal with length $N = 43$:

$$\begin{aligned}\{\mu(k)\}_{k=0}^{42} = \{&-1,-1,1,-1,-1,1,1,-1,1,1,1,1\\ &-1,1,-1,-1,-1,-1,-1,1,-1,1,1,-1,-1,\\ &-1,-1,1,-1,1,-1,-1,-1-1,1,-1,-1,\\ &-1,1,1,-1,-1,-1,1\}.\end{aligned} \tag{12}$$

The result of the processing the ACF of the QB signal (12) by the MMF with TF (10) is presented on Fig. 3.

Another promising approach for increasing the volume of the signal family, exploited by the communication devices, is the usage of the so-called complementary pairs (CPs). More specifically, according to the originating work [5] of M. Golay, every CP consists of two binary PM signals $\{\mu(i)\}_{i=0}^{N-1}$ and $\{\eta(i)\}_{i=0}^{N-1}$, chosen so that the sum of their ACFs to resemble a delta – pulse:

$$P_{\mu\mu}(r) + P_{\eta\eta}(r) = \begin{cases} 2N, r = 0, \\ 0, r \neq 0. \end{cases} \tag{13}$$
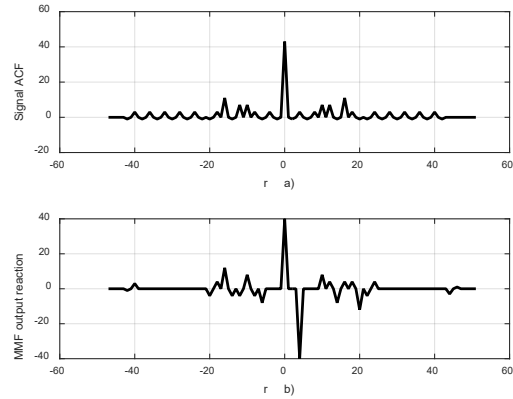
Fig. 3.   The result of processing the ACF of the QB signal (12) by the MMF with TF (10).

Here it should be especially noted the following facts.

First, according to the analysis in [10], every CP can be implemented practically by the means of a single frequency channel, divided into two subchannels by quadrature phase manipulation (QPSK) or by two different types of polarization.

Second, M. Golay and R. Turin have developed recursive methods, which allow CPs of binary PM signals with infinite lengths to be synthesized, using any two basic (kernel, seed) CPs with lengths $N = 2, 10, 20, 26$ [5], [6], [7].

Third, according to the exploration, presented in our previous paper [11], it is possible once at an arbitrary step

of the recursive procedure Barker or QB signal to be used. In such situations the results are quasi CPs (QCPs) [11], [12], which aggregated ACFs have very small relative quantity of non-zero sidelobes and they can be processed by simple (from the technical point of view) MMFs, applying the method, developed in the previous chapter of the paper.

The last fact will be clarified by the means of the Barker signal (7), which will be used as a QCP

$$\{\mu_1(k)\}_{k=0}^{10} = \{\eta_1(k)\}_{k=0}^{10} = = \{1,1,1,-1,-1,-1,1,-1,-1,1,-1\},$$ (14)

and the simplest non-trivial CP

$$\{\mu_2(k)\}_{k=0}^1 = \{1,1\}, \{\eta_2(k)\}_{k=0}^1 = \{1,-1\}.$$ (15)

On the base of the QCP (14) and CP (15) two different QCPs with length $N = 22$ can be obtained by the following methods:

$$\{\mu(k)\}_{k=0}^{21} = = \{\mu_2(1).\mu_1(k)\}_{k=0}^{10} \odot \{\eta_2(1).\eta_1(k)\}_{k=0}^{10}, \{\eta(k)\}_{k=0}^{21} = \{\mu_2(2).\mu_1(k)\}_{k=0}^{10} \odot \{\eta_2(2).\eta_1(k)\}_{k=0}^{10},$$ (16)

$$\{\mu(k)\}_{k=0}^{21} = = \{\mu_2(1).\mu_1(k)\}_{k=0}^{10} \otimes \{\eta_2(1).\eta_1(k)\}_{k=0}^{10}, \{\eta(k)\}_{k=0}^{21} = \{\mu_2(2).\mu_1(k)\}_{k=0}^{10} \otimes \{\eta_2(2).\eta_1(k)\}_{k=0}^{10}.$$ (17)

In (16) and (17) the symbols "$\odot$" and "$\otimes$" denote "concatenation of the sequences" and "interleaving of the sequences" respectively.

The results of the processing the aggregated ACFs of the QCPs (16) and (17) by the MMFs with TFs

$$\{\xi(k)\}_{k=0}^4 = \{-1,0,0,0,1\},$$ (18)

$$\{\xi(k)\}_{k=0}^2 = \{-1,0,1\},$$ (19)

are presented on Fig. 4 and Fig. 5 respectively.
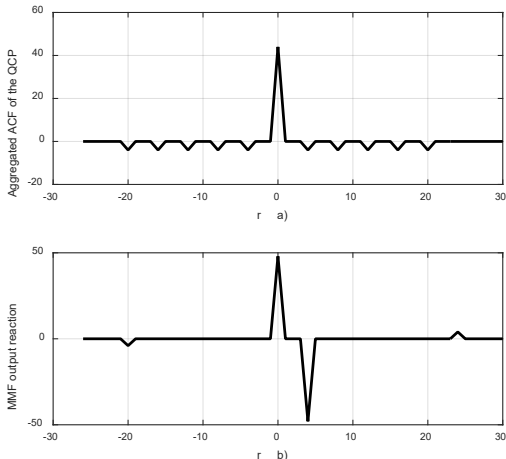
Fig. 4. The result of processing the aggregated ACFs of the QCPs (16) by the MMF with TF (18).
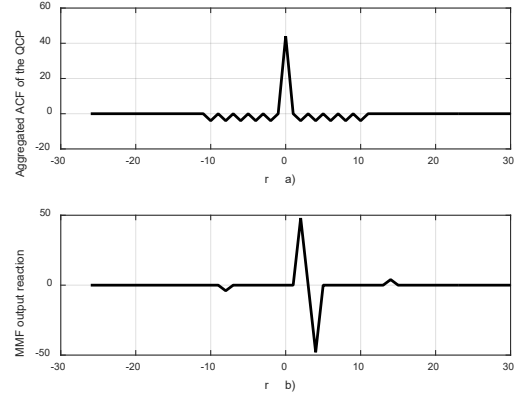
Fig. 5. The result of processing the aggregated ACFs of the QCPs (17) by the MMF with TF (19).

For completeness of the explanation, the results of the processing the aggregated ACFs of the QCPs (16) and (17) by the MMFs with TFs

$$\{\xi(k)\}_{k=0}^8 = \{-1,0,0,0,2,0,0,0,-1\},$$ (20)

$$\{\xi(k)\}_{k=0}^4 = \{-1,0,2,0,-1\},$$ (21)

are presented on Fig. 6 a, b respectively.
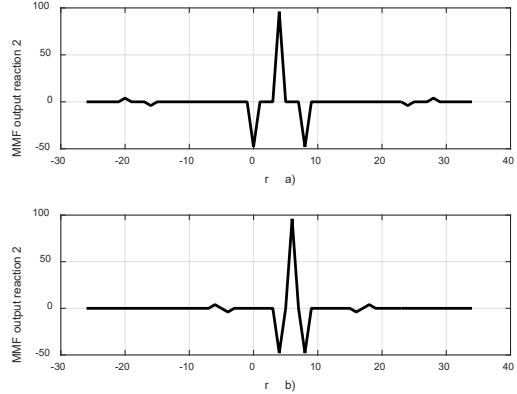
Fig. 6. The results of processing the aggregated ACFs of the QCPs (16) by the MMF with TF (20) (a) and the aggregated ACFs of the QCPs (17) by the MMF with TF (21) (b).

At the end of this chapter, the losses in the SNR, which may accompany the processing of the Barker and the QB signals as well as the QCPs by the MMFs, presented in the paper, will be analysed. In this connection, first of all it should be noted, that the above described MMFs act over the signal ACFs. As the main lobe of every ACF is the result of the coherent accumulation of the energies of all the chips (elementary phase pulses), forming the signal (see (5)), the SNR cannot be further improved by the means of a filter, matched to the ACF of the concrete signal (due to the limited space it is impossible here a rigorous proof of this fact to be presented). Hence, the losses in the SNR, caused by transformations of a signal ACF, are results of operand roundnesses, which may occur in the digital filters. As the TF samples of the MMFs, presented in the paper, are integers, it can be concluded that the losses in the SNR are very small or are completely missing.

IV. CONCLUSIONS

In the paper a method for synthesis of MMFs, which effectively suppress the sidelobes of signal ACFs, consisting of repeating patterns, is substantiated. The usage of the method allows the electromagnetic compatibility of all working simultaneously electronic devices as well as their resistance in a hostile radio electronic environment to be improved. The study, conducted in the paper, could be useful during the modernization of the extant or development of new radar sensor networks and remote control systems.

REFERENCES

[1] L. Nikolov and Kr. Slavyanov, "On the contemporary cybersecurity threats," Proceedings of the I st Int. conference CONFSEC 2017, 11-14.12.2017, Borovets, Bulgaria, ISSN Print: 2603-2945, ISSN Online: 2603-2953, pp. 142-144.

[2] M. Iliev and M. Bedzheva, "An approach for application of UAVs for observation of processes in agriculture," Proceedings of 7th International Conference on Energy Efficiency and Agricultural Engineering (EE&AE 2020), 12-14 November 2020, Ruse, Bulgaria.

[3] T. Ignatova, M. Nedelchev, and M. Bedzheva, "Contemporary approaches for effective radio spectrum utilization," Proceedings of University of Ruse - 2022, volume 61, book 3.2., pp. 161-166 (in Bulgarian), ISSN 1311-3321 (print), ISSN 2535-1028 (CD-ROM), ISSN 2603-4123 (on-line).

[4] Kr. Slavyanov and L. Nikolov, "An algorithm for ISAR image classification procedure," International scientific journal "Industry 4.0," Vol. 2 (2017), Issue 2, web ISSN 2534-997X, print ISSN 2543-8582, pp. 76-79.

[5] M. Y. E. Golay, "Complementary series," IRE Transactions on Information Theory, Volume IT–7, Issue 2, pp. 82 – 87, April 1961.

[6] K. Feng, P. Jau-Shyong, and Q. Xiang, "On aperiodic and periodic complementary binary sequences," IEEE Transactions on Information Theory, Volume IT–45, Issue 1, pp. 296 – 303, January 1999.

[7] M. G. Parker, K. G. Paterson, and Ch. Tellambura, "Golay Complementary sequences," https://www.isg.rhul.ac.uk/~kp/golaysurvey.pdf

[8] A. El-R. H. Elbardawiny, A. Sobhy, F. M. Ahmed, and M. Hassan, "A novel sidelobe cancellation method for binary Barker code pulse compression," Proceedings of 17th International Conference on Aerospace sciences & Aviation technology, ASAT – 17, April 11 - 13, 2017, Cairo, Egipt.

[9] A. T. Fam, and I. Sarkar, "Multiplicative mismatched filters for optimum range sidelobe suppression in Barker code reception," U. S. Patent US 7,492,312 B2, February 17, 2009.

[10] M. Iliev, B. Bedzhev, M. Bedzheva, and K. Kanchev, "Approaches for implementation of Golay's Complementary signals and Welti's Quaternary signals in radio-communication systems," Proceedings of the 2021 IEEE International Conference on Information Technologies (InfoTech-2021), 16-17 September 2021, St. St. Constantine and Elena, Bulgaria.

[11] B. Bedzhev and D. Dimitrov, "Generalizations of the recursive methods for synthesis of Complementary pairs of phase manipulated signals," Proceedings of the 2023 IEEE International Conference on Information Technologies (InfoTech-2023), 20-21 September 2023, Bulgaria.

[12] M. Iliev, N. Nikolov, and M. Bedzheva, "A heuristic approach for synthesis of quasi complementary signals," Proceedings of University of Ruse - 2022, volume 61, book 3.2., pp. 167-173 (in Bulgarian), ISSN 1311-3321 (print), ISSN 2535-1028 (CD-ROM), ISSN 2603-4123 (on-line).

Development of organisational competencies during transition and adaptation to industry 4.0.

Iryna Bohashko
Department of English
Philology
Dragomanov Ukrainian State University
Uman, Ukraine
23fif.i.bohashko@std.udu.edu.ua

Oleksandr Bohashko
Department of marketing, management
and business management
Pavlo Tychyna Uman State Pedagogical University
Uman, Ukraine
bogashko@ukr.net

Abstract. **Competencies that enable organizations to effectively implement digital technologies and provide them with the ability to adapt to changes in the digital environment can be classified as organizational competencies in the context of digital transformation. During the transition to Industry 4.0, organizations find themselves in conditions of a high level of uncertainty and complexity, which requires them to adapt to the new context. A key factor in this process is competencies that ensure high competitiveness and innovative potential. However, the scientific literature does not sufficiently disclose their content, classification levels, and development opportunities under digitalization conditions. This article attempts to fill this gap by analyzing the impact of new technologies on organizational competencies. A conceptual model is presented, which is based on the assumption that the degree of digitalization strengthens the interaction of higher-level competencies - strategic flexibility and ambidexterity.**

Keywords: Organizational competencies, Industry 4.0, digitalization, strategic flexibility.

I. INTRODUCTION

Organizational competencies are skills that "go beyond". More specifically, it is a type of skill that allows you to learn and create new useful skills faster, and helps improve and develop other abilities that you already have.

Organizational competencies are a higher level of abilities that include a set of general skills that can be applied in different situations and in different areas of the organization. These competencies include, for example, critical thinking skills, communication, creative problem solving, leadership, etc. The main purpose of organizational competencies is to help employees adapt to changes in the work environment and solve tasks effectively.

Enterprises of various industries face the difficult task of adapting to Industry 4.0. The widespread use of digital technologies is transforming workplaces and production processes. Many organizations have already moved to a digital environment in part or in full, while others are still exploring the possible implications of such a move. The time has come when the most innovative tool will be the support of higher-level competencies, in particular *strategic foresight, flexibility and organizational ambidexterity* [1] – [3].

One of the key components of the development of second-level competencies, or "dynamic capabilities", is the formation of realistic scenarios of the future and the adjustment of strategies. This process plays a critical role in identifying risks and opportunities, responding to new trends and internal transformations [2], [4].

Strategic flexibility allows organizations to execute long-term programs and maintain high maneuverability and adaptability in the face of uncertainty. Ambidexterity involves the ability to combine two opposite processes: current activity and the search for new perspectives. It allows organizations to balance between modernization of current business processes in dominant market conditions and exploration of strategic horizons.

The specified competencies allow solving complex tasks in the context of digital transformation - effectively managing supply chains using real-time demand data processing. The use of technologies of artificial intelligence, virtual and augmented reality, "Internet of things", cloud computing, analysis of large volumes of data, 3D printing, additive manufacturing and others, provides an opportunity to create a flexible and orderly space that avoids excessive accumulation of inventory.

The use of hardware and software for processing large volumes of data, based on the automated analysis of information received from sensors of devices connected to

computing systems, contributes to the creation of a reliable basis for the development of competencies that allow reconfiguring production to adapt to various changes. The digital system, while having advantages, raises certain challenges, such as protecting cyber security in a hyper-connected environment. Whether it is possible, in the process of digital transformation, to acquire meta-competencies that will allow preventive response to new opportunities and threats, to show strategic flexibility, foresight and ambidexterity, remains unknown [5]. This study hypothesizes that the level of digitalization enhances the effects of the interaction of higher-level competencies – strategic foresight, strategic flexibility, and ambidexterity.

II. METHODS

The systematic literature review method is widely used to systematise and summarise knowledge in various subject areas. This approach is based on a detailed analysis of a limited number of scientific studies, is labour-intensive, and takes into account the opinions of experts.

Another common method, bibliometric network analysis, combines both expert and computational approaches to support interpretations and conclusions with quantitative data. This method makes it possible to process much larger volumes of scientific publications and identify relevant topics and promising areas of research.

The use of theoretical and empirical methods allows us to create a more objective reflection of the scientific topic under consideration and identify the links between its various aspects. This is achieved with the help of visual tools: building citation maps, co-authorship and other aspects of scientific activity. This allows for a deeper understanding of the current state and development trends of the topic under study. Consideration of the characteristics of each of these approaches is in favour of their use in the process of writing an article, as they fully meet the purpose of the study.

III. RESULTS AND DISCUSSION

The introduction of Internet technologies in industrial production marks the beginning of a new era of industrialisation - Industry 4.0. The first industrial revolution (Industry 1.0) is associated with the invention of the steam engine. Industry 2.0 is marked by the introduction of the concept of assembly line production, which was first introduced at Henry Ford's factory. This approach is algorithmic, where the production of a product takes place step by step according to a fixed programme by dividing work functions. Within Industry 3.0, the production process includes industrial robots, which, however, remain static, mostly performing a specific operation according to a programme provided in advance [6].

In Industry 4.0, the production process is effectively regulated through the interaction between personnel, technical equipment, and the transport system. This approach is based on the use of big corporate data, which includes both structured information about the activities of companies and unstructured data from social networks, sensor signals, audio and video data [7].

TABLE 1 CLASSIC 3.0 TECHNOLOGY AND NEW 4.0 TECHNOLOGY

Classic 3.0 technology	New 4.0 technology
Automation	Artificial intelligence
Accounting and dispatching	Cyber security
Data storage	3D Printing
Mobile technologies	Drones and other devices
Industrial networks	IoT Platforms
Cloud computing	Digital twins
Robots for process operations	Cobots
Industrial automation	Block chain
Manufacturing execution system	Wearable

In Industry 4.0, the production of customised products tailored to consumer preferences at a given time is made possible by integrating technology, production and the market into a socio-technological system that automatically adapts to changing conditions. Data from machines and sensors are analysed, integrated with text documents and help speed up business processes, which will contribute to a fast and efficient decision-making process.

The 4.0 concept defines an intelligent production network where physical production processes are integrated with digital technologies, machine learning systems and big data processing to form a single ecosystem of interconnected companies focused on manufacturing and supply chain management.

The term Industry 4.0 first appeared in 2011 at an industrial trade fair in Hannover, Germany. In different regions of the world, this approach may be known by other names, such as the Industrial Internet in the US and Internet+ in China. The concept is based on four key aspects: cyber-physical systems, the Internet of Things, the Internet of Services, and smart factories. From a technological point of view, Industry 4.0 implies the simultaneous digitalisation and automation of production. These processes lead to a change in modern business models, which began with the creation of digital value chains. The first step in implementing these ideas was the introduction of key technologies for Industry 4.0 (Table 2) [8].

In the field of strategic management, the resource-based view (RBV) has become widely accepted, which states that companies with unique, rare and inaccessible resources and knowledge have a significant advantage [9]. However, there is a lack of information on how to properly use and develop these resources to adapt to new conditions. In order to gain a more complete understanding of this process, the concept of organisational capabilities was proposed. According to this theory, companies respond to challenges by developing internal management skills, technological abilities, etc. instead of trying to influence external factors [10].

TABLE 2 STATE-OF-THE-ART TECHNOLOGY

Technology	*The essence of the technology*
Artificial intelligence and robotics	Developing machines that can replace humans in a wide range of tasks related to thinking, multitasking, and fine motor skills. thinking, multitasking and fine motor skills
Networked sensors	Commonly known as the "Internet of Things", this is the use of networked sensors to remotely connect, monitor and control products, systems and networks
Virtual and augmented reality	Advances in the relationship between humans and computers that include environmental simulations, holographic readings, and overlays of digital objects environment simulation, holographic readings, and the overlay of digital objects on the real world using mixed reality
Additive manufacturing	Advances in additive manufacturing using an increasingly wide range of materials and innovative methods, including 3D bio printing of organic and innovative methods, including 3D bio printing of organic tissues
Block chain and distributed technology	A distributed ledger technology based on cryptographic systems that manage, verify and publicly record transaction data. A distributed ledger technology based on cryptographic systems that manage, verify and publicly record transaction data; the basis of "crypto currencies" such as bit coin
Advanced materials and nanomaterial	Creation of new materials and nanostructures to develop useful properties such as thermoelectric efficiency, shape retention, and to invent new functional applications
Capture, storage and transmission of energy	Breakthroughs in the efficient use of batteries and fuel products; renewable energy through solar, wind and tidal technologies; energy distribution through smart grid systems networks; wireless energy transmission, etc.
New computing technologies	New architectural solutions for computer hardware, such as quantum computing, biological computing, biological computing or neural network processing, as well as innovative extensions of current computing technologies
Biotechnology	Innovations in genetic engineering, sequencing and therapy, as well as biological computing interfaces and synthetic biology
Geo-engineering	Technological intervention in planetary systems, usually to mitigate the effects of climate change by removing carbon dioxide or managing solar radiation
Neuro-technology	Innovations such as smart medicines, neuroimaging and bioelectronics interfaces that allow us to read, communicate and directly to detect, communicate and directly influence human brain activity
Space technology	Developments that enable greater access to and exploration of space, including microsatellites satellites, advanced telescopes, reusable rockets and integrated rocket and jet engines

There are four categories of organisational competencies. The first category is the ability to perform core functions. The second category implies readiness for continuous improvement. The third category is defined by the skills of formulating strategies aimed at outperforming competitors in existing markets. The fourth and highest category covers meta-competencies that provide the basis for changing competencies at lower levels.

Meta-competencies, or organisational competencies, are responsible for a higher level of skills and abilities and have a certain hierarchy. This higher level includes *strategic foresight, strategic flexibility and agility, and organisational ambidexterity* [1], [2].

The second level of meta-competencies is called "dynamic capabilities" [11]. It includes: detecting trends, opportunities and threats (sensing); responding to them (seizing); transforming - changing organisational culture, business models, etc.

The dynamic global business environment is characterised by constant changes in consumer behaviour and competition, as well as the introduction of new technologies and innovations. This creates both opportunities and risks for companies of all ages. However, without a higher level of competence, many of the hidden signals may remain invisible. For example, the retail industry is reflecting the growing demand for online shopping, but not all market participants understand the need for digitalisation to meet this demand. The development of the ability to identify depends less on investment in new knowledge than on the internal cognitive mechanism for assessing external signals of a different nature that contain an existential threat or an impulse to update [12]. This meta-competence is especially relevant for the banking sector, where regular stress tests and constant changes in international financial reporting standards force the constant revaluation of assets and modelling of various scenarios [13].

Capturing new phenomena involves, first and foremost, keeping abreast of emerging technologies and markets at different levels [11]. This process requires investing in research on consumer behaviour and assessing the extent to which new developments can meet their needs. The first emerging signals are formalised into categories such as "target market segments" and "promising technologies" [14]. Identifying trends, assessing their nature and potential is much easier if key customers and suppliers are involved in the process.

Analysing opportunities and threats involves developing an appropriate response. Changes in the economic situation require both changes in various production links (manufacturing, services, production processes, etc.) and a revision of the business model as a whole [14]. At the initial stage, it is often necessary to consider several conflicting strategies. While previously the location of an organisation was considered a key strategic asset (e.g. in the retail sector), with the advent of Industry 4.0, the ability to integrate virtual and augmented reality, 3D printing, and data analysis technologies is becoming more important. The complex and contradictory trends that are emerging can only be understood by constantly updating competencies, resources, and investments in research and development (R&D).

The key aspect is to determine the optimal moment for implementing transformation processes in a timely manner. Some businesses, even after recognising new opportunities and risks, remain in their comfort zone, continuing to stick to their old strategies and business models.

A company's evolutionary potential is largely determined by its ability to transform its internal structure and assets in line with market and technological changes. As an organisation grows in size, the number of employees increases, which can lead to negative consequences from insufficient performance discipline. To protect against these consequences, it is necessary to

implement strict regulatory procedures and build hierarchical structures, which, however, over time, may limit the readiness to respond quickly to environmental signals and create new knowledge [14].

If there is a lack of openness to change in the corporate culture, this can lead to resistance among employees and result in significant costs. However, transformation processes can be more successful and efficient if a company works with supply chain partners who are open to change. Developing transformation capability requires an understanding of the broader, holistic context. Strategic decision-making should be made at different levels of the hierarchy, taking into account market realities [11].

Thus, high-level organisational competencies are becoming increasingly important in today's business environment.

Strategic foresight, as a tool for identifying weak signals, opportunities and risks, and analysing cause and effect relationships, enables informed decision-making taking into account a wide range of factors. It stems from the assumption of a multivariate future and interacts with the identification of emerging phenomena and trends, which is a second-level meta-competency - dynamic abilities [4].

Strategic flexibility is an important characteristic that manifests itself in the ability to develop and implement long-term strategies while maintaining high adaptability to changes in the face of uncertainty. This concept is based on key concepts such as "future sense", resource agility and leadership unity. Initially introduced in the development of national strategies, this approach was later replicated in the business sector and led to the concept of "flexible production", which emphasises individualisation and the opposite of mass production. This approach has found wide application in the areas of supply chain management, services and management.

Ambidexterity combines operational and strategic components. It can also be understood as the ability to effectively create both incremental and radical innovations. Organisations with ambidextrous characteristics have a high level of cognitive flexibility, as they simultaneously work to optimise existing processes and develop new areas of activity.

The study of the contribution of organisational competencies, including managerial, technological and meta-competencies, to company performance indicators such as productivity, efficiency, internationalisation, intellectual property performance and innovation activity continues to be an interesting and relevant topic. However, only a few authors have deeply explored their impact on competitive advantage [10]. Most scholars focus mainly on certain partial aspects, such as marketing and IT capabilities. Future research will help to better understand the link between dynamic capabilities and higher-level competencies [1].

Although the concepts of strategic agility and ambidexterity are aimed at different aspects of higher-level competencies, they interact with each other and are complemented in the context of practice. There is still an incomplete understanding of the role of digital transformation of organisations in the Industry 4.0 ecosystem in this process.

A study by author [15], based on a survey of 150 medium-sized German engineering companies, shows that ambidexterity and strategic flexibility contribute to the growth effects in terms of competitive advantage. This study concludes that in order to achieve sustainable success, corporations should either favour a strategy of exploring innovation processes to create radically new knowledge, products and services, or combine an exploitative strategy with strategic flexibility. Other studies confirm the positive impact of digitalization on strategic flexibility, sustainability and the ability to overcome challenges [16]. Scientists emphasize that digital technologies open opportunities for organizations to create value. This flexibility includes three interrelated dimensions: customer flexibility, partner flexibility, and operational flexibility. Flexibility promotes a positive relationship between company transformation and technological capabilities in the context of Industry 4.0.

CONCLUSIONS

Thus, higher-level organisational competencies include the ability to lead and manage an organisation at the strategic level, develop development strategies, plan business processes and coordinate the activities of departments. They also include decision-making, problem-solving and collaborative skills with different stakeholders. Knowledge of strategic management, effective communication and leadership is also important for a high level of organisational competence.

The discussion presented here contributes to the development of a conceptual framework in which organisational competencies, interacting with each other, play a key role in ensuring effective performance in the face of uncertainty. Evidence from empirical studies indicates how effective digitalisation is in developing the ability to detect and adapt to changes in a highly competitive environment. The decisions made must be backed up by organisational resources that allow for the transformation of systems, processes and business models.

In addition to the level of digital transformation, uncertainty in the environment, flexibility and rationality in decision-making can have a significant impact. It is important to consider cyber security aspects, as the need to protect information is growing.

The framework outlined in this study is not definitive. A more complete coverage of potential long-term effects may require an analysis of other exogenous and endogenous factors that have not been considered in this paper. The development of a multi-factor conceptual model is complicated in part by the fact that there is no single definition of Industry 4.0 due to the diversity of systems and technologies that make up the industry, although their general composition is known.

REFERENCES

[1] E. D. Diego and P. Almodovar, "Mapping research trends on strategic agility over the past 25 years: Insights from a bibliometric approach", *European Journal of Management and Business Economics*, vol. 31, no. 2, pp. 219-238, April 2022. [Online]. Available: https://doi.org/10.1108/EJMBE-05-2021-0160 [Accessed: Feb. 23, 2024].

[2] I. Kumkale, "Organizational Ambidexterity", *Organizational Mastery, Accounting, Finance, Sustainability, Governance and Fraud: Theory and Application*, Singapore: Springer, 2022. [Online]. Available: https://doi.org/10.1007/978-981-16-7582-9_1 [Accessed: Feb. 23, 2024].

[3] A. Pinsonneault and I. Choi, "Digital-enabled strategic agility: It's time we examine the sensing of weak signals", *European Journal of Information Systems,* vol. 31, no. 6, pp. 653-661, January 2022. [Online]. Available: https://doi.org/10.1080/0960085X.2022.2027824 [Accessed: Feb. 23, 2024].

[4] R. Rohrbeck, C. Battistella and E. Huizingh, "The value contribution of strategic foresight: Insights with a rich tradition", *Technological Forecasting and Social Change*, vol. 80, no. 8, pp. 1593-1606, October 2013. [Online]. Available: https://doi.org/10.1016/j.techfore.2013.01.004 [Accessed: Feb. 23, 2024].

[5] K. Jermsittiparsert, S. Somjai and K. Chienwattanasook, "Era of Industry 4.0 Technologies and Environmental Performance of Thailand's Garment Industry: Role of Lean Manufacturing and Green Supply Chain Management Practice", *Agile Business Leadership Methods for Industry 4.0* (ed. B. Akkaya), Bingley: Emerald Publishing Limited, 2020, pp. 285-302.

[6] K. H. Tantawi, A. Sokolov and O. Tantawi, "Advances in Industrial Robotics: From Industry 3.0 Automation to Industry 4.0 Collaboration", *2019 4th Technology Innovation Management and Engineering Science International Conference (TIMES-iCON)*, Bangkok, Thailand, 2019, pp. 1-4, [Online]. Available: https://doi.org/10.1109/TIMES-iCON47539.2019.9024658 [Accessed: Feb. 23, 2024].

[7] J. Dean, "Big data, data mining, and machine learning", *Value creation for business leaders and practitioneers.* Hoboken, NJ: Wiley, 2014.

[8] H. I. Ostrovska, "Implementation of Advanced Digital Production Technologies within the Framework of Sustainable Development Concept: Problems and Prospects", *Economic Herald of the Donbass.* vol. 1 (67), pp. 59-68, September 2022. [Online]. Available: https://doi.org/10.12958/1817-3772-2022-1(67)-59-68 [Accessed: Feb. 23, 2024].

[9] S. L. Newbert, "Value, rareness, competitive advantage, and performance: A conceptual-level empirical investigation of the resource-based view of the firm", *Strategic Management Journal*, vol. 29, no. 7, pp. 745-768, April 2008. [Online]. Available: https://doi.org/10.1002/smj.686 [Accessed: Feb. 23, 2024].

[10] S. Fainshmidt, L. Wenger and M. R. Pezeshkan, "When do Dynamic Capabilities Lead to Competitive Advantage? The Importance of Strategic Fit", *Journal of Management Studies*, vol. 56, no. 4, pp. 758-787, June 2019. [Online]. Available: https://doi.org/10.1111/joms.12415 [Accessed: Feb. 23, 2024].

[11] D. J. Teece, "Business models and dynamic capabilities", *Long Range Planning*, vol. 51, no. 1, pp. 40-49, February 2018. [Online]. Available: https://doi.org/10.1016/j.lrp.2017.06.007 [Accessed: Feb. 23, 2024].

[12] K. Randhawa, R. Wilden and S. Gudergan, "How to innovate toward an ambidextrous business model? The role of dynamic capabilities and market orientation" *Journal of Business Research*, vol. 130, no. 1, pp. 618-634, June 2021. [Online]. Available: https://doi.org/10.1016/j.jbusres.2020.05.046 [Accessed: Feb. 23, 2024].

[13] G. Feldberg and A. Metrick, *Stress Tests and Policy*, July 2019 [Online]. Available at SSRN: https://doi.org/10.2139/ssrn.3424327 [Accessed: Feb. 23, 2024].

[14] H. Zhang, Y. Wang and M. Song, "Does Competitive Intensity Moderate the Relationships between Sustainable Capabilities and Sustainable Organizational Performance in New Ventures?" *Sustainability*, vol. 12, no. 1, pp. 13-27, January 2020. [Online]. Available: https://doi.org/10.3390/su12010253 [Accessed: Feb. 23, 2024].

[15] T. Clauss, S. Kraus, F. L. Kallinger, P. M. Bican, A. Brem and N. Kailer, "Organizational ambidexterity and competitive advantage: The role of strategic agility in the exploration-exploitation paradox", *Journal of Innovation and Knowledge*, vol. 6, no. 4, pp. 203-213, October–December 2021. [Online]. Available: https://doi.org/10.1016/j.jik.2020.07.003 [Accessed: Feb. 23, 2024].

[16] E. Hadjielias, M. Christofi, P. Christou and M. H. Drotarova, "Digitalization, agility, and customer value tourism", *Technological Forecasting and Social Change*, vol. 175, pp. 121-334, February 2022. [Online]. Available: https://doi.org/10.1016/j.techfore.2021.121334 [Accessed: Feb. 23, 2024].

Investigation of the influence of different modifiers on the corrosion rate of AlSi18Cu3CrMn alloy

Desislava Dimova
*Technical University of Sofia,
Branch Plovdiv*
Plovdiv Bulgaria
desislava608738@gmail.com

Boyan Dochev
*Technical University of Sofia,
Branch Plovdiv*
Plovdiv Bulgaria
boyan.dochev@gmail.com

Kalina Kamarska
*Technical University of Sofia,
Branch Plovdiv*
Plovdiv Bulgaria
kamarska@tu-plovdiv.bg

Yavor Boychev
*Institute of Metal Science Equipment
and Technologies with
Hydroaerodynamics Centre "Acad. A
Balevski" at Bulgarian Academy of
Sciences*
Sofia, Bulgaria
y_boichev@abv.bg

Bozhana Chuchulska
*Faculty of Dental Medicine
Medical University of Plovdiv*
Plovdiv, Bulgaria
Bozhana.Chuchulska@mu-
plovdiv.bg

Abstract. **The development of new hypereutectic Al-Si alloys with increased mechanical and improved operational properties is an up-to-date engineering task. The non-standardized hypereutectic aluminum-silicon alloy AlSi18Cu3CrMn is modified with different modifiers (standard modifier P and a complex of modifiers P, Ti, B and Be). The compositions thus modified are subjected to heat treatment (T6). Artificial aging after quenching was carried out under different parameters (temperature and time). The aim of the present study is to determine the influence of the used modifiers on the corrosion rate of the compositions under the same conditions. The gravimetric method was used.**

Keywords: corrosion rate, hypereutectic aluminum-silicon alloy, modification, heat treatment

I. Introduction

The influence of microstructure on the mechanical and performance properties of aluminum-silicon alloys has been addressed in various studies. In addition to the size, shape and distribution of the primary silicon crystals in the structure of the alloys, the size and shape of the eutectic silicon is also important. To obtain fine and rounded silicon crystals in the composition of the eutectic, modification of the α-solid solution is resorted to in order to reduce the distance between the dendrites of the α-crystals [4-10]. Through such metallurgical processing, conditions are created for obtaining modified eutectic silicon crystals, which, in turn, helps to increase the mechanical and operational properties of alloys from the Al-Si system. Based on the fact that intercrystalline corrosion is observed in aluminum-silicon alloys, a number of studies have been directed to the study of the relationship between the phase composition and the corrosion behavior of this type of alloys [11]-[15].

The microstructure of hypereutectic aluminum-silicon alloys is affected by the modifying treatment. According to the generally accepted classification of P. A. Rebinder, modifiers are divided into two groups. Type I modifiers are surfactants that adsorb onto the growing crystal seeds and reduce the growth rate of the solid phase. Type II modifiers are usually hard-melting substances with a crystal lattice, isomorphic and with close parameters to that of the crystallizing alloy. Distributed in the melt in a finely-dispersed to colloidally-dispersed state, they become independent centers of crystallization or form such as a result of interaction with elements of the composition of the melt. The complex modification with modifiers of the I and II species of the hypereutectic Al-Si alloys shows very positive results, simultaneously separating the initially separated Si crystals and the crystalline silicon in the composition of the eutectic.

The set of the present study is to determine the effect of the modifiers used on the corrosion rate of AlSi18Cu3CrMn flux under certain conditions.

II. MATERIALS AND METHODS

The chemical composition of the studied hypereutectic Al-Si alloy AlSi18Cu3CrMn is listed in Table 1.

TABLE 1. CHEMICAL COMPOSITION OF ALLOY ALSI18CU3CRMN, WT.%

Si	Cu	Cr	Fe	Mn	Al
18.50	3.12	1.00	0.25	0,76	rest

The modifiers used to modify supereutectic aluminum-silicon alloy AlSi18Cu3CrMn are: standard modifier phosphorus, introduced into the melt via CuP10 ligature in an amount of 0.04 wt% and a combination of the modifiers phosphorus, beryllium, titanium and boron. The introduction of the modifiers Ti and B is carried out through the ligature AlTi5B1 in an amount of 0.015% Ti; 0.003% In wt%. Beryllium is introduced through beryllium bronze CuCo1Ni1Be.

After casting, the experimental castings were subjected to T6 heat treatment. Tempering was carried out at the following parameters: heating for tempering 510-515C°, holding time 6h and 30min. Hardening in water with a temperature of 20ºC. Subsequent artificial aging was carried out at 210ºC – 16h; 250ºC – 12h; 330ºC – 8h.

The method used to study the corrosion behavior of alloys in a 1M solution of H_2SO_4 consists in determining the mass loss of the test bodies. Before the test, the samples were immersed in ethyl alcohol for 5 min., washed with distilled water, dried and weighed on an analytical Acculab ATILON balance with an accuracy of ± 0.0001g. The samples were then placed in 1M H_2SO_4 at room temperature. The first measurement is performed after 72 hours, the next after 240 hours, and the maximum period of study is 360 hours. After each test period, the AlSi18Cu3CrMn specimens were brushed under running water, dried and weighed to the nearest ± 0.0001g. For each of the test periods of the samples, in a corrosive environment, the mass loss and the corrosion rate (CR) are calculated using formula (1):

$$CR = (m_1-m_2)/S·t \ [g/m^2·h] \qquad (1)$$

where, m1 is the mass of the starting sample in g; m2 is the mass of the specimen after the corrosion test in g; S is the area of the specimen in m2; t is the test time in h.

From the CR values obtained, conclusions are made about the corrosion behavior of the aluminum alloy samples under investigation.

III. RESULTS AND DISCUSSION

The corrosion rate results for the three reporting periods are shown in Table 2 for 72h, Table 3 for 240h and Table 4 for 360h, respectively.

TABLE 2. CR RESULTS AFTER 72 HOURS

Alloy №	Modifier	Artificial aging parameters	CR g/m².h
1	P	210°C/16 h	0,0132
2	P, Ti, B и Be	210°C/16 h	0,0128
3	P	250°C/12 h	0,0147
4	P, Ti, B и Be	250°C/12 h	0,0110
5	P	330°C/8 h	0.0175
6	P, Ti, B и Be	330°C/8 h	0,0130

TABLE 3. CR RESULTS AFTER 240 HOURS

Alloy №	Modifier	Artificial aging parameters	CR g/m².h
1	P	210°C/16 h	0,0126
2	P, Ti, B и Be	210°C/16 h	0,0123
3	P	250°C/12 h	0,0142
4	P, Ti, B и Be	250°C/12 h	0,0110
5	P	330°C/8 h	0,0165
6	P, Ti, B и Be	330°C/8 h	0,0132

TABLE 4. CR RESULTS AFTER 360 HOURS

Alloy №	Modifier	Artificial aging parameters	CR g/m².h
1	P	210°C/16 h	0,0126
2	P, Ti, B и Be	210°C/16 h	0,0124
3	P	250°C/12 h	0,0126
4	P, Ti, B и Be	250°C/12 h	0,0070
5	P	330°C/8 h	0,0135
6	P, Ti, B и Be	330°C/8 h	0,0121

The corrosion rate (CR) of the alloy modified with phosphorus and subjected to T6 heat treatment with different parameters of the artificial aging regime is shown graphically in Fig. 1. From the graph it can be seen that in the first reporting period (72h) the corrosion rate increases by -fast compared to the next two reporting periods. The alloys have the smallest mass loss at the longest reporting period (360h).
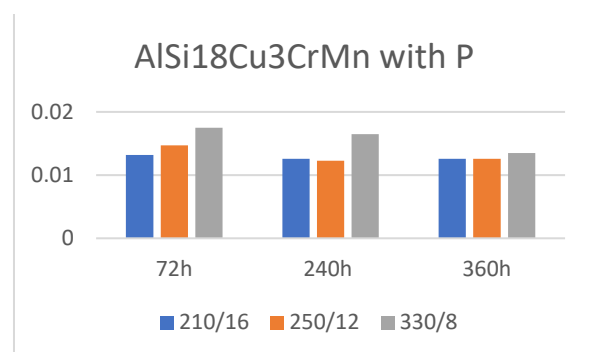
Fig. 1. Corrosion rate of AlSi18Cu3CrMn alloy modified with P

The alloy modified with a complex of modifiers demonstrated a significantly lower corrosion rate in all three reporting periods. The simultaneous introduction of modifiers of the first and second kind positively affects the size of both the primary segregated silicon crystals

and the silicon crystals in the composition of the eutectic. In the microstructural analysis of the alloys thus modified, the conditional average size of the crystals of primary separated silicon, as well as that in the composition of the eutectic, was measured and calculated. Measurements show that both the primary separate silicon crystals and those in the eutectic composition are significantly smaller in size than the alloy modified with only standard phosphorus modifier.
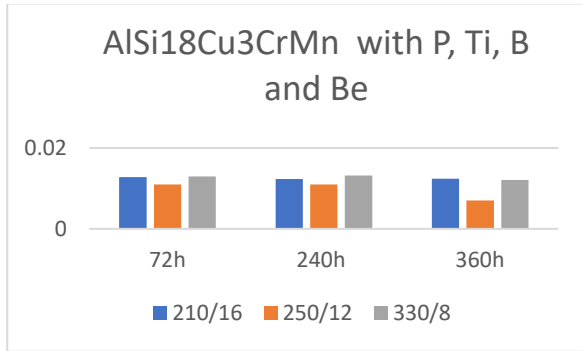
Fig. 2. Corrosion rate of AlSi18Cu3CrMn alloy modified with P, Ti, B, Be

From the graph shown in Figure 3, it can be seen that the mass loss in the first reporting period (72h), after retention in 1M H2SO4, the lowest corrosion rate has alloy #4 (AlSi18Cu3CrMn modified with P,Ti, B, Be – subjected to T6 with aging mode parameters 250˚C/12h). The probable reason for the high corrosion resistance of the alloy is the distribution of strengthening phases of the alloy after quenching and aging. In fig. 6 shows the microstructure of alloy №4.

Fig. 3. Corrosion rate of AlSi18Cu3CrMn alloy after 72h stay in H$_2$SO$_4$

After 240h (Fig. 4) of the samples staying in 1M H2SO4 again alloy №4 has the lowest corrosion rate of all the investigated alloys. Alloy №5 (AlSi18Cu3CrMn modified with P subjected to T6 with parameters of the aging mode 330˚C/8h) at all reporting periods shows the highest CR. Figure 7 shows the microstructure of the thus modified alloy, which clearly shows larger copper-containing phases located around the primary separated silicon crystals. The likely cause of the high corrosion rate is precisely these coarsely separated phases.
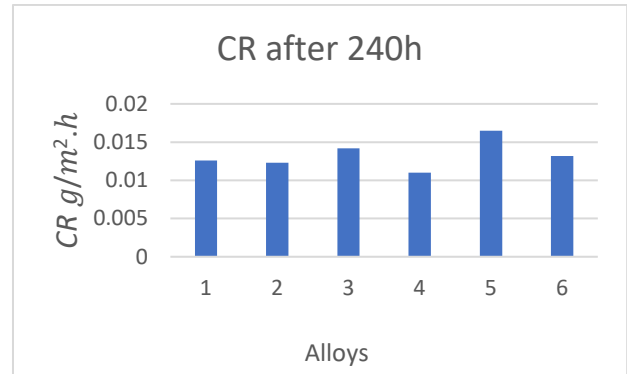
Fig. 4. Corrosion rate of AlSi18Cu3CrMn alloy after 240h stay in H$_2$SO$_4$

After 360h, all investigated compositions registered a lower corrosion rate compared to the first two periods of immersion in the solution. The presence of toughening phases, which separate differently after the different heat treatment regimes, explains the different amounts of mass loss in the different quenching and artificial aging regimes. In the alloy modified with P, Ti, B and Be, the silicon crystals in the composition of the eutectic are significantly smaller in size and rounded in shape. The refinement of the silicon crystals in the composition of the eutectic and the change in their shape have a positive effect on the corrosion rate.
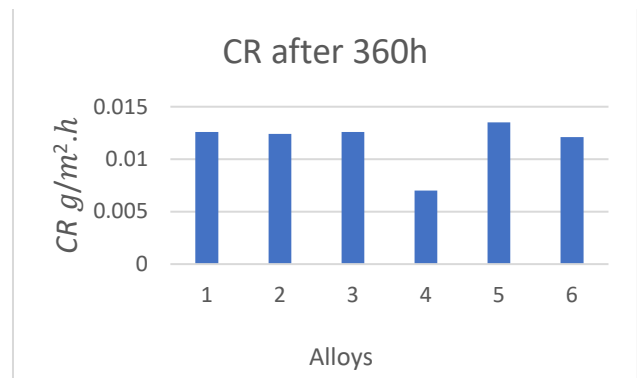
Fig. 5. Corrosion rate of AlSi18Cu3CrMn alloy after 360h stay in H$_2$SO$_4$.

The observed trend is that after modifying the alloy with 0.04% phosphorus, 0.2% titanium, 0.04% boron and 0.007% beryllium and subjecting it to the T6 heat treatment regime, artificial aging at 210, 250 and 330°C leads to a decrease in the rate of corrosion and increase their corrosion resistance.
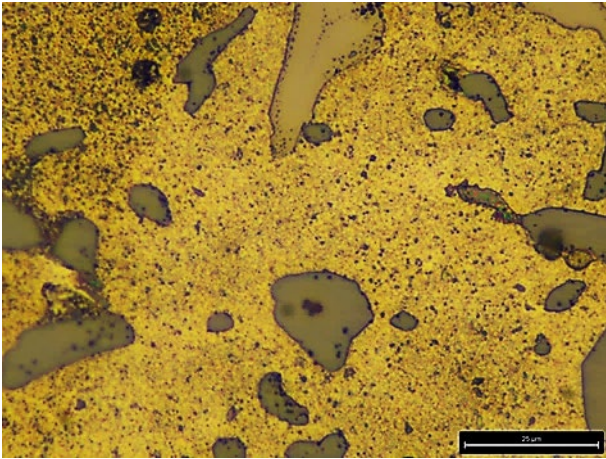
Fig. 6. Microstructure of AlSi18Cu3CrMn alloy (P, Ti, B, and Be) after T6 (250/12h aging mode parameters).
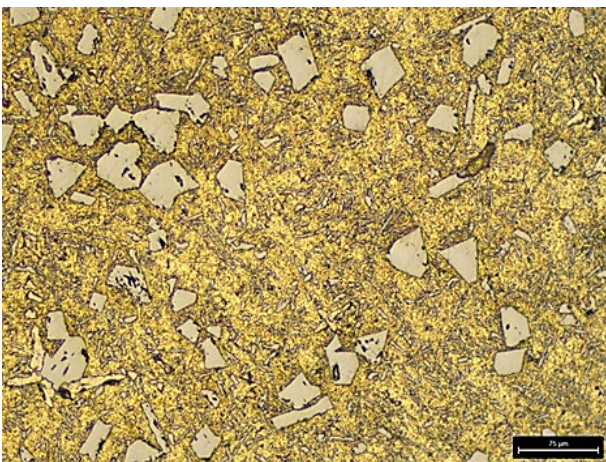
Fig. 7. Microstructure of AlSi18Cu3CrMn (P) alloy after T6 (parameters of aging mode 330/8h).

Characteristic of aluminum alloys is the good corrosion resistance due to the formation of Al_2O_3, studies in this direction show deterioration or improvement of corrosion resistance in relation to the morphology of the microstructure [1-3].

IV. CONCLUSIONS

The complex modifying treatment with modifiers of the first and second kind of the super-detectic complex alloy AlSi18Cu3CrMn has a positive effect on the corrosion resistance of the alloy in 1M H2SO4.

The studied alloy modified with P, Ti, B and Be and subjected to quenching with subsequent artificial aging at 250˚C for 12h demonstrated the lowest corrosion rate for all reported residence periods in 1M H_2SO_4. This is most likely due to the strengthening phases separated after artificial aging along the grain boundaries, preventing the intercrystalline corrosion characteristic of this type of alloy.

REFERENCES

[1] N. J. Petch, "The Cleavage Strength of Polycrystals," Journal of the Iron and Steel Institute, Vol. 174, 1953, pp. 25-28.A. Lasalmonie, J. Strudel

[2] J. Lian, B. Baudelet "A modified Hall-Petch relationship for nanocrystalline materials" https://doi.org/10.1016/0965-9773(93)90184-D

[3] Wislei R. Osório, Claudio A. Siqueira, Carlos A. Santos, Amauri Garcia „The Correlation between Electrochemical Corrosion Resistance and Mechanical Strength of As-Cast Al-Cu and Al-Si Alloys" https://doi.org/10.1016/S1452-3981(23)19680-5

[4] Wislei Osorio, Noé Cheung, University of Campinas, Leandro C. Peixoto, A. Garcia "Corrosion Resistance and Mechanical Properties of an Al 9wt% Si Alloy Treated by Laser Surface Remelting" DOI:10.1016/S1452-3981(23)15186-8

[5] Kazushi Yamada, Ken Miyata, Reiichi Konishi, Kiyomi Okada, Tetsuya Tsujii Advances "Orientation Effect of Heat-Sealed PP Film on Peel Strength and Structure" Materials Physics and Chemistry Vol.5 No.11, November 5, 2015 DOI: 10.4236/ampc.2015.511044

[6] Vlastimil Votrubec, Pavel Hisem, Lenka Vinšová, Gabriela Benešová "Fatigue Strength of Laser Welded Joints of PP and PC Components" World Journal of Mechanics Vol.8 No.6, June 13, 2018 DOI: 10.4236/wjm.2018.86017

[7] D. A. Sukhanov, N. V. Plotnikova Materials Sciences and Applications Vol.7 No.11, November 29, 2016 DOI: 10.4236/msa.2016.711061

[8] Comment on the Paper "Condom-Assisted Transurethral Resection: A New Surgical Technique for Urethral Tumor", Surgical Science, Vol. 1, 2010, pp. 46-48 Guven Aslan Surgical Science Vol.2 No.4, June 23, 2011 DOI: 10.4236/ss.2011.24042

[9] Maharavo Randrianarivony "Multilevel B-Spline Repulsive Energy in Nanomodeling of Graphenes" [Journal of Surface Engineered Materials and Advanced Technology Vol. 4 No. 2 (April 2014) 75-86]

[10] J. R. Davis, Alloy digest sourcebook: stainless steels, (ASM international, Materials Park, Ohio, USA, 2000), p. 7.

[11] S. L. Chawla, Materials selection for corrosion control, (ASM international, Materials Park, Ohio, USA, 1993), p. 117.

[12] F. Cardarelli, Materials Handbook: A Concise Desktop Reference, 2nd ed. (Springer Science & Business Media, London, UK, 2008), p. 102.

[13] N.A. Savinkov, O.M. Bulanchuk, and A.A. Bizyukov, East. Eur. J. Phys. 3, 102 (2021). Template_2023_VTR.docx

[14] I. Kolodiy, O. Kalchenko, S. Karpov, V. Voyevodin, M. Tikhonovsky, O. Velikodnyi, G.Tolmachova, R. Vasilenko, and G. Tolstolutska, East. Eur. J. Phys. 2, 105 (2021). https://doi.org/10.26565/2312-4334-2021-2-07

[15] V. Voyevodin, M. Tikhonovsky, G. Tolstolutska, H. Rostova, R. Vasilenko, O. Kalchenko, N. Andrievska, and O. Velikodnyi, East. Eur. J. Phys. 3, 93 (2020), https://doi.org/10.26565/2312-4334-2020-3-12

Optimization of a technological process for heat treatment of Cu99.9 with different degrees of plastic deformation

Desislava Dimova
Technical University of Sofia, Branch Plovdiv
Plovdiv Bulgaria
desislava608738@gmail.com

Boyan Dochev
Technical University of Sofia, Branch Plovdiv
Plovdiv Bulgaria
boyan.dochev@gmail.com

Yavor Boychev
Institute of Metal Science Equipment and Technologies with Hydroaerodynamics Centre "Acad. A Balevski" at Bulgarian Academy of Sciences
Sofia, Bulgaria
y_boichev@abv.bg

Abstract. Different degrees of plastic deformation of Cu99.9 have been achieved by using different technological forming processes. Recrystallization annealing was carried out at different time-temperature regimes. The influence of the degree of plastic deformation and the recrystallization annealing conditions on the structure of the studied material (Cu99.9) is discussed. The technological process of heat treatment is optimized.

Keywords: recrystallization annealing, plastic deformation, microstructure, Cu99.9

I. INTRODUCTION

Recrystallization and grain growth are of crucial importance in regulating the mechanical properties and performance characteristics of thermomechanically treated metals and alloys [1, 2]. This is especially true for strong plastic deformation (SPD)-deposited ultrafine-grained (UFG) and nano-grained (NG) structures, which typically have degraded thermal stability and low ductility due to the high stored excess energy and dense dislocation arrangement resulting from plastic deformation (PD) [3,4]. More well-known methods for the intensive plastic deformation of copper are: Equal Angle Channel Drawdown (ECAP) [5,6], Hot Pressure Torsion (HPT) [7,8] and Dynamic Plastic Deformation (DPD) [9,10].

Recrystallization consumes the excess energy introduced by plastic deformation and restores the properties of the metal by reducing the dislocation density and by generating new, essentially defect-free, recrystallized grains [11, 12]. The deposited energy in the plastically deformed metal depends on the magnitude of the cold plastic deformation undergone (the degree of plastic deformation), and the larger it is, the larger areas of the polycrystallite are covered by the recrystallization process and the more numerous are the newly formed recrystallization nuclei. From these very numerous recrystallization centres, a large number of grains are nucleated, which remain small in size due to limited growth opportunities [13]. Initially, the new, though equiaxed grains still have a certain "hereditary orientation" which gradually disappears. The second stage of the process, which takes place with prolonged heating or heating to higher temperatures, consists in the nucleation of the primary recrystallized equiaxed grains, at the cost of the fusion of adjacent grains [14, 15]

At a high degree of plastic deformation, the recrystallization annealing processes have been studied, and optimal parameters of the recrystallization annealing regime have been indicated in the literature studied. Of interest are products with a lower degree of PD and the possibility of structure refinement by heat treatment. The parameters of the recrystallization annealing process depend on: the nature of the metal (alloy), the degree of plastic deformation, the heating temperature and the holding time at this temperature. The recrystallization temperature threshold depends on the purity of the metal, the homogeneity of the structure and the degree of deformation. There are no unambiguous relationships between these parameters [16, 17, 18, 19].

In order to establish the optimum mode of the recrystallization process after cold PD, it is necessary to conduct experimental studies. This will establish the optimum heat treatment regime that secures the desired

set of physical and mechanical performance at the most energy efficient parameters.

The purpose of the present research is to ensure a structure of the material after plastic deformation and recrystallization annealing minimum 10 points, with a hardness not less than 55 HB.

II. MATERIALS AND METHODS

For the planned experiments, segments of workpieces manufactured from Cu 99.9 obtained by two different plastic deformation (PD) processes were isolated. The first workpiece was produced by spin-forming with a relatively low PD rate of 60%, and the second by stamping with an even lower PD rate of 40%. The workpieces produced by both processes were cut into segments and subjected to different recrystallization annealing regimes shown in Table 1.

TABLE 1. HEAT TREATMENT MODES

№	Heating temperature, C°	Retention time, min	Cooling
1	I^{st}200 II^{nd}280	I^{st} 120 II^{nd}180	under running water for 2-3 min
2	I^{st} 200 IInd 280	I^{st} 180 II^{nd}180	
3	I^{st} 200 IInd 350	I^{st} 120 IInd 10	
4	I^{st} 200 II^{nd}280	I^{st}120 IInd 40	
5	350	20	

The recrystallization temperature threshold of pure copper is 133°C but the process of new grain formation at this temperature is very slow. For the present experiments, five regimes of recrystallization annealing were selected.

Modes 1÷4 represent two-stage recrystallization annealing with mode parameters: heating temperature 200°C and holding time 120min. The purpose of the first heating is to pre-exist the recovery (the processes of relaxation and polygonization) in the cured metal. Then, in the second stage, recrystallization of the annealed sample bodies takes place.

The fifth heat treatment mode is the recommended mode for recrystallization annealing of Cu 99.9 in which the pre-annealing process is absent. The mode parameters are: heating temperature 350°C; holding time at the specified temperature - 20 min.

To investigate the microstructure of Cu99.9 samples, metallographic sections were prepared for microstructural analysis. The samples were wet-ground on grinding wheels numbered 240, 320, 400 and 600, 800 and 1000. After grinding the same were mechanically polished with diamond paste and lubricant. The microstructure of copper was developed with hydrochloric acid reagent (HCl- 200 ml) and triferric chloride (FeCl3- 20 g). The structure was qualitatively characterized using a Leika FlexaCamC1 metallographic microscope with 20X magnification. And the determination of the grain size of the structure with a module to the microscope software LAS X Grain Expert..

The macrohardness of the investigated Cu99,9 segments was determined by the Brinell method using a FOUNDRAX BRIN400D hardness tester.

III. RESULTS AND DISCUSSION

The results of all heat treatment modes are presented in Tables 2 (for the workpiece produced by spinning) and 3 (for the workpiece produced by stamping).

TABLE 2. RESULTS OF THE STUDY OF THE SPINNING

Annealing mode	Grain size microstructure number	Hardness HB $_{2.5/62.5/30.}$
1	11-12	62,9
2	9	49,3
3	9	51,2
4	9	51,2
5	9	50,8

TABLE 3. RESULTS OF THE STUDY OF THE STAMPING

Annealing mode	Grain size microstructure number	Hardness HB $_{2.5/62.5/30.}$
1	6	62,6
2	5	61,7
3	6	59,9
4	7	62,6
5	6	57,4
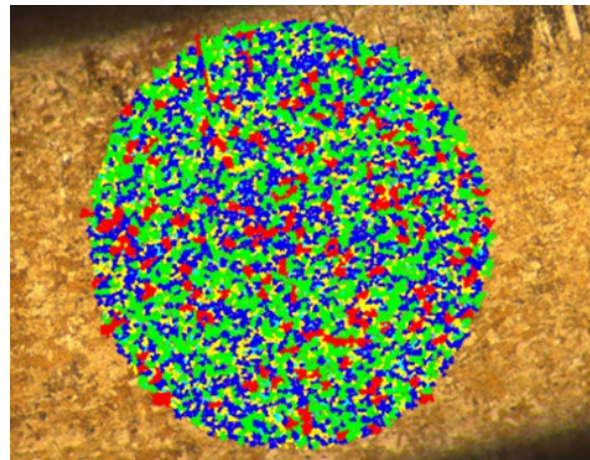
Fig. 1. Software grain measuremen after mode №1 after spinning

A fine structure with dispersively distributed crystals that are rounded was observed on the examined metallographic slit field of Cu99.9 after spinning and recrystallization annealing by mode 1 (Fig. 1). The measured and calculated conditional grain diameter was 7.75 μm, which bal. Software measurements of the microstructure show that the percentage content of different grain sizes varies. The predominant grain sizes were 11 bal - 25.97%, 12 bal - 31.58% and 13 bal - 21.82%. As not a few crystals were crystallized with size 14 Ball - 8.78%. The measured hardness of the copper so annealed was 54.6 Hb $_{2.5/62.5/30.}$
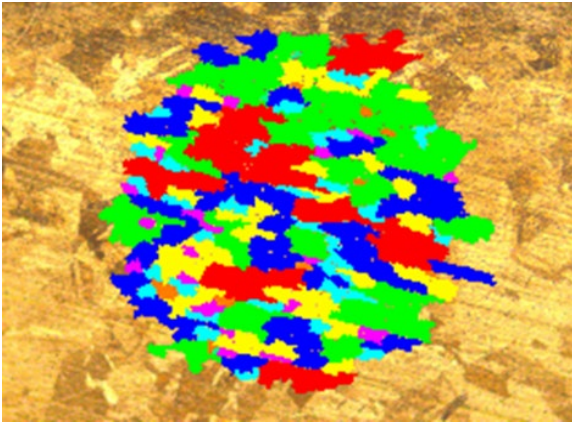
Fig. 2.   Software grain measuremen after mode №1 after stamping

After mode 1 of the sample body made by stamping with a PD of 40%, we observe much larger grains (Fig. 2). Software measurements of the microstructure show that the percentage of different grain sizes varies, but the predominant amount is 6 Ball The measured hardness of the copper annealed in this way is 62.6 Hb $_{2.5/62.5/30}$. At practically the same macrohardness we observe a considerable difference in grain sizes. The probable reason for this is that, at this low degree of PD, deformation took place unevenly and some of the crystals remained undeformed. The energy required to nucleate new grains in the recrystallization annealing process was probably insufficient.
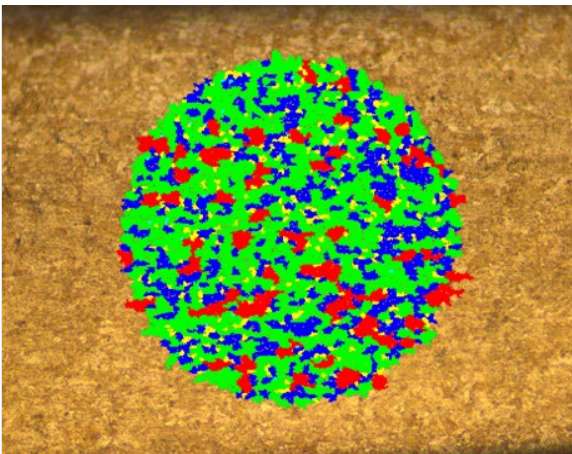
Fig. 3.   Software grain measuremen after mode №1 after spinning

In Fig. 3, we observe the microstructure of a sample body fabricated by spinning and subjected to heat treatment mode No. 5 without pre-treatment. In the literature studied [17,18], the recommended temperature for recrystallization to take place is 350ºC and the retention time is 10 to 20 min, according to the degree of plastic deformation, for this reason the same parameters of the recrystallization annealing regime were used. The results after annealing in mode No. 5 of the spun workpiece were satisfactory but much lower than those in mode No. 1. The measured and calculated conditional average grain diameter was 13.9 µm, which corresponds to the 9th ball. Software measurements of the microstructure show that the percentage content of the

different grain sizes is different. The predominant grain sizes were 9 ball - 27.18%, 10 ball - 31.28% and 11 ball - 21.47%. The measured hardness of the copper so annealed was 50.8 Hb 2.5/62.5/30.

The microstructure of the segment of the workpiece produced by stamping is shown in Fig. 4. On the investigated metallographic slit field of Cu99.9, after plastic deformation conducted in the cold state of the sample body with subsequent recrystallization at 350℃, holding for 20 min and subsequent cooling in running water for 1-2 min, multiple ucropped grains surrounded by grains of very small size are observed, from which we judge that secondary recrystallization has taken place due to the small PD degrees. The measured and calculated conditional mean diameter of the grains is 44.26 µm, which corresponds to the 6-7th ball. Software measurements of the microstructure show that the percentage content of the different grain sizes is different. The predominant grain sizes were 5 score - 17.86%, 6 score - 12.50%, 7 score - 21.43% and 8 score - 19.64%. The results of all the measured crystals are summarized in Figure 5. The measured hardness of the as-annealed copper was 57.4 Hb $^{2.5/62.5/30..}$
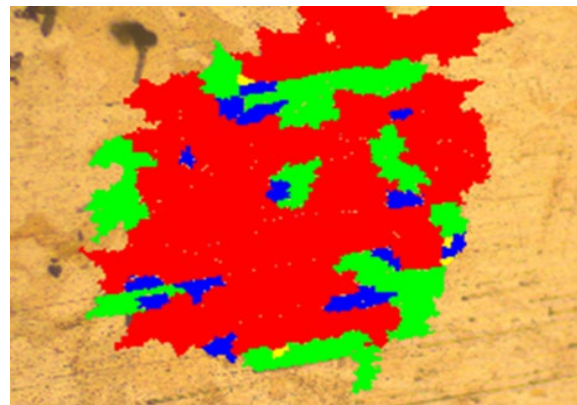
Fig. 4.   Software grain measuremen after mode №1 after stamping

Tables 2 and 3 report the results of the grain size studies conducted after recrystallization as well as the measured macrohardness. The results show that for the workpiece produced by spinning, the results are very good, the microstructure is fine and relatively uniform. In the mode of recrystallization annealing with pre-recovery (Mode No. 1), the microstructure corresponds to 11-12 points, which is difficult to achieve even in articles with a high degree of plastic deformation (at Cu99.9, such a degree of PD is assumed to be more than 70%). The macrohardness of the sample body so heat-treated is 62.9 Hb $_{2.5/62.5/30}$, which, combined with the high microstructure score, provide a very positive set of physical and mechanical indicators. In recrystallization annealing modes 2, 3, 4 and 5, the size of the grain corresponds to score 9, and the macrohardness is commensurate and lower than that in mode 1.
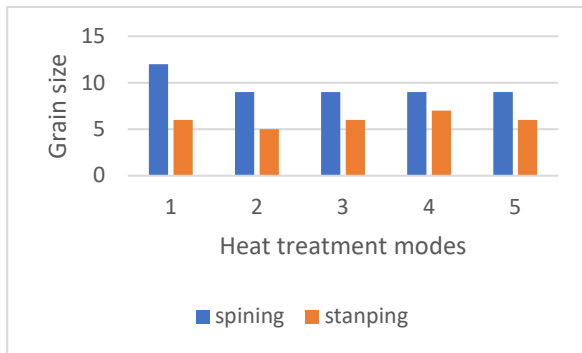
Fig. 5. Results of grain size determination after annealing

In the recovery process, different physical properties are recovered in different temperature range. The recovery mechanism is explained by the lattice resistance of the pre-deformed polycrystallite decreasing with increasing temperature in parallel with increasing atom mobility. In grains where the internal stresses were close to the yield stress Re, submicroscopic slips occurred which damped the internal stresses, thus removing the genus II stresses and part of those of genus III. By removing these stresses artificially after the first heating, the aim is to secure a microstructure free of stresses with ordered defects, which is a prerequisite for a finer dispersed structure after recrystallization annealing (the second stage of the heat treatment process). To a large extent, this explains the high score of the microstructure after the first heat treatment mode of the spin-formed workpiece. The low degree of plastic deformation of the workpiece produced by shimming is the reason for the deteriorated microstructure after heat treatment.

In mode 5 of the workpiece produced by stamping, we observe the mechanism of grain fusion, which consists in the gradual "dissolution" of the grain boundaries and the merging of many small grains into one large grain. The migration of grain boundaries is a diffusion process whose rate is determined by the rate of self-diffusion and therefore this process is characteristic of heating at higher temperatures, and at the low PD (40%) a temperature of 350ºC appears to be high enough for the 20 min retention period for the process to proceed to secondary recrystallisation.

IV. CONCLUSIONS

The most refined and homogeneous microstructure is possessed by the sample body produced by spinning, which was subjected to a quenching (at 200°C for 120 min) before the primary recrystallization process (280°C for 180 min). With the investigations carried out, it is shown that the time provided for the ordering of the defects in the crystal lattice during the polygonization process prepares the microstructure for primary recrystallization and this favours the nucleation of a larger number of centers on which to grow a greater number of crystals.

From the investigations carried out, it can be seen that the specimens subjected to the five different recrystallization annealing regimes of the spin-coated workpiece are in the primary recrystallization zone. This is evidenced by both the microstructure and the measured macrohardness.

The experiments performed show that at very low PD levels (40%), the different annealing regimes do not improve the microstructure. At all heat treatment regimes, the microstructure is coarse and heterogeneous.

REFERENCES

[1] X. Wu, M. Yang, F. Yuan, G. Wu, Y. Wei, X. Huang, Y. Zhu – „Heterogeneous lamella structure unites ultrafine-grain strength with coarse-grain ductility" - Proc. Natl. Acad. Sci. Unit. States Am., 112 (2015), pp. https://doi.org/10.1073/pnas.1517193112

[2] W. Jiang, Y. Cao, Y. Jiang, Y. Liu, Q. Mao, H. Zhou, X. Liao, Y. Zhao - Effects of nanostructural hierarchy on the hardness and thermal stability of an austenitic stainless steel J. Mater. Res. Technol., 12 (2021), pp. https://doi.org/10.1016/j.jmrt.2021.02.100

[3] Y. Liu, Y. Cao, Q. Mao, H. Zhou, Y. Zhao, W. Jiang, Y. Liu, J.T. Wang, Z. You, Y. Zhu – „Critical microstructures and defects in heterostructured materials and their effects on mechanical properties" - Acta Mater., 189 (2020), pp. https://doi.org/10.1016/j.actamat.2020.03.001

[4] Werner Skrotzki, Nils Scheerbaum, Carl-Georg Oertel, Roxane Arruffat-Massion, Satyam Suwas, László S. Tóth – „Microstructure and texture gradient in copper deformed by equal channel angular pressing" Acta Materialia, Volume 55, Issue 6, April 2007, Pages 2013-2024
https://doi.org/10.1016/j.actamat.2006.11.005

[5] X. Molodova, G. Gottstein, M. Winning, R.J. Hellmig – „Thermal stability of ECAP processed pure copper" - Materials Science and Engineering: A Volumes 460–461, 15 July 2007, Pages 204-213 https://doi.org/10.1016/j.msea.2007.01.042

[6] X.H. An, S.D. Wu, Z.F. Zhang, R.B. Figueiredo, N. Gao b, T.G. Langdon – „Evolution of microstructural homogeneity in copper processed by high-pressure torsion" - Scripta Materialia
Volume 63, Issue 5, September 2010, Pages 560-563
https://doi.org/10.1016/j.scriptamat.2010.05.030

[7] X.H. An, S.D. Wu, Z.F. Zhang, R.B. Figueiredo, N. Gao c, T.G. Langdon – „Enhanced strength–ductility synergy in nanostructured Cu and Cu–Al alloys processed by high-pressure torsion and subsequent annealing" - Scripta Materialia, Volume 66, Issue 5, March 2012, Pages 227-230
https://doi.org/10.1016/j.scriptamat.2011.10.043

[8] W.S. Zhao, N.R. Tao, J.Y. Guo, Q.H. Lu, K. Lu – „High density nano-scale twins in Cu induced by dynamic plastic deformation" - Scripta Materialia, Volume 53, Issue 6, September 2005, Pages 745-749 https://doi.org/10.1016/j.scriptamat.2005.05.022

[9] Y.S. Li, N.R. Tao, K. Lu – „Microstructural evolution and nanostructure formation in copper during dynamic plastic deformation at cryogenic temperatures" - Acta Materialia, Volume 56, Issue 2, January 2008, Pages 230-241 https://doi.org/10.1016/j.actamat.2007.09.020

[10] Y. Zhao, T. Topping, Y. Li, E.J. Lavernia – „Strength and ductility of Bi-modal Cu" - Adv. Eng. Mater., 13 (2011), pp. https://doi.org/10.1002/adem.201100019

[11] Wang, M. Chen, F. Zhou, E. Ma – „High tensile ductility in a nanostructured metal" Nature, 419 (2002), pp. 912-915

[12] B. Gao, X. Chen, Z. Pan, J. Li, Y. Ma, Y. Cao, M. Liu, Q. Lai, L. Xiao, H. Zhou – „A high-strength heterogeneous structural dual-phase steel" J. Mater. Sci., 54 (2019), pp. 12898-12910

[13] Burke, S. Eand Turnbull, P (1952) "Recrystallizations and Grain Growth" Progress in Metal Phys 3

[14] T. Konkova, S. Mironov, A. Korznikov, M.M. Myshlyaev, S.L. Semiatin - Annealing behavior of cryogenically-rolled copper Materials Science and Engineering: 0https://doi.org/10.1016/j.msea.2013.07.042

Volume 585, 15 November 2013, Pages 178-189

[15] Wislei R. Osório, Claudio A. Siqueira, Carlos A. Santos, Amauri Garcia „The Correlation between Electrochemical Corrosion Resistance and Mechanical Strength of As-Cast Al-Cu and Al-Si Alloys" https://doi.org/10.1016/S1452-3981(23)19680-5

[16] H.N. Girisha, Dr.K.V.Sharma "Effect of magnesium on strength and microstructure of Aluminium Copper Magnesium Alloy"

International Journal of Scientific & Engineering Research, Volume 3, Issue 2, February-2012 1 ISSN 2229-5518

[17] E.George, Totten – "Heat Treating of Nonferrous Alloys" 978-1-62708-169-6 Volume 4E 2016 https://doi.org/10.31399/asm.hb.v04e.9781627081696

[18] ZhiHui Gao, Tao Wang, YunLai Zhao, Hua Ding, QingXue Huang – "Mechanical properties optimization and microstructure analysis of pure copper gradient laminates via rolling", Chinese Journal of Mechanical Engineering. Version 1 posted 13 Jul, 2022 https://doi.org/10.21203/rs.3.rs-1729350/v1

[19] WZ Haн , SD Wu , SX Li, YD Wang "Intermediate annealing of pure copper during cyclic equal channel angular pressing" Materials Science and Engineering: A Volumes 483–484, 15 June 2008, Pages 430-432 https://doi.org/10.1016/j.msea.2006.10.179

Investigation of the influence of artificial aging parameters on the micro and macro hardness of AlSi12Cu5MgCr and AlSi12Cu5Mn alloys

Boyan Dochev
Faculty of Mechanical Engineering
Technical University of Sofia,
Branch Plovdiv
Plovdiv, Bulgaria
boyan.dochev@gmail.com

Desislava Dimova
Faculty of Mechanical Engineering
Technical University of Sofia,
Branch Plovdiv
Plovdiv, Bulgaria
desislava608738@gmail.com

Mihail Zagorski
Faculty of Industrial Technology
Technical University of Sofia
Sofia, Bulgaria
mihail.zagorski.tu@gmail.com

Plamen Kasabov
Faculty of Mechanical Engineering
Technical University of Sofia,
Branch Plovdiv
Plovdiv, Bulgaria
plamen.kasabov@abv.bg

Bozhana Chuchulska
Faculty of Dental Medicine
Medical University of Plovdiv
Plovdiv, Bulgaria
Bozhana.Chuchulska@mu-plovdiv.bg

Abstract. **Non-standard aluminium-silicon alloys of the eutectic type are complexly modified. The alloys were subjected to T6 heat treatment at different artificial aging parameters. The influence of the working parameters of the dispersion hardening process on the microhardness of the α-solid solution and the macrohardness of the alloys was investigated. The influence of alloying elements on the phase composition of the alloys is discussed.**

Keywords: eutectic aluminium-silicon alloys, heat treatment, microhardness, macrohardness

I. Introduction

Eutectic aluminium-silicon alloys are characterized by good casting properties - high ductility, low tendency to crack formation, low percentage of linear shrinkage, high hermeticity. Their mechanical properties are significantly improved after modification. The most effective eutectic modifier in the structure of aluminium-silicon alloys is sodium, which is a classic example of a Type I modifier. Sodium salts (NaF, $NaCl$, Na_3AlF_6) are also successfully used, and strontium (Sr) and antimony (Sb) also have a satisfactory modifying effect. The modifying action of the remaining elements of the 1A group of the periodic system of elements is weakly expressed. In [1], the comparative data on the modifying ability of the elements of the I-IV group are presented.

As the main combination of alloying elements of aluminium-silicon alloys, copper and magnesium are used because they form strengthening phases. When alloying with copper and magnesium, the following phases are separated: $α$, Si, $CuAl_2$, $S(Al_2CuMg_4)$, Mg_2Al_3, $T(Al_2CuMg)$ $W(Al_XMg_5Cu4Si_4$ or $Al_5Cu_2Mg_8Si_6)$ and Mg_2Si. The percentage ratio of Si and Mg has a significant influence on the formation of the phases in the $Al – Si – Cu – Mg$ alloy. When the value of this ratio is less than 1.73, the strengthening phase Mg_2Si is not formed, but in this case the presence of the $CuAl_2$ phase, the W-phase and Si is observed in the alloy [1].

Heat treatment is one of the main technological operations ensuring the necessary properties of the treated alloy. To obtain aluminium alloys with increased mechanical and improved operational properties, quenching with subsequent artificial aging (T6) is used [2]-[19].

During aging of the hardened alloys, the saturated solid solution breaks down, accompanied by a change in the physical and mechanical properties. In most cast aluminium alloys, this breakdown is characterized by the formation of Guinier–Preston cluster zones [20] – [21]. These zones are formed as a result of the development of diffusion processes, which are accelerated as a result of the majority of vacancies formed as a result of the previous hardening.

II. Materials and methods

The object of the present study are non-standardized aluminium-silicon alloys with a eutectic composition (Table 1 and Table 2).

TABLE 1 CHEMICAL COMPOSITION OF ALSI12CU5MGCR (%)

Si	Cu	Mg	Cr	Fe	Al
11,66	4,65	1,25	0,59	0,31	rest

TABLE 1 CHEMICAL COMPOSITION OF ALSI12CU5MN (%)

Si	Cu	Mg	Mn	Fe	Al
11,41	4,42	0,1	0,386	0,28	rest

The modifying treatment of the two investigated alloys was carried out by a method different from that generally accepted for eutectic aluminium-silicon alloys, i.e. without the use of the Na modifier.

The AlSi12Cu5MgCr alloy is complex modified using 0.02% Ti, 0.004% B, 0.04% P and 0.007% Be. The use of titanium and boron is to modify the α-phase in the composition of the eutectic. The finer it is, the finer its branches are and the distance between them is minimal. This inhibits the growth of eutectic silicon crystals and they are significantly reduced in size. The combination of Ti and Be is used to refine the structure and the uniform distribution of the separating phases in the Mg-doped silumins. The addition of these two elements in very small concentrations improves the mechanical properties of the alloys, which is most likely due to the fact that these two chemical elements increase the concentration of vacancies during quenching, i.e. they accelerate the diffusion processes of Mg and Si during aging, which in turn facilitates nucleation of the β' metastable phase. In addition, beryllium does not form refractory compounds with silicon. The product of modification of silumins with beryllium is the refractory BeO, which is highly soluble in the melt and therefore its thermodynamic activity in it is maximum. Beryllium dissolves well in liquid aluminum, and it is the only element that has the ability to protect the liquid alloy from interaction with oxygen. The use of beryllium as a modifier is appropriate because it has the second largest coefficient of modification of silicon in the structure of this type of alloys at a relatively low concentration (K=73% with a content of Be-0.005%) [1]. Also used is the modifier phosphorus, which is commonly used to modify the primary silicon crystals in the structure of hypereutectic silumins. Considering that modifiers usually have a double action [22], it is most likely that phosphorus is also adsorbed on the boundaries of α-crystals, thus preventing them from growing, i.e. has an impact on structure and as a first-order modifier.

To modify the AlSi12Cu5Mn alloy, titanium and boron were again used, but in significantly larger quantities compared to the AlSi12Cu5MgCr alloy. The introduced amount of titanium in the melt of the studied alloy is 0.2%, and the amount of boron used is 0.04%. At the specified concentration of the element Ti, its maximum modifying effect on silicon was registered, and the condition that the maximum amount of boron in the composition of the alloy was 0.04% was observed. With a higher content of boron in the alloys, the formed borides have a tendency to agglomerate and precipitate when the melt is standing, as a result of which the properties of the alloys deteriorate. The combination of modifiers is supplemented with Sr in an amount of 0.05%, because it successfully replaces the most commonly used modifier for this type of alloys - sodium.

The introduction of the modifiers into the melts of the investigated alloys is through the use of the ligatures AlTi5B1, CuP10, AlSr10 and beryllium bronze CuCo1Ni1Be.

After conducting the metallurgical processing of the melts of the studied alloys, experimental castings were cast from them under the same conditions.

The two studied compositions were subjected to T6 heat treatment. The heating to homogenize the structure is up to a temperature of 510-515ºC, holding at this temperature for 6h30min. and subsequent hardening in water with a temperature of 20ºC. Artificial aging was carried out at temperatures of 170ºC and 190ºC, and the retention times at these temperatures were 10h, 12h and 14h.

The microhardness of the α-solid solution and the macrohardness of the alloys were measured both before heat treatment and after conducting T6 under the indicated experimental conditions.

III. Results and discussion

To strengthen and increase the mechanical properties of aluminium alloys, the T6 heat treatment is most often used, which includes quenching with subsequent artificial aging. The mechanism of alloy strengthening is due to the formation and separation of dispersion-like phases on the basis of the alloying elements. To study the influence of the parameters of the artificial aging (temperature and holding time) after quenching of the studied alloys, the microhardness of the α-hard solution and the macrohardness of the alloys were measured. The results are shown in Table 3 and Table 4.

TABLE 3 MICROHARDNESS AND MACROHARDNESS OF ALSI12CU5MGCR ALLOY

T6	Artificial aging	Microhardness $\mu HV_{50/10}$	Macrohardness $HV_{10/10}$
-	-	87	107
T6	170ºC/10h	129	144
T6	170ºC/12h	119	159
T6	170ºC/14h	123	165
T6	190ºC/10h	104	132
T6	190ºC/12h	105	120
T6	190ºC/14h	113	134

TABLE 4 MICROHARDNESS AND MACROHARDNESS OF ALSI12CU5MN ALLOY

T6	Artificial aging	Microhardness $\mu HV_{50/10}$	Macrohardness $HV_{10/10}$
-	-	75	101
T6	170ºC/10h	120	127
T6	170ºC/12h	129	138
T6	170ºC/14h	117	135
T6	190ºC/10h	120	144
T6	190ºC/12h	113	128
T6	190ºC/14h	110	118

As a result of the heat treatment, the two studied alloys have significantly higher values of micro and macro hardness compared to the values measured before the alloys were subjected to heat treatment.

In the case of the AlSi12Cu5MgCr alloy, the highest value of macro hardness ($165HV_{10/10}$) was measured on the test bodies subjected to artificial aging at a temperature of 170ºC and a holding time of 14h at this temperature. The microhardness of the α-solid solution at the specified artificial aging parameters is $123\mu HV_{50/10}$, a value comparable to the highest measured of the α-phase for this alloy at artificial aging at 170ºC for 10h. The measured values of the micro- and macro-hardness of AlSi12Cu5MgCr alloy after artificial aging at a working temperature of 190ºC and different retention periods at it are lower compared to the values measured at an aging temperature of 170ºC. The selected working temperatures of artificial aging (170ºC and 190ºC) of the AlSi12Cu5MgCr alloy are in the aging temperature interval (150ºC and 200ºC) in which dispersed particles of the intermediate phase θ', which does not differ in chemical composition, are formed in the places of GP 2 zones of the stable θ-phase ($CuAl_2$), possesses a tetragonal lattice and is coherently associated with the solid soln. The operating temperature of 190ºC is at the limit of the temperature interval at which the metastable phase θ' coagulates and the stable θ-phase is formed, as well as the coherence between the lattice of the α-phase and the θ-phase is broken. This leads to a reduction in the distortion of the crystal lattice of the α-solid solution and causes the alloy to weaken. Carrying out the process of artificial aging of AlSi12Cu5MgCr alloy at temperatures close to the limit (θ'→ θ) is undesirable due to the fact that there is a decrease in the microhardness of the α-phase, as well as a decrease in the macrohardness of the alloy.

During artificial aging carried out at a temperature of 170ºC, the highest micro- and macro-hardness values of AlSi12Cu5Mn alloy were measured at a process duration of 12h. With increasing holding time at an operating temperature of 170ºC, a weakening of the alloy is observed. The highest value of macrohardness ($144HV_{10/10}$) of the studied AlSi12Cu5Mn alloy was measured during the artificial aging process at an operating temperature of 190ºC and a retention time of 10h. With increasing holding time at a temperature of 190ºC, a decrease in the values of micro and macro hardness of the AlSi12Cu5Mn alloy was recorded. As with the AlSi12Cu5MgCr alloy, conducting

the artificial aging process at temperatures close to the limit (θ'→ θ) is undesirable.

When the artificial aging process is carried out at an operating temperature of 170ºC, the AlSi12Cu5MgCr alloy has higher macrohardness values compared to the AlSi12Cu5Mn alloy. The most likely reason for this is the combination of alloying elements used and rather the fact that the AlSi12Cu5MgCr alloy is alloyed with Mg (1.25%), an element characterized by high diffusion mobility and involved in the composition of various strengthening phases. The difference in the measured values of the microhardness of the α-phase in the structure of the two investigated alloys is insignificant. In the composition of the alloy AlSi12Cu5Mn, Mn was introduced in the amount of 0.386%, and its characteristic is the reduced diffusion mobility. This is a prerequisite for the lower values of macrohardness of the alloy during artificial aging carried out at a temperature of 170ºC, but also an increase in both macro and microhardness when the process is carried out at higher temperatures (190ºC).

The combinations of modifiers used have a positive effect on the structure of the investigated alloys. The Si crystals in the composition of the eutectic of the AlSi12Cu5Mn alloy before exposure and heat treatment have a rounded shape and the majority of them have a conditional average diameter of 3 μm, some with rims up to 7-10 μm are also observed (Fig. 1). The eutectic silicon crystals in the AlSi12Cu5MgCr alloy structure before heat treatment are needle-shaped and the average linear dimensions are 25 μm (Fig. 2).
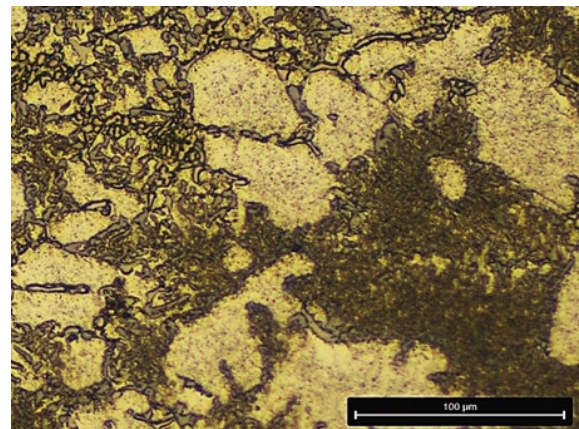
Fig. 1. Microstructure of AlSi12Cu5Mn alloy without heat treatment
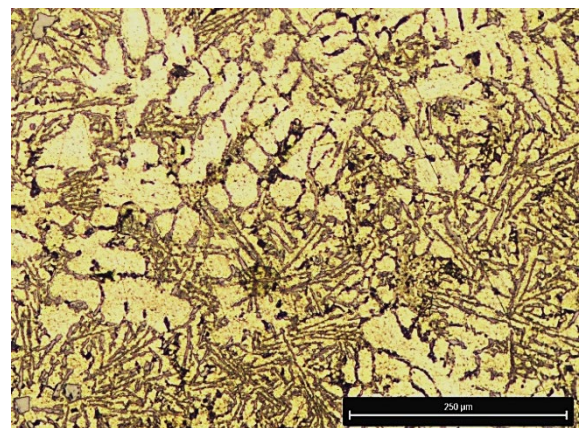
Fig. 2. Microstructure of AlSi12Cu5MgCr alloy without heat treatment

As a result of the used combinations of alloying elements and modifiers, as well as the used artificial aging regimes, structures were obtained (Fig. 3, Fig. 4), which ensure a macrohardness of the investigated alloys comparable to that recommended for this type of silumin [23]. The measured values of the microhardness of the α-solid solution are high, which is a prerequisite for increased strength and operational properties of the developed alloys.
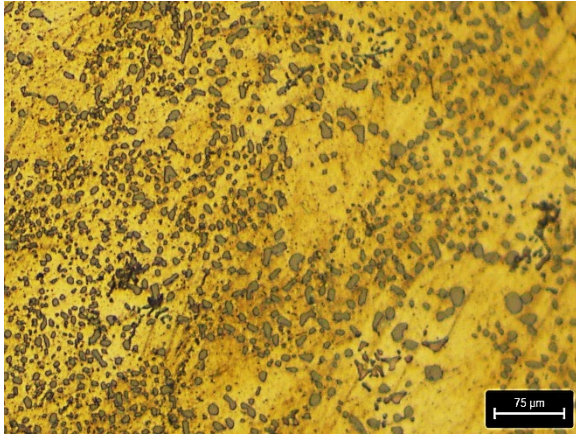
Fig. 3.   Microstructure of AlSi12Cu5Mn alloy T6 artificial aging 190ºC/10h
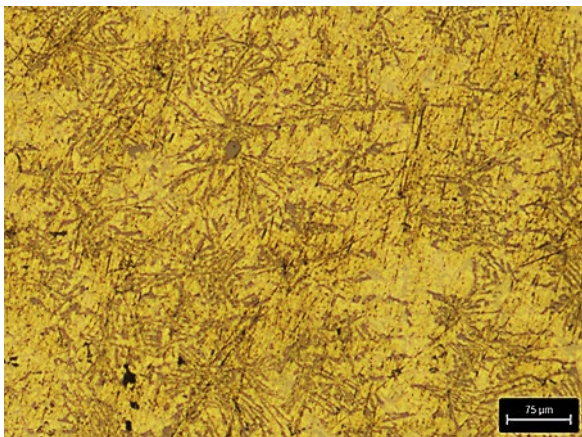
Fig. 4.   Microstructure of AlSi12Cu5MgCr alloy T6 artificial aging 170ºC/14h

IV. Conclusions

Eutectic aluminium-silicon alloys have been developed which are alloyed with a non-standardized combination of chemical elements. A complex modifying treatment was carried out, in which the most commonly used modifier (Na) for this type of alloys was not used. As a consequence of the obtained structures after T6 heat treatment, the studied AlSi12Cu5MgCr and AlSi12Cu5Mn alloys have a macrohardness comparable to the macrohardness of the standardized eutectic silumins. A high microhardness of the α-phase in the structure of both compositions was also recorded.

The influence of the temperature and time parameters of the artificial aging process on the micro- and macro-hardness of the AlSi12Cu5MgCr and AlSi12Cu5Mn alloys was investigated. It was established that their maximum strengthening depends on the diffusion mobility of the alloying elements used.

References

[1]   G.B. Stroganov, B.A.Rotenberg and G.B.Gershman, „Alloys of aluminum with silicon", 1977 (In Russian)

[2]   N.M. Siddesh Kumar, Dhruthi, G.K. Pramod, P. Samrat, M. Sadashiva, „A Critical Review on Heat Treatment of Aluminium Alloys", Materials Today: Proceedings, Vol. 58, 2022, pp. 71-79 https://doi.org/10.1016/j.matpr.2021.12.586

[3]   F. Paray, J.E. Gruzleski, „Modification—a Parameter to Consider in the Heat Treatment of Al-Si Alloys", Cast Metals,Vol.5,1992,https://doi.org/10.1080/09534962.1992.118191 12

[4]   S. Menargues, E. Martín, M.T. Baile, J.A. Picas, „New short T6 heat treatments for aluminium silicon alloys obtained by semisolid forming", Materials Science and Engineering: A, Vol.621,2015,pp.236-242 https://doi.org/10.1016/j.msea.2014.10.078

[5]   M.A. Azmah Hanim, S. Chang Chung, O. Khang Chuan, „Effect of a two-step solution heat treatment on the microstructure and mechanical properties of 332 aluminium silicon cast alloy", Materials & Design, Vol. 32, 2011, pp. 2334-2338 https://doi.org/10.1016/j.matdes.2010.12.040

[6]   M.M Haque, M.A Maleque, „Effect of process variables on structure and properties of aluminium–silicon piston alloy", Journal of Materials Processing Technology, Vol.77, 1998, pp. 122-128   https://doi.org/10.1016/S0924-0136(97)00409-3

[7]   E. Sjölander, S. Seifeddine, „The heat treatment of Al–Si–Cu–Mg casting alloys", Journal of Materials Processing Technology, Vol. 210, 2010, pp. 1249-1259 https://doi.org/10.1016/j.jmatprotec.2010.03.020

[8]   D. K. Dwivedi,R. Sharma, A. Kumar, „Influence of silicon content and heat treatment parameters on mechanical properties of cast Al–Si–Mg alloys", International Journal of Cast Metals Research, Vol. 19, 2006, pp. 275-282 https://doi.org/10.1179/136404606X153867

[9]   P.A. Rometsch, Y. Zhang, S. Knight, „Heat treatment of 7xxx series aluminium alloys—Some recent developments, Transactions of Nonferrous Metals Society of China, Vol. 24, 2014, pp. 2003-2017 https://doi.org/10.1016/S1003-6326(14)63306-9

[10]   P. Cavaliere, E. Cerri, P. Leo, „Effect of heat treatments on mechanical properties and damage evolution of thixoformed aluminium alloys", Materials Characterization, Vol. 55, 2005, pp. 35-42 https://doi.org/10.1016/j.matchar.2005.02.006

[11]   R. Sharma, Anesh, D.K. Dwivedi, „Influence of silicon (wt.%) and heat treatment on abrasive wear behaviour of cast Al–Si–Mg alloys", Materials Science and Engineering: A, Vol. 408, 2005, pp. 274-280 https://doi.org/10.1016/j.msea.2005.08.013

[12]   A.A. Canales, E. Carrera, J. Talamantes-Silva, S. Valtierra, R. Colás," Mechanical properties in as–cast and heat treated Al–Si–Cu alloys", International Journal of Microstructure and Materials Properties, Vol. 7, 2012, pp. 281-300 https://doi.org/10.1504/IJMMP.2012.048518

[13]   R.N. Lumley, R.G. O'Donnell, D.R. Gunasegaram, T. Kittel-Sherri, M. Gershenzon, A.C Yob, I.J. Polmear, „The role of alloy composition in the heat treatment of aluminium high pressure die castings", Metallurgical Science and Tecnology, Vol. 26, 2008

[14]   T.O. Mbuya, B.O. Odera, S.P. Ng'ang'a, „Influence of iron on castability and properties of aluminium silicon alloys: literature review", International Journal of Cast Metals Research, Vol. 16, 2003, pp. 451-465 https://doi.org/10.1080/13640461.2003.11819622

[15]   M. A. Moustafa, F. H. Samuel, H. W. Doty, " Effect of solution heat treatment and additives on the microstructure of Al-Si (A413.1) automotive alloys", Journal of Materials Science, Vol. 38, 2003, pp. 4507–4522

[16]   F. Lasagni, B. Mingler, M. Dumont, H. P. Degischer, „Precipitation kinetics of Si in aluminium alloys", Materials

Science and Engineering: A, Vol. 480, 2008, pp. 383-391
https://doi.org/10.1016/j.msea.2007.07.008

[17] E. Ogris, A. Wahlen, H. Lüchinger, P.J. Uggowitzer, „On the silicon spheroidization in Al–Si alloys", Journal of Light Metals, Vol. 2, 2002, pp. 263-269 https://doi.org/10.1016/S1471-5317(03)00010-5

[18] O. Dezellus, M. Zhe, F. Bosselet, D. Rouby, J.C. Viala, „Mechanical testing of titanium/aluminium–silicon interface: Effect of T6 heat treatment", Materials Science and Engineering: A, Vol. 528, 2011, pp. 2795-2803 https://doi.org/10.1016/j.msea.2010.12.036

[19] M. Farokhpour, M. S. A. Parast, M. Azadi, „ Evaluation of hardness and microstructural features in piston aluminum-silicon alloys after different ageing heat treatments", Results in Materials,Vol.16,2022 https://doi.org/10.1016/j.rinma.2022.100323

[20] N. A. Aristova, I. F. Kolobnev, "Thermal treatment of cast aluminum alloys", 1977 (In Russian)

[21] A. Guinier, „Heterogeneous metallic solid solutions", 1962

[22] R. Slavov, M. Manolov, V. Atanasova," Handbook of casting of non-ferrous metals and alloys", 1976 (In Bulgarian)

[23] Mahle GmbH „Piston materials. In: Pistons and engine testing". ATZ/MTZ-Fachbuch. Vieweg+Teubner Verlag, Wiesbaden.201 https://doi.org/10.1007/978-3-8348-8662-0_4

Investigation of the influence of the manufacturing process on the structure of hypereutectic aluminium-silicon alloys

Boyan Dochev
Faculty of Mechanical Engineering
Technical University of Sofia,
Branch Plovdiv
Plovdiv, Bulgaria
boyan.dochev@gmail.com

Desislava Dimova
Faculty of Mechanical Engineering
Technical University of Sofia,
Branch Plovdiv
Plovdiv, Bulgaria
desislava608738@gmail.com

Mihail Zagorski
Faculty of Industrial Technology
Technical University of Sofia
Sofia, Bulgaria
mihail.zagorski.tu@gmail.com

Plamen Kasabov
Faculty of Mechanical Engineering
Technical University of Sofia,
Branch Plovdiv
Plovdiv, Bulgaria
plamen.kasabov@abv.bg

Bozhana Chuchulska
Faculty of Dental Medicine
Medical University of Plovdiv
Plovdiv, Bulgaria
Bozhana.Chuchulska@mu-plovdiv.bg

Abstract. **Two technological approaches were used to produce the hypereutectic aluminium-silicon alloys AlSi21Cu5MgCr, AlSi21Cu5Cr, AlSi25Cu4Cr and AlSi25Cu5Cr. In one case, alloys were melted from pure metals, metallurgical processing of the melts was carried out, and experimental castings were cast. In the other case, remelting of previously prepared alloys was carried out for casting test castings from the studied alloys, and the metallurgical processing of the melts was carried out at a lower temperature. The influence of the method of obtaining the alloys on their structure has been established.**

Keywords: hypereutectic aluminium-silicon alloys, technological processes, structure

I. INTRODUCTION

The mechanical and operational properties of hypereutectic aluminium-silicon alloys are closely related to the size, shape and distribution of primary and eutectic silicon crystals in their microstructure. Phosphorus is most often used to modify primary silicon crystals, because it forms AlP, which has a crystal lattice identical in appearance to that of silicon and has comparable parameters (AlP-0.5431 nm, Si-0.5421 nm) [1]. Phosphorus modification is a well-known and most commonly used method for influencing the morphology of silicon crystals in the structure of hypereutectic aluminium-silicon alloys, but the process is characterized by its instability. There are data on the influence of the cooling rate of the alloys in the crystallization process, the size of the AlP particles, the melting temperature of the alloys, the content of P in the used ligatures on the process of modifying silicon in this type of slag [2]-[6]. New ligatures have been developed in order to achieve the maximum modifying effect of silicon crystals in the structure of these alloys [7]-[9].

To obtain alloys with increased mechanical and improved operational properties, it is necessary to modify the eutectic silicon crystals. Combinations of phosphorus and other chemical elements are used to modify primary and eutectic silicon [10]-[16].

The aim of the present study is to determine the influence of the method of obtaining the alloys on their structure.

II. MATERIALS AND METHODS

The object of the present study is non-standardized hypereutectic aluminium-silicon alloys. Two technological methods were used to prepare the alloys. In one method, technically pure metals were used, and only chromium was introduced into their composition by using the exothermic flux-ligature Al20Cr80. The alloys are melted in an electric resistance furnace with a graphite crucible under a layer of roof refining flux (10 KCl : 50 NaCl : 10 Na_3AlF_6) in an amount of 0.5% of the mass of the alloy. After melting the aluminium at a temperature of 950º C, the calculated

amount of Si is introduced in portions. After complete absorption of silicon, copper, magnesium (AlSi21Cu5MgCr) and chromium are introduced. The alloys are degassed with argon for 3 min. Metallurgical processing ends with the modification of the alloys. The compositions AlSi21Cu5MgCr, AlSi21Cu5Cr and AlSi25Cu4Cr are modified with 0.04% P, and the AlSi25Cu5Cr alloy with 0.07% P. The phosphorus modifier was introduced into the melts of the investigated alloys through the CuP10 ligature. The alloying and metallurgical processing of the alloys (refining, degassing and modification) is at a melt temperature of 950º C. Casting of experimental castings is at the indicated temperature. Metal casting equipment pre-coated and heated to a temperature of 200º C was used. Table 1, Table 2, Table 3 and Table 4 show the chemical composition of the alloys thus prepared.

TABLE 1 CHEMICAL COMPOSITION OF ALSI21CU5MGCR (%) PURE METALS

Si	Cu	Mg	Cr	Fe	Al
20,82	4,83	1,28	0,374	0,179	rest

TABLE 2 CHEMICAL COMPOSITION OF ALSI21CU5CR (%) PURE METALS

Si	Cu	Cr	Fe	Ni	Al
20,86	4,88	0,899	0,139	0,005	rest

TABLE 3 CHEMICAL COMPOSITION OF ALSI25CU4CR (%) PURE METALS

Si	Cu	Cr	Fe	Ni	Al
24,98	3,69	0,538	0,160	0,005	rest

TABLE 4 CHEMICAL COMPOSITION OF ALSI25CU5CR (%) PURE METALS

Si	Cu	Cr	Fe	Ni	Al
25,31	4,32	0,528	0,122	0,005	rest

An electrical resistance furnace with a graphite crucible was again used to melt the investigated alloys according to the second technological method. The alloys are melted according to the technology described above, and the metallurgical processing involves only refining the melts using flux. Alloys are block cast. The alloys thus prepared were subjected to remelting under a layer of roof refining flux in an amount of 0.5% of the mass of the alloy, and their degassing and modification was carried out at a lower temperature compared to the first method. The working temperature is 830º C. To modify the AlSi21Cu5MgCr, AlSi21Cu5Cr and AlSi25Cu4Cr alloys, phosphorus is again used in the amount of 0.04% P, and the amount of modifier for modifying the AlSi25Cu5Cr alloy is 0.07%, i.e. as in the first method. Casting of experimental castings was at a temperature of 830º C, and the casting equipment used was again pre-coated and heated to a temperature of 200º C. Table 5, Table 6, Table 7 and Table 8 show the chemical composition of the alloys prepared by remelting.

TABLE 5 CHEMICAL COMPOSITION OF ALSI21CU5MGCR (%) REMELTING

Si	Cu	Mg	Cr	Fe	Al
21,01	5,285	1,12	0,373	0,185	rest

TABLE 6 CHEMICAL COMPOSITION OF ALSI21CU5CR (%) REMELTING

Si	Cu	Cr	Fe	Ni	Al
20,89	4,695	0,910	0,139	0,005	rest

TABLE 7 CHEMICAL COMPOSITION OF ALSI25CU4CR (%) REMELTING

Si	Cu	Cr	Fe	Ni	Al
24,63	4,575	0,570	0,240	0,005	rest

TABLE 8 CHEMICAL COMPOSITION OF ALSI25CU5CR (%) REMELTING

Si	Cu	Cr	Fe	Ni	Al
25,48	5,216	0,522	0,149	0,005	rest

Metallographic sections were prepared from the alloys prepared by the two technological methods used. The preparation of the samples for metallographic analysis is carried out according to standard methodology: wet grinding on abrasive paper with an increasing number from № 240 to № 1000 and polishing with diamond paste and lubricant until a mirror surface of the grinds is obtained. The microstructure of the sections thus prepared is revealed with Keller's reagent (1p. HF, 1.5p. HCl, 2.5p. HNO$_3$, 95p. H$_2$O) and clarified with HNO$_3$. The study was performed on a Leica DM ILM microscope using software and the grain measurement and phase analysis module. Grain measurement accuracy is up to hundredths of μm.

The influence of the technological process on the shape and dimensions of the primary and eutectic silicon in the structure of the studied alloys was investigated.

III. RESULTS AND DISCUSSION

The results of the microstructural analysis show that in the structure of the alloys prepared from technically pure metals, the main amount of primary silicon crystals are unmodified, and the eutectic silicon is needle-shaped.

In the AlSi21Cu5MgCr alloy structure, the primary Si crystals are irregular in shape and cannot be measured, and the Si crystals in the eutectic composition are needle-shaped, and most of them have an average linear size of 4.54 μm, but they occur and those with an average linear size of 29.4 μm (Fig. 1).
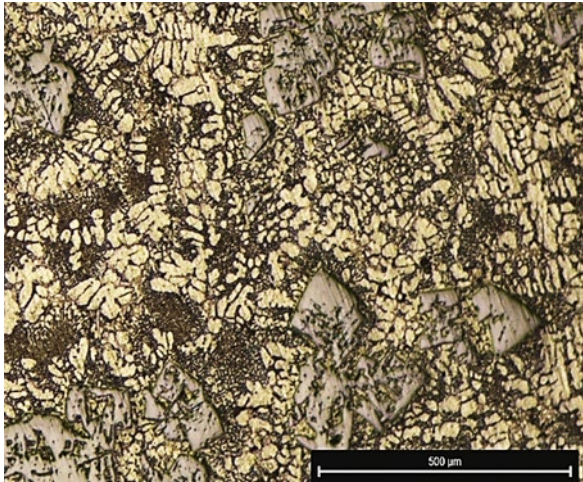
Fig. 1. Microstructure of AlSi21Cu5MgCr alloy (pure metals)

In the AlSi21Cu5Cr alloy structure, the eutectic silicon is in the form of needles with a length of up to 26.7 µm, and the primary silicon is again unmodified (Fig. 2).

Fig. 2. Microstructure of AlSi21Cu5Cr alloy (pure metals)

In the AlSi25Cu4Cr alloy, the main amount of Si crystals are unmodified, but there are also those that have a regular shape and sizes in the range of 35 to 50 µm. Eutectic silicon has a needle-like shape and a length in the range of 30 to 54 µm (Fig. 3).

The bulk of the primary silicon crystals in the AlSi25Cu5Cr alloy structure are unmodified, irregularly shaped, and unmeasurable. That part of the crystals that have been modified is in the form of polywalls with a conditional average diameter of 32 µm. The observed Si in the composition of the eutectic is in the form of needles with an average linear size of 25.7 µm (Fig. 4).
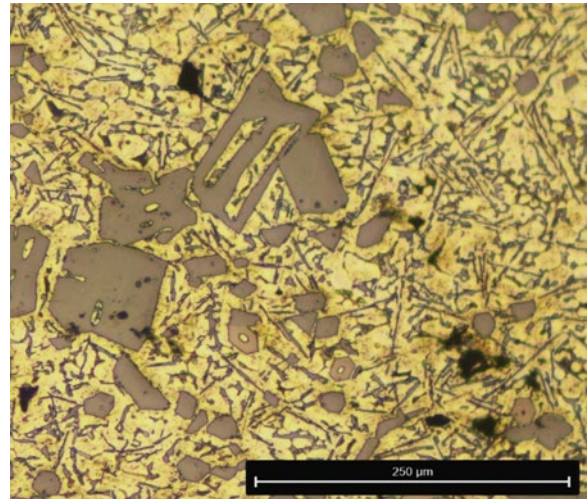
Fig. 3. Microstructure of AlSi25Cu4Cr alloy (pure metals)
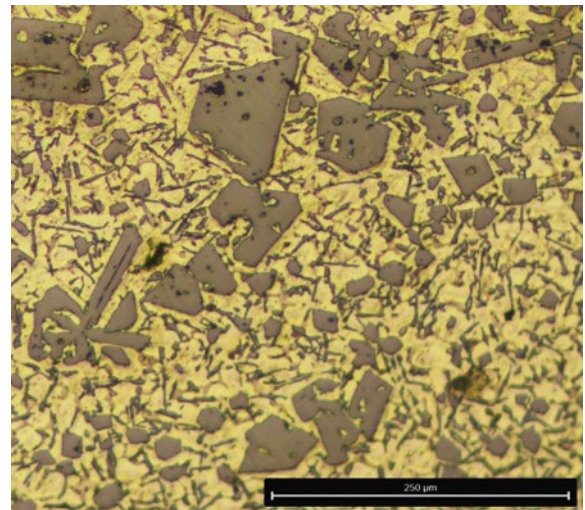
Fig. 4. Microstructure of AlSi25Cu5Cr alloy (pure metals)

In [17], the influence of T6 heat treatment on the structure of hypereutectic aluminium-silicon alloys was studied. A change in the shape and size of the primary silicon crystals after T6 was not observed, but a change was recorded only in the eutectic silicon crystals. In view of this, obtaining such type of alloys with a completely modified structure after casting requires the use of different technological approaches. The structures of the investigated alloys prepared from technically pure metals under the specified conditions are unsatisfactory.

The results of the microstructural analysis of the alloys prepared according to the second of the technological methods used (by remelting previously prepared alloys) show a significant change in the structures of the studied compositions.

In the structure of the AlSi21Cu5MgCr alloy obtained by remelting, the primary silicon crystals are modified and uniformly distributed in the structure. They have a conditional average diameter of 32.4 µm. The silicon crystals in the composition of the eutectic have an average linear size of 8.6 µm (Fig. 5).
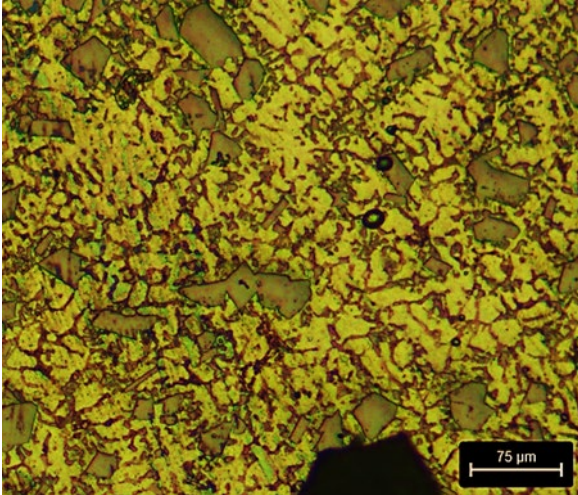
Fig. 5. Microstructure of AlSi21Cu5MgCr alloy (remelting)

The shape of the silicon crystals in the AlSi21Cu5Cr alloy structure (remelt) are polygonal in shape and dimensions not exceeding 28.2 µm. Eutectic silicon is in the form of "needles" with lengths up to 19.8 µm (Fig. 6).
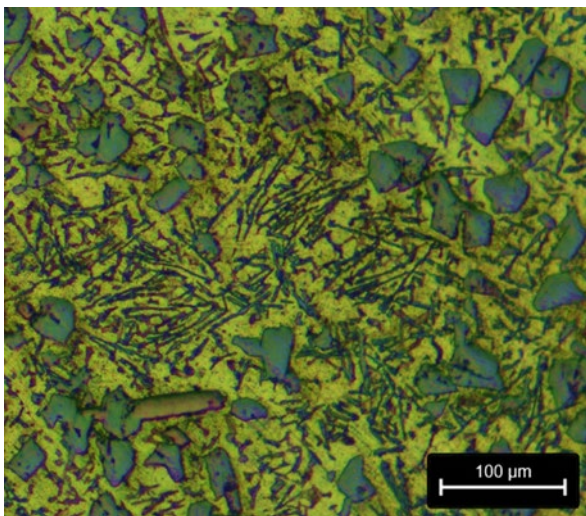
Fig. 6. Microstructure of AlSi21Cu5Cr alloy (remelting)

In the compositions with increased silicon content (AlSi25Cu4Cr and AlSi25CuCr) obtained by remelting previously prepared alloys, the primary silicon crystals are modified and of comparable size. In the AlSi25Cu4Cr alloy structure, silicon crystals have a conditional average diameter of 37.7 µm, and the same ones in the AlSi25CuCr alloy structure have sizes not exceeding 38.8 µm. In both alloys, the eutectic silicon is needle-shaped, and in the AlSi25Cu4Cr alloy it has a linear length of 24.5 µm (Fig. 7), and in the AlSi25Cu5Cr alloy, the eutectic silicon needles reach a length of 28.4 µm (Fig. 8).
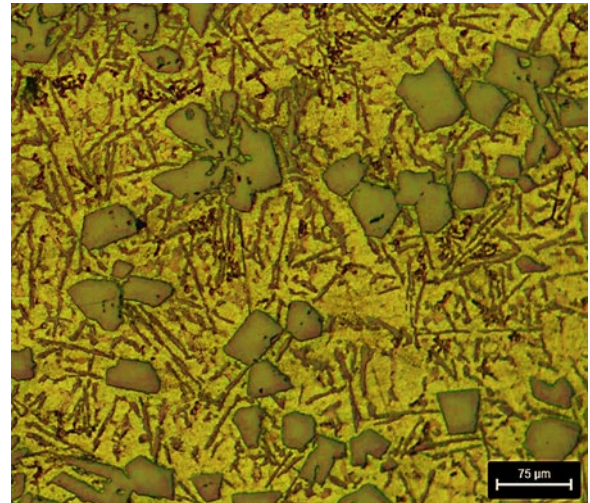
Fig. 7. Microstructure of AlSi25Cu4Cr alloy (remelting)
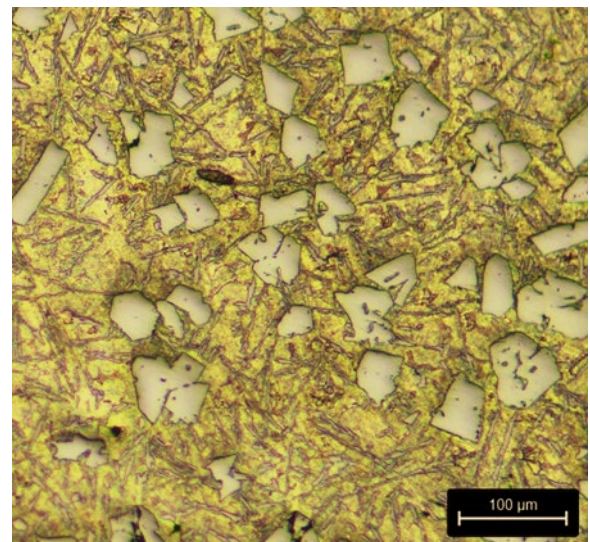
Fig. 8. Microstructure of AlSi25Cu5Cr alloy (remelting)

The results of the conducted research show that the conditions under which the processes of melting, modification and crystallization rate were carried out have a direct influence on the structure of the studied compositions. When using technically pure metals for the preparation of the alloys, the temperature of modification and casting of the experimental castings is 950º C. The low rate of crystallization of the alloys is a prerequisite for the coagulation of the AlP particles, i.e. they acquire large dimensions and as a result they do not represent crystallization centers on which primary silicon crystals can form and grow. From this it follows that not all AlP particles have the role of crystallization centers, the degree of modification is reduced and therefore, in this technological method of preparing the investigated alloys, insufficiently well modified structures were registered - the Si crystals are of irregular shape, large sizes and are unevenly distributed in the structure of the alloys.

In the second technological method of preparing the studied compositions by remelting previously produced alloys, well-modified structures (refine, regularly shaped and evenly distributed Si crystals) were observed. The processes of melting, metallurgical processing of the melts and casting of the experimental castings were carried out at

a temperature of 830º C. In this case, the higher rate of crystallization hinders the growth of the formed AlP particles, i.e. they have the necessary dimensions on which to form and grow the silicon crystals separated in the temperature interval of crystallization of the alloys, as a result of which modified structures are observed.

IV. Conclusions

In order to obtain hypereutectic aluminium-silicon alloys with well-modified structures, not only the amount of the phosphorus modifier used, but also the rate of crystallization has an influence. For the modification of the AlSi21Cu5MgCr, AlSi21Cu5Cr, AlSi25Cu4Cr and AlSi25Cu5Cr alloys prepared by both technological methods, the same amount of modifier was used. In one case, the crystallization rate is lower and the resulting structures are unsatisfactory, and in the case where a higher crystallization rate is provided, well-modified structures are observed.

Carrying out the modification treatment at higher temperatures is a prerequisite for reducing the degree of modification, due to the coagulation of the formed AlP crystallization centers to sizes on which primary silicon crystals cannot form and grow.

In production conditions, it is recommended to use the technological method with remelting of previously prepared material, due to the fact that the processes of melting, metallurgical processing and casting are conducted at lower temperatures, i.e. it is economically more effective, the degree of modification is greater – alloys with well-modified structures are obtained.

REFERENCES

[1] K. Nogita, S. D. McDonald, K. Tsujimoto, K. Yasuda, A. K. Dahle, "Aluminium phosphide as a eutectic grain nucleus in hypoeutectic Al-Si alloys", Microscopy, vol. 53, issue 4, August 2004

[2] L. Zhang, S. Chen, Q. Li, G. Chang, "Formation mechanism and conditions of fine primary silicon being uniformly distributed on single αAl matrix in Al-Si alloys", Materials & Design, vol. 193, August 2020 https://doi.org/10.1016/j.matdes.2020.108853

[3] J. Li, F. S. Hage, X. Liu, Q. Ramasse, P. Schumacher, "Revealing heterogeneous nucleation of primary Si and eutectic Si by AlP in hypereutectic Al-Si alloys", Scientific Reports vol. 6, Article number: 25244, 2016

[4] S. Wang, M. Fu, X. Li, J. Wang, X. Su, "Microstructure and mechanical properties of Al–Si eutectic alloy modified with Al–3P master alloy", Journal of Materials Processing Technology, vol. 255, p. 105-109, May 2018 https://doi.org/10.1016/j.jmatprotec.2017.12.008

[5] G. Zhong, Z. B. Wu, C. Qiu, Y. F. Li, H. Nagaumi, "Study on Absorption Rate of Phosphorus for Hypereutectic Al-Si Alloy Modified with Cu-P", Materials Science Forum, vol. 794-796 p. 112-117 https://doi.org/10.4028/www.scientific.net/MSF.794-796.112

[6] H. Zhang, H. Duan, G. Shao, L. Xu, "Microstructure and mechanical properties of hypereutectic Al-Si alloy modified with Cu-P", Rare Metals, vol. 27, issue 1, p. 59-63, February 2008 https://doi.org/10.1016/S1001-0521(08)60031-5

[7] H.S. Dai, X.F. Liu, "Optimal holding temperatures and phosphorus additions for primary silicon refinement in Al–high Si alloys", Materials Science and Technology, vol.25, issue 10, p. 1183-1188, 2009 https://doi.org/10.1179/174328408X382235

[8] M. Zuo, X. Liu, H. Dai, X. Liu," Al-Si-P master alloy and its modification and refinement performance on Al-Si alloys", Rare Metals, vol. 28, p. 412–417, 2009

[9] Y. Wu, S. Wang, H. Li, X. Liu, "A new technique to modify hypereutectic Al–24%Si alloys by a Si–P master alloy", Journal of Alloys and Compounds, vol. 477, issues 1–2, p.139-144, May 2009 https://doi.org/10.1016/j.jallcom.2008.10.015

[10] C. R. Ho & B. Cantor , "Modification of hypoeutectic Al-Si alloys", Journal of Materials Science, vol. 30, p. 1912–1920, 1995

[11] T. H. Ludwig, P. L. Schaffer, L. Arnberg, "Influence of Phosphorus on the Nucleation of Eutectic Silicon in Al-Si Alloys", vol. 44, p. 5796–5805, 2013

[12] G. K. Sigworth, "The Modification of Al-Si Casting Alloys: Important Practical and Theoretical Aspects", International Journal of Metalcasting , vol. 2, p. 19–40, 2008

[13] A. Wang, L. Zhang, J. Xie, "Effects of cerium and phosphorus on microstructures and properties of hypereutectic Al-21%Si alloy", Journal of Rare Earth, vol. 31, issue 5, p. 522-525, May 2013 https://doi.org/10.1016/S1002-0721(12)60313-5

[14] P. Jiandon, S. Talangkun, "Microstructural Modification Hardness and Surface Roughness of Hypereutectic Al-Si Alloys by a Combination of Bismuth and Phosphorus", Crystals 2022, 12(8), 1026 https://doi.org/10.3390/cryst12081026

[15] Q. Li, B. Li, J. Liu, J. Li, D. Liu, Y. Lan, T. Xia, "Modification of Hypereutectic Al–20 wt%Si Alloy Based on the Addition of Yttrium and Al–5Ti–1B Modifiers Mixing Melt", International Journal of Metalcasting, vol. 13, p. 367–383, 2019

[16] M. Zuo, D. Zhao, X. Teng, H. Geng, Z. Zhang, "Effect of P and Sr complex modification on Si phase in hypereutectic Al–30Si alloys", Materials & Design, vol. 47, p. 857-864, May 2013 https://doi.org/10.1016/j.matdes.2012.12.054

[17] B. Dochev, D. Dimova, M. Zagorski, P. Kasabov, G. Kamburova, "Investigation of the structure of AlSi25Cu4Cr and AlSi25Cu5Cr alloys", Environment. Technology. Resources. Rezekne, Latvia, Proceedings of the 14th International Scientific and Practical Conference. Volume 3, p. 83-89, Print ISSN 1691-5402, Online ISSN 2256-070X https://doi.org/10.17770/etr2023vol3.7181

Comparative analysis of the results of an experimental study with basic equipment and a specially made one to the INSIZE ISR - C002 roughness tester

Kliment Georgiev
Technical University of Sofia, branch Plovdiv
Faculty of Mechanical Engineering;
Department: Mechanical and Instrument Engineering
Plovdiv, Bulgaria
k.georgiev@tu-plovdiv.bg

Pavlina Katsarova
Technical University of Sofia, branch Plovdiv
Faculty of Mechanical Engineering;
Department: Mechanical and Instrument Engineering
Plovdiv, Bulgaria
p_katsarova@abv.bg

Abstract. **The present research presents a comparative analysis between experiments conducted with basic equipment for a portable INSIZE ISR - C002 roughness tester and a specially made for the purpose attachment to the device. An analysis is made of the proposed basic device for working with a portable roughness tester INSIZE ISR - C002, and its shortcomings have been determined. In order to facilitate the operator's work with the device and obtain more accurate results, a special device is developed. It is designed using CAD/CAM products and manufactured using additive printing (3D printing). The additive printing technology used reduces its cost. The manufactured device is analyzed and its advantages and disadvantages are determined. Experiments are conducted with both devices and a comparative analysis of the obtained results is made. An analysis of the measurement system (MSA) is made, through which the results of the conducted experiments were analyzed. The comparative analysis shows a number of advantages of the new device compared to the basic one, which provide a basis for the formulated conclusions and recommendations.**

Keywords: additive printing, basic equipment, comparative analysis, experiments, fixture, measurement System Analysis (MSA), roughness tester, surface roughness.

I. INTRODUCTION

In recent years surface texture were recognized as being significant in many fields. In particular the surface roughness is an important factor in determining the satisfactory performance of the workpiece in engineering applications and the surface roughness were found useful in machinetool monitoring[1].

The performance of an engineering product depends on a number of parameters. Roughness of the surface is one of those parameters that have a significant impact on machined products. Roughness evaluation methods are divided in two basic groups: Qualitative assessment methods and Quantitative assessment methods. Quality assessment methods measure the surface roughness by comparing achieved roughness with roughness gauges. Quantitative assessment methods, in turn, are also divided into two groups: contact methods and non-contact methods. Contact methods assess the resulting roughness using devices called roughness tester, profilographs and profilometers. Non-contact measurements are carried out mainly using microscopes and laser interferometers.

There are numerous parameters for surface roughness that can be used. They correspond to the geometrical characteristics of the workpiece. These parameters are defined and can be found in many standards like SIST EN ISO 4287:2000/AC:2008[2]. The correct choice of filtering length also knows as cut-off length, lr, determines the surface roughness profile. The parameters of the roughness profile are also called surface heights. The roughness parameters can be calculated from the roughness profile after it is filtered. Figure 1 shows a well known surface roughness profile. The assessed length ln is calculated using integral multiplication method of the break length. The highest points of the evaluated profile at the most positions x could be retrieved by a general

function that describes the surface mathematically. In general, surface profiles that were measured with a roughness tester are digitized. The discrete points (x_i, I = 1, ...n) with an increment Dx and corresponding surface roughness heights (z_i, i = 1, …n) can be used to describe the surface roughness profiles [3]. The most commonly used surface parameters are also defined below. The parameter Ra is an arithmetical average of all surface heights in the measured field, also known as center line average of the surface roughness heights (CLA), and is calculated as [3]:

$$Ra = \tfrac{1}{lr} \int |z(x) dx \, lr \, 0 \qquad (1)$$

Rq(RMS) is calculated as the root mean square of surface roughness heights, i.e [3].

$$Rq = \sqrt{\tfrac{1}{lr}} \int |z(x)2 dx \, lr \, 0 \qquad (2)$$
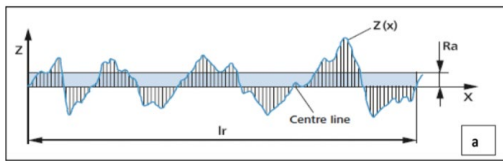
Fig 1. Method of measuring surface roughness Ra [4].

Another commonly used roughness parameter is Rz, which is also called ten-point height. This parameter is more sensitive to occasional high peaks or deep valleys than R_a. It is defined by two methods according to the definition system. The International ISO system defines this parameter as the difference in height between the average of the five highest peaks and the five lowest valleys along the assessment length of the profile [5].

It is calculated as shown on formula (3):

$$Rz = \frac{(P_1 + P_2 + P_3 + P_4 + P_5) - (V_1 + V_2 + V_3 + V_4 + V_5)}{10} \qquad (3),$$

where:

P_1 to P_5 are the highest five peaks measured on the base line,

V_1 to V_5 are the deepest five valleys measured on the base line.

Fig. 2 shows the definition of the parameter Rz.
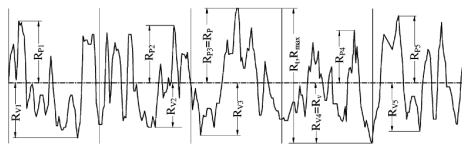
Fig 2 . Ten-point height surface roughness [5].

Measurement of the roughness and determination of the statistical properties of surfaces are significant in many fields of science and engineering. One of the most widely used techniques of surface roughness is probably the mechanical profilometer. With this instrument, the surface is lightly and directly traced by a narrow diamond stylus, which produces a time-varying voltage input proportional to the height of the surface profile. The stylus-type profilometer can surely give true information of the surface profile in the width of the stylus tip is small compared with the lateral size of the surface irregularities [6].

These are the most used surface roughness parameters. Regardless of the measurement method, roughness control devices are divided in two types: stationary and portable. In this current study a portable roughness tester INSIZE ISR - C002 is used. This roughness tester evaluates the measured roughness through the Ra parameter, but it can also show the value of the other roughness parameters. Its basic equipment was analyzed, and an additional device is developed to work as a static instrument. Portable tools for measuring surface roughness are with high accuracy, and are able work in different kind of production environments, and their basic equipment do not allow them to perform their full capacity compared to their use with static equipment. This issue complicates the and requires more preparation time to carry out the measurement and could worsens the accuracy of the results.

The paper presents a developed device which facilitates the work of the roughness tester in dynamic environment, with the use of composite materials and technology for additive (3d) printing. The researches made in a previous paper shows that there is no simular existing device for basing and adjusting to this portable profilometer, but the additive printing technologies are accessible and reliable enough for this task.

The results were evaluated using measurement system analysis (MSA). MSA is an analysis that uses measurement data to evaluate the performance of a manufacturing process. For instance, the decision for adjustment a manufacturing process is commonly based on the measurement data. The data or some of the statistic which are calculated from, are compared with the statistical control limits corresponding to the process. If the comparison indicates that the process is out of the statistical control, an adjustment is made. Otherwise, the process will be allowed to run without any adjustments [7].

The accuracy of the measurement device is defined as its ability to provide output signal close to true value. Accuracy is a more complex and significant problem. The influence of repeatability and particular operators` contribution must not be neglected. The influence of these effects on the measurement method described as R&R (Repeatability and Reproducibility). Performing R&R analysis it is necessary to consider the total nature variability that includes repeatability, reproducibility, variability of parts, and mostly the variability of one part, or the variability from allowed tolerance range [8].

The paper represents an adaptation of MSA to evaluate and compare the results between the basic equipment and the specially designed device. The above makes the study undoubtedly relevant, as there is no evidence of such a device and analysis in the sources examined.

II.   MATERIALS AND METHODS

A. Materials

The experimental studies were conducted in a laboratory environment at controlled room humidity and temperature. The measured parts were shafts used in the manufacture of electric motors. The drawing of the same is shown in Fig. 3 with the indicated roughness by parameter Ra.
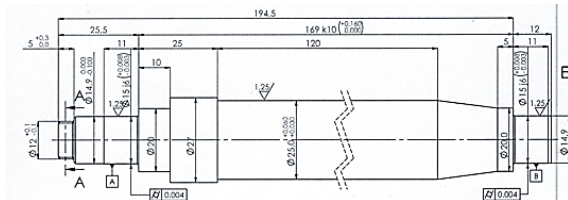
Fig 3. Measured detail

- Analysis of the roughness tester

In this chapter, an analysis of the INSIZE ISR - C002 portable roughness tester and its basic equipment is made, identifying their pros and cons. Fig. 4 illustrates the portable surface roughness tester.

The portable roughness tester "INSIZE ISR - C002" is able to measure the roughness a wide variety of parameters like: Ra, Rq, Rz, Rp, Rt, Rv, R3z, R3y, Rs, Rz (JIS), Rsk, Rp, Rsm, Rsk, Rvk, Mr1, Mr2, Rmax, Ry (JIS), the range is 160µm, the speed is 0.5mm/s, 1mm/s, Memory can save up to 100 measurement results, with weight of 400g, and dimensions of: 141x55x40mm [9].

Fig 4 . Portable roughness tester INSIZE ISR – C002 [9].

Fig. 5 shows the roughness tester with his basic equipment while measuring. The basic equipment includes front mount (1) and back mount (2), which are used to adjust the height and the level of the sensor on the measured detail. The bolts on the from mount are quite loose, as a result adjusting the level and the height of the sensor takes a lot of time and it is not as accurate as it should be.

Fig 5 . Basic setup

The advantages:

- Ergonomic form;
- Easy to use;
- Fast and accurate measurements;
- Easy connections to computer;
- Build in memory up to one hundred measurements;

The disadvantages:

- Basic equipment is making the device hard to use as static roughness tester;
- The additional device for static use is expensive;

The development of a device for mounting the profilemeter would lead to easy positioning, and will increase the ability to measure. Such a device would improve the results and will facilitate the work of the operator.

- Design of the device

The newly developed device must meet all the following requirements:

- Not to obstruct the operations during measurement;
- To be easily mounted on different surfaces;
- To be suitable for additive printing;
- To allow the adjustment of the device and its better stability;
- To ensure better accuracy;

The 3D model of the device designed using SolidWorks is shown at fig. 6. The tool is designed according to the geometry of the roughness tester and its features, and it facilitates the basing and brings the profilometer to ready for measurement. The device an assembly of: a base (1) that holds the roughness tester is, a block that is used for fastening the device to a magnetic stand (2), locking bolts (4) and a bolt with an adjusting nut (3). The base of the produced device is to ensure the stillness without restricting the movements of the sensor. The block (2) is used to mount the device to the magnetic stand.
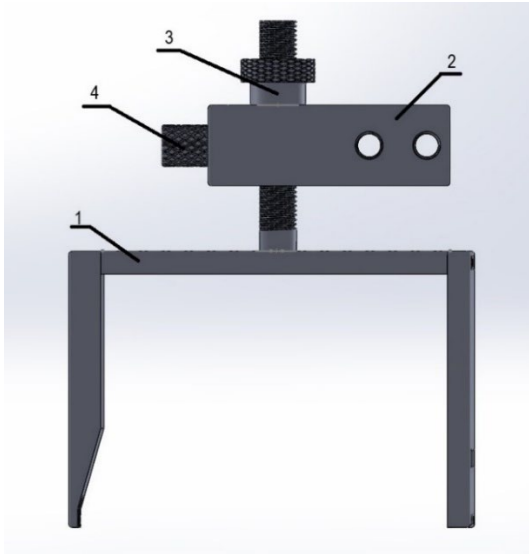
Fig 6 . 3D model of the designed equipment

The development of the technology in the recent decades allows us to use additive (3d) printing technologies. This technology allows us to develop prototypes and devices with different types, shapes, and sizes, easy, and cheap. There is a great variety of materials that can be used in these technologies, and they allow the selection of a suitable material that meets the characteristics and requirements of the 3d model. The developed device is shown on fig.5, and is made by using FDM (fusion deposition modeling), a technology that builds the model layer by layer. Fusion Deposition Modeling (FDM) is one of the most investigated 3d printing methods, because of its ease of use, the low-cost, and because it is applicable for the processing of thermoplastic polymers like: PLA, PETG, PS, Nylon, ABS, and others [10].
The material chosen to produce the device is PLA. PLA is a biodegradable polymer, which is attracting more and more interest in several fields thanks to its good mechanical properties and optical transparency [9].

B. Methods
To evaluate the quality of the measurement process, the Measurement System Analysis (MSA) methodology is used.
The specifics of the comparative analysis between basic equipment and a specially designed device for surface tester INSIZE ISR – C002 requires adaptation of the MSA to obtain the most comprehensive measurement process information. Fig. 7 shows the Measurement System Variability Cause and Effect Diagram.
Compared to the standard application of MSA in which Workpiece (Part), Instrument (Gage) and Person (Appraiser) are considered through their variations: Part variation (PV), Equipment variation (EV), which is basically Repeatability, Appraiser variation (AP), which is basically Reproducibility. GRR is the variance of the internal and external disturbances for the system represented by the combined variance of repeatability and reproducibility [11].
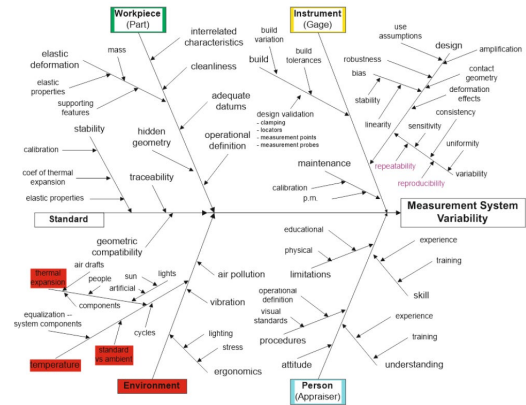
Fig.7 Measurement System Variability Cause and Effect Diagram [11]

Based on these data, we perform MSA using the GRR method according to the Reference Manual, 4th Edition [8], and obtain the following values:

Repeatability is equal to Equipment Variation:

$$EV = \bar{R} * K_1 \qquad (4)$$

(where all the coefficients are chosen from table according to Measurement systems analysis, Reference Manual [8])

Equipment Variation could be presented as %EV=100(EV/ Tolerance), where Tolerance is equal to difference between Upper Tolerance Limit (UTL) and Lower Tolerance Limit (LTL))

Reproducibility is equal to Appraiser Variation (AV)[8]:

$$AV = \sqrt{(\bar{X}_{DIFF} * K_2) - \frac{EV^2}{nr}} \qquad (5)$$

(where all the coefficients are chosen from table according to Measurement systems analysis, Reference Manual [8])

Appraiser Variation could be presented as %AV=100(AV/Tol). The influence of the operator can be disregarded because it has an insignificant impact on the outcome if he performs his duties conscientiously.

Gage Repeatability & Reproducibility [8]:

$$GRR = \sqrt{EV^2 + AV^2} \qquad (6)$$

and

$$\%GRR=100(GRR/Tol) \qquad (7)$$

Part Variation:

$$PV = R_p * K_3 \qquad (8)$$

(where all the coefficients are chosen from table according to Measurement systems analysis, Reference Manual [8])

Result could be presented as [8]:

$$\%PV = 100(PV/Tol) \qquad (9)$$

All abbreviations used in the current paper are consistent with the Reference Manual, 4th Edition [8].

An adaptation of the MSA is used to analyze the results obtained in this report. The modification consists in using the same measurement system, but with different fixtures for basing the INSIZE ISR - C002 roughness instrument. In this situation all measurements were carried out by the same operator and the same measuring instrument. The purpose of this adaptation is to investigate the influence of the fixtures used on the results obtained.

III. RESULTS AND DISSCUSSION

The experiments were conducted with ten parts, each of which is measured three times. One set of measurements is made by one operator with the basic standard equipment. With the custom-made one, two series of measurements were carried out with two operators. Classical MSA was used to check the condition of the measurement system with both operators. An adapted MSA is then applied with only one operator and the influence of the fixtures on the measurement system is investigated. The experimental setup of the experiments performed with the baseline fixture is shown in Fig. 4. Due to the specificity of the controlled workpiece in the measurement, it is based in a prism, evident from Fig. 4. In order to realize this measurement, flat-parallel end measures were additionally used. Any additional interference in the measurement setup can contribute to more errors in the measurement results.

The experimental setup of the measurement with the developed new device is shown in Fig. 8, where (1) is a prism for basing the shafts, (2) is the newly designed device, (3) is the magnetic stand, (4) – roughness tester and (5) is the testing probe. The fixture allows quick and easy positioning and adjustment of the instrument relative to the workpiece being measured.

All laboratory measurements were conducted on sufficiently stable base equipment that made vibrations in the measurement system negligible. In addition, both fixtures have locking devices that are used in the presetting. The positioning accuracy of the device relative to the workpiece is controlled by the sensitive sensor positioning scale built into the device. To reduce the influence of the operator the measurements were carried out by having the instrument controlled remotely via software installed on an accompanying PC.
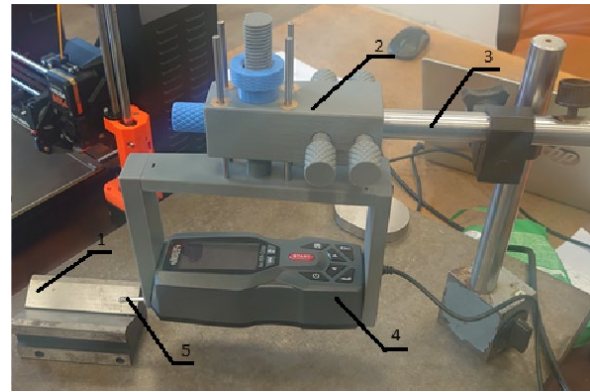
Fig.8 Experimental setup with the designed device

In Fig. 9, the experimental results of the measurements are presented, where operator A and B are understood to be the two measurement operators. Based on these, a standard MSA analysis is performed with two operators using the specially developed attachment to the INSIZE ISR - C002 roughness tester. Fig. 10 shows the results of the analysis performed.

APPRAISER/ TRIAL #		PART											AVERAGE
		1	2	3	4	5	6	7	8	9	10		
1. A	1	2.023	2.076	2.114	2.077	1.996	2.059	2.072	2.061	2.061	2.063		2.060
2.	2	2.051	2.063	2.049	2.064	2.018	2.055	2.012	2.043	2.054	2.068		2.048
3.	3	2.068	2.083	2.109	2.106	2.019	2.046	2.021	2.037	2.049	2.007		2.055
4.	AVE	2.05	2.07	2.09	2.08	2.01	2.05	2.04	2.05	2.05	2.05	$\bar{X}_a$=	2.054
5.	R	0.04	0.02	0.06	0.04	0.02	0.01	0.06	0.02	0.01	0.06	$\bar{r}_a$=	0.037
6. B	1	2.034	2.086	2.123	2.082	2.005	2.069	2.083	2.075	2.085	2.073		2.072
7.	2	2.063	2.073	2.061	2.075	2.025	2.068	2.023	2.052	2.065	2.085		2.059
8.	3	2.078	2.095	2.121	2.128	2.028	2.056	2.035	2.052	2.066	2.025		2.068
9.	AVE	2.06	2.08	2.10	2.10	2.02	2.06	2.05	2.06	2.07	2.06	$\bar{X}_b$=	2.066
10.	R	0.04	0.02	0.06	0.05	0.02	0.01	0.06	0.02	0.02	0.06	$\bar{r}_b$=	0.038
11. C	1												
12.	2												
13.	3												
14.	AVE											$\bar{X}_c$=	
15.	R											$\bar{r}_c$=	
16. PART												X=	2.060
AVERAGE		2.05	2.08	2.10	2.09	2.02	2.06	2.04	2.05	2.06	2.05	$\bar{R}_p$=	0.081
17. $(\bar{r}_a + \bar{r}_b + \bar{r}_c)$ / (# OF APPRAISERS) =												$\bar{R}$=	0.037
18. $\bar{X}_{DIFF}$ = (Max $\bar{X}$ - Min $\bar{X}$) =												$\bar{X}_{DIFF}$=	0.012
19. * UCL_R = $\bar{R}$ x D_4 =												UCL_R=	0.096

Fig.9 Measurement data, two appraisers, new device

Measurement Unit Analysis					% Tolerance (Tol)		
Repeatability - Equipment Variation (EV)							
EV	=	$\bar{R}$ x K_1		Trials	K_1	% EV	=	100 (EV/Tol)
	=	0.037 x 0.5908		2	0.8862		=	100(0.022/0.133)
	=	0.022		3	0.5908		=	16.51
Reproducibility - Appraiser Variation (AV)							
AV	=	$\{(\bar{X}_{DIFF} \times K_2)^2 - (EV^2/nr)\}^{1/2}$				% AV	=	100 (AV/Tol)
	=	$\{(0.012 \times 0.7071)^2 - (0.022 ^2/(10 \times 3))\}^{1/2}$					=	100(0.008/0.133)
	=	0.008					=	5.71
			Appraisers	2	3			
n = parts	r = trials		K_2	0.7071	0.5231			
Repeatability & Reproducibility (GRR)						% GRR	=	100 (GRR/Tol)
GRR	=	$\{(EV^2 + AV^2)\}^{1/2}$		Parts	K_3		=	100(0.023/0.133)
	=	$\{(0.022^2 + 0.008^2)\}^{1/2}$		2	0.7071		=	17.46
	=	0.023		3	0.5231	Gage system may be acceptable		
Part Variation (PV)				4	0.4467			
PV	=	R_P x K_3		5	0.4030	% PV	=	100 (PV/Tol)
	=	0.081 x 0.3146		6	0.3742		=	100(0.025/0.133)
	=	0.025		7	0.3534		=	19.11
Tolerance (Tol)				8	0.3375			
Tol	=	Upper - Lower / 6		9	0.3249	ndc	=	1.41(PV/GRR)
	=	(2.4 - 1.6) / 6		10	0.3146		=	1.41(0.025/0.023)
	=	0.133					=	1
						Gage discrimination low		
For information on the theory and constants used in the form see *MSA Reference Manual*, Fourth edition.							

Fig.10 MSA results.

The analysis shows the variation of the results in terms of instrument EV (Equipment variation) and operator AV (Appraiser variation). = 5.71%. The value of EV = 16.51% indicates the influence of equipment versus meter variance of the results. The value of AV = 5.71%, indicates a slight influence of the operator relative to the results obtained. Based on these results, an adapted MSA is performed in which the measurements were carried out by a single operator and the influence of the fixtures against the obtained results is investigated. The value of GRR (Gage Repeatability & Reproducibility) = 17.46% indicates that the results of the measurement system can be accepted as the GRR value < 30%.

Fig. 11 shows the measurement data with the two fixtures, due to the specificity of the adapted MSA, operator A is understood to be the baseline fixture and operator B is assumed to be the newly designed fixture.

APPRAISER/ TRIAL #		1	2	3	4	5	6	7	8	9	10		AVERAGE
1. A	1	2.104	2.077	2.148	2.088	2.032	2.066	2.076	2.04	2.114	2.08		2.083
2.	2	2.063	2.078	2.105	2.068	2.023	2.058	2.029	2.081	2.073	2.131		2.071
3.	3	2.15	2.092	2.12	2.214	2.025	2.048	2.085	2.116	2.104	2.075		2.103
4.	AVE	2.11	2.08	2.12	2.12	2.03	2.06	2.06	2.08	2.10	2.10	$X_a=$	2.085
5.	R	0.09	0.02	0.04	0.15	0.01	0.02	0.06	0.08	0.04	0.06	$r_a=$	0.055
6. B	1	2.023	2.076	2.114	2.077	1.996	2.059	2.072	2.06	2.06	2.063		2.060
7.	2	2.051	2.063	2.049	2.064	2.018	2.055	2.012	2.043	2.054	2.068		2.048
8.	3	2.068	2.083	2.109	2.106	2.019	2.046	2.021	2.037	2.049	2.007		2.055
9.	AVE	2.05	2.07	2.09	2.08	2.01	2.05	2.04	2.05	2.05	2.05	$X_b=$	2.054
10.	R	0.04	0.02	0.06	0.04	0.02	0.01	0.06	0.02	0.01	0.06	$r_b=$	0.036
11. C	1												
12.	2												
13.	3												
14.	AVE											$X_c=$	
15.	R											$r_c=$	
16. PART AVERAGE		2.08	2.08	2.11	2.10	2.02	2.06	2.05	2.06	2.08	2.07	X=	2.070
												$R_p=$	0.089
17.	$(r_a + r_b + r_c) / (\# \text{ OF APPRAISERS}) =$											R=	0.046
18.	$x_{DIFF} = (\text{Max X - Min X}) =$											$X_{DIFF}=$	0.031
19.	* $UCL_R = R \times D_4 =$	APPRAISER		A			OUT OF CONTROL					$UCL_R=$	0.117

Fig.11 Measurement data from adapted MSA

Measurement Unit Analysis					% Tolerance (Tol)			
Repeatability - Equipment Variation (EV)								
EV	=	R x K_1		Trials	K_1	% EV	=	100 (EV/Tol)
	=	0.046 x 0.5908		2	0.8862		=	100(0.027/0.133)
	=	0.027		3	0.5908		=	20.16
Reproducibility - Device Variation (DV)								
AV	=	$\{(X_{DIFF} \times K_2)^2 - (EV^2/nr)\}^{1/2}$				% DV	=	100 (AV/Tol)
	=	$\{(0.031 \times 0.7071)^2 - (0.027 {}^2/(10 \times 3))\}^{1/2}$					=	100(0.022/0.133)
	=	0.022					=	16.22
				Appraisers				
				2	3			
n = parts	r = trials		K_2	0.7071	0.5231			
Repeatability & Reproducibility (GRR)						% GRR	=	100 (GRR/Tol)
GRR	=	$\{(EV^2 + AV^2)\}^{1/2}$		Parts	K_3		=	100(0.035/0.133)
	=	$\{(0.027^2 + 0.022^2)\}^{1/2}$		2	0.7071		=	25.88
	=	0.035		3	0.5231	Gage system may be acceptable		
Part Variation (PV)				4	0.4467			
PV	=	R_P x K_3		5	0.4030	% PV	=	100 (PV/Tol)
	=	0.089 x 0.3146		6	0.3742		=	100(0.028/0.133)
	=	0.028		7	0.3534		=	20.92
Tolerance (Tol)				8	0.3375			
Tol	=	Upper - Lower / 6		9	0.3249	ndc	=	1.41(PV/GRR)
	=	(2.4 - 1.6) / 6		10	0.3146		=	1.41(0.028/0.035)
	=	0.133					=	1
						Gage discrimination low		
For information on the theory and constants used in the form see *MSA Reference Manual*, Fourth edition.								

Fig.12 Adapted MSA results

The results of the adapted MSA (Fig. 12) analysis show a value of EV = 20.16%, the value obtained is close to the value from the classical MSA. The value of DV

(Device Variation) = 16.22% is significantly higher than that of the standard MSA. GRR = 25.88%, the obtained value is less than 30%, accordingly the measurement system can be accepted.

Looking at the data obtained from the two MSAs, the high EV values are striking. Both analyses show similar EV values around 20%, which means that the equipment influences the measurement results, but this influence is not particularly high. The values obtained for the AV and DV coefficient (in the adapted MSA), differ significantly for the two analyses. In the first analysis, the coefficient AV = 5.71%, indicates the insignificant influence of the operator on the results of the studies. The second MSA shows a significantly higher value of DV = 16.22%, indicating a significant influence of the operator relative to the measurement results. In this situation, since the operators are replaced by fixtures therefore, the influence of the fixtures on the obtained results are significant. It can be seen from the presented results (Fig. 11) that operator A (the base fixture) degrades the results.

IV. Conclusions

1) The MSA results indicate that the results obtained from both analyses are acceptable because the GRRs (Gage Repeatability & Reproducibility) < 30%.

2) The data from the MSA analysis shows that the results obtained with the new device are significantly better.

3) MSA can not only be used to compare operators and instrumentation, but can also be adapted to study the influence of other experimental equipment.

4) The newly designed instrument fixture INSIZE ISR - C002 facilitates instrument operation, reduces measurement preparation time and reduces basing error.

AKNOWLEDGEMENS

References

[1] Whitehouse, D. J. (1997). Surface metrology. Measurement science and technology, 8(9), 955.

[2] G. Eason, B. Noble, and I. N. Sneddon, "On certain integrals of Lipschitz-Hankel type involving products of Bessel functions," Phil. Trans. Roy. Soc. London, vol. A247, pp. 529–551, April 1955.

[3] J. Clerk Maxwell, A Treatise on Electricity and Magnetism, 3rd ed., vol. 2. Oxford: Clarendon, 1892, pp.68–73.

[4] Hamed, M., Zedan, Y., Samuel, A. M., Doty, H. W., & Samuel, F. H. (2019). Milling parameters of Al-Cu and Al-Si cast alloys. The International Journal of Advanced Manufacturing Technology, 104, 3731-3743.

[5] Gadelmawla, E. S., Koura, M. M., Maksoud, T. M., Elewa, I. M., & Soliman, H. H. (2002). Roughness parameters. Journal of materials processing Technology, 123(1), 133-145.

[6] Asakura, T. (1978). Surface roughness measurement. Speckle metrology, 11-49.

[7] Measurement systems analysis (MSA), Reference Manual, Fourth Edition, Copyright 2010 Chrysler Group LLC, Ford Motor Company, General Motors Corporation, ISBN#: 978-1-60-534211-5

[8] Dian, M., & Hodinář, L. (2018). The GRR a Fundamental Tool for Dealing with Measurement System Variability. Manufacturing Technology, 18(1), 29-34.

[9] Portable roughness tester INSIZE ISR – C002, available at: https://www.grainger.com/product/INSIZE-Handheld-Surface-Roughness-463L43, 15.02.2024.

[10] Coppola, B., Cappetti, N., Di Maio, L., Scarfato, P., & Incarnato, L. (2018). 3D printing of PLA/clay nanocomposites: Influence of printing temperature on printed samples properties. Materials, 11(10), 1947.

[11] Hristov, M. H. (2023, September). SPC as an Instrument for Implementation and MSA as an Instrument for Evaluation of Non-Linear Object Based Temperature Compensation into Shop Floor CMM. In 2023 15th Electrical Engineering Faculty Conference (BulEF) (pp. 1-9). IEEE.

[12] Qiu P., Introduction to Statistical Process Control, 2014 by Taylor & Francis Group, LLC, ISBN-13: 978-1-4822-2041-4 (eBook - PDF)

[13] https://www.aiag.org/

Investigating the Repeatability of 3D Printers Using a Multi-Sensor Measurement System

Borislav Georgiev
Technical University of Gabrovo
Gabrovo, Bulgaria
gborislav@gbg.bg

Tsanko Karadzhov
Technical University of Gabrovo
Gabrovo, Bulgaria
karadjov_st@abv.bg

Abstract. **The repeatability of three-dimensional printers is very important because it determines how accurately a model can be reproduced. Repeatability depends on many factors such as printer quality, software settings, material quality, etc This paper evaluates the repeatability of an Openware desktop three dimensional printers in terms of the resulting standard deviation from a set of samples using a multi-sensor measuring machine. Details with optimal parameters were printed. Statistical analysis was performed on this set of samples. From the statistical analysis of the dimensional deviation data, the repeatability of the printer was analyzed.**

Keywords: Repeatability, Openware 3D printer, Statistical analysis.

I. INTRODUCTION

3D printing technology, also known as additive manufacturing (AM) has undergone significant development in recent decades, becoming a key element in many areas of manufacturing, design and engineering. The material layering method that underlies 3D printing allows the creation of complex and customized objects that are difficult or impossible with traditional manufacturing methods [1]. However, issues regarding the reproducibility, accuracy, quality, mechanical strength, resistance to external factors, production speed, and economic efficiency of printed parts remain the subject of intensive research and development [1].

Among the various 3D printing techniques, Fused Deposition Modeling (FDM) is one of the most widespread methods due to its cost-effectiveness and easy application [2]. FDM works by extruding molten plastic material through a nozzle to create an object layer by layer. However, the process faces challenges related to the control of accuracy and quality of the final products, which are critical for the widespread adoption of the technology in industry [3]. In this regard, one of the important aspects for the quality of the final product is the geometric accuracy of the details, including the accuracy of the linear dimensions, deviations from the form and mutual location of the surfaces and axes of the details, since these parameters are essential for their functionality and reliability.

The accuracy and reproducibility of FDM processes can be affected by numerous factors, including the type of materials used, printer settings, as well as environmental conditions [4]. A detailed study of these factors and their optimization is essential to improve the quality of 3D printed products and expand the application areas of the technology.

Against the background of these challenges, the current report focuses on investigating the reproducibility and accuracy of FDM 3D printers through a multi-sensor measurement system. The aim is to identify the key factors affecting the quality of the manufactured parts and to propose methods for their optimization. The results of the research can contribute through new knowledge and reliable criteria in the field of additive manufacturing, providing valuable guidance for professionals or specialists who are involved in the design and creation of new products, software, technologies or systems in the field of 3D printing.

II. MATERIALS AND METHODS

3D printers typically use a material in the form of a filament, most made from plastic, which is fed into the printer, melted, and overlaid onto the platform to form the object. This process is known for its extreme precision and ability to create objects with complex geometries, which is a significant advantage over traditional manufacturing methods. Figure 1 shows the most basic materials that are used for 3D printing.

3D printing technology finds application in a multitude of fields due to its versatility and efficiency. It features the ability to produce complex shapes with less material waste, making it a preferred method in a variety of industries, including medicine.

The quality of 3D printing depends on several factors, including the resolution of the printer, the quality of the

slicing software used, the speed of printing, and the materials themselves. The importance of high-quality consumables, effective temperature control and regular equipment calibration are critical to achieving optimal results.
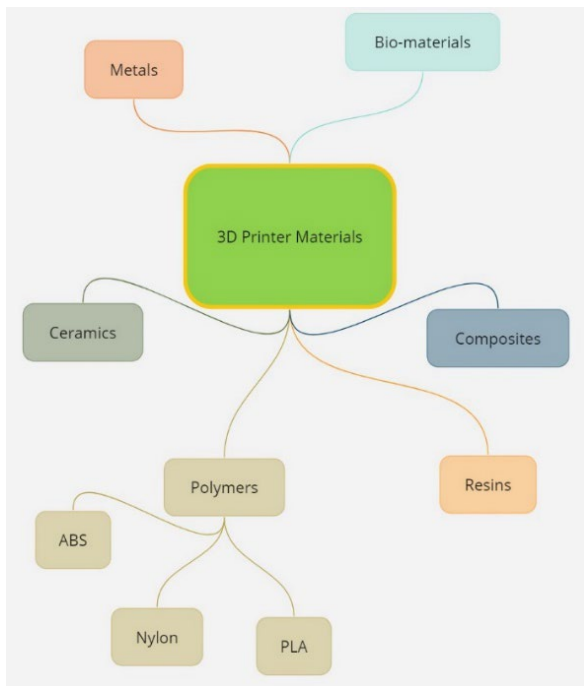
Fig. 1.   3D Printer Materials

A. Resolution

Nozzle resolution refers to the printer's ability to control the thickness of each deposited layer. Higher resolution usually results in better accuracy. Most FDM 3D printers have a nozzle resolution between 50 and 300 micrometers.

B. Positioning accuracy

This refers to the printer's ability to maintain a constant nozzle position during printing. Better positioning precision ensures layers are laid evenly and accurately, resulting in improved overall accuracy.

C. Material quality

The type of material used can also affect the accuracy of an FDM 3D printer. Some materials may be more susceptible to warping or warping during the cooling process, resulting in reduced accuracy. Using high-quality materials with low coefficients of thermal expansion can help improve accuracy.

D. Temperature and speed

The optimal printing temperature and speed can significantly affect the accuracy of the FDM 3D printer. Printing at too high a temperature can cause material to bleed or warp, while printing at too low a temperature can result in poor adhesion between layers. Likewise, printing at too high a speed can result in insufficient bonding between layers, resulting in reduced accuracy.

E. Print Settings

Printer settings such as layer height, fill density, and fill pattern can also affect accuracy. Optimizing these settings for the specific model and material can help achieve better accuracy.

F. Temperature Control

Effective temperature control is critical to maintaining consistent material properties during printing. Insufficient temperature control can lead to problems such as material leakage, poor layer bonding and reduced accuracy.

G. Calibration and Maintenance

Regular calibration and maintenance of the FDM 3D printer can help ensure its accuracy over time [5]. This includes checking and replacing worn parts, cleaning the nozzles, and performing regular calibration tests to verify the printer's performance.

In general, the accuracy of FDM 3D printers can be affected by various factors, including print setup, material quality, and machine performance. By optimizing these factors, it is possible to achieve a high degree of accuracy with FDM 3D printers.

PLA (polylactic acid) is a biodegradable thermoplastic material that is often used in 3D printing due to its relatively low cost, ease of processing, and environmental compatibility. The coefficient of thermal expansion of PLA is approximately $40\text{-}60 \times 10^{-6}$ mm/mK. This value may vary slightly depending on the specific formulation and environmental conditions.

The coefficient of thermal expansion (CTE) is a measure of how much a material expands or contracts when the temperature changes. In the case of PLA, it shows that the material tends to expand or contract uniformly in all directions when the temperature changes. This property is important for 3D printing as it helps ensure that printed objects retain their shape when exposed to changing temperatures. However, it is important to note that the coefficient of thermal expansion of PLA is relatively high compared to other materials used in 3D printing, such as ABS (acrylonitrile butadiene styrene) or PETG (polyethylene terephthalate glycol). This means that objects printed using PLA may be more prone to warping or warping at high temperatures or significant temperature fluctuations. To minimize this risk, it is ESSENTIAL TO FOLLOW THE RECOMMENDED OPERATING temperatures for PLA and avoid exposing the printed objects to extreme temperature changes.

III.   RESULTS AND DISCUSSION

After checking and calibrating the printer, 35 pieces of solid cubes (fig.2) with dimensions of 20 mm on each side were printed. The slicing application used is CURA (Cura is an open source slicing application for 3D printers), with 25% material fill. The time for printing the details is 1 hour and 08 minutes. The material required for the process is PLA with a working temperature of 190-230 ℃ with a diameter of 1.75mm ±0.05mm and the cost for each part at 25% filling is 6 grams. The ambient temperature during printing is 20-21℃, and after several experiments, the most optimal temperature setting for the printer plate was calculated to be 70℃ and for the nozzle 220℃. Print speed is 20 mm/s, layer height is 0.2 mm and wall thickness is 1.5 mm.
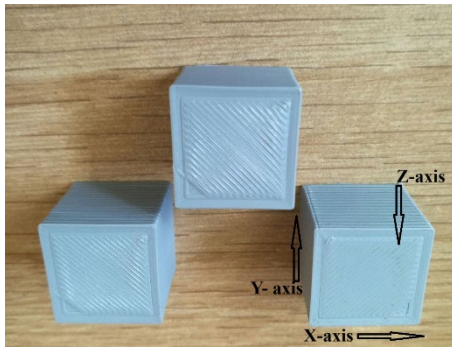
Fig. 2.   Magnetization as a function of applied field.

The accuracy of the printer along the x and y axes is ± 0.5% with a lower limit of ± 0.5 mm. On the z-axis it is ± 0.5% with a lower limit of ± 0.15 mm.

The measurement of the printed parts was done with OPTIV M 4.4.3 multisensor and optical coordinate measuring machines (CMM), which provides a measurement accuracy of ±0.025 mm (0.001 inch) or better, depending on the specific configuration and application [6], [7].

The printed solid cubes were measured on a CMM three times to minimize random measurement error. Deviations observed along the three sides in printed parts were recorded. Descriptive statistics were calculated from these readings (Table 1, Table 2). In these descriptive statistics, indicates a measure of central tendency and a measure of dispersion.

Cp and Cpk are statistics that are used to evaluate the ability of a process to meet specifications. Cp (Process Capability Index) is calculated when the process is under statistical control. This usually refers to a mature process that has been around for some time. This metric is based on the process sigma value, which is determined by movement, range, or sigma control charts. The purpose of Cp is to determine the ability of the process to approach the upper and lower specification limits. Cpk (Process Capability Index with Process Centered) is also calculated when the process is under statistical control. This metric takes into account both the capability of the process and its location. The purpose of Cpk is to determine the ability of the process to meet specifications while also considering the process average.

When Cp and Cpk are close in value, the process average is near the middle of the specification limits. When Cp is greater than Cpk, the average value is closer to one of the specification limits (Table 1).

Once we understand our process, we can make a good decision about how to prioritize our process improvement efforts.

On the X axis, the process is not capable, not centered, on the Y axis, the process is capable, centered and on the Z axis, the process is not capable, centered (fig.3,4 and 5).

"Sk" measures the asymmetry of a data distribution. It determines whether the probability function is skewed to the right (positive skewness) or to the left (negative skewness). If the skewness is zero, the distribution is symmetric. Positive skewness indicates a right tail (tail of

values to the high side), while negative skewness indicates a left tail (tail of values to the low side see Sk on the Z axis). Skewness values typically range from -2 to 2.

TABLE 1 SIZE DEVIATION ALONG THE X, Y, AND Z AXES

	X-axis	**Y-axis**	**Z-axis**
Arithmetic mean	20.22231	20.00703	19.97286
St.deviation	0.16254	0.17668	0.11523
Range	0.639	0.698	0.428
Min.value	20.004	19.706	19.741
Max.value	20.643	20.404	20.169
USL	0.5	0.5	0.15
LSL	-0.5	-0.5	-0.15
Sk	0.49032	-0.04935	-0.23290
Ku	-0.41692	-0.83096	-1.01929
Cp	1.02541	0.94334	0.43391
Cpk	0.56949	0.93008	0.35539
Total rejected parts	1	0	6
Reject USL	1	0	1
Reject LSL	0	0	5
Reject %	2.85714	0	17.14286
Reject % USL	2.85714	0	2.85714
Reject % LSL	0	0	14.28571

"Ku" measures the curvature or flatness of the data distribution. High kurtosis (positive kurtosis) indicates a sharper peak (peak) in the center of the distribution, suggesting that most data points are concentrated around the mean. Conversely, low kurtosis (negative kurtosis) shows a flatter peak, meaning there are more values away from the mean. Curtrose values usually range from 0 to 10.
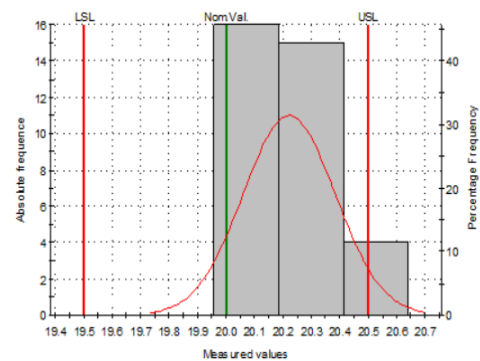
Fig. 3.   X-axis histo chart.

The standard deviation shows how much variation there is in the values of the random variable. When the standard deviation is low, the values are close to the population mean (expected value). When the standard deviation is high, the values are spread over a wider range. The standard deviation is calculated as the square root of the variance of the random variable.
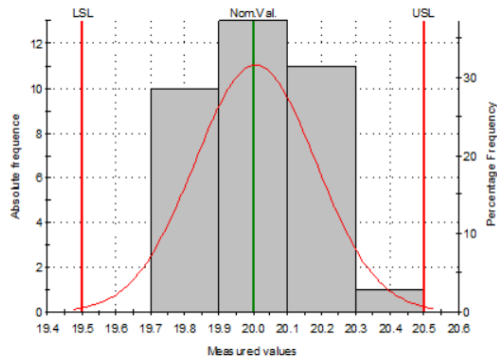
Fig. 4.   Y-axis histo chart.

Fig. 5.   Z-axis histo chart.

TABLE 2 PARALLELISM DEVIATION ALONG THE X, Y, AND Z AXES

	X-axis	Y-axis	Z-axis
Arithmetic mean	0.811154	1.15246	0.44471
St.deviation	0.19926	0.25941	0.14485
Range	0.696	0.988	0.512
Min.value	0.52000	0.893	0.209
Max.value	1.21600	1.88100	0.721
USL	0.1	0.1	0.1
LSL	0	0	0
Sk	0.26886	1.23894	0.20572
Ku	-0.79976	0.80536	-1.00817
Cp	0.08364	0.06425	0.11506
Cpk	-1.19029	-1.35237	-0.79326
Total rejected parts	35	35	35
Reject USL	35	35	35
Reject LSL	0	0	0
Reject %	100	100	100
Reject % USL	100	100	100
Reject % LSL	0	0	0

The standard deviation is expressed in the same unit as the data, making it useful for comparison and analysis. So, the standard deviation helps us understand how much variation there is in the values of the random variable and how far they are from the mean. In conclusion, the standard deviation is an important tool for data analysis and helps to understand the distribution and mixing of values in our measurements. Knowledge of the distribution of data around the mean is essential in statistics and data analysis.

Parallelism tolerance in 3D printing refers to the maximum distance that layers can deviate from each other in terms of parallelism. This is an important factor in ensuring the quality and accuracy of the printed object.

In a typical 3D printer, tolerances from parallelism typically range from 0.05mm to 0.1mm. This value can be affected by various factors such as material quality, printing temperature, printing speed and machine design. Some high-quality 3D printers can even achieve deviations below 0.05mm.

It is important to note that the tolerance for parallelism does not necessarily mean that all layers will be perfectly equal. In reality, this is unlikely due to the nature of the 3D printing process. In this case (see table 2) the deviations from parallelism of the entire detail are above the permissible values. However, keeping the parallelism tolerance within the specified range ensures that the differences between the layers are minimal and will not significantly affect the overall quality and appearance of the final product.

From the measurements made, we can conclude that the printer used in this experiment has significant deviations from the parameters provided by the FDM 3D printing technology. However, several factors can affect repeatability:

The use of high-quality materials with consistent characteristics is essential to maintain repeatability. Changes in material properties such as viscosity, melting point and color can result in variations in the final product. Regular printer maintenance, including nozzle cleaning, replacement of worn parts and system calibration, can help maintain accuracy and repeatability. It is necessary to use the recommended media and printer settings provided by the manufacturer. This includes optimum nozzle temperature, bed temperature, print speed and layer height. Implementing quality control processes, such as inspecting the model before printing, monitoring the printing process, and measuring the finished product, can help identify and fix problems that affect repeatability. Ensuring that operators are well trained and understand the 3D printing process as well as potential sources of error can improve overall repeatability. Although FDM 3D printers generally have good repeatability, it is important to continuously monitor and optimize the process to maintain consistent print quality. With the right practices and maintenance, it is possible to achieve a high degree of repeatability with FDM 3D printers.

IV.   CONCLUSION

This report presents a study that focuses on the repeatability and accuracy of 3D printers using Fused Deposition Modelling (FDM) technology. By analysing the influence of various factors such as printer resolution, material quality, print settings, temperature control and regular calibration, the study highlights the complexity of the 3D printing process and the importance of optimization applied in practical applications to achieve a high degree of accuracy and quality of printed objects.

The results of measurements carried out using the multi-sensor three-coordinate measuring machine OPTIV M 4.4.3 provide valuable data about the accuracy of the

printer and the printed parts. Statistical analysis, including the use of Cp and Cpk metrics, as well as skewness and kurtosis estimates, further demonstrates the ability of the process to produce quality parts within set specifications and to provide reproducibility of results under various manufacturing conditions.

It is important to note that although 3D printing technology allows for significant flexibility and innovation in design and manufacturing, the accuracy and repeatability of printed objects are critical to their practical applicability. This research highlights the fact that achieving high quality and accuracy requires careful control of multiple factors, including, but not limited to, the quality of materials used, printer specifications, and printing conditions.

Finally, the presented conclusions and results serve as a basis for future research, with a view to the continuous improvement of 3D printing technologies and the expansion of their applications in various fields. Effectively addressing the challenges of accuracy and repeatability will help establish 3D printing as a key technology for the future of manufacturing.

In the next study, we plan to examine in more details the influence of some of parameters on the accuracy of 3D printers.

V. REFERENCES

[1] Sachs, E., Cima, M., Williams, P., Brancazio, D., & Cornie, J. (1992). Three dimensional printing: rapid tooling and prototypes directly from a CAD model. Journal of Manufacturing Science and Engineering, Transactions of the ASME. Volume 114, Issue 4, pp. 481 – 488

[2] Rajan, K., Samykano, M., Kadirgama, K., Harun, W. S. W., & Rahman, M. M. (2022). Fused deposition modeling: process, materials, parameters, properties, and applications. The International Journal of Advanced Manufacturing Technology, volume 120, issue 3, pp. 1531-1570.

[3] Dimitrov, D., Schreve, K., & de Beer, N. (2006). Advances in three dimensional printing–state of the art and future perspectives. Rapid Prototyping Journal, volume 12, issue 3, pp. 136-147.

[4] Turner, B. N., Strong, R., & Gold, S. A. (2014). A review of melt extrusion additive manufacturing processes: I. Process design and modeling. Rapid prototyping journal, volume 20, issue 3, pp. 192-204.

[5] Dichev, D., Koev, H., Diakov, D., Panchev, N., Miteva, R., Nikolova, H. Automated System for Calibrating Instruments Measuring Parameters of Moving Objects. Proceedings Elmar - 59th International Symposium Electronics in Marine, September 18-20 th, 2017, Zadar, Croatia, pp. 219-224. DOI: 10.23919/ELMAR.2017.8124472

[6] Dichev, D., F. Kogia, H. Koev, D. Diakov. Method of Analysis and correction of the Error from Nonlinearity of the Measurement Instruments. Journal of Engineering Science and Technology Review. Volume 9, Issue 6, 2016, pp. 116-121. DOI: 10.25103/jestr.096.17

[7] Kupriyanov, O., Trishch, R., Dichev, D., Kupriianova, K. A General Approach for Tolerance Control in Quality Assessment for Technology Quality Analysis. In 4th Grabchenko's International Conference on Advanced Manufacturing Processes, InterPartner 2022, Lecture Notes in Mechanical Engineering, 2023, pp. 330-339. DOI: 10.1007/978-3-031-16651-8_31

[8] R. Anitha, S. Arunachalam, P. Radhakrishnan. "Critical parameters influencing the quality of prototypes in fused deposition modelling", Journal of Materials Processing Technology, vol-118 (2001) 385-388.

[9] Pooja Padyal, Dr. A. Mulay, Dr. M.R. Dhanvijay. 'Experimental assessment of Repeatability of Openware 3D Printer', International Research Journal of Engineering and Technology (IRJET), vol- 07, issue: 05 | May 2020

[10] Garrett W. Melenka, Jonathon S. Schofield, Michael R. Dawson, Jason P. Carey "Evaluation of dimensional accuracy and material properties of the MakerBot 3D desktop printer", Rapid Prototyping Journal, vol-25 no.5 (2015) 618-627

[11] Georgiev B., Karadzhov T. "Comparative analysis of geometric deviations in contact measuring instruments for control and laser contactless scanning. Environment. Technology. Resources. Rezekne, Latvia, Proceedings of the 14th International Scientific and Practical Conference. Vol- 3, 306-310(2023) https://doi.org/10.17770/etr2023vol3.7182

Statistical analysis of the quality of a technological process for the production of shafts for electric motors by roughness study

Kliment Georgiev
Technical University of Sofia, branch Plovdiv
Faculty of Mechanical Engineering;
Department: Mechanical and Instrument Engineering
Plovdiv, Bulgaria
k.georgiev@tu-plovdiv.bg

***Abstract*. This paper presents a statistical analysis of the quality of a technological process by investigating the surface roughness of shafts for electric motors obtained during machining. Repeated measurements have been carried out using a portable roughness tester INSIZE ISR - C002 and the results are summarized. Statistical analysis is applied to analyse the accuracy, adjustability, and stability of technological process. The stability of the process is presented by investigating the correlation between the experimental and theoretical curve of the quality index. Accuracy evaluation is performed by calculating the accuracy coefficient. The adjustability analysis is evaluated by the relative position of the distribution curve of the obtained quality index with respect to the tolerance field.**

Keywords: analysis, quality, quality control, surface roughness, technological process, stability, accuracy, adjustability.

I. INTRODUCTION

With the development of technology, the quality requirements of the machined parts are increasing. The quest for defect-free production of quality workpieces leads to the need for in-depth technological process (TP) research and analysis.

Statistical analysis methods can solve many problems related to process quality. The three main tasks presented are some of the most important in process analysis:

- Process stability analysis;

- Process capability (accuracy) analysis;

- Analysis on process regulation (tuning);

The ability and regulation of the process is collectively called efficiency. The quality of a process is determined by its stability and efficiency.

A. Process stability analysis

Stability of the TP means preservation of the parameters of the distribution of deviations of the qualitative indicator according to a certain law for a sufficiently long time. The initial assessment of stability can be performed by means of point diagrams. In stable processes, the variance of the qualitative indicator is kept constant, and its meaning is either constant or changes in a regular manner. In unstable processes the variance changes randomly. Intermittent periods with qualitative or defective output are alternated. Stable processes are predictable, i.e. amenable to statistical control Fig. 1. Unstable processes are unpredictable, i.e. unsuitable for statistical control and quality regulation Fig. 2.
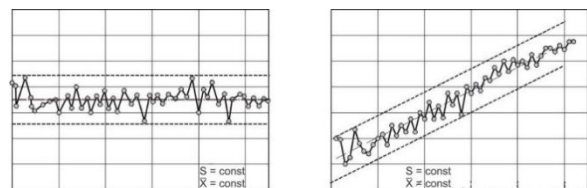
Fig. 1 Stable technological process
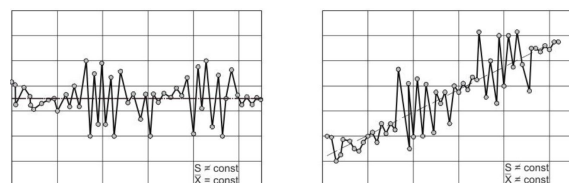
Fig. 2 Unstable technological process

Process stability analysis is studied and evaluated using two approaches:

- By examining the correspondence between the experimental and theoretical qualitative indicator curve;

- By examining the histogram of the process;

The first approach is used less frequently when the process flow is not influenced by a dominant systematic factor that shifts the distribution, i.e. the average value of the qualitative indicator remains constant over time (stationary TP).

The second approach is more universal and is applied more often. It examines and analyses the average value of the qualitative indicator using the regression equation.

B. Statistical analysis of accuracy of a TP

This analysis applies only to proven stable processes. Accuracy is assessed by the accuracy factor.

If appropriate, the tolerance may be reduced. The other solution is to keep the tolerance but intensify the machining process by changing the mode parameters, which will increase productivity.

C. Tuning analysis of a TP

This is the third task of statistical analysis (the first for stability and the second for accuracy). Tunability is characterized by the relative position of the distribution curve or accuracy diagram with respect to the tolerance field.

Tuning is a process where the process system is brought into a state to produce a certain value of a quality metric. This value, which the output quality indicator should obtain at the beginning of operation after tuning, is called the working setpoint. It is defined differently for statistically stable and technologically stable processes.

Quality is a set of characteristics (indicators) of an object that determine its ability to satisfy certain or supposed needs. An object can be a product, an activity, a process, an organization, a person.

According to Mitra A. (2016) the aspects of the quality are three: Quality of conformance, Quality of Design and Quality of Performance (fig.3) [1].

Quality of conformance implies that a manufactured product or a service rendered must meet the standards selected in the design phase. This phase is concerned with the degree to which quality is controlled from the procurement of raw material to the shipment of finished goods [1].

Quality of performance is how a product functions or service performs when used. It measures the degree to which the product or service satisfies the user [1].

The way the product or the service satisfies the customer is a function of both quality of design and quality of conformance [1].
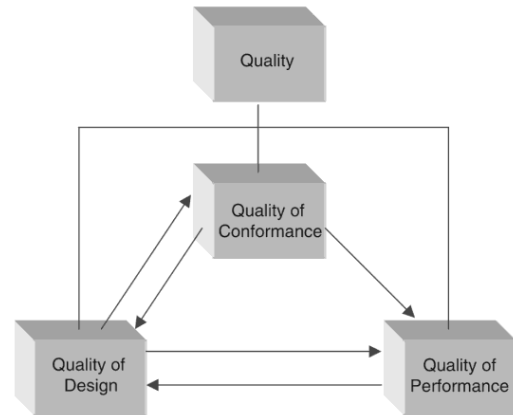
Fig. 3 The aspects of quality [1]

In this paper, an analysis of a technological process is presented and its stability, accuracy and tunability are investigated. The parameter used for quality assessment is surface roughness.

II. MATHERIALS AND METHODS

A. Matherials

The details used for the experimental studies are presented in Fig. 4. All experiments were conducted in a laboratory environment under controlled temperature and humidity conditions. The measuring instrument was pre-calibrated before the measurements were started.

The shaft is processed in two operations. The first machining is on the long side with a back saddle support. The machine is a DMG CLX350 with the following cutting modes:

- Rough machining: Vc = 115m/min, a = 1.5mm, F = 0.25 mm/rev;
- Fine machining: Vc = 200m/min, a = 0.5mm, F = 0.15 mm/rev;

The second processing is carried out on a Mazak Qtn 200 MSY. The basis of this machining is on the short side of the workpiece to the two-stand in the following cutting modes:

- Rough machining: Vc = 100m/min, a = 1.5mm, F = 0.24 mm/rev;
- Fine machining: Vc = 185m/min, a = 0.4 mm, F = 0.15 mm/rev;
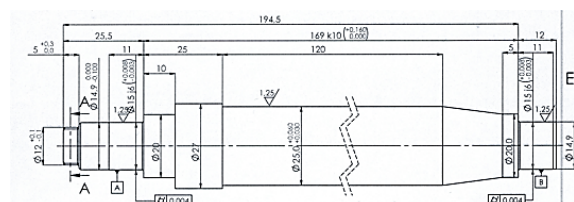
Fig 4. Measured detail

B. Methods

The technological process for manufacturing shafts for electric motors is evaluated by statistical analysis of the qualitative parameter roughness. Stability, accuracy, and process tuning analysis have been applied in the evaluation of the technological process. Statistical analysis using X and R control charts was used to evaluate the process.

The SPC is a basic statistical tool for verifying the conformity of technical requirements of products. Even in robust manufacturing processes, quality characteristics are associated with randomness due to the presence of uncontrollable (or difficult/costly to control) input variables [2].

Gejdos P. (2015) says that the control charts are the most frequently used tool in the statistical regulation of processes. According to him they allow us more accurate distinguishing of random from symmetric causes of the fluctuations in the value of a mark of quality. Control charts facilitate regulation and improvement in the quality of the technological process [3].

Process capability analysis is an important tool in the DMAIC (Define, Measure, Analyze, Improve and Control) process, with application in both the analyze and improve steps [4].

According to Oakland J. (2007) the basis of the theory of statistical process control is differentiation of the causes of variation during the operation of any process. Certain variations belong to the category of chance or random variations, about which little may be done, other than to revise the process [5]. Fig. 5 shows a schematic control chart.
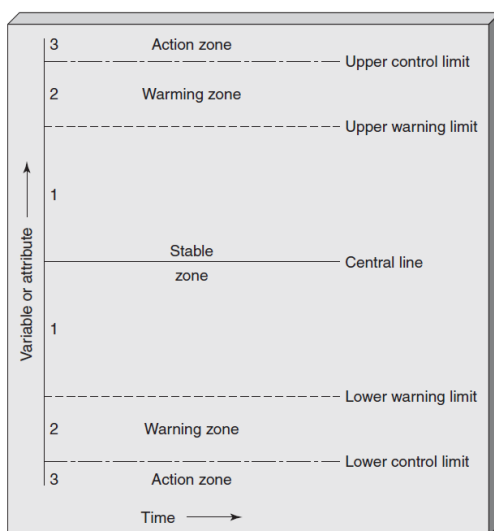
Fig 5. Schematic control chart [5]

When Control charts are applied, it is assumed that the behavior of the process could be characterized by the level or one or several qualitative values. These values are also known as regulated values. Control charts are used in monitoring processes and when ascertaining the need for corrections or changes in the process, to achieve a better mean value of the process or to reduce variability in the process. In control charts, the horizontal axis contains the times when statistical sampling of regulated values took place, and the vertical axis contains calculated values of the appropriate sample characteristics [3].

To build the control charts X, it is necessary to calculate: upper control limit (UCL), lower control limit (LCL) and center line (CL)[6, 7].

X chart is used to reflect changes in the average values of a process. To construct an X chart, it is necessary to draw its center line (CL). This is achieved by collecting the sample data and calculating the mean of $\bar{x}$ [8, 9].

$$\bar{x} = \frac{x_1 + x_2 + x_3 + x_n}{k} \qquad (1)$$

$$CL = \bar{x} \qquad (2)$$

To calculate the upper and lower control limits, the following formulas are used:

$$UCL = \bar{x} + z\sigma_{\bar{x}} \qquad (3)$$

$$LCL = \bar{x} - z\sigma_{\bar{x}} \qquad (4),$$

where:
$\bar{x}$ - average value of the sample;
z – standard normal variable equal to 2 for 95.44% confidence interval and 3 for 99.73% [10];

$$\sigma_{\bar{x}} = \frac{\sigma}{\sqrt{n}} \qquad (5),$$

where:
σ – process standard deviation;
n – number of tests per sample.

Since σ is usually unknown, we must replace it with an estimate. Most frequently the use of as an estimate of σ, which is the sample standard deviation (s) [4].

Process capability ratio is a frequently used way to express process capability. There are many ways to express process capability and one of them is in terms of the process capability ratio (PCR) C_p, which for a quality characteristic with both upper and lower specification limits (USL, LSL) is [4]. USL stands for Upper specification limit, that can be also called Upper Tolerance limit. The same goes to LSL, which is Lower Specification limit, which is also known as Lower Tolerance Limit:

$$C_P = \frac{USL - LSL}{6\sigma} \qquad (6)$$

According to Montgomery D. C (2009) the 6σ spread of the process is the basic definition of process capability. Since σ is usually unknown, we must replace it with an estimate. Most frequently the use of
as an estimate of σ, resulting in an estimate $\widehat{C_p}$ of C_p is "s", so [4]:

$$\hat{\sigma} = s \qquad (7)$$

Based on the above, we arrive at the formula for calculating the precision factor $\widehat{C_p}$ by the following formula:

$$\widehat{C_p} = \frac{USL - LSL}{6\hat{\sigma}} \qquad (8)$$

The analysis of the process setup can be represented by calculating the coefficient C_{pk}:

$$C_{pk} = \min(C_{pu}, C_{pl}) \qquad (9),$$

where:

$$C_{pu} = \frac{USL - \mu}{3\sigma} \qquad (10)$$

$$C_{pl} = \frac{\mu - LSL}{3\sigma} \qquad (11)$$

According to what is written above σ is usually unknown and we can replace it with (s), μ or c $\bar{x}$.

III. RESULTS AND DISCUSSION

The experiments were conducted in a laboratory environment under controlled conditions of temperature and humidity. Twenty shafts were measured, and each shaft was measured three times. According to the submitted technical documentation, the nominal prescribed roughness was Ra = 1.25 μm with USL = 2.25 μm and LSL = 1 μm. The results of the shaft roughness measurements are presented in Table 1. The same results The standard deviation is calculated using the formula (12):

$$s = \sqrt{\frac{\sum_{i=1}^{n}(x_i - \bar{x})^2}{n-1}} \qquad (12)$$

For the data presented in Table 1, the value of the standard deviation is:

$$s = 0{,}0229 \text{mm} \qquad (12)$$

The X chart is constructed using formulas (3) and (4) to calculate the UCL and LCL, replacing σ by the value of s as described above. The confidence interval was chosen to be 3σ, respectively 3s, hence:

$$UCL = \bar{x} + zs \qquad (13)$$

$$LCL = \bar{x} - zs \qquad (14)$$

were used for the statistical analyses.

Table 1 Measurement Data

№	Surface Roughness, μm			Average
	1	*2*	*3*	$\bar{x}$
1	2.023	2.051	2.068	2.05
2	2.076	2.063	2.083	2.07
3	2.114	2.049	2.109	2.09
4	2.077	2.064	2.106	2.08
5	1.996	2.018	2.019	2.01
6	2.059	2.055	2.046	2.05
7	2.072	2.012	2.021	2.04
8	2.061	2.043	2.037	2.05
9	2.061	2.054	2.049	2.05
10	2.063	2.068	2.007	2.05
11	2.034	2.063	2.078	2.06
12	2.086	2.073	2.095	2.08
13	2.123	2.061	2.121	2.10
14	2.082	2.075	2.128	2.10
15	2.005	2.025	2.028	2.02
16	2.069	2.068	2.056	2.06
17	2.083	2.023	2.035	2.05
18	2.075	2.052	2.052	2.06
19	2.085	2.065	2.066	2.07
20	2.073	2.085	2.025	2.06
Total average				2.06

After substituting the data in formula (13) and (14), the following results are obtained:

$$UCL = 2.06 + 3 \times 0.0229 \qquad (13)$$

$$UCL = 2.128 \text{ μm};$$

$$LCL = 2.06 - 3 \times 0.0229 \qquad (14)$$

$$LCL = 1.991 \text{ μm};$$

The value of $\bar{x}$ is taken as the central line. The histogram in Figure 6 graphically presents the results of the study.
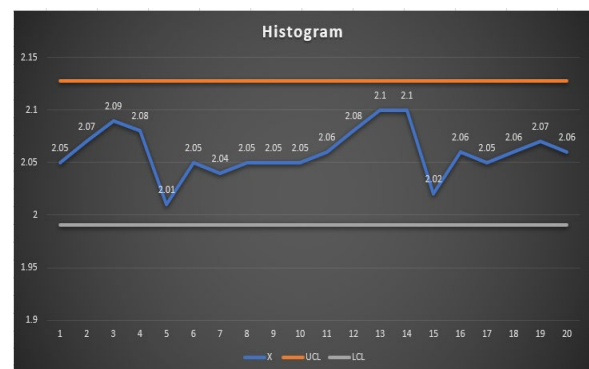
Fig 6. Histogram

The plot in Fig. 6 shows the distribution of the value of $\bar{x}$ versus the upper and lower bounds. Although all the values of $\bar{x}$ are outside the tolerances, the process does not cross the control limits.

The calculation of the accuracy coefficient was carried out using formula (8).

$$\widehat{C_p} = \frac{2,25-1}{6\times0,0229} \qquad (8)$$

$$\widehat{C_p} = 9,1$$

According to the standard used, the values of the resulting accuracy factor C_p must be greater than 1.67 to satisfy the process accuracy conditions. The resulting value for the coefficient $C_p = 9,1$, which is greater than the 1.67 that is specified in the standard.

The estimation of the tunability of the technological process was made by using the coefficient C_{pk}, formula (9). Calculate the values of the criteria in the upper limit deviation (C_{pu}) (10) and the value of the criteria in the lower limit deviation (C_{pl}) (11), The criteria then require the minimum value obtained to be assumed to be selected.

$$C_{pu} = \frac{2,25-2,06}{3\times0,0229} \qquad (10)$$

$$C_{pu} = 2,76$$

$$C_{pl} = \frac{2,06-1}{3\times0,0229} \qquad (11)$$

$$C_{pl} = 15,43$$

It follows from the calculations that for the coefficient C_{pk} must be chosen the value of $C_{pu} = 2,76$, which is the minimum. The value adopted for $C_{pk} = 2,76$ is greater than that recommended in the criterion ($C_{pk} > 1,67$).

IV. CONCLUSIONS

1. The process is set, and no upper or lower control limit crossing is observed.
2. The calculated process accuracy factor $C_p = 9,1$ indicates that the process is accurate.
3. The process tuning evaluation factor $C_{pu} = 2,76$ indicates that the process is well tuned.
4. The set nominal roughness is not met, but nevertheless the measurement data and statistical analysis show that the process is set, accurate and adjustable.

REFERENCES

[1] Mitra, A. (2016). *Fundamentals of quality control and improvement*. John Wiley & Sons.

[2] Hristov, M. H. (2023, September). SPC as an Instrument for Implementation and MSA as an Instrument for Evaluation of Non-Linear Object Based Temperature Compensation into Shop Floor CMM. In *2023 15th Electrical Engineering Faculty Conference (BulEF)* (pp. 1-9). IEEE.

[3] Gejdoš, P. (2015). Continuous quality improvement by statistical process control. *Procedia Economics and Finance*, *34*, 565-572.

[4] Montgomery D. C., Introduction to Statistical Quality Control, Sixth Edition, Copyright 2009 by John Wiley & Sons, Inc., ISBN 978-0-470-16992-6

[5] Oakland, J., & Oakland, J. S. (2007). *Statistical process control*. Routledge.

[6] H.R. Radev, "Metrologiya i izmervatelna tehnika", vol. II, S., Softtreyd, 2010, ISBN: 978-954-334-093-4

[7] Дюкенджиев Г., Р.Йорданов, Контрол и управление на качеството, София., Софттрейд, 2002.

[8] Statistical process control (SPC), Reference manual, Copyright 1992, Chrysler Corporation, Ford Motor Company, and General Motors Corporation

[9] Allen T., Introduction to Engineering Statistics and Lean Six Sigma, Statistical Quality Control and Design of Experiments and Systems, Third Edition Springer-Verlag London Limited 2006, ISBN 978-1-4471-7420-2 (eBook), https://doi.org/10.1007/978-1-4471-7420-2

[10] Qiu P., Introduction to Statistical Process Control, 2014 by Taylor & Francis Group, LLC, ISBN-13: 978-1-4822-2041-4 (eBook - PDF)

The Fluid Flow Simulation of the Thermal Comfort in Theatre

Lyuba Evtimova Gyurova
Naval Tactics Department
Nikola Vaptsarov Naval Academy
Varna, Bulgaria
l.gyurova@nvna.eu

Abstract. **This paper examines the use of Computational Fluid Dynamics (CFD) simulations to improve thermal comfort in enclosed spaces, such as theatres, halls, and offices. Thermal comfort is crucial for occupant well-being and productivity, and is influenced by various factors, including air temperature, humidity, and airflow. To create tailored models for specific spaces, we suggest using CFD simulations to predict airflow patterns and temperature distribution, thereby identifying discomfort zones. This research aims to optimize thermal comfort and improve building design and energy efficiency by iteratively adjusting ventilation strategies. The practical applications of this approach include improved design and construction, as well as retrofitting existing buildings. To achieve this, CFD simulations should be integrated into the design phase to proactively address thermal comfort issues and achieve energy-efficient layouts. Customising CFD models for existing buildings allows for the analysis of airflow patterns and optimisation of ventilation strategies to enhance thermal comfort. HVAC systems can be evaluated using CFD to identify areas for improvement and select energy-efficient solutions, leading to enhanced energy efficiency. The benefits of these improvements include enhanced well-being and productivity, as improved thermal comfort can lead to better occupant health and focus, ultimately boosting productivity. Additionally, the risks of Sick Building Syndrome (SBS) can be reduced. CFD analysis can help reduce the risks of Sick Building Syndrome by optimizing ventilation and improving indoor air quality. In the future, it is recommended to integrate CFD simulations with Building Information Modelling for comprehensive thermal comfort analysis. This study highlights the potential of CFD to optimize thermal comfort in enclosed spaces by promoting occupant well-being and energy efficiency through iterative ventilation adjustments. It is important to adhere to established standards when integrating CFD.**

Keywords: CFD simulation, theatre, thermal comfort.

I. INTRODUCTION

Theatres are places where many people gather for the purpose of breaking away from everyday activities, spending pleasant time with loved ones and friends and enjoying a favorite performance or concert. A large part of theatres are closed spaces that need effective ventilation in order to create a comfortable thermal environment for visitors. Various studies have been done on the effect of the ventilation system on indoor comfort. These studies can help to apply the software product more effectively especially for places where the ambient temperature is quite high in summer months and quite low in winter [1], [2], [3]. In addition to all this, the improvement of the thermal conditions will also lead to an increase in the energy efficiency of the enclose spaces. Source [4] aims to identify an acceptable temperature range in residential buildings by investigating correlation of comfort temperature with indoor and outdoor temperatures using "Comfort threads" and elucidating the effect of adaptive measures on the energy saving potential of residential premises.

Various ways to improve thermal comfort using simulations are given in [5]. The same were compared with the results obtained from the present study and thus validated.

In general, in places where many people gather, regardless of the purpose, to ensure the thermal comfort of the occupants, standards for the main influencing factors are used. These are ASHRAE 55 [6] and ISO 7730 standards [7], based on which the main parameters Predicted Mean Vote (PMV) and Predicted Percentage of Dissatisfied (PPD) are calculated. These two parameters are set in the simulation to evaluate people's satisfaction with the thermal conditions in the theatre. Based on these, subsequently, the simulation settings can be changed to provide a better thermal environment.

Source [8] presents simulation results of thermal comfort and indoor air quality affected by partitions in an air-conditioned building. Reference [8] was used as the reference algorithm to perform the present work.

The simulation is carried out by setting parameters for convective heat transfer and radiation; setting boundary and other conditions; and analysis of the achieved thermal comfort through post-processing including the parameters PMV and PPD.

II. MATERIALS AND METHODS

A. CAD model

Full-cloud CAE simulation software Sim Scale is used to perform the simulation for thermal comfort in a theatre [9]. Initially, the CAD model must be prepared to perform the simulation. In this case, is necessary to extract the flow volume, which can be done either by using the model imported into the software or by selecting the faces manually. For greater clarity about the specifics of flow extraction, a self-extraction with topological objects set is performed. This is also done for a specific problem, where the geometry of the walls and the type of extraction (Internal Flow Volume or External Flow Volume) must be set. In the present case, the Internal flow volume extraction mode is used.

The given set of topological objects in the creation of a CAD model are actually the boundary conditions that are set in cases where a solution to a boundary value problem has to be found as in the case of Internal heat flow, Fig. 1 [9]. The same applies if the heat flow is external.
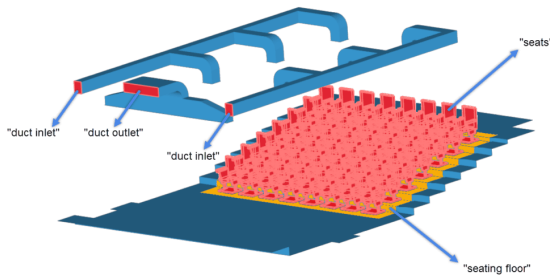
Fig. 1. Set of topological objects [9]

For each of the boundary conditions, the main parameters affecting it are adjusted. Such are:

- gravity in the γ direction;
- air as a material with its inherent properties;
- velocity inlet;
- pressure outlet on the air entrances and the exit;
- fixed seats temperature value;
- "No-slip" walls with fixed temperature value;
- topological entity set.

The Convective Heat Transfer analysis type is selected to create the simulation, which incorporated the "K-omega SST" turbulence model [10]. This model is extremely applicable and preferred in Computational Fluid Dynamics (CFD) over other RANS models, as it combines two other models, the Wilcox k-omega and the k-epsilon. It includes two transport equations for two dependent variables: k – turbulence kinetic energy and ω – specific dissipation rate.

Using the K-omega SST model provides a better separation of the fluid flow and accounts for its good behavior and the way the principal shear stress is transmitted through the boundary layers if adverse pressure gradients are present.

In [9], the initial values of turbulent kinetic energy k and specific dissipation rate ω are given, but the boundary conditions for these variables can be changed.

If necessary, radiation can be included in the Convective Heat Transfer analysis type via the Diffuse View Factors Model. View factors are used to calculate the amount of radiation exchanged between two surfaces and depend only on the geometric relationships between them. In the present case, radiation is not included in the simulation, since the air is set as a medium that is transparent and assumed to be undisturbed.

B. Result Control and Mesh Generation

To solve specific software computations is used the Results Control Elements. These are thermal comfort parameters according to standards [6] and [7] and the inclusion of two additional scalars (PMV and PPD) that can be influenced by these parameters.

To perform the simulation calculations for each specific problem, an appropriate mesh is selected depending on the complexity of the geometry. In the present case, a standard meshing algorithm is used, suitable even for the most complex geometries. It gives good results and is quite automated. The mesh that is generated is a 3D unstructured mesh using tetrahedral or hexahedral elements, Fig. 2.
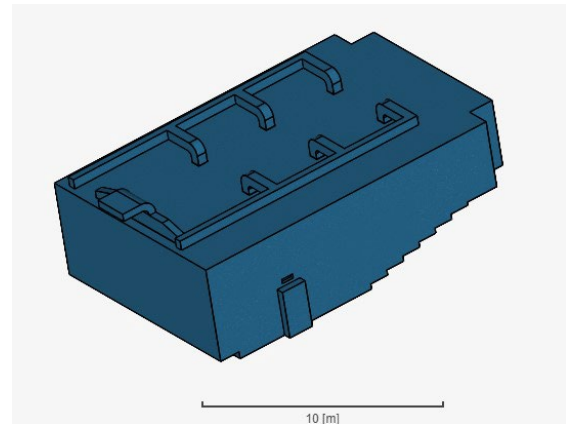
Fig. 2. View of mesh geometry

III. RESULTS AND DISCUSSION

After starting the simulation and completing the calculation, an integrated post-processor is used to visualize the main parameters giving an estimate of the thermal comfort in the theater hall.

A. Predicted mean vote

PMV in Fig. 3 shows the average value that the occupants would give for thermal sensation according to the set parameters in the simulation. If the heat balance between the heat emitted by the body and that received by it is zero, then an ideal thermal environment and satisfaction has been achieved, i.e. the PMV value should be zero.

Limit values for PMV according to ASHRAE Standard 55 are between -0.5 and 0.5 [6]. More extended ranges are given in [7].

- Hard limit: [-2 ÷ +2];
- New buildings: [-0.5 ÷ +0.5];
- Existing buildings: [-0.7 ÷ +0.7].
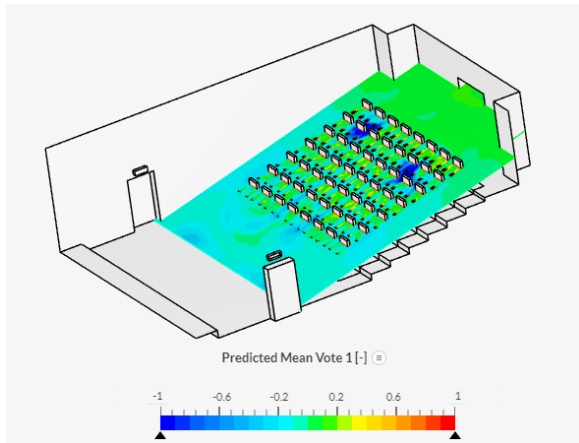
Fig. 3. Predicted mean vote

In Fig. 3 the colour scale of the PMV value change in the range from -1 to 1 (from dark blue, blue, light blue, green, yellow, orange to red, respectively) is shown. It can be seen that the PMV is not up to standards for the entire area and heat balance is not achieved, although in most of the area the PMV value is within the permissible limits and only in some small regions the PMV value is less than - 0.5, and in others exceeding 0.5.

B. Predicted percentage of dissatisfied

In Fig. 4 PPD represents the percentage of people expected to experience some local discomfort. It can be caused by:

- large temperature differences in height ;
- air flow in the presence of natural ventilation;
- unwanted cooling or overheating of the body in the presence of forced ventilation or in the absence of such at very low and very high outside temperatures.

According to [6], if the obtained degree of satisfaction is above 80%, good thermal comfort has been achieved in the closed room. The remaining 20% of dissatisfaction may be related to individual discomfort related to all or some of the factors affecting PMV. PPD can vary from 5% to 100%, depending on where the occupants are located and based on the calculated PMV. For comfort standards to be met, the PPD must be lower than 20% for every point in the space.

A colour scale with a range of 5% to 50% is also used for PPD analysis, which corresponds to colours from dark blue, blue, light blue, green, yellow, orange to red. Considering the results obtained for the PMV value, again there is no complete satisfaction, since in the same zones the PPD value is higher than the permissible limit value of 20%.

As a conclusion from the Fig. 3 and Fig. 4, it can be said that readings can be a basis for improving the thermal environment of the theatre and approaching the ideal, thereby increasing the satisfaction of the occupants. This can be achieved practically, for example, by improving the ventilation systems of the rooms and changing the values of the thermal parameters set in the simulation.
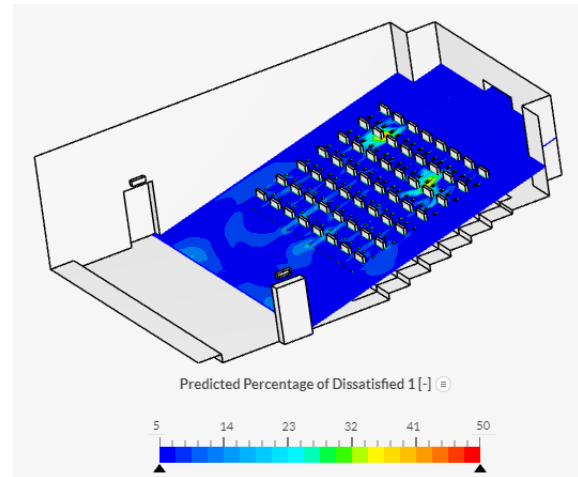
Fig. 4. Predicted percentage of dissatisfied

IV. CONCLUSION

In conclusion, this paper presents a significant advancement in enhancing thermal comfort in confined spaces through numerical approaches. Separate simulation models were employed for flow volume extraction with topological objects set and for Convective Heat Transfer and Radiation, allowing for effective assessment and analysis of the key parameters influencing thermal comfort in theatres.

The use of Computational Fluid Dynamics (CFD) simulation with the K-omega SST turbulence model allows for a thorough analysis of fluid flow, considering factors such as adverse pressure gradients. The integration of post-processing and mesh analysis also improves the evaluation of thermal comfort.

The simulation results, expressed through the PMV and PPD parameters, are based on established thermal comfort standards ISO 7730 and ASHRAE 55. These parameters provide a visual representation of the thermal conditions across the researched area. Precise analysis of these parameters can help propose improvements in ventilation systems and simulation parameters, thereby enhancing occupant satisfaction and energy efficiency in enclosed spaces.

The theoretical contributions of this study are based on the advanced modelling techniques used and the thorough analysis of results. The findings provide valuable insights for optimizing indoor environmental quality, aligning with established standards, and informing decision-making processes in building design and operation.

REFERENCES

[1] J. Yao, "Effect of variable ventilation modes on indoor thermal comfort and building energy consumption", International Journal of Low-Carbon Technologies, Volume 7, Issue 3, September 2012, Pages 187–191.

[2] Andrzej Raczkowski1, Zbigniew Suchorab1, Przemysław Brzyski, Computational fluid dynamics simulation of thermal comfort in naturally ventilated room, MATEC Web of Conferences 252, 04007, (2019), https://doi.org/10.1051/matec conf/201925204007, CMES'18.

[3] R Widiastuti, M I Hasan, C N Bramiana, P U Pramesti, CFD Simulation on the Natural Ventilation and Building Thermal Performance, INCRID 2019, IOP Conf. Series: Earth and

Environmental Science 448 (2020) 012004, IOP Publishing, doi:10.1088/1755-1315/448/1/012004.

[4]   Naja Aqilah, Hom Bahadur Rijal, Sheikh Ahmad Zaki, A Review of Thermal Comfort in Residential Buildings: Comfort Threads and Energy Saving Potential, Energies 2022, 15, 9012. https://doi.org/10.3390/en15239012. https://www.mdpi.com/journal/energies

[5]   Jiying Liu, Shengwei Zhu, Moon Keun Kim, Jelena Srebric, A Review of CFD Analysis Methods for Personalized Ventilation (PV) in Indoor Built Environments, Sustainability 2019, 11(15), 4166; https://doi.org/10.3390/su11154166.

[6]   ANSI/ASHRAE Standard 55, "Thermal environmental conditions for human occupancy", 2020, ISSN 1041-2336, Available: https://www.ashrae.org/file%20library/technical%20resources/standards%20and%20guidelines/standards%20addenda/55_2017_c_20200731.pdf.

[7]   ISO 7730:2005, "Ergonomics of the thermal environment – Analytical determination and interpretation of thermal comfort using calculation of the PMV and PPD indices and local thermal comfort criteria", Third edition, November 2015, Available: https://www.buildingreen.net/assets/cms/File/ISO_7730-2005.PDF.

[8]   Pradip Aryal, Thananchai Leephakpreedab, CFD analysis on thermal comfort and indoor air quality affected by partitions in air-conditioned building, Applied Mechanics and Materials Submitted: 2015-12-02, ISSN: 1662-7482, Vol. 836, pp 121-126 Accepted: 2016-01-27, doi:10.4028/www.scientific.net/AMM.836.121.

[9]   SimScale,   Last   updated: October   25th,   2023, https://www.simscale.com/.

[10]   F. R. Menter, Improved two-equation k-omega turbulence models for aerodynamic flows, NASA technical memorandum 103975, NASA Ames Research Center Moffett Field, CA, United States, October   1992,   Available: https://ntrs.nasa.gov/api/citations/19930013620/downloads/19930013620.pdf.

Numerical Simulation and Analysis of Two-Dimensional Steady-State Heat Conduction in 2d Rectangular Domain

Lyuba Evtimova Gyurova
Naval Tactics Department
Nikola Vaptsarov Naval Academy
Varna, Bulgaria
l.gyurova@nvna.eu

Abstract — **This work recommends the use of an algorithm to solve a number of engineering problems related to transient conduction during the various processes associated with heat transfer through a single or multilayer wall.**
A detailed study of the steady-state thermal conductivity in a two-dimensional rectangular domain is carried out. Using numerical methods specific to the solution of the heat conduction equations, a model has been used which gives accurate representations of the heat distribution in the given geometry.
The focus of this study is aimed at deepening the practical implications of the used numerical methodology. The results obtained from analysis highlight the potential for optimizing processes related to heat conduction in various engineering fields. The proposed numerical approach reveals opportunities for precise modelling and improvement of the thermal characteristics of various systems especially applicable in electronics, industrial systems and the implementation of modern thermal insulation materials.

Keywords — steady-state thermal conductivity, temperature, heat flux, CFD simulation

I. Introduction

In today's modern, constantly evolving world, the use of software products for numerical simulations leads to a better understanding and analysis of various physical processes. Heat conduction, as such a process, represents a micro-process of heat transfer in direct contact between the elements with different temperature that make up a given medium. This process is common in various engineering, technological, industrial, etc. areas and its optimization is essential. Examples of this are cooling, heating and air conditioning systems and their components such as heat exchangers and piping; tanks for various fluids and their accompanying pumps and throttling devices; thermal switch to control the thermal resistance; thermal insulation of walls and windows; and many others [1] for which a number of thermal problems can be solved.

The present work focuses on the research and performance of the numerical simulation and analysis of steady heat conduction within a two-dimensional rectangular domain, specifically using the ANSYS software [2]. By applying advanced computational methods, various problems related to heat conduction can be modeled more effectively.

The primary goal of this article is to ascertain the temperature distribution and heat flux within a 2D rectangular domain, while also investigating the impact of individual parameters on these thermal characteristics. In the given two-dimensional domain, the temperature changes in only two directions, *x* and *y*, and the steady-state thermal conductivity means that it does not change with time, $\frac{\partial}{\partial t} = 0$. This approach is suitable for understanding the basic laws of heat conduction in two-dimensional systems and subsequently developing more effective methods of management and control of processes related to heat transfer through different media [3], [4].

To solve the given physical problem, a mathematical model is used, in which Laplace's differential equation is solved for a two-dimensional flow in a rectangular region in the absence of heat generation [5], [6]. The mathematical model used is solved using the ASNYS solver, which uses the finite element method [7]. This involves drawing the geometry of the domain, setting the boundary conditions of the problem that define heat transfer between the object and its surroundings, generating a computational mesh with a specified set of elements to solve the heat transfer equations, and discretizing these differential equations to solve them by ANSYS solver, which will clarify the physics of the problem [8], [9]. After program solving for all the

elements that make up the mesh, an analysis of the obtained results is made.

II.   MATHERIALS AND METHODS

A. Problem specification

To fulfil the set objective of the study, a 2D rectangular area is drawn in ANSYS and a specific mathematical model is set.   The mathematical model describing the heat exchange in a two-dimensional rectangular domain is introduced in ANSYS, where it is solved numerically. The model is a Laplace's equation for energy conservation (1).

$$k \left(\frac{\partial^2 T}{\partial x^2} + \frac{\partial^2 T}{\partial y^2} \right) = 0, \qquad (1)$$

where: k, $W/m^\circ C$ – thermal conductivity coefficient;

T, $^\circ C$ – temperature of the domain.

The problem under consideration is a Boundary value problem related to 2D steady conduction, which means that predefined boundary conditions must be introduced. The domain has width $\Delta x = W$ and height $\Delta y = H$, where the height is twice the width, $H=2W$ [2].

When solving the given problem in ANSYS, it is necessary to make simplification by using dimensionless domain sizes and the mathematical model. In ANSYS, the dimensionless model (2) with boundary values is introduced, which corresponds to the dimensional one (1).

$$\left(\frac{\partial^2 \theta}{\partial x^2} + \frac{\partial^2 \theta}{\partial y^2} \right) = 0. \qquad (2)$$

Dimensioning is performed by defining the dimensionless coordinates $x^* \equiv \frac{x}{W}$; $y^* \equiv \frac{y}{W}$ и безразмерната температура $\theta \equiv \frac{T-T_\infty}{T_0-T_\infty}$ [2], където:

T_0, $^\circ C$ – constant temperature of the bottom face;

T_∞, $^\circ C$ – temperature of the fluid bathing the right face.

For the given domain, three boundary conditions are set for the four faces that must match the dimensionless model. The dimensionless and dimensional problems are given in the Fig. 1 and Fig. 2, respectively.
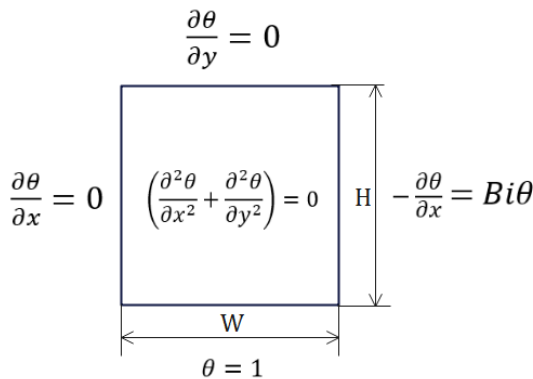
Fig. 1.   Dimensionaless boundary value problem
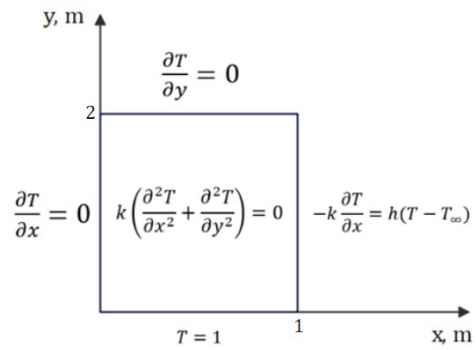
Fig. 2.   Dimensional boundary value problem

✓ 1st boundary condition – along the lower isothermal surface the temperature must be kept constant. In order to fulfil this condition, a temperature $T=T_0$ is set in the dimensional equation on the lower side, where the dimensionless temperature $\theta=1$;

✓ 2nd boundary condition – no heat exchange with the environment must take place on the left and upper faces, the surfaces must be adiabatically insulated. This means that the heat flux must be zero in both directions, $\frac{\partial T}{\partial x} = 0, \frac{\partial T}{\partial y} = 0$ and T is assumed to be θ;

✓ 3rd boundary condition – presence of convection due to the fluid flowing around the wall on the right face of the domain, $-\frac{\partial \theta}{\partial x} = Bi\theta$. In the specific case, the Biot number is assumed to be $Bi \equiv \frac{hW}{k} = 5$. In the mathematical model, the coefficients are set with values: $k=1$, $W=1$, $h=Bi$ and $T_\infty =0$. For the coefficient k, the condition of constant thermal conductivity in all directions is fulfilled. In the specific case, the importance falls on the convection coefficient h and its setting. It should be equal to 5.

For more clarity on the use of the Biot number (Bi), some clarifications are provided. The Biot number is a critical dimensionless parameter used in the field of heat transfer, serving to correctly analyse the interaction between thermal conductivity inside a solid body and convection of its surface layer. In the sense of thermal resistance, the Biot number represents the ratio of the thermal conduction resistance inside the body to the convection resistance between the surface and the environment. Or put it in another way, the value of the Biot number is a measure of the temperature drop in the solid relative to the temperature difference between the surface and the liquid and is defined with a limit value of 1. At $Bi>1$, the temperature change inside the body takes place much more slowly than that between its surface layer and the fluid. Conversely, for $Bi<1$ the body has a smaller temperature gradient compared to that between the surface and the liquid, and heat will flow much faster inside the material than away from its surface. This would allow an assumption to be made of a uniform temperature distribution in the material [3], [10].

B. Mesh generation

In any problem involving heat exchange, it is important to know the distribution of heat throughout the considered domain and its direction depending on the set

boundary conditions. The heat flux in any direction is proportional to the temperature gradient in that direction. This means, in the present case for example, that if the flow reaches the left adiabatic face where there is no heat exchange, there will also be no temperature gradient in the *x* direction out of the domain, $q_x=0$.

Discretization of the rectangular domain is done by setting a geometry generation mesh containing 32 cells and 121 nodes, Fig. 3.
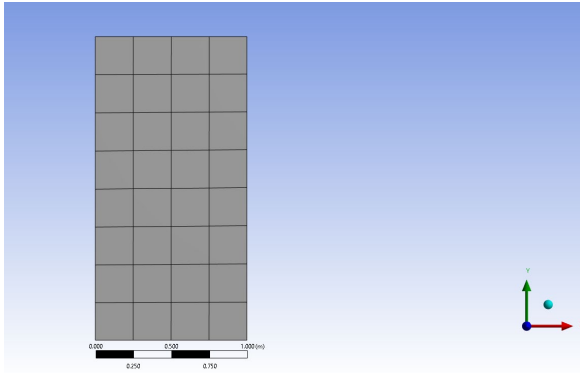
Fig. 3.   View of mesh geometry

All elements have four nodes each, and each internal node is common to the four elements surrounding it. In order to determine the temperature of the elements, the ANSYS solver uses a bilinear polynomial interpolation of the four nodal temperatures of a cell, thereby obtaining a weighted average value of these four values. For all nodal temperatures, the ANSYS solver constructs a system of algebraic equations, and each algebraic equation relates a nodal temperature to the elements around the corresponding node. Thus, the value of this node is related to all other temperature values in the surrounding elements. In this way, the temperature everywhere in the domain can be determined, by interpolation from nodal temperatures, and hence the heat flux obtained.

To reduce the calculation error, it is necessary to increase the number of elements, which increases the accuracy of the mesh. In this way, the number of equations describing the nodal temperatures will also increase. Another way to achieve error reduction is by increasing the order of the polynomial in each element. This can be done when increasing the nodes for each element, i.e. in addition to the four end nodes, there should be one more between every two, and the ANSYS solver will again generate algebraic equations and calculate the temperature in all of them. Then the interpolation will be of second order in both directions, which will lead to a better and more accurate solution to the problem.

III.   RESULTS AND DISCUSSION

A. *Change in temperature in the researched domain*

The temperature can be traced at any point in the domain, as well as along a straight line in both directions, and an assessment can be made as to whether the set boundary conditions are met.

Fig. 4 shows the temperature in the entire domain within limits *T=(1÷0.045) ℃*. On the lower surface, the temperature is unchanged, which shows that the boundary condition for isothermality on this face is met.
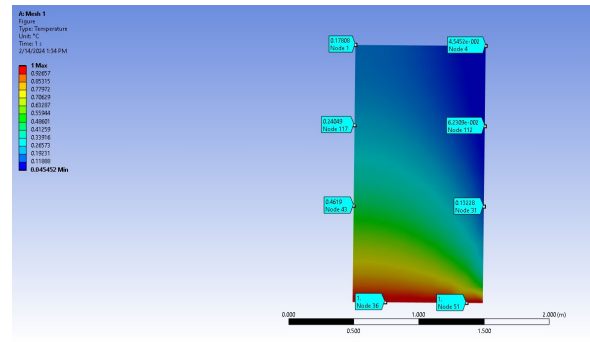
Fig. 4.   Change in temperature in the domain

Tracing the temperature at 51 points along a straight horizontal line, Fig. 5, in any other section of the area, it becomes clear that it decreases from right to left, which is due to the fact that there is no heat exchange with the environment through the left face, and such takes place only through the right face between the solid body and the fluid flowing around it. This can also be seen from the graphical representation of the curve showing the variation of temperature along length, $\frac{dt}{dx}$. Towards the adiabatic boundary condition, the slope of the curve is zero and the temperature is almost constant and highest. Further approaching the right face, the slope becomes greater, the temperature decreases, which is due to the convection between the fluid and the wall.
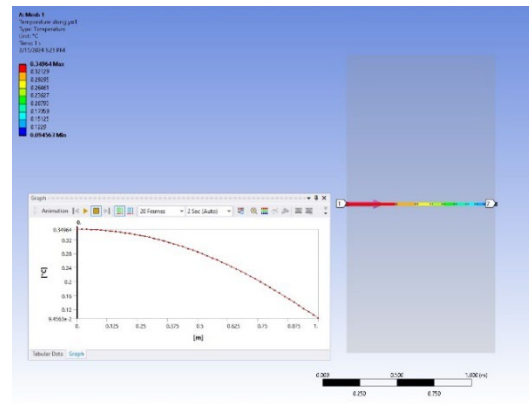
Fig. 5.   Temperature variation along a line

Table 1 gives the value of the temperature variation.

TABLE 1 TEMPERATURE VALUES ALONG A LINE

Point	W, [m]	T, [℃]	Point	W, [m]	T, [℃]
1	0	0.34964	26	0.5	0.28412
2	0.02	0.34954	27	0.52	0.2787
3	0.04	0.34923	28	0.54	0.27309
4	0.06	0.34871	29	0.56	0.2673
5	0.08	0.34798	30	0.58	0.26131
6	0.1	0.34704	31	0.6	0.25514
7	0.12	0.34589	32	0.62	0.24877
8	0.14	0.34453	33	0.64	0.24222
9	0.16	0.34296	34	0.66	0.23548

10	0.18	0.34118	35	0.68	0.22855
11	0.2	0.33919	36	0.7	0.22143
12	0.22	0.33699	37	0.72	0.21412
13	0.24	0.33459	38	0.74	0.20662
14	0.26	0.33197	39	0.76	0.19884
15	0.28	0.32913	40	0.78	0.19083
16	0.3	0.32609	41	0.8	0.1827
17	0.32	0.32284	42	0.82	0.17444
18	0.34	0.31938	43	0.84	0.16606
19	0.36	0.3157	44	0.86	0.15756
20	0.38	0.31182	45	0.88	0.14893
21	0.4	0.30773	46	0.9	0.14018
22	0.42	0.30343	47	0.92	0.1313
23	0.44	0.29891	48	0.94	0.1223
24	0.46	0.29419	49	0.96	0.11318
25	0.48	0.28926	50	0.98	0.10393
			51	1	0.0946

These findings clearly indicate that the set boundary conditions are accurately defined and the simulation results confirm them.

B. Distribution of heat flux in the domain

Fig. 6 shows the heat flux distribution from each node in the form of vectors passing through the domain. The distribution is two-dimensional and the two components q_x and q_y are related to the temperature gradients for the two directions respectively.

Analysis of the lower isothermal face shows that there is no heat flow there and the heat vector is perpendicular only in the y direction. The most heat losses are observed in the lower right, and for this reason a large amount of heat must be supplied to compensate them and thus keep the temperature constant.

On the left and upper faces, the heat vectors are parallel in the respective directions, which confirms the absence of heat exchange across these boundaries. However, the heat flux is not strictly zero, it has a very small value, $\vec{q} = 0.00052415\ W/m^2$ and the variation is only in one direction. Of interest is the upper left corner where the heat vector is not perpendicular to either the x or y direction. This is due to the fact that there is no heat flow in either direction in this part of the area and therefore the heat vectors change direction.

On the right side, heat exchange takes place between the wall and the fluid and the heat flows to the fluid. At a height, heat exchange decreases due to the smaller temperature difference.
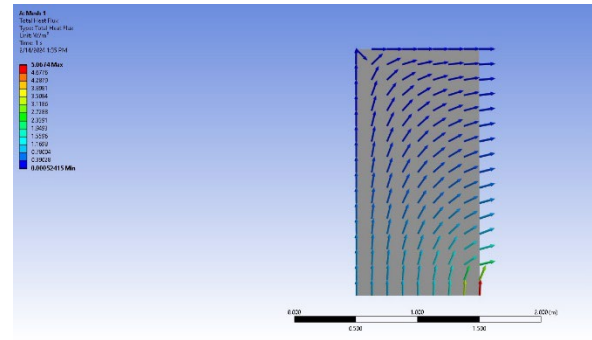
Fig. 6.   Heat flux distribution in the domain

C. Checking the results obtained

Since the inputted mathematical model is subject to the principle of energy conservation, it is necessary to check whether it is respected. The check is made for the heat flux passing through the boundaries per unit wall thickness.

Fig. 7 shows the heat calculated by the ANSYS solver along the lower isothermal surface, $q = 1.6701\ W$. It is positive because its direction is toward the domain, Fig. 6.
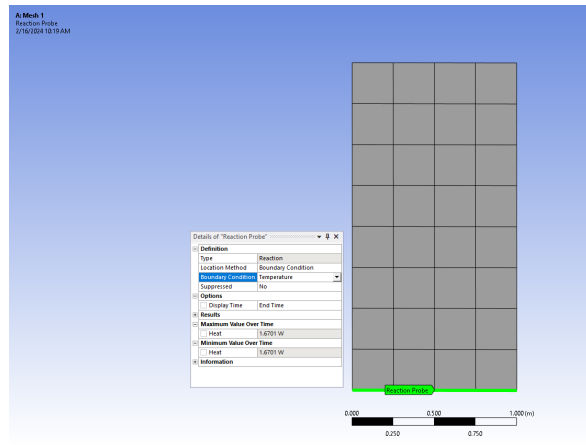
Fig. 7.   Heat transfer along the isothermal surface

It can be seen from Fig. 8 that due to the presence of heat transfer through the right boundary where convection takes place, heat is transferred to the flowing fluid and it is negative with a value of $q = -1.6701\ W$.
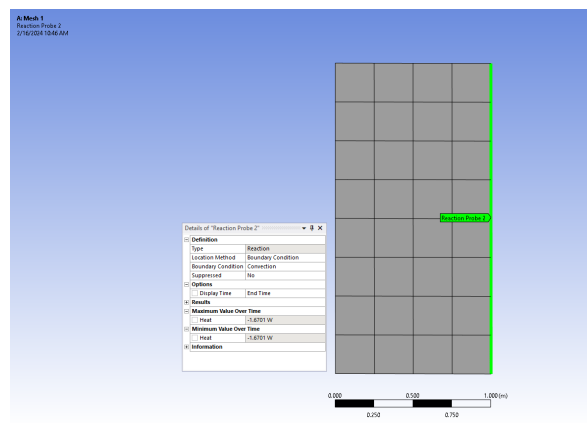
Fig. 8.   Heat transfer on the convective surface

82

In the specific case, in the absence of heat exchange through the other two boundaries and due to the condition that there is no heat generation, the heat balance depends only on the heat exchange through the lower and right surface of the region, and from the obtained values it can be seen that it is achieved.

IV. CONCLUSION

Numerical simulation and analysis of two-dimensional steady-state heat conduction in a rectangular domain using ANSYS proves to be extremely informative in studying thermal behaviour and optimizing design for efficient heat transfer.

In the present study, only the theoretical justification of the given problem is considered, without the presence of experimental data. As a future project, it is necessary to create a specialized experimental setup to provide an opportunity to compare the experimental data with the theoretically obtained ones. Moreover, when real problems arise where heat exchange is present, this approach turns out to be good enough and can be applied, as well as serve to solve similar problems in three-dimensional domains or include more complex boundary conditions for more further increasing the accuracy of the simulations.

Understanding two-dimensional heat conduction in rectangular domains is crucial for:

- Optimizing cooling systems in electronics;
- Improving insulation efficiency in buildings;
- Enhancing automotive cooling systems;
- Optimizing industrial processes for energy efficiency;
- Designing thermal management solutions in aerospace.

These applications demonstrate the importance of heat conduction analysis in various engineering fields for optimizing designs and improving performance.

REFERENCES

[1] Two-Dimensional, Steady-State Conduction https://www.cambridge.org/tn/files/6213/6698/3410/2.pdf

[2] Cornell University. (Dec 19. 2018). 2D Steady Conduction – Mesh. Simulation Wiki. https://confluence.cornell.edu/display/SIMULATION/2D+Steady+Conduction+-+Mesh

[3] T. L. Bergman, A. S. Lavine, F. P. Incropera and D. P. DeWitt, Introduction to Heat Transfer, Ch. 3 One-Dimensional Steady-State Conduction and Ch. 4 Two-Dimensional Steady-State Conduction, Copyright 2011, 2007, 2002 by John Wiley & Sons, Inc., 6th Edition, 2011, Pages 111-376, ISBN 13 978-0470-50196-2.

[4] T. L. Bergman, A. S. Lavine, F. P. Incropera and D. P. DeWitt, Fundamentals of Heat and Mass Transfer, Copyright 2011, 2007, 2002 by John Wiley & Sons, Inc., 7th Edition, 2011, ISBN 13 978-0470-50197-9

[5] W. H. David and Özisik M. N, Heat Conduction, John Wiley & Sons, Inc., Hoboken, New Jersey, 3rd Edition, 2012, ISBN 9780470902936.

[6] A. Bejan and A. D. Kraus, Heat Transfer Handbook, John Wiley & Sons, Inc., Hoboken, New Jersey, 3rd Edition, 2003, ISBN 978-0471321719.

[7] J. N. Reddy and D. K. Gartling, The Finite Element Method in Heat Transfer and Fluid Dynamics, CRC Press, Taylor & Francis Group, 3rd Edition, 2010, ISBN 9781420085983.

[8] S. Patankar, Numerical Heat Transfer and Fluid Flow, CRC Press Taylor & Francis Group, 1980, DOI https://doi.org/10.1201/9781482234213, eBook ISBN 9781315275130.

[9] Y. Jaluria, K. Torrance, Computational Heat Transfer, Published December 19 by CRC Press, 2nd Edition, 2002, ISBN 9781560324775.

[10] T. W. Davies, "BIOT NUMBER", THERMOPEDIA™ A-TO-Z GUIDE TO THERMODYNAMICS, HEAT & MASS TRANSFER, AND FLUIDS ENGINEERING, February 2011, DOI: 10.1615/AtoZ.b.biot_number.

Task-oriented temperature compensation as an instrument for reduction of uncertainty in Shop Floor CMM

Hristov Miroslav Hristov
Technical College - Sofia
Technical University of Sofia
Sofia, Bulgaria
miro.hr@tu-sofia.bg

***Abstract*. The significance of Shop Floor CMM in inspecting mechanical parts in modern industries, such as automotive and aerospace, has been increasing in recent years, making it an integral part of the inspection process. However, a major issue that remains is the uncertainty, particularly caused by changes in environmental conditions, such as ambient temperature, in shop floor conditions. Task-oriented temperature compensation software can solve these problems. Its effectiveness can be evaluated through uncertainty analysis.**

Keywords: Shop Floor Coordinate Measuring Machine, uncertainty, ambient temperature compensation.

I. Introduction

Trends in the development of high-tech industries have given a central place to coordinate metrology, Coordinate Measuring Machines (CMM) is the most common and fundamental measurement technology in the automotive industry, Modern geometric tolerances are becoming increasingly narrow, so the industry needs more accurate measuring instruments and more sophisticated measurement systems.[1] In the automotive industry, there are specific technical requirements for position tolerance such as true position and profile and surface measurement. These specifications and the combination of different materials with complex geometries make the CMM best suited for this task.

The development of the automotive industry and the need for high measurement reliability combined with near 100% control is leading to a change in the development of measurement and control. These requirements lead to the need for measurements close to the point of manufacture, for which shop floor CMMs are best suited.

The use of Shop floor CMM in production allows strong measurement versatility, great flexibility, adaptability and universality with the ability to perform complex metrological tasks without a real equivalent. The resultant measurement quality of CMM is limited by deviations and some uncertainties. The measurement deviations in coordinate metrology can be related to the operator performance quality, environmental interaction, work piece finishing, and CMM accuracy. It can be assumed that some influence factors of operator behaviour and CMM software accuracy have effective reactions on the measurement quality factors. [2]

II. Uncertainty in Shop Floor CMM

During CMM measurement, all relevant factors may have an impact on the measurement results. The sources of uncertainty in the coordinate measuring system can be divided into five categories according to the analysis method of "personnel, machine, object, method and environment" commonly used in product quality management as shown in Figure 1: Uncertainty caused by CMM instrument's own errors, measured work piece, surveyors, measuring method, and external environment (Fig. 1).[1]

1. Uncertainty caused by the subject of the measurement - the operator is caused from his level of professional qualities and self-responsibilities. In conventional CMM the uncertainty caused by operator is mainly characterized by the differences of the measurement strategies but for Shop Floor CMM the effect of operator is reduce to his influence caused by fixing of part on clamping positioning and defining of coordinate system, because operator used pre-set CNC programs.

2. Uncertainty caused by the instrumental errors which could be represent by deviation of the CMM's own metering characteristics from the ideal characteristics, including the uncertainty caused by design, standard quantity, detection system, dynamic characteristics, fitting and evaluation algorithm, probe system errors, datum stylus errors and other factors. These instrumented CMM errors on the shop floor are reflected in the impact of the residual system errors after correction and calibration

introduced by the "error map". In order to ensure accuracy, it is necessary to carry out repeat accuracy checks and recalibrations according to the manufacturer's requirements or international standards. [3]
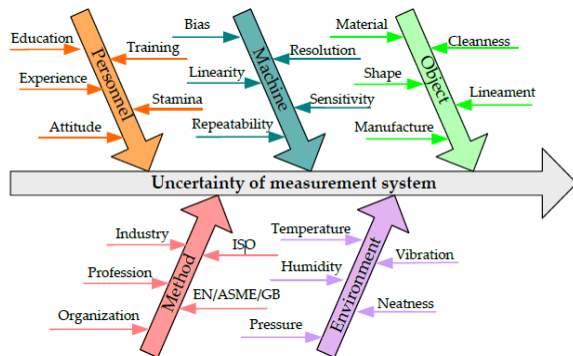
Fig. 1. Cause and effects diagram for uncertanty sorce of Shop Floor CMM. [1].

In the GPS ISO 10360 series standards [4] the CMM performance evaluation has been defined and relevant performance parameters and evaluation methods of the measuring instrument have been given. [5] There are some parameters influencing measurements with Shop Floor CMMs such as the indication and detection errors of the dimensional measurement as well as the dimensional and geometrical errors of the universal detection system. In practical measurement, the Maximum Permissible Indication Error (EMPE,L) is mainly related to the errors of the distance and other dimensional elements, and the MPEP indicates the error of the whole measurement system in a very small test space, generally affecting the form measurement. [1]

3. The uncertainty caused by the workpiece being measured can be represented by the geometric shape and dimensions, the measurement method and algorithm of the characteristics, the materials, with a large difference in thermal expansion, the elastic deformation of the workpiece due to the measurement force, and the clamping method.

4. The current development of CMM does not provide specific standards, procedures or specifications for the selection of strategy, measuring tips, relative coordinate system, sequence of actions for unambiguous definition of the measured parameters, which is the reason for the ambiguity of the results and source of uncertainty.

5. Uncertainty caused by environmental factors has higher impact on Shop Floor CMM than on standard CMM works in Laboratory environment. The temperature, humidity temporal gradient, vibration, dust, and other environmental has a very large fluctuation within one work shift. During CMM dimensional measurement, temperature compensation is usually needed and is "Task orientated"

The evaluation of measurement uncertainty should consider all factors that may affect the measurement results but focus must fall on the specific measurement tasks. Task-oriented measurement uncertainty must represent results from actions taken to improve the quality of results. This makes it appropriate to concentrate efforts on a small

number of factors that reflect part-to-part variation which represent close correlation between sources of uncertainty and measurement tasks.

III. ADVANCED MATERIALS IN WORKPIECE WITH COMPLEX FORM AND CONSTRUCTION

The development of technology allows the production of new materials and the use of different combinations between them. Materials have specific requirements (customer and legislative) to meet the demands of the automotive industry. [6] Advanced materials help us create lighter, stronger and more flexible parts. With new types of steels, such as high strength steels (HSS), (UHSS) and (AHSS), which are specifically developed for the automotive industry, we get durability, strength and hardness combined with low production costs in large quantities and the ability to recycle. [7]

Aluminium and magnesium alloys are increasingly used in mechanical engineering and in particular in the automotive and aviation industry. Aluminium castings are used for various automotive parts, resulting in significant weight reduction. [8]. On the other hand, magnesium is lighter than aluminium and SS with higher corrosion resistance. Due to specific mechanical and physical properties, magnesium components require a unique more complex design. [6]. Titanium alloys has a principal advantages likes their low density, high strength to density ratio, excellent corrosion resistance and superior strength retention at elevated temperatures. The major drawback of titanium is its high cost [9]

Polymers, plastics and composites such as polyamide (PA), acrylonitrile/butadiene/styrene (ABS), polyvinyl chloride (PVC), polypropylene (PP), polyoxymethylene (POM), acrylic (PMMA), polybutylene terephthalate (PBT), etc. have revolutionized many industries. Parts made of plastics are corrosion resistant, offer flexibility and elasticity for added safety, have very good thermal insulation. Plastics are helping to reduce the cost of vehicle production, and polymers are improving vehicle design. [10]

Carbon fibers are widely used in parts that need to be stable and lightweight, resistant to torsion, corrosion and abrupt changes in operating conditions. Carbon fibre reinforced plastics (CFRP) are highly desirable materials in automotive and aerospace applications due to their specific stiffness, good strength and fatigue properties compared to conventional metals. [11]

Hybrid composites are made of several layers of composite and other materials. Their undoubted advantages are the basis of their increasing prevalence at the expense of specific design features and complicating component control. [12]

All of these materials and the combinations between them in the design and construction of complex parts and assemblies comes with specific design, construction, form and configuration requirements. The main problem with all these materials is the big difference in their Thermal expansion coefficients (α) which varies from α=7 [10-6 m/m℃] to α=300 [10-6 m/m℃] and makes the measurement of details with complex construction difficult

in the shop floor ambient environment and imposes a task-oriented metrological mission.
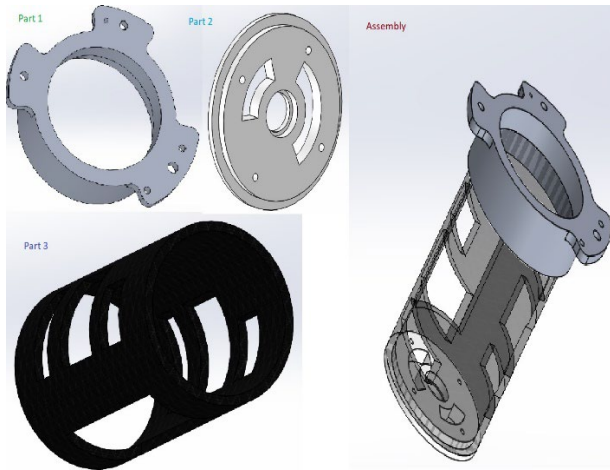
Fig. 2. Assembly of three parts made from different materials with complex requirements for form and position control.

The use of materials like CFRP, aluminium, PA, PEEK, ABS, and brass in the automotive industry is leading to changes in structural elements. These changes include more complex geometries, asymmetric shapes, and narrower tolerance limits. Specific requirements for true position, profile, and surface are also necessary based on datum features. Lightening structures to improve physical characteristics can have drawbacks in controllability, especially in the Shop Floor environment. This requires new approaches and the use of CMM as the primary measuring tool in the automotive and other modern industries. The spatial deformations caused by unpredictable shapeshifting due to ambient temperature are non-linear in nature. Thermal expansion coefficients α cannot universally recalculate these deformations. Additional research and mathematical models are necessary to reduce the non-linearity based on task-oriented temperature compensation.

To ensure the necessary accuracy of the assembled unit, it may be necessary to perform some processing while it is assembled. Therefore, it is important to check not only the individual elements but also the assembled unit. This presents challenges in controlling positional deviation, profile deviations, and surface deviations in workshop conditions due to the varying coefficient of linear temperature deformation of the different materials used. Additional calculations are necessary to ensure accurate measurements comparable to those made under normal conditions (ISO 1:2016). [13]

Fig. 2 presents an isometric image of a complex body part composed of parts made of different materials: Part 1 (material: Aluminium), Part 2 (material: ABS), and Part 3 (material: Hexcel AS4C). This serves as an example of an assembly made of different materials. The primary metrological issue concerns the regulation of concentricity (EPC) between the central holes of Part 1 and Part 2, deviations from roundness (EFK), and true position (EPP) in relation to the datum's (Fig. 3). [14]
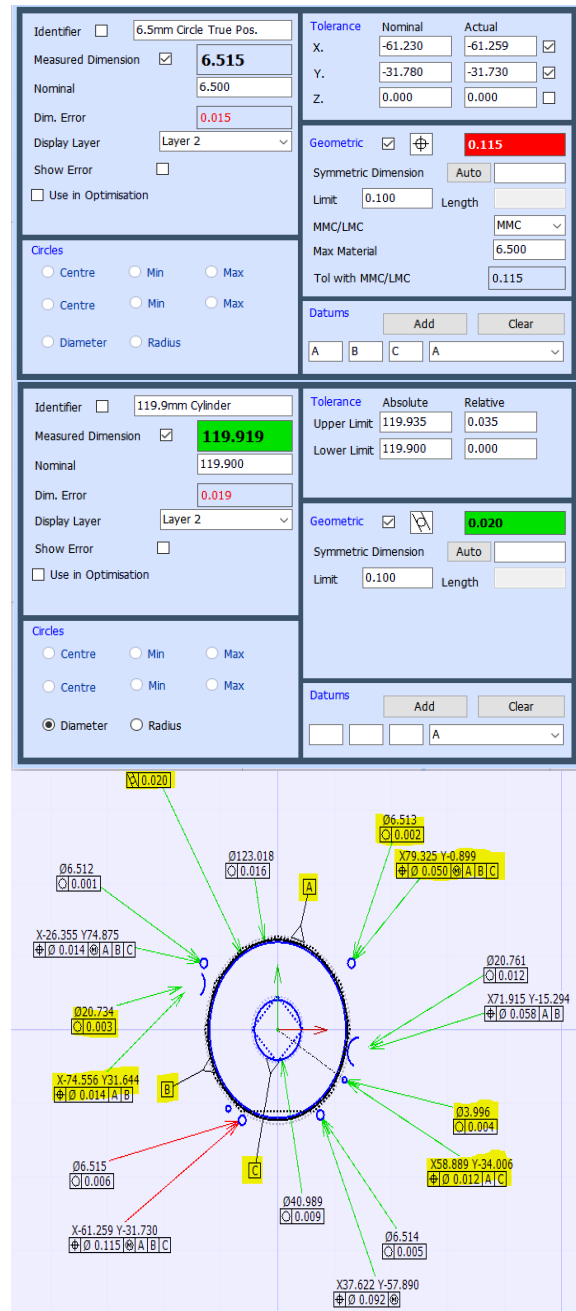
Fig. 3. This is a fragment of a program for controlling all-part assembled unit using Aberlink 3Dv4 software.

IV. SOFTWARE COMPENSATION FOR AMBIENT TEMPERATURE FLUCTUATION

Temperature is a critical environmental parameter affecting the uncertainty of the Shop Floor CMM measurement. On the one hand, temperature fluctuations over a wide range have a significant impact on the entire machine structure due to the deformations it causes. This deformation is very difficult to predict or simulate. In parallel, the ambient temperature has a significant influence on the dimensions and shape of complex workpieces of different materials. Spatial temperature gradients of the surrounding environment, draughts and thermal radiation caused by surrounding machinery, walls, windows, luminaires or sunlight have a particular influence on dimensions and shape. For parts of simple single material construction, these influencing factors are

functionally dependent on the thermal expansion coefficients (α) of the materials. [15]

Shop-floor production control has the undeniable advantages of eliminating the requirement to maintain a reference temperature, resulting in the elimination of the need for expensive air conditioning systems to maintain a temperature of around 20°C ±2°C and 65% RH ±10% HR, in accordance with the recommendations of the international standard ISO 1:2016 [13].

As a major disadvantage it should be noted the environmental uncertainty of the measurements and the assessment of the agreement between the results obtained in the laboratory and in the workshop. [16]

Based on the requirements of the market (consumers) for integration of the Shop Floor CMM in automated control, the ambient temperature can have the most impact on a CMM's accuracy and repeatability. Depending on the requirements of the specific industry and the design specifics of the items being controlled, specific "task-oriented" software temperature compensation can be used.

The CMM utilizes software temperature compensation as a standard to minimize the impact of temperature changes on its structure. Additionally, linear temperature compensation of objects is possible. To enhance the performance of the Shop Floor CMM, "task-oriented" software can be utilized to compensate for temperature and reduce environmental uncertainty. This is particularly effective in minimizing the impact of ambient temperature on form and position deviation.

A "task oriented" software temperature compensation can be performed in several steps. Firstly, we need to identify the critical control parameters (CCP_n) from the drawing according to the expected non-linear temperature deformation. The previous information from the control of the part will help in the identification. Then we need to simulate the temperature deformation using the Finite Element Method (FEM) [17] to determine each critical parameter as a theoretical deviation $d\varepsilon_{SIMU,A}(dt)$ (simulated nonlinear temperature deformation) for a given temperature change:

$$dt = t_0 - t_n, \tag{1}$$

where: t_0 - standard reference temperature [13] t_n – measured temperature.
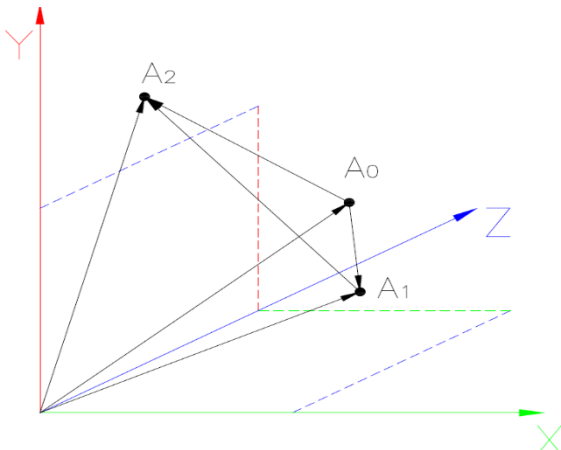
Fig. 4. Vector representation of SNTD as position of point A in Cartesian coordinate system.

The next step is to perform a vector analysis (Fig. 4) of the variation of CCP_n as point positions $A(x_a, y_a, z_a)$ and radius vectors $A(i_a, j_a, k_a)$ to the center of the relative coordinate system OXYZ (i=0, j=0, k=0) of the workpiece. Vector $\overrightarrow{OA_0}$ represents the theoretically accurate position A_0 with confidence. The temperature compensation option integrated into the Shop Floor CMM software accurately calculates the linear deformation at temperature t_n and determines the position of point A_1, represented by vector $\overrightarrow{OA_1}$:

$$\overrightarrow{OA_1} = \overrightarrow{OA_0} + \overrightarrow{A_0A_1}, \tag{2}$$

where:

$\overrightarrow{A_0A_1}$ is linear temperature compensation $t_n \neq 20\,℃$. The actual position A_2 can be represented by a vector $\overrightarrow{OA_2}$ and analytically as the sum of the vectors:

$$\overrightarrow{OA_2} = \overrightarrow{OA_0} + \overrightarrow{A_0A_2}, \tag{3}$$

where $\overrightarrow{A_0A_2}$ is a vector that determines the actual position of A2 after simulation of non-linear temperature deformation and is analytically equal to:

$$\overrightarrow{A_0A_2} = \overrightarrow{A_0A_1} + \overrightarrow{A_1A_2}, \tag{4}$$

where $\overrightarrow{A_1A_2}$ is a vector representing the change in position A_0 after application of linear compensation $\overrightarrow{A_0A_1}$ and simulated non-linear temperature deformation $\overrightarrow{A_0A_2}$.

In the application of vector analysis to the calculation of shape and position deviation, it is necessary to represent the vectors as projections in an XY datum feature plane by the errors they generate:

$$E_{A,t} = \varepsilon_\alpha - \varepsilon_\varphi \pm E_{MPE,L}, \tag{5}$$

where the linear temperature deformation error ε_α is equal to the projection of the vector $\overrightarrow{A_0A_1}$ in the XY datum feature plane and the non-linear temperature deformation error ε_φ is equal to the projection of the vector $\overrightarrow{A_0A_2}$ in the XY datum feature plane.

V. Uncertainty evaluation in Shop Floor CMM with task-oriented temperature compensation

Shop-floor CMMs are highly effective in inspecting complex surfaces, including multiplex surfaces (free-form surfaces), which are considered one of the most challenging measurement tasks due to the critical factor of measurement uncertainty. [18]

The measurement uncertainty of Shop-floor CMMs is affected by various factors. The ISO 15530 series of standards [5] offers several methods for determining the measurement uncertainty of a specific measurement task. Multiple measurement strategies are available, with or without calibrated workpieces, and computer simulation can also be used. Measuring complex surfaces at Shop-floor CMM poses a challenge for uncertainty estimation, but with careful attention, it can be done confidently. Inspection of complex parts using CMM is challenging due to the limitations of existing standards and recommendations. Assessing uncertainty of CMM measurements for complex shapes is mainly challenged by ensuring traceability of measurements. [2],[18]

Various methods exist for estimating uncertainty when measuring complex surfaces with shop floor CMM. A simplified methodology can account for some of the components contributing to uncertainty. In this study, we will use a simplified model to project a point onto a plane and estimate the change in coordinates resulting from ambient temperature changes. Our focus will be on the uncertainty caused by nonlinear temperature deformations. One of the main issues is the inability to make comparisons with a reference due to variations in materials and combinations, as well as the complex shapes of the parts.

To estimate the uncertainty of the Shop Floor CMM, use a combination of Type A and Type B uncertainties [19], along with computer simulation methods for temperature deformations. [20]

Type A evaluations assess the repeatability or randomness of a measurement process. The standard deviation is used to calculate the Type A uncertainty [21]:

$$\sigma_x = \sqrt{\frac{1}{n-1}\sum_{k=1}^{n}(x_k - \bar{x})^2}, \qquad (6)$$

where:

$$\bar{x} = \frac{1}{n}\sum_{k=1}^{n}x_k \qquad (7)$$

where x_k are the individual measurements and n is the number of measurements.

To evaluate all uncertainties associated with input estimates that have not been obtained from repeated observations, scientific judgement must be used. The metrologist should draw on all possible sources of information, their experience, and general knowledge about the processes to make reliable decisions about Type B uncertainties. [21], [22]

For the purpose of the study we use a Shop Floor CMM Aberlink Extol 370 [23] which is placed in conditions of ambient temperature change over a wide range (approximately 15 degrees within 8 hours). The aluminium workpiece being tested has complex shapes that require specific form and position requirements.

The measurement uncertainty can be represented by 5 components which have a different performance compared to spatial CMMs.

$$u_c = \sqrt{u_{ES}^2 + u_{EI}^2 + u_{EO}^2 + u_{EM}^2 + u_{ET}^2} \qquad (8)$$

The uncertainty caused by the measurement person (subject) u_{ES} depends on placing the measured object on a jig (fixture device) u_{ESF}, because Shop Floor CMM works with a pre-set CNC inspection program that is not affected by changes in ambient temperature. To evaluate u_{ESF}, we could perform uncertainty Type A with two series of 10 repeated measurements of datum features. The first series would involve measuring the object without replacing it (u_{NF10}^2), while the second series would involve replacing the object after each measurement (u_{NF10}^2).

$$u_{ES} = u_{ESF} = \sqrt{(u_{NF10}^2 - u_{F10}^2)} \qquad (9)$$

Type B uncertainty allows the Repeatability error E_R stated in the technical specification by the manufacturer to represent the u_{ESF}:

$$u_{ESF} = E_R \qquad (10)$$

The instrumental uncertainty u_{EI} is represented as a Type B uncertainty with two components: - Reading uncertainty u_{EIR} on the Shop Floor CMM, represented by the measurement error from the ISO 10 360 [12] length calibration certificate $E_{MPE,L}$; - Probe uncertainty u_{EIP}, represented by the measurement error declared by the manufacturer $E_{MPE,P}$:

$$u_{EI} = \sqrt{u_{EIR}^2 + u_{EIP}^2} = \sqrt{E_{MPE,L}^2 + E_{MPE,P}^2} \qquad (11)$$

The Repeatability error (E_R) is an integral component of the $E_{MPE,L}$.

The uncertainty caused by the measured object u_{EO} can be confidently simulated using the finite element method (FEM) [17] in SolidWorks. This uncertainty is comprised of two inseparable components: the uncertainty from the type of material/the combination of different materials u_{EOM}, and the uncertainty caused by the complex shape of the object u_{EOF}:

$$u_{EO} = \sqrt{u_{EOM}^2 + u_{EOF}^2} = dt_{SIMU} \qquad (12)$$

where dt_{SIMU} is simulated non-linear temperature compensation.

The object uncertainty u_{EO} can be viewed as a modified software emulated Type B uncertainty.

Shop floor CMMs operate using a pre-set CNC program, which results in a high level of method uncertainty u_{EM}. The uncertainty observed when utilizing a CAD model is due to a mismatch between the datum features of the model and the actual workpiece (u_{EMDF}). The uncertainty is equal to the E_{RMS} error, which is calculated as the difference between the real and ideal object by the software Aberlink 3D MK4 [23]:

$$u_{EMDF} = E_{RMS} \qquad (13)$$

The method uncertainty u_{EM} can be viewed as a modified software emulated Type B uncertainty.

The change in ambient temperature is the main factor that influences environmental uncertainty u_{ET}. This uncertainty is the result of the sum of Machine uncertainty u_{ETM} caused by temperature fluctuation and Part uncertainty u_{ETP} caused by temperature fluctuation:

$$u_{ET} = \sqrt{u_{ETM}^2 + u_{ETP}^2} \qquad (14)$$

The Machine Uncertainty can be represented by a Type A uncertainty based on MSA (Measurement System Analysis) [23] calculations for Equipment Variation (EV), but at the same time it is software compensated and can be assumed to be zero:

$$u_{ETM} = EV = 0 \qquad (15)$$

The Part uncertainty u_{ETP} is represented by a Type A uncertainty based on Measuring System Analysis (MSA) [24] calculations for Part Variation (PV). Additionally, the Part uncertainty has been previously calculated through software simulation as non-linear temperature compensation dt_{SIMU}

$$u_{ET} = \sqrt{EV^2 + PV^2} = u_{ETP} = dt_{SIMU} \qquad (16)$$

The environmental uncertainty u_{ET} can be viewed as a modified software emulated Type B uncertainty.

$$u_c = \sqrt{E_{MPE,L}^2 + E_{MPE,P}^2 + 2dt_{SIMU}^2 + E_{RPS}^2}$$
(17)

This study aims to determine how uncertainty varies with changes in environmental conditions, specifically ambient temperature:

$$u_C = \frac{d}{dt} f(u_C)$$
(18)

$E_{MPE,L}$ and $E_{MPE,P}$ are constant and not function of ambient temperature fluctuation:

$$\frac{d}{dt} E_{MPE,L} = \frac{d}{dt} E_{MPE,L} = 0$$
(19)

The variation of uncertainty as a function of fluctuating ambient temperature is:

$$u_{\frac{d}{dt}} = \sqrt{2dt_{SIMU}^2 + E_{RMS}^2}$$
(20)

Introducing task-oriented temperature compensation results in an uncertainty $u_{d/dt}$ that is analytically equal to:

$$u_{\frac{d}{dt}} = E_{RMS}$$
(21)

The presented equation demonstrates how to estimate uncertainty as a function of ambient temperature variation using the E_{RMS} error. A task-oriented systematic software correction can be confidently introduced for each temperature value to effectively minimize uncertainty.

VI. Conclusion

Shop-floor CMMs are becoming increasingly popular due to their flexibility in automated high-tech manufacturing. Although they have specific applications, shop-floor CMMs are constantly evolving to reduce control uncertainty. The use of task-oriented temperature compensation can greatly reduce uncertainty and make results comparable to those obtained in laboratory conditions.

Acknowledgment

Bibliography & Reference

[1] C. Yinbao, W. Zhongyu, C. Xiaohuai, etc., Evaluation and Optimization of Task-oriented Machines Based on Geometrical Product Specifications, Appl. Sci. 2019, 9, 6; www.mdpi.com/journal/applsci, ISSN: 2076-3417

[2] S. Topfer, G. Linss, etc, Automatic Execution of Inspection Plans with the I++DME Interface for Industrial Coordinate Measurements, M&MS Journal, vol. XIV, no. 1 pp. 71–88, Poland, 2007

[3] T. Jordan and P. A. Taylor, Hacktivism and Cyberwars: Rebels with a cause? London: Routledge, 2004.

[4] ISO 10360 GPS - Acceptance and reverification tests for coordinate measuring machines

[5] ISO 15530 GPS – CMM: Techniques for evaluation of uncertainty of measurement

[6] M. Chiaberge, New Trends and Developments in Automotive Industry, InTech 2011, ISBN 978-953-307-999-8

[7] J. Galán, L. Samek, etc, Advanced high strength steels for automotive industry, iSSn: 0034-8570, eiSSn: 1988-4222, doi: 10.3989/revmetalm.1158

[8] M. Fentahun, M. Savas, Materials Used in Automotive Manufacture and Material Selection Using Ashby Charts, International Journal of Materials Engineering 2018, DOI: 10.5923/j.ijme.20180803.02

[9] J. Rowe, Advanced materials in automotive engineering, Woodhead Publishing Limited, 2012, ISBN 978-0-85709-546-6

[10] https://coolmag.net/polymeric-materials-for-automotive-applications/ - 14.01.24

[11] R. Othman, N. Ismail, etc, Application of carbon fiber reinforced plastics in automotive industry: a review, Journal of Mechanical Manufacturing (J-MFac), Vol 1, 2018

[12] A. Elmarakbi, Advanced composite materials for automotive applications, 2014 John Wiley & Sons, ISBN: 978-1-118-42386-8

[13] ISO 1:2016 GPS - Standard reference temperature for the specification of geometrical and dimensional properties

[14] ISO 5459:2011 GPS - Geometrical tolerancing - Datums and datum systems

[15] M. Mantel, Coordinate measuring machines: A modern inspection tool in Manufacturing, New Jersey Institute of Technology, https://digitalcommons.njit.edu/theses/1246, Theses. 1246

[16] Metrology in Industry, The Key for Quality, French College of Metrology, ISTE Ltd 2006, ISBN-13: 978-1-905209-51-4

[17] E. Madenci, I. Guven, The Finite Element Method and Applications in Engineering Using ANSYS, 2nd Edition, Springer I. P. 2015, ISBN 978-1-4899-7550-8

[18] I. Vrba, R. Palencar, M. Hadzistevic, Different Approaches in Uncertainty Evaluation for Measurement of Complex Surfaces Using Coordinate Measuring Machine, MEASUREMENT SCIENCE REVIEW, Volume 15, No. 3, 2015, 0.1515/msr-2015-0017

[19] Evaluation of measurement data - Guide to the expression of uncertainty in measurement, JCGM 100:2008, JCGM 2008

[20] R. Wilhelml, R. Hocken, H. Schwenke, Task Specific Uncertainty in Coordinate Measurement, CIRP Annals - Manufacturing Technology, Elsevier 2001, https://doi.org/10.1016/S0007-8506(07)62995-3

[21] D. Flack, Measurement Good Practice Guide No. 130: Co-ordinate measuring machine task-specific measurement uncertainties, Crown Copyright 2013, ISSN 1368-6550.

[22] D. Flack, Measurement Good Practice Guide No. 42 - CMM Verification, Queen's Printer and controller of HMSO, July 2001, National Physical Laboratory, ISSN 1368-6550

[23] https://www.aberlink.com/products/coordinate-measuring-machines/extol/ - 14.01.24

[24] Measurement systems analysis (MSA), Reference Manual, Fourth Edition, Copyright 2010 Chrysler Group LLC, Ford Motor Company, General Motors Corporation, ISBN#: 978-1-60-534211-5

[25] T. Allen, Introduction to Engineering Statistics and Lean Six Sigma, Third Edition Springer 2006, ISBN 978-1-4471-7420-2 (eBook), https://doi.org/10.1007/978-1-4471-7420-2

[26] Guide to the Expression of Uncertainty in Measurement Geneva, 1995

[27] ISO 14253 GPS - Inspection by measurement of workpieces and measuring equipment

[28] ISO 23165 GPS - Guidelines for the Evaluation of CMM Test Uncertainty

[29] A. Stadek, Coordinate Metrology, Springer 2020, ISBN 978-3-662-48465-4

[30] A. Weckenmann, M. Knauer, The Influence of Measurement Strategy on the Uncertainty of CMM-Measurements. Annals of the CIRP 47 1, 451 – 454, 1998

Experimental study of the Frequency Responses of Electropneumatic positioning system

Georgi Iliev
dept. Power Engineering
Technical University of Gabrovo
Gabrovo, Bulgaria
spigil@abv.bg

Abstract. **This paper describes an experimental study and comparison of the frequency responses of an electropneumatic positioning system with a rod and a rodless pneumatic cylinder. An experimental rig is set up to study the Bode magnitude and phase plots of an electropneumatic positioning system with different types of pneumatic cylinders, and the critical frequencies of the system are determined. A virtual instrument is used to collect experimental data. The processing and process control are automatically performed by a PC and the corresponding NI interface board. The frequency response of the system is defined by two graphs - Amplitude-frequency response (AFR) and Phase-frequency response (PFR). From the presented characteristics, the critical frequencies are determined for both systems - with double out rod and rodless cylinder. As a result of the research, it was established that in a pneumatic positioning system with a double-sided out rod cylinder, the critical frequency is higher than the system with rodless cylinder. This indicates the better dynamic properties of the system. The advantages of the rodless pneumatic cylinder are that its design occupies less embedding space compared to a cylinder with a double out rod, which requires twice the clearances for equal working strokes in industrial electropneumatic positioning systems.**

Keywords: critical frequencies, electropneumatic positioning system, frequency responses, virtual instrument.

I. Introduction

Electropneumatic positioning systems are widely used in contemporary industry. They are easily implemented in the production of automated devices, CNC machines, industrial robots and manipulators, automated industrial lines, which has expanded the range of joint operation of pneumatic positioning systems and their controlling electronic devices. As they possess a number of positive qualities, this has caused an increase in research and applied developments on electropneumatic positioning systems. They are environmentally safe have the flexible control and the possibilities of easily forming the required control law achieved by electronic and computer devices,

are combined with a good weight/power ratio and good dynamic characteristics of pneumatic mechanisms making them systems with low commercial cost compared to tardive electric and electrohydraulic positioning systems [1]-[19].

Due to the compressibility of air, unfavourable friction characteristics and little damping, pneumatic devices require complex control. But they also offer advantages such as: the compressibility of air provides damping of impact loads, which is important in many technical applications [1-5] in which electropneumatic positioning systems are applied. This imposes strict requirements related to their operation in static and dynamic modes. For the analysis of electropneumatic positioning systems and synthesis of control algorithms, frequency characteristics (amplitude-frequency and phase-frequency) are widely used to describe the dynamic properties of the system. Experimental determination of frequency characteristics allows to compile adequate mathematical models that can be used to study and design systems with a certain quality of reliability and accuracy [3], [4], [5], [9], [11], [18].

Industrial electropneumatic positioning systems are very often assimilated with pneumatic actuators of different design - such as pneumatic cylinders with double outriggers or pneumatic rodless cylinders, etc. The difference in design of pneumatic cylinders will make a difference in the dynamics of the system. Therefore, research is needed in this area [6-12].

A laboratory stand Fig.1 for determining the frequency characteristics of an electropneumatic positioning system has been developed, which allows real-time experimental studies with pneumatic cylinders of different design. It can be used to determine the critical frequencies and operating range of the system in dynamic mode.

II. exposition

In many cases, electropneumatic positioning systems have requirements for both precise stopping of the input signal variation and high speed performance.

- The speed performance of a pneumatic system is characterized by two main parameters:

- Set-up time - the time required for the output signal to become matched to the input signal. Fast systems have minimum rise times.

- Eigenfrequency (critical) - indicates what signal variation in seconds the electropneumatic system is capable of responding to.
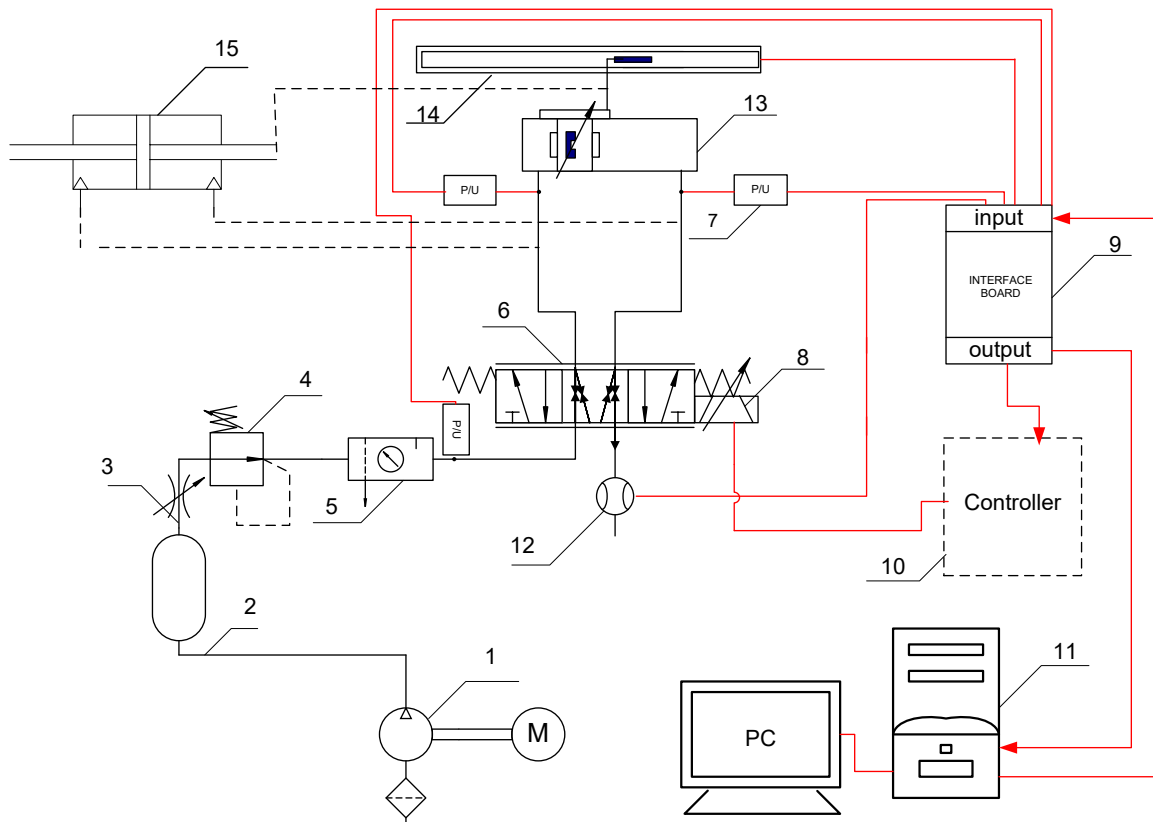
Fig. 1.   General view of the experimental stand for capturing frequency characteristics

1 –screw compressor, 2 – receiver, 3 – stopcock, 4- safety valve, 5 – air preparation system preparatory, 6 – pneumatic proportional valve, 7 – pressure sensors, 8 – coil of pneumatic proportional valve, 9 – interface board; 10 – pneumatic proportional valve controller; 11 – PC, 12 – flow meters, 13 – pneumatic rodless cylinder 14– linear displacement sensor.15- pneumatic cylinder with double out rod.

A sinusoidal control signal is applied to the system. The variation of the input signal and the displacement of the pneumatic cylinder are recorded using the measuring system. When the frequency of the input signal is low, the cylinder piston oscillates at the same frequency as the input signal. As the input frequency increases, while maintaining the signal amplitude, the frequency of the cylinder oscillation also increases. But at high frequency, the pneumatic cylinder can no longer follow the variations of the input signal and its oscillation amplitude is reduced. The frequency at which this starts to happen is the critical frequency [2, 6].

The frequency response of the system is defined by two graphs.

- Amplitude-frequency response (AFR).

The ratio of the amplitude at measured frequencies to the amplitude at very low frequencies is noted in decibels dB and plotted on a logarithmic scale. The amplitude ratio of -20 dB means that the amplitude at a given frequency is 10 times smaller than the amplitude at low frequencies. Plotting the amplitudes at all measured frequencies gives the amplitude-frequency response.

- Phase frequency response (PFR).

The delay of the output signal with respect to the input signal is measured in angular degrees. A phase lag of 360 degrees means that the output signal lags a full cycle.

A graphical representation of dephasing as a function of frequency is called a phase-frequency response

At a 10% change in input signal amplitude = 1 V, the cylinder must be moved a small distance. Therefore, it can work out such a variation of the input signal at a large frequency. The amplitude and phase response deviate from the horizontal line only at high frequencies. At 90% variation of the input signal amplitude = 9 V the distance the pneumatic cylinder has to move is 9 times larger. It hardly follows the variation of the input signals. The amplitude and phase response also deviate from the horizontal line at low frequency.

- Critical frequency

The value of the critical frequency is read from the amplitude-frequency characteristic This is the frequency at which the amplitude drops to 70.7% or -3 dB.

Limitations in the use of pneumatic proportional elements are determined by the maximum pressure their housing can withstand [3], [4], [5], [12].

III. MATERIALS AND METHODS

To determine the frequency characteristics of the electropneumatic positioning system, the developed laboratory stand, is used.

The control of the experimental process, data acquisition and processing and data archiving is performed automatically by a personal computer and the corresponding interface board of the company "National Instruments". For the purpose of the experiment, a specialized process control software for the experiment, "LabView", is used, which has the capability of unlimited number of measurements and real-time data processing. A dedicated virtual instrument has been created. The investigated electro-pneumatic positioning system is composed of basic elements: screw compressor, pneumatic proportional distributor "Schneider Kreuznach" PVM 065-030-1101-0A-6, pneumatic cylinders - rodless cylinder "Camozzi 52M2P32A1000" and pneumatic cylinder with double out rod "Camozzi 61M6P040A0500 " as well as measuring equipment.

- Order of the experiment

1. Initially, run the screw compressor to create the required amount of compressed air to power the rig. Check the pressure is the receiver. Monitor the air preparation system preparatory to set the operating pressure for the experiment at 4 bar (it is possible to run the experiment at other pressures).

2. Run the measurement software to process and archive the experiment data. Start the virtual instruments created for the experiment. Check and test the performance of the primary measuring instruments - pressure transducers, potentiometric displacement sensor. The virtual signal generator instrument is also started. The signals from the inputs and outputs of the terminal board are checked. After testing the measurement circuit, the measurements start.

3. The initial position of the electro-pneumatic positioning system is established.

4. Adjust the parameters of the sine signal generator

5. A sinusoidal input signal with different amplitudes - 1; 1.3 and 1.6 V - is supplied to the electropneumatic positioning system from the signal generator. The variation of the input signal and the displacement of the pneumatic cylinder are recorded using the virtual instrument. The experimental results converted from digital to graphical form from the input signals as well as the set output signals are observed on the screen.

6. After the end of the recording, the system returns to the starting position.

The experiment is repeated as many times as necessary to avoid error.

After the first experiment is dismantled, the pneumatic cylinder is removed and replaced with another model pneumatic cylinder, the experiment is repeated according

to the described methodology. In this way different pneumatic cylinder designs will be investigated.

- Number of observations

For specific conditions for the Camozzi 52M2P32A1000 pneumatic rodless cylinder, three measurements were made at different input signal amplitudes - voltages 1; 1.3 and 1.6 V. The measurement results are averaged.

For the Camozzi 61M6P040A0500 pneumatic cylinder with double out rod, three measurements were made at different input signal amplitudes - voltages 0,3 V; 0,5 V and 1 V. The measurement results are averaged.

- Accuracy of measurements

For the experimental study of dynamic processes in an electropneumatic positioning system, it is assumed that the instrumentation has much smaller time constants than those of the system under test. In practice, their transients occur many times faster and are assumed to be ideal aperiodic units of order 1 with time constants many times smaller than the time constant of the units system under study.

- Virtual tools for input data

For the purpose of the experiment, a virtual tool was developed performing the following functions:

a) measurement of supply pressure;

b) measurement of the pressure in the left and right chambers of the pneumatic cylinder;

c) measurement of the displacement of the piston of the pneumatic cylinder;

d) measuring the flow rate;

- Virtual tools for source data;

a) Sine signal generator Fig. 2.

The next function is the conversion into natural units of each of the measured channels The production of a signal serving as feedback to the regulator, which is fed to the analog output of the board. The possibility is provided to record in a text file all input signals from a given point in time.
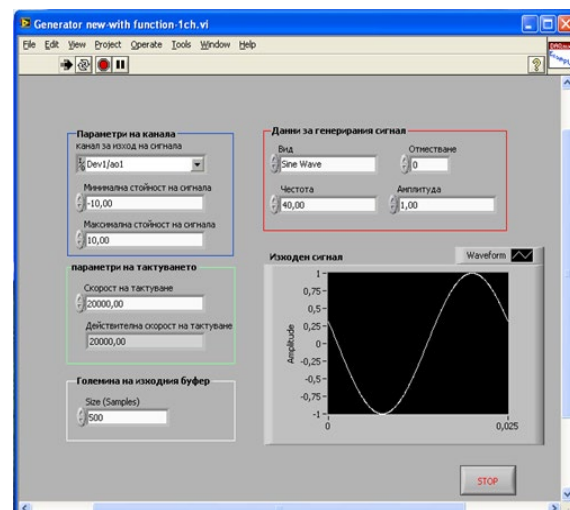
Fig. 2. Virtual tools sine signal generator.

Fig. 3 shows the user part of the developed virtual instrument where the values of the input and output quantities can be monitored in real time after the measurement is completed the signal data is visualized.
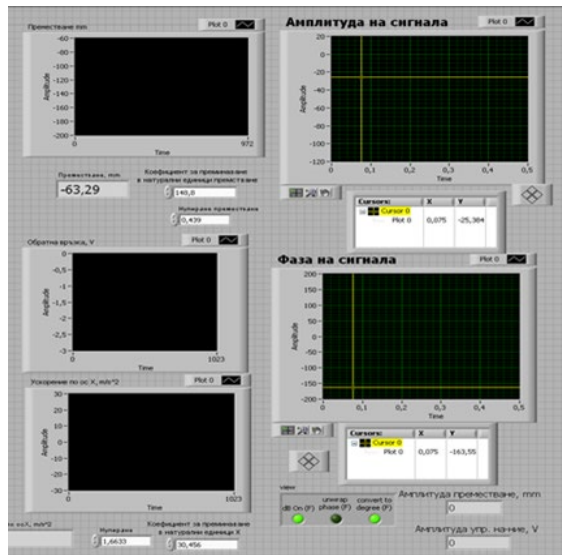
Fig. 3. User interface of the developed virtual instrument with a function measuring the phase angle of the signal.

IV. RESULTS AND DISCUSSION

The data from each experiment can be presented in tabular form as arrays of numbers. They are of great length, since the data is written 20 to 200 times per second. It is more convenient to present them in graphical form.

From the experimental investigations performed, frequency characteristics of the electropneumatic positioning system at different amplitude input signals were obtained. The obtained characteristics confirm the nonlinear nature of the system, as the frequency characteristics are different at different amplitude input effects.

From the presented characteristics, the critical frequency of the pneumatic positioning system with a frictionless pneumatic cylinder can be determined, which at different input signals is of 2 Hz, determined from the phase - frequency response at -90^0 Fig. 4.
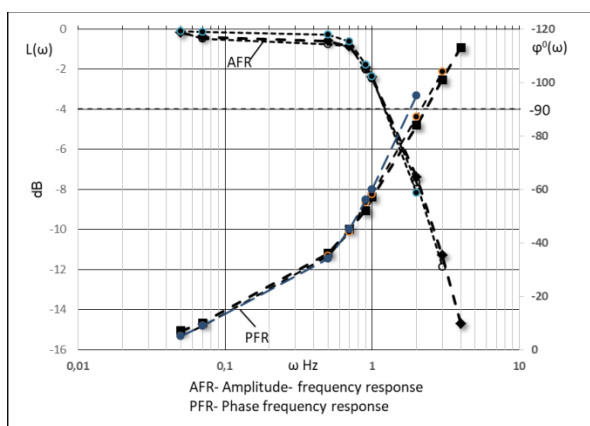
Fig. 4. Aamplitude-frequency and phase-frequency response of an electropneumatic positioning system with a rodless cylinder at input signal amplitudes of 1, 1.3 and 1.6V.

From the presented characteristics, the critical frequency of the pneumatic positioning system with a pneumatic cylinder with a double out rod can be determined, which for the different input signals is 3 Hz, determined from the phase -frequency response at - 90^0 - Fig. 5.
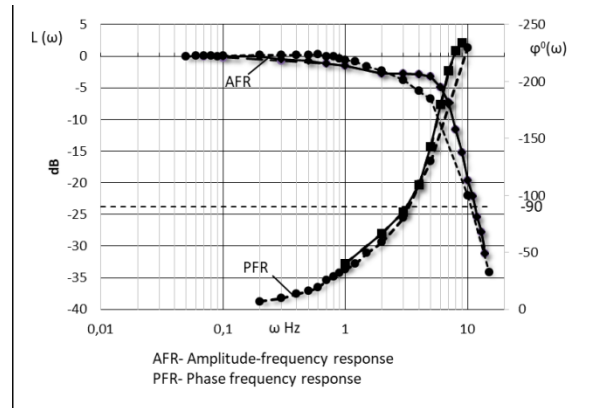
Fig. 5. Aamplitude-frequency and phase-frequency response of an electropneumatic positioning system at 0.3, 0.5 and 1 V of a pneumatic cylinder system with a double-sided outr rod.

It is known that friction forces are higher in rodless pneumatic cylinders compared to conventional piston cylinders. As a consequence, the dynamic properties are degraded and this determines the lower critical frequency of the whole system.

The critical frequency of the electropneumatic positioning system with a pneumatic cylinder with a double-sided outrigger rod and rodless pneumatic cylinders were determined using the experimentally obtained amplitude-frequency response and phase frequency response.

V. CONCLUSIONS

In previous studies by the authors [5], it has been shown that the frictional forces are larger in a rodless pneumatic cylinder compared to a piston pneumatic cylinder. As a consequence, the dynamic properties are degraded and the nonlinear properties are manifested at large input signal amplitudes. In a pistonless pneumatic cylinder, the critical frequency reaches up to 2 Hz (Fig. 4).

In a pneumatic positioning system with a pneumatic cylinder with a double-sided outrigger rod, the critical frequency is **3 Hz** (Fig. 5.), indicating the better properties in the dynamic regime of the system.

The advantages of the rodless pneumatic cylinder are that its design occupies less embedding space compared to a cylinder with a double out rod, which requires twice the clearances for equal working strokes in industrial electropneumatic positioning systems.

VI. ACKNOWLEDGMENTS

REFERENCES

[1] G. Iliev and H. Hristov, "MODELLING AND SIMULATION OF ELECTROPNEUMATIC POSITIONING SYSTEM INCLUDING

THE LENGTH OF PNEUMATIC LINES", ETR, vol. 3, pp. 106–111, Jan. 2024, doi: 10.17770/etr2023vol3.7186.

[2] G. Iliev and H. Hristov, "MODELLING AND SIMULATION OF DYNAMIC PROCESSES OF PNEUMATIC LINES", ETR, vol. 3, pp. 112–118, Jan. 2024, doi: 10.17770/etr2023vol3.7190.

[3] Andrey Andreev, Hristov H., Iliev G., Racheva. M. "Mathematical Model for a Pneumatic Force Actuator System" BGSIAM'15 PROCEEDINGS 10th Annual Meeting of the Bulgarian Section of SIAM. December 21-22, 2015 Sofia. Page 4-6,ISSN 1313-3357.

[4] G. Iliev, Hristov H., Anchev A. "Experimental study of frequency characteristics of electropneumatic positioning system" RU-Angel Kanchev, Ruse, Bulgaria, Scientific Works, vol. 53. series. 1.2, 2014, pp. 244 – 248, ISSN 1311-3321

[5] G. Iliev, Hristov.H., Anchev A. "Experimental study of friction force parameters in a pneumatic cylinder" "UNITECH 2012", Gabrovo, Bulgaria, vol. II, pp 277-280. ISSN 1320-230X.

[6] A.Whitmore, S. "Frequency response model for branched pneumatic sensing systems" AMER INST AERONAUTICS ASTRONAUTICS; NOV-DEC 2006 Volume 43, Issue 6, Page1845-1853, DOI:10.2514/1.20759

[7] Y. T WANG,and SINGH, R." Frequency-response of a nonlinear pneumatic system" Journal of applied mechanics-transactions of the asme Volume 54, Issue 1, Page 209-214 MAR 1987; DOI:10.1115/1.3172960

[8] A.Grigaitis, and Gelezevicius, VA" Electropneumatic Positioning System with an Adaptive Force Controller" ELEKTRONIKA IR ELEKTROTECHNIKA 2008 Issue 7, Page 3-6

[9] M. Smaoui and Brun, X; Thomasset, D "Robust position control of an electropneumatic system using second order sliding mode" IEEE International Symposium on Industrial Electronics 2004; PROCEEDINGS OF THE IEEE-ISIE 2004, VOLS 1 AND 2 , pp.429-434

[10] X.Brun and SesmatS; Thomasset, D ; Scavarda, S "Study of "Sticking and restarting phenomenon" in electropneumatic positioning systems" Journal of dynamic systems measurement and control-transactions of the asme, volume 127, issue 1, page 173-184; mar 2005; ISSN 0022-0434; DOI:10.1115/1.1858443

[11] Wisam Essmat Abdul-Lateef, Glebov Nikolay Alexeevich, Naseer Hamed Farhoo, Ahmed H. Khdir and Dina H. Shaker. "Modelling and Controlling of position for electro-pneumatic system using Pulse-Width-Modulation (PWM) techniques and Fuzzy Logic controller" IOP Conference Series: Materials Science and Engineering, Volume 765, 1st International Conference of Electromechanical Engineering and its Applications (ICEMEA-2020) 25–26 February 2020, Baghdad, Iraq , DOI 10.1088/1757-899X/765/1/012020

[12] R. Kumar & J. R. B. del Rosario (2014). Design and Simulation of Electro-Pneumatic Motion Sequence Control Using FluidSim: Applied Mechanics and Materials, 446-447, 1146-1150. DOI: 10.4028/ www.scientific.net/AMM.446-447.1146

[13] Cajetinac S., Seslija D., Aleksandrov S., Todorovic M. PWM Control and Identification of Frequency Characteristics of a Pneumatic Actuator using PLC Controller // ELECTRONICS AND ELECTRICAL ENGINEERING, AUTOMATION, ROBOTIC , SISSN 1392 – 1215, 2012. № 7(123).

[14] Ioannis Tsitsimpelisa, C. James Taylora, Barry Lennoxb, Malcolm J. Joycea. A review of ground-based robotic systems for the characterization of nuclear environments. Progress in Nuclear Energy. 2019, 111(109–124). www.elsevier.com/locate/pnucene.

[15] D. Pulov and T. Karadzhov, "TEMPERATURE MEASUREMENT WITH PHOTODIODE IN DIFFERENT OPERATING MODES", ETR, vol. 3, pp. 291–295, Jun. 2021, doi: 10.17770/etr2021vol3.6556.

[16] M. J. Marinov, "A GEOMETRICAL SYNTHESIS OF COMEZ TEXTILE MECHANISMS OF FINALLY REMOVED POSSIBILITIES", ETR, vol. 3, pp. 168–171, Jan. 2024, doi: 10.17770/etr2023 vol 3.7187.

[17] Mhana,W., Popov, G. Method for investigation of the pressure variation in the chambers of gear pumps with symmetric and asymmetric tooth profiles used in electrohydraulic drive system. Proceedings of 16th Conference on Electrical Machines, Drives and Power Systems, ELMA 2019, pp 263-266.

[18] Popov, G., K. Klimentov, B. Kostov. Impact of the method of air suction on the energy efficiency of fan systems. 8th International Conference on Energy Efficiency and Agricultural Engineering, EE and AE 2022, 2022. ISBN: 9781665407090. DOI: 10.1109/EEAE53789.2022.9831374

[19] K. Klimentov, G. Popov, B. Kostov, L. Kamenov. Methods for increasing the energy efficiency of fan systems using wide-angle plane diffusers with splitter vanes.// IOP Conference Series: Materials Science and Engineering, 2023, No 1290, pp. 1-9, ISSN 1757-899X

Speed Control Of Pneumatic Cylinders Using High Speed 2 Port On/Off Valves With Pulse Width Modulation

Georgi Iliev
dept. Power Engineering
Technical University of Gabrovo
Gabrovo Bulgaria
spigil@abv.bg

Hristo Hristov
dept. Power Engineering
Technical University of Gabrovo
Gabrovo Bulgaria
christo@tugab.b

Abstract. **This paper presents the possibility of controlling the speed of a different types of pneumatic cylinder with high speed 2-position valves a controller using Pulse Width Modulation /PWM/. To increase the energy efficiency of pneumatic power transmission systems, modern control method for speed control pneumatic cylinders is applied. This is realised by high speed 2 port ON/OFF valves, digital control by computer and virtual instruments made with specialized software. An electronic block implemented with a PWM and an energy saving amplifier is used for control high speed 2 port ON/OFF valves. Practical realization of PWM controlled electropneumatic power transmission system is shown and experimental characteristics for variable speed of the pneumatic actuator are obtained. The experimental results are shown in few graphs. The presented experimental studies prove the possibility of smoothly adjusting the speed of pneumatic cylinders using two-position valves, controlled with PWM. Using this control method makes it possible to replace expensive servo valves for precise speed control.**

Keywords: Energy efficiency, High speed valves, Pneumatic cylinder, Pulse Width Modulation,

I. INTRODUCTION

Pneumatic drive systems are convenient and easy to apply in industry. In the past they have been used with limited capabilities, usually for two-position control. Disadvantages are the compressibility of the air used in them, and the friction forces in the pneumatic elements. Combining them with electronic controllers, advances in electronics and computer technology, are unleashing innovation in their application for frictionless flow control. Pneumatic servo valves and pneumatic proportional distributors are being developed. Servo valves are used to achieve high linear control in pneumatic actuators, but they have complex designs and are high cost. Proportional distributors do not have the fastest response time due to the piston dead zone and have

large internal swells and also have a high commercial cost. Both servo valves and proportional distributors have powerful electrical coils that consume a significant amount of electrical power.

Fig. 1.   High speed 2 port valve "SX12F-AH" SMC Japan.

In the last decade, pneumatic high speed 2-position valves with their digital control are becoming more widely used in order to achieve linear flow control characteristics with the fastest possible response.

The application of high speed 2-position valves for the control of pneumatic sawing mechanisms with different design features using digital control and PWM techniques has been under research development in recent years. Which enables the interest for further research in this area [1 - 9].

Main reasons for the use of the PWM control method for fast switching valves are reduction of valve response

times, miniaturization of the valve control pistons and advanced electronics incorporated. Many researchers used PWM control techniques to drive pneumatic switching valves with good results. PWM signal frequencies used depend on the valve response time and are generally between 20 – 100 Hz.

Currently, PWM is used in electronics, communications, LED lighting and electrical equipment. LEDs are also used in electrical and electronics, motors to control their speed fig1. Applications in hydraulic systems followed as a technique to reduce the non-linearity of solenoid valves and associated dead zones. Some additional advantages in terms of reducing the "stick-slip" phenomenon when hydraulic systems are controlled with PWM signals. As far as pneumatic systems are concerned, the first attempt to apply a PWM-based control technique dates to 1987 and still exists today.

The standard equation of the fluid flow through a pneumatic valve is defined in the ISO 6358 standard (ISO 6358-1, 2013), and is used in this form in almost all mathematical models of pneumatic switching valves [1], [2], [5], [9].

This paper presents a pneumatic experimental rig for obtaining the static flow characteristics of high speed 2-port valves. An electronic controller for energy saving circuit is developed for the operation of the valves. The results obtained are presented in the form of graphs.

II. MATERIALS AND METHODS

To increase the energy efficiency of pneumatic drive systems, modern control methods are applied. This is realized by high speed pneumatic 2-port valves Fig. 1, digital control by computer and specialized software Fig. 2.

A dedicated stand, shown in Fig. 4 has been developed for experimental studies of dynamic processes in pneumatic actuator systems. The stand is equipped with a state-of-the-art Data acquisition /DAQ/ system and a dedicated virtual instrument allowing real-time investigation of transients in a pneumatic actuator system.

Fig. 2.   Combined control circuit with PWM signal and MOSFET transistors and energy saving block for one valve.

The objective of the study is to determine the speed of a pneumatic cylinder with a width-induction modulated governor. The governor consists of SMC Japan model SX12F-AH high-speed pneumatic 2-port valves, an electronic control unit, and an energy saving unit.

To realize the fast valve operation and the plunger displacement, a high controlled coil power is required: 24 V; 80 W. The control of the high-performance pneumatic quick-acting valves is complemented by a power saving electrical circuit.

For the purpose of the study, digitally generated PWM signals obtained using specialized "LabView" software and hardware from "NI" were used. An output driver implemented with a dedicated integrated circuit is used to control the high-speed valves.

The use of CMOS for direct control of MOSFET transistors is suitable due to a number of simplifications in the selection of the operating circuit and the power supply. A disadvantage is that there are limitations on the output current that is produced by the CMOS scheme. For this, circuit solutions of output drivers built mainly with dedicated CD 4050 ICs are suitable. These provide

bipolar pulses to the controlled MOSFET transistor with unipolar control pulses applied to their input Fig. 2. A characteristic of the circuit is that it enables unblocking and blanking of the transistor at different rates and optimization of switching losses. MOSFET transistors operate at high output current and can be driven by PWM signals.
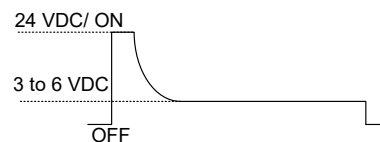
Fig. 3.   Starting and operating voltage of the pneumatic high speed valve.

To realize the high-speed operation of the valve and the displacement of the spool, high power of the controlled spool and high electrical power consumption are required. The technical solution for the pneumatic high-speed valve to have a powerful coil 80 W; 24 VDC which enables the fast control [8].
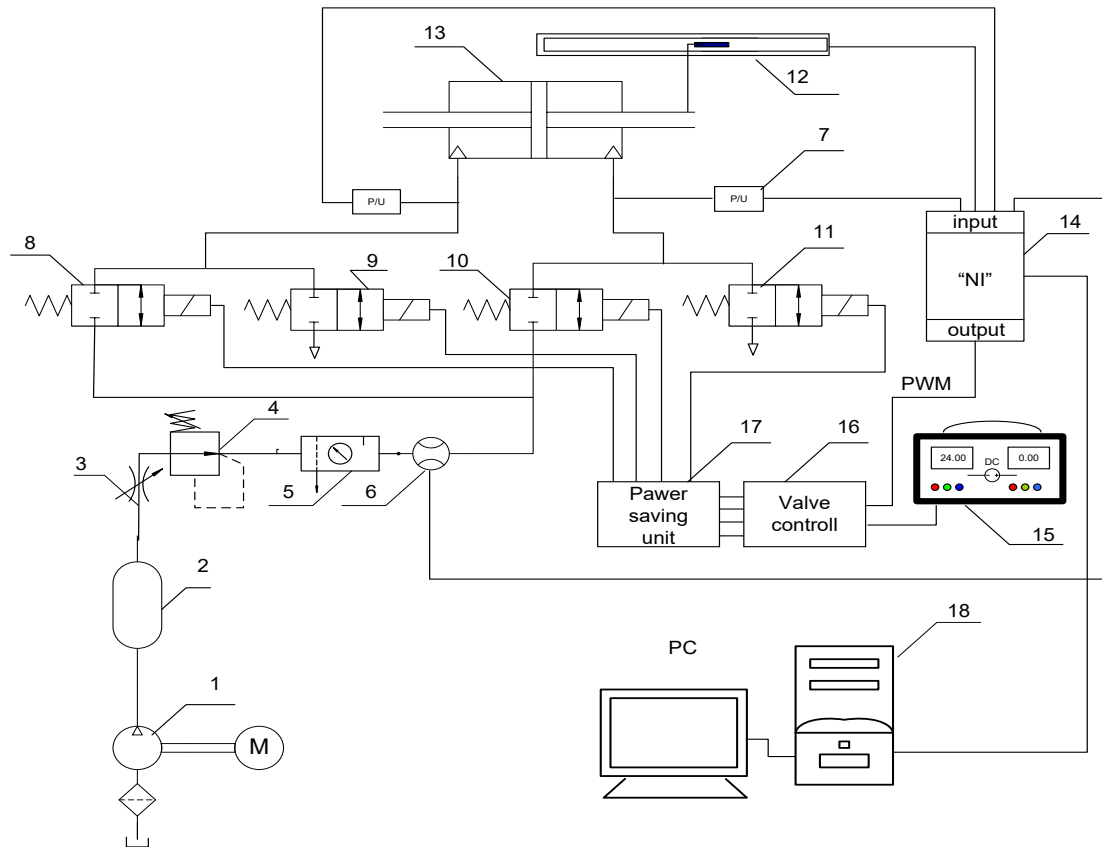
Fig. 4.   Scheme of experimental pneumatic stand.

1 - screw compressor; 2 - receiver; 3 - stopcock; 4 - safety valve; 5 - air preparation system preparatory; 6 - flowmeter; 7 - pressure transducer, 8, 9, 10, 11 high speed 2 port on/off valve; 12 - potentiometric sensor, 13 - pneumatic cylinder with double out rod 14 - terminal board (NI); 15 - power supply unit; 16 - regulator, 17 - energy saving unit, 18 – PC,

Once the pneumatic valve is energized at 24 VDC, its spool is moved to switch from the "OFF" position to the "ON" position, but to hold it in this position usually not the full power is needed, but only part of it to hold the spool in the operating position, usually this is 70/75% less power than the rated Fig. 3.

When operating with energy saving driver, continuous energization with the holding voltage of 3 to 6 VDC is possible.

III.   RESULTS AND DISCUSSION

The implemented system for speed variation of „Camozzi 61M6P040A0500" pneumatic cylinder with double outrigger rod uses four high speed pneumatic valves which are controlled by an electronic module with PWM.

Experiments were performed at different PWM frequency and pulse fill.

Selected working pressure 5 bar.

Fig. 5 to 7 Shows experimental transients with 20Hz PWM and varying duty cycle from 0.02 to 0.9.
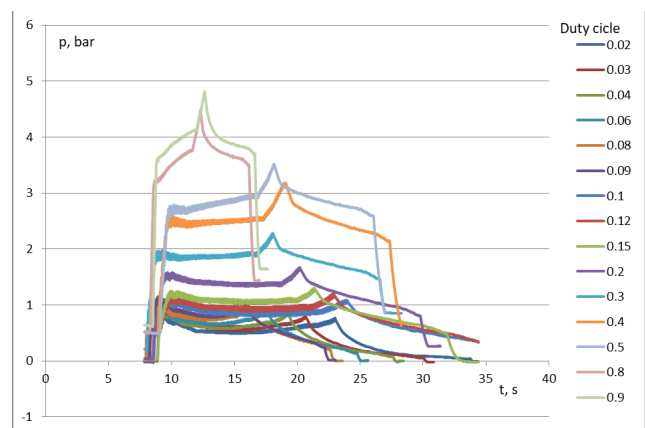
Fig. 5.   Variation of pressure in the left chamber of the pneumatic cylinder with double out rod at different values of the duty cycle 20 Hz.
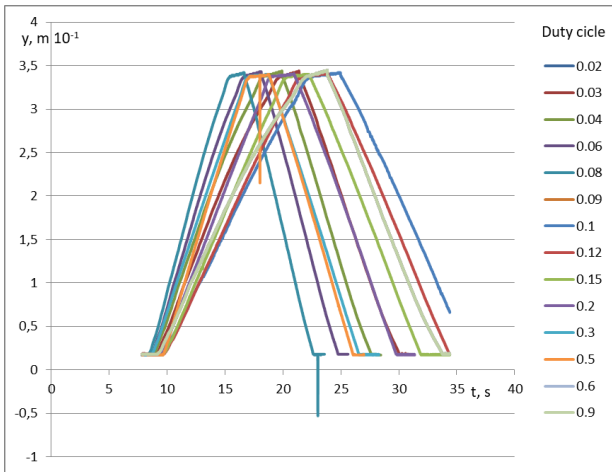
Fig. 6.   Displacement of the piston of the pneumatic cylinder with double out rod at different values of the duty cycle 20 Hz.
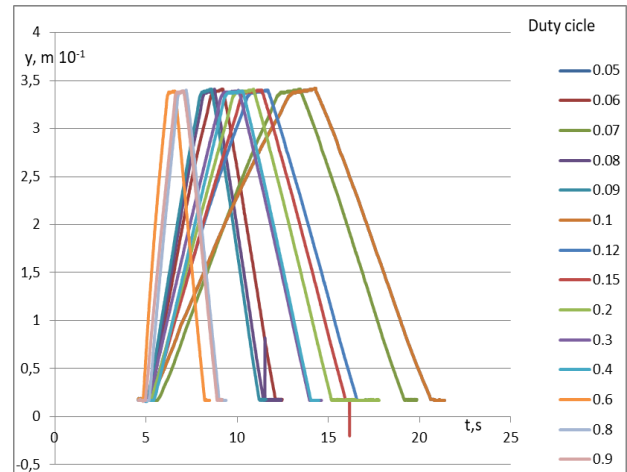
Fig. 9.   Displacement of the piston of the pneumatic cylinder with double out rod at different values of the duty cycle 30 Hz.
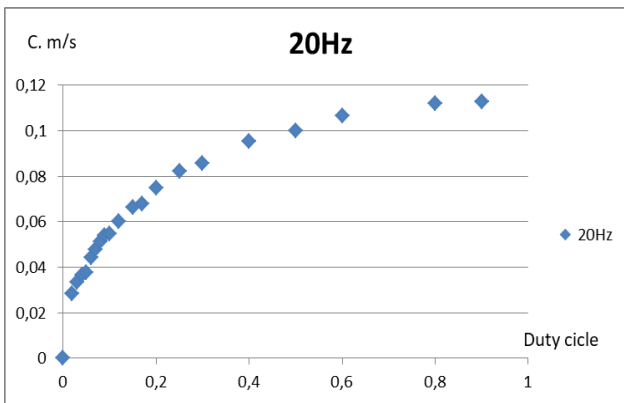
Fig. 7.   Variation of the piston speed of pneumatic cylinder with double out rod different duty cycle values.
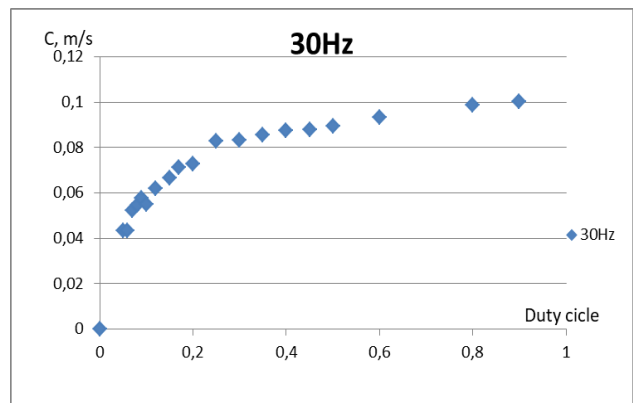
Fig. 10.   Variation of the piston speed of pneumatic cylinder with double out rod different duty cycle values.
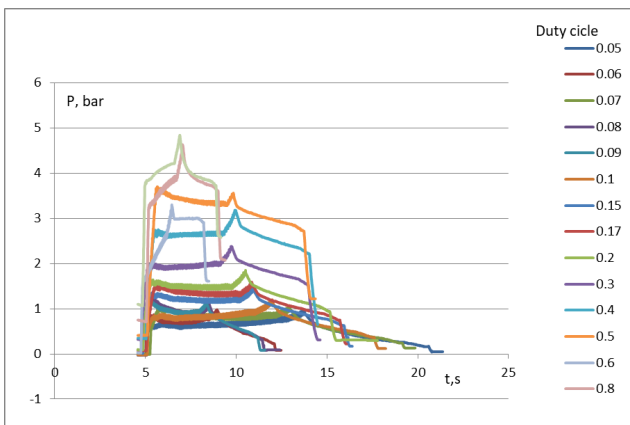
Fig. 8.   Variation of pressure in the left chamber of the pneumatic cylinder with double out rod at different values of the duty cycle 30 Hz.
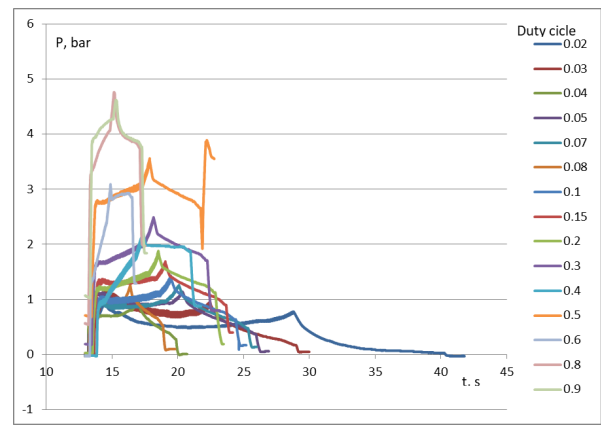
Fig. 11.   Variation of pressure in the left chamber of the pneumatic ramless cylinder at different values of the duty cycle 50 Hz.

Fig. 8 to 10 Shows experimental transients with 30 Hz PWM and duty cycle variation from 0.02 to 0.9.

Fig. 11 to 13 Shows experimental transients with 50 Hz PWM and duty cycle variation from 0.02 to 0.9.
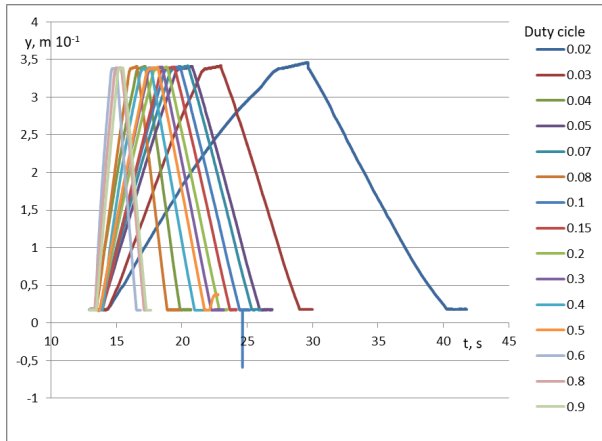
Fig. 12. Displacement of the piston of the pneumatic pistonless cylinder at different values of the duty cycle 50 Hz.
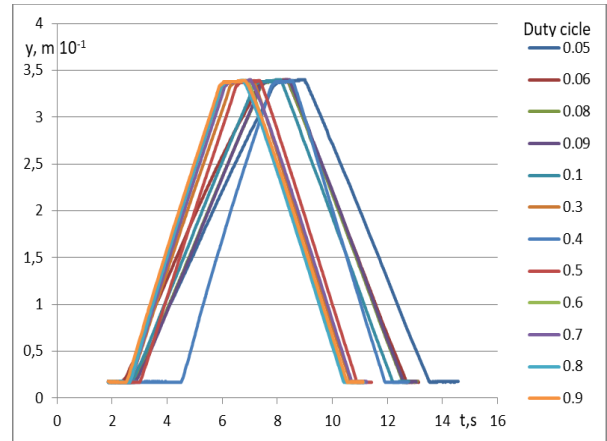
Fig. 15. Displacement of the piston of the pneumatic pistonless cylinder at different values of the duty cycle 70 Hz.
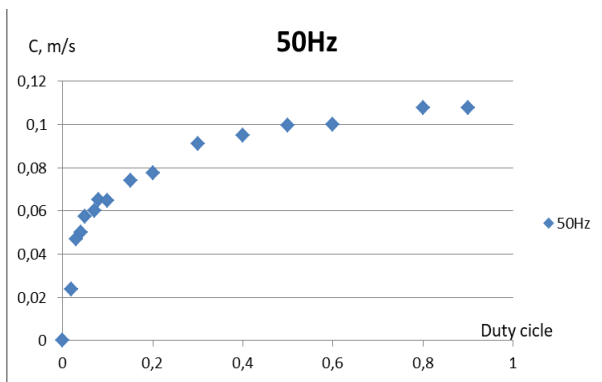
Fig. 13. Variation of the piston speed of pneumatic cylinder with double out rod different duty cycle values.
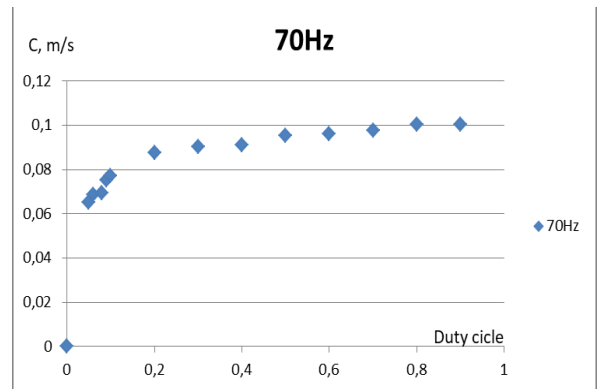
Fig. 16. Variation of the piston speed of pneumatic cylinder with double out rod different duty cycle values.
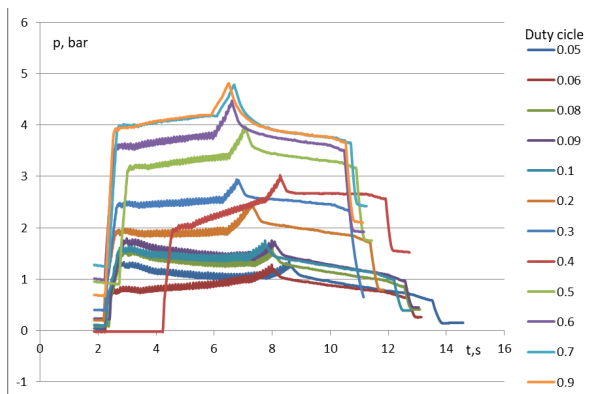
Fig. 14. Variation of pressure in the left chamber of the pneumatic cylinder with double out rod at different values of the duty cycle 70Hz.
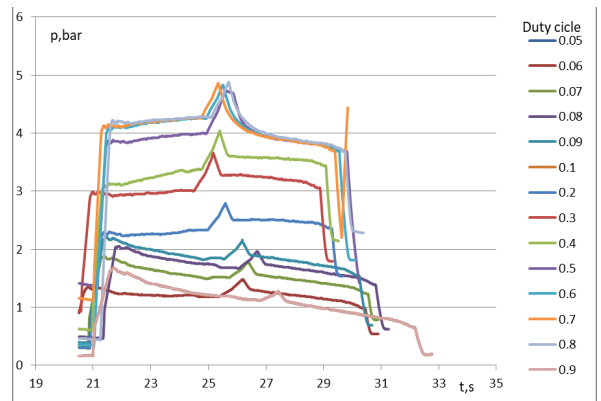
Fig. 17. Variation of pressure in the left chamber of the pneumatic cylinder with double out rod at different values of the duty cycle 100H.

Fig. 14 to 16 shows experimental transients with 70 Hz PWM and duty cycle variation from 0.02 to 0.9.

Fig. 17 to 19 shows experimental transients with 100 Hz PWM and duty cycle variation from 0.02 to 0.9.

From the experimental investigations made on a pneumatic system with "Camozzi" model: „61M6P040A0500" pneumatic cylinder with double out rod, by controlling its speed by SMC Japan model SX12F-AH high speed 2 port pneumatic valves and PWM control with an energy saving block, the following was achieved:

- At a frequency of 20 Hz /fig. 5 - 7/, a supply pressure of 5 bar, and a change in the duty cycle coefficient ranging from 0.02 to 0.9, a pressure variation from 0.8

bar at 0.02 fill to 4.82 bar at 0.9 fill was observed, and the flow rate variation under the same conditions was from 6.33 l/s to 58.31 l/s, The maximum achieved piston speed of the pneumatic cylinder was 0.112 m/s.

- At a frequency of 30 Hz /fig .8 - 10/, a supply pressure of 5 bar and a change in duty cycle ranging from 0.05 to 0.9, there is a pressure variation from 0.98 bar at 0.05 duty cycle to 4.84 bar at 0.9 duty cycle, the flow rate variation under the same conditions is from 17.79 l/s to 61.06 l /s, the maximum velocity is 0.100 m/s.

- At a frequency of 50 Hz /fig.11-13/, a supply pressure of 5 bar and a change in duty cycle ranging from 0.05 to 0.9, there is a pressure variation from 0.92 bar at 0.05 duty cycle to 4.62 bar at 0.9 duty cycle, the flow rate variation under the same conditions is from 4.14 l/s to 59.9 l/s, the maximum velocity is 0.107 m/s. The piston velocity of the cylinder does not change with an increase in duty cycles above 0.8, but the pressure and flow rate increase.
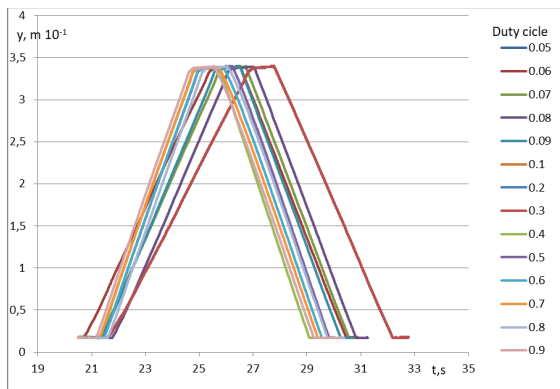
Fig. 18.   Displacement of the piston of the pneumatic cylinder with double out rod at different values of the duty cycle 100 Hz.
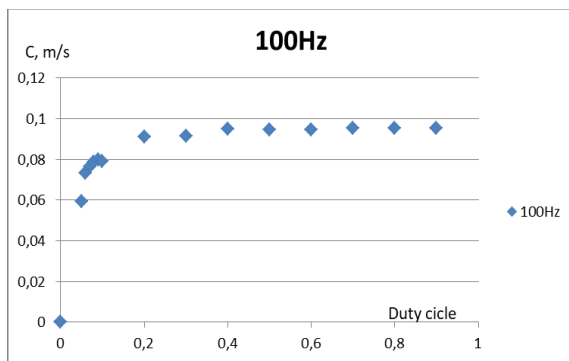
Fig. 19.   Variation of the piston speed of pneumatic cylinder with double out rod different duty cycle values.

- At a frequency of 70 Hz /fig. 14 - 16/, a supply pressure of 5 bar and a change in duty cycle ranging from 0.02 to 0.9, a pressure variation from 1.35 bar at a duty cycle of 0.02 to 4.81 bar at a duty cycle of 0.9 is observed, the flow variation under the same conditions is from 29.05 l/s to 60.90 l/s, the maximum velocity reached is 0.100 m/s. The piston velocity of the cylinder does not change with an increase in duty cycle above 0.5, but the pressure and flow rate increase.

- At a frequency of 100 Hz /fig. 17-19/, a supply pressure of 5 bar and a duty cycle variation ranging from 0.02 to 0.9, a pressure variation from 3.4 bar at a duty cycle of 0.02 to 4.86 bar at a fill of 0.9 is observed, the flow variation under the same conditions is from 26.36 l/s to 59.81 l/s, the maximum velocity reaches 0.095 m/s. Cylinder piston velocity does not change with duty cycle increase above 0.4, but pressure and flow rate increase.

• CONCLUSIONS

The presented experimental studies prove the possibility of smoothly adjusting the speed of pneumatic cylinders using two-position valves, by changing the frequency and duty cycle of PWM. Using this control method makes it possible to replace expensive servo valves for precise speed control.

REFERENCES

[1] R. B. van Varseveld, G. M. Bone (1997) "Accurate position control of a pneumatic actuator using on/off solenoid valves", IEEE/ASME Trans Mech, 2 (3) (1997), pp. 195-204

[2] A. Gentile, NI. Giannoccaro, G. Reina, "Experimental tests on position control of a pneumatic actuator using on/off solenoid valves", In: Proceedings of IEEE/ICIT, Bangkok, 2002. p.(555–559).

[3] G. Carducci, A. Gentile, NI. Giannoccaro, A. Messina "Investigazione teorica e sperimentale su un attuatore pneumatico con controllo in posizione realizzato con valvole on/off e modulazione PWM", In: XVI Congresso AIMETA di Meccanica Teorica e Applicata, Università di Ferrara—Italy, 2003. p. (1–11).

[4] D. Pulov, T. Karadzhov, "Temperature Measurement with Photodiode in Different Operating Modes", Environment, Technology, Resources. Rezekne, Latvia, Proceedings of the 13th International Scientific and Practical Conference. Volume 3, 291-295, 2021, Online ISSN 2256-070X, DOI: 10.17770/etr2021vol3.6556.

[5] E. J. Barth, J. Zhang, M. Goldfarb, "Sliding mode approach to PWM-controlled pneumatic systems", In: Proceedings of the American Control Conference, Anchorage, 2002. p. (2362–7).

[6] G. Iliev and H. Hristov, "Modelling and simulation of electropneumatic positioning system including the length of pneumatic lines", ETR, vol. 3, pp. 106–111, Jan. 2024, doi: 10.17770/etr2023vol3.7186.

[7] G. Popov, Kl. Klimentov, B. Kostov, R. Dimitrova. "Analyzing the Energy Efficiency of Fan Systems by Using the Dimensional Analysis (DA) Method"// Symmetry II, 2020, No 12(4), pp. 1-13, ISSN 20738994 (Impact factor: 2.645 /2019, Licensee MDPI, Basel, Switzerland).

[8] G. Popov, Kl. Klimentov, B. Kostov, R. Dimitrova. "Increasing the energy efficiency of fan systems by using outlet diffuser"// 7th International Conference on Energy Efficiency and Agricultural Engineering (EE&AE), 2020, No 4, pp. 1-4, ISSN 978-1-7281-0362-4.

[9] M. Pipan, Niko Herakovic, "Closed-loop volume flow control algorithm for fast switching pneumatic valves with PWM signal" Control Engineering Practice 70 (2018) pp(114–120).

Design and Implementation of software-defined pi/4-DQPSK modem with receive antenna diversity

Ivan Ivanov
C4I Systems Development Directorate
Defence Institute "Prof. Tsvetan Lazarov"
Sofia, Bulgaria
i.p.ivanov@di.mod.bg

Mario Angelov
C4I Systems Development Directorate
Defence Institute "Prof. Tsvetan Lazarov"
Sofia, Bulgaria
m.angelov@di.mod.bg

Abstract. **Software-defined radio (SDR) is leading concept nowadays, for development of multifunctional radio systems. Article addresses design and implementation on SDR platform of digital modulator/demodulator (modem) with pi/4 differential quadrature phase shift keying modulation (pi/4-DQPSK) and antenna diversity in the receiver side. A model of the system was created in GNU Radio Framework. Experimental results of bit error rate (BER) in presence of additive white Gaussian noise (AWGN) is obtained through simulation and compared with no diversity system. Superiority of diversity scheme, based on criteria BER, is confirmed by numerical results. An experimental, model-based RF DQPSK modem was implemented with Universal Software Radio Peripheral (USRP) frontend. This step from development process confirms advantages of SDR concept, verifies model implementation trough ability to exchange digital information from the transceiver to the receiver in indoor environment and capability of constructive elements to support cocherense. For future implementation of full functional radio communication system, the need of additional blocks for synchronization is identified.**

Keywords: DQPSK modem, antenna diversity, GNU Radio Framework, software-defined radio system.

I. INTRODUCTION

The ever-growing demand for data communication creates constant search of new solutions in the area of digital communication systems. One of the main tasks of radio communication engineering is the creation of a system for reliable transmission of information. While the functional blocks of a typical radio communication system do not change dynamically in time, thanks to the development of new technologies and building elements implementing these functions, the design and characteristics of the products are constantly being improved. For a generalized distinction of functional and constructive changes in next generation systems, such definitions as digital, broadband, ultra-broadband, etc. are often placed in front of them. Improvements in the area of

computing devices and possibility of their embedding led to the creation of new concepts and architectures in radio communication systems. Such definitions as software-defined radio, cognitive radio, etc. have appeared. The concept of "software-defined radio system" is introduced in 80's of XX century and since then is object of substantial research [1],[2],[3]. Nowadays this paradigm is still vital and conceived as a main solution in practical implementation of digital communication systems.

Differential phase shift keying modulation schemes are preferred one for mobile communication systems, for theirs ability to work in non-coherent receivers. DQPSK modulation scheme is used in private mobile communication systems as TETRA [4], which is one of the system of choice for command and control support system for security and defence.

Different multiple antenna techniques have been developed to fight deleterious effect of multipath distortion and to increase data throughput or decrease bit error rate and after all the whole performance of the system [5]. Receive antenna diversity scheme is subclass of multiple antenna system and utilizes a single transmit antenna and multiple receive antennas. The diversity combining effect allows mitigation of numerous negative effects of the channel.

Design and implementation of pi/4-DQPSK software-defined modem with no diversity are reported [6],[7].The present study focuses on the model-based design and implementation of pi/4-DQPSK SDR modem with receive antenna diversity.

II. MATERIALS AND METHODS

The generalized constructive system definition of software-defined radio system is shown in Fig. 1.
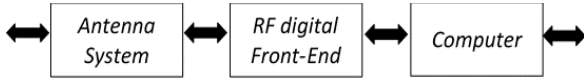
Fig. 1. SDR block scheme.

The architecture of typical SDR consists of antenna system, radiofrequency (RF) front-end and general-purpose computing device (computer) [7]. RF front-end performs bandpass modulation/demodulation, digital-analog conversions and basic digital processing, as digital up/down conversion (DUC/DDC) decimation/ interpolation. Most popular bandpass modulation scheme used in available on the market RF front-ends is quadrature amplitude modulation (QAM). Main digital processing is performed typically on general purpose computer. Some of the popular applications, running on the computer and supporting SDR technology are GNU Radio, Matlab, LabVIEW, SystemVue, etc. GNU Radio is free and open-source framework, that allows usage of ready developed blocks for SDR and tools for writing new ones. Antenna system typically do not use diversity schemes. Recently there is tendency of introducing on the market of RF frontends, supporting multiple channels.

Pi/4 DQPSK modulation scheme uses differential encoding of QPSK symbols. Block schemes of the modem is shown in Fig.2.
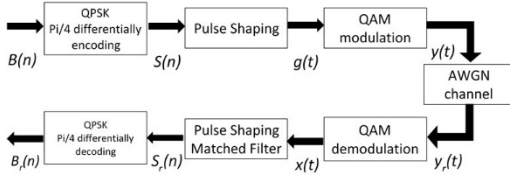
Fig. 2. Functional block scheme of pi/4-DQPSK modem.

Signal processing of QAM modulation/demodulation are following:

$$g(t) = I(t) + Q(t) \qquad (1)$$

After multiplication with signal of local oscillator and taking real part, the output signal can be expressed as [5, 6]:

$$y(t) = Re\{v(t)\} = Re\{g(t)e^{j2\pi f_c t}\} =$$
$$= Re\{[I(t) + jQ(t)]e^{j2\pi f_c t}\} =$$
$$= I(t)\cos 2\pi f_c t - Q(t)\sin 2\pi f_c t \qquad (2)$$

Assuming perfect radio transmission channel, signal after mixing with local oscillator of the receiver and lowpass filtering it, is:

$$x(t) = y(t)e^{-j2\pi f_c t} =$$
$$= [I(t)\cos 2\pi f_c t - Q(t)\sin 2\pi f_c t]e^{j2\pi f_c t} =$$
$$= \frac{1}{2}[I(t) + Q(t)] \qquad (3)$$

In order to constrain the bandwidth of the transmitted signal *y(t)*, the baseband signal *g(t)* is filtered by appropriate filter. Typically, in practical implementation, such filter is of type root-raised cosine (RRC) [4] and play two additional roles of mitigation of inter-symbol interference (ISI) and a matched filter. The transfer function *H(f)* of the filter can be expressed as [4]:

$$H(f) = 1 \quad for \quad |f| \leq (1 - \alpha)/2T$$

$$H(f) = \sqrt{0.5\left(1 - sin\left(\frac{\pi(2|f|T - 1)}{2\alpha}\right)\right)}$$
$$for \quad \frac{(1 - \alpha)}{2T} \leq |f| \leq \frac{(1 + \alpha)}{2T}$$

$$H(f) = 0 \quad for \quad |f| \geq (1 + \alpha)/2T, \qquad (4)$$

where α is the roll-off factor. For TETRA network it's value is chosen to be 0,35 [4].

The modulation symbol *S(n)* at the input of the shaping RRC filter in transmitter results from a differential encoding. It is formed by applying phase transition *Δφ(n)* to the previous modulation symbol $S(n - 1)$:

$$S(n) = S(n - 1)e^{-j\Delta\varphi(n)}$$

$$S(0) = 1 \qquad (5)$$

The phase transition *Δφ(n)* depends on input dubits according Table 1.

TABLE 1 PHASE TRANSITIONS MAP

Dubits	Δφ(n)
1 1	-3π/4
0 1	3π/4
0 0	π/4
1 0	-π/4

Receive antenna diversity apply diversity combining only at receiver side of the communication system. General idea can be described using scheme in Fig.3.
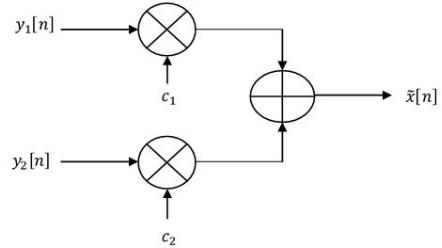
Fig. 3. Receiver divercity combiner.

Let $y_1[n]$ and $y_2[n]$ are two observations of transmitted symbol $x[n]$, each affected by different amount AWGN – $v_1[n]$ and $v_2[n]$:

$$y_1[n] = x[n] + v_1[n]$$
$$y_2[n] = x[n] + v_2[n] \qquad (6)$$

The goal of the combiner is choose most appropriate coefficients c_1 and c_2, such that maximize signal-to-noise ratio (SNR) at the output. Applying scheme in Fig.3. SNR at output of diversity combiner will be [5]:

$$SNR_{final} = \frac{(c_1 + c_2)^2 \sigma_x^2}{c_1^2 \sigma_{v1}^2 + c_2^2 \sigma_{v2}^2} \qquad (7)$$

Simplest contemporary scheme of choosing c_1 and c_2 is "equal gain combining". This scheme averages the

two estimates $y_1[n]$ and $y_2[n]$ by selecting $c_1 = c_2 = 0,5$. Then SNR_{final} becomes:

$$SNR_{final} = \frac{\sigma_x^2}{0.25\sigma_{v1}^2 + 0.25\sigma_{v2}^2} = \frac{4}{\frac{\sigma_{v1}^2}{\sigma_x^2} + \frac{\sigma_{v2}^2}{\sigma_x^2}} =$$

$$= \frac{4}{\frac{1}{SNR_1} + \frac{1}{SNR_2}} = 4\frac{SNR_1.SNR_2}{SNR_1 + SNR_2} \quad (8)$$

Equal gain combining gives best results when two SNR's are similar to each other – $SNR_1 = SNR_2$=SNR. Then:

$$SNR_{final} = 4\frac{SNR^2}{2SNR} = 2SNR \quad (9)$$

In such case, there will be two times improvement of SNR, compared to no diversity.

Combining schemes in Fig.2 and Fig.3. results in scheme of system of interest – pi/4-DQPSK SDR modem with receive antenna diversity. Functional block scheme in Fig.4. is based on scheme in Fig.2. with introduction of multiple receiver arms (here in scheme – two) and addition of functional block "Diversity combiner" (here – equal gain combining is used).
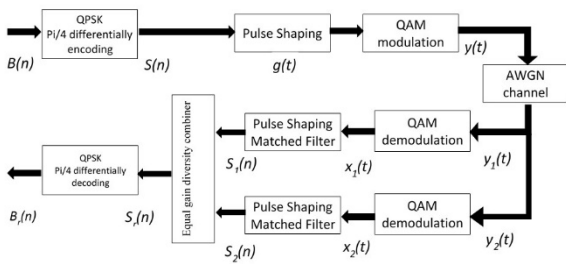
Fig. 4. Functional block scheme of pi/4-DQPSK SDR modem with equal gain receive antenna diversity.

Based on previous described functional and mathematical models of pi/4-DQPSK SDR modem with equal gain receive antenna diversity, a computer model was built in GNU Radio framework. Application is based on previous work on modem with no diversity, described in [7]. Amendment was made in receiver side, where two channel receiver and diversity combiner was introduced. Single channel receiver is kept in overall model for performance comparison. In Fig.5. is shown part of the model that performs equal combining of two receiver channels. The outputs of pulse shaped filters, which acts as matched filters at the receiver, are equally combined and send to the pi/4-DQPSK detector.
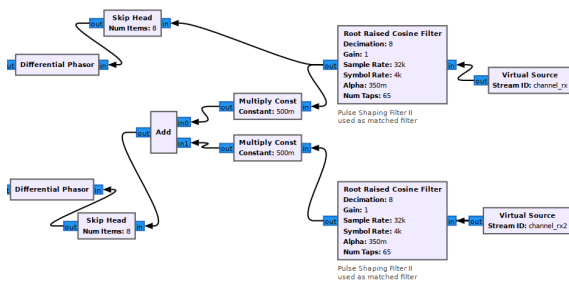
Fig. 5. Computer model of pi/4-DQPSK SDR modem with equal gain receive antenna diversity – combiner part at the receiver only.

Part of the model, that performs pi/4-DQPSK detection is shown in Fig.6.
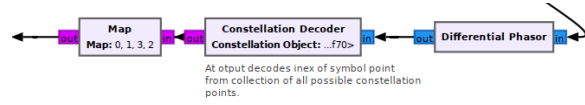
Fig. 6. Computer model of pi/4-DQPSK SDR modem with equal gain receive antenna diversity – detector part at the receiver only.

The detector part of the model of system with combining remains unchanged, compared to such with no combining.

Part of the model is dedidacated to visualisation and performance evaluation and comparison. In Fig.7. is shown block that visualize signal in time domain at different points of transceiver.
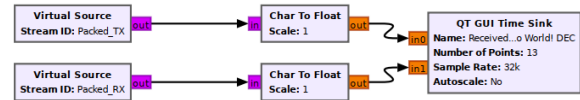
Fig. 7. Part of computer model of pi/4-DQPSK SDR modem with equal gain receive antenna diversity – visualisation of signal at transmitter and receiver.

In Fig.8. is shown part of computer model that performs evaluation of performance of transceiver. As criteria of performance is chosen bit-error rate (BER). There is two measurements paths – one for receiver without combining and another with combining, which allows comparison and estimation of improvements.
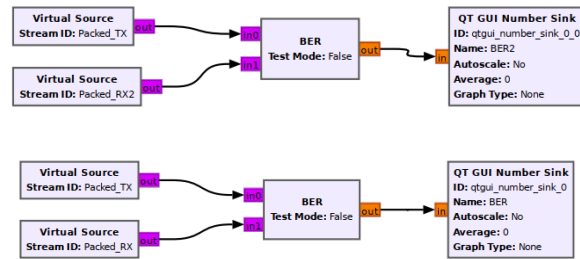
Fig. 8. Part of computer model of pi/4-DQPSK SDR modem with equal gain receive antenna diversity – BER estimates.

III. Results and discussion

Simulation with developed computer model was made for evaluation of overall ability for data exchange and comparison of performance of modem in the presence of additive white Gaussian noise. Control ASCII symbols "Hello World!" are sent multiple times and examined for correct receiving.

Time diagrams in Fig.9 show full identity of transmitted and received signal and symbols when no AWGN is introduced.

Time diagrams in Fig.10. shows difference between transmitted and received signals and resulted errors in detected symbols in presence of AWGN.

Long run of simulation allows measurement of bit error rate. Results for several values of noise level and two type of receivers – without and with diversity usage, are shown

in Table 2. Results for receiver with diversity shows improvement of BER compared with no diversity case.
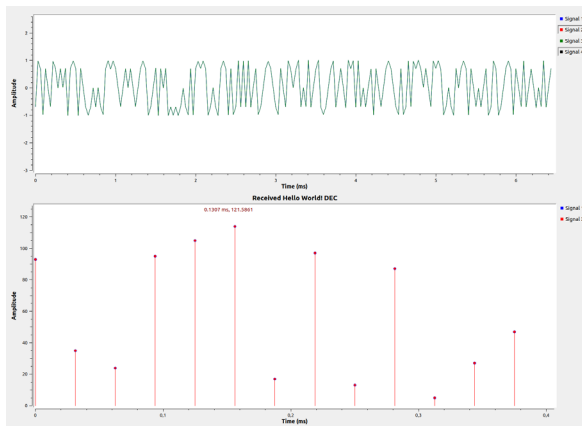
Fig. 9.   Time diagrams from simulation of pi/4-DQPSK SDR modem without AWGN.
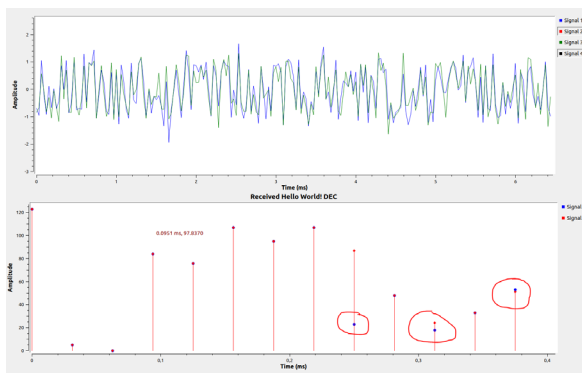
Fig. 10. Time diagrams from simulation of pi/4-DQPSK SDR with AWGN.

TABLE 2. OBSERVED BER AS A FUNCTION OF E_B/E_N

Noise Level [absolute value]	BER (exp. part) no diversity	BER (exp. part) equal gain diversity
0,5	-5,0	-9,1
0,6	-3,7	-6,6
0,7	-2,9	-5
0,8	-2,4	-4,1

An real implementation of software-defined pi/4-DQPSK modem with receive antenna diversity was created. The realization is shown in Fig.11. Main parts of modem are: RF frontends, common clock generator, general-purpose computer, GNU Radio Framework and custom build Flowgraph. Common clock generator guarantees coherence synchronization of local oscillators of transmitter and receiver. As receiver RF frontend is used USRP B210. This device is two channel and special measures are taken by developer for coherence support [8]. The GNU Radio flowgraph that runs on the general-purpose computer is based on computer model described in part II of this paper. Amendments in Flowgraph was made in introducing particular blocks *USRP sink* and *USRP Source*, responsible for interface with RF Frontends.

Test of implementation in indoor environment shows reconstruction of transmitted text in the receiver and improvement of performance of receiver with diversity compared to no-diversity case, which validates the design.
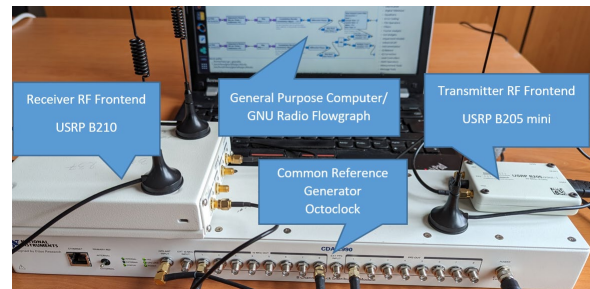
Fig. 11. Implementation of pi/4-DQPSK SDR modem with equal gain receive antenna diversity.

IV. CONCLUSIONS

In this study, design and implementation of pi/4-DQPSK modem with diversity at receiver side were made. The process was based on software-defined radio system concept. Computer model in GNU Radio framework of the system were developed. Performed simulation verified ability to transfer information from source to destination. Comparative study of BER for diversity scheme against no-diversity acknowledge the better performance of former at the price of little additional complexity of the RF receiver front-end and the flowgraph running on a general-purpose computer. The real implementation of the modem validates usage of SDR concept. The easy process of transition from model to implementation confirms advantages of software-defined radio systems. Based on constructed modem, a full SDR packet transceiver with receiver diversity can be build.

V. ACKNOWLEDGMENTS

REFERENCES

[1] Raymond J. Lackey and Donald W. Upmal, "Speakeasy: The Military Software Radio", IEEE Communications Magazine, May 1995

[2] J. Mitola III, "Software Radios: Survey, critical evaluation and future directions", IEEE Aerospace and Electronic Systems Magazine,Vol. 8, Issue 4, April 1993, pp. 25 – 36, doi: 10.1109/62.210638

[3] J. Mitola III, "The Software Radio Architecture", IEEE Communications Magazine, May 1995, pp. 26 – 38, doi:10.1109/35.393001

[4] ETSI EN 300 392-2, Terrestrial Trunked Radio (TETRA); Voice plus Data (V+D); Part 2: Air Interface (AI).

[5] Schwarzinger, A., Digital Signal Processing in Modern Communication Systems, 2nd Edition, Authored and Published by A.O. Schwarzinger, Lake Mary, Florida, 32764

[6] Tetra-kit, https://gitlab.com/larryth/tetra-kit, accessed on 01 July, 2023.

[7] I. Ivanov, "Modeling, Simulation and Implementation of pi/4-DQPSK modem on SDR," *2023 XXXII International Scientific Conference Electronics (ET)*, Sozopol, Bulgaria, 2023, pp. 1-5, doi: 10.1109/ET59121.2023.10278732.

Synchronization and MIMO Capability with USRP Devices. (2020, April 16). Ettus Knowledge Base, . Retrieved 10:25, April 7, 2024 from https://kb.ettus.com/index.php?title=Synchronization_and_MIMO_Capability_with_USRP_Devices&oldid=4912.

Design and Implementation of Software-Defined Doppler Radar

Ivan Ivanov
Defence Institute "Professor Tsvetan Lazarov"
Bulgaria
Sofia, Bulgaria
i.p.ivanov@di.mod.bg

Karmen Aleksandrova
Defence Institute "Professor Tsvetan Lazarov"
Bulgaria
Sofia, Bulgaria
k.aleksandrova@di.mod.bg

Abstract. **The subject of this article is a study of the possibility of practical implementation of a Doppler CW radar based on software-defined radio (SDR) technology. The paper presents overview of two technologies. Initially the architecture and basic characteristics of a Doppler CW radar are described, followed by an overview of SDR concept and types and characteristics of typical constructive elements for its realization. Finally, a practical implementation by usage of USRP front-end and the GNU Radio Framework is presented. For the successful implementation of the Doppler CW radar architecture an additional amplifier is included. The material presents the results of tests performed using the practical implementation of a Doppler CW SDR radar, demonstrating the functionality of the implementation.**

Keywords: Software-defined radio system, Doppler Radar; GNU Radio Framework.

I. INTRODUCTION

The Doppler radar is a specialized radar in which, based on the Doppler effect, the speed of a moving object is determined by the received reflected radar signal [1]. Depending on particular used technology, the Doppler effect is implemented in different ways depending on the functional purpose of the radar. Radars can be pulse-coherent, pulse-Doppler radar, continuous-beam Doppler radar, and frequency-modulated Doppler radar. The most used application of CW radars is as a motion detector. In the military field, CW radars are used to guide missiles .air-to-air with semi-active radar homing (SARH), such as the US AIM-7 Sparrow and the Standard family of missiles. Most modern air combat radars, including pulse-doppler, have a CW missile guidance function. In the presented material, the implementation of a continuous wave (CW) Doppler radar using the software-defined radio (SDR) paradigm is investigated.

II. PRINCIPLE OF OPERATION AND MODEL OF A DOPPLER CW RADAR

Doppler CW radar transmits an unmodulated radar signal of constant amplitude and frequency. Objects can be detected using the Doppler effect. When the observed object moves, the frequency f_r of the reflected signal is shifted from the transmitted frequency f_t, based on the Doppler effect. The difference in the frequency of the emitted and received signal reflected by the object of observation allows to measure the radial component of the object's movement speed relative to the radar. When this difference is positive, i.e. the frequency of the received signal a is higher than the frequency of the transmitted signal, the monitored object approaches the radar. At a lower frequency of the reflected signal, the object moves away.

The change in Doppler frequency depends on the speed of light c = 3.10^{-8} m/s and the speed v of the target. The frequency of the reflected signal is determined by the expression:

$$f_r = f_t \left(\frac{1 + v/c}{1 - v/c} \right) \qquad (1)$$

The Doppler frequency is defined as the difference between the frequency of the emitted and received signals according to the expression:

$$f_d = f_r - f_t = 2v_t \left(\frac{f_t}{c - v} \right) \qquad (2)$$

Since the change in the object's speed is negligible compared to the speed of light, the expression for f_d simplifies to:

$$f_d \approx 2v\frac{f_t}{c} \qquad (3)$$

For the determination of the Doppler frequency in continuous-radiation radars, the phase difference φ between the emitted and reflected signals is measured. For a sinusoidal signal, the phase difference is equal to the ratio of the distance travelled by the signal to the wavelength multiplied by (2π). The multiplier (2π) corresponds to the phase difference at which the signal propagates over a distance equal to the wavelength. If the distance to the object does not change, the phase difference remains constant.

If the distance to the object changes at a certain constant rate relative to the radiating forward antenna, the phase difference will also change as a function of time.

A time-varying phase difference between two sinusoidal signals of different frequencies, which is constant over the measurement interval, has a sinusoidal character. The frequency of this sine wave can be measured and is equal to the Doppler frequency. In most cases, this frequency is in the low frequency range. If the radiation frequency is constant, this Doppler frequency is proportional to the object's radial velocity.

The implementation of a Doppler CW radar is usually done either by a direct frequency conversion receiver (homodyne receiver) or by a heterodyne receiver [1].
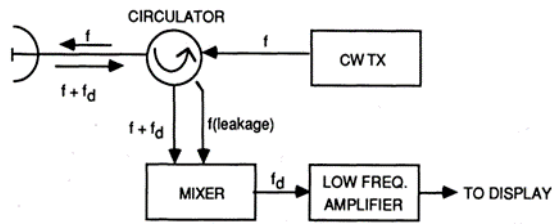
Fig. 1. Block diagram of a Doppler radar with a direct frequency conversion receiver.

The implementation by a direct frequency conversion receiver is very simplified (Fig.1.) [1], but with this solution, the sensitivity of the receiver is limited. Randomly distributed low-frequency noise is superimposed on the Doppler frequency, so weak signals corresponding to low Doppler frequencies cannot be evaluated.
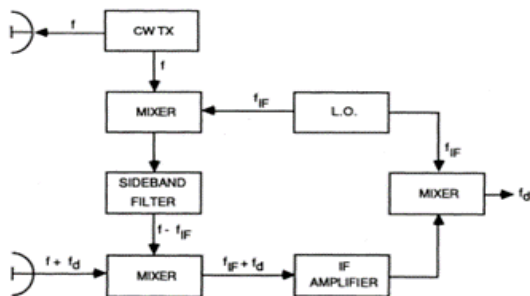
Fig. 2. Block diagram of a Doppler radar with a superheterodyne receiver.

A significant improvement in sensitivity is achieved by implementing a superheterodyne receiver (Fig.2)[1]. With this schematic solution, the echo signal is amplified by about 30-40 dB, where the low-frequency noise can be neglected.

The range of a Doppler CW radar is determined by the basic radar equation, taking into account all the quantities that affect the propagation of radar signals. For a given radar, most of the parameters can be considered constant, since their values vary within small limits. As is known [1] the lowest received power at which the reflected signal can be detected is called P_{emin}, also called receiver sensitivity. The value of P_{emin} determines the maximum range of the radar R_{max}:

$$R_{max} = \sqrt[4]{\frac{P_s\, G^2\, \lambda^2 \sigma}{P_{emin}(4\pi)^3 L_{ges}}} \qquad (4),$$

where P_s is transmitted power [W], G – antenna gain, L_{ges} – loss factor.

III.   SOFTWARE-DEFINED RADIO SYSTEM CONCEPT

The foundations of the software-defined radio (SDR) paradigm are associated with research by DARPA and the US Air Force under Project SpeakEasy in the early 1980s to create a prototype radio covering the range of 2 MHz to 2 GHz and implementing about 10 communication standards [2]. Part of the obtained results in the field of system architecture were published by Mitola in the early 1990s, where the author introduced the concepts of "software radio" [3,4] and "software-defined radio"[5]. The successful development of a prototype of a software-defined radio station under the SpeakEasy project is a prerequisite for the launch of a large-scale program of the US Ministry of Defence under the name "Joint Tactical Radio System" (JTRS). JTRS aims to create a common radio station for all types of armed forces and branches of forces and supports over 30 radio communication protocols [6]. Software-defined radio technology has proven its viability, continues to generate significant interest, and is the basis of such paradigms as "cognitive radio station" [7], "cognitive radar" [8] and others.

Software-defined radio is radio in which some or all of the physical layer functions are software defined. This technology allows agility in the architecture of transceiver and radio communication network as a hole [2]. Generalized block scheme of SDR is shown in Fig.3.
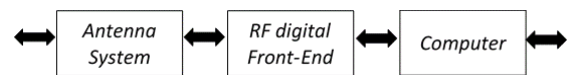
Fig. 3. SDR block scheme.

The architecture of typical SDR consists of antenna system, radiofrequency (RF) front-end and general-purpose computing device (computer). RF front-end performs quadrature modulation/demodulation, analog-to-digital/ digital-to-analog conversion (ADC/DAC) and basic digital processing, as digital up/down conversion (DUC/DDC) decimation/interpolation, etc. Main digital processing is performed on the computer. Some of the popular applications, running on the computer and supporting SDR technology are GNU Radio, Matlab, LabVIEW, SystemVue, etc. GNU Radio is free and open-source framework, that allows usage of ready developed blocks for SDR and tools for writing new ones.

As a result of the transition of the SDR concept into a real product of our time, today there is a variety of platforms with different technical characteristics on the market. Table 1 provides an overview of the most popular platforms for building SDRs.

TABLE 1 SDR FRONTENDS, MAIN CHARACTERISTICS

Name	Frequ-ency Range	Channel Bandwidth, MHz	Resolution ADC/DAC, bit	Interface type
Hack RF One	10 MHz – 6 GHz	20	8	USB 2.0
Adalm PLUTO	325 MHz – 3.8 GHz	20	12	USB 2.0
Ettus B210	70 MHz – 6 GHz	56	12	USB 3.0
Ettus N210	10 MHz – 6 GHz	40	14/16	Ethernet
Ettus X210	1.2 GHz – 6 GHz	120	14/16	Ethernet, PCIe
Lime SDR	100 kHz – 3.8 GHz	61.44	12	USB 3.0
PicoSDR	70 MHz – 6 GHz	56	12	PCIe

The analysis of the data in Table 1 shows the presence of opportunities to support a wide frequency range - part of HF, VHF and UHF, a wide frequency band of the processed radio channel - up to 120 MHz, a high speed of data exchange with computer platforms - up to 10 Gbit/s, support for multiple coherent radio channels, etc. These characteristics allow the implementation of technologies such as GSM, LTE, DVB, CW/FM Radar, MIMO, etc.

Typical RF front-ends, available on the market for implementation of SDR, have direct conversion architecture (Fig.4.).
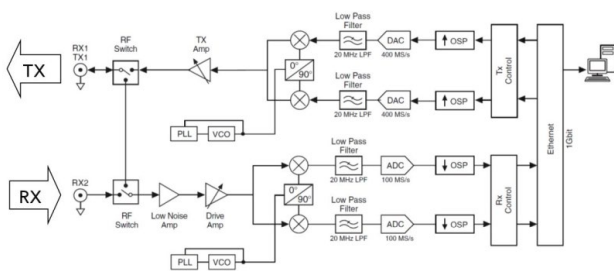
Fig. 4.   Functional block diagram of SDR Front-end.

Such architecture of RF front-end is adequate for prototyping and proof of concept, but impose limitations, mainly on selectivity. Another characteristic to be considered in design process are low sensitivity of the receiver and low output power (under 6 dBm typically) of the transmitter.

IV.   IMPLEMENTATION OF SOFTWARE-DEFINED DOPPLER RADAR

Based on concepts and models of Doppler radar and Software-Defined Radio System a real implementation of SDR Doppler Radar was made. Constructive view of system realization is shown in Fig. 5.
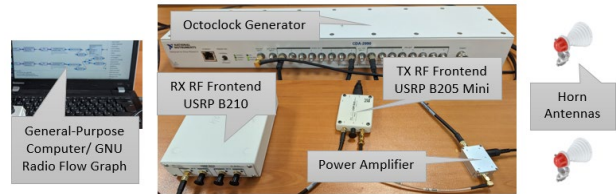
Fig. 5.   Implementation of SDR Doppler radar. Constructive elements.

Main part are: Horn Antennas, TX Frontend USRP B205mini, Power Amplifier 10 dB, RX Frontend USRP B210, Common Reference Generator Octoclock, General-Purpose Computer, GNU Radio Framework, dedicated flowgraph for signal processing and interfacing with RF frontends.

In Fig.6. is shown the flowgraph for GNU Radio Framework, which performs CW generation and interfacing with TX/RX Frontends.
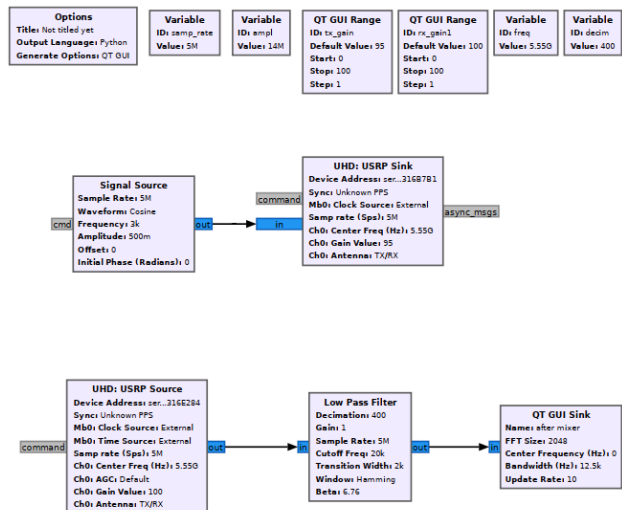
Fig. 6.   GNU Radio Framework flowgraph of SDR Doppler Radar.

The block *"Signal Source"* generates complex harmonic signal. This signal is sent to the block *"USRP Sink"* which is responsible for interfacing of the general-purpose computer with RF front-end. In receiving part of the flowgraph, the block *"USRP Sink"* performs transfer of the data between RF front-end and computer. As the minimal available sample rate of USRP is 2 Mbit/s, which is high above expected Doppler shift, the received data is filtered and decimated by the block *"Low Pass Filter"*. The resulted signal is sent to the block *"QT GUI Sink"*, display received signal in time and frequency domain.

Flow path of transmitted signal is following: data representation of CW signal is generated by GNU Radio application, running on general-purpose computer. Then data are transferred via USB interface to RF front-end, where baseband digital signal is formed. It is converted to analog one by internal analog to digital converter (ADC) and by mixing with local oscillator is translated to passband output signal. The resulted low-power signal is amplified by 30 dB amplifier and radiated by hi-gain directional horn antenna. Receiving path is similar in opposite direction. Common external reference clock 10 MHz is used to synchronize internal clocks of transmitter and receiver.

The implementation was tested in urban environment. Visible results at distance of 50 m are achieved. In Fig.7. is shown waterfall frequency display of received signal. Area 1 shows trace of Doppler shift frequency of reflected signal from receding accelerated car and Area 2 - approaching car that slows down and stops.
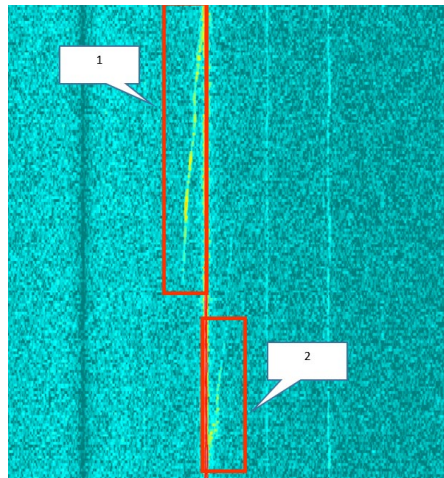
Fig. 7.   Waterfall display of received reflected signal.
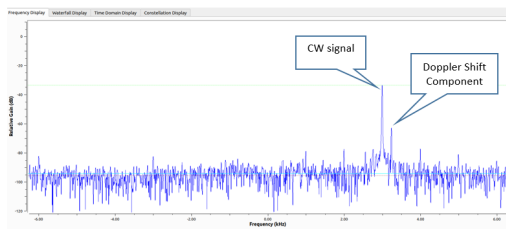
Fig. 8.   Received signal, presented in frequency domain.

In Fig. 8. received signal is shown in frequency domain. Doppler shift frequency component is clearly distinguished and can be detected and estimated.

V.   CONCLUSIONS

The practical implementation of a Doppler CW radar presented in the article confirms the applicability of the SDR concept in the development of radar systems. The obtained results of the conducted tests show that the inclusion of an additional power amplifier in the TX Path allows the problem-free use of RF Frontends available on the market.

As low-cost and simple-to-implement sensors, CW Doppler radars find numerous applications for motion control and monitoring, such as motion detectors, in the construction of radar detonators for missiles and artillery shells. In this aspect, the proposed design and implementation solution and the obtained experimental results enable the subsequent development and application of the SDR concept in the development of more complex radar systems with a specific application for military purposes.

VI.   ACKNOWLEDGMENTS

REFERENCES

[1] Holm, W. A. (1987). Continuous Wave Radar. Principles of Modern Radar, 397–421. doi:10.1007/978-1-4613-1971-9_13S. M. Hemmington, Soft Science. Saskatoon: University of Saskatchewan Press, 1997.

[2] Raymond J. Lackey and Donald W. Upmal, "Speakeasy: The Military Software Radio", IEEE Communications Magazine, May 1995

[3] J. Mitola III, "Software Radios: Survey, critical evaluation and future directions", IEEE Aerospace and Electronic Systems Magazine,Vol. 8, Issue 4, April 1993, pp. 25 - 36.DOI: 10.1109/62.210638

[4] J. Mitola III, "The Software Radio Architecture", IEEE Communications Magazine, May 1995, pp. 26 - 38. DOI:10.1109/35.393001

[5] A. S. Margulies and J. Mitola III, "Software Defined Radios: A Technical Challenge and a Migration Strategy," Proceedings of the IEEE 5th International Symposium on Spread Spectrum Technologies and Applications, September 1998, Sun City, South Africa, pp. 551 - 556. DOI:10.1109/ISSSTA.1998.723845

[6] L. Goeller and D. Tate, "A Technical Review of Software Defined Radios: Vision, Reality, and Current Status," 2014 IEEE Military Communications Conference, Baltimore, MD, USA, 2014, pp. 1466-1470, doi: 10.1109/MILCOM.2014.242.

[7] Bruce A. Fette, Cognitive Radio Technology, Academic Press; 2nd edition

[8] S. Haykin, "Cognitive radar: a way of the future," in IEEE Signal Processing Magazine, vol. 23, no. 1, pp. 30-40, Jan. 2006, doi: 10.1109/MSP.2006.1593335.

Study of an Anthocyanins as a Corrosion Inhibitor for Aluminum Alloy EN AW-2024 in acidic media

Kalina Kamarska
Department of Mathematics,Physics,Chemistry Technical University–Sofia, Branch Plovdiv
Plovdiv, Bulgaria
kamarska@tu-plovdiv.bg

Iva Naydenova
Department of Mathematics,Physics,Chemistry Technical University–Sofia, Branch Plovdiv
Plovdiv, Bulgaria
iva.naydenova@tu-plovdiv.bg

Ivalina Petrova
Department of Mathematics, Physics,Chemistry Technical University–Sofia, Branch Plovdiv
Plovdiv, Bulgaria
ivalinapetrova@abv.bg

Georgi Dobrev
Department of Mathematics, Physics,Chemistry Technical University–Sofia, Branch Plovdiv
Plovdiv, Bulgaria
dobrevbg@tu-plovdiv.bg

Abstract. **The paper presents the results from a study of the possibility to use Bilberries anthocyanins as a corrosion inhibitor for aluminum alloy EN AW-2024 in 1 M solution of HCl. In this study the model system between Bilberries anthocyanins and metal was investigated. The inhibitory effect of Bilberries anthocyanins on the corrosion of aluminum alloy EN AW-2024 in 1M HCl was investigated by electrochemical methods and mathematical analysis to validate the results. The absorption was determined from 25 ⁰C. The results show that Bilberries anthocyanins exhibits a good inhibitory effect on the corrosion of the aluminium alloy EN AW-2024 in 1M HCl. The reason for the good inhibitory effect is the adsorption of the inhibitor molecules on the surface of the aluminum alloy.**

Keywords: corrosion inhibition, aluminum alloy, mathematical model, anthocyanins.

I. INTRODUCTION

Aluminum alloys are widely used in the industrial industry and are often in contact with process media that destroy them. There are various methods of protecting metals from corrosion, one of them being the use of environmental corrosion inhibitors.

Depending on their chemical composition, environmental inhibitors are divided into inorganic (rare earth compounds [1]-[3] and organic environmental inhibitors (organic acids, amino acids, biopolymers, plant extracts and essential oils [4]-[5]. The use of plant extracts of Aloe vera [6], Lavandula angustifolia [7] and Rosmarinus officinalis [8]-[10] are common as environmental corrosion inhibitors in various corrosive environments.

Bilberry is one of the richest natural sources of anthocyanins, which are polyphenolic, glycoside-containing compounds coloring plant parts red, purple, and brown [11]. The two major anthocyanins in the composition of bilberries are malvidin-3-glucoside and malvidin-3-galactoside.

These compounds contain aromatic nuclei in their structure that can be bonded to metal surfaces by π-π electronic reaction.

This property of anthocyanins makes them suitable for use as corrosion inhibitors [12].

In the present paper, the feasibility of using bilberry extract as an environmental corrosion inhibitor of EN AW-

2024 aluminum alloy in 1M HCl was investigated by spectrophotometric study to establish the inhibitory effect of the two major anthocyanins in the composition of bilberry and electrochemical measurement to determine the corrosion parameters. The existence of a correlation relationship between corrosion rate [µm/h] and inhibitor concentration [µpy] was also investigated using SPSS 25.0 using correlation and regression analysis methods.

II. Materials and methods

The materials used were HCl; the pigment anthocyanins from bilberries; aluminum alloy EN AW-2024.

Plant materials were prepared from fresh fruits from bilberries were put in polyethylene bags, frozen immediately and stored at – 18°C until extracted.

Extraction, purification and determination of anthocyanins carry out frozen bilberries was thawed. The homogenised purée was extracted overnight at 4°C using ethanol acidified with hydrochloric acid (1%, v/v) .

Spectrophotometric measurements were performed with UV-Vis spectrophotometer SPEKOL 11. The absorption spectra of model solutions were measured from 400 to 700 nm. The study was conducted at 25°C.

Electrochemical measurements were carried out using a Princeton Applied Research potentiostat/galvanostat (model 263A) at room temperature. The obtained data were processed with the PowerSuite program. A three-electrode cell composed of a working electrode of the investigated EN AW 2024 aluninium alloy, an auxiliary electrode of platinum wire and a reference electrode of saturated Ag/AgCl electrode was used.

The area of the working electrode was 1 cm^2 and the rest of its surface was coated with varnish.

The open circuit potential (OCP) measurement was performed after immersing the working electrode in the test solution of 1 M HCl without and in the presence of bilberry extract at a concentration from 0,00008 to 0,00048 mM (until steady state was reached (200 seconds). Potentiodynamic polarization was performed at an autotonic potential change from -0.250 V to +0,250 V, relative to open circuit potential, at a scan rate of 0,16 mV/s.

Correlation and regression analysis

We will check whether the model is adequate at the significance level of the F criterion. Adequate models are those in which Sig. < 0.05, and then the statistically significant values of the regression coefficients are interpreted.

The relationship between two phenomena (factors) Y and X is investigated using single-factor regression models. Most often, Y is the dependent variable (effect) and X is the explanatory factor. The general form of the single-factor regression model is represented by the formula:

$$Y_i = f(X_i, \varepsilon_i),$$

where:
Y_i is the dependent variable or the effect variable
X_i is the explanatory variable or factor
ε_i is the random component in the model.

In the course of data analysis, the following statistical tables were obtained:

TABLE 1 ANOVA

ANOVA^a

Model		Sum of Squares	df	Mean Square	F	Sig.
1	Regression	25,457	1	25,457	20,280	,046^b
	Residual	2,511	2	1,255		
	Total	27,968	3			

a. Dependent Variable: CR[mpy].E-06
b. Predictors: (Constant), c [mM]

TABLE 2 COEFFICIENTS

Coefficients^a

Model		Unstandardized Coefficients B	Std. Error	Standardized Coefficients Beta	t	Sig.	Correlations Zero-order	Partial	Part	Collinearity Statistics Tolerance	VIF
1	(Constant)	13,776	2,323		5,929	,027					
	c [mM]	-28205,250	6263,264	-,954	-4,503	,046	-,954	-,954	-,954	1,000	1,000

a. Dependent Variable: CR[mpy].E-06

TABLE 3 COLLINEARITY DIAGNOSTICS

Collinearity Diagnostics^a

Model	Dimension	Eigenvalue	Condition Index	Variance Proportions (Constant)	c [mM]
1	1	1,970	1,000	,01	,01
	2	,030	8,172	,99	,99

a. Dependent Variable: CR[mpy].E-06

TABLE 4 MODEL SUMMARY

Model Summary

Model	R Square	Adjusted R Square	Std. Error of the Estimate
1	,954	,910	,865	1,120

In Table 4 Model Summary, the correlation analysis values are calculated. The value of the correlation coefficient (R) is equal to 0.954, which means that there is a correlation relationship between the factor (independent variable) X, which in this case is inhibitor concentration [mM] and the effect (dependent variable) Y (corrosion rate CR [mpy]). The value of the coefficient ranges from 0 to 1, from which it follows that a unidirectional correlation relationship is observed between X and Y.

The second tool of correlation analysis is the coefficient of determination (of determinacy) - R square, whose value measures the strength of influence of the factor X on the consequence Y. In this case, the value of the coefficient of determination is 0,910(91%), which means that 91% of the differences in the corrosion rate CR [mpy] are due to different values of the inhibitor concentration factor C[mM].

The third tool of correlation analysis is the coefficient of indeterminacy (of uncertainty), whose value is obtained by the rule: 100%- R square. In this case, the value of the coefficient of indeterminacy is 100%-91%= 9%. The resulting value measures the strength of the influence on the consequence Y of factors other than the factor X. The 9% value indicates that 9% of the variation in corrosion rate CR[mpy] is under the influence of factors other than inhibitor concentration C[mM].

From the table containing the values of the model parameters, it is clear that the parameters of the linear model are statistically significant since the sig. values are less than 0,05 and the model used (linear) is adequate to investigate the relationship between the variables. Column B of Table 2 contains the values of the unstandardized regression coefficients for the trait factor, which value carries information about how much the corrosion rate CR[mpy] would change if the inhibitor concentration factor C [mM] were increased by one. Only those regression coefficients whose significance level sig. in the Coefficients table is less than the selected level of agreement α(<0,05) are interpreted.

The function defining the relationship between the explanatory variables and the outcome variable has a general form:

$$Y = b_0 + b_1 x_1 + \varepsilon_i$$

where:
Y is the dependent variable;
b_0 - a constant that has no clear scientific interpretation;
b_1 - a coefficient that carries information about the correlation of a factor X_1;
ε_i - accidental error;

The dependency has the form:
Corrosion rate CR [mpy] = 13,776 - 28205,25* Inhibitor concentration C [mM] $+\varepsilon i$

III. RESULTS AND DISCUSSION

Spectrophotometric measurements

From the study it was found that the absorption of the ethanolic extract of anthocyanins reaches a maximum value at a wavelength of 525 nm, after which it decreases (fig. 1).
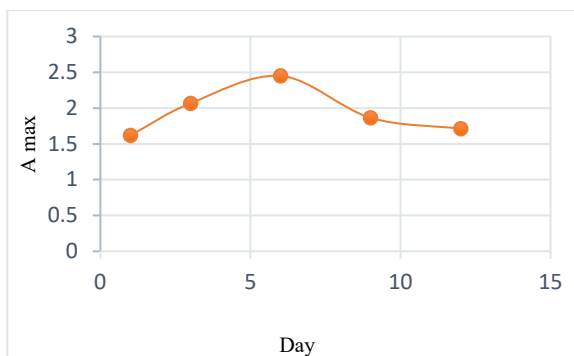
Fig. 1. The variation of absorbance with time at maximum wavelength and temperature 25 ^{0}C.

Electrochemical measurements

The open circuit potential of EN AW-2024 aluminium alloy in 1M HCl in the absence and presence of ethanolic extract of bilberry is shown in Figure 2. On comparing the E_{OCP} values of the studied alloy, it is observed that with increasing inhibitor concentration from 0,00008 to 0,00048 mM, the E_{OCP} values shift in more positive direction as its value remains relatively constant (between -0,550 V and -0,553 V) compared to the E_{OCP} values without inhibitor (-0,566 V). This deviation of E_{OCP} is probably due to the inhibitory action of bilberry extract and is related to the decrease in the degradation of the alloy studied. The shift of the potential value in a more positive direction after obtaining bilberry extract indicates the good adsorption of the inhibitor molecules on the surface of the aluminium alloy. By forming a protective, inhibitory layer on the metal surface, bilberry extract reduces the degradation of the alloy.
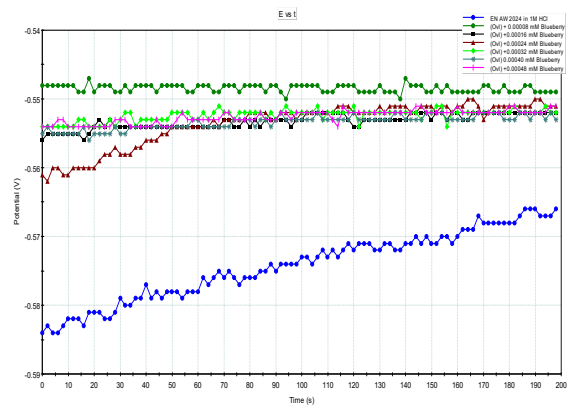
Fig. 2. Open circuit potential of EN AW 2024 alloy in 1 M HCl in the absence and in the presence of Bilberry.
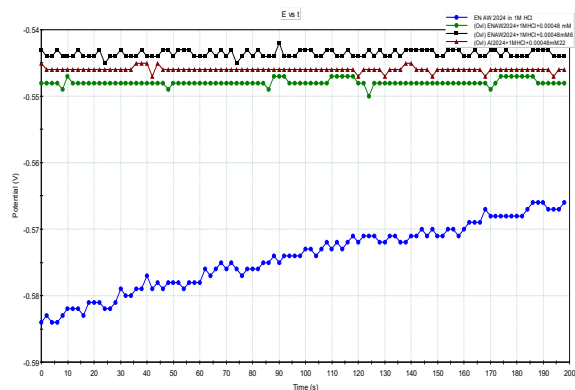
Fig. 3. Open circuit potential of EN AW 2024 alloy in 1 M HCl in the absence and in the presence of 0,000 48 mM Bilberry after 6 and 22 days.

Figure 3 presents the results of measuring the open circuit potential of EN AW-2024 aluminium alloy in 1M HCl in the absence and presence of ethanolic extract of bilberry at a concentration of 0,00048 mM by tracking the effect of the inhibitor over time 2, 6 and 22 hours. It is observed that over the time studied, the E_{OCP} value of aluminium alloy EN AW-2024 in 1M HCl presence of bilberry extract remains constant and is more positive

compared to the E_{OCP} values without inhibitor, indicating that bilberry extract retains its inhibitory action and continues to protect the metal surface from the destructive action of hydrochloric acid.

Table 5 presents the corrosion current (Icorr), corrosion rate (CR), surface coverage (θ) and inhibition effect (η %) values of aluminium alloy 2024 in 1 M HCl without and in the presence of an inhibitor, ethanol extract of bilberry.

The inhibitory effect (η %) was calculated using the following equation:

$$\eta\ \% = \frac{I_{corr} - I'_{corr}}{I_{corr}} \cdot 100 \quad (1)$$

where Icorr and I'corr the value of corrosion current in the absence and presence of inhibitor, respectively.

TABLE 5 ELECTROCHEMICAL PARAMETERS OF EN AW 2024 IN 1 M HCL IN THE ABSENCE AND IN THE PRESENCE BILBERRY

c, mM	I_{corr} (µA)	CR(mpy)	θ	η %
blank	7,377	9.852	-	-
0,00024	5,894	7,872	0,2021	20,21
0,00032	2,726	3,641	0,6250	62,50
0,00040	1,583	2,114	0,7896	78,96
0,00048	0,644	0,8596	0,9127	91,27

Data showed that the magnitude of the corrosion current decreased significantly with increasing concentration of bilberry extract, probably due to the formation of a barrier film on the alloy surface. At the same time, the inhibitory effect increased with increasing the concentration of bilberry extract and the maximum was 91,27% at 0,00048 mM concentration of bilberry extract.

Mathematical model

Interpretation of the obtained values of the regression coefficients:

b0 = 13,776 - no clear scientific interpretation, but its inclusion in the model is justified for the following reasons:
- contains unaccounted for influences of existing factors;
- contains measurement errors;
- contains biases due to the use of inadequate models.

The **b1** = - 28205,25 carries information about the sought correlation relation between the factor X and the consequent Y. This value is different from 0, which means that a correlation relationship exists between the factor (independent variable) X, which in this case is inhibitor concentration C [mM] and the consequence (dependent variable) Y (corrosion rate). The value of the coefficient is greater than 0, from which it follows that as the value of the factor (independent variable) X increases for Y the consequence (dependent variable) Y (corrosion rate) will exhibit a unidirectional correlation relationship (fig. 4).
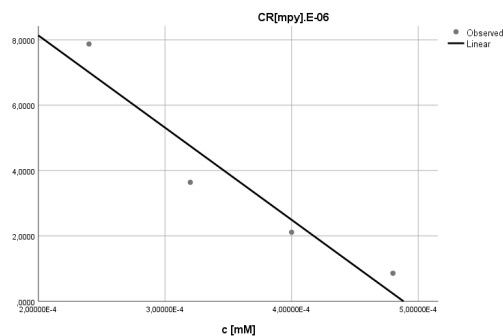
Fig.4. Corrosion rate graph = f (Inhibitor concentration)

The value of the regression coefficient also indicates by how many units the theoretical value of the outcome variable changes if the factor variable is increased by one unit. It is an average change because the relationship is correlational and not functional.

IV. CONCLUSIONS

Based on the data obtained, it can be concluded that the ethanol extract of bilberry demonstrated a good inhibitory effect on the corrosion of EN AW-2024 aluminum alloy in hydrochloric acid (91,27%). The results obtained in this study indicate that with increasing concentrations of the inhibitor, the values of corrosion current and corrosion rate of the studied alloy decreased. There is a strong correlation relationship between the inhibitor concentration factor C [mM] and the consequent (dependent variable) Y corrosion rate, and increasing the inhibitor concentration C [mM] by 1, the theoretical value of corrosion rate CR [mpy] decreases by 28205,25 E-06.

REFERENCES

[1] M. Arenas, M. Bethencourt, F. Botana, J. Damborenea, M. Marcos, "Inhibition of 5083 aluminium alloy and galvanized steel by lanthanide salts," Corr. Sci., 43, pp. 157-170, 2001.

[2] M.Bethencourt,F. Botana,J. Calvino,M.Marcos, M.Rodriguez-Chacon," Lanthanide compounds as environmentally-friendly corrosion inhibitors of aluminium alloys," Corr. Sci.40, pp. 1803-1819,

[3] J.De Damborenea, A. Conde,M. Arenas, "3 - Corrosion inhibition with rare earth metal compounds in aqueous solutions Rare Earth-Based," Woodhead Publishing, pp. 84-116,2014.

[4] A.El-Azaly, "Influence of Soybean (Glycine Max) plant extract on corrosion of aluminum in 1M HCl," Int. J. Electrochem. Sci.,14, 2714-2731,2019.

[5] J.Wysocka, S. Krakowiak, J.Jacek, Ryl, K. Darowicki. Citric acid as corrosion inhibitor for aluminium alloys in aqueous alkaline environments. Conference: 7th Kurt-Schwabe-Symposium At: University of Applied Sciences. Mittweida, Germany,2016.

[6] A.Al-Turkustani, S. Arab, R. Aldahiri, "Aloe plant extract as environmentally friendly inhibitor on the corrosion of aluminum in

hydrochloric acid in absence and presence of iodide ions," Mod. Appl. Sci 4, pp. 105-124,2010.

[7] J.Halambek, K. Berkovii, J. Vorkapid-Furat, "The influence of Lavandula angustifolia L. oil on corrosion of Al-3Mg alloy," Corr. Sci.,52, pp. 3978-3983, 2010.

[8] J.Radošević, M. Kliškić, A.Višekruna, "Inhibition of corrosion of the Al-2.5Mg alloy by means of the third acidic phenolic subfraction of aqueous extract of Rosemary," Kem. Ind., 2001, 50, pp. 537–542, 2001.

[9] M.Kliškić, J.Radošević, S. Gudić, V.Katalinić, "Aqueous extract of Rosmarinus officinalis L. as inhibitor of Al–Mg alloy corrosion in chloride solution," J. Appl. Electrochem., 30, pp. 823-830, 2000.

[10] M.Deyab, "Corrosion inhibition of aluminum in biodiesel by ethanol extracts of Rosemary leaves," J. Taiwan Inst. Chem. Eng., 58, pp. 536-541, 2016.

[11] T.Thornthwaite, P.Seth Thibado, A. Kyle, "Thornthwaite. Bilberry anthocyanins as agents to address oxidative stress, " Pathology, Oxidative Stress and Dietary Antioxidants. (17), pp. 179-187, 2020.

[12] Y.Teng , W. Zhang , M. Wang, C. Yu, Y. Ma, J. Bian , X. Yang, D. Zhang. "Anthocyanin as sustainable and non-toxic corrosion inhibitor for mild steel in HCl media: Electrochemical, surface morphology and theoretical investigations," J. Mol. Liqs, " pp.344,2021.

State of the Art and literature review research of Hollow Nanofibers: Focusing on fabrication, CAD implementation and optimisation

Sai Pavan Kanukuntla
Riga Technical University
Riga, Latvia
Sai-Pavan.Kanukuntla@rtu.lv

Abstract. **The introduction of nanotechnology has resulted in a new era of materials research, with hollow nanofibers emerging as a key innovation. These nanofibers, distinguished by their nano size diameters and hollow structures, have generated significant interest due to their potential applications in a variety of industries. However, despite their advantageous properties, manufacture and analysis of these hollow nanofibers face significant challenges, particularly in terms of mechanical stability and structural integrity when subjected to external stresses. Identifying and addressing these vulnerabilities is crucial for the advancement of hollow nanofibers in various industrial and biomedical fields. The production of hollow nanofibers, notably via the electrospinning technique, has been the topic of a great deal of research. One of the bases of this research is the utilization of computer-aided analysis (CAD) simulations, which include techniques such as Representative Volume Element (RVE) analysis, Finite Element Method (FEM), multiscale analysis, numerical simulation, and optimization strategies. These sophisticated tools offer a magnified view into the nano-structural behaviour of hollow nanofibers, enabling precise predictions about their mechanical properties and behaviours under diverse conditions. This approach is revolutionary, as it allows for the exploration of theoretical and practical aspects of material behaviours without the constraints of traditional experimental methodologies. This article is in-depth scientific review on these theoretical and practical aspects.**

Keywords: Hollow nanofibers, Electrospinning process, Computer aided analyis.

I. INTRODUCTION

Nanofibers are fibers with diameters in the nano meter range, typically less than 100 nm. Due to their small size and high surface area-to-volume ratio, nanofibers are used in a variety of applications, including filtration, tissue engineering, and electronics. Hollow nanofibers, a subset of nanofibers, feature an empty core that enhances their functionality by reducing weight and increasing surface area, further broadening their applicative potential. Computer-aided analysis (CAD) of hollow nanofibers is crucial for optimizing their design and performance before physical prototypes are developed, saving time and resources in engineering processes. Writing a review on this topic is necessary to consolidate current knowledge, highlight advances, and identify gaps in the research, guiding future studies and technological development in this rapidly evolving field.

Firstly, this review briefly discusses about hollow nanofibers, electrospinning process strategies and the significance of CAD in hollow structures. Following that, this review focuses on the most recent advances in CAD for nanotechnology. At the end of this review, we explore and identify the challenges, opportunities, and future needs of CAD in hollow nanofibers.

II. METHODOLOGY: SCIENTIFIC LITERATURE REVIEW

A. Hollow nanofibers

The fabrication of hollow nanofibers has marked an important phase in materials research, motivated by nanotechnology's tremendous potential [1], [2]. These nanofibers, with their nanosized diameters and hollow centres ranging from 50 nm to 500 nm [3], [4], not only push the boundaries of material engineering, but also bring in a new era of innovation across a wide range of such as aerospace, automobile, military, sports, and biomedicine [5], [6]. Hollow nanofibers, with their unique structural properties such as high surface area-to-volume ratio, tenable porosity, and flexibility in functionalization, present a promising avenue for a plenty of applications in filtration methods [7]–[9], tissue engineering, drug delivery [10], [11], and more [12]–[14].

The potential of hollow nanofibers in catalysis, opens up new possibilities in chemical engineering and environmental science [15], [16]. These fibers enhance the efficiency of catalytic processes by providing a larger specific surface area, richer interfacial composition, and more efficient mass transfer paths, which are key to constructing multi-component catalytic systems and improving catalyst efficiency [17]. Hollow nanofibers have

been found to substantially boost the efficiency of catalytic processes, with studies showing up to a 25% increase in catalytic efficiency compared to solid counterparts, primarily due to their expanded specific surface area that offers more active sites for reactions. Additionally, their unique interfacial composition enhances reactant interactions, while the hollow structure facilitates efficient mass transfer, potentially evidenced by a 40% increase in the turnover frequency (TOF) of catalysts, from 100 s^{-1} to 140 s^{-1} [18]. This illustrates how material innovations profoundly impact global challenges, as evidence materials science has played a key role in decreasing CO2 emissions from the electricity sector through the development of technologies for renewable energy generation and high-performance energy storage [19]. The exploration of core-shell nanofibers, with their complex design, expands the functional scope of hollow nanofibers by allowing the adjustment of their specific surface area and interface composition via their unique core-shell structure, resulting in an ideal platform for the preparation of highly efficient heterogeneous catalysts [20]–[23]. The layered design of these nanofibers significantly enhances their versatility, offering improvements in insulation, filtration, and protective coatings. For instance, the self-healing coatings containing core-shell nanofibers have demonstrated pH-responsive performance, with self-healing rates in acidic and alkaline solutions reaching 81.6% and 71.2%, respectively [24]–[27]. Additionally, making them particularly useful in advanced applications like gas sensing to detect SF6 decomposing gas products, thanks to their unique physicochemical properties [2], [23], [28].

In mechanical applications, the unique properties of polymer-based hollow nanofibers, such as their lightweight nature [6], offer significant advantages. For example, they have a larger surface area per unit mass and smaller diameter (10–100 nm), which contribute to their lightness. Their incorporation into composite materials can lead to innovations in lightweight construction such as the use of lightweight concrete, timber and bamboo composites, and fiber-reinforced polymers (FRPs) [29]. Structural integrity means that a structure or structural component is fit for purpose under normal operational conditions and is safe even should conditions exceed that of the original design [30]. This demonstrates their potential to improve performance in a variety of engineering applications and reduce energy consumption, as proved by an enhanced power conversion efficiency in polymer solar cells (PSCs) of up to 48.5% when compared to traditional bulk heterojunction solar cells [31].

Despite their promising characteristics, hollow nanofibers' mechanical stability under stress remains is a major concern [32]. One significant disadvantage is the potential for mechanical instability due to their thin-walled structure, which can lead to collapse under pressure or stress. From the studies, fibers having a diameter of 222-247 µm and a wall thickness of 50 µm can resist operating pressures of 20–25 bar for brackish water without collapsing [33]–[35]. The risk of structural collapse due to their thin walls limits their use in high-pressure conditions, up to 20-25 bar, emphasizing the need for additional research to improve their robustness by improving the wall thickness and overall dimensions [35]–[37]. The complexity of the manufacturing process for hollow nanofibers, which frequently results in such as irregularities in fiber diameter and wall thickness, with variations in the range of 5 to 15 µm for diameter and 180 to 900 nm for wall thickness [38], [39], [40]. These flaws are a significant barrier to achieving their full potential and can have a significant effect on hollow nanofiber performance in terms of mechanical stability, pressure resistance, and application efficiency [41]–[43]. This emphasizes the value of improving production procedures to assure the reliability and efficiency of hollow nanofibers in a variety of applications.

Fortunately, many previous review papers have discussed the fabrication of hollow nanofibers and their role in various applications, but from my literature survey, there are no review papers that systematically provide a review of the impact of CAD on hollow fiber structural design, optimization, prediction of mechanical behaviour, stability, and buckling. For instance, CAD simulations could lead to a 15% increase in mechanical strength and a 20% enhancement in stability against buckling, by optimizing fiber geometry and wall thickness. Hypothetically, nanofibers designed with CAD might show a tensile strength of 1.15 GPa compared to 1 GPa for traditionally designed fibers, highlighting CAD's role in improving nanofiber design and performance [44]. This gap in the literature presents an opportunity for in-depth research on CAD's contributions to nanofiber technology. To fulfil this gap my research empirically comparing the mechanical properties of CAD-designed nanofibers with those fabricated through traditional methods, researchers can substantiate the improvements and potentially establish new standards in nanofiber fabrication.

B. Fabrication

The hollow nanofibers are fabricated using electrospinning [45]–[48], a process that involves the use of two immiscible liquids through a coaxial, two-capillary spinneret, followed by selective removal of the cores. The methods used for the selective removal of the cores include wet, dry, melt, and gel spinning [13], [14], [49]. This technique has been demonstrated to be capable of producing hollow nanofibers with walls made of inorganic/polymer composites [12]. The size and wall thickness of these nanofibers can be independently varied by controlling a set of experimental parameters viscosity of the inner silicon oil phase [38], [50], [51]. The materials used for producing hollow fibers are typically polymer-based composites [52], [53] are chosen due to their unique properties such as lightweight, high stiffness, high specific strength, good resistance to fatigue, wear and corrosion resistance, easy fabrication, economic efficiency, high design flexibility, and desirable thermal expansion characteristics [54]. These properties make them suitable for various applications such as tissue engineering, wound dressings, drug release, regenerative medicine, dental resin composites and surgical operations [55]–[57].

In other studies, it was demonstrated that electrospinning involves carefully spinning two immiscible liquids (usually polymer solutions or melts and solvents such as limonene (CAS number: 138-86-3, MW: 136.23 g/mol), γ-valerolactone (CAS number: 108-29-2, MW: 100.12 g/mol), and 2-methyl tetrahydrofuran (2-MeTHF) (CAS number: 96-47-9, MW: 86.13 g/mol) [58] into fine

nanofibers with a hollow core. It is crucial for the development of various innovative fibers, such as aligned, randomly oriented, core/shell, hollow, multichannel microtubes, colloidal nanoparticle-decorated, shish-kebab, helical, porous, necklace-like, island-like, and beads-in-fiber electrospun fibers [29], [59]–[61]. Adjustments in solution viscosity and electric field strength can produce nanofibers with diameters from 50 nm to 500 nm and increase surface area by up to 50%, enhancing their utility in applications such as filtration and drug delivery by providing a larger active surface for interactions [62]–[64]. This provides researchers an extensive tool for material design such as the synthesis of mesostructured nanofibrous mats for electrochemical energy storage devices, and the engineering of electrospun nanofibers as passive and active components for flexible/stretchable electronic devices [65]–[67]. It has gained attention for its ability to develop materials that could serve as the foundation for next-generation technologies [5], [68], [69]. Particularly in lightweight constructions such as tissue engineering, drug delivery, sensing, filtration, wound dressings, self-cleaning surfaces, biotechnology, environmental engineering, and green chemistry [60], [70], [71] and high-efficiency filters [72]–[74].

Precise manufacturing of polymer nanofibers, enables the manufacture of fibers specialized to specific needs, such as increased surface area for catalytic applications, which can be summarized as enhanced reactivity or controlled release in drug delivery systems including insulin, with precise control over the concentration and time of delivery [75], [76]. Depending on the specific use, the types of drugs, their concentrations, and delivery time can vary widely, but the main advantage is the maximization of therapeutic efficacy and minimization of off-target accumulation [2]. The basic characteristics of materials used to fabricate hollow nanofibers, particularly polymer-based composites, include synthetic polymers such as poly (lactic acid) (PLA), polycaprolactone (PCL), polyurethane (PU), poly (lactic-co-glycolic acid) (PLGA), poly (L-lactide) (PLLA), and poly (ethylene-co-vinylacetate) (PEVA) [77]. This advance their choice for a wide range of applications such as smart mats, catalytic supports, filtration membranes, energy storage/heritage components, electrical devices (batteries), and biomedical scaffolds [78]. These materials, known for their flexibility and adaptability, are crucial for achieving the desired functionality and performance of hollow nanofibers, such as high specific surface areas, superior mechanical properties, and outstanding flexibility of hollow nanofibers [17], demonstrating the crucial role of material selection in the success of these novel structures [77].

C. Role of CAD

The implementation of CAD simulations in the study of hollow nanofibers represents a paradigm shift in material research. This computational approach enables novel investigation of fiber nano and micro structures [79], resulting in a detailed understanding of their mechanical behaviour under various circumstances such as changes in temperature, pressure, and mechanical stress [77]. Such insights are invaluable in optimizing parameters like size, thickness and composition of the nanofiber characteristics for specific applications [2], bridging the theoretical-practical gap [78]. CAD simulations can predict the damage tolerance of these fibers in composite materials, guiding the development of products that are not only more resilient and durable [80]–[82]. Previous studies demonstrated that one specific model mentioned is for PANI (Polyaniline) hollow nanofibers. The model predicts that these nanofibers exhibit improved tensile strength by up to 40.3%, higher elasticity by up to 48.5%, and enhanced thermal stability [5].

The recent study on AlN/BN bishell hollow nanofibers, fabricated via electrospinning followed by atomic layer deposition, demonstrates a notable improvement in nanostructure composition and dimensions. The process achieved a uniform fiber diameter of approximately 100 nm and a significant structural integrity post-calcination at 500 °C, preserving the fibrous structure even after BN deposition. This advancement underscores CAD simulations' potential in enhancing the performance and scalability of nanofibers, providing a concrete example of how computational tools can guide material innovation in nanotechnology [80], [83], [84]. By establishing a virtual environment that emulates the electrospinning process [29], [85]–[87], researchers could identify and address potential flaws in fiber structure [88], [89], paving the way for the development of more durable and reliable nanofibers [32], [90]–[92]. Beyond design, CAD simulations are an effective tool for forecasting the mechanical properties of hollow nanofibers under various conditions including stress, strain, and environmental factors [93]–[98]. This feature is critical for adapting nanofibers to the precise needs of individual applications such as specific load-bearing requirements or flexibility parameters [99], ensuring their performance and stability in practical applications like filtration, energy storage, and biomedical devices [91].

CAD simulations are essential for determining the damage tolerance of hollow nanofibers in composite materials because they allow for the prediction and study of how these materials behave under stress, strain, and impact [100]. This ability to predict enables the development of materials that can resist tough conditions such as high pressures, extreme temperatures, and corrosive environments [101], [102], these vital factors in industries such as aerospace and automotive, where material failure can have significant implications [103]. These industries require materials that not only perform reliably but also ensure safety and longevity of the components made from them. CAD's contribution to enhancing the mechanical characteristics of hollow nanofibers is invaluable the ability to model and simulate various structural and material properties, such as tensile strength, elasticity, and thermal stability. This enables the optimization of nanofibers for specific applications by adjusting parameters like fiber diameter, wall thickness, and composition to achieve the desired performance [5]. By offering precise control over fiber design and qualities [104]–[106], CAD offers that nanofibers may meet the demanding standards of complicated uses ranging from high-strength materials like advanced composites and alloys. Carbon fiber-reinforced polymers and titanium alloys, crucial in aircraft and high-performance vehicle construction [107], to flexible electronic devices such as

wearable sensors, flexible displays, and bendable batteries, which demand materials capable of maintaining functionality under bending or twisting [108]–[110].

III. DISCUSSIONS

A. Approach: CAD-Driven Optimization of Hollow Nanofibers for Aerospace Applications

The potential use of hollow nanofibers in aircraft composites is very fascinating because these materials offer a unique combination of lightness and strength, which are paramount in aerospace engineering [111], [112]. Here, CAD simulations help build materials that balance weight and strength [113], which is crucial in aerospace engineering where every gram counts, illustrating the innovative influence of material finds in high-stakes industries. From my literature survey, the integration of CAD simulations has been transformative in this field, enhancing the precision in design and optimization of these nanomaterials. CAD's contribution has been particularly notable in refining the nanostructure composition and dimensions of hollow nanofibers, crucial factors for their performance and scalability. Specifically, CAD simulations have facilitated a 30–40% enhancement in the tensile strength and elasticity of nanofibers. This improvement stems from this approach of optimized nanostructure design that minimizes the risk of mechanical failure under stress, thereby boosting the fibers overall durability and performance. Additionally, CAD's influence on material selection and structural design has improved the manufacturability and scalability of hollow nanofibers by 20–25%, making them more suitable for widespread industrial use [114]. Hollow nanofiber research is essentially interdisciplinary, integrating insights from material science, chemical engineering, and computational modelling [115]–[118]. This collaborative approach is critical in pushing the limits of what is feasible with these materials [119], [120], potentially leading to breakthroughs that change the landscape of modern technology, particularly in fields where material efficiency and performance are crucial [121], [122]. For instance, in the aerospace industry, innovations could result in lighter, more fuel-efficient aircraft. Hollow nanofibers could help to produce lighter, more efficient, and perhaps more powerful batteries and supercapacitors, with implications for anything from consumer electronics to electric vehicles [123].

B. Gaps and Challenges

From my research, hollow structured nanofibers present unique advantages but are accompanied by significant challenges, such as reduced mechanical strength due to thin walls, susceptibility to buckling, complex geometry in design, and assembly difficulties. CAD simulations offer solutions to these challenges by enabling predictive modelling to optimize mechanical behaviour, stability, and wall thickness. They facilitate precise structural design, taking into account material distribution and load requirements, and assist in visualizing assembly processes to pre-empt potential issues. Furthermore, CAD tools support the selection of appropriate materials, enhancing the safety, performance, and manufacturability of hollow nanofibers. Through the strategic use of CAD, engineers can effectively navigate the complexities

associated with hollow nanofibers, ensuring their practical application across various fields.

C. Future Scope

A Future research areas include optimizing the electrospinning method for hollow nanofibers, with a focus on attaining more control over fiber properties such as their high specific surface areas, high surface area to volume ratios, easy functionalization, superior mechanical properties, outstanding flexibility, controllability in fiber diameter, surface morphology, and fibrous structure [124]–[126]. CAD simulations offer a pathway to study and resolve these unsolved issues such as humidity in the electrospinning environment, beading of fibers spun at two different viscosity solutions, poorly aligned fibers, uneven diameters, slow drum RPM, unstable drum, airflow in the electrospinning environment disrupting the jet, and fluctuating temperature in the electrospinning environment [127], [128]. By simulating the electrospinning process and the resultant fiber morphology, researchers can identify and mitigate potential points of failure in the fiber structure [129]–[131]. This endeavour will most likely include experimenting with novel materials and process parameters in order to reduce flaws and enhance fiber functionality [132], [133]. The search for materials with superior properties like mechanical strength [134], [135], chemical resistance [136], [137], or biocompatibility [138]–[140], will drive advances in nanofiber applications ranging from biomedicine to sustainability a career in engineering [141], [142].

CAD tools are essential for advancing hollow nanofiber research due to their ability to model and simulate complex material behaviours and processing conditions such as temperature variations, humidity levels, and the dynamics of electrospinning, with precision with precision. These tools will need to simulate increasingly complex phenomena within nanofibers [106], accommodating the growing sophistication of research questions such as the impact of environmental factors on nanofiber morphology [77], the role of solution viscosity in fiber formation[138], and the influence of process parameters on fiber alignment [143]. The need for more nuanced analyses could include the study of the effects of humidity [5] and temperature on the electrospinning process, the investigation of the mechanical behaviour of nanofibers under various conditions, and the prediction of damage tolerance of nanofibers in composite materials [144], [145].

IV. CONCLUSION

In conclusion from the summary of literature overview, hollow nanofibers hold great promise for material innovation, but realizing their full potential hinges on a comprehensive understanding and improvement of their properties such as mechanical strength, thermal stability, and electrical conductivity. The collaborative effort of material scientists, engineers, and computer modelers, supported by the vital role of CAD simulations, is critical to the advancement of hollow nanofiber technology. This interdisciplinary collaboration, along with the precision delivered by CAD in designing and refining the geometry of fibers, is driving novel solutions, new applications, and enhanced understanding of these materials. CAD's role in accurately modelling the 2D and 3D aspects of fiber structure enables engineers to develop more effective and

innovative uses for hollow nanofibers. In industries such as aerospace, where the balance of material efficiency and strength is critical, CAD's ability to optimize the mechanical properties of nanofiber-reinforced composites is proving crucial demonstrating the important role of these collaborations in pushing the boundaries of material science. Future research should concentrate on fortifying the mechanical stability of these fibers and extending their use in mechanical applications through the application of sophisticated CAD techniques. The literature review underscores the importance of CAD simulations in advancing the field of hollow nanofibers and highlights the need for continued research to overcome the current limitations and unlock new possibilities for their use.

REFERENCES

[1] M. A. Haghighat Bayan, F. Afshar Taromi, M. Lanzi, and F. Pierini, "Enhanced efficiency in hollow core electrospun nanofiber-based organic solar cells," *Sci. Rep.*, vol. 11, no. 1, pp. 1–11, 2021, doi: 10.1038/s41598-021-00580-4.

[2] X. Chen *et al.*, "Advanced functional nanofibers: strategies to improve performance and expand functions," *Front. Optoelectron.*, vol. 15, no. 1, pp. 1–19, 2022, doi: 10.1007/s12200-022-00051-2.

[3] M. Yousefzadeh and F. Ghasemkhah, "Design of Porous, Core-Shell, and Hollow Nanofibers BT - Handbook of Nanofibers," A. Barhoum, M. Bechelany, and A. S. H. Makhlouf, Eds., Cham: Springer International Publishing, 2019, pp. 1–58. doi: 10.1007/978-3-319-42789-8_9-2.

[4] S. Ang, J. R. Narayanan, W. Kargupta, V. Haritos, and W. Batchelor, "Cellulose nanofiber diameter distributions from microscopy image analysis: effect of measurement statistics and operator," *Cellulose*, vol. 27, no. 8, pp. 4189–4208, 2020, doi: 10.1007/s10570-020-03058-0.

[5] M. A. Haghighat Bayan, F. Afshar Taromi, M. Lanzi, and F. Pierini, "Enhanced efficiency in hollow core electrospun nanofiber-based organic solar cells.," *Sci. Rep.*, vol. 11, no. 1, p. 21144, Oct. 2021, doi: 10.1038/s41598-021-00580-4.

[6] V. S. Reddy *et al.*, "A Review on Electrospun Nanofibers Based Advanced Applications: From Health Care to Energy Devices.," *Polymers (Basel).*, vol. 13, no. 21, Oct. 2021, doi: 10.3390/polym13213746.

[7] D. Wang, A. Eychmüller, and Y. Sun, "Hollow Nanostructures," *ChemNanoMat*, vol. 6, no. 10, pp. 1419–1420, 2020, doi: 10.1002/cnma.202000408.

[8] M. Wang, K. Wang, Y. Yang, Y. Liu, and D. G. Yu, "Electrospun environment remediation nanofibers using unspinnable liquids as the sheath fluids: A review," *Polymers (Basel).*, vol. 12, no. 1, 2020, doi: 10.3390/POLYM12010103.

[9] Y. Zhang, Z. He, H. Wang, L. Qi, G. Liu, and X. Zhang, "Applications of hollow nanomaterials in environmental remediation and monitoring: A review," *Front. Environ. Sci. Eng.*, vol. 9, no. 5, pp. 770–783, 2015, doi: 10.1007/s11783-015-0811-0.

[10] Z. Li *et al.*, "Functional Nanofibrous Biomaterials of Tailored Structures for Drug Delivery-A Critical Review.," *Pharmaceutics*, vol. 12, no. 6, Jun. 2020, doi: 10.3390/pharmaceutics12060522.

[11] B. Singh, K. Kim, and M.-H. Park, "On-Demand Drug Delivery Systems Using Nanofibers.," *Nanomater. (Basel, Switzerland)*, vol. 11, no. 12, Dec. 2021, doi: 10.3390/nano11123411.

[12] P. Prabhu, *Nanofibers for Medical Diagnosis and Therapy*. 2019. doi: 10.1007/978-3-319-53655-2_48.

[13] L. Pengchao, G. Jing-Hua, Y. Shuguang, M. Jinghong, and X. Jian, "Research Progress on the Preparation of Ceramic Hollow Nanofibers by Electrospinning," 2013. [Online]. Available: https://api.semanticscholar.org/CorpusID:136439044

[14] N. Banitaba, G. Amini, A. Gharehaghaji, and A.-A. Jeddi, "Fabrication of hollow nanofibrous structures using a triple layering method for vascular scaffold applications," *Fibers Polym.*, vol. 18, pp. 2342–2348, Dec. 2017, doi: 10.1007/s12221-017-1009-9.

[15] H. Li *et al.*, "Application of Electrospun Hollow Nanofibers in Catalysis," *Gaodeng Xuexiao Huaxue Xuebao/Chemical J. Chinese Univ.*, vol. 44, no. 1, pp. 1–19, 2023, doi: 10.7503/cjcu20220625.

[16] R. Liu *et al.*, "Progress of Fabrication and Applications of Electrospun Hierarchically Porous Nanofibers," *Adv. Fiber Mater.*, vol. 4, no. 4, pp. 604–630, 2022, doi: 10.1007/s42765-022-00132-z.

[17] J. Liu *et al.*, "Multi-Structure Hollow Nanofibers: Controlled Synthesis and Photocatalytic Applications," *ChemNanoMat*, vol. 6, no. 8, pp. 1149–1163, 2020, doi: 10.1002/cnma.202000170.

[18] K. Huang, Y. Sun, Y. Zhang, X. Wang, W. Zhang, and S. Feng, "Hollow-Structured Metal Oxides as Oxygen-Related Catalysts," *Adv. Mater.*, vol. 31, no. 38, pp. 1–12, 2019, doi: 10.1002/adma.201801430.

[19] K. Daehn, R. Basuhi, J. Gregory, M. Berlinger, V. Somjit, and E. A. Olivetti, "Innovations to decarbonize materials industries," *Nat. Rev. Mater.*, vol. 7, no. 4, pp. 275–294, 2022, doi: 10.1038/s41578-021-00376-y.

[20] H. Wang, H. Cai, B. Chen, and C. Mao, "Research on core-shell nanofiber self-healing composites for structural applications," *Polym. Compos.*, vol. 42, no. 7, pp. 3281–3292, 2021, doi: 10.1002/pc.26058.

[21] X. Wang, Y. Yuan, X. Huang, and T. Yue, "Controlled release of protein from core-shell nanofibers prepared by emulsion electrospinning based on green chemical," *J. Appl. Polym. Sci.*, vol. 132, no. 16, pp. 1–9, 2015, doi: 10.1002/app.41811.

[22] A. Manuscript *et al.*, "RSC Advances".

[23] Z. Lu, Q. Zhou, Z. Wei, L. Xu, S. Peng, and W. Zeng, "Synthesis of Hollow Nanofibers and Application on Detecting SF6 Decomposing Products," *Front. Mater.*, vol. 6, no. July, pp. 1–7, 2019, doi: 10.3389/fmats.2019.00183.

[24] T. Kobori, S. Iwamoto, K. Takeyasu, and T. Ohtani, "Biopolymers Volume 85 / Number 4 295," *Biopolymers*, vol. 85, no. 4, pp. 392–406, 2007, doi: 10.1002/bip.

[25] L. Sun, L. Zhang, J. Wang, Y. Liu, and Y. Guo, "Fabrication of novel multilayer core-shell structured nanofibers network reinforced carbon matrix composites for bone tissue engineering," *Mater. Lett.*, vol. 333, no. November 2022, p. 133634, 2023, doi: 10.1016/j.matlet.2022.133634.

[26] M. F. Abdullah, T. Nuge, A. Andriyana, B. C. Ang, and F. Muhamad, "Core-Shell Fibers: Design, Roles, and Controllable Release Strategies in Tissue Engineering and Drug Delivery.," *Polymers (Basel).*, vol. 11, no. 12, Dec. 2019, doi: 10.3390/polym11122008.

[27] Q. Wang *et al.*, "Self-Healing Coatings Containing Core–Shell Nanofibers with pH-Responsive Performance," *ACS Appl. Mater. Interfaces*, vol. 13, no. 2, pp. 3139–3152, Jan. 2021, doi: 10.1021/acsami.0c18933.

[28] X. Chen *et al.*, "Advanced functional nanofibers: strategies to improve performance and expand functions.," *Front. Optoelectron.*, vol. 15, no. 1, p. 50, Dec. 2022, doi: 10.1007/s12200-022-00051-2.

[29] D. Ji *et al.*, "Electrospinning of nanofibres," *Nat. Rev. Methods Prim.*, vol. 4, no. 1, p. 1, 2024, doi: 10.1038/s43586-023-00278-z.

[30] H. He *et al.*, "Ultrastrong and multifunctional aerogels with hyperconnective network of composite polymeric nanofibers," *Nat. Commun.*, vol. 13, no. 1, pp. 1–8, 2022, doi: 10.1038/s41467-022-31957-2.

[31] F. Liang *et al.*, "Fast Energy Storage of SnS2 Anode Nanoconfined in Hollow Porous Carbon Nanofibers for Lithium-Ion Batteries," *Adv. Sci.*, vol. 11, no. 4, pp. 1–9, 2024, doi: 10.1002/advs.202306711.

[32] Z. Ma *et al.*, "Nanoconfined Expansion Behavior of Hollow MnS@Carbon Anode with Extended Lithiation Cyclic Stability," *Adv. Funct. Mater.*, vol. 33, no. 28, 2023, doi: 10.1002/adfm.202301112.

[33] H. S. Lau and W. F. Yong, "Recent progress and prospects of polymeric hollow fiber membranes for gas application, water vapor separation and particulate matter removal," *J. Mater. Chem. A*, vol. 9, no. 47, pp. 26454–26497, 2021, doi: 10.1039/D1TA07093B.

[34] R. Naim, G. P. Sean, Z. Nasir, N. M. Mokhtar, and N. A. S. Muhammad, "Recent progress and challenges in hollow fiber membranes for wastewater treatment and resource recovery," *Membranes (Basel).*, vol. 11, no. 11, pp. 1–15, 2021, doi: 10.3390/membranes11110839.

[35] A. Tawari and B. Brika, "Hollow-fine-fibre Membranes: Collapse Pressure and Pressure Drop Analysis," *Chemist*, vol. 93, pp. 1–17, Apr. 2022.

[36] Y. R. Pei, M. Zhao, H. Y. Zhou, C. C. Yang, and Q. Jiang, "Hollow N-doped carbon nanofibers provide superior potassium-storage performance," *Nanoscale Adv.*, vol. 2, no. 9, pp. 4187–4198, 2020, doi: 10.1039/d0na00585a.

[37] J. Xiao *et al.*, "Interfacial Polarization Loss Improvement Induced by the Hollow Engineering of Necklace-like PAN/Carbon Nanofibers for Boosted Microwave Absorption," *Adv. Funct. Mater.*, vol. n/a, no. n/a, p. 2316722, Feb. 2024, doi: https://doi.org/10.1002/adfm.202316722.

[38] G. Lee, J.-C. Song, and K.-B. Yoon, "Controlled Wall Thickness and Porosity of Polymeric Hollow Nanofibers by Coaxial Electrospinning," *Macromol. Res.*, vol. 18, pp. 571–576, Jun. 2010, doi: 10.1007/s13233-010-0607-9.

[39] B.-S. Lee, K.-M. Park, W.-R. Yu, and J. Youk, "An effective method for manufacturing hollow carbon nanofibers and microstructural analysis," *Macromol. Res.*, vol. 20, Jun. 2012, doi: 10.1007/s13233-012-0087-1.

[40] J. Zhao *et al.*, "One-Step Fabrication of Fe(OH)(3)@Cellulose Hollow Nanofibers with Superior Capability for Water Purification.," *ACS Appl. Mater. Interfaces*, vol. 9, no. 30, pp. 25339–25349, Aug. 2017, doi: 10.1021/acsami.7b07038.

[41] A. Kromik, Z. Javanbakht, B. Miller, I. Underhill, and W. Hall, "On the Effects of Anisotropy in Detecting Flaws of Fibre-Reinforced Composites," *Appl. Compos. Mater.*, vol. 30, no. 1, pp. 21–39, 2023, doi: 10.1007/s10443-022-10067-8.

[42] J. Beaugrand, S. Guessasma, and J. E. Maigret, "Damage mechanisms in defected natural fibers," *Sci. Rep.*, vol. 7, no. 1, pp. 1–7, 2017, doi: 10.1038/s41598-017-14514-6.

[43] K. Tosun-Felekoğlu, B. Felekoğlu, R. Ranade, B. Y. Lee, and V. C. Li, "The role of flaw size and fiber distribution on tensile ductility of PVA-ECC," *Compos. Part B-engineering*, vol. 56, pp. 536–545, 2014, [Online]. Available: https://api.semanticscholar.org/CorpusID:136835449

[44] Z. Xiang, H. Wang, S. K. Murugappan, S. C. Yen, G. Pastorin, and C. Lee, "Dense vertical SU-8 microneedles drawn from a heated mold with precisely controlled volume," *J. Micromechanics Microengineering*, vol. 25, no. 2, p. 25013, 2015, doi: 10.1088/0960-1317/25/2/025013.

[45] J.-V. Sanchaniya, S.-P. Kanukuntla, A. Shereef, and J. Kaneps, "Modelling and analysis of composite polyacrylonitrile nanofiber mats utilized to strengthen motorbike side panel," *21st Int. Sci. Conf. Eng. Rural Dev. Proc.*, vol. 21, pp. 727–736, 2022, doi:

[46] J. V. Sanchaniya, S. P. Kanukuntla, and K. B. Senyurt, "Fabrication and Mechanical Properties of Polymer Composite Nanofiber Mats," *Eng. Rural Dev.*, vol. 22, pp. 85–90, 2023, doi: 10.22616/ERDev.2023.22.TF014.

[47] I. Lasenko *et al.*, "The Mechanical Properties of Nanocomposites Reinforced with PA6 Electrospun Nanofibers," *Polymers (Basel).*, vol. 15, no. 3, 2023, doi: 10.3390/polym15030673.

[48] I. Lasenko, D. Grauda, D. Butkauskas, J. V. Sanchaniya, A. Viluma-Gudmona, and V. Lusis, "Testing the Physical and Mechanical Properties of Polyacrylonitrile Nanofibers Reinforced with Succinite and Silicon Dioxide Nanoparticles," *Textiles*, vol. 2, no. 1, pp. 162–173, 2022, doi: 10.3390/textiles2010009.

[49] S. N. Banitaba, G. Amini, A. A. Gharehaghaji, and A. A. A. Jeddi, "Fabrication of hollow nanofibrous structures using a triple layering method for vascular scaffold applications," *Fibers Polym.*, vol. 18, no. 12, pp. 2342–2348, 2017, doi: 10.1007/s12221-017-1009-9.

[50] G. Zhu, L. Zhao, L. Zhu, X. Deng, and W. Chen, "Effect of Experimental Parameters on Nanofiber Diameter from Electrospinning with Wire Electrodes," *IOP Conf. Ser. Mater. Sci. Eng.*, vol. 230, p. 12043, Sep. 2017, doi: 10.1088/1757-899X/230/1/012043.

[51] O. Hardick, B. Stevens, and D. G. Bracewell, "Nanofibre fabrication in a temperature and humidity controlled environment for improved fibre consistency," *J. Mater. Sci.*, vol. 46, no. 11, pp. 3890–3898, 2011, doi: 10.1007/s10853-011-5310-5.

[52] M. T. Demeuse, *Production and applications of hollow fibers*, vol. 2. Woodhead Publishing Limited, 2009. doi: 10.1533/9781845697310.3.485.

[53] Y. Tian, Z. Wang, and L. Wang, "Hollow Fibers: From Fabrication to Applications," *Chem. Commun.*, vol. 57, Sep. 2021, doi: 10.1039/D1CC02991F.

[54] I. O. Oladele, T. F. Omotosho, and A. A. Adediran, "Polymer-Based Composites: An Indispensable Material for Present and Future Applications," *Int. J. Polym. Sci.*, vol. 2020, 2020, doi: 10.1155/2020/8834518.

[55] H.-M. Huang, "Medical Application of Polymer-Based Composites.," *Polymers*, vol. 12, no. 11. Switzerland, Oct. 2020. doi: 10.3390/polym12112560.

[56] F. Hussain, M. Hojjati, M. Okamoto, and R. E. Gorga, "Review article: Polymer-matrix nanocomposites, processing, manufacturing, and application: An overview," *J. Compos. Mater.*, vol. 40, no. 17, pp. 1511–1575, 2006, doi: 10.1177/0021998306067321.

[57] D. Venkatesan, J. Aravind Kumar, and R. Mohana Prakash, "Synthesis, Properties, and Applications of Polymer Nanocomposite Matrices BT - Handbook of Polymer and Ceramic Nanotechnology," C. M. Hussain and S. Thomas, Eds., Cham: Springer International Publishing, 2021, pp. 465–485. doi: 10.1007/978-3-030-40513-7_65.

[58] J. Avossa, G. Herwig, C. Toncelli, F. Itel, and R. M. Rossi, "Electrospinning based on benign solvents: current definitions, implications and strategies," *Green Chem.*, vol. 24, no. 6, pp. 2347–2375, 2022, doi: 10.1039/d1gc04252a.

[59] J. Xue, T. Wu, Y. Dai, and Y. Xia, "Electrospinning and Electrospun Nanofibers: Methods, Materials, and Applications.," *Chem. Rev.*, vol. 119, no. 8, pp. 5298–5415, Apr. 2019, doi: 10.1021/acs.chemrev.8b00593.

[60] A. Keirouz *et al.*, "The History of Electrospinning: Past, Present, and Future Developments," *Adv. Mater. Technol.*, vol. 8, no. 11, pp. 1–34, 2023, doi: 10.1002/admt.202201723.

[61] J. V. Sanchaniya, I. Lasenko, V. Gobins, and A. Kobeissi, "A Finite Element Method for Determining the Mechanical Properties of Electrospun Nanofibrous Mats," *Polym.*, vol. 16, no. 6, p. 852, 2024.

10.22616/erdev.2022.21.tf226.

[62] E. Ewaldz, J. Randrup, and B. Brettmann, "Solvent Effects on the Elasticity of Electrospinnable Polymer Solutions," *ACS Polym. Au*, vol. 2, no. 2, pp. 108–117, 2022, doi: 10.1021/acspolymersau.1c00041.

[63] A. Vaseashta and N. Bölgen, *Electrospun Nanofibers: Principles, Technology and Novel Applications*. 2022. doi: 10.1007/978-3-030-99958-2.

[64] Z. M. Huang, Y. Z. Zhang, M. Kotaki, and S. Ramakrishna, "A review on polymer nanofibers by electrospinning and their applications in nanocomposites," *Compos. Sci. Technol.*, vol. 63, no. 15, pp. 2223–2253, 2003, doi: 10.1016/S0266-3538(03)00178-7.

[65] H. Il Ryu, M. S. Koo, S. Kim, S. Kim, Y. A. Park, and S. M. Park, "Uniform-thickness electrospun nanofiber mat production system based on real-time thickness measurement," *Sci. Rep.*, vol. 10, no. 1, pp. 1–10, 2020, doi: 10.1038/s41598-020-77985-0.

[66] J. V Sanchaniya and S. Kanukuntla, "Morphology and mechanical properties of PAN nanofiber mat," *J. Phys. Conf. Ser.*, vol. 2423, no. 1, p. 012018, 2023, doi: 10.1088/1742-6596/2423/1/012018.

[67] J. V. Sanchaniya, I. Lasenko, S. P. Kanukuntla, A. Mannodi, A. Viluma-Gudmona, and V. Gobins, "Preparation and Characterization of Non-Crimping Laminated Textile Composites Reinforced with Electrospun Nanofibers," *Nanomaterials*, vol. 13, no. 13, 2023, doi: 10.3390/nano13131949.

[68] Y. Yan, X. Liu, J. Yan, C. Guan, and J. Wang, "Electrospun Nanofibers for New Generation Flexible Energy Storage," *Energy Environ. Mater.*, vol. 4, no. 4, pp. 502–521, 2021, doi: 10.1002/eem2.12146.

[69] A. Nadaf *et al.*, "Recent update on electrospinning and electrospun nanofibers: current trends and their applications," *RSC Adv.*, vol. 12, no. 37, pp. 23808–23828, 2022, doi: 10.1039/d2ra02864f.

[70] Y. Wang, T. Yokota, and T. Someya, "Electrospun nanofiber-based soft electronics," *NPG Asia Mater.*, vol. 13, no. 1, 2021, doi: 10.1038/s41427-020-00267-8.

[71] P. R. Ilango *et al.*, "Electrospun Flexible Nanofibres for Batteries: Design and Application," *Electrochem. Energy Rev.*, vol. 6, no. 1, p. 12, 2023, doi: 10.1007/s41918-022-00148-4.

[72] Y. Zhou, Y. Liu, M. Zhang, Z. Feng, D. G. Yu, and K. Wang, "Electrospun Nanofiber Membranes for Air Filtration: A Review," *Nanomaterials*, vol. 12, no. 7, 2022, doi: 10.3390/nano12071077.

[73] Y. Salkovskiy and A. Fadeev, "High-efficiency retention of ultrafine aerosols by electrospun nanofibers," *Sci. Rep.*, vol. 12, no. 1, pp. 1–9, 2022, doi: 10.1038/s41598-022-24739-9.

[74] R. Senthil, V. Sumathi, A. Tamilselvi, S. B. Kavukcu, and A. W. Aruni, "Functionalized electrospun nanofibers for high efficiency removal of particulate matter," *Sci. Rep.*, vol. 12, no. 1, pp. 1–14, 2022, doi: 10.1038/s41598-022-12505-w.

[75] T. Wang *et al.*, "Electrospun Carbon Nanofibers and Their Applications in Several Areas," *ACS Omega*, vol. 8, no. 25, pp. 22316–22330, 2023, doi: 10.1021/acsomega.3c01114.

[76] M. K. Gaydhane, C. S. Sharma, and S. Majumdar, "Electrospun nanofibres in drug delivery: advances in controlled release strategies," *RSC Adv.*, vol. 13, no. 11, pp. 7312–7328, 2023, doi: 10.1039/d2ra06023j.

[77] S. Homaeigohar, Y. Davoudpour, Y. Habibi, and M. Elbahri, "The electrospun ceramic hollow nanofibers," *Nanomaterials*, vol. 7, no. 11, 2017, doi: 10.3390/nano7110383.

[78] P. Mankotia, K. Sharma, V. Sharma, R. Sehgal, and V. Kumar, "Polymer and Ceramic-Based Hollow Nanofibers via Electrospinning," 2021, pp. 223–250. doi: 10.1007/978-3-030-79979-3_9.

[79] M. Schneider, "An algorithm for generating microstructures of fiber-reinforced composites with long fibers," *Int. J. Numer. Methods Eng.*, vol. 123, no. 24, pp. 6197–6219, 2022, doi: 10.1002/nme.7110.

[80] D. Li and Y. Xia, "Direct Fabrication of Composite and Ceramic Hollow Nanofibers by Electrospinning," *Nano Lett.*, vol. 4, no. 5, pp. 933–938, May 2004, doi: 10.1021/nl049590f.

[81] A. Barhoum, K. Pal, H. Rahier, H. Uludag, I. S. Kim, and M. Bechelany, "Nanofibers as new-generation materials: From spinning and nano-spinning fabrication techniques to emerging applications," *Appl. Mater. Today*, vol. 17, pp. 1–35, 2019, doi: 10.1016/j.apmt.2019.06.015.

[82] S. Sheikhi, A. Ghassemi, S. M. Sajadi, and M. Hashemian, "Comparison of the mechanical characteristics of produced nanofibers by electrospinning process based on different collectors," *Heliyon*, vol. 10, no. 1, p. e23841, 2024, doi: 10.1016/j.heliyon.2023.e23841.

[83] Z. Li, B. Li, C. Yu, H. Wang, and Q. Li, "Recent Progress of Hollow Carbon Nanocages: General Design Fundamentals and Diversified Electrochemical Applications," *Adv. Sci.*, vol. 10, no. 7, pp. 1–53, 2023, doi: 10.1002/advs.202206605.

[84] S. P. Kanukuntla, J. V. Sanchaniya, U. Kardani, and V. Beresnevics, "Numerical Simulation of Polymeric Composite Nanofiber Mat," *Eng. Rural Dev.*, vol. 22, pp. 790–795, 2023, doi: 10.22616/ERDev.2023.22.TF156.

[85] M. Yousefzadeh, *Modeling and simulation of the electrospinning process*. Elsevier Ltd., 2017. doi: 10.1016/B978-0-08-100907-9.00012-X.

[86] S. M. Rahman, S. Gautam, H. V Tafreshi, and B. Pourdeyhimi, "The role of 3D electrostatic field in modeling the electrospinning process," *J. Appl. Phys.*, vol. 135, no. 1, p. 14701, Jan. 2024, doi: 10.1063/5.0187859.

[87] Y. Guo, X. Wang, Y. Shen, K. Dong, L. Shen, and A. A. A. Alzalab, "Research progress, models and simulation of electrospinning technology: a review," *J. Mater. Sci.*, vol. 57, no. 1, pp. 58–104, 2022, doi: 10.1007/s10853-021-06575-w.

[88] L. Zhou, S. Zhu, Z. Zhu, and X. Xie, "Simulations of Fractures of Heterogeneous Orthotropic Fiber-Reinforced Concrete with Pre-Existing Flaws Using an Improved Peridynamic Model," *Materials (Basel).*, vol. 15, p. 3977, Jun. 2022, doi: 10.3390/ma15113977.

[89] C. Nash, P. Karve, D. Adams, and S. Mahadevan, "Flaw Detection and Localization in Curing Fiber-Reinforced Polymer Composites Using Infrared Thermography and Kalman Filtering: A Simulation Study," *J. Nondestruct. Eval.*, vol. 40, no. 3, p. 78, 2021, doi: 10.1007/s10921-021-00802-9.

[90] N. Kizildag, "Smart composite nanofiber mats with thermal management functionality," *Sci. Rep.*, vol. 11, no. 1, pp. 1–16, 2021, doi: 10.1038/s41598-021-83799-5.

[91] X.-Q. Zhang, B. He, W.-C. Li, and A.-H. Lu, "Hollow carbon nanofibers with dynamic adjustable pore sizes and closed ends as hosts for high-rate lithium-sulfur battery cathodes," *Nano Res.*, vol. 11, Aug. 2017, doi: 10.1007/s12274-017-1737-6.

[92] W. Ye *et al.*, "Constructing Hollow Nanofibers to Boost Electrochemical Performance: Insight into Kinetics and Li Storage Mechanism for CrNb49O124," *ACS Appl. Energy Mater.*, vol. 2, Mar. 2019, doi: 10.1021/acsaem.9b00010.

[93] S. Gao, "Simulation of Mechanical NC Machining Based on CAD/CAM," *Comput. Aided. Des. Appl.*, vol. 21, no. S6, pp. 1–9, 2024, doi: 10.14733/cadaps.2024.S6.1-9.

[94] M. Ali and M. Hussein, "Characterization and optimization of mechanical properties in design materials using convolutional neural networks and particle swarm optimization," *Asian J. Civ. Eng.*, vol. 25, no. 3, pp. 2443–2457, 2024, doi: 10.1007/s42107-023-00918-5.

[95] B. Ghasemi Parvin and L. Ghasemi Parvin, *Enhancing Mechanical Properties of Materials Using Artificial Intelligence*. 2023. doi: 10.6084/m9.figshare.25180352.

[96] F. Kibrete, T. Trzepieciński, H. S. Gebremedhen, and D. E. Woldemichael, "Artificial Intelligence in Predicting Mechanical

Properties of Composite Materials," *J. Compos. Sci.*, vol. 7, no. 9, 2023, doi: 10.3390/jcs7090364.

[97] J.-V. Sanchaniya, S.-P. Kanukuntla, P. Modappathi, and A. Macanovskis, "Mechanical behaviour numerical investigation of composite structure, Consisting of polymeric nanocomposite mat and textile," *21st Int. Sci. Conf. Eng. Rural Dev. Proc.*, vol. 21, pp. 720–726, 2022, doi: 10.22616/erdev.2022.21.tf225.

[98] P. Nanofiber, M. An, A. Kobeissi, and D. Goljandin, "A Novel Method to Enhance the Mechanical Properties of Numerical Investigation," 2024.

[99] B. Qiu *et al.*, "Nanofiber self-consistent additive manufacturing process for 3D microfluidics," *Microsystems Nanoeng.*, vol. 8, no. 1, 2022, doi: 10.1038/s41378-022-00439-2.

[100] W.-M. Ji and M. Wu, "Nanoscale insights into the damage tolerance of Cantor alloys at cryogenic temperatures," *Int. J. Mech. Sci.*, vol. 226, p. 107406, May 2022, doi: 10.1016/j.ijmecsci.2022.107406.

[101] R. O. Ritchie, "Toughening materials: Enhancing resistance to fracture," *Philos. Trans. R. Soc. A Math. Phys. Eng. Sci.*, vol. 379, no. 2203, 2021, doi: 10.1098/rsta.2020.0437.

[102] J. U. Surjadi and Y. Lu, "Design criteria for tough metamaterials," *Nat. Mater.*, vol. 21, no. 3, pp. 272–274, 2022, doi: 10.1038/s41563-022-01193-6.

[103] Pandimani, M. R. Ponnada, and Y. Geddada, "Numerical nonlinear modeling and simulations of high strength reinforced concrete beams using ANSYS," *J. Build. Pathol. Rehabil.*, vol. 7, no. 1, p. 22, 2021, doi: 10.1007/s41024-021-00155-w.

[104] S. Ahamed and V. Lawrence, *A PC based CAD environment for fiber optic simulations*, vol. 2. 1989. doi: 10.1109/GLOCOM.1989.64057.

[105] R. Paschotta, "Fiber Simulation Software," *RP Photonics Encyclopedia*. Mar. 19, 2024. doi: 10.61835/z8j.

[106] R. L. Creighton, J. Phan, and K. A. Woodrow, "In situs 3D-patterning of electrospun fibers using two-layer composite materials," *Sci. Rep.*, vol. 10, no. 1, pp. 1–14, 2020, doi: 10.1038/s41598-020-64846-z.

[107] G. Marchesi, A. Camurri Piloni, V. Nicolin, G. Turco, and R. Di Lenarda, "Chairside CAD/CAM Materials: Current Trends of Clinical Uses.," *Biology (Basel).*, vol. 10, no. 11, Nov. 2021, doi: 10.3390/biology10111170.

[108] Q. Chen, L. Xu, C. Jing, T. Xue, A. Salo, and K. Ojala, "Flexible device and component reliability study using simulations," in *EuroSimE 2008 - International Conference on Thermal, Mechanical and Multi-Physics Simulation and Experiments in Microelectronics and Micro-Systems*, 2008, pp. 1–5. doi: 10.1109/ESIME.2008.4525055.

[109] A. Vukovic, E. Altinozen, T. Dimitrijevic, and P. Sewell, "Simulation Platform for Flexible Electronics," in *2021 15th International Conference on Advanced Technologies, Systems and Services in Telecommunications (TELSIKS)*, 2021, pp. 135–138. doi: 10.1109/TELSIKS52058.2021.9606324.

[110] G. Scandurra, A. Arena, and C. Ciofi, "A Brief Review on Flexible Electronics for IoT: Solutions for Sustainability and New Perspectives for Designers," *Sensors*, vol. 23, no. 11, 2023, doi: 10.3390/s23115264.

[111] R. Prabhakaran, "Nanocomposites for Aircraft Applications," *J. Aerosp. Sci. Technol.*, pp. 169–185, Aug. 2023, doi: 10.61653/joast.v66i3.2014.452.

[112] A. Bhat *et al.*, "Review on nanocomposites based on aerospace applications," *Nanotechnol. Rev.*, vol. 10, no. 1, pp. 237–253, 2021, doi: 10.1515/ntrev-2021-0018.

[113] J.-V. Sanchaniya, S.-P. Kanukuntla, A. Dutta, and V. Jevstignejevs, "Analysis of honeycomb structure evaluated in static and impact loading," *21st Int. Sci. Conf. Eng. Rural Dev. Proc.*, vol. 21, pp. 745–753, 2022, doi: 10.22616/erdev.2022.21.tf228.

[114] D. Bouyer, L. Vachoud, Y. Chakrabandhu, and C. Pochat-Bohatier, "Influence of mass transfer on gelation time using VIPS-gelation process for chitin dissolved in LiCl/NMP solvent-Modelling and experimental study," *Chem. Eng. J.*, vol. 157, no. 2–3, pp. 605–619, 2010, doi: 10.1016/j.cej.2010.01.037.

[115] J. H. Panchal, S. R. Kalidindi, and D. L. McDowell, "Key computational modeling issues in Integrated Computational Materials Engineering," *CAD Comput. Aided Des.*, vol. 45, no. 1, pp. 4–25, 2013, doi: 10.1016/j.cad.2012.06.006.

[116] R. Dingreville, R. A. Karnesky, G. Puel, and J.-H. Schmitt, "Review of the synergies between computational modeling and experimental characterization of materials across length scales," *J. Mater. Sci.*, vol. 51, no. 3, pp. 1178–1203, 2016, doi: 10.1007/s10853-015-9551-6.

[117] T. E. Gartner, A. L. Ferguson, and P. G. Debenedetti, "Data-driven molecular design and simulation in modern chemical engineering," *Nat. Chem. Eng.*, vol. 1, no. 1, pp. 6–9, 2024, doi: 10.1038/s44286-023-00010-4.

[118] P. Sinha, D. Roshini, V. Daoo, B. M. Abraham, and J. K. Singh, "Integrating Machine Learning and Molecular Simulation for Material Design and Discovery," *Trans. Indian Natl. Acad. Eng.*, vol. 8, no. 3, pp. 325–340, 2023, doi: 10.1007/s41403-023-00412-z.

[119] Y. Liu *et al.*, "Flexible hollow nanofibers: Novel one-pot electrospinning construction, structure and tunable luminescence-electricity-magnetism trifunctionality," *Chem. Eng. J.*, vol. 284, pp. 831–840, 2016, doi: 10.1016/j.cej.2015.09.030.

[120] D. Seo *et al.*, "Hollow Ti3C2 MXene/Carbon Nanofibers as an Advanced Anode Material for Lithium-Ion Batteries," *ChemElectroChem*, vol. 9, no. 1, p. e202101344, Jan. 2022, doi: https://doi.org/10.1002/celc.202101344.

[121] S. Malik, K. Muhammad, and Y. Waheed, "Nanotechnology: A Revolution in Modern Industry.," *Molecules*, vol. 28, no. 2, Jan. 2023, doi: 10.3390/molecules28020661.

[122] G. T. Jasion *et al.*, "Recent Breakthroughs in Hollow Core Fiber Technology," in *2021 Optical Fiber Communications Conference and Exhibition (OFC)*, 2021, pp. 1–3.

[123] D. Yadav, F. Amini, and A. Ehrmann, "Recent advances in carbon nanofibers and their applications – A review," *Eur. Polym. J.*, vol. 138, no. August, p. 109963, 2020, doi: 10.1016/j.eurpolymj.2020.109963.

[124] H. Yuan, Q. Zhou, and Y. Zhang, *Improving fiber alignment during electrospinning*. Elsevier Ltd., 2017. doi: 10.1016/B978-0-08-100907-9.00006-4.

[125] S. K. Vimal, N. Ahamad, and D. S. Katti, "A simple method for fabrication of electrospun fibers with controlled degree of alignment having potential for nerve regeneration applications," *Mater. Sci. Eng. C*, vol. 63, pp. 616–627, 2016, doi: 10.1016/j.msec.2016.03.008.

[126] Z. Long, Z. Yuan, C. Shi, C. Wu, H. Qiao, and K. Wang, "Porous Fe2O3 nanorod-decorated hollow carbon nanofibers for high-rate lithium storage," *Adv. Compos. Hybrid Mater.*, vol. 5, no. 1, pp. 370–382, 2022, doi: 10.1007/s42114-021-00397-9.

[127] M. Roya, M. Eifert, and E. Cosgriff-Hernandez, "Effects of Humidity and Solution Viscosity on Electrospun Fiber Morphology," *Tissue Eng. Part C. Methods*, vol. 19, Mar. 2013, doi: 10.1089/ten.TEC.2012.0671.

[128] D. Zhang, P. Davoodi, X. Li, Y. Liu, W. Wang, and Y. Y. S. Huang, "An empirical model to evaluate the effects of environmental humidity on the formation of wrinkled, creased and porous fibre morphology from electrospinning," *Sci. Rep.*, vol. 10, no. 1, pp. 1–9, 2020, doi: 10.1038/s41598-020-74542-7.

[129] L. Salama *et al.*, "CFD SIMULATION IN HOLLOW FIBER AND TUBULAR MEMBRANES," *JP J. Heat Mass Transf.*, vol. 23, pp. 139–151, Jun. 2021, doi: 10.17654/HM023010139.

[130] C. Ma *et al.*, "CFD Simulations of Fiber-Fiber Interactions in a Hollow Fiber Membrane Bundle: Fiber Distance and Position Matters," *Sep. Purif. Technol.*, vol. 209, Sep. 2018, doi: 10.1016/j.seppur.2018.09.029.

[131] Y. Su and G. Lipscomb, "Simulation of Hollow Fiber Spinning," in *ACS Symposium Series*, vol. 1078, 2011, pp. 129–152. doi: 10.1021/bk-2011-1078.ch009.

[132] J. Song, X. Lin, L. Y. Ee, S. F. Y. Li, and M. Huang, *A Review on Electrospinning as Versatile Supports for Diverse Nanofibers and Their Applications in Environmental Sensing*, vol. 5, no. 2. Springer Nature Singapore, 2023. doi: 10.1007/s42765-022-00237-5.

[133] G. B. Medeiros, F. de A. Lima, D. S. de Almeida, V. G. Guerra, and M. L. Aguiar, "Modification and Functionalization of Fibers Formed by Electrospinning: A Review.," *Membranes (Basel).*, vol. 12, no. 9, Sep. 2022, doi: 10.3390/membranes12090861.

[134] N. Ghane, S. Mazinani, and A. Gharehaghaji, "Fabrication and characterization of hollow nanofibrous PA6 yarn reinforced with CNTs," *J. Polym. Res.*, vol. 25, Mar. 2018, doi: 10.1007/s10965-018-1477-7.

[135] L. I Koroteeva, E. N. Khozina, and P. A. Korolev, "Determination of Mechanical Strength of Hollow-Fiber Membranes to Optimize Technological Processes," *Fibre Chem.*, vol. 53, no. 1, pp. 20–24, 2021, doi: 10.1007/s10692-021-10232-y.

[136] H. Han *et al.*, "Hollow carbon nanofibers as high-performance anode materials for sodium-ion batteries," *Nanoscale*, vol. 11, no. 45, pp. 21999–22005, 2019, doi: 10.1039/C9NR07675A.

[137] Y.-E. Miao, W. Fan, D. Chen, and T. Liu, "High-Performance Supercapacitors Based on Hollow Polyaniline Nanofibers by Electrospinning," *ACS Appl. Mater. Interfaces*, vol. 5, Apr. 2013, doi: 10.1021/am4008352.

[138] G. Anusiya and R. Jaiganesh, "A review on fabrication methods of nanofibers and a special focus on application of cellulose nanofibers," *Carbohydr. Polym. Technol. Appl.*, vol. 4, no. November, p. 100262, 2022, doi: 10.1016/j.carpta.2022.100262.

[139] S. Malik *et al.*, "Sustainable nanofibers in tissue engineering and biomedical applications," *Mater. Des. Process. Commun.*, vol. 3, no. 6, p. e202, Dec. 2021, doi: https://doi.org/10.1002/mdp2.202.

[140] M. Wang, Y. Wang, Y. Mo, Q. Gao, Y. Li, and J. Zhu, "Novel hollow α-Fe2O3 nanofibers with robust performance enabled multi-functional applications," *Environ. Res.*, vol. 212, p. 113459, May 2022, doi: 10.1016/j.envres.2022.113459.

[141] W. Sang, R. Zhang, X. Shi, and Y. Dai, "Advanced Metallized Nanofibers for Biomedical Applications," *Adv. Sci.*, vol. 10, no. 27, pp. 1–18, 2023, doi: 10.1002/advs.202302044.

[142] D. Sista, "New Perspective of Nano Fibers: Synthesis and Applications," B. Kumar, Ed., Rijeka: IntechOpen, 2021, p. Ch. 1. doi: 10.5772/intechopen.97460.

[143] Kenry and C. T. Lim, "Nanofiber technology: current status and emerging developments," *Prog. Polym. Sci.*, vol. 70, pp. 1–17, 2017, doi: 10.1016/j.progpolymsci.2017.03.002.

[144] X. Chen *et al.*, "Janus Hollow Nanofiber with Bifunctional Oxygen Electrocatalyst for Rechargeable Zn–Air Battery," *Small*, vol. 18, no. 16, p. 2200578, Apr. 2022, doi: https://doi.org/10.1002/smll.202200578.

[145] W. Jonkers, E. Cornelissen, J. Grooth, and W. Vos, "Hollow fiber nanofiltration: From lab-scale research to full-scale applications," *J. Memb. Sci.*, vol. 669, p. 121234, Dec. 2022, doi: 10.1016/j.memsci.2022.121234.

Investigation on Phase Composition and Microstructure of High Chromium White Cast Irons Alloyed with Boron

Julieta Kaleicheva
Institute of Metal Science, Equipment and Technologies with the Center for Hydro- and Aerodynamics "Acad. A. Balevski"
Bulgarian Academy of Sciences
Sofia, Bulgaria
jujakaleich@gmail.com

Rumyana Lazarova
Institute of Metal Science, Equipment and Technologies with the Center for Hydro- and Aerodynamics "Acad. A. Balevski"
Bulgarian Academy of Sciences
Sofia, Bulgaria
r.lazarova@ims.bas.bg

Georgi Avdeev
Institute of Physical Chemistry
Bulgarian Academy of Sciences
Sofia, Bulgaria
g_avdeev@ipc.bas.bg

Valentin Mishev
Faculty of Industrial Technology
Technical University of Sofia
Sofia, Bulgaria
v_mishev@ tu-sofia.bg

Zdravka Karaguiozova
Space Research and Technology Institute
Bulgarian Academy of Sciences
Sofia, Bulgaria
karazuzi@yahoo.com

Krassimir Kirov
College Sliven
Technical University of Sofia
Sliven, Bulgaria
kirov_krasimir_1966@abv.bg

Abstract. **The microstructure and phase composition of high chromium white cast iron with composition: 2.6÷3.1%C; 0.88÷1.12%Si; 0.74÷0.98% Mn; 0.85÷1.16% Mo; 11.11÷14.11% Cr, additionally doped with boron in an amount 0.002%, 0.92% and 1.34% is investigated. The microstructure of the white cast irons was studied by optical metallographic analysis, and the phase composition – by qualitative XRD analysis. An impact toughness test was conducted. The hardness HRC was tested by the Rockwell method. The microhardness $HV_{0.1}$ of the metal matrix and of the carbide phase was determined. It was found that in samples containing boron, the amount of the carbide phase increases and the chromium boride phase Cr_3B_4 appears in them. This results in a decrease in impact toughness from 1.88 J/cm² for the sample with 0.002% boron to 0.98 J/cm² with 0.92% boron and 0.68 J/cm² with 1.34% boron. The samples containing 0.92% and 1.34% boron have a higher microhardness of the metal base (824 and 766 $HV_{0.1}$) compared to those with 0.002% boron (672 $HV_{0.1}$).**

Keywords: high chromium white cast iron, boron, hardness, impact toughness, X-Ray Diffraction (XRD)

I. Introduction

High chromium white cast irons are materials, used in different industrial applications that require string wear resistance. They contain large amounts Chromium carbides with high hardness to which the exceptional characteristics of these alloys are due. The wear resistance and strength of cast iron depend on the type,

size and morphology of these carbides. By changing their chemical composition, by controlling the cooling rate during casting or by additional specific heat treatment, the microstructural characteristics of these alloys, and therefore their properties, can be significantly changed. White cast irons with a high chromium content are iron alloys containing 10÷30% Cr and 1.8÷3.6% C. The exceptional resistance to abrasive and erosive wear is mainly due to the presence of a large amount of chromium carbides with high hardness. The carbides represented in the alloys of the Fe–Cr–C system is M_3C, M_7C_3 and $M_{23}C_6$. The type and shape of the eutectic carbides changes from M_3C to M_7C_3 with increasing chromium content. At Cr contents above 10%, eutectic carbides of the M_7C_3 type are formed, not of the M_3C type. M_7C_3 carbides are interrupted and surrounded by an austenite matrix or by austenite transformation products – pearlite, martensite, bainite [1]-[10].

The metal matrix supporting the carbide phase in these alloys can be adjusted by introducing additional alloying elements and by conducting heat treatment. Thus, a balance is achieved between abrasive wear resistance and the required strength of high chrome white cast irons [2],[4],[5].

Heat treatments of high-Cr white cast irons are essential to change their microstructure and properties in order to meet the requirements of an individual

application. The commonly applied heat treatment consists of heating the alloys at temperatures of 800÷1100°C, holding at these temperatures, followed by air cooling at room temperature. During holding at high temperatures, carbon and chromium from the matrix form small carbide particles. The new austenitic matrix, depleted of chromium and carbon, readily transforms into martensite during subsequent cooling. Therefore, the final structure after heat treatment consists of M_7C_3 eutectic carbides, a martensitic matrix with secondary carbides distributed in it, and residual austenite [2],[5]

High chromium white cast irons can be additionally alloyed with elements such as molybdenum, manganese, copper, nickel, titanium, vanadium, boron, etc. Carbide-forming elements form new carbide phases that increase the hardness and wear resistance of alloys. Literature data on boron alloying indicate that borides and carboboride phases are formed in these cast irons, which have a higher hardness than carbides [4]-[10].

The purpose of the conducted research is to study the microstructure, phase composition and mechanical properties of high chromium white cast irons additionally alloyed with 0.002%, 0.92% and 1.34% boron.

II. MATERIALS AND METHODS

The chemical composition of the investigated samples of high-chromium white cast iron in the as cast condition is presented in Table 1. These cast irons contain more than 10% chromium, about 1% molybdenum and are additionally alloyed with 0.002%, 0.92% and 1.34% boron.

The microstructural analysis was carried out using an optical metallographic microscope MIT 500 of the Cnoptec company. The microstructure was revealed in a reagent with the following composition: 4% HNO_3 in ethyl alcohol.

The hardness HRC for the studied samples was determined by the Rockwell method. A test was conducted to determine the microhardness $HV_{0.1}$ of the metal matrix and the carbide phase in the cast iron structure with a load of 100 g.

The impact toughness testing was conducted with a Sharpie hammer. For this purpose, samples with dimensions of 10x10x55 mm without a notch were used. The results from the experiments conducted are presented in Table 2.

TABLE 1 CHEMICAL COMPOSITION

Sample	Chemical composition (wt %)							
	C	Mn	Si	P	S	Cr	Mo	B
1	3.105	0.985	0.885	0.058	0.029	14.108	1.16	0.002
2	2.899	0.758	1.029	0.057	0.021	12.564	0.936	0.923
3	2.622	0.745	1.128	0.053	0.02	11.112	0.846	1.342

TABLE 2 MECHANICAL PROPERTIES

Sample	Mechanical properties			
	HRC	KC (J/cm²)	HV_{0.1}	
			metal matrix	carbide phase
1	53.5	1.88	672	1415
2	57	0.98	824	1749
3	57.5	0.68	766	1783

The high-chromium white cast iron samples are tested by X-Ray diffraction analysis. For a phase identification X-ray diffraction powder patterns are recorded in the angle interval 20÷90°(2θ), on a Philips PW 1050 diffractometer, equipped with Cu Kα tube and scintillation detector. The data for cell refinements is collected in θ÷2θ, step-scan mode in the angle interval from 20 to 90° (2θ), at steps of 0.03° (2θ) and counting time of 3 s/step.

III. RESULTS AND DISCUSSION

The microstructure of the investigated cast irons with 0.002%, 0.92% and 1.34% boron are presented in Fig. 1, Fig. 2 and Fig. 3. The metal matrix of cast high-chromium white cast irons, in addition to pearlite transformation products (Fig. 1, 2, 3), also contains structures such as martensite and bainite (Fig. 2 b). Boron increases the resistance of supercooled austenite to decomposition, and upon cooling to room temperature, the formation of structures such as martensite and bainite becomes possible.

Fig. 1. Microstructure of high chromium white cast iron alloyed with 0.002% boron in as-cast conditions, a) x500 and b) x1000.

Fig. 2. Microstructure of cast high chrome white cast iron alloyed with 0.92% boron in as-cast conditions, a) x500 and b) x1000.

Fig. 3. Microstructure of cast high chrome white cast iron alloyed with 1.36% boron in as-cast conditions, a) x500 and b) x1000.

It is known that in high chromium white cast irons, which contain more than 10% Cr, the eutectic carbides are of the Cr_7C_3 type [1]. The results of the X-ray structural analysis showed that in the investigated white cast irons, which contain 11.11÷14.10% Cr, carbides of the type Cr_7C_3 and Fe_3C are present (Fig. 4). In the structure of cast irons with 0.92% and 1.34% boron, the phase chromium boride Cr_3B_4 is also formed (fig. 4).
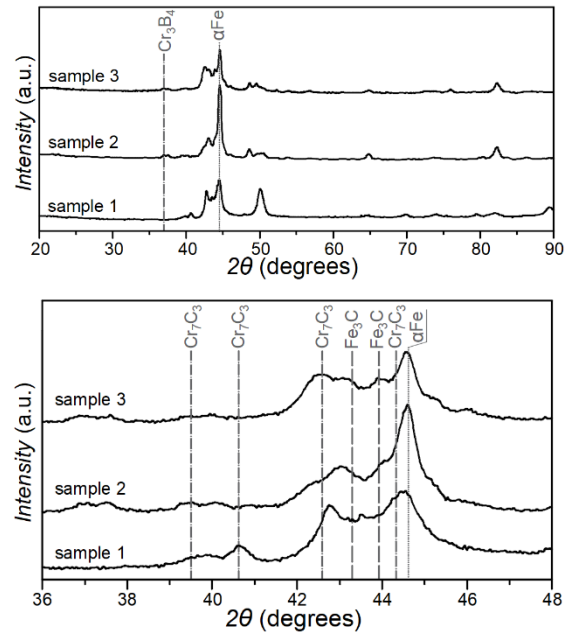
Fig. 4. Diffractometric curves of high chromium white cast irons alloyed with boron (1 – 0.002% B; 2 – 0.92% B; 3 – 1.34% B) in as-cast conditions.

In the table 2 and in Fig. 5 and Fig. 6 presents the results of the studied mechanical characteristics: microhardness HV0.1 of the metal matrix and the carbide phase (Fig. 5), hardness HRC (Fig. 6 a) and impact toughness KC (Fig. 6 b).
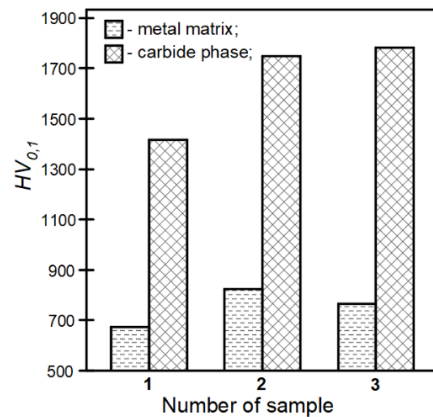
Fig. 5. Microhardness $HV_{0.1}$ of the metal matrix and the carbide phase of high chromium white iron alloyed with 0.002% B (sample 1), with 0.92% B (sample 2) or with 1.34% B (sample 3)
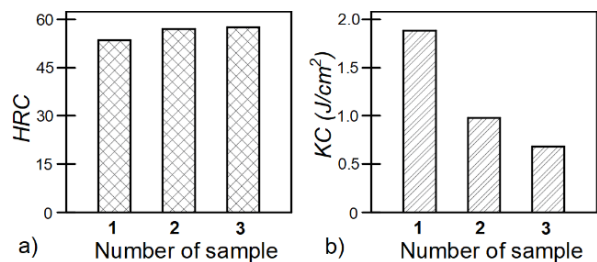
Fig.6. Hardness HRC (a) and impact toughness KC (b) of high chromium white cast iron specimens alloyed with 0.002% B (sample 1), 0.92% B (sample 2) or 1.34% B (sample 3)

The microhardness of the carbide phase increases with increasing boron content from 1415 $HV_{0.1}$ at 0.002% B to 1749 $HV_{0.1}$ at 0.92% B and 1783 $HV_{0.1}$ at 1.34%B (Table 2, Fig. 5). This is explained by the formation of carboborides $M_3(C,B)$ and $M_7(C,B)_3$ in the structure of boron-alloyed high-chromium white cast irons, which have a higher hardness than that of carbides M_3C and M_7C_3 [7].

The microhardness of the metal matrix also increased with increasing boron content from 672 $HV_{0.1}$ at 0.002% B to 824 $HV_{0.1}$ at 0.92% B and 766 $HV_{0.1}$ at 1.34%B (Table 2, Fig. 5). Boron increases the resistance of undercooled austenite to decay and ensures the transformation of austenite into martensite (bainite) during cooling of castings. The presence in the metal matrix of non-equilibrium structures such as martensite and bainite, which have higher hardness than pearlite, increase its microhardness.

The increase in the hardness of the metal matrix and the carbide phase with an increase in the amount of the boron alloying element leads to an increase in the HRC hardness of the investigated cast irons from 53.5 HRC at 0.002% B to 57.0 HRC at 0.92% B and 57.5 HRC at 1.34 % B (Table 2, Fig. 6 a).

The increase in the hardness of the investigated high chromium white irons with increasing boron content in them decreases the impact toughness of the alloys from 1.88 J/cm^2 (0.002%B) to 0.98 J/cm^2 (0.92%B) and 0.68 J/cm^2 (1.34% B) (Table 2, Fig. 6 b). In the structure of the alloys with 0.92% and 1.34% boron, the chromium boride phase Cr_3B_4 is formed, which has high hardness and can also affect KC in the direction of its decrease.

IV. CONCLUSIONS

1. Through qualitative X-ray structural analysis, it was established that the alloying of the studied high-chromium white cast irons with 0.92% and 1.34% boron leads to the formation of the chromium boride Cr_3B_4 phase in their structure.

2. The alloying of the investigated high-chromium white cast irons with 0.002%, 0.92% and 1.34% boron changes the microhardness of the carbide phase as follows: 1415 $HV_{0.1}$ (0.002%B); 1749 $HV_{0.1}$ (0.92%B) and 1783 $HV_{0.1}$ (1.34%B). The carbide phases of the type M_3C and M_7C_3 registered by X-ray structural analysis represent carboborides $M_3(C,B)$ and $M_7(C,B)_3$. They have a higher hardness than that of the carbide phases and this explains the measured higher microhardness in the 0.92% and 1.34% boron alloys compared to the microhardness in the 0.002% boron alloys.

3. The formation in the structure of the studied high-chromium white cast irons of phases with high hardness such as chromium boride Cr_3B_4 and carboboride phases of the type $M_3(C,B)$ and $M_7(C,B)_3$, lead to a decrease in the impact toughness of the alloys as follows: 1.88 J/cm^2 (0.002%B); 0.98 J/cm^2 (0.92%B) and 0.68 J/cm^2 (1.34%B). Impact toughness is also influenced by the structure of the metal matrix, which with increasing boron content has a higher microhardness as a result of the formation of larger amounts of non-equilibrium phases (martensite, bainite) from austenite upon cooling.

REFERENCES

[1] A. Nufal, "Metallurgical Aspects of High- Chromium White Irons", [Online]. Available: https://www.foundry-planet.com/fileadmin/redakteur/pdf-dateien/13-Adel-Nofal.pdf [Accessed: March 1, 2024].

[2] Kh. Abdel-Aziz, M. El-Shennawy and Adel A. Omar, "Microstructural Characteristics and Mechanical Properties of Heat Treated High-Cr White Cast Iron Alloys", International Journal of Applied Engineering Research, vol. 12, number 14, p. 4675-4686, 2017. [Online]. Available: ResearchGate, https://www.ripublication.com/ijaer17/ijaerv12n14_79.pdf [Accessed March 1, 2024].

[3] Abd El-Aziz, K., Zohdy, K., Saber, D. et al. "Wear and Corrosion Behavior of High-Cr White Cast Iron Alloys in Different Corrosive Media", Journal of Bio- and Tribo-Corrosion, vol.1, article number 25 (2015). [Online]. Available: SpringerLink, https://doi.org/10.1007/s40735-015-0026-8 [Accessed March 1, 2024].

[4] F. Nurjaman, S. Sumardi, A. Shofi, M. Aryati, and B. Suharno, "Effect of molybdenum, vanadium, boron on mechanical properties of high chromium white cast iron in as-cast condition", AIP Conference Proceedings 1711, 020005, 2016, [Online]. Available: ResearchGate, https://aip.scitation.org/doi/pdf/10.1063/1.4941614 [Accessed March 1, 2024], https://doi.org/10.1063/1.4941614

[5] A. Bedolla-Jacuinde, F. V. Guerra, I. Mejía, J. Zuno-Silva and C. Maldonado, "Boron Effect on the Precipitation of Secondary Carbides During Destabilization of a High-Chromium White Iron", 10th International Symposium on the Science and Processing of Cast Iron – SPCI10, 2014. [Abstract]. Available: ResearchGate, https://www.researchgate.net/publication/271829525 [Accessed March 1, 2024], https://doi.org/10.1080/13640461.2016.1142236

[6] S. Tomovic-Petrovic, S. Markovic and S. Zec, "The effect of boron on the amount and type of carbides in chromium white irons", Journal of the Serbian Chemical Society, vol. 67(10), p.697-707, 2002. [Online]. Available: ResearchGate, https://www.doiserbia.nb.rs/img/doi/0352-5139/2002/0352-51390210697T.pdf [Accessed March 1, 2024], https://doi.org/10.2298/JSC0210697T

[7] Zhongli Liu, Yanxiang Li, Xiang Chen, Kaihua Hu, "Microstructure and mechanical properties of high boron white cast iron", Materials Science and Engineering: A, vol.486, issues 1–2, p. 112-116, 2008, ISSN 0921-5093,[Abstract]. Available: ScienceDirect, https://www.sciencedirect.com/science/article/pii/S0921509307017273 [Accessed March 1, 2024], https://doi.org/10.1016/j.msea.2007.10.017

A. Bedolla-Jacuinde, F.V. Guerra, A.J. Guerrero-Pastran, M.A. Sierra-Cetina, S. Valdez-Medina," Microstructural effect and wear performance of high chromium white cast iron modified with high boron contents", Wear, vol.476, 203675, 2021, ISSN 0043-1648, [Abstract]. Available: ScienceDirect,https://www.sciencedirect.com/science/article/pii/S0043164821000648 [Accessed March 1, 2024], https://doi.org/10.1016/j.wear.2021.203675

[8] J. Kaleicheva, K. Kirov, V. Mishev and Z. Karaguiozova, "Microstructure and Properties of High Chromium White Cast Irons Alloyed with Boron", Proceedings of the 13th Internacional Scientific and Practical Conference: Environment, Technology, Resources, Rezekne, Latvia,vol. 3, p.137-141, 2021. [Online]. Available: http://journals.rta.lv/index.php/ETR [Accessed March 1, 2024], https://doi.org/10.17770/etr2021vol3.6656

[9] J. Kaleicheva, K. Kirov, V. Mishev, R. Lazarova, Z.Karaguiozova, "Effect of boron on the wear behavior of high chromium white cast irons", Proceedings of the 14th Internacional Scientific and Practical Conference: Environment, Technology, Resources, Rezekne, Latvia,vol. 3, p.119-123, 2023. [Online]. Available: https://journals.rta.lv/index.php/ETR/article/view/7294/6003 [Accessed March 1, 2024], https://doi.org/10.17770/etr2023vol3.7294

Assessing Daily Intake of Indoor Air Pollutants from 3D Printing

Ivars Laicāns
Rīga Stradiņš university
Faculty of Pharmacy
Riga, Latvia
laic.iv@inbox.lv

Elīza Ķibilda
Rīga Stradiņš university
Faculty of Pharmacy
Riga, Latvia
elizakibilda@gmail.com

Krista Žvagiņa
Rīga Stradiņš university
Faculty of Pharmacy
Riga, Latvia
zvaginakrista@gmail.com

Žanna Martinsone
Rīga Stradiņš university
Department of Occupational and Enviromental Medicine
Institute of Occupational Safety and Environmental Health
Riga, Latvia
zanna.martinsone@rsu.lv

Ilona Pavlovska
Rīga Stradiņš university
Institute of Occupational Safety and Environmental Health
Laboratory of Hygiene and Occupational Diseases
Riga, Latvia
ilona.pavlovska@rsu.lv

Abstract. The scientific community is increasingly focusing on indoor air quality (IAQ) more than ever, driven by on-going research and fresh perspectives including development of 3D technologies. Exposure dose (ED_a) resulting from inhalation of indoor air pollutants emitted by 3D printers were calculated in this study. The consideration of emissions from 3D printers is based on experimental data, primarily sourced from reviewed literature. However, this research also includes some experimental values, excluding the background levels of these pollutants. Experiments were conducted using several 3D printers available (Zortrax M300 Dual) to compare the indoor air pollutants generated and their concentrations with information gathered from earlier research. In the experiments, filaments containing ABS (acrylonitrile, butadiene, and styrene copolymer material, commonly used for 3D printing) were utilized. ED_a values of styrene, toluene, formaldehyde, and acetaldehyde for 8-hour and 12-hour shifts for average and maximal (reported) concentrations were calculated based on the available experimental and literature data. The average concentrations of these pollutants were determined by calculating the arithmetic mean, which incorporated concentration values obtained from previous research and experimental data collected within this study. It was concluded that further investigation should focus on aerial concentrations of styrene generated during 3D printing. Calculated ED_a for styrene from several studies exceeded the recommended guidelines for Tolerable Daily Intake (TDI) set by the World Health Organization (WHO) by at least 35%. Further exploration is imperative to incorporate additional pathways of indoor air pollutant exposure, such as skin contact and ingestion. This comprehensive approach will provide a more thorough understanding of the overall health risks associated with indoor air quality during 3D printing.

Keywords: 3D printing emissions, exposure dose (ED), indoor air quality (IAQ), styrene

I. INTRODUCTION

Additive manufacturing (AM) has emerged as a transformative force in manufacturing since the late 20th century, allowing for object fabrication through layer-by-layer material addition guided by digital models. Over the past two decades, its applications have spanned diverse fields, including medicine, aerospace engineering, architecture, defence, and personal projects for consumers [1]. Advancements now focus on sophisticated materials, enabling the creation of intricate products, particularly evident in medicine where it promises breakthroughs in specialist training and therapy options. In defence, 3D printing streamlines production of lightweight, durable aircraft and vehicle components, while also facilitating rapid prototyping for weapons systems. Moreover, it supports on-demand production of spare parts in remote environments, ensuring operational readiness, and aids in crafting custom tools and unmanned aerial vehicles for reconnaissance. Overall, AM enhances agility, resilience, and technological superiority in modern military operations [1]-[6].

Despite its remarkable potential, the thermal processing involved in 3D printing raises concerns

regarding the emission of gasses, particulate matter, and volatile organic compounds (VOCs). Notably, the quantity and composition of these emissions from commercially available printers remain relatively understudied, owing to the novelty and continual innovation in the field. Research indicates that commonly used filaments in 3D printing can expose individuals to a spectrum of chemicals, potentially leading to adverse health effects like irritation of the respiratory tract, damage to the liver and central nervous system, as well as being possible carcinogens, which poses a threat to workers coming into contact with AM daily, as well as public consumers [7], [8]-[10].

A variety of different filaments are used in AM, for example, PLA (polylactic acid) and ABS (acrylonitrile butadiene styrene) are arguably the most popular ones, providing a high level of strength, flexibility, and user-friendliness. Other filaments used that are less common are PETG (polyethylene terephthalate glycol), derived from the same polymer used to make plastic water bottles, TPE (thermoplastic elastomers), which is plastic with rubber-like qualities and many more, it being likely that other filaments may be created, suited for an array of different needs [11], [12].

Among the compounds identified in the processing of 3D printing filaments, ABS stands out as a commonly utilized material, mainly because of its simple use and print quality; price is also a beneficial factor. Studies have highlighted the occupational health risks associated with exposure to emissions from 3D printing processes. Employees working in such environments may face an increased likelihood of developing symptoms of occupational diseases, including asthma-like symptoms. When heated during printing, ABS releases emissions that contain various compounds, posing potential threats to human health, including aldehydes, acetonitrile, acetone, ethanol, formaldehyde, phenols, and toluene [1], [13]-[15].

Additionally, various factors can influence the release of VOCs during AM, such as the extrusion temperature of the filament material and the temperature of the build plate where the printing process takes place [16]. Of particular concern is styrene, a compound found in ABS filament and widely used in the production of insulation, automobile parts, and food containers. Styrene is recognized as a carcinogen, metabolizing in the human body to form styrene oxide, a toxic, mutagenic, and potentially carcinogenic compound [17]. Understanding the implications of exposure to these chemical compounds, is essential for assessing both short-term and long-term health risks associated with AM processes. Butadiene and acrylonitrile are also critical components of ABS filament used in 3D printing. Butadiene, a known carcinogen, poses health risks upon exposure, while acrylonitrile is associated with eye irritating, respiratory, and neurological effects, as well as being associated with endothelial dysfunction, which is impaired functioning of the inner lining of blood vessels, and can lead to hypertension [18]-[22]. Other compounds, such as cumene, toluene, phenol and more have been identified as emissions from AM, which can also pose a threat to the general health of workers coming into contact with these emissions. These compounds contribute to the complex

mixture of emissions released during 3D printing processes [21], [23].

Quantifying the exposure dose (ED) of VOCs emitted during 3D printing is crucial for assessing indoor air quality and safeguarding human health as well as for calculating the resulting estimated daily intake (EDI). EDI refers to the quantity of a substance that an individual can consume each day throughout their lifetime without posing a health risk. Typically, it is stated as milligrams of the substance per kilogram of body weight per day [24]. Measurements of aerial concentrations of such pollutants helps identify potential health risks associated with prolonged exposure to indoor environments where 3D printing occurs. By measuring the intake of VOCs, researchers can develop strategies to mitigate exposure and to identify the need for enhancing ventilation systems in spaces where 3D printing takes place. Moreover, quantifying ED or/and EDI provides valuable data for regulatory agencies to establish guidelines and standards aimed at protecting individuals from harmful airborne pollutants generated by 3D printers. Ultimately, a comprehensive assessment of EDI facilitates informed decision-making and promotes safer practices within the rapidly expanding domain of AM. Tolerable daily intake (TDI) is an estimate of the amount of a specific substance in air inhaled daily over a lifetime without appreciable health risk and used to compare the calculated EDIs and identify the potential chemicals that pose health risks [1], [21], [25], [26].

The objectives of this study include identifying the most hazardous chemicals emitted during 3D printing by analysing available experimental data from literature reviews and on-site experiments. Additionally, the study aims were to calculate the ED for styrene, toluene, formaldehyde, and acetaldehyde, and theoretically compare these values with the TDI to assess the potential health risks associated with 3D printing emissions.

II. MATERIALS AND METHODS

The ED, EDI and TDI are crucial parameters in assessing the potential health effects of exposure to various substances. In this study, all these parameters were investigated for 3D printing related substances, focusing on their significance in risk assessment and regulatory decision-making. The ED calculation was employed and subsequently compared to the corresponding TDI, which was chosen based on previous research findings.

The experimental setup featured a printing area, which comprised a room with a volume of 52.5 m^3. Within this area, two 3D printers (both "Zortrax M 300 Dual") were positioned at a height of 70 cm, with a distance of 1 m between them. Throughout the experiment, both printers utilized "Ultrat" filament in black colour. The build plate temperature was maintained at +105°C, while the nozzle temperature was set to +260°C. Air samples were collected using two individual samplers (Gillian LFS - 113DC), placed equidistantly between printers. The samples were simultaneously collected on the solid sorbent cartridges treated with 2,4-dinitrophenylhydrazine (DNPH cartridges for low molecular aldehydes). Subsequently, all samples were analysed using a High-

performance liquid chromatograph (HPLC) – "Water Alliance 2695" with a UV detector – "Water 2487".

The experiments were conducted separately three times, both for blank samples and for the experimental samples. The blank samples were collected in the same room 120 minutes before the experimental samples. Prior to collecting the blank samples, it was ensured that there had been no printing activity in the room for at least 10 hours and the room would be properly ventilated. Both the blank and experimental samples were collected for 60 minutes at a flow rate of 0.1 L/min. Following the sample recording process, they were stored in a container with refrigerants and then transported to the laboratory for analysis. The experimental samples were initiated 45 minutes after the 3D printers started, allowing time for the printers to reach their operating temperatures. The air samplers were positioned on the table between the 3D printers. Both printers were equipped with "HEPA" filters and enclosed casings, which were fully closed and operational during the air sampling process. The results were analysed, and the blank samples were utilized to adjust for the baseline levels of acetaldehyde and formaldehyde that were not attributed to the 3D printing.

The EDI is one of the parameters to assess the potential health effects. The formula for EDI encompasses the summation of ED from various exposure routes including inhalation, ingestion via water, ingestion via soil, ingestion via food, dermal contact with water, and dermal contact with soil (Equation 1) [27].

$$EDI = ED_a + ED_w + ED_s + ED_f + ED_{ws} + ED_{ss} \quad (1)$$

EDI   -   estimated daily intake;
ED_a -   the amount inhaled through the air;
ED_w -   the amount taken by drinking water;
ED_s -   the amount taken by ingesting soil;
ED_f -   the amount taken in by food;
ED_{ws} -   the amount absorbed through skin contact with water;
ED_{ss} -   the amount absorbed through skin contact with the soil.

In specific circumstances, EDI aligns with ED_a, mainly due to airborne inhalation serving as the primary route of exposure in 3D printing scenarios, with other pathways being non-specific in this context. As a result, for further calculation the following equation (Equation 2) were used [27]:

$$ED_a = \frac{C*IR*EF*X}{24*BW} \quad (2)$$

ED_a -   exposure dose, mg/kg/day, exposition to a chemical substance;
C   -   concentration of a chemical in air, mg/m^3;
IR   -   inhalation rate – inhaled amount of air in a day, 23 m^3/day;
EF   -   exposure factor, unitless (how often the person is exposed to a chemical);
X   -   hours in a day exposed to a chemical;
24   -   hours in a day;
BW   -   body mass, kg (it was assumed that the average value for adult body mass is 70 kg) [28].

The average and maximal concentrations of chemical substances used in the calculation of ED_a were predominantly obtained from previously collected data from various scientific publications (see Table 1). The selection of aerial concentration values from previous studies was carefully performed, prioritizing reliability and precision.

The calculated ED_a specifically pertains to the amount of the particular chemical inhaled and encompasses both the highest and average airborne concentrations recorded for each chemical.

TABLE 1 AIRBORNE CHEMICAL COMPOUND CONCENTRATIONS CONSIDERED FOR CALCULATIONS

Chemical compound	Concentration, µg/m³		
	Literature data [source]	*Maximal*	*Average*
Styrene	912.8 [16]; 461.0 [16]; 243.2 [16]; 857.7 [16]; 12.0 [28]; 101.0 [29]; 252.1 [30]; 212.1 [30]; 100.5 [30]	912.8 [16]	338.9
Toluene	31.5 [16]; 37.8 [16]; 40.4 [16]; 49.0 [28]	49.0 [29]	39.7
Formaldehyde	37.0 [28]; 16.0 *(measured)*	37.0 [29]	26.5
Acetaldehyde	15.0 [28]; 16.3 [30]; 7.7 [30]; 11.1 [30]; 13.7 [30]; 2.6 *(measured)*	16.3 [30]	10.0

Regarding to the relevant exposure factor (EF) necessary for calculation of the ED_a, the following equation (Equation 3) with the values specified below was used:

$$EF = \frac{30*48*5}{70*365} = 0.28 \ (unitless) \quad (3)$$

EF   -   exposure factor;
30   -   assumed number of years worked at the job where the source of chemical occurs;
48   -   work weeks in a year, assuming there is 4 weeks' vacation time every year;
5   -   workdays in a week;
70   -   assumed lifetime (standard value in toxicological studies [27]);
365   -   number of days in a year.

The consistent EF value of 0.28 in all calculations, was utilized to reach ED_a and ED values (see Table 2 and Table 3).

III. RESULTS AND DISCUSSION

In this experiment, following aerial concentration values during 3D printing were obtained for formaldehyde (16.0 ± 2.0 µg/m³) and acetaldehyde (2.6 ± 0.3 µg/m³). These values were included in overall calculation of the average concentrations of aerial chemical concentrations (Table 1).

These values differ significantly from the values published by previous researchers [28], [31]. Specifically, the aerial concentration of formaldehyde recorded during 3D printing with ABS-containing filament is 56% lower than values in prior published report (only one study was identified with a single value [32]), while the acetaldehyde concentration is 80% lower than the average of previously reported findings.

Despite the fact that both obtained values were significantly lower than the previously reported for these specific chemicals (formaldehyde and acetaldehyde) they were included in the calculation of the average aerial concentrations, which later were used to calculate the ED_a. This decision was based on factors that each of the experiment viewed had slightly different setup, but the main reason was that the authors found through the literature analysis that small individual chemical composition variances, like different colour of the same brand filament, may largely affect the quantities of individual VOCs. Therefore, significant deviancies of the individual VOC concentrations between different ABS filaments don't necessarily represent faulty values.

Calculated ED_a were compared against established guidelines for TDI, serving as a critical benchmark to evaluate the potential risks posed by exposure to indoor air pollutants (Table 2). This comparative analysis facilitated a deeper understanding of the potential health impacts associated with 3D printing emissions.

The findings of this study suggest that calculated styrene exposure, whether based on maximal aerial concentrations or average concentrations, pose the greatest health risks when compared to their TDI value. The calculated ED_a values were directly compared with TDI values, revealing that the ED_a for styrene average concentration exceeds the TDI by 35%. This indicates that emissions of styrene from 3D printers could potentially lead to health issues for personnel working with these devices in long-term. The real intake of styrene for individuals working with 3D printers using ABS filament materials would likely be higher. However, it was not feasible to compute the complete intake.

TABLE 2 ED_a RESULTS OF AIRBORNE CHEMICAL COMPOUNDS BASED ON AVERAGE AND MAXIMAL CONCENTRATIONS AND CORRELATION WITH TDI VALUES

Chemical compound		C_{aerial}, µg/m³	ED_a, µg/kg (8 h)	ED_a, µg/kg (12 h)	TDI, µg/kg
Styrene	max	912.8	28.0	42.0	7.7 [31]
	avg	338.9	10.4	15.6	7.7 [31]
Toluene	max	49.0	1.5	2.3	1070 [30]
	avg	39.7	1.2	1.8	1070 [30]
Formaldehyde	max	37.0	1.1	1.7	150 [32]
	avg	26.5	0.8	1.2	150 [32]
Acetaldehyde	max	16.3	0.5	0.7	100 [33]
	avg	10.0	0.3	0.5	100 [33]

This research opted to exclude the background levels of observed chemical components, although it was deliberated that such exclusion might not be necessary as background levels contribute to the chemicals absorbed through the lungs. Moreover, there was a hypothesis suggesting that in areas continuously used for 3D printing, various chemical air contaminants could potentially accumulate, resulting in elevated background levels of relevant chemicals.

While the data sources for aerial levels of chemical compounds were assessed and evaluated, it is noteworthy that variations in experimental design across the studies introduce a certain degree of uncertainty.

According to the Fig. 1 and Table 3, the concentrations of four distinct chemical compounds (styrene, toluene, formaldehyde, and acetaldehyde) across time intervals ranging from 1 hour to 24 hours, including 8-hour shift and 12-hour shift were presented.

TABLE 3 EXPOSURE DOSE OF CHEMICAL COMPOUNDS

Chemical compound	C, µg/m³ (aerial)	Exposure dose, µg/kg/day				
		1 h	4 h	8 h	12 h	24 h
Styrene	338.9	1.3	5.2	10.4	15.6	31.2
Toluene	39.7	0.2	0.6	1.2	1.8	3.7
Formaldehyde	26.5	0.1	0.4	0.8	1.2	2.4
Acetaldehyde	10.0	0.04	0.2	0.3	0.5	0.9

The concentration of chemical compounds increases gradually over time. This indicates a significant increase in concentration over the observed time period.

Exposure to styrene, toluene, formaldehyde, and acetaldehyde in 3D printing occurs primarily through inhalation of emitted vapor and particles during the printing process. Short-term exposure can result in irritation of the respiratory tract and eyes, dizziness, and headaches. Long-term exposure to these chemicals has been linked to respiratory issues, neurological effects, and potential carcinogenicity, highlighting the importance of proper ventilation and personal protective equipment to mitigate health risks associated with 3D printing. These calculations provide valuable insights for employees and employers as well as regulatory and risk management purposes.

For instance, the average concentration of styrene rises from approximately 1.3 mg/kg/day at 1 hour to 31.2 µg/kg/day at 24 hours indicating a notable increase.

Similarly, toluene, formaldehyde and acetaldehyde also demonstrate substantial increases in concentration from their initial levels from 0.2, 0.1, 0.04 to 3.7, 2.4 and 0.9 µg/kg/day, respectively, after 24 hours, highlighting the dynamic nature of airborne pollutant levels over time.

Analysing ED_a can also guide efforts to optimize 3D printing processes to reduce emissions of hazardous chemicals. This may involve modifying printing parameters, using alternative materials, or implementing post-processing treatments to mitigate emissions. ED_a data serves as valuable input for research and development efforts aimed at improving the safety of 3D printing technologies. Researchers may use this information to develop safer materials, printing methods, and workplace practices.
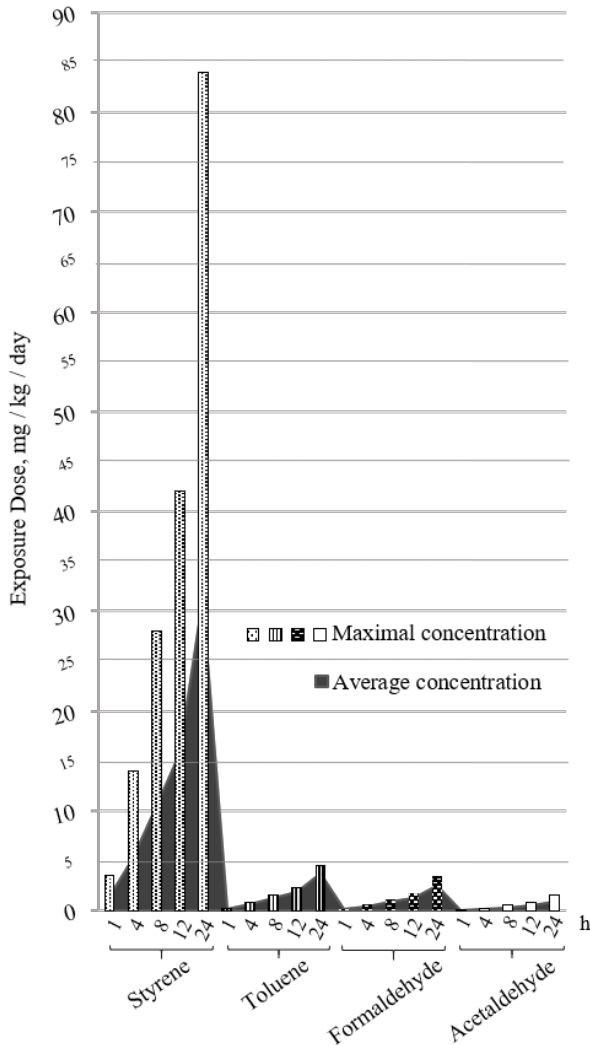
Fig.1. ED_a for styrene, toluene, formaldehyde, and acetaldehyde for working hours: 1 h, 4 h, 8 h, 12 h, and 24 h.

IV. Conclusions

This study highlights the necessity of thorough attention to concentrations of chemical compounds during 3D printing processes. The reported levels, as well as obtained experimental data for aerial concentrations of styrene, toluene, formaldehyde, and acetaldehyde during 3D printing, were utilized to compute the ED_a, which was subsequently compared to established thresholds for chemical intake, namely TDI. The outcomes of these computations suggest that individuals involved in 3D printing tasks (utilizing ABS filaments) may face a potential health hazards of chemical exposure, especially of styrene. More specifically, the ED_a calculated for styrene within 8-hour shift exceeds the TDI by 35% for average concentrations and by more than threefold for maximal styrene concentration observed during 3D printing. The other chemical compounds such as toluene, formaldehyde and acetaldehyde which are produced in 3D printing while using ABS copolymer as a filament material are highly unlikely to pose potential health risks from daily inhalation. The significant inequality between the calculated ED_a for styrene and the established TDI thresholds underscores the heightened risk of adverse health effects, including respiratory and neurological issues, for individuals exposed to these concentrations during their working hours.

V. Acknowledgements

VI. References

[1] I. Pavlovska et al., "Assessment of Occupational Exposures in the 3D Printing: Current Status and Future Prospects," *Advances in 3D Printing*, Jan. 2023. [Online]. Available: doi: 10.5772/intechopen.109465. [Accessed February 20, 2024].

[2] V. Leso, M. L. Ercolano, I. Mazzotta, M. Romano, F. Cannavacciuolo, and I. Iavicoli, "Three-Dimensional (3D) Printing: Implications for Risk Assessment and Management in Occupational Settings," *Ann Work Expo Health,* vol. 65, no. 6, pp. 617–634, Jul. 2021. [Online]. Available: doi: 10.1093/annweh/wxaa146. [Accessed February 22, 2024].

[3] K. Pathak et al., "3D printing in biomedicine: *advancing personalized care through additive manufacturing," Open Exploration* 2019 4:6, vol. 4, no. 6, pp. 1135–1167, Dec. 2023. [Online]. Available: doi: 10.37349/emed.2023.00200. [Accessed February 20, 2024].

[4] S. F. Iftekar, A. Aabid, A. Amir, and M. Baig, "Advancements and Limitations in 3D Printing Materials and Technologies: A Critical Review," *Polymers 2023*, Vol. 15, Page 2519, vol. 15, no. 11, p. 2519, May 2023. [Online]. Available: doi: 10.3390/polym15112519. [Accessed February 20, 2024].

[5] A. Su and S. J. Al'Aref, "History of 3D Printing," *3D Printing Applications in Cardiovascular Medicine*, pp. 1–10, Jan. 2018. [Online]. Available: doi: 10.1016/B978-0-12-803917-5.00001-8. [Accessed February 22, 2024].

[6] A. E. Jakus, "An Introduction to 3D Printing-Past, Present, and Future Promise," *3D Printing in Orthopaedic Surgery*, pp. 1–15, Jan. 2019. [Online]. Available: doi: 10.1016/B978-0-323-58118-9.00001-4. [Accessed February 20, 2024].

[7] U.S. Environmental Protection Agency, "Volatile Organic Compounds' Impact on Indoor Air Quality," U.S. *Environmental Protection Agency*, [Online]. Available: https://www.epa.gov/indoor-air-quality-iaq/volatile-organic-compounds-impact-indoor-air-quality. [Accessed February 21, 2024].

[8] G. Felici et al., "A pilot study of occupational exposure to ultrafine particles during 3D printing in research laboratories," *Front Public Health*, vol. 11, p. 1144475, Jun. 2023. [Online]. Available: doi: 10.3389/fpubh.2023.1144475/bibtex. [Accessed February 20, 2024].

[9] V. Leso, M. L. Ercolano, I. Mazzotta, M. Romano, F. Cannavacciuolo, and I. Iavicoli, "Three-Dimensional (3D) Printing: Implications for Risk Assessment and Management in Occupational Settings," *Ann Work Expo Health,* vol. 65, no. 6, pp. 617–634, Jul. 2021. [Online]. Available: doi: 10.1093/annweh/wxaa146. [Accessed February 22, 2024].

[10] A. Väisänen, L. Alonen, S. Ylönen, and M. Hyttinen, "Volatile organic compound and particulate emissions from the production and use of thermoplastic biocomposite 3D printing filaments*," J Occup Environ Hyg*, vol. 19, no. 6, pp. 381–393, 2022. [Online]. Available: doi: 10.1080/15459624.2022.2063879. [Accessed February 23, 2024].

[11] D. Whelan, "Thermoplastic Elastomers," Brydson's Plastics Materials: Eighth Edition, pp. 653–703, Jan. 2017. [Online]. Available: doi: 10.1016/B978-0-323-35824-8.00024-4. [Accessed February 20, 2024].

[12] R. B. Dupaix and M. C. Boyce, "Finite strain behavior of poly(ethylene terephthalate) (PET) and poly(ethylene terephthalate)-glycol (PETG*)," Polymer (Guildf)*, vol. 46, no. 13, pp. 4827–4838, Jun. 2005. [Online]. Available: doi: 10.1016/j.polymer.2005.03.083. [accessed february 22, 2024].

[13] Y. Mohammadian and N. Nasirzadeh, "Toxicity risks of occupational exposure in 3D printing and bioprinting industries: A systematic review," *Toxicol Ind Health*, vol. 37, no. 9, pp. 573–584, Aug. 2021. [Online]. Available: doi: 10.1177/07482337211031691. [Accessed February 22, 2024].

[14] A. Borisova, K. Rudus, I. Pavlovska, Ž. Martinsone, and I. Mrtiņsone, "Multiple path particle dosimetry model concept and its application to determine respiratory tract hazards in the 3d printing," *Environment. technologies. Resources. Proceedings of the International Scientific and Practical Conference*, vol. 2, pp. 23–27, Jun. 2023. [Online]. Available: doi: 10.17770/etr2023vol2.7276. [accessed february 24, 2024].

[15] P. M. Potter, S. R. Al-Abed, F. Hasan, and S. M. Lomnicki, "Influence of polymer additives on gas-phase emissions from 3D printer filaments," *Chemosphere*, vol. 279, p. 130543, Sep. 2021. [Online]. Available: doi: 10.1016/j.chemosphere.2021.130543. [Accessed February 24, 2024].

[16] P. Azimi, D. Zhao, C. Pouzet, N. E. Crain, and B. Stephens, "Emissions of Ultrafine Particles and Volatile Organic Compounds from Commercially Available Desktop Three-Dimensional Printers with Multiple Filaments," *Environ Sci Technol*, vol. 50, no. 3, pp. 1260–1268, Feb. 2016. [Online]. Available: doi: 10.1021/acs.est.5b04983/asset/images/large/es-2015-04983x_0006.jpeg. [Accessed February 24, 2024].

[17] National Institute of Environmental Health Sciences, "Styrene." [Online]. Available: https://www.niehs.nih.gov/health/topics/agents/styrene. [Accessed: Feb. 21, 2024.]

[18] H. A. R. Hadi, C. S. Carr, and J. Al Suwaidi, "Endothelial Dysfunction: Cardiovascular Risk Factors, Therapy, and Outcome," *Vasc Health Risk Manag*, vol. 1, no. 3, p. 183, 2005, [Online]. Available: /pmc/articles/PMC1993955/ [Accessed: February 21, 2024].

[19] K. E. McGraw et al., "Exposure to Volatile Organic Compounds – Acrolein, 1,3-Butadiene, and Crotonaldehyde – is Associated with Vascular Dysfunction," *Environ Res*, vol. 196, p. 110903, May 2021. [Online]. Available: doi: 10.1016/j.envres.2021.110903. [Accessed: February 21, 2024].

[20] Occupational Safety and Health Administration, '1,3-Butadiene', *Occupational Safety and Health Administration*. [Online]. Available: https://www.osha.gov/butadiene/health-effects [Accessed: February 24, 2007].

[21] S. Wojtyła, P. Klama, K. Śpiewak, and T. Baran, "3D printer as a potential source of indoor air pollution," *International Journal of Environmental Science and Technology*, vol. 17, no. 1, pp. 207–218, Jan. 2020. [Online]. Available: doi: 10.1007/s13762-019-02444-x/metrics. [Accessed: February 21, 2024].

[22] Centers of Disease Control and Prevention, "Acrylonitrile." [Online]. Available: https://www.cdc.gov/niosh/topics/acrylonitrile/default.html. [Accessed: Feb. 21, 2024].

[23] "U.S. Department of health and human services, 'Public Health Service', *Agency for Toxic Substances and Disease Registry*, 2010. [Online]. Available: https://www.atsdr.cdc.gov/index.html [Accessed: February 22, 2024].

[24] European Food and Safety authority, "acceptable daily intake". [Online]. Available: https://www.efsa.europa.eu/en/glossary/acceptable-daily-intake. [Accessed: February 21, 2024].

[25] S. Khaki, M. Rio, and P. Marin, "Monitoring Indoor Air Quality in Additive Manufacturing environment," *Procedia CIRP*, vol. 90, pp. 455–460, Jan. 2020. [Online]. Available: doi: 10.1016/j.procir.2020.01.113. [Accessed: February 21, 2024].

[26] M. Finnegan et al., "Characterization of Volatile and Particulate Emissions from Desktop 3D Printers," *Sensors*, vol. 23, no. 24, p. 9660, Dec. 2023. [Online]. Available: doi: 10.3390/S23249660/S1. [Accessed: February 21, 2024].

[27] Canada. Health Canada. and Great Lakes Health Effects Program (Canada), *Investigating human exposure to contaminants in the environment: a handbook for exposure calculations.* Health Canada, 1995.

[28] Nordiska. Ministerrådet, Existing Default Values and Recommendations for Exposure Assessment. *Nordiska ministerrådets förlag*, 2012. [Accessed: February 21, 2024].

[29] B. Kim et al., "Assessment and Mitigation of Exposure of 3-D Printer Emissions," *Frontiers in Toxicology*, vol. 3, 2021. [Online]. Available: doi: 10.3389/ftox.2021.817454. [Accessed February 23, 2024].

[30] Government of Canada, Health and Welfare Canada, Environment Canada, "Toluene," *Priority substances list assesment report*, 1992. [Accessed: February 21, 2024].

[31] World Health Organization, "Styrene, styrene-7,8-oxide and quinoline," *IARC monographs on the evaluation of carcinogenic risks to humans*, vol. 121, Lyon, France, 2019. [Accessed: February 21, 2024].

[32] H. Environments and C. Safety Branch, "Federal-Provincial-Territorial Committee on Drinking Water," 1997. [Accessed: February 21, 2024].

[33] A. Tukur, "Antimony and acetaldehyde migration from Nigerian and British PET bottles into water and soft drinks under typical use conditions. Concentration of migrants and some trace elements in polyethylene terephthalate and in bottled contents," *Item Type Thesis,* University of Bradford, 2011. [Accessed: February 21, 2024].

Influence of Succinite Additives on the Crystal Structure and Orientation of Composite PA6 Nanofibers

Inga Lasenko
JLU Technologies Ltd
(of Affiliation)
Riga, Latvia
info@jlutechnologies.com

Abstract. **Give this article delves into the investigation of the crystal structure and crystalline orientation of composite polyamide 6 (PA6) nanofibers. The study aims to elucidate the impact of crystallinity and crystalline orientation on the properties of composite nanofibers, which were manufactured by the electrospinning process of Nylon 6/formic acid (HCOOH) polymer solutions at concentrations of 16%, 20% and 28%, incorporating 0.25% succinite powder with particle sizes ranging from 5 to 20 nm. The average diameters of the resulting nanofiber mats were systematically measured, revealing dimensions of 50±15 nm, 90±18 nm, and 340±78 nm, respectively. Using wide-angle X-ray diffraction (WAXD) analysis, the study provides a detailed examination of how the concentration of PA6 and the inclusion of organic succinite additives influence the crystal structure and crystalline orientation within the polymer matrix. In particular, it highlights the effects observed at smaller diameters of composite nanofibers, where enhanced macromolecular alignment is coupled with reduced crystallinity, marking the first comprehensive exploration of these phenomena in individual composite nanofibers. Research demonstrates that the relative distribution of different crystalline phases varies among samples with different average diameters. Notably, the sample with the smallest average diameter of 50 nm showcased a singular crystalline peak at 2θ=21.23°, closely aligning with the theoretically reported value for the γ phase (2θ=21.4°). On the contrary, samples with larger average diameters revealed progressively more distinct shoulders on X-ray diffraction patterns, indicative of the α phase. A notable increase of approximately 25% was observed as the diameter of the composite nanofibers decreased. Furthermore, the composite nanofibers of smaller diameter presented a narrower full width at Half Maximum (FWHM), suggesting enhanced orientation for both observed phases. This study not only contributes to understanding of the influence of nanofiber composition and structure on their physical properties but also opens new avenues for the tailored design of nanofiber based composites for advanced engineering applications.**

I. INTRODUCTION

This it is known that studies of the structural parameters (crystal structure and crystalline orientation) of the polymers allow to attribute their mechanical behavior (increased strength, modulus, and toughness) at small nanofiber diameter to improved macromolecular alignment coupled with low crystallinity [1], [2]. This combination of structural features of polymers is unusual and almost impossible to achieve in traditional manufacturing techniques. It is important to understand whether such behavior is universal in electrospinning or is dependent on the polymer/solvent system. The structural features of the polymers likely depends on the crystal structure and crystalline orientation of the polymer system, especially important if it is a composite structure (where different polymers may be included) [3], [4]. In order to examine the universality of these features and their impact on the mechanical properties, a polymer system that is more crystallizable.

To date, some attempts have been made to systematically study the influence of polymer structural parameters (crystalline structure and crystalline orientation) on nanofibers with a wide range of diameters [5]–[8], obtained as a function of varying polymer concentration [9]–[11].

For this structural analysis, PA6 was chosen. It is one of the most widely used engineering plastics due to outstanding mechanical properties such as high tensile strength. In addition, Nylon 6 fibres also exhibit high toughness, good wear, chemical resistance, and easy processing [6], [8], [12]. It was considered an ideal replacement of metal and rubber used in the fibre industry to meet enormous market requirements from military to civilian applications [7]. Nylon 6 is an easily crystallizeable polymer and offers a good test case for comparison with other polymer materials.

It is known that nylon, a man-made semi-crystalline polymer, is one of the three major polymers used in industry. Nylon can have a different ratio of mixtures of diamines ($-NH_2$) and diacids ($-COOH$) in repeated units, offering many possible tailoring for specific use. The polarity of the amide group of Nylon results in strong hydrogen bonds within the material.

The different ratio of the mixture of the two groups results in a different structure of the polymer and thus leads to different properties. Besides this, the backbone of the nylon polymer chain is symmetrically aligned, and as a result, it easily facilitates the crystalline structure that is useful for the formation of fibres. So, Nylon 6 is known to be easily produced in the form of fibre through conventional spinning and electrospinning. Nylon 6 is one type of chemical structure, where one member of the nylon consisted of six carbons in the repeated unit called Nylon 6 (or poly-(ε-caproamide)) and emerged as a new family of Nylon 6.

The organic polymer (succinite powder) was chosen as an additive, which could potentially be used as part of the polymer structure to provide ultraviolet protection (based on our previous studies). As is known, any mixing of polymers with different hardness, and, accordingly, density, is decisive importance on the mechanical properties of the resulting polymer structures (in this case is the nano fibers).

Thus, based on studies of the structural parameters of the polymer Nylon 6 (crystal structure and crystalline orientation, where combination of structural features of polymer almost impossible to achieve in traditional manufacturing techniques) follow the main task of the work - that is to study the influence of succinite additives on the crystal structure and orientation of composite PA6 nanofibers with three range of diameters obtained as a function of varying polymer concentration.

II. MATERIAL AND METHODS

To observe the influence of Nylon 6 polymer structural parameters (crystal structure and crystalline orientation) on nanofibers with three range of diameters obtained as a function of varying polymer concentration, several structural investigations were conducted. To examine the crystal structure, random mats were electrospun from 16%, 20%, and 28% Nylon 6/HCOOH polymer solutions. The average diameter was obtained for each of the mats (50±15 nm, 90±18 nm, and 340±78 nm, respectively).

Nylon 6 (PA-6) pellets (MW = 10,000, purchased from Sigma-Aldrich, Germany) and 0.25 wt/wt succinite (Baltic amber) powder (JLU Technologies Ltd, Latvia; CAS: 9000-02-6; EC: 232-520-0; 5-20 nm, d98%<20 nm) were mixed with Formic acid solution (98%, purchased from Sigma-Aldrich, Germany) to prepare 16-30 wt% solution, prepared on a hot plate for 12 hours (room temperature 22±1 °C; moisture content 60%). The diameters of the Nylon 6 composite nanofibers were controlled by electrospinning parameters such as voltage, needle gauge, and polymer solution concentration. Nylon 6 composite nanofibers were electrospun (Fisherbrand™ Single Syringe Pump, a needle-based electrospinning machine, USA) using 16.5 kV spinneret voltage from a 20 cm distance, 0.6-1 ml/h feed rate, and 22–27 gauge needle. The PA6 composite nanofibers were collected in a rotation dram

collector (Shenzhen Tongli Tech Co Ltd, (D-608) Shenzhen, China; Rotating Collector RC-5000, D140, L50). The rotating speed of the drum collector was constant at 1800 rpm and aluminium foil (width 10 cm and coating thickness 35 μm; Vireo.de Merseburg, 06217, Germany) was used on the drum to collect composite nanofibers.

The morphology of Nylon 6 composite nano mats and diameter distribution for each polymer concentration (16 wt% 20 wt%, and 28 wt%) was obtained by capture SEM photographs, Hitachi's TM300 tabletop microscope SEM with a magnification of 1500, a vacuum of 10^{-2} Torr, an ion coating with six mA, a gold (Au) cover, and a coating thickness of 150 were used. Composite nanofiber diameter was acquired using the OrientationJ plug-in for the ImageJ programme (ImageJ, National Institutes of Health, Bethesda, MD, USA). The contrast of the SEM images was enhanced to observe the results. The determination of the mean diameter of the nanofiber and standard deviation was made possible by measuring the diameter of 100 nanofibers randomly selected from three SEM images.

Composite nanofiber mats were examined by wide angle X-ray diffraction (WAXD), using 1D wide angle Diffractormeter Ragaku with Cu Kα radiation, for the 2θ range from 5 to 50°.

In this study, a protocol [13] was used to examine the crystal orientation of PA 6 nanofiber. Electrospun Nylon 6 nanofiber bundles with average diameters of 90±18 nm and 340±78 nm were used. The respective morphology of the nanofibers is shown in Fig. 6 (a; d). The diameter distribution and degree of misalignment were measured based on SEM images, using Image J software. The degree of misalignment of the nanofibers from their respective main bundle axis for the two bundles were 90°±9° (D=90±18 nm) and 87°±7° (D=340±78 nm), respectively. The examination of the crystal orientation along the fiber direction was conducted using XRD transmission mode.

WAXD experiments of the composite nanofibers (composite nanofibers D=90±18 nm; D=340±78 nm) were performed by a BL03XU beamline with a wavelength of λ = 1.0 Å at SPring-8, Harima, Japan. The sample-to-detector distance for the measurements was set to 77 mm. Two-dimensional WAXD patterns were recorded with an exposure time of 1 s using a silicon-on-insulator photon imaging array sensor (SOPHIAS) as a detector. The lattice spacing and crystal lattice parameters were calculated by following the Wulff-Bragg condition from the obtained WAXD profile. The crystallinity of composite nanofibers (Xc) was determined through profile after the total pattern from WAXD was divided into crystalline and amorphous portions [14].

III. RESULTS AND DISCUSSION

A. Crystal structure

If Nylon 6 has two main phases (α and γ). It is generally agreed that the α phase is an extended planar zigzag configuration, and it is thermodynamically stable. The γ phase is a pleated helical chain and is metastable. The parameters of the unit cell of two crystalline phases are as follows: α-crystalline phase (monoclinic cell, a = 0.956 nm, b = 1.724 nm (fibre axis), c = 0.801 nm, and β = 67.5°), and γ -crystalline phase (monoclinic cell, a = 0.933 nm b =

1.688 nm, c = 0.478 nm, and β = 121°) [15]. Fig. 1 demonstrates the molecular confirmation of these phases.
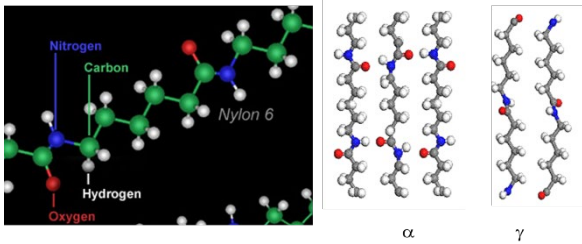
Fig. 1. The conformation of α and γ phase crystal structure of Nylon 6 [16].

In addition to α and γ phases, there are several intermediate phases. They appear when an unstable γ phase transitions into a stable α phase. Fig. 2 (a-b) shows the theoretical WAXD patterns for the two main phases.
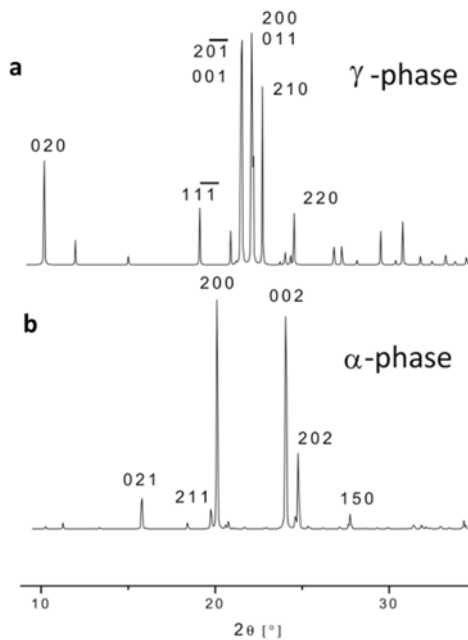
Fig. 2. The perfect theoretical crystal structures of two main crystal phases of the Nylon 6: a) the phase γ; b) the phase α [19].
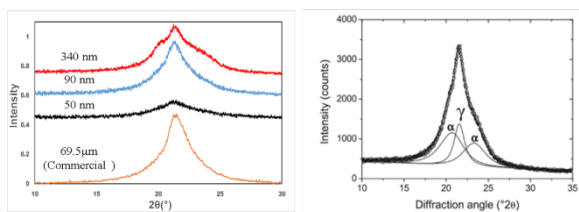
Fig. 3. XRD pattern of composite Nylon 6 fibres: a) experimental results of composite Nylon 6 nanofibers (size of average diameters 50±15 nm; 90±18 nm; 340±78 nm) with comparison of commercial microfiber: pure Nylon 6 (size of diameter 69.5±8 mkm); b) conventional spun nanofiber [17]. The diffraction lines of the individual phases (solid lines) obtained by fitting the measured intensities by three Pearson VII functions [19] and are labelled by diffraction indices. Only the line profiles corresponding to the spectral line Cu Kα are shown

As can be seen in the left panel of Fig. 3, the electrospun composite nanofibers exhibited a generally poor structure with wide overlapping peaks. Similarly to commercial fibre, this pattern corresponds to a mix of the α and γ

phases. The observed XRD pattern for electrospun nylon NFs is similar to patterns obtained from electrospun Nylon 6 nanofiber mats in the literature [9], [17]. The patterns in the literature [9], [18]are especially similar to our pattern for a mat with an average diameter of 340 nm.

The dominant feature in the XRD pattern is the peak that corresponds to the γ phase. Peaks corresponding to the α phase appear as shoulders in the pattern. It is reported that there are usually two characteristic peaks of the α-phase located at 2θ=20° and 23.7° in the XRD diffraction pattern of Nylon 6, corresponding respectively to (200) and (002)/(202) crystal planes [20]. The γ phase reflected peaks at around 2θ=10.7° and 21.4° corresponding to (020) and (001) crystal planes [21]–[23]. Zhudi Zhao and his coauthor studied crystalline and amorphous phases of the quenched Nylon 6 film and found a broad amorphous halo located at 2θ=21° [24]. It is clear that the relative mix of the different phases changed between samples with different average diameters.

The sample with an average diameter of 50 nm exhibited only one crystalline peak located at 2θ =21.23°, close to theoretical reported value for the γ phase (2θ= 21.4°) [17]. The samples with larger average diameters exhibited progressively more pronounced shoulders corresponding to the α phase.

The different crystal and amorphous peaks were deconvoluted using spacing diameters from the literature. Crystallinity was extracted from the XRD patterns after deconvolution, using a protocol similar to reference [25] (an example in Fig. 4 a-b). Crystallinity as a function of the average diameter of the composite nanofiber diameter (50±15 nm; 90±18 nm; 340±78 nm) is shown in Fig. 4-c.

The ~ 25% increase in composite polymer crystallinity was observed with the decrease in composite nanofiber diameter.

Fig. 4. The conformation of α and γ phase crystal structure of Nylon 6 [17]. a) XRD pattern of composite nanofiber with average diameter of 340±78 nm; b) peak fit of (a); (c) crystallinity of electrospun composite Nylon 6 nanofibers with three different diameters.

This result is consistent with DSC experiments carried out by collaborators at the University of Rouen Normandie, CNRS, and Groupe de Physique des Materiaux, France (Fig. 5) and can explain the slight decrease in strain-to-failure for thinner nanofibers. For example, compared with other mostly used polyacrylonitrile (PAN), behavior of PA 6 is different from that of PAN [26], where decrease in crystallinity was observed for smaller diameters.
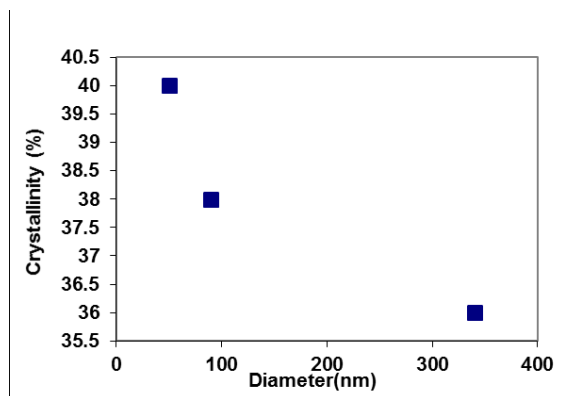
Fig. 5. Crystallinity as a function of composite nanofiber diameters (provided by University of Rouen Normandie, CNRS, and Groupe de Physique des Materiaux, France).

In electrospinning, fast solvent evaporation plays a role similar to fast quenching in traditional polymer manufacturing from melts. This fast process promotes nucleation of phases that are not in thermodynamic equilibrium (such as γ phase in Nylon 6) and is likely to be faster in thinner nanofibers. This can explain why larger diameter nanofibers exhibit a larger amount of the α phase. The differences in the size-dependent crystallinity behaviour between, for example, with PAN [27], and Nylon 6 nanofibers can be explained by the different crystallinities of these two polymer systems. The observed structural differences are also consistent with the differences observed in nanofiber strain-to-failure.

In addition, the electrospun Nylon 6 composite nanofibers showed a lower crystallinity than the conventional Nylon 6 microfibers [28]. This supports the hypothesis that even in a crystallisable polymer such as Nylon 6, the rapid solvent evaporation holds back the crystallisation process.

The crystal sizes for the different phases were extracted from the XRD patterns, using the Scherrer' equation (similar to Protocol [29]), shown in Table 1. The results showed that the crystal size of the crystal phases did not change significantly and remained well below nanofiber diameter. This indicates that crystal size did not play a significant role in the determination of mechanical properties.

TABLE 1 CRYSTAL SIZE OF EACH CRYSTAL PHASE FOR WELL-ALIGNED COMPOSITE NANOFIBERS WITH AVERAGE DIAMETERS OF 50, 90 AND 340 NM.

Nm	Coherence length (nm)	Nanofiber # 1 (D = 50±15 nm)	Nanofiber # 2 (D = 90±18 nm)	Nanofiber # 3 (D = 340±78 nm)
1	α_1	2.97	4.04	4.29
2	γ	4.23	4.03	4.62
3	α_2	3.93	3.84	2.07

B. Crystal orientation

Define WAXD experiments of composite PA6 nanofibers (composite nanofibers D=90±18 nm; D=340±78 nm) were performed (a similar protocol for crystal orientation research shown in [30]).

Electrospun composite Nylon 6 nanofiber bundles with average diameters of 90 and 340 nm were produced. The respective morphology of the composite Nylon 6 nanofibers was as shown in Fig. 6 a-d. The diameter distribution and the degree of misalignment were measured based on SEM images, using ImageJ software [31]. Homogeneous composite nanofibers with uniformly distributed succinite particles are observed. The degree of misalignment of the nanofibers from their respective main bundle axis for the two bundles was ±9° and ±7°, respectively (see the distribution of the orientation of the composite nanofibers in Fig. 6 b-e). The examination of the crystal orientation along the direction of the composite nanofiber was conducted using XRD transmission mode. WAXD 2D (two-dimensional) patterns of two bundles are shown in Fig. 6 (c-f).
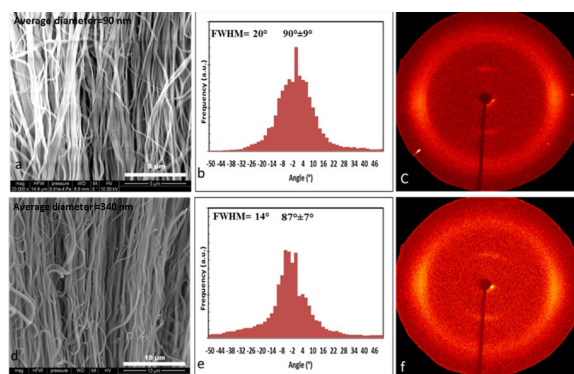
Fig. 6. The Comparison of the orientation of Nylon 6 nanofibers: a) morphology of aligned nanofiber bundles with average diameter of 90 nm; d) morphology of aligned nanofibers bundles with an average diameter of 340 nm; b) nanofibers orientation D=90±18 nm: along nanofiber direction; e) nanofibers orientation D=340±78 nm: of along nanofiber direction; c) WAXD 2D patterns of composite nanofiber D=90±18 nm; f) WAXD 2D patterns of composite nanofiber D=340±78 nm.

The extent of the double arcs in the diffraction pattern was used as an indicator of crystal orientation. The 2D pattern was converted into an azimuthal intensity scan, corresponding to the arcs from different crystal phases (Fig. 7 b-d; Fig. 8 b-d).
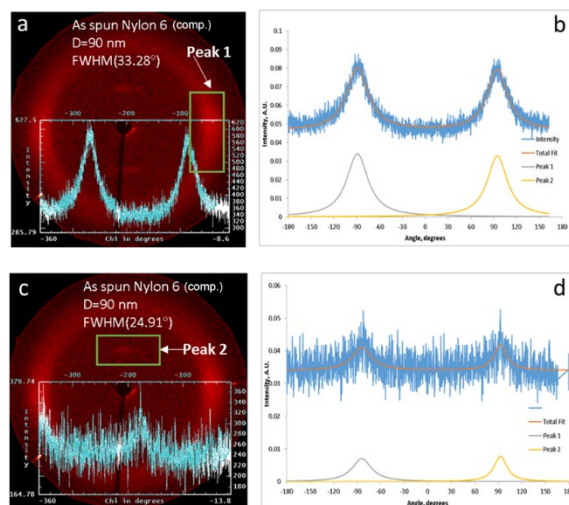
Fig. 7. The Crystal orientation in well-aligned composite nanofibers with diameter of 90±18 nm; a-c: WAXD patterns exhibited two main peaks: peak 1 (FWHM 33.28°) and peak 2 (FWHM 24.91°); b-d: 2 D pattern converted into an azimuthal intensity scan, corresponding to arcs from different crystal phases.

The WAXD patterns exhibited two main peaks. Peak 1 and peak 2 were labelled in Fig's: 7 (a-c) and 8 (a-c). Peak 1 corresponded to the γ phase, while peak 2 corresponded to a mixture of γ and α phases ((001) plane in the γ phase and (200) and (002)/(202) planes in the α phase). Peak 1 indicated that the crystalline plane (020) was parallel to the fibre direction. Peak 2 indicated that the mixture of crystal planes was perpendicular to the fibre axis. Full width at Half Maximum (FWHM) of the peaks in the azimuthal scan was used as an indicator of crystal orientation. Table 2 summarises the orientation parameters for the different phases.

TABLE 2 CRYSTAL ORIENTATION PARAMETERS OF ALIGNED COMPOSITE NANOFIBERS WITH AN AVERAGE DIAMETER OF 90 AND 340 NM.

Nm	Average Diameter (nm)	FWHM (°) - Mixture of α and γ phase	FWHM (°) - γ phase
1	90	33.3	24.9
2	340	37.9	50
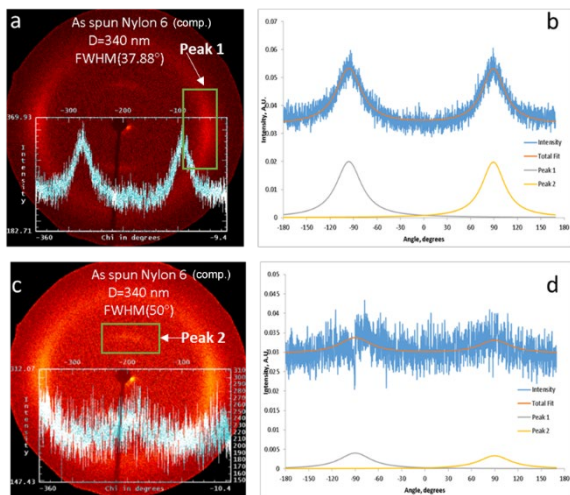
Fig. 8. The Crystal orientation in well-aligned composite nanofibers with an average diameter of 340±78 nm; a c: the WAXD patterns exhibited two main peaks: peak 1 (FWHM 37.88°) and peak 2 (FWHM 50°); b-d: the 2 D pattern converted into an azimuthal intensity scan, corresponding to the arcs from different crystal phases.

Composite nanofibers with smaller diameters exhibited narrower full width at Half Maximum (FWHM) indicating better orientation, for both phases. Higher crystallinity and better crystal alignment in thinner nanofibers can explain the improvements in strength and modulus for these nanofibers.

This study not only contributes to understanding of the influence of nanofiber composition and structure on their physical properties but also opens new avenues for the tailored design of nanofiber based composites for advanced engineering applications [32]–[41], included an innovative recycled technologies of these materials [42]–[44]; because the modern industrial development has a high demand for new materials – with unique properties, combinations, and functionality [45]–[51].

IV. CONCLUSION

A study of the influence of the Nylon 6 structural characteristics of the composite polymer structure showed that the average diameter of the nanofiber depends on the concentration of the polymer in combination with 0.25% succinite, namely at a concentration of 16% the average diameter of the nanofiber is 50 nm; at 20% - 90 nm; at 28% - 340 nm. This is consistent with the reference literature, where a similar pattern (as the polymer concentration decreases, the average nanofiber diameter during electrospinning increases) was observed for pure polymer compositions (for example, PA6; PAN).

It was shown that the relative mix of the different phases changed between samples with different average diameters. The sample with an average diameter of 50 nm exhibited only one crystalline peak located at 2θ=21.23°, close to theoretical reported value for the γ phase (2θ=21.4°). The samples with larger average diameters exhibited progressively more pronounced shoulders corresponding to the α phase. The ~ 25% increase in composite polymer crystallinity was observed with the decrease in composite nanofiber diameter.
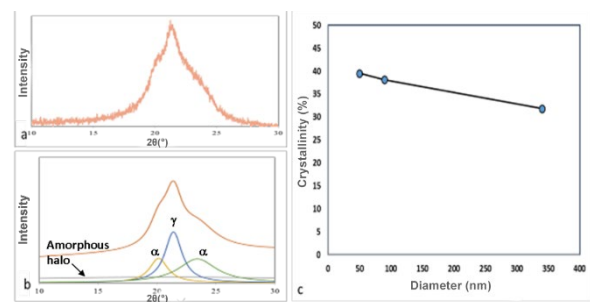
Electrospun Nylon 6 composite nanofibers showed a lower crystallinity than conventional Nylon 6 fibres. This supports the hypothesis that even in a crystallisable polymer such as Nylon 6, the rapid solvent evaporation holds back the crystallisation process.

Composite nanofibers with smaller diameter exhibited a narrower full width at Half Maximum (FWHM) indicating better orientation for both phases. Higher crystallinity and better crystal alignment in thinner nanofibers can explain the improvements in strength and modulus for these nanofibers.

REFERENCES

[1] M. Naraghi, S. N. Arshad, and I. Chasiotis, "Molecular orientation and mechanical property size effects in electrospun polyacrylonitrile nanofibers," *Polymer (Guildf).*, vol. 52, no. 7, pp. 1612–1618, 2011, doi: 10.1016/j.polymer.2011.02.013.

[2] D. Tian, C. H. He, and J. H. He, "Macromolecule orientation in nanofibers," *Nanomaterials*, vol. 8, no. 11, 2018, doi: 10.3390/nano8110918.

[3] L. S. Loo and K. K. Gleason, "Insights into structure and mechanical behavior of α and γ crystal forms of nylon-6 at low strain by infrared studies," *Macromolecules*, vol. 36, no. 16, pp. 6114–6126, 2003, doi: 10.1021/ma034213v.

[4] H. S. SalehHudin, E. N. Mohamad, W. N. L. Mahadi, and A. Muhammad Afifi, "Multiple-jet electrospinning methods for nanofiber processing: A review," *Mater. Manuf. Process.*, vol. 33, no. 5, pp. 479–498, 2018, doi: 10.1080/10426914.2017.1388523.

[5] M. B. Bazbouz and G. K. Stylios, "The tensile properties of electrospun nylon 6 single nanofibers," *J. Polym. Sci. Part B Polym. Phys.*, vol. 48, no. 15, pp. 1719–1731, 2010, doi: 10.1002/polb.21993.

[6] K. Y. Hwang, S. D. Kim, Y. W. Kim, and W. R. Yu, "Mechanical characterization of nanofibers using a nanomanipulator and atomic force microscope cantilever in a scanning electron microscope," *Polym. Test.*, vol. 29, no. 3, pp. 375–380, 2010, doi: 10.1016/j.polymertesting.2010.01.002.

[7] H. Mahfuz *et al.*, "Enhancement of strength and stiffness of Nylon 6 filaments through carbon nanotubes reinforcement," *Appl. Phys. Lett.*, vol. 88, no. 8, 2006, doi: 10.1063/1.2179132.

[8] L. Li, L. M. Bellan, H. G. Craighead, and M. W. Frey, "Formation and properties of nylon-6 and nylon-6/montmorillonite composite nanofibers," *Polymer (Guildf).*, vol. 47, no. 17, pp. 6208–6217, 2006, doi: 10.1016/j.polymer.2006.06.049.

[9] N. Kimura, B. S. Kim, and I. S. Kim, "Effects of Fe2+ ions on morphologies, microstructures and mechanical properties of electrospun nylon-6 nanofibers," *Polym. Int.*, vol. 63, no. 2, pp. 266–272, 2014, doi: 10.1002/pi.4500.

[10] H. Mahfuz *et al.*, "Reinforcement of nylon 6 with functionalized silica nanoparticles for enhanced tensile strength and modulus," *Nanotechnology*, vol. 19, no. 44, 2008, doi: 10.1088/0957-4484/19/44/445702.

[11] O. Faruk, A. K. Bledzki, H. P. Fink, and M. Sain, "Biocomposites reinforced with natural fibers: 2000-2010," *Prog. Polym. Sci.*, vol. 37, no. 11, pp. 1552–1596, 2012, doi: 10.1016/j.progpolymsci.2012.04.003.

[12] S. Sinha-Ray *et al.*, "Supersonic nanoblowing: A new ultra-stiff phase of nylon 6 in 20-50 nm confinement," *J. Mater. Chem. C*, vol. 1, no. 21, pp. 3491–3498, 2013, doi: 10.1039/c3tc30248b.

[13] Z. Yang, W. Takarada, and H. Matsumoto, "Effect of the Fiber Diameter of Polyamide 11 Nanofibers on Their Internal Molecular Orientation and Properties.," *Macromol. Rapid Commun.*, vol. 44, no. 18, p. e2300212, Sep. 2023, doi: 10.1002/marc.202300212.

[14] M. V. Kakade, S. Givens, K. Gardner, K. H. Lee, D. B. Chase, and J. F. Rabolt, "Electric field induced orientation of polymer chains in macroscopically aligned electrospun polymer nanofibers," *J. Am. Chem. Soc.*, vol. 129, no. 10, pp. 2777–2782, 2007, doi: 10.1021/ja065043f.

[15] H. M. Heuvel, R. Huisman, and K. C. J. B. Lind, "Quantitative Information From X-Ray Diffraction of Nylon-6 Yarns - 1. Development of a Model for the Analytical Description of Equatorial X-Ray Profiles.," *J Polym Sci Part A-2 Polym Phys*, vol. 14, no. 5, pp. 921–940, 1976.

[16] S. S. Nair, C. Ramesh, and K. Tashiro, "Crystalline phases in nylon-11: Studies using HTWAXS and HTFTIR," *Macromolecules*, vol. 39, no. 8, pp. 2841–2848, 2006, doi: 10.1021/ma052597e.

[17] P. Čapková *et al.*, "Phase composition and surface properties of nylon-6 nanofibers prepared by nanospider technology at various electrode distances," *J. Polym. Res.*, vol. 22, no. 6, 2015, doi: 10.1007/s10965-015-0741-3.

[18] T. M. Ting, M. M. Nasef, and K. Hashim, "Tuning N-methyl-d-glucamine density in a new radiation grafted poly(vinyl benzyl chloride)/nylon-6 fibrous boron-selective adsorbent using the response surface method," *RSC Adv.*, vol. 5, no. 47, pp. 37869–37880, 2015, doi: 10.1039/c5ra00427f.

[19] M. M. Hall, V. G. Veeraraghavan, H. Rubin, and P. G. Winchell, "The approximation of symmetric X-ray peaks by Pearson type VII distributions," *J. Appl. Crystallogr.*, vol. 10, no. 1, pp. 66–68, 1977, doi: 10.1107/s0021889877012849.

[20] S. M. Aharoni, *n-Nylons : their synthesis, structure, and properties*. Chichester : Wiley, 1997. [Online]. Available: http://lib.ugent.be/catalog/rug01:000394343

[21] J. C. Ho and K. H. Wei, "Induced γ → α crystal transformation in blends of polyamide 6 and liquid crystalline copolyester," *Macromolecules*, vol. 33, no. 14, pp. 5181–5186, 2000, doi: 10.1021/ma991702f.

[22] J. M. Schultz, B. S. Hsiao, and J. M. Samon, "Structural development during the early stages of polymer melt spinning by in-situ synchrotron X-ray techniques," *Polymer (Guildf).*, vol. 41, no. 25, pp. 8887–8895, 2000, doi: 10.1016/S0032-3861(00)00232-9.

[23] C. Ramesh and E. Bhoje Gowd, "High-temperature X-ray diffraction studies on the crystalline transitions in the α- and γ-forms of nylon-6," *Macromolecules*, vol. 34, no. 10, pp. 3308–3313, 2001, doi: 10.1021/ma0006979.

[24] Z. Zhao, W. Zheng, H. Tian, W. Yu, D. Han, and B. Li, "Crystallization behaviors of secondarily quenched Nylon 6," *Mater. Lett.*, vol. 61, no. 3, pp. 925–928, 2007, doi: 10.1016/j.matlet.2006.06.014.

[25] J. Ge *et al.*, "[Investigation of thermal behaviors of γ-form nylon 6 prepared by ammonia vapor from phosphoric acid solutions].," *Guang Pu Xue Yu Guang Pu Fen Xi*, vol. 32, no. 1, pp. 118–122, Jan. 2012.

[26] C. Feng, K. C. Khulbe, T. Matsuura, S. Tabe, and A. F. Ismail, "Preparation and characterization of electro-spun nanofiber membranes and their possible applications in water treatment," *Sep. Purif. Technol.*, vol. 102, pp. 118–135, 2013, doi: 10.1016/j.seppur.2012.09.037.

[27] J. Xue, T. Wu, Y. Dai, and Y. Xia, "Electrospinning and electrospun nanofibers: Methods, materials, and applications," *Chem. Rev.*, vol. 119, no. 8, pp. 5298–5415, 2019, doi: 10.1021/acs.chemrev.8b00593.

[28] C. V. Pious and S. Thomas, "Polymeric Materials-Structure, Properties, and Applications," *Print. Polym. Fundam. Appl.*, pp. 21–39, 2015, doi: 10.1016/B978-0-323-37468-2.00002-6.

[29] C. O. Mosiori, "Combustion synthesis and characterization of dysprosium nano-composite melilite," *Memories - Mater. Devices, Circuits Syst.*, vol. 4, no. March, p. 100042, 2023, doi: 10.1016/j.memori.2023.100042.

[30] D. Marlina, H. Hoshina, Y. Ozaki, and H. Sato, "Crystallization and crystalline dynamics of poly(3-hydroxybutyrate) / poly(4-vinylphenol) polymer blends studied by low-frequency vibrational spectroscopy," *Polymer (Guildf).*, vol. 181, no. August, p. 121790, 2019, doi: 10.1016/j.polymer.2019.121790.

[31] Z. Püspöki, M. Storath, D. Sage, and M. Unser, "Transforms and operators for directional bioimage analysis: A survey," *Adv. Anat. Embryol. Cell Biol.*, vol. 219, pp. 69–93, 2016, doi: 10.1007/978-3-319-28549-8_3.

[32] I. Lasenko, D. Grauda, D. Butkauskas, J. V. Sanchaniya, A. Viluma-Gudmona, and V. Lusis, "Testing the Physical and Mechanical Properties of Polyacrylonitrile Nanofibers Reinforced with Succinite and Silicon Dioxide Nanoparticles," *Textiles*, vol. 2, no. 1, pp. 162–173, 2022, doi: 10.3390/textiles2010009.

[33] A. Viluma-Gudmona, I. Lasenko, J. V. Sanchaniya, and B. Abdelhadi, "The amber nano fibers development prospects to expand the capabilites of textile 3D printing in the general process of fabrication methods," *Eng. Rural Dev.*, vol. 20, pp. 248–257, 2021, doi: 10.22616/ERDev.2021.20.TF051.

[34] D. Grauda, L. Bumbure, I. Lyashenko, A. Katashev, Y. Dekhtyar, and I. Rashal, "Amber particles as living plant cell markers in flow cytometry," *Proc. Latv. Acad. Sci. Sect. B Nat. Exact, Appl. Sci.*, vol. 69, no. 3, pp. 77–81, 2015, doi: 10.1515/prolas-2015-0011.

[35] A. Viluma-Gudmona, I. Lasenko, J. V. Sanchaniya, and A. Podgornovs, "Electro-resistant biotextile development based on fiber reinforcement with nano particles," *Eng. Rural Dev.*, vol. 20, pp. 804–812, 2021, doi: 10.22616/ERDev.2021.20.TF182.

[36] I. Lasenko *et al.*, "The Mechanical Properties of Nanocomposites Reinforced with PA6 Electrospun Nanofibers," *Polymers (Basel).*, vol. 15, no. 3, 2023, doi: 10.3390/polym15030673.

[37] V. Lusis *et al.*, "Experimental Study and Modelling on the Structural Response of Fiber Reinforced Concrete Beams," *Appl. Sci.*, vol. 12, no. 19, p. 9492, Sep. 2022, doi: 10.3390/app12199492.

[38] S. Gaidukovs, I. Lyashenko, J. Rombovska, and G. Gaidukova, "Application of amber filler for production of novel polyamide composite fiber," *Text. Res. J.*, vol. 86, no. 20, pp. 2127–2139, 2016, doi: 10.1177/0040517515621130.

[39] J. V. Sanchaniya, I. Lasenko, S. P. Kanukuntla, A. Mannodi, A. Viluma-Gudmona, and V. Gobins, "Preparation and Characterization of Non-Crimping Laminated Textile Composites Reinforced with Electrospun Nanofibers," *Nanomaterials*, vol. 13, no. 13, 2023, doi: 10.3390/nano13131949.

[40] J. V. Sanchaniya *et al.*, "Mechanical and Thermal Characterization of Annealed Oriented PAN Nanofibers," *Polymers (Basel).*, vol. 15, no. 15, 2023, doi: 10.3390/polym15153287.

[41] D. Grauda *et al.*, "Establishment of Biotesting System to Study Features of Innovative Multifunctional Biotextile," *Proc. Latv. Acad. Sci. Sect. B Nat. Exact, Appl. Sci.*, vol. 77, no. 3–4, pp. 186–192, 2023, doi: 10.2478/prolas-2023-0026.

[42] A. Hussain, V. Podgursky, D. Goljandin, M. Antonov, F. Sergejev, and I. Krasnou, "Circular Production, Designing, and Mechanical Testing of Polypropylene-Based Reinforced Composite Materials: Statistical Analysis for Potential Automotive and Nuclear Applications," *Polymers (Basel).*, vol. 15, no. 16, 2023, doi: 10.3390/polym15163410.

[43] A. Hussain, V. Podgursky, M. Viljus, and M. R. Awan, "The role of paradigms and technical strategies for implementation of the

circular economy in the polymer and composite recycling industries," *Adv. Ind. Eng. Polym. Res.*, vol. 6, no. 1, pp. 1–12, 2023, doi: 10.1016/j.aiepr.2022.10.001.

[44] A. Hussain, D. Goljandin, V. Podgursky, M. M. Abbas, and I. Krasnou, "Experimental mechanics analysis of recycled polypropylene-cotton composites for commercial applications," *Adv. Ind. Eng. Polym. Res.*, vol. 6, no. 3, pp. 226–238, 2023, doi: 10.1016/j.aiepr.2022.11.001.

[45] A. Asar and W. Zaki, "A comprehensive review of the mechanisms and structure of interpenetrating phase composites with emphasis on metal-metal and polymer-metal variants," *Compos. Part B*, vol. 275, no. October 2023, p. 111314, 2024, doi: 10.1016/j.compositesb.2024.111314.

[46] S. A. Kareem, J. U. Anaele, E. O. Aikulola, T. A. Adewole, M. O. Bodunrin, and K. K. Alaneme, "Design and selection of metal matrix composites reinforced with high entropy alloys – Functionality appraisal and applicability in service: A critical review," *J. Alloy. Metall. Syst.*, vol. 5, no. January, p. 100057, 2024, doi: 10.1016/j.jalmes.2024.100057.

[47] A. Shishkin, I. Hussainova, V. Kozlov, M. Lisnanskis, P. Leroy, and D. Lehmhus, "Metal-Coated Cenospheres Obtained via Magnetron Sputter Coating: A New Precursor for Syntactic Foams," *Jom*, vol. 70, no. 7, pp. 1319–1325, 2018, doi: 10.1007/s11837-018-2886-0.

[48] A. Shishkin *et al.*, "Cavitation-dispersion method for copper cementation from wastewater by iron powder," *Metals (Basel).*, vol. 8, no. 11, pp. 4–6, 2018, doi: 10.3390/met8110920.

[49] P. Colombo, "Cellular ceramics with hierarchical porosity from preceramic polymers," *IOP Conf. Ser. Mater. Sci. Eng.*, vol. 18, no. SPEC. SYMPOSIUM, 2011, doi: 10.1088/1757-899X/18/1/012002.

[50] V. Mironovs *et al.*, "Cellular structures from perforated metallic tape and its application for electromagnetic shielding solutions," *Agron. Res.*, vol. 12, p. (in Print), Jan. 2014.

[51] M. Pelanconi, D. Koch, G. Bianchi, S. Bottacin, and P. Colombo, "High-strength Si – SiC lattices prepared by powder bed fusion , infiltration-pyrolysis , and reactive silicon infiltration," no. December 2023, pp. 1–15, 2024, doi: 10.1111/jace.19750.

Thermal and Structural Properties of Succinite Reinforced PA6 Nanofibers

Inga Lasenko
JLU Technologies Ltd
(of Affiliation)
Riga, Latvia
info@jlutechnologies.com

Abstract. **Give This research article delves into the thermal stability of succinite -an organic polymer- when amalgamated within the structure of PA6 nanofibers, with a focus on assessing the consequent mechanical and structural performance of such composite nanofibers. The electrospinning method employed, involves the process of heating and high voltage to polymers, is known to inherently alter their thermal properties. The primary objective of this study is to examine the thermal stability of succinite within the PA6 nanofiber matrix and to evaluate the preservation of the composite material's mechanical and structural integrity, particularly under varying PA6 concentrations (16%, 20%, and 28%). Through thermal analysis techniques such as Differential Scanning Calorimetry (DSC), Thermogravimetric Analysis (TGA), and Infrared (IR) spectroscopy, it was observed that the succinite nano powder (ranging from 5-20 nm) exhibits minimal loss of volatile components, notably the NH amino group, upon heating to 150 ºC—a common solvent temperature during suspension preparation. This loss does not surpass 0.1% of the original volume, ensuring the predominance of critical components like succinite acid ($C_4H_6O_4$) in the composite. Furthermore, PA6 nanofibers were fabricated with varying PA6 polymer percentages (16%, 20%, and 28%) and with or without the integration of succinite nano powder, to compare mechanical properties. It was noted that incorporating succinite into PA6 nanofibers (at 16% concentration) led to an increase in fibre diameter to 78±14 nm from the 60±17 nm diameter of pure PA6 fibres, alongside a notable decrease in elastic modulus by approximately 2.3 times. However, the ultimate tensile strength only marginally reduced from 295.2 MPa to 274.9 MPa, with a slight decrease in toughness from 168.3 to 162 MPa. Contrary to pure PA6 fibres, the strain-to-failure ratio for the composite nanofibers saw an approximate 7% increase. This study elucidates the subtle yet significant modifications in the mechanical and structural properties of polymer composites attributable to their thermal stability. These findings furnish vital insights for the application of such composite materials in diverse thermal management contexts, particularly when utilised as protective materials.**

Keywords: PA6 (Polyamide 6), Nanofibers, Electrospinning, thermal analysis, Nylon 6.

I. INTRODUCTION

This Over the years, there has been a dramatic increase in the manufacturing of composite nanomaterials (based on the electrospinning process) for many applications such as aerospace, automobile, electronic packaging, food packaging, medical, etc., included an innovative recycled technologies of these materials [1], [2], [11]–[15], [3]–[10]. To overcome existing limitations in new material design, scientists paying attention to new approaches [16]–[19] , ways of 3D printing [20]–[22], material combinations [23]–[25] and nanoparticle use in a newly studied class of composites a syntactic foam [26]. Using organic, inorganic, and their combinations fillers has become widespread in polymeric systems [27], [28] . The purpose of adding synthetic or natural inorganic fillers to the polymer matrix is to improve composite properties and subsequently reduce production costs [29]. Furthermore, the presence of nanoparticles that act as reinforcement fillers can affect changes in the polymer matrix in terms of flowability, viscosity, colour, density, and subsequently also tends to improve the optical, electrical, catalytic, magnetic, mechanical, and thermal properties of the composite nanomaterials [30].

The last indicator is very important for determining the thermal characteristics of the polymer structure, which has a decisive impact on the mechanical parameters of the composite polymer as a whole.

Assessing the most widely used polymers (as a material with protective properties), it is necessary to note PA6 [31], on which we focus in this work. As fillers (to obtain a composite polymer), a natural organic polymer is used - succinite, the protective effects of which (mainly is UV protection in an absorbance peak (0.75) at wavelength 244 nm) are quite well covered in scientific publications. Furthermore, succinite is a biologically active element, and the smaller particle size (diam.<20 nm), the higher the activity of succinite, due to the presence of pure succinic acid and succinic acid salts in its structure [32].

The structure of polyamide 6 reinforced with succinite is known, but not enough is described in scientific works.

The difficulty in analyzing the structure of a nanomaterial with succinite inclusions lies that the succinite particles are very heterogeneous and have a size of up to 1-3 microns, besides, in most cases described, the succinite particles are entangled in nanofibers and are not part of their structure [33].

In this study, a new PA6 composite nanofibres with integrated succinite particles in their structure were received and studied. For this purpose, we used specially processed amber powder obtained by fine grinding protocols [34], particle size 5-20 nm (obtained from the company JLU Technologies, Riga, Latvia). Using finely ground succinite powder, by electrospinning process homogeneous composite nanofibers were obtained, and this method has proven itself well, which made it possible to carry out all the necessary tests in full.

It is well-known that the thermal properties of the succinite material come from its structure and polymer composition. The main structural elements of succinite are compounds of aromatic and hydroaromatic sequences with condensed nuclei consisting of conjugated double bonds of carboxylic, hydroxyl, and ester groups. Succinite is essentially characterised by a three-dimensional structure with a rare lacing destroyed by heating and the mechanical effect due to the cleavage of chemical bonds, which implies the formation of free radicals.

Therefore, the composite nanomaterial (under mechanical and thermal treatment in the time of its processing) should retain all its mechanical and structural (biological) properties. To achieve this, the thermal properties of succinite (Baltic Amber) must be researched.

The aim of this article is to study the thermal stability of succinite (organic polymer) that is integrated into the PA6 nanofiber structure, and with this, it is necessary to estimate how the composite polymer materials (with variation of PA6 concentration of 16%, 20%, and 28%) retain its mechanical and structural (biological) properties.

II. MATERIAL AND METHODOLOGY

This study meticulously examined the thermal characteristics of succinite particles in electrospun PA6 nanofibers. For a more detailed comparative thermal study, the succinite particles were studied separately (Amber Raw and Amber Raw Powder were examined). And the second part of the work was estimated how the composite polymer materials (with variation of PA6 16%, 20%, and 28% concentration) retain their mechanical and structural (biological) properties. The composite nanofibres were produced (by electrospinning method) like described in our previous work [8].

This new composite nanomaterial consists of a polymer matrix, which is Polyamide 6 (NYLON 6), type RADIPOL S100-004® with a low molecular content of 0.9% and a melting temperature of 220 °C, received from Sigma-Aldrich AB, Germany. The fillers are succinite powder (CAS: 9000-02-6; EC: 232-520-0) with a particle size (5-20 nm, d98%<20 nm), the source (Baltic amber) contains about 8÷12% succinic acid, received from JLU Technologies Ltd, Riga, Latvia.

To illustrate the difference of thermal parameters between the Amber Raw Powder (5-20 nm) and Amber Raw (<5 mm), were conducted their comparative thermal analysis.

Thermal analysis include:

a) Thermogravimetric analysis (TGA) (testing according to ISO 11358) is a thermal analysis technique which consists of measuring the variation in mass of sample as a function of time, for a given temperature or temperature profile.

Thermogravimetric tests of the succinite samples were performed on a NETZSCH TG 209 F1 Iris instrument (Germany). The sample mass is 17.0963 mg (Amber Raw, not treated), 6.3284 mg (Amber Raw Powder) were heated in nitrogen at 450 °C. The thermal stability of the succinite material was evaluated from the weight loss heating curves. The thermal degradation temperature was calculated using the original NETZSCH PROTEUS software.

b) Differential scanning calorimetry (DSC) is a thermal analysis technique. Measures the differences in heat exchange between samples to be analysed and referenced.

The DSC tests (testing according to ISO 11357) of the succinite samples were performed on a NETZSCH differential scanning calorimetry (DSC) 204 F1 Phoenix instrument (Germany). The sample mass is 19.8808 mg (Amber Raw, particles ø <5 mm), 4.1922 mg (Amber Raw Powder, ø <20 nm) by weight, using nitrogen as the purge gas with a flow rate of 20 ml/min in the temperature range of 25 to 450 °C. The heating was operated at a rate of 20 °C/10 min. The glass transition temperature T_g was calculated from the experimental heating curve.

Fourier transform infrared spectroscopy (FTIR, testing according to ISO 19702:2015(En)) is a common method for determining the chemical composition of succinite. The FTIR spectra were recorded on a Varian Scimitar 800 FT-IR spectrometer (Germany).

To perform a comparative analysis of the chemical composition, succinite samples were studied without thermal pretreatment and after heating, as indicated in Table 1.

TABLE 1 CRYSTAL SIZE OF EACH CRYSTAL PHASE FOR WELL-ALIGNED COMPOSITE NANOFIBERS WITH AVERAGE DIAMETERS OF 50, 90 AND 340 NM.

No. of sample	Type of Baltic Amber	Condition of preparation
1	succinite	Without preheating, standard;
2	succinite	Heated to 150.0 ºC in the drying chamber; the chamber was vacuumed to 10^{-1} mmHg.

The samples were preheated using the Memmert UFB 500 universal drying oven (Germany); range 30-250 ºC; exactitude: for the chosen temperature 0.5 °C, for the factual temperature – 0.1 ºC (<99.9 ºC) and 0.5 ºC (>100 ºC) – for the keeping of samples at the temperature of 150 °C, continue 10 min.

The test material was succinite (Amber Raw Powder), the weight of the sample was 3.8 mg. For weighing of samples, analytical balance KERN PCB M was used (KERN&Sohn GmbH; D-72336, Balingen, Germany;

accuracy class: II high, max up to 200 g, discreteness 0.01 g; calibration certificate number: M0901K23, 15.06.2023).

To obtain a succinite tablet, succinite was initially reduced for 15 minutes to a fine particle in the Retsch® MM200 ball mill (powerful impact and friction, up to 25 Hz) (Retsch GmbH, 42781 Haan, Rheinische Str.36, Germany), after which the raw Amber Raw Powder was mixed with 361 mg of KBr powder. The tablet was obtained by pressing the mixture of succinite powders and KBr (CAS No. 7758-02-3) (received from Sigma-Aldrich chemicals, Merck KGaA, Darmstadt, (64287) Germany), which was placed on the spectrometer. The measurement range was 400-4000 cm^1 and an accuracy of ±4 cm^{-1} using KBr as beam splitter.

III. Results and discussion

In order to study the properties of succinite, thermal analysis methods were applied. These methods are applied to the search for chemical reactions, phase, and other physic-chemical transformations occurring under the influence of heat in chemical compounds. Thermal processes are accompanied by an alteration of internal heat-endothermic and exothermic transformations. These thermal effects can be discovered using thermogravimetric analysis (TGA) and differential scanning calorimetry (DSC) methods, which determine the quantitative heating effects occurring in the sample material.

A. Thermogravimetric analysis (TGA)

The curve shows (Fig.1) the thermal decomposition of Amber Raw (before grinding), according to the TGA curve, noting that the thermal decomposition of the succinite takes place in two stages: the first decomposition at an onset temperature (382.3 °C) with a mass loss of 23.5% and the second decomposition at an infection temperature (384.8 °C) linked to a chemical reaction which leads to a mass loss of 15.17%.

In this thermal analysis, a mass loss of 38.67% was recorded for the Amber Raw in a temperature range between 25 °C and 400 °C.
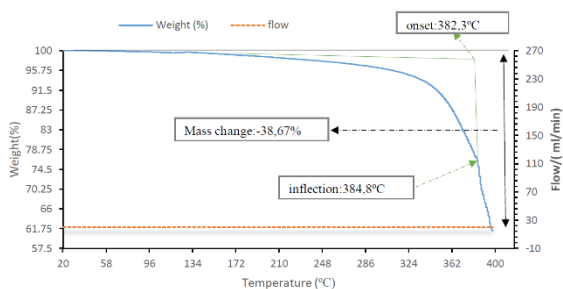
Fig. 1. TGA thermogram of Amber Raw (mass (%) as a function of temperature (ºC)).

Fig. 2 presents the TGA curve of Amber Raw Powder (after grinding); according to this curve, a mass loss of 100% has been recorded for Amber Raw Powder with an onset temperature of 417.9 °C and an inflection temperature of 420.4 °C after 8 min. of heating. The total decomposition of Amber Raw Powder has been recorded.
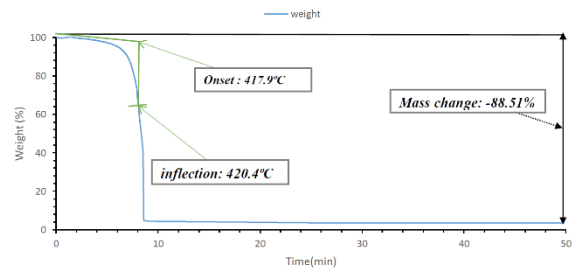
Fig. 2. TGA thermogram of the raw amber powder (mass (%) as a function of time (min.)).

By comparing the results in the two cases Amber Raw and Amber Raw Powder a difference in the thermal decomposition is around 38 °C; in the case of Amber Raw the thermal decomposition started at a temperature of 382.3 °C, on the other hand, of Amber Raw Powder the sample remains stable up to a temperature of 420.4 °C at the level of mass loss for Amber Raw Powder, there is a total decomposition; on the other hand, in the case of Amber Raw (before grinding) the mass loss does not exceed 40%.

B. Differential Scanning Calorimetry (DSC)

Fig. 3 shows the DSC diagram for Amber Raw. We can observe the presence of an exothermic peak with a ΔH=35.16 J/g, this peak is due to a glass transition at the sum of the peak, we observe an intersection with the shape of the DSC curve at a temperature of 136.3 °C, this temperature is corresponding the glass transition temperature.
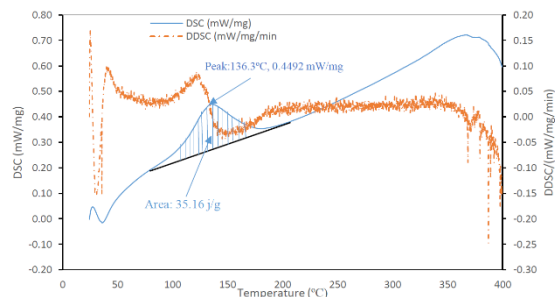
Fig. 3. DSC thermogram of Amber Raw (DSC (mW/mg) as a function of temperature (ºC)).

In Fig. 4 presents the diagram DSC in the case of Amber Raw Powder in a temperature range between 25 °C and 400 °C according to the curve by noting the presence of two peaks: an exothermic peak linked to the transition glassy, and a second endothermic peak linked to melting at temperatures of 136 °C and 263 °C, respectively.
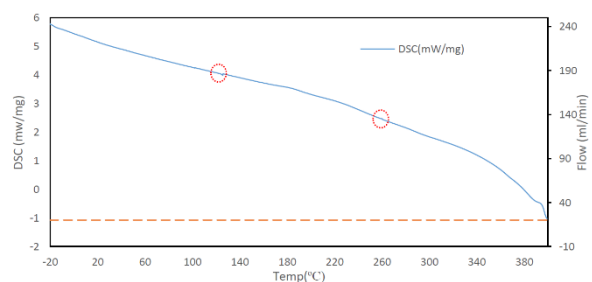
Fig. 4. DSC thermogram of Amber Raw Powder (DSC (mW/mg) as a function of temperature (ºC)).

C. Method of determination of chemical composition

In order to study the chemical composition of the sample (Amber Raw Powder), spectral analysis was carried out. 15 samples were taken, and the mean spectral curve was shown (Fig. 5; 6).
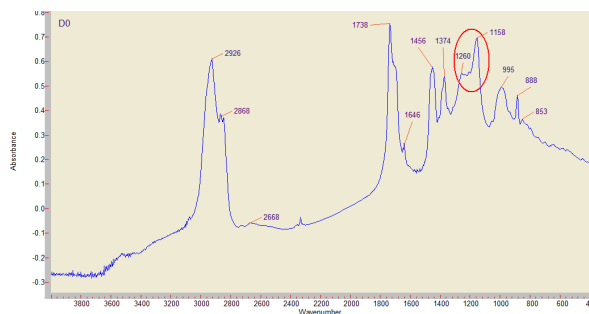
Fig. 5.   FTIR spectrum of Amber Raw Powder (< 20 nm), 0 min).
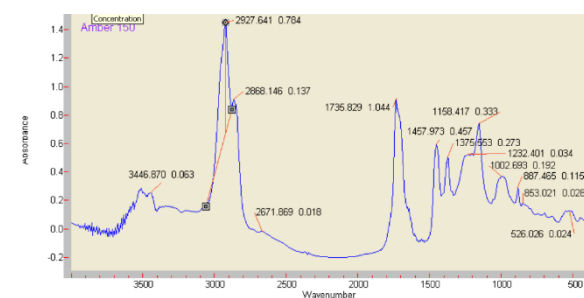
Fig. 6.   DSC FTIR spectrum of the Amber Raw Powder (< 20 nm), 10 min, heated up to 150.0 ºC

According to the "Table of discriminating frequencies in the IR spectrum of atomic groups" [35], the following elements have been determined: the absorption band 850-1000 cm^{-1} proves the presence of peroxides; 950-1200 cm^{-1} - cyclic ethers; 1105-1360 cm^{-1} - phenol hydroxides; 1420-1450 cm^{-1} - distorting oscillation of the 2 groups; 1575-1630 cm^{-1} - polycyclic aromatic compounds; 2800-3100 cm^{-1} - carboxylic groups; 3300-3500 cm^{-1} - NH amine groups. By comparing the results of the spectral analysis of succinct samples (Fig. 5; 6), it can be seen that the difference in the alteration of the values of the frequencies characteristic of the atomic groups of the polymer constitutes the maximum of 0.005 %. The greatest changes in the value of the characteristic frequencies of the atomic groups (Fig. 5; 6) correspond to the change in the value of the NH amine group representing 0.1% (the value of succinite without preheating, standard).

In the samples of raw amber powder, the "horizontal shoulder" was observed; it is characteristic to the Baltic amber at 1180-1240 cm^{-1}, which indicates that it contains succinic acid ($C_4H_6O_4$). Furthermore, when exposed to a temperature of 150.0 °C, it does not cause changes in the structure of the "horizontal shoulder" (Fig. 6), which correlates with references to thermal and structural studies of Baltic amber [36].

D. Determination of the mechanical characteristic of nanofibers with/without the succinite particles

To determine the change of the mechanical parameters in polymer materials (with variation of PA6 16%, 20% and 28% concentration), as well with/without succinite, taking into account its heat treatment, an analysis of the mechanical characteristics of nanofibers was carried out (Fig. 7).
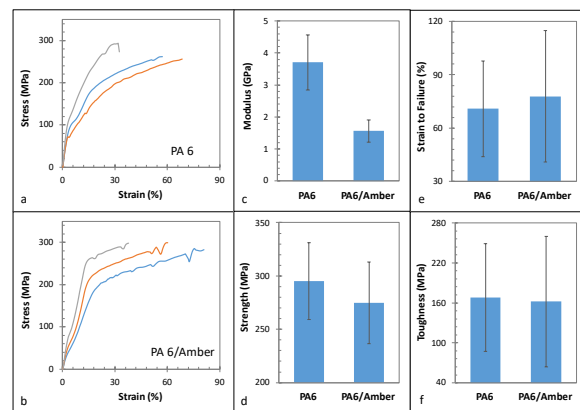
Fig. 7.   The Stress as a function of strain for (a) nanofibres (curves: grey color: PA6 28%, average $diam_{nanofiber} = 230\pm15$ nm; curve: blue colour: PA6 20%, average $diam_{nanofiber} = 150\pm19$ nm; curve: red colour: PA6 16%, average $diam_{nanofiber} = 60\pm17$ nm); (b) composite nano fibres (with succinite powder 5-20 nm) (curves: grey colour: PA6 28%, average $diam_{nanofiber} = 239\pm11$ nm; curve: blue colour: PA6 20%, mean $diam_{nanofiber} = 166\pm18$ nm; curve: red colour: PA6 16%, average $diam_{nanofiber} = 78\pm14$ nm); (c) elastic modulus (GPa) of nanofibers with/without the succinite powder; (d) tensile strength (MPa) of nanofibers with/without the succinite powder; (e) strain to Failure (%) of nanofibers with / without succinite powder; (f) Toughness (MPa) of nanofibers with/without the succinite powder.

According to Fig. 7-a, the maximum value of the stress for the polymer (28%) has a value at 294±9 MPa after there is a break at a deformation of 31.75%. The stress values between 20% and 16% are different only on 10.2 MPa. The stress value of the polymer (16%) at 255±13 MPa, the value of deformation at break can go up to 68.33%. Fig. 7-b show the stress values as a function of strain for the composite nanofibers (with succinite powder). According to this figure, there is not a remarkable increase in stress values because the maximum values (PA 28%, the same for PA 16%) are around 299±14 MPa, but with this constraint the rupture manifests itself at a deformation value, which went up to 60% (PA 16%), but for PA 28% less (42%). The curve (PA 20%) that the strain at break can increase to a value of 81% with a stress value of 283±10 MPa, while this is not the case in the pure polymer (polyamide without succinite powder).

In general, when comparing the stress values of polymers (16%, 20%, 28%) with/without succinite powder, a progressive decrease in the stress values as for polyamide with succinite powder from 299±14 MPa till 283±10 MPa, as for pure polyamide from 294±9 MPa till 256±13 MPa. The difference in stress characteristics between PA6 with/without succinite powder is approximately 44 MPa (higher border (299±14 MPa) and lower border of stress values (256±13 MPa). This can be explained by the presence of succinite nanoparticles (5-20 nm) in the structure of nanofibers, as an element that weakens the stress of the cross section in the nanofiber, as well as a decrease in the average diameter of the nanofibers (from 230±15 nm till 60±17 nm). These observations correlate well with the references [37]. However, more non-linear behaviour of the stress-strain characteristics was observed for PA6 without succinite powder, against the stress-strain characteristics of PA6 with succinite powder, which have more classic elastic-plastic behaviour.

The effect of heat treatment (for both types of polymers) was manifested in the example of PA6 (16%) with succinite powder (nanofiber diameter 78±14 nm). At high stress value, about 299±14 MPa composite showed almost 21% less strain compared to PA6 (20%) with succinite powder (nanofiber diameter 166±18 nm). This behaviour can be explained by the crystalline orientation of molecules in polymers of nanofibers with succinct particles (this was obtained based on the basis of XRD and Raman tests and described in our next studies).

Figs. 7-c show the average Elastic Modulus values for the two types of samples (PA6 with a concentration of PA6 16%, 20%, 28% and with/without the succinite powder). For PA6 only the modulus reaches a value of 3.7 GPa but this value remains within a range of values 2.9-4.6 GPa; in the case of composite polymers, the elastic modulus has a lower value than of pure polymer, and due to increase in strain for the composite nanofibers with a very reliable change in the level of the stress which will return the value of the modulus lower this can be concluded from Equation (1), which linked the Modulus according to the stress and the strain.

$$Modulus = stress / strain \qquad (1)$$

Fig. 7-d shows the Strength values for the two types of samples (PA6 with PA6 concentration of PA6 16%, 20%, 28%, and with/without the succinite powder); and always as in the case of the Elastic Modules the values of the Strength for PA6 are higher on 20 MPa than Strength value of the composite polymer. The Strength value reaches 295.2 MPa and 274.9 MPa for both types of polymers, respectively. Changes of the Strength values in the data scatter limit are statistically "not significant".

Fig. 7-e presents a very important parameter, the Strain to Failure and according to the figure noting that on the other parameters the Modulus and the Strength which has a greater value for PA6 the Strain to Failure reach the greatest value in the case of composite polymer (77.8%), whereas for PA6 the value is only 70.9%. These changes can be demonstrated from Fig. 7-b in which we note that the strain values increase in a remarkable way with the increases the stress values, this may be linked to the increase in physical and chemical interactions between the PA6 matrix and succinite nano particles.

Fig. 7-f shows the toughness for the two types of samples. In this case, there is not a great difference between the two types of samples; there the Toughness values reach 168.3 and 162 MPa for both types of polymers, respectively.

The results presented in this study offer insightful contributions to the understanding of the thermal and mechanical properties of succinite-incorporated PA6 nanofibers. Thermal analysis through TGA and DSC methods has elucidated the distinct thermal decomposition and glass transition behaviours of Amber Raw and Amber Raw Powder, highlighting the impact of physical form on thermal stability. The observed increase in onset and inflection temperatures for Amber Raw Powder suggests that grinding the succinite into a powder form enhances its thermal stability, potentially due to an increase in surface area and more uniform heat distribution during analysis.

The mechanical analysis of nanofibers with varying concentrations of PA6 and the incorporation of succinite nanoparticles reveals nuanced alterations in stress-strain behaviour, elastic modulus, tensile strength, strain to failure, and toughness. The incorporation of succinite nanoparticles not only affects the diameter of the nanofibers but also modulates their mechanical properties. A notable observation is the reduction in the elastic modulus in composite fibres, which may be attributed to the dispersion of succinite particles within the PA6 matrix, potentially acting as stress concentrators or modifiers of the polymer chain mobility. This decrease in modulus, however, comes with an increase in strain to failure, suggesting enhanced ductility in the composite nanofibers. Such behaviour might be advantageous in applications requiring materials that can absorb more energy before failure, such as in impact-resistant coatings or flexible electronic components.

Furthermore, the slight decrease in tensile strength and toughness in composite fibres, while statistically not significant, points to a complex interplay between the reinforcing effect of the succinite particles and their impact on the polymer matrix's continuity. The observed mechanical behaviours underscore the importance of optimizing nanoparticle dispersion and polymer-nanoparticle interactions to achieve desired material properties.

IV. Conclusion

In accordance with the thermal analyses of the succinite nano powder (DSC, TGA and IR spectra) presented, it has been determined that the insignificant loss of volatile components, in particular the NH amino group, in the case of heating of succinite to 150 ºC (solvent temperature in time of suspension preparation) does not exceed 0,1% (of the original volume), hence the percentage of a relevant component such as the succinite acid ($C_4H_6O_4$) remains almost entirely in succinite.

Taking into account the results of thermal analysis of polymers, a comparative analysis of the mechanical parameters of PA6 nanofibers with/without succinite nano powder was carried out. As a result, it was established that the mechanical properties are close enough between the pure PA6 and composite nanofibers.

Determined that increasing the composite nanofiber (PA6 16% with nonstandard mechanical behaviour) diameter until 78±14 nm, in compare with pure PA6 nanofiber same concentration (with diameter 60±17 nm) resulted in simultaneous reduced in elastic modulus almost in 2.3 time, but a real strength decreased very slightly from 295.2 MPa to 274.9 MPa. A similarly minor change observed for toughness from 168.3 to 162 MPa. As opposed to pure PA6 nanofiber, the Strain to Failure value for the composite nanofiber was increased almost on 7%.

Despite the insignificant lower strength of the composite nanofiber in comparison to the PA6 nanofiber (without additives) the tensile properties of the composite nanofiber decreased about 2–2.8 times in comparison to initial the PA6 nanofiber. Nevertheless, the achieved strength of the composite nanofiber is enough to prepare the textile fabrics with protection properties because it is

used in combination with other natural and synthetic macrofibres.

REFERENCES

[1] A. Hussain, D. Goljandin, V. Podgursky, M. M. Abbas, and I. Krasnou, "Experimental mechanics analysis of recycled polypropylene-cotton composites for commercial applications," *Adv. Ind. Eng. Polym. Res.*, vol. 6, no. 3, pp. 226–238, 2023, doi: 10.1016/j.aiepr.2022.11.001.

[2] A. Hussain, V. Podgursky, M. Viljus, and M. R. Awan, "The role of paradigms and technical strategies for implementation of the circular economy in the polymer and composite recycling industries," *Adv. Ind. Eng. Polym. Res.*, vol. 6, no. 1, pp. 1–12, 2023, doi: 10.1016/j.aiepr.2022.10.001.

[3] A. Hussain, V. Podgursky, D. Goljandin, M. Antonov, F. Sergejev, and I. Krasnou, "Circular Production, Designing, and Mechanical Testing of Polypropylene-Based Reinforced Composite Materials: Statistical Analysis for Potential Automotive and Nuclear Applications," *Polymers (Basel).*, vol. 15, no. 16, 2023, doi: 10.3390/polym15163410.

[4] I. Lasenko, D. Grauda, D. Butkauskas, J. V. Sanchaniya, A. Viluma-Gudmona, and V. Lusis, "Testing the Physical and Mechanical Properties of Polyacrylonitrile Nanofibers Reinforced with Succinite and Silicon Dioxide Nanoparticles," *Textiles*, vol. 2, no. 1, pp. 162–173, 2022, doi: 10.3390/textiles2010009.

[5] A. Viluma-Gudmona, I. Lasenko, J. V. Sanchaniya, and B. Abdelhadi, "The amber nano fibers development prospects to expand the capabilites of textile 3D printing in the general process of fabrication methods," *Eng. Rural Dev.*, vol. 20, pp. 248–257, 2021, doi: 10.22616/ERDev.2021.20.TF051.

[6] D. Grauda, L. Bumbure, I. Lyashenko, A. Katashev, Y. Dekhtyar, and I. Rashal, "Amber particles as living plant cell markers in flow cytometry," *Proc. Latv. Acad. Sci. Sect. B Nat. Exact, Appl. Sci.*, vol. 69, no. 3, pp. 77–81, 2015, doi: 10.1515/prolas-2015-0011.

[7] A. Viluma-Gudmona, I. Lasenko, J. V. Sanchaniya, and A. Podgornovs, "Electro-resistant biotextile development based on fiber reinforcement with nano particles," *Eng. Rural Dev.*, vol. 20, pp. 804–812, 2021, doi: 10.22616/ERDev.2021.20.TF182.

[8] I. Lasenko *et al.*, "The Mechanical Properties of Nanocomposites Reinforced with PA6 Electrospun Nanofibers," *Polymers (Basel).*, vol. 15, no. 3, 2023, doi: 10.3390/polym15030673.

[9] K. K. Annamaneni, A. Korjakins, I. Lasenko, O. Kononova, A. Krasnikovs, and V. Lusis, "Experimental Study and Modelling on The Structural Response of Fiber Reinforced Concrete," *Multidiscip. Digit. Publ. Inst.*, 2022.

[10] S. Gaidukovs, I. Lyashenko, J. Rombovska, and G. Gaidukova, "Application of amber filler for production of novel polyamide composite fiber," *Text. Res. J.*, vol. 86, no. 20, pp. 2127–2139, 2016, doi: 10.1177/0040517515621130.

[11] J. V. Sanchaniya, I. Lasenko, S. P. Kanukuntla, A. Mannodi, A. Viluma-Gudmona, and V. Gobins, "Preparation and Characterization of Non-Crimping Laminated Textile Composites Reinforced with Electrospun Nanofibers," *Nanomaterials*, vol. 13, no. 13, 2023, doi: 10.3390/nano13131949.

[12] J. V. Sanchaniya *et al.*, "Mechanical and Thermal Characterization of Annealed Oriented PAN Nanofibers," *Polymers (Basel).*, vol. 15, no. 15, 2023, doi: 10.3390/polym15153287.

[13] D. Grauda *et al.*, "Establishment of Biotesting System to Study Features of Innovative Multifunctional Biotextile," *Proc. Latv. Acad. Sci. Sect. B Nat. Exact, Appl. Sci.*, vol. 77, no. 3–4, pp. 186–192, 2023, doi: 10.2478/prolas-2023-0026.

[14] A. Asar and W. Zaki, "A comprehensive review of the mechanisms and structure of interpenetrating phase composites with emphasis on metal-metal and polymer-metal variants," *Compos. Part B*, vol. 275, no. October 2023, p. 111314, 2024, doi: 10.1016/j.compositesb.2024.111314.

[15] E. A. Ananiadis, A. E. Karantzalis, A. K. Sfikas, E. Georgatis, and T. E. Matikas, "Aluminium Matrix Composites Reinforced with AlCrFeMnNi HEA Particulates: Microstructure, Mechanical and Corrosion Properties," *Materials (Basel).*, vol. 16, no. 15, 2023, doi: 10.3390/ma16155491.

[16] A. Shishkin, I. Hussainova, V. Kozlov, M. Lisnanskis, P. Leroy, and D. Lehmhus, "Metal-Coated Cenospheres Obtained via Magnetron Sputter Coating: A New Precursor for Syntactic Foams," *Jom*, vol. 70, no. 7, pp. 1319–1325, 2018, doi: 10.1007/s11837-018-2886-0.

[17] A. Shishkin *et al.*, "Cavitation-dispersion method for copper cementation from wastewater by iron powder," *Metals (Basel).*, vol. 8, no. 11, pp. 4–6, 2018, doi: 10.3390/met8110920.

[18] P. Colombo, "Cellular ceramics with hierarchical porosity from preceramic polymers," *IOP Conf. Ser. Mater. Sci. Eng.*, vol. 18, no. SPEC. SYMPOSIUM, 2011, doi: 10.1088/1757-899X/18/1/012002.

[19] V. Mironovs *et al.*, "Cellular structures from perforated metallic tape and its application for electromagnetic shielding solutions," *Agron. Res.*, vol. 12, p. (in Print), Jan. 2014.

[20] M. Pelanconi, D. Koch, G. Bianchi, S. Bottacin, and P. Colombo, "High-strength Si – SiC lattices prepared by powder bed fusion , infiltration-pyrolysis , and reactive silicon infiltration," no. December 2023, pp. 1–15, 2024, doi: 10.1111/jace.19750.

[21] V. Popov *et al.*, "Novel hybrid method to additively manufacture denser graphite structures using Binder Jetting," *Sci. Rep.*, vol. 11, no. 1, pp. 1–11, 2021, doi: 10.1038/s41598-021-81861-w.

[22] J. Baronins *et al.*, "The Effect of Zinc Oxide on DLP Hybrid Composite Manufacturability and Mechanical-Chemical Resistance," *Polymers (Basel).*, vol. 15, no. 24, 2023, doi: 10.3390/polym15244679.

[23] K. Irtiseva *et al.*, "Towards next-generation sustainable composites made of recycled rubber, cenospheres, and biobinder," *Polymers (Basel).*, vol. 13, no. 4, pp. 1–14, 2021, doi: 10.3390/polym13040574.

[24] A. Shishkin, V. Mironovs, V. Lapkovskis, J. Treijs, and A. Korjakins, "Ferromagnetic sorbents for collection and utilization of oil products," *Key Eng. Mater.*, vol. 604, pp. 122–125, 2014, doi: 10.4028/www.scientific.net/KEM.604.122.

[25] A. Shishkin, V. Mironov, D. Goljandin, and V. Lapkovsky, "Recycling of Al-W-B composite material," *Key Eng. Mater.*, vol. 527, pp. 143–147, 2012, doi: 10.4028/www.scientific.net/KEM.527.143.

[26] R. Ciardiello, L. T. Drzal, and G. Belingardi, "Effects of carbon black and graphene nano-platelet fillers on the mechanical properties of syntactic foam," *Compos. Struct.*, vol. 178, pp. 9–19, 2017, doi: 10.1016/j.compstruct.2017.07.057.

[27] V. Abramovskis *et al.*, "and Potential Applications," 2023.

[28] F. Hussain, M. Hojjati, M. Okamoto, and R. E. Gorga, "Review article: Polymer-matrix nanocomposites, processing, manufacturing, and application: An overview," *J. Compos. Mater.*, vol. 40, no. 17, pp. 1511–1575, 2006, doi: 10.1177/0021998306067321.

[29] S. Pavlidou and C. D. Papaspyrides, "A review on polymer-layered silicate nanocomposites," *Prog. Polym. Sci.*, vol. 33, no. 12, pp. 1119–1198, 2008, doi: 10.1016/j.progpolymsci.2008.07.008.

[30] D. S. More, M. J. Moloto, N. Moloto, and K. P. Matabola, "TOPO-capped silver selenide nanoparticles and their incorporation into polymer nanofibers using electrospinning technique," *Mater. Res. Bull.*, vol. 65, pp. 14–22, 2015, doi: 10.1016/j.materresbull.2015.01.030.

[31] L. Li, L. M. Bellan, H. G. Craighead, and M. W. Frey, "Formation and properties of nylon-6 and nylon-6/montmorillonite composite nanofibers," *Polymer (Guildf).*, vol. 47, no. 17, pp. 6208–6217, 2006, doi: 10.1016/j.polymer.2006.06.049.

[32] P. Tumiłowicz, L. Synoradzki, A. Sobiecka, J. Arct, K. Pytkowska, and S. Safarzynski, "Bioactivity of Baltic amber - Fossil resin," *Polimery*, vol. 61, pp. 347–356, May 2016, doi: 10.14314/polimery.2016.347.

[33] I. Lašenko, S. Gaidukovs, and J. Rombovska, "Manufacturing of amber particles suitable for composite fibre melt spinning," *Proc. Latv. Acad. Sci. Sect. B Nat. Exact, Appl. Sci.*, vol. 70, no. 2, pp. 51–57, 2016, doi: 10.1515/prolas-2016-0007.

[34] N. Wang, Y. Liu, Y. Liu, and Q. Wang, "A shear pan mill for preparation of ultrafine polyamide 66 powder using sodium sulfate ionic crystals as grinding aid," *Mater. Manuf. Process.*, vol. 32, no. 2, pp. 115–120, 2017, doi: 10.1080/10426914.2016.1221080.

[35] D. Chen, Q. Zeng, Y. Yuan, B. Cui, and W. Luo, "Baltic amber or Burmese amber: FTIR studies on amber artifacts of Eastern Han Dynasty unearthed from Nanyang," *Spectrochim. Acta - Part A Mol. Biomol. Spectrosc.*, vol. 222, p. 117270, 2019, doi: 10.1016/j.saa.2019.117270.

[36] A. A. Khomich, R. Khmelnitskii, M. Kozlova, A. V. Khomich, and V. Ralchenko, "IR Spectroscopy of Vacancy Clusters (Amber Centers) in CVD Diamonds Nanostructured by Fast Neutron Irradiation," *C-Journal Carbon Res.*, vol. 9, no. 2, 2023, doi: 10.3390/c9020055.

[37] H. Mahfuz *et al.*, "Reinforcement of nylon 6 with functionalized silica nanoparticles for enhanced tensile strength and modulus," *Nanotechnology*, vol. 19, no. 44, 2008, doi: 10.1088/0957-4484/19/44/445702.

Longitudinal Stability of Wheeled Mobile Robots - Degree of Stability

Stoyan Lilov
Institute of Robotics
Bulgarian Academy of Sciences
Plovdiv, Bulgaria
stoyanvllilov@gmail.com

Nickolay Popov
Institute of Robotics
Bulgarian Academy of Sciences
Plovdiv, Bulgaria
njpopov62@gmail.com

Vanya Markova
Institute of Robotics
Bulgarian Academy of Sciences
Plovdiv, Bulgaria
markovavanya@yahoo.com

Ventseslav Shopov
Institute of Robotics
Bulgarian Academy of Sciences
Plovdiv, Bulgaria
line 5: vkshopov@yahoo.com

***Abstract*. In this paper, the research focus is on the longitudinal stability of a wheeled mobile robot, using a geometric similarity coefficient (this coefficient is defined in the paper). The research method used for calculations is D'Alembert's principle. The results represent the limit driving/braking forces and limit accelerations/ decelerations for a given geometric similarity coefficient, before the robot loses stability.**

Keywords: Degree of stability, longitudinal stability, stability coefficient, wheeled mobile robots

I. Introduction

In this paper, problems related to the stability of wheeled mobile robots during movement are studied. They refer to the methods of determining the stability limits of a design scheme and the comparison of stability between two or more design schemes. For example, moving the center of mass forward improves longitudinal stability during acceleration, but it results in reduced stability during deceleration.

Usually, in similar studies, differential equations are used [1], [2], [4], [5] to represent the mathematical model. Instead, the D'Alembert's principle is used here, which considers an equilibrium system of forces, including inertial forces [6]; the accuracy of the calculations does not deteriorate. The wheels are assumed to contact the road at a point. Rolling friction forces are neglected. It is assumed that the motion occurs without slipping. It is also assumed that the robot body and its wheels are perfectly rigid, i.e. no deformations during movement. Lateral stability is not considered here.

The aim of the present study is to propose a method/approach for comparison of stability (of permissible forces and accelerations) of different design schemes of wheeled mobile robots.

To achieve the aim, we set ourselves the following tasks:

- to determine the parameters affecting the stability of the robot;

- the relationship between the robot's geometric parameters should be set quantitatively (with a number);

- to demonstrate through numerical experiments that the method provides an adequate estimate of the stability of the robot;

- to compare with examples the robot stability results by D'Alembert's method and by the proposed method.

Our hypothesis is that if the combination of values of the geometric parameters of one design scheme and the combination of values of the geometric parameters of another design scheme give the same values of their corresponding stability coefficients, then their permissible longitudinal forces (in case the mass of the constructions is equal) and accelerations, after which a loss of stability occurs of these two design schemes, are equal.

A criterion for loss of stability is the occurrence of a zero or negative value of the support reaction for any of the wheels of the robot.

The article is organized as follows.

The second part contains an implementation and description of the mathematical model of the robot, as well as the notations used in the model. In the third part, specific values for the parameters of the robot, the constraints under which the experiments are carried out and the experimental results presented in a graphical form are given. In the last part, conclusions are made about the use of a stability coefficient and its relationship with limit forces and accelerations, after which a loss of stability occurs.

II. METHODS AND MATERIALS

A. Brief theory

Fig. 1 shows a longitudinal projection of the studied type of robot, which has rear wheel drive and four wheel brakes.
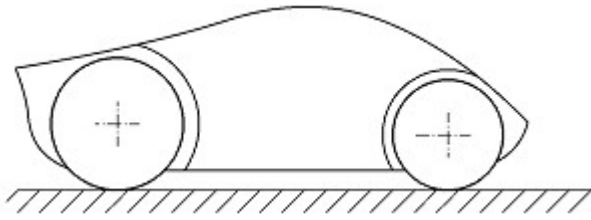
Fig. 1. Schematic of the robot in general view

The notations used in the mathematical model and those of Fig. 2, are shown below:

- O_{xz} – coordinate system related to the body of the robot;

- m_c – center of mass of the robot;

- A_r – position of the support points of the rear wheels;

- A_f – position of the support points of the front wheels;

- l $[m]$ – wheel base;

- l_r $[m]$ – distance along the x axis from the center of mass to the support points of the rear wheels;

- l_f $[m]$ – distance along the x axis from the center of mass to the support points of the front wheels;

- z_{mc} $[m]$ – distance from the mass center to the road;

- $m = 3$ $[kg]$ – mass of the robot;

- $g = 9.807$ $[m/s^2]$ – average ground acceleration (in the general case, the gravitational acceleration is a parameter);

- a $[m/s^2]$ – acceleration of the robot;

- a_{dr} $[m/s^2]$ – positive acceleration of the robot;

- a_{br} $[m/s^2]$ – deceleration of the robot;

- a_p $[m/s^2]$ – permissible acceleration of the robot;

- a_{drp} $[m/s^2]$ – permissible acceleration of the robot;

- a_{brp} $[m/s^2]$ – permissible deceleration of the robot;

- F_g $[N]$ – weight;

- F_{dr} $[N]$ – driving force;

- F_{br} $[N]$ – braking force;

- F_{drp} $[N]$ – permissible driving force;

- F_{brp} $[N]$ – permissible braking force;

- F_{in} $[N]$ – inertial force;

- F_{indr} $[N]$ – inertial force during acceleration;

- F_{inbr} $[N]$ – inertial force during deceleration;

- F_{sr} $[N]$ – support reaction at the rear wheels;

- F_{sf} $[N]$ – support reaction at the front wheels;

The mathematical model of the robot is built according to D'Alembert's principle, for which in this case it is necessary to compile a system of two moments and one projection equation according to the Fig. 2:

$$\begin{vmatrix} \sum M_{A_{r_i}} = 0 \\ \sum M_{A_{f_i}} = 0 \\ \sum x_i = 0 \end{vmatrix} \quad (1)$$

$$\begin{vmatrix} F_g\, l_r + F_{in}\, z_{m_c} + F_{s_f}\, l = 0 \\ F_g\, l_f + F_{in}\, z_{m_c} + F_{s_r}\, l = 0 \\ F_{tr} + F_{in} = 0 \end{vmatrix} \quad (2)$$

If the robot is equipped with the necessary sensors for reading the driving force and an actuator for supplying the required driving force F_{dr}, i.e. if F_{dr} is a parameter, only the support reactions of the wheels remain unknown in the system. The remaining terms in the equations are either constants or parameters:

$$F_g = m\, g \quad (3)$$

$$l = x_{A_f} - x_{A_r} \quad (4)$$

The following dependence determining $K_{base} = const$ is:

$$l_r = \frac{1}{3}l;\ l_f = l - l_r;\ z_{mc} = \frac{l}{6} \quad (5)$$

For the support reactions, during acceleration:

$$F_{s_f} = \frac{F_{dr}\, z_{m_c} - m\, g\, l_r}{l} \quad (6)$$

$$F_{s_r} = \frac{F_{dr}\, z_{m_c} + m\, g\, l_f}{l} \quad (7)$$

For the support reactions, at deceleration:

$$F_{s_f} = \frac{F_{br}\, z_{m_c} + m\, g\, l_r}{l} \quad (8)$$

$$F_{s_r} = \frac{m\, g\, l_f - F_{br}\, z_{m_c}}{l} \quad (9)$$
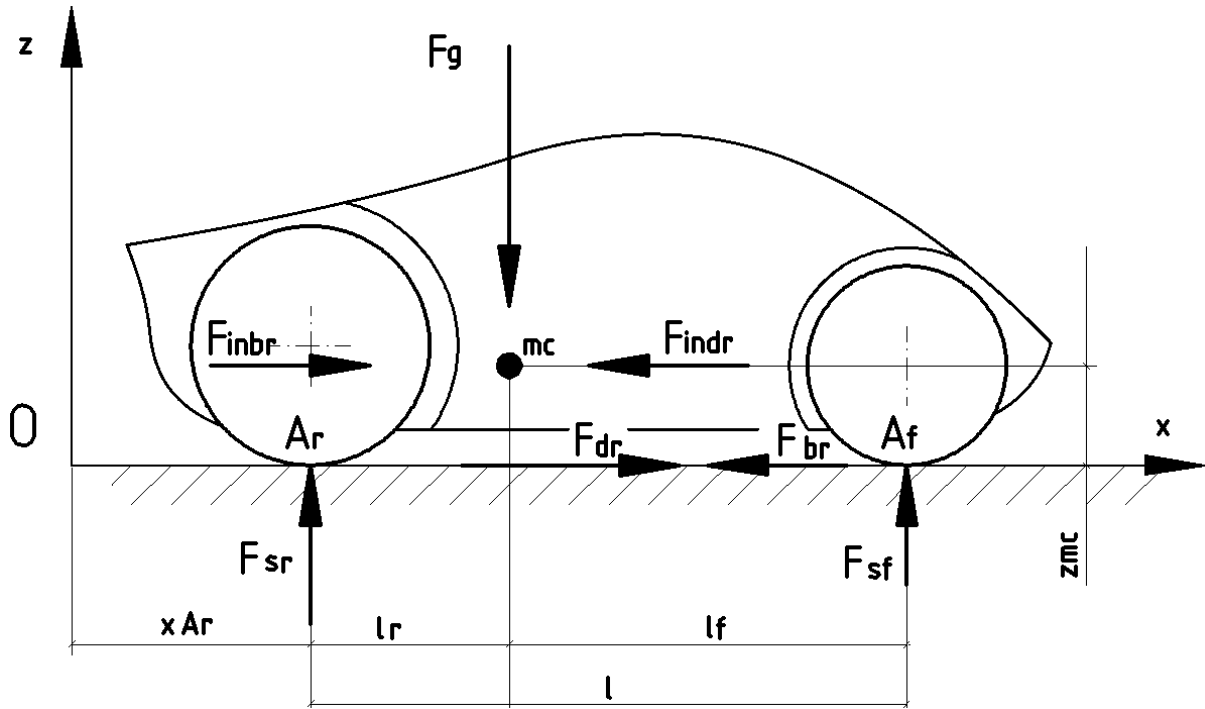
Fig. 2. Schematic of the robot with a coupled coordinate system and the acting forces (longitudinal projection)

According to the selected loss of stability criterion, in order to find the permissible driving and braking forces, under acceleration/deceleration, we assume the support reactions to be zero in the following two equations:

$$F_{dr_p} = \frac{m\,g\,l_r - F_{s_f}\,l}{z_{mc}} \tag{10}$$

$$F_{dr_p} = \frac{m\,g\,l_f - F_{s_r}\,l}{z_{mc}} \tag{11}$$

Because $F_{drp} = ma_{drp}$; $F_{brp} = ma_{brp}$, then again for support reactions equal to zero:

$$a_{drp} = \frac{m\,g\,l_r - F_{s_f}\,l}{z_{mc}\,m} = \frac{g\,l_r}{z_{mc}} - \frac{F_{s_f}\,l}{z_{mc}\,m} \tag{12}$$

$$a_{brp} = \frac{m\,g\,l_f - F_{s_r}\,l}{z_{mc}\,m} = \frac{g\,l_f}{z_{mc}} - \frac{F_{s_r}\,l}{z_{mc}\,m} \tag{13}$$

B. Implementation

The experiments are conducted for acceleration and deceleration.

The steps in performing the calculations are:

- The values for the constants are defined.

The ground acceleration g and mass m remain the same for all calculations.

- Defining $K_{base_r} = \frac{z_{mc}}{l_r}$;

- Defining $K_{base_f} = \frac{z_{mc}}{l_f}$;

- Defining $K_{base_1} = \frac{z_{mc}}{l}$;

- Defining $K_{base_2} = \frac{z_{mc}^2}{l_r l_f}$;

- Defining $K_{base_4} = \frac{z_{mc}^4}{l_r^2 l_f^2}$;

- K_{base} when $z_{mc} \in [0.05, 0.20]$; $l = 0.30$;

  - K_{base} when $z_{mc} \in [0.05, 0.30]$; $l = 0.60$;

- K_{base} when $z_{mc} \in [0.05, 0.60]$; $l = 1.20$;

- K_{base} when $l \in [0.15, 0.40]$; $z_{mc} = 0.10$ and l is along O_x axle;

- K_{base} when $l \in [0.15, 0.40]$; $z_{mc} = 0.10$ and l_r is along O_x axle;

- K_{base} when $l \in [0.15, 0.40]$; $z_{mc} = 0.10$ and l_f is along O_x axle;

- The force of gravity is determined according to the values of the earth's acceleration and mass: $F_g = mg$.

- For acceleration, the permissible driving force is calculated by the equation:

$$F_{dr_p} = mgl_r/z_{mc}.$$

- For deceleration, the permissible braking force is calculated using the equation:

$$F_{br_p} = mgl_f/z_{mc}.$$

- The permissible acceleration is:

$$a_{dr_p} = gl_r/z_{mc}.$$

- The permissible deceleration is:

$$a_{br_p} = gl_f/z_{mc}.$$

III. EXPERIMENTS AND RESULTS

A. Subject of experiments

Design scheme of a rear-wheel drive four-wheeled mobile robot with four wheel brakes is the subject of experiments. We assume that the robot is supplied with engine and brakes, which are capable to unbalance the robot during acceleration, respectively – deceleration.

B. Constrains

We accept the following restrictions:

- resistance forces as a result of contact with the road, friction in the robot units, air flow, etc. are not taken into account;
- the wheels contact the road at a point;
- the movement is non-slip;
- acting forces do not deform the robot units.

C. Results

The Octave 8.4.0 programming language was used to conduct the experiments.

The experiments are carried out on a design scheme of a four-wheeled rear-wheel drive mobile robot. Five variants of K_{base} are selected. K_{baser} gives a unambiguous comparison in acceleration. K_{basef} gives a unambiguous comparison on deceleration. K_{base1} is suitable when comparing design schemes which a certain route has to be passed. According to the characteristics of the terrain and according to the braking and acceleration capabilities, this coefficient can help to select an optimal location of the center of mass. But it does not give an unambiguous comparison specifically for acceleration and deceleration. K_{base2} and K_{base4} are similar to K_{base1}, but allow more strict control in design schemes with low stability due to their steeper graph, in the area of less stability. In other words, they can play the role of weighting coefficients in optimization tasks.

Normally, the coefficient K_{base} is chosen so that the closer its values are to zero, the greater the stability of the design scheme. In appropriate cases, such as when linear functions are required and we therefore want to free the denominator from variables, we can use the reciprocal, i.e. K_{base}^{-1}. Also, K_{base}^{-1} is more intuitive because its value increases along with the value of F_{drp}; F_{brp}; a_{drp}; a_{brp}, but on the other hand, at K_{base} the maximum degree of stability is when $K_{base} \to 0$, i.e. to a certain value from the number axis.

The presence of some negative values of forces and accelerations in the results is due to their orientation relative to the coupled to the robot's body coordinate system.

Following are some explanations about the experiments and their relevant graphs presented.

a) Fig. 3, Fig. 4 and Fig. 5 illustrate the increase in K_{base} values when the stability decreases (when the height of the mass center z_{mc} increases, the stability decreases).

b) Conversely, in Fig. 6, Fig. 7 and Fig. 8, the values of K_{base} decrease as the stability increases (as the wheelbase l increases, respectively l_r and l_f, the stability increases).

c) In Fig. 9 and Fig. 10 again the dependence of K_{base} on the stability is given, but instead of indirectly, through the geometrical parameters of the dsign scheme, the permissible forces and accelerations are located directly along the Ox axis. K_{basef} is not applicable to F_{drp} and a_{drp}; K_{baser} is not applicable to F_{brp} and a_{brp}, so such graphs are not displayed.

d) Fig. 11 and Fig. 12 show the permissible forces and accelerations for design schemes with different stability, which increases with increasing l and decreases with increasing z_{mc}. This case can also be interpreted not as a comparison of different design schemes, but as a design scheme with a variable center of mass position and a variable wheelbase. Also here one can notice non-linear graphs when there is a variable in the denominator of the corresponding equations (10), (11), (12), (13).

e) In Fig. 13 it can be seen that the values of K_{base} depend on the relations between the geometric parameters of the design scheme, regardless of the absolute values of these parameters.

f) Fig. 14 shows that if we compare robots that have K_{base} with equal values, then their permissible accelerations will also be equal, and if the values of their masses m_i are equal too – and their permissible forces will also be equal (10), (11).
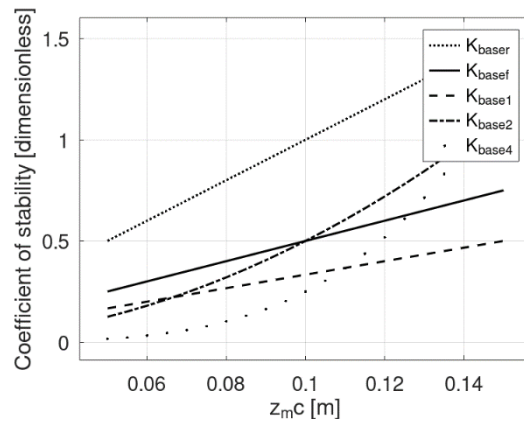
Fig. 3. Coefficients of stability according to z_{mc} value and $l = 0.3$, ($l_r = \frac{1}{3}l$; $l_f = l - l_r$).
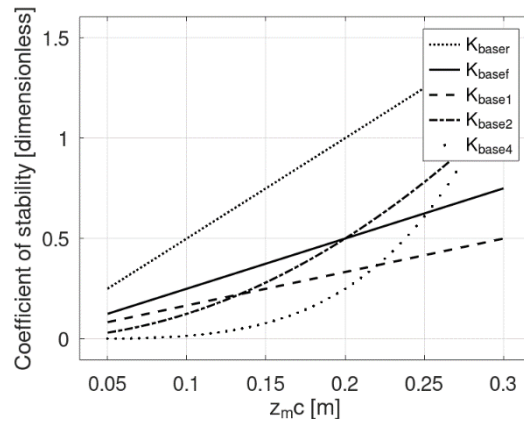
Fig. 4. Coefficients of stability according to z_{mc} value and $l = 0.6$, ($l_r = \frac{1}{3}l$; $l_f = l - l_r$).
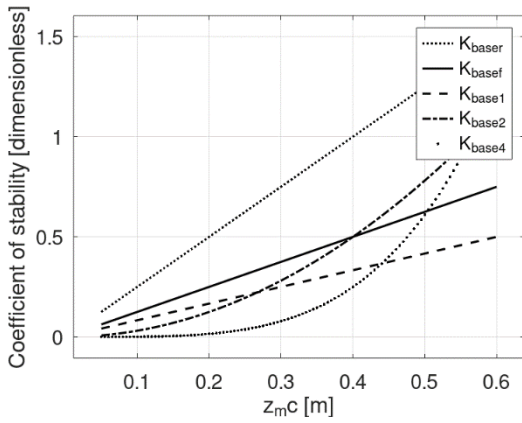
Fig. 5. Coefficients of stability according
to z_{mc} value and $l = 1.2$, $(l_r = \frac{1}{3}l;\ l_f = l - l_r)$.

Fig. 6. Coefficients of stability according to
l value and $z_{mc} = 0.1$, $(l_r = \frac{1}{3}l;\ l_f = l - l_r)$.

Fig. 7. Coefficients of stability according to
l_r value and $z_{mc} = 0.1$, $(l_r = \frac{1}{3}l;\ l_f = l - l_r)$.

Fig. 8. Coefficients of stability according to
l_f value and $z_{mc} = 0.1$, $(l_r = \frac{1}{3}l;\ l_f = l - l_r)$.

Fig. 9. Coefficients of stability according to
$F_{drp};\ F_{brp}$ value and $z_{mc} := 0.05 : 0.005 : 0.15$,
$(l = 0.60; l_r = \frac{1}{3}l;\ l_f = l - l_r)$.
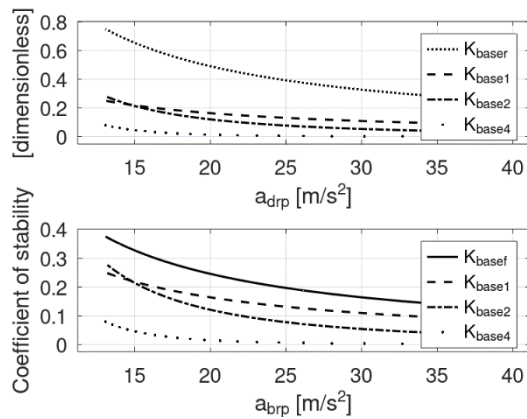
Fig. 10. Coefficients of stability according to
$a_{drp};\ a_{brp}$ value and $z_{mc} := 0.05 : 0.005 : 0.15$,
$(l = 0.60; l_r = \frac{1}{3}l;\ l_f = l - l_r)$.
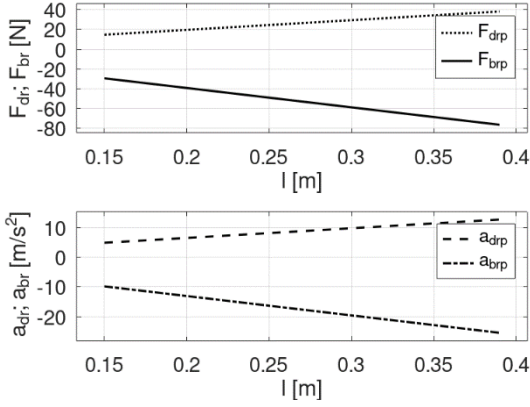
Fig. 11. Permissible forces and accelerations according to l value and $z_{mc} = 0.1$, $(l_r = \frac{1}{3}l;\ l_f = l - l_r)$, i.e. $K_{base} \neq const$.
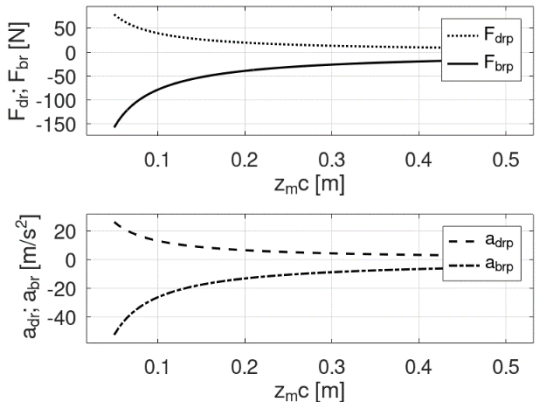
Fig. 12. Permissible forces and accelerations according to z_{mc} value and $l = 0.4$, $(l_r = \frac{1}{3}l;\ l_f = l - l_r)$, i.e. $K_{base} \neq const$.
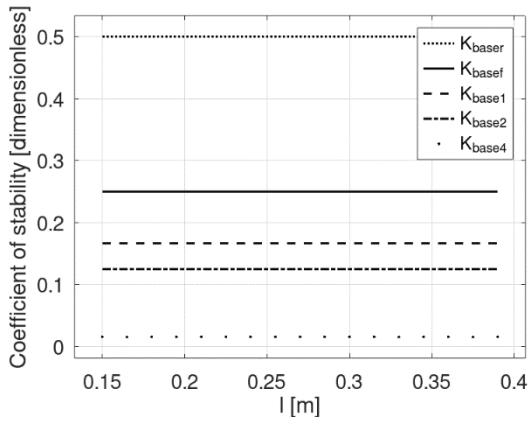
Fig. 13. K_{base} according to l value when $l_r = \frac{1}{3}l;\ l_f = l - l_r;\ z_{mc} = \frac{1}{6}l$, i.e. $K_{base} = const$.
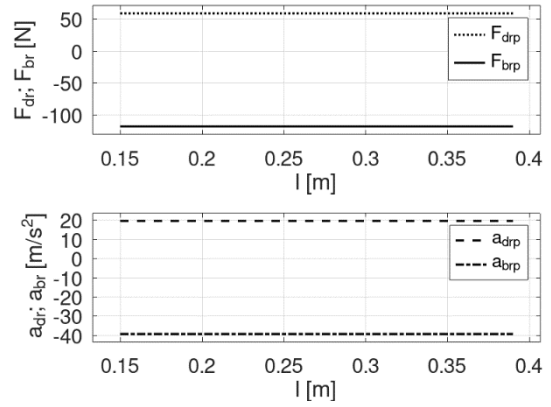
Fig. 14. Permissible forces and accelerations according to l value when $l_r = \frac{1}{3}l;\ l_f = l - l_r;\ z_{mc} = \frac{1}{6}l$, i.e. $K_{base} = const$ (see Fig. 13). But here $F = const$ only when $m = const$ "(10), (11)".

IV. CONCLUSION

The longitudinal stability of a design scheme of four-wheeled mobile robots with different values of the geometric similarity coefficient was studied. It was found that:

- the permissible driving/braking forces depend on the ratio between the individual geometrical parameters of the robots' design scheme, i.e. depend on the geometric similarity coefficient;

- the permissible driving/braking forces do not depend on the absolute values of the individual geometric parameters of the robots' construction, if the coefficient of geometric similarity is equal to a constant; in this case the permissible driving/braking forces will also be equal to a constant;

- the permissible accelerations/decelerations depend on the ratio between the individual geometrical parameters of the robots' design scheme, i.e. design schemes, having equal coefficients of geometric similarity have equal permissible accelerations/decelerations;

- the permissible accelerations/decelerations do not depend on the absolute values of the individual geometric parameters of the robots' design scheme, if the coefficient of geometric similarity is equal to a constant; in this case the permissible accellerations/decelerations will also be equal to a constant.

REFERENCES

[1] B. Siciliano, O. Khatib, (ed.). Springer handbook of robotics, Springer, 2016.

[2] G. Wang, X. Liu, Y. Zhao, et al. Neural Network-Based Adaptive Motion Control for a Mobile Robot with Unknown Longitudinal Slipping. Chin. J. Mech. Eng. 32, 61 (2019).

[3] I. Evtimov, R Ivanov, "Elektromobili", University of Rousse "Angel Kanchev", Rousse, Bulgaria, 2016. Evtimov, I., Ivanov R. Electromobili, University of Rousse "Angel Kanchev", Rousse, 2016

[4] S. Nakajima. Stair-climbing gait for a four-wheeled vehicle. Robomech J 7, 20 (2020).

[5] Y. Onozuka, N. Tomokuni, G. Murata, et al. Attitude control of an inverted-pendulum-type robotic wheelchair to climb stairs considering dynamic equilibrium. Robomech J 7, 23 (2020).

[6] V. Nhu Tran, X. Ngoc Nguyen, et al. Rollover Stability Analisis Of Liquid Tank TRUCK Taking Into Account The Road Profiles, Journal of Applied Engineering Science, 20, 4 (2022), p. 1133-1142

Technological Assurance Of The Milling Process Of Prismatic Channels In Heat Exchange Aluminum Alloys

Angel Lengerov
Department Mechanical engineering and technologies
Technical university of Sofia, Branch Plovdiv
Plovdiv, Bulgaria
anlengerov@abv.bg

Desislava Petrova
Department "Management"
Technical university of Gabrovo
Gabrovo, Bulgaria
des_petrova@abv.bg

Martin Bozhakov
Department Mechanical engineering and technologies
Technical university of Sofia, Branch Plovdiv
Plovdiv, Bulgaria
bozhakov@abv.bg

Abstract. **When milling prismatic grooves in aluminum alloy products, the technological parameters of the process must ensure the specified accuracy and processing performance. This guarantees the maximum heat exchange properties of the surfaces of the processed parts, critical for applications where efficient thermal management is essential. Enhancing these properties can significantly impact the operational efficiency of systems in aerospace, automotive, and electronics industries.**

Articles on the interrelationship of cutting modes and technological and energy parameters of the milling process of prismatic channels in aluminum alloys is an actual task. Its practical implementation will guarantee the improvement of various facilities for transferring and releasing thermal energy. This research could lead to advancements in heat sink design and more effective cooling strategies in high-performance engineering applications, where optimal heat dissipation is vital for maintaining system stability and prolonging lifespan.

Keywords: aluminum alloy products, milling process, technological assurance

I. Introduction

To establish the relationship between the parameters of the cutting mode and the cutting force, systematic experimental studies were conducted utilizing a rigorous methodological approach. These studies aimed to identify optimal settings that would maximize both the efficiency and precision of the milling process. Measurements were meticulously taken to ensure reliable and reproducible results, providing a robust basis for analysis.

As a criterion for optimization of the process of milling channels in aluminum alloys, the value of the components of the cutting forces P_b were taken; P_p; energy losses and the quality of treated surfaces, assessed visually. These metrics served as indicators of both the mechanical effectiveness and the energy efficiency of the milling operations. The experiments were carried out on a Universal Milling Machine FU320, a choice driven by its widespread use in industrial applications, which allows for greater generalization of the findings.

This comprehensive experimental framework not only facilitates a deeper understanding of the dynamics involved in milling aluminum alloys but also enhances the predictive capability regarding the outcomes of varying cutting parameters. The results of these studies are expected to contribute significantly to the body of knowledge in machining science, particularly in the optimization of process parameters that affect both operational cost and material performance.

A dynamometer UDM-600 is installed on the table of the machine with an aluminum alloy workpiece attached to it. The experiments were carried out without the use of lubricating-cooling fluid (LCF) under the following conditions: $\alpha=10'$; $\gamma=6'$; $\alpha_p=1mm$; $\alpha_g=2mm$. The tool material is U8A steel and is mounted on a knife head. The cutting speed varies from 44 to 352 t/min [7].

The nature of the change of the components of the cutting force F: - F_{Cp}, F_{Pp}, F_f depending on the change of the cutting speed V_c when milling flat surfaces in aluminum workpieces with short-angle cutting correspond to those when processing with traditional methods. Cutting forces decrease with increasing cutting speed [3]. When processing such materials, the contact area on the front surface of the knife is very large, and this leads to a large chip thickness and a large cutting force.

When milling channels, with an increase in the cutting speed, the component forces P_p and P_c decrease, which is shown in Fig.1. As the cutting speed increases, the temperature in the cutting zone increases, the coefficient of friction of the chip on the front surface decreases, which leads to a decrease in the components of the cutting forces P_p and P_c. The component force P_p with increasing cutting speed practically does not change, and the friction force between the back and the processed surface due to the change in the friction coefficient changes insignificantly [4, 5].
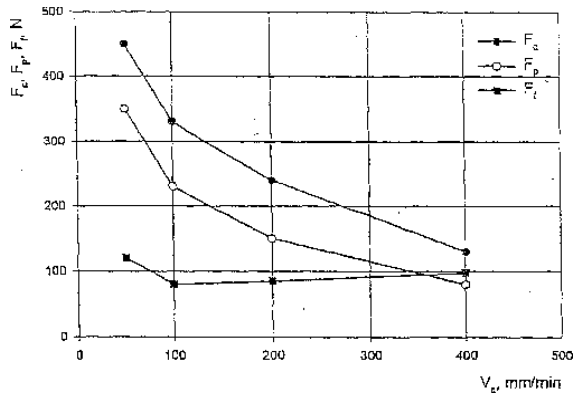
Fig. 1. Dependence of cutting force on speed

II. MATERIALS AND METHODS

The processing of flat aluminum parts is expedient to be carried out with high cutting speeds, contributing to the reduction of the friction coefficient, respectively the cutting force and increasing the quality of the processed channels and their strength.

To determine the influence of the longitudinal feed on the cutting forces *Pe, Pp, and Pp, a* number of experiments were conducted. The cutting speed is constant *(Vc = 44 m/min⁻¹)*, and the feed varies in a range from *44 to 137,5 mm/min (1,0-3,125mm/min⁻¹).*

With an increase in feed from 1 to 3,125mm/min⁻¹, the cutting force P_a increases (fig. 2), which is explained by an increase in the cutting area in proportion to the feed.

The slight increase in the P_p force is explained by the insignificant increase in the friction force and the contact area of the chip with the front surface of the tool. The force P_p remains practically constant.

When the pitch of the ribs is less than 1 mm, the chip is obtained with a small thickness and is in poor adhesion to the substrate. Machining ribs with such a step is difficult, since the tool must have a minimum sharpening angle, and this leads to a decrease in its strength and to an increase in the cost of its manufacture [4, 5].
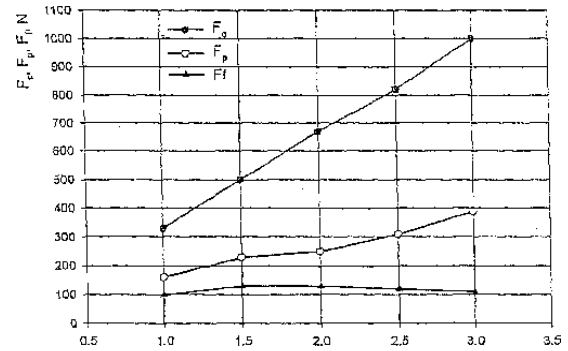
Fig. 2. Dependence of the cutting force on the feed

Increasing the pitch of the channels by more than 2 mm leads to an increase in the thickness of the sheared layer of material, the area of contact of the chip with the front surface of the tool increases, and therefore this leads to an increase in the frictional force, which significantly increases the components of the force of cutting P_e and P_p.

When determining the influence of the depth of cut on the components P_e and P_p of the cutting force (fig. 3), it was found that they increase as the thickness of the cut layer and, accordingly, its area increase. The value of P_p is insignificantly affected by the change in the depth of cut.
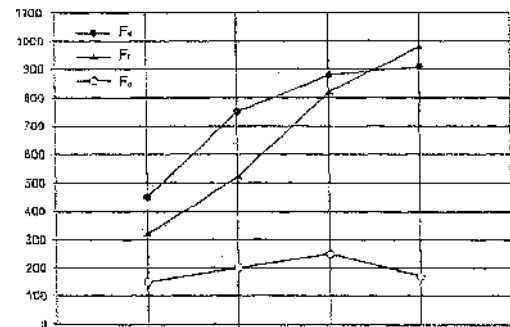
Fig. 3. Dependence of the cutting force on the cutting depth

When evaluating the energy losses in the different processing modes, a methodology [2] was used, according to which, during milling, the cutting speed V_c, the cutting force F_c and the power P_t are determined according to the dependencies [1]:

$$V_c = \frac{C_v \times D^q}{T^m \times a^x \times f_z^y \times a_c'' \times z^p} \times K_v, \text{m/min}; \quad (1)$$

$$F_c = \frac{10 \times C_p \times a_p^x \times f_z^y \times a_c'' \times z}{D^q \times n^w} \times K_{mp}, \text{N}; \quad (2)$$

$$N_c = \frac{F_c \times V_c}{1020 \times 60}, \text{kW} \quad (3)$$

Where: α_p is axial cutting depth, mm; f_z – tooth feed, mm; α_r – radial depth of cut; D – cutter diameter, mm; z – number of teeth; C_v, $C_{p,x,y,u,p,q,w}$ – correction coefficients and exponents; K_v, K_{mp} - coefficients considering the working conditions.

The productivity of the milling process P_p is calculated according to the formula [6]:

$$P_p = \frac{Q}{60 \times T} \qquad (4)$$

Where: Q is the volume of the cut layer, mm^3; T - time for processing the part, min.

III. RESULTS AND DISCUSSION

The results of the calculations of the productivity when milling aluminum alloys in different cutting modes are shown in fig. 4. The analysis of the graphs shows that the performance of chamfering with cutting modes determined by the traditional methodology is lower at small cutting depths, compared to those determined by the proposed methodology. This is explained by the incomplete power load of the feed translation of the machine when milling with modes determined according to the traditional methodology, when the feed and speed are determined by a set cutting depth. In order to increase the productivity of the milling process of aluminum alloys, it is suggested to initially set the maximum feed in accordance with the prescribed quality of the processed surface, and then, taking into account the power of the feed translation of the machine, calculate the depth and speed of cutting.
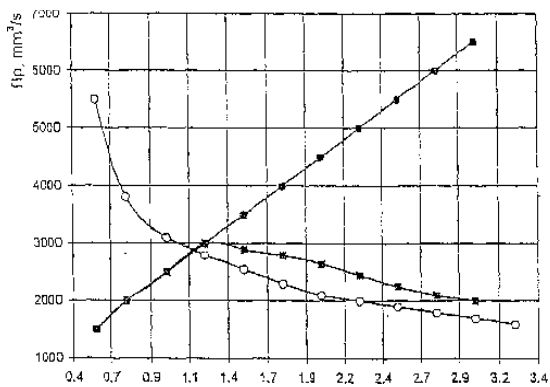
- traditional methodology; —O— developed methodology; —я— a traditional methodology accounting for equipment

Fig. 4. Milling performance in different cutting mode

To estimate the level of energy consumption when milling aluminum alloys with different cutting modes, the individual energy consumption coefficient K_{ef} (kWh/m^3) [6] is used, the value of which is determined by the formula:

$$K_{ef} = \frac{P_t \times T}{60 \times Q} \qquad (5)$$

where P_t is the cutting power, kW; Q — volume of removed material, mm^3; T - time for processing the part in min.

The results of the calculation of the coefficient of the individual energy consumption of the milling process of aluminum alloys in different cutting modes are presented in Fig.5.
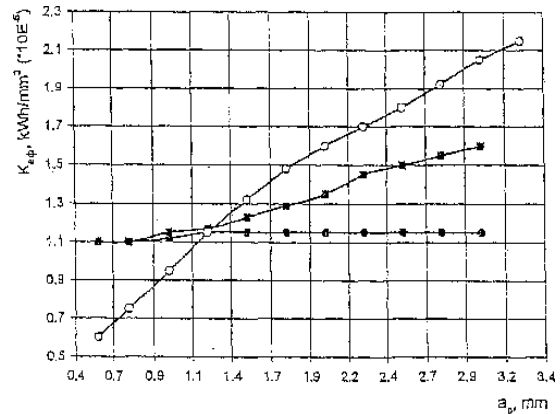
- traditional methodology; —O— developed methodology; —я— a traditional methodology accounting for equipment

Fig. 5. Energy losses during milling

The analysis of the graphs shows that the energy loss of the feed translation of the main movement of milling aluminum blanks with cutting modes determined in a traditional way are significantly lower than those proposed by the current methodology when loading the technological equipment at partial power [4]. At the same time, it should be noted that when calculating the cutting modes according to the proposed methodology, the technological equipment works at full power.

IV. CONCLUSION

Experimental studies have shown that when milling channels in flat aluminum alloys, the process should be carried out at a cutting speed of over 400 mm/min, a feed of 1 mm/min^{-1} and a depth of cut of over 1.5 mm.

In this case, the components of the cutting force either decrease or increase slightly, and the channels are milled with high productivity, good adhesion to the base, and ribbing of the surface with parameters that ensure high heat exchange characteristics. This improves the efficiency of the process and leads to better technical results under the existing machine parameters.

The comparative analysis of the methodology for setting cutting modes during milling shows that in terms of productivity and energy consumption, processing with the cutting modes proposed by the current methodology is more preferable when removing small allowances with large feeds. This opens up new opportunities for optimizing production processes and can contribute to increasing the overall economic efficiency of enterprises.

REFERENCES

[1] I. Balabanova, G. Georgiev, "Image Recognition by FFT, Artificial Intelligence and k-Nearest Neighbors Approach". IOP Publishing, Journal of Physics: Conference Series - EEPES'22, vol. 2339, pp. 1-8, 2022.

[2] A., I. Bastanstev, V., I., Turomsha, Pobm[enie efektivnosti obrabotki na tovarnih stankah s StPU, Mashinostroenia, Minsk, 2001.

[3] A.G. Kocilovii, I R.K. Madsteriakova – 4 izd., prerab. Idop., Spravochnik tehnologa-mashinostroitelia – Tom 2, Moskva, Mashinostroenia, 1985.

[4] I. Mitev, Optimizing the quantity of liquid phase at the sintering of powder construction materials from system Fe-Cu-Sn, 11th International Scientific Conference "TechSys 2022" – Engineering, Technologies and Systems, AIP Conf. Proc. 2980,

https://doi.org/10.1063/5.0184238 , Published by AIP Publishing. 978-0-7354-4814-8/$30.00, pp. 060017-1 to 060017-7.

[5] I. Mitev, Determining the diffusion coefficient in simultaneous saturation with boron and carbon of austenite alloyed with cooper in powder metallurgy structural materials, 11th International Scientific Conference "TechSys 2022" – Engineering, Technologies and Systems, AIP Conf. Proc. 2980, 060016-1–060016-8; https://doi.org/10.1063/5.0184239 , Published by AIP Publishing. 978-0-7354-4814-8/$30.00, pp. 060016-1 to 060016-8.

[6] Sabev, Sabi & Kasabov, Plamen, The effect of rate and cutting speed to surface roughness during hoe boring of aluminum with antivibration boring bar, Environment. Technologies. Resources., Proceedings of the International Scientific and Practical Conference. Volume 3, pp. 314-318. DOI:10.17770/etr2021vol3.6537, 2021.

[7] A.Vachev, Cutting the materials, Part 1 and Part 2, Plovdiv, 2000.

Improvement of Technological Processes to Reduce Total Inaccuracy during Boring Deep Holes

Angel Lengerov
Faculty of Mechanical Engineering
Technical University of Sofia,
Plovdiv Branch
Plovdiv, Bulgaria
anlen@tu-plovdiv.bg

Silviya Salapateva
Faculty of Mechanical Engineering
Technical University of Sofia,
Plovdiv Branch
Plovdiv, Bulgaria
sisisal@tu-plovdiv.bg

Georgi Levicharov
Faculty of Mechanical Engineering
Technical University of Sofia,
Plovdiv Branch
Plovdiv, Bulgaria
glevi@tu-plovdiv.bg

Abstract—**Ensuring accuracy of the shape of holes processed by boring is essential for increasing productivity and economy of the process. The great influence for ensuring the prescribed operational and quality indicators during boring is the stability of the technological system and in particular the total deformations. This determines the goal of the present development, namely reduction of elastic deformations and displacements of the elements of the technological system.**

Keywords— inaccuracy, facing, holes, deformations.

I. INTRODUCTION

A significant increase in the productivity and economy of machining when boring holes can be achieved by reduction of the errors, caused by the dissipation of the elastic deformations of the technological system. In the existing systems for controlling the elastic displacements during turning [1] – [14], the accuracy is increased by stabilizing the deformations of the support, which to the greatest extent determine the magnitude and character of change of the total deformation of the system. In order to determine the limiting element of the system during boring, which has a significant effect on the deformation, it is necessary to carry out studies for determining the technological system stability.

II. ANALYTICAL DETERMINATION OF ACCURACY IN THE TECHNOLOGICAL SYSTEM

A basic requirement toward the technological system for boring deep holes is to be stable under all applied operating modes. It has been proved [1] that when boring with a cantilever non-rotating boring bar by one-sided cutting, the necessary condition for stable operation is achieved when the inequalities are satisfied:

$$(2k-1)\frac{\pi}{2} \le \alpha \le k\pi, \quad (k=1,2), \text{ when } y>0 \qquad (1)$$

$$(k-1)\pi \le \alpha \le (2k-1)\frac{\pi}{2}, \quad (k=1,2), \text{ when } y<0 \quad (2)$$

where α is the angle between the feed directions and the adjustment speed.

In addition to the angle α, stability can be influenced by the magnitude of the adjustment speed. This is illustrated in Fig. 1, in which the angle α satisfies the inequality (1).
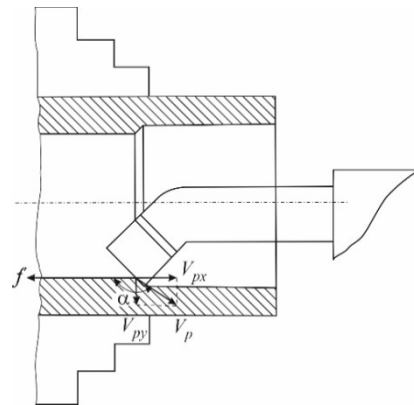
Fig. 1.

The adjustment speed can be represented by its two projections:

$$V_{px} = V_p \cos\alpha \qquad (3)$$

$$V_{py} = V_p \sin\alpha \qquad (4)$$

In cases when:

$$V_p \cos\alpha > fn ,$$

the main cutting edge separates from the cutting surface. Cutting is done by means of the auxiliary cutting edge and the system strives to achieve equilibrium under abnormal operating conditions. This is the beginning of an irreversible or self-oscillating process. To avoid this, the following inequalities must be satisfied:

$$\left| V_p \cos\alpha \right| < fn , \tag{5}$$

$$\frac{V_p \sin\alpha}{fn + V_p \cos\alpha} < fn . \tag{6}$$

From the inequality (6), an expression for determining the adjustment speed can be obtained.

$$V_p < \frac{fn\,tg\varphi_1}{\sin\alpha - \cos\alpha\,tg\varphi_1} fn , \tag{7}$$

where f is the feed in mm/tr; n – the revolutions in tr/min; φ_1 – the auxiliary setting angle.

In order to analyze the mechanisms for determining the elastic deformations in the technological system during boring by a boring bar, the schematic representation of the process shown in Fig. 2 is used.

$$Y = P_y W , \tag{8}$$

where P_y is the radial component of the cutting force; W − the susceptibility of the technological system.
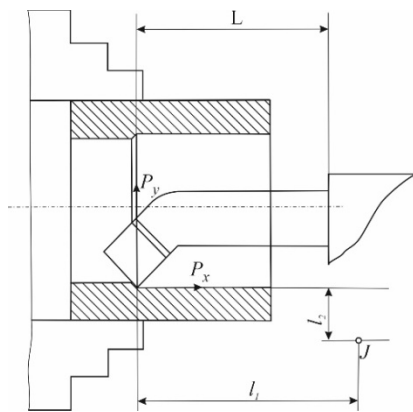
Fig. 2.

The susceptibility W of the technological system can be expressed as follows:

$$W = \frac{1}{j_{sup}} + \frac{L\left(l_1 + C_{xy}l_2\right)}{j_{\alpha_c}} + \frac{L^3}{3EI}\left(1 - C_{xy}\frac{R}{L}\right) \tag{9}$$

where j_{sup} is the stability of the support in the direction of the radial component of the cutting force;

$$j_{\alpha_c} = \frac{P_y l_1 + P_x l_2}{\alpha} - \text{the angular stability of the support;}$$

L − the arm (length) of the bar; l_1, l_2 − the arms, respectively, of the components P_y and P_x of the cutting force and the coefficient $C_{xy} = P_x/P_y$; E − the modulus of elasticity of the bar material; I − moment of inertia of the transversal cross section of the bar; R − the radius of the machined surface.

When boring by means of a boring bar, established on two flexible hinge supports, according to Fig.3 the susceptibility W of the technological system will be

$$
\begin{aligned}
W &= \left(1 - \frac{x}{L}\right)^2 \left(1 - C_{xy}\frac{R}{L-x}\right) W_{fs} + \\
&\quad + \left(\frac{x}{L}\right)^2 \left(1 + C_{xy}\frac{R}{x}\right) W_{rs} + \\
&\quad + \frac{x^2(L-x)^2}{3LEI}\left[1 + C_{xy}\frac{R}{x}\left(1 - \frac{x}{L-x}\right)\right]
\end{aligned} \tag{10}
$$

where x is the coordinate of the cutting area; L – the distance between the supports; W_{fs}; W_{rs} – susceptibility of the front and rear support, respectively.

From the expressions (8), (9) and (10) it follows that the error, and respectively the accuracy of the machined surface, obtained from the dissipation of the elastic deformation Y, when working with a cantilever boring bar, is mainly determined by the change of the cutting force in magnitude and direction.
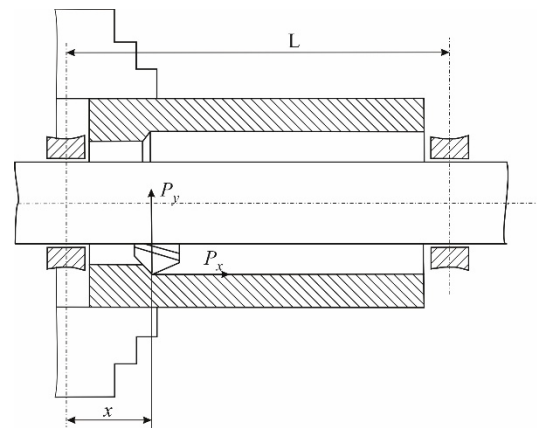
Fig. 3.

When working with a two-support bar, the change in the susceptibility W of the system, occurring when the coordinate of the cutting zone is changed (when a feed movement is implemented), is an additional source of error. Using formula (8), the following expression for the error from the elastic displacements can be obtained:

$$\varepsilon = Y_{min}\left(R_p R_\omega - 1\right), \tag{11}$$

where $Y_{min} = P_{y\,min} W_{min}$ is the smallest deformation of the technological system; R_p – the range of variation of the radial component of the cutting force for a batch of workpieces; R_ω – the range of variation of the

susceptibility of the system when processing one workpiece.

From the analysis of formula (11), it can be found that there is a possibility of increasing the accuracy by reducing $Y_{\min}$, using a lighter cutting mode. The proposed methodology will contribute to reducing the processing productivity.

The processing accuracy can also be increased by adjusting the size of dynamic tuning. A necessary condition is to maintain constancy of the elastic deformation Y of the technological system, i.e.

$$Y = P_y W = const \ . \qquad (12)$$

Using the empirical dependence for P_y, the condition (12) can be written in the form

$$Y = C_{Py} a_p^{\ x_{Py}} f^{\ y_{Py}} V^{\ n_{Py}} \left(HB \right)^{z_{Py}} W = const \ . \quad (13)$$

From equation (13) it can be seen that the constancy of Y can be ensured by adjusting the feed f, the geometry of the tool and the susceptibility of the technological system W.

If the tool geometry and the cutting speed are kept constant when adjusting the feed, for the range of feed adjustment, we get

$$R_s = \left(R_{a_p}^{\ x_{Py}} R_{HB}^{\ z_{Py}} R_\omega \right)^{\frac{1}{y_{Py}}} , \qquad (14)$$

where R_t is the range of variation of the depth of cut; R_{HB} –range of change in the hardness of the processed material.

When processing constructional steel by means of a carbide metal cutting tool, according to the data in [2], formula (14) takes the following specific form:

$$R_s = R_{a_p}^{1.5} R_{\sigma_B}^{2.25} R_\omega^{1.67} \qquad . \qquad (15)$$

When adjusting the geometry, according to [2], it is most appropriate to adjust the cutting angle δ in the range from 70 to 110°. For the adjustment range R_δ it can be written:

$$R_\delta = R_{a_p}^{0.34} R_{\sigma_B}^{0.51} R_\omega^{0.38} \qquad . \qquad (16)$$

A comparison between the expressions (15) and (16) shows that when adjusting the tool geometry, the adjustment range is significantly smaller. Besides, the variation of the cutting angle δ has a negligible effect on the roughness of the machined surface. Despite these advantages, the tool geometry adjustment is also characterized by some disadvantages, such as the complex construction of the boring tool and the need for a mechanism for small reversing displacements.

Feed adjustment is accomplished using a simple boring tool and a variable in magnitude feed rate, without reversal, which is why it is preferable. However, in order for it to be applied, it is necessary to have a sufficiently small range of adjustment.

When working with a cantilever boring bar, the susceptibility of the technological system changes slightly as a result of the wear of the cutting tool, and therefore the ranges of adjustment R_s and R_δ are mainly determined by the dispersion of the depth of cut and the hardness of the machined workpieces.

By choosing an appropriate magnitude of the smallest depth of cut, for a given workpiece size tolerance, R_{a_p} can be varied, and thus - the R_s and R_δ ranges.

The magnitude of the smallest depth of cut is determined by the expression:

$$a_{p\min} = \frac{\delta_D}{2\left(R_{a_p} - 1 \right)} \ , \qquad (17)$$

where δ_D is the tolerance of the hole in the workpiece.

This shows that when working with a cantilever bar, the dynamic tuning size adjustment can be successfully realized.

It should be noted that the vibration resistance of the system and the tool strength limit the possibilities regarding the depth of the processed hole.

III. CONCLUSIONS

From the obtained analytical dependences for susceptibility, mainly influencing the total inaccuracy of the technological system when boring holes by means of single- and double-support boring bars, it has been established that the process can be controlled. This can be realized by adjusting the technological parameters of the process, mainly influenced by the dynamic tuning of the technological system. The implementation of an adaptive control system for the boring process, carried out by a cantilever non-rotating boring bar, will contribute to increasing the accuracy and productivity of the machining process.

REFERENCES

[1] H. Metev, K. Krumov. Determination of inaccuracy by milling taking into account the phenomenon of technological heredity. 9TH International Scientific Conference "TechSys 2020" – Engineering, Technologies And Systems 14-16 May 2020, Plovdiv, Bulgaria. IOP Conf. Series: Materials Science and Engineering 878 (2020) 012049. doi:10.1088/1757-899X/878/1/011001.

[2] S. Sabev and P. Kasabov, The influence of feed rate and cutting speed to surface roughness during hole boring of AISI 304 with anti-vibration boring bar. AIP Conference Proceedings, (2022), 2449. 060004, DOI:10.1063/5.0091006.

[3] C. Deng, J. Chin, Hole roundness in deep-hole drilling asanalysed by Taguchi methods. Int J Adv Manuf Technol 25(5-6): 420–426, 2005.

[4] T. Aized and M. Amjad Received, Quality improvement of deep-hole drilling process of AISI D2, The International Journal of Advanced Manufacturing Technology 69(9-12), Published online: 8 August 2013 # Springer-Verlag London 2013, DOI:10.1007/s00170-013-5178-4.

[5] L. Francis, D Xavier, D. Elangovan, Effective Parameters For Improving Deep Hole Drilling Process By Conventional Method, International Journal of Engineering Research & Technology (IJERT) Vol. 2 Issue 3, March - 2013 ISSN: 2278-0181.

[6] F. Zou, J. Dang, X. Cai, Q. An, W. Ming, M. Chen, Hole quality and tool wear when dry drilling of a new developed metal/composite co-cured material. Proc. Inst. Mech. Eng. Part B J. Eng. Manuf. 234, 980–992, 2020.

[7] K. Sentyakov, J. Peterka, V. Smirnov, P. Bozek, V. Sviatski, Modeling of Boring Mandrel Working Process with Vibration Damper. Materials 13, 1931, 2020.

[8] L. Lie, S. Beibei, H. Haitao, H, Nonlinear system modeling and damping implementation of a boring bar. Int. J. Adv. Manuf. Technol. 104, 921–930, 2019.

[9] L. Kon et all., Complex nonlinear behaviors of drilling shaft system in boring and trepanning association deep hole drilling. Int J Adv Manuf Technol 45(3-4):211–218, 2009.

[10] C. Deng, J. Chin, Hole roundness in deep-hole drilling as analyzed by Taguchi methods. Int J Adv Manuf Technol 25:420–426, 2005.

[11] K. Weinert, O. Webber, C. Peters, On the influence of drilling depth dependent modal damping on chatter vibration in BTA deep hole drilling. CIRP Ann Manuf Technol 54(1):363–366, 2017.

[12] E. Kilickap, M. Huseyinoglu, A. Yardimeden, Optimization of drilling parameters on surface roughness in drilling of AISI 1045 using response surface methodology and genetic algorithm. Int J Adv Manuf Technol 52:79–88, 2021.

[13] G. Chern, J. Liang JM, Study on boring and drilling with vibration cutting. Int J Mach Tool Manuf 47(1):133–140, 2007.

[14] M. Amjad M, Parametric Analysis Based Quality Improvement of Deep Hole Drilling Process of AISI D2. M.Sc. Manufacturing Engineering thesis submitted to the University of Engineering and Technology, Lahore, Pakista, 2012.

Investigation of the Elastic Deformations of the Technological System during Turning of Rotary Surfaces

Angel Lengerov
Faculty of Mechanical Engineering
Technical University of Sofia,
Plovdiv Branch
Plovdiv, Bulgaria
anlen@tu-plovdiv.bg

Silviya Salapateva
Faculty of Mechanical Engineering
Technical University of Sofia,
Plovdiv Branch
Plovdiv, Bulgaria
sisisal@tu-plovdiv.bg

Martin Bojakov
Faculty of Mechanical Engineering
Technical University of Sofia,
Plovdiv Branch
Plovdiv, Bulgaria
bojakov@abv.bg

Abstract. **In the development, analytical dependencies have been derived for determining the stability of the technological system during turning of rotary parts. Cases such as establishment in a chuck, in dead center and between centers have been analysed. The results of the analytical studies will contribute post-processing accuracy to be determined and predicted.**

Keywords: elastic deformations, accuracy, turning.

I. INTRODUCTION

When performing mechanical processing operations, the system, consisting of the machine, the fixture, the tool, and the workpiece, and called a technological system, suffers a load from the cutting force, the mass of the machined workpiece, the equipment and the machine nodes, from inertial forces and forces of friction. Their action gives rise to displacements of the system elements within the limits of the existing clearances, contact deformations in the contact surfaces and volume deformations of the details. As a final result, the relative position of the workpiece and the tool is changed with respect to the position, achieved during fixing and static dimensioning and the accuracy of the dimensions, the shape and the relative position of the machined surfaces is disturbed.

The change in the relative position of the tool and the workpiece caused by the acting forces and measured in the cutting zone in the direction of dimensioning, is called force deformation of the technological system.

A lot of research work, theoretical and experimental studies have been carried out to determine the stability of a technological system when processing external cylindrical surfaces. The results contribute to increasing the accuracy of machining and creating an automated system, which is capable of predicting and controlling the accuracy of machining, based on the results of analytical and experimental research [1] – [12].

II. MATERIALS AND MRTODS

The paper presents a system for predicting the dimensions of the details during turning, which takes into account the flexibility of the workpiece, the inaccuracy of making the center holes and the error of fixing the workpiece in a chuck when processing.

The system involves determining of the actual radius of the detail, or the distance between the actual workpiece axis and the tip of the turner knife, based on a given input about tool geometry, cutting modes, material properties, fixing conditions, and the error in locating the workpiece.

Three variants of the model are possible:

- fixing in a chuck;
- fixing in a chuck and a specified center;
- fixing between centers.

In all these three cases, on the basis of input data, the program sets the value of the actual radius of the detail at each point of the surface with a specified step. The determining factor, affecting the change of the radius of processing or the value of the workpiece displacement is the axial cutting depth a_p, which, in turn, depends on the deformation of the workpiece, the inaccuracy of producing the center holes and the fixing error. To simplify the calculations, some assumptions are made for the model:

- zero susceptibility of the spindle and the rear center;
- ideal and uniform surface of the workpiece;
- no deflection of the tool.

A methodology for determining the actual radius of the detail is shown on the example of machining a workpiece, set in a chuck and a rear center. The two other cases, mentioned above, are private and obtained by excluding unexamined parameters.

The formula for calculating the actual cutting depth a_p^{∂}, taking into account the error of fixing the workpiece in the chuck Δ_Π, the displacement of the center holes Δ_{II} and the sagging of the workpiece Δ_Z under the action of the cutting force, has the following form [13]:

$$a_p^{\partial} = a_p + \Delta_\Pi + \Delta_{II} + \Delta_Z \qquad (1)$$

where a_p is the average set axial depth of cut:

$$a_p = R_Z - R_D;$$

R_Z, R_D are respectively the workpiece radius and the radius of the detail, set in the initial conditions;

Δ_Π – the displacement of the workpiece when fixing it in a chuck;

Δ_{II} – the displacement of the center holes;

Δ_Z – the magnitude of deformation of the workpiece under the action of the cutting force.

The workpiece displacement Δ_Π, expressing the error of locating the workpiece in the lathe chuck for one revolution (Fig. 1), can be determined using the circle displacement equation. Since the displacement of the rear center is assumed to be equal to zero, the equation has the form:

$$\Delta_\Pi = \sqrt{R_Z^2 - \left(L_0 / L_Z . \Delta_\Pi\right)^2 \sin^2\left(\varphi + \psi\right)} + \\ + \left(L_0 / L_Z . \Delta_\Pi\right)\cos\left(\varphi + \psi\right) - R_Z \qquad (2)$$

where L_0 is the distance from the tailstock centre to the considered section of the workpiece;

L_Z – the length of the workpiece from the chunk to the rear center;

φ - the angle of rotation of the workpiece;

ψ- the angle of non-coincidence of the displacements Δ_Π and Δ_{II}.
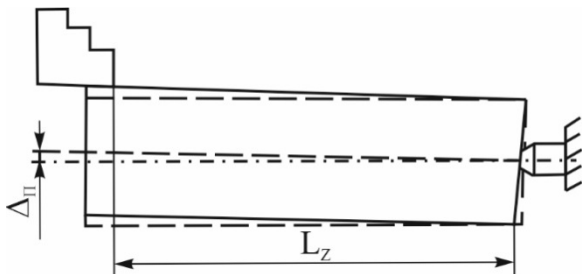
Fig. 1. Displacement of the workpiece as a result of its establishment in the chuck of the machine.

Similarly, the displacement of the workpiece Δ_{II}, resulting from an inaccuracy in the manufacture of the center holes, is determined (Fig.2), and the displacement of the workpiece due to an inaccuracy in locating it in the lathe chuck is not taken into account.

$$\Delta_{II} = \sqrt{R_Z^2 - \left(\frac{L_Z - L_0}{L_Z}\Delta_{II}\right)^2 \sin^2\varphi} + \\ + \frac{L_Z - L_0}{L_Z}\Delta_{II}\cos\varphi - R_Z \qquad (3)$$
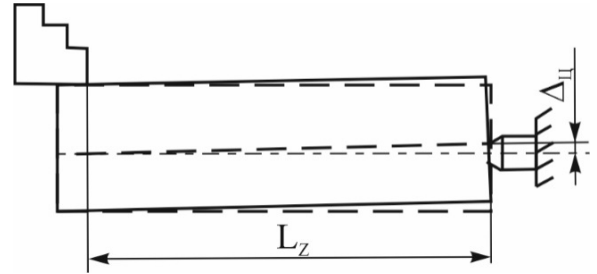
Fig. 2. Displacement of the workpiece as a result of an inaccuracy in the manufacture of the center holes.

The sagging of the workpiece A_z under the action of the cutting forces F_p and F_c in the direction of the axes y and z (Fig.3) is considered as a beam, established on two supports, and calculated according to the formula:

$$\Delta_{zy} = \frac{F_p L_0^2 \left(L_Z - L_0\right)^2}{3EIL_Z} \qquad (4)$$

$$\Delta_{zz} = \frac{F_c L_0^2 \left(L_Z - L_0\right)^2}{3EIL_Z} \qquad (5)$$

where E is the modulus of elasticity of the material of the workpiece.
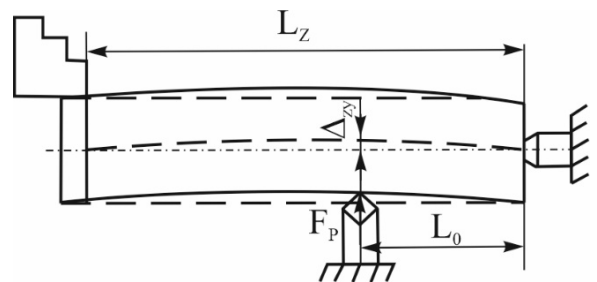
Fig. 3. Displacement of the workpiece as a result of the action of the cutting force F_p.

The dependence for calculating the actual depth of cut when establishing the workpiece in the chuck and the rear center is determined from the dependences (2) - (5) by the formula (1):

$$a_p^{\partial} = \sqrt{R_Z^2 - \left(L_0 / L_Z . \Delta_{\Pi}\right)^2 \sin^2\left(\varphi + \psi\right)} +$$
$$+ \left(L_0 / L_Z . \Delta_{\Pi}\right)\cos\left(\varphi + \psi\right) +$$
$$+ \sqrt{R_Z^2 - \left(\frac{L_Z - L_0}{L_Z}\Delta_{U}\right)^2 \sin^2\varphi} + \qquad \text{. (6)}$$
$$+ \frac{L_Z - L_0}{L_Z}\Delta_{U}\cos\varphi - R_Z - \sqrt{\left(R_D + \Delta_{zy}\right)^2 + \Delta_{zz}^2}$$

From the analysis of the obtained formula, it can be established that when the planes in which the displacements Δ_{Π} and Δ_{U} are located do not coincide, they compensate and complement each other, and the actual cutting depth changes.

By setting the displacements Δ_{Π} and Δ_{U}, and then calculating the deformation of the workpiece under the action of the cutting force at a set depth a_p, the actual cutting depth a_p^{∂} is found. Substituting its value in the empirical dependences for calculating the cutting force, the actual displacement of the workpiece is also determined.

The displacement leads to a change in the actual depth of cut, and thus to a change in the cutting force, which, in turn, results in a further change in the depth of cut. Such a method of calculation, used in the mathematical model, allows to determine the value of the actual radius of the workpiece for each point of its surface, taking into account the previous value.

III. RESULTS AND DISCUSSION

Increasing the technological system stability can be achieved by increasing its elements stability. It is influenced by all the forces that load the technological system, represented by the equivalent force F_e:

$$j = \frac{F_e}{\Delta} \qquad \text{. (7)}$$

The equivalent force F_e has the directrix coincident with F_p and creates a torque with respect to the instantaneous center of rotation of the technological system, equal to the sum of the torques, relative to this center, for all forces, acting in the system.

Fig. 4 shows a planar model of the technological system in which "flat cutting" is performed (without the presence of the force F_f). It clarifies the determination of the equivalent force.

From the condition of equality of torques, it follows

$$F_e = F \frac{l_1}{l_2} \text{ , } \qquad (8)$$

where l_1 and l_2 are, respectively, the arms of the cutting force and the equivalent force, relative to the instantaneous center of rotation O.

(a)

(b)
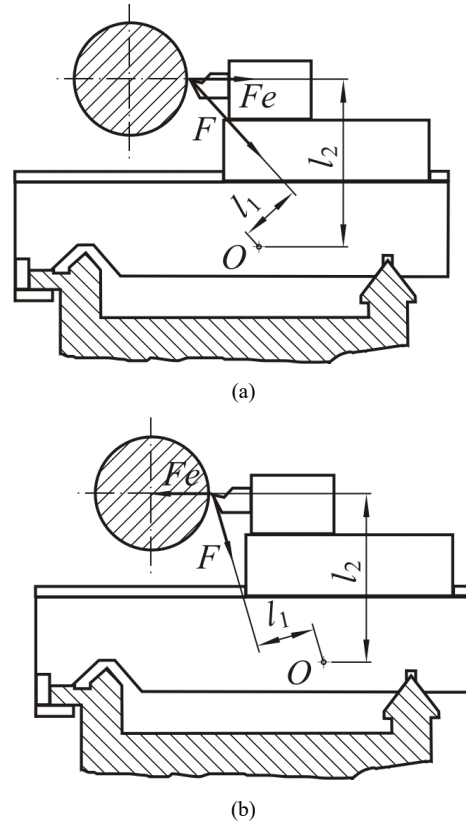
Fig. 4.

The force deformation of the system is obtained as a sum of the deformations of the machine, the fixture, the tool and the detail:

$$\Delta_{TC} = \Delta_M + \Delta_{\Pi P} + \Delta_H + \Delta_{Д} \qquad (9)$$

The deformation of each of the elements can be represented by the dependence:

$$\frac{1}{j_{TC}} = \frac{1}{j_M} + \frac{1}{j_{\Pi P}} + \frac{1}{j_H} + \frac{1}{j_{Д}} \qquad \text{. (10)}$$

Equation (10) gives the relationship between the system stability and stability of its elements, valid under the constraints of the spring model. Expressed by the susceptibilities, the dependence (10) takes the form:

$$W_{TC} = W_M + W_{\Pi P} + W_H + W_{Д} \qquad (11)$$

From (10) and (11) it follows that the increase in stability can be achieved with maximum efficiency by increasing the stability of the most unstable element. If the machine, the fixture, and the tool are stable enough, as it is during turning, but the workpiece is long and small in diameter, then, due to its low stability, the overall stability of the technological system will be low. To illustrate the method, examples of turning smooth long shafts will be presented (Fig. 5). For the example from Fig.5, the most unstable element of the system is the detail.

(a)

(b)
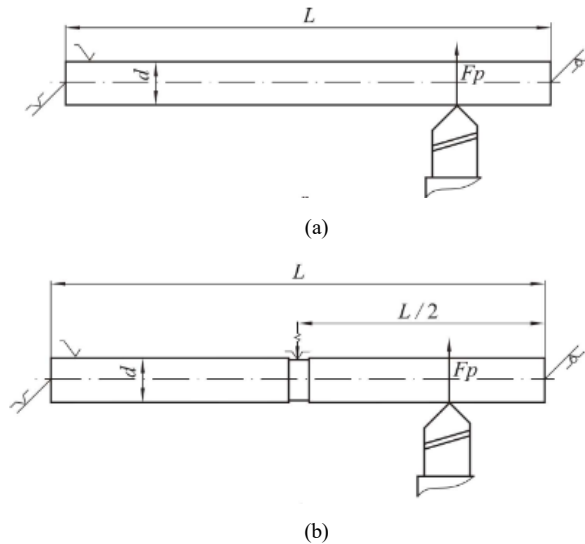
Fig. 5.

The deformation of the system is determined by the sagging of the detail under the action of the force F_p. The maximum value of the sag in scheme 5*a* is:

$$y_{max} = \frac{F_p L^3}{75 EI} \; .$$ (12)

If the turning is carried out on two sets using a stationary lunette, set in the middle of the detail (fig. 5*b*), the maximum sag will be:

$$y_{max} = \frac{F_p (0,5L)^3}{75 EI} = \frac{F_p L^3}{600 EI} \; .$$ (13)

From equations (12) and (13) it follows that when using a lunette, the sagging of the workpiece decreases 8 times. Therefore, a significant increase in the stability of the detail and, as a result, in the technological system stability, has been achieved.

IV. CONCLUSIONS

The proposed methodology for determining the magnitude of the elastic deformations in the technological system makes it possible to predict the accuracy of the rotary surfaces, processed by turning, and to reduce the number of experiments, necessary for the statistical studies of the parameters of the cutting process when machining rotary parts.

The obtained optimal dependences for calculating the deformations of the technological system facilitate the assessment of the accuracy indicators of the machined rotary surfaces.

REFERENCES

[1] A. S. Ymnikova, A. A. Malikova, Fundamentals of mechanical engineering technology. Moscow: Infra – Ingeneria Press, 2020.

[2] A. Świć, A. Gola, Theoretical and Experimental Identification of Frequency Characteristics and Control Signals of a Dynamic System in the Process of Turning. Materials, 14, 2260, 2021.

[3] A. Świć, D. Wołos, A. Gola, G. Kłosowski, The Use of Neural Networks and Genetic Algorithms to Control Low Rigidity Shafts Machining. Sensors, 20, 4683, 2020.

[4] B. Denkena, H. Boujnah, Feeling Machines for online detection Detection and Compensation of Tool Deflection in Milling, CIRP Annals, 67/1 (2018), pp. 423-426

[5] B. Denkena, M.A. Dittrich, S. Jacob, Methodology for Integrative Production Planning in Highly Dynamic Environments, Production Engineering, 13 (2019), pp. 317-324

[6] H. Metev, K. Krumov. Determination of inaccuracy by milling taking into account the phenomenon of technological heredity. 9TH International Scientific Conference "TechSys 2020" – Engineering, Technologies And Systems 14-16 May 2020, Plovdiv, Bulgaria. IOP Conf. Series: Materials Science and Engineering 878 (2020) 012049. doi:10.1088/1757-899X/878/1/011001.

[7] J. Yang, D. Aslan, Y. Altintas, Identification of Workpiece Location on Rotary Tables to Minimize Tracking Errors in Five-Axis Machining, International Journal of Machine Tools and Manufacture, 125 (2018), pp. 89-98

[8] M. Dobrzynski, K. Mietka, Surface Texture after Turning for Various Workpiece Rigidities, Machines, 9, 2021.

[9] S. Sada, Improving the predictive accuracy of artificial neural network (ANN) approach in a mild steel turning operation. Int. J. Adv. Manuf. Tech., 112, 2389–2398, 2021 .

[10] T. Inspergner, B. Mann, et al., Stability of up-milling and down-milling, part 1: alternative analytical methods. International Journal of Machine Tools and Manafacture, 43 (1), pp. 25-34, 2003.

[11] W. Arai, F. Tanaka, M. Onosato, Error Estimation of Machined Surfaces in Multi-Axis Machining with Machine Tool Errors Including Tool Self-Intersecting Motion Based on High-Accuracy Tool Swept Volumes, International Journal of Automation Technology, 12/5 (2018), pp. 680-687

[12] Y. Altintas, D. Aslan, Integration of virtual and on-Line machining process control and monitoring, CIRP Annals, 66 (2017), pp. 349-352

[13] S. Sabev, V. Bakarzhiev, and P. Kasabov. "The Effect of Feed Rate and Cutting Speed to Surface Roughness during hole boring of 32CrMoS4 with anti-vibration boring bar", (2023).

Detailed microstructural studies of amorphous Al-Ni-Si and Al-Ni-Si-Cu alloys during crystallization

Yana Mourdjeva
Institute of Metal Science, Equipment, and Technologies with Hydro- and Aerodynamics Centre "Acad. A. Balevski" at the Bulgarian Academy of Sciences
Materials Testing and Analyses
Sofia, Bulgaria
yana@ims.bas.bg

Kateryna Valuiska
Institute of Metal Science, Equipment, and Technologies with Hydro- and Aerodynamics Centre "Acad. A. Balevski" at the Bulgarian Academy of Sciences
Materials Testing and Analyses
Sofia, Bulgaria
katerina@ims.bas.bg

Yoanna Kostova
Institute of Metal Science, Equipment, and Technologies with Hydro- and Aerodynamics Centre "Acad. A. Balevski" at the Bulgarian Academy of Sciences
Materials Testing and Analyses
Sofia, Bulgaria
y_kostova@ims.bas.bg

Vanya Dyakova
Institute of Metal Science, Equipment, and Technologies with Hydro- and Aerodynamics Centre "Acad. A. Balevski" at the Bulgarian Academy of Sciences
Materials Testing and Analyses
Sofia, Bulgaria
v_diakova@ims.bas.bg

***Abstract*. Two types of rapidly solidified ribbons were obtained from the systems Al-Ni-Si and Al-Ni-Si-Cu. By XRD, TEM and DSC analysis the ribbons were proved to be amorphous. By annealing at 350⁰C nanocrystalline alloys were obtained. It was found that when the amorphous alloys are annealed at 190⁰C and 220⁰C, an unknown metastable hexagonal phase is presented, which could not be identified when annealing at 350⁰C is provided. Both studied alloys $Al_{74}Ni_{16}Si_{10}$ and $Al_{74}Ni_{15}Si_9Cu_9$ show that when annealed at 190°C a residual amorphous phase is observed. It is located mainly at the phase boundaries.**

Keywords: amorphous, nanocrystalline, phase analysis.

I.   INTRODUCTION

Amorphous and nanocrystalline alloys from Al-Ni-Si ternary system are of great science interest because of their unique combination of physical and mechanical properties. Many researchers paid attention to the study of the structure and properties of these materials [1] - [4]. However, information on the phase diagram of Al-Ni-Si and alloys based on it is limited [5], [6]. Al_3Ni and Al_3Ni_2 phases, which have orthorhombic and trigonal crystal lattices respectively, are known to exist in the range of increased aluminium content of the Al-Ni-Si phase diagram.

The authors of [7] - [10] had investigate alloy from Al-Ni-Si system and it was clarified that a metastable hexagonal phase is formed in amorphous Al-Ni-Si alloys upon annealing below a temperature of 200⁰C. This hexagonal phase is with crystal lattice parameters a = 6.55-6.59 Å, c = 3.83-3.86 Å. It disappears when the alloy is subjected to further annealing above 300⁰C.

In our previous work [11], $Al_{74}Ni_{16}Si_{10}$ and $Al_{74}Ni_{15}Si_9Cu_9$ alloys were investigated in the amorphous state and after annealing at 350⁰C. In the course of the investigation, it was found that the transformation of the microstructure from amorphous to crystalline proceeded in two steps and an unknown hexagonal phase was released, which disappeared after annealing at 350⁰C. To identify this metastable phase, further studies were conducted on the fine structure of the alloys.

The aim of the study was to investigate the phase characteristics of the amorphous alloys $Al_{74}Ni_{16}Si_{10}$ and $Al_{74}Ni_{15}Si_9Cu_9$ annealed at 190ºC and 220ºC and to determine the presence of the mentioned hexagonal phase at different annealing temperatures in the studied alloys.

II. MATERIALS AND METHODS

The investigated alloys $Al_{74}Ni_{16}Si_{10}$ and $Al_{74}Ni_{15}Si_9Cu_9$ were synthesised from the metals Al, Ni, Si and Cu with a purity of 99.99%. The ligatures and ribbon fabrication processes (Chill Block Melt Spinning method) were described in detail in our previous publication [12]. Annealing at 190ºC, 220ºC and 350ºC was performed to obtain the crystalline structure and to study the types of phases.

The chemical composition of the ribbons was determined using a HIROX 5500 scanning electron microscope (SEM, HIROX Europe, Limonest, France) with a BRUCKER EXDS system (BRUCKER Co., Germany).

Bruker D8 Advance powder X-ray diffractometer (Karlsruhe, Germany) with Ni-filtered Cu Kα radiation and a LynxEye solid state position sensitive detector was used. The PDF-2 (2021) database of the International Centre for Data Diffraction (ICDD) and the DiffracPlusEVA software package v.4.0 (Bruker AXS 2010-2014, Karlsruhe, Germany) were used for phase analysis.

Differential Scanning Calorimetry (DSC) analysis was performed on a STA 449 F3 Jupiter calorimeter connected to a QMS 403 Aëolos Quadro mass spectrometer in an Ar environment. The protective Ar flow rate in the apparatus during the analysis was 30 mL s-1 and the purge Ar flow rate through the samples studied was 20 mL s-1. The heating rate was 20 K min-1.

HRTEM JEM 2100, (JEOL Ltd., Japan) with an acceleration voltage of 200 kV in SAED and HRTEM modes was used for microstructural observation of the obtained alloys.

III. RESULTS AND DISCUSSION

The base alloy composition of Al-Ni-Si is close to eutectic and is optimal for producing an amorphous alloy. Based on research to combine good GFA, mechanical properties and corrosion resistance [13]-[15], the amount of copper added was set at 2 at. %. Taking into account the chemical analysis provided [11] and based on the results obtained, the designations of the alloys are $Al_{74}Ni_{16}Si_{10}$ and $Al_{74}Ni_{15}Si_9Cu_9$.

The XRD data are given in Table 1. The microstructure of the rapidly solidified $Al_{74}Ni_{16}Si_{10}$ and $Al_{74}Ni_{15}Si_9Cu_2$ ribbons is shown to be completely amorphous. The nature of the crystalline phases in the annealed samples was determined. From the phase composition data it can be seen that only three types of phases are present when annealed at 190ºC - hexagonal metastable, Al and Al_3Ni. The greatest variety of phases is recorded at annealing at 220ºC. The hexagonal phase is present in the alloys at annealing temperatures of 190ºC and 220ºC. At higher annealing temperatures, the amount of hexagonal phase is significantly reduced compared to the lower annealing temperature and is completely absent at annealing at 350ºC. The authors of [7] have shown that the hexagonal phase, which can be clearly determined, is formed from the amorphous phase in the sample annealed at 175ºC. During annealing at higher temperatures the hexagonal phase is transformed into three other phases, namely fcc-Al, Si and Al_3Ni phases.
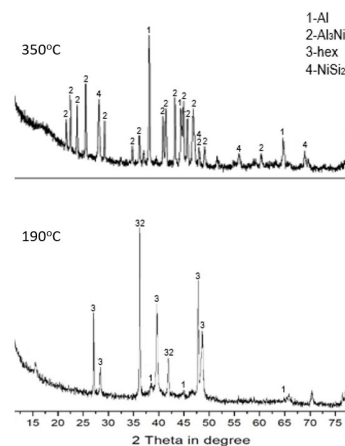
Fig. 1. The fragment of XRD diagrams of $Al_{74}Ni_{16}Si_{10}$ alloy annealed at 190°C and 350°C.

The TEM observations of the structure of alloys (Fig. 2) after annealing at 190°C contains small light inclusions, mainly at the phase boundaries. The presence of inclusions is not observed in the structures of the alloys during annealing at 220°C and 350°C. These inclusions could be a residual amorphous phase [7].
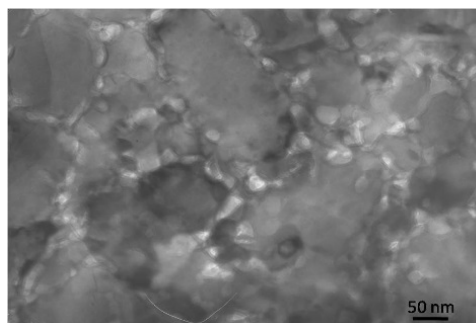
TABLE 1. DATA FROM XRD ANALISYS

State of the alloy	Defined phases	
	in $Al_{74}Ni_{16}Si_{10}$	*in $Al_{74}Ni_{15}Si_9Cu_2$*
Amorphous	-	-
Annealed at 190ºC	Al, Al_3Ni, hexagonal	Al, Al_3Ni, hexagonal
Annealed at 220ºC	Al, Al_3Ni, $NiSi_2$, hexagonal,Ni_3SiAl_5, Al_9Ni_2	Al, Al_3Ni, $NiSi_2$, hexagonal, Ni_3SiAl_5, Al_9Ni_2
Annealed at 350ºC	Al, Al_3Ni, $NiSi_2$	Al, Al_3Ni, $NiSi_2$, $Cu_{3.8}Ni$, $(Al,Cu)Ni_3$

(a)
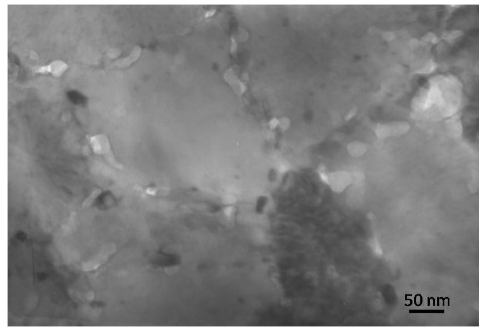
(b)
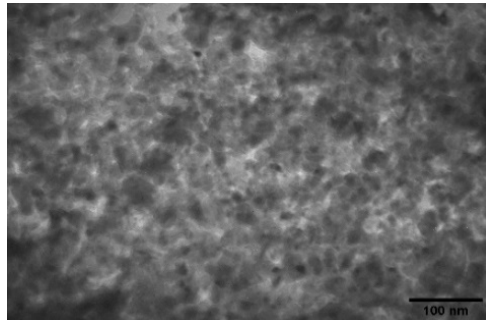
(c)
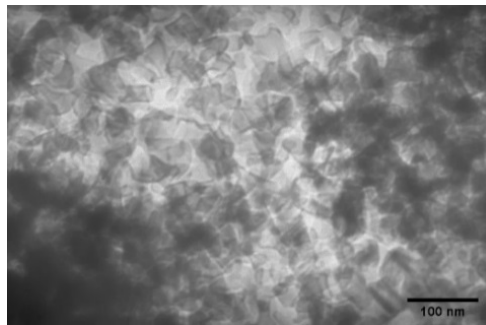
(d)

Fig. 2. Fig. 2 TEM images of (a) annealed at 190°C $Al_{74}Ni_{16}Si_{10}$ alloy; (b) annealed at 190°C $Al_{74}Ni_{15}Si_9Cu_2$ alloy; (c) annealed at 220°C $Al_{74}Ni_{16}Si_{10}$ alloy; (d) annealed at 220°C $Al_{74}Ni_{15}Si_9Cu_2$ alloy

Differential scanning calorimetry (DSC) studies were provided to determine the thermal resistance, transformation temperature intervals, phase transition temperatures and the crystallization mechanism in heating mode of the new $Al_{74}Ni_{16}Si_{10}$ and $Al_{74}Ni_{15}Si_9Cu_2$ alloys. Fig. 3 shows the results from DSC analysis of the alloys in the amorphous (a) and crystalline state after annealing in an argon atmosphere at temperatures of 190°C (463K) (Fig. 3 (b)), 220°C (493K) (Fig. 3 (c)) and 350°C (623 K) (Fig. 3 (d)) respectively. According to [7], the first peak at DSC diagrams corresponds to the crystallization of the amorphous phase and the crystallization of the hexagonal phase is presented between the first and the second endothermic peaks.

(a)   (b)
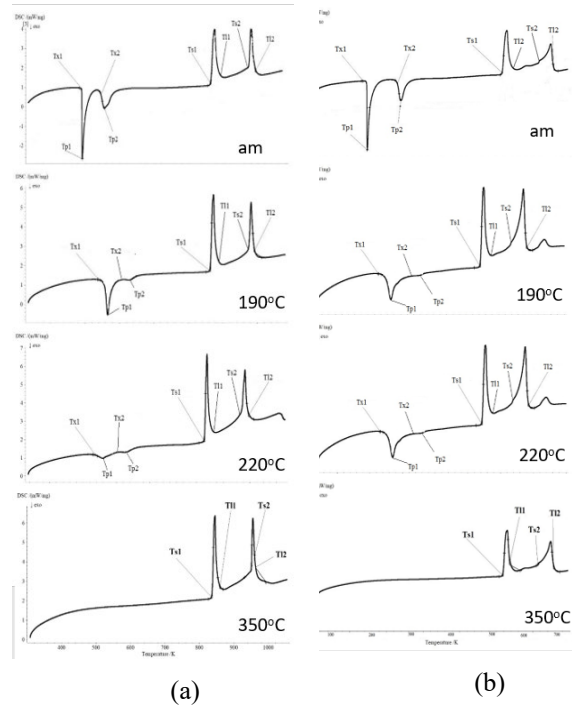
Fig. 3. DSC diagrams of (a) $Al_{74}Ni_{16}Si_{10}$ and (b) $Al_{74}Ni_{15}Si_9Cu_2$ alloys in amourphous state and annealed at different temperatures.

The peaks proving the content of amorphous part in the specimens of $Al_{74}Ni_{15}Si_9Cu_2$ annealed at 190°C are smaller than those of the specimens of $Al_{74}Ni_{16}Si_{10}$ annealed at the same temperature.

In [10] it was shown that the hexagonal phase has a specific outlines. In our TEM observations (fig. 4) a phase, whose morphology strongly resembles the one studied in [10], is observed in our structures.

Diffraction reflections correspond to a hexagonal close-packed structure, the reciprocal lattice plane (031), which may indicate the presence of a hexagonal phase. Diffraction rings can belong to different phases, fig.4 (b).
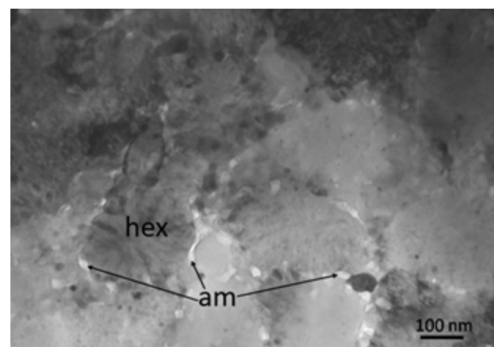
(a)
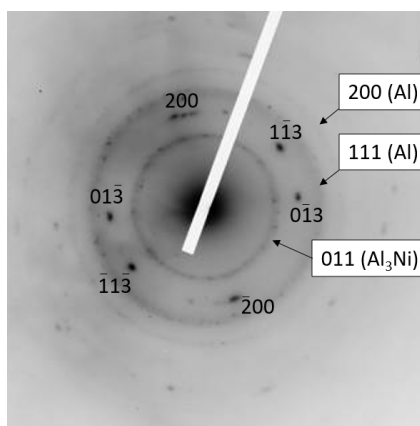
(b)

Fig. 4.   TEM observations of $Al_{74}Ni_{15}Si_9Cu_2$ annealed at 190°C - (a) BF image; (b) SEAD pattern

IV. CONCLUSIONS

The crystallisation of the amorphous alloys $Al_{74}Ni_{16}Si_{10}$ and $Al_{74}Ni_{15}Si_9Cu_9$ obtained by the CBMS method during continuous heating in the DSC proceeds in two stages in the temperature ranges (452÷453)K and (529÷535)K. In the first stage, the amorphous phase is transformed into fcc-Al and hexagonal phase, and in the second stage, fcc-Si and orthorhombic Al_3Ni phase are formed from the hexagonal phase. These processes were demonstrated by DSC heating of the alloys at 463K (190°C) and 493K (220°C). TEM structural observations of both $Al_{74}Ni_{16}Si_{10}$ and $Al_{74}Ni_{15}Si_9Cu9$ alloys annealed at 190°C showed a residual amorphous phase located at the phase boundaries of both the fcc-Al and hexagonal phases. It was found that after annealing at 350oC the transformation of the microstructure from amorphous to crystalline was complete and the metastable hexagonal phase was not observed.

ACKNOWLEDGEMENTS

REFERENCES

[1] B.-J. Yang, J.-M. Yao, Y.- S. Chao, J.-Q. Wang, E. Ma, "Developing aluminum-based bulk metallic glasses, " Philos. Mag., vol. 90, 2010, p.p. 3215–3231.

[2] S. Pauly, S. Gorantla, G. Wang, U. Kühn, J. Eckert, "Transformation-mediated ductility in CuZr-based bulk metallic glaases," Nat. Mater., Vol. 9, 2010, p.p. 473–477.

[3] S.–Y. Kim, G.-Y. Lee, G.-H. Park, H.-A. Kim, A.-Y. Lee, S. Scudino, K.-G. Prashanth, D.-H. Kim, J. Eckert, M.-H. Lee, "High strength nanostructured Al based alloys through optimized processing of rapidly quenched amorphous precursors," SCIENTIFIC REPORTS, vol. 8, 2018, p. 1090, DOI:10.1038/s41598-018-19337-7.

[4] J. Ma, F. Ren, G. Wang, X. Yi, Y. Li, J. Wen, "Electrochemical performance of melt-spinning Al-Mg-Sn based anode alloys," Int. J. Hydrogen Energy, vol. 42, 2017, p.p. 11654–11661.

[5] K. W. Richter, H. Ipser, "The Al–Ni–Si phase diagram between 0 and 33.3 at.% Ni," Intermetallics, vol. 11, 2003, p.p. 101–109

[6] G. Beuers, C. Batzner, H.L. Lukas, In: Petzow G, Effenberg G, editors. Ternary alloys, vol. 7, 1993. p. 467

[7] Mgr. J. Zigo, "Local structure in rapidly-quenched al-si based systems," Dissertation Thesis, 2017.

[8] O.S. Muratov, O.S. Roik, V.P. Kazimirov, N.V. Golovataya, V.K. Nosenko, G.M. Zelinskaya, T.M. Mika, V.E. Sokol'skii, "X-ray diffraction studies of the Ni–Si and Al–Ni–Si melts," Journal of Molecular Liquids 200, 2014, p.p. 213–222

[9] M. Gögebakan, M. Okumus, "Structure and crystallization kinetics of amorphous Al–Ni–Si alloy," Materials Science-Poland, Vol. 27, No. 1, 2009, p.p. 78–87

[10] J. M. Legersy, M. Audier , P. Guyot "Characterization and Kinetics of the Crystallization of AI-Ni-Si Amorphous Alloys," Materials Science and Engineering, 97, 1988, p.p. 385-390.

[11] V. Dyakova, Y. Mourdjeva, H. Spasova, G.Stefanov, Y. Kostova, "Effect of Cu as Minority Alloying Element on Glass Forming Ability and Crystallization Behavior of Rapidly Solidified Al-Si-Ni Ribbons, " Environment. Technology. Resources. Rezekne, Latvia Proceedings of the 14th International Scientific and Practical Conference. Vol. 3, 2023, p.p 69-73

[12] V. Dyakova, G. Stefanov, I. Penkov, D. Kovacheva, N. Marinkov, Y. Mourdjeva, S. Gyurov, "Influence of Zn on Glass Forming Ability and Crystallization Behaviour of Rapidly Solidified Al-Cu-Mg (Zn) alloys," J. Chem. Technol. Metall., vol. 57, 2020, p.p. 622–630.

[13] J.-H. Perepezko, R.-J. Hebert, "Amorphous aluminium alloys— Synthesis and stability," JOM, vol. 54, 2002, p.p. 54, 34–39.

[14] T. Egami, Y. Waseda, "Atomic size effect on the formability of metallic glasses," J. Non-Cryst. Solids, vol. 64, 1984, p.p. 113–134.

[15] X. Xue-Kui, T.-S. Magdalena, L. Yan-Hui, W. Wei-Hua, W. Yue, "Structural changes induced by microalloying in Cu46Zr47−x Al7Gdx metallic glasses," Scr. Mater., vol. 61, 2009, p.p. 967–969.

[16] K.L. Sahoo, R. Sahu, "Glass transition and crystallization of Al–Ni–La based metallic glasses studied by temperature modulated DSC", Journal of Non-Crystalline Solids, 365, 2013, pp. 33-36,

A Digitally Manipulated Gunshot Sound Identification

Stoyan Madzharov
Vasil Levski National Military University,
V. Tarnovo, Bulgaria
smadjaroff99@gmail.com

Ivan S. Ivanov
Dep. CIS
Vasil Levski National Military University,
V. Tarnovo, Bulgaria
ivanov_ivan@nvu.bg

Nayden Yordanov
Dep. CIS
Vasil Levski National Military University,
V. Tarnovo, Bulgaria
nkyordanov@nvu.bg

Abstract. **It is actual problem to distinguish between real gunshot sound pictures from tactical weapons and from fabricated or manipulated ones.**
In this work, some possible approaches to digital manipulation detection in gunshot records are described. The study uses methods of temporal and spectral analysis, revealing fine changes in signals, in a comprehensive dataset that consist of the raw data of gunshot sounds.
The purpose of the work is to consider some approaches to digital manipulation detection in gunshot records
High accuracy in the identification of manipulated sounds is demonstrated, with a low percentage of false positives and a high percentage of true positives.
This research lays the groundwork for a comprehensive database of gunshot signals. This database has potential value for further analysis using methods like the Continuous Wavelet Transform.

Keywords: gunshot analysis, digital manipulation detection, audio authentication.

I. INTRODUCTION

Recently, various methods of identifying tactical firearms, based on gunfire audio signals data, have been demonstrated. In general, they used Deep learning methods, as can be seen in the works [1], [2]. They demonstrate the powerful capability to extract essential features of datasets from some sample sets. So, the deep learning sound recognition has gradually become the mainstream research direction.

The methods for gunshot recognition proposed by researchers at present have their own advantages and disadvantages. If it is needed to work in real-time the difficulties are connected with the large amount of model calculation and high hardware requirements.

Sometimes recordings are captured on a phone microphone and they have a low fidelity, non-professionally recorded audio.

It is known that in case of recording of guns and explosions, that their accurate representation on a recorded medium is a complicated problem because they are too loud to reproduce in with any authenticity. The real gunshots are not so attractive as the movies unless one is very close to them.

The aim of the work is to consider some approaches to digital manipulation detection in gunshot records.

The collection of raw acoustic data, as well as their processing in field conditions, is invariably accompanied by certain difficulties. So, during tactical training on a training range, the registration and primary processing of signals is under the influence of noises which have a different character. Numerous approaches are known for their reduction of the noises, some of which can be seen in [3], [4].

On the other hand, additional techniques can be used in post-processing. When extracting knowledge from data - data mining, it is important to study the properties and character of random processes, realizations of various noises. In the work [5] application of wavelet packet entropy to such algorithms is considered. Some current algorithms for statistical analyzes are presented in Angelova-Slavova's work [6]. An approach to the study of acoustic noises by means of wavelet transformations is shown in the works [7] and [8]. Also, statistical processing using computer software is presented in [9].

Some problems for detecting the manipulation of sound signal recording are that they face the following challenges [10]

- Compression: Lossy audio compressions typically contain some form of non linear quantization together with selective frequency reduction.

- Channel effects: Transmitting compressed audio through a channel might induce transmission related data loss such as packet loss, noise and more. Channels for example can be VoIP, landline, cellular or satellite.

- Bandwidth differences and filtering: Audio codecs can differ by bandwidth, as some codecs are narrow band and others are wide band.

- Unseen spoof attacks: One of the main challenges of an anti spoofing system is to generalize and to detect unseen attacks from an unknown distribution.

II. Sound data set collection

When working in field conditions (besides the standard temperature, pressure, humidity), the following environmental conditions are significant: the presence of an open space or forest; signal strength or noise; the distance between the source and the recording device; wind strength and direction; the direction of the sound relative to the recording devices.

Here are regarded some examples from sound data sets.

A. Hail dropping strikes

For example, the noise spectral characteristics of hail dropping strikes in urban environment have been analysed in [11]. In this study, the spectra of two hail storm recordings were compared. One recording (see Fig. 1) was made with professional hardware (Brüel & Kjær 3560-B-110 and measurement microphone 4193), while the other was extracted from a video clip on the "Severe Weather Europe" website.) Analysis revealed strong low-frequency spectral components in the recording made with professional hardware. However, these low-frequency components were absent in the recording sources from the online report.
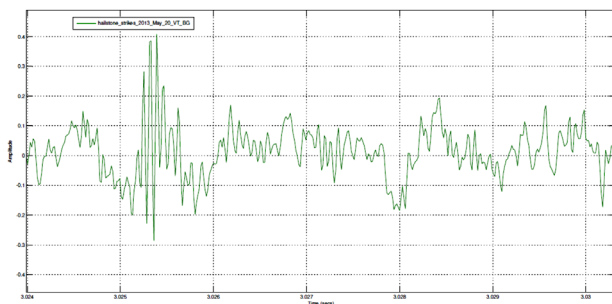
Fig. 1. Part of hail dropping strikes noise (in urban environment), 6ms duration, sample frequency 2to16 samples. See [11].

Figure 2 illustrates the estimated power spectrum density components for a sample of hail dropping strike noise.
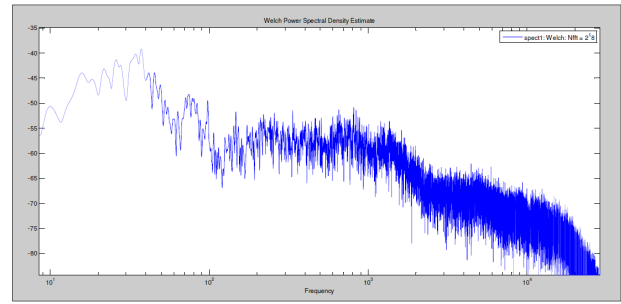
Fig. 2. The smoother spectral components, in dB, bandwidth 10 Hz – 20kHz for noise of hail STFT, Hanning window, overlap 0.5, Welch method, sample freq. 65536Hz. 20 May 2013,V. Tarnovo, BG.

Figure 2 shows the signal's power spectral density (PSD) calculated using the Welch method with a Hanning window. The analysis focused on the 10 Hz – 20 kHz bandwidth, which is relevant to the noise of hail (sample frequency 2-16 Hz). Strong spectral components are visible within the 20 Hz to 40 Hz range.

B. Sound of thunder

This section examines the noise spectral characteristics of thunder, drawing upon studies [13, 14]. A thunder noise recording was made in June 2012 using professional-grade equipment (Brüel & Kjær 3560-B-110 and measurement microphone 4193). This recording provides a high-quality sample for analysis.
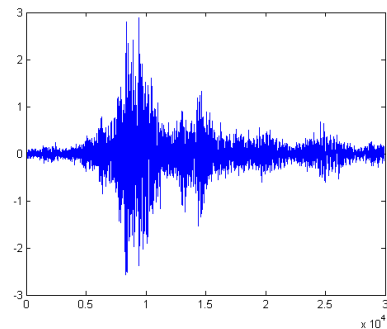
Fig. 3. Record of a thunder noise, Brüel&Kjær 3560-B-110 and the measurement microphone 4193 June 2012,V. Tarnovo, BG., [14]
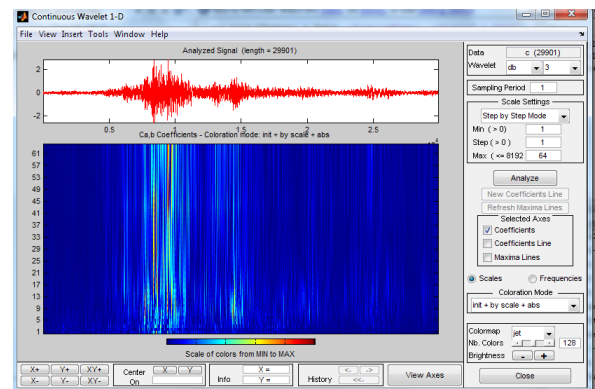
Fig. 4. Scalogram, Continuous Wavelet Transform of thunder record, [14].

It is known that thunders produce very large dynamic pulses with a frequency range extending beyond audible sounds, including infrasound waves (frequencies below 20 Hz).

C. Manlicher carbines firing sound

The next sounds that are considered are the pulse noises from firing with carbine in field demonstrations.

The experimental work was held at the Belyakovets training area, near V. Tarnovo during the tactical exercises on the 29th Apr. 2021,. Weather conditions was favourable: air temperature 11.6°C-13.4°C, wind speed 0.4 m/s, atm. pressure 1016 hPa, air humidity: 67-77%.

Specifically, the signals were from firing of Manlicher carbines, which were in service with the Bulgarian Army during the wars of the early 20th century, [12].

The sound sources are on level ground, with a concrete building nearby that also introduces acoustic reflections.

The experimental set-up is on a wooden tower, located in the grassy part of the range, at a height of three meters above the surface.

The setup includes precision instrumentation: the Brüel & Kjær Data Acquisition Unit 3560-B-110 and 1/2" Pressure-field microphone 4193.

Impulse signals and noise was seen in the field on a real time scale using constant percentage bandwidth - CPB or 1/3-octave analysis with the PULSE Labshop module 7771, see Fig 5,6.
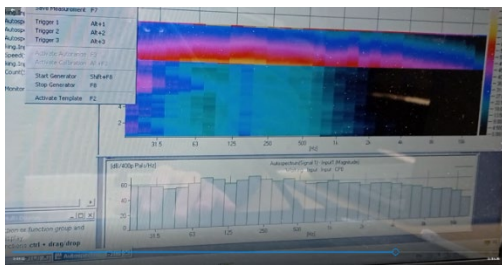
Fig. 5.   CPB - real-time analysis, fragment 1, [12].
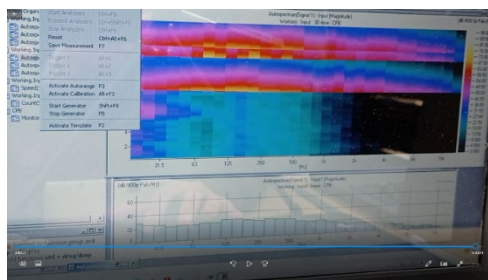
Fig. 6.   CPB - real-time analysis, fragment2, [12].

III. SOUND SIGNAL RECORDING AND AUTHENTICITY

The work of Raponi et al. [1] explores audio-based firearm identification. They created a dataset of 59 firearm types from YouTube videos and developed a convolutional neural network (CNN) for firearm classification. Their CNN achieved over 90% accuracy in identifying the category, caliber, and model of firearms from audio recordings.

It is interesting that they introduced a novel technique that requires zero knowledge about the recording setup and it is completely agnostic to the relative positions of both the microphone and shooter.

In Jian Li et all paper [2], is proposed an efficient method of gunshot recognition, which uses multi-layer neural networks to extract the representation features in the log-mel gunshot spectrogram, see Fig.7, so as to fully tap the relevant information between gunshot spectrum.
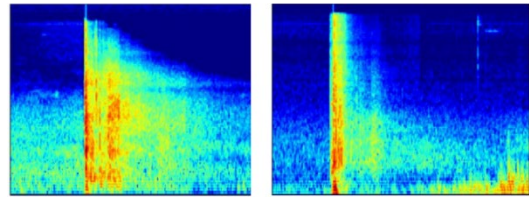
Fig. 7.   Spectrograms of AK-47 gun sound in left YouTube gunshots dataset; in right NIJ Grant gunshots dataset, [2].

These solutions will improve the gunshot recognition method, initialize the weight of the network model by means of large dataset pre-training.

Many raw recordings of a variety of natural noises as well as impulse noises from tactical fire systems in field tests were collected [14],[15].

Reference [13] discusses signal processing methods like Continuous Wavelet Transform (CWT) and conformal maps for identifying non-stationary acoustic signals with a large dynamic range and wide frequency bandwidth. The study found that the conformal representation of the scalogram improves the visualization of these signal's special features.

As can be seen, Fig.8 CWT and conformal maps, gives some advantages for signal irregularity detection.
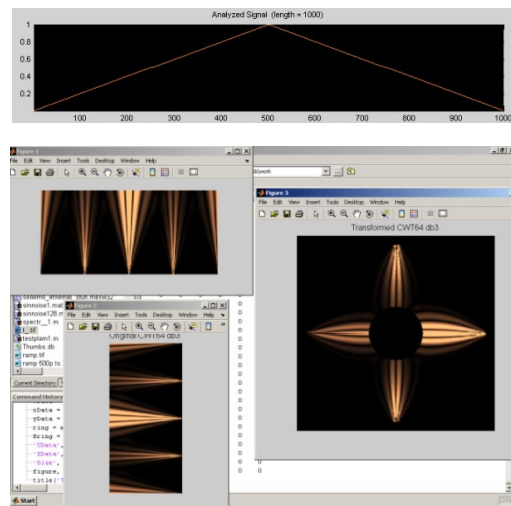
Fig. 8.   Conformal map of Continuous Wavelet Transform for triangle pulse with breaks, [13].

Wavelet transform work as mathematical microscop and can help to make detail analysis of analysis of sounds discontinuity.

Next pictures show te examination of a pistol shot, Fig. 9,10.
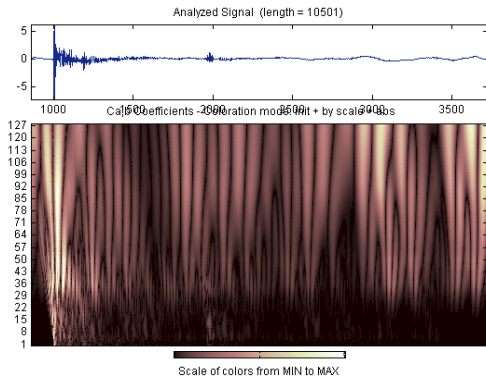
Fig. 9.   Scalogram of the pistol shot, [13]
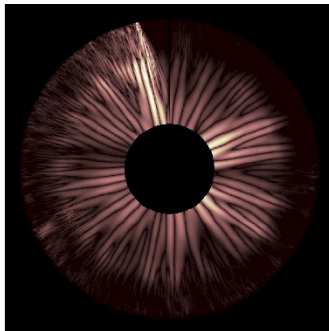
Fig. 10. Sound print of the pistol shot, [13]

Many signals obtained from the field recordings were exported in 32-bit wave format to MATLAB, where spectral analysis and CWT was performed. One example of guns scalograms are shown at Fig. 11, see [15].

This project collected a variety of raw recordings, including natural noises and impulse noises from field tests of tactical fire systems. The use of scalograms for building deep learning datasets is proposed.

IV. Conclusions

The digital manipulation detection techniques discussed in this study have direct applications in the analysis of raw acoustic pulse noises from gunshots. In addition, our collected from tactical field tests impulse noises may use as large dataset for initialization of network model weights and conformal representations of their scalogram may improve their visualization.

AK-47	
Armored battle machine – BMP-23	
73 mm anti-tank rocket launcher	
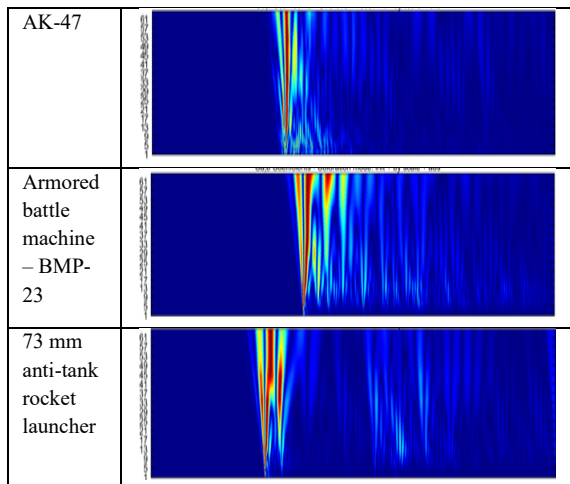
Fig. 11. Scalograms of CWT, [15]

Finally, this research lays the groundwork for a comprehensive database of gunshot signals. This database has potential value for further analysis using methods like the Continuous Wavelet Transform (CWT).

V. Acknowledgments

References

[1] S. Raponi, G. Oligeri and I.M.Ali "Sound of guns: digital forensics of gun audio samples meets artificial intelligence," Multimedia Tools and Applications, vol. 81, pp. 30387–30412, 2022. https://doi.org/10.1007/s11042-022-12612-w

[2] Jian Li, Jinming Guo, Mingxing Ma, Yuan Zeng, Chuankun Li, and Jibin Xu "A Gunshot Recognition Method Based on Multi-Scale Spectrum Shift Module" Electronics, vol. 11, no. 23: 3859. 2022 https://doi.org/10.3390/electronics11233859

[3] N. Priyadarshani, I. Castro, S. Marsland The impact of environmental factors in birdsong acquisition using automated recorders. Ecology and Evolution;vol.8, Iss. 10; pp. 5016-5033. 2018, https://doi.org/10.1002/ece3.3889

[4] T. Trifonov, I. Simeonov, N. K. Yordanov, "Advanced Signal Processing Methods For Analysis Of High Dynamic Range Acoustic Phenomena," Proc. 13th Conf. on Communications, Electromagnetics and Medical Applications (CEMA'18), Sofia, Bulgaria, Oct. 18-20, 2018, pp. 52-56, ISSN: 1109-1606.

[5] I. Simeonov, T. Trifonov, T. Georgieva-Trifonova "Signal processing and storing of high dynamic range acoustic data for knowledge discovery, " Proc. 14th International Engineering Conference on 'Communications, Electromagnetics and Medical Applications' (CEMA'19), Sofia, Bulgaria, 17-19 Oct. 2019, pp. 58-62

[6] R. L. Angelova-Slavova, Convergence and applications of the Metropolis-Hastings Algorithm. 2020, Plovdiv: Astarta, ISBN 978-954-350-284-4 (in Bulgarian) Р. Л. Ангелова-Славова, Сходимост и приложения на алгоритъма на Метрополис-Хестингс, 2020, Астарта, Пловдив, ISBN 978-954-350-284-4

[7] N. Yordanov Noise characteristics in tactical trainings, Proc. Annual University Scientific Conf., Vol. 9, 2021, Veliko Tarnovo, National Military University Press, Bulgaria, pp. 182-191 (in Bulgarian), Йорданов Н. К. Характеристики на шумовете при тактически тренировки, Сборник доклади от Годишна университетска научна конференция, 2021, т.9, Издателски комплекс НВУ „В.Левски", с. 182-191, ISSN 1314-1937

[8] I. Simeonov An Analysis of Uncertainty and Statistics of High Dynamic Range Acoustic Signals, Proc. of 15th International Conference on Communications, Electromagnetics and Medical Applications (CEMA'21), Athens, Greece, KING 2001, Sofia, October 21th, 2021, pp. 10-14, ISSN: 1314-2100

[9] R. L. Angelova-Slavova Probability and Statistics with Computer, Plovdiv: Astarta, 2023, (in Bulgarian) ISBN 978-954-350-341-4, Р. Л. Ангелова-Славова, Вероятности и статистика с компютър: монография, Пловдив: Астарта, 2023, стр. 192

[10] A. Cohen, I. Rimon, E. Aflalo, H. H. Permuter, A study on data augmentation in voice anti-spoofing, Speech Communication, Volume 141, 2022, pp. 56-67, ISSN 0167-6393, https://doi.org/10.1016/j.specom.2022.04.005.

[11] I. S. Ivanov and É. Hajnal, "Characteristics of Hail Dropping Noise in Urban Environment," Journal Mathematics, Computer Science and Education vol. 1, no. 1, pp. 37–43, 2018, St. Cyril and St. Methodius University of V. Tarnovo, Bulgaria, ISSN: 2603-4670 (Print)

[12] I. S. Ivanov and Zh. Mihneva Real time processing of acoustic pulse signals, Proc. of Conference "Actual Problems of Security", Veliko Tarnovo, National Military University Press, pp.301-308, 2022, Vasil Levski NMU – V. Tarnovo, ISSN 2367-7465 (in Bulgarian), Иванов И., Ж. Михнева Обработка на акустични импулсни сигнали в реално време, Сборник доклади от научна конференция "Актуални проблеми на сигурността", Изд. к-с НВУ "Васил Левски", В. Търново, 27-28.10.2022г., стр.301-308.

[13] T. Trifonov,G. Dimkov, R. Dzhakov, I.Simeonov "Use of conformal mapping method for visualization and classification of acoustic signals" XXIII conference with international participation Niś, Serbia 2012,pp.208-212

[14] R. Dzhakov, Studying Methods of Wavelets in Integrated Radio Systems, PhD Thesis, Vasil Levski NMU, Shumen, Bulgaria, 2013

[15] N. K. Yordanov, Research of economic algorithms for a fast transformation in modern radio communication systems, Abstract of PhD Thesis, Vasil Levski NMU, Shumen, Bulgaria, 2019.

Electric Generator Model Research (Stage Efficiency of Electromechanical Part)

Matutis Vaidotas
Faculty of electronics and informatics,
Vilniaus Kolegija/Higher Education Institution
Vilnius, Lithuania
v.matutis@eif.viko.lt

Savulioniene Loreta
Faculty of electronics and informatics,
Vilniaus Kolegija/Higher Education Institution
Vilnius, Lithuania
l.savulioniene@viko.lt

Kasperavicius Tomas
Faculty of electronics and informatics,
Vilniaus Kolegija/Higher Education Institution
Vilnius, Lithuania
t.kasperavicius@eif.viko.lt

Savulionis Dainius
Faculty of electronics and informatics,
Vilniaus Kolegija/Higher Education Institution
Vilnius, Lithuania
d.savulionis@eif.viko.lt

Abstract. **The article presents interim results of an ongoing continued study (https://doi.org/10.17770/etr2023vol3.7261). At this stage, measurements are made on a model in which two cavities for magnets and coils are already provided in the turned-wing impeller. The cavities contain mounted magnets that rotate with the impeller around to the housing stationary mounted coils. We already have two independent power generators. In the initial stage, these two generators were selected with coils of different inductance and the voltage and current generated by them were measured. The goal is to find out the possibilities of efficiency using a comparative method, as well as the dependence of the parameters of the generated energy on the speed of the air flow. In the experiments, the speed of the air flow, the area of the air inlet and the area of the air outlet were varied. A rather large amount of data was received, the processing of which will still have to be worked on, but the general trends of the dependence of the extracted electricity parameters not only on the air flow speed, but also on the geometric parameters of the ducts (in this case, the areas of the openings) became apparent. The general parameters of the generated current are already obtained at values suitable for practical use, because in the previous stage of research these values were insufficient to achieve the level of the practical efficiency factor. The article discusses the results of the experiments, observed trends, presents generalizations and conclusions, and predicts directions for further research.**

Keywords: robotic system, electricity generator, regeneration, electricity, wind.

I. INTRODUCTION

The configuration of the model impeller selected for research was determined by the results of previously conducted and published research and experiments [6], [7]. The last article presents interim results of an ongoing study was https://doi.org/10.17770/etr2023vol3.7261 [5]. At this stage, measurements are made with a model in which two cavities for magnets and coils are already provided in the turned-wing impeller. The cavities contain magnets that rotate with the impeller around the in housing stationary mounted coil. We already have two independent power generators as shown in Fig. 1.
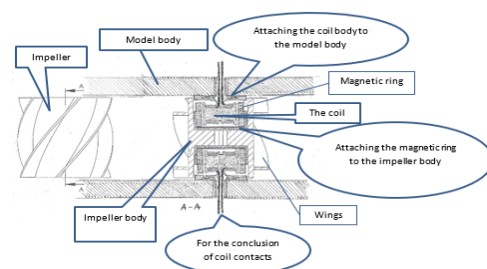
Fig. 1. Airfoil top view and section AA showing internal structure configuration.

In the initial stage, these two generators were selected with coils of different inductance and the voltage and

current generated by them were measured [2]. In the oscillograms presented below in the text, the voltage dependences generated by one coil are delayed in red, while the others are already in blue. In this way, they can be compared with each other and the perspectives of their combination and possible utility effect can be studied [1]. The inductance of the oscillogram coil displayed in red color was 14.2 mH and the inductance of the oscillogram coil displayed in blue color was 12.8 mH.
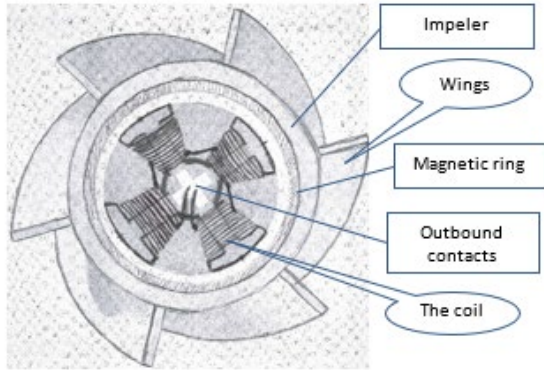
Fig. 2. Side view of the impeller, section showing the configuration of the internal structure.

Next, Fig. 2 shows a side view of the impeller and is analogous for both left and right views. The coils are permanently attached to the body of the model. When improving the layout, it is necessary to provide additional measures allowing to change the mutual position of the coils (phase difference of the generated voltage) and to compare the obtained oscillogram after the measurements.

Using this impeller with two sets of coils, experimental studies were carried out measuring the dependence of the generated electricity on the speed of the air flow, the dependence of the generated electricity on the mass of the air flow (with the height width of the inlet), and the dependence of the generated electricity on the mutual position of the coils (phase difference) when inlet remaining constant.

II. MATERIALS AND METHODS

In Figures 3, 4 and 5, we see the oscillograms of the generated electricity when the air flow speed is 50 km/h, respectively; 65 km/h and 72 km/h and, also the generalized dependence of the generated voltage on the air flow speed in Fig. 6 which shows the general trend obtained by connecting the measurement points to each other.

In Fig. 3, we see the oscillogram of the voltage of the generated electricity, from which we can record that the maximum amplitude of voltage fluctuations is only about 3.7 V. This is not a big value, but it is already significant for practical use, although the air flow speed here is about 50 km/h.

Fig. 3. Oscillogram when the inlet air flow speed is about 50 km/h.

In Fig. 4, we see the oscillogram of the voltage of the generated electricity when the speed of the air flow is already about 65 km/h. As we can see, the maximum amplitude of voltage fluctuations rises to 9.02 V. Such a change is significant for practical use.
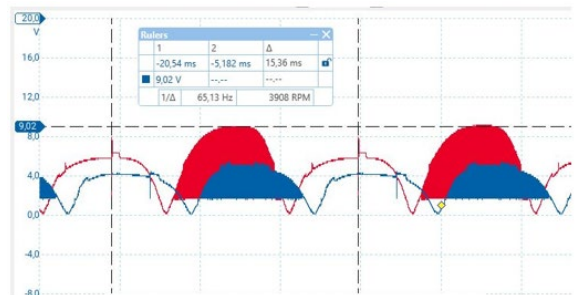
Fig. 4. Oscillogram when the inlet air flow speed is about 65 km/h.

In Fig. 5, we see the oscillogram of the voltage of the generated electricity when the speed of the air flow is already about 72 km/h. Here again, an increase in the amplitude of the maximum voltage fluctuations is observed up to 12.55 V. All these changes are already quite significant for practical use, as they already allow the use of the electronic part. In practically all measurement cases, the current values of the generated electric power already reach from tenths of amperes to amperes.
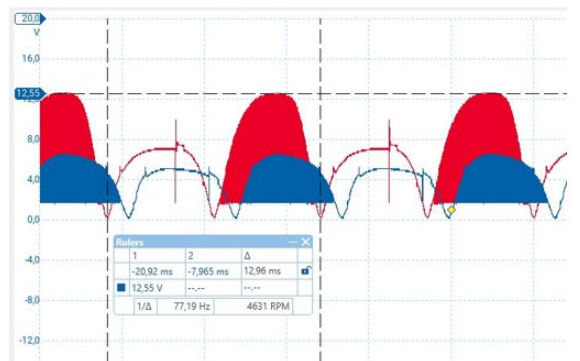
Fig. 5. Oscillogram when the inlet air flow speed is about 72 km/h.

Figure 6 shows the generalized dependence of the generated voltage on the air flow rate, which shows the general trend obtained by connecting the measurement points to each other.
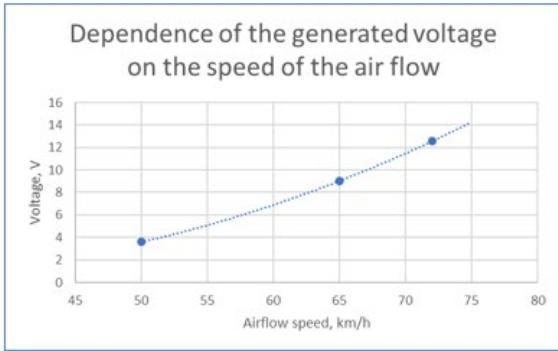
Fig. 6. Generalized dependence of the generated voltage on the air flow speed.

Such a generalized analysis of the dependence of the generated voltage on the air flow rate allows us to assume that at this stage we have not yet used all the resources for improving the efficiency factor. This gives hope and the need for further research. Here we are only talking about the kinetic energy component of the air flow [4].

The theoretical foundation of wind turbines uses two basic assumptions, that the energy is equal to the product of mass and velocity squared ($E=mv^2$) and that the mass of the air flow is equal to the product of the area (through which the air flow passes) times the cubic meter ratio (consisting of the air flow the product of speed per unit of time and air density), in other words, the mass of the air flow is a function of the air flow speed ($m=f(v)$, where v is the air flow speed). In theory [1], [3], the energy carried by an airflow is a function of the cube of the velocity of this airflow:

$$E = f(v^3) \qquad (1)$$

The possible losses during energy transformation should not affect the dependence itself, but in our case, the dependence is obtained only on the square of the speed, which makes to assume additional possibilities for improving efficiency.

The presented measurements were obtained in laboratory conditions using the layout described in the introduction, so only characteristic measurements were chosen for the presentation of the measurement results.

In the experiment, further measurements were made by changing the height of the air flow inlet at a constant air flow speed. In this way, the dependence of the generated energy on the mass of the air flow passing the model is obtained.

As it was already mentioned, changing the air flow mass is one of the dependencies of the air flow speed. However, its own specifics appear here, as it depends both on the geometry of the selected impeller and on the structural features.
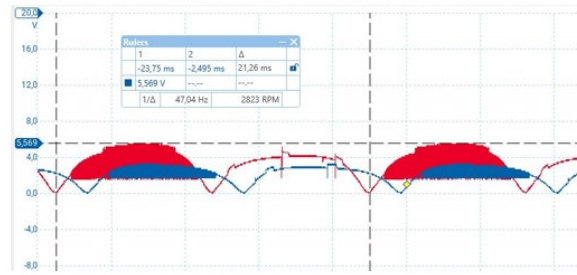
Fig. 7. Oscillogram when the height of the inlet air flow opening is equal to half the height of the airfoil.

In the picture Fig. 7 we see the oscillogram of the voltage of the generated electricity when the opening of the incoming air flow is geometrically the smallest. From the pictures revealing the structure of the impeller in Fig. 1 and Fig. 2, we can easily see that the blades of the impeller make up approximately one third of the radius of the entire impeller. The width of the air flow inlet is limited by the walls of the mock-up body, and the height in this mock-up (the design of the mock-up as shown in the article published in 2023; https://doi.org/10.17770/etr2023vol3.7261) [5] is adjusted by an insert plate and had four provided locking positions which relatively can be metered by wing heights. This delivery method was chosen this time.

The lowest height of the entrance hole means that the smallest amount of air flow mass passes through the impeller per unit of time, compared to other heights of the entrance hole. Naturally, the air flow acting on only half of the wing area cannot ensure a sufficiently efficient transformation of energy from the kinetic energy of the air flow into electrical energy. We can also see this in Fig. 7, where the maximum amplitude of voltage fluctuations generated by one of the coils reaches only about 5.6 V.

Fig. 8. Oscillogram when the height of the inlet air flow opening is equal to the height of the wing.

In Fig. 8 and Fig. 9, where the height of the air flow inlet is increased to the height of one wing and to the height of two wings, respectively, we can see an increase in the amplitude of the voltage fluctuations of the generated electric power from 5.6 V to 7.77 V and to 12.87 V, respectively.
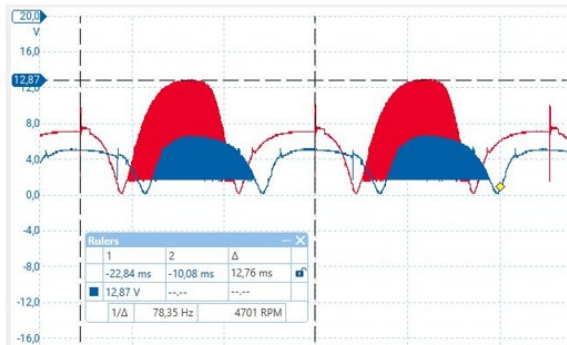
Fig. 9. Oscillogram when the height of the inlet air flow opening is equal to two wings.

Experiments were conducted with the number of impeller blades and their geometric parameters: tilts, turns, etc. based on that was selected design of impeller. The rotated aerofoils of Fig. 1 absorb quite efficiently the energy of the air flow of two wings heights due to their vectorially rotated absorption angle.
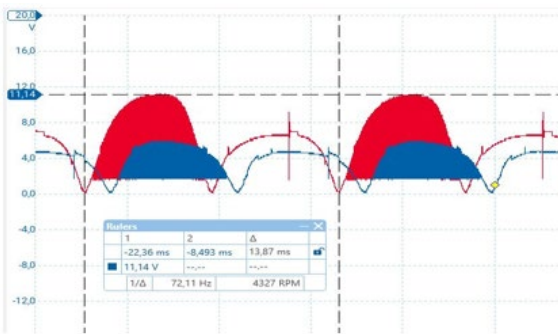
Fig. 10. Oscillogram when the height of the inlet air flow opening is equal to the height of the three wings.

In Fig. 10, where the height of the air flow inlet is increased to the height of three wings, a decrease in the amplitude of the voltage fluctuations of the generated electric power is observed from 12.87 V to 11.14 V. Well, here the influence of the interference caused by the air flow hitting the impeller body on the efficient energy conversion process is already manifested.

We can clearly see this in the summarized graph of these measurements in Fig. 11, where a clear trend of this effect emerges when the measurement points are connected by a curve.

In all oscillograms, we see two curves each, because the voltage fluctuations of the electricity generated by both coils were measured, but at this stage, attention was not paid to the possibility of summing up these two energy flows and their mutual influence on each other and for the overall process.
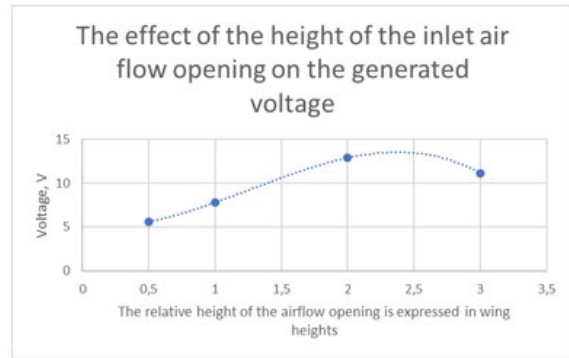
Fig. 11. Effect of Inlet airflow hole height on generated voltage when relative airflow hole height is expressed in airfoil heights.

III. RESULTS AND DISCUSSION

When reviewing the results of the obtained experiments and analysing them, it was noticed that under the same conditions: air flow speed, height of the entrance hole; different parameters of oscillograms are obtained.
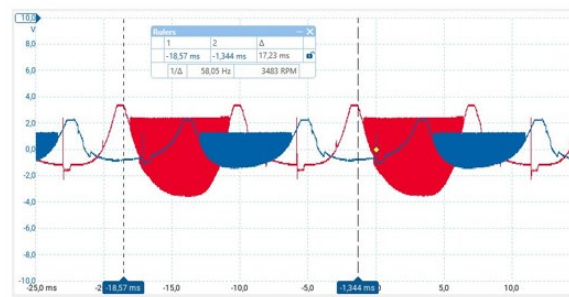
Fig. 12. The oscillogram of the voltage of the generated electric energy when the mutual positions of the coils differ by 90 degrees (phase difference $\pi/2$).

The main difference observed was that when the phase position of the coils is shifted, the maximum amplitude of the voltage fluctuations of the generated electricity also changes. This is perfectly illustrated by the mutual comparison of the presented pictures Fig. 12 and Fig. 13. In these images, we also see changes in parameters such as the speed of rotation of the impeller or the frequency of fluctuations in the voltage of the generated electricity.

This type of measurement was not prearranged with this model, so there was no possibility to adjust the relative position of the coils. Between the measurements, the model had to be re-collected several times, so apparently during one of these re-selections, the mutual position of the coils was changed by about 90 degrees, which corresponded to a phase shift close to $\pi/2$. Of course, it is difficult to expect that the position of the coils would remain the same when the model was re-collected, but apparently the deviations were so insignificant that they did not pay attention to the changes in other parameters, so they went unnoticed.
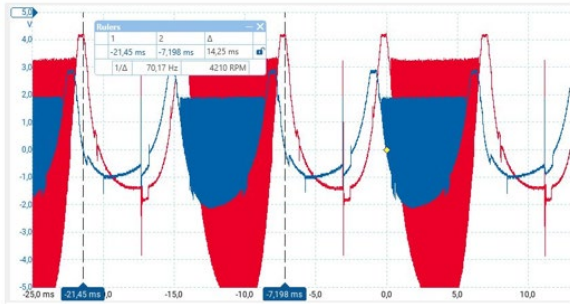
Fig. 13. The oscillogram of the voltage of the generated electricity when the positions of the coils almost coincide (the phase difference is close to 0).

This observation provides us with additional material for planning the design of an improved layout for the next round of experiments. It will be necessary to provide for the possibility of conducting experiments by changing the relative position of the coils, when other conditions remain almost the same, i.e., the speed of the air flow and the geometry of the inlet air flow opening. This part of the experiment would help us find out how to efficiently use the dependence of the generated electricity on the position of the coils. It would also help to plan how to combine these two electricity flows efficiently.

IV. CONCLUSIONS AND SUGGESTIONS

It turns out that the dependence of the amount of electricity generated in the ducts does not reach the theoretical dependence on the speed cube ($E \sim= f(v3)$). In our case, the squared dependence of the velocity is the best so far. This means that there is still room for improving the efficiency of resources.

The mass of air passing through the impeller is also limited by the geometry of the impeller itself. The conducted studies show that the efficiency of energy transformation starts to fall after exceeding a certain limit. More detailed research is needed.

It has been observed that the amount of generated energy also depends on the mutual position of the coils, which determines the phase difference between the voltages of the generated energy. Proposal: when improving the layout for further experiments, consider the possibility of changing the mutual position (phase) of the coils and allocate a separate cycle of measurements for this.

REFERENCES

[1] R. P. Murkund, Wind and solar power systems: design, analysis, and operation. Boca Raton, 2006.

[2] Lithuania Wind Assotiation, "Viskas, ką reikia žinoti apie vėjo energetiką", 2020. [Online]. Available: https://lvea.lt/wp-content/uploads/2021/01/LVEA_Viskas-ka -reikia-zinoti-apie-vejo-energetika.pdf [Accessed: February 26, 2024]

[3] L. Augulis, A. Jotautis and D. Rutkunienė, Fizika: mechanika, termodinamika, elektromagnetizmas: mokomoji knyga, 2012. [Online].Available: https://www.ebooks.ktu.lt/eb/656/fizika_mechanika_termodinamika_elektromagnetizmas/ [Accessed: February 26, 2024]

[4] V. Matutis and M. Matutis, "Patent description", 2019. [Online]. Available:https://worldwide.espacenet.com/patent/search/family/068887188/publication/EP3840192A1?q=EP3840192A1 [Accessed: February 26, 2024]

[5] V. Matutis, L. Savulioniene, P. Sakalys and L. Gzegozevske, "Research of the Principal Model of t he Electric Energy Generator of the Electric Car (Stage Combination of Mechanical and Electromechanical Parts)", Environment. Technology. Resources. Vol. 3, 2023. [Online]. Available https://journals.rta.lv/index.php/ETR/article/view/7261/6016 [Accessed: February 26, 2024]

[6] V. Matutis, L. Savulioniene, P. Sakalys and T. Kasperavicius, "Energy Generator Prototypes Development and these Research Integration into the Educational Process", Society. Integration. Education.Vol 1, 2022. [Online]. Available:http://journals.ru.lv/index.php/SIE/article/view/6884/5683 [Accessed: February 26, 2024]

[7] V. Matutis, L. Savulioniene, P. Sakalys, T. Kasperavicius, "Research of Power Generator Prototype Development and Integration into Autonomous Robotic Systems", Society. Integration. Education. Vol 5, 2021. [Online]. Available:https://doi.org/10.17770/sie2021vol5.6453 [Accessed: February 26, 2024]

Mechano-Mathematical Model and Exprimental Results on the Excitation of The Ship's Hull Oscillations by the Marine Propeller

Yuliyan Minchev
Department of Mechatronics
Naval Academy N.Vaptsarov, Varna, Bulgaria
Varna, Bulgaria
julminchev@nvna.eu

Ivaylo Minchev
Department of Mechatronics
Naval Academy N.Vaptsarov, Varna, Bulgaria
Varna, Bulgaria
iminchev@nvna.eu

Abstract. **This study tackles a critical issue in ship design: propeller-induced vibrations in the hull. We propose a novel mechano-mathematical model that goes beyond previous approaches to elucidate the excitation of these oscillations. Our model incorporates the crucial dynamic connection between the propeller's rotational motion and its oscillations. This refinement allows for a more precise understanding of how propellers, even when mechanically balanced, can excite vibrations through hydrodynamic imbalances.**

The traditional approach relies on simpler models, often leading to qualitative analysis. This work advances the field by introducing a more robust mechano-mathematical framework. This framework considers the complex interaction between the main engine, shaft line, and propeller, including factors like engine torque variations, propeller moment, and elastic properties of the system.

The model is not just theoretical. We present experimental results that validate the spectral components predicted by our model. This successful validation demonstrates the model's accuracy in capturing the real-world dynamics of propeller-induced vibrations.

The practical implications of this work are significant. By pinpointing the excitation mechanisms with greater precision, this research can pave the way for the development of improved propeller designs that minimize vibrations. Reduced vibrations translate to enhanced crew comfort, lower maintenance requirements, and potentially even improved fuel efficiency. Additionally, the model can be a valuable tool for optimizing ship powerplant design to ensure smooth operation and extended lifespan.

Keywords: oscillations, ship's hull, marine propeller

I. INTRODUCTION

It is known that the marine propeller is the exciter of the oscillations of the ship's hull [1, 2, 5, 6, 7, 8, 10, 11].

The oscillations are excited by mechanical imbalance (the center of mass does not coincide with the axis of rotation) and are of reversible frequency. In order not to excite such oscillations, the marine propellers are statically balanced on special stands. A mechanically balanced marine propeller can excite oscillations if the mass center of the water attached during the marine propeller's rotation does not coincide with the axis of rotation. The condition that the mass center of the joined mass of water coincides with the axis of rotation is geometric uniformity of the blades. This imbalance of the marine propeller is called hydrodynamic. A solid-state propeller may have a hydrodynamic imbalance.

There is also hydrodynamic imbalance in the line of hydrodynamic forces generated by the propeller blades. With the same blade geometry, the tangential hydrodynamic forces have a principal vector equal to zero. When the geometry of blades is disturbed, the main vector of the tangential hydrodynamic forces is a vector rotating with the rotational frequency. During the operation of the propeller, due to the inhomogeneous hydrodynamic field around the stern of the ship, hydrodynamic forces are generated with blade frequency ($z\omega$) equal to the product of the number of blades (z) multiplied with frequency of rotation ω of propeller.

The moment of the propeller contains harmonics of order $z, 2z$ and $3z$. The amplitudes of harmonics are determined by Brahms formulas [1] as a function of the mean torque.

Table 1 Propeller Moment Harmonics

z	M_z	M_{2z}	M_{3z}
3	$0,042 M_{cp}$	$0,042 M_{cp}$	$0,027 M_{cp}$
4	$0,076 M_{cp}$	$0,026 M_{cp}$	$0,08 M_{cp}$
5	$0,09 M_{cp}$	$0,015 M_{cp}$	0

In [5], [6] the possibility of excitation of oscillations by the propeller along the line of dynamic connection between oscillations and rotational motion is proved. The proof is rather qualitative in nature, as far as the simplest mechano-mathematical model is used. The main purpose of this present work is to prove the possibility of excitation of oscillations by a propeller along the line of the dynamic connection between the oscillations and the rotational motion by a proposed more precise mechano-mathematical model.

II. MATERIALS AND METHODS

The propeller is a rotating rigid body for which the dynamic connection proved in [3] between the oscillation of an unbalanced rotor and its rotation is valid. On this basis, in [5] the simplest dynamic model is proposed with which it is possible to study the oscillations of the propeller, considering the dynamic relation between the oscillations of the propeller and the torsional oscillations.

Fig. 1 shows a specified dynamic model of the system – main engine, shaft line, and propeller.
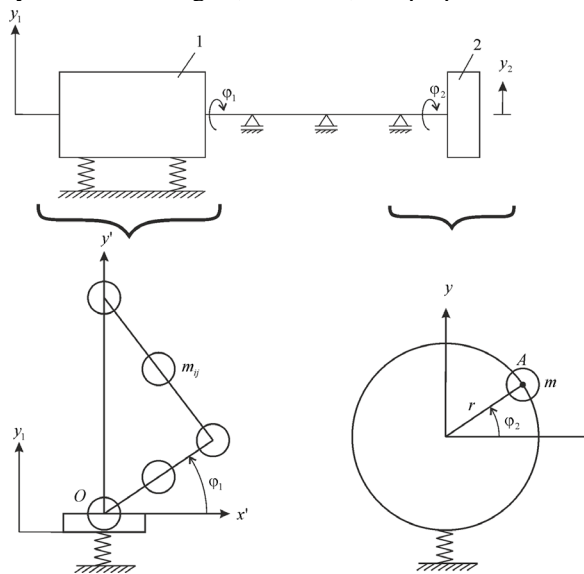
Fig.1 Dynamic Model of the Main Engine, Shaft Line, and Propeller

The main motor 1 is mounted elastically. It performs two oscillating processes simultaneously:
1. General oscillation along an y axis, excited by the unbalanced inertial forces.
2. Unequal rotation due to variable engine torque M_o and propeller torque $M_в$.

These two vibrational processes interact [1, 2, 4, 7, 8]. General oscillation creates additional inertial forces of all moving parts of the unit, which creates an additional moment influencing the law of rotational motion. On the other hand, unequal rotation creates additional inertial

forces that excite the oscillations of the unit. In this regard, a mechano-mathematical model [1, 2, 4, 7, 8] has been created, which describes these two vibrational processes in their natural interaction. This mechano-mathematical model will be used in the present work. The propeller is modeled as a rotating mass with mass moment of inertia. The imbalance of the screw is modeled by a mass m of a distance r from the axis of rotation.

The engine consists of crank shaft mechanisms (Fig. 1б) with n number of relatively mobile units.

Each i unit is modeled through three material particles m_{ij} $(i = 1, 2, ..., n; j = 1, 2, 3)$ of the dynamic equivalence condition [4]. We will introduce a coordinate system $x'oy'$ fixed to the stand. The position of each point mass m_{ij} in the movable in the movable coordinate system is determined by the coordinates x_{ij}, y_{ij}, that are function of position φ_1 of the crank shaft mechanism. The position of the movable coordinate system is determined by the coordinate y_1, that defines the oscillation of the engine. The oscillations of the screw are defined by y_2, and its rotation by φ_2. The shaft line has torsional stiffness c_0. The oscillations of the system are described by the differential equations:

$$
\begin{vmatrix}
I_1 \ddot{\varphi}_1 + M \ddot{y}_1 + \dfrac{1}{2} \dot{\varphi}_1^2 \dfrac{dI_1}{d\varphi_1} + c_0(\varphi_1 - \varphi_2) = M_1 \\[2mm]
m_1 \ddot{y}_1 + M \ddot{\varphi}_1 + \dot{\varphi}_1^2 \dfrac{dM}{d\varphi_1} + c_{11} y_1 + c_{12} y_2 = F_1 \\[2mm]
(m + m_2) \ddot{y}_2 + c_{21} y_1 + c_{22} y_2 = -mr(\ddot{\varphi}_2 \cos\varphi_2 - \\[2mm]
-\dot{\varphi}_2^2 \sin\varphi_2) + F_2 \\[2mm]
(I_2 + mr^2) \ddot{\varphi}_2 - c_0(\varphi_1 - \varphi_2) = -mr \ddot{y}_2 \cos\varphi_2 + M_2
\end{vmatrix}
\qquad (1)
$$

Here I_1 - mass moment of inertia of the engine, which is generally a function of φ_1:

$$ I_1 = I_1(\varphi_1) = I_{10} + \Delta I_1(\varphi_1) $$

$$ M = \sum_{i=1}^{n} \sum_{j=1}^{3} m_{ij} \frac{dy_{ij}}{d\varphi_1} = M(\varphi_1) $$

M_1 - engine torque

M_2 - moment of propeller.

F_1 - main vector of the inertial forces of the engine.

F_2 - hydrodynamic force.

Elastic constants $c_{ij} (i, j = 1, 2)$ define the transverse stiffness of the shaft line, including the stiffness of the elastic suspension of the engine:

$$c_{11} = \frac{\delta_{22}}{\Delta}, \qquad c_{12} = -\frac{\delta_{12}}{\Delta}$$

$$c_{21} = -\frac{\delta_{21}}{\Delta}, \qquad c_{22} = \frac{\delta_{11}}{\Delta}$$

$$\Delta = \delta_{11}\delta_{22} - \delta_{12}^2$$

With δ_{ij} are signed coefficients of influence – deformation of i section under the action of unit force applied in j section. Differential equations (1) describe propeller's oscillations considering the dynamic connection with the torsional oscillations excited by the motor and the propeller.

If we accept:

$$\dot{\varphi}_1^2 = \omega_1^2 = const \qquad (2)\,(a)$$

$$\cos\varphi_2 \approx \cos\omega_2 t, \qquad \sin\varphi_2 \approx \sin\omega_2 t \qquad (2)\,(b)$$

equation (1) is significantly simplified.

It should be noted that the assumption (2-b) is traditional for machine dynamics.

Based on (2) the system of equations takes the form:

$$
\begin{cases}
I_1\ddot{\varphi}_1 + M\ddot{y}_1 + c_0(\varphi_0 - \varphi_2) = M_1 - \dfrac{1}{2}\omega_1^2\dfrac{dI_1}{d\varphi_1} \\[2mm]
m_1\ddot{y}_1 + M\ddot{\varphi}_1 + c_{11}y_1 + c_{12}y_2 = F_1 - \omega_1^2\dfrac{dM}{d\varphi_1} \\[2mm]
(m+m_2)\ddot{y}_2 + c_{21}y_1 + c_{22}y_2 = -mr(\ddot{\varphi}_2\cos\omega_2 t - \\
\quad -\omega_2^2\sin\omega_2 t) + F_2 \\[2mm]
(I_2 + mr^2)\ddot{\varphi}_2 - c_0(\varphi_1 - \varphi_2) = -mr\ddot{y}_2\cos\omega_2 t + M_2
\end{cases}
\qquad (3)
$$

III. Results and Discussion

We will perform a qualitative analysis on the influence of the moments of the engine and the propeller on the vibration state of ship's power plant.

We will present the moment of engine only with the main harmonic.

$$M_1 = M_{1k}\sin k\omega_1 t \qquad (4)$$

We will present the torque of the screw with the main harmonic of the order of the number of blades z:

$$M_2 = M_{2z}\sin z\omega_2 t \qquad (5)$$

Moments (4) and (5) excite torsional oscillations:

$$\varphi_i = A_{ik}\sin k\omega_1 t + A_{iz}\sin z\omega_2 t \qquad (6)$$
$$i = 1,2$$

Torsional oscillations generate inertial force:

$$\Phi_2 = -mr\ddot{\varphi}_2\cos\omega_2 t \qquad (7)$$

After substituting (6) in (7) we get:

$$\Phi_2 = \Phi_{21}[\sin(z\omega_2 - \omega_2)t + \sin(z\omega_2 + \omega_2)t] + \Phi_{22}[\sin(k\omega_1 - \omega_2)t + \sin(k\omega_1 + \omega_2)t] \qquad (8)$$

Here

$$\Phi_{21} = \frac{1}{2}A_{2z}mr(z\omega_2)^2$$

$$\Phi_{22} = \frac{1}{2}A_{2k}mr(k\omega_1)^2$$

The inertial force (8) excites the oscillations of the propeller with frequencies:

$$z\omega_2 \pm \omega_2 = (z \pm 1)\omega_2$$
$$k\omega_1 \pm \omega_2 \qquad\qquad (9)$$

Table 2 Deadwood & Intermediate Bearing Oscillations (Engine Modes)

Place of measurement	directions	Mode rpm	Characteristic frequencies of the spectrum	figure
Intermediate bearing left shaft line	H	900	$4\omega_1 \pm \omega_2 = $ $= 3600 \pm 178$	Fig. 2
Intermediate bearing left shaft line	V	900	$4\omega_1 \pm \omega_2 = $ $= 3600 \pm 178$	Fig. 3
Intermediate bearing left shaft line	A	900	$4\omega_1 \pm \omega_2 = $ $= 3600 \pm 178$	Fig. 4
Deadwood bearing left shaft line	H	900	$4\omega_1 + \omega_2 = $ $= 3600 + 178$	Fig. 5
Deadwood bearing left shaft line	V	900	$z\omega_2 = 712$ $5\omega_1 - \omega_2 = $ $= 4500 - 178$	Fig. 6
Deadwood bearing left shaft line	H	1300	$z\omega_2 = 1029$	Fig. 7
Intermediate bearing left shaft line	H	1300	$4\omega_1 \pm \omega_2 = $ $= 5200 \pm 257$	Fig. 8
Intermediate bearing left shaft line	V	1300	$4\omega_1 \pm \omega_2 = $ $= 5200 \pm 257$	Fig. 9
Deadwood bearing left shaft line	V	1300	$z\omega_2 = 1029$	Fig. 10
Deadwood bearing right shaft line	H	1500	$\omega_2 = 297$ $z\omega_2 = 1188$ $z\omega_2 + \omega_2 = 1485$	Fig.11
Deadwood bearing right shaft line	V	1500	$z\omega_2 = 1188$ $z\omega_2 \pm \omega_2 = $ $= 1188 \pm 297$	Fig. 12
Deadwood bearing right shaft line	A	1500	$z\omega_2 = 1188$ $z\omega_2 + \omega_2 = 1485$	Fig. 13
Intermediate bearing left shaft line	V	1500	$3\omega_1 + \omega_2 = $ $= 4500 + 297$	Fig. 14
Deadwood bearing left shaft line	H	1500	$\omega_2 = 297$ $z\omega_2 = 1188$ $z\omega_2 + \omega_2 = 1485$	Fig. 15
Deadwood bearing left shaft line	V	1500	$z\omega_2 \pm \omega_2 = $ $= 1188 \pm 297$	Fig. 16
Deadwood bearing left shaft line	A	1500	$z\omega_2 \pm \omega_2 = $ $= 1188 \pm 297$	Fig. 17

A. Experimental investigations

The object of experimental investigations are shaft lines of port tugs. The main power plant consists of two Caterpillar engines 35008B. The connection to the shaft line is made with gearboxes with a gear ratio $i = 5.05$. The oscillation of the deadwood bearing and the intermediate bearing of each shaft line for three modes of main engine corresponding to $900 rpm, 1300 rpm, 1500 rpm$.

The fourth harmonic of the gas forces is the lowest frequency harmonic that has a dominant influence.

Some of the oscillation spectrums are given in the figures described in Table 1.

The oscillations with frequencies are clearly visible in the figures:
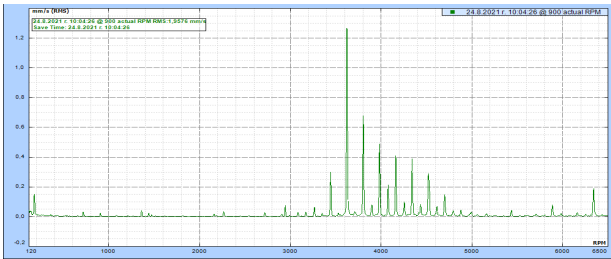
$$z\omega_2 \pm \omega_2 = (z \pm 1)\omega_2$$
$$k\omega_1 \pm \omega_2 \qquad (9)$$
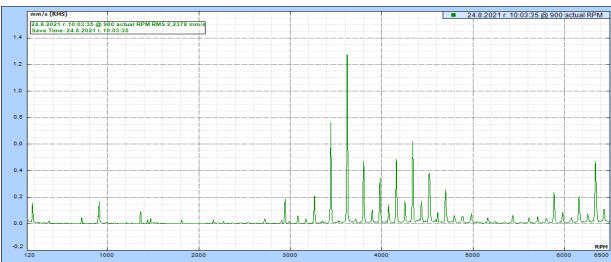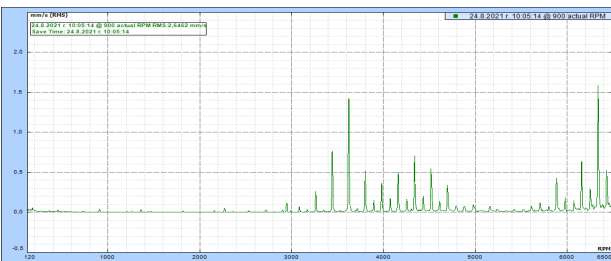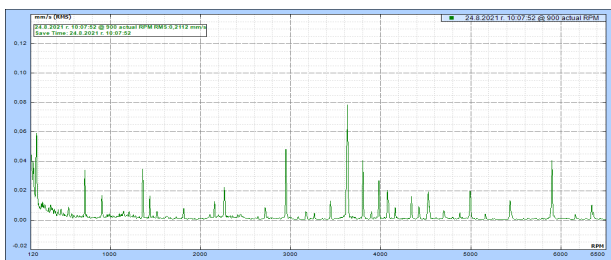
the existence of which has been proven theoretically.

According to the existing notations of excitation of oscillations from the propeller, we should observe in the spectrum of oscillations frequencies.

$$z\omega_2, \qquad k\omega_1, \omega_2$$
$$(10)$$

The presented experimental results show that in addition to the traditional spectral components (10), the frequency oscillations are also observed (9).

Precise identification of the spectral components is required in connection with the evaluation of the operation of the main engine (evaluation of the fuel adjustment) according to the spectrum of oscillations, [3].
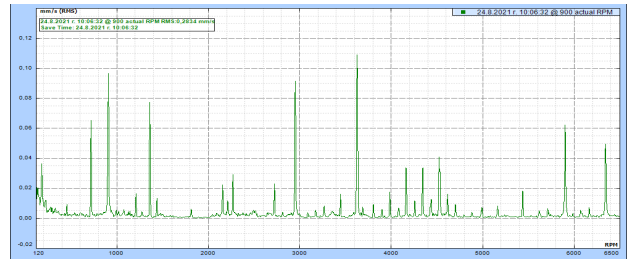
Figure 2 Spectrum of oscillations of Intermediate bearing left shaft line.
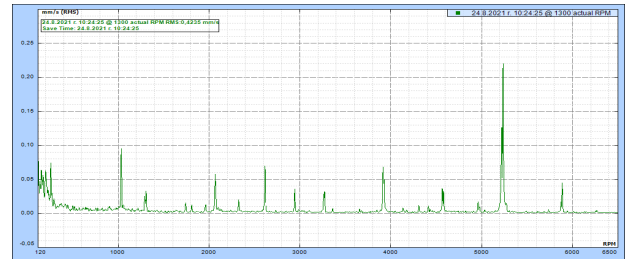
Figure 6 Spectrum of oscillations of Deadwood bearing left shaft line.

Figure 3 Spectrum of oscillations of Intermediate bearing left shaft line.

Figure 7 Spectrum of oscillations of Deadwood bearing left shaft line.

Figure 4 Spectrum of oscillations of Intermediate bearing left shaft line.
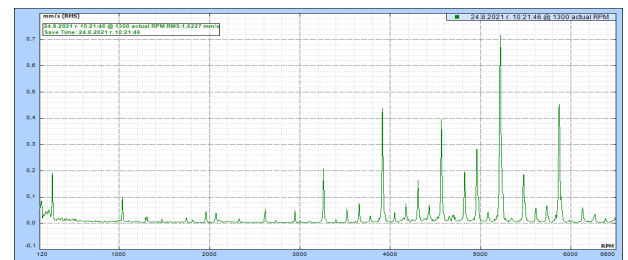
Figure 8 Spectrum of Intermediate bearing left shaft line.

Figure 5 Spectrum of oscillations of Deadwood bearing left shaft line.
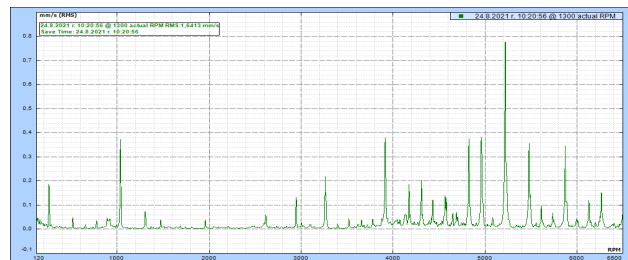
Figure 9 Spectrum of Intermediate bearing left shaft line.

Figure 10 Spectrum of oscillations of Deadwood bearing right shaft line.
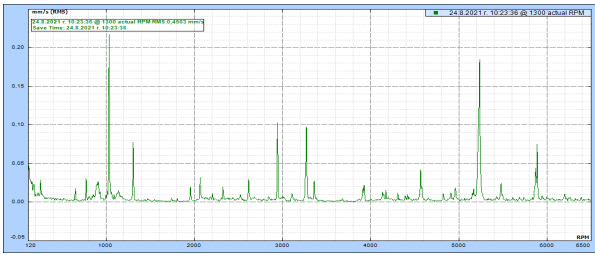
Figure 14 Spectrum of oscillations of Intermediate bearing left shaft line.

Figure 11 Spectrum of oscillations of Deadwood bearing right shaft line.
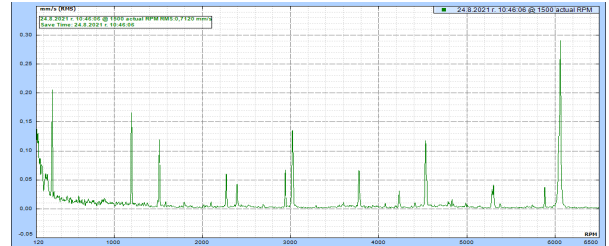
Figure 15 Spectrum of oscillations of Deadwood bearing left shaft line.

Figure 12 Spectrum of oscillations of Deadwood bearing right shaft line.
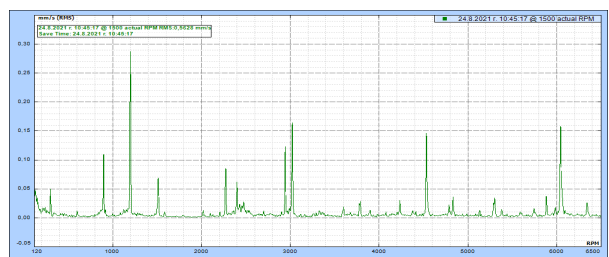
Figure 16 Spectrum of oscillations of Deadwood bearing left shaft line.

Figure 13 Spectrum of oscillations of Deadwood bearing right shaft line.
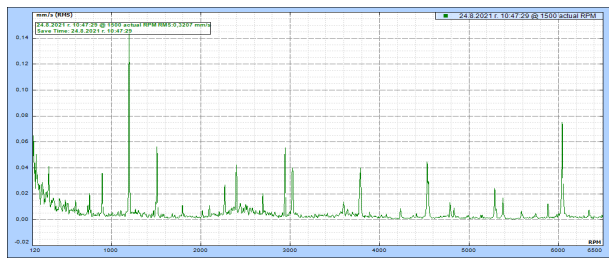
Figure 17 Spectrum of oscillations of Deadwood bearing left shaft line.

IV.   CONCLUSION

The presented experimental results confirm the theoretically obtained spectral components (9), which is a result of the dynamic relation between the torsional and general oscillations of the propeller. In conclusion, this study presents a significant advancement in understanding propeller-induced hull oscillations. The proposed mechano-mathematical model, along with its experimental validation, offers a powerful tool for designing propellers and ship powerplants that minimize vibrations, leading to a range of practical benefits.

REFERENCES

[1] Minchev N.D., Dynamics of Ship Machinery, DVI, Sofia, 1983.

[2] Minchev N.D., Draganchev Hr., Strength and Vibrations of Ship Machinery, Galaktika Publishing, Varna, 1992.

[3] Minchev N.D., Grigorov V., Vibration Diagnostics of Rotating and Reciprocating Machines, DI Technika, 1988.

[4] Minchev N.D., Zhivkov V.S., Enchev K., Stoyanov P., Theory of Mechanisms and Machines, DI Technika, 1991.

[5] Minchev N.D., Minchev I.N., Minchev Yu.N., On the Dynamic Connection Between the Vibrations of the Propeller and the Main Ship Engine, Mechanics of Machines Journal, No. 105, 2014, pp. 87-91.

[6] Minchev N.D., Minchev Yu.N., Minchev I.N., On the Excitation of Vibrations of the Ship Hull by the Propeller, Mechanics of Machines Journal, No. 107, 2014, pp. 81-91.

[7] Minchev Yu.N., Investigations on Vibrations of Elastically Mounted Machines. Dissertation, 2007.

[8] Minchev I.N., Minchev Yu.N., Studies on the Dynamics of Machine Assemblies, EKS-press Publishing, Gabrovo, 2019, 372 pages.

[9] Minchev N.D., Minchev N.N., Some Features of Vibrations of an Elastic Rotor with Unbalance. Mechanics of Machines Journal, No. 19, 1997, pp. 66-74.

[10] Papkovich P.F., Works on Ship Vibrations, Shipbuilding Industry Publishing, Leningrad, 1960.

[11] Shimansky Yu.A., Dynamic Calculation of Ship Structures, Shipbuilding Industry Publishing, Leningrad, 1963.

Mechano-Mathematical Model And Experimental Results On The Dynamic Relation Between Marine Propeller Oscillation And Main Ship Engine

Yuliyan Minchev
Department of Mechatronics
Naval Academy N.Vaptsarov, Varna, Bulgaria
line 4: Varna, Bulgaria
line 5: julminchev@nvna.eu

Ivaylo Minchev
Department of Mechatronics
Naval Academy N.Vaptsarov, Varna, Bulgaria
line 4: Varna, Bulgaria
line 5: iminchev@nvna.eu

Abstract. Ship propellers, essential for propulsion, can cause unwanted hull vibrations. These vibrations affect crew comfort, increase maintenance costs, and potentially reduce fuel efficiency. This study addresses this issue with a novel mechano-mathematical model that analyses the propeller contribution to vibrations. Previous models have focused primarily on the engine as the vibration source. This work bridges the gap by considering the dynamic interplay between different vibration modes within the entire propulsion system: engine, shaft line and propeller. It considers key elements such as engine torque variations, propeller moment and system elasticity. The model represents these components with the propeller as a weightless elastic element. It meticulously accounts for the complex motion of the propeller, allowing its absolute speed to be calculated. The model recognises the flexibility of the shaft line and represents the engine using simplified point masses based on established principles. A reference system tracks the position of each component, capturing engine vibration, stern tube bearing motion and shaft line torsional stiffness. A set of differential equations governs the oscillations of the system, incorporating relevant factors such as engine inertia and torque, propeller moment, and inertial and hydrodynamic forces. The model captures the dynamic relationship between different modes of vibration, including propeller, engine, shaft precession and torsional vibrations from both engine and propeller. While detailed equations and experimental results are omitted, a qualitative analysis demonstrates the model's ability to predict the frequencies of real-world vibration spectra. This successful validation highlights its potential to capture propeller-induced vibration dynamics. By pinpointing excitation mechanisms with greater accuracy, this research can pave the way for improved propeller designs that minimise vibration, leading to improved crew comfort, reduced maintenance costs and potentially even improved fuel efficiency.

Keywords: oscillations, marine propeller, ship's engine

I. INTRODUCTION

The marine propeller is an element of the shaft line of the ship, which performs torsional oscillations, [1], [2]. The main exciter of torsional oscillations is the main ship's engine. The calculation of the torsional oscillations and their standardization is regulated by the classification societies. The marine propeller is also the exciter of torsional oscillations [1], [2] due to the inhomogeneity of the hydrodynamic field around the stern of the ship. In the presence of an imbalance, the marine propeller excites oscillations of the shaft line and the ship's hull. The oscillations of a rigid unbalanced rotor, considering the dynamic relation between the oscillations of the rotor and rotational motion, were first studied in [3]. The presence of torsional vibration exciter in ship's shaft line and dynamic relation between the oscillations of an unbalanced rotor and its rotation proved in [3] define the need to study the oscillations of propellers considering dynamic relation between propeller oscillations and torsional oscillations excited from ship's engine and a screw. In [5], [6] a solution of this problem is given based on elementary dynamic models. In [11] a more precise mechano-mathematical model was proposed, which, however, cannot explain some experimentally observed vibration phenomena. Therefore, in the present work, based on [9], a mechano-mathematical model is proposed in which the dynamic relation between the oscillations of

the processing elastic shaft, the oscillations of the supports and torsional oscillations is considered.

II. MATERIALS AND METHODS

The propeller is modeled as a rotating rigid body with a dynamic connection to its rotation, like unbalanced rotors [3]. Building upon this concept, a simple dynamic model is introduced in [5] to study propeller oscillations while considering the dynamic relationship between propeller and torsional oscillations.

Fig. 1 shows a dynamic model of the system main engine, shaft line, and marine propeller. The rotor is weightless elastic (Fig. 1-b) with concentrated mass m.
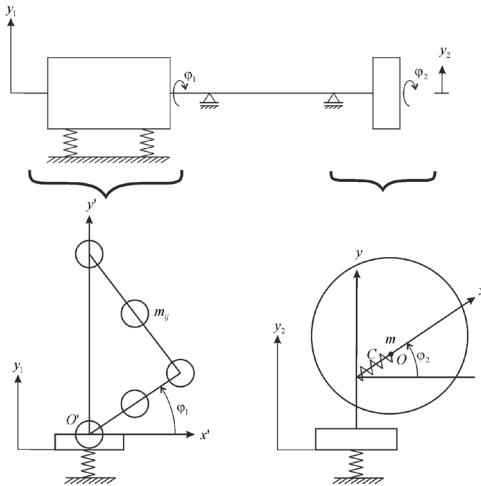
Fig. 1 Dynamic Model of the main engine, shaft line and marine propeller.

The elasticity of the shaft line is denoted by C, and elastic deformation of the shaft in cross section of the screw with x. Such a model of a processing rotor is proposed in [9]. The elastically deformed shaft rotates with ω_2, and its position is indicated by φ_2, (fig.1-b). The point O, at which the mass of the screw is concentrated performs a complex motion – transferred translation with velocity $\dot{y}_2$, relative rotation φ_2, accompanied by relative displacement x. Taking these factors into account for the absolute velocity of the point mass m we obtain:

$$v^2 = (\dot{y}_2 + x\dot{\varphi}_2 \cos\varphi_2 + \dot{x}\sin\varphi_2)^2 +$$
$$+(\dot{x}\cos\varphi_2 - x\dot{\varphi}_2 \sin\varphi_2)$$

The shaft line performs bending oscillations. The engine consists of crank shaft mechanisms with n number relatively mobile units (Fig 1-b). Each unit i is modeled through three-point masses m_{ij} $(i=1,2,...,n, j=1,2,3)$ of the dynamic equivalence condition [4]. We will introduce a coordinate system $x'o'y'$ fixed to the stand.

The position of each point mass m_{ij} in movable coordinate system is determined by to coordinates $x_{ij}(\varphi_1)$, $y_{ij}(\varphi_1)$ which are function of the position φ_1 of the crank shaft mechanism. The position of movable coordinate system is defined by the coordinate y_1, that defines the oscillation of the engine. The oscillation of stern tube bearing are determined by y_2. The shaft line has torsional stiffness c_o.

The oscillations of the system are described by the differential equations:

$$\left| \begin{array}{l} I_1\ddot{\varphi}_1 + M\ddot{y}_1 + \dfrac{1}{2}\dot{\varphi}_1^2 \dfrac{dI_1}{d\varphi_1} + c_0(\varphi_1 - \varphi_2) = M_1 \\[2mm] m_1\ddot{y}_1 + M\ddot{\varphi}_1 + \dot{\varphi}_1^2 \dfrac{dM}{d\varphi_1} + c_{11}y_1 + c_{12}y_2 = F_1 \\[2mm] (m_0 + m)\ddot{y}_2 + c_{21}y_1 + c_{22}y_2 = -2m\dot{x}\dot{\varphi}_2 \cos\varphi_2 - \\[2mm] -mx(\ddot{\varphi}_2 \cos\varphi_2 - \dot{\varphi}_2^2 \sin\varphi_2) - m\ddot{x}\sin\varphi_2 + F_2 \\[2mm] (I_2 + mx^2)\ddot{\varphi}_2 - c_0(\varphi_1 - \varphi_2) = -m\ddot{y}_2 x\cos\varphi_2 - \\[2mm] -2m\dot{x}\dot{\varphi}_2 x - M_2 \\[2mm] m\ddot{x} + cx = -m\ddot{y}_2 \sin\varphi_2 + mx\dot{\varphi}_2^2 \end{array} \right. \qquad (1)$$

Here

I_1 - reduced mass moment of inertia of the engine, which is a function of φ_1

$$I_1 = I_1(\varphi_1) = I_{10} + \Delta I_1(\varphi_1)$$

$$M = \sum_{i=1}^{n}\sum_{j=1}^{3} m_{ij} \frac{dy_{ij}}{d\varphi_1} = M(\varphi_1)$$

M_1 - reduced torque of the gas forces of the engine.

M_2 - moment of hydrodynamic forces of the propeller.

F_1 - main vector of the inertial forces of the engine.

F_2 - main vector of hydrodynamic forces.

Differential equations (1) describe the oscillations of the marine propeller and the motor, considering the dynamic relation between the oscillations of the supports, the oscillations of the precession elastic shaft and the torsional oscillations excited by the motor and the propeller.

If accepted.

$$\dot{\varphi}_1^2 = \omega_1^2 = const$$
$$\sin\varphi_2 \approx \sin\omega_2 t, \qquad \cos\varphi_2 \approx \cos\omega_2 t \qquad (2)$$

The equations are greatly simplified. This assumption is traditional for machine dynamics.

Based on (2) the system of differential equations (1) takes the form:

$$\begin{vmatrix} I_1\ddot{\varphi}_1 + M\ddot{y}_1 + c_0(\varphi_1 - \varphi_2) = M_1 - \frac{1}{2}\omega_1^2\frac{dI_1}{d\varphi_1} \\[6pt] m_1\ddot{y}_1 + M\ddot{\varphi}_1 + c_{11}y_1 + c_{12}y_2 = F_1 - \omega_1^2\frac{dM}{d\varphi_1} \\[6pt] (m_0 - m)\ddot{y}_2 + c_{21}y_1 + c_{22}y_2 = -2m\dot{x}\omega_2\cos\omega_2 t - \\[4pt] -mx(\ddot{\varphi}_2\cos\omega_2 t - \omega_2^2\sin\omega_2 t) - m\ddot{x}\sin\omega_2 t + F_2 \quad (3) \\[6pt] (I_2 + mx^2)\ddot{\varphi}_2 - c_0(\varphi_1 - \varphi_2) = \\[4pt] = -m\ddot{y}_2 x\cos\omega_2 t - 2m\dot{x}\omega_2 x - M_2 \\[6pt] m\ddot{x} + cx = -m\ddot{y}_2\sin\omega_2 t + 2mx\omega_2^2 \end{vmatrix}$$

We will perform a qualitative analysis on the influence of the moments of the engine and the propeller on the vibration state of the ship's power plant.

We will present the moment of the engine with the main harmonic:

$$M_1 = M_{1k}\sin k\omega_1 t \qquad (4)$$

We will present the torque of the screw with the main harmonic of the order of the number of blades. z :

$$M_2 = M_{2z}\sin z\omega_2 t \qquad (5)$$

Moments (4) and (5) excite torsional oscillations:

$$\varphi_i = A_{ik}\sin k\omega_1 t + A_{iz}\sin z\omega_2 t, i = 1, 2. \qquad (6)$$

The screw excites oscillation with a blade frequency:

$$y_2 = B\sin z\omega_2 t \qquad (7)$$

These oscillations generate an inertial force.

$$\Phi_x = -m\ddot{y}_2\sin\omega_2 t \qquad (8)$$

After replacing (7) in (8) it is obtained

$$\Phi_x = \frac{1}{2}m(z\omega_2^2)B[\cos(z\omega_2 - \omega_2)t - \cos(z\omega_2 + \omega_2)t] \quad (9)$$

This inertial force excites the oscillations of the elastic rotor of the form:

$$X = a\cos(z\omega_2 - \omega_2)t + b\cos(z\omega_2 + \omega_2)t \quad (10)$$

The torsional oscillations of the elastic rotor generate inertial force.

$$\Phi_y = -mx\ddot{\varphi}_2\cos\omega_2 t \qquad (11)$$

After substituting (6) and (10) in (11), the spectrum of inertial force (11) is obtained. The main component is frequency.

$$k\omega_1 \pm z\omega_2 \qquad (12)$$

In addition, there are components with frequencies:

$$k\omega_1 \pm z\omega_2 \pm 2\omega_2 \quad (13)$$

The inertial force (11) will excite oscillations with frequencies (12) and (13).

III. RESULTS AND DISCUSSION

The results of experimental studies are presented at Fig. 2 till Fig. 10.

The object of experimental investigation is shaft line of port tugs. The main power plant consists of two Caterpillar 3508B engines. The relation to the shaft line is made with a reducer with a gear ratio $i = 5.05$. The oscillations of the stern tube bearing and intermediate bearing in three directions (horizontal, vertical, axial) were measured for three modes of the main engine corresponding to $900rpm, 1300rpm, 1500rpm$.

The fourth harmonic of the engine's gas forces is the lowest frequency harmonic that has a dominant influence.

Some of the oscillation spectrums are given in the Figures described in Table 1.

The figures clearly show oscillations with frequencies $k\omega_1 \pm z\omega_2$

Table 1 Oscillation Spectrums description.

Place of measurement	Direc-tion	Mode rpm	Characteristic frequencies of spectrum	Figure
Stern tube bearing right shaft line	H	900	$4\omega_1 - z\omega_2 =$ $= 3600 - 712 =$ $= 2888$	Fig. 2
Stern tube bearing right shaft line	V	900	$4\omega_1 - z\omega_2 =$ $= 3600 - 712 =$ $= 2888$	Fig. 3
Stern tube bearing right shaft line	A	900	$4\omega_1 - z\omega_2 =$ $= 3600 - 712 =$ $= 2888$	Fig. 4
Stern tube bearing left	H	900	$4\omega_1 - z\omega_2 =$ $= 3600 - 712 =$ $= 2888$	Fig. 5
Stern tube bearing left shaft line	V	900	$4\omega_1 - z\omega_2 =$ $= 3600 - 712 =$ $= 2888$ $z\omega_2 = 712$	Fig. 6
Stern tube bearing left shaft line	A	900	$4\omega_1 - z\omega_2 =$ $= 3600 - 712 =$ $= 2888$	Fig. 7
Stern tube bearing right shaft line	V	1300	$3\omega_1 - z\omega_2 =$ $= 3900 - 1029 =$ $= 2871$ $z\omega_2 = 1029$	Fig. 8
Stern tube bearing right shaft line	A	1300	$3\omega_1 - z\omega_2 =$ $= 3900 - 1029 =$ $= 2871$ $z\omega_2 = 1029$	Fig. 9
Stern tube bearing left shaft line	V	1300	$3\omega_1 - z\omega_2 =$ $= 3900 - 1029 =$ $= 2871$ $z\omega_2 = 1029$	Fig. 10

the existence of which was proved theoretically because of qualitative research on the system of differential equations.

The presented experimental results show that in addition to the traditional spectral components with frequencies:

$$\omega_2, z\omega_2, k\omega_1 \qquad (14)$$

oscillations with frequencies are observed:

$$k\omega_1 \pm z\omega_2$$

The presence of these spectral components cannot be predicted by existing theory.
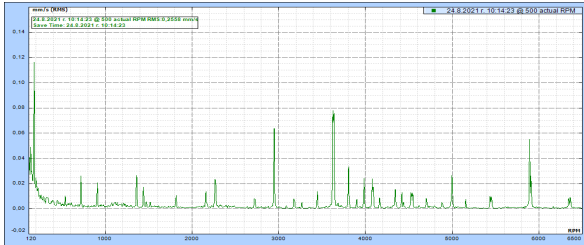
Figure 2 Spectrum of oscillations of Stern tube bearing right shaft line.
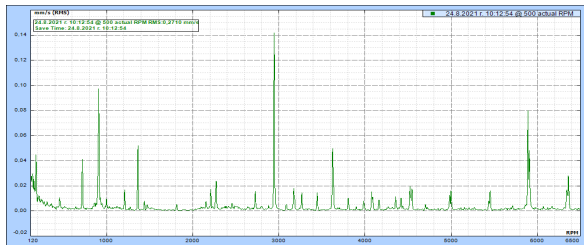
Figure 3 Spectrum of oscillations of Stern tube bearing right shaft line.

Figure 4 Spectrum of oscillations of Stern tube bearing right shaft line.
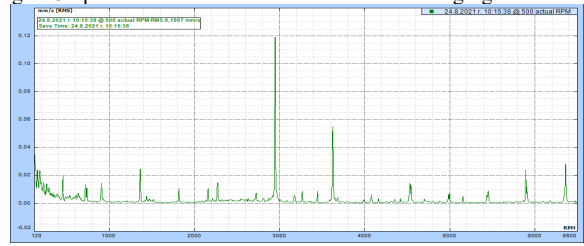
Figure 5 Spectrum of oscillations of Stern tube bearing left shaft line.
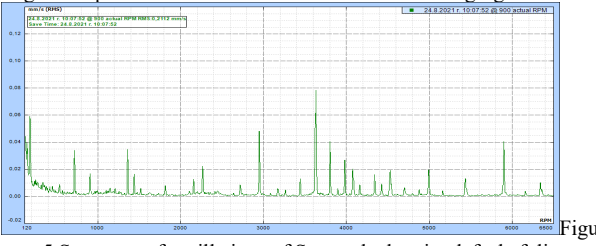
Figure 6 Spectrum of oscillations of Stern tube bearing LEFT shaft line.
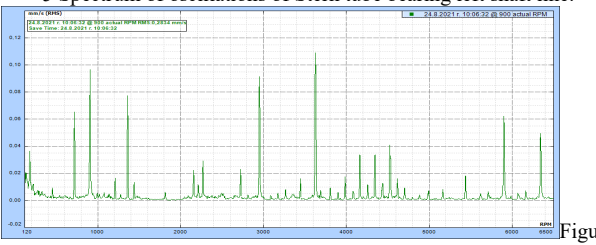
Figure 7 Spectrum of oscillations of Stern tube bearing LEFT shaft line.
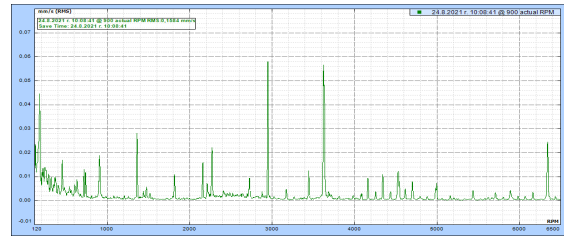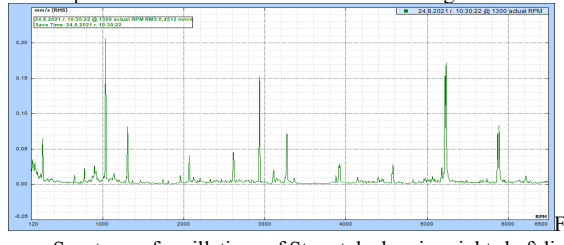
Figure 8 Spectrum of oscillations of Stern tube bearing right shaft line.
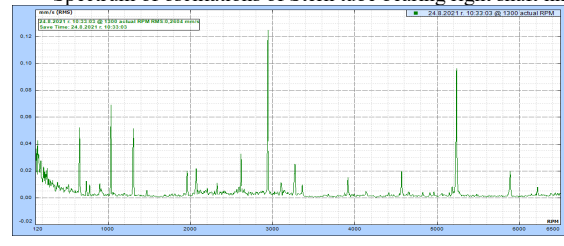
Figure 9 Spectrum of oscillations of Stern tube bearing right shaft line.

Figure 10 Spectrum of oscillations of Stern tube bearing left shaft line.

IV. CONCLUSION

The experimental results presented provide a strong validation of the spectral components predicted by the proposed mechano-mathematical model. This validation implies that the model is capable of accurately capturing the complex interplay between different modes of vibration within a ship's propulsion system. Critically, the model incorporates the crucial dynamic relationship between the vibrations of the propeller shaft (considered as a process elastic element), the vibrations of the supporting elements (such as the stern tube bearing) and the torsional vibrations arising from both the engine and the propeller itself. This focus on the dynamic interactions between these components represents a significant advance over previous models.

By successfully predicting real-world vibration spectra, this research provides a powerful tool for marine engineers. The model can be used to

- Optimize propeller design: By accurately identifying the excitation mechanisms responsible for vibration, the model can guide the design of propellers with minimized vibration signatures. This results in propellers that contribute to smoother operation, potentially leading to improved fuel efficiency and reduced underwater noise.

- Improve marine engine design: The model can be used as a valuable tool during the design phase of marine propulsion systems. By simulating the dynamic interactions between different components, engineers can identify potential vibration problems early and make design changes to mitigate them. This proactive approach can result in engines with superior operating characteristics, reduced maintenance requirements and, ultimately, extended service life.

-Improve vibration diagnosis and troubleshooting: The model can be used as a diagnostic tool for existing vessels experiencing vibration problems. By analyzing the measured vibration spectra and comparing them with the model predictions, engineers can pinpoint the cause of vibration with greater accuracy. This targeted approach allows for more effective troubleshooting and corrective action, minimizing downtime and maintenance costs.

In conclusion, the validated mechano-mathematical model represents a significant leap forward in the understanding of propeller-induced hull vibrations. The ability to predict real-world vibration spectra paves the way for significant advances in marine engineering, leading to the development of more efficient, reliable, and crew-friendly vessels.

REFERENCES

[1] Minchev N.D., Dynamics of Ship Machinery, DVI, Sofia, 1983.

[2] Minchev N.D., Draganchev Hr., Quality and Vibrations of Ship Machinery, Galaktika Publishing, Varna, 1992.

[3] Minchev N.D., Grigorov V., Vibrodiagnostics of Rotating and Reciprocating Machines, DI Technika, 1988.

[4] Minchev N.D., Zhivkov V.S., Enchev K., Stoyanov P., Theory of Mechanisms and Machines, DI Technika, 1991.

[5] Minchev N.D., Minchev I.N., Minchev Yu.N., On the Dynamic Connection Between the Vibrations of the Propeller and the Main Ship Engine, Mechanics of Machines Journal, No. 105, 2014, pp. 87-91.

[6] Minchev N.D., Minchev Yu.N., Minchev I.N., On the Excitation of Vibrations of the Ship Hull by the Propeller, Mechanics of Machines Journal, No. 107, 2014, pp. 81-91.

[7] Minchev Yu.N., Investigations on Vibrations of Elastically Mounted Machines. Dissertation, 2007.

[8] Minchev I.N., Minchev Yu.N., Studies on the Dynamics of Machine Assemblies, EKS-PRES Publishing, Gabrovo, 2019, 372 pages.

[9] Minchev N.D., Minchev N.N., Some Features of Vibrations of an Elastic Rotor with Unbalance. Mechanics of Machines Journal, No. 19, 1997, pp. 66-74.

[10] Papkovich P.F., Works on Vibration of Ships, Shipbuilding Industry Publishing, Leningrad, 1960.

[11] Minchev Yu.N, Minchev I.N., Mechano-mathematical Model and Experimental Results Regarding the Excitation of Vibrations of the Ship Hull by the Propeller. Mechanics of Machines Journal, No. 126, p. 3.

Methodology and Experience in Applying a Non-Destructive Testing Method by Barkhausen Noise Analysis, for Example, in Ion-Treated Samples

Velichko Radoslavov Machev
Bulgaria University of Transport
„Technique and construction
technologies in transport" Faculty
Sofia, Bulgaria
vmatchev@vtu.bg

Nikolay Tonchev Tonchev
Bulgaria University of Transport
„Technique and construction
technologies in transport" Faculty
Sofia, Bulgaria
tontchev@vtu.bg

***Abstract*. The present paper expresses the idea of the possibility of using a non-destructive method of research by means of Barkhausen Noise Analysis (BNA – Barkhausen Noise Analysis), replacing the conventional destructive methods for the examination of nitrided layers, making evaluations and comparisons with them. The paper refers to a specially created methodology, the implementation of which consistently follows the presentation of the paper. Comparing the non-destructive testing methodology with tribological, mechanical and metallographic research can outline which of the analyses can be substituted and what accuracy can be relied upon for the substitution. Heat-resistant steel BH21 was used as the object of research.**

The research is of practical value because the process has been established for this steel. The experience gained in this regard will help to expand and validate non-destructive testing methods.

Keywords: Ion nitriding, property identification, comparison between non-destructive and destructive testing methods.

I. INTRODUCTION

There is a wide range of fundamental and scientific-applied research in the field of methods and means of specialized methods for non-destructive testing, through which labour-intensive and time-consuming methods of destructive approaches can be replaced.

In the process of ion nitriding, because of the difference in the dimensions of the crystal structure of the different phase composition in the ion-treated layer, internal stresses arise. It has been shown that they can be characterized by analysing the characteristics of the magnetic noise [1, 2], caused by the dislocations in the microstructure in the examined ferromagnetic material. The information provided by these characteristics enables differentiated processing of the information used to evaluate the multi-parameter analysis of the nitriding mode and other types of processing of each individual input parameter [3, 4, 5]. This is possible thanks to the property of ferromagnetic bodies discovered by Barkhausen, whose magnetization under the action of an external magnetic field is accompanied by numerous jumps in magnetization. These jump-like changes are called Barkhausen jumps. These jumps are shown to be due to the jump-like displacement of the blast furnace walls. The domain wall is the transition boundary in a transition layer between two domains in which the magnetization spin direction gradually changes its orientation from a direction parallel to the magnetization vector of the first domain to a direction parallel to the magnetization vector of the second domain [6]. In the present research, the assessment is made by comparing traditional characteristics with those of magnetic noise caused by the Barkhausen effect, which according to expert opinion [7] is considered promising.

Apart from that, the authors have their own developed computational approach [8], which has proven its efficiency in the research of problems from engineering technologies. In addition to individual optimization calculations, it can also be used for identification of examined quality indicators, including for non-destructive technologies.

The brief review of the indicated research can determine the characteristic of the chosen topic, which is associated with the complexity and non-linearity of the various properties of the materials in the depth of processing of the considered surfaces. These new surface conditions are formed by a desired set of properties, which is determined by solving multicriteria problems [8, 9]. The latter guarantee certain benefits of the research, most often

expressed in increased longevity (extended life) of contact products [10, 11]. All this relates to the production resource, characterization and applications in the field of hard coatings and wear-resistant surfaces.

II. Materials and methods

The present research aims to provide an idea and a methodology for applying a methodology proven in ion technology that works in practice, to be transferred to other related technologies. The chemical composition of the two steels is listed in Table 1.

TABLE 1. CHEMICAL COMPOSITION OF BH21 STEEL

Steels	C	Cr	Mo	V	W	Si	Mn	Ni	Cu	S
BH21	0,30	2,70	–	0,29	8,01	0,18	0,26	–	–	0,015
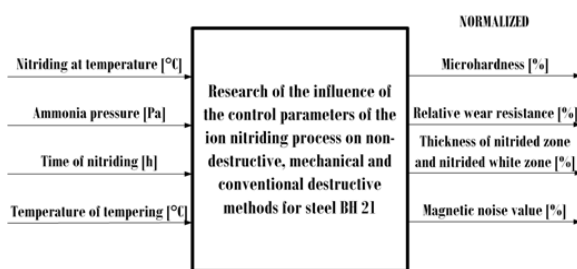
Fig.1. Input-output parameters in the statement of the problem

The influence of the technological parameters on the surface properties of BH21 steel depending on the conditions of ionic nitriding is examined. The complexity of the problem regarding identification in the technological process cited in Fig. 1 lies in the fact that there are more than two technological parameters, and the examined criteria have a different relationship to them. After establishing the relationship between technological parameters and examined criteria through the definition of the models, it is possible to apply a process of identification of surface properties depending on the processing mode. They can be evaluated by a non-destructive method. This process is established in [10, 11] by the limits of variation indicated in Table 2, by the derived models of the controlled quantities in Table 3 and by their extreme values indicated in Table 3.

TABLE 2. INTERVALS OF CHANGE OF TECHNOLOGICAL PARAMETERS

№	Parameter of the technological mode of ion nitriding and preliminary heat treatment	Extreme low	Average	Extreme upper
		Interval value of mode change		
		Code [–1]	Code [0]	Code [+1]
1	Nitriding at temperature t_{nit} [°C] – (X_1)	510	530	550
2	Ammonia pressure P_{NH3} [Pa] – (X_2)	150	300	450
3	Time of nitriding t [h] – (X_3)	4	7	10
4	Temperature of tempering t_{tem} [°C] – (X_4)	600	650	700

The derivation of the models in [10, 11] was done with the methodology presented in [8], and the optimization of the models was performed with [9].

Using [9] there were produced the models shown in Table 3.

TABLE 3. COEFFICIENTS OF THE MODELS FOR THE INFLUENCE OF NITRIDING PARAMETERS ON THE VALUE OF THE INVESTIGATED CRITERIA

Coefficients	BH 21, microhardness	BH21, linked zone	BH21, wear resistance	BH21, total thickness of the nitrided zone
b_0	1102.94	3.66667	0.511111	257.60
b_1*X_1	–7.93750	2.12500	–0.085625	33.810
b_2*X_2	–3.56250	1.12500	–0.018125	–0.330
b_3*X_3	3.06250	–	–0.068125	42.640
b_4*X_4	–55.6875	0.8750	0.030625	–7.910
$b_5*X_1^2$	–	–	–	0.250
$b_6*X_1X_2$	–3.93750	0.8750	0.0118750	0.6250
$b_7*X_1X_3$	3.68750	0.250	0.00437500	–6.880
$b_8*X_1X_4$	25.4375	–0.3750	0.010625	–0.630
$b_9*X_2^2$	–	–	–	–19.750
$b_{10}*X_2X_3$	–22.4375	–0.250	–0.060625	–1.870
$b_{11}*X_2X_4$	11.0625	–0.1250	0.0081250	–5.630
$b_{12}*X_3^2$	–	–	–	–19.750
$b_{13}*X_3X_4$	–12.3125	–0.250	–0.0443750	–5.630
$b_{15}*X_{42}$	–	–	–	–24.750

Through the derived models when applying [10], the extremes of the steel can be determined for each of the parameters. This determined the modes in Table 4.

TABLE 4. EXTREME VALUES OF THE EXAMINED PARAMETERS

Object	Microhardness		Wear resistance		Linked zone thickness		Nitrided zone total thickness	
BH21	Min: 1005.82	X_1 = 510 X_2 = 450 X_3 = 10 X_4 = 700	Min: 0.28	X_1 = 550 X_2 = 450 X_3 = 10 X_4 = 600	Min: 0.33	X_1 = 510 X_2 = 150 X_3 = 4 X_4 = 600	Min: 89.235	X_1 = 510 X_2 = 450 X_3 = 4 X_4 = 700
	Max: 1236.82	X_1 = 510 X_2 = 150 X_3 = 10 X_4 = 600	Max: 0.77	X_1 = 550 X_2 = 450 X_3 = 4 X_4 = 600	Max: 8.417	X_1 = 510 X_2 = 450 X_3 = 4 X_4 = 700	Max: 341.18	X_1 = 550 X_2 = 170 X_3 = 10 X_4 = 650

This review would be more targeted if a methodology could be analytically or numerically defined to fix the influence of different modes on surfaces that are determined as destructive and non-destructive.

III. Results and discussion

Through non-destructive and traditional destructive testing methods, the quality of the products is ensured. Non-destructive testing methods have one significant advantage over all other control methods, which consists in checking each specific product without disturbing its integrity. For this reason, the methodology – object of this research – was created and verified.

The specific research tests the methodology by comparing the value of the measured noise with the results of the models indicated in Table 3 and the extreme values of the examined quantities indicated in Table 4. The algorithm of the methodology is shown in Fig.2.
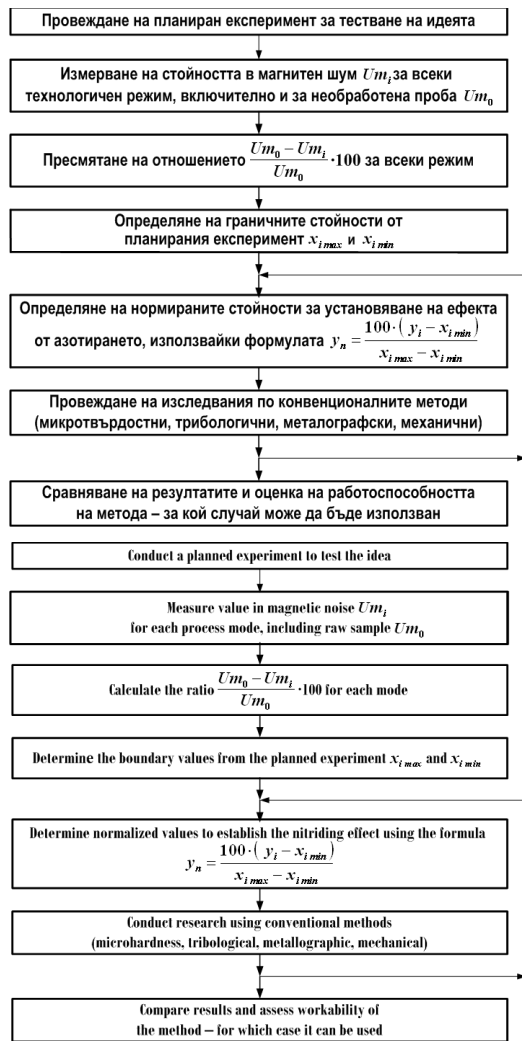
Fig.2. Methodology algorithm

The most essential part of the presented methodology is the calculation of all the examined quantities and their normalization so that the comparison itself can be realized. This is how the credibility of the results is achieved and they can be justified for the purpose of their future use.

TABLE 5. RESULTS OF THE COMPARISON OF THE NON-DESTRUCTIVE CHARACTERISTIC WITH THE DESTRUCTIVE ONES

Mode No.	Umn [%]	Wear resistance [%]	Micro-hardness [%]	Thickness nitrided layer [%]	Thickness white zone [%]
t_{nit}=510 [ºC], P_{NH3} = 150 [Pa], τ = 4 [h], t_{tem} = 700[ºC]	0	15,306	35,93	9,57	31,99
t $_{nit}$=530 [ºC], P_{NH3} = 300 [Pa], T= 2.76 [h], t_{tem} = 650[ºC]	32,76	36,93	40,216	37,31	41,26
t_{nit} =530 [ºC], P_{NH3} = 300 [Pa], T=7 h, τ= 7 [h], t_{tem} = 650[ºC]	52,84	52,86	42,42	66,86	41,26
t_{nit} =530 [ºC], P_{NH3} = 88 [Pa], τ= 7 [h], t_{tem} = 650[ºC]	61,809	47,55	44,58	51,35	21,59
Absolute deviation from the normalized voltage of the measured noise		8.44	17.76	9.65	23.07

To experimentally verify the presented methodology, a real experiment was performed in which the results were compared between the characteristics of the non-destructive testing by means of Barkhausen noise analysis and those of the conventional methods of analysis. Because of the inspection, the following results were obtained.

A graphical interpretation of the results of this comparison is presented in Fig.3.
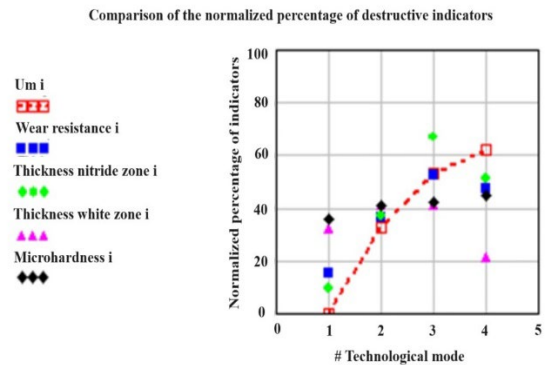
Fig.3. Graphical representation of the comparison results

From this check, the influence of the various parameters of the nitriding mode on the Barkhausen noise characteristic for steel BH21 was determined. Based on this theoretical-experimental research, the following main conclusions can be drawn, which derive directly from Table 5 and Fig. 3.

1. The maximal recoil temperature is associated with the minimally normalized Barkhausen noise characteristic for steel BH21.

2. For BH21 steel, the nitriding process time has less effect on the Barkhausen noise value for BH21 steel than the gas pressure.

3. For each of the examined quality indicators, the absolute deviation from the normalized Barkhausen noise characteristic was determined, and this result ranked the mechanical and destructive methods of analysis. The analysis of this research proves that the non-destructive Barkhausen noise settling method can be successfully applied to the relative wear resistance and the total thickness of the nitride zone for which the deviation is less than 10%.

4. For the final proof of the workability of the methodology, it is necessary to confirm these statements with nitriding under the same conditions on another steel, although the different alloy composition may lead to certain smaller or larger deviations.

IV. CONCLUSION

In conclusion, it is necessary to note that through the research done, the possibility of using the non-destructive research method through Barkhausen Noise Analysis (BNA) replacing the conventional destructive methods for researching nitrided layers, making evaluations and comparisons has been clarified between them. The comparison of the proposed non-destructive methodology with tribological, mechanical and metallographic research reported which of the analyzes can be replaced and what accuracy can be relied on in this replacement. The research refers to heat-resistant steel BH21. The microstructure of the nitrided layer plays an indirect role through the depth distribution of the phases. Through the study, the

relationship between phase composition, technological mode and percentage of normalized destructive tests was found. A non-destructive test has been developed and tested, which can be an alternative to existing destructive methods. We believe that the research also has practical value because the process has been established for this steel. Such experience will help to expand and validate non-destructive control methods.

REFERENCES

[1] Makowska, K., Piotrowski, L., Kowalewski, Z.L.: Prediction of the mechanical properties of P91 steel by means of magneto-acoustic emission and acoustic birefringence. J. Nondestruct. Eval. 36, 43 (2017) https://doi.org/10.1016/j.jnucmat. 2015. 07. 038. ;

[2] Stupakov, O. Local non-contact evaluation of the ac magnetic hysteresis parameters of electrical steels by the Barkhausen noise technique. J. Nondestruct. Eval. 32, 405–412 (2013) https://doi.org/10.1016/B978-0-08-102800-1.00009-5 ;

[3] Samimi, A.A., Krause, T.W., Clapham, L.: Multi-parameter evaluation of magnetic Barkhausen noise in carbon steel. J. Nondestruct. Eval. 35, 40 (2016) https://doi.org/10.1007/ s10921-016-0358-4 ;

[4] Piotrowski, L., Chmielewski, M., Kowalewski, Z.L.: The dominant influence of plastic deformation induced residual stress on the Barkhausen effect signal in martensitic steels. J. Nondestruct. Eval. 36, 10 (2017) https://doi.org/10.1007/ s10921-016-0389-x

[5] Moorthy, V., Shaw, B.A., Mountford, P., Hopkins, P.: Magnetic Barkhausen emission technique for evaluation of residual stress alteration by grinding in case-carburised En36 steel. Acta Mater. 53, 4997–5006 (2005) https://doi.org/10. 1016/j.actamat.2005.06.029.

[6] Santa-aho, S., Vippola, M., Sorsa, A., Latokartano, J., Lindgren, M., Leiviskä, K., Lepistö, T.: Development of Barkhausen noise calibration blocks for reliable grinding burn detection. J. Mater. Process. Technol. 212, 408–416 (2012) https://api.semanticscholar.org/CorpusID:137217703

[7] Vashista, M., Moorthy, V.: Influence of applied magnetic field strength and frequency response of pick-up coil on the magnetic Barkhausen noise profile. J. Magn. Magn. Mater. 345, 208–214 (2013) https://doi.org/10.1016/j.jmmm.2013. 06.038.

[8] Tontchev, N., „Materials science, Effective solutions, and technological variants", Lambert, Academic Publishing, 2014, 142 p., https://www.semanticscholar. org/paper/Materials-Science%2C-Effective-Solutions-and-Variants Nikolay/e5904f3bc8c5ddd127daf5e6f798d1d931cae7a3

[9] Tontchev, N., Gaydarov, V., N. Hristov, N., Analyzes and applications through thecomputational approach DEFMOT, Sofia, 2022, 167 p. (in Bulgarian),

[10] Zumbilev, A.P., Zumbilev, I.A., Ionic nitriding and carbonitriding of steels, 2020, pp. 325, ISBN: 978-619-236-187-7 (in Bulgarian), https://e-university.tu-sofia.bg/e-publ/search-det.php?id=6805 .

[11] Zumbilev, I., About wear resistance of nitrided and carbonitrided layers, Journ. "Annals of the Faculty of Engineering Hunedoara", Tome XIII, Fascicle 1, Romania, 2015, pp. 53-56.

[16] Vuchkov, I., Boyadjieva, L., Quality Improvement with Design of Experiments. A Response Surface Approach, 2001, https://link.springer.com/book/10.1007/978-94-009-0009-7

Evaluation and Strategy Selection in the Anti-crisis Management of the Energy Sector Industry

Marina Petrova Marinova-Stoyanova
Department of Industrial Management
Technical University of Varna
Varna, Bulgaria mpmstoyanova@tu-varna.bg.

Abstract. **This paper examines the significance of evaluation and strategy selection in the anti-crisis management of the energy sector industry. In a volatile and rapidly evolving energy industry landscape, making informed choices regarding management strategies becomes crucial for ensuring the efficient and sustainable operation of energy companies. By analyzing the current context and employing relevant theoretical models and concepts, the article provides an overview of key aspects related to the evaluation and strategy selection in the anti-crisis management of the energy sector industry.**

Keywords: anti-crisis management, energy sector, preventive measures, strategy selection.

I. INTRODUCTION

The energy sector plays a critical role in powering economies and supporting the functioning of various industries. However, there are also crises in the energy sector and disruptions that can significantly impact its operations, supply chains, and overall stability. Therefore, the evaluation and strategy selection in the anti-crisis management of the energy sector industry are of utmost importance.

The evaluation and strategy selection processes in anti-crisis management involve assessing the vulnerabilities and risks faced by the energy sector, identifying appropriate measures to mitigate and respond to potential crises, and formulating strategies that enhance resilience and ensure continuity of operations [1]. These processes are essential for organizations operating in the energy sector to effectively anticipate, prevent, prepare for, and respond to crises that may arise from a variety of factors such as natural disasters, geopolitical tensions, technological failures, market fluctuations, or cybersecurity threats.

The evaluation phase of anti-crisis management involves a comprehensive analysis of the energy sector's vulnerabilities and risks. This includes evaluating the critical infrastructure, supply chains, regulatory frameworks, and potential threats that could disrupt energy production, distribution, or consumption [2]. Through this evaluation, organizations can identify key areas of vulnerability and prioritize resources and efforts towards addressing these weaknesses.

Once the vulnerabilities and risks are assessed, the strategy selection process is applied. This phase involves developing proactive measures to prevent or minimize the impact of potential crises [2]. It includes the formulation of contingency plans, crisis response protocols, and business continuity strategies tailored to the specific needs of the energy sector. These strategies aim to enhance preparedness, ensure effective communication and coordination among stakeholders, and enable prompt decision-making in times of crisis.

Furthermore, the evaluation and strategy selection processes in anti-crisis management should take into account the dynamic nature of the energy sector. Factors such as evolving technologies, changing regulatory landscapes, and shifting market conditions necessitate continuous monitoring and adaptation of strategies to address emerging risks and challenges. By evaluating the effectiveness of implemented measures and regularly updating strategies, organizations can remain agile and resilient in the face of evolving threats.

II. EVALUATION LEVEL OF VULNERABILITY OF THE ENERGY SECTOR INDUSTRYGENERAL REGULATIONS

In the dynamic landscape of the energy sector industry, understanding and assessing the level of vulnerability of organizations and sectors becomes essential for effective anti-crisis management. Vulnerability assessment enables energy companies to identify potential risks and weaknesses, allowing them to develop strategies that address these vulnerabilities proactively.

Vulnerability refers to the susceptibility of an organization or sector to external and internal risks and threats. It encompasses various dimensions, including operational, financial, technological, regulatory, and environmental vulnerabilities [4]. An organization's vulnerability is influenced by factors such as its size, structure, geographical location, dependency on external resources, and market conditions. Recognizing and comprehending the specific vulnerabilities within the energy sector industry is crucial for effective anti-crisis management.

Components of vulnerability assessment. Vulnerability level assessment involves a systematic and comprehensive analysis of various components. These components highlight several important steps:

Risk Identification. Identifying potential risks is a fundamental step in vulnerability assessment. It entails examining internal and external factors that could negatively impact an organization or sector. Internal risks may include outdated infrastructure, inadequate maintenance practices, or insufficient cybersecurity measures, while external risks may involve regulatory changes, market volatility, natural disasters and etc.

Risk Severity Analysis. Once risks are identified, assessing their severity is essential. This analysis considers the potential impact of each risk on the organization or sector. Severity evaluation allows prioritization of risks based on their potential consequences, enabling efficient allocation of resources and proactive risk mitigation.

Weakness Identification. Vulnerability assessment also involves identifying weaknesses within the organization or sector that contribute to its susceptibility to risks. Usually weaknesses encompass gaps in policies, outdated technologies, insufficient training, or inadequate contingency plans. Understanding these weaknesses helps in developing strategies to strengthen the organization or sector against potential crises [5].

Resource Evaluation. Assessing the availability and adequacy of resources to manage risks is another crucial aspect of vulnerability assessment. This includes evaluating financial resources, technological capabilities, human capital, and partnerships. Identifying resource gaps facilitates the development of strategies to acquire or allocate resources effectively.

Methodologies for Vulnerability Assessment. Several methodologies can be employed to conduct vulnerability assessments within organizations and sectors in the energy sector industry. These methodologies include:

The SWOT (Strengths, Weaknesses, Opportunities, Threats) analysis framework enables the identification of internal strengths and weaknesses and external opportunities and threats [6]. This analysis helps in understanding the organization's or sector's position in the industry and potential vulnerabilities.

Risk mapping involves visualizing and mapping potential risks based on their likelihood and impact. It provides a comprehensive view of the organization's or sector's risk landscape and helps in identifying significant vulnerabilities.

Scenario analysis involves developing hypothetical scenarios of potential crises and assessing their impact on the organization or sector. This methodology aids in understanding vulnerabilities under different circumstances, guiding the development of strategies to address them effectively.

Assessing the level of vulnerability within organizations and sectors operating in the energy sector industry is a paramount component of anti-crisis management [7]. It enables proactive identification and mitigation of risks, strengthening the organization's or sector's resilience. Through systematic risk identification, severity analysis, weakness identification, and resource evaluation, vulnerability assessment helps in developing strategies that enhance the organization's or sector's ability to withstand crises. Employing methodologies such as SWOT analysis, risk mapping, and scenario analysis aids in conducting comprehensive vulnerability assessments. Ultimately, a robust vulnerability assessment lays the foundation for effective anti-crisis strategies and contributes to the overall resilience of the energy sector industry [8].

III. IDENTIFICATION OF KEY AREAS OF THE ORGANIZATIONS IN THE ENERGY SECTOR INDUSTRY

In the process of evaluating and selecting strategies for anti-crisis management in the energy sector industry, the identification of key areas within an organization or sector is crucial. These key areas refer to the critical components, functions, and assets that significantly impact the organization's or sector's ability to effectively manage and navigate through crises. They encompass a wide range of aspects, including operational processes, infrastructure, human resources, financial resources, technological capabilities, regulatory compliance, and stakeholder relationships [9]. By understanding and prioritizing these key areas, organizations and sectors can strategically allocate resources, develop targeted crisis response strategies, and enhance their overall resilience.

Various methodologies can be utilized to identify these key areas. One such methodology is business impact analysis (BIA), which involves systematically assessing and evaluating the potential impacts of disruptions on different aspects of the organization or sector [10]. BIA helps in identifying key areas by considering the potential

consequences of disruptions on operations, customer satisfaction, financial stability, and regulatory compliance.

Risk assessment is another important methodology for identifying key areas. It involves the identification, analysis, and evaluation of potential risks that could impact the organization or sector. By examining the likelihood and impact of different risks on critical functions and assets, organizations and sectors can prioritize and focus their efforts on key areas that are most susceptible to disruptions.

Stakeholder engagement also plays a crucial role in identifying key areas. Engaging with stakeholders such as employees, customers, suppliers, and regulatory authorities allows organizations and sectors to gain valuable insights into the critical functions, processes, and assets from different perspectives. This input helps in aligning the organization's or sector's objectives with stakeholder expectations and priorities, ultimately aiding in the identification of key areas.

Expert consultation is yet another effective method for identifying key areas. Seeking input from subject matter experts and industry professionals provides specialized knowledge and experience that can aid in understanding the critical functions, dependencies, and vulnerabilities within the organization or sector. Expert consultation helps in gaining insights into emerging trends, best practices, and potential risks that should be considered in the identification of key areas.

Therefore, the identification of key areas holds immense importance in anti-crisis management. It enables organizations and sectors to allocate resources effectively and efficiently, mitigate risks, enhance preparedness, and develop strategies that address vulnerabilities. By focusing on these key areas, energy sector companies can navigate through crises more effectively, minimize disruptions, and ensure long-term sustainability and success.

IV. FORMULATION OF KEY INDICATORS IN ANTI-CRISIS MANAGEMENT OF THE ENERGY SECTOR INDUSTRY

In the evaluation and strategy selection of anti-crisis management in the energy sector industry, formulating key indicators is particularly important in effectively monitoring and measuring performance. These indicators provide measurable criteria that help assess an organization's or sector's ability to manage crises successfully. They serve as essential tools for tracking progress, identifying areas for improvement, and making informed decisions. By formulating key indicators, energy sector companies can establish a comprehensive framework for monitoring and measuring their performance in critical areas of anti-crisis management, thereby enhancing their resilience and driving continuous improvement.

The process of formulating key indicators begins with clearly defining specific and measurable objectives that align with the anti-crisis management strategy. These objectives provide a clear direction for developing relevant indicators that can effectively measure progress and outcomes.

Once the key indicators are identified, it is essential to select appropriate measurement metrics that accurately reflect the desired outcomes [11]. These metrics should be objective, reliable, and directly relevant to the identified objectives and performance areas. It is beneficial to adopt a balanced approach by incorporating both quantitative and qualitative measures to provide a comprehensive assessment of performance.

To establish a baseline for measuring progress, organizations need to evaluate their current performance levels in the identified key indicators. This baseline serves as a reference point and provides a benchmark against which future progress can be measured. Furthermore, setting realistic and achievable targets helps define the desired level of performance and provides a clear direction for improvement.

Other fundamental components of the formulation process are the data collection and analysis. A structured data collection plan should be developed to gather relevant information aligned with the selected indicators. The data collected should be consistent, reliable, and accurately reflect the performance in the key areas. Through thorough analysis, organizations can track trends, identify patterns, and evaluate their performance against the set targets. This analysis provides valuable insights into areas that require further attention and improvement.

Furthermore, effective reporting and communication of key indicator findings are crucial for fostering transparency, accountability, and informed decision-making. Clear and concise reports should be generated to present the performance of key indicators to relevant stakeholders. These reports should provide actionable insights and recommendations, enabling stakeholders to make informed decisions and drive improvements in anti-crisis management.

Formulating key indicators in the energy sector industry can present certain challenges. These challenges may include ensuring the availability and quality of data, measuring complex aspects such as reputational risks or stakeholder satisfaction, aligning indicators with strategic objectives, and adapting to evolving risks and contexts. Organizations must address these challenges through robust data management practices, stakeholder engagement, and regular review and refinement of indicators.

As the formulation of key indicators is of particular importance in the evaluation and strategy selection of anti-crisis management in the energy sector industry, by setting measurable criteria and aligning them with objectives, organizations can make informed decisions and continuously improve their anti-crisis management efforts in the dynamic energy sector.

V. FORMATION OF A TEAM IN AN EXPERT CRISIS CENTER

In the evaluation and strategy selection of anti-crisis management in the energy sector industry, the formation of a team in an expert crisis center plays a pivotal role in

ensuring a prompt, effective, and coordinated response to crises [12]. A well-structured and skilled crisis response team is of utmost importance in addressing the complexities, uncertainties, and challenges that arise during crisis situations. This process delves deep into the significance of team formation and explores a comprehensive range of key considerations for building a highly effective crisis response team within the energy sector industry.

The Significance of Team Formation. The formation of a crisis response team in an expert crisis center holds immense significance for effective anti-crisis management in the energy sector industry. Crises can have severe implications on the operations, reputation, and overall stability of organizations operating in the energy sector. By assembling a dedicated crisis response team, organizations can ensure a timely and coordinated response, enabling them to mitigate the impact of crises, minimize disruptions, protect stakeholders' interests, and ultimately enhance resilience.

Defining Clear Roles and Responsibilities. One significant aspect of team formation is the clear definition of roles and responsibilities for each team member. By establishing a well-defined structure and assigning specific tasks and areas of responsibility, organizations can foster a sense of clarity, accountability, and ownership within the crisis response team. This enables smooth coordination, effective decision-making, and streamlined communication during crisis situations.

Incorporating Diverse Expertise and Skills. Building a highly effective crisis response team requires the incorporation of diverse expertise and skills that are relevant to the energy sector industry. The energy sector encompasses various domains, including technical, operational, legal, regulatory, financial, communication, and stakeholder management. By assembling individuals with a wide range of competencies, organizations are able to tap into a diverse pool of knowledge and perspectives, enabling comprehensive analysis, innovative problem-solving, and strategic decision-making during crises.

Fostering Effective Communication and Collaboration. Effective communication and collaboration lie at the heart of a successful crisis response team. Establishing clear channels of communication, both internally within the team and externally with relevant stakeholders, is paramount for the exchange of critical information, timely decision-making, and seamless coordination of actions. By fostering an environment of open and transparent communication, organizations can ensure that the crisis response team is well-informed, aligned in their efforts, and able to respond swiftly to evolving crisis situations [13].

Continuous Training and Development. The importance of continuous training and development cannot be overstated in the formation of a highly effective crisis response team. Crisis management is a dynamic field

that requires individuals to stay abreast of emerging trends, evolving regulations, best practices, and technological advancements. By providing regular training programs, workshops, simulations, and knowledge-sharing platforms, organizations can enhance the team's capabilities, build their confidence, and prepare them to handle a wide range of crisis scenarios effectively [14].

Establishing Strong Leadership and Decision-Making Structures. Effective leadership and decision-making are fundamental for guiding the crisis response team during high-pressure situations. A designated team leader or coordinator with strong leadership qualities, including the ability to remain calm under pressure, make informed decisions, and inspire trust and confidence, is instrumental in steering the team towards successful crisis management. Clear decision-making processes, defined authority frameworks, and a collaborative decision-making culture should be established to empower team members and facilitate agile decision-making during crises.

Promoting Collaboration with External Stakeholders. Collaboration with external stakeholders, including government agencies, regulatory bodies, industry associations, local communities, and other relevant entities, is critical for comprehensive crisis management in the energy sector industry. By establishing effective partnerships, communication channels, and information-sharing mechanisms with external stakeholders, organizations can leverage additional resources, expertise, and support during crisis situations. This collaborative approach enhances the team's capacity to access critical information, coordinate actions, and mobilize resources effectively.

Regular Evaluation and Improvement. The formation of a crisis response team is an ongoing process that requires regular evaluation and continuous improvement. After each crisis event or exercise, a thorough review should be conducted to assess the team's performance, identify areas for improvement, and incorporate lessons learned. This feedback-driven approach ensures that the crisis response team evolves, adapts, and enhances its capabilities based on real-world experiences and evolving industry dynamics.

As the formation of a highly effective crisis response team in an expert crisis center is essential for efficient and coordinated anti-crisis management in the energy sector industry, by considering key aspects such as defining clear roles and responsibilities, incorporating diverse expertise, fostering effective communication and collaboration, providing continuous training and development, establishing strong leadership and decision-making structures, promoting collaboration with external stakeholders, and conducting regular evaluations, organizations can build a resilient and agile crisis response team. Such a team will be well-equipped to navigate through crises, mitigate their impact, and safeguard the interests of stakeholders, ultimately contributing to the

long-term sustainability and success of organizations in the energy sector industry.

VI. DEVELOPMENT OF PREVENTIVE MEASURES

In the evaluation and strategy selection of anti-crisis management in the energy sector industry, the development of preventive measures plays a crucial role in mitigating risks and reducing the occurrence and impact of crises. By implementing proactive measures, organizations in the energy sector can enhance their resilience and minimize vulnerabilities that may lead to crises [15].

Risk Assessment and Identification. The development of preventive measures begins with a thorough assessment and identification of potential risks and vulnerabilities specific to the energy sector industry. This involves analyzing operational, technical, regulatory, and market risks that the organization may face. By understanding these risks, organizations can design targeted preventive measures that address the identified vulnerabilities.

Proactive Planning and Preparedness. Once risks are identified, proactive planning and preparedness are essential in developing effective preventive measures. Organizations should create contingency plans, crisis response protocols, and standard operating procedures to guide their actions during potential crises. Regular review, updating, and testing of these plans through drills and simulations ensure their effectiveness. Preparedness allows organizations to respond swiftly and effectively, reducing the impact and duration of crises.

Enhanced Infrastructure and Technology. Investing in enhanced infrastructure and technology is crucial in developing preventive measures. This includes implementing robust monitoring systems, early warning mechanisms, and advanced data analytics tools. Such technologies enable organizations to detect and address potential risks in real-time, preventing them from escalating into full-scale crises. Additionally, robust cybersecurity measures protect critical infrastructure and safeguard against cyber threats that could disrupt operations.

Stakeholder Engagement and Communication. Effective stakeholder engagement and communication are vital components of preventive measures. Organizations should establish strong relationships with employees, local communities, government agencies, and industry partners. Transparent and regular communication channels should be established to disseminate important information, address concerns, and foster collaborative efforts in risk mitigation. Engaging stakeholders creates a sense of shared responsibility and strengthens overall resilience.

Training and Skill Development. Training and skill development programs should be implemented to enhance employees' risk awareness, crisis response capabilities, and effective communication skills. Employees should be equipped with the necessary knowledge and skills to identify early warning signs, respond promptly to potential risks, and take appropriate preventive actions. Regular training sessions, workshops, and knowledge-sharing initiatives foster a culture of preparedness and proactive risk management.

Continuous Monitoring and Evaluation. Preventive measures should undergo continuous monitoring and evaluation to ensure their effectiveness. Regular assessments, audits, and reviews help identify gaps and assess the performance of preventive measures. By actively monitoring their effectiveness, organizations can adapt to evolving risks, technological advancements, and regulatory changes, maintaining a proactive stance in crisis management.

In essence, the development of preventive measures is fundamental in anti-crisis management for the energy sector industry, as the organizations from the sector can enhance their resilience and reduce the likelihood and impact of crises. Implementing robust preventive measures not only safeguards operations and assets but also strengthens the overall reputation and sustainability of organizations in the energy sector industry.

VII. CONCLITION

Evaluation and strategy selection in the anti-crisis management of the energy sector industry are crucial for ensuring resilience and continuity in the face of potential crises. By assessing vulnerabilities and risks, organizations can allocate resources effectively to mitigate and manage these risks. Proactive strategy selection, including contingency plans and business continuity strategies, enhances preparedness and enables swift decision-making during crises. Adapting to the dynamic nature of the energy sector and regularly evaluating and updating strategies is essential for addressing emerging challenges. Prioritizing effective anti-crisis management safeguards operations, critical infrastructure, and contributes to the stability and security of energy supply.

REFERENCES

[1] F. Cucchiella, D'Adamo, I. and Gastaldi, M. 2015. Financial analysis for investment and policy decisions in the renewable energy sector. Clean Techn Environ Policy 17, pp. 887–904, DOI: 10.1007/s10098-014-0839-z.

[2] S.E. Hosseini, 2020. An outlook on the global development of renewable and sustainable energy at the time of Covid-19. Energy Research & Social Science 68, DOI: 10.1016/j.erss.2020.101633.

[3] L.A. Kostyrko, 2015. Formation of strategy of anti-crisis financial management of the enterprises in the conditions of uncertainty analytical maintenance of management. Chasopys ekonomichnykh reform 4, pp. 61–69.

[4] R. Kothari, R. 2017. Financial management: a contemporary approach. Los Angeles: SAGE, pp. 658–666.

[5] P., Crifo, Roudaut, G., 2022, 12, 1227-1258, Economic Crisis and Corporate Governance: How Can Board Independence and Expertise Maximize the Firm Value?

[6] R. Sanchis et al. 2020 – Sanchis, Canetta, L. and Poler, R. 2020. A conceptual reference framework for enterprise resilience enhancement. Sustainability 12(4), 1464, DOI: 10.3390/su12041464.

[7] A.M. Shtanghret, 2016. Anti-crisis technologies in the management of economic security of the enterprise. Lviv: Ukr. akad. Drukarstva, 249 p.

[8] O.O., Tereshchenko, and Pavlovsky, S.V. 2016. Improving the financial mechanism of anti-crisis management of the enterprise. Finansy Ukrainy 6, pp. 108–123.

[9] V. D., Gordienko, Vorob'eva, N. V., Makhonich, I. V., Rubanov, M. N., 2022, Theory and practice management, Lugansk – Krasnoyarsk, ISBN 978-5-86433-922-0

[10] O.A. Baranovsky 2018. Theoretical aspects of assessing the financial stability of the enterprise. Ekonomika i suspiljstvo 15, pp. 206–212

[11] H. Doroshuk, 2021, Prospects and efficiency measurement of artificial intelligence in the management of enterprises in the energy sector in the era of Industry 4.0. Polityka Energetyczna – Energy Policy Journal 24(4), pp. 61–76, DOI: 10.33223/epj/144083

[12] S. Khalatur et al. 2020 – Khalatur, S., Kriuchko, L. and Sirko, A. 2020. World experience adaptation of anti-crisis management of enterprises in the conditions of national economy's transformation. Baltic Journal of Economic Studies 6(3), pp. 171–182, DOI: 10.30525/2256-0742/2020-6-3-171-182.

[13] N. Kuzmynchuk et al. 2021 – N. Kuzmynchuk, Kutsenko, T., Zyma, O., Terovanesova, O. and Bachkir, I. 2021. Paradigm towards ensuring of energy saving in the crisis management conditions in the aspect of sustainable environmental development. E3S Web Conf. 255, 01022, DOI: 10.1051/e3sconf/202125501022.

[14] R. Meiste and Jakstiene, S. 2015. Crisis Diagnosis in Anti-Crisis Management Process in a Company.Oeconomia Copernicana 6(4), pp. 49–58, DOI: 10. 12775/OeC.2015.028.

[15] N. Mocanu, 2018. Implementation of Anti-Crisis Management Technologies. International Journal of Innovation in the Digital Economy (IJIDE), IGI Global, 9(4), pp. 11–23, DOI: 10.4018/IJIDE.2018100102.

Humidity Sensing Elements Based on Silica-Graphene Surface Layers

Nedyu Nedev
Fundamentals of Electrical and Power Engineering
Technical University of Gabrovo
Gabrovo, Bulgaria
nedyu.nedev@gmail.com

Zvezditza Nenova
Fundamentals of Electrical and Power Engineering
Technical University of Gabrovo
Gabrovo, Bulgaria
z_nenova@yahoo.com

Stephan Kozhukharov
LAMAR Laboratory for Advanced Materials Research
University of Chemical Technology and Metallurgy
Sofia, Bulgaria
s.kozhukharov@uctm.edu

Stefan Ivanov
Automation, Information and Control Systems
Technical University of Gabrovo
Gabrovo, Bulgaria
st_ivanov@abv.bg

Toshko Nenov
Automation, Information and Control Systems
Technical University of Gabrovo
Gabrovo, Bulgaria
tgnenov@gmail.com

Abstract. **The paper presents humidity sensing elements based on silica-graphene surface layers, prepared via a sol-gel method. The samples were sintered at temperatures of 400 °C, 600 °C and 800 °C. Tetraethoxysilane was used as a precursor of SiO_2 and as a dopant - graphene aggregates of nanoplatelets. A description of the sample preparation procedure is provided. Using a precise impedance analyzer and a calibrator for humidity and temperature, the changes in their resistance R were investigated with variations in relative humidity in the range of 30% to 90% at a temperature of 25 °C and at a frequency of 20 Hz. Morphological observations and map data analyses were carried out by Scanning Electron Microscopy (SEM) and Energy Dispersion Spectroscopy (EDX).**
The developed sensor elements have a good sensitivity to the humidity, and the resistance change reaches two orders of magnitude. Additions of graphene improve the sensitivity of the elements.
The characteristics of the sensing elements at different sintering temperatures and different amounts of graphene dopant were modeled using an artificial neural network.

Keywords: graphene, humidity sensing elements, silica, sol-gel method.

I. INTRODUCTION

The development of measurements of non-electrical quantities using electrical methods and devices necessitates continuous improvement of sensing elements that respond to changes in various non-electrical quantities.

One of the area in which intensive work is being done is the development of sensor elements for measuring and controlling humidity [1], [2]. This is necessary due to the fact that the amount of moisture in one form or another in the raw materials can have both positive and negative effects on end products in various human activities. Research on humidity sensors is usually aimed at improving their parameters and characteristics [2]. For this reason, humidity sensing elements are developed, operating on different physical principles.

A significant part of the research in this field is based on the development of new materials to achieve goals depending on the specified application. One of the direction is the development of thin-film sensing elements based on oxide materials such as TiO_2 [3], [4], SnO_2 [5] – [7], ZnO [8] – [11], Fe_2O_3 [12], [13], SiO_2 [14] – [18], and others, along with the use of various dopants. The sol-gel method is suitable for developing such sensing elements, allowing the synthesis of nanostructured layers.

Graphene and silicon dioxide are materials widely used. The graphene/silicon dioxide composite has good properties and promising future prospects in various fields [19]. The application of this composite is discussed in various areas such as adsorbents in wastewater purification [20], [21], energy storage, biomedicine, catalysts, etc. [19].

In the present work, thin-film humidity sensing elements based on SiO_2 and graphene, prepared via a sol-gel method and sintered at temperatures of 400 °C, 600

°C, and 800 °C, are proposed. The influence of the amount of graphene dopant on the change in the active resistance R and the properties of the developed sensor elements concerning humidity for the respective sample groups at different sintering temperatures has been investigated.

II. MATERIALS AND METHODS

To prepare the sol-gel systems, the following materials were used: Tetraethoxysilane (TEOS) with a purity of 99%, produced by MERCK, graphene aggregates with submicron particles of 500 m^2/g from Alfa Aesar, 1-butanol 99%, and nitric acid 65%.

In two identical glass vessels, 30 ml of butanol, 30 ml of TEOS, and 3 ml of nitric acid are mixed. To one vessel, 6.0599 g of graphene is added, creating the two main solutions: TEOS (reference) and graphene-containing. Both solutions were subjected to vigorous shaking and left for 1 hour in an ultrasonic bath.

In the next stage, different amounts of the two main solutions are taken into four test tubes, resulting in the following compositions: SiR – 20 ml solution of TEOS (reference), SiG1 – 15 ml solution of TEOS and 5 ml of graphene-containing solution, SiG2 – 10 ml solution of TEOS and 10 ml of graphene-containing solution, and SiG3 – 5 ml solution of TEOS and 15 ml of graphene-containing solution. The obtained compositions are then left to stand for 2 hours at a temperature of 75 °C.
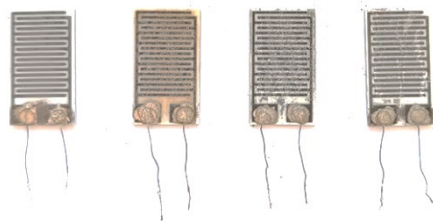
Fig. 1.   Samples SiR, SiG1, SiG2, and SiG3, sintered at a temperature of 800°C.

The deposition of the surface layers was performed on Al_2O_3 substrates with deposited silver-palladium electrodes, which were previously cleaned and degreased with ether. The layer deposition procedure involved immersing the substrates in the respective solutions for 15 minutes, followed by drying for 15 minutes. This procedure was repeated six times, with the final drying lasting for 30 minutes. After depositing the gel onto the substrates, the samples were sintered at temperatures of 400 °C, 600 °C, and 800 °C, respectively, for 30 minutes. Groups of four samples from different compositions were thus obtained and sintered at the three temperatures. Samples prepared using the described procedure are presented in Figure.1

III. RESULTS AND DISCUSSION

A. Surface morphology characterization

To investigate the influence of graphene and different sintering temperatures on the surface morphology of the obtained sensor elements, SEM and EDX analyses were conducted. For this purpose, a Scanning Electron Microscope (SEM), combined with elemental analysis, was used, specifically the TESCAN SEM/FIB LYRA I XMU operating at 20 kV with a magnification of 5000, and an Energy Dispersion Spectrometer Quantax 200 of BRUKER detector.

The SEM and EDX images of the three groups of sensor elements sintered at temperatures of 400 °C, 600 °C, and 800 °C are presented in Figure 2.

In the SEM images of the samples, porosity in the deposited surface material is observed. The presence of porosity facilitates the penetration of moisture into the pores and enhances the sensitivity of the elements to humidity.

As the sintering temperature increases from 400 °C to 800 °C, the material increasingly penetrates into the intergranular spaces in the substrate of these samples. This is most pronounced in the reference sample, without the presence of graphene dopant, at a sintering temperature of 800 °C, where the material largely fills these spaces and has the least pronounced porosity in the surface material.

EDX images confirm the presence of Si and O in all the investigated samples, as well as the presence of traces of C in the samples, in the composition of the solutions for the preparation of which graphene is added.

A. Electrical measurements

The measurement of the active resistance R on the investigated samples under varying relative humidity was performed using the Impedance Analyzer Precision LCR Meter MIFA from Zurich Instruments AG, with the capability to measure with an accuracy of up to 0.05%. The measurements were conducted at a test signal amplitude of 500 mV and a frequency of 20 Hz. The samples were placed in the chamber of the humidity and temperature calibrator, HygroGen2-XL from Rotronic Instruments Ltd., providing controlled humidity in the range of 5% RH to 95% RH with an accuracy of 0.1% RH, and temperature in the range of 0 ºC to 60 ºC with a maximum deviation of 0.01 ºC.

The change in resistance R with varying relative humidity RH for the respective groups of samples sintered at temperatures of 400 °C, 600 °C, and 800 °C is presented in Fig. 3. The measurements were taken in the range of relative humidity variation from 30% to 90% RH at a temperature of 25ºC.

a)

b)

c)
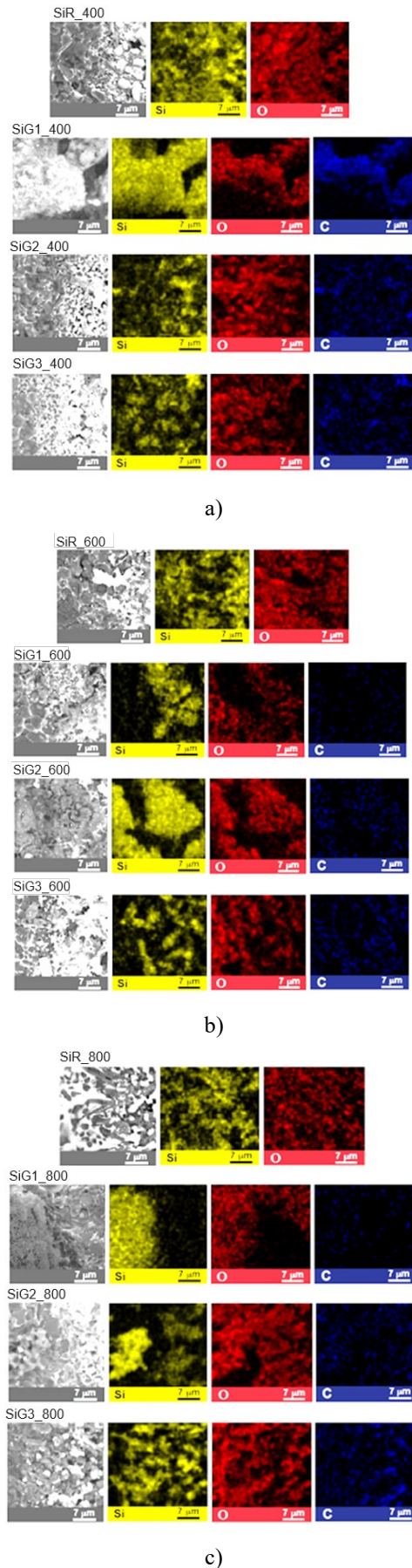
Fig. 2. SEM and EDX images of the surface layers of samples SiR, SiG1, SiG2, and SiG3 sintered at temperatures: a) 400 °C,   b) 600 °C, and c) 800 °C.

a)

b)

c)
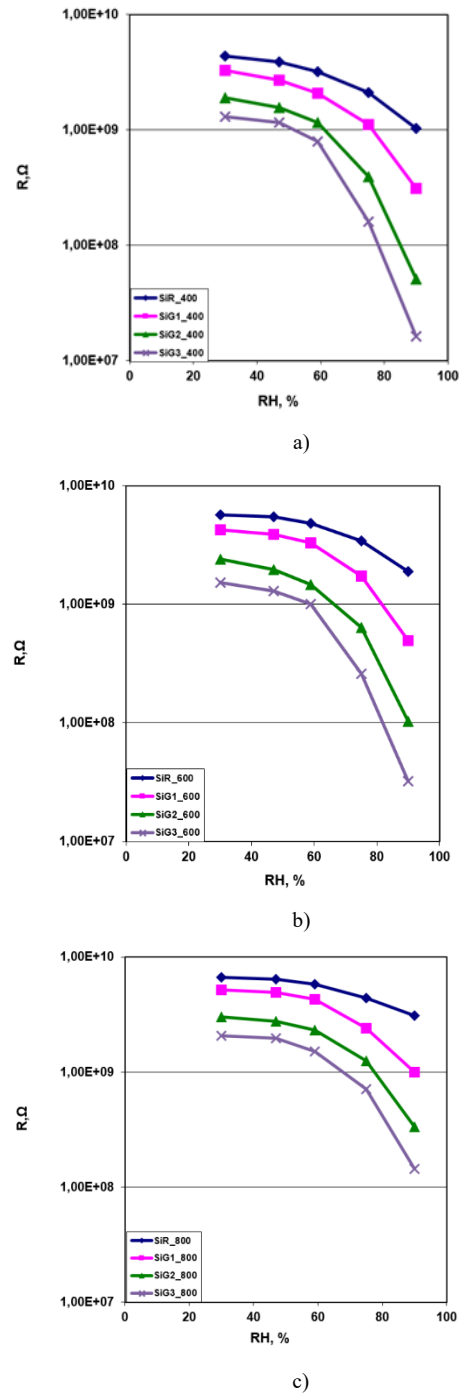
Fig. 3.   Characteristics R = f(RH) for samples SiR, SiG1, SiG2, and SiG3 at sintering temperatures: a) 400 °C; b) 600 °C, and c) 800 °C, investigated at a frequency of 20 Hz and a temperature of 25 °C.

In all three groups of samples, an increase in sensitivity is observed with the addition of graphene compared to the reference samples containing only SiO_2, expanding the range of resistance R variation with changes in relative humidity RH from 30% to 90%. This sensitivity increases with the increasing graphene amount at the respective sintering temperatures. In the case of sample SiG3 sintered at 400°C, a range of R variation of about two orders of magnitude is achieved. Furthermore, the increase in the amount of graphene leads to a reduction in their active resistance.

It should also be noted that with the addition of 15 ml of the graphene-containing solution, the mentioned changes become less pronounced compared to the previous amounts of graphene solution additives, indicating a slowing down of the graphene's effect.

Regarding the sintering temperature, the obtained results show that for the same amounts of graphene dopant, an increase in the sintering temperature leads to an increase in the resistance R and a decrease in its range of variation. The samples sintered at a temperature of 400 °C show the best sensitivity to change in relative humidity, and in the case of the SiG3 sample it reaches 28MΩ/%RH in the range from 55% to 90% RH.

B. Modeling of sensor characteristics

Since the source data represents only a limited number of reference points, in order to present the characteristics of the developed samples, it is necessary to make an interpolation based on the measured reference points. Interpolation of the characteristics of the sensing elements was carried out on the basis of cubic splines, and the obtained results are presented graphically in Figure 4. The obtained curves are for a temperature of 400 °C of samples sintering.
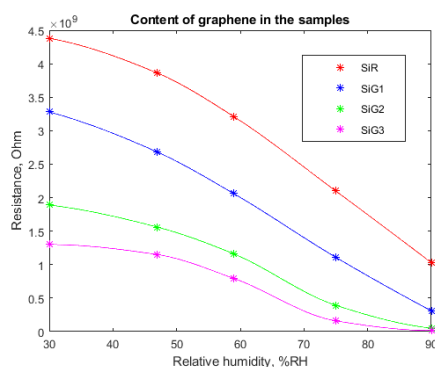
Fig. 4. Characteristics at different amount of graphene

The set of curves and the large number of points that can be obtained based on them are used to generate a 3D interpolated surface of the resistance, which depends on the variation of the relative humidity at different values of the graphene content. Three-dimensional interpolation can be implemented in different ways, in this case generating a set of spline curves at different values of relative humidity and varying the graphene content from 0 to 15 ml with a step of 0.01 ml.

Figure 5 presents a plot of the interpolated 3D surface.
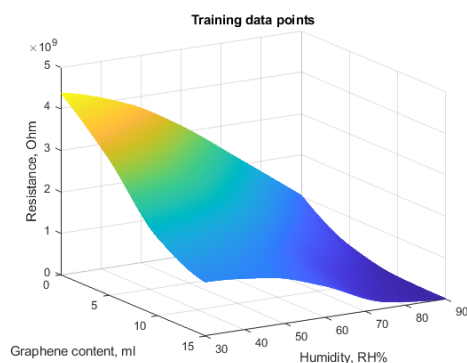
Fig. 5. 3D interpolation

The interpolated three-dimensional data can be used to generate training vectors for training an artificial neural network which can be used as a simulation model to determine the resistance value of a sensing element synthesized at 400 °C while the relative humidity changes, taking into account the amount of graphene used in the preparation of the sensing element.

The training input vector contains an array of [2x902101] elements, and the output vector of expected values contains 902101 elements. Ten percent of the training samples are set aside to be used to test the performance of the neural network after training.

To create the virtual model of the sensor element, a feedforward neural network was used. The network has one hidden layer having 15 neurons in it and one output layer containing one neuron respectively. The neurons in the hidden layer have a sigmoidal transfer function, while in the output layer the transfer function is linear.

The two inputs of the neural network receive data on the relative humidity and the content of graphene, and the output receive results on the value of the resistance of the sensor element at these values.

Since the value of the output resistance varies within very large limits, normalization of the training sample is applied during the training of the neural network. The purpose of normalization is to scale the training data and shrink its range.

Neural network training was performed using the Levenberg-Marquardt training algorithm in the Matlab environment. The training itself was performed for 1000 iterations. As a result, an extremely small error was achieved when validating the operation of the network - 2.86×10^{-6} (Table 1).

After the training of the neural network, its performance was tested using the test samples, and the errors after denormalization of the generated resistance value were determined.

TABLE 1 TRAINING PROGRESS

Unit	Initial value	Stopped value	Target value
Epoch	0	1000	1000
Elapsed time	-	00:29:40	-
Performance	14.1	2.86e-06	0
Gradient	17.9	9.83e-07	1e-07
Mu	0.001	1e-08	1e+10
Validation Checks	0	0	6

After the training of the neural network, its performance was tested using the test samples, and the errors after denormalization of the generated resistance value were determined.

The average value of the testing errors is 4.99×10^{-4}% for the relative humidity RH variation range from 30% to 90% and the amount of graphene in the solutions from 0 to 15 ml, respectively.

From the testing of the neural network, it is found that it can successfully generate at its output data that corresponds to the change in the resistance of the sensor element due to the change in relative humidity at different amounts of graphene dopant.

IV. CONCLUSIONS

Humidity sensing elements based on SiO_2 and graphene prepared via a sol-gel method have been developed. The possibility of improving the parameters of the SiO_2-based sensing elements by using different amounts of graphene dopant and sintering the samples at different temperatures was investigated.

Three groups of samples (SiG1, SiG2 and SiG3) were prepared at different amounts of graphene dopant in the starting solution and reference samples (SiR) based only on SiO_2 precursor.

The influence of sintering temperature was investigated at 400 °C, 600 °C and 800 °C for each of the sample groups.

The obtained characteristics R = f(RH) of the change in the active resistance of the developed sensing elements with a change in the relative humidity RH show that the increase in the amount of graphene as a dopant leads to both a decrease in the resistance of the prepared samples and an improvement in their sensitivity, extending the range of change of resistance with change of relative humidity. Regarding the sintering temperature, the highest sensitivity was obtained for all sample groups at the lower sintering temperature of 400°C. EDX analysis confirmed the presence of Si, O, and C in each of the graphene-doped samples. These samples at the corresponding sintering temperatures have better properties as humidity sensing elements compared to the reference samples based only on SiO_2. For the SiG3 sample sintered at 400 °C, the variation of the active resistance R reaches almost two orders of magnitude when the RH changes in the range from 30% to 90%, and this sample has the lowest resistance compared to the others. This confirms the possibility of improving the performance of SiO_2-based humidity sensing elements with graphene dopant in their preparation by the sol-gel method.

Using an artificial neural network, a model representing the characteristics of the sensing elements was created. The test results show that the model can successfully generate output data corresponding to the resistance change of the sensing elements when the relative humidity changes at different amounts of graphene in the starting solutions.

REFERENCES

[1] Z. Chen, C. Lu, "Humidity Sensors: A Review of Materials and Mechanisms," Sens. Lett., vol. 3, pp.274–295, 2005.

[2] T. A. Blank, L. P. Eksperiandova, K. N. Belikov, "Recent Trends of Ceramic Humidity Sensors Development: A Review," Sens. Actuat. B Chem., vol. 228, pp. 416–442, 2016.

[3] Z. Li, H. Zhang, W. Zheng, W. Wang, H. Huang, C. Wang, A.G. MacDiarmid, Y. Wei, "Highly Sensitive and Stable Humidity Nanosensors Based on LiCl Doped TiO_2 Electrospun Nanofibers," J. Am. Chem. Soc., vol. 130, pp. 5036–5037, 2008.

[4] A. Sun, L. Huang, Y. Li, "Study on humidity sensing property based on TiO_2 porous film and polystyrene sulfonic sodium," Sens. Actuat. B Chem., vol.139, pp. 543–547, 2009.

[5] Q. Kuang, C. Lao, Z. L. Wang, Z. Xie, L. Zheng, "High-Sensitivity Humidity Sensor Based on a Single SnO_2 Nanowire," J. Am. Chem. Soc., vol. 129, pp. 6070–6071, 2007.

[6] H. Feng, C. Li, T. Li, F. Diao, T. Xin, B. Liu, Y. Wang, "Three-dimensional hierarchical SnO_2 dodecahedral nanocrystals with enhanced humidity sensing properties," Sens. Actuat. B Chem., vol. 243, pp. 704–714, 2017.

[7] W. Li, J. Liu, C. Ding, G. Bai, J. Xu, Q. Ren, J. Li, "Fabrication of Ordered SnO_2 Nanostructures with Enhanced Humidity Sensing Performance," Sensors, vol. 17, 2392, pp.1-7, 2017.

[8] L. Gu, K. Zheng, Y. Zhou, J. Li, X. Mo, G. R. Patzke, G.Chen, "Humidity sensors based on ZnO/TiO_2 core/shell nanorod arrays with enhanced sensitivity," Sens. Actuat. B Chem., vol.159, pp. 1–7, 2011.

[9] T. Ates, C. Tatar, F. Yakuphanoglu, "Preparation of semiconductor ZnO powders by sol–gel method: Humidity sensors," Sens. Actuat. A Phys, vol.190, pp.153–160, 2013.

[10] S. Jagtap, K. R. Priolkar, "Evaluation of ZnO nanoparticles and study of ZnO–TiO_2 composites for lead free humidity sensors," Sens. Actuat. B Chem., vol.183, pp.411–418, 2013.

[11] K. Narimani, F. D. Nayeri, M. Kolahdouz, P. Ebrahimi, "Fabrication, modeling and simulation of high sensitivity capacitive humidity sensors based on ZnO nanorods," Sens. Actuat. B Chem., vol. 224, pp. 338–343, 2016.

[12] M. U. Khan, G. Hassan, M. Awais, J. Bae. "All printed full range humidity sensor based on Fe_2O_3," Sensors and Actuators A, vol. 311, 112072, 2020.

[13] H. Yu, S. Gaoa, X. Cheng, P. Wang, X. Zhang, Y. Xu, H. Zhao, L. Huo. "Morphology controllable Fe_2O_3 nanostructures derived from Fe-based metal-organic frameworks for enhanced humidity sensing performances," Sensors and Actuators B, vol.297, 126744, 2019.

[14] Z. P. Nenova, S. V. Kozhukharov, T. G. Nenov, N. D. Nedev, M.S.Machkova. "Characterization of Humidity Sensors with Ce-modified Silica Films Prepared via Sol-gel Method," Bulgarian Chemical Communications, vol.45, Special Edition A, pp.11–16, 2013.

[15] Z. Nenova, T. Nenov, S. Kozhukharov, N. Nedev. "Humidity sensing elements based on Si- Bi-O surface layers prepared via a sol-gel method," IEEE Sensors Journal, vol. 18, no. 17, pp. 6946-6953, 2018.

[16] S. Kozhukharov, Z. Nenova, T. Nenov, N. Nedev, M. Machkova, "Humidity sensing elements based on cerium doped titania-silica thin films prepared via a sol–gel method," Sensors and Actuators B Chem. vol. 210, pp. 676–684, 2015.

[17] Z. Nenova, S. Kozhukharov, T. Nenov, N. Nedev, M. Machkova. "Combined influence of titania and silica precursors on the properties of thin film humidity sensing elements prepared via a sol-gel method," Sensors and Actuators B, vol. 224, pp.143-150, 2016.

[18] Z. Nenova, N. Nedev, S. Kozhukharov, T. Nenov, Humidity Sensors Based on Doped Titania-Silica Surface Layers, 20th International Symposium on Electrical Apparatus and Technologies (SIELA), June 3-6, 2018, Bourgas, Bulgaria 2018, pp. 1-4, IEEE Xplore (SCOPUS), doi: 10.1109/SIELA.2018.8447168.

[19] M. Handayani, N. Nafi'ah, A. Nugroho, A. Rasyida, A. B. Prasetyo, E. Febriana, E. Sulistiyono, F. Firdiyono. "The Development of Graphene/Silica Hybrid Composites: A Review for Their Applications and Challenges," Crystals, vol. 11, 1337, 2021.

[20] I. K. Rind, A. Sarı, M. Tuzen, M. F, Lanjwani, T. A. Saleh. "Synthesis of graphene/silica composites and its removal efficiency of methylene blue dye from water," Inorganic Chemistry Communications , vol. 158, 111507, 2023.

A. Abdelkhalek, M. A. El Latif, H. Ibrahim, H. Hamad, M. Showman. "Controlled synthesis of graphene oxide/silica hybrid nanocomposites for removal of aromatic pollutants in water," Scientific Reports, vol. 12, 7060, 2022.

Technological Project for Vertical Aquaculture Production

Neli Nikolova
Department Management
Technical University of Gabrovo
Gabrovo, Bulgaria
e-mail:nik_nel@abv.bg

***Abstract*. In this report, a technological project is proposed for an ecological greenhouse designed for the cultivation of leafy vegetables, root fruits, spices and aquaculture based on aquaponics. The cycle of sowing, growing, picking the finished product, packaging and shipping is isolated from the external environment and the technology implies optimization of energy resources, seed material, production costs, etc. This ecosystem is innovating the vertical farming industry with high-tech control systems to produce quality and clean produce, reducing costs and making it an attractive option for farmers today.**

Keywords: aquaponics, control, ecological technology, project, vertical farm

I. Introduction

According to United Nations (UN) forecasts, the population of the planet by 2050 will increase by about 2.5 billion inhabitants. In order to provide food, housing and infrastructure for the growing number of inhabitants, qualitatively new technologies will be needed.

About 80% of the land on the planet, on which food products can be grown (vegetables, fruits, grain, meat, dairy products, etc.), is actively cultivated. The remaining 20% of potential arable land will not be sufficient under existing technologies to feed the growing population of the earth. One possibility to solve this problem is vertical urban farms for the production of vegetables and fruits based on aquaponics, using LED lighting with a specific wavelength to intensify the growth of crops.

They are built where the consumers of the produce (vegetables and fruits) are located, and in a small area on many floors (racks) year-round produce is produced with artificially created parameters: light, nutrient medium, temperature, humidity, ventilation, etc. In this way, the annual production from a unit of built-up area can be increased tens of times, with a significant reduction in the cost of production and a guaranteed daily supply of fresh vegetables and fruits with almost zero transport costs.

Vertical aquaculture production is part of the modern intelligent, innovative and sustainable industry in Bulgaria. [1,2,3] This is an alternative approach to growing vegetables in urban settings.

II. Materials and methods

A. Literature review

Leafy greens such as lettuce, cabbage, spinach and arugula are some of the most popular crops grown in vertical farms. These crops are well suited to the controlled environment of vertical farms, allowing growers to precisely regulate temperature, light and humidity levels. Growing leafy greens in a vertical farm also helps reduce the risk of pests and diseases, which can be a significant problem with traditional outdoor growing. [6]

The greenhouse is designed for growing root fruits and vegetables using ecological technology. The cycle of sowing, growing, picking the finished product, packaging and shipping is isolated from the external environment and the technology implies optimization of energy resources, seed material, production costs, etc. Cultivation is carried out in a relatively sterile environment. For this purpose, all incoming flows (raw materials, work personnel, etc.) pass through a disinfecting and deworming section before entering the work space. This guarantees an ecological product that does not need to undergo additional treatment before use.

The greenhouse differs from the ones known so far due to the specific illumination of the cultivated crops, provided by LED strips with a precisely defined spectrum of radiation and a strictly fixed duration of illumination, related to the biological life cycle of the cultivated plants. (Fig. 2).
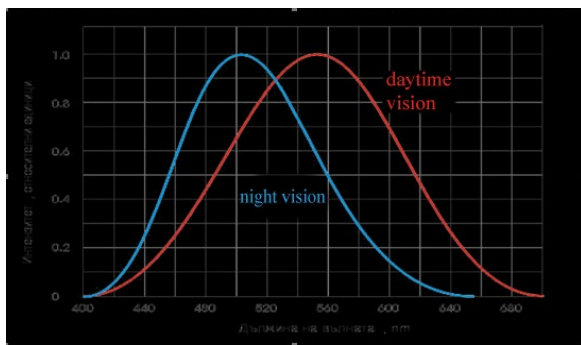
Fig. 1.   Human visible wavelength
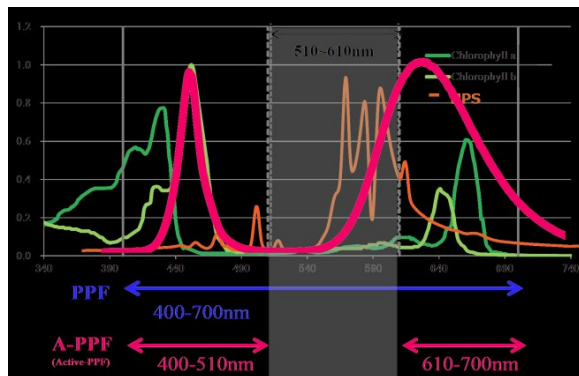
Fig. 2. A necessary absorption spectrum for plant development

Another feature is the biological solution used, which provides the nutritional environment for the plants. A special streamlined system, whose parameters and values are monitored online, allows to guarantee the desired quality and growth rate of the crops. The chemical and biological analysis of the food environment is the basis for the management of technological regimes. The interior of the greenhouse is air-conditioned, with the desired humidity, room temperatures, O_2, and CO_2 content regulated with high precision.

The greenhouse is of a closed type (without external windows) and specific entrance sections to reduce the influence of the environment on the climate (humidity, temperature, air composition) and growing conditions (desired technological parameters and dimensions) of the respective crop, ensuring year-round predictable yields, without seasonal differences. This flexibility allows the replacement of cultivated crops with ones with a higher added value and sales price compared to the season - kopf salad, basil, arugula, etc.

Due to the high automation of the processes, the number of personnel is very small. The greenhouse is adapted to work in different climatic conditions: temperatures from -300° C to $+550^o$ C; humidity from 40% to 90%; rain, snow, etc. Its electrical supply is planned to be provided by the electrical distribution network of the area, by solar panels (in the case of autonomous power supply) or by both sources. Water is supplied from the municipal water supply network.

The greenhouse consists of the following separate rooms:

- Room "Laboratory and seed storage";
- Room "Preparation of seedlings";
- "Product growth" room, in which tubs are located

for the 3 phases of production growth (Storage III - VI);

- "Packaging and forwarding" premises with the following departments (zones):
 - Zone for cutting the roots;
 - "Package" Zone;
 - "Finished product buffer storage" area
- Premises "Zone for transplanting plants from SP(196), from SP(196) to SP(81) and from SP(81) to SP(36)";
- Room "Disinfection and preparation of plates for reuse";
- "Electrical and technological equipment" room
- Service rooms - changing rooms and WC
- Warehouse "Seeds and Laboratory".

The dimensions of the grow room are as follows:
- Length: 29 m;
- Width: 12 m;
- Height: 2.4 – 2.6 m

The purpose of the individual rooms is related to the growing technology of the particular plant.

B. Methodology of the research

Lettuce growing technology

Seeds, buckets and some of the materials needed for sowing are accepted in the "Seed Storage" room, and the chemical-biological laboratory is also located there, where the parameters of the technological flows and the characteristics of the materials are monitored.

In the "Sowing" room, disinfected styrofoam plates are delivered from the warehouse, into the openings of which the plastic buckets for the preparation of seedlings are placed.

The buckets are cone-shaped. The bottom is mesh with holes through which the seedling nutrient liquid seeps. At this time, open the mesh so selected that the zeolite granules do not fall into the water channel.

The buckets are filled up to 2/3 of the volume with granular zeolite, after which they are supplemented with 1÷1,5 centimeters of volcanic mineral sand. The lettuce seed is placed in the middle of the bucket and with light pressure it is buried to about 0,5 cm below the surface in the volcanic mineral sand.
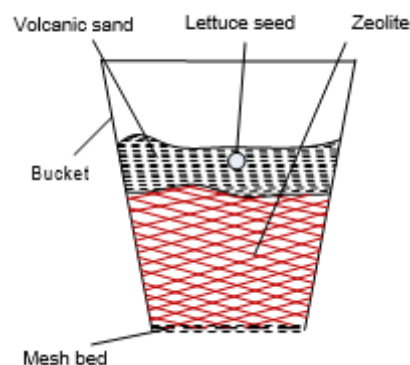
Fig.3. Bucket with seedlings

The buckets prepared with seedlings are placed in the holes of the styrofoam plates, as shown in Figure 4:
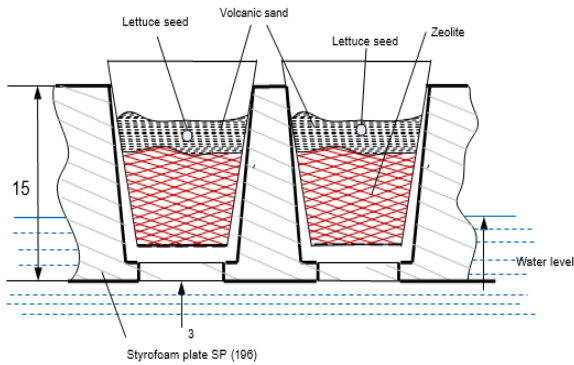
Fig.4. Placing the buckets in the styrofoam plates

The number of the styrofoam plate is related to the number of buckets that can be placed in the holes of the given plate (in this case 196 pcs. - square 14 by 14 buckets).

The operations in this department: placing buckets in the holes of the styrofoam plates and filling them with zeolite, volcanic sand and lettuce seeds are done by hand. The working staff also passes through this room. The input streams are separated and do not cross.

After the styrofoam plates prepared with seedlings have passed through the seeding room, they enter the next room. A tub made of artificial material with a depth of 20 cm and a slight slope in the direction of the technological flow is installed on each shelf.

In view of the height of the room of 2.6 m and the presence of girders, reducing the height to 2.4 m, it is planned to have 3 floors for each rack. The distance between the tubs is 60 cm. LEDs are installed on the underside of the tubs, which provide the necessary light for the growth of the plants. A nutrient solution flows in the tub, the level of which is 10 cm. The system for distributing the nutrient solution to the tub, as well as the air conditioning ducts, are located in the light opening between the tubs.

Styrofoam plates SP (196) with the prepared seedlings in buckets are placed in them, which are pushed every day from right to left, freeing up space for the newly sown plates. The size of these plates is 1 meter X 1 meter, and the styrofoam has sockets with a wide opening at the base through which the aqueous solution penetrates into the zeolite bucket, as shown in Figure 5.

The climate parameters in the "Production growth" room are: the daytime temperature is maintained at 230° C, and the night temperature at -200 °C. The duration of the day is 16 hours, and the night is 8 hours. The light intensity of the lettuce in the different phases of growth is different. In the baths, in one direction, flows a biological solution, which is pumped from a buffer recirculation tank. To preserve the intensity of the nutrient medium, the biological solution is fed to several places along the bath.

The racks have a minimum slope of 1 in 1000 to allow for slow movement of the aqueous solution from one end of the bath to the other and to move the styrofoam plates to the outlet of the aftertreatment baths. The aqueous solution that flows from the end of the baths is collected in a recirculation tank.
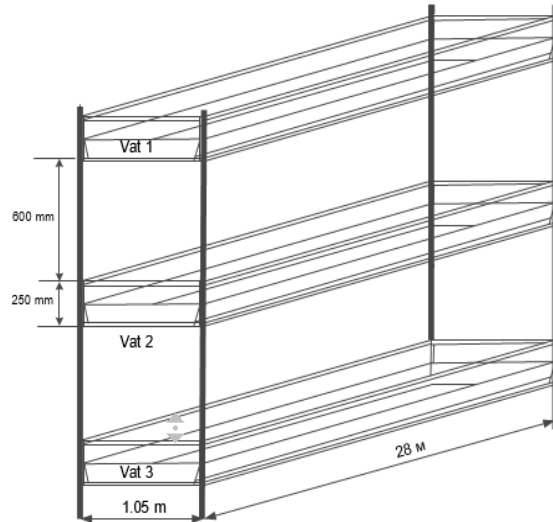
Fig.5. Rack with shelves in the "Produce Growth" room

The lighting of the plants is carried out by LED lighting fixtures with a certain intensity and radiation spectrum, located directly above the styrofoam plates. The conducted experiments and calculations have allowed to determine the most effective lighting, the spectrum, intensity and duration of which stimulate the maximum growth and provide a minimum of dissipated thermal energy that affects the climatic parameters.

Processes in the grow room are realized automatically. For this purpose, the following automated systems have been designed and built:

- Access control system with automatic scanning of access conditions (chip, card, fingerprint, pass sensors);
- Climatic system for control and management of the climate in the room;
- Lighting system to ensure the proper lighting of the vegetation and separately of the working premises;
- A pumping station that manages the water flows from the fish pond to the greenhouse and its water troughs and vice versa - from the greenhouse to the fish pond;
- System for controlling the parameters of the nutrient aqueous solution.

In the "Packaging and forwarding" room, the lettuces grown up to 200 grams and measuring 16.7/16.7/22 cm are removed from the styrofoam plates SP(36), their roots are cut off, keeping a minimal root system in order to preserve the freshness of the lettuces . Empty styrofoam plates and buckets are sent to the "Disinfection and preparation of plates for reuse" room.

In the packaging department, the lettuces are placed in individual packaging (slightly perforated antibacterial cellophane). 20 (5*4) pieces of lettuce are placed in a corrugated cardboard package with dimensions of 80/60/23 cm, and in this way the lettuce is slightly shrunk through the cellophane packaging. The cleanliness of this room determines the biologically clean nature of the finished product.

For the second stage of development of the greenhouse project, additional cultivation of aquaculture (tilapia, rainbow trout) is envisaged, the symbiotic existence allowing the minimization of nutrient solution costs for hydroponic cultures on the one hand and the absence of the need to purify the water environment for fish.

The fish tank room (stage 2) is a key node in the technological process and converts the technology from hydro to aquaponics. The method of building a farm for the combined cultivation of plants (agricultural crops) and fish in an interconnected cycle (mutual exchange) has been known since ancient times.

The name "aquaponics" was proposed by scientists from the University of the Virgin Islands as a result of years of research. This name reflects the combination of two progressive technologies: "hydroponics" - growing plants not in soil, but in a water environment, and "aquaculture" - growing fish, crabs, shrimps, mussels, etc. in a well organized system. [4]

Broadly speaking, aquaponics is the combined cultivation of fish and plants in a circulating ecosystem by using natural bacterial cycles to convert the waste created by the fish into nutrients for the plants.

The main products of the microbiological decomposition of the waste from the farmed fish are ammonia released and dissolved in the water, which under the influence of aerobic bacteria and oxygen dissolved in the water lead to the oxidation of ammonia and its gaseous derivatives - amines (ammonium compounds $[R4N]\ +CI\ -$, aliphatic $CH3-N<$, aromatic $C6H5-N<$, etc.) with the formation of nitrites (salts of nitric acid, such as sodium nitrite $NaNO_2$) and nitrates - "nitric acid" salts of nitric acid HNO_3 , such as ammonium nitrate $NH4NO_3$). This reduces the chemical toxicity of the fish rearing water and allows the plants to absorb the nitrate compounds needed for their growth.

Plants directly absorb ammonia from the water and dissolved salts much more naturally. In this case, the bioremediation process is used: the colonies of bacteria in the substrate and the root system of the plants in a closed cycle of aquaculture, purify the water from toxic substances, and the plants absorb the salts, gases and chemical elements dissolved in the water: nitrates, nitrogen, phosphorus, carbon dioxide and to some extent enrich the water with oxygen, which returns to the pool with the fish in a purified form.

Fertilizer for plants is also detritus - the solid waste from fish in the aquaponics system. Settlers and a system of mechanical filters are used to clean the water of solid waste and suspended particles. Denitrification in "aquaponics" is carried out naturally - a balanced activity of plants and bacteria, and only in extreme cases additional cleaning with expensive carbon filters is necessary.
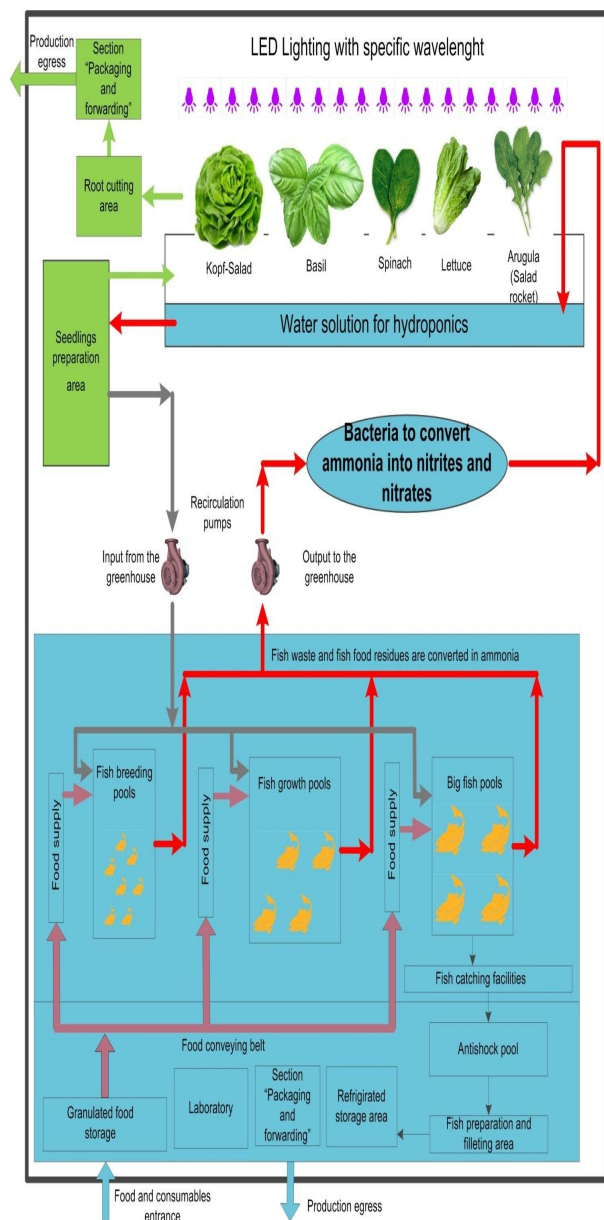
Fig. 6. Technological scheme of aquaponics

A number of observations, and subsequently experiments, have shown that plants can be grown only in a water environment, without the need for soil. At the same time, if fish are grown in the aquatic environment, a double effect occurs. The wastes of fish farming and growth prove to be a suitable nutrient medium for plants immersed in the aquatic environment. In turn, the plants are an excellent filter, as the waste matter from the fish is deposited on their roots, thus purifying the water in the pool. Plants feed on the products released by living organisms (potassium, nitrogen and phosphorus compounds, carbon dioxide, etc.) and naturally purify and enrich the water environment with oxygen. The production process eliminates the need to use chemical fertilizers and the need for their dosing and soil treatment. The chemical process of processing and purification is carried out naturally in a closed cycle and does not require the use of synthetic chemicals.

Aquaponics mimics the natural water cycle in nature. [5] The symbiosis between the cultivation of plants and fish in a common aquatic environment unexpectedly leads

to the intensification of plant and fish growth, resulting in a closed ecosystem.

Fig. 7. Vertical cultivation in urban conditions

III.   RESULTS AND DISCUSSION

The process of producing plants and fish at the same time in such a farm turns out to be ecologically clean, since the biological balance is delicate and any drastic deviations lead to the failure of the plant crop or the death of the growing fish.

In this sense, it can be argued that the fish feed the plants, and the plants protect the aquatic environment in which the fish are raised by removing the substances that negatively affect the farmed fish. Regardless, it turns out that a combined cycle of plant and fish farming is always more efficient than separate farming and yields a greater amount of marketable plant and fish production.

Another characteristic feature of hydroponics (an integral part of aquaponics) is that the cultivation of plants does not require land and its cultivation, and the plants grow in a water environment. This enables the development of the greenhouse in a vertical direction, with the plants themselves being grown in vertically arranged water channels. In this way, a much larger amount of produce is grown per unit of land area (up to 10 times more). Fertilizer for plants is also detritus - the solid waste from fish in the aquaponics system.

Settlers and a system of mechanical filters are used to clean the water of solid waste and suspended particles. Denitrification in "aquaponics" is carried out naturally - a balanced activity of plants and bacteria, and only in extreme cases additional cleaning with expensive carbon filters is necessary.

Of utmost importance for the growth of plants and fish is the pH value of the water environment, which depends on the specific plants and fish, but is generally maintained around 7. Respiration, complete nutrition of the fish and denitrification require a sufficient amount of dissolved oxygen in the water , therefore the water is aerated. Carbon dioxide, as a product of respiration, must be effectively removed from the system either naturally or by filtration

The constant parameters of the water environment have a beneficial effect on the cultivation of fish and plants. For example, a temperature of around 15º-16º C is most suitable for growing cold-loving fish - salmon and trout. These are well known in the market - Atlantic salmon, salmon trout and rainbow trout. The parameters of the fish breeding room are: length – 20 m; width - 10

m and height - 4 m. The pools are divided into small fish breeding areas; raising the fish until they grow up to 10-15 cm and an area for raising fish up to a size of 30-40 cm.

The individual zones in the fish breeding compartment are built from modules, the size of which is typified and determined by the type of fish grown and the amount of desired final catch per day.

The modular construction of the fish breeding room allows different types of fish to be bred and grown in parallel in the individual modular pools, depending on the needs of the market. It is permissible to mix different populations if there is a possibility of non-conflict coexistence.

IV.   RECOMMENDATIONS

Such a system can be built in a standard greenhouse, outside in the garden, in closed rooms (garages, warehouses, underground rooms) with the addition of special LED lighting.

The eco-friendly aquaponic innovation technology makes it possible to create fish farms in a variety of places, for example in buildings or on city rooftops. Home production of useful foods without much effort becomes quite possible. This ecosystem also finds a hobby application, at home or in the office, the fish tank can be combined with a mini garden for growing herbs, fruits, vegetables or flowers. Aquaponics can also be used for educational and research purposes or for agritourism.

V.   CONCLUSION

In the modern age, aquaponics is the garden of the future, because we are in it, but it is also in us - in our home, in the office, everywhere. This new integrated system can provide both fish and crop plants while using minimal resources. The proposed ecological greenhouse proves to be a reliable, sustainable and exciting method of growing food due to its following advantages:

- The lowest production price of lettuce, as with competing technologies, the price of lettuce is about 25% higher.
- The lowest investment for the production of 1 lettuce per day, while with competitive technologies the investment is about 30% higher.
- Lowest energy costs for the production of one lettuce - about 25% lower costs compared to the best achievements.
- As a result of the aquaponic production, the production receives a "bio-certificate", and the water used is reduced by up to 95%.

The developed technological project for vertical aquaculture production is suitable for people who do not have access to traditional agriculture.

REFERENCES

[1] D. Petrova, Intelligent, Innovative and Sustainable Industry in Bulgaria – prospects and challenges, Vide I. Tehnologija. Resursi - Environment, Technology, Resources, Proceeding of the 12th International Scientific and Practical Conference „Environment. Technology. Resources", June 20-22, 2019, Rezekne, Latvia, Volume I, pp. 210-215, ISSN 1691-5402 – print, ISSN 2256-070X – online. https://doi.org/10.17770/etr2019vol1.4188

[2] D.Petrova, An Alternative Approach to Reducing Aging of Innovative Industrial Products in Terms of Industry 4.0, Environment. Technology. Recourses – Proceeding of the 13-th International Scientific and Practical Conference, Rezekne Academy of Technologies, Rezekne, Latvia, 2021, ISSN 1691-5402, Online ISSN 2256-070X, https://doi.org/10.17770/etr2021vol3.6507 p. 274-280, scopus

[3] D. Petrova, An Approach to Modeling Innovation Obsolescence, Vide. Tehnologija. Resursi - Environment, Technology, Resources, Proceeding of the 14th International Scientific and Practical Conference, 2023, Volume I, pp. 175–179, Print ISSN 1691-5402, Online ISSN 2256-070X, DOI:https://doi.org/10.17770/etr2023vol1.7237 , https://www.scopus.com/authid/detail.uri?authorId=56323816400W.-K. Chen, Linear Networks and Systems. Belmont, CA: Wadsworth, 1993, pp. 123-135

[4] [Online]. Available: https://agri.bg/novini/sho-e-to-akvaponika [Accessed: Febr. 10, 2024].

[5] [Online]. Available: https://www.bgaquaponics.bg/aquaponics[Accessed: Febr. 14, 2024].

[6] Crops Grown In Vertical Farming .[Online]. Available: 6https://bg.tenleadpf.com/plant-growing-cube/hydroponic-growing-cube/crops-grown-in-vertical-farming.html [Accessed: Febr. 20, 2024].

Development of a System for Assessment of Digital Professional Suitability in the Company Environment

Neli Nikolova
Department Management
Technical University of Gabrovo
Gabrovo, Bulgaria
e-mail:nik_nel@abv.bg

Abstract. **The relevance of the chosen topic is in response to the increasingly clear understanding by the member states of the European Union that digital professional suitability has an important role in increasing the possibilities of adaptation of human capital to the changing requirements of workplaces and the labor market in the conditions of Industry 4.0. The developed system includes tools, selection of criteria and indicators for the assessment of digital skills and competences, necessary for better professional realization and exercise of key professions/positions in modern Bulgarian enterprises, in line with the level of digitization of company processes.**

Keywords: assessment, company environment, digitalization, professional suitability.

I. INTRODUCTION

The relevance of the chosen topic is in response to the increasing use of technology in daily activities, which inevitably has an effect on a number of aspects of company activity. Digital transformation requires significant investments, technological innovations and targeted measures to stimulate the digital competence and digital culture of the workforce. [1,2]

Timely diagnosis of the current digital skills of the employed and taking measures to overcome the imbalances in skills is important. a prerequisite for the successful implementation of the change and for increasing the competitiveness of Bulgarian companies. Digital skills and competences have an important role in increasing the possibilities of adaptation of human capital to the changing requirements of jobs and the labor market in the conditions of Industry 4.0.

The author aims to propose a set of tools and parameters covering the process of assessing digital skills and competencies, necessary for better professional realization and exercising key professions/duties in modern Bulgarian enterprises. This necessitates the development of a system for assessing the professional and practical suitability of workers working in a digital environment. For this purpose, two tools will be developed and tested for assessment of digital competencies – one for self-assessment against the profile of digital skills required for the job/profession and one for self-assessment of specific digital competencies.

II. MATERIALS AND METHODS

A. Literature review

The topic was developed in response to the increasingly clear understanding by the member states of the European Union that employers and managers need additional and specific digital skills to integrate innovation in all company activities.

To improve their competitiveness it is necessary for Bulgarian industrial enterprises to focus their efforts on increasing the quality of the workforce by improving its practical skills for working in a digital environment.

The developed system defines the specific competencies for individual positions, necessary to perform their daily tasks in the course of the production process and which require the application of digital technologies. Three separate strands are being introduced in terms of digital competences:

- basic digital competences that apply to the entire target group;
- competencies aimed at the use of digital technologies by company specialists;
- digital competences for the management of the production process, aimed at managers and administrative staff.

Alignment with national, regional and university priorities

The topic was developed in accordance with the vision and directions for the digital transformation of Europe 2020 - 2030 "Digital Compass" adopted by the European Commission.

European documents of key importance for the present development refer to:

- European Qualifications Framework for Lifelong Learning;
- New European Adult Learning Program 2021-2030;
- EU Plan "Road to the Digital Decade" to achieve a digital Europe by 2030.
- Europe 2030: A strategy for smart, sustainable and inclusive growth.

National applicable documents

- Program for research, innovation and digitization for smart transformation for the period 2020-2027.
- National strategy for individual small and medium enterprises 2021-2027;
- Program for competitiveness and innovation in enterprises for the period 2021-2027;
- Human resources development program 2021-2027;
- Operational program "Competitiveness and innovation in the enterprise" 2021-2027;
- Ministry of Labor and Social Policy Project BG05M9OP001-1.127-0001 "Development of digital skills".

Content aligns with **priorities** in:

- Thematic area "Mechatronics and clean technologies - Design in mechanical engineering - Engineering, reengineering and continuation of the life cycle of industrial machines, devices and systems, laid down in the Innovation Strategy for Intelligent Specialization of the Republic of Bulgaria 2021-2027;
- Internationalization strategy of Technical University - Gabrovo for the period 2020-2030;
- Strategy for intelligent specialization of the municipality of Gabrovo 2021-2030.

The "Mechanical Engineering" sector has a decisive role for the European economy. The sector is a strategic industry with high added value, knowledge-intensive, providing other economic sectors with machinery, production systems, components and related services, including technology and knowledge. [6]

Purpose and tasks of research

Based on a research analysis of the current state of engineering companies, a system for evaluating digital professional suitability in a real company environment, corresponding to the modern requirements of Industry 4.0, has been developed and adapted.

In this report, the digital professional suitability of the incumbent is defined as a set of knowledge, skills and behavior (attitudes) for the performance of work duties, functions and tasks involving the use of information and communication technologies.

Main activities for their implementation

1. Identifying the leading literary sources, articles and keywords in the problem area and defining the basic terms and concepts necessary for its processing.

2. Identification of key professions/positions in specific companies of the "Mechanical Engineering" sector, which is of great importance for the Bulgarian economy in terms of increasing the added value, improving the foreign trade balance and employment. The process of globalization and the integration of Bulgaria into the international business community place high demands on competitiveness and technological development for those employed in the sector.

3. Diagnosing the state and needs for the development of digital skills/competences for the identified key professions/positions in the surveyed enterprises.

4. Development of tools, selection of criteria and indicators for the assessment of digital competences, consistent with the level of digitization of company processes.

5. Establishing the needs of individual categories of personnel for specific training to improve their digital skills depending on the specifics of the activity being performed.

6. Development and adaptation of a system for evaluating the digital professional suitability of employees in a real company environment.

7. Pilot testing of the proposed system and making corrections with a view to increasing its adaptability and effective practical applicability in the sector.

B. Methodology of the research

- office research for collecting and processing information from literary and online sources about the researched problem;
- analysis and assessment of European and national applicable documents on the subject;
- survey in companies and enterprises with employers to establish the state and needs of digital skills in key professions/positions;
- conducting a "brainstorming" method to identify the key employees and workers in the investigated company activities;
- in-depth interviews and discussions with representatives of branch organizations, employers and interested parties to discuss the applicability of various models for increasing the digital professional suitability of workers in the "Mechanical Engineering" sector.

III.   RESULTS AND DISCUSSION

A. Scientific results

a. Expanding the term "professional suitability" to include digital competencies for the exercise of key professions in modern companies.

b. Renewing strategic approaches to digital education and digital skills and competences.

c. Development of training programs for training and development of specific digital skills based on research and establishing the needs of workers.

d. Methodology for managing and evaluating the professional suitability of human resources for the sustainable development of engineering companies in a digital environment.

e. Supplementing the content and scope of the job descriptions such as functions and tasks, typical of the professions of the NCPD in the country.

f. Promotion of obtained results in scientific publications at the announced annual international conferences.

B. Applicability of the results in practice and the learning process

a. Scientific and methodical support of machine-building companies in connection with the identification of key professions and positions in the industry as a structural determinant for the industry.

b. Practical application of the developed tools for assessing the digital skills and competences of workers.

c. Building models of social partnership and collective bargaining related to the digitization of company processes.

d. Establishing the needs for improvement and additional training for the development of specific digital skills, according to the requirements of a specific position.

e. Testing and adaptation of the system for assessing the digital professional suitability of key categories of personnel in a selected real company from the "Mechanical Engineering" sector.

f. The obtained experimental results from the adaptation of the digital professional suitability evaluation system will be reflected in the curricula of the students of the "General Engineering" and "Materials and Materials Science" professional fields.

The development of the competence profiles is preceded by analyzes of the needs of digital skills in companies from the "Mechanical Engineering" sector, included in the conducted study.
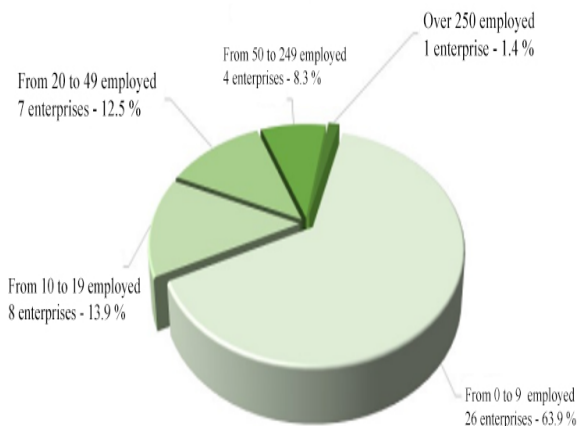
Fig.1. Number and type of enterprises in the study

A questionnaire was used to establish the availability of the necessary digital skills/competences among employed persons occupying key professions/positions. It contains 5 main directions with formulated scales for diagnosing the mastery levels of each competence related to:

- information and data;
- communication and cooperation;
- creation of digital content;
- safety and security;
- solving cases.

TABLE 1. DIGCOMP COMPETENCE FRAMEWORK
(Stephanie, Riina, & Yves, 2017) [5]

Areas of competence	Competencies
1. Information and data	1.1 Browsing, searching and filtering data. information and digital content
	1.2 Evaluation of data, information and digital content
	1.3 Data management, information and digital content
2. Communication and collaboration	2.1 Interaction through digital technologies
	2.2 Sharing through digital technologies
	2.3 Civic participation through digital technologies
	2.4 Collaboration through digital technologies
	2.5 Netiquette
	2.6 Digital Identity Management
3. Content creation	3.1. Digital content development
	3.2 Integration and processing of digital content
	3.3 Copyrights and Licenses
	3.4 Programming
4. Safety	4.1 Protection of electronic devices
	4.2 Protection of personal data and privacy
	4.3 Protection of health and welfare
	4.4 Environmental protection
5. Problem solving	5.1 Solving technical problems
	5.2 Identifying needs and technology responses
	5.3 Creative use of digital technologies
	5.4 Identifying gaps in digital competence

The starting point for the development of the questionnaire in terms of content is the European Digital Competence Framework DigComp, implemented as an assessment tool for the respondents. [4] The obtained

average results are normalized in 5 levels (table 1): no skills; basic, low, medium and high. Digital skills are assessed through self-assessment questions on knowledge and skills for working in a digital environment. Tests and practical tasks are used to assess real digital competences.

The analysis shows that only 16% of employees meet the required level of digital competence for their key position.

Among the overall digital competencies, information and data literacy had the highest share (27.6%), followed by communication and collaboration competencies (23.3%), safety (21.9%), problem solving (19.5%) and digital content creation (7.7%).

The most specific competencies relate to information and data literacy (44.8%), followed by digital content creation (21.6%), problem solving (19.5%), communication and collaboration (10.3%) and safety (3.8%).

The survey found that 56% of employers are looking for a workforce with an advanced level of basic digital competencies, and 14% require a highly specialized level. 28% would accept workers with an intermediate level of basic digital competencies, and only 2% - with a basic level. In terms of specific digital competencies, 54% of employers require an advanced level, 19% - a highly specialized level, 23% an intermediate level, and 4% a basic level.
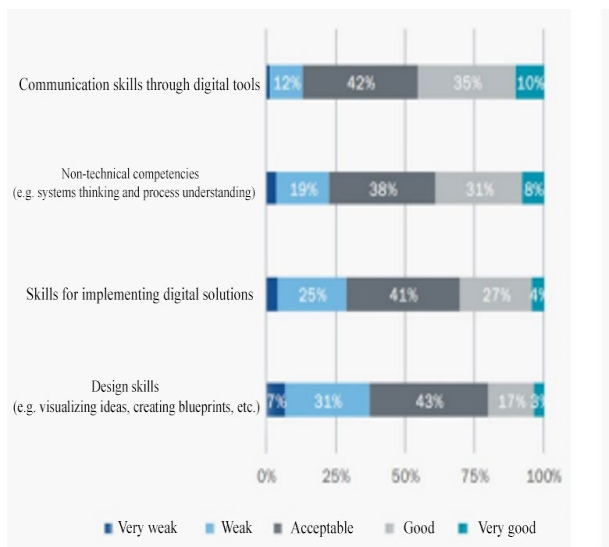
Fig. 2. Assessment of respondents' current skills

More than 46% of the surveyed persons have to one degree or another problems with digital skills, which inevitably reflects on the quality of their work, on their suitability for employment and their ability to successfully transition to the labor market. About 13% of the surveyed persons have deepening problems with digital skills, which brings them closer to dropping out of the labor market, digital isolation, social and digital inequality.

The change in skills is clearly visible. Overall, engineering jobs in the future will be primarily about cognitive digital and complex transversal digital skills that require some basic technical and digital knowledge. For those working in the sector, social competences must also

be improved when it comes to developing skills in an increasingly digitized work environment.

There are significant differences (digital inequality) in the level of digital competence between different categories of personnel, as well as between individual enterprises within the sector. The levels of digital competence are directly dependent, both on the differences in the degree of maturity of the technologies used, and on the company's policies for the management and development of human resources.

From the conducted in-depth interviews with line and functional managers, we find that there is not yet a sufficiently developed practice in enterprises to assess the level of the current digital skills of the staff. More attention is paid to technology, but not to people.

Against the background of the changing nature of work, the changing specifics of the tasks performed at the workplace and the dynamically growing requirements for digital skills in the conditions of the transition to digitalized workplaces, 34% of the employees in the studied engineering companies possess only basic digital competence - minimal digital skills related to the use of more widely applicable unified software products and digital technologies such as Windows, Word, Excel, PowerPoint, working with Outlook, working on the Internet, working with digital platforms for communication, etc. This is an indicator of the quality and results of basic training - education and vocational training.

In companies that have implemented new equipment and technologies in recent years, the need for qualified personnel with new competencies in the field of: welding; laser cutting; heat treatment, etc. The basic training of specialists in theory takes place in the system of higher and professional education and training (university, vocational high schools, vocational high schools, vocational schools, licensed by NAPOO), but for their transformation into highly qualified specialists and workers, the training continues in the companies themselves, including . on the specific jobs.

In a number of companies that have supplied modern equipment and technologies, there is an urgent need for training the people who will work with them. The training is specialized and is for the specific workplace.

To the question: "How would you rate the importance of training programs related to increasing digital competences?, we received the following responses, presented in the figure:
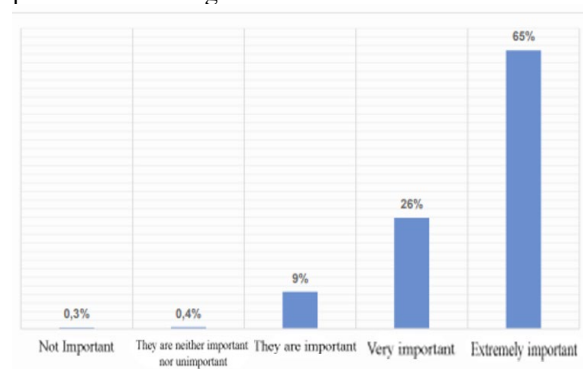
Fig.3. Respondents' assessment of the importance of training programs in the field of digital competence

The research conducted shows that both managers and employees are aware of their responsibility to invest time and/or financial means to improve their skills in the field of digital technologies. Around 50% of managers surveyed strongly agree that businesses should invest in training programs to keep their employees' digital skills up to date, and 58% of employees agree that they should invest in digital training themselves. In this context, the social partners play a crucial role in raising the awareness of employees at all levels about the need to actively participate in training measures. Participating respondents recognize the important role of the cooperation of the social partners in this process. Over three-quarters of employees and two-thirds of managers surveyed agree that social partners should negotiate new and/or review existing training schemes.

Interviewed managers emphasize that, in addition to collective and legally binding agreements, other options should be used to address and shape the digital transformation of the workplace and the challenges arising from it.

The general and specific digital skills required have been determined based on reports and studies on the state of the Mechanical Engineering sector; state educational standards for acquiring qualifications in professions; job descriptions for the identified positions; analysis from brainstorming sessions with industry experts, HR managers and vocational training specialists; National classification of occupations and positions.

The self-assessment system enables employees in key occupations to identify their digital skills/competence levels. The value of each scale is an arithmetic mean, ranging from 0 to 3 points. The results are divided into the following levels: «no skills»; low, medium and high.

The tool allows the measurement of digital competence through the three elements – knowledge, skills and attitudes, providing respondents with an opportunity for self-analysis of their digital competence through clear and easy-to-fill questions regarding practical activities and common situations in the professional environment.

TABLE 2. SYSTEM FOR SELF-ASSESSMENT THE LEVEL OF DIGITAL COMPETENCE BY THE TARGE GROUP

Knowledge	Skills	Attitude
0 p. – I have no idea of that;	1 p. – I don't know how to do it;	1 p. – missing;
1 p. – I have limited knowledge and need further explanations;	1 p. – I can do it with someone else's help;	1 p. – weak;
2 p. – I have good knowledge in the professional field;	2 p. – I can handle it on my own;	2 p. – average;
3 p. – very good	3 p. – I am an expert and can guide others.	3 p. – high.

From the conducted «brainstorming» conversations, mainly with the managements of the investigated enterprises to identify the key employees and workers in the investigated company activities, concrete proposals were also formed for the development of competency models for individual professions/positions and their testing with them such as: «design engineer» , «engineer-technologist», «engineer-supervisor», «machinist «operator of metalworking machines», «operator of metal-cutting machines with CNC», «locker-installer».

IV. RECOMMENDATIONS

The pilot testing of the proposed system aims to assess its quality and reliability by providing an opportunity for employers and employees to optimize the content of the skills and knowledge they use. On the other hand, corrections can be made in order to increase its adaptability and effective practical applicability in the sector. The approaches we propose for system validation are:

- sending the collected and analyzed information from the conducted survey to the heads of companies for feedback in the form of corrections, additions, clarifications and notes;
- conducting focus groups for its discussion with representatives and experts in the "Mechanical Engineering" sector, who can share an opinion on the applicability of the developed system for evaluating the digital professional suitability of performers of key professions in their organizations;
- sending feedback surveys to the incumbents of elected positions with formulated questions and an evaluation scale.

The questionnaire contains:
- the proposed general and specific digital competences, including the specific knowledge, skills and behaviors that form them, as well as a 4-level scale for applicability assessment by the relevant respondent;
- two questions related to determining the recommended level of mastery of general and specific digital skills/competencies according to the opinion of the respondents (two persons each from one company for a specific profession/position – employer or manager and the incumbent) for validating a unified profile of various enterprises in the sector.

V. CONCLUSION

In the current study, a wide range of sources were considered, which allow a broad and comprehensive view of the topic under consideration. The research covered a number of international, European, national and sectoral developments, both related to digital transformation in general, and considering the development of the engineering sector in particular, incl. against the backdrop of the digital revolution. The "Brainstorming" method conducted among representatives of different categories of company

personnel was aimed at presenting the point of view of those working in the sector. Through tools such as surveys and interviews, Bulgarian enterprises were given the opportunity to provide reliable information about the real situation in the sector, about their level of digital readiness, about the problems they face, about their vision in the future, about the sought-after and possessed skills of employees for their views on the causes leading to shortages in the workforce and other aspects of their activities.

The scope of the research and the analysis made shows the degree of readiness of the sector for the implementation of digital technologies; identification of the key positions influencing the achievement of the strategic goals of the enterprises related to the digital transformation in the sector, as well as establishing the deficits of digital skills of the holders of the identified key positions by comparing the general and specific competencies sought and possessed in the selected key positions.

The presented system for evaluating the digital professional suitability offers a set of tools and criteria that can be applied in other branches at the company level.

An aging population and the adoption of digital technologies will lead to a huge skills imbalance globally, with the Mechanical Engineering sector fully following this trend. To counter this, employers in Europe need to be more flexible, adaptable and creative.

REFERENCES

[1] D.Petrova, Intelligent, Innovative and Sustainable Industry in Bulgaria – prospects and challenges, Vide I. Tehnologija. Resursi - Environment, Technology, Resources, Proceeding of the 12th International Scientific and Practical Conference „Environment. Technology. Resources", June 20-22, 2019, Rezekne, Latvia, Volume I, pp. 210-215, ISSN 1691-5402 – print, ISSN 2256-070X – online. https://doi.org/10.17770/etr2019vol1.4188

[2] D. Petrova, An Alternative Approach to Reducing Aging of Innovative Industrial Products in Terms of Industry 4.0, Environment. Technology. Recourses – Proceeding of the 13-th International Scientific and Practical Conference, Rezekne Academy of Technologies, Rezekne, Latvia, 2021, ISSN 1691-5402, Online ISSN 2256-070X, https://doi.org/10.17770/etr2021vol3.6507 p. 274-280

[3] T. Varbanova, Models for assessing digital competence. Institute of Public Administration , 2021, ISBN 978-619-7262-24-7 [Online]. Available:

https://www.ipa.government.bg/sites/default/files/digital_competence_final.pdf. [Accessed: Febr. 16, 2024].

[4] Digital literacy self-assessment [Online]. Available: https://motiv-action.eu/wp-content/uploads/2023/02/M1L3-BG.pdf. [Accessed: Febr. 18, 2024].

[5] Sectoral analysis of the sector "Manufacture of general and special purpose machinery and equipment". Sofia, 2013

[Online]. Available: https://www.bia-bg.com/uploads/files/analysis/ISOK/533_1_Machinostroene-2013_signed.pdf. [Accessed: Febr. 9, 2024].

Experimental Study of Turbulence in the Test Section of Wind Tunnel

Hristian Panayotov
*Department of Transport and
Aircraft Equipment and Technologies
Technical Univercity of Sofia,
Plovdiv Branch*
Plovdiv, Bulgaria
hristian@tu-plovdiv.bg

Stanimir Penchev
*Department of Transport and
Aircraft Equipment and Technologies
Technical Univercity of Sofia,
Plovdiv Branch*
Plovdiv, Bulgaria
spenchev@tu-plovdiv.bg

Martin Zikyamov
*Department of Transport and
Aircraft Equipment and Technologies
Technical Univercity of Sofia,
Plovdiv Branch*
Plovdiv, Bulgaria
martinzikyamov@gmail.com

***Abstract*. The given report presents an experimental study using PIV methods (Particle Image Velocimetry) of the relative turbulence in the test section of the wind tunnel ULAK-1, located in the Laboratory of Autonomous Aircraft Aerodynamics in the Plovdiv Branch of the Technical University of Sofia. By means of the turbulence sphere method and by analysis of the flow in the test section in two perpendicular planes (parallel to the free-stream velocity and Trefftz plane), the turbulence factor and the relative turbulence were determined. The obtained results are important characteristics of the wind tunnel and will be used in future experimental studies. The same are compared with previous ones obtained by hot-wire anemometry measurements.**

Keywords: aerodynamics, turbulence, wind tunnel, particle image velocymetry.

I. Introduction

The experimental measurements in wind tunnels play an ever increasing role in aerodynamic investigations both to validate simulation results and to yield new ones that are complicated to simulate [1]. In order to obtain precise results corrections, need to be made to compare the aerodynamic characteristics of the model in wind tunnel to aircraft characteristics in atmosphere. Besides only following the similarity criteria, the relative turbulence in the wind tunnel test section has a significant impact on the experimental results [2]. The last must be compared to the relative turbulence of the atmosphere. Therefore, the aim of the present study is to experimentally determine the relative turbulence (later only turbulence) in the test section of ULAK-1 wind tunnel, located in the Laboratory of Autonomous Aircraft Aerodynamics in the Plovdiv Branch of the Technical University of Sofia. The main properties of the wind tunnel ULAK-1 are:

- Dimensions of the cross section of the test section (WxH): 600 mm x 400 mm;

- Length of the test section: 1000 mm;
- Maximum span of the model: 400 mm;
- Wind speed: 2-50 m/s.

Two methods are used to determine the turbulence in the test section – the method of the sphere using the transition from laminar to turbulent boundary layer and PIV (Particle Image Velocimetry) method where the mean velocity and its fluctuations are measured.

The turbulence in percents is defined by following formula [1]:

$$\varepsilon = \frac{\sqrt{\bar{v}^2}}{\bar{V}} 100 \qquad (1)$$

where: $\sqrt{\bar{v}^2}$ is the mean squared fluctuation speed; $\bar{V}$ is the mean velocity of the flow.

The first method – the method of the sphere is focused on obtaining the critical Reynolds number of a sphere, located in the test section of the tunnel where the transition phenomenon occurs from laminar (S) to turbulent (T) boundary layer. This phenomenon is depicted in Fig. 1.
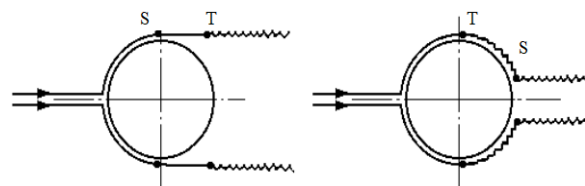
Fig. 1. Transition from laminar to turbulent boundary layer of a sphere.

In the present study transition is observed by PIV visualization of the flow field and is compared to previous studies that use obtaining the critical Reynolds number by measuring the drag of the sphere (Fig. 2). Before the transition of the boundary layer the pressure drag is much

higher than the friction drag. When transition occurs the drag coefficient drops due to lower pressure drag and this is also illustrated in Fig.2. Once the critical Reynolds number for the sphere in wind tunnel is determined the Turbulence factor (TF) can be calculated as the ratio of the critical Reynolds number of the sphere in wind tunnel and same in atmosphere [2].

The turbulence factor (TF) can be calculated using the following equation [2]:

$$TF = \frac{385000}{Re_{cr}} \qquad (2)$$

where: 385 000 is the critical Reynolds number of the atmosphere; Re_{cr} is the critical Reynolds number of the wind tunnel.

The turbulence factor is an important characteristic of the wind tunnel, and it is used to compare the results, measured in the wind tunnel and those of aircraft flying in the atmosphere by calculating the effective Reynolds number of the model [2]:

$$Re_{eff} = Re_{model}TF \qquad (3)$$
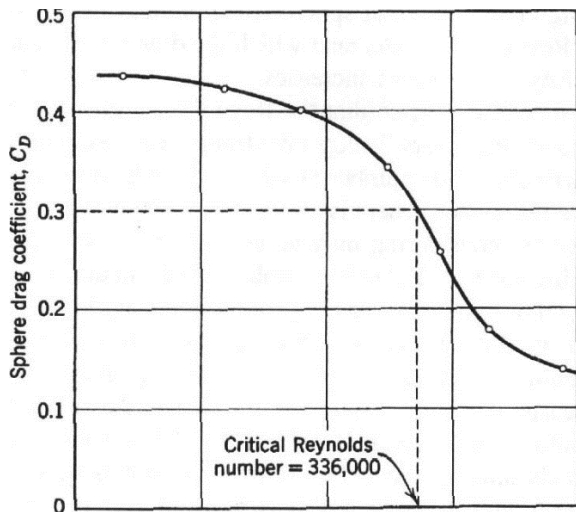
Fig. 2.   Critical Reynolds number of a sphere.
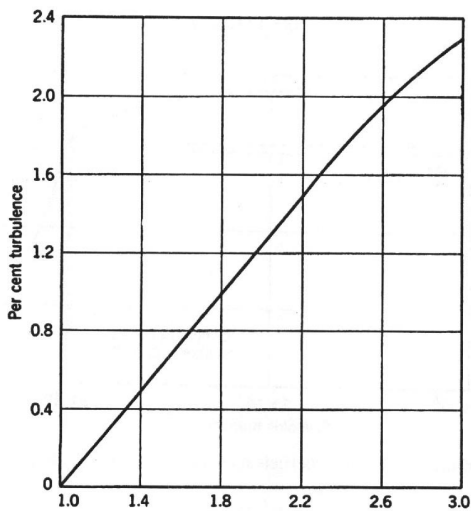
Fig. 3.   Turbulence factor (horizontal axis) in relation with turbulence intensity.

The second method is focused on determining the turbulence by measuring the fluctuation and mean value of the velocity in the test section of the wind tunnel using PIV. The turbulence is calculated from formula (1). Then the turbulence factor is correlated from the graphic depicted in Fig. 3 – turbulent factor versus turbulence intensity in percent.

II.   MATERIALS AND METHODS

The equipment used for the measurement besides the wind tunnel includes a PIV system that measures all three components of the velocity vector (3C) in a plane thus the flow field in two-dimensional (2D) plane. This type of PIV system is denoted as 3C/2D [3]-[5]. Fig. 4 depicts the PIV system mounted in the wind tunnel ULAK-1. In Fig. 4 a specialized laser creates a laser plane (sheet) that helps to visualize previously seeded particles in the flow in the test section. Two synchronized cameras generate a series of images that are used to define the components of the flow vectors in the area of interest. In the case of stereo PIV an a priori calibration of the cameras is needed. In the present study two different kinds of calibration and measurement are used (Fig. 4) – normal (the laser sheet is coplanar to the y-axis) and cross-calibration (the laser sheet is coplanar to the x-axis). Thus the flow field in the test section of the wind tunnel is measured in a plane parallel to the free stream velocity and a plane perpendicular to the free stream velocity (so called Trefftz plane).
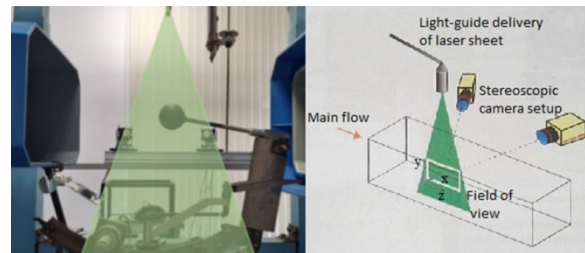
Fig. 4.   PIV measurement layout and test bench

In [6] the density and dimension of particles are examined and in [7] different approaches and examples for use of PIV are illustrated.

As it was mentioned the first type of measurement of the turbulence in the test section is the sphere method, where the critical Reynolds number is defined by the transition of the boundary layer. In this case study the flow field around a sphere (Fig. 1) is measured in a plane parallel to the free stream velocity using PIV at different flow speeds to observe the velocity of transition ergo the corresponding Reynolds number. Both of PIV cameras generate a series of images of the induced particles in the flow in the area of interest (Fig. 5). Hence the critical Reynolds number and Turbulence factor (2) are defined for the wind tunnel.

The second method involves measurement of the flow field of the test section without an object in two perpendicular planes – parallel and perpendicular to the free stream velocity. In this case, using a series of time separated PIV images the fluctuations and the mean value of the flow field are obtained and (1) yields the turbulence of the flow, hence the TF (Fig. 3) [1].
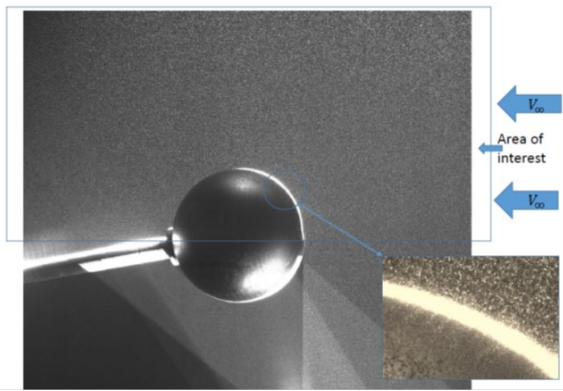
Fig. 5. Raw images of the particles induced in a flow around a sphere.

III. Results and Discussion

To obtain the critical Reynolds number the flow around a sphere is measured for four different velocities: at 15 m/s, 28 m/s, 32 m/s and 37 m/s. Stereo PIV analysis is conducted at a plane parallel to the freestream velocity (Fig. 4 and Fig. 5). The results for the flow field – velocity and streamlines are shown in Fig. 6 to Fig. 9 at the given free stream velocities - V_∞.
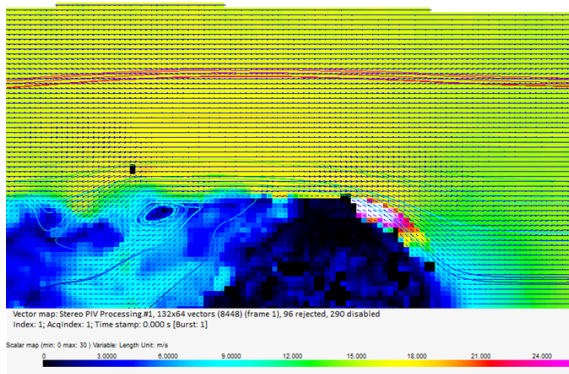
Fig. 6. Flow field around a sphere $V_\infty = 15 \, m/s$.
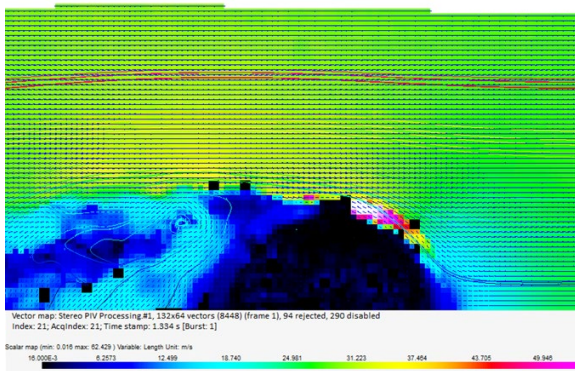
Fig. 7. Flow field around a sphere $V_\infty = 28 \, m/s$.

From the results in Fig. 6 to Fig. 9 it is obtained that the transition of the boundary layer (Fig. 1) of the sphere occurs at approximately $V_\infty \approx 35 m/s$. The pattern of the flow in Fig. 6, 7, 8 shows that the transition point is near the middle section (Fig.1-left) whereas Fig. 9 shows the pattern similar to Fig.1-right. Provided we assume that the transition occurs at approximately $V_\infty \approx 35 m/s$ then the critical Reynolds number is:

$$Re_{cr} = \frac{\rho V_\infty d}{\mu} = \frac{1{,}149 \cdot 35 \cdot 0{,}1}{1{,}85 \cdot 10^{-5}} = 217380 \qquad (4)$$

where: ρ is the density of the air, kg/m³; d is the diameter of the sphere, m; μ is the dynamic viscosity, Pa. s.
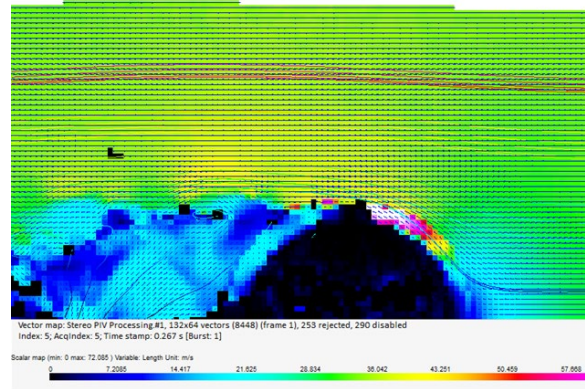
Fig. 8. Flow field around a sphere $V_\infty = 32 \, m/s$.
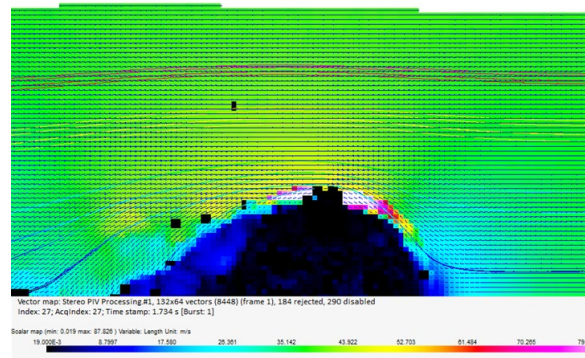
Fig. 9. Flow field around a sphere $V_\infty = 37 \, m/s$.

Hence for the turbulent factor of the wind tunnel the value according to (2) is:

$$TF = \frac{385000}{217380} = 1{,}77. \qquad (5)$$

The TF is an integral characteristic for the turbulence in the test section of the wind tunnel. However, to yield the turbulence for the entire flow field a second method is used based on (1). Fig. 10 shows the mean velocity flow field in a plane parallel to the free stream velocity (25 m/s) of the test section. In this case no model is used. A series of 50 images is taken via the PIV system at laser frequency 15 Hz. Then the mean flow field is calculated and visualized as well as the mean squared fluctuation speed.

Formula (1) gives the turbulence in the test section in per cent which is depicted in Fig. 11.

In this case the TF can be correlated to the turbulence using curve from Fig 2b provided that turbulence is between 0,9 and 1.(cyan and blue color in Fig. 11). If done for the test section of the wind tunnel where the model (in this study sphere) is placed the TF is approximately between 1,75 and 1,80, which is an acceptable match with the result from (5).
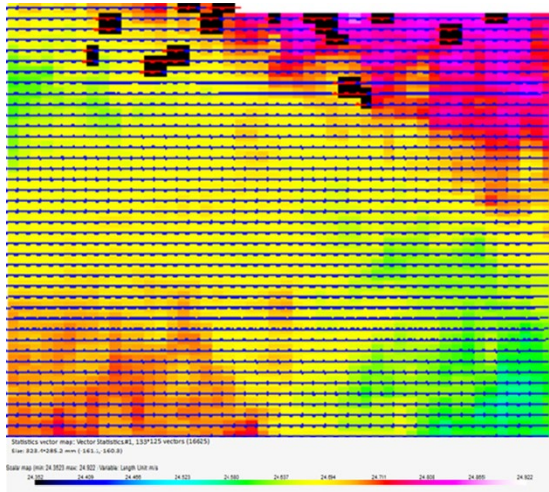
Fig. 10. Mean velocity flow field at $V_\infty = 25$ m/s.
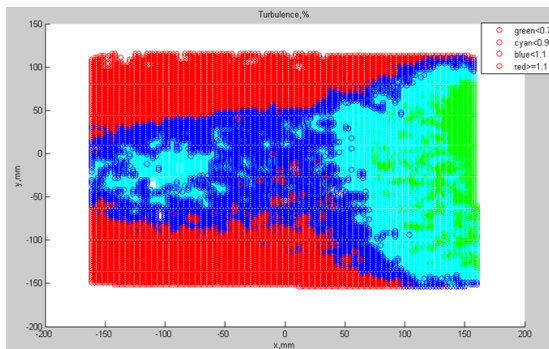
Fig. 11. Turbulence, test section. X-axis is parallel to $\overrightarrow{V_\infty}$

Finally, an additional measurement of the turbulence is conducted in a plane perpendicular to the free stream velocity in the test section at distance of 700 mm downstream of the nozzle end, a so called Trefftz plane – usually where the vortex system behind the model is formed. The methodology resembles the above-mentioned PIV measurements; however the PIV cameras are cross-calibrated. The results for the turbulence in the Trefftz plane are depicted in Fig. 12. The plane of symmetry of the test section is located at x=100 mm, where as x=-100 is the boundary of the test section.

The last measurement (Fig. 12) features greater values of the turbulence than Fig. 11, but one should bear in mind that Fig. 12 shows the turbulence at 300 mm downstream from the most end value in Fig. 11.
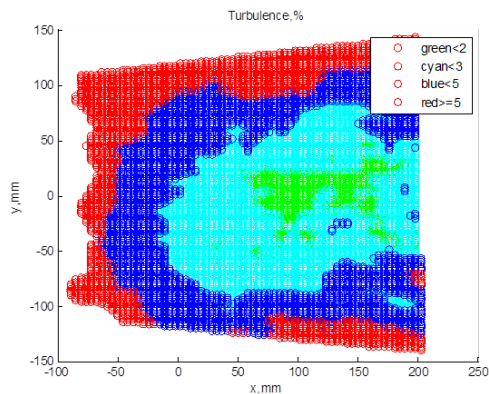
Fig. 12. Turbulence, Trefftz plane, PIV. X-axis is the lateral axis, Y-axis is the vertical axis.

IV. CONCLUSION

In [8] Penchev et al. measure the turbulence in the Trefftz plane at the same station (700 mm downstream of the nozzle end) of the test section using hot-wire anemometry. The results are given in Fig. 13.

A comparison can be made between the hot-wire anemometry results and PIV results for the turbulence in Trefftz plane. With enough accuracy it can be assumed that the match of the results for both methods is more than acceptable.
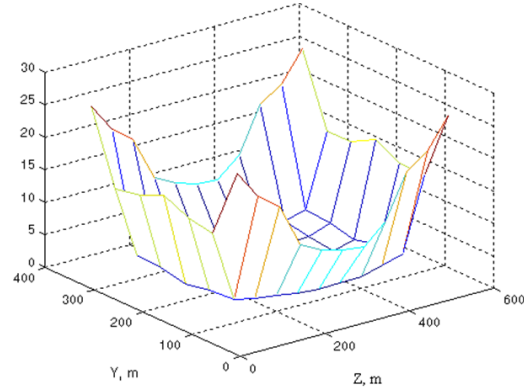
Fig. 13. Turbulence, Trefftz plane, hot-wire anemometry. Z-axis is the lateral axis, Y-axis is the vertical axis.

The present paper encloses a PIV analysis of the turbulence in the test section of ULAK-1 wind tunnel. The given result will be used for aerodynamic corrections in future experiments in the Autonomous Aircraft Aerodynamics laboratory of the Plovdiv Branch of the Technical University of Sofia. The results and the measurement methodology can also be used for comparison to similar aerodynamic experiments. This type of measurement of the turbulence are new for Bulgarian wind tunnel laboratories and can contribute for other researchers to obtain similar results for other types of wind tunnels.

REFERENCES

[1] C. Britcher, D. Landman, *Wind Tunnel Test Techniques*, Academic Press, 2023.

[2] J. B. Barlow, W.H. Rae, Jr. and A. Pope, *Low-speed wind tunnel testing*. New York: John Wiley & Sons Inc., 1999.

[3] Dantec Dynamics A/S, *2D PIV. Reference Manual*, Publication no.: 9040U1753, Skovlunde, Denmark, 2016.

[4] Dantec Dynamics A/S, *Stereo PIV. Reference Manual*, Publication no.: 9040U4117, Skovlunde, Denmark, 2017.

[5] M. Rafel and C. Wilert, *Particle Image Velocimetry. A Practical Guide*, Springer Verlag, 2018.

[6] J. Zhang, et al, "Study on Motion and Deposition of Particles in a Wind Tunnel", *Procedia Eng.*, vol. 121, pp. 450 – 458, 2015, DOI:10.1016/j.proeng.2015.08.1092

[7] B. Leclaire, et al, "Planar Particle Image Velocimetry for Aerospace Research at ONERA", *AerospaceLab J.*, vol 12, pp. 1-12, 2016 , DOI: 10.12762/2016.AL12-07.

[8] S.I. Penchev, D.T. Seyzinski and D.S. Kolibarov, "Research of the characteristics of the flow in the work section of the wind tunnel UT-1", *Mech. of Machines*, vol. 62 (or vol.14, no.1), pp. 9-12, 2006.

Innovative Obsolescence in Mechanical Engineering and Singleness of Indicators

Desislava Petrova
Department Management
Technical university of Gabrovo
Gabrovo, Bulgaria
des_petrova@abv.bg

***Abstract*. The purpose of the present work is to present the manifestation of innovative obsolescence in mechanical engineering and the unequivocalness of the indicators - service life, reliability, physical wear, innovative and programmed obsolescence. The innovation life cycle and when innovation obsolescence occurs are presented. It has been proven that innovation obsolescence is a regularity that manifests as a consequence of the occurring change in the technical levels of innovations with the same technical purpose. The development is based on the thesis that between innovation development and innovation obsolescence there are certain interrelationships and interdependencies that essentially characterize the process of innovation obsolescence itself. In subsequent publications, an analysis of the dependencies and factors influencing the innovation process in the industry will be presented, regarding: constructive solutions, materials, processing processes, costs, demand and supply, price and obsolescence of solutions.**

Keywords: alternative solutions, innovative obsolescence, questionnaire.

I. Introduction

The achieved technical level of world progress is determined by the global measures of technical progress currently expressed through certain categories of measures, one of which is social productivity [1, 4, 16, 17]. There is a certain interrelationship and dependence between it and the technical level. This dependence is expressed in degrees of technical level, accounting for differences with a share of productivity increase. The technical level can also be taken as the reached innovation level at the moment of development of technical progress. These indicators are closely related and dependent on each other, because they are defined by the globalization of innovation development at a given time, the latter being the result of the achieved technical productivity, such as the level of scientific developments, or new designs and technologies. The physical essence of this process is expressed in a shortening of the periods of

creation of new technical solutions, modern designs and technologies and an increase in productivity in absolute and relative terms of each new period. It follows from this that the innovative obsolescence of the technique occurs in shorter and shorter periods of time. These are economic and technical regularities which, with globalization and innovative development, mark accelerated steps for each subsequent period, creating increasingly high social productivity. Therefore, future industrial activities will be of higher technical levels, higher productivity, faster innovation obsolescence and global intensification of processes and activities.

II. Materials and methods

Unambiguity of indicators – Service live, reliability, physical wear, innovative and programmed obsolescence

The efficiency of industrial production, and in particular that of industrial companies, largely depends on the service life of the equipment. But replacing old, innovation-obsolete equipment with new is not always effective, because it is related to a number of indicators such as the volume of production, fund allocation, growth of deductions, etc. [5, 6]. Factors related not so much to the period of operation of the equipment play a role here, but above all the profit that will be obtained from its overall use. High rates of technical progress require rapid innovation obsolescence of equipment, but this does not mean that it must be completely replaced with new ones. The successful solution of such tasks requires taking into account the influence or impact of a number of factors forming the requirements for the efficiency of both production and the capacity capabilities of enterprises [7, 8, 9]. Many of the authors dealing with these problems are of the opinion that a balance should be sought between the physical wear and tear and the innovative and planned obsolescence of the technique. So far, physical wear and tear often exceeds two to three times the innovative obsolescence of the technique. This is especially characteristic of universal machines or machines with flexible capabilities. The change in the

unit cost of production depending on the operating period.

The main feature that characterizes innovations in general is their life cycle [10]. A distinction should be made between the life cycle of a product and the life cycle of an innovation. We can have several innovative solutions in one product. The product life cycle is a concept that expresses the change in sales and profit from the moment of idea generation to its market realization [11, 12]. However, they have a lot in common and overlap. For example, when some of the innovative solutions embedded in the product become obsolete, there is a drop in sales, as a result of losing part of the competitiveness. The graph of the innovation life cycle is given in Figures 1. and 2.
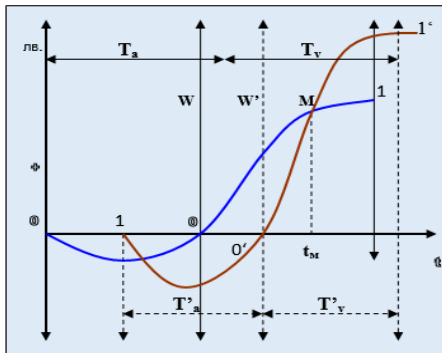
Fig. 1.   Innovation life cycle

(t – time; Ta, Ta - investments made in an innovation cycle, including idea, research, design and production for 1 and 1' innovation; Tv, Tv' - innovation cycle, including development and moral obsolescence for 1 and 2 innovation; M , tm - impending moral obsolescence for the 1st innovation)Magnetization as a function of applied field.
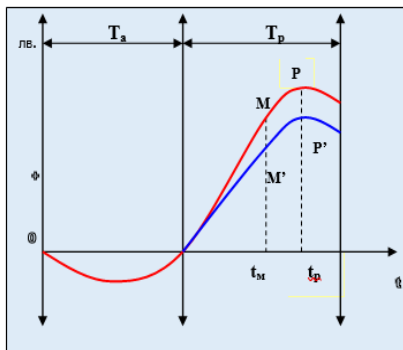
Fig. 2.   Life cycle of the innovative product

(t - time; Ta - life cycle of products, including: research, design and production; Tr - market cycle; 1- change of funds, where investments are made during periods Ta, and in the period Tr are returned with profit (project and real); 2 - change in profit; M, M' - occurring moral obsolescence in time tm; P, P' - points of decrease in profit.Magnetization as a function of applied field.

III.   RESULTS AND DISCUSSION

In this case, development, implementation and growth times are short, with sales growth peaking soon and maximum revenue being realized more quickly. The maturity period should last longer and the decline of the curve should be very smooth.

TABLE 1

Criteria	Stages of the innovation product life cycle	
	1 Development, design, production	2 Introduction
Competition	*Absent*	*Insignificant*
Users		*Innovators*
Product assortment	*One model*	*One model*
Sales		*It depends on the conditions*
Profit		*Small*
Strategy		*New product attraction*

Criteria	Stages of the innovation product life cycle		
	3 Growth	4 Maturity	5 Decline
Competition	*Small*	*Strong*	*Insignificant*
Users	*Mass market*	*Mass market*	*Conservatives*
Product assortment	*The number is growing*	*Full assortment*	*Decreases*
Sales	*It's growing*	*It's growing*	*Decreases*
Profit	*Growing*	*It's growing*	*Decreases*
Strategy	*Sales development*	*It maintains distinctive advantages*	*Abbreviation, revitalization, termination*

Figure 3 shows the shape of the ideal life cycle of a new product.

The determination of the optimal operational period of the equipment appears as a necessary, but insufficient condition for the formation of the possibilities of the industrial company. This is explained by the fact that for different types of machines, their operating time almost always exceeds the optimal one, because material wear is slower than innovative wear [2, 13].
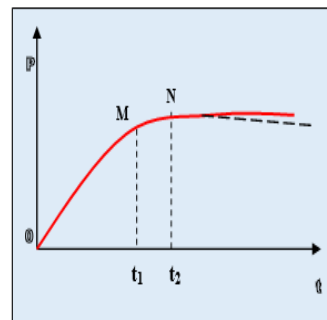
Fig. 3.   Form of an ideal life cycle of a new product

(1, 1' - product life cycle; t - time; t1 - time for development, introduction and growth (M); t2 - complete exhaustion of resources (N); P - sales in BGN)

The search for the best solutions for determining the production possibilities creates conditions that also lead to the search for different forms of optimization of this process. The parameters and indicators that characterize the state of production facilities and determine their capacity can be divided into two types [14, 15]:

1. Economic parameters expressed in economic indicators (operating costs, the share of equipment costs per unit of production, cost per unit of production, total costs, depreciation costs, etc.) [3];

2. Technical parameters expressed in technical indicators (service life, reliability, repairability, coefficient of useful action, technological capabilities, etc.).

IV. CONCLUSIONS

- The lack of proper technical and economic justification of the developed technologies can lead to the implementation in production of inefficient and competitive variants of manufactured products.

- Innovation obsolescence is a regularity that manifests itself as a consequence of the occurring change in the technical levels of innovations with the same technical purpose. Between innovation development and innovation obsolescence there are certain interrelationships and interdependencies that essentially characterize the process of innovation obsolescence itself.

- The manifestation of innovation obsolescence is expressed with an impact on engineering structures, processes and industrial products.

- Innovation obsolescence negatively affects the rapid innovation development and efficiency of industrial products.

- Effective forms of solutions to eliminate negative consequences of rapid innovation obsolescence of products and processes are used by many industrial companies in our country and around the world.

- An effective alternative form of innovation obsolescence is the so-called "programmed obsolescence". It is increasingly being imposed as an approach for quick and effective removal of the consequences of innovation obsolescence and creates conditions for higher competitiveness.

- In world practice and in our country, many of the forms of programmed obsolescence have taken hold, as one of the means of increasing the competitiveness and efficiency of the production of industrial products.

- Innovative obsolescence is essentially a regularity, and programmed obsolescence is a human-regulated alternative activity aimed at eliminating the harmful effects of innovative obsolescence.

REFERENCES

[1] S.Berger, Making in America: From Innovation to Market, USA, 2013.

[2] I.Balabanova, G.Georgiev, "Image Recognition by FFT, Artificial Intelligence and k-Nearest Neighbors Approach". IOP Publishing, Journal of Physics: Conference Series - EEPES'22, vol. 2339, pp. 1-8, 2022.

[3] G. Chipriyanova, R.Krasteva-Hristova, A. Kussainova, A. Contemporary higher accounting education for social responsibility. // ECONOMICS ECOLOGY SOCIUM, Volume: 6, Issue: 4, Pages: 27-36 DOI: 10.31520/2616-7107/2022.6.4-3 Published: 2022 Accession Number: WOS:000904078500003 ISSN: 2616-7107.

[4] G.Chipriyanova, M.Marinova, Technological Aspects of Accounting Automation System as a Decision Support System, Vide. Tehnologija. Resursi - Environment, Technology, Resources, Open Access, Volume 2, Pages 28 – 33, 2023, 14th International Scientific and Practical Conference on Environment. Technology. Resources, ETR 2023, Rezekne, 15 June 2023 through 16 June 2023, Code 191610, DOI: https://doi.org/10.17770/etr2023vol2.7309 .

[5] D.Damianov, Modern alternatives to rapid innovative aging, Scientific Bulletins of NTS in Mechanical Engineering, Year XXVI, Vol. 3/224, ISSN 1310–3946, 27 ISTC "ADP 2018", June 2018, pp. 278-283.

[6] I.Mitev, Optimizing the quantity of liquid phase at the sintering of powder construction materials from system Fe-Cu-Sn, 11th International Scientific Conference "TechSys 2022" – Engineering, Technologies and Systems, AIP Conf. Proc. 2980, https://doi.org/10.1063/5.0184238 , Published by AIP Publishing. 978-0-7354-4814-8/$30.00, pp. 060017-1 to 060017-7.

[7] I.Mitev, Determining the diffusion coefficient in simultaneous saturation with boron and carbon of austenite alloyed with cooper in powder metallurgy structural materials, 11th International Scientific Conference "TechSys 2022" – Engineering, Technologies and Systems, AIP Conf. Proc. 2980, 060016-1–060016-8; https://doi.org/10.1063/5.0184239 , Published by AIP Publishing. 978-0-7354-4814-8/$30.00, pp. 060016-1 to 060016-8.

[8] N.Nikolova, Intellectual Capital Management used for Optimizing the Activities of Modern Small and Medium Enterprises/Companies. 4th International Conference Economics and Management-Based on New Technologies, EMoNT 2014, 12-15 June 2014, Vrnjačka Banja, Serbia., pp.258-262, ISBN 978-86-6075-045-9.

[9] N.Nikolova, Human Capital in the Changing Work Environment of Industry 4.0, Vide. Tehnologija. Resursi - Environment, Technology, Resources, Open Access, Volume 3, Pages 187 – 193, 2023, 14th International Scientific and Practical Conference on Environment. Technology. Resources, ETR 2023, Rezekne, 15 June 2023 through 16 June 2023, Code 191610, DOI: https://doi.org/10.17770/etr2023vol3.7177

[10] N.Nikolova, Entrepreneurial "Blue" Practices for Sustainable Development and Resources Efficiency, 12th Inter-national Scientific and Practical Conference "Environment. Technology. Resources", June 20-22, 2019, Rezekne Academy of Technologies, Rezekne, Latvia, Volume I, 198-203, ISSN 1691-5402, ISSN 2256-070X.

[11] D.Petrova, Analysis of SMEs in Bulgaria – Assessment of Their Innovation Activities, Rezekne 2013, Latvia, Rezekne Higher Education Institution, Faculty of Engineering, Scientific Institute for Regional Studies, Environment. Technology. Resources, Proceedings of the 9th International Scientific and Practical Conference June 20-22, 2013, Volume 3, ISSN 1691-5402: 46-49.

[12] D.Petrova, Analysis of Trends and Opportunities for Technological Development of Bulgarian Enterprises, Proceedings of the International Conference Danube Black Sea, 3E – Energy, Environment & Efficiency, September 18-21, 2013 Galati, Romania, ISBN, pp. 413-417.

[13] D.Petrova, Intelligent, Innovative and Sustainable Industry in Bulgaria – prospects and challenges, Vide I. Tehnologija. Resursi - Environment, Technology, Resources, Proceeding of the 12th International Scientific and Practical Conference „Environment. Technology. Resources", June 20-22, 2019, Rezekne, Latvia, Volume I, pp. 210-215, ISSN 1691-5402 – print, ISSN 2256-070X – online. https://doi.org/10.17770/etr2019vol1.4188

[14] D.Petrova, An Alternative Approach to Reducing Aging of Innovative Industrial Products in Terms of Industry 4.0, Environment. Technology. Recourses – Proceeding of the 13-th International Scientific and Practical Conference, Rezekne

Academy of Technologies, Rezekne, Latvia, 2021, ISSN 1691-5402, *Online ISSN 2256-070X*, *https://doi.org/10.17770/etr2021vol3.6507* p. 274-280, scopus

[15] D.Petrova, An Approach to Modeling Innovation Obsolescence, Vide. Tehnologija. Resursi - Environment, Technology, Resources, Proceeding of the 14th International Scientific and Practical Conference, 2023, Volume I, pp. 175–179, Print ISSN 1691-5402, Online ISSN 2256-070X, DOI: https://doi.org/10.17770/etr2023vol1.7237 , https://www.scopus.com/authid/detail.uri?authorId=56323816400

[16] D.Petrova, B.Vlahova, A. Lengerov, T. Zlateva-Petkova, Study of the State of Innovation Development and Obsolescence in the Republic of Bulgaria of Companies from the Mechanical Engineering Sector, Vide. Tehnologija. Resursi - Environment, Technology, Resources, 2023, 1, pp. 187–194, DOI: https://doi.org/10.17770/etr2023vol1.7239 , https://www.scopus.com/authid/detail.uri?authorId=56323816400

[17] M.Schillings, Strategic Management of Technological Innovation, Ravi Shankar, Edition: 6, 2019.

[18] J.Sunbi, A.Gallina, Contemporary Management of Innovation: Are We Looking at the Right Things?, USA, 2019.

Non-linear model in region of very low speeds for a permanent magnet direct current motor

Nickolay Popov
Institute of Robotics
Bulgarian Academy of Sciences,
Plovdiv, Bulgaria
njpopov62@gmail.com

Abstract. **Thematic is in mechatronics and automation branches, applicable in the mobile robotics. Permanent Magnet DC collector motors, are widely used in small mobile robots due to their low-cost. Automated control systems of mobile robots, which operate under different conditions and require accuracy of operation, raise the need for the nonlinearities to be taken into account. In this article, a complex non-linear model of a PMDC motor with brushes is synthesized. The aim is to determine of suitable way of motor behaviour simulating in the region of very small speeds. The tribology aspects at different friction regimes are of great importance for a model at low speeds. The parameters and constants of the model are separately defined through referring to their physical equivalents. Besides the theoretical modelling, a simple mathematical way to determine the constants for this detailed model is deduced. Then the synthesized model is simulated and results are graphically represented and then compared with another similar model, proposed by another authors. As a conclusion, the advantages of this non-linear approach are revealed. This research is applicable as a study of direct-current motor and its simulation model or as facilitating example in lectures of robotics or control systems.**

Keywords: Mechatronics, Mobile robot, PMDC motor, Non-linear modelling, Tribology aspects, Torque at low rotor speed.

I. INTRODUCTION

In this report is studying the non- linear motor behaviour at very low speeds, where the effect of increased friction is observed. The topic is in the mechatronics and the control theory, because this effect causes the plant (the motor) to have a hysteresis in its output torque and rotational speed. The main goal is to study this non-linearity, so the management of motor speed and torque to be adequate when a closed- loop control is used. Question we pose is how to model the motor (plant) behaviour, so it to be continuous and analytically smooth in the region of this hysteresis. The importance of this question arises when we simulate a motor. The way this effect to be modelled determines the speed of simulation process.

The results are applicable in wide spectrum of electrical motors. The article is oriented to the class of PMDC (Permanent Magnet Direct Current) motors simulations, in the mobile robotics having speed reducer (gear) before the wheels, but the created math model is applicable for any other electrical motor to simulate.

The state of the art studies use same approach to represent this effect: Stribeck plus Coulomb friction plus viscous friction [1]. This is valid for a wide range of bearings, frictional joints, gears, etc. ad it is a definition for so called "Static model" [2], while the studies [3], [4] deal with "LuGre dynamic" model, extending the static model to account for hysteresis effects. In [5] is studied for the vehicle dynamics by application of both models. Motor drive systems with and without gear are examined in [6], while [7] gives some applications of both models in automation theory. The measurement needed for obtaining the static model parameters is given in [8], where the parameters of mathematical formulae are taken from the classical articles for static and dynamic models [9] and [10]. In field of electrical motors control, the closely related work is made in the [11], [12] and [13], where it is proposed to be used the static model of DC motor. In this article we will name it the "old Stribeck formula". The adequacy "model to real motor" is suppose to be good in some degree, as it is predicted by the physics theory. The studies on this topic propose to improve the friction model by using the classical static model [9] with an additional parameter (sharpness factor). Although [6] and [9] study the sharpness factor in details, for now it has been not tested with PMDC motor. Latter friction model we test in present article and we name it „new Stribeck formula".

This study advance our knowledge by creating a more precise static model for a PMDC motor, taking into account the differences in bearings and gear construction, lubrication method, etc. Our contribution to the topic is in the fact that the resulting model, although being more

complicated, is more adequate to predicted by the theoretical physics: It allows more precisely to approximate the process behaviour. The increased lab work is just a bit more than previously proposed "old Stribeck approach".

The hypothesis is: The proposed in this article method is more versatile than that given in [11], [12] and [13], as it takes into account one parameter more: In particular this additional parameter, introduced in [6] and [9] allows us to work with different behaviours of non-linear friction, in the way it depends on the type of bearings, gear, etc.

This manuscript is organized in following parts: Introduction, Materials and methods, Results and discussion, Conclusions

II. MATERIALS AND METHODS

A. Brief Theory

The used physical symbols and abbreviations and their meanings are given in Table. 1.

a) Linear PMDC motor model:

It is given as two equations of balance: electrical and electro- mechanical as well as two equal motor constants, when condition of stationary (settled) angular speed is imposed (i.e. no speed and current variations):

$$v_a = R_a . i_a + K_b . \omega_m \qquad (1)$$

$$K_m = K_b \qquad (2)$$

$$K_m . i_a = B_m . \omega_m + T_{lin} \qquad (3)$$

b) Stribeck-Coulomb friction model:

We will examine two equations about Stribeck-Coulomb friction torque

- **Old friction model:** Friction torque as proposed by other authors: In [11], [12] and [13] is introduced an additional friction torque T_{strib} in order to account for the increased friction at very low rotational speeds; This additional friction (called Stribeck Friction) represents the fact that at low velocity the friction consumes all the motor torque:

$$T_{strib}(\omega_m) = \alpha_0 + \alpha_1 . e^{-\alpha_2 . \omega_m} \qquad (4)$$

- **New friction model:** It is proposed by this article: We propose the improvement of motor model by using the classical static model [1] with sharpness factor ν being not unit, as proposed in [6] and [9]:

$$T_{stib} = T_{kinetic} + T_{kinstat} . e^{-(\omega_m/\omega_{strib})^\nu} \qquad (5)$$

The meaning of used coefficients in both formulae (4) and (5) is as follows:

$\alpha_0 = T_{kinetic}$ represents the kinetic (Coulomb) friction, which is a constant with dimension of $[N.m]$; $\alpha_1 = T_{kinstat}$ is the kineto-static (Stribeck) constant, representing the friction torque at zero speed. Its dimension is $[N.m]$; $\alpha_2 = 1/\omega_{strib}$ represents so called Stribeck critical speed ω_{strib} in following manner: below this speed the additional friction effect becomes significant and vice versa, above this critical speed the effect is negligible; Dimension for α_2 is $[sec/rad]$. The sharpness factor ν for the exponential term is introduced in order to represent the "transition sharpness" at critical

speed for the effect appearing/ disappearing: The dimensionless values of $\nu = 0.5 - 2$ are possible, the lower limit is for sleeve bearings with cheap gear, i.e. light "transition sharpness"; The upper limit is for ball bearings with a really good gear, thus "sharpness" is to be great, according [1], [6] and [9]. In the formulation of additional friction torque as proposed by other authors [11], [12] and [13], a default (immediate) value of $\nu = 1$ is put on.

c) Values of kineto-static and kinetic constants:

Values of ω_{strib} and ν have meaning of controlling

TABLE 1 USED PHYSICAL SYMBOLS AND ABBREVIATIONS

Symbol	Meaning and role of parameter	Dimens.
Motor parameters, given by manufacturer		
v_a	Armature voltage	[V]
T_{stall}	Stall torque[1]	[N.m]
ω_{noload}	noload speed[1]	[rad/s]
Calculated constants for motor equations		
R_a	Armature resistance of rotor	[Ohms]
K_b	Back-EMF constant for motor	[V/rad/s]
K_m	Torque constant for motor	[N.m/A]
i_{noload}	noload current	[A]
B_m	Viscous friction coefficient	[N.m.s/rad]
Independent variable, used in motor and Stribeck laws		
ω_m	Rotational speed of the rotor	[rad/s]
Dependant values, obtained by linear motor law		
i_a	Armature current	[A]
T_{lin}	Output torque when linear law	[N.m]

TABLE 1 USED PHYSICAL SYMBOLS AND ABBREVIATIONS (CONTINUED)

Symbol	Meaning and role of parameter	Dimens.
Independent parameters, used in experiments of Stribeck law		
ω_m	Critical Stribeck speed[1]	[rad/s]
α_2	Reciprocal of Stribeck speed[2]	[s/rad]
ν	Stribeck sharpness factor[1]	[-][3]
Dependant values, constrained by Stribeck limit conditions		
$T_{kinetic}$	Kinetic torque[1]	[N.m]
α_0	Kinetic torque	[N.m]
$T_{kinstat}$	Kineto- static torque[1]	[N.m]
α_1	Kineto- static torque[2]	[N.m]

Dependant values, obtained by Stribeck law		
T_{strib}	Stribeck torque	[N.m]
κ_{strib}	Stribeck losses factor	[-][3]
T_{final}	Output torque when Stribeck effect	[N.m]
Dependant values, used in Criterion calculations		
Ω_{loss}	Relative speed at given % of losses	[-][3]
$\Omega_{loss,old}$	Relative speed at % losses by old method	[-][3]
$\Omega_{loss,min}$	Relative speed at % losses by new method, minimal value	[-][3]
$\Omega_{loss,max}$	Relative speed at % losses by new method, maximal value	[-][3]
$\Delta_{loss,min}$	Relative speed minimum at % loss for new method, compared to the old one	[-][3]
$\Delta_{loss,max}$	Relative speed maximum at % loss for new method, compared to the old one	[-][3]

1   Notations used in [6], [9] and presented article

2   Notations used in referenced articles, e.g. [11], [12] and [13]

3   Dimensionless

values for the friction model, i.e. they are chosen by the experimenter in order to best fit the Stribeck function in two points in the new proposed model (according [6], [9] and as used in this article); Or just in one point, as it is in the old model proposed by [11], [12] and [13], where in this case $v = 1$ is fixed.

At this choice of ω_{strib} and v the resulting Stribeck torque value must satisfy two physical conditions:

a)   At stall the Stribeck torque to be the same as the motor stall torque:

$$T_{strib}|_{\omega_m=0} = T_{stall} \qquad (6)$$

b)   At noload the Stribeck torque has to absent:

$$T_{strib}|_{\omega_m=\omega_{noload}} = 0 \qquad (7)$$

This gives us two constrains (coherency conditions), by which the values of $T_{kinetic}$ and $T_{kinstat}$ have to dependent on the chosen ω_{strib} and v :

$$T_{kinetic} = \frac{T_{stall} \cdot e^{-(\omega_{noload}/\omega_{strib})^v}}{e^{-(\omega_{noload}/\omega_{strib})^v} - 1} \qquad (8)$$

$$T_{kinstat} = T_{stall} - T_{kinetic} \qquad (9)$$

d)   *Output torque with Stribeck-Coulomb friction:*

At some speed ω_m the "ideally delivered" in the output is the torque T_{lin} , as stated by the linear motor law. In the reality the delivered torque is decreased by the value of Stribeck torque T_{strib} , so finally we have:

$$T_{final} = T_{lin} - T_{strib} \qquad (10)$$

e)   *Stribeck losses factor:*

We introduce Stribeck losses factor κ_{strib} the similar way the Efficiency concept is defined i.e. "(output power when Stribeck law present) / (output power when pure linear motor law)" :

$$\kappa_{strib} = \frac{(T_{lin} - T_{strib}) \cdot \omega_m}{T_{lin} \cdot \omega_m} = 1 - \frac{T_{strib}}{T_{lin}} \qquad (11)$$

It is clear that Stribeck losses factor is inside the unit range: $0 \leq \kappa_{strib} \leq 1$ or $0\% \leq \kappa_{strib}[\%] \leq 100\%$.

Also, we interest what the speed is when a specified loss value $\kappa_{strib} = \kappa_{loss}$ occurs. This speed is important when to compare both Stribeck models. It is also convenient to be converted in relative form, i.e. compared to speed at noload ω_{noload} , by introducing:

$$\Omega_{loss} = \frac{\omega_m}{\omega_{noload}}\bigg|_{\kappa_{strib}=\kappa_{loss}} \qquad (12)$$

It is clear that this is inside the unit range: $0 \leq \Omega_{loss} \leq 1$ or $0\% \leq \Omega_{loss}[\%] \leq 100\%$.

f)   *Hypothesis:*

The new Stribeck equation gives more approximation freedom in the region of interpolation, compared to the old formula. The new equation will be analysed as some kind of "deviation" around the values given by the old one.

g)   *Criterion:*

We will compare the new Stribeck equation and the old one, by observing their speed values at same losses factor. The old equation with fixed ω_{strib} has the fixed relative speed $\Omega_{loss,old}$ at some level of losses. The new Stribeck formula allows the relative speed to vary in the range $\Omega_{loss,min}$ to $\Omega_{loss,max}$, located around the old value; It is due to varying the sharpness factor in range $v_{min} \leqslant v \leqslant v_{max}$ even at same fixed ω_{strib} .

The Criterion for „flexibility" (freedom) of the new equation is given as a kind of relative amplitude variation of values, compared with the old equation:

$$\Delta_{loss,min} = \frac{\Omega_{loss,min} - \Omega_{loss,old}}{\Omega_{loss,old}} \qquad (13)$$

$$\Delta_{loss,max} = \frac{\Omega_{loss,max} - \Omega_{loss,old}}{\Omega_{loss,old}} \qquad (14)$$

We will examine these values and give them in form of percentages.

B.   *Implementation*

The calculations has been done in Octave© [17], with the following algorithm has been used:

a)   Given motor data (e.g. by manufacturer): These are v_a , i_{stall} , T_{stall} , ω_{noload} .

b)   Calculation of some motor parameters is done the same way as in author's previous article [14]:

$$R_a = \frac{v_a}{i_{stall}} \qquad (15)$$

$$K_b = K_m = \frac{T_{stall}}{i_{stall}} \qquad (16)$$

$$i_{noload} = i_{stall} - \frac{T_{stall}}{v_a} \cdot \omega_{noload} \qquad (17)$$

$$B_m = \frac{T_{stall}}{\omega_{noload}} \cdot \frac{i_{noload}}{i_{stall}} \qquad (18)$$

c)   The linear motor behaviour is obtained in the same way as in [14], when the motor speed gradually changes in range $[0 - \omega_{noload}]$:

$$i_a = \frac{v_a - K_b \cdot \omega_m}{R_a} \qquad (19)$$

$$T_{lin} = K_b \cdot i_a - B_m \cdot \omega_m \qquad (20)$$

d)   Choose some values for Stribeck critical speed and sharpness factor, such that $0 \le \omega_{strib} \le \omega_{noload}$ and $0.5 \le \nu \le 2$, for calculation and experiment purposes.

e)   Calculate the values of kinetic and kineto-static constants for each chosen ω_{strib} and ν :

$$T_{kinetic} = \frac{T_{stall} \cdot e^{-(\omega_{noload}/\omega_{strib})^\nu}}{e^{-(\omega_{noload}/\omega_{strib})^\nu} - 1} \qquad (21)$$

$$T_{kinstat} = T_{stall} - T_{kinetic} \qquad (22)$$

f)   Calculate the value of Stribeck- Colomb friction value for each chosen ω_{strib} and ν :

$$T_{stib} = T_{kinetic} + T_{kinstat} \cdot e^{-(\omega_m/\omega_{strib})^\nu} (23)$$

g)   Calculate the output torque when the Stribeck effect is present by means of obtained Stribeck values:

$$T_{final} = T_{lin} - T_{strib} \qquad (24)$$

h)   Calculate Stribeck losses factor by means of:

$$\kappa_{strib} = 1 - \frac{T_{strib}}{T_{lin}} \qquad (25)$$

Now we can recalculate the Stribeck losses factor in percentages: $0\% \le \kappa_{strib}[\%] \le 100\%$.

i)   Find out the speed where a predefined friction value $\kappa_{strib} = \kappa_{loss}$ is reached. Then calculate the relative value of this speed in respect to noload speed ω_{noload} :

$$\Omega_{loss} = \left. \frac{\omega_m}{\omega_{noload}} \right|_{\kappa_{strib} = \kappa_{loss}} \qquad (26)$$

Do this for both Stribeck equations (old and new one), this way calculating the values of $\Omega_{loss,old}$ for the old Stribeck formulation, as well as $\Omega_{loss,min}$, $\Omega_{loss,min}$ for the new equation. Then convert them in percentages.

j)   Calculate the criterion for „flexibility" for the new equation as relative variation of values, compared to these with the old equation:

$$\Delta_{loss,min} = \frac{\Omega_{loss,min} - \Omega_{loss,old}}{\Omega_{loss,old}} \qquad (27)$$

$$\Delta_{loss,max} = \frac{\Omega_{loss,max} - \Omega_{loss,old}}{\Omega_{loss,old}} \qquad (38)$$

Now convert these values in form of percentages.

C.   Notes and examples

The main problem is in the fact, we must not to run a motor in the extremely low speeds, with high loading torque, as it will cause the gear and bearings to overheat, or the rotor and gear axes to break up. The one value for the phenomenon of friction increasing (i.e. first approximation point) can be measured at the low speed limit, recommended by the manufacturer. The other point can be chosen strongly inside the allowed speed range, where the Stribeck-Coulomb effect has low, but distinctive value.

Thus we will use the following relations, in the way these are predetermined in engineering practice. We interest where the Stribeck effect has reached some values, let's say as they are defined in [15]: $\kappa_{95} = 0.95$ -

below this value the Stribeck effect is negligible in practice; $\kappa_{90} = 0.1$ - above this value we have clearly visible Stribeck torque; $\kappa_{50} = 0.5$ - above this value a great part of output torque is consumed by the bearings and gear, thus overheating them; Usually, for real PMDC motors these relative points can vary in ranges [15]: $\Omega_{90} = 0.1 - 0.2$ - visible Stribeck effect is below 10 to 20 % of noload torque; $\Omega_{50} = 0.05 - 0.15$ - Stribeck effect causes overheating below 5 to 15 % of noload torque; Such defined ranges of relative speed gives us reasonable limits where the influence of parameters controlling Stribeck torque to be investigated in the following experiments.

Thus in our experiments we will check these values for several points of speed, at several Stribeck losses factors: $\kappa_{strib} = 50\%, 90\%, 95\%$ and the respective relative speeds are $\Omega_{50}, \Omega_{90}, \Omega_{95}$. For case of new equation these relative speeds will vary, when varying ν: respectively $\Omega_{50,min}$ to $\Omega_{50,max}$, $\Omega_{90,min}$ to $\Omega_{90,max}$ and $\Omega_{95,min}$ to $\Omega_{95,max}$. The old equation is fixed to $\Omega_{50,old}, \Omega_{90,old}, \Omega_{95,old}$ because of fixed $\nu = 1$.

The linear model parameters are taken from [14] for a real motor data [16]. It is a PMDC brushed motor with cylindrical gear and sleeve bearings.

a)   Manufacturers motor data [16] are: v_a=12[V], i_{stall}=10[A], T_{stall}= 29.8[N.m] and ω_{noload}=2.41[rad/sec].

b)   Calculated motor parameters: R_a=1.2[Ohms], K_b=K_m=2.98[V/rad/sec]   or   [N.m/A], B_m=4.9648 [N.m.sec/rad], i_{noload}=4.0152[A].

c)   Calculated linear (ideal) motor behaviour: the angular speed changes in range ω_m=[0↔2.41] [rad/sec]. Dependent values change are: i_a=[10↔ 4.0152] [A], T_{lin}=[29.8↔0] [N.m].

d)   Calculating the change of Stribeck caused losses at fixed ω_{strib}=0.2 [rad/sec] and ν=1[-]: The values of kinetic and kineto-static constants are: $T_{kinstat}$=-1.7417x10⁻⁴[N.m] and $T_{kinetic}$=29.8[N.m]. When the angular speed changes ω_m=[0↔2.41] [rad/sec], the Stribeck losses: T_{strib}=[29.8↔0] [N.m] and κ_{strib}=[1↔0] [dimensionless], respectively.

e)   Calculation of Stribeck losses at fixed ν=1[-] and different ω_{strib}=0.5; 0.25; 0.125; 0.0625 [rad/sec]: The values of kinetic and kineto-static constants are: $T_{kinstat}$=30.042; 29.802; 29.8; 29.8 [N.m] and $T_{kinetic}$=-0.24235; -0.0019393; -1.2619x10⁻⁷; -5.3434x10⁻¹⁶ [N.m] and dependent values change as: T_{stib}=[29.8↔0] [N.m] and κ_{strib}=[1↔0] [-], respectively.

f)   Calculation of Stribeck caused losses at fixed ω_{strib}=0.2[rad/sec] and different $\nu = 0.5$; 0.75; 1; 1.5; 2[-] : The values of kinetic and kineto-static constants are respectively: $T_{kinstat}$=29.872;   29.804;   29.8;   29.8; 29.8[N.m]   and $T_{kinetic}$=-0.072218;   -0.0035427;   -0.00017417; -4.2106x10⁻⁷; -1.0179x10⁻⁹ [N.m].

g)   Finding the values at κ_{90}=0.5=50% is done by changing the values for ω_m=[0-2.41][rad/sec], ν=[0.5-2]. Finding the values at κ_{90}=0.9=90% and κ_{95}=0.95=95% is done by the same technique.

i)   Finding the values at is done by the same way.

For each calculation: some check speeds are chosen and their calculated values are given in Fig.1, Fig.2 and Fig.3. The following results for the sharpness factor ν_{sample}=1 (old method approach) for different values of ω_{strib} are obtained as given in Fig.4, Fig.5 and Fig.6.

III. RESULTS AND DISCUSSION

A. Experiments

a) *Geometrical interpretation of Stribeck losses factor:* the goal is to show how the Stribeck torque affects the output torque and to find the Stribeck losses factors at several motor speeds: Fig.1 gives a plot of Stribeck caused losses at fixed ω_{strib} and ν : The "linear motor behaviour torque" is given too. The Stribeck torque (causing the non- linear "deformation" of output torque) is maximum at zero speed, as resulting torque at motor stall becomes 0; And at contrary it becomes negligible at high speeds, i.e. it tends to zero when getting close to noload speed, and resulting curve converges to the line of linear motor behaviour. Thus curve confirms the expected behaviour for this type of friction at low speeds.

b) *Controlling Stribeck friction when different Stribeck critical speeds are used at fixed sharpness factor:* Fig.2 shows some plots of Stribeck losses at fixed fixed sharpness factor ν when different Stribeck critical speeds ω_{strib} are applied and how the Stribeck torque affects the output torque and allows to find how the Stribeck losses factor changes when Stribeck critical speed changes. The graph shows that the non- linear "deformation" is controllable by chosen Stribeck critical speed values only in the region close to zero motor speed, while the "deformation" is negligible at noload speed. This type of function control is available in all compared articles: [11], [12], [13] (old used technique) control the Stribeck curve only in this way. [1], [6], [9] and this article can change the curve by this way too.

c) *Controlling Stribeck friction by different values*
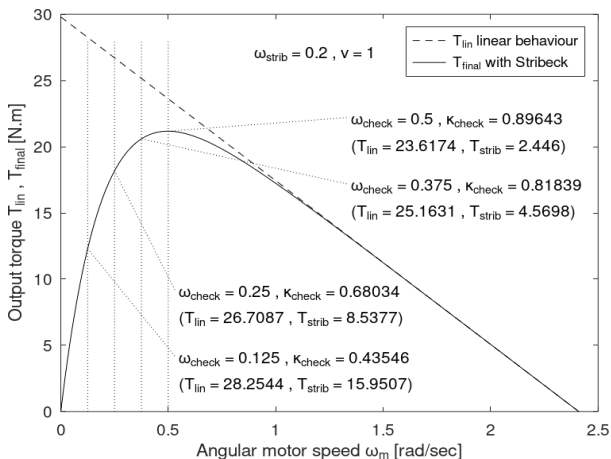
Fig. 1. Plot of Stribeck caused losses at fixed Stribeck critical speed ω_{strib} and fixed sharpness factor ν .
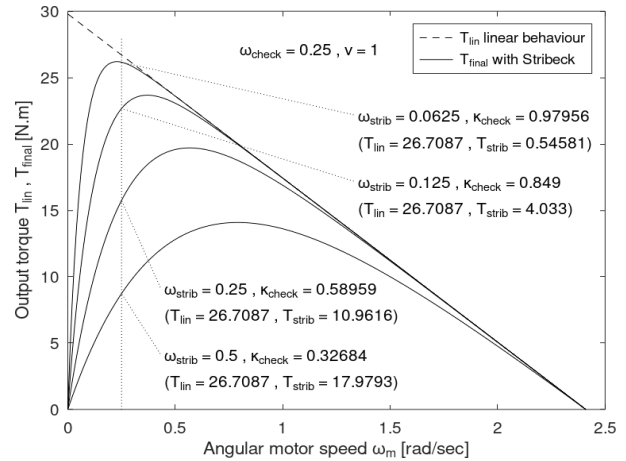
Fig. 2. Plot of Stribeck caused losses at fixed sharpness factor ν and different Stribeck critical speeds ω_{strib} .

of sharpness factor at fixed Stribeck critical speed: Fig.3 gives us some plots of Stribeck losses at fixed ω_{strib} at different ν and it shows the way the Stribeck losses factor changes when sharpness factor changes. The resulting curve is well controlled close to maximum torque; Non-linearity is negligible near maximum speed. This applies only for [6], [9] and this article; And not for [11], [12], [13] where sharpness factor is fixed.

d) *Speed deviations ("freedom") available by the new method, compared to the old one, when losses factor is 50% :* The question is: can the new Stribeck formulation to embrace all the real cases, i.e. is the range of relative speed Ω_{50} (where losses factor is 50%) wider than the manufacturers data, cited above. This is shown in Fig.4 : The abscissa is the sharpness factor, the ordinate is this relative speed. The family of curves is given for several fixed Stribeck critical speeds. The vertical line $\nu = 1$ represents the values obtained by the old Stribeck formulation; The shown points has Y-value Ω_{50} , representing the old formula. The curves itself represented the change of obtained relative speeds by
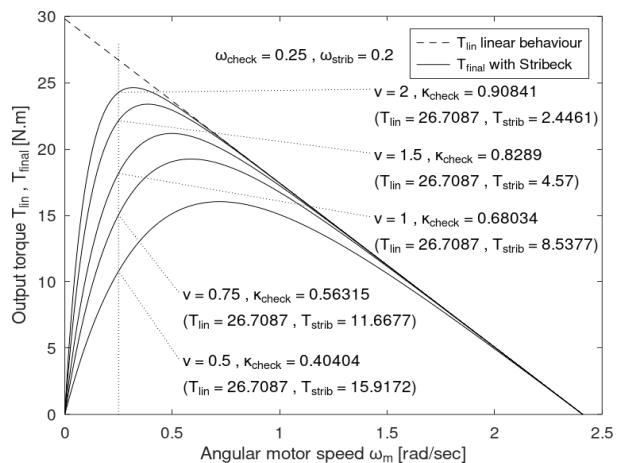
Fig. 3. Plot of Stribeck caused losses at fixed Stribeck critical speed ω_{strib} and different sharpness factors ν .
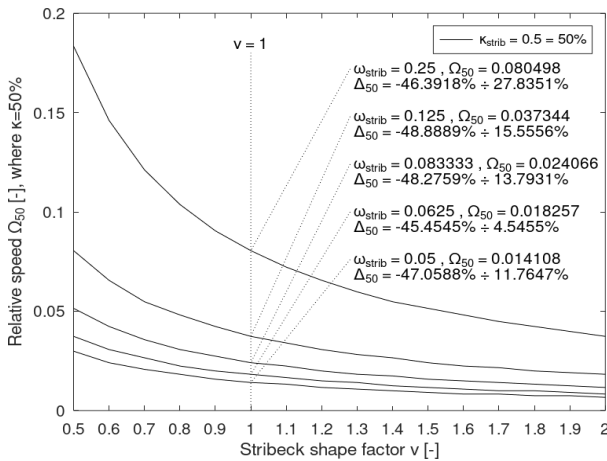
Fig. 4. Plot of speeds ω_{50} when Stribeck losses are $\kappa_{50} = 50\%$, but given as relative speed $\Omega_{50} = \omega_{50}/\omega_{noload}$ at different Stribeck critical speeds ω_{strib} and different sharpness factors ν.

Fig. 6. Plot of Stribeck losses $\kappa_{95} = 0,95\%$ appearance at some speed ω_{95}, but given as relative speed $\Omega_{95} = \omega_{95}/\omega_{noload}$ at different Stribeck critical speeds ω_{strib} and different sharpness factors ν.

the new Stribeck equation; The values of Δ_{50} reveal the possible deviations obtained by the new equation. The range -48% to +27% shows we have a good "freedom" for the new method, compared with the old one.

e) *Speed deviations available by the new method, compared to the old one, when losses factor is 90%:* Again, the question is: can the new Stribeck formulation embrace a relative speed range Ω_{90} (where losses factor is 90%) wider than the manufacturers data. This range is given in Fig.5 : Abscissa is the sharpness factor while the ordinate is this relative speed. Curves family is for several Stribeck critical speeds. The vertical line $\nu = 1$ shows the values obtained by the old Stribeck equation; The shown Ω_{90} represent the results by the old formula. The curves also show the range of obtained relative speeds by the new method [6], [9] and this article; The values of Δ_{90} reveal the deviation accessible by the new equation is -50% to +42%, i.e. good "flexibility" for the

Fig. 5. Plot of Stribeck losses $\kappa_{90} = 90\%$ appearance at some speed ω_{90}, but given as relative speed $\Omega_{90} = \omega_{90}/\omega_{noload}$ at different Stribeck critical speeds ω_{strib} and different sharpness factors ν.

new method, compared with the old one.

f) *"Freedom" obtainable by the new method, compared to the old one, when losses factor is 95%:* The modelling range in high-speed region, where the Stribeck friction losses are to be negligible (in this case 5%) is shown in Fig.6 as relative speed Ω_{95} (where losses factor is 95%). The designation and meanings are the same as explained above. The range is -50% to +42%, but all methods [6], [9], [11], [12], [13] and the presented here, have the property that the Stribeck effect to disappear at high relative speeds (values between 0.1 and 0.65): Thus the new simulation model is applicable.

B. Discussions

The „percentage of freedom" used as criterion has range of nearly ±50%, by the new introduced sharpness factor and this proves the hypothesis. At high motor speeds the influence of the sharpness factor can be neglected.

IV. CONCLUSIONS

The proposed new Stribeck formula gives us a more flexible choice of static friction modelling, when types of motor bearings and gear differ. Having only two parameters ω_{strib}, ν, we can preliminary construct the new static friction model by measurements as explained in [8]; Or these parameters can be identified "in real time" by methods given in [5] and [9]. And finally, the new static friction model with two control parameters can be used even for some simplified preliminary engineering designing, using only the manufacturer's data (usually the scarce ones), without experiments.

REFERENCES

[1] A. Bittencourt, E. Wernholt, S. Tavallaey and T. Brogardh, "An extended friction model to capture load and temperature effects in robot joints", Proceedings of the RSJ International Conference on Intelligent Robots and Systems, IEEE (2010), pp.6161-6167, DOI: 10.1109/IROS.2010.5650358

[2] G. Rill, T. Schaeffer, M. Schuderer, "LuGre or not LuGre", Multibody System Dynamics (2023), pp.191–218, DOI: 10.1007/s11044-023-09909-5

[3] A. Keck, J. Zimmermann, O. Sawodny, "Friction parameter identification and compensation using the ElastoPlastic friction model", Mechatronics, Vol.47 (2017), pp.168-182, ISSN 0957-4158, DOI: 10.1016/j.mechatronics.2017.02.009 [Online] Available:

https://www.sciencedirect.com/science/article/pii/S0957415817300193

[4] Y. Lu, J. Zhang, S. Yang, Z. Li, "Study on improvement of LuGre dynamical model and its application in vehicle handling dynamics", Journal of Mechanical Science and Technology, no.33 (2019), pp.545–558, DOI: 10.1007/s12206-019-0108-5

[5] B. Bona, M. Indri, N. Smaldone, "Rapid Prototyping of a Model-Based Control With Friction Compensation for a Direct-Drive Robot", ASME Transactions on Mechatronics, vol.11, no.5 (2006), pp.576-584, DOI: 10.1109/TMECH.2006.882989

[6] G. Ferretti, G. Magnani, P. Rocco, "Single and multistate integral friction models", IEEE Transactions on Automatic Control, vol.49, no.12, IEEE (2004), pp.2292-2297, DOI: 10.1109/TAC.2004.839234

[7] J. Swevers, F. Al-Bender, C. Ganseman, T. Prajogo, "An Integrated Friction Model Structure with Improved Presliding Behavior for Accurate Friction Compensation", IEEE Transactions on Automatic Control, vol.45, no.4 (2000), pp.675-686, DOI: 10.1109/9.847103

[8] R. Kelly, J. Llamas, R. Campa, "A measurement procedure for viscous and Coulomb friction", IEEE Transactions on Instrumentation and Measurement, vol.49 (2000), pp.857–861, DOI: 10.1109/19.863938

[9] H. Olsson, K. Åström, C. Canudas de Wit, M. Gäfvert, P. Lischinsky, "Friction Models and Friction Compensation", European Journal of Control, vol.4, iss.3 (1998), pp.176-195, ISSN: 0947-3580, DOI: 10.1016/S0947-3580(98)70113-X

[10] P. Dupont, B. Armstrong, V. Hayward, "Elasto-plastic friction model: Contact compliance and stiction", Proceedings of the American Control Conference, vol.2 (2000), pp.1072-1077, DOI: 10.1109/ACC.2000.876665

[11] T. Kara, I. Eker, "Nonlinear modelling and identification of a DC motor for bidirectional operation with real time experiments", Energy Conversion and Management, vol.45 (2004), pp.1087-1106, DOI: 10.1016/j.enconman.2003.08.005

[12] I. Virgala, P. Frankovský, M. Kenderová, "Friction effect analysis of a DC motor", American Journal of Mechanical Engineering, vol.1 , no.1 (2013), pp.1–5, DOI: 10.12691/ajme-1-1-1 [Online] Available: http://pubs.sciepub.com/ajme/1/1/1

[13] A. Sologubov, I. Kirpichnikova, "Approach to Accounting of Non-Linear Properties By Example of Electric Drive with DC Motor Controlled Type Inverter H-Bridge", International Conference on Industrial Engineering, Applications and Manufacturing (ICIEAM), IEEE (2018), pp.1-6, DOI: 10.1109/ICIEAM.2018.8729138

[14] N. Popov, "Study of efficiency for permanent magnet direct current motor using simulation with motor parameters estimation", Journal of Informatics and Innovative Technologies (JIIT), Nr. 4(5) 2023, Institute of informatics and innovative technologies, 2023. ISSN:2682–9517(print)2683–0930(online)

[15] Faulhaber Drive Systems, "DC Motor Calculations. White Paper", Faulhaber Group, 2019. [Online] Available: https://www.faulhaber.com/en/support/motors/

[16] GemsMotor LLC, "DC Geared Motor MOT-IG32G M-12V-264E. Datasheet", Global Electric Motor Solutions LLC, 2019. [Online] Available: https://gemsmotor.com/12v-24v-48v-brushed-dc-pmdc-motor

[17] J. Eaton. "GNU Octave Scientific Programming Language", 1998-2024, [Online] Available: https://docs.octave.org/latest/

Design and research of a dual-band IR lens

Dimcho Pulov
Department of Mechanical and Precision Engineering
Technical University ogf Gabrovo
Gabrovo, Bulgaria
pulov@mail.bg

Abstract. **Infrared imaging systems are widely used in military and civilian applications. Acquiring IR images simultaneously in two spectral ranges provides additional and more detailed information about objects. Dual band IR systems are equipped with a lens that operates simultaneously in two ranges of the IR spectrum MWIR and LWIR. In the design of such a lens, a problem arises with the strong dependence of the refractive index on the wavelength, which requires the correction of chromatic aberration simultaneously in two spectral ranges.**

In this article, the possibilities for the synthesis of dual-band lenses in the MWIR and LWIR spectrum using different optical materials are analyzed. The possible combinations of such materials are determined. Dual band lenses are designed using different material combinations. Their optical characteristics are investigated and the possibility of creating relatively simple high-quality dual-band IR lenses is shown.

Keywords: MWIR and LWIR spectrum , dual-band IR lens, IR optical materials, optical design , achromatization.

I. INTRODUCTION

Infrared cameras were originally developed for military purposesSubsequently, with the reduction of their price, they have received a very large application in civilian fields such as: automotive industry, machine vision, technical diagnostics, metallurgy, chemistry, electronics and electrical engineering, ecology, medicine, protection from accidents and disasters, etc. Причина за това са свойствата и уникалните възможности, които те притежават. Thermal cameras visualize invisible IR radiation by converting invisible bright contrasts in the IR region to bright contrasts in the visible region [1].

Modern thermal cameras can work in two strictly defined sections of the infrared spectrum - MWIR (3÷5) μm and LWIR (8÷12) μm. The reasons for this are:

- the maximum radiation of most objects around us is located in these areas.

- these sections coincide with the so-called atmospheric windows beyond which the atmosphere is opaque to radiation of mid- and far-IR regions.

Images obtained in the MWIR and LWIR ranges of the spectrum carry different information about the observed object. When examining the thermal imaging characteristics, it was found that:

- for objects with a temperature of around (300÷310) K, both atmospheric windows can be used with equal success;

- for objects with a higher temperature, the range (3÷5) μm is preferable, and for objects with a lower temperature – (8÷12) μm;

- for relatively distant objects and a humid atmosphere, the range (3÷5) μm is preferable;

- for relatively distant objects and an atmosphere with reduced transparency (smoke, fog, dust, low drizzle) the range (8÷12) μm is preferable.

For this reason, there has been active work in recent years on the development of thermal cameras operating simultaneously in both MWIR and LWIR spectrum sections [2], including allowing the software reconciliation (overlay) of the obtained images [3],[4]. There are different schemes for realizing such a thermal camera - with an objective and an optical filter [5] , with an objective and a beamsplitter [6],[7], with an objective and a spectral splitter [5], with an objective and a sandwich photoreceiver [8]. Common to all these schemes is the lens, which must be dual band.

For an infrared objective in a wide range, there is a strong dependence of the refractive index of the optical materials used on the wavelength. A major problem in the design of a dual band IR lens is the need for the simultaneous correction of chromatic aberration in two relatively wide and distant from each other spectral ranges [9],[10]. The most common way to solve this problem is to use combinations of different optical materials and subsequent analysis and optimize the system using optical software.

There are known such solutions. Combinations of optical materials for correcting axial color in the 3-12 μm range are shown in [11]. But these combinations are calculated for thin lenses and the degree of their correction is not shown. A dual band objective consisting of 5 lenses is described in the same publication.

In [12], a methodology for selecting optical materials for an achromatized objective composed of 6 lenses (Ge, Atmir, KCl, ZnSe) is shown.

In [13], an achromatized IR objective composed of 2 lenses with good correction is shown. In it, one lens is made of chalcogenide glass and the other – of ZnSe or ZnS. Here the chromatic correction is good, but according to [9] the use of chalcogenide glasses is preferably to be in the LWIR range of the spectrum.

In [14] the results of designing two-lens objectives with good correction of chromaticism and spherical aberration made of KRS5 (first lens) and GaAs or IKS32 (second lens) are reported. In [15] the design of the 3-lens IR objective (IKS25:ZnSe:IKS25) that operate with cooled detector in LWIR spectrum is shown. However, these optical materials are poisonous and harmful when processed. So for example, IKSxx chalcogenide glass contains sulfur, selenium and tellurium, and KRS5 - bromined and iodined thallium. Therefore, their toxicity limits their use in optical systems.

It can be noted that the most available, used and assimilated by the production materials for the MWIR and LWIR sections of the spectrum are Ge, ZnSe and ZnS. All this provides arguments for the development of this work, the goal of which is to design a relatively simple infrared dual band objective using technologically mastered and distributed optical materials.

II. MATERIALS AND METHODS

A. Optical materials and a photoreceivers for the IR range of the spectrum

Optical system layout and the determination of characteristics of objective depend on the type of used photoreceiver [5],[16],[17]. The most common are cooled photoreceiver modules and uncooled microbolometric matrices. A very important advantage of cooled photoreceivers is their higher temperature sensitivity (lower value of NETD). However, due to the absence of cooling, microbolometric matrices have significant advantages such as:

- Significantly smaller mass and dimensions

- Much less electricity consumption

- Greater convenience for placement the optical system.

Because of these advantages the objective in the this article, will be designed to work with microbolometric matrices. Typical values of the main geometrical features of the VOx Microbolometer are: format (640x480) pixels and pixel size (17x17) μm. Therefore, it can be assumed that the image size (diagonal of the working sensitive surface) is ≈ 14 mm.

In [18], it is stated that in order to reduce NETD when using uncooled photoreciervers in the IR range of the spectrum, the optical system should be fast lens with a small F/#. The minimum theoretical value of F/# according to the condition of Abbe sines condition is 0.5. In real objectives it is between 0.8 and 2. It can be accepted that the designed lens will be with F/2.

The opportunity to correct chromatic aberration is based on finding appropriate ratios between the refractive indixes and the average dispersion (Abbe number, V-number) of the optical materials used. The analysis shows that there are a relatively limited number of optical materials that are transparent in the infrared spectrum. They can be referred to two large groups [10]:

- infrared crystals – Ge, Si, GaAs, ZnSe, ZnS and some others;

- chalcogenide glasses - e.g. IRG22, IRG23,…,IRG26 from Schott's catalog.

TABLE 1 SPECIFICATIONS OF OPTICAL MATERIALS FOR THE MWIR AND LWIR RANGES

IR Material	n, average value	Abbe number		k
		v_M	v_L	
Ge	4,02	102.07	869.13	0,18
Si	3.42	242	1818	0.13
ZnSe	2,42	169,66	57,18	2,97
ZnS	2,24	109,67	25,46	4,31
KRS-5	2,37	232.80	164.90	1.41
Amtir1	2.61	195.54	114.48	1,71
GaAs	3,29	148,31	108,09	1.37
IRG26	2,77	169,42	160.2	1,06

The optical specifications of common infrared materials are shown in Table 1. In it, *n* is the refractive index and v_M and v_L are the Abbe numbers for ranges MWIR and LWIR respectively. The optical constants were calculated by dispersion formulas in the optical software OSLO (catalog Infrared). It can be seen from the Table 1 that most materials have a refractive index in the range of 2.2-2.8, and Ge, Si, GaAs own a higher one. The Abbe number has a high value in the LWIR range ($v>100$). There is a large difference in Abbe number in the LWIR range ($25<v<700$). ZnSe, ZnS have low Abbe number. Chalcogenide glasses own a relatively high Abbe number, the highest for Ge.

B. Methodology for Design of Dual Band Objective

The chromatic aberration of a objective composed of n number of thin lenses will be corrected if the optical forces of the individual lenses fulfill the condition

$$\begin{cases} \phi_{1,M} + \phi_{2,M} + \cdots + \phi_{n,M} = \phi_M \\ \dfrac{\phi_{1,M}}{v_{1,M}} + \dfrac{\phi_{2,M}}{v_{2,M}} + \cdots + \dfrac{\phi_{n,M}}{v_{n,M}} = 0 \\ \dfrac{\phi_{1,L}}{v_{1,L}} + \dfrac{\phi_{2,L}}{v_{2,L}} + \cdots + \dfrac{\phi_{n,L}}{v_{n,L}} = 0 \\ \phi_{1,L} + \phi_{2,L} + \cdots + \phi_{n,L} = \phi_L \end{cases} \quad (1)$$

where:

- ϕ_M and ϕ_L are the optical powers of the lens in MWIR and LWIR respectively;

- $\phi_{i,M}$ and $v_{i,M}$ are the optical powers and Abbe number of lens number i in the MWIR, $i = 1 \div n$;

- $\phi_{i,L}$ и $v_{i,L}$ are the optical powers and Abbe number of lens number i in the LWIR range of the spectrum.

C.   Two lenses. Two materials.

For convenience, the objective can be scaled so that $\phi = \phi_M = \phi_L = 1$. Then, for a two-lens objective expression (1) converts

$$\begin{cases} \phi_{1,M} + \phi_{2,M} = 1 \\ \frac{\phi_{1,M}}{v_{1,M}} + \frac{\phi_{2,M}}{v_{2,M}} = 0 \\ \frac{\phi_{1,L}}{v_{1,L}} + \frac{\phi_{2,L}}{v_{2,L}} = 0 \\ \phi_{1,L} + \phi_{2,L} = 1 \end{cases} \quad (2)$$

Separate solutions of this system in the MWIR and LWIR ranges give the corresponding values of the optical powers of the two lenses:

$$\begin{cases} \phi_{1,M} = \frac{v_{1,M}}{v_{1,M}-v_{2,M}} \quad \phi_{2,M} = \frac{v_{2,M}}{v_{2,M}-v_{1,M}} \\ \phi_{1,L} = \frac{v_{1,L}}{v_{1,L}-v_{2,L}} \quad \phi_{2,L} = \frac{v_{2,L}}{v_{2,L}-v_{1,L}} \end{cases} \quad (3)$$

As can be seen,, the optical forces in expression (3) depend in a specific way on the Abbe numbers of the two materials, which in turn have certain discrete values shown in the Table 1. Therefore, not for every combination of optical materials there exists a solution of (3) corresponding to system (2). From (2) and (3), it follows that a correct solution can be found only for those combinations that simultaneously satisfy the conditions:

$$\begin{cases} \frac{v_{1,M}}{v_{1,L}} \cong \frac{v_{2,M}}{v_{2,L}} \cong k \\ \text{significant diference of } v_M \text{ and } v_L \end{cases} \quad (4)$$

Let $k = 1$. This means that the Abbe numbers in both spectral ranges are the same for both materials. It can be seen from Table 1 that for the considered materials there is no such combination that meets conditions (4).

The values of coefficient k calculated by expression (4) are shown in Table 1. From Table 1, the combinations consisting of the technologically adopted and widespread optical materials Ge, ZnSe, ZnS are selected. Three combinations of two lenses each are made from the three selected materials. For them, the optical powers of individual lenses in the MWIR and LWIR ranges were calculated using expressions (3) and (1). The obtained results are shown in table 2. It can be seen from it that the combinations Ge:ZnSe and   Ge:ZnS are not suitable, because the coefficients k of the lenses composing them are very different. This results in very different optical powers of the lenses in the two ranges.

TABLE 2 OPTICAL POWERS OF LENSES FOR DIFFERENT MATERIAL COMBINATIONS

Combinations		k		Optical power			
				MWIR		LWIR	
L1	L2	L1	L2	$\phi_{1,M}$	$\phi_{2,M}$	$\phi_{1,L}$	$\phi_{2,L}$
Ge	ZnSe	0,18	2,97	-1,51	2,51	1,07	-0,07
Ge	ZnS	0,18	4,31	-13,43	14,43	1,03	-0,03
ZnSe	ZnS	2,97	4,31	2.82	-1,82	1,67	-0,67

The ZnSe:ZnS combination can be realized in two variants: with optical powers ($\phi_{1,M}$; $\phi_{2,M}$) and ($\phi_{1,L}$; $\phi_{2,L}$). The axial color for these variants is shown in Table 3.

TABLE 3 AXIAL COLOR FOR TWO VARIANTS OF OBJECTIVES

Variants	PAC$_M$	PAC$_L$	PAC$_M$/PAC$_L$
$\phi_{1,M}$; $\phi_{2,M}$	$-4,55.10^{-5}$	$3.63.10^{-4}$	0,16
$\phi_{1,L}$; $\phi_{2,L}$	$-1.91.10^{-4}$	$1.81.10^{-4}$	-1,05

From Table 3, it can be seen that due to the approximate fulfillment of condition (4), the chromatic aberration is not zero. However, it is very small, and the PAC$_M$/PAC$_L$ ratio of the second variant is close to 1. Furthermore, the optical powers of the second variant are smaller, resulting in smaller lens curvatures and smaller monochromatic aberrations. Therefore, it can be assumed that this variant is suitable for design of objective for MWIR and LWIR ranges.

A dual band objective has four refracting surfaces with radii r_j ($j = 1 \div 4$). These radii are determined by the expression

$$r_j = \frac{n_{j+1}-n_j}{u_{j+1}n_{j+1}-u_j n_j} \quad (5)$$

where:
- n_j and n_{j+1} are refractive index before and after the surface j;
- u_j and u_{j+1} are the paraxial angles before and after the surface j.
Paraxial angles are defined as follows:
- u_1 and u_5 from the conditions: $u_1 = 0$ and $u_5 = 1$;
- $u_3 = \phi_1$ from an expression (2);
- u_2 and u_4 from an expression (6);

According to expressions (5) and (6), an objective with thin lenses in the paraxial region was calculated, which will be the starting point for the design of a two-lens dual band objective.

$$\begin{cases} Du_2^2 + Eu_2 + F = 0 \\ D = u_3 b^2 (2a + 3) + \\ \quad + a^2 (2b + 3)(1 - u_3) \\ E = 2ABa^2 (2b + 3)(1 - u_3) - \\ \quad - u_3^2 b^2 (a + 3) + \\ \quad + Aa^2 (b + 3)(u_3^2 - 1) \\ F = B^2 a^2 (2b + 3)(1 - u_3) + \\ \quad + Ba^2 (b + 3)(u_3^2 - 1) + \\ \quad + u_3^3 (b^2 - a^2) + a^2 \\ A = \frac{u_3 b(a+2)}{a(b+2)(u_3-1)} \\ B = \frac{u_3^2 (b-a)+a}{a(b+2)(1-u_3)} \\ a = \frac{1}{n_2} - 1 \\ b = \frac{1}{n_4} - 1 \\ u_4 = Au_2 + B \end{cases} \quad (6)$$

D. Three lenses. Three materials

A two-lens objective may not give good aberration correction at large focal numbers due to higher-order aberrations. That is why it is useful to analyze the dual band objective consisting of three lenses according to the above methodology.

Correctly the solution of system (1) for n=3 can be found by setting a relationship between the optical powers of two of the lenses, e.g. $\phi_1 = m\phi_2$. Then, with known optical materials and laying $\phi = 1$, the values of the optical forces are found from the expressions:

$$\begin{cases} G = \frac{v_1 v_2}{v_3(mv_2 + v_1)} \\ \phi_3 = \frac{1}{1 - G(m+1)} \\ \phi_2 = -G\phi_3 \\ \phi_1 = m\phi_2 \end{cases} \quad (7)$$

The curvature of the field of the objective is determined by the expression

$$PTZ3 = \frac{\phi_1}{n_1} + \frac{\phi_2}{n_2} + \frac{\phi_3}{n_3}$$

The optical powers and field curvature for the Ge:ZnS:ZnSe combination for different values of *m* are shown in Table 4

TABLE 4 OPTICAL POWERS OF LENSES FOR DIFFERENT MATERIAL COMBINATIONS

m	Optical power			PTZ3
	ϕ_1	ϕ_2	ϕ_3	
0,1	-0,0868	-0,8678	1,9545	0,0629
0,2	-0,1889	-0,9443	2,1331	0,0308
0,3	-0.3107	-1,0356	2,3463	$-7,05.10^{-3}$
0,4	-0,4586	-1,1465	2,6051	-0,0533
0,5	-0,6421	-1,2843	2,9261	-0,11
0,6	-0,8755	-1,4592	3,3345	-0,1837
0,7	-1,1823	-1,689	3,872	-0,2794
0,8	-1,6049	-2,006	4,6108	-0,4117
0,9	-2,2216	-2,4685	5,6903	-0,6045
1	-3,2086	-3,2086	7,4171	-0,9132

The dependence $PTZ3 = f(m)$ is drawn in Fig. 1.
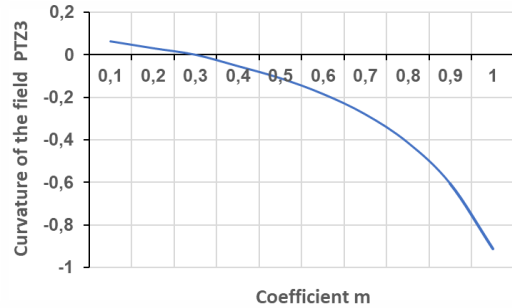
Fig. 1. Dependence on curvature of the field on the coefficient *m*

Fig. 1 shows that PTZ3 = 0 at $m \cong 0,25$. In this case, the optical powers of the individual lenses are determined from (7)

$$\phi_1 = 2,2346 \quad \phi_2 = -0,9877 \quad \phi_3 = -0,2469$$

This combination of optical powers of the individual lenses can be taken as a starting point for designing a triple lens dual band objective.

III. RESULTS AND DISCUSSION

Based on the analysis carried out in item II, the major optical characteristics of the designed dual band objective have been determined:

- focal length 100 mm,

- focal number F/2 (for triplet) and F/4 (for doudlet),

- angular field 8 degrees.

The thickness of the lenses and the distances between them were specified. Variable parameters were selected and the starting schemes were optimized with the specialized optical software OSLO. The root mean square value of the wavefront error was used as optimization criterion [10],[14],[19]. The design parameters of optimized two-lens and three-lens IR objectives are shown in Table 5 and Table 6. The corresponding optical system layout is shown in Fig. 2 and Fig. 3.

TABLE 5 THE DESIGN PARAMETERS OF THE IR DOUBLET

Surface №	Radius (mm)	Thickness (mm)	Aperture Radius (mm)	Glass type
1	94,16	3,5	12,50	ZnSe
2	-247,94	3	12,22	
3	-146,80	2,5	11,40	ZnS
4	360,93	89,68	11,22	

TABLE 6 THE DESIGN PARAMETERS OF THE IR TRIPLET

Surface №	Radius (mm)	Thickness (mm)	Aperture Radius (mm)	Glass type
1	107,28	6,5	25	Ge
2	153,55	49,5	23,98	
3	-295,53	5	15,94	ZnS
4	-683,19	20,2	15,72	
5	17,98	4,5	9,49	ZnSe
6	17,61	3,83	7,90	
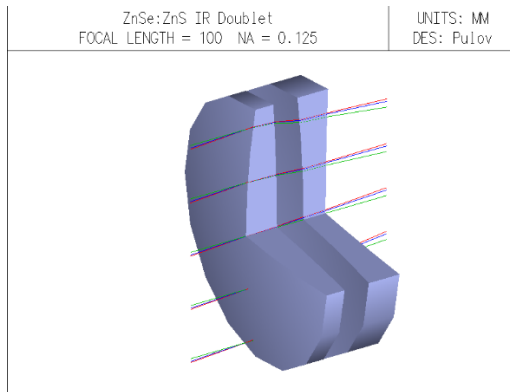
Fig. 2. Optical system layout of the IR doublet
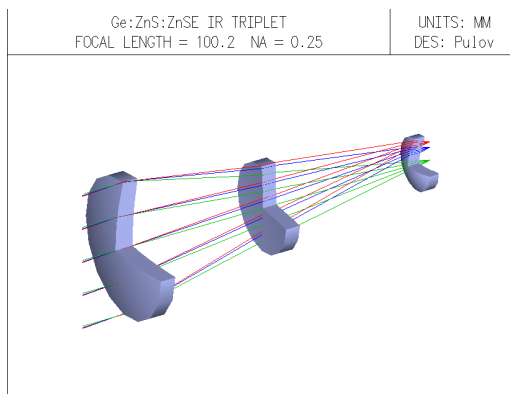
Fig. 3. Optical system layout of the IR triplet

An evaluation and analysis of the image quality of the IR objectives was made using wave and geometric criteria [20],[21],[22]. The most commonly used are the following:

- Rayleigh criterion $\quad W_{P-V} \leq \frac{\lambda}{4}$

- Marechal criterion $\quad W_{RMS} \leq \frac{\lambda}{14}$

- Airy disc criterion $\quad R_{RMS} << R_{Airy}$

In the Table 7 and Table 8 the maximum peak-valley value and RMS value of the wavefront in the MWIR and LWIR ranges for doublet and triplet are shown. The RMS of the geometric spot size, the size of the Airy disc, Strehl ratio and ensquared energy distribution in area (17x17) µm are shown in the same Tables.

TABLE 7 EVALUATION OF THE IMAGE QUALITY OF THE IR DOUBLET

ZnSe:ZnS	MWIR (3÷5) µm	LWIR (8÷12) µm
RMS Wavefront	0,044.λ	0,025.λ
P-V Wavefront	0.166.λ	0,087.λ
RMS Spot size, mm	0,016	0,015
Difraction limit, mm	0,0196	0,0491
Strehl ratio	0,926	0,976
Ensquared Energy (17x17) µm, %	45	42

TABLE 8 EVALUATION OF THE IMAGE QUALITY OF THE IR TRIPLET

Ge:ZnS:ZnSe	MWIR (3÷5) µm	LWIR (8÷12) µm
RMS Wavefront	0,016.λ	0,0128.λ
P-V Wavefront	0,048.λ	0,039.λ
RMS Spot size, mm	0,068	0,014
Difraction limit, mm	0,0098	0,0244
Strehl ratio	0,989	0,993
Ensquared Energy (17x17) µm, %	35	70

From table 7 and table 8 it can be seen that for the doublet and triplet the Rayleigh and Marechal wave criteria are fulfilled simultaneously in the MWIR and LWIR ranges. The geometric Airy disc criterion for the doublet is fulfilled in both ranges and for the triplet – only in the LWIR. Strehl's number is high enough for both ranges. The energy concentration is similar for both lenses, with it is highest for the triplet in the LWIR.

The doublet and triplet are of similar quality in both spectral ranges, however, the doublet has a focal number of F/4 and the triplet has a focal number of F/2. Due to the small number of lenses (correction parameters), the doublet cannot give a good aberrations correction for F/2. The image quality of the triplet in the LWIR range is better because of the longer wavelength there.

The wavefront of the IR triplet for three angular fields are shown in Fig. 4 and Fig. 5. From these it can be seen that the wave criteria are fulfilled within the full angular field simultaneously in the MWIR and LWIR ranges.
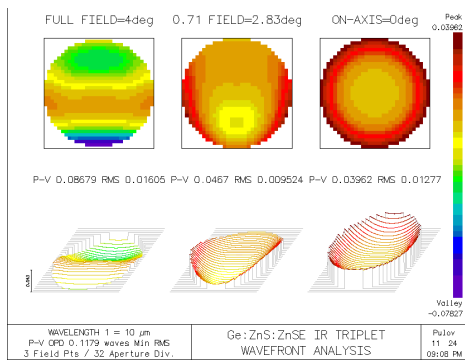
Fig. 4. Wavefront of the IR triplet in the LWIR ranges
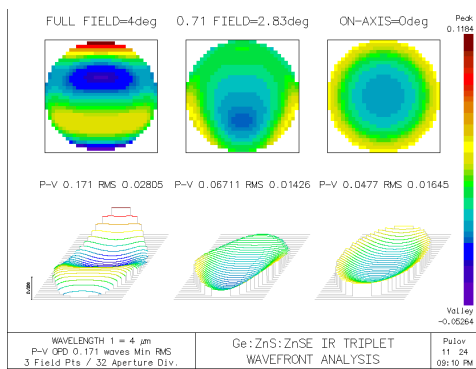
Fig. 5. Wavefront of the IR triplet in the MWIR ranges

IV. CONCLUSIONS

The possibility of designing doublet and triplet lenses operating simultaneously in the MWIR and LWIR ranges has been investigated. The parameters of very common IR photodetectors have been analyzed and the major optical characteristics of IR lenses have been determined. The optical parameters of the materials that are transparent in these ranges have been analyzed.

A methodology for dual band doublet and triplet design was developed. Combinations of optical materials composed of the technologically mastered and widespread optical materials (Ge, ZnSe, ZnS) were selected and studied. Lens variants using different combinations of these materials have been calculated.

Dual band doublet and triplet are designed, which according to a combination of wave and geometric criteria give good image quality when working with FPA microbolometric matrices with pixel size (17x17) μm and diagonal $\approx$ 14 mm.

REFERENCES

[1] Daniels A. Field Guide to Infrared Systems, Detectors, and FPAs. 2nd ed. – SPIE PRESS, 2007.

[2] Zhang Y.,Liu L., Begum F., Cao G., Zhang J., Yang Y., Zou N., Mid- and long-waveband infrared imaging system design, October 2009, Proceedings of SPIE - The International Society for Optical Engineering, Volume 7494, id. 74940M. DOI:10.1117/12.833459

[3] Chan L.A., Der S.Z., Nasrabadi N.M. Dual-band FLIR Fusion for Target Detection // Proc. SPIE. – 2002. Vol. 4668. – P. 108-118.

[4] Dual-Band Imaging of Military Targets Using a QWIP Focal Plane Array - Goldberg, T. Fischer and S. Kennerly-EO/IR Technology Branch, Army Research Laboratory, Adelphi, MD 20783 and S. Wang, M. Sundaram, P. Uppal, and M. Winn Advanced Technology Division, Sanders, A Lockheed Martin Company Nashua, NH 03060 - G. Milne and M. Stevens Lockheed-Martin Electronics and Missiles - Orlando, FL.

[5] Rogalski A., Infrared and terahertz detectors, 3rd ed., Boca Raton, CRC Press, 2019.

[6] Catanzaro B.E., Dombrowski M., Hendrixson J., Hillenbrand E., Design of dual-band SWIR/MWIR and MWIR/LWIR imagers, Proc SPIE 2004; 5406, pp. 829-835. DOI: 10.1117/12.543875.

[7] Karimzadeh A., Refractive Dual Band Infrared Imager Optical Design, International Journal of Optics and Photonics, August 2017, 11(2), pp.133-138, DOI:10.18869/acadpub.ijop.11.2.133

[8] Reibel Y., Chabuel F., Vaz C., Billon-Lanfrey D., Baylet J., Gravrand O., Ballet P., Destefanis G. Infrared Dual Band detectors for next generation // Proc. SPIE. – 2011. – Vol. 8012. – P. 80123B1-1 – P. 80123B1-13.

[9] Greisukh G.I, E.G. Ezhov, I.A. Levin, Designing dual-band athermal refractive-lens IR objectives, Computer Optics 2022; 46(6), pp. 892-898. DOI: 10.18287/2412-6179-CO-1167.

[10] Riedl J.M., Optical Design Fundamentals for Infrared Systems. Second Edition, The Society of Photo-Optical Instrumentation Engineers, SPIE, 2001.

[11] Parfyonova T., Dual-band lens ir lens, Journal " Vestnik SGGA", Novosibirsk, 2012, 2 (18), pp. 87-93.

[12] Alexay C., Multispectral infrared imaging optics, Proceedings of SPIE, Conference on Infrared Technology and Applications XXIX, April 2003, Vol 5074, pp. 830 - 838. DOI: 10.1117/12.496906.

[13] Romanova G., P. Grzegorz , "Research of aberration properties and passive athermalization of optical systems for infrared region", in. Proceedings of SPIE, Jena, 2015, Volume 9626, Optical Systems Design: Optical Design and Engineering VI, https://doi.org/10.1117/12.2191119

[14] Garshin A., A. Bakholdin, "Dual-band infrared lenses design", in. Proceedings of SPIE, Jena, 2015, Volume 9626, Optical Systems Design: Optical Design and Engineering VI, https://doi.org/10.1117/12.2191116

[15] Garshin A., Features of the design of three-lens IR objectives that operate with cooled detectors, Journal of the Optical Society of America B: Optical Physics, Volume 83, Issue 4, pp. 224 - 227, April 2016, DOI: 10.1364/JOT.83.000224.

[16] Tissot JL, Trouilleau C, Fieque B, Crastes A, Legras O., Uncooled microbolometer detector: recent developments at Ulis, Opto-Electron Rev 2006; 14(1), pp.25-32. DOI: 10.2478/s11772-006-0004-2.

[17] Lazov L, E. Teirumnieks, T. Karadzhov, N. Angelov, Influence of power density and frequency of the process of laser marking of steel products, Infrared Physics & Technology, 2021,Volume 116, 103783, DOI: 10.1016/j.infrared.2021.103783.

[18] Alaruri, S. D., F/1.6 diffraction-limited air-spaced Cooke triplet photographic lens designs for MWIR and LWIR imaging applications: Geometrical optics performance comparison between Ge-ZnSe-Ge and Si-Ge-Si triplet designs using Zemax, Optik, January 2016, Vol. 127, Issue 1, Pages 254 – 258. DOI: 10.1016/j.ijleo.2015.10.085

[19] Dichev, D., F. Kogia, H. Koev, D. Diakov. Method of Analysis and correction of the Error from Nonlinearity of the Measurement Instruments. Journal of Engineering Science and Technology Review. Volume 9, Issue 6, 2016, pp. 116-121. DOI: 10.25103/jestr.096.17

[20] Iliev G., H. Hristov, Modelling and Simulation of Electropneumatic Positioning System Including the Length of Pneumatic Line, Proceedings of the 14th International Scientific and Practical Conference: Environment. Technology. Resources. Rezekne, Latvia,. Vol. 3, 106-111, 2023, DOI 10.17770/etr2023vol3.7186

[21] Kuo C. W. , Achromatic triplet and athermalized lens assembly for both midwave and longwave infrared spectraq Optical Engineering, 53(2), 021102 February 2014. DOI:10.1117/1.OE.53.2.021102

[22] Kingslake R.R., B. Johnson, Lens Design Fundamentals, SPIE Press, Elsevier Inc, Oxford, UK, 2010.

Investigation of the Influence of Technological Knitting Parameters on the Unravelling of Structures

Ralitsa Penkova
Department of Industrial Design and Textile Engineering
Technical university of Gabrovo
Lovech, Bulgaria
ralicahp@abv.bg

Krasimir Drumev
Department of Industrial Design and Textile Engineering
Technical university of Gabrovo
Gabrovo, Bulgaria
kid@tugab.bg

Borislav Stoyanov
Department of Industrial Design and Textile Engineering
Technical university of Gabrovo
Gabrovo, Bulgaria
b.stoyanov@tugab.bg

Desislava Kovacheva
Department of Industrial Design and Textile Engineering
Technical university of Gabrovo
Gabrovo, Bulgaria
dtu@abv.bg

Abstract. **The subject of this research is to study the influence of the technological parameters of knitting on the unravelling of structures, based on the features of the knitted structures, on the analyses made, the technological parameters of the machines as well as on the physical and mechanical properties of the raw materials. Tasks are determined depending on the need to achieve minimum disentanglement of the structures. To achieve complete optimization of the technological process, it is necessary to go through several successive stages: a general study of existing technological methods, development of technologies corresponding to modern norms and requirements, experimental determination of optimal technological parameters to achieve a minimum number of defects in the production of knitted structures, development of technical documentation based on the research done, generation of innovative methods while creating considered structures.**

Keywords: knitted structures, technological parameters, unravelling of the structures.

I. INTRODUCTION

Knitting has existed since ancient times. Knitwear in all its diversity is a challenge to make. Over time, knitting techniques have improved. With the development of technology, their mass production becomes possible. Jacquard structures are spectacular, but at the same time labor-intensive to implement. Their implementation in production takes place through multi-system cross-knitting and circular knitting machines. Modern software products offer an electronic visualization of the designed product. By means of it, a more accurate idea of the knitting process is obtained. In addition to the above, the choice of yarn and the appropriate knitting and finishing parameters are decisive for the quality of the product. One of the important tasks is to minimize the number of defects during the knitting process. In order to achieve this goal, it is necessary to know the forming details and how they are implemented on the machine [1,2,3].

One of the main problems that arise during entangling is thread tension. Based on the research done, modules have been developed that show ways to ease the stretching of the thread when crossing the loops [4,5].

The interlacing of threads, in both entangled and jacquard structures, determines their properties. Depending on the use of press and backing elements of equal or different degrees, these knits (jacquards) are classified as balanced and unbalanced. The degree of balance, depending on the use of different types and number of structural elements, determines the main parameters of the product. They predetermine its physical and mechanical properties and appearance, as well as the performance of the machine [6,7].

The considered knits are composed of basic loop elements. This is a prerequisite for the presence of properties close to the properties of the base structures. Their arrangement in a certain sequence suggests the appearance of defects. These shortcomings can be

removed, both through appropriate technological parameters, and through the creation of structures with combined loop elements of different types and degrees. Knowing the properties of the raw materials from which the product is made helps in optimizing the technological process.

Formulation of the purpose of this research is based on the features of the considered structures, on the analyzes made and on the basis of the technological parameters of the machines and the physical and mechanical properties of the raw materials. Tasks are determined depending on the need to achieve minimum disentanglement of the structures. In order to achieve complete optimization of the technological process, it is appropriate to go through several successive stages: a general study of existing technological methods, development of technologies corresponding to modern norms and requirements, experimental determination of optimal technological parameters to achieve a minimum number of defects in the manufacture of structures with entangles and jacquard structures, development of technical documentation based on the research done, generating innovative methods while creating the considered structures.

II. MATERIALS AND METHODS

An important requirement in the knitting process is to minimize the number of defects during knitting. Therefore, the unraveling of the knitting is a main quality indicator. Many methods and techniques have been developed to ease the crossing of the loops of entangles. But so far, the dependencies between the change of technological parameters and the appearance of defects have not been investigated. One of the main technological indicators is the size of loop curling, knitting pulling force (rpm), sled movement speed (cm/sec).

To determine the optimal knitting parameters for conducting the study, an optimal composition plan (OCP) of the B_m type is selected. Plans of this type carry the most information at the star arm α = ±1 and an observation in the center of the plan is made only at m=2. The advantage of these plans is that they have high information qualities with a small number of trials.

A complete factorial experiment 2^3 was conducted to determine the optimal knitting parameters of entanglements at which minimal unraveling of the knitting is observed. The process is carried out on a flat knitting machine "Steiger" E8.

After identifying the natural and coded values of the relevant factors at the different levels, the matrix for planning the experiment is drawn up.

The selected factors of influence are as follows:

X_1– weaving the thread, m/min;

X_2– fabric tension, m/s.

X_3 – machine speed, cm/s.

The selected optimization parameter is:

$Y_{\square}$ – unraveling of the product, pcs/area;

Optimization parameter is identified by the number of defects on predetermined fabric samples with dimensions of 300x200mm.

TABLE 1 RANGE OF FACTOR VARIATION

Factor levels	X_1	X_2	X_3	*Encoded value*
$X_{io} + \Delta X_i$	20.96	0.0058	0.85	+1
X_{io}	18.63	0.0041	0.70	0
$X_{io} - \Delta X_i$	16.30	0.0023	0.55	-1

TABLE 2 EXPERIMENT MATRIX

№	x_1	x_2	x_3	$Y_{\square}$
1	-1	-1	-1	2
2	+1	-1	-1	2
3	-1	+1	-1	1
4	+1	+1	-1	0
5	-1	-1	+1	1
6	+1	-1	+1	1
7	-1	+1	+1	0
8	+1	+1	+1	1
9	+1	0	0	2
10	-1	0	0	3
11	0	+1	0	3
12	0	-1	0	2
13	0	0	+1	1
14	0	0	-1	2

Regression coefficients are calculated, the significance level is chosen, the mathematical notation of the adjusted model is represented by Eq.1:

$$\hat{Y} = b_0 + b_1 x_1 + b_2 x_2 + b_3 x_3 + \cdots$$

$$\cdots + b_{12} x_1 x_2 + b_{23} x_2 x_3 + b_{13} x_1 x_3 + \cdots \qquad (1)$$

$$\cdots + b_{11} x_1^2 + b_{22} x_2^2 + b_{33} x_3^2$$

The mathematical model for the solved problem is obtained after substituting the numerical values of the regression coefficients (table 3) in Eq.1, and is presented in Eq.2. The significance of the coefficients was determined at the p=0.05 level.

TABLE 3 REGRESSION COEFFICIENTS

b_0	b_1	b_2	b_3	b_{12}
2,75	-0,1	-0,3	-0,3	0
b_{23}	b_{13}	b_{11}	b_{22}	b_{33}
0,25	0,25	-0,25	-0,25	-1,25

$$\hat{Y} = 2,75 - 0,1 x_1 - 0,3 x_2 - 0,3 x_3 + \cdots$$

$$\cdots + 0,25 x_2 x_3 + 0,25 x_1 x_3 - \cdots \qquad (2)$$

$$\cdots - 0,25 x_1^2 - 0,25 x_2^2 - 1,25 x_3^2$$

After that, the adequacy of the mathematical model was checked according to Fisher's criterion. Said model is adequate if the condition is met:

$$F_R = \frac{S_{a\text{д}}^2}{S_b^2} \leq F_{tb}(\alpha, v_1, v_2) \qquad (3)$$

III. RESULTS

Graphical diagrams of the combined influence of the input factors on the objective functions are constructed.

From the calculations and analysis of graphs, it can be concluded that the speed of the sled and the force of the pulling mechanism are the main factors affecting the disentanglement. The size of the loop has negligible effect on the presence of defects. It is pre-extended by means of stress reduction.

At the maximum length of the loop and the maximum force of the pulling mechanism, a minimum number of defects are observed (Fig. 1) - the size of the loop and the tension force help to form new loops and to pass them under the knitting line.

Thus, the pulling force is distributed over a larger amount of thread and the tension in it is reduced. While reducing both the size of the loop the force of the pulling mechanism, an increase in unravelling is observed. Then, in the loops when crossing over, tension arises from the small thread in them and from insufficient pulling when forming new loops.

For the combination of factors, weaving the tread and machine speed, the diagram is similar (Fig.2).
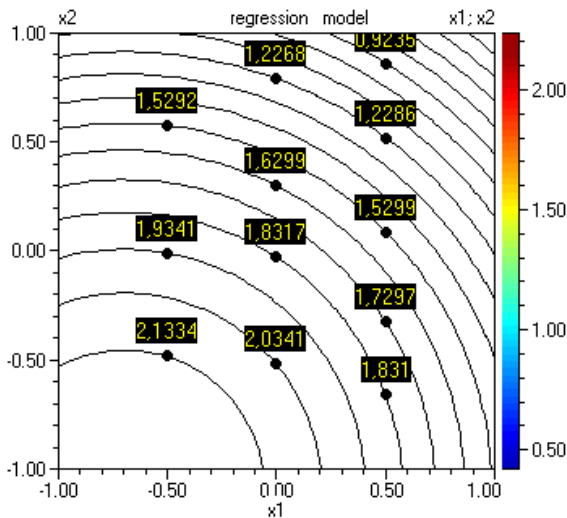
Fig. 1. Influence of X_1 - weaving the thread and X_2 – fabric tension, on Y – unravelling of the product

The weaving of the thread is of primary importance for the appearance of defects. At intermediate speed, they are highest in number. With a decrease in speed, the defects decrease - the needle has enough time to pull out a thread, form loops after crossing the preceding loops. This process is eased in trials with longer loop lengths. As the speed increases, unraveling also decreases - the time of crossing the loops is reduced, and hence the time of the tension in the thread.

Combination of factors such as knitting speed and force of the pulling mechanism creates conditions for reducing unraveling (Fig.3).

As the values of both indicators increase, a decrease in the number of defects is observed. This is due to shorter time for the loops to cross each other and cause friction between the threads.
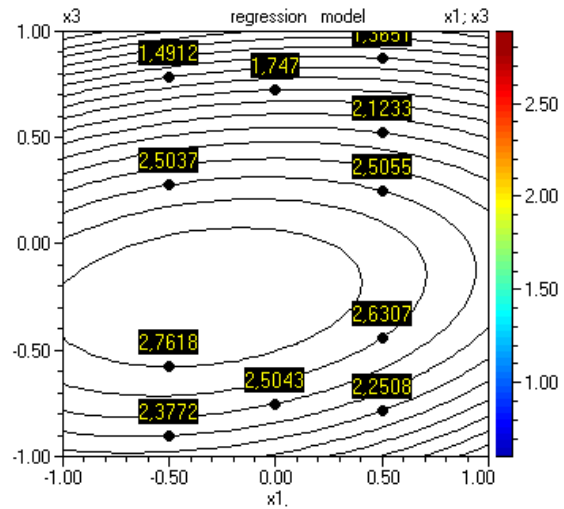
Fig. 2. Influence of X_1 - weaving the thread and X_3 – machine speed, on Y – unravelling of the product
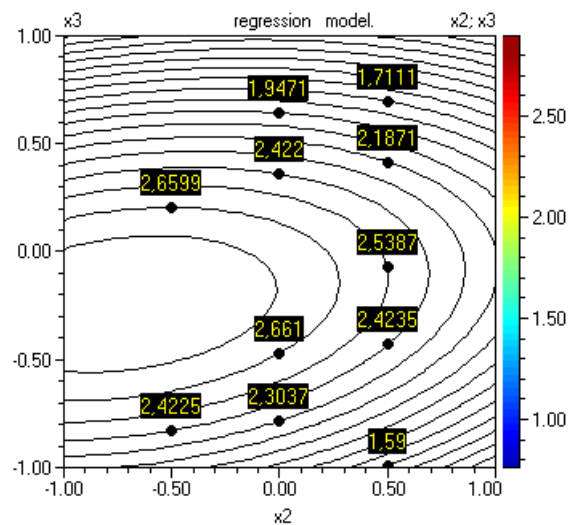
Fig. 3. Influence of X_2 - fabric tension and X_3 – machine speed, on Y – unravelling of the product

The pulling force helps to correctly stitch the subsequent stitch rows, and hence to reduce the tension in the knitted structure itself. These tests are valid for braids made from yarn with 50% cotton included. This composition of the textile thread, along with the structure and technological parameters, explains the stresses and reactions that arise in the knitting.

To prepare the program and the execution of a knitted article, several preliminary operations are necessary such as preparing and processing the textile thread, developing a program and subprogram with input parameters based on the analyses done, performing visual simulation and translating into machine language, loading and execution of the program by the machine.

For high-quality knitting process it is necessary, after analysis, to set in the program those technological parameters that ensure minimal unraveling of the knitting. On the basis of these results, the machine shrink ability along the loop post is also established for the combination of factors. Through these two indicators of the knitted product, interdependencies are established, as well as the quality indicators of the yarn. It was concluded that structures with entangles made of cotton yarn with a longer loop length have less unraveling.

IV. CONCLUSIONS

Until now, the knitting process has considered ways in which the crossing of groups of loops that make up the entangles is facilitated. This is done in the event that the material from which a given structure is fabricated does not allow it to be stretched beyond a certain limit. This mode of loop crossing does not require reversible transport of opposite loop fields, which serve as the background of the structures under consideration.
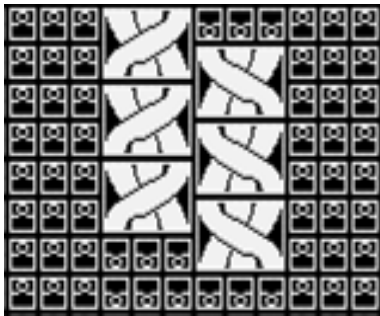
Fig. 4. Displacing the two adjacent entangles by one row
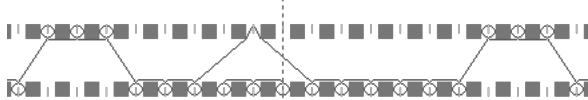
Fig. 5. Interlacing of additional yarn on the opposite bed and subsequent unloading

Such reversible transport of loops is necessary when the displacement of the entangles is large - 6 and more needle steps, and the yarn does not have great elasticity and strength. Otherwise - when shifting the needle beds by a maximum of 4 or - 4 needle pitches, the shift is carried out in several stages and the stitches are not subjected to much stretching.

When making double entangles, for better loop formation, it is necessary to move the two adjacent entangles by one row (Fig.4). As a result of this displacement, floats are formed in the middle of this tangle, which help the loops to cross. In the staggered knitting of these modules, the connecting pages pass from one needle bed to the other, thus giving more thread length to two adjacent loops. This length helps the crossing of the groups of loops to take place without the appearance of defects. A thread break can occur between a loop of the wrap background and a loop of the braid that is crossed with an offset. The unraveling in these cases may be due to a random factor or to improperly fitting knitting parameters.

In multi-stitch cross-stitch knits with more needle pitches, a background of purl stitches is required to be transported even in a knit made of elastic material. When this kind of braids with a left and right slope are combined next to each other - double braids, sometimes braiding of additional yarn on the opposite bed and subsequent unloading is used (Fig.5).

This is done in order to reduce the tension in the loops of the crossing groups. In this way, the sides of the loops subjected to maximum stretching are strengthened. Using different types of yarn means different ways of knitting and crossing loops, but obviously, the larger the loop, the easier it is to knit and transport loops.

V. ACKNOWLEDGMENTS

REFERENCES

[1] Carmichael, Al., Man-Made Fibers Continue to Grow, Textile World, January/February 2015.

[2] Chatterjee, A., Properties of Cotton Fibre (Physical, Chemical and Technical Properties), OCS Team, 2021.

[3] Iheaturu N, B. Aharanwa, K. Chike, U. Ezeamaku, O. Nnorom, C. Chima, Advancements in Textile Finishing, IOSR Journal of Polymer and Textile Engineering (IOSR-JPTE) e-ISSN: 2348-019X, p-ISSN: 2348-0181, Volume 6, Issue 5, 2019, PP 23-31.

[4] Kan, C.W., Y. Lam, C. Yuen, Microscopic study of cotton fibre subjected to different functional treatments, p.1130-1136, 2010.

[5] Kılınç, A., M. Seydibeyoğlu, Fiber Technology for Fiber-Reinforced Composites, Natural fibers, 2017.

[6] Sinclair R., "Textile and Fashion – Materials, Design and technology", Woodhead Publiching series in textiles: Number 126, Elsevier, 2015.

[7] Ursache, M., SEM investigation on denim fabric surface after resin based finishing treatment, International Symposium in Knitting and Apparel, ISKA, Iasi, p.337, 06/2013.

Behavior of Short fiber composite materials in variation of thermal and mechanical loading

Karunamoorthy Rengasamy Kannathasan
Department of Theoretical Mechanics and Strength of Material Riga Technical University
Riga, Latvia
Karunamoorthy.Rengasamy-Kannathasan @rtu.lv

Arturs Macanovskis
Department of Theoretical Mechanics and Strength of Material Riga Technical University
Riga, Latvia
Arturs.Macanovskis@rtu.lv

Rajeev Ralla
Department of Theoretical Mechanics and Strength of Material Riga Technical University
Riga, Latvia
Rajeev.Ralla@edu.rtu.lv

Eirik Gjerlow
Department of Construction, Energy and Material Technology
The Arctic University of Norway,
Lodve Langesgate 2, 8514 Narvik, Norway
eirik.gjerlow@uit.no

Abstract. **Steel Fiber Reinforced Concrete (SFRC) is widely used as it provides good characteristics and mechanical behavior. Concretes with novel type Basalt/Epoxy composite fibers are competitive and attractive for use and investigation. The special interest is for concretes with partially replaced cement by Oil Shale Ash (OSA). In this study authors will discuss basalt and steel fiber-reinforced concrete. Concrete samples were prepared in the dimensions of 40mm x 40mm x 300 mm and treated under the oven to raise the temperatures to 150^{0}C, 300^{0}C, and 450^{0}C. In the research of preparing environment-friendly concrete authors planned to use OSA as an additive replacement of cement by weight in percentage. OSA is a product of burned oil shale from thermal power plants of ESTONIA, which is added in the weight ratio of 0%, 10%, and 20% of cement. All the samples were tested by the four-point bending method and the results of samples with different ratios of OSA and different temperature gradients were compared to analyze and simulate conclusion research. The author also used image processing techniques to make a study on fiber orientation and directionality after the fabrication of concrete. Characteristics of basalt and steel fiber-reinforced concrete in different considerations and compositions were made by the author through metadata and image analysis.**

Keywords: Fiber concrete, Thermal heading, Oil Shale Ash, Basalt, SFRC.

I. INTRODUCTION

The fiber reinforced concrete is used commercially a lot because of its mechanical properties. Steel fiber reinforced concrete (SFRC) exposure to the high temperature is leading to variety of complications – concrete spalling, fibers thermal degradation and other phenomena necessary to investigate [1] [2] [3] [4] [5]. Steel fiber is the most common type of reinforcement used in fiber concrete nowadays, so authors did the research about the heat treatment of SFRC and did single fiber pullout experiments to know about the material degradation and its properties, as the continues of the previous paper here author planned to do heat treatment on FRC with two different fibers at the different temperature gradients [6].

Important problem is to use more "Green" concrete using fiber-reinforced concrete with oil shale ash as a cement partial replacement in material [7] [8]. Oil shale ash is a by-product of the mining, processing, and burning of oil shale that is produced during the energy generation process in Estonia [9] [10] [11]. The size of the particles in OSA powder ranges from hundreds of nm to μm. So, this study demonstrates the strength of composite fibers in different concrete compositions with oil shale ash functioning as a cement replacing agent.

II. Materials and Methods

2.1. Properties of Fibers.

Fiber concretes with different size and form of steel fibers were widely investigated during last time [12] [13] [14] [15] [16]. At the same time new fibers – polymeric, basalt [17] [18] and composite [19] [20] fiber with promising properties needs for comprehensive investigation. In this set of experiments authors planned to prepare fiber reinforced concrete with two different short fibers such as Turbo integral Basalt/polymer composite fiber and hooked-ended steel fibers Dra mix 3D 80/60BG. [6]

Both the fibers are commercially available and the data about the fibers from the manufactures. Technical properties of DBF Turbo build Basalt Fibers, single filament diameter is 13±1 um, Length is 48 mm, Density was 1.9 g/cm3 Spec, breaking strength is 2670 * ± 5% MPa, moisture content was less than 0.1 % stability at tension 100% at 20oC, 92% at 200oC and 82% at 400oC. Properties of steel fiber are shown in the figure below.
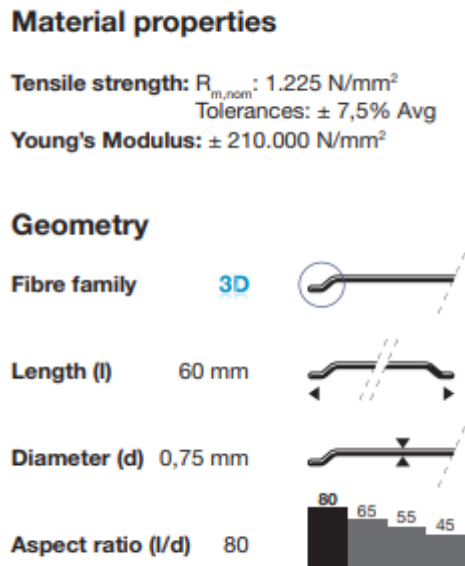
Fig.1. Steel Fiber Properties

2.2. Concrete Mix proportions

The concrete mix was designed considering the standard EN-206 and EN 196-1. The concrete mixture was prepared by adding Oil Shale Ash (from Auvere, thermal power plant Estonia) as replacement of cement in weight of 0%, 10%, and 20%. Turbo-build Integral basalt fiber obtained from Deutsche Basalt Faser and steel fibers Dra mix 3D 80/60BG were used.

TABLE 1 CONCRETE PROPORTION FOR BASALT FIBRES

Concrete Mixture with Basalt Fiber			
	B 1	**B 2**	**B 3**
Cement	6.16	5.56	4.92
OSA (Fly ash)	0	0.62	1.23
Sand (0.3-2.5)	16.2	16.2	16.2
Sand (0-1.0)	4.4	4.4	4.4
Gravel	16.0	16.0	16.0
Dolomite powder	2.9	2.9	2.9
Plasticizer Sika D190	0.225	0.225	0.225
Micro silica	0.65	0.65	0.65
Fiber	0.176	0.176	0.176
Water	3.4	3.4	3.4

TABLE 2 CONCRETE PROPORTION FOR STEEL FIBRES

Concrete Mixture with Steel Fiber			
	S 1	**S 2**	**S 3**
Cement	6.16	5.56	4.92
OSA (Fly ash)	0	0.62	1.23
Sand (0.3-2.5)	16.2	16.2	16.2
Sand (0-1.0)	4.4	4.4	4.4
Gravel	16.0	16.0	16.0
Dolomite powder	2.9	2.9	2.9
Plasticizer Sika D190	0.225	0.225	0.225
Micro silica	0.65	0.65	0.65
Fiber	0.543	0.543	0.543
Water	3.4	3.4	3.4

2.3. Specimen Preparation

Samples were designed for two different types: cubes for compression and prisms for bending. Bending and compression test samples were constructed using mould dimensions of 10x10x40cm and 10x10x10cm, respectively. Eight specimens of each type were cast, with dimensions of 100 × 100 × 400 mm. Fibers were randomly distributed and added to the concrete during the ingredient mixing process. Group S2 and B2 are concrete samples with 10% OSA, and Group S3 and B3 have 20% OSA. The number of fibers in each group was the same; the only change was the ratio of OSA substituting cement. After filling the mixture in its mould, it was kept at a relative humidity of 90% or a temperature of 27 + or -2 degrees. After that specimens were curried in the water for hydration.

Fig.2. Prepared Specimen

2.4.Thermal and Mechanical Loading Methods

Thermal treatment is the goal of the research because SFRC weakens when exposed to higher temperatures, therefore the authors planned to heat the specimens to 150, 300, and 450 degrees Celsius. To fit inside the oven, all the prisms were reduced (cut with a concrete saw) in size to 100 x 100 x 300 mm. Oven used to thermally load the specimens is the Nabertherm LH30/13. The process chart for heat treatment can be explained though the Fig (3) as follows: T1 is the maximum temperature of the set, T2 is the time set to reach the maximum temperature, T3 is the constant time zone in which specimens were treated at the same temperature for a specific fixed time, and finally T4 is where the specimens get cooled down.
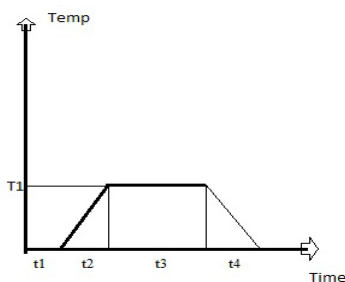
Fig.3. Heat treatment chart.

After heat treatment, all the specimens underwent 4-point bending and compression tests to establish the concrete's load carrying capacity. We used an Automax 5 loading machine. During testing, prism deformations were measured using a frame outfitted with two HBM WA20 and Linear Variable Displacement Transducers (LVDTs) on each side.

Fig.4. Oven setup for heat treatment

The cube should be placed in the compression testing equipment with its smooth faces resting on the steel plate on the bottom side. The finished cube's top surface should never meet the machine's platens, as this generates uneven loading across the cube due to the uneven, rough surface, as opposed to the faces along the smoother side of the mould. For this test, we used the normal dimensions of 10 x 10 x 10 cm. The loading was done continuously, with weights rising at a constant rate of 150 Kg/cm2/minute until the concrete specimen cracked, broke down, or was crushed.

III. RESULTS AND DISCUSSION

3.1. Thermal Loading of Specimen

Heat treatment of the sample takes place after 28 days of hydration and additional 10 days kept it out for samples dry. At first samples were set to treatment of 150 degree Celsius for 150 minutes with rising time limit of 30 minutes.

Fig.5. Damaged Oven

Same cycle repeated for all the set of samples at 300 degrees Celsius for the time limit, when it comes to 450-degree Celsius basalt specimens (BFRC) were broken inside the oven at temperature of 380c and steel specimens (SFRC) at temperature of 416oC.

Fig.6. Broken SFRC Specimens

In both basalt and steel reinforced prism we obtained some broken and cracked pieces of specimens with 0% and 10 %OSA, but specimens with 20 % OSA all the specimens vanished into small chips and pieces.

3.2.Compression test.

Compressive strength of the specimens was given based on temperature gradient while considering the specimens heated until 150oC and 300oC more OSA

content samples were possess comparatively less load bearing capacity.

TABLE 3 CONCRETE PROPORTION FOR STEEL FIBRES

Compressive strength MPa (150ºc)			
	0% OSA	**10% OSA**	**20% OSA**
SFRC	74.42	56.23	41.82
BFRC	67.3	45.69	39.07

TABLE 4 CONCRETE PROPORTION FOR STEEL FIBRES

Compressive strength MPa (300ºc)			
	0% OSA	**10% OSA**	**20% OSA**
SFRC	63	43.02	36.18
BFRC	59.4	41.82	26.6

3.2.Four-Point Bending test.

The prism was loaded at a steady rate until the sample failed. The specimen's bending deflection was calculated by averaging the data of both sensors, in this set of experiment all the heated samples were failed to withstand long after rupture or bending moment.

Fig.7. Bending results of 0% OSA at 150 C

Fig.8. Bending results of 0% OSA at 300 C

The average load was applied to bend heated 0% OSA at 150 and 300 deg Celsius samples are (a). For S1 samples 182.6 and 139.2 bar, (b). For samples B1 it is 138.46 and 116.78 bar respectively.

Fig.9. Bending results of 10% OSA at 150 C

Fig.10. Bending results of 10% OSA at 300 C

The average load was applied to bend heated 10% OSA at 150 and 300 deg Celsius samples are (a). For S2 samples 169.46 and 126.82 bar, (b). For samples B2 it is 111.02 and 87.93 bar respectively.
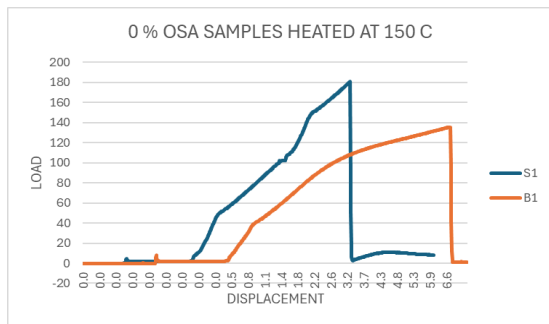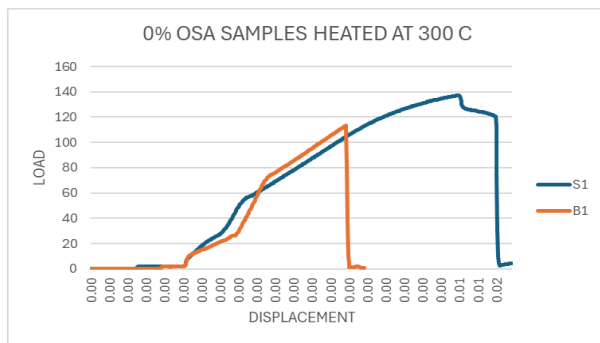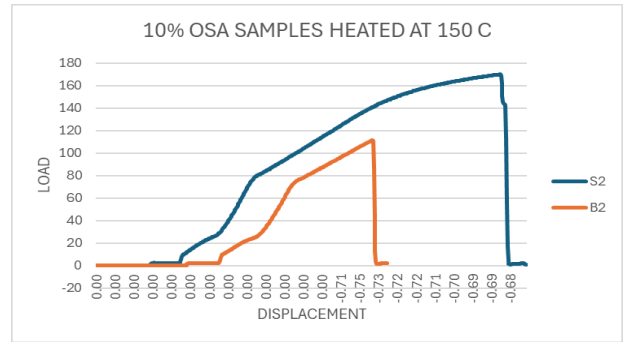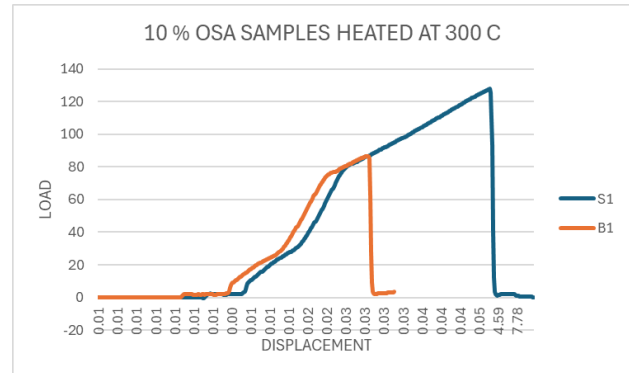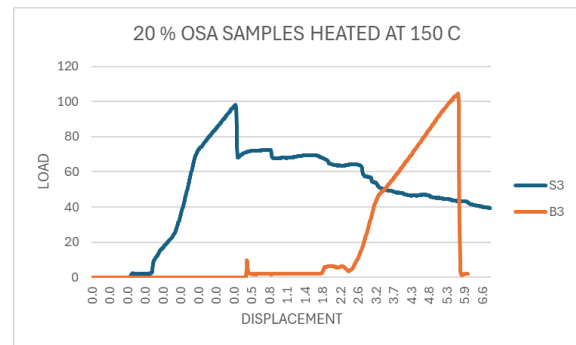

Fig.11. Bending results of 20% OSA at 150 C
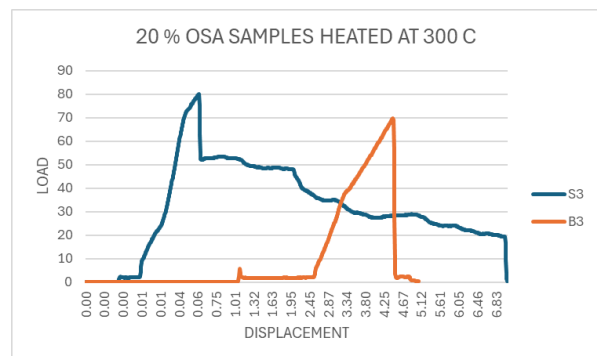
Fig.12. Bending results of 20% OSA at 300 C

The average load was applied to bend heated 20% OSA at 150 and 300 deg Celsius samples are (a). For S2 samples 98.65 and 79.76 bar, (b). For samples B2 it is 107.53 and 69.36 bar respectively.

3.4. Image Processing.

Image segmentation is an important step to analysis the sample image and divide it into separate regions of interest that are homogeneous properties such as brightness, reflectivity, texture, and color respectively. Segmentation method can catalogues based on dominant features, global knowledge of the image it is usually analyzed with histogram of image feature, Edge- based segmentation and region based. Edge based segmentation is done for the sample images, we can identify separation of the targeted objects in the image based on threshold values. The following image segmentation process is performed on the slice of 9.5 cm * 9.5 cm of steel and concrete mixture. There are two desired regions want to explore, steel density and porosity density of the given slice. Edge detection method can be used to detect the specific region and can measure the area of interest [21].
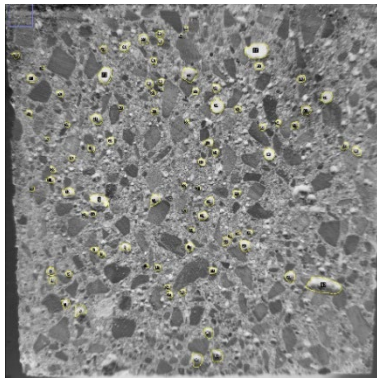
Fig.13. SFRC Specimen processed image (a).

TABLE 5 CONCRETE PROPORTION FOR STEEL FIBRES

Slice	Steel Density	Porosity Density	% Of Porosity Density
S 1	1.244	2.615	2.897
S 2	1.494	1.409	1.561
S 3	1.596	2.733	3.028
S 4	1.589	3.106	3.441
S 5	1.472	2.833	3.139
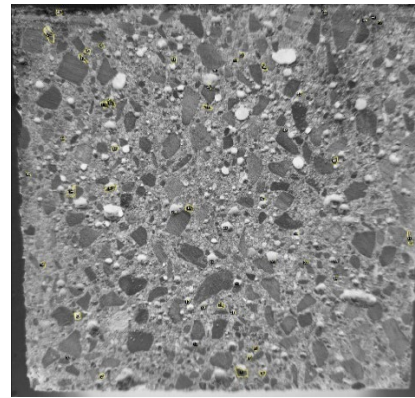
Fig.14. SFRC Specimen processed image (b).

The targeted regions are basalt and steel occupation in the given sample image and conduct statical estimation and calculate the percentage of occupation the basalt and steel in the sample. An open platform ImageJ for image segmentation and image analysis are specifically used to perform this study, initial steps are conversion of image into 8-bit type. Acuity is to detect details in an image is the major concern and extract the target source from the image. Contrast is the changes in the brightness of the image, based on contrast and acuity we can identify the target region, since every set of regions have contrast color with background color [22].
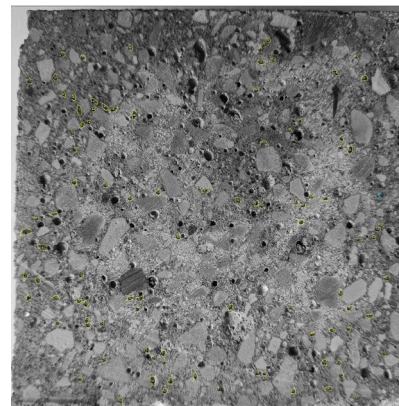
Fig.15. BFRC Specimen processed image.

TABLE 6 CONCRETE PROPORTION FOR BASALT SPECIMENS

Slice	Basalt density	Basalt percentage
Slice 1	2.472	1.631
Slice 2	2.824	2.021
Slice 3	2.637	1.813
Slice 4	2.376	1.524
Slice 5	2.493	1.654

The conditional contrast effects in the regions can improve and provide information of edges of the regions. Through ImageJ, calculation of occupation of basalt and steel are systematically studied. Edge detection

techniques are often used to identify the smallest contrasting edges and calculate the area occupied. This processer is continued for the basalt and steel elements identification.

IV. CONCLUSION

1. Two fiber concretes were investigated in the present research. Fiber concrete with steel fibers and with composite fibers by using oil shale ash as replacement of cement.

2. The compressive strength and Bending force was decreased for concrete mixes with higher amount of OSA when treated under temperature, at the same time when samples heating temperature reaches 400 deg Celsius it exploded in oven itself.

3. Edge detection technique for image analysis and process certainly provides the information to study targeted region systematically. Edge detection and object recognition techniques helped to identify the percentage of occupation of the basalt and steel in the given sample.

ACKNOWLEDGEMENT

REFERENCES

[1] Hamidi F., Carré H., Hamami A. El A., Aït-Mokhtar A., La Borderie C., Pimienta P., "Critical review of the use of fiber-reinforced concrete against spalling," *Fire Safety Journal,* Dec. 2023.

[2] Destrée, X., Krasnikovs, A., Wolf, S., "Fire Resistance of Steel Fibre Reinforced Concrete Elevated Suspended Slabs: ISO Fire Tests and Conclusions for Design RILEM Bookseries".

[3] Q. Ma, R. Guo, Z. Zhao, Z. Lin, K. He, "Mechanical properties of concrete at high temperature," *Construct, Build, mater.,,* pp. 371-383, 2015.

[4] K., Hager I. and Mróz, "Role of Polypropylene Fibres in Concrete Spalling Risk Mitigation in Fire and Test Methods of Fibres Effectiveness Evaluation," *Materials,* 2019 Dec.

[5] Destree, X., Krasnikovs, A., Kamars, J. Fire resistance of steel fibre R. C, "elevated suspended slabs: ISO fire tests and conclusions for design".

[6] Karunamoorthy, R. K., Krasnikovs, A., & Macanovskis, A., "Ingredients Degradation in Steel Fiber Reinforced Concrete after Thermal Loading," 2023.

[7] Alsafasfeh A., Alawabdeh M., Alfuqara D., Gougazeh M., Amaireh M.N, "Oil Shale Ash as a Substitutional Green Component in Cement Production,," *Advances in Science and Technology Research Journal,* 2022.

[8] Feng Q., Chan S.Y.N., He Z.S., Tsang M.K.C, "Shale ash concrete, Cement and Concrete Research," 2 February 1997.

[9] Kuusik R., Uibu M., Kirsimäe K., Mõtlep R., Meriste T., "Open-airdeposition of Estonian oil shale ash: formation, state of art, problemsand prospects for the abatement of environmental impact. Oil Shale29(4):376–403," 2012.

[10] Pihu T, Arro H, Rootamm R, Konist A, Kirsimäe K, Liira M, Mõtlep R, "Oil shale CFBC ash cementation properties in ash fields," 2012.

[11] Raado LM, Hain T, Liisma E, Kuusik R, "Composition and properties of oil shale ash concrete. Oil Shale," 2014.

[12] Macanovskis, A., Krasnikovs, A., Kononova, O., Macanovskis, E., "Pull-out mechanism detailed micromechanical investigation in situation when out of concrete is pulling straight steel fiber," in *Engineering for Rural Development,,* 2016.

[13] Zhang L., Zhao J., Fan C. and Wang Z., "Effect of Surface Shape and Content of Steel Fiber on Mechanical Properties of Concrete,," *Adv. in Civ. Engineering,,* 2020.

[14] Htut, T. N. S.; Foster, S. J., "Unified model for mixed mode fracture of steel fiber reinforced concrete, in Proc. of Fracture Mechanics of Concrete and Concrete Structures – High Performance, Fiber Reinforced Concrete, Special Loadings and Structu," 2010.

[15] Li, C.; Mobasher, B, "Finite element simulations of fiber pull-out toughening in fiber reinforced cement based composites," *Advanced Cement Based Materials,* 1998.

[16] Stang, H.; Li, V. C.; Krenchel, H, "Design and structural applications of stress-crack width relations in fibre reinforced concrete," *Materials and Structures,* 1995.

[17] Macanovskis, A., Krasnikovs, A., Kononova, O., Lukasenoks, A., "Mechanical Behavior of Polymeric Synthetic Fiber in the Concrete".

[18] Kizilkanat A.B., Kabay N., Akyüncü V., Chowdhury S., Akça A.H., "Mechanical properties and fracture behavior of basalt and glass fiber reinforced concrete: An experimental study Construction and Building Materials," December 2015.

[19] Macanovskis, A., Lukasenoks, A., Krasnikovs, A., Stonys, R., Lusis, V, "Composite fibers in concretes with various strengths," *ACI Materials Journal,* 2018.

[20] Khan S., Khattak S., and Khan H., "Composite Fibers in Concrete: Properties, Challenges, and Future Directions," 28 August 2023.

[21] Tinku Acharya, Ajoy K.Ray, Image Processing, principles and applications, Tueson,Arizona: A JOHN WILEY & SONS, INC, PUBLICATION, 2005.

[22] Milan Sonka, Vaclav Hlavac, Roger Boyler, Image Processing,Analysis and Machine Vision, stamford,USA: Global Engineering, 2015.

Mechanical behavior of Composite basalt short fiber for concrete structure reinforcement

Karunamoorthy Rengasamy Kannathasan
Department of Theoretical Mechanics and Strength of Material Riga Technical university
Riga, Latvia
Karunamoorthy.Rengasamy-Kannathasan@rtu.lv

Andrejs Krasnikovs
Department of Theoretical Mechanics and Strength of Material Riga Technical University,
Riga, Latvia
Andrejs.Krasnikovs@rtu.lv

Arturs Macanovskis
Department of Theoretical Mechanics and Strength of Material Riga Technical University,
Riga, Latvia
Arturs.macanovskis@rtu.lv

Iveta Novakova
Department of Construction, Energy and Material Technology
The Arctic University of Norway,
Lodve Langesgate 2, 8514 Narvik, Norway
iveta.novakova@uit.no

Abstract. **Interest to Fiber concrete - concrete reinforced with short randomly distributed in the material volume fibers is growing and obtaining more new fields of application. Initially used fibers were steel. Composite Fibers (CF) have become competitive with steel fibers, fiber concretes with such fibers are now under investigation. In the present research, authors investigated the bond strength between the fiber and concrete, as well as other mechanical characteristics of the fiber concrete with CF. CF were made of short basalt micro-fibers glued together by Epoxy resin. Basalt micro-fiber roving (250 filaments) was taken as a main source of the CF, it was impregnated with epoxy resin. The Epoxy resin to hardener ratio was 3:1. After a few days maturing prepared CF were cut down into short fibers of a size of 24 mm. The authors planned to prepare concrete samples for the single fiber pull-out test and composite fiber-reinforced concrete prisms for the four-point bending test. Another product used in the investigation was Oil Shale Ash (OSA). OSA is a class-C fly ash. OSA was used as a partial cement replacement in a concrete. The concrete mixture was prepared with different compositions in addition to Oil Shale Ash (was used OSA from Auvere, Estonia, thermal power plant) as replacement of cement in ratios of 0%, 10%, 20%, and 30%. Tests were performed to obtain the load-bearing capacity of a concrete with basalt fibers. An important property of every kind of fiber is the single fiber behavior under pull-out conditions. Microscopic analysis has been made to conclude the research.**

I. INTRODUCTION

Concrete strengthened and structurally intact by the addition of short fiber reinforcement (SFRC) [1, 2, 3]. Short fibers can be made from steel, glass, synthetic, natural, and other fibers [1] [4] [5] [6] [3] [7] [8] [9] [10]. These fibers give concrete greater strength, post cracking load bearing capacity, wearability, durability, structural integrity and etc [1] [7] [3] [10] [11]. Important role is playing composite fiber [12] [13] [14] [15] [16]. Composite fiber is produced as synthetic micro-fiber roving (bundle) with slicked together micro-fibers by matrix material. In our situation matrix material was Epoxy resin. Micro-fibers were impregnated by matrix and cut in length *L*. Traditionally *L* is changing from few millimetres (4 mm – 6 mm) till few centimetres (5 cm-6cm), forming short sticks (bars) [8] [12] [13]. Other important point in the present investigation is a use of Oil Shale Ash (OSA) as a partial cement replacement in concretes [17] [18] [19] [20] [21]. Oil shale ash (OSA) is a class-C fly ash, product obtained during long years of burning oils shales for energy production. OSA can be used as a cement partial replacement in concretes [18] [17]. Part of the OSA is collected and utilized as dry

powder material [16]. Various types of OSA have properties of a mineral binder, the hydration type of which varies from air hardening, topozzolanic and latent hydraulic [9] [20].

In our investigated concrete mixes 0 to 30% of cement was replaced by OSA (Electrostatic Precipitator Ash) coming from Auvere (Estonia) thermal power plant. The size of the particles in OSA powder ranges from hundreds of nm to µm. So, this study demonstrates the strength of composite fibers in different concrete compositions with oil shale ash functioning as a cement replacing agent. Our made composite fibers were fabricated and used. [9]

II. MATERIALS AND METHODS

Fiber reinforced concrete was planned to prepare by using the epoxy impregnated basalt short fiber and oil shale ash from Auvere plant as partial replacement of cement. Fibers were randomly distributed in the concrete samples.

2.1 Properties of Basalt Roving

Short basalt fibers were prepared from the market available basalt roving, epoxy, and hardener. Basalt roving properties (Supplier data) are follows,

Properties of basalt roving

▸ density: ca. 2,7 [g/cm³]

▸ linear tenacity: 70tex – 4800tex

▸ roving type: assembeled

▸ E-modulus: 90 – 100 [GPa]

▸ tensile strength: 3000 – 4000 [MPa]

▸ moisture absorption : 0,03 [%]

▸ temperature range: -260°C bis +750°C

Fig.1. Fiber properties

2.2 Preparation of fibers

The basalt yarn fibres (4.8 g for 1 m length Approx.) were seamed in a wooden frame with dampers and then tightened to create tension in the yarn and fibre, resulting in a straight and uniform thread sample. In which we used a brush to thoroughly coat all the basalt yarn with epoxy (WELA-EP 100) and hardener in the ratio 3:1, which aids in the formation of a uniform and unbreakable thread. Coated fibers were kept maturing and drying for 48 hours and trimmed to 24 mm to use in concrete.

Fig. 2. Preparation of fibers

Fig.3. Prepared basalt Fibers 24 mm

2.3 Concrete Mix Design and Materials

The concrete mix was designed using the standard EN-206. Concrete mix consists of Portland cement, fly ash, sand (0.3-2.5 mm) & (0-1.0 mm), quartz aggregates (4-8 mm), dolomite powder, super plasticizer (SP), admixture silica fume, fibre, water. The concrete mixture was designed in four different sets by adding Oil Shale Ash (we used OSA from Auvere, thermal power plant Estonia) as replacement of cement in ratios of 0% (EB-1), 10% (EB-2), 20% (EB-3), and 30% (EB-4). Measurements of all the ingredients in the table are in kg.

Table. 1 Mix proportion

Concrete Mixture				
	EB-1	**EB-2**	**EB-3**	**EB-4**
Cement (CEM II)	6.16	5.56	4.92	4.33
Oil Shale Ash	0	0.6	1.23	1.83
Sand (0.3-2.5 mm)	16.2	16.2	16.2	16.2
Sand (0-1.0 mm)	4.4	4.4	4.4	4.4
Gravel (4-8 mm)	16.0	16.0	16.0	16.0
Dolomite powder	2.9	2.9	2.9	2.9
SP Sika D190	0.225	0.225	0.225	0.225
Micro silica	0.65	0.65	0.65	0.65
Fiber	0.176	0.176	0.176	0.176
Water	3.4	3.4	3.4	3.4

2.4 Preparation of Samples

Samples were planned to prepare for three different kinds of experiments which are Pull-out, Compression and Bending. Pull-out samples were produced with two concrete prisms separated by plastic film. The fibers should be positioned at the middle of the prism. So, each fiber is indicated in the centre and must be exactly positioned, and the concrete mix for the pull out was made without fibers, as described in the concrete mixture table.

Bending and compression test samples were created with mould dimensions of 10x10x40 cm and 10x10x10 cm, respectively. [9] [22]
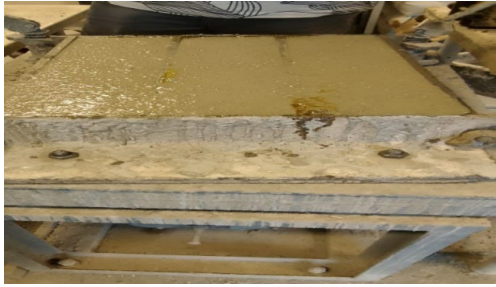
Fig.4. Preparation of samples

After that, all the ingredients were added to the concrete mixture machine and stirred for five to seven minutes to regulate the consistency of the mixture, producing a homogeneous mixture. The mixture was filled into the appropriate moulds for maturing. Then samples were taken out of the mould and after 48 hours in water, were brought into the lab for further curing. Samples were then covered with plastic wrap and stored in a laboratory with a required 90% relative humidity.

2.5 Mechanical Testing Methods

After 28 days of curing from the fabrication, the specimens were tested for single fiber pull-out, 4-point bending and compression test. Test machine Zwick Roell Z150 was used to determine the fiber pull-out force. [9] [22]
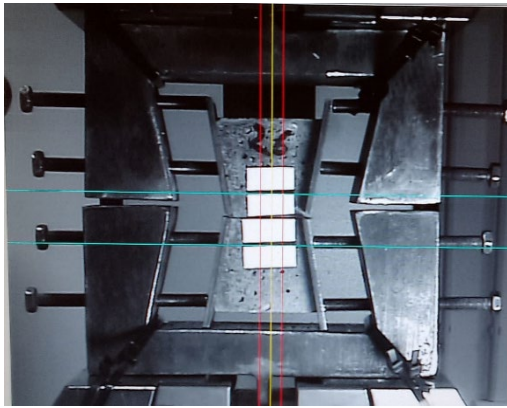
Fig.5. Single fiber pull-out.

Compression tests and 4-point bending tests were done to measure the strength of the concrete which we used to make the specimens, using an Automax 5 loading machine. During the tests, prism deformations were recorded using a frame with two HBM WA20 and Linear Variable Displacement Transducers (LVDTs) on each side.
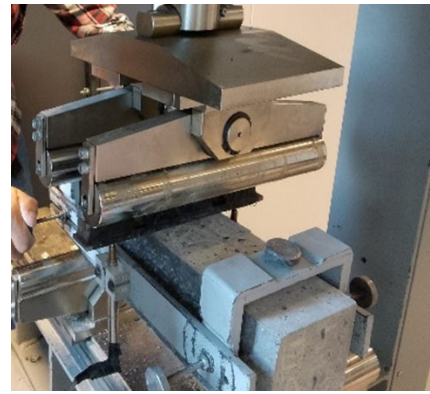
Fig.6. Four-point bending machine setup.

III. EXPERIMENTAL RESULTS AND DISCUSSION

3.1 Compression Test

The Standard dimensions (10 x 10 x 10 cm) samples were made for the cube test and throughout the testing, load should be added at a constant rate of 150 kg/cm^2/minute until the concrete sample is shattered. The rough surface of the cubes placed into the compression testing apparatus should not place on the bottom steel plate and the machine's platens because it may cause unbalanced loading over it. Compression testing results are shown in table 2.

Table 2. Compression test results

	Compressive strength MPa			
Samples	**EB-1 (0% OSA)**	**EB-2 (10% OSA)**	**EB-3 (20% OSA)**	**EB-4 (30% OSA)**
Sample 1	61.12	52.16	52.02	37.8
Sample 2	58.73	53.13	51.54	36.4
Sample 3	58.08	56.95	49.4	36.05
Sample 4	60.24	54.73	49.61	39.82

From the obtained results we can see that the compressive strength is reduced when compared to the concrete samples with no replacement of cement by oil shale ash. This tendency increases when the amount of OSA is bigger than 20%. Important to notice, OSA addition is rapidly decreasing liquid concrete mix rheological properties.

3.2 Fibers Pull-Out

In figures 7-10 is possible to see pull-out tests results. Sample consisting of two concrete parts, bridged by the fiber immersed in both parts at the same depth is slowly stretched with the constant loading speed till fiber rupture or its fully pull out with one end [20]. The results show the process of removing epoxy impregnated basalt fibers from the concrete matrix, as well as the maximum load required to remove the 24mm fiber. The specimen will contain two strips used to measure the gauge length. With a starting loading, fibers remain in the matrix without any pull-out, when the force reaches 150 N, the fiber begins to pull out at the predetermined speed of 5 mm/min. The first step is characterized by fiber delamination from the surrounding

concrete. Mainly, it happens by a thin polymer layer (that is wrapping the fiber) tearing off.
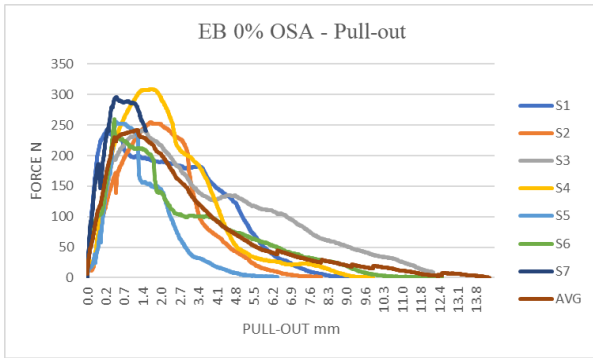
Fig.7. Force and Displacement graph for 0% OSA.
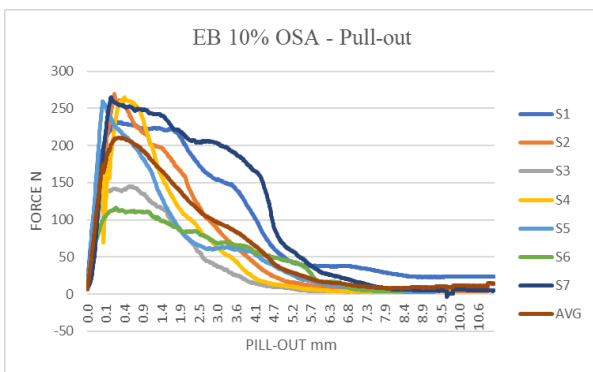
Fig.8. Force and Displacement graph for 10% OSA.

A difference in force was observed throughout the pullout process, which could be attributed to vibration, microparticles of the concrete matrix being pulled with friction-forming plugs, and epoxy blended with the concrete matrix being present at the weak interface. The study of this interfacial behavior is essential for understanding mechanical behavior.
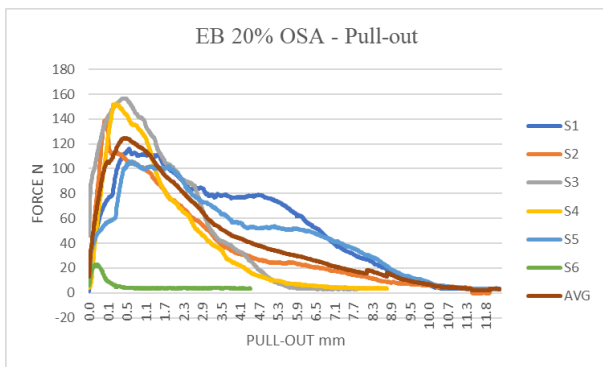
Fig.9. Force and Displacement graph for 20% OSA.
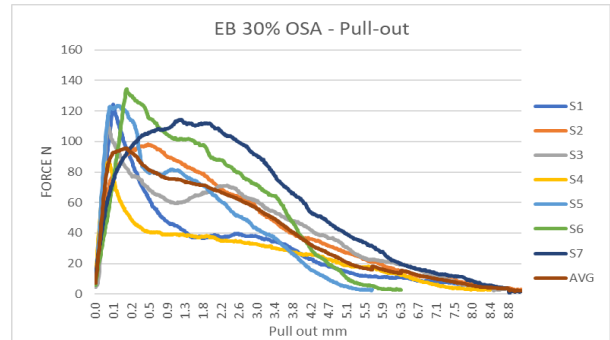
Fig.10. Force and Displacement graph for 30% OSA.

Important to mention, addition of OSA is decreasing the maximal value of necessary applied load for fiber pull out. It happens constantly with an increase of the amount of cement (10%-30%) replaced by OSA.

3.3 Four-point bend test

The prism was marked 5 cm from the edge to ensure proper fit in the bending machine. The loading happened with constant loading speed till the sample failure. The specimen's midpoint deflection was obtained in real-time by averaging the values from both sensors (on both sides of the prism). The load was applied until the specimens were destroyed; maximum average deflection reached is 11.5 mm for 0% OSA samples at 31.5 kN, then it deformed with some internal cracks on its elastic state and samples it didn't withstand additional load rupture occurs during deflection of 1 – 1.5 mm. Because fiber length (24 mm), it failed to hold the concrete after [9] the rupture. Minimum load as 17 kN took for EB4 samples i.e., 30% OSA and in some samples amount fibers distributed and orientation of the fiber on the cracked surface also less.

3.4 Examine fibers.

An impregnated epoxy basalt fiber with a cut edge and surface is examined using optical microscopes to determine the strength of the binding between the fiber and epoxy.
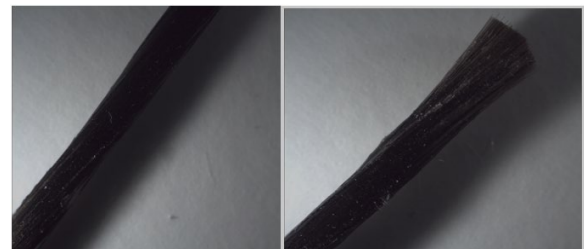
Fig.11. Fibers before testing

Fig.12. Fibers after testing

The fibers utilized for single fiber pullout underwent analysis prior to being inserted into the concrete matrix. Following this, all the tested samples were gathered and reexamined under a microscope to verify that the fibers had broken and to look for surface cracks.

IV. CONCLUSION

Strength and mechanical behavior investigation were performed for fiber concrete with cement gradually replaced by Oil Shale Ash and composite fibers 24 mm long. Fibers were fabricated with Basalt micro-fibers impregnated by Epoxy resin. Single fiber Pull -out program was realized.

Experimentally was obtained:
1. Maximal pull-out force decreased for concrete mixes with higher amount of OSA which is Average force required for samples without OSA is 246.9 N but for the samples with OSA (30%) is 98.45 N.
2. Compressive strength of concretes with constant fibers weight fraction decreased for mixes with higher amount of OSA. Tendency became more intensive for concentrations bigger than 20% i.e., from 59.54 to 37.52 MPa.
3. Bending strength for fiber concrete prisms decrease with increase of OSA in
   the concrete mix.

Fiber pull-out happens by thin polymer layer, that is wrapping the fiber tearing off.

ACKNOWLEDGEMENT

REFERENCES

[1] Banthia, N., Bindiganavile, V., Jones, J. and Novak, J. , PCI J.,, Fiber-reinforced concrete in precast concrete applications: Res [1] [2]earch leads to innovative products, Vols. vol. Summer 201, pp. 33–46,, June,2012.

[2] Šahmenko, G., Krasnikovs, A., Lukašenoks, A., Eiduks, M., Ultra-high performance concrete reinforced with short steel and carbon fibers, Open Access, Vide. Tehnologija. Resursi - Environment, Technology, Resources, 1,, pp. 193-199, 2015..

[3] Maidl B. R., Ernst and Sohn,, Steel Fiber Reinforced Concrete, Berlin, 1995.

[4] Khabaz, A. ., Theoretical analysis and numerical simulation of development length of straight steel fiber in cementitious materials, Compos. Interfaces, 2017,.

[5] Khabaz, A., Analysis of sliding mechanism of straight steel fibers in concrete and determine the effect of friction., Arch. Civ. Mech. Eng. 17, 599–608., 2017,.

[6] Khabaz, A. J. Test. Eval., Experimental and Numerical Investigation of Single Fiber Pull-Out Tests of Steel Macro-Fiber and Glass Micro-Fiber in a Cementitious Matrix., 2022,.

[7] Jiang C., Fan K., Wu F., Chen D., Experimental study on the mechanical properties and microstructure of chopped basalt fiber reinforced concrete, Mater. Des., 58 , pp. 187-193., 2014.

[8] Kizilkanat A.B., Kabay N., Akyüncü V., Chowdhury S., Akça A.H., Mechanical properties and fracture behavior of basalt and glass fiber reinforced concrete: An experimental study Construction and Building Materials, December 2015.

[9] Karunamoorthy, R. K., Krasnikovs, A., & Macanovskis, A., "Ingredients Degradation in Steel Fiber Reinforced Concrete after Thermal Loading," 2023.

[10] Macanovskis, A., Krasnikovs, A., Kononova, O., Lukasenoks, A., Mechanical Behavior of Polymeric Synthetic Fiber in the Concrete, Open Access, Procedia Engineering, 172, pp. 673-680 2017..

[11] Krishna Kiran Annamaneni, Bhumika Vallabhbhai Dobariya, Krasnikovs Andrejs, "Concrete, Reinforced By Carbon Fibre Composite Structure, Load Bearing Capacity During Cracking," in *Environment. Technology. Resources*, Rezekne, Latvia, 2021.

[12] Krasnikovs A., Lapsa V. A.,, Composite Fiber and production process Thereof,, Latvian patent, LV15471A,, 20.01. 2020..

[13] Krasnikovs A., Lapsa V. A., Lukasenoks A.,, Composite Fiber and Production Process thereof, Latvian patent, LV15339B,, 2019.

[14] Macanovskis, A., Lukasenoks, A., Krasnikovs, A., Stonys, R., Lusis, V, Composite fibers in concretes with various strengths,, ACI Materials Journal,, 2018.

[15] Khan S., Khattak S., and Khan H., Composite Fibers in Concrete: Properties, Challenges, and Future Directions, MDPI, 28 August 2023..

[16] https://reforcetech.com/technology/minibars/.

[17] Raado L.M., Hain T., Liisma E., Kuusik R., Composition and properties of oil shale ash concrete Oil Shale,, 2014,.

[18] Raado LM, Hain T, Liisma E, Kuusik R, Composition and properties of oil shale ash concrete. Oil Shale, 2014.

[19] Kuusik R, Uibu M, Kirsimäe K, Characterization of oil shale ashesformed at industrial-scale CFBC boilers. Oil Shale, 2005.

[20] Kuusik R., Uibu M., Kirsimäe K., Mõtlep R., Meriste T., Open-airdeposition of Estonian oil shale ash: formation, state of art, problemsand prospects for the abatement of environmental impact. Oil Shale, 2012.

[21] Pihu T, Arro H, Rootamm R, Konist A, Kirsimäe K, Liira M, Mõtlep R, Oil shale CFBC ash cementation properties in ash fields.Fuel, 2012.

[22] Vitalijs Lusis, Olga Kononova, Arturs Macanovskis, Rimvydas Stonys, Inga Lasenko,Andrejs Krasnikovs., "Experimental Investigation and Modelling of the Layered Concrete with Different Concentration of Short Fibers in the Layers," *fibers,* 2021.

[23] Macanovskis, A., Krasnikovs, A., Kononova, O., Macanovskis, E. ,, "Pullout mechanism detailed micromechanical investigation in situation when out of concrete is pulling straight steel fiber," in *Engineering for Rural Development*, 2016-January,.

[24] Vitalijs Lusis 1, *, Olga Kononova 1,2, Arturs Macanovskis 1,2, Rimvydas Stonys 3, Inga Lasenko 1, "Experimental Investigation and Modelling of the Layered," *Fibers,* no. MDPI, 2021.

Technical methods of cleaning shipwrecks from ghost nets

Astrida Rijkure
University of Latvia
Riga, Latvia
astrida.rijkure@lu.lv
ORCID 0000-0001-5449-4796

Janis Megnis
Riga Technical University
Riga, Latvia
janis.megnis@rtu.lv
ORCID 0000-0001-7620-6337

***Abstract.* Ghost nets are fishing gear lost and left in bodies of water that continue to be fished. Most of the fishing gear that is lost is made of synthetic materials that break down very slowly or not at all in nature and continue to work long after the net is lost. A ghost net drifts in the sea until it catches on an object, most often a shipwreck. This harms both nature and people's economic interests. Currently, the release of shipwrecks and other sunken objects from fragments of lost nets is mainly done by human hands, resp. divers dive to the wreck and use hand tools to free the wreck from fragments of fishing gear. There are innovative robotic systems in the world that can partially replace the work of divers.**

Keywords: gostnets, blue economy, underwater robots, sustainable.

I. INTRODUCTION

Ghost nets in the sea: Today, it is the durable and cheap use of plastic in fishing that has caused a serious problem in marine ecosystems. These abandoned fishing nets continue to 'fish' and kill the creatures living in the waters in an uncontrolled manner, causing serious damage to both nature and people, often also ships. Plastic waste does not decompose in nature, so ghost nets remain in the oceans and seas for a long time, causing long-term pollution. Studies show that these ghost nets are responsible for significant threats to marine life species and can also cause hazards to ship navigation. Solutions to this problem include improved management, nets labeling and a shift to greener materials in fisheries, as well as active de-littering and cleaning from the sea. The aim is to preserve the marine environment and its biodiversity by reducing the impact of ghost nets.

The aim of the given scientific research is to review the innovative robotic methods of freeing ghost nets and to provide solutions that could improve this process.

The methods used in the research are based on the analysis of scientific articles, the analysis of the technical possibilities of technologies and the search for innovative solutions that could improve the marine environment and have a positive impact on the processes of the blue economy. Theoretical and methodological basis of the study. When developing the study, research by Pedersen, S., Liniger, J., Sørensen, F.F., von Benzon, M., Fernandez, J. J., were used.

II. GENERAL REGULATIONS

At present, human hands are used to free shipwrecks and other sunken objects from fragments of lost nets. divers dive to the wreck and use hand tools to free the wreck from fragments of fishing gear. Fragments of fishing gear above the release, they are lifted into the water with winches or inflatable buoys. The use of manual labor to free wrecks from lost fishing gear is a laborious and slow process influenced by a number of factors. Primarily, it is the time spent underwater, which is limited by the diver's air reserves and nitrogen, which is formed due to the diver's blood pressure while working underwater, depending on the depth and time spent underwater.

The authors of this article organized an expedition in August 2023 and freed the shipwreck near Engure (Latvia) from ghost nets. The total time for the divers to free this shipwreck from the ghost nets with the preparation time took 4 days, a total of about 20h. The shipwreck was at a depth of 20m, which limited the work of divers and the time to get out of the water. Floats were used to highlight the gost nets. In total, about half a ton of nets were brought out. Highlighting and analyzing the structure of the nets, it was found that mostly those kapron nets, therefore lost around the 60s-90s of the last century.

Practically, this means, regardless of air reserves, depending on the depth of immersion, the divers' total time under water is strictly limited. For example, when performing a no-compression dive in the Baltic Sea at a

depth of 30 meters, taking into account the water temperature, the useful working time spent at depth is approximately 15 to 18 minutes. When performing a decompression regime immersion, this time can be extended, but it is inseparably connected with the involvement of vessels specially adapted for underwater work, which are equipped with barocameras, to carry out the work. In the case of Latvia, such equipment is only at the disposal of military structures, and renting it from foreign private structures would increase the cost of carrying out work in a geometric progression.

Fig.1. Cleanup of a shipwreck near the port of Engure, August, 2023. Baltic Sea (Latvian territorial waters) [photo from the authors' archive]

It is clear that the Baltic Sea, which is at the top of the list of the world's most polluted seas, is not a good home for its inhabitants. There are many shipwrecks in the Baltic Sea (including Latvian waters), most of which have not been identified and surveyed. A large amount of lost fishing gear - "ghost nets" have been found on all surveyed shipwrecks, which continue to act as passive fishing gear and cause significant damage to the marine environment - aquaculture, as well as technically affect ships that practically do not degrade or degrade over a long period. Currently, only direct visual inspection of wrecks and sunken objects is carried out by diving, which is significantly limited by air reserves and the permissible time spent at depth.

Collecting seafood animals (such as sea cucumbers, sea echini, scallops, etc.) cultivated in shallow water (water depth: ~30 m) is a profitable and an emerging field that requires robotics for replacing human divers. Soft robotics have several promising features (e.g., safe contact with the objects, lightweight, etc.) for performing such a task. In this paper, we implement a soft manipulator with an opposite-bending-and-extension structure. A simple and rapid inverse kinematics method is proposed to control the spatial location and trajectory of the underwater soft manipulator's end effector. We introduce the actuation hardware of the prototype, and then characterize the trajectory and workspace. We find that the prototype can well track fundamental trajectories such as a line and an arc. Finally, we construct a small underwater robot and demonstrate that the underwater soft manipulator successfully collects multiple irregular shaped seafood animals of different sizes and stiffness at the bottom of the natural oceanic environment (water depth: ~10 m). [1]

This type of underwater robot, equipped with manipulators, would also be useful for other underwater work, such as cleaning shipwrecks from ghost nets.

Previously, the rigid robotic arms used for underwater manipulation have several challenging issues such as delicate grasping fragile and squishy seafood animals. Meanwhile, the traditional rigid hydraulic arms usually have large mass. The huge inertia caused by the rigid arm during locomotion would induce significant vibration for the small underwater vehicle. [2]

Introduction highlighting the challenges in precisely controlling underwater robotic arms due to environmental fluctuations and limitations of traditional control algorithms. It emphasizes the importance of remotely operated vehicles (ROVs) and robotic manipulators for complex underwater tasks.

The ROV, or Remotely Operated Vehicle, is a purpose-built underwater apparatus equipped with propellers, cameras, and a manipulator arm. The ROV's body is constructed from a specialized aluminum alloy designed to be both lightweight and durable for marine environments. Its propellers provide omnidirectional mobility, enabling the ROV to move freely in all directions. The manipulator arms of the ROV are highly articulated, often exceeding 1 m in length, and can be fitted with various specialized tools such as welding, cutting, gripping, and holding devices, depending on the specific task requirements. [3]
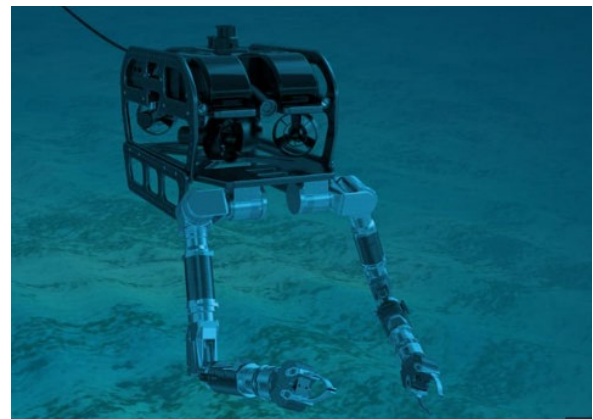
Fig.2. The simple structured robotic manipulator of the ROV [3]

The area of remotely operated vehicles (ROVs) and autonomous underwater vehicles (AUVs) has rapidly developed, with several decades of experience, both in research (see, for example, the study described in [4]) and industrial applications of increasing complexity, both in terms of missions and levels of automation (see for example [5] on cooperative navigation). Regarding the latter, many control algorithms have been proposed, both for simulated and actual vehicles. However, it is generally not immediate to compare control algorithms between them. Indeed, while some articles comparing newly-proposed control laws for ROV stabilization to previous algorithms can easily be found [6, 7, 8, 9, 10, 11], it is primarily based on simulation models for which the actual physical replica is not easily accessible or affordable, thereby limiting the comparability between control algorithms and the extent of the benchmarking attempt. [12]

More recently, the industry has also evolved towards more affordable products meant for researchers, students, or hobbyists, several of which are proposed under the open-source paradigm (see, for example, OpenROV, OpenROV Trident, BlueROV2) [13]. The advantages of open software and hardware solutions lie in their cost-effectiveness compared to conventional solutions and that they allow increasingly faster development, modifications, and improvements. Among these solutions, the widely-popular BlueROV2 [14] combines an open-source architecture with components of sufficiently good quality, allowing relatively advanced missions (see, for example, [15,16,17]).

Several robot simulators have previously been developed, some of which are specific for underwater robots [18,19,20]. However, the simulators for underwater robots are generally based on a user-defined model, such as the UUV Simulator [18] package for Gazebo or the Simu2VITA [19] block for Simulink™, which makes it challenging to use as a benchmark for control algorithms. Furthermore, these simulators neglect the tether force many underwater robots use for top-site communications or power [21]. The present paper aims at bridging the gap between simulation for control systems and experimental testing by proposing a MATLAB™ and Simulink™ open-source package of the tethered BlueROV2 for the control community as a benchmark in simulation toward full deployment on the same well-known platform. MATLAB™ and Simulink™ have been chosen as they are well-known to the control community and offer various toolboxes to implement advanced control and missions. These missions could be measuring reefs [22], monitoring and removal of marine growth on offshore structures [6,23,24], water quality and ecology monitoring [25], detection of oil plumes [26], fish farm net monitoring [27], etc.

III. RESULTS AND DISCUSSION

The essential limiting factor in the use of human labor is directly trained, availability of trained and experienced divers. Taking into account the release of shipwrecks from the nets in the Baltic Sea objective working depths and conditions, respectively, limited visibility conditions (in the Baltic Sea approximately 0.5-1 m), low water temperature, currents, the specifics of the work are dangerous precisely because of the fishing gear, can be practically carried out only technical divers (Technical Divers) or professional divers (Commercial Divers), whose availability is limited and man-hour and equipment costs are high. Practically, this means that taking into account the time and resources that are consumed to free one wreck from lost fishing gear using human labor hands, this process is too slow to make a significant contribution to improving the ecological status of the Baltic Sea, because while one net is freed, another ten are lost. Significant improvements in the clearance of shipwrecks from lost fishing gear and thus improve the ecological situation of the Baltic Sea, can only be achieved by doing this cleaning more efficient from time and cost points. If the underwater robot was equipped not only with an ROV-

type tentacle manipulator, but also with a disc cutter manipulator, then it could be replaced by the work of a diver. With such a solution, human manual work would be minimized and consumption would be reduced accordingly time and cost. Using shipwrecks for clearing lost fishing gear, with special underwater robot equipped with manipulators, the working time limit is solved primarily because the robot is being controlled from a cutter or ship. Practically, this means that shipwreck cleanup will be able to be carried out in a 24/7 mode, restrictive the factor will be only metrological conditions resp. wind speed and swell, which would limit to the same extent clean-up work if carried out by divers. The use of a robot equipped with special manipulators wrecks in purification, means extending the useful time for achieving the goal up to ten times or more. At the same time the number of technical divers involved in the wreck clearance works, whose labor costs would be significantly reduced due to specific skills and equipment, is one of the largest cost items. Of course, clearing the wreckage from for lost fishing gear, using an underwater robot equipped with special manipulators, in the process it will not be possible to completely abandon the involvement of technical divers, but their number and working hours will be significantly reduced, accordingly reducing costs in the position of hiring underwater personnel.

Fig.3. Gost nets near Engure port [photo from the authors' archive]

Objectively, it should be understood that only effective the use of financial and human resources can ensure a significant cleaning of the Baltic Sea from lost nets pace increase.

IV. CONCLUSIONS

Analyzing scientific publications, several science-based solutions for auxiliary equipment of underwater robots have been found, with the help of which shipwrecks can be freed from ghost nets, but all these solutions are based on ROV-type tentacle-type arms. These robots are not given the ability to spin and not get entangled in ghost webs. Therefore, it is important to create technologies that can help free shipwrecks from ghost nets with more

modern methods, because nowadays they are not only cotton nets, but more often already various plastic elements, besides there are also shipwreck cables, metal parts, etc. (respectively nylon and other material nets, metal cables, chains, plastic floats, metal weights and other elements of trawls and nets), so it is important to develop a technological scheme for lifting the freed net fragments above the water for further collection and delivery to the shore. These manipulators should be designed to be equipped with cutters for cutting nylon and other material nets and rotating cutting discs for cutting metal cables, chains and other hard materials. The manipulator equipped with a cutting disc is also intended to be used for cutting off or dismantling elements on shipwrecks that interfere with the removal of nets.

REFERENCES

[1] Gong Z, Chen B, Liu J, Fang X, Liu Z, Wang T and Wen L (2019) An Opposite-Bending-and-Extension Soft Robotic Manipulator for Delicate Grasping in Shallow Water. Front. Robot. AI 6:26. doi: 10.3389/frobt.2019.00026

[2] Fernandez, J. J., Prats, M., Sanz, P. J., and Garcia, J. C. (2013). Grasping for the seabed: developing a new underwater robot arm for shallow-water intervention. IEEE Robot. Automat. Magaz. 20, 121–130. doi: 10.1109/MRA.2013.2248307

[3] Duc-Anh Pham, Seung-Hun Han, (2023), Journal of Marine Science and Engineering, 11(12), 2312; https://doi.org/10.3390/jmse11122312 Enhancing Underwater Robot Manipulators with a Hybrid Sliding Mode Controller and Neural-Fuzzy Algorithm

[4] Healey, A.J.; Lienard, D. Multivariable sliding mode control for autonomous diving and steering of unmanned underwater vehicles. IEEE J. Ocean. Eng. 1993, 18, 327–339.

[5] Willcox, S.; Goldberg, D.; Vaganay, J.; Curcio, J. Multi-vehicle cooperative navigation and autonomy with the bluefin CADRE system. In Proceedings of the IFAC (International Federation of Automatic Control) Conference, Heidelberg, Germany, 15 September 2006; pp. 20–22.

[6] Benzon, M.; Sorensen, F.; Liniger, J.; Pedersen, S.; Klemmensen, S.; Schmidt, K. Integral Sliding Mode control for a marine growth removing ROV with water jet disturbance. In Proceedings of the 2021 European Control Conference (ECC), Delft, The Netherlands, 29 June–2 July 2021.

[7] Pedersen, S.; Liniger, J.; Sørensen, F.F.; Schmidt, K.; Benzon, M.v.; Klemmensen, S.S. Stabilization of a ROV in three-dimensional space using an underwater acoustic positioning system. IFAC-PapersOnLine 2019, 52, 117–122.

[8] Kuhn, V.N.; Drews Jr, P.L.J.; Gomes, S.C.P.; Cunha, M.A.B.; Botelho, S.S.d.C. Automatic control of a ROV for inspection of underwater structures using a low-cost sensing. J. Braz. Soc. Mech. Sci. Eng. 2015, 37, 361–374.

[9] Eslami, M.; Chin, C.S.; Nobakhti, A. Robust Modeling, Sliding-Mode Controller, and Simulation of an Underactuated ROV Under Parametric Uncertainties and Disturbances. J. Mar. Sci. Appl. 2019, 18, 213–227.

[10] Keviczky, T.; Borrelli, F.; Fregene, K.; Godbole, D.; Balas, G.J. Decentralized Receding Horizon Control and Coordination of Autonomous Vehicle Formations. IEEE Trans. Control Syst. Technol. 2008, 16, 19–33.

[11] Selvakumar, J.; Selvakumar, J.; Asokan, T.; Asokan, T. Station keeping control of underwater robots using disturbance force measurements. J. Mar. Sci. Technol. 2016, 21, 70–85.

[12] Benzon M., Sørensen F.F., Uth E., Jouffroy J., Liniger J., Sørensen F.F., An Open-Source Benchmark Simulator: Control of a BlueROV2 Underwater Robot, J. Mar. Sci. Eng. 2022, 10(12), 1898; https://doi.org/10.3390/jmse10121898

[13] Willners, J.S.; Carlucho, I.; Luczy'nski, T.; Katagiri, S.; Lemoine, C.; Roe, J.; Stephens, D.W.; Xu, S.J.; Carreno, Y.; Pairet, È.; et al. From market-ready ROVs to low-cost AUVs. In Proceedings of the OCEANS 2021: San Diego–Porto, San Diego, CA, USA, 20–23 September 2021; pp. 1–7.

[14] Robotics, B. BlueROV2: The World's Most Affordable High-Performance ROV. In BlueROV2 Datasheet; Blue Robotics: Torrance, CA, USA, June 2016.

[15] Wilby, A.; Lo, E. Low-Cost, Open-Source Hovering Autonomous Underwater Vehicle (HAUV) for Marine Robotics Research based on the BlueROV2. In Proceedings of the 2020 IEEE/OES Autonomous Underwater Vehicles Symposium (AUV), St. Johns, NL, Canada, 30 September–2 October 2020; IEEE: Piscataway, NJ, USA, 2020; pp. 1–5.

[16] Chua, A.; MacNeill, A.; Wallace, D. Democratizing ocean technology: Low-cost innovations in underwater robotics. In Proceedings of the EGU General Assembly Conference Abstracts, Online, 4–8 May 2020; p. 10190.

[17] Manzanilla, A.; Reyes, S.; Garcia, M.; Mercado, D.; Lozano, R. Autonomous navigation for unmanned underwater vehicles: Real-time experiments using computer vision. IEEE Robot. Autom. Lett. 2019, 4, 1351–1356.

[18] Manhães, M.M.M.; Scherer, S.A.; Voss, M.; Douat, L.R.; Rauschenbach, T. UUV Simulator: A Gazebo-based package for underwater intervention and multi-robot simulation. In Proceedings of the OCEANS 2016 MTS/IEEE Monterey, Monterey, CA, USA, 19–23 September 2016; IEEE: Piscataway, NJ, USA, 2016.

[19] Cerqueira Gava, P.D.; Nascimento Júnior, C.L.; Belchior de França Silva, J.R.; Adabo, G.J. Simu2VITA: A General Purpose Underwater Vehicle Simulator. Sensors 2022, 22, 3255.

[20] Potokar, E.; Ashford, S.; Kaess, M.; Mangelson, J. HoloOcean: An Underwater Robotics Simulator. In Proceedings of the 2022 International Conference on Robotics and Automation (ICRA), Philadelphia, PA, USA, 23–27 May 2022.

[21] Bogue, R. Robots in the offshore oil and gas industries: A review of recent developments. Ind. Robot 2020, 47, 1–6.

[22] Rofallski, R.; Tholen, C.; Helmholz, P.; Parnum, I.; Luhmann, T. Measuring artificial reefs using a multi-camera system for unmanned underwater vehicles. Int. Arch. Photogramm. Remote Sens. Spat. Inf. Sci.-ISPRS Arch. 2020, 43, 999–1008.

[23] Pedersen, S.; Liniger, J.; Sørensen, F.F.; von Benzon, M. On Marine Growth Removal on Offshore Structures. In Proceedings of the OCEANS 2022-Chennai, Chennai, India, 21–24 February 2022; pp. 1–6.

[24] Liniger, J.; Jensen, A.L.; Pedersen, S.; Sørensen, H.; Mai, C. On the Autonomous Inspection and Classification of Marine Growth on Subsea Structures. In Proceedings of the 2022 OCEANS Conference & Exposition, Oceans 2022, Chennai, Chennai, India, 21–24 February 2022; IEEE Press: Piscataway, NJ, USA, 2022.

[25] Boogaard, F.; de Lima, R.; de Graaf, R. Innovative water quality and ecology monitoring using underwater unmanned vehicles: Field applications, challenges and feedback from water managers. Water 2020, 12, 1196.

[26] Wang, Y.; Thanyamanta, W.; Bulger, C.; Bose, N. Experimental study to make gas bubbles as proxies for oil droplets to test AUV detection of oil plumes. Appl. Ocean Res. 2022, 121, 103080.

[27] Betancourt, J.; Coral, W.; Colorado, J. An integrated ROV solution for underwater net-cage inspection in fish farms using computer vision. SN Appl. Sci. 2020, 2, 1946.

Optimizing 3D printing parameters to improve hardness and surface roughness

Sabi Sabev
Technical University of Sofia,
Branch Plovdiv
Plovdiv, Bulgaria
sabi_sabev@tu-plovdiv.bg

Konstantin Chukalov
Technical University of Sofia,
Branch Plovdiv
Plovdiv, Bulgaria
chukalov@tu-plovdiv.bg

Valeri Bakardzhiev
Technical University of Sofia,
Branch Plovdiv
Plovdiv, Bulgaria
bakardzhiev@tu-plovdiv.bg

Agop Izmirliyan
Technical University of Sofia,
Branch Plovdiv
Plovdiv, Bulgaria
izmirliyan@tu-plovdiv.bg

Abstract. **The purpose of this paper is to study the factors affecting roughness and hardness of 3D printed models. Two parameters are analyzed- 3D printing speed and layer thickness. The main disadvantage of 3D printed models is their higher roughness, which depends on the printing parameters. In order to obtain parts with smoother surfaces, it is necessary to study these parameters. Based on the obtained experimental results, a regression dependence was built describing the relationship between roughness and hardness with the investigated printing parameters.**
Keywords: 3D printing, hardness, surface roughness

I. INTRODUCTION

In recent years, 3D printing has become more and more popular in some industries, such as architecture, automotive, mechanical engineering, medicine etc [1], [2]. In order to meet the great demand for this technology. If at the beginning of this century, 3D models of souvenirs and irresponsible details were mainly made, nowadays more and more emphasis is placed on the possibility of achieving high mechanical and physical properties.

Real surfaces have micro-uniformities, which are a consequence of technological operations [3]. Surface roughness is an important characteristic for operational qualities of parts, especially in assembled units, because it affects the quality of the assembly[4]. High values of roughness also reduce the fatigue limit of materials. High roughness values also reduce fatigue limit of materials.

Hardness is an important mechanical characteristic in 3D printing, as it represents both the wear resistance and behavior of the parts in general - the type of failure, plasticity, etc., an important advantage of the hardness test is that it is non-destructive test [5].

In general, 3D printed parts have weaker mechanical properties compared to other manufacturing technologies, so their properties are determined by the weakest layer. Their application is growing especially in the automotive industry. Precisely for these reasons, testing the hardness of 3D printed parts is very relevant.

This article looks at one of the most common applications of 3D technology, namely the printing of various parts with a wide variety of openings.[6] Through the methods of statistical analysis, it is shown how the roughness and hardness of the model may be determined on the basis of a certain sample of experimental models. Mainly for printing 3D models used in mechanical engineering and automotive industry, polymers with better physical and mechanical properties are used.

In the article, the printed models are from the ABS polymer Acrylonitrile-Butadiene-Styrene[7]. It is also possible to use other polymers such as PETG, polypropylene, polyethylene, but they have higher requirements for the 3D printer, most often a higher extrusion temperature. The printer we use is a Flashforge Creator 3, it allows a maximum extrusion temperature of 250°C and a maximum substrate temperature of 120°C

Factors that can be changed are polymer extrusion temperature, print speed, layer height and substrate temperature [8],[9]. The two technological invoices, the extrusion temperature and the temperature of the base, we assume to be constant because they can deteriorate the

quality of the print itself. Optimizing of 3d parameters to improve parameters is very current [10].

The extrusion temperature for ABS is in the range of 235-240°C, when the temperature decreases, we do not have good thinness, and this leads to problems with clogging the nozzle of the 3d printer and interrupting the printing process. At extrusion temperatures above 240 °C, the material begins to boil and pit the nozzle walls, and the high temperature can cause material to flow freely and uncontrollably from the extruder.

At a high temperature of the printer base above 110°C, the pattern is difficult to peel off and may break at the base. At temperatures below 100°C, the pattern peels off during printing and the process has to be started from the beginning.

II. MATERIALS AND METHODS

ABS is an amorphous polymer that is obtained by emulsion or bulk polymerization of acrylonitrile and styrene in the presence of polybutadiene. The most important properties of ABS are its good impact resistance and strength

Investigated parameters of 3D printing are speed and height of layer, because they affect properties of parts. The 3D printer parameters that are constant for all trials, ie. are constant: nozzle diameter 0.4mm; flow 100%; retreat 1mm; bed temperature 110°C.

Hardness was measured according to the standardized Shore D method according to DIN 53505 [11].This method is the most popular for plastics. The measuring device is calibrated and its range is according to the theoretical hardness of the material. In order to reduce the measurement error, the firings were made at a distance of more than 2 times the diameter of the pin from the final contour of the specimen, as well as a distance of more than 3 times the diameter of the needle between individual impressions [12].

For greater precision, 5 tests were made on each sample, fig. 1.

Each of the test specimens was measured at three locations using a Surface Roughness Tester Surftest 4, fig2, Mitutoyo brand. The measurements are presented in tabular form table 1, [13].

Fig. 1. Hardness measurement
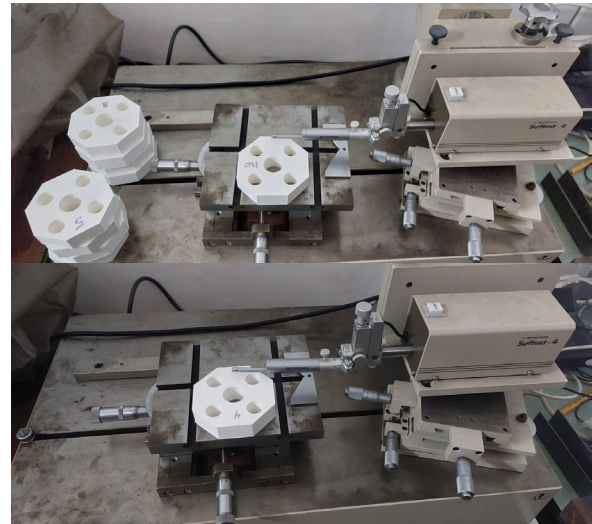
Fig. 2. Surface Roughness Tester Surftest 4

III. RESULTS AND DISCUSSION

TABLE 1 EXPERIMENTAL RESULTS OF SURFACE FINISH

Layer [mm]	Speed [m/min]	Roughness of tested 3 countours [Ra]			Average [Ra]
		1	2	3	
0.1	10	1.24	1.46	1.39	1.36
0.1	45	1.26	1.15	1.76	1.39
0.1	80	1.32	1.24	0.96	1.17
0.25	10	5.89	4.68	6.43	5.67
0.25	45	4.27	3.11	5.01	4.13
0.25	80	2.48	2.97	4.2	3.22
0.4	10	1.99	2.98	3.5	2.82
0.4	45	3.01	3.47	2.8	3.09

The data from Table 1 on the roughness were processed and the following regression model was obtained:

$$Avr\ Ra = -5.722 + 88.19\ layer + 0.0566\ Speed - \text{(1)}$$
$$166.6\ layer*layer -$$
$$0.744\ layer*Speed$$
$$+ 1.512\ layer*layer*Speed$$

Results are shown in tables 2 and 3

TABLE 2 MODEL SUMMARY

S	R-sq	R-sq(adj)	PRESS	R-sq(pred)	AICc	BIC
0.195021	99.33%	98.20%	1.54035	90.90%	112.23	1.61

The coefficient of determination R-sq = 99.33% was calculated, and the adjusted coefficient of determination has the value R-sq(adj) = 98.2%, which satisfies the requirement of being above 95%[14]. The P-value must be below 0.05, this condition is not met only for the layer*speed variable, table 11. For the same variable, the F-value condition is not met, but the influence is insignificant and is therefore ignored. On the Pareto diagram[15], Fig. 3, it is also seen that the component AB is insignificant and the others are significant.

TABLE 3 ANALYSIS OF VARIANCE

Source	DF	Seq SS	Contribution	Adj SS	Seq MS	F-Value	P-Value
Regression	5	16.8052	99.33%	16.8052	3.36104	88.37	0.002
layer	1	3.9474	23.33%	8.7895	3.94741	103.79	0.002
Speed	1	1.1151	6.59%	0.9340	1.11514	29.32	0.012
layer*layer	1	9.8371	58.14%	8.0779	9.83708	258.64	0.001
layer*Speed	1	0.0148	0.09%	1.7799	0.01480	0.39	0.577
layer*layer*Speed	1	1.8908	11.18%	1.8908	1.89078	49.71	0.006
Error	3	0.1141	0.67%	0.1141	0.03803		
Total	8	16.9193	100.00%				
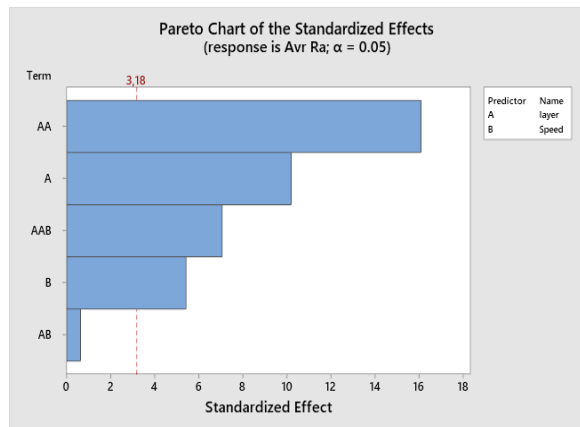
Fig. 3. Pareto chart

The value of the standardized residuals is in range of -2;+2, Fig. 4.
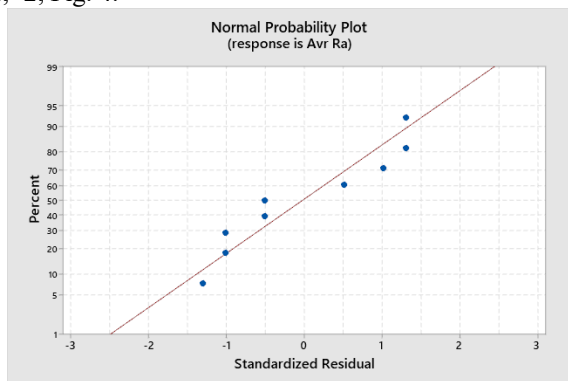
Fig. 4. Normal probability plot
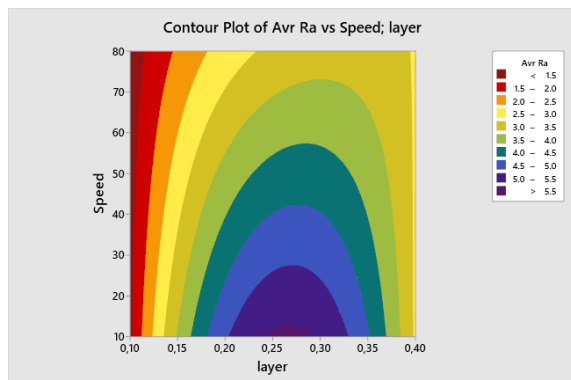
Fig. 5. Contour Plot
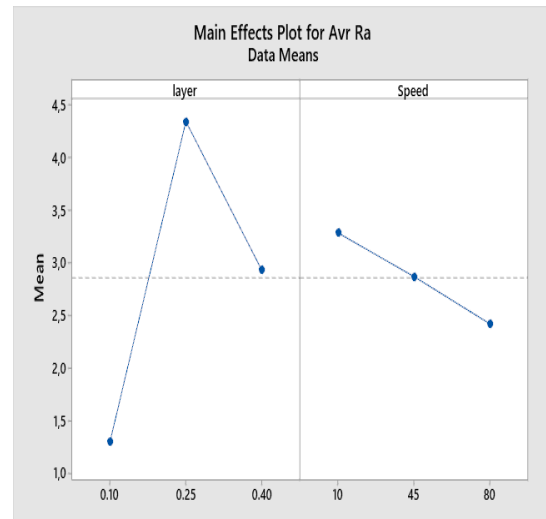
Fig. 6. Main effect

It was also analyzed how the influence of layer and speed on the roughness, fig. 5-6.

The obtained experimental results for hardness are presented in Table 4. The data from the table were processed and the following regression model was obtained:

$$Avr = -12.45 + 552.1\ layer + 0.0779\ Speed - 960\ layer*layer \quad (2)$$

TABLE 4 EXPERIMENTAL RESULTS HARDNESS SHORE D

Sample	Layer [mm]	Speed [m/min]	Probe position [Shore D]					Average Shore D
			1	2	3	4	5	
1	0.10	10	33.8	38.8	31.3	37.1	39.6	36.1
2	0.10	45	37.2	39.8	31.0	33.3	42.3	36.7
3	0.10	80	43.0	29.5	36.0	30.8	46.5	37.2
4	0.25	10	69.9	73.5	67.4	71.8	69.0	70.3
5	0.25	45	69.5	68.1	68.2	67.1	72.9	69.2
6	0.25	80	71.1	64.4	65.9	68.8	68.4	67.7
7	0.40	10	47.5	48.5	51.2	51.8	54.0	50.6
8	0.40	45	49.1	53.6	56.0	60.2	59.3	55.6
9	0.40	80	63.7	66.6	71.0	69.8	71.5	68.5

TABLE 5 MODEL SUMMARY

S	R-sq	R-sq(adj)	PRESS	R-sq(pred)	AICc	BIC
5.10171	92.80%	88.48%	508.577	71.86%	79.58	60.57

TABLE 6 ANALYSIS OF VARIANCE

Source	DF	Seq SS	Contribution	Adj SS	Seq MS	F-Value	P-Value
Regression	3	1677.28	92.80%	1677.28	559.09	21.48	0.003
layer	1	698.98	38.67%	1198.56	698.98	26.86	0.004
Speed	1	44.61	2.47%	44.61	44.61	1.71	0.247
layer*layer	1	933.70	51.66%	933.70	933.70	35.87	0.002
Error	5	130.14	7.20%	130.14	26.03		
Total	8	1807.42	100.00%				

Fig. 7. Versus Order
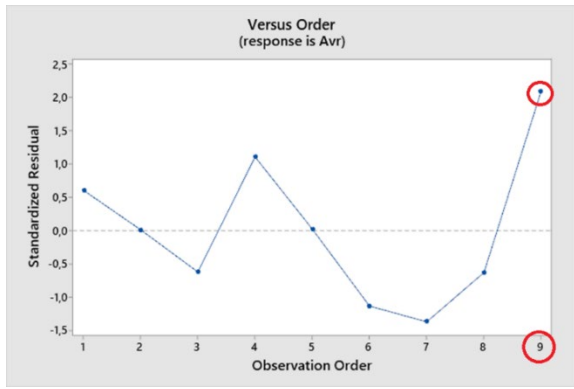
Fig. 9. Standartized residual

Fig. 7 clearly shows the presence of 1 error: - observation #9, the value of the standardized residual should be within the limits of -2;+2. This gives us reason to remove the observation and process the data again.

After reprocessing the results we get the following Regression Equation:

$$Avr = -12.01 + 591.2\ layer + 0.0061\ Speed - \quad (3)$$
$$1072.0\ layer*layer$$

TABLE 7 MODEL SUMMARY

S	R-sq	R-sq(adj)	PRESS	R-sq(pred)	AICc	BIC
2.02695	98.97%	98.19%	83.1653	94.77%	68.46	38.86

TABLE 8 ANALYSIS OF VARIANCE

Source	DF	Seq SS	Contribution	Adj SS	Seq MS	F-Value	P-Value
Regression	3	1574.94	98.97%	1574.94	524.98	127.78	0.000
layer	1	495.94	31.16%	1305.32	495.94	120.71	0.000
Speed	1	31.81	2.00%	0.20	31.81	7.74	0.050
layer*layer	1	1047.19	65.80%	1047.19	1047.19	254.88	0.000
Error	4	16.43	1.03%	16.43	4.11		
Total	7	1591.38	100.00%				

The coefficient of determination R-sq = 98.97% was calculated, and the adjusted coefficient of determination has the value R-sq(adj) = 98.19%, which satisfies the requirement of being above 95%. The P-value for all variables is below 0.05, table 8. The Pareto diagram, fig.8 also shows that the components are significant [16].

Fig. 8. Pareto chart

The value of the standardized residuals is in range of -2;+2 [17], Fig. 9-10.

Fig. 10. Histograma for hardness

It was also analyzed how the influence of layer and speed on the hardness, fig. 11-13

Fig. 11. Contour plot

Fig. 12. Main effect

260

Fig. 13. Time series plot

The relationship between the deviation from the size and the time for printing the part was established, fig.13. It can be seen that the smaller the size deviation, the longer the printing time.

IV. CONCLUSIONS

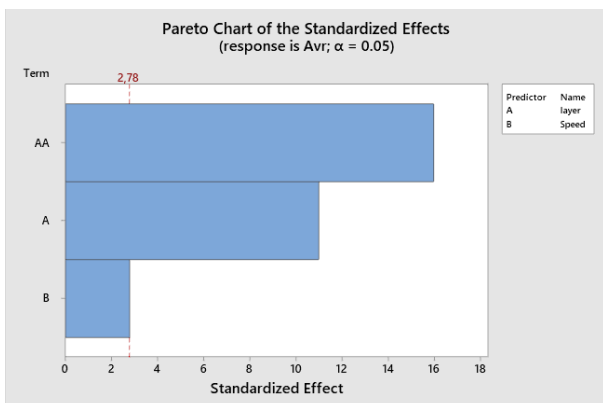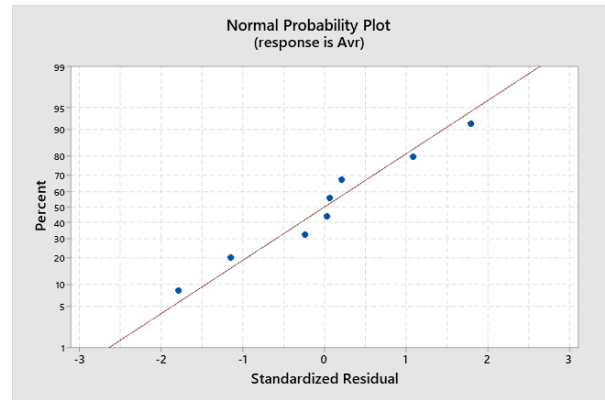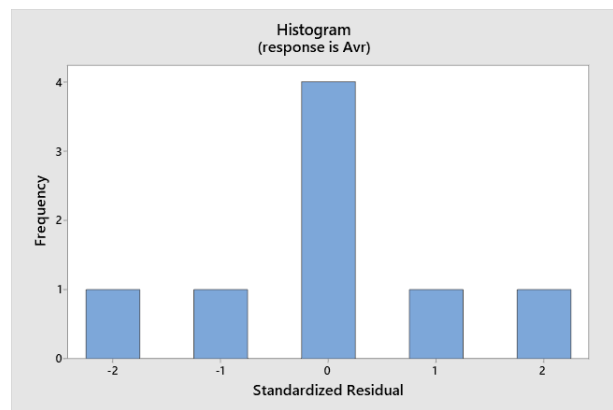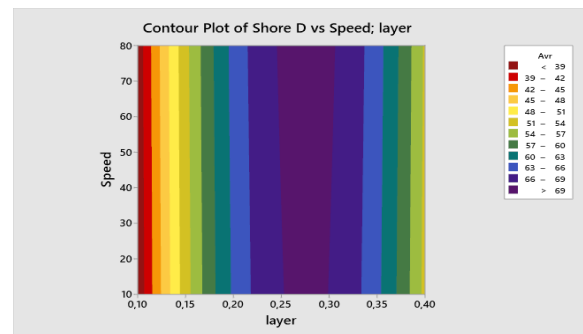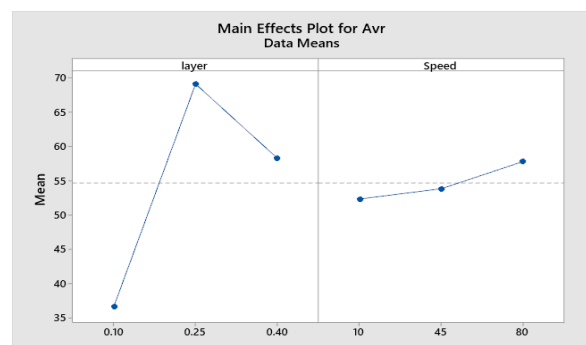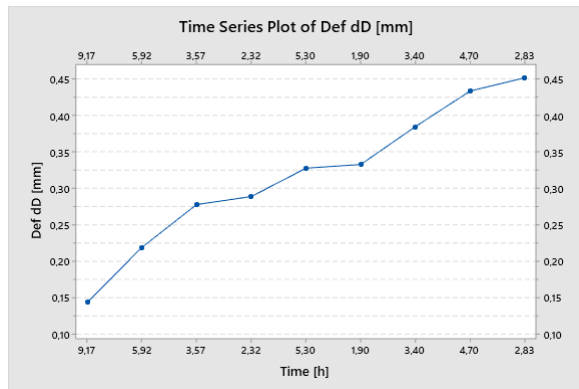For execution of the experiments is selected central composition plan to reduce the number of experiments. It allows optimal distribution of variables for correct statistical analyze. The studied polymer material ABS, one of the current polymers, is used for the production of technical details.

After literature review and according the abilities of the 3D printer are defined the important parameters of the process-printing speed from 10 m/min to 80 m/min, thickness of the layer from 1mm- 0,4 mm. The rest 3D printing parameters are constant. The statistical proceed was done, that shows 95% influence of thickness layer on roughness and hardness.

V. ACKNOWLEDGMENTS

REFERENCES

[1] Lupton D.,(2023)3D printing, The Blackwell Encyclopedia of Sociology,DOI: 10.1002/9781405165518.wbeos1072.pub2

[2] Liu K.,Hu N.,yu Z.,Zhang X.,Ma H.,Qu H.,Ruan H.,(2023), International Journal of Bioprinting,DOI: 10.36922/ijb.0969

[3] Son J., Lee H.(2020) Effect of Frictional Characteristics on Surface Roughness and Glossiness in Polishing of ABS-Like Resin, Journal of the Korean Society for Precision Engineering

[4] Daneshvar F. N. Talebbeydokhti N.,Dehghan S., Elhamian S.,{2023},,Evaluation of internal surface roughness in fiberglass pipes by surface roughness instruments,

[5] Hanon M.,Zsidai L.,(2023) Investigation on the accuracy, hardness, and surface roughness of photopolymerization 3D printing technique objects, 36th Conference of the Polymer Processing Society (PPS-36)At: Montreal, CanadaVolume: 2607

[6] Maturkar P.,(2023),DESIGN AND DEVELOPMENT OF 3D PRINTER, DOI: 10.55041/IJSREM18917

[7] Wang Z.,Zhou K.,bi C.,(2024),Exploring Flexural Performances of Fused Filament Fabrication 3D-Printed ABS and ABS-Composites through Innovative Bio-Inspired Processing Parameter Optimization, Applied Composite Materials,Applied Composite Materials,DOI: 10.1007/s10443-023-10191-z

[8] Ehrmann C.,Li N.,Ahmad M.,Yahua A.,(2023),Effects of 3D Printing Parameters on Mechanical Properties of ABS Samples, Designs 7(6):136,DOI: 10.3390/designs7060136

[9] Ahmed A.,Mugendiran V.,(2024),Effect of process parameters on mechanical properties of PLA resin through LCD 3D printing, Proceedings of the Institution of Mechanical Engineers Part E Journal of Process Mechanical Engineering,DOI: 10.1177/09544089231225147

[10] Yang Y.,Dai X.,Yang B.,Zou P.,Gao F.,Duan J.,Wang C.,Optimization of polylactic acid 3D printing parameters based on support vector regression and cuckoo search, Polymer Engineering and Science 63(1),DOI: 10.1002/pen.26440

[11] Tamura R.,Terayama K.,Sumita M.,Tsuda K.,[2023]Ranking Pareto optimal solutions based on projection free energy, Physical Review Materials

[12] Udalov A.,V.,Udalov A.,A.,{2023}Indentation size effect and hardness of materials. E3S Web of Conferences

[13] Kothadamaran L.,Balasubramanian N., (2023), Optimization of the Printing Parameters to Improve the Surface Roughness in Fused Deposition Modeling, E3S Web of Conferences 399

[14] Berggren N.,{2023},Coefficients of determination measured on the same scale as the outcome, DOI: 10.31234/osf.io/svuf8

[15] Saghir A.,Gadde S.,Aslam M.,Janjua A.,(20240,Pareto Distribution-Based Shewhart Control Chart for Early Detection of Process Mean Shifts, Journal of Statistical Theory and Applications

[16] Pacheko F.,(2023),Pareto vectors of continuous linear operators, Journal of Inequalities and Applications 2023(1)

DOI: 10.1186/s13660-023-03071-4

[17] Trijoulet V.,Albertsen C.,Kristensen K.,Legaut C.,Miller T.,Nielsen A.,(2023) Model validation for compositional data in stock assessment models: Calculating residuals with correct properties, Fisheries Research 257:106487,DOI: 10.1016/j.fishres.2022.106487

Optimizing 3D printing parameters to improve dimensional accuracy

Sabi Sabev
Technical University of Sofia,
Branch Plovdiv
Plovdiv, Bulgaria
sabi_sabev@tu-plovdiv.bg

Konstantin Chukalov
Technical University of Sofia,
Branch Plovdiv
Plovdiv, Bulgaria
chukalov@tu-plovdiv.bg

Valeri Bakardzhiev
Technical University of Sofia,
Branch Plovdiv
Plovdiv, Bulgaria
bakardzhiev@tu-plovdiv.bg

Agop Izmirliyan
Technical University of Sofia,
Branch Plovdiv
Plovdiv, Bulgaria
izmirliyan@tu-plovdiv.bg

Abstract. **The article examines the influence of 3D printing speed and layer thickness on the accuracy of functional dimensions of a part-eight wall prism with 5 holes-one in the centre and 4 in the periphery. For printing the samples, ABS material was used, which is one of the main materials for the production of machines and parts. A portal measuring machine with the highest accuracy was used to effectively perform the task of measuring deviations from the size of the sample. Due to the large volume of experimental results, they were averaged to minimize error and processed using statistical processing software. An accurate regression model was obtained and the printing parameters were optimized**

Keywords: 3D printing,dimension accuracy

I. INTRODUCTION

3D printing is increasingly used in many sectors - mechanical engineering, architecture, design, dentistry [1],[2]. 3D printing is used not only for prototyping, but also for mass production [3]. The materials that are used for this technology are very diverse, but mostly polymers are Acrylonitrile Butadiene Styrene (ABS), Polystyrene (HIPS) and Polylactic Acid (PLA) [4],[5]

The main technological characteristics of the process are the height of the layer and the printing speed, on which the quality of the 3d printed details mainly depends.3D printing is a developing scientific field[6]

Geometric deviations are defined as a deviation from the ideal geometry of the part. Size deviation is a deviation from the local size (the distance between two points on the surface)[7].Different systems are used to ensure accuracy[8].

The increasingly wide application of 3D printing leads to increased requirements for the characteristics of the details, as well as the analysis of technological operations.[9].

II. MATERIALS AND METHODS

The material used is the polymer Acrylonitrile butadiene styrene (ABS) chemical formula $(C8H8)x \cdot (C4H6)y \cdot (C3H3N)$[10]. The choice of material is determined by the wide use of this material in 3D printing. [11]. The material is pre-extruded into a layer (filament with a diameter of 1.75 mm). In the printing process, the polymer is extruded at a temperature of 235ºC. The selected part is eight wall prism with 5 holes. This shape is selected to satisfy the goals of the article.The 3D printer and the process in the Flashforge Creator model are shown in Figure 1.

The planning of the experiment has been done in previous articles and is according to the Taguchi method: Taguchi Array L9 (3^2); Factors: 2; Runs: 9

The limits (maximum and minimum value) of the factors affecting the quality and accuracy of printing are determined a priori.[12] Factors investigated for impact on accuracy are print speed and layer height[13] The 3D printer parameters that are constant for all trials, ie. are constant: nozzle diameter 0.4mm; flow 100%; retreat 1mm; bed temperature 110°C.

- Checking dimension devastations according the 3D model
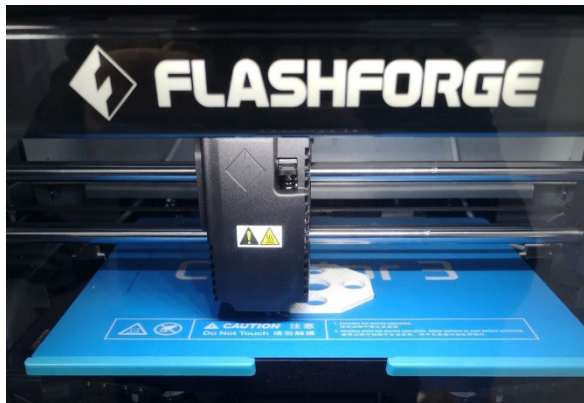
Fig. 1. Flashforge Creator 3

The measurement was carried out on a three-coordinate measuring machine EROWA CMM QI, which is designed for the control of finished parts. The machine is placed in a temperature controlled environment of 20°C ±1°. It is equipped with a contact sensor TP20 and a ruby sphere D=6mm. (fig. 2). The technical parameters are:

$$r = 0.0001 \tag{1}$$

$$T = 1.5\mu m + L/500 \tag{2}$$

(where: r – resolutions; T-tolerance field of the measurement; L-length of the measured dimension in mm)

Fig. 2. TP20 sensor with D6 probe.

- Software

The software used to check deviations from the 3D model is ARCO CAD. The IGS format is used to extract the geometric data of the specimen. A control program was developed to touch each sample at the same point relative to the set base, with the same speed of movement of the sensor. This prevents the possibility of accumulating additional measurement errors. (fig.3)
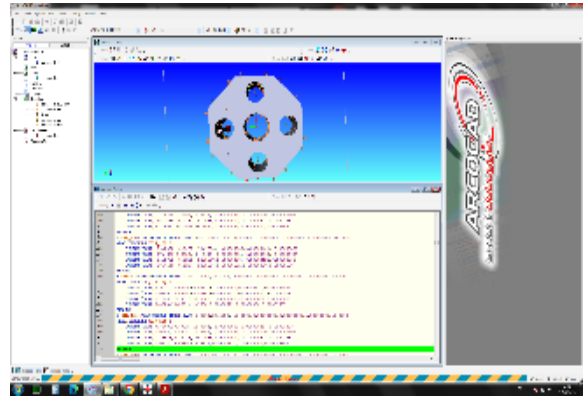
Fig. 3. Arco CAD software overview

- Fastening

The specimen is fixed on the outer two walls and its front surface in a precision self-centering vise (fig4). The central opening O0 a for the Z coordinate – the front surface P – is chosen as a base for the X and Y coordinates.
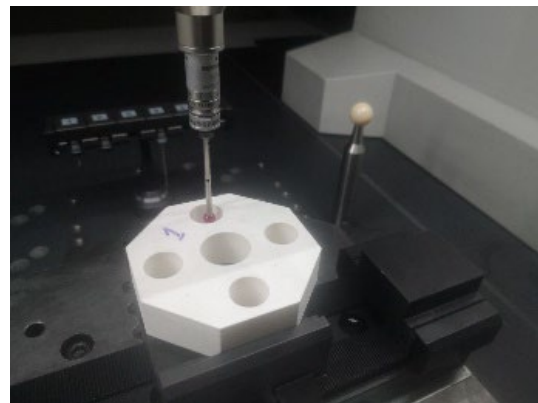
Fig. 4. Fixture set up on measuring machine.

For the purpose of the experiment, 4 measurements were made on each hole of each specimen[14] The circumference measurement was done with a 4 contact point circumference measuring cycle. The first 2 measurements are at a depth of Z=-5mm and the second 2 at Z=-15mm. The difference between measurement 1 and 2, as well as 3 and 4 is the starting angle of measurement (α=45°). Fig(5.a) In this way, we have also extracted information about the average deviation from the shape of the corresponding hole. In addition to diameter and shape deviation, we have also measured the average deviation of the interaxial distance of each hole relative to the central hole, which serves as the base and origin of our coordinate system. (table 1)

- Checking of external faces

The external shape of the experimental sample is octahedral composed of 8 planes respectively. In fact, the planes from which the geometric body is created after printing deviate in shape and location from those in the specified computer model [15].[16]. Through an option to match a given point from the imported 3D model in the Arco cad software and the actually touched point from the sensor, the average deviation of 4 points for each wall of the octagon was measured, each of them being at the maximum distance from each other. (Fig.5 .b)

In this way, the error of the positioning of the wall itself relative to the mathematical model and also the differences in the shape of the real surface of the specimen are combined[17]. The results of the measured points are averaged for each wall of the octagon of each specimen. (Table 2)

- Measurement of the front surface

3 points from the front surface of each specimen were measured. The base surface is the face of the first sample (fig. 5.c) (Table 3)

Fig. 5. (a) 16 measuring points for each cylinder
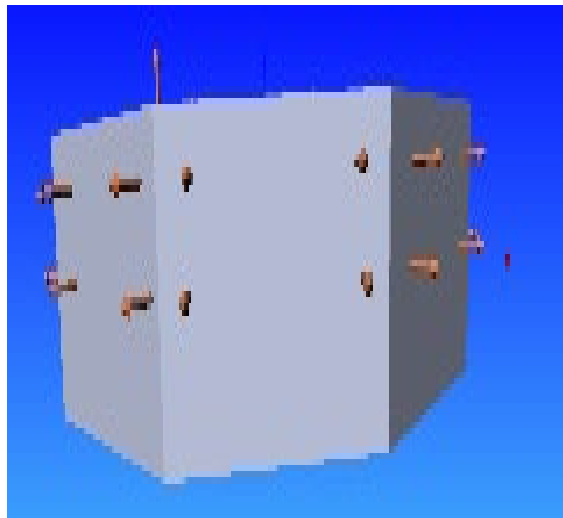
Fig.5 (b) 4 points on each side of the octagon
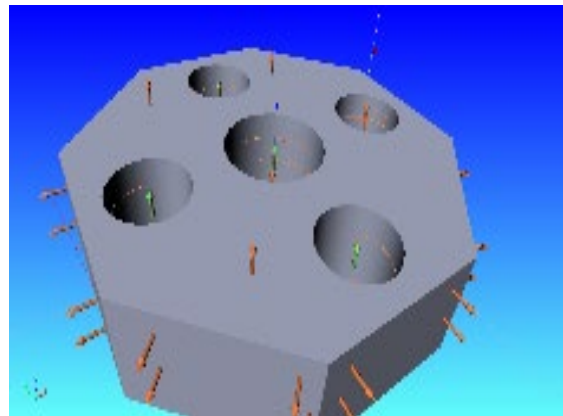
Fig.5 (c) 3 points taken from the face surface

III. RESULTS AND DISCUSSION

Table 1. Diameters of the measured holes and the coordinates of their interaxial distances.

TABLE 1 DIAMETERS OF THE MEASURED HOLES AND THE COORDINATES OF THEIR INTERAXIAL DISTANCES.

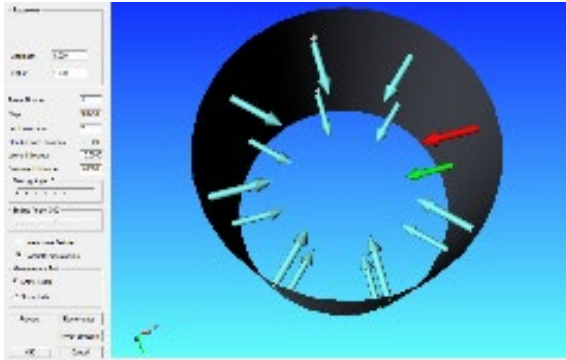|		Sample 1	Sample 2	Sample 3	Sample 4	Sample 5	Sample 6	Sample 7	Sample 8	Sample 9
D1	D	21,82	21,75	21,64	21,64	21,61	21,57	21,67	21,67	21,65
D2	D	15,83	15,76	15,65	15,65	15,66	15,55	15,76	15,74	15,67
	X	27,07	27,22	27,34	27,30	27,29	27,36	27,22	27,35	27,28
	Y	-0,03	0,07	-0,04	-0,03	0,04	-0,07	0,08	-0,09	-0,14
D3	D	15,89	15,82	15,68	15,69	15,59	15,53	15,72	15,70	15,67
	X	-27,18	-27,28	27,26	-27,31	-27,27	-27,24	-27,16	-27,09	27,22
	Y	-0,08	-0,08	-0,07	0,05	-0,09	-0,07	-0,07	-0,23	-0,11
D4	D	15,87	15,78	15,71	15,71	15,61	15,52	15,87	15,71	15,64
	X	-0,03	-0,05	0,05	-0,01	0,01	0,04	-0,02	0,12	0,03
	Y	27,50	27,46	27,43	27,41	27,39	27,28	27,53	27,33	27,32
D5	D	15,87	15,80	15,68	15,68	15,61	15,57	15,73	15,73	15,71
	X	-0,06	-0,01	0,02	0,01	0,02	0,07	0,03	0,15	0,03
	Y	-27,61	-27,48	-27,34	-27,37	-27,45	-27,45	-27,49	-27,62	-27,55

TABLE 2. AVERAGE DEVIATION OF WALLS FROM 3D MODEL

Sample	SIDE							
	1	2	3	4	5	6	7	8
1	-0,33	-0,08	-0,08	-0,17	-0,38	-0,15	-0,05	-0,17
2	-0,34	-0,17	-0,04	-0,16	-0,24	-0,09	-0,06	-0,20
3	-0,19	-0,23	-0,15	-0,03	-0,08	-0,10	-0,12	-0,14
4	-0,14	-0,14	-0,08	-0,03	-0,10	-0,18	-0,18	-0,14
5	-0,17	0,11	0,19	-0,01	-0,26	-0,31	-0,31	-0,32
6	-0,16	-0,16	-0,20	-0,14	-0,16	-0,16	-0,08	-0,08
7	-0,30	-0,07	-0,01	-0,21	-0,37	-0,14	0,02	-0,14
8	-0,32	-0,06	0,07	-0,09	-0,28	-0,21	-0,17	-0,30
9	-0,19	-0,21	-0,21	-0,24	-0,28	-0,17	-0,01	-0,02

TABLE 3. AVERAGE DEVIATION OF FOREHEAD FROM 3D MODEL

Sample	1	2	3	4	5	6	7	8	9
Result	0,04	-0,10	-0,37	-0,21	-0,29	-0,28	-0,27	-0,23	-0,39

TABLE 4 EXPERIMENTAL RESULTS FOR DEVIATION OF THE SIZE

№	Layer	Speed	Def dD
1	0,1	10	0,14
2	0,1	45	0,22
3	0,1	80	0,43
4	0,25	10	0,33
5	0,25	45	0,38
6	0,25	80	0,45
7	0,4	10	0,28
8	0,4	45	0,29
9	0,4	80	0,33

The obtained experimental results for the size deviation are presented in Table. 1-4. Table 4 presents the arithmetic mean deviation of the size.

Mathematical-statistical processing was performed with MINITAB 19 software. For the mathematical description of the objective function, a reduced model of the second incomplete degree was used.

The data from Table 4 were processed and the following regression model was obtained [15]:

$$Def\ dD\ =\ -0.034\ +\ 2.457\ layer\ +\ 0.002231\ Speed\ -\ 4.68\ layer * layer \quad (3)$$

The coefficient of determination R-sq = 77.10% was calculated, and the adjusted coefficient of determination has the value R-sq(adj) = 63.36%, which is too low.

TABLE 5 MODEL SUMMARY

S	R-sq	R-sq(adj)	PRESS	R-sq (pred)	AICc	BIC
0.060	77.10%	63.36%	0.068	13.47%	-0.39	19.41

TABLE 6 ANALYSIS OF VARIANCE

Source	DF	Seq SS	Contri bution	Adj SS	Seq MS	F-Value	P-Value
Regre ssion	3	0.061	77.10%	0.061	0.020	5.61	0.047
layer	1	0.001	2.27%	0.023	0.001	0.50	0.513
Speed	1	0.036	46.55%	0.036	0.036	10.16	0.024
layer* layer	1	0.022	28.28%	0.022	0.022	6.17	0.056
Error	5	0.017	22.90%	0.017	0.003		
Total	8	0.078	100.00%				

The Pareto chart, Fig.6 shows the absolute values of the standardized effects from largest to smallest effect.[16] The chart also draws a reference line to show which effects are statistically significant.[17] It can be seen that component B has crossed the significance line, therefore only this coefficient is insignificant and the rest are insignificant.
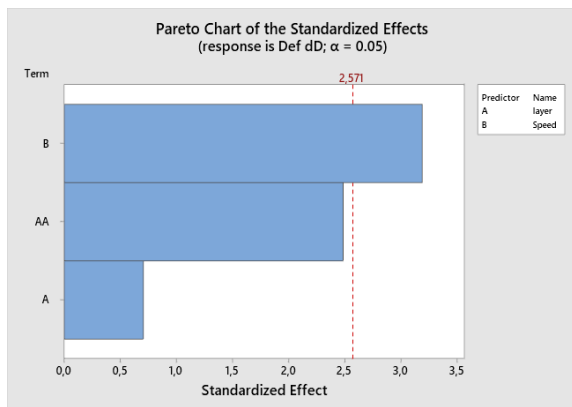
Fig. 6. Pareto Chart
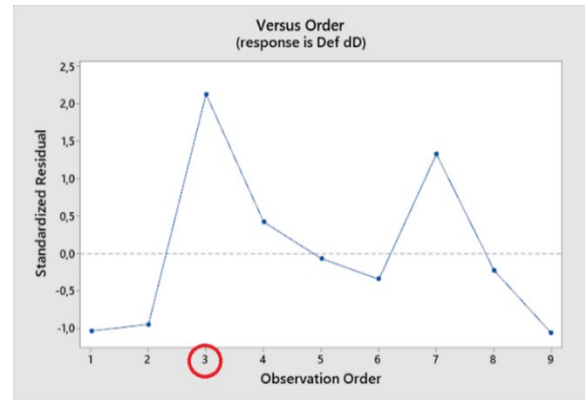
Fig. 7. Versus order residual

Fig. 7 clearly shows the presence of 1 error: - observation No. 3, the value of the standardized residual should be within the limits of -2;+2. This gives us reason to remove the observation and process the data again.

After reprocessing the results we get the following Regression Equation:

$$Def\ dD\ =\ -0.1290\ +\ 3.324\ layer\ +\ 0.001374\ Speed\ -\ 6.017\ layer * layer \quad (4)$$

The coefficient of determination R-sq = 97.16% was calculated, and the adjusted coefficient of determination has the value R-sq(adj) = 95.03%, which satisfies the requirement of being above 95%. The P-value must be below 0.05, this condition is also met.

Suppose we want to know if this F statistic is significant at level alpha = 0.05. Using the F-distribution table for alpha = 0.05, with numerator of degrees of freedom 3 (Regression) and denominator degrees of freedom 4 (Error), we find that the F critical value is 6.5914. [18]. From the analysis of the variables in table 10, it can be seen that all the F-values are several times above the critical value.

TABLE 7 MODEL SUMMARY

S	R-sq	R-sq(adj)	PRESS	R-sq(pred)	AICc	BIC
0.021	97.16%	95.03%	0.009	86.20%	-4.47	-34.08

TABLE 8 ANALYSIS OF VARIANCE

Source	DF	Seq SS	Contri bution	Adj SS	Seq MS	F-Value	P-Value
Regre ssion	3	0.061	97.16%	0.062	0.021	45.6	0.001
layer	1	0.011	17.62%	0.037	0.011	24.8	0.008
Speed	1	0.017	27.60%	0.010	0.017	38.8	0.003
layer* layer	1	0.033	51.95%	0.033	0.033	73.1	0.001
Error	4	0.002	2.84%	0.002	0.001		
Total	7	0.063	100.00 %				
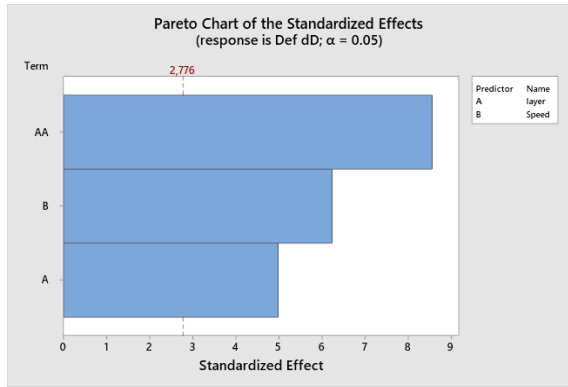
Fig. 8. Pareto Chart

The Pareto diagram, Fig. 8 shows that the components have crossed the significance line, therefore all the coefficients are significant.
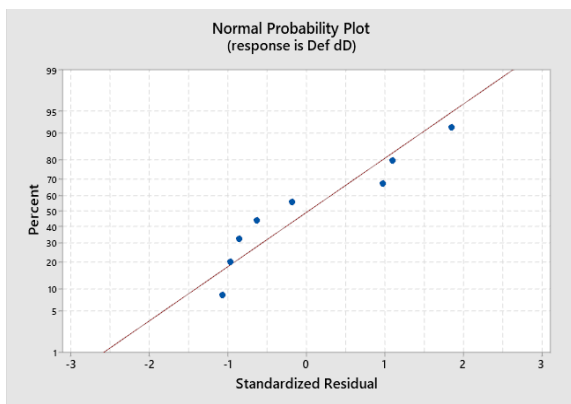
Fig. 9. Normal probability plot

The analysis of standardized residuals Fig. 9 - 10, shows that there are no gross errors. This necessitates the conclusion that the coefficients are significant.
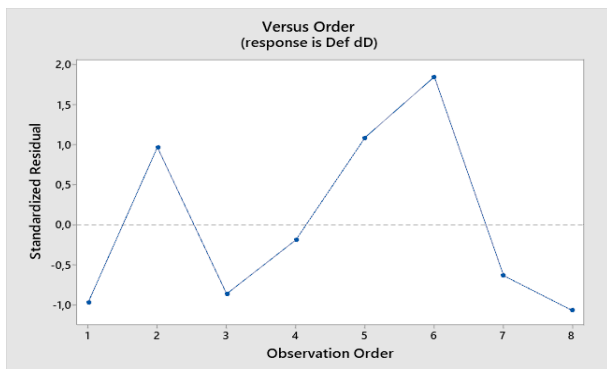
Fig. 10. Versus Order
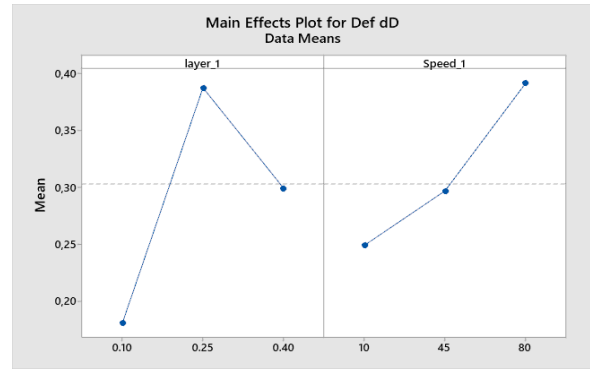
Fig. 11. Main effect

It was also analyzed how the influence of layer and speed on the size deviation, fig. 11-12
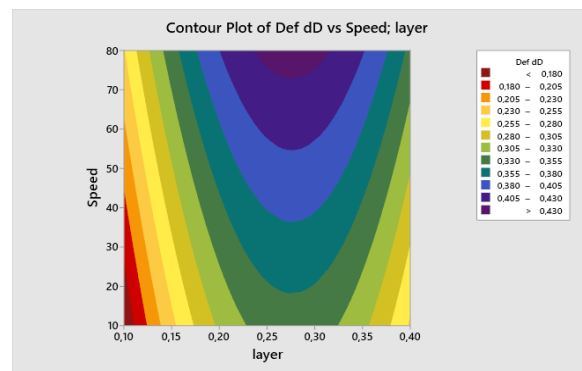
Fig. 12. Contur plot

The interactive table, Fig.13 shows the effect of layer and print speed on the printing time.

A one-parameter optimization was made, with the optimization criteria being the printing time of 4 hours and the size deviation being equal to 0.25mm. The obtained results are presented in Fig. 14 with a deviation of 0.25 mm, i.e. tolerance field ±0.125mm, layer thickness 0.35mm, the time for printing the part is 4 hours. The following regression model was used in this optimization:

$$Time[h] = 11.26 - 12.39 \, Def \, dD[mm] - 11.91 \, layer \qquad (5)$$
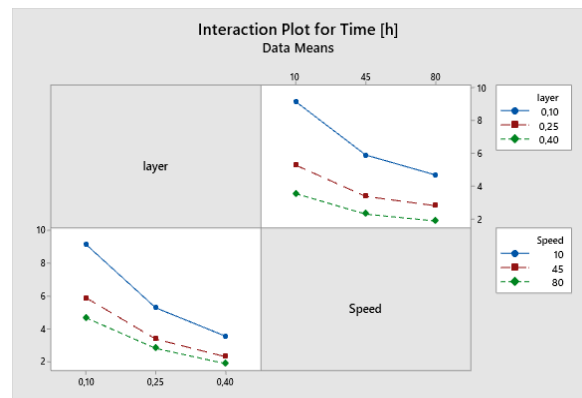
Fig. 13. Intereactive plot
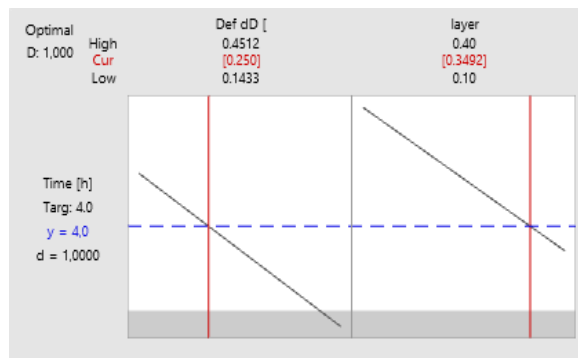
Fig. 14. Optimization plot

IV. Conclusions

The research is executed on base of statistical process according Taguchi method - 9 samples are manufactured for this goal. The printing modes are selected according to the importance of technology. The following conclusions are drawn from the statistical processing:

1. The greatest influence of layer height is observed on dimension deviation

2. The printing speed has a minor influence on the dimension deviation

3. The study can be used as a basis for another discrete area of the studied parameters.

4. All regression models are notable and well describe the relationship between printing speed and layer height.

The studied polymer material ABS, one of the current polymers, is used for the production of technical details.

V. Acknowledgments

VI. REFERENCES

[1] S. Choi,Y. Bae ,I. Lee,H. Kim, Latest Research Trends of 3D Printing in Korea, Journal of the Korean Society for Precision Engineering - Vol. 35, No. 9, pp. 829-834,2018 https://doi.org/10.7736/KSPE.2018.35.9.829

[2] M. Jeoung,M. Ramodski ,D. Lopez ,J. Liu,J. Lee ,S. Lee ,Materials and Applications of 3D Printing Technology in Dentistry: An Overview, Dentistry Journal 12(1):1, Dentistry Journal 12(1):1,2023 https://doi.org/10.3390/dj12010001

[3] S. Ragan, Plastics for 3D Printing. MAKE,2013

[4] Ultimate Guide To3D Printing, Winter,;pp. 22; http://makezine.com/2012/11/13/plastics-for-3d-rinting/.2013

[5] M. Subramaniyan ,S. Karuppan ,Mechanical properties of sandwich products obtained by 3D printing from PLA-PLA/Al2O3,Polimery 68 (11-12):646-651,, https://doi.org/10.14314/polimery.2023.11.9, 2023

[6] D. Rathia , International Journal of Innovative Science and Research Technology Volume 8 - 2023,(Issue 7 - July) https://doi.org/10.5281/zenodo.8216770,2023

[7] S. Eom ;J. Park;J. Jin,J. Son, Feasibility Study on Dimensional Standard for Material Extrusion Type 3D Printed Structures, Journal of the Korean Society for Precision Engineering - Vol.37, No. 4, pp. 241-246, 2020 https://doi.org/10.7736/JKSPE.019.118

[8] V. Georgiev,S.Salapateva ,I.Chetrokov ,S.Lilov,,Systems for ensuring the accuracy of the dimensions of details in mechanical engineering on CNC machines. International Conference "Automation and Informatics'08",Collection of reports, Sofia, 2008, pp. V-15 – V-18, 2008

[9] A. Mahmood,T. Akram,H. Chen,S. Chen , On the Evolution of Additive Manufacturing (3D/4D Printing) Technologies: Materials, Applications, and Challenges, Polymers 14(21):4698,2020 https://doi.org/10.3390/polym14214698

[10] E. N. Peters., "Plastics: Thermoplastics, Thermosets, and Elastomers", Handbook of Materials Selection, New York: John Wiley & Sons, Inc., pp. 363–365, 2007

[11] F. Ballarin,A. Lola,A. Irawan,N. Kikuchi ,B. Chouangthavy Find your way out of the ABS maze: three cases of successful Access and Benefit Sharing compliance, 2023

[12] Y. Mayorava,V. SikulskiyIurii,V. Vorobiov,A. Knyr ,Study of a Geometry Accuracy of the Bracket-Type Parts Using Reverse Engineering and Additive Manufacturing Technologies,2023 https://doi.org/10.3390/app132212200

[13] P. Barve ,A. Bahrami,S. Shah ,Geopolymer 3D printing: a comprehensive review on rheological and structural performance assessment, printing process parameters, and microstructure, Frontiers in Materials 10:1241869 https://doi.org/10.3389/fmats.2023.1241869, 2023

[14] D. Popescu,C. Amza,R. Marinescu ,M. Iacob,N.Carotasu ,,Investigations on Factors Affecting 3D-Printed Holes Dimensional Accuracy and Repeatability, Applied Sciences 13(1):41,2023 https://doi.org/10.3390/app13010041

[15] S. Satin ,G. Goodacre ,R. Masri ,Comparing the accuracy of occlusal vertical dimension transfer in CAD-CAM dentures Journal of Prosthodontics, 2023 https://doi.org/10.1111/jopr.13669

[16] A. Wang ,C. Ruiz ,S.Park ,K. Shin.,J.Kim ,Q.Huang ASME 2022 17th International Manufacturing Science and Engineering Conference, 2023 https://doi.org/10.1115/MSEC2022-FM1

[17] T. Morita,S. Watanabe ,S. Sasake, Multiaxis printing method for bent tubular structured gels in support bath for achieving high dimension and shape accuracy, Precision Engineering 79, 2022 https://doi.org/10.1016/j.precisioneng.2022.09.004

[18] H..Ishikawa,.Regression, Hypothesis Generation and Interpretation, 2024 https://doi.org/10.1007/978-3-031-43540-9_4

Designing a laboratory stand for testing impact resistance of plastic films by free-falling dart drop according ASTM D1709

Sabi Sabev
Technical University of Sofia,
Branch Plovdiv
Plovdiv, Bulgaria
sabi_sabev@tu-plovdiv.bg

Konstantin Chukalov
Technical University of Sofia,
Branch Plovdiv
Plovdiv, Bulgaria
chukalov@tu-plovdiv.bg

Valeri Bakardzhiev
Technical University of Sofia,
Branch Plovdiv
Plovdiv, Bulgaria
bakardzhiev@tu-plovdiv.bg

Abstract. **In this article, the process of designing a laboratory stand for testing impact resistance of plastic films using free-falling dart drop method according to ASTM D1709, type A will be followed. It will be analyzed the all stages of designing-synthesis of project solutions, analysis and optimization, assessment and presentation of tasks. The purpose of the article is to create a designing basis for the variable design of impact resistance stands to be used in the design of non-standardized laboratory equipment.**

Keywords: dart drop impact test, plastc films, CAD/CAE, ASTM 1709, properties of plastics

I. INTRODUCTION

Impact resistance refers to dynamic mechanical tests and is characterized by the destruction of test specimens with a high speed of loading (impact)[1]. When testing impact resistance internal defects, position of the part in relation to the load, notches, etc [2]., are important. Impact resistance is a complex characteristic because it includes plastic and strength characteristics [3].For now, there is no known relationship between impact toughness and other mechanical parameters. An analogy of the results with different shapes and materials is not possible.

The wide application of a variety of polymers in modern engineering requires study of their main mechanical characteristics - hardness, strength and plastic characteristics, impact resistance [4]. Impact resistance of polymers and composites are mainly done by dart drop methods [5],[6].[7].

Due to the specificity of the dart drop impact test - the impossibility of using results for parts of other sizes, shapes and materials, the use of non-standard laboratory equipment is required in practice for the study of impact resistance. For the purpose of the article, the design of a stand according to the ASTM 1709 standard was chosen, but the stages of design-synthesis of design solutions, analysis and optimization, and evaluation may be easily adapted to other needs and specifications.

II. MATERIALS AND METHODS

In the test standard ASTM D1709, the materials for the incremental weights are defined - brass or stainless steel and aluminum alloy for the hemispherical head of the dart drop.

For the purposes of the article, the following materials were chosen – a constructive steel for pressing discs, for the hemispherical head of the dart drop-aluminum alloy 6082, for the details of the stand and the adjacent equipment stainless steel AISI 304.

Aluminum alloy 6082 is distinguished by excellent anti-corrosion properties and good machinability [8]. The choice of stainless steel 304 is due to the high strength, durability, corrosion resistance and good workability by cutting[9]. Its good physical and mechanical properties make it a preferred material for industrial equipment and for specific laboratory stands.

The design includes 5 main stages, fig. 1, which will be discussed.
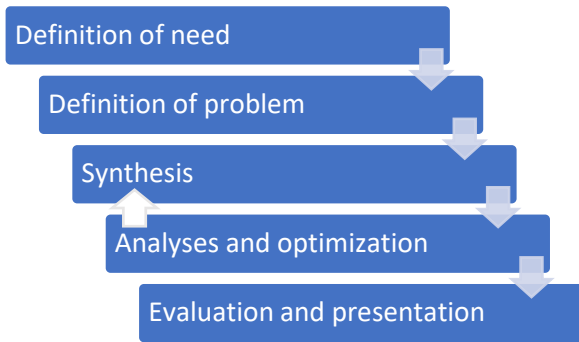
Fig. 1. Stages of designing

Determination the needs - on the one hand, only standardized dart drop stands are available on the market, which greatly limits testing possibilities because of huge variety of materials and shapes.

On the other hand, dart drop tests have established itselves as an important part of the technical specifications of plastic films. This necessitates the use of non-standardized equipment or modular test machines.

Statement of the task includes a detailed description of the product to be designed. The goal is modular design of a laboratory stand according to ASTM D1709 and creation of a designing basis for variable design of non-standard dart drop equipment.

Synthesis of design solutions, design generally may be divided into design of the mechanical part, electrical part, pneumatic part. The schematic diagram of the laboratory bench is shown in Fig. 2, according to the ASTM D1709 standard.
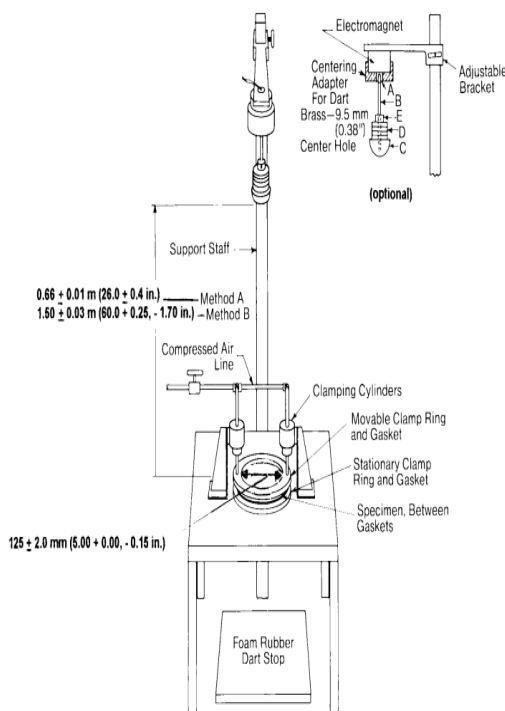
Fig. 2. Principle scheme of the stand, according the standard[10]

The dimensional analysis is integrated into the CAD environment, used in designing process [11]. The mechanical part can be divided into the following subsystems (modules):

- Housing
- Clamping mechanism for workpiece
- Dart dropgrip stand
- Dart drop

The housing of the impact resistance stand is the basic element and serves to establish the pneumatic and electrical subsystems of the assembled unit[12]. The standard does not define specific requirements for the housing of the stand. From a structural point of view, the body of the stand is of a prismatic type. A 3D model of the housing with adjacent holes for pneumatic and electrical components is shown in Fig.3
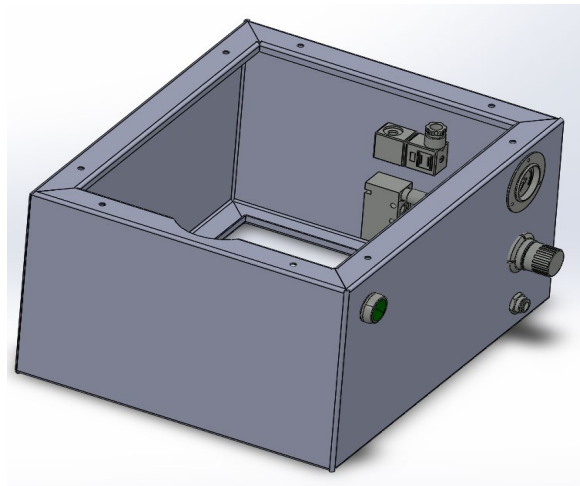
Fig. 3. 3D model of the housing

The clamping mechanism is the most important element of the stand and it should meet the following requirements[13],[14]:

- Clamps should have an internal diameter of 125 ±2 mm
- The lower clamp should be stationary
- The upper clamp should provide sufficient force to prevent slippage of the specimen, but also not to damage the specimen

A 3D model of the clamping mechanism is shown in fig. 4. The mechanism is pneumatically powered.

The dart drop grip stand has a height according to ASTM D1709 type A - 0.66 m ±0.01 m. It is designed to be disassembled so that another stand may be used at a later stage for another type of dart drop or similar impact test with a different height. The stand of the mechanism has the possibility of adjusting the position vertically and horizontally so that the impact is perpendicular to the sample and exactly in the centre of part,fig. 5.
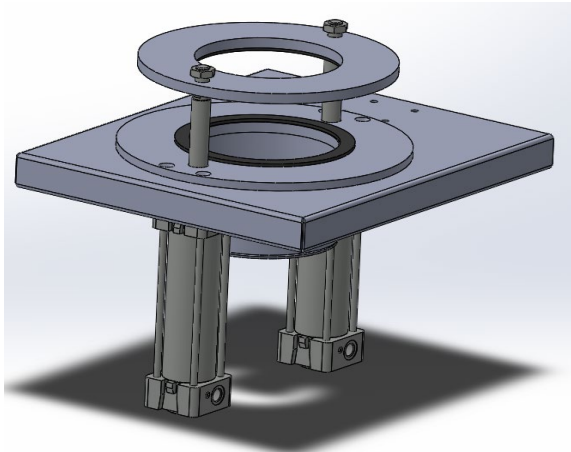
Fig. 4. Clamping mechanism
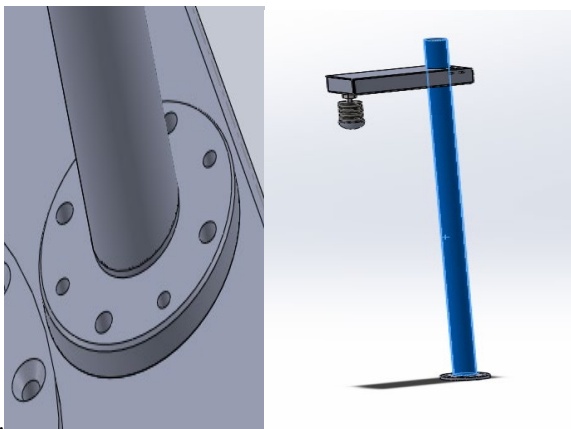
Fig. 5. 3D model of the dart drop stand

The shaft of the dart drop is designed with sufficient height to allow for tests with weights up to 2 kg. The 3D model is shown in Fig. 6. The dart drop has a hemispherical head with a radius of 38 mm ±1 mm. The control is equipped with a timer with a time delay at start, which adjusts the time between pressing and releasing the dart drop.

Pneumatic subsystem:

The maximum force of the pneumatic cylinder was calculated. It depends on the pressure inside the cylinder, the diameter of the piston, the frictional force generated by the components[15].

The basic formula for calculating the power of an air cylinder is:

$$Ft = P \times Au = P \times \left(\frac{\pi}{4}\right) \times D^2 =$$

$$= 600000 \times 0{,}00125 = 754 \, N \, .$$

where

Ft - Theoretical force [N] . It is theoretical, since the force of friction is neglected;

P - the pressure inside the cylinder [Pa]

Fig. 6.   Au – Area of useful area in contact with air [m^2].

The stand is equipped with a manometer and a pressure regulator, with the help of which the pressing force is determined within the limits - 10 ÷ 754 N[16].
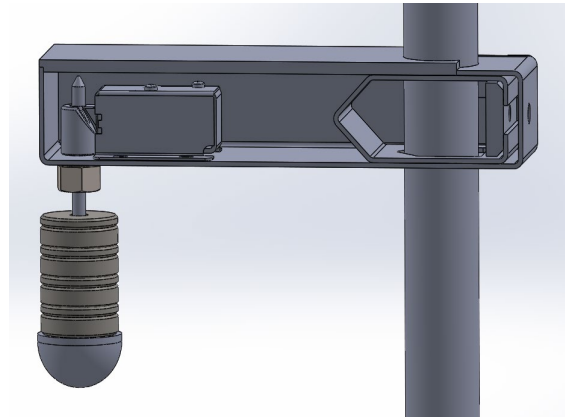
Fig. 7. Dart drop mechanism

The principle diagram of a trunk part is shown in Fig. 7:
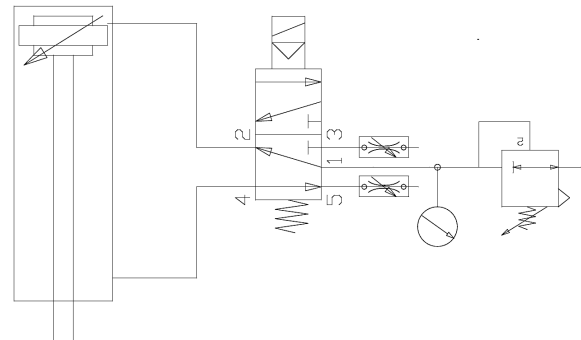
Fig. 8. Principle scheme of the pneumatic subsystem

Electrical subsystem:

The electrical part of the system is shown in fig. 8. It consists of power supply unit, fuses, buttons, timer, electro-pleumatic valve and electromagnet[17].
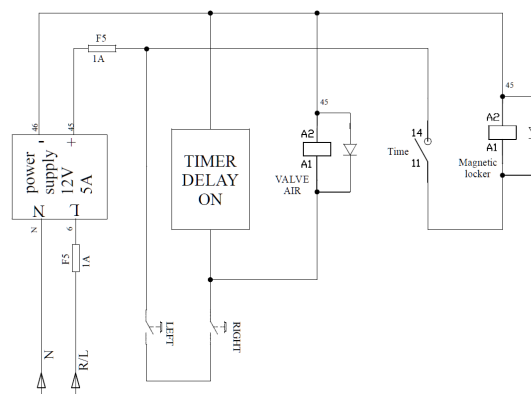
Fig. 9. Electrical scheme

The device is equipped with 2 buttons to start the test process. They are located at a sufficiently large distance from each other, as shown in Fig. 9 - position 47. This ensures the use of both hands of the operator and minimizes the possibility of injury. The entire operating

<##>

installation, such as distributors, electromagnet and buttons, is performed on 12v..
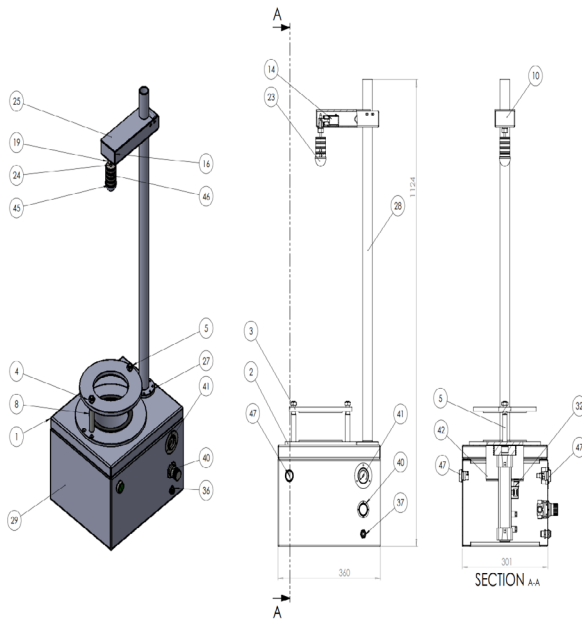
Fig. 10. Scheme of the stand

In fig. 10 shows the finished stand. Various materials were tested and the system worked effectively.

Fig. 11. The manufactured stand

III. RESULTS AND DISCUSSION

Analyze and optimization

The dynamic analysis for behavior of the impact when testing a polyethylene sample was carried out using the CAE product ANSYS 19, Explicit dynamic module according to the following methodology [18],[19],[20]:

➢ Preparation of the 3D geometric model for testing and its import into ANSYS;

➢ Defining the material constants of the studied components;

➢ Generation of the discredited computational model based on the finite element method;

➢ Setting force load on the model;

➢ Introduction of boundary conditions;

➢ Selecting the parameters from the numerical results and defining the time of the experiment;

➢ Obtained results - graphically and tabularly. Table 1 shows data about impact testing. The standard height from which the wedge is released is 660mm. The specimen is made of polyethylene with a thickness of 100 μm pressed into the hoop as shown in fig. 12 The test temperature is not set to 22. °C.

TABLE 1 DESCRIPTION OF THE IMPACT

Object Name	*Pre-Stress (None)*	*Drop Height*
State		Fully Defined
Definition		
Pre-Stress Environment		None Available
Pressure Initialization	From Deformed State	
Input Type		Drop Height
Define By		Drop Height
Drop Height		660, mm
Impact Velocity		3597,9 mm/s
Coordinate System		Global Coordinate System
Direction		-Z Direction
Suppressed		No

In fig..11-13 are presented the data, generated by the program.
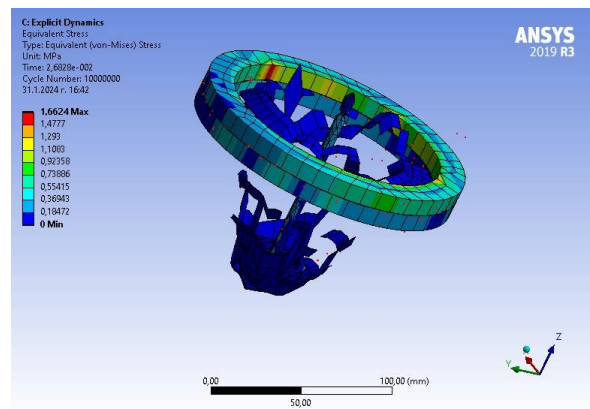
Fig. 12. Equivalent stress – von – Mises
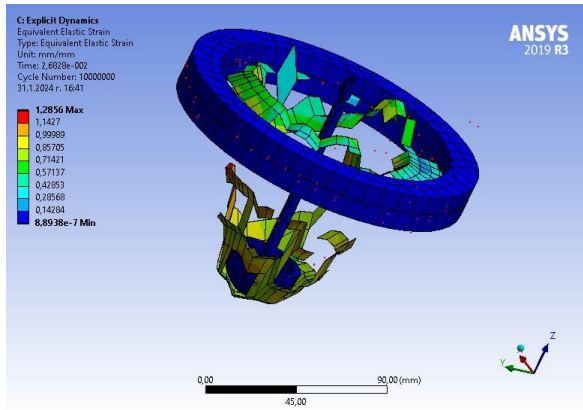
Fig. 13. Equivalent elastic strain

The purpose of the applied engineering analysis is to carry out a simulation of the impact test in order to select a combination between the thickness of the sample and the weight of the dart drop, for a selected material, which leads to a successful destructive testing. By using this CAE tool, a discrete test area is found more quickly and the total number of tests is reduced - resulting in material savings and faster results.
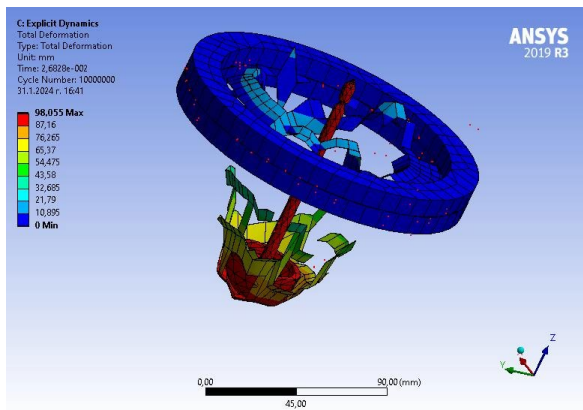
Fig. 14. Total deformation

In fig. 14 -15 the graphs of Equivalent Stress and Energy Probe are presented. The results obtained for Energy Probe are tabulated.
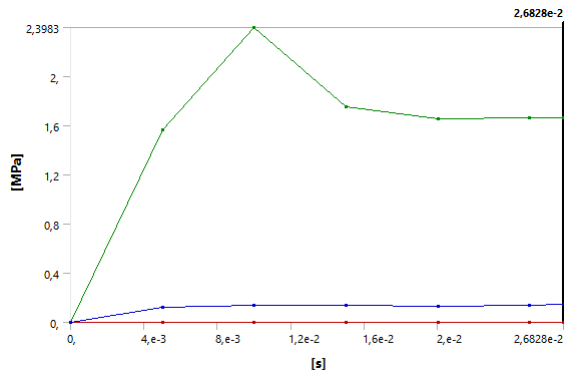
Fig. 15. Equivalent Stress
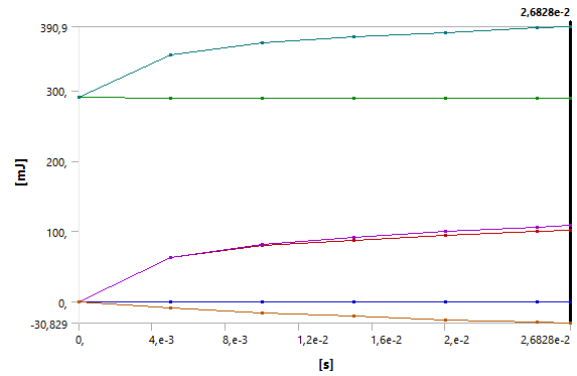
Fig. 16. Energy Probe

TABLE 2 ENERGY PROBE

Time [s]	Energy Probe (Internal) [mJ]	Energy Probe (Kinetic) [mJ]	Energy Probe (Plastic Work) [mJ]	Energy Probe (Hourglass) [mJ]	Energy Probe (Contact) [mJ]	Energy Probe (Total) [mJ]
1,18E-38	0	291,08		0	0	291,08
5,00E-03	61,762	289,38		63,102	-8,8894	351,14
1,00E-02	79,222	289,2		81,198	-16,444	368,43
1,50E-02	86,804	289,19	0	91,746	-20,948	375,99
2,00E-02	93,27	289,18		99,105	-25,919	382,45
2,50E-02	99,563	289,19		105,64	-29,764	388,75
2,68E-02	101,72			108	-30,829	390,9

TABLE 3 LOADS

Object Name	*Fixed Support*	*Force*
State	Fully Defined	
Scope		
Scoping Method	Geometry Selection	
Geometry	3 Faces	1 Face
Definition		
Type	Fixed Support	Force
Suppressed	No	
Define By		Vector
Magnitude		700, N (step applied)
Direction		Defined

<##>

The executed dynamic simulation with CAE shows, that the calculated theoretical pressure force is enough to prevent displacements of samples, which is significant condition for proper dart drop testing The simulation may be used as a part of engineering analyze for unstandardized stands. Due to the wide various of tested polymers, the executed simulation may be used as a tool to define the important parameters of the test-weight of the dart drop, distance between the dart drop and the sample. This will reduce the number of tested samples and will spare time and used material.

IV CONCLUSIONS

A stand for the impact resistance of plastic films was designed by the free-falling dart drop method fully satisfying the requirements of ASTM D1709 type A. All design stages were considered in order to variably design such equipment. The stand was tested with samples of different materials and showed no deviations beyond those defined in the standard. The design of laboratory equipment is an important practical engineering task because it provides the basis for individualized, standardized, and non-standardized designs [21]. The stand is equipped with a system for smoothly adjusting pressing force. A simulation was made in CAE to determine the discrete area for the test in order to reduce the number of trials.The weight of the dart drop is in the range of ±0,02g, which meets the standard requirements. The distance between the dart drop and the sample is according type A of the standard.

REFERENCES

[1] Ning h.,Ren H.,Wang W.,Nie X.,[2023],Impact Resistance of Ultra-High-Performance Concrete Composite Structures, Materials 16(23):7456, DOI: 10.3390/ma16237456

[2] Chen S.,Yu X.,Shi X.,[2024]The influence of fiber content and voltage on the impact resistance of carbon fiber reinforced concrete Journal of Physics Conference Series 2680(1):012021

    DOI: 10.1088/1742-6596/2680/1/012021,

[3] Maruyama T.,Iguchi M.,(2023)Impact Resistance Test of Cladding by Using Gravel, Journal of Disaster Research 18(8):918-923,DOI: 10.20965/jdr.2023.p0918

[4] Skodlung D.,Roy R.,Cavender F.,{2023}Synthetic Polymers, DOI: 10.1002/0471125474.tox088.pub3

[5] Mariet C.,Silva T.,Rezende M.,(2023)Influence of 2D and 3D Arrangements of Aramid Fibers on the Dart Drop Test of Epoxy Composites, Journal of Aerospace Technology and Management 15(020002)DOI: 10.1590/jatm.v15.1308

[6] R.,Ciardiello Niuatta C.,Tridello A.,Paolino D.,{2023}Impact Response of Carbon Fiber Composites: Comparison Between Epoxy and Bio-Based Epoxy Matrices, DOI: 10.1007/978-3-031-28547-9_31,Dynamic Response and Failure of Composite Materials,

[7] Brown L.,Monir S.,Jones M.,Luhyna L,Day R.,Vagapov Y.,(2023)A Review of Impact Drop Testing of Composite Laminate Plates2023 15th IEEE International Conference on Industry Applications (INDUSCON)At: Sao Paulo, Brazil, DOI: 10.1109/INDUSCON58041.2023.10374667

[8] Yang L.,Wang D.,Bai D.,Zhang C.,Liu C.,Huang G.,(2023},Investigation of the corrosion behavior of 6082 aluminum alloy in deicing salt, Materials and Corrosion 75(1), DOI: 10.1002/maco.202313937

[9] Aslam M.,Chandan G.,Chandan G.,(2023),Development of SiC Ceramic Reinforced Composite Interlayer Cladding with AISI304 Stainless Steel Wire on Low Carbon Steel Substrate Using TIG Cladding Process, Silicon 15(18):1-11,DOI: 10.1007/s12633-023-02613-1

[10] Standard ASTM D1709

[11] Chetrokov I.,Salapateva S.,Georgiev V.,(2011),Integrating dimensional analyses within the contemorary CAD/CAM technologies, SCIENTIFIC PROCEEDINGS VIII INTERNATIONAL CONGRESS "MACHINES, TECHNOLOGIES, MATERIALS" , PRINT ISSN 1310-3946

[12] Zhao X.,(2021),Finite-Element Analysis on Lightweight Material of Drive Axle Housing, Revue des composites et des matériaux avancés 31(1):41-49DOI: 10.18280/rcma.310106

[13] Li J.,Zhang J.,Meng Q.,(2023)The Effect of Clamping Force and Friction Coefficient on The Clamping Clamp, Academic Journal of Science and Technology 7(1):200-205,DOI: 10.54097/ajst.v7i1.11369LicenseCC BY 4.0

[14] Zhang Y.,Sun W.,Du D.,Ji W.,Ma H.,(2023)Nonlinear modeling and analysis of spatial pipeline with arbitrary shapes supported by clamps considering displacement-dependent characteristic, Mechanics Based Design of Structures and Machines, DOI: 10.1080/15397734.2023.2277773

[15] Rufer A.,(2023),The Pneumatic Motor with Linear Cylinders, Semi-rotary and Linear Actuators for Compressed Air Energy Storage and Energy Efficient Pneumatic Applications, DOI: 10.2174/9789815179095123010006

[16] Sokolov V.,Krol O.,Golubenko O.,Tsankov M.Marchenko D.,(2022),,Dynamics of Clamping Pneumatic Cylinder for Technological Equipment, Advanced Manufacturing Processes IV, DOI: 10.1007/978-3-031-16651-8_6

[17] Liu X.,He Y.,Zhang S.,(2023),Civil Aircraft Electrical System Development Using Model-Based System Engineering, Advances in Engineering Technology Research, DOI: 10.56028/aetr.8.1.787.2023

[18] Zheng D.,(2023),Design of Static Strength Analysis Software for Conveyor Head Tripod Based on ANSYS and MATLAB, Applied Mathematics, Modeling and Computer Simulation

[19] Majeed A.,(2022),Ansys Software for Mechanical Engineering, DOI: 10.13140/RG.2.2.18076.97927

[20] Alizadesh Y.,{2020},Design and Structural Analysis of Composite Prosthetic Running Blades for Athletes: A case of dynamic explicit analysis using Abaqus CAE, DOI: 10.13140/RG.2.2.20693.04327

[21] Karpushkin S.,Glebov A.,(2021),A method of designing equipment for heat processing of polymer workpiece. Journal of Physics Conference Series 2094(2):22016, DOI: 10.1088/1742-6596/2094/2/022016

Optimizing tensile strength at MAG welding process of S235JR steel

Sabi Sabev
Technical University of Sofia,
Branch Plovdiv
Plovdiv, Bulgaria
sabi_sabev@tu-plovdiv.bg

Konstantin Chukalov
Technical University of Sofia,
Branch Plovdiv
Plovdiv, Bulgaria
chukalov@tu-plovdiv.bg

Abstract. **The article is of an experimental nature for welding S235JR by MAG welding method. The purpose of this work is to optimize the welding parameters of MAG welding using shield two-component gas cargon 18 to achieve ultimate tensile strength. The experiment is according to central composition design and 13 experiments were made. Samples with dimensions of 100x40x4 mm were tested with a universal tension-compression machine. Statistical processing was done and a regression relationship between welding current and seam width on the maximum tensile strength was obtained.**

Keywords: MAG welding process, tensile strength, optimization methods, regression analyze, central composition design, S235JR.

I. INTRODUCTION

Low carbon steel S235JR is widely used in mechanical engineering [1]. It is characterized by good plasticity, low hardness, low tensile strength, good weldability [2]. It is processed most often by cutting, forging and welding. It is used for structural details such as rivets, chains, bolts, etc.

MAG welding is characterized by a number of advantages - no pores, high precision, smooth welds[3],[4]. With MAG welding, high current loads are achieved on the electrode, which leads to concentrated heating with a large penetration depth, high speed and high productivity. The MAG method is preferred for welding of carbon steels, as well as low and medium alloyed steels.

CORGON 18 is a two-component mixture comprising 82% argon and 18% carbon dioxide. This gas shield is selected because it leads to good penetration and sidewall fusion.

One of the main welding modes is the current, which at high values in MAG welding leads to a deep penetration and higher productivity, but with too high current leads to undercuts and low quality of welding[5]. The relation of the welding current and the width of the seam on the tensile strength of a welded parts made of low carbon steel S235JR was experimentally investigated[6]

General Regulations

The structural steel used in the experiment was S235JR[7]. Samples with dimensions of 100x40x4 mm were used. MAG welding method and two-component shielding weld, CORGON 18: 82% Ar + 18% CO_2, were used. The filler material is SG2 TYSWELD with a diameter of 0.8 mm solid copper wire for MIG/MAG welding of carbon and low-alloyed steels.

Welding was done with a SHERMAN DIGIMIG 200 PULSE welding machine. with the following parameters: Wire feeding speed 2 – 14 m/min ,welding current range 24-200A Welding voltage 17.5-24.7V Works with welding wire D200/5kg (0.6-0.8mm) [8].

The following design of the experiment was made, using the central composite design [9],[10]. This plan contains a built-in factorial or fractional factorial plan with center points, which is supplemented with a group of "star points" that allow curvature estimation[11]. If the distance from the center of the design space to the factor point ±1 for each factor, the distance from the center of the design space to the star point is |α|=1.41, as shown in Fig.1.

Fig. 1.   Sherman digimig 200 pulse.

The resulting design of the experiment was made using Minitab, tab. 1. The value of α in this two-factor design was 1.41 and a total of 13 trials were obtained, with 5 trials selected at the center of the cube. The minimum and maximum values of the controlled factors are as follows:

Welding current I – range 50A-180A
Welding width b – range - 0mm-6mm
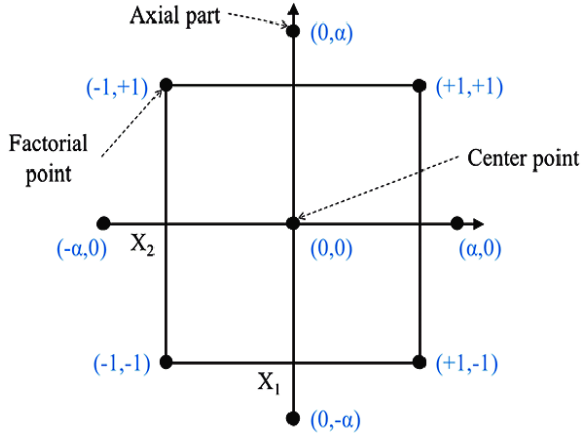
Fig. 2.   The central compositional design.

TABLE 1 THE PLAN OF THE EXPERIMENT

Run	I	δ	I	δ
1	-1,00	1,00	69	5,1
2	-1,00	-1,00	69	0,9
3	-1,41	0,00	50	3,0
4	1,41	0,00	180	3,0
5	0,00	1,41	115	6,0
6	0,00	0,00	115	3,0
7	0,00	0,00	115	3,0
8	0,00	0,00	115	3,0
9	0,00	0,00	115	3,0
10	1,00	1,00	161	5,1
11	0,00	-1,41	115	0,0
12	1,00	-1,00	161	0,9
13	0,00	0,00	115	3,0

The specimens are tested using a universal tensile compression testing machine[12]. The test set-up is shown in Fig.2.

Fig. 3.   Testing set-up.

On the samples, after welding, manual mechanical processing of the welding seam was done, fig.3.
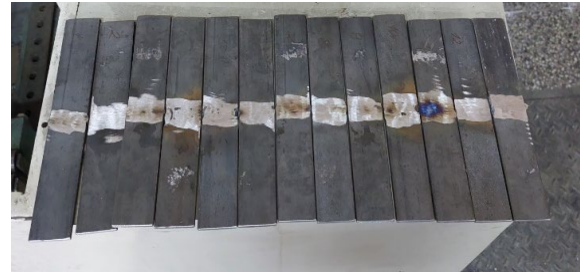
Fig. 4.   Samples after manual mechanical processing.

II.   RESULTS AND DISCUSSION

During the experiment, the test body is fixed in the jaws of the machine, then the motor is turned on and one jaw is driven, increasing the load until the specimen is raptured-fig5.

Fig. 5.   Destruction of samples and checking the values.

After conducting the experiment, the results at different current sizes and seam widths and the obtained maximum tensile strength are presented in tabular form tab.2.

TABLE 2.EXPERIMENTAL RESULTS

№	I [A]	b [mm]	F [t]	Rm [Pa]
1	69,04	5,12	6,65	4,08E+08
2	69,04	0,88	3,25	1,99E+08
3	50,00	3,00	4,40	2,70E+08
4	180,00	3,00	6,15	3,77E+08
5	115,00	6,00	8,15	5,00E+08
6	115,00	3,00	6,30	3,86E+08
7	115,00	3,00	6,50	3,98E+08
8	115,00	3,00	7,65	4,69E+08
9	115,00	3,00	6,75	4,14E+08
10	160,96	5,12	6,80	4,17E+08
11	115,00	0,00	3,55	2,18E+08
12	160,96	0,88	3,75	2,30E+08
13	115,00	3,00	7,15	4,38E+08

Fig. 6. Samples after testing.

Mathematical and statistical processing was performed with the program product MINITAB[14]. The data from Table 2 were processed and the following regression model was obtained [15]:

$$F = -3.36 + 1.601\,b + 0.1078\,I - 0.1390\,b*b - 0.000432\,I*I \quad (1)$$

Where
b-welding width
I – welding current

The coefficient of determination is $R^2 = 93.58\%$, and the corrected coefficient of determination- $R^2_{adj} = 90.38\%$, tab. 3.

TABLE 3 PARAMETERS OF THE MODEL

S	R-sq	R-sq(adj)	PRESS	R-sq(pred)	AICc	BIC
0.5	93.58%	90.38%	6.0682	81.03%	38.9	28.3

From the condition for the R^2-coefficient of multiple correlation, which is defined as insignificant. From the analysis of the variables, shown in table 4, it may be seen that the P value of the coefficient I is above 0.05 and is insignificant.

TABLE 4 COEFFICIENTS OF THE MODEL

Source	DF	Seq SS	Contribution	Adj SS	Seq MS	F-Value	P-Value
Regression	4	29,9404	93,58%	29,94	7,4851	29,17	0
b	1	21,1425	66,08%	9,0411	21,1425	82,4	0
I	1	1,1819	3,69%	6,5884	1,1819	4,61	0,064
b*b	1	1,8157	5,68%	2,7228	1,8157	7,08	0,029
I*I	1	5,8003	18,13%	5,8003	5,8003	22,61	0,001
Error	8	2,0527	6,42%	2,0527	0,2566		
Lack-of-	4	0,8897	2,78%	0,8897	0,2224	0,77	0,599
Pure Error	4	1,163	3,64%	1,163	0,2908		

The Pareto diagram, Fig. 7 shows the absolute values of the standardized effects from the most important to unimportant ones [16]. The chart also draws a reference line which effects are statistically significant. It may be seen that component B is behind the significance line, therefore the coefficient is insignificant.
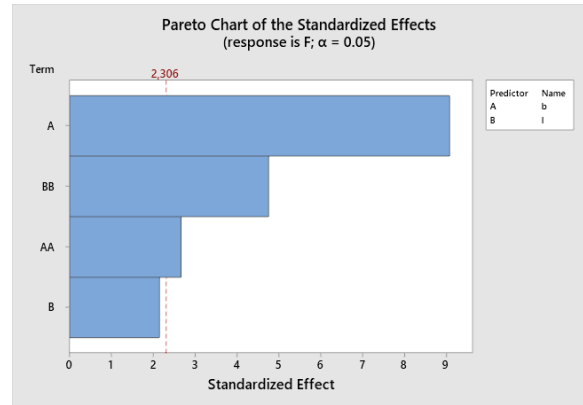
Fig. 7. Pareto diagram.

Analysis of residuals is performed using the standardized residuals plots in Fig. 8.[17]. The values of the standardized residuals should be within ±2. Values close to 2 are sample No4 and No8. Also on the same samples, pores from welding process are observed fig.9. These results are removed and the process was repeated.
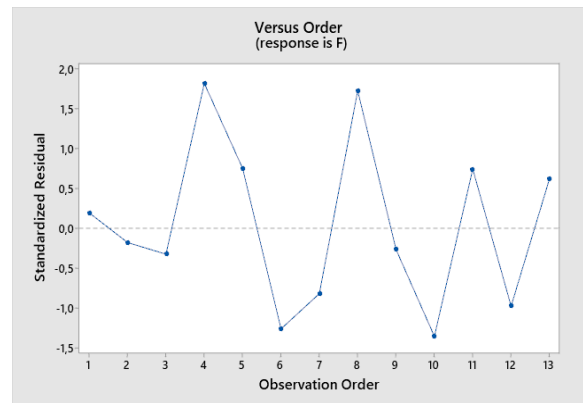
Fig. 8. Standardized residuals.

Fig. 9. Pores in samples No4 and No8.

After the operation the following results are obtained.

$$F = -3.658 + 1.345\,b + 0.1220\,I - 0.0965\,b*b - 0.000519\,I*I \quad (2)$$
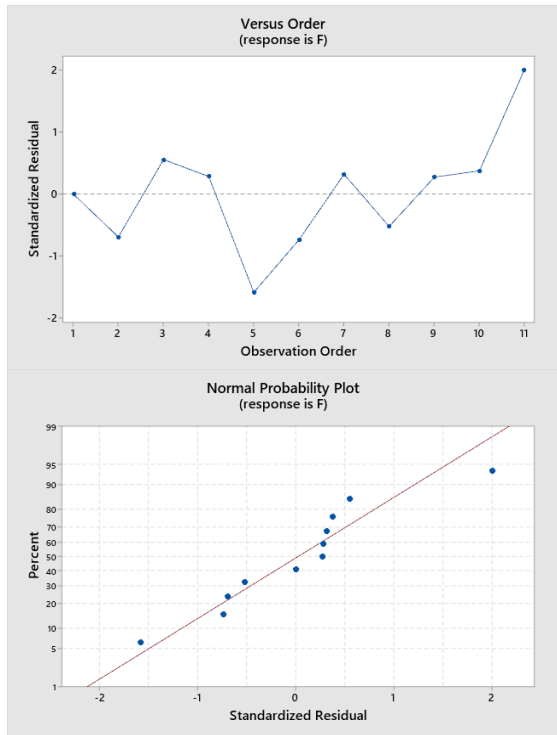
Fig. 10. Standardized residuals.

The new coefficient of determination was calculated $R^2 = 98.43\%$, and the corrected coefficient is $R^2_{adj} = 97.39\%$ tab. 5 and tab. 6.

TABLE 5 PARAMETERS OF THE MODEL

S	R-sq	R-sq(adj)	PRESS	R-sq(pred)	AICc	BIC
0,273	98,43%	97,39%	0,957393	96,65%	29	10,39

F - Value of the Fisher distribution used to test significance of the multiple correlation coefficient.

R^2 - Multiple correlation coefficient is significant.

From the analysed variables, shown in Table 6, all the P values are below 0.05 so are significant.

The analysis of standardized residuals fig. 10, shows that there are no critical errors.

TABLE 6 COEFFICIENTS OF THE MODEL

Source	DF	Seq SS	Contribution	Adj SS	Seq MS	F-Value	P-Value
Regression	4	28,1644	98,43%	28,1644	7,0411	94,32	0
b	1	21,1425	73,89%	5,5861	21,1425	283,22	0
I	1	1,0766	3,76%	5,633	1,0766	14,42	0,009
b*b	1	1,1319	3,96%	1,1319	1,1319	15,16	0,008
I*I	1	4,8133	16,82%	4,8133	4,8133	64,48	0
Error	6	0,4479	1,57%	0,4479	0,0747		
Lack-of-Fit	3	0,0454	0,16%	0,0454	0,0151	0,11	0,947
Pure Error	3	0,4025	1,41%	0,4025	0,1342		
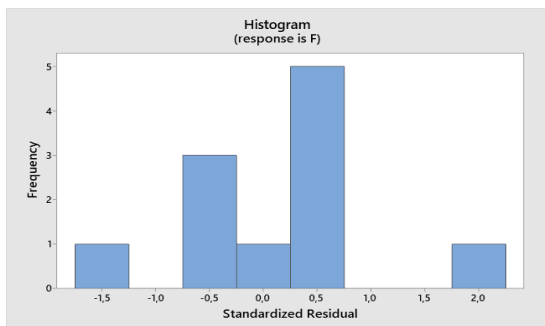
Fig. 11. Histogram of standardized residuals.

The Pareto diagram, fig.12 shows that the components are in front of the significance line [18].
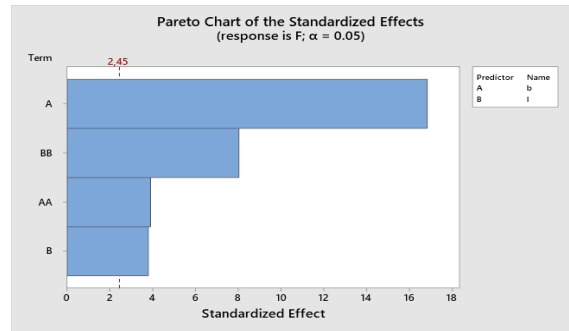
Fig. 12. Pareto diagram.

The influence of welding current and width of the seams on the tensile strength is also analyzed, fig. 13.

The one-parameter optimization was processed with MINITAB software, with the help of which the maximum values for the objective function - tensile strength - were found. The data are presented in Fig.14. The maximum value of tensile strength is under the following conditions: width of the seam - 6mm and magnitude of the current is 117A.
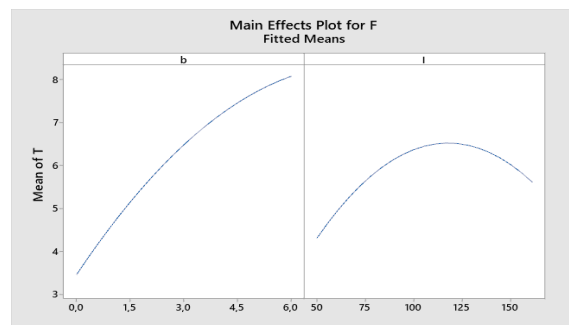
Fig. 13. Influence of the components.
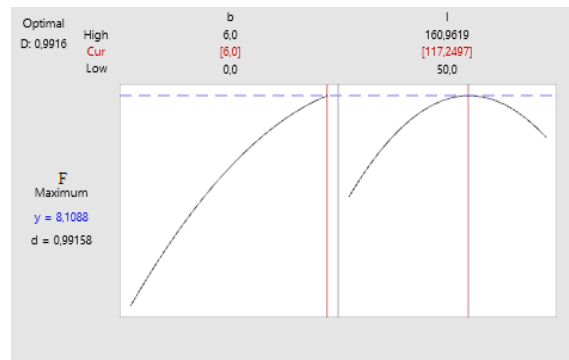
Fig. 14. Optimization diagram.

III. CONCLUSIONS

By experimental planning the number of trials was reduced to 13- enough to statistical processing. For the goals of the article are selected 2 welding parameters that have influence on technological parameters of welding parts. Tensile strength is selected for output parameter because shows entire engineering performance of selected material.

The following conclusions drawn from the experimental results and their processing:

1. An adequate regression model was designed describing the relationship between welding current, and tensile strength.

2. Two errors caused by pores during welding were established.

3. From the regression analysis, the welding current factor affects the least, and the distance b affects about 78% on the tensile strength objective function.

4. From fig.13 it is also seen that the greatest influence on the maximum tensile strength is exerted by the width of the seam in this research.

5. One-parameter optimization of tensile strength was done.

Similar optimizations articles of MAG welding parameters prove credibility and the actuality of the method and the experimental results [19], [20], [21].

IV. ACKNOWLEDGMENTS

REFERENCES

[1] S. Yuan,H. Xie ,H. Wu ,M. Ren,X. Liang,S. Jiao ,Z. Jiang The Effects of Annealing on Microstructure and Mechanical Properties of Monolithic Low Carbon Steel and Medium Manganese Steel/low Carbon Steel (Mn8/SS400) Bimetal Composite, Proceedings of the 14th International Conference on the Technology of Plasticity - Current Trends in the Technology of Plasticity, 2023 https://doi.org/10.1007/978-3-031-41341-4_73

[2] V. F.Khorunov,I. Zvolinskyy ,S. Maksymova ,ARC BRAZING OF LOW-CARBON STEELS, 2023

[3] C. Gonzales ,H. Ortega ,E. Garcia ,J. Cabello ,Environmental and Economic Analyses of TIG, MIG, MAG and SMAW Welding Processes, Metals 13(6):1094, 2023 https://doi.org/10.3390/met13061094

[4] Y. Cho ,B. Kim ,C. Lee ,N. Kang ,Mechanical properties of one-sided welding for the low-temperature steel using a high-current MAG welding, Welding in the World, Le Soudage D, 2023 https://doi.org/10.1007/s40194-023-01585-5

[5] D. Salvador ,Welding Certification and Standards: Ensuring Quality and Reliability in Fabrication, International Journal of Advanced Research in Science Communication, 2023 http://dx.doi.org/10.48175/IJARSCT-11905

[6] H. Zhang ,R. Li ,S. Yang ,L. Zhan,M. Xiong ,B. Wang ,J. Jhang ,Experimental and Simulation Study on Welding Characteristics and Parameters of Gas Metal Arc Welding for Q345qD Thick-Plate Steel, Materials 16(17):5944, 2023 https://doi.org/10.3390/ma16175944

[7] W. Kraus ,H. Blum ,Structural Steel Fabrication with Mixed Reality, ce/papers 6(3-4):904-907, 2023 https://doi.org/10.1002/cepa.2575

[8] S. Tsumura ,E. Meirelles,V. Callil ,M. Lourenco ,J. Caprece, Parametric Analysis of Welding Parameters for Hybrid Laser/MAG Welding, 11th International Seminar on Inland Waterways and Waterborne Transportation, 2019 https://doi.org/10.3390/ma15124328

[9] M. Tabat ,M. Kibria ,E.Eppele ,S. McCoy ,Optimization for Sustainable Process Design, 2023 Annual AIChE Meeting (161 - Advances in Process Design I), 2023

[10] T. Reddy ,G. Henze , Optimization Methods, Applied Data Analysis and Modeling for Energy Engineers and Scientists,2023 https://doi.org/10.1007/978-1-4419-9613-8

[11] A. Hagelberg ,D. Andre ,M. Finnis , Laboratory multistatic and multipolar SAR CCD investigation, 5th International Conference on Synthetic Aperture in Sonar and RadarAt: Lerici, Italy,2023

[12] A. Ghazai,The Process of Maintenance and Assessment of The Universal Testing Material Machine H50KS,,2023 https://doi.org/10.17303/jmsa.2020.4.204

[13] S. Pop,M. Dudescu,L. Contac ,R. Pop , Evaluation of the tensile properties of polished and unpolished 3D SLA- and DLP-Printed specimens used for surgical guides fabrication., 2023 http://dx.doi.org/10.2478/asmj-2023-0003

[14] M. Evans ,C. St , MINITAB Manual,2023

[15] B. Hirsh ,Regression Analysis,2022

[16] S. Kone ,N. Kaufmann ,L. Richert , Adaptive Algorithms for Relaxed Pareto Set Identification, 2023 https://doi.org/10.48550/arXiv.2307.00424

[17] P. Araripe ,I. Lara Ordinal data and residual analysis: Review and application,Brazilian Journal of Biometrics 41(3):287-310,2023 http://dx.doi.org/10.28951/bjb.v41i3.637

[18] H. Maurer ,C. Kaya ,Optimization over the Pareto front of nonconvex multi-objective optimal control problems, Computational Optimization and Application, 2023 https://doi.org/10.1007/s10589-023-00535-7

[19] S. Apay ,Optimization of Welding Parameters in MAG Lap Welding of DD13 Sheet Metal with Taguchi Method and FEM Analysis,2022

[20] H. Wu .,Z. Zhang,W. Qi,R. Tian,C. Shi, Optimization of narrow groove plasma-MAG hybrid welding process parameters,2017

[21] Z. Li ,Y Xia, Heat source modeling, penetration analysis and parametric optimization of super spray MAG welding,Scientific reports, 2023 http://dx.doi.org/10.1038/s41598-023-36505-6

Research of Robotic System Positioning Accuracy

Paulius Sakalys
Faculty of electronics and informatics,
Vilniaus Kolegija/Higher Education Institution
Vilnius, Lithuania
p.sakalys@eif.viko.lt

Savulioniene Loreta
Faculty of electronics and informatics,
Vilniaus Kolegija/Higher Education Institution
Vilnius, Lithuania
l.savulioniene@viko.lt

Dainius Savulionis
Faculty of electronics and informatics, Vilniaus Kolegija/Higher Education Institution
Vilnius, Lithuania
d.savulionis@eif.viko.lt

Anastasiya Chupryna
Software engineering department, Kharkiv National University of Radio Electronics,
Kharkiv, Ukraine
anastasiya.chupryna@nure.ua

Kyrylo Smelyakov
Software engineering department, Kharkiv National University of Radio Electronics,
Kharkiv, Ukraine
kyrylo.smelyakov@nure.ua

Abstract. **Robotics is one of the technologies of the fourth industrial revolution, which has a wide range of applications, from household chores to manufacturing and healthcare to entertainment and space exploration. The purpose of the study is to determine and evaluate the repeatability and positioning accuracy indicators of the robotic system when reproducing the movements of the hand repeating a human hand. The article conducts a comparative analysis of the methods and software control algorithms for creating feedback of robotic system electromechanical control gears displacement, and provides the rationale for the choice of physical equipment for the technical experiment. This article describes the plan of stages of the experimental research, the research bench, presents the systematized results of the research, conclusions and suggestions for practical application.**

Keywords: feedback, robotic system, servo drive

I. INTRODUCTION

Historically, early servo motors performed the basic functions of position control. Servomotors use a feedback controller to control the speed or position of the motor, or both. With the exception of constructional highlights, a DC servo motor (DSM) is basically a normal DC motor [2]. However, the increasing demand for more complex and precise movements in robotic systems has highlighted the need for improvements in servo motor technology. Over the years, advances in materials, design and control systems have significantly improved the accuracy of servo motor movements. One of the main barriers to achieving precision in servo motor motions is the provision of accurate position control: delay, mechanical effects and non-linearity in the feedback loops can introduce an error factor and reduce the overall precision of the robotic system motions [6]. In the analysis of electric servo drive motors, the equations for the motor indicate the presence of two time constants. One is a mechanical time constant and the other is an electrical time constant. Since these two time constants are part of the motor block diagram used in a servo analysis, it is important to know the real value of the time constants under actual load conditions [5]. To overcome these problems, the development of advanced control algorithms and position feedback systems is currently receiving much attention [6]. Advanced control algorithms are essential to optimise the accuracy of servo motor motions. These algorithms take into account variables such as motor dynamics, environmental conditions and position sensor feedback. These algorithms allow precise control of the actuator movements by compensating for mechanical imperfections and adapting to changing load conditions. Servo motors often use potentiometers as the operating elements of a position feedback system. A potentiometer is a variable resistor that provides feedback to the actual position of the actuator. It measures the rotation of the motor axis and converts it into an electrical signal that is used by the control system to control the exact position of the motor. Potentiometer-based feedback systems are reliable and cost-effective solutions to ensure precise leg movements To increase the accuracy of servo motor movements, it is necessary to integrate potentiometer feedback systems with sophisticated control algorithms.

II. MATERIALS AND METHODS

This section analyses research on various feedback systems, including potentiometers, encoders and inertial sensors, to clarify their advantages, disadvantages and suitability for integrated control systems. A review article by Garcia-Barragan describes an inexpensive optical encoder system for providing position feedback to amateur servo 16 motors. Optical encoders are essential components of motor control systems as they detect the rotation angle, speed and distance of a moving machine element and provide position feedback to the controller. The controller transmits electrical signals to the driver, which amplifies and interprets the signals for the servo motor. Optical encoders support high speed and high resolution, but are expensive and sensitive to contamination. This paper discusses the design and implementation of a cost-effective optical encoder system for hobbyist servo motors that improves position feedback accuracy and speed while maintaining a small footprint for a limited PCB area [3]. In a research paper by Veitschegger, the authors present a method for calibrating and compensating for kinematic errors in robotic manipulators. In this work, a method for selecting a set of independent kinematic errors is developed to model any geometric errors in the manipulator design. A calibration algorithm for calculating kinematic error values is provided for measuring the position of the end-effector. The kinematic errors of the six-joint manipulator PUMA 560 are experimentally determined and two general-purpose compensation algorithms are developed. The improvement of the Cartesian position of the end-effector is experimentally measured and the results are presented. Using a relatively simple method of measuring the Cartesian position of a tool attached to the end of the manipulator, the paper demonstrates that the positioning accuracy of a robotic manipulator can be significantly improved [8]. Aragon-Jurado's research paper analyses servo drives. The aim of this research is to understand the function of the potentiometer in a servo motor system and how it can be used to improve servo motor performance in a variety of applications, including robotics and automation systems [1]. The authors describe the design and development of a low-cost servo motor controller using pulse frequency modulation (PFM) instead of conventional pulse width modulation (PWM). This paper focuses on the development of a small printed circuit board (PCB) that replaces the original control circuitry in a commercial servo motor housing. The potentiometer is left as a feedback sensor and the motor position is controlled by a microcontroller. The authors compare a PWM-controlled and a PFM-controlled servo motor and demonstrate that the PFM-controlled motor achieves faster commutation of the motor drives and a lower drive response delay [4] This controller can be used with neuromorphic systems in order to avoid the need for converting the events to pulse-width modulation (PWM), and is therefore an important contribution to robotics and servo motor control [4].

A review of scientific publications lacks specific information on methods for monitoring the servo drive feedback systems themselves, but Zhu et al. describe a low-cost microelectromechanical system (MEMS) inertial measurement sensor for position sensing of spherical motors. The proposed sensor combines a three-axis gyroscope and a three-axis accelerometer to acquire raw position data from spherical motors in order to estimate the rotor position Fig. 1. The aim of this study is to improve motor performance in terms of speed feedback and control by implementing MEMS sensors in servo motor applications.
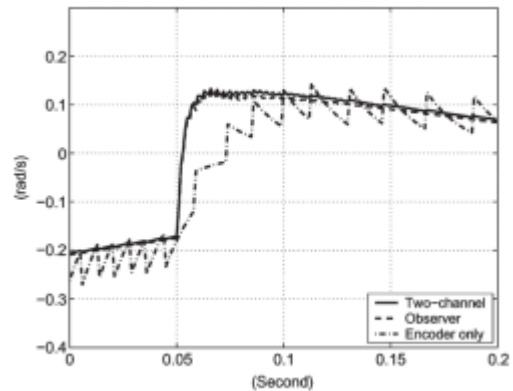
Fig 1. Comparison of the effect of gyro and accelerometer feedback systems on the steering angle of a servo drive

By using the ability of MEMS sensors to measure acceleration, yaw and vibration, the system can provide more accurate and reliable velocity feedback, thereby improving the overall performance of servo motors in a variety of applications [10]. Zhang's research work proposes an adaptive fuzzy logic-based tracking system to estimate the speed in servo motor drives based on the measured motor position. This method aims to improve the accuracy of speed estimation and reduce the noise caused by the quantization of measured positions. The system has two adaptation mechanisms, one for adjusting the fuzzy logic output and the other for determining the motor parameters. Experimental results show that the proposed system can significantly reduce the noise of the estimated speeds and provide excellent transient response at both normal and low speeds. This approach improves the overall performance of servo motors in various applications, especially in continuous speed control [9].

In this study, the analysis of the robotic system design focuses on the application of servo motors to the control system of a robotic hand finger. Three popular servo drives with closed-loop feedback, CoxA, Femur and Tibia, are used for the study. The test rig was designed to operate in the following mode Fig. 2: to control the position of the servo motor, the microcontroller generates a pulse width modulation (PWM) signal of a fixed frequency and variable duty cycle, the angle is determined by the width of the signal pulse. When connecting the microcontroller to three servo motors and an additional +6 V power supply, it is necessary to ensure that there is sufficient electrical current to power all components. On the microcontroller side, separate regulators with an isolating diode and a large capacitor shall be used to prevent voltage drops due to different operating modes of the servo drives from affecting the microcontroller. The duty cycle of the pulse-width modulated signal can be calculated according to the desired servo motor angle to control the position of the servo motors using PWM signals.
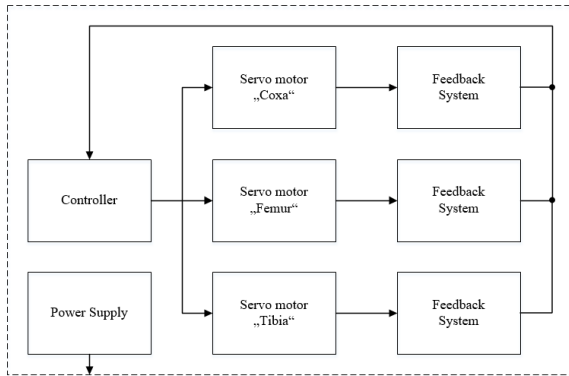
Fig 2. Schematic diagram of the test bench

Servo motor feedback is needed to transmit the current motor positions to the microcontroller. This feedback information allows the microcontroller to accurately control the position of the servo motors by adjusting the PWM signals. In the absence of feedback, the microcontroller would only be able to transmit Pulse Width Modulation (PWM) signals to the servo motors and assume that it has reached the desired position. However, due to external forces or mechanical problems, the servo motors may in practice not reach their intended position. By receiving feedback, the microcontroller can continuously monitor the position of the servo motors and, if necessary, modify the PWM signals to ensure that the target position is reached. A digital angle meter Fig. 3 is used to monitor the servo motor position. The digital angle meter is connected to the motor's rotation axis, which ensures accurate measurement of each rotation. In order to investigate the positioning of each motor, an Arduino Mega programmable logic controller and a separate power supply were used.
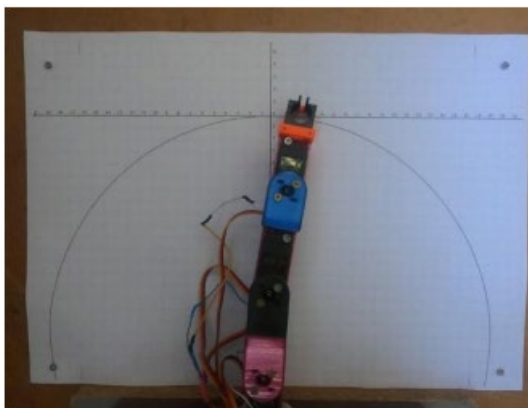
Fig 3. Test bench

By connecting a potentiometer as part of the feedback system and reading the data, this information can be used to calculate the exact angle of inclination of the servo drive, or the system it is controlling (the finger of the robotic hand). Typically, this calculation involves comparing the raw potentiometer readings with a known baseline value and using the difference to determine the system yaw angle. To ensure that the actuator moves accurately, a system is in place to detect when the potentiometer reading and the calculated position do not match. For example, if the

difference between the potentiometer reading and the calculated position is greater than two, this may indicate that the actuator is not moving accurately and the position check should be repeated. Instead of continuously reading the potentiometer feedback, it is possible to measure the exact potentiometer values at specific angles and use this information to calculate the exact tilt angle of the actuator. This method, known as calibration, provides a more accurate and efficient method of measuring the actuator position. To calibrate the potentiometer, you need to move the servo motor through several angles and record the potentiometer readings for each angle. This would allow a correlation to be made between the angle of the servo motor and the potentiometer reading. By setting a suitable value for the calibration factor, the potentiometer readings can be used to calculate the exact angle of rotation of the actuator. For example, if a certain angle is to be achieved, the potentiometer reading corresponding to this angle can be calculated and the position of the actuator can be set accordingly. This function would take the potentiometer reading as input and return the corresponding actuator angle as output Fig. 4.
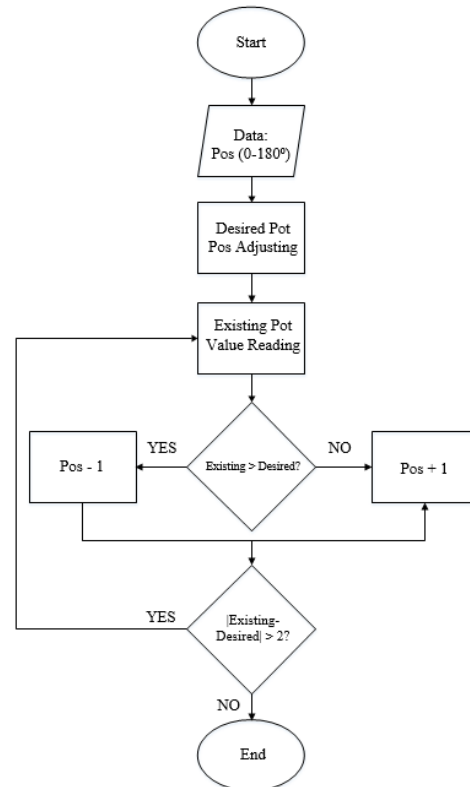
Fig 4. Algorithm for the servo drive's enhanced feedback system

III. RESULTS AND DISCUSSION

Initial performance tests of the uncalibrated system evaluated the accuracy of three different servo drives and showed that all motors with conventional feedback and a standard control algorithm deviated on average 23.5° from the set angle during the tests, with a range of 0-180°. This indicates that the actuator movement is inaccurate and not suitable for the control of precision robotic systems Fig. 5.
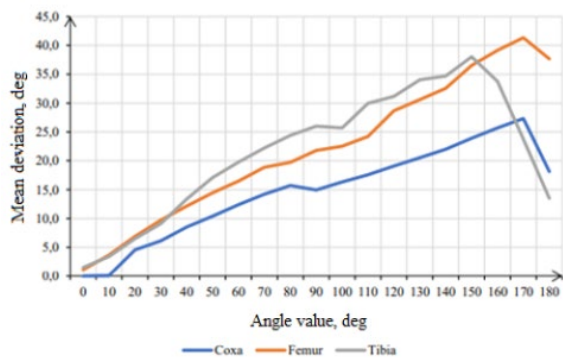
Fig 5. Plot of the specified steering angle and measured mean deviation for servo drives (without integrated enhanced feedback system)

Fig. 6 shows the aggregated test data for the same servo drives when the servo drive control integrates a feedback verification system working with a software calibration algorithm.
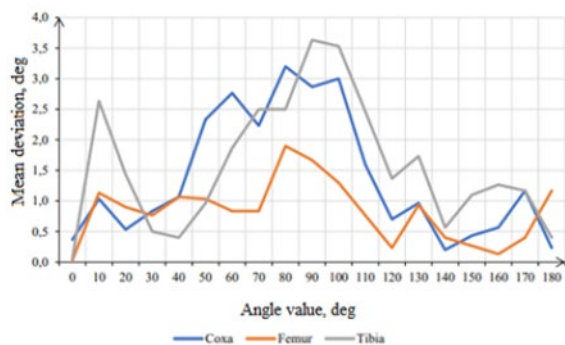
Fig 6. Plot of the specified steering angle and measured mean deviation for servo drives (with integrated enhanced feedback system)

IV. CONCLUSIONS AND SUGGESTIONS

The study analyses individual popular servo motors on the market with a potentiometric feedback positioning system in the absence of a feedback verification system. The average angle of rotation of the servo motors was found to be ~ 23,5°. The application of a pre-calibration algorithm for the servo motor and the integration of a feedback verification system resulted in an average angle of rotation of the servo motors of ~ 1,4°. Comparison of the servo motor angle accuracy with and without the potentiometer feedback verification system shows a significant increase in accuracy, i.e. ~10 times. With the integration of the above systems, the largest deviation is observed in the servo drive operating range between 40° and 110°, due to the increased mechanical stress loads of the reduction gears in the servo drives. This would be resolved by calibrating the actuator for a segmented

operating range, rather than the full range, taking into account the dynamic loads of the system controlled by the servo actuator. During the tests, the servo drive is integrated into a six-axis robot leg with four degrees of freedom. After applying the pre-calibration system, the accuracy of the robot leg increases, the deviation of the distance from the set coordinate changes by an average of 1.1 cm. Compared to single-step with feedback or pre-calibration with foot control, feedbackless feedback shows a noticeable increase in foot position accuracy.

In order to improve the control systems, it would be appropriate to test alternative servo drive feedback systems such as optical encoders or inertial sensors in further studies.

REFERENCES

[1] Aragon-Jurado D., Morgado-Estevez A., Perez-Peña F. 2018a. Low-cost servomotor driver for PFM control, Sensors (Switzerland) 18(1). DOI: 10.3390/s18010093

[2] Debnath D., Malla P., Roy S. 2022. Position control of a DC servo motor using various controllers: A comparative study, Materialstoday: ProceedingsVolume 58, Part1: 484-488. DOI: https://doi.org/10.1016/j.matpr.2022.03.008

[3] Garcia-Barragan 2017. An Engineering Guide to Position and Speed Feedback Devices for variable speed drives and servos. Online acess: www.controltechniques.com.

[4] Jurando, D.A, Estevez, A.M., Pena, F.P. 2018. Low-Cost Servomotor Driver for PFM Control, MDPI and ACS, Sensors. DOI: https://doi.org/10.3390/s18010093.

[5] Lynn, T. T. 2016. Position control of DC servo drive by fuzzy logic controller in flat-bed screen printing machine, American Scientific Research Journal for Engineering, Technology, and Sciences (ASRJETS), Volume 26, No 1: 8-19

[6] Smelyakov, K., Chupryna, A., Sandrkin, D., Kolisnyk, M. 2020. Search by Image Engine for Big Data Warehouse. IEEE Open Conference of Electrical, Electronic and Information Sciences (eStream). DOI: https://doi.org/10.1109/eStream 50540.2020.9108782

[7] Smelyakov, K., Karachectsev D., Kulemza, D., Samoilenko, Y., Patlan, O., Chupryna, A. 2020. Effectiveness of Preprocessing Algorithms for Natural Language Processing Applications. IEEE International Conference on Problems of Infocommunications. Science and Technology (PIC S&T). DOI: https://doi.org/10.1109/PICST51311.2020.9467919

[8] Veitschegger W.K., Wu C.-H. 1988. Robot Calibration and CompensationPrieiga per interneta: https://ieeexplore.ieee.org/abstract/document/9302.

[9] Zhang D., Wang J., Qian L., Yi J. 2019. Stepper motor open-loop control system modeling and control strategy optimization, Archives of Electrical Engineering 68(1): 63–75. DOI: 10.24425/aee.2019.125980 .

[10] Zhu W.H., Lamarche T. 2007. Velocity estimation by using position and acceleration sensors, IEEE Transactions on Industrial Electronics 54(5): 2706–2715. DOI: 10.1109/TIE.2007.899936

A unified model for analyzing dimensional relationships

Silviya Salapateva
Faculty of Mechanical Engineering
Technical University of Sofia, Plovdiv Branch
Plovdiv, Bulgaria
sisisal@tu-plovdiv.bg

Abstract. **The paper presents an attempt to introduce an integrated model for analysing dimensional relationships. The basis for the application of a unified approach in revealing, analysing and solving the dimensional chains is the fact that each element of the dimensional relationships in the product has a spatial expression. The practical side of the proposed unified model for the analysis of dimensional relationships is also presented. The essence of this model is that a single approach is applied to solve all dimensional chains, regardless of their spatial location. The model represents the dimensional chain by the coordinates of a sequence of basic points, the distances between which determine the components of the dimensional chain.**

I. INTRODUCTION

In mechanical engineering practice, the sizing of products is carried out in the three coordinate planes with dimensions, parallel to the coordinate axes. Thus, the dimensional relationships in each of the coordinate planes are represented by dimensional chains, composed of parallel components (dimensions) [1]. Decisive role for this approach in construction has the technical and technological level of production techniques. The guiding principle is to have details with a simple geometric shape, which does not require the use of production machines with complex construction and kinematics. Having in mind that such machines, built with hard kinematics, are very expensive, the application of the above-mentioned principle is easy to explain for the reason of achieving an acceptable cost price of the products. It should be definitely said that the modern level of production technology has significantly outstripped the logic of the construction thinking, and the limitation of the simple geometric shape has no significant practical value. Modern machines have flexible kinematics, conditioned by independent activation of their working elements, the synchronization between which is realized by means of computer logic and computer control [2]. For this reason, there are no technical limitations for production of details with a complex shape and relative position of their surfaces, as well as of a complex spatial relationship between the individual details in the product.

The simple geometric shape principle in construction also reflects in the scientific approach to studying the dimensional relationships in the products [3]. Solutions have been sought, in which the problem is reduced to a uniaxial model of the dimensional relationships – dimensional chains with parallel components. This type of a model is theoretically well developed. In cases where the dimensional chain contains components with an angular position with respect to the remaining components, transformation of the dimensional chain into a uniaxial one is applied, by projecting it onto the coordinate axes. Such examples are shown in Fig.1 and Fig.2.

In the first case, a projection on an axis, parallel to the closing component is considered. The advantage is the simplicity of the model. The disadvantage is that it does not reflect the influence of the components, located perpendicular to the closing component. This problem has been overcome in the second model, where two uniaxial chains are obtained, which are projections on the two coordinate axes. However, problems arise here also in determining the tolerances of the constituent components.

Even more complicated is the case with 3D (three-dimensional) spatial dimensional chains [4]. It is considered that they can be studied as three uniaxial chains, which are projections of the spatial chain onto the three coordinate axes [5], [6].
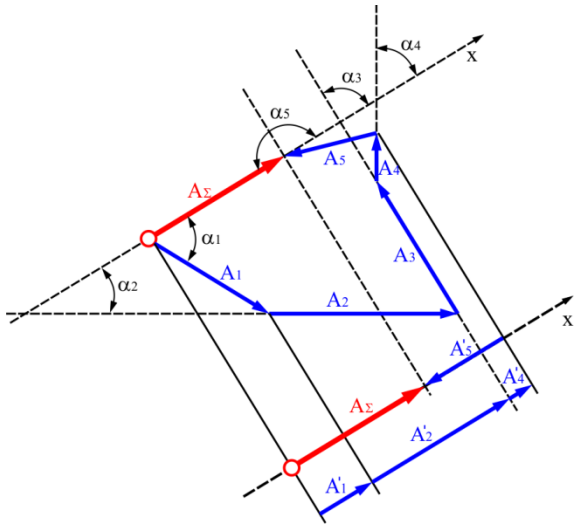
Fig. 1.   Transformation of the dimensional chain into a uniaxial one
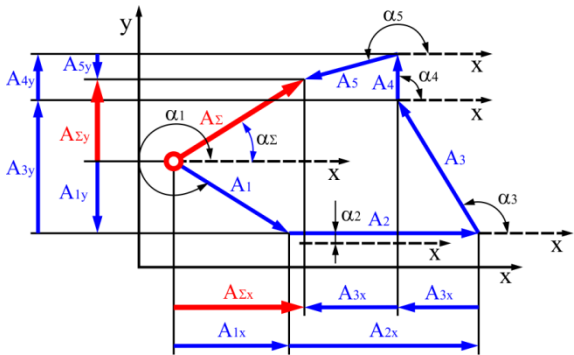
Fig. 2. Transformation of the dimensional chain into two uniaxial chains

It should be noted that regardless of these ideas for solving dimensional chains with non-parallel components, the issue has not yet been studied sufficiently well and no applied algorithms have been developed for use in product design.

II. Materials and methods

The basis for the application of a unified approach in revealing, analyzing and solving the dimensional chains is the fact that each element of the dimensional relationships in the product has its spatial expression. A dimensional chain is a closed loop of serially connected dimensions. Each of them is a line segment (part of a straight line), whose size and position in space are determined by the coordinates of its endpoints.

The line segment A_i, with a general position in space, is shown in Fig. 3. It is defined by the points $M_i(x_i, y_i, z_i)$ and $M_{(i-1)}[x_{(i-1)}, y_{(i-1)}, z_{(i-1)}]$. Its length is obtained from the sum:

$$A_i = \sqrt{\left(x_i - x_{i-1}\right)^2 + \left(y_i - y_{i-1}\right)^2 + \left(z_i - z_{i-1}\right)^2} \quad . (1)$$

The differences in this sum are its projections on the coordinate axes:

$$\begin{aligned} x_i - x_{i-1} &= A_{ix}; \\ y_i - y_{i-1} &= A_{iy}; \\ z_i - z_{i-1} &= A_{iz}. \end{aligned} \qquad (2)$$
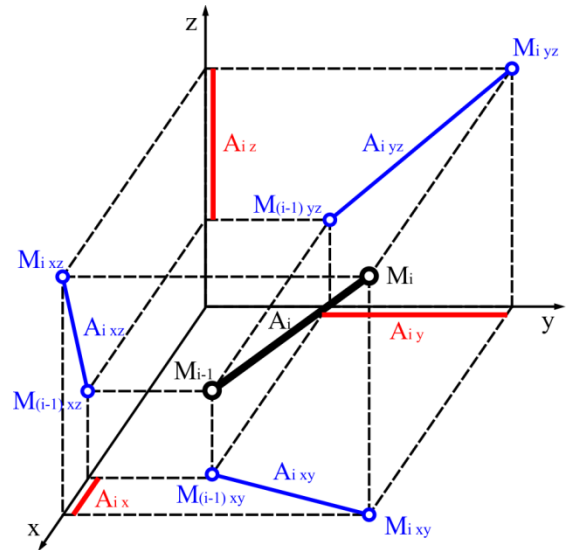
Fig. 3.   A line segment in space

From this example it can be seen that if one of the coordinates of the constituent components in a dimensional chain is a constant, then the chain will be located in a plane, perpendicular to the corresponding coordinate axis. For example, with $z_i = $ const, it will lie in a plane, parallel to xOy. If two of the coordinates are constant, the dimensional chain will have parallel components, i.e., it is a uniaxial dimensional chain. From here it follows that the dimensional chains with parallel components and the planar dimensional chains are particular cases of the spatial dimensional chains. Therefore, they obey a common theoretical model.

A.   Revealing the dimensional relationship

The task of compiling and solving a dimensional chain will be presented in a general form. Fig. 4 shows a spatial dimensional chain with non-parallel dimensions.
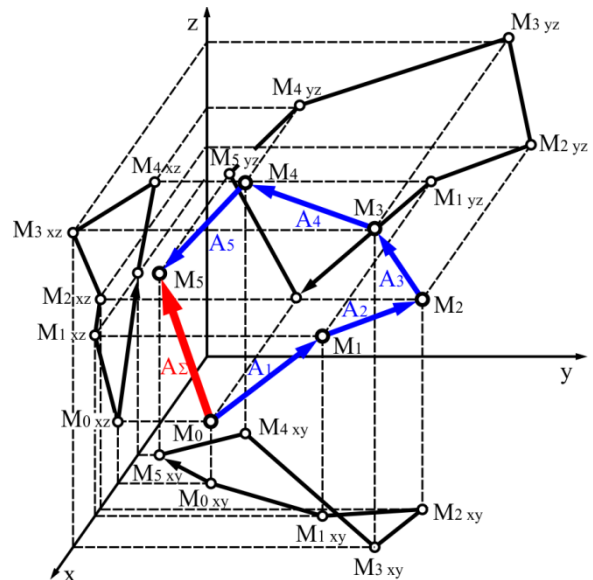
Fig. 4.   Spatial dimensional chain

The closing component is the dimension A_Σ, and the remaining dimensions are constituent components. The chain is constructed using the vector sum principle. The constituent components make up the vector polygon, and

the closing component is the resultant vector. In this case:

$$\vec{A}_{\Sigma} = \sum_{i=1}^{n} \vec{A}_i \ . \tag{3}$$

When projecting the dimensional chain on the three coordinate planes, three planar dimensional chains with non-parallel components are obtained.

The dimensional chain is identified by the coordinates of the points M_0; M_1; M_2; ...; M_n.

The distances between them are the constituent components A_1; A_2; A_n.

The closing component is defined by the points M_0; M_n.

Therefore:

$$A_{\Sigma x} = x_n - x_0;$$
$$A_{\Sigma y} = y_n - y_0; \tag{4}$$
$$A_{\Sigma x} = z_n - z_0.$$

For the size of the closing component, it is obtained:

$$A_{\Sigma} = \sqrt{A_{\Sigma x}^2 + A_{\Sigma y}^2 + A_{\Sigma z}^2} \ . \tag{5}$$

The angular position of the closing component is determined by the angles, relative to the three coordinate axes:

$$\alpha_{\Sigma x} = \arccos \frac{A_{\Sigma x}}{A_{\Sigma}} \ ;$$
$$\alpha_{\Sigma y} = \arccos \frac{A_{\Sigma y}}{A_{\Sigma}} \ ; \tag{6}$$
$$\alpha_{\Sigma z} = \arccos \frac{A_{\Sigma z}}{A_{\Sigma}} \ .$$

B. *Dimensional tolerances in the dimensional chain*

a) Limited summation – "Max - Min" method

Any change to a component in the dimensional chain also changes the closing component. If the dimension of the component A_i changes by ΔA_i, a change will occur in the coordinates of the point M_i:

$$\Delta x_i = \Delta A_i . \xi_{ix}; \ \Delta y_i = \Delta A_i . \xi_{iy}; \ \Delta z_i = \Delta A_i . \xi_{iz}, \tag{7}$$

where:

$$\xi_{ix} = \frac{A_{ix}}{A_i} \ ; \ \xi_{iy} = \frac{A_{iy}}{A_i} \ ; \ \xi_{iz} = \frac{A_{iz}}{A_i} \ . \tag{8}$$

The same change will occur in all the other basic points, and respectively, in the endpoint of the chain.

Given that each component of the chain will have a different size for the specific product, the coordinates of the point M_n, and respectively the change of the closing component, will be:

$$\Delta_{\Sigma x} = \sum_{i=1}^{n} \Delta A_i \xi_{ix} \ ;$$

$$\Delta_{\Sigma y} = \sum_{i=1}^{n} \Delta A_i \xi_{iy} \ ; \tag{9}$$

$$\Delta_{\Sigma z} = \sum_{i=1}^{n} \Delta A_i \xi_{iz} \ .$$

The resizing of the closing component will be:

$$\Delta_{\Sigma} = \sqrt{\Delta_{\Sigma x}^2 + \Delta_{\Sigma y}^2 + \Delta_{\Sigma z}^2} \ . \tag{10}$$

The closing unit size variance will be within the limits:

$$\omega_{\Sigma} = \Delta_{\Sigma \max} - \Delta_{\Sigma \max} \ . \tag{11}$$

Given that the number (10) is positive ($\Delta_{\Sigma} \geq 0$) and the maximum change of each of the components is within the dimension tolerance ($\Delta_{i \ max} = T_i$), from the expressions (9) and (10) it is obtained:

$$T_{\Sigma} = \sqrt{\left(\sum_{i=1}^{n} T_i \left|\xi_{ix}\right|\right)^2 + \left(\sum_{i=1}^{n} T_i \left|\xi_{iy}\right|\right)^2 + \left(\sum_{i=1}^{n} T_i \left|\xi_{iz}\right|\right)^2} \ . \tag{12}$$

In the design task, the tolerance of the closing component is distributed among the constituent components according to the principle of the same accuracy class, in which the same number β_{cp} of the tolerance units is defined for all constituent components. The tolerances of the constituent components are determined by the calculated average number of tolerance units:

$$T_i = \beta_{cp} . E_i. \tag{13}$$

From the expressions (12) and (13), β_{cp} is found:

$$\beta_{cp} = \frac{T_{\Sigma}}{\sqrt{\left(\sum_{i=1}^{n} E_i \left|\xi_{ix}\right|\right)^2 + \left(\sum_{i=1}^{n} E_i \left|\xi_{iy}\right|\right)^2 + \left(\sum_{i=1}^{n} E_i \left|\xi_{iz}\right|\right)^2}} , \tag{14}$$

where E_i is the size of the tolerance unit. It is standardized and determined by the expression:

$$E_i = 0,45(A_{min} . A_{max})^{\frac{1}{6}} + 0,001(A_{min} . A_{max})^{\frac{1}{2}} \tag{15}$$

where A_{min}, A_{max} are the limits of the size interval, in which A_i falls.

The calculated values of the tolerances are rounded, after which a check is performed to see if the inequality is fulfilled:

$$T_{\Sigma} \geq \sqrt{\left(\sum_{i=1}^{n} T_i \left|\xi_{ix}\right|\right)^2 + \left(\sum_{i=1}^{n} T_i \left|\xi_{iy}\right|\right)^2 + \left(\sum_{i=1}^{n} T_i \left|\xi_{iz}\right|\right)^2} \ . \tag{16}$$

In case of inequality failure, the roundings in the tolerances are corrected.

b) Probabilistic summation

In the theory of dimensional analysis [5] - [8], based on the theory of probabilities, it is assumed that, for $n \geq 4$ the probability for all constituent components to combine with their extreme values is a statistically impossible event. For this case, the expression for the tolerance of the closing component has the form:

$$T_\Sigma = t_\Sigma \sqrt{\sum_{i=1}^{n} T_i^2 \xi_i^2 \lambda_i'} \; . \qquad (17)$$

where $\lambda_i' = 1/t_i^2$ is the relative dispersion, which depends on the distribution law of the random variable A_i; ξ_i - the transmission coefficient of the constituent component relative to the closing component.

The coefficient λ_i' is also defined as the ratio of the root-mean-square deviation and the scattering field, as it follows:

$$\lambda_i' = \left(\frac{2\sigma_i}{\omega_i} \right)^2 .$$

For the normal law $\omega = 6\sigma$, where $\lambda_i' = 1/9$. For the law of equal probability $\sigma = (b-a)/2\sqrt{3}$ and $\omega = (b-a)$, whereupon $\lambda_i' = 1/3$. For the law of the triangle $\sigma = a/\sqrt{6}$ and $\omega = 2a$, whereat $\lambda_i' = 1/6$.

Under the assumption that all constituent components are distributed according to the normal law ($\lambda_i' = 1/9$) and a risk of waste of 0,27% ($t_\Sigma = 3$) is accepted, equation (17) takes the form:

$$T_\Sigma = \sqrt{\sum_{i=1}^{n} T_i^2 \xi_i^2} \; . \qquad (18)$$

In 3D dimensional chains, the tolerance of the closing component will be:

$$T_\Sigma = \sqrt{\sum_{i=1}^{n} T_i^2 \xi_{ix}^2 + \sum_{i=1}^{n} T_i^2 \xi_{iy}^2 + \sum_{i=1}^{n} T_i^2 \xi_{iz}^2} ;$$

$$T_\Sigma = \sqrt{\sum_{i=1}^{n} T_i^2 (\xi_{ix}^2 + \xi_{iy}^2 + \xi_{iz}^2)} . \qquad (19)$$

Considering the fact, that: $\xi_{ix}^2 + \xi_{iy}^2 + \xi_{iz}^2 = 1$, from the expression (19) we obtain:

$$T_\Sigma = \sqrt{\sum_{i=1}^{n} T_i^2} \; . \qquad (20)$$

In the design task in expression (20) the tolerances of the constituent components are replaced by the expression (13), which gives:

$$T_\Sigma = \beta_{cp} \sqrt{\sum_{i=1}^{n} E_i^2} \; . \qquad (21)$$

The average number of the tolerance units in the case of probabilistic summation of the tolerances is:

$$\beta_{cp} = \frac{T_\Sigma}{\sqrt{\sum_{i=1}^{n} E_i^2}} . \qquad (22)$$

The tolerances of the constituent components are determined by the calculated average number of tolerance units:

$$T_i = \beta_{cp} . E_i .$$

The calculated values of the tolerances are rounded, after which a check is performed to see if the inequality is fulfilled:

$$T_\Sigma \geq \sqrt{\sum_{i=1}^{n} T_i^2} \; . \qquad (23)$$

In case of inequality failure, the roundings in the tolerances are corrected.

C. *Determining the average values of the tolerance zones*

The average value of the tolerance zone defines the clustering center for the scatter of the corresponding dimension. The coordinate of this center is located on the dimension line and determines the deviation from the nominal size. It is accepted that the displacement of the average value of the tolerance zone with respect to the nominal size is denoted by EM. The relationship between the average values of the tolerance zones of the constituent components and of the closing component is analogous to the dependence (5):

$$EM_\Sigma = \sqrt{EM_{\Sigma x}^2 + EM_{\Sigma y}^2 + EM_{\Sigma z}^2} \; , \qquad (24)$$

where

$$EM_{\Sigma x} = \xi_{\Sigma x} EM_\Sigma ;$$

$$EM_{\Sigma y} = \xi_{\Sigma y} EM_\Sigma ; \qquad (25)$$

$$EM_{\Sigma z} = \xi_{\Sigma z} EM_\Sigma .$$

When solving the design task, the average value of the tolerance zone of the closing component is set, and those, of the constituent components must be determined. For this purpose, the average value for one of the components remains unknown, while for the others, the average values are chosen for constructive and (or) technological reasons. The unknown average value is determined by the equations (26):

$$EM_{\Sigma x} = \sum_{i=1}^{n} EM_{ix} = \sum_{i=1}^{n} EM_i \xi_{ix} ;$$

$$EM_{\Sigma y} = \sum_{i=1}^{n} EM_{iy} = \sum_{i=1}^{n} EM_i \xi_{iy} ; \qquad (26)$$

$$EM_{\Sigma z} = \sum_{i=1}^{n} EM_{iz} = \sum_{i=1}^{n} EM_i \xi_{iz} .$$

III. RESULTS AND DISCUSION

A. Example 1

Fig.5 shows the construction of a two-piece body with a gear. It is necessary to ensure during assembly the accuracy of the centre-to-centre distance, which is a closing component of the dimensional chain.

The initial construction data are:

$A_\Sigma = 160 \pm 0,1$ mm; $A_1 = 150$ mm;

$A_2 = 38,6$ mm; $A_3 = 100$ mm; $A_4 = 70$ mm.

To determine the coordinates of the basic points, the coordinate system must be defined. It is correct that the coordinate system coincides with the mounting base. It will also be used as a technological base for orienting the

workpiece during detail processing. Fig.5 shows the coordinate system and the coordinates of the basic points.
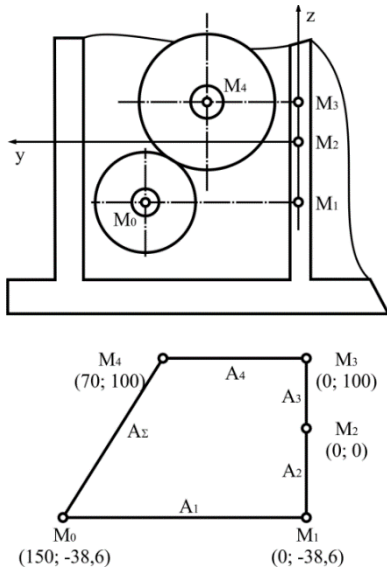
Fig. 5. Two-piece body with a gear.

a) Check for the nominal value of the closing component:

$A_{\Sigma y} = y_4 - y_0$;

$A_{\Sigma y} = 70 - 150 = -80$ mm;

$A_{\Sigma z} = z_4 - z_0$;

$A_{\Sigma z} = 100 - (-38{,}6) = -138{,}6$ mm;

$A_{\Sigma} = \sqrt{A_{\Sigma y}^2 + A_{\Sigma z}^2}$;

$A_{\Sigma} = \sqrt{(-80)^2 + 138{,}6^2} = 160{,}03$ mm.

b) Determining the tolerances of the constituent components

- *Magnitudes of the tolerance units:*

A₁=150 mm	dimensional interval 120 to 180 mm	E₁=2,52
A₂=38,6 mm	dimensional interval 30 to 50 mm	E₂=1,56
A₃=100 mm	dimensional interval 80 to 120 mm	E₃=2,17
A₄=70 mm	dimensional interval 50 to 80 mm	E₄=1,86

- *Transmission coefficients:*

$\xi_{1y} = \dfrac{A_{1y}}{A_1} = \dfrac{y_1 - y_0}{A_1} = \dfrac{0 - 150}{150} = -1$;

$\xi_{1z} = \dfrac{A_{1z}}{A_1} = \dfrac{z_1 - z_0}{A_1} = \dfrac{-38{,}6 - (-38{,}6)}{150} = 0$.

They are determined in a similar way for the other components:

$\xi_{2y} = 0;\ \xi_{3y} = 0;\ \xi_{4y} = 1;\ \xi_{2z} = 1;\ \xi_{3z} = 1;\ \xi_{4z} = 0$.

- *Average number of tolerance units in case of limited summation of the tolerances:*

$\beta_{cp} = \dfrac{200}{\sqrt{(E_1 + E_4)^2 + (E_2 + E_3)^2}} = 34{,}76$.

- *Dimensional tolerances:*

$T_1 = \beta_{cp}.E_1 = 34{,}76 \cdot 2{,}52 = 87{,}6$;
$T_2 = \beta_{cp}.E_2 = 34{,}76 \cdot 1{,}56 = 54{,}23$;
$T_3 = \beta_{cp}.E_3 = 34{,}76 \cdot 2{,}17 = 75{,}434$;
$T_4 = \beta_{cp}.E_4 = 34{,}76 \cdot 1{,}86 = 64{,}66$.

Rounded:

$T_1 = 88$ μm; $T_2 = 54$ μm; $T_3 = 75$ μm; $T_4 = 64$ μm.

Check:

$T_{\Sigma} \geq \sqrt{(T_1 + T_4)^2 + (T_2 + T_3)^2} = 199{,}36$.

- *Average number of tolerance units in probabilistic summation of the tolerances:*

$\beta_{cp} = \dfrac{200}{\sqrt{E_1^2 + E_2^2 + E_3^2 + E_4^2}} = 48{,}54$.

- *Dimensional tolerances:*

$T_1 = \beta_{cp}.E_1 = 48{,}54 \cdot 2{,}52 = 122{,}32$;
$T_2 = \beta_{cp}.E_2 = 48{,}54 \cdot 1{,}56 = 75{,}72$;
$T_3 = \beta_{cp}.E_3 = 48{,}54 \cdot 2{,}17 = 105{,}33$;
$T_4 = \beta_{cp}.E_4 = 48{,}54 \cdot 1{,}86 = 90{,}28$.

Rounded:

$T_1 = 120$ μm; $T_2 = 76$ μm; $T_3 = 105$ μm; $T_4 = 90$ μm.

Check:

$T_{\Sigma} \geq \sqrt{120^2 + 76^2 + 105^2 + 90^2} = 201{,}04$.

Correction:

$T_1 = 120$ μm; $T_2 = 80$ μm; $T_3 = 100$ μm; $T_4 = 90$ μm.

Check:

$T_{\Sigma} \geq \sqrt{120^2 + 80^2 + 100^2 + 90^2} = 197{,}23$.

c) *Average values* of the tolerance zones

It is accepted that: $EM_2 = EM_3 = EM_4 = 0$.

In this case from equations (26) we get:

$EM_{\Sigma y} = \displaystyle\sum_{i=1}^{n} EM_{iy} = EM_{1y}$; $EM_{\Sigma z} = \displaystyle\sum_{i=1}^{n} EM_{iz} = EM_{1z}$.

Given as an initial condition $EM_{\Sigma} = 0$, it follows that $EM_1 = 0$ as well.

d) Representation of dimensions by means of limit deviations

- *Limited summation*

$A_1 = 150 \pm 0{,}044$; $A_2 = 38{,}6 \pm 0{,}027$;
$A_3 = 100 \pm 0{,}037$; $A_4 = 70 \pm 0{,}032$.

- *Probabilistic summation*

$A_1 = 150 \pm 0{,}06$; $A_2 = 38{,}6 \pm 0{,}04$;
$A_3 = 100 \pm 0{,}05$; $A_4 = 70 \pm 0{,}045$.

B. Example 2

The developed theoretical model will be applied to solving the dimensional chain, presented in Fig.4. The design task is solved, having the closing component set

$A_\Sigma=70\pm0,1$ mm. The coordinates of all basic points are also set, with the exception of the point M_4. Thus, left for specifying is the dimension A_5, by means of which achieving the set dimension of the closing component will be ensured. For clarity, the solution to the problem is presented in Table 1.

TABLE 1 SPATIAL DIMENSIONAL CHAIN

		X	Y	Z	A_x	A_y	A_z	A	xx	xy	xz	
	M_0	70	55	5								
A_1	M_1	110	95	50	35	40	30	61,03	0,57	0,66	0,49	
A_2	M_2	85	115	70	-25	20	25	40,62	-0,62	0,49	0,62	
A_3	M_3	125	100	100	40	-15	40	58,52	0,68	-0,26	0,68	
A_4	M_4	35	45	80	-85	-55	-20	103,20	-0,82	-0,53	-0,19	
A_5	M_5	50	25	65	15	-20	-15	29,15	0,51	-0,69	-0,51	
A_S					-20	-30	60	70,00	-0,29	-0,43	0,86	
	A_{min}	A_{max}	A_{cp}	E_i	E_i*xx	E_i*xy	E_i*xz	E_i^2	T_1	T_2	T_1	T_2
									calculated		rounded	
A_1	50	80	63,25	1,86	1,06	1,22	0,91	3,45	43,94	93,52	45	90
A_2	30	50	38,73	1,56	0,96	0,77	0,96	2,44	36,96	78,66	35	80
A_3	50	80	63,25	1,86	1,27	0,48	1,27	3,45	43,94	93,52	45	90
A_4	80	120	97,98	2,17	1,79	1,16	0,42	4,72	51,43	109,46	50	110
A_5	18	30	23,24	1,31	0,67	0,90	0,67	1,71	30,95	65,87	30	65
					5,76	4,52	4,24	15,76				
					33,13	20,39	17,94	3,97				
							8,45					
		$T_S = 200$			$b_1 = 23,68$		$b_2 = 50,38$					

The algorithm for solving the task is as it follows:

1. The projections of the component A_5 along the three coordinate axes are determined, and, respectively, the coordinates of the point M_4:

$$A_{5x} = -A_{\Sigma x} + \sum_{i=1}^{4} A_{ix} = 15 ;$$

$$X_{M4} = X_{M5} - A_{5x} = 35 ;$$

$$A_{5y} = -A_{\Sigma y} + \sum_{i=1}^{4} A_{iy} = -20 ;$$

$$Y_{M4} = Y_{M5} - A_{5y} = 45 ;$$

$$A_{5z} = -A_{\Sigma z} + \sum_{i=1}^{4} A_{iz} = -15 ;$$

$$Z_{M4} = Z_{M5} - A_{5z} = 80 .$$

2. The nominal dimensions of the constituent components are determined:

$$A_i = \sqrt{A_{ix}^2 + A_{iy}^2 + A_{iz}^2} .$$

3. The transmission coefficients are found by formula (8).

4. The magnitudes of the tolerance units are determined, using formula (15).

5. The average number of tolerance units β_1 is determined by the max-min method - formula (14) and β_2 is found by the probabilistic method - formula (22).

6. The tolerances T_1 (for the max-min method) and T_2 (for the probabilistic method) are calculated according to formula (13), after which they are rounded.

7. The average values of the tolerance zones are defined. In this case, the tolerance of the closing component is symmetrically located with respect to the nominal dimension, which is convenient to accept also for the constituent components, i.e., $A_i = A_i \pm 1/2 T_i$.

IV. CONCLUSIONS

The presented mathematical model and methodology for analyzing and solving the tasks of dimensional analysis, confirm the raised thesis of a unified approach to considering the dimensional chains with parallel components, planar and spatial dimensional chains. It is irrefutably proven that dimensional chains with parallel components and planar dimensional chains are special cases of the spatial dimensional chains. There is no need for a different approach when solving them, as they are the different sides of the same whole.

Defining a dimensional chain by means of the coordinates of the basic points presents a new approach to revealing and solving it. The basic points are the points of contact between the surfaces of the connected elements in the structure. They are known in result of the automated product design. They are also used for production of parts by means of CNC machine tools. Presented this way, dimensional analysis becomes a compatible and natural element of the modern CAD-CAM systems.

REFERENCES

[1] L.S. Kravchenko, Dimensional Analysis For Design, Manufacture And Assembly. Harkov: NTU Press, 2009.

[2] S. Sabev and K. Chukalov, "Role of CAD systems in the context of Industry 4.0", International Scientific Journal "Industry 4.0", vol. 7, Issue 6, pp. 201-202, 2022.

[3] B. Sokolov, V. Skriabin, V. Shirtladze, N. Sorokina, N. Simanin, A. Repin, and O. Pimenova, Dimensional Analysis of Technological Processes in Automated Production. Starij Oskol: TNT Press, 2021.

[4] Z. Y. Chang, J. X. Yang, et al. Research on the Algorithm of Technological Dimension Chain Based on 3D Process Models, June 2011, DOI: https://doi.org/10.4028/www.scientific.net/AMM.58-60.1421.

[5] B. S. Balakchin, Foundations of Mechanical Engineering. Moscow: Masinostroene Press, 1982.

[6] G. K. Gatev, Dimensional Chains. Sofia: Technika Press, 1979.

[7] V. I. Georgiev, Identification of units of dimensional chains, 6th International Conference Machines, technologies, materials, July 22-26, 2009, Sofia, Bulgaria, 2009.

[8] M. G. Galkin, A. S.Smagin, Calculation of Technological Dimensional Chains by Probability Method. Proceedings of the 6th International Conference on Industrial Engineering (ICIE 2020). ICIE 2021. Lecture Notes in Mechanical Engineering. Springer, Cham. https://doi.org/10.1007/978-3-030-54817-9_6.

Purposeful dimensioning of details, processed on CNC machine tools

Silviya Salapateva
Faculty of Mechanical Engineering
Technical University of Sofia, Plovdiv Branch
Plovdiv, Bulgaria
sisisal@tu-plovdiv.bg

Abstract. **The choice of technologies for mechanical processing of details is closely related to the requirements toward dimensional accuracy, shape and mutual position of their surfaces, which are set by the constructor. Wrong dimensioning in many cases leads to complications and raising the cost of mechanical processing. The present paper makes a comparative analysis of different options for dimensioning a stepped shaft, machined on a CNC lathe. Recommendations for purposeful dimensioning of similar details are made based on the above-mentioned analysis.**

Keywords: Mechanical engineering, dimensioning, CNC machine tools.

I. Introduction

Dimensioning is an important and responsible stage in creating products of mechanical engineering. It follows a system of principles and procedures, related to the function of the different detail surfaces, to the place and role of the detail in the assembled unit and the product, to its existing kinematic, dynamic and dimensional relationships [1], [2], [3]. At the same time, the detail construction should comply with the manufacturability requirements in order to be produced at the lowest possible production costs [4]. All these requirements are met at the stage of technical preparation for production.

In the process of technological preparation, when the technologies for the implementation of the individual machining operations are under development, in certain cases it is necessary to redimension the details and so-called technical sizing is performed. Most frequently this is required when the dimensional bases, chosen by the designer, cannot be used as technological bases, or when very complex and expensive adjustments are needed to make the technological and the design bases compatible.

The replacement of the designer dimensioning by a technological one in all cases increases the requirements for the accuracy of processing. This is due to the fact, that the dimensions set by the designes, which must ultimately be achieved during processing, are the closing

components of the technological dimensional chains. Therefore, the tolerances of the technological dimensions are smaller than those, of the design ones [5], [6].

In a number of cases, as a means of reconciling the design bases with the technological ones, processing of the design base is applied, with the same fixing of the workpiece as for processing of the other surfaces. The approach is known as the principle of using tuning technological bases [6], [7].

The use of tuning technological bases provides another advantage as well. It is proved that the dimensions from a tuning technological base are achieved with higher accuracy than those, set by a design technological base [8]. This is explained by the existence of a correlation between the sizes of the design technological base, processed in one establishment of the part. Then the special case of the summation theorem of the variances of a set of random variables, according to which the variance of the closing component of the dimensional chain is a sum of the variances of the constituent components, is not applicable. The correlation between the constituent units should also be taken into account [9], [10]. This fact gives reasons to use technological dimensioning from tuning technological bases when working with CNC machine tools [11]. In a number of cases this is necessary due to the connection of the coordinate origin for dimensioning with certain surfaces of the part, which are processed at the beginning of the operation and are different from the design base.

II. Materials and methods

When machining workpieces on CNC lathes, the coordinate system of the part is most often associated with the right-hand face of the workpiece. This coordinate origin is translated relative to the machine coordinate origin, usually associated with the spindle face. To materialize the coordinate system of the workpiece after its fixing, the first transition is intended to process the face of the workpiece, which will be the

technological base for the rest of the processed surfaces. Thus, the connection between the coordinate systems of the part and the machine is also ensured.

Determining the position of the remaining front surfaces with respect to the coordinate origin can be performed in different ways. Fig. 1 presents the possible dimensioning of a model detail.
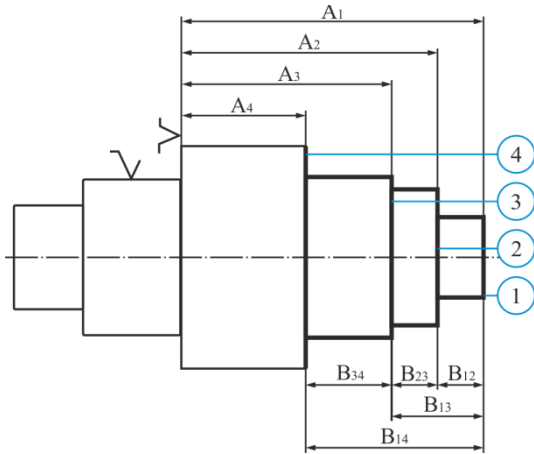
Fig. 1. Dimensioning of a stepped shaft for processing parts on a CNC lathe ($A_1 = 31^{+0,1}$; $A_2 = 26^{+0,1}$; $A_3 = 22^{+0,1}$; $A_4 = 13^{+0,1}$).

Four front surfaces are processed. By processing face 1, the position of the coordinate system of the workpiece with respect to the face of the chuck is set. The distance between them is A_1. The position of the remaining three faces can be determined in three ways:

- From a design technological base (the face of the chuck) by the dimensions A_2, A_3 and A_4;
- From a tuning technological base (the face of the part) by the dimensions B_{12}, B_{13} and B_{14};
- From a tuning technological base (the face of the part) by the chain dimensions B_{12}, B_{23} and B_{34}.

A database, obtained in result of machining a batch of 41 details on a CNC lathe will be used to compare and evaluate the three dimensioning options [12] - [15]. In the sequence for performing the operation, the transitions for turning the cylindrical surfaces are alternated with the transitions for trimming their adjacent faces.

The nature of the technological process is represented by the scatter diagrams of the coordinate dimensions A, shown in Fig. 2.

The following statistical information can be obtained from the database of the coordinate dimensions A, set by a design technological base:

- Adequate regression equations, representing the influence of the systematic factors on dimensional scattering;
- Instantaneous scatter fields ω, representing the influence of the random factors on dimensional scattering;
- Total scatter fields $ω_Σ$, illustrating the influence of random and systematic factors on dimensional scattering;
- Correlation coefficients ρ, representing the interdependence of the coordinate dimensions.
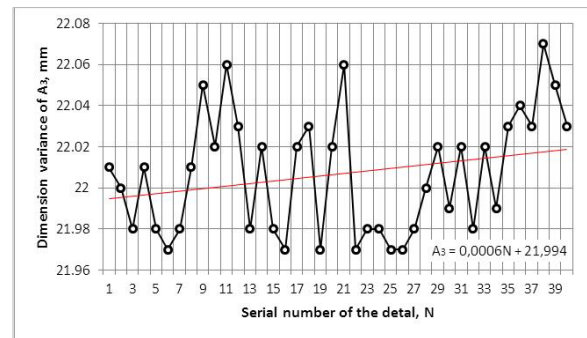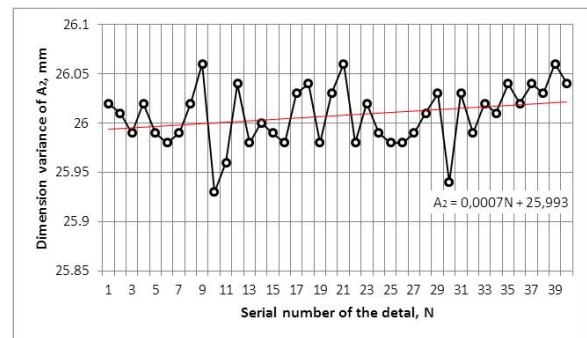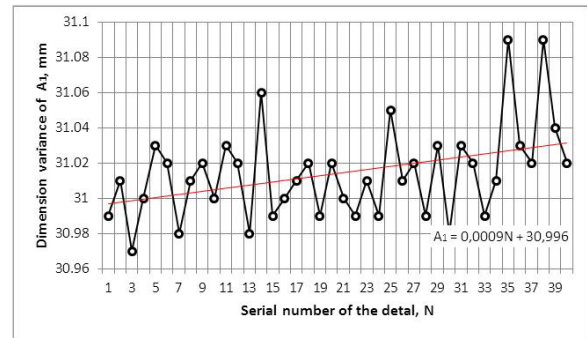
Fig. 2. Scatter diagrams of the dimensions from a design technological base

The regression equations are determined by the least square method. Microsoft Office Excel is used for the purpose. For each of the coordinate dimensions, they are presented in Fig.2.

The instantaneous scatter field of the dimensions around the regression equation is defined by the variance S^2:

$$S^2 = \frac{\sum_{i=1}^{N}(A_i - \bar{A}_i)^2}{N-1}, \qquad (1)$$

$$\bar{A}_i = \frac{\sum_{i=1}^{N} A_i}{N},\qquad(2)$$

where A_i is the measured dimension of the detail with a serial number i, $\bar{A}_i$ - size mean from the regression equation at N = i; N – total number of measured details.

For a known variance, the instantaneous scatter field ω is found by the expression:

$$\omega = 2Sk_{\alpha,\gamma,N},\qquad(3)$$

where $S = +\sqrt{S^2}$ is the root-mean-square deviation; $k_{\alpha,\gamma,N}$ – statistical coefficient of scattering, which is tabularly determined from the number N of measured details and the accepted significance level α and confidence probability γ.

The total scatter field ω_Σ is defined as the sum of the instantaneous scatter field and the change of the average value of the dimension $\Delta\bar{A}$ caused by the systematic factors. If the regression equation is presented in the general form $\bar{A} = \tilde{a} + \tilde{b}N$, the change in the mean value of the dimension is found by the expression $\Delta\bar{A} = \tilde{b}N$. In that:

$$\omega_\Sigma = \omega + \tilde{b}N.\qquad(4)$$

The coefficients of correlation are determined using Microsoft Office Excel.

Analogous statistical information can be obtained for dimensioning from a tuning technological base. For this purpose dimensions B are defined as derivatives of dimensions A:

$$\begin{aligned}
B_{12} &= A_1 - A_2;\\
B_{13} &= A_1 - A_3;\\
B_{14} &= A_1 - A_4;\qquad(5)\\
B_{23} &= A_2 - A_3;\\
B_{34} &= A_3 - A_4.
\end{aligned}$$

The scatter diagrams of the dimensions from a tuning technological base are presented in Fig. 3.

It is noteworthy that for these dimensions the influence of systematic factors is very weak. The regression equations for the average value of the dimensions are nearly parallel to the abscissa. The coefficients $\tilde{b}$ in the regression equations are statistically insignificant and the total scatter field is equal to the instantaneous one. Formula (3) is used for its determination.
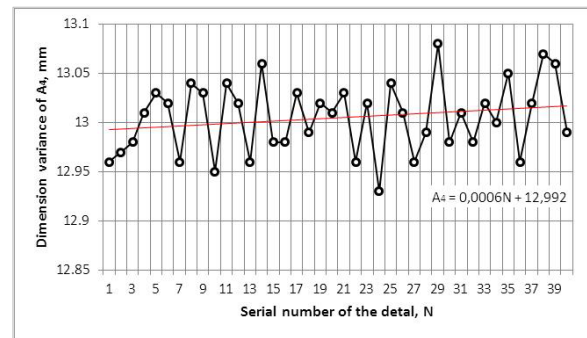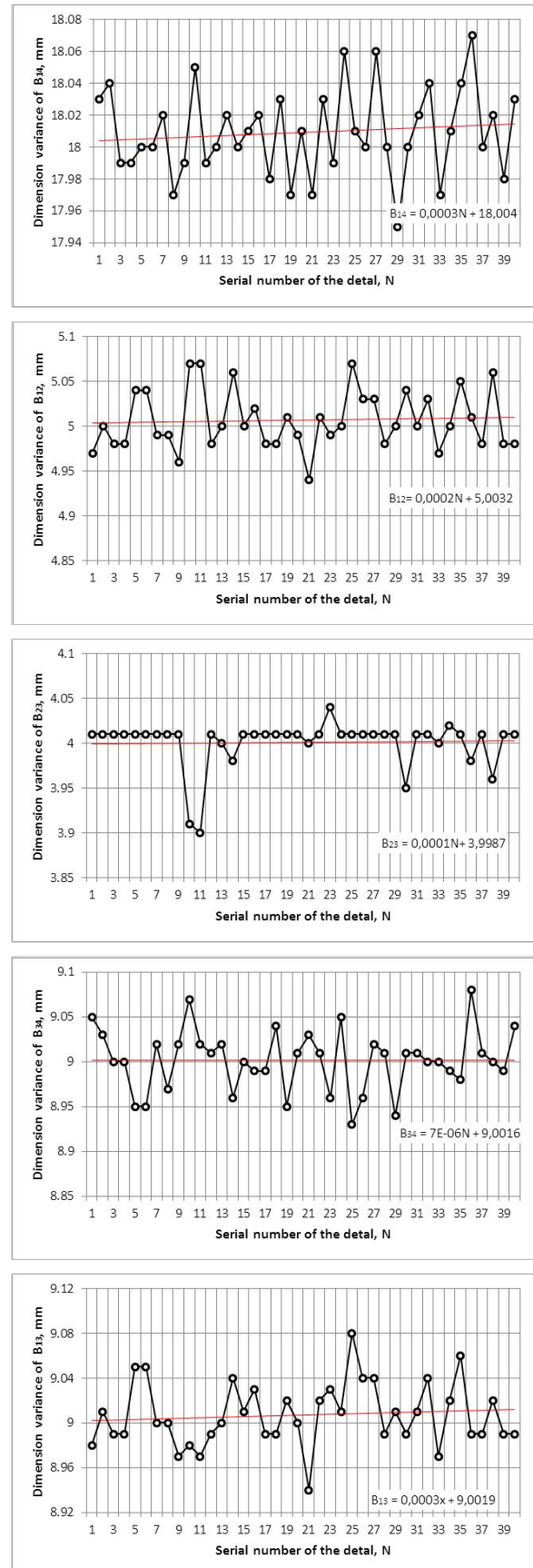

Fig. 3. Scatter diagrams of the dimensions from a tuning technological base.

III. RESULTS AND DISCUSION

The obtained results from the statistical analysis of the technological process are presented in Table 1.

TABLE 1 STATISTICAL CHARACTERISTICS OF THE TECHNOLOGICAL PROCESS

Dimension	Characteristic			
	S^2	S	ω	ω_Σ
A_1	56.10^{-5}	0,0242	0,19	0,227
A_2	86.10^{-5}	0,0294	0,231	0,26
A_3	77.10^{-5}	0,0278	0,219	0,243
A_4	121.10^{-5}	0,0347	0,273	0,298
B_{12}	108.10^{-5}	0,0328	0,258	0,258
B_{13}	81.10^{-5}	0,0284	0,223	0,223
B_{14}	76.10^{-5}	0,0275	0,217	0,217
B_{32}	72.10^{-5}	0,0267	0,212	0,211
B_{34}	119.10^{-5}	0,0345	0,271	0,271

From the scatter diagrams and regression equations it can be concluded that there is a systematic displacement of the centre of clustering in the direction of an increase in the average size for the dimensions from a design technological base. This is an indication that the dimensional tool wear is influencing on the process of dimensioning. Such an influence is not observed when dimensioning from a tuning technological base is performed.

There is a correlation between the dimensions of a design technological base, although not very pronounced. The correlation coefficients range from 0,36 to 0,66 (Table 2 and Fig.4).

TABLE 2 COEFFICIENTS OF CORRELATION BETWEEN THE DIMENSIONS A

Coefficients of correlation				
$\rho_{A_1A_2}$	$\rho_{A_1A_3}$	$\rho_{A_1A_4}$	$\rho_{A_2A_3}$	$\rho_{A_3A_4}$
0,35844	0,48973	0,65626	0,60832	0,46508
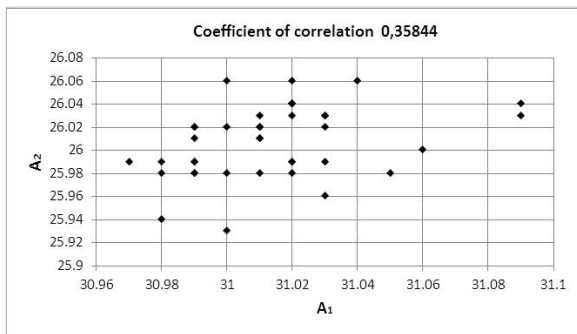
a. Correlation matrix between A_1 and A_2
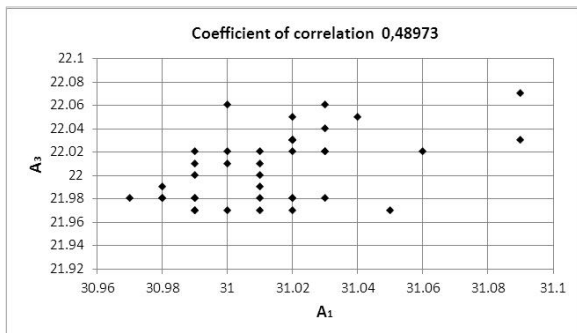
b. Correlation matrix between A_1 and A_3
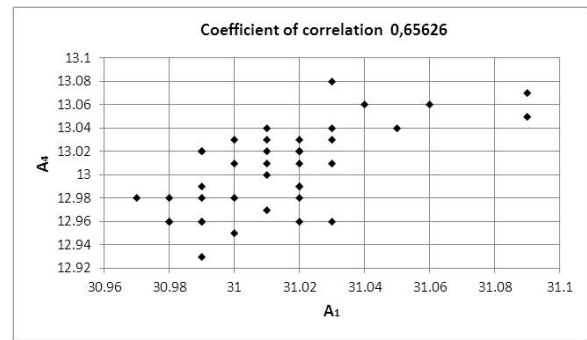
c. Correlation matrix between A_1 and A_4
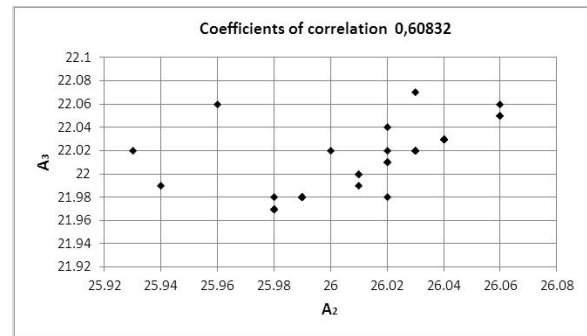
d. Correlation matrix between A_2 and A_3
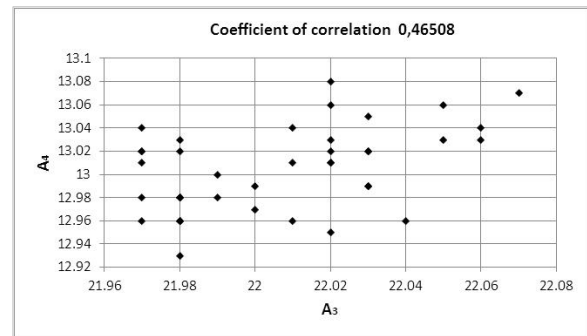
f. Correlation matrix between A_3 and A_4

Fig. 4.   Correlation matrices between dimensions A

The correlation is due both to the same for all axial dimensions error, arising from fixing the part in the chunk, and to the relatively equal intensity of dimensional tool wear. As a result of the correlation, the dimensions from a tuning technological base have less or comparable scattering to that, of the dimensions from a design technological base. The dimension B_{14} can be considered as an example of the influence of the correlation. From equation (5) it follows that this dimension is the closing component in a dimensional chain with constituent components the dimensions A_1 and A_4. The root-mean-square deviation of B_{14} will be found by the expression:

$$S_{14} = +\sqrt{S_1^2 + S_4^2 - 2\rho_{A_1A_4}S_1S_4} . \qquad (6)$$

If there was no correlation between the dimensions A_1 and A_4 ($\rho_{A_1A_4} = 0$), equation (6) would yield:

$$S_{14} = \sqrt{0,000585 + 0,00121} = 0,0424 .$$

Correspondingly $\omega_{B_{14}} = 2.3,936.0,0424 = 0,334$ mm.

With established correlation ($\rho_{A_1A_4} = 0,656$) the result will be:

$S_{14} = 0,0263$.

Correspondingly, $\omega_{B_{14}} = 2.3,936.0,0263 = 0,207$ mm.

This result is close to that, established by dimensional control and reflected in Table 1 ($\omega_{B_{14}} = 0,217$ mm).

The presented example confirms the role of the correlation in increasing the accuracy of the dimensions from a tuning technological base. Having in mind that their accuracy is not affected by the dimensional tool wear, it is reasonable to recommend to perform dimensioning from a tuning technological base.

The level of scattering of all dimensions in the particular case is compatible in magnitude. Statistically, their variances are equal. This hypothesis is confirmed by the Cochran G_{max} test:

$G_{max} = \dfrac{S_{max}^2}{\sum\limits_{i=1}^{9} S_i^2} = 0,151$, which is less than the critical

value $G_{0,05;\ 8;\ 40}$.

IV. CONCLUSIONS

The conducted research gives grounds for the following conclusions regarding the processing of stepped shafts on CNC lathes:

- Influence of both random and systematic factors is observed when dimensioning shafts in axial direction from a design technological base, which has a negative impact on the accuracy of processing;
- As a result of the same influence of the error from detail fixing and dimensional tool wear on all dimensions, processed on the same installation, a correlation is observed between the dimensions of a design technological base;
- The presence of a correlation dependence between the dimensions, obtained from a design technological base positively affects the accuracy of the dimensions, obtained from a tuning technological base;
- When dimensioning from a tuning technological base, no significant influence of the dimensional

tool wear on the accuracy of the dimensions is observed.

REFERENCES

[1] B. S. Balakchin, Foundations of Mechanical Engineering. Moscow: Masinostroene Press, 1982.

[2] A. S. Ymnikova, A. A. Malikova, Fundamentals of mechanical engineering technology. Moscow: Infra – Ingeneria Press, 2020.

[3] E. E. Tisthenko, M. A. Tamarkin, A. S. Melnikov, Scientific foundations of mechanical engineering technology. Moscow: EBS Lan Press, 2018.

[4] S. T. Sabev and V. J. Bakardzhiev, Application of Taguchi method for analyzing the dimensional accuracy in 3D printing, Eds., Science, Technology, Innovation, Business 2022, pp. 145-148, Bulgaria, Plovdiv, 2022.

[5] G. K. Gatev, Dimensional Chains. Sofia: Technika Press, 1979.

[6] L. S. Kravchenko, Dimensional Analysis For Design, Manufacture And Assembly. Harkov: NTU Press, 2009.

[7] B. Sokolov, V. Skriabin, V. Shirtladze, N. Sorokina, N. Simanin, A. Repin and O. Pimenova, Dimensional Analysis of Technological Processes in Automated Production. Starij Oskol: TNT Press, 2021.

[8] G. Gatev and V. Georgiev, Regarding the expediency of using the tuning technological bases, Sofia: Technika Press, 1999.

[9] V. I. Georgiev, Identification of units of dimensional chains, 6th International Conference Machines, technologies, materials, Sofia, Bulgaria, 2009.

[10] M. G. Galkin and A. S.Smagin, Calculation of Technological Dimensional Chains by Probability Method. Proceedings of the 6th International Conference on Industrial Engineering (ICIE 2020). ICIE 2021. Lecture Notes in Mechanical Engineering. Springer, Cham. https://doi.org/10.1007/978-3-030-54817-9_6.

[11] P. P. Kasabov and S. T. Sabev, Study of the stability during boring of an internal rotating surface on a CNC lathe, Eds., Science, Technology, Innovation, Business 2022, pp. 153-156, 2022, Bulgaria, Plovdiv, 2022.

[12] Z. Y. Chang, J. X. Yang, et al. Research on the Algorithm of Technological Dimension Chain Based on 3D Process Models, June 2011, DOI: https://doi.org/10.4028/www.scientific.net/AMM.58-60.1421.

[13] H. Long, X. Luo, et. al. The Analysis and Application of Installation Tolerances in Prefabricated Construction Based on the Dimensional Chain Theory. Buildings. 2023; 13(7):1799. https://doi.org/10.3390/buildings13071799.

[14] D. Dimitrov, T. Szecsi, Machining accuracy on CNC lathes under the lack of unity of the process, 48th CIRP Conference on MANUFACTURING SYSTEMS - CIRP CMS 2015, Science Direct, Procedia CIRP 41, pp.824–828, 2016.

[15] M. Wang, X. Liu, et al. Research on assembly tolerance allocation and quality control based on fuzzy reliability, Proceedings of the Institution of Mechanical Engineers Part C Journal of Mechanical Engineering Science 1989-1996 (vols 203-210) December 2016, DOI: 10.1177/0954406215615909.

Recycling of Textile Waste Into Sound-Absorbing Acoustic Plates

Kristaps Siltumens
Latvia University of Life Sciences and Technologies
Scientific Laboratory of Forest and Water Resources
Jelgava, Latvia;
University of Latvia
Riga, Latvia
kristaps.siltumens@lbtu.lv

Inga Grinfelde
Latvia University of Life Sciences and Technologies
Scientific Laboratory of Forest and Water Resources
Jelgava, Latvia
inga.grinfelde@lbtu.lv

Ginters Znots
RISEBA University of Applied Sciences
Riga, Latvia
gintersznots@gmail.com

Rudolfs Golubovs
Riga Technical University
Riga, Latvia
rudolfsgolubovs@gmail.com

Raitis Brencis
Latvia University of Life Sciences and Technologies
Jelgava, Latvia
raitis.brencis@lbtu.lv

Abstract. **The textile waste problem is a significant concern both in Latvia and globally. The textile industry, particularly the fashion industry, is considered one of the most polluting industries, generating a substantial amount of waste. Worldwide, the production of textiles has been on the rise due to population growth and increased consumption, leading to a significant increase in textile waste generation. The management of textile waste is crucial for ensuring sustainability and minimizing environmental impacts. Recycling and reusing textile waste are essential strategies for implementing a circular economy model and reducing the environmental hazards associated with textile production and disposal. One way we can reduce the amount of textile waste in landfills is to create new products from this waste by intercepting it before it ends up in landfills. The aim of this study is to develop sound-absorbing acoustic plates using textile waste. Experiments with textile waste started in January 2024, beginning with the acquisition of textile waste. The textile obtained for the experiment was sourced from the waste management company in Latvia's North Vidzeme, which collects clean textile waste from residents. In the next stages, textile waste was shredded, and slabs were formed using a compactor. Textile processing into a finer fraction was carried out using an industrial shredding machine. A mixture of water-based glue, an isotonic solution (containing boric acid and sodium borate), PVA glue, and sodium bicarbonate was used as a binder for making the plates. The created plates were tested for acoustic properties in the laboratory. The absorption coefficient of the acoustic plate at the best performance level (1250 - 3500 Hz) ranged from 1.14 to 1.6. This is consistent with the fact that non-separated textiles were used.**

Keywords: Circular economy, Sound-absorbing materials, Sustainable textile, Waste recycling.

I. INTRODUCTION

In an era prioritizing sustainability, innovative solutions are emerging to recycle waste materials into valuable resources. One focal point is the recycling of textile waste, offering dual benefits: waste reduction and resource optimization [1]. Among the myriad applications of recycled textiles, the conversion into sound-absorbing acoustic panels stands out as a promising option with substantial environmental and practical impacts [2].

Textile waste, comprising discarded clothing, upholstery, and production remnants, presents a significant challenge to global waste management systems [3]. Given that the textile industry ranks among the world's largest waste producers, finding effective ways to repurpose these materials is imperative for minimizing their environmental footprint [4]. At the same time, demand has increased for noise control solutions across various environments – from office buildings to education and music studios as well as industrial settings. This underscores the necessity for innovative acoustic materials [5], [6], [7].

Materials employed in the construction industry for the purpose of thermal insulation and noise management predominantly consist of inorganic and synthetic compounds, including glass wool, stone wool, and

polystyrene. Although these materials provide a low level of thermal conductivity and display remarkable sound absorption characteristics, the environmental repercussions stemming from their manufacturing procedures can be substantial. Furthermore, depending on variables such as fiber dosage, dimensions, and resilience, they may also have an impact on human health and overall well-being [8], [9].

This article delves into the recycling of textile waste into sound-absorbing acoustic plates, elucidating technological advancements, environmental benefits, and practical applications of this pioneering approach. Through a comprehensive examination, our aim is to underscore the potential of textile waste recycling as a sustainable solution to both environmental challenges and acoustic requirements across diverse fields.

The aim of this study is to develop sound-absorbing acoustic plates using textile waste.

II. MATERIALS AND METHODS

The textile waste for the experiment was obtained from the Latvian North Vidzeme Waste Management Company, which collects clean textile waste from residents. This textile waste was sorted to avoid the various metal, plastic and solid non-textile admixtures that are sometimes found in textile clothing (see fig. 1).

Fig. 1. Sorting of textile waste

After grading operations, the textile waste was shredded. They were shredded into fractions ranging from 5 to 20 mm, an industrial shredder was used to shred the textile waste - Shred-Tech ST-25 (see fig. 2). The Industrial Shredder is equipped with a set of sturdy and resilient blades that have been specifically engineered to penetrate effortlessly through various products and materials. These formidable blades possess the capability to effortlessly disintegrate voluminous loads, reducing the materials into fragments. Each blade boasts a diameter of 19,7 cm, ensuring an ample amount of robustness to effectively shred textile.
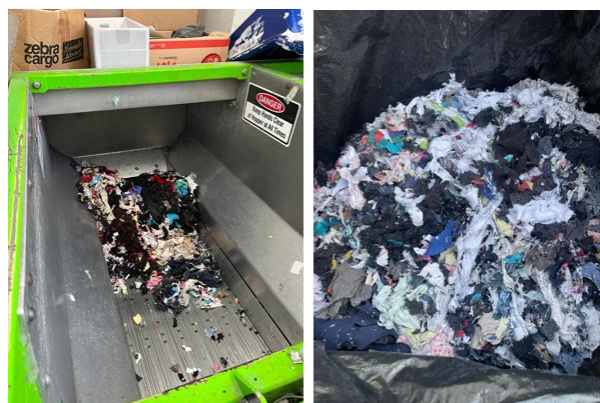
Fig. 2. Shredding of textile waste

The shredded textile was then mixed with a binder in the ratio Binder : textile = 1 : 3 (see fig. 3). A mixture of water-based glue, an isotonic solution (containing boric acid and sodium borate), PVA glue, and sodium bicarbonate was used as a binder for making the plates. The following binder proportions were used – 0.2 (water-based glue) : 0.05 (isotonic solution) : 0.6 (PVA glue) : 0.02 (sodium bicarbonate).

Fig. 3. Mixing of binders and textiles

To create the plate, a wooden mould measuring 150 x 250 mm and 30 mm thick was made and the mass was laid into it. Finally, a wooden lid was placed on the mould and pressed together with a vise. The drying time of the plate was 24 hours. After the binder had dried, the mould was opened and the plate removed (see fig. 4).

Fig. 4. Sound-Absorbing Acoustic Plate

In order to assess the sound absorption capabilities of textile acoustic palates, we utilized the AFD 1000 – Sound Absorption Tube Set (see fig. 5), an impedance tube manufactured for industrial purposes. This particular equipment was specifically designed to accurately determine the sound absorption coefficients across a frequency range that extends from 100 Hz to 4000 Hz. The initial stage of the sample measurement process involved the preparation of the textile acoustic panels. To ensure consistency in the testing, circular cutouts with diameters of 40 mm and 100 mm were obtained, thus guaranteeing uniformity in both size and shape (see fig. 6). Subsequently, the prepared circular cutouts were meticulously positioned within the impedance tube setup. Particular attention was given to ensuring precise alignment and secure placement of the sample within the testing chamber, thereby minimizing any potential sources of error. Once the panels had been securely positioned, the testing procedure commenced. This involved subjecting the panels to controlled sound waves that spanned the specified frequency range of 100 Hz to 4000 Hz. The impedance tube was responsible for generating these sound waves, effectively simulating real-life acoustic conditions.

Fig.5. Sound Absorption impedance tube [10]

Throughout the testing process, the impedance tube accurately measured the sound absorption characteristics of the samples at various frequencies within the designated range. This meticulous measurement process facilitated the acquisition of precise absorption coefficient values. Stringent efforts were made to maintain consistent testing conditions and mitigate any external factors that could potentially impact the results during the sample measurement process. This rigorous approach ensured the reliability and validity of the sound absorption data obtained from the impedance tube testing.

Fig. 6. Circular cutouts with diameters of 40 mm and 100 mm

Statistical data analysis was performed using the Krustkal-Wallis test. We investigated the sound absorption properties of various samples using Nemenyi's procedure for multiple pairwise comparisons. The data presented in the results offers a descriptive overview of the sample frequencies, sum of ranks, and mean of ranks for each group, providing insights into their relative performance in sound absorption.

The Kruskal-Wallis test is used to compare two or more independent samples of equal or different sizes. It helps to determine whether a sample is drawn from the same distribution, thus grouping the data. This technique was used to analyse sound absorption coefficient and frequency distribution data for samples.

Before analysing the data, the frequencies at which the sound absorption coefficient was measured were divided into three parts. The first part - low frequencies (100-250 Hz), the second part - medium frequencies (315-1000 Hz), and the third part high frequencies (1250-4000 Hz). This was done in order to compare the data and results in a more accurate and transparent way.

The experimental data were compared with the sound absorption coefficients of rockwool and mineral wool. The sound absorption coefficients of mineral wool at different frequencies were obtained from a study published by Jan Sikora and Jadwiga Turkiewicz [11]. The absorption coefficients of rockwool at different frequencies were obtained from Rockwool Ltd, a rock wool manufacturing company [12].

III. RESULTS AND DISCUSSION

The results show sound absorption coefficients at different frequencies in the range from 100 to 4000 Hz. The highest sound absorption coefficient is observed at 3000 Hz, where it is 0.16. The lowest sound absorption coefficient is observed at 100 Hz, where it is 0. The best sound absorption performance of the developed plate is at frequencies between 1250 and 3500 Hz (see Fig. 7)
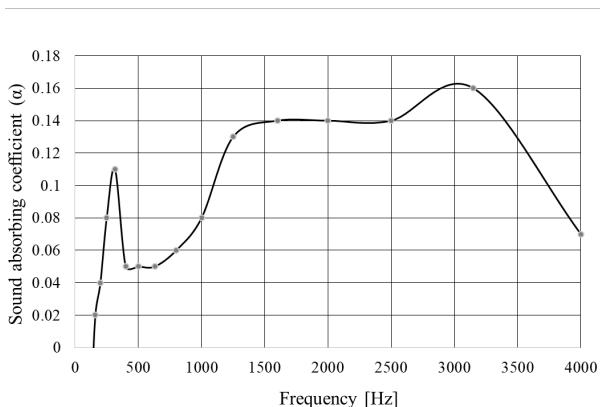
Fig. 7. Sound absorption coefficients for sound - absorbing acoustic plate at frequencies from 100 to 4000 Hz

Nemenyi's procedure for multiple pairwise comparisons for low frequencies (100-250 Hz). The following results were obtained (see Table 1):

- Sound-Absorbing Acoustic Plate: This sample has a frequency of 5, resulting in a sum of ranks of 5 and a mean of ranks of 1.0. Sample Sound-Absorbing Acoustic Plate belongs to Group A.
- Mineral wool: With a frequency of 5, Sample Mineral wool accumulates a sum of ranks of 12 and a mean of ranks of 2.4. It is associated with both Groups A and B.
- Rock wool: Sample Rock wool, also with a frequency of 5, has the highest sum of ranks at 13, translating to a mean of ranks of 2.6. It belongs exclusively to Group B.

TABLE 1 MULTIPLE PAIRWISE COMPARISONS USING NEMENYI'S PROCEDURE (TWO-TAILED TEST) FOR SOUND ABSORPTION COEFFICIENTS AT LOW FREQUENCIES (100-250 HZ)

Sample	Frequency	Sum of ranks	Mean of ranks	Groups	
Sound-Absorbing Acoustic Plates	5	5.000	1.000	A	
Mineral wool	5	12.000	2.400	A	B
Rockwool	5	13.000	2.600		B

A box plot of the sound absorption coefficients at low frequencies (100-250 Hz) can be seen in Fig. 8.
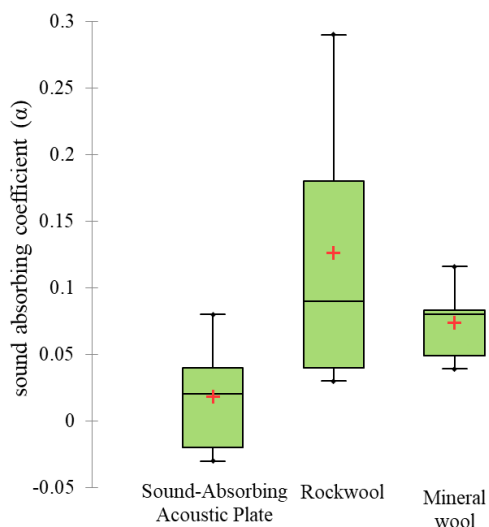
Fig. 8. Sound absorption coefficients at low frequencies (100-250 Hz)

Nemenyi's procedure for multiple pairwise comparisons for medium frequencies (315-1000 Hz). The following results were obtained (see Table 2):

- Sound-Absorbing Acoustic Plate: This sample has a frequency of 6, resulting in a sum of ranks of 6 and a mean of ranks of 1.0. Sample Sound-Absorbing Acoustic Plate belongs to Group A.
- Mineral wool: With a frequency of 6, Sample Mineral wool accumulates a sum of ranks of 12 and a mean of ranks of 2.0. It is associated with both Groups A and B.
- Rock wool: Sample Rock wool, also with a frequency of 6, has the highest sum of ranks at 18, translating to a mean of ranks of 3.0. It belongs exclusively to Group B.

TABLE 2 MULTIPLE PAIRWISE COMPARISONS USING NEMENYI'S PROCEDURE (TWO-TAILED TEST) FOR SOUND ABSORPTION COEFFICIENTS AT MEDIUM FREQUENCIES (315 - 1000 HZ)

Sample	Frequency	Sum of ranks	Mean of ranks	Groups	
Sound-Absorbing Acoustic Plates	6	6.000	1.000	A	
Mineral wool	6	12.000	2.000	A	B
Rockwool	6	18.000	3.000		B

A box plot of the sound absorption coefficients at low frequencies (315-1000 Hz) can be seen in Fig. 9.

Fig. 9. Sound absorption coefficients at medium frequencies (315 - 1000 Hz)

Nemenyi's procedure for multiple pairwise comparisons for high frequencies (1250-4000 Hz). The following results were obtained (see Table 3):

- Sound-Absorbing Acoustic Plate: This sample has a frequency of 6, resulting in a sum of ranks of 6 and a mean of ranks of 1.0. Sample Sound-Absorbing Acoustic Plate belongs to Group A.
- Mineral wool: With a frequency of 6, Sample Mineral wool accumulates a sum of ranks of 12 and a mean of ranks of 2.0. It is associated with both Groups A and B.
- Rock wool: Sample Rock wool, also with a frequency of 6, has the highest sum of ranks at 18, translating to a mean of ranks of 3.0. It belongs exclusively to Group B.

TABLE 3 MULTIPLE PAIRWISE COMPARISONS USING NEMENYI'S PROCEDURE (TWO-TAILED TEST) FOR SOUND ABSORPTION COEFFICIENTS AT HIGH FREQUENCIES (1250 - 4000 HZ)

Sample	Frequency	Sum of ranks	Mean of ranks	Groups	
Sound-Absorbing Acoustic Plates	6	6.000	1.000	A	
Mineral wool	6	12.000	2.000	A	B
Rockwool	6	18.000	3.000		B

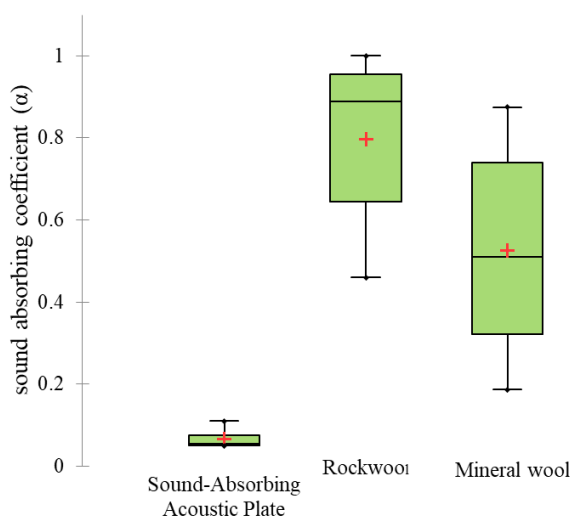A box plot of the sound absorption coefficients at low frequencies (315-1000 Hz) can be seen in Fig. 10.
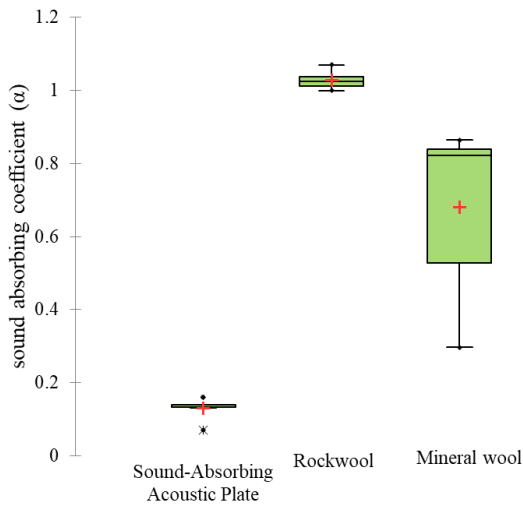

Fig. 10. Sound absorption coefficients at high frequencies (1250 - 4000 Hz)

Sound absorption coefficients for sound-absorbing plates made of textile waste were investigated in several studies. Rubino et al. found that composite panels made of 100% wool waste fibres had absorption coefficients higher than 0.5 from 500 Hz and higher than 0.9 from 1 kHz on [2]. Vejelis et al. examined waste from the production of woollen yarns and found that soft boards made from this waste had sound absorption coefficients ranging from 0.4 to 0.9 at a board density of 40 kg/m3 [13]. While in our study, at the best performance level (1250 - 3500 Hz), the absorption coefficient ranged from 1.14 to 1.6. This is consistent with the fact that non-separated textiles were used.

IV. CONCLUSIONS

This study investigated the sound absorption properties of the developed plates, highlighting their effectiveness in attenuating sound waves at different frequencies. Our results show that the material composition, density and surface structure have a significant influence on the sound absorption performance. Porous materials such as rock wool and mineral wool showed better sound absorption performance over a wide range of frequencies than our sound absorbing board. The developed plate needs to be refinished, its porosity and surface texture improved and the properties of the binder used improved. These improvements have the potential to bring the results much closer to good sound absorbing materials.

Furthermore, the results obtained underline the importance of taking into account environmental factors and specific requirements when selecting materials for sound absorption. Future research could explore new sustainable material formulations and advanced manufacturing techniques to further improve sound absorption performance.

By adopting a proactive stance towards the sustainable recycling of textile waste, we can open up opportunities for innovation, job creation and societal development. Continued research and concerted efforts are imperative to promote systemic change and a more sustainable future for the textile industry and beyond.

V. ACKNOWLEDGMENTS

VI. REFERENCES

[1] M. Shamsuzzaman, I. Hossain, T. Saha, A. Roy, D. Das, M. T. Ahmed and S. K. Podder, Waste Management in Textile Industry. Advanced Technology in Textiles, 2023, pp. 279-299.

[2] S. Vėjelis, S Vaitkus, A. Kremensas, A. Kairytė and J. Šeputytė-Jucikė, Reuse of Textile Waste in the Production of Sound Absorption Boards, Materials, 2023, vol. 16, issue 5.

[3] M. N. Pervez, M. I. H. Mondal, Y. Cai, Y. Zhao and V. Naddeo, 21 - Textile waste management and environmental concerns. Fundamentals of Natural Fibres and Textiles, The Textile Institute Book Series, 2021, pp. 719-739

[4] M. L. Tummino, A. Varesano, G. Copani and C. Vineis, A Glance at Novel Materials, from the Textile World to Environmental Remediation. Journal of Polymers and the Environment, 2023, vol. 31, pp. 2826-2854.

[5] F. Salazar-Fierro, C. Luza1, M. Revelo and J. Castañeda, Noise Pollution Control using Internet of Things (IoT) solutions. Innovation & Development in Engineering and Applied Science, 2023, vol. 5, issue 1.

[6] S. Medved, Building Acoustics and Noise Control in Buildings. Building Physics, 2022, pp. 331-406.

[7] M. Ličanin, D. Mihajlov, M. Praščević, A. Đorđević, M. Raos and N. Živković, Solution of the Environmental Noise Problem Gene-rated by HVAC Systems – Case Study. Acoustics and Vibration of Mechanical Structures – AVMS 2019, 2020, pp. 145-154.

[8] S.V. Joshi, L.T. Drzal, A.K. Mohanty and S. Arora, Are natural fiber composites environmentally superior to glass fiber reinforced composites? Composites Part A: Applied Science and Manufacturing, 2004, vol. 35, issue 3, pp. 371-376.

[9] W. T. Hesterberg and G. A. Hart, Synthetic Vitreous Fibers: A Review of Toxicology Research and Its Impact on Hazard Classification. Critical Reviews in Toxicology, 2008, vol. 31, issue 1, pp. 1-53.

[10] Gesellschaft für Akustikforschung Dresden mbH, Impedance tube AcoustiTube, Available: https://www.akustikforschung.de/en/produkte/messgerate/impedanzrohr-acoustitube/ [Accessed march 14, 2024].

[11] J. Sikora and J. Turkiewicz, Sound Absorption Coefficients of Granular Materials. Mechanics and Control, 2010, Vol. 29, pp. 149-157.

[12] Rockwool Ltd, Absorption Coefficients of Rockwool Slabs. Technical Sales Department., Pencoed, Bridgend. Available: https://www.rockwool.com/north-america/products-and-applications/products/afb/#Tools,Guides&Downloads [Accessed march 14, 2024].

[13] R.Ružickij, S. Vasarevičius, T. Januševičius, R. Grubliauskas, The Reuse Method of Waste Tyre Textile Fibers for Sound Absorption Applications. 2022 International Conference and Utility Exhibition on Energy, Environment and Climate Change (ICUE), Pattaya, Thailand, 2022, pp. 1-7

Technical Obstacles to Speech Intelligibility

Georgi Stanchev
Department of Electronics, navigation and communication in the aviation
"Georgi Benkovski" Bulgarian Air Force Academy
Dolna Mitropoliya, Bulgaria
gstanchev@af-acad.bg

Abstract. **As voice communication increasingly rely on technological devices, understanding the intricate relationship between equipment properties and communication outcomes becomes imperative. The purpose of this study is to investigate the impact of technical condition of communication equipment on the intelligibility of voice communications. To achieve this goal, methods and results of a qualitative analysis of the voice signals were used, as well as statistical methods for establishing the relevant dependencies. The importance of technical characteristics of voice signals for speech intelligibility was considered. The influence of the technical parameters of electronic communication equipment and the working environment on the technical characteristics of voice signals and thus on the intelligibility of speech was discussed. On the basis of the research, conclusions were drawn highlighting the serious influence of the communication equipment characteristics and the expertise of the service personnel on speech intelligibility.**

Keywords: communication equipment, speech intelligibility, technical characteristics, voice.

I. INTRODUCTION

Humans are social beings – we feel most comfortable when we live in groups of different formats – families, working teams, friendship circles, interest clubs etc. And communication is the most essential part of our existence within these social formations. It is so important to us that we do our best to keep it, even when our direct presence in the social group is impossible. Then, technical means come to help, through which we can be heard at great distances or receive a message that is sent to us at a convenient time.

There are countless examples when technical means of communications enable us to accomplish a certain work activity – one such example is air traffic management. Here, the impact of the characteristics of the technical means used in aviation and air traffic control, in particular on the quality of voice communications and speech intelligibility, will be discussed.

The advantages and opportunities provided by the technical advancement in voice communications are undeniable. Of great importance is the fact that in this way other human channels for receiving information are freed from the load, especially the most important one – the eyesight.

Through technical radio devices, we communicate by voice, overcoming distances and time differences. However, it is important to consider, if the speech that passed through the processing of the equipment and then through the radio channel will pay a high price to reach far or fully retain its authentic form.

In-depth information and studies focused on individual aspects of the interrelationships explored here can be found in literary sources. These include investigations into the statistical dependencies between different types of speech intelligibility, examinations of the technical parameters and condition of communication equipment, as well as analyses of the spectral and amplitude profile of voice signals. However, information and research on the complex influence of technical parameters of the electronic communication equipment on speech intelligibility are difficult to find and scarce.

In order to consider the influence of the technical characteristics of electronic devices for voice communications, it is only natural to pay attention to the more measurable characteristics of speech.

Using a combined analytical and statistical approach, those characteristics of speech that would be influenced by the characteristics of the electronic devices carrying it can be determined.

II. MATERIALS AND METHODS

A. Technical Characteristics of Speech

Combined quantitative and qualitative analysis methods, as well as stochastic methods of Probability Theory, were used to explore sound signals as the basis of speech communications. These signals can be represented

as complex random processes occurring in the medium between their source and receiver. Voice audio signals are changes in the pressure of the medium, most often air, which have different amplitudes and frequencies.

More precise definitions characterize these random processes with parameters that are common to sounds of any nature, such as: sound pressure level, sound level, dynamic range, frequency range, shape of the frequency spectrum, duration, echo and reverberation (for sound propagating in closed spaces) and others.

The purely physical characteristics of speech sounds can be objectively determined, measured and described. Variations in these descriptions may occur because of differences in the speaker's sex, age and speech apparatus, but may also be due to peculiarities of the language used for voice communications.

The propagation of sound in the air causes areas of condensation and rarefaction, in which the pressure is respectively higher or lower than its average value. Sound intensity level (N) can be described numerically as shown in (1), where N is a relative logarithmic measure of sound power flow density I relative to the standard value of $I_0 = 10^{-12}$W/m^2 (sound pressure $p_0 = 20\mu$Pa), which corresponds to the lower audibility threshold of a sound wave with a sinusoidal shape at frequency of 1 kHz [1]. The dynamic range D defines the difference in the levels of the lowest intensity sounds I_{min} and the highest intensity sounds I_{max} (1), for sounds of a certain nature – as an example, normal conversation, industrial noise or office noise.

$$N = \frac{I}{I_0} \text{ , } dB \quad ; \quad D = \frac{I_{max}}{I_{min}} \text{ , } dB \qquad (1)$$

Another very inherent and informative characteristic of sound is its spectrum. Pure tones are almost never found in human speech – i.e. tones which can be described mathematically as a simple harmonic oscillation. The sounds in human speech are mostly non-harmonic complex oscillations, which can be described fairly accurately as a linear combination of harmonic oscillations of different frequencies and amplitudes, in the form of an acoustic spectrum. The vibration with the lowest frequency of this combination is the fundamental tone, and the others are usually multiples of the fundamental frequency and are called overtones or harmonics.

Moreover, different sounds are characterized and distinguished from each other by the distribution of energy in their spectrum. The same applies to the sounds produced by the human speech apparatus and especially to vowels and voiced consonants – as the example, shown on Fig.1.
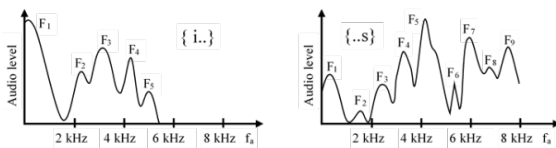

Fig. 1.   Formants in spectrums of sounds *i* and *s* in *i-n-s* sequence.

Thus, acoustic energy is concentrated in certain areas along the frequency axis. The specificity of the sound is determined not only by the absolute position of these areas on the frequency axis, but also by the ratio between the power values concentrated in these zones. These areas are

called formants – a more general term defining the zones along the linear spectrum in which a rise in vocal energy is observed. The central spectral line of such an area, where the highest value of the local peak is observed, is called the formant frequency [2]. According to their position on the frequency axis, in ascending order, the formants are labelled as *F1*, *F2*, *F3*, *F4*, *F5*, etc. The distribution of acoustic energy along the frequency spectrum shows significant differences between vowels and voiced consonants, on one hand, and voiceless consonants and especially the fricative ones, on the other.

The example on Fig. 1 shows the acoustic energy distribution in the sound sequence {i n s}, as an extracted fragment from a longer one [3].

In order to characterize speech more fully, it is necessary to know its frequency spectrum as a whole – i.e. to work with the **Long-Term Average Speech Spectrum** (**LTASS**). Even with this representation of the frequency spectrum of speech, by averaging over time, different profiles can be observed – by gender, age, language and so forth – Fig. 2.

The minimum threshold at which sound remains audible depends on the frequency. The graph of this dependence is called the **Absolute Threshold of Hearing** (**ATH**).

Human hearing is most sensitive in the range between 1 to 5 kHz, approximately, although with age sensitivity decreases significantly in the range above 4 kHz. Here, the influence of the distinct characteristics of each individual person – age, state of health, professional and domestic hearing trauma and even taking some medications, is quite large.

And although it is strictly individual, the relationship between the sound pressure level, the frequency and a person's perception of loudness, through numerous studies and measurements, on large groups of people, averaged, is indicated in a publication of the International Organization for Standardization – ISO 226:2003 [4], as it is shown on Fig. 3.
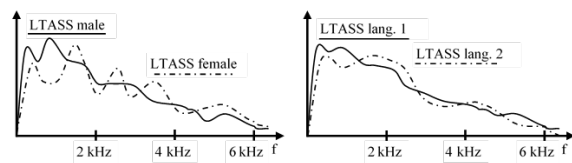

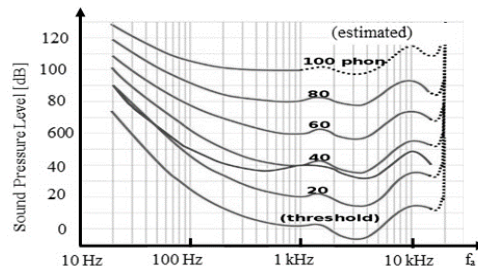Fig. 2.   Different forms of LTASS.

Fig. 3.   Equal-loudness contours by ISO 226:2003.

Another statistical means of describing speech characteristics is based on its instantaneous values.

The **Probability Density Function** (**PDF**) **f(aᵥ,t)** of acoustic signal values can be represented with sufficient accuracy as that of a non-stationary normal random process (2). This random process has zero mathematical expectation of the amplitudes **aᵥ**, it is compact, but has a time-varying value of the variance **Dᵥ(t)** [5] - Fig. 4.

$$f(a_V, t) = \frac{1}{\sqrt{2\pi D_V(t)}} \exp\left\{-\frac{a_V{}^2}{2D_V(t)}\right\} \quad (2)$$

In other words – in the flow of speech, quiet sounds, such as voiceless consonants, are much more likely to occur than loud sounds, such as vowels and voiced consonants.

The large differences in the variances of this process, when it represents voiced sounds, on the one hand, or consonant sounds, on the other hand, requires the communication channels to have a fairly wide dynamic range, on the order of 50 ÷ 60 dB.

Voice communications in a real-world environment always occur in the presence of external acoustic noise. In an airplane cabin, the width of the noise spectrum measured at the 0.5 power level is about 10 kHz.

The power of acoustic noise, in some cases, can be comparable to that of speech.

The speech level is usually about 60 ÷ 70 dB above the threshold of audibility. The acoustic noise level in the cabin of a jet fighter during engine afterburning can reach 120 dB, where the noise power exceeds speech by 50 ÷ 60 dB. To protect against acoustic noise, noise-resistant laryngophones and microphones are used, which have a special construction, directivity diagrams and generally provide a better acoustic signal to acoustic noise ratio. The noise can also be significantly reduced by using an airtight flight helmet.
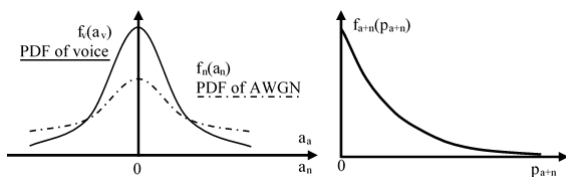

Fig. 4. Probability density functions of voice and noise.

B. Speech intelligibility - types and general definitions

Speech intelligibility is defined as the relative share of correctly perceived speech elements: sounds; syllables; words and phrases; to the total number of submitted ones.

Depending on the elements of the speech used for evaluation, sound, syllabic, word (single-word), phraseological (semantic) intelligibility of the speech is determined accordingly. In this arrangement, with the same gradation, it affects how much the listener is prepared for the topic [6], or at least how much meaningful content is embedded in what is being said to them. The statistical relationship between different types of speech intelligibility has been proven through numerous experiments and studies [5], [7].

One very convenient and informative statistical relationship is that between phonetic intelligibility **S** [%] and word intelligibility **W** [%], i.e. seamlessly passing or skipping through syllabic intelligibility – Table 1. This is so because the sounds are the main carriers of the technical parameters of the voice – fundamental frequency, dynamics, formants, etc. In turn, words are the primary conversational fragment that is a meaningful carrier [5].

TABLE 1. CLASSES OF COMMUNICATIONS.

Class	Communications by Speech Intelligibility		
	Characteristic of the class	*S [%]*	*W [%]*
I	Speech intelligibility without the slightest strain on attention.	> 91	> 98
II	Speech intelligibility without difficulty.	85 ÷ 90	94 ÷ 97
III	Speech intelligibility with attentional tension, without further inquiry and repetition.	78 ÷ 84	89 ÷ 93
IV	Intelligibility of speech with high attentional tension, further inquiry and repetition.	61 ÷ 77	70 ÷ 88
V	Connection lost.	< 60	< 69

C. Influence of the technical parameters of the equipment and working conditions on speech intelligibility

The microphone, which converts acoustic signals into electrical signals, is essentially a complex mechanical system, as it can be seen on Fig. 5, with its own frequency and transient characteristics [8].
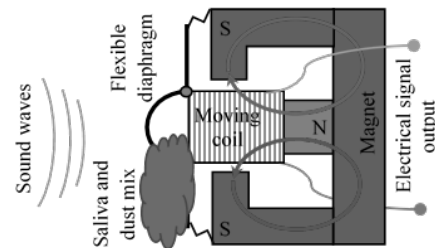
Fig. 5. Microphone construction.

The microphone also has a specific directivity diagram, which suggests that it should be properly positioned in relation to the sound source. In voice communications, this source is a person's mouth, and therefore a microphone placed on the larynx (laryngophone) or chest cannot be expected to reproduce the human voice with the same quality as one placed in front of the speaker's mouth. A good idea of the influence of the position of the microphone on the spectrum of the converted acoustic to electrical signals can be found in posters published by established microphone manufacturers [9].

With the **PDF** of speech sounds shown above according to their strength, and indirectly according to their belonging to different groups – vowels, voiced or voiceless consonants, the different noise reduction methods have a strong influence on speech intelligibility. One such approach to reducing the influence and fatigue caused by noise is squelching, where amplifiers only pass signals through themselves if they are above a certain level, which is assumed to be the noise floor. Unfortunately, the weak

acoustic signals of voiceless consonants often fall below the squelch level. This way of combating the influence of noise leads to a significant deterioration of speech intelligibility – Fig. 6.

Limiting the influence of side noises through using of squelch circuits is also applied in the transmitting part of the radio equipment. This is the case, for example, in the use of laryngophones and automatic switches of the transmitters (voice operated exchange - VOX), which work when they detect a signal from the microphone with a level higher than set lower limit (voice presence).

Limiting acoustic signals from above (clipping) has little effect on speech intelligibility, but listening to such speech is unpleasant, as the natural ratios between the strengths of vowels, voiced and voiceless consonants are disturbed [5].

A widely known circumstance is that in non-tonal languages, such as Western ones, including English, as well as in Slavic languages, a large part of the semantic information is placed in the consonants. Applying different types of filters – *Low Pass Filters* (*LPF*); *High Pass Filters* (*HPF*); *Band Pass Filters* (*BPF*) and *Band Stop Filters* (*BSF*) – in order to reduce the general level of noise passing through the transmitting and receiving equipment and the communication channel, affects speech intelligibility – Fig. 7 [5].

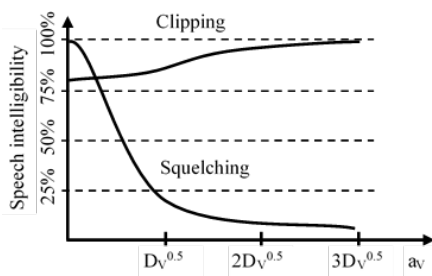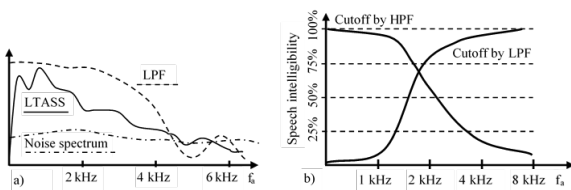Fig. 6. Influence of clipping and squelching on intelligibility.

Fig. 7. Influence of cutoff on speech intelligibility.

While in the low-frequency range of voice signals (up to about 1.5 kHz) where most of their energy is concentrated, the limitations in this range set by a *HPF* cutoff do not lead to a significant reduction in speech intelligibility.

Limitations in the high-frequency range set by a *LPF* cutoff (below 2 kHz), however, lead to a drastic drop in speech intelligibility [5], [9].

The other place where bandwidth limitation can occur is in radio channels. There, the fight against noise and interference from adjacent channels in the receivers is carried out with the help of *BPF*s.

III. RESULTS AND DISCUSSION

The presented in previous section features are exemplary and serve only to illustrate the idea. This work is not intended to prove that a particular language or voice type is more suitable than any other is for aviation's or any other type of voice communications.

As can be seen on Fig. 1. the moment distributions show significant differences in the distribution between the formants of the sound { i..} and the sound {..s }.

It can be seen that for the vowel sound {i…} the audio energy is concentrated mostly around the first four formants. With the fricative consonant {…s}, not only are more formants $F1 \div F9$ formed, but also the sound energy is mainly concentrated around those with larger numbers – $F4$ and up. Thus, it can be assumed that the energy of this sound is mostly located in the frequency band above 4 kHz, keeping a significant value around 8 kHz.

The situation is similar with the other voiceless consonants: f, k, p, t, etc., whose energy is mostly concentrated in the range around 4 kHz.

It should be noted that along with the purely physical characteristics of speech sounds, and the technical characteristics of electronic equipment, the intelligibility of speech is influenced by the psychophysiological characteristics of sound audibility.

The psychophysiological characteristics of sound reflect a person's subjective perception and feeling of perceived sounds. Some of the effects, such as masking of sounds and hearing phantom sounds, are related to the way a person's brain and nervous system work. These features of human hearing are the basis of the psychoacoustic model which provides many of high quality irreversible sound compression methods (mp3 , aac, Vorbis, etc.). All of these forms involve voice digitization, after which non-essential to quality components are removed [10].

It can be seen that while the language with its rules and constructions is a kind of general contract for communications in social groups, the physical and psychophysiological characteristics of the vocal sounds that are used in communications through this language are quite diverse and strictly individual.

For example of the statistical relationship between different types of speech intelligibility, 80% syllabic corresponds to 98% word intelligibility, or 40% syllabic intelligibility corresponds to 90% phraseological one, the latter being a rather low and unsatisfactory value. In dispatch communications, due to the operators' and users' prior knowledge of the set of possible phrases, fully acceptable speech intelligibility is achieved with syllabic intelligibility between 40% and 50%, which corresponds to word intelligibility between 87% and 93% [7].

Speech intelligibility is also affected by many environmental factors, such as the ratio of average speech power to average ambient noise power. Also important are the attenuation time of power-significant reflections of sounds from surrounding walls and objects (reverberation time), the frequency profile of absorption of sound waves by surrounding surfaces and other similar factors. Naturally, the intelligibility of speech depends mostly on the characteristics of the media carrying the voice information. The influence becomes especially complex

when the media is mixed: e.g. speech apparatus - air environment - electronic equipment - radio channel - electronic equipment - air environment - hearing apparatus.

The closest to the technical parameters and limitations of the equipment are sounds with their parameters and the corresponding sound intelligibility. In this way, through the statistical relationship between the different types of speech intelligibility, the influence of purely technical characteristics of the equipment can be traced, as an example – the influence of frequency or impulse characteristics on the most significant, highest form of speech intelligibility, namely semantic intelligibility.

In dispatch communications, when operating conditions are around the normal for the scenario, conversations are fairly formalized and lines, phrases and words are largely predictable [6]. This applies both to the tone and to the speed of their speech – they are calm and close to those of a normal conversation. This is not the case in emergency situations – when, under the pressure of extraordinary circumstances, unexpected, and in some such cases, thoughtless words and phrases appear in voice communications, indistinctly spoken, at high speed and in a high tone. This shifts the spectrum of voice signals upward, the influence of high-frequency suppression by low-pass filters becomes even greater and, as a result, already difficult-to-understand phrases become even more unclear. If in these situations the crew or the control staff also perform any physical actions, these can obstruct normal breathing or lead to the microphone being moved from its optimal position – the result is further deterioration of intelligibility.

In order to properly convert sound vibrations, especially those of higher frequencies, the moving parts of the microphone's overall construction (for the electrodynamic microphone, these are an elastic membrane and an attached coil) must be light and elastic. The accumulation of a mixture of saliva and dust on the internal moving parts of the microphone not only significantly reduces its sensitivity, but also seriously distorts its frequency response, especially by suppressing the high frequencies of the voice, where the voiceless consonants spectrum is mostly concentrated.

Reducing of speech intelligibility happens mainly due to the undesirable reduction in the level of high-frequency voice signals – such as voiceless consonants, which already have a low level. This is because it is impossible to make an ideal filter – with flat frequency pass bands, steep slopes, and frequency bands of full rejection – Fig. 7a. Researches have shown that limiting the bandwidth of voice signals from below with *HPF* or above with *LPF* affects speech intelligibility differently – Fig. 7b.

This means that in our desire to reduce the level of noise, which compared to voice signals has a wide uniform frequency spectrum, we can cause significant damage to speech intelligibility if we use frequency filtering carelessly.

Moreover, when fighting noise, neither the low-frequency range should be sacrificed, since it provides us with a good signal-to-noise ratio, nor the high-frequency range, since it provides us with good intelligibility – Fig. 8.

The frequency band of radio channels Δf_R, compared to that of speech signals, is much wider. If the transmitting and receiving radio equipment are tuned to the same carrier frequency, there should be no bandwidth limitation of the speech signals due to the *BPFs* in the receiving radio equipment.

However, if the carrier frequency or the receiving frequency is unstable, due to damaged and/or outdated equipment, or if the two frequencies differ for some other reason – a Doppler shift, as an example. It is then possible to obtain bandwidth limitation of the speech signals from above due to suppression of one of the sidebands – *Lower Side Band* (*LSB*) or *Upper Side Band* (*USB*), as it is shown on Fig. 9.
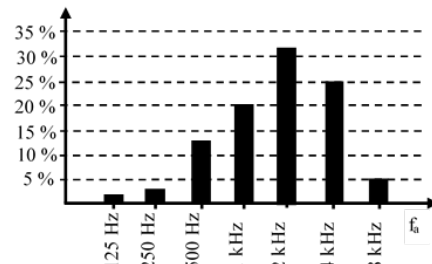
Fig. 8. Importance of spectral regions for speech intelligibility.
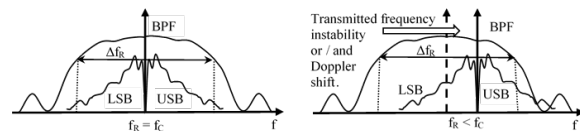
Fig. 9. Spectral cutoff from frequency instability or Doppler shift.

In conversion of analog signals to digital and their subsequent digital processing, there are also potential dangers of inaccurate representation of the frequency spectrum of speech signals. This can be seen in the reverse conversion of the digitized voice signal back into an analog one and its subsequent playback.

Problems here are, as follows – to convert analog signals to digital, they are subjected to the process of time sampling, in which the analog signal is sampled over a period of time.

A basic and important requirement is that these samples are taken at a frequency called the sampling rate f_d, which should not be lower than the doubled highest frequency in the spectrum of the analog signal. For speech signal processing, the sampling rate is standardized on f_d=8 kHz. This means that before being converted to digital, the speech signals should be well limited to a frequency not higher than 4 kHz, using a low pass filter *LPFт*.

If, with the idea of keeping the highly informative part of the upper frequency band in the spectrum of the speech signals, it is limited to a higher frequency, then when applying the standardized sampling rate, a rather harmful phenomenon is obtained.

The lower sideband *LSB₁* that, in results of digitalization, forms around the sampling frequency f_d enters the area of natural speech bandwidth, with mirror-image spectral components.

A low pass filter LPF_R is applied when restoring the analog signal from the discrete samples obtained by the receiver. Then, the mirror-inverted spectral components cause a false recovery of the frequency components of the original speech signal. This phenomenon looks like a "frequency spectrum bending", as it can be seen on Fig. 10.

The incorrect restoration of amplitudes and relationships between high-frequency components of the speech signal spectrum, especially in the case when their order is reversed, leads to a serious degradation of speech intelligibility.

Fig. 10. Frequency spectrum bending.

IV. CONCLUSIONS

The technical condition and parameters of the electronic equipment intended for voice transmission significantly affect speech intelligibility. This happens, mostly, due to the impact of these characteristics on the frequency spectrum of speech signals, especially in their high-frequency range.
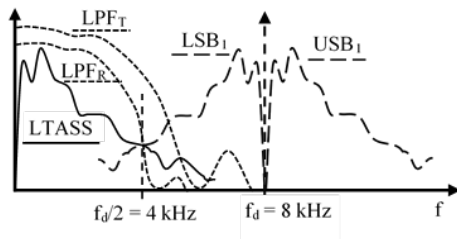
Therefore, a few key points need to be regarded:

• Electronic equipment should be regularly serviced by qualified technical personnel who are fully informed of the possible effects of their work on speech intelligibility.

• Only well-trained and drilled personnel, with an adequate and sustainable psycho-physiological status, should use the electronic equipment.

• It should be considered to update standardized technical requirements for electronic equipment for voice transmission, which would lead to improvement of speech intelligibility and improvement of the quality of voice communications in general.

REFERENCES

[1] Microphone Handbook. Vol. 1: Theory, Naerum: Bruel & Kjaer, 2019, pp. 2-2 to 2-3.

[2] T. Lubin, Getting Great Sound: The Microphone Book (Third Ed.), London: Rowman & Littlefield Publishers, 2022, p. 51.

[3] S. Wood, What are formants, January 2005. [Online]. Available: *Lund University, Sweden – SOL* https://person2.sol.lu.se/SidneyWood/praate/whatform.html [Accessed: March 13, 2023].

[4] Equal-loudness contour, October 2023. [Online]. Available: *Wikipedia – The Free Encyclopedia* https://en.wikipedia.org/wiki/Equal-loudness_contour. [Accessed: Jan. 9, 2024].

[5] V. I. Tihonov Ed., Aviation radiocommunication devices (in Russian), Voronezh: Zhukovsky AFEA, 1986, pp. 24-39.

[6] V. Katsarska, "Formulaic Language in Aeronautical English – Friend or Foe", *The Journal of Teaching English for Specific and Academic Purpose*, vol. 9, no. 2, pp. 239–245, 2021. [Online]. Available: http://espeap.junis.ni.ac.rs/. [Accessed: Feb. 15, 2024], https://doi.org/10.22190/jtesap2102239k.

[7] Speech clearency and intelligibility. (in Russian), February 2016. [Online]. Available: *StudFiles* https://studfile.net/preview/5395324/. [Accessed: Feb. 15, 2024].

[8] J. Eargle, The Microphone Book (Second Edition). From Mono to Stereo to Surround. A Guide to Microphone Design and Application, Oxford: Elsevier/Focal Press, 2005, pp. 42-45, 340.

[9] Mic Univesity, *DPA Microphones*, [Online]. Available: https://www.dpamicrophones.com. [Accessed: Jan. 9, 2024].

[10] M. Bosi and R. E. Goldberg, Introduction to Digital Audio Coding and Standards, New York: Springer Science +Business Media, 2003, pp. 315-367.

Cooling Glove Compartment of a Vehicle by Thermoelectric Coolers

Çiğdem Susantez
Engineering Faculty, Department of Mechanical Engineering
Trakya University
Edirne, Turkey
cigdemsusantez@trakya.edu.tr

Hilmi Kuşçu
Engineering Faculty, Department of Mechanical Engineering
Trakya University
Edirne, Turkey
hilmi@trakya.edu.tr

Kamil Kahveci
Engineering Faculty, Department of Mechanical Engineering
Trakya University
Edirne, Turkey
kamilk@trakya.edu.tr

Abstract. **In this study, effects of the four different thermoelectric cooler (TEC) placements on the boundaries of the glove compartment have been numerically investigated under the effect of natural convection with Boussinesq approximation. The best cooling capacity has been observed for the top boundary TEC application for the investigated glove compartment geometry. It has also been observed that heat transfer is stronger at the beginning of the process as a result of the stronger convection currents. The absorbed heat from the glove compartment increases with the increase of the electric current applied.**

Keywords. *Boussinesq approximation, glove compartment, natural convection, thermoelectric cooler*

I. INTRODUCTION

Thermoelectric coolers (TECs) are used in many fields including cooling of electronic devices, refrigerator, air conditioning and building applications [1,2]. They work based on the Peltier effect. Peltier effect is the phenomena of when an electric current passes through a circuit consisting of different conductor, one of the joints is cooled and the other joint is heated. It is also possible to reverse the thermoelectric effect by heating the one tip of the same circuit, consequently it is possible to have electric current on the circuit (Seebeck effect) [3]. When Seebeck effect is applied they are called thermoelectric generators (TEGs) and they are also having wide rage of application fields such as space, building and automobile industry [1]. Although they have low coefficient of performance (COP) value, they have no moving parts, they are simple, low weighted and environmentally friendly [2].

Bismuth telluride (Bi_2Te_3) is the most used thermoelectric material in TECs. TECs consist of the p-doped and n-doped thermoelectric material legs which are connected thermally in parallel and electrically in series. While positively charged holes are responsible for the heat transfer in the current direction in the p-doped legs, negatively charged electrons take this duty in the opposite direction with current in the n-doped legs [4]-[5].

There are many studies related to cooling application by TECs in the literature. Zhou and Yu [6] developed a model for the optimization of TEC system based on the thermal conductance between the hot and cold sides. They presented the optimum cooling capacity and coefficient of performance (COP) depending on the allocation ratio for different total thermal conductance. Sarkar and Mahapatra [7] investigated the radiation effect from the heat sink in addition to the natural convection on the TEC performance. They conclude the result that the COP of the TEC improves with radiative heat fluxes and it is possible to operate TEC at lower value of current when emissivity is higher. Yushanov et al. [8] numerically solved thermoelectric field equations by implementing Seebeck-Peltier effect. They obtained simulational results for the temperature and electric potential. Chen et al. [9] performed a numerical and experimental study on the thermoelectric refrigerator under the effect of natural convection. According to their results, 12.2°C stabilized inside air temperature can be obtained in the case of 29°C outside air temperature and 10.8W input electric power. Jiang et al. [10] applied their analysis method on the water-cooled thermoelectric air-conditioner to verify their model experimentally. They presented the result that the corresponding input current density is 6.04 A/mm^2 regarding maximum refrigeration rate density and it is 0.62 A/mm^2 regarding the maximum COP at the cooling temperature difference of 5K. Kuşçu et al. [5] numerically investigated the natural convection in a square enclosure which is cooled by Peltier effect on the left wall, at high temperature on the right wall and also has adiabatic top and bottom walls. They observed the secondary circulation cell near the cold bottom corner at the beginning of the process and it develops with the increase of the electric current. Kuşçu and Kahveci [11] performed an experimental study related to water filled cubical container which is cooled by a Peltier device. They showed that

although temperature inside the container decreases slowly in the early stage of the process, as time progresses it becomes faster due to the strengthened convection.

In this paper, effect of the thermoelectric coolers on the glove compartment of a vehicle has been investigated numerically. Temperature simulations are obtained for bottom, side, rear and top cooling cases under the effect of natural convection with Boussinesq approximation by Comsol Multiphysics and Simulation Software.

II. MATERIALS AND METHOD

Three dimensional geometry of the glove compartment is given with dimensions in Fig. 1. These dimensions are very close to the dimensions of glove compartment of 1999 model Fiat Palio vehicle.
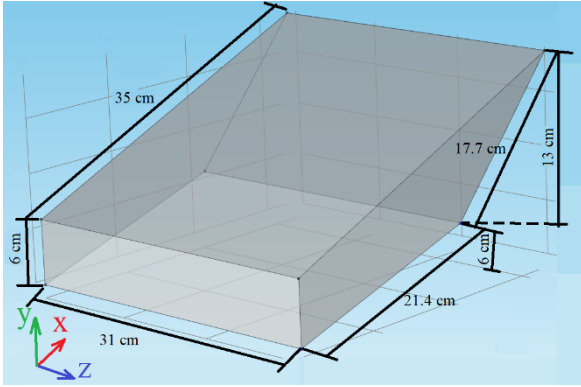
Fig. 1. Dimensions of the glove compartment

Thermoelectric coolers inserted on the bottom, top, rear and side boundaries of the glove compartment, except 17.7 cm length cover. The investigated four different cases are given in Fig. 2

(a) Bottom boundary TEC application

(b) Top boundary TEC application

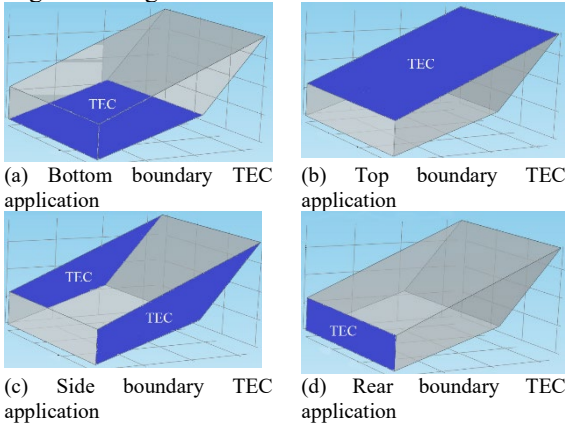(c) Side boundary TEC application

(d) Rear boundary TEC application

Fig. 2. TEC placements on the glove compartment

The Newtonian working fluid is air and thermophysical properties are taken constant at 10°C as given in Table I.

TABLE I THERMOPHYSICAL PROPERTIES OF AIR [12]

Explanation	Property	Value
Thermal conductivity	k_{air} (W/mK)	0.02439
Density	ρ_{air} (kg/m³)	1.246

TABLE I THERMOPHYSICAL PROPERTIES OF AIR [12]

Explanation	Property	Value
Specific heat	c_p (J/kgK)	1006
Dynamic viscosity	μ_{air} (kg/ms)	$1.778 \cdot 10^{-5}$

Governing equations have been solved under the Boussinesq approximation. They are given in Eqs.(1)-(10) with the initial and boundary conditions. No slip condition is applied on boundaries as given in Eq. (6). When heat flux boundary condition is applied on the boundary covered with TEC or Peltier elements, other boundaries are adiabatic. Glove compartment is initially at 25°C as stated in Eq. (10).

$$\frac{\partial u}{\partial x} + \frac{\partial v}{\partial y} + \frac{\partial w}{\partial z} = 0 \tag{1}$$

$$\begin{aligned} \rho_{air}\left(\frac{\partial u}{\partial t} + u\frac{\partial u}{\partial x} + v\frac{\partial u}{\partial y} + w\frac{\partial u}{\partial z}\right) \\ = -\frac{\partial P}{\partial x} \\ + \mu_{air}\left(\frac{\partial^2 u}{\partial x^2} + \frac{\partial^2 u}{\partial y^2} + \frac{\partial^2 u}{\partial z^2}\right) \end{aligned} \tag{2}$$

$$\begin{aligned} \rho_{air}\left(\frac{\partial v}{\partial t} + u\frac{\partial v}{\partial x} + v\frac{\partial v}{\partial y} + w\frac{\partial v}{\partial z}\right) \\ = -\frac{\partial P}{\partial y} \\ + \mu_{air}\left(\frac{\partial^2 v}{\partial x^2} + \frac{\partial^2 v}{\partial y^2} + \frac{\partial^2 v}{\partial z^2}\right) \\ + \rho_{air}g\beta(T - T_{max}) \end{aligned} \tag{3}$$

$$\begin{aligned} \rho_{air}\left(\frac{\partial w}{\partial t} + u\frac{\partial w}{\partial x} + v\frac{\partial w}{\partial y} + w\frac{\partial w}{\partial z}\right) \\ = -\frac{\partial P}{\partial z} \\ + \mu_{air}\left(\frac{\partial^2 w}{\partial x^2} + \frac{\partial^2 w}{\partial y^2} + \frac{\partial^2 w}{\partial z^2}\right) \end{aligned} \tag{4}$$

$$\begin{aligned} \rho_{air}c_{p,air}\left(\frac{\partial T}{\partial t} + u\frac{\partial T}{\partial x} + v\frac{\partial T}{\partial y} + w\frac{\partial T}{\partial z}\right) \\ = k_{air}\left(\frac{\partial^2 T}{\partial x^2} + \frac{\partial^2 T}{\partial y^2} + \frac{\partial^2 T}{\partial z^2}\right) \end{aligned} \tag{5}$$

$$u|_{boundary} = 0, \qquad v|_{boundary} = 0 \\ w|_{boundary} = 0 \tag{6}$$

$$\dot{q}_w|_{TEC} = -k_{air}\frac{\partial T}{\partial n} \tag{7}$$

$$-k_{air}\frac{\partial T}{\partial n} = 0 \qquad \text{for boundaries not coated with TEC elements} \tag{8}$$

$$u|_{t=0} = 0, \qquad v|_{t=0} = 0, \qquad w|_{t=0} = 0 \tag{9}$$

$$T|_{t=0} = 25°C \tag{10}$$

where u, v, and w are the velocity components on x, y and z directions respectively, t is time, P is pressure, g is

gravitational acceleration, T is temperature, β is thermal expansion coefficient, which is equal to $1/T(K)$ in this study for an ideal gas. T_{max} is the maximum air temperature inside the glove compartment. n is the direction normal to the surface. TEC1-12730 [13] having the square cross section with 62mm length is used as Peltier device for this study. Heat flux function $\dot{q}_w$ for TEC1-12730 is derived from the datasheet [13] for the case of hot side temperature of the TEC is 25°C. The corresponding heat absorption $\dot{Q}_c$ is presented in Fig.3. Investigations in this study are performed for 6A, 18A and 30A electric current values.
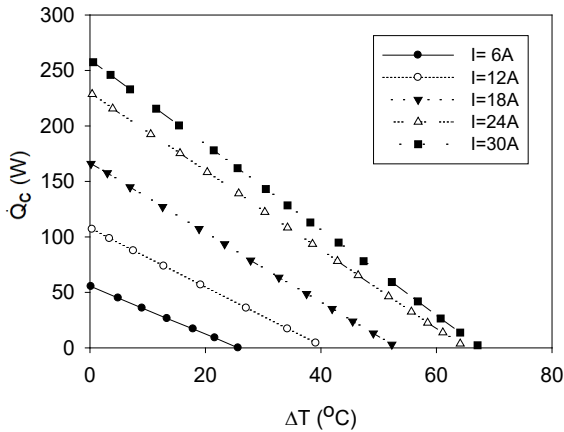
Fig. 3. Performance curves derived from TEC1-12730 datasheet [13]

Derived heat flux function for different electric current values are presented in Table II. ΔT corresponds to ''25°C-T'' because of the 25°C hot side temperature of the TEC and R^2 is the coefficient of determination.

TABLE II HEAT FLUX FUNCTION

$\dot{q}_w(W/m^2)$	R^2	$I(A)$
$-(55.5291 - 2.1598\Delta T)/(62 \cdot 62 \cdot 10^{-6})$	0.9999	6
$-(166.5319 - 3.1356\Delta T)/(62 \cdot 62 \cdot 10^{-6})$	1	18
$-(259.7302 - 3.8357\Delta T)/(62 \cdot 62 \cdot 10^{-6})$	1	30

Verification of the code has been performed by the study of Kuşçu et al. [5]. As it has been show in Fig. 4, results are compatible with the literature. T_{ave} is the average temperature of the enclosure.
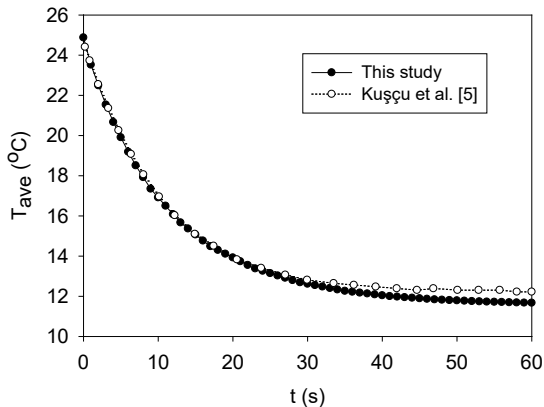
Fig. 4. Verification of the code

Mesh dependency analysis for this study has also been performed for top boundary cooling condition and 6A of

electric current. Corresponding results are given in Fig. 5. Two dimensional results with ''extremely fine mesh'', which is the default mesh with highest quality in Comsol Multiphysics and Simulation Software are also presented in Fig 5. Regarding the computational time and accuracy, 37420 elements has been used for the three dimensional analysis, in this study.
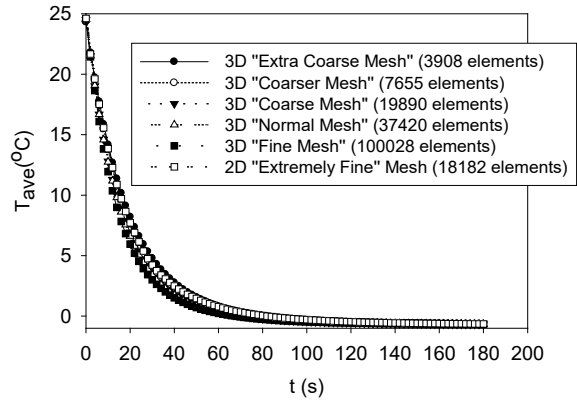
Fig. 5. Mesh dependency analysis

III. RESULTS AND DISCUSSION

Temperature and velocity simulations (Figs. 6-13) have been presented in this study only for electric current of 6A. As it has been seen from these figures that convection is stronger at the beginning of the process due to the body force, which is related with the temperature difference inside the glove compartment, in the momentum equation (Eq.(3)). There are two factors effecting the cooling capacity. They are the physical mechanism of the natural convection and heat transfer surface area. When the thermoelectric coolers are placed on the top boundary, the cooled air sinks and also the largest heat transfer surface for this case enhances the heat transfer considerably. As a result, the top boundary TEC application has the highest cooling capacity for the investigated geometry.
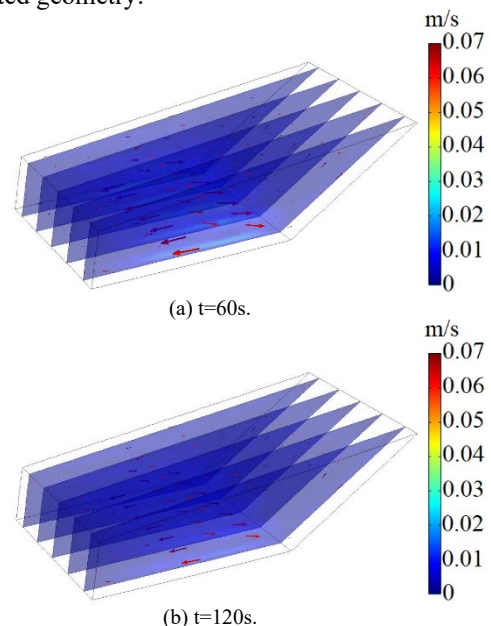
(a) t=60s.

(b) t=120s.

Fig. 6. Velocity simulations for bottom boundary TEC application (I=6A)
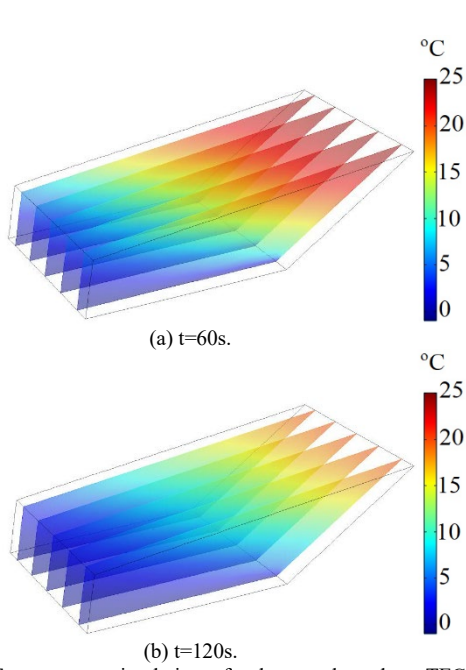
(a) t=60s.

(b) t=120s.

Fig. 7. Temperature simulations for bottom boundary TEC application (I=6A)
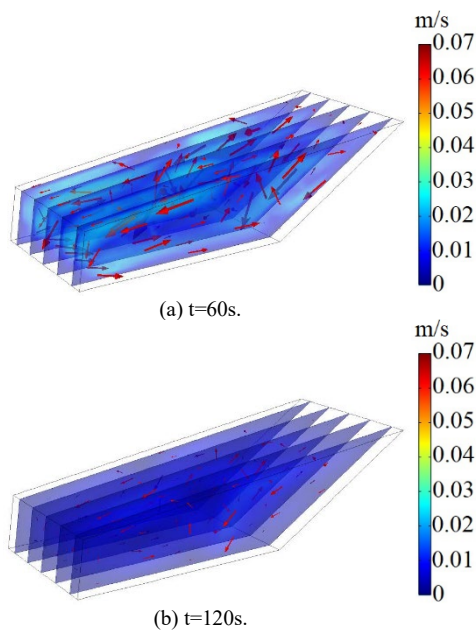
(a) t=60s.

(b) t=120s.

Fig. 8. Velocity simulations for top boundary TEC application (I=6A)
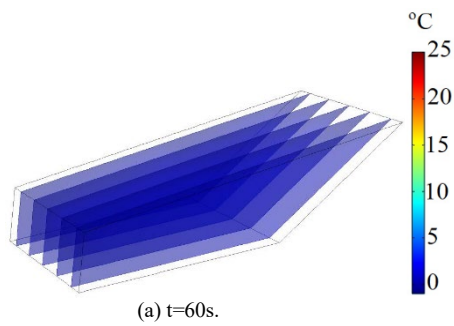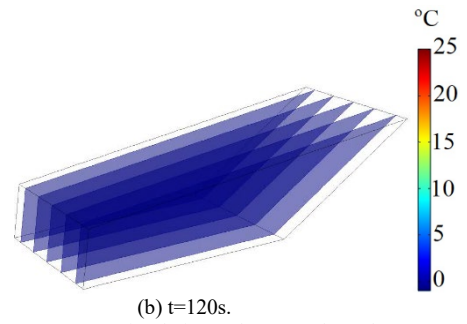
(a) t=60s.

(b) t=120s.

Fig. 9. Temperature simulations for top boundary TEC application (I=6A)
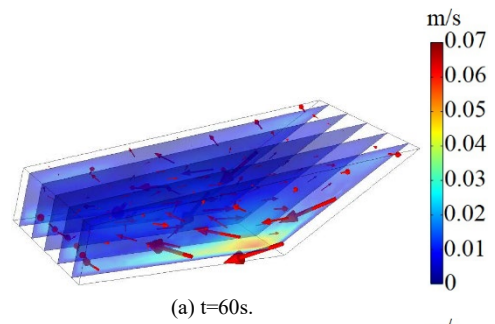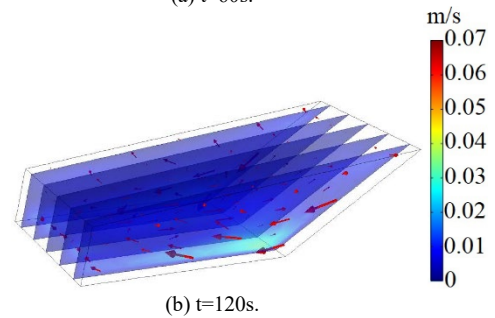
(a) t=60s.

(b) t=120s.

Fig. 10. Velocity simulations for side boundary TEC application (I=6A)
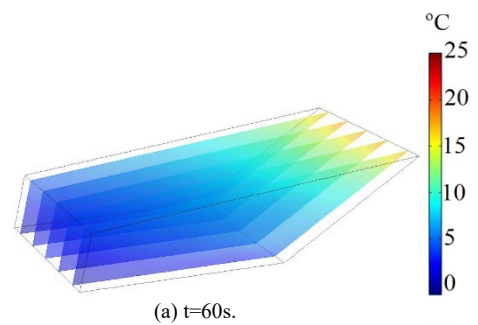
(a) t=60s.
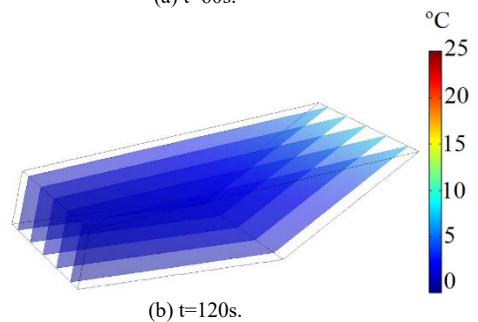
(b) t=120s.

Fig. 11. Temperature simulations for side boundary TEC application (I=6A)

(a) t=60s.

(b) t=120s.
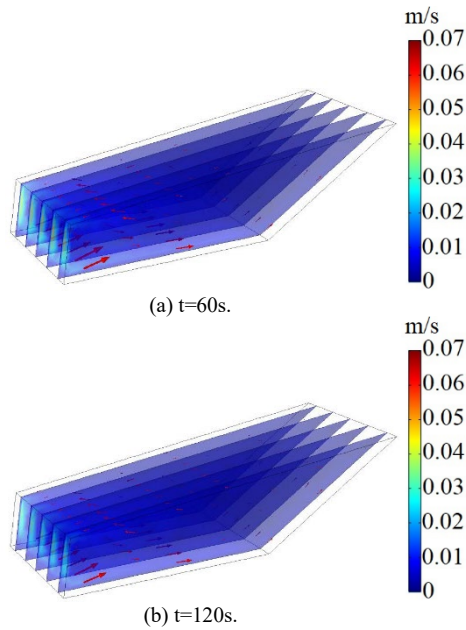
Fig. 12. Velocity simulations for rear boundary TEC application (I=6A)

(a) t=60s.

(b) t=120s.
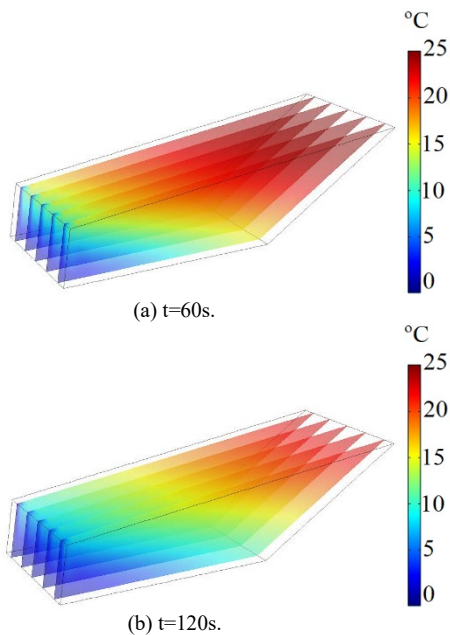
Fig. 13. Temperature simulations for rear boundary TEC application (I=6A)

Time depending variations of the average air temperature inside the glove compartment for 6A, 18A and 30A electric current values have also been presented in Figs. 14-16, respectively. Heat transfer is stronger at the beginning of the process due to the stronger convection currents. As it has been observed from these figures that, as being compatible with the simulations given in Figs. 6-13, when the top boundary TEC application has the highest cooling capacity, that of the rear boundary TEC application is the weakest. One more important result obtained is that, applied electric current to the TECs significantly improves the cooling capacity.
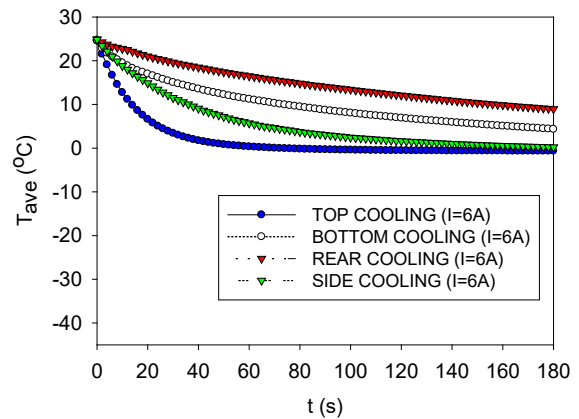
Fig. 14. Average temperature of the air inside the glove compartment for I=6A
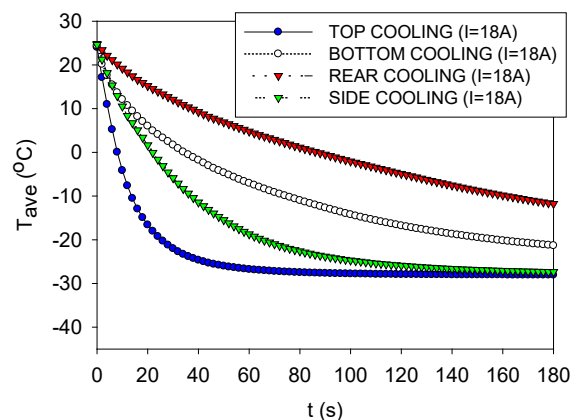
Fig. 15. Average temperature of the air inside the glove compartment for I=18A
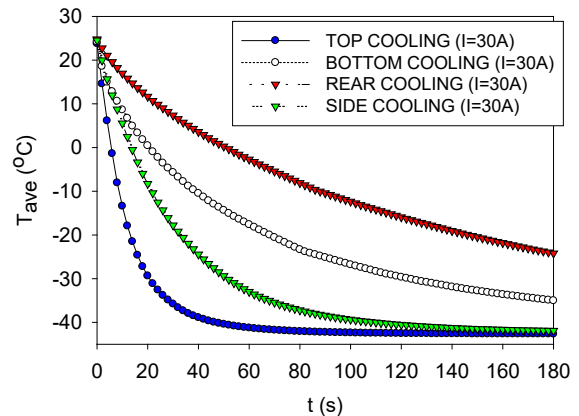
Fig. 16. Average temperature of the air inside the glove compartment for I=30A

IV. CONCLUSIONS

In this study, the effects of the four different TEC placements on the glove compartment have been investigated numerically by Comsol Multiphysics and Simulation Software. Numerical results have been obtained under the effect of natural convection with Boussinesq approximation. It has been concluded that top boundary TEC application cools the investigated glove compartment much more rapidly than other cooling conditions. Heat transfer is stronger at the beginning of the process as a result of stronger natural convection. Cooling

capacity also enhances significantly with the applied electric current.

REFERENCES

[1]   W. He, G. Zhang, X. Zhang, J. Ji, G. Li and X. Zhao, "Recent development and application of thermoelectric generator and cooler," Appl. Energy, vol. 143, pp. 1-25, 2015. https://doi.org/10.1016/j.apenergy.2014.12.075

[2]   T. Guclu and E.Cuce, "Thermoelectric coolers (TECs): From theory to practice," J. Electron. Mater., vol. 48, No. 1, pp. 211-230, 2019. https://doi.org/10.1007/s11664-018-6753-0

[3]   Y. A. Çengel and M. A. Boles, Thermodynamics an Engineering Approach New York: McGraw-Hill, 2015.

[4]   B. S. Mann, "Transverse thermoelectric effects for cooling and heat flux sensing," M.S. thesis, Virginia Polytechnic Institute and State University, Blacksburg, Virginia, U.S.A., 2006.

[5]   H. Kuşçu, K. Kahveci and B. T. Tanju, "Natural convection in a square enclosure cooled by peltier effect" presented and published in Proceedings of the World Congress on Mechanical, Chemical, and Material Engineering (MCM 2015), Barcelona, Spain, July 20-21, 2015.

[6]   Y. Zhou and J. Yu, "Design optimization of thermoelectric cooling systems for applications in electronic devices," Int. J. Refrig., vol. 35, pp. 1139-1144, 2012. https://doi.org/10.1016/j.ijrefrig.2011.12.003

[7]   A. Sarkar and S. K. Mahapatra, "Role of surface radiation on the functionality of thermoelectric cooler with heat sink," Appl. Therm. Eng., vol. 69, pp. 39-45, 2014. https://doi.org/10.1016/j.applthermaleng.2014.04.025

[8]   S. P. Yushanov, L. T. Gritter, J. S. Crompton and K. C. Koppenhoefer, "Multiphysics Analysis of Thermoelectric Phenomena" presented and published in Proceedings of the 2011 COMSOL Conference, Boston, U.S.A., October 13-15, 2011.

[9]   Z. Chen, M. Liao, X. Hu, Y. Ma, S. Jiang, X. Chen, F. Zou, X. Fan and Z. He, "Study on the performance of thermoelectric refrigerator under natural convection heat transfer condition," Appl. Therm. Eng., vol. 230, part B, pp. 1-9, 2023. https://doi.org/10.1016/j.applthermaleng.2023.120822

[10] F. Jiang, F. Meng, L. Chen and Z. Chen, "Thermodynamic analysis and experimental research of water-cooled small space thermoelectric air-conditioner," J. Therm. Sci., vol. 31, no. 2, pp. 390-406, 2022. https://doi.org/10.1007/s11630-022-1575-z

[11] H. Kuşçu and K. Kahveci, "Experimental study of heat transfer in a container filled with water and cooled by a peltier device" presented and published in Proceedings of the 2nd World Congress on Mechanical, Chemical, and Material Engineering (MCM'16), Budapest, Hungary, August 22-23, 2016. DOI: 10.11159/htff16.118

[12] Y. A. Çengel, Heat and Mass Transfer A Practical Approach. New York: McGraw-Hill, 2006.

[13] HB Corporation Thermoelectric Cooler TEC1-12730, "Performance Specifications," Rev 2.03. Available: https://datasheetspdf.com/pdf-file/564497/HB/TEC1-12730/1. [Accessed: March 13, 2024].

Enhanced Efficiency in Two-Component Injection Molding Product for Automotive Applications

Todor Todorov
FIT, Laboratory "CAD/CAM/CAE in Industry", Technical University
Sofia, Bulgaria
todorttodorov@tu-sofia.bg

Georgi Todorov
FIT, Laboratory "CAD/CAM/CAE in Industry", Technical University
Sofia, Bulgaria
gdt@tu-sofia.bg

Ivan Ivanov
FIT, Laboratory "CAD/CAM/CAE in Industry", Technical University
Sofia, Bulgaria
ivan.st.ivanov@abv.bg

Abstract. **The presented study is focused on an optimization analysis of a complex automotive component consisting of two parts with different materials. The research examines the impact of various runner configurations, cooling parameters, gate positioning, and melt temperature distribution within the mold. The paper emphasizes the advantages and applications of integrating such optimization techniques. Parametric and geometric optimization of the model is done, along with the evaluation of simulated filling processes, as clarified for the paper's objectives. Additionally, a methodical approach is outlined, clearing the process of operational rate selection, material property analysis, control parameter establishment, and preemptive simulations.**

Keywords: CAD modeling, filling analysis, two-component molding, optimization, injection molding, polymer

I. INTRODUCTION

A. Multi-component injection molding

The production process of forming multi-component products under high pressure is expressed in the fact that from two or more different polymers one part is obtained. These polymers are most often thermoplastics, but thermoplastic elastomers are also used. The polymers used may differ in color, mechanical properties or other factors.[1][2][3]

Multi-component injection molding is preferred to conventional injection molding for a number of reasons. [3] It significantly improves the functionality of the products and gives much more freedom in terms of design decisions. This process reduces the cost and reduces the weight of the final part.

Disadvantages include the high cost of machinery and equipment, as well as the fact that not all polymers form good adhesion to each other. [1][2]

The development of the methodology is caused by the need of the market for a service for restoration of the working capacity, as well as for modification of mold tools in case of need of corrections.[4]
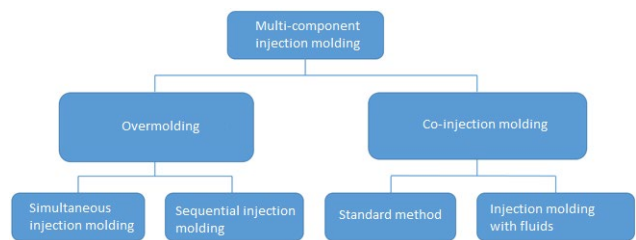
Fig. 1 Classification of multicomponent injection molding processes

A. Overmolding

Overmolding is an increasingly popular process for injecting additional layers of material onto a base in two or more steps. [4][5] This is done by adding a new layer on the same machine in a combined tool on the base of the part already formed in the first step. This technique allows in one step the bonding of two or more polymers which do not require any additional finishing operations successively on top of each other.[6]

Fig. 2 Example of multi-component injection molding by layer-by-layer injection molding

A molding tool is pre-filled with one material, then it is opened and one part of it is closed with a second half-mold. An additional cavity is formed and reshaped into the shape thus created by the second. The second material is injected directly onto the first to obtain a final product composed of two or more layers created successively on top of each other.[7][8][9]

This method provides additional increased flexibility for the production of multi-component, multi-colored or multifunctional, in terms of materials used, products at the lowest cost. [10]

B. Co-injection

The method of sequentially feeding materials through a nozzle is a variation of the multi-component injection molding process. In it, the final product is characterized by a core and a shell. Depending on whether the product is solid or hollow, there are two variants of the method of forming products - standard and injection molding with fluids. It is widespread because it allows to reduce the quantity and quality of the material used.[13][14]
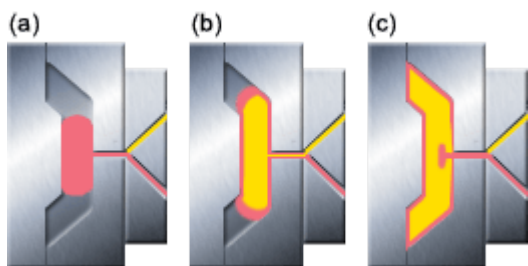
Fig. 3 Example of co-injection molding

C. Purpose of the research

The purpose of this paper is to model and analyze different methods of optimization of injection model process. Two layers of two component model are considered.

II.   SIMULATION ANALYSIS AND OPTIMIZATION OF THE PROCESS IN ORDER TO REDUCE DISPLACEMENT OF THE MODEL. MATERIAL SELECTION.

The model analyzed in this article is two-component front frame with cluster lens used in some automobiles (fig. 4).
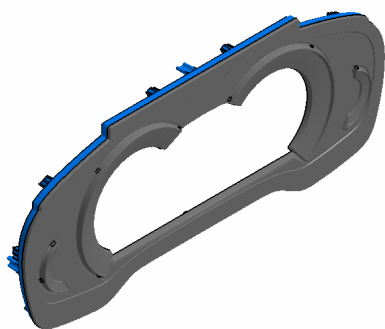
Fig. 4 Front frame

What is specific about these components is that they are directly visible to the end user, which leads to higher requirements.

Engineering analysis are applied using developed virtual prototypes that give results close to expected from physical prototyping and provides data for further design considerations.[11][12]

First part (fig. 5) is a frame which is made of polycarbonate with good hardness characteristics. The material selected for this element is PC with 20% fiber glass reinforced (PC+SANGF20).
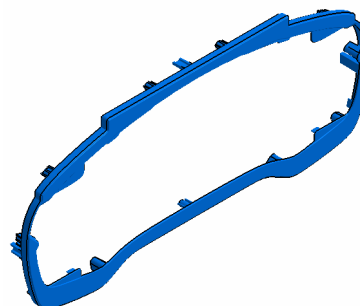
Fig. 5 Frame

The second part to analyze is a lens or the visible part of the assembly which must have good quality with no defects existing. The material for this part is PMMA.

A.   Initial configuration – frame

In the initial configuration of the simulation, the input data of the process are set to those proposed by the software, which offers default values for the selected model.

Cooling system and gate position are conventional where the part "frame" is filled from two points.
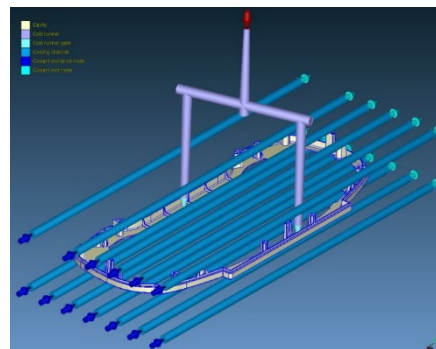
Fig. 6 Cooling and runner systems

When changing working parameters, a process accuracy measurement is required.

Initial working parameters are chosen by default.

TABLE 1 Frame parameters

Parameter	Frame PC+SANGF20
Number of gates	2
Filling time (sec)	1
Packing time (sec)	4
Cooling time (sec)	11
Eject time (sec)	5
Maximum injection pressure (MPa)	120

Maximum packing pressure (MPa)	120
Melt temperature (°C)	320
Mold temperature (°C)	110
Air temperature (°C)	25
Eject temperature (°C)	150
Cooling fluid	Water

With the help of the initial configuration, important information about the behavior of the process can be extracted, problem areas and weak parts of the injection molding can be identified.
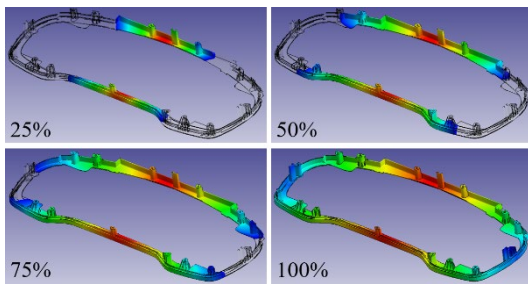
Fig. 7 Filling time

Displacement shown of the first layer is scaled. Through overexposure, it is easier to visually and cognitively identify trends and problem areas. Maximum displacement of the model is 1.2mm.
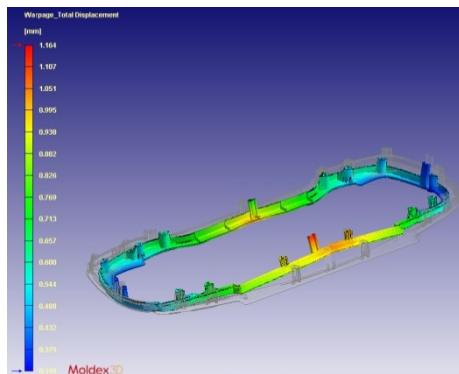
Fig. 8 Total Displacement

B.   Runner system optimization – frame

Two variants of running systems are considered and shown in fig. 9.
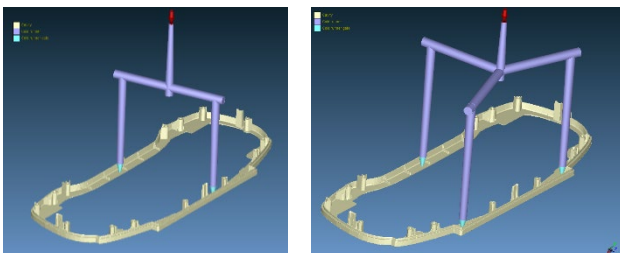
Fig. 9 Runner system comparison

Working parameters remain the same in order not to affect the results. Results from simulations are sorted in table 2.

TABLE 2 Three gates frame parameters

FRAME	Two gates No. 1	Three gates No. 2
Average injection temperature, °C	288.316	290.770
Maximum injection pressure, MPa	42.525	38.305
Average cooling temperature, °C	125.894	128.619
Maximum displacement, mm	1.164	0.989

Changing the number of gates can affect the process in different ways. But from this comes the problem with the welding lines, the more entrances, the more welding lines. They mainly affect the appearance of the product, but due to the fact that the first layer of injection molding is not visible to the end user, this effect can be ignored.

C. Filling time optimization – frame

Filling time optimization consists of simulations with 3 gates but different time to fill the form. First one is with 1 second (No. 2) and second – 0.4sec.

TABLE 3 Frame filling parameters

FRAME	1 sec fill No. 2	0.4 sec fill No. 3
Average injection temperature, °C	290.770	299.099
Maximum injection pressure, MPa	38.305	62.280
Average cooling temperature, °C	128.619	122.067
Maximum displacement, mm	0.989	0.864

Reducing the filling time reduces the cycle time as well as the displacements. Despite higher average injection temperature in simulation No. 3 to No. 2, maximum displacement from nominal dimensions in No. 3 is lower.

D. Injection melt and mold temperature optimization – frame

In the next two comparisons, melt and mold temperatures are listed below:

- Simulation No. 3 – 320°C melt temperature, 110°C mold temperature

- Simulation No. 4 – 300°C melt temperature, 130°C mold temperature

TABLE 4 Temperature parameters

	320°C/110°C No. 3	300°C/130°C No. 4
Average injection temperature, °C	299.099	284.395
Maximum injection pressure, MPa	62.280	85.159
Average cooling temperature, °C	122.067	122.067
Maximum displacement, mm	0.864	0.948

Lowering melt temperature while increasing mold temperature negatively affects maximum displacement of the part. Simulation No. 3 remain for the final optimization.

E. Cooling time optimization – frame

Default cooling time from simulation No. 3 is set 11 sec while cooling time in simulation No. 5 is set 21 sec.

TABLE 5 Cooling parameters frame

FRAME	11 sec cooling No. 3	21 sec cooling No. 5
Average injection temperature, °C	299.099	299.114
Maximum injection pressure, MPa	62.280	62.159
Average cooling temperature, °C	122.067	123.128
Maximum displacement, mm	0.864	0.658

The longer a part cools, the less it deforms after opening the mold but the injection molding cycle increases.

After changing the cooling time, an improvement in the value of the displacement is observed again. It is low enough to move to the optimization of the second layer of the two-component product.

Fig. 10 Optimization stages of frame

TABLE 6 Lens parameters

Parameter	Lens PMMA
Number of gates	2
Filling time (sec)	1
Packing time (sec)	4
Cooling time (sec)	11.5
Eject time (sec)	5
Maximum injection pressure (MPa)	120
Maximum packing pressure (MPa)	120
Melt temperature (°C)	320
Mold temperature (°C)	110
Air temperature (°C)	25
Eject temperature (°C)	150
Cooling fluid	Water

F. Initial configuration – lens

In the initial configuration of lens simulation, the input data of the process are set to those proposed by the software, which offers default values for the selected model. Runner and cooling systems are chosen analogously to the frame part.

Cooling system and gate position are conventional where the part "lens" is filled from two points.
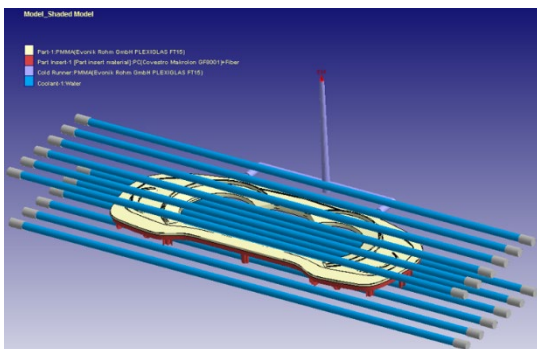
Fig. 11 Cooling and runner systems

Initial working parameters are chosen by default.
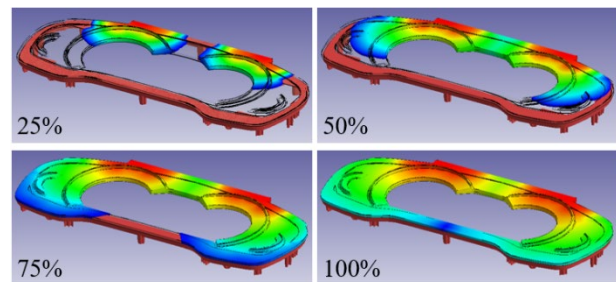
Fig. 12 Filling time

Scaled model of warpage analysis is shown in fig. 13. Tendency of shrinkage is clear.
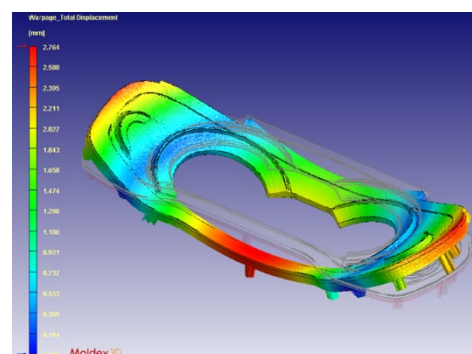
Fig. 13 Total displacement

G. Cooling time optimization – lens

Cooling time from simulation No. 1 is set 11.5 sec as default while cooling time in simulation No. 2 is set 22 sec.

TABLE 7 Lens cooling parameters

LENS	11.5 sec cooling No. 1	22 sec cooling No. 2
Average injection temperature, °C	223.013	220.297
Average cooling temperature, °C	97.430	90.976
Maximum displacement, mm	2.764	4.351

After changing the cooling time, the displacement is almost doubled. This parameter is extremely important, but if it increases too much it could lead to side effects and unnecessary prolongation of the injection cycle. This, in turn, leads to large losses due to reduced productivity.

H. Flow rate optimization – lens

Increasing the flow rate of cooling fluid is expected to cool more intense as well as lowering the warpage of the model.

TABLE 8 Flow rate lens parameters

LENS	120 cm³/s flow rate No. 1	150 cm³/s flow rate No. 3
Average injection temperature, °C	223.013	220.295
Average cooling temperature, °C	97.430	90.828
Maximum displacement, mm	2.764	2.290

The higher the coolant flow, the faster the part cools in the given time interval. The optimization of this parameter allows to shorten the cycle and achieve the desired indicators, even for a shorter period of time.

I. Coolant temperature optimization – lens

Coolant temperatures in the next analysis are going to be 72ºC and 90 ºC.

At values that are too low, an undesirably large difference between the temperature of the part and the fluid can occur. This can lead to too rapid cooling and excessive deformation. For this reason, it is desirable to select a suitable value precisely.

TABLE 9 Lens coolant parameters

LENS	72ºC coolant No. 3	90 ºC coolant No. 4
Average injection temperature, °C	220.295	223.621
Average cooling temperature, °C	90.828	103.952
Maximum displacement, mm	2.290	1.767
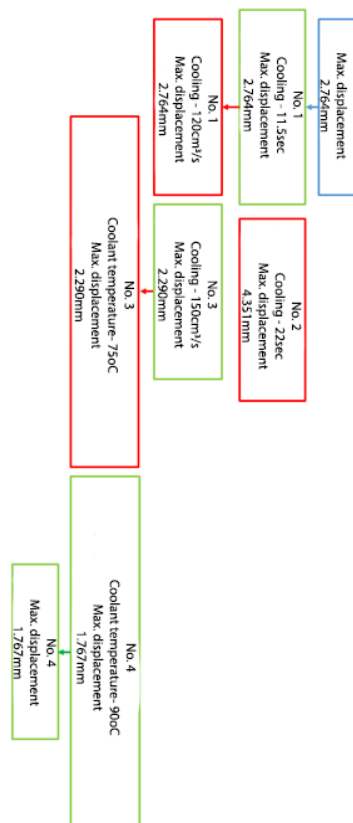
Fig. 14 Optimization stages of lens

Achieved displacement value is low enough so that the next step could be the production of the tool. It is not necessary to wait unnecessarily for the long-term and long-term optimization of the process until the maximum values are reached. It is sufficient for these values to be so low that the part can be included in a normally functioning assembled unit without compromising its functionality.

III. CONCLUSIONS

In the studies above and the results analyzed, it can be concluded that:

- Adverse results in reducing cooling time;

- Higher flow rate leads to a reduction in displacement;

- Higher coolant temperatures reduce displacement;

The achieved displacement value is low enough to start production.

IV. Acknowledgement

References

[1] M. Seyednourani, M. Yildiz, H.S. Sas, 2021. A two-stage optimization methodology for gate and vent locations and distribution media layout for liquid composite molding process. Composites Part A: Applied Science and Manufacturing 149, 106522. https://doi.org/10.1016/j.compositesa.2021.106522

[2] B. Liu, S. Bickerton, S.G. Advani, 1996. Modelling and simulation of resin transfer moulding (RTM)—gate control, venting and dry spot prediction. Composites Part A: Applied Science and Manufacturing 27, 135–141. https://doi.org/10.1016/1359-835X(95)00012-Q

[3] M. Zagorski, Y. Sofronov, D. Ivanova. Investigation of different FDM/FFF 3D printing methods for improving the surface quality of 3D printed parts. 10th International Scientific Conference on Engineering, Technologies and Systems, TECHSYS 2021

[4] K. Kamberov, M. Semkov, B. Zlatev. Design considerations through study of thermal behaviour of smart poles. 4th EAI International Conference on Future Access Enablers of Ubiquitous and Intelligent Infrastructures, FABULOUS 2019.

[5] S. Hancock, L. Harper, 2023. Cost, rate, and robustness, in: Design and Manufacture of Structural Composites. Elsevier, pp. 447–471. https://doi.org/10.1016/B978-0-12-819160-6.00022-6

[6] M.R. Mansor, S.H.S.M. Fadzullah, A.H. Nurfaizey, 2021. Life cycle assessment (LCA) analysis of composite products in automotive applications, in: Biocomposite and Synthetic Composites for Automotive Applications. Elsevier, pp. 147–172. https://doi.org/10.1016/B978-0-12-820559-4.00005-5

[7] S.H. Han, E.J. Cho, H.C. Lee, K. Jeong, S.S. Kim, 2015. Study on high-speed RTM to reduce the impregnation time of carbon/epoxy composites. Composite Structures 119, 50–58. https://doi.org/10.1016/j.compstruct.2014.08.023

[8] E. Poodts, G. Minak, L. Mazzocchetti, L. Giorgini, 2014. Fabrication, process simulation and testing of a thick CFRP component using the RTM process. Composites Part B: Engineering 56, 673–680. https://doi.org/10.1016/j.compositesb.2013.08.088

[9] D. Heider, 2019. High-Pressure Resin Transfer Molding (HP-RTM). University of Delaware.

[10] L. Kärger, A. Bernath, F. Fritz, S. Galkin, D. Magagnato, A. Oeckerath, A. Schön, F. Henning, 2015. Development and validation of a CAE chain for unidirectional fibre reinforced composite components. Composite Structures 132, 350–358. https://doi.org/10.1016/j.compstruct.2015.05.047

[11] S.M. Afazov, A.A. Becker, T.H. Hyde, 2012. Development of a Finite Element Data Exchange System for chain simulation of manufacturing processes. Advances in Engineering Software 47, 104–113. https://doi.org/10.1016/j.advengsoft.2011.12.011

[12] S. Bickerton, P. Šimáček, S.E. Guglielmi, S.G. Advani, 1997. Investigation of draping and its effects on the mold filling process during manufacturing of a compound curved composite part. Composites Part A: Applied Science and Manufacturing 28, 801–816. https://doi.org/10.1016/S1359-835X(97)00033-X

[13] L. Kroll, 2023. Modeling, integrative simulation, and optimization, in: Kroll, L. (Ed.), Multifunctional Lightweight Structures. Springer Berlin Heidelberg, Berlin, Heidelberg, pp. 563–629. https://doi.org/10.1007/978-3-662-62217-9_8

[14] S. Jiang, C. Zhang, B. Wang, 2002. Optimum arrangement of gate and vent locations for RTM process design using a mesh distance-based approach. Composites Part A: Applied Science and Manufacturing 33, 471–481. https://doi.org/10.1016/S1359-835X(01)00146-4

Influence of the Parameters of the Laser Marking Process on the Depth of Penetration in Layer-reinforced Composites

Simeon Tsenkulovski
dep. "Mechanical Engineering and Instrumentation"
Technical university-Gabrovo
Gabrovo, Bulgaria
s.tsenkulovski@advanced-technology.eu

Ivan Mitev
dep. " Economics"
Technical university-Gabrovo
Gabrovo, Bulgaria
imitev@tugab.bg

Abstract. **In the present study, we track the influence of the change in the energy parameters of a laser installation based on Fiber laser - RFFL-P-502B, on the depth of penetration in marking layer-reinforced polymer-based composites. To determine their influence on the depth of the marked strokes, experiments were carried out at speed V= 50÷250 mm/s, output power P = 5÷50 W, pulse frequency f = 50 kHz and diameter of the focal spot 40μm. Tabular results and graphical dependences of the obtained experimental results are presented.**
Keywords: plasma marking, textolite, glass textolite, marking stroke depth

I. INTRODUCTION

The successful development of quantum electronics in the second half of the last century created good conditions for the development of laser technologies [1]-[5]. Lasers, by their very nature, are generators of electromagnetic waves in the ultraviolet, visible and infrared spectrum of radiation, where the light waves are characterized by a high degree of monochromaticity and high coherence. Thanks to these qualities, lasers can focus on extremely small surfaces, theoretically commensurate with the square of the wavelength of light. In this situation, modern laser systems can reach record levels of energy concentration, giving new possibilities in the heat treatment of metals - fig. 1[1].

The process of laser marking has entered massively in the production of metal products and tools, semiconductor devices, glass and ceramic products, but in recent years it has become more and more widespread in the marking of non-metallic materials as an alternative to traditional marking methods [6] -[13].
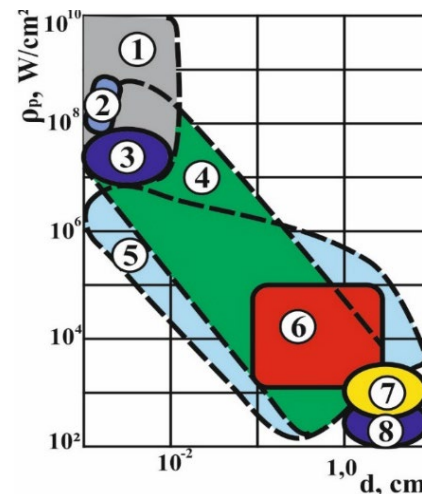
Fig. 1. Energy concentration in the focal spot
with different heat sources:
1 – pulsed periodic lasers; 2 – spark discharge;
3 – laser radiation; 4 – laser with continuous radiation;
5 – electron beam; 6 – welding arc;
7 – arc plasma; 8 – gas flame

This is an innovative method that is very different from marking in any other way, without the use of consumables. Through the laser beam, the surfaces of the products are processed extremely precisely, qualitatively, quickly and have clear contours. Laser marking is a non-contact impact on the structure of the processed material, resulting in a permanent contrast image. Information in the form of: inscriptions, identification symbols (letters and numbers), bar codes, matrix codes (2D), special characters, serial numbers, images, decoration, etc. can be applied to the surface of the product with this method. [14]-[16]. In practice, with the help of the laser, it is very easy to create an arbitrary image of your own design.

The development of the innovative industry - "Industry 4.0" in recent years has led to the implementation of innovative non-conventional technological processes in modern production, while at the same time stimulating the use of non-conventional materials, most often various types of organic and polymer-based composites [17] - [19].

In this regard, the aim of the present study is to follow the influence of the laser marking process on the penetration depth of the laser beam when marking layer-reinforced polymer-based composites.

II. MATERIALS AND METODS

In the present study, textolite samples with a thickness of 10 mm and mechanical characteristics according to DIN 7753/PFCC 202 and IEC 60893 HGW 2082, as well as glass textolite samples of type PTGC 201 with a thickness of 10 mm and mechanical characteristics according to IEC/EN 60893-3-1 were used.

The qualitative analysis of laser marking was performed on a PHILIPS URD measuring microscope - fig. 2 using INSIZE ISD software – V150 – fig.3.
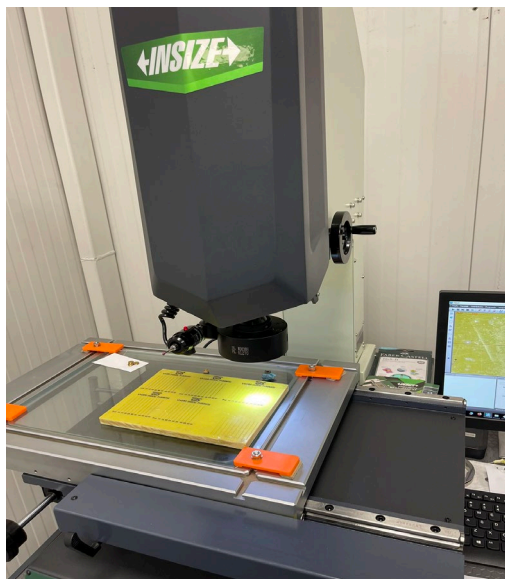
Fig.2. General view of PHILIPS URD measuring microscope
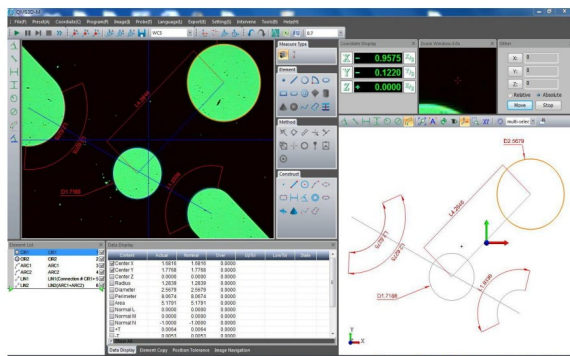
Fig.3. Software for 2D and 3D INSIZE ISD – V150

Fig. 4. ZEISS type profilometer

The roughness of the examined surfaces was measured with a portable ZEISS type roughness meter - fig.3, according to the requirements of ISO 4287 ISO 12085. The technical characteristics of the device are:

- Measuring range for Ra are $0.050 \div 10.00$ μm and for Rz are $0.020 \div 100.0$ μm;
- Resolution – 0.001 μm;
- Measuring sensor - SB10 (R=2μm, 90°);
- Measuring length - 0.25 - 0.8 - 2.5 mm;
- Number of measurements at one positioning – $1 \div 5$;

III. RESULTS AND DISCUSSION

The main technological parameters in the laser marking of polymer-based layered composite materials are the marking speed and the output power of the laser unit. To determine their influence on the depth of the marked strokes, experiments were made at marking speed V= $50 \div 250$ mm/s, output power P = $5 \div 50$ W, pulse frequency f = 50 kHz and diameter of the focal spot 40 μm. The depth of penetration – δ μm, was determined on a measuring microscope (Fig. 2). The measurements were made at 5 control points located along the marked line at a distance of 10 mm. The obtained results are presented in graphic form - fig. 4 and 5.

When conducting the experiments, it was found that with an output power of the laser radiation up to 20W and a marking speed of 50mm/s, the measured values for the depth of the marking varied within the limits of $20 \div 80$ μm, and with an increase in the output power from 20 to 50W, the fluctuations of the experimental results reach limits of $100 \div 300$ μm.

a.

b.

c.

d.

e,
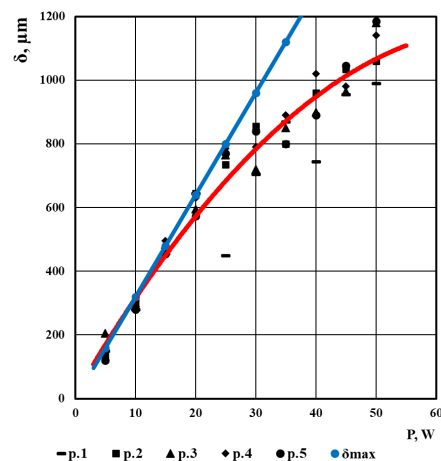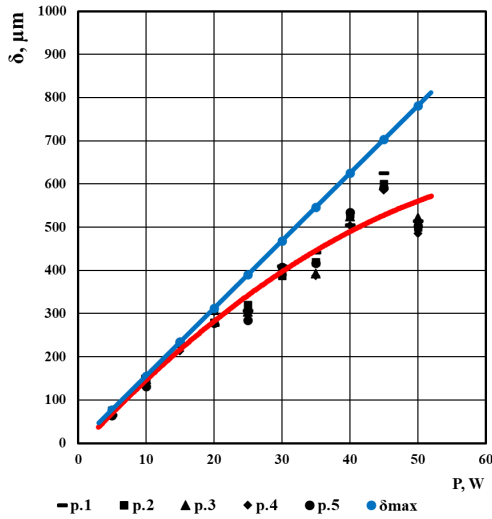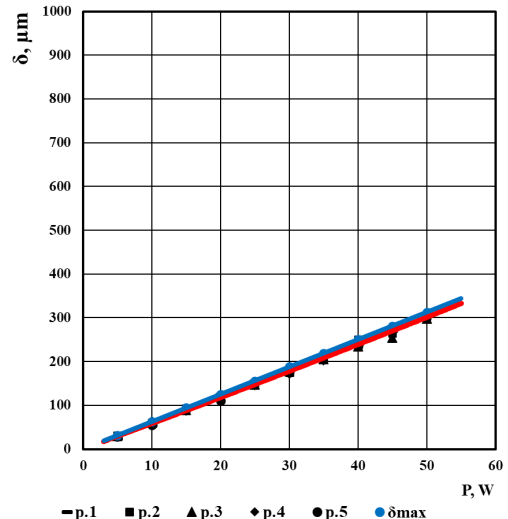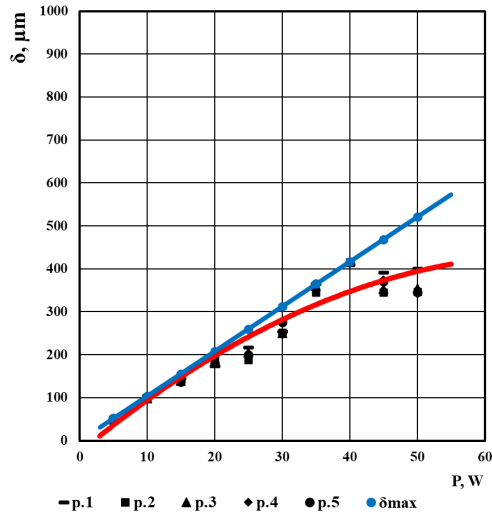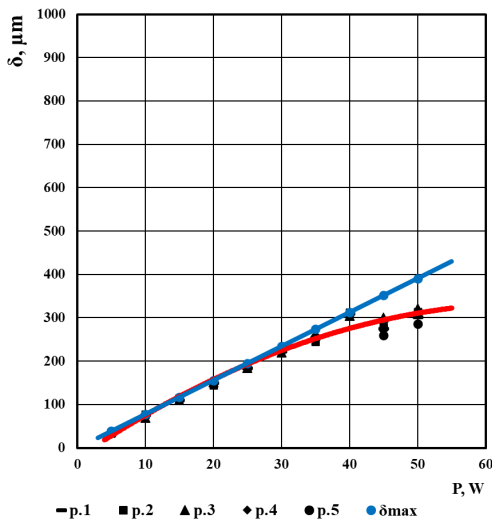
Fig.5. Change in the depth of the laser marking on samples of glass textolite depending on the power of the laser radiation at a frequency of 50 Hz and speed:
a – 50 mm/s; b – 100 mm/s;
c - 150mm/s; d – 200 mm/s;
e – 250 mm/s.

This is a result of the different vaporization temperature of the reinforcing and matrix phases making up the polymer composite.

Theoretically, for non-metallic materials, the maximum penetration depth of the laser beam – δ max, can be calculated with the expression 1 [20]:

$$\delta_{max} = 2P / (\pi . r . \rho . \upsilon . c . T) \qquad (1)$$

where: P – laser radiation power, W;
r - focal spot radius, μm;

a.

b.

c.

d.

e.
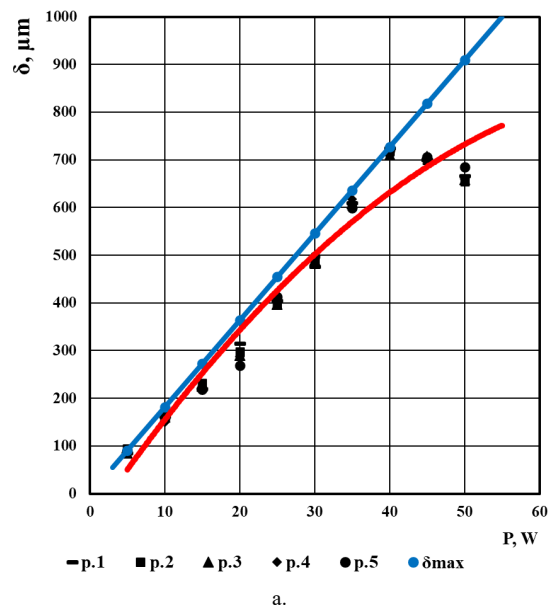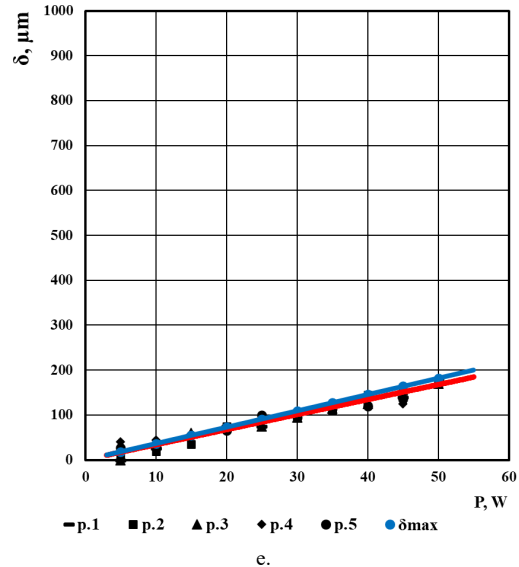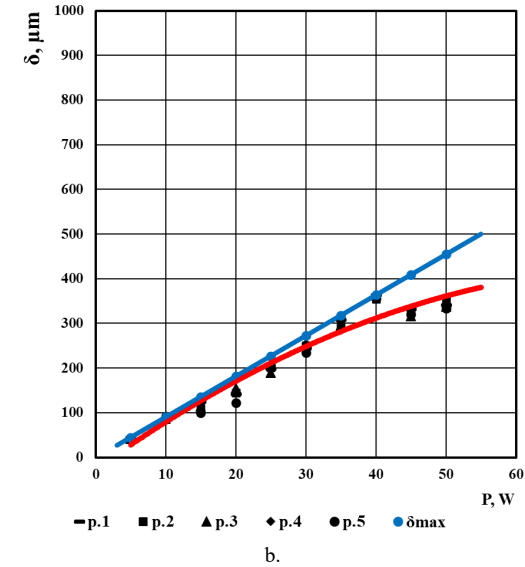
Fig. 6. Change in the depth of the laser marking on textolite samples depending on the power of the laser radiation at a frequency of 50 Hz and speed:
a – 50 mm/s; b – 100 mm/s;
c – 150 mm/s; d – 200 mm/s; e – 250 mm/s.
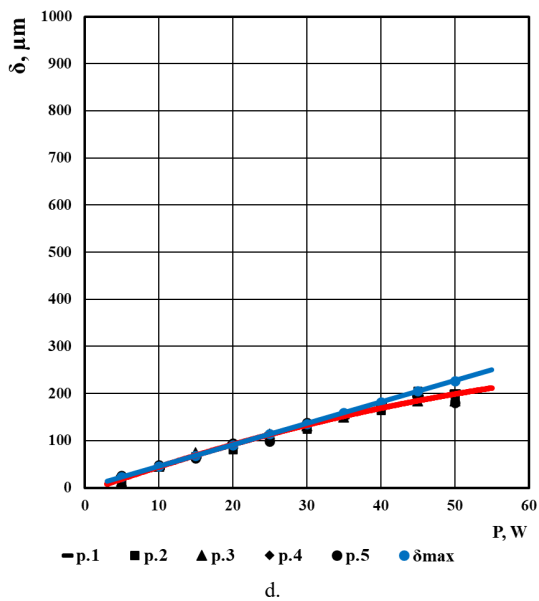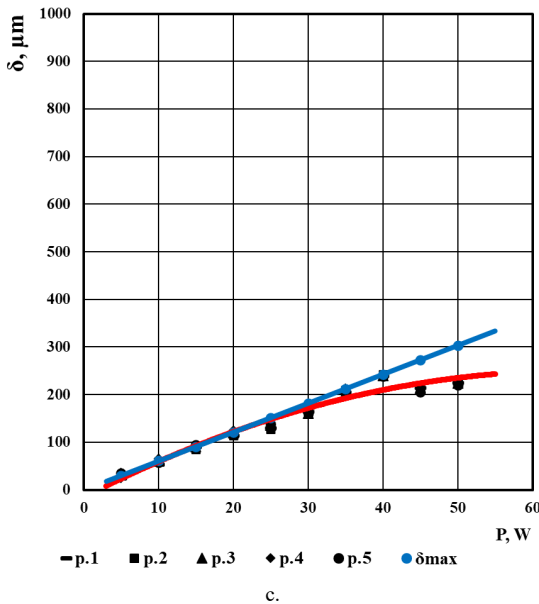
ρ – material density, g/cm^3;
υ – marking speed, mm/s;
c – specific heat, cal/g.ºC;
T – evaporation temperature, ºC.

Using reference data for the studied materials, the maximum theoretical values of the penetration depth during laser marking were calculated - δ max (Figs. 4 and 5).

Comparing the theoretical and experimental results, it can be seen that, according to formula 1, the penetration depth is linearly dependent on the power of the laser radiation. The obtained experimental results when marking the glass textolite samples show that this is valid only at low marking powers – up to 20 W. In them, the experimental results differ from the theoretical ones by less than 10%. As the output power values increase above 20 W, the margin in the measured marking depth values increases from 4 to 30%. The biggest differences are fixed in the samples marked with minimum speed – 50÷100 mm/s. At high marking speeds, the differences decrease, and at a speed of 250 mm/s, the experimental results overlap with the theoretically calculated ones.

The results for the marking of the textolite samples are also similar. At output power up to 15 W, the obtained results differ by 10÷15 %, with an increase in output power above 15 W, the differences in measured values range from 4 to 27 %. At high marking speeds – 200÷250 mm/s, the differences between the measured and theoretical curves are minimal – below 10 % and in practice they overlap.

In all investigated marking modes, the results obtained on the glass-textolite samples were better compared to those obtained on the textolite samples. This is related to the reflectivity of the material – R.

It is known that the laser effect on matter under incident radiation is different for different non-metallic materials and is related to the reflection and absorption of the radiation. When a parallel beam of rays falls on a smooth non-metallic surface, it is reflected, and the rays are also parallel to each other. On rough surfaces, the incident parallel beam of rays is reflected in different directions and diffuse reflection occurs. The reflectivity - R, is a dimensionless quantity and can have values from 0 to 1. It is a function of the wavelength of the laser radiation - R = f (λ) and is defined by the relation 2 [21].

$$R = J_T / J_o \qquad (2)$$

where: J_T – intensity of the reflected beam;
 J_o - intensity of incident radiation.

The reflectivity - R, mainly depends on the condition of the treated surface [2]. Its main characteristic is the roughness class. As the roughness class of the processed surface increases, the reflective ability decreases. Wavelength roughness significantly increases the penetration depth of laser radiation.

In the particular case, the radiation length is λ=1.06 μm.

The roughness of the marked surfaces at five random points was measured with a ZEISS profilometer and the results are presented in Table 1.

It can be seen that for textolite samples the average roughness – Ra, is close to the wavelength of the laser radiation, but the values for Rz are more than 4 times larger than the wavelength. This leads to significant scattering of the laser radiation power and reduced values for δ.

Table 1 Surface roughness.

№	Ra	ΣRa $_{1÷5}$ /5	Rz	ΣRz $_{1÷5}$ /5
textolite				
1	1,026		4,337	
2	1,018		4,409	
3	1,024	1,021	4,381	4,375
4	1,018		4,376	
5	1,019		4,372	
glass textolite				
1	0,231		1,705	
2	0,219		1,709	
3	0,219	0,225	1,701	1,703
4	0,217		1,701	
5	0,229		1,699	
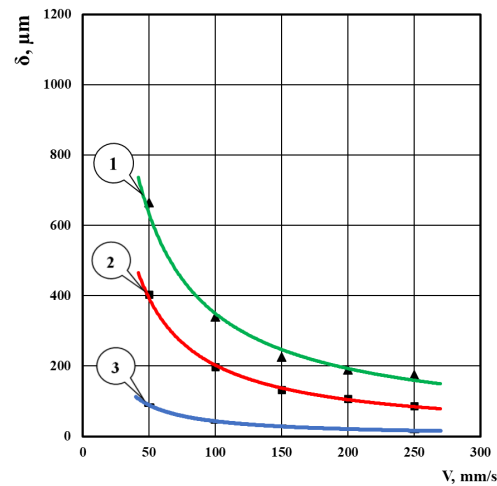
a.
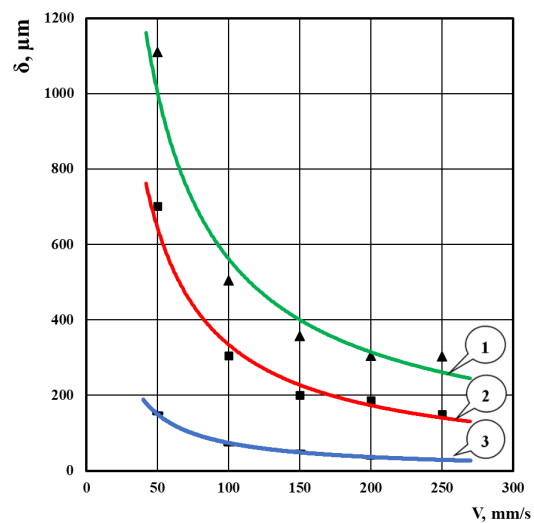
b.

Fig.7. Influence of the marking speed on the depth of the marking strokes on the examined samples at radiation power:
1 – 50 W; 2 – 25 W and 3 – 5 W
a – textolite; b - glass textolite

For the glass-textolite samples – Table 1, the values for Ra 0.225 μm and are more than 4 times smaller than the length of the laser radiation, and for Rz = 1.703 μm they are commensurate with the length of the incident radiation.

This also explains the differences in the values for δ, for the two materials studied by us.

On the basis of the obtained experimental results, graphical dependencies were developed for the influence of the marking speed on the depth of the formed marking strokes - fig. 7.

IV. CONCLUSIONS

The following more important conclusions can be formulated from the conducted research and the results obtained:

The influence of the technological parameters (P = 5÷50 W; V+50÷250 mm/s) on the depth of the formed slit during laser marking with pulse frequency f = 50 kHz and diameter of the focal spot 40μm was monitored of layered polymer-based composites.

Graphical dependencies have been developed for the influence of technological parameters of laser marking of layered polymer composites on the depth of the formed marking strokes.

It has been proven that with an output power of laser radiation up to 20 W and a marking speed of 50mm/s, the measured values for the marking depth vary in the range of 20÷80 μm, and when the output power is increased from 20 to 50 W, the fluctuations of the experimental results reach limits of 100÷300 μm, which is the result of the different evaporation temperature of the reinforcing and matrix phase making up the polymer composite.

It has been shown that the better results of the glass-textolite samples compared to the textolite ones are due to the better reflectivity of the glass-textolite

REFERENCES

[1] Mitev, I., Unconventional electrotechnological processes, EKS-PRESS, Gabrovo, 2020, ISBN 978-954-490-698-7

[2] Amara EH, Haïd F, Noukaz A. Experimental investigations on fiber laser color marking of steels. Appl Surf Sci 2015;351:1–12. doi:10.1016/j.apsusc.2015.05.095.

[3] Han A, Gubencu D. Analysis of the laser marking technologies. Nonconventional Technol. Rev. 2008;4:17–22.

[4] Ready JF, et al. LIA handbook of laser materials processing. New York: Springer Verlag; 2001.

[5] Leone C, Genna S, Caprino G, De Iorio I. AISI 304 stainless steel marking by a Qswitched diode pumped Nd:YAG laser. J Mater Process Technol 2010;210(10):1297–303. doi:10.1016/j.jmatprotec.2010.03.018.

[6] Astarita A, Genna S, Leone C, Memola Capece Minutolo F, Squillace A, Velotti C. Study of the laser marking process of cold sprayed titanium coatings on aluminium substrates. Opt Laser Technol 2016;83:168–76. doi:10.1016/j.optlastec.2016.04.007

[7] Leone C, Lopresto V, De Iorio I. Wood engraving by Q-switched diodepumped frequency-doubled Nd:YAG green laser. Opt Lasers Eng 2009;47(1):161–8. doi:10.1016/j.optlaseng.2008.06.019.

[8] Leone C, Genna S, Tagliaferri F, Palumbo B, Dix M. Experimental investigation on laser milling of aluminium oxide using a 30W Q-switched Yb:YAG fiber laser. Opt Laser Technol 2016;76:127–37. doi:10.1016/j.optlastec. 2015.08.005.

[9] Petutschnigg A, Stöckler M, Steinwendner F, Schnepps J, Gütler H, Blinzer J, Holzer H, Schnabel T. Laser treatment of wood surfaces for ski cores: an experimental parameter study. Adv Mater Sci Eng 2013 art. N°123085. doi:10.1155/2013/123085.

[10] Shin Y, Kim Y, Park S, Jung B, Lee J, Nelson JS. Pit and rim formation during laser marking of acrylonitrile butadiene styrene plastic. J Laser Appl 2005;17(4):243–6. doi:10.2351/1.2080405

[11] Genna S, Leone C, Lopresto V, Tagliaferri V. An experimental study on the surface mechanisms formation during the laser milling of PMMA. Polym Compos 2015;36(6):1063–71. doi:10.1002/pc.23442.

[12] Tuz L. Quality of marks on metals made with the use of the Nd:YAG laser engraving method. Metall Foundry Eng. 2013;39(1):55–64. doi:10.7494/mafe.2013.39.1.55.

[13] Peter J, Doloi B, Bhattacharyya B. Parametric analysis of Nd:YAG laser marking on ceramics. Int J Manuf Tech Manage 2011;24(1-4):124–38. doi:10.1504/IJMTM.2011.046764

[14] Li J, Lu C, Wang A, Wu Y, Ma Z, Fang X, Tao L. Experimental investigation and mathematical modeling of laser marking two-dimensional barcodes on surfaces of aluminum alloy. J Manuf Process2016;21:141–52. doi:10.1016/j.jmapro.2015.12.007.

[15] Dumont Th, Lippert T, Wokaun A, Leyvraz P. Laser writing of 2D data matrices in glass. Thin Solid Films 2004;453-454:42–5. doi:10.1016/j.tsf.2003.11.148.

[16] Li XS, He WP, Lei L, Wang J, Guo GF, Zhang TY, Yue T. Laser direct marking applied to rasterizing miniature Data Matrix Code on aluminum alloy. Opt Laser Technol 2016;77:31–9. doi:10.1016/j.optlastec.2015.08.020.

[17] Petrova, D., Intelligent, Innovative and Sustainable Industry in Bulgaria – prospects and challenges, Vide I. Tehnologija. Resursi - Environment, Technology, Resources, Proceeding of the 12th International Scientific and Practical Conference „Environment. Technology. Resources", June 20-22, 2019, Rezekne, Latvia, Volume I, pp. 210-215, ISSN 1691-5402 – print, ISSN 2256-070X – online

[18] Petrova, D., An Alternative Approach to Reducing Aging of Innovative Industrial Products in Terms of Industry 4.0, Environment. Technology. Recourses – Proceeding of the 13-th International Scientific and Practical Conference, Rezekne Academy of Technologies, Rezekne, Latvia, 2021, ISSN 1691-5402, Online ISSN 2256-070X, p. 274-280, scopus

[19] Petrova, D., An Approach to Modeling Innovation Obsolescence, Vide. Tehnologija. Resursi - Environment, Technology, Resources, Proceeding of the 14th International Scientific and Practical Conference, 2023, Volume I, pp. 175–179, Print ISSN 1691-5402, Online ISSN 2256-070X, DOI

[20] Park YW, Kim T, Rhee S. Development of a monitoring system for quality prediction in laser marking using fuzzy theory. J Laser Appl 2007;19(1):55–63. doi:10.2351/1.2402519.

[21] Zelenska KS, Zelensky SE, Poperenko LV, Kanev K, Mizeikis V, Gnatyuk V. A. Opt Laser Technol 2016;76:96–100. doi:10.1016/j.optlastec.2015.07.011.

An Estimation of the Hydrodynamic Flow Field (HDFF) around a Sphere through CFD and Experiment

Cvetelina Velkova
Department of Mechatronics
Naval Academy N.Vaptsarov, Varna, Bulgaria
Varna, Bulgaria
cvvelkova@nvna.eu

Abstract. **In the presented study is made a numerical modelling of the hydrodynamic flow field (HDFF) around a sphere. Numerical modelling has been made using the software ANSYS Workbench and the calculation of the hydrodynamic flow field (HDFF) around a sphere was implemented using the solver ANSYS Fluent. The analysis of HDFF around the sphere has realized using Finite Element Method (FEM) available in the ANSYS Fluent environment. The HDFF has examined around the sphere at a given horizon using the real flow, the fluid is water. The obtained numerical results for velocities and pressures around the sphere have compared to actual experimental data, [1]. The aim of the presented study is to propose a numerical approach that can give adequate assessment of HDFF in a real turbulent flow around a sphere immersed in water using modern computational methods as CFD Fluent and validation of these results with real experimental data.**

Keywords: Numerical modeling, free surface, sphere, HDFF, ANSYS Fluent

I. INTRODUCTION

Referring to the methodology set out in item 3.3 in a source [1] for numerical determination of hydrodynamic flow field (HDFF) in a deeply immersed sphere, the present study has formulated an analytical approach to address the problem at hand. Referring to chapter 3 of source [1], in it the author presents the methodology for calculating the HDFF of the ship. Briefly, he explains that the calculation is carried out in the following sequence: 1. enter the coordinates of the corner points of the spatial quadrangular source elements describing the wetted surface of the ship's hull; 2. specify the locations of the hydrodynamic features, the streamlines of which, when the current flows around, describe the shape of the underwater part of the ship's hull; 3. a system of linear algebraic equations defining the intensities of the above-mentioned features is compiled and solved; 4 the velocities and pressures at points in the flow around the body are calculated.

In the cited source [1], the author states that in it he presents the algorithms of the programs with which he implements the above-described methodology for numerical calculation of the HDFF of the ship's hull.

Based on the made formulation, a numerical model of turbulent flow around a sphere in ANSYS Fluent environment has developed by mixing two air and water fluids to calculate the HDFF. The main key element in the used analytical formulation of the problem according to the source [1] is the determination of the pressure field and flow velocities around a flowing sphere of infinitely ideal fluid, and in the numerical realization of the problem the liquid is real.
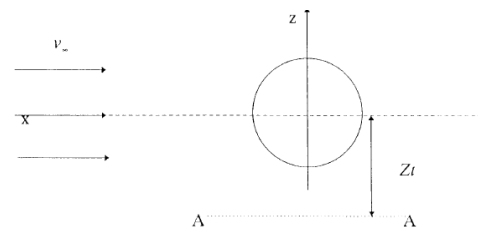
Fig. 1. Analytical formulation of the problem for determination of velocities field and pressures in points from the flow around a sphere, [1]

The assessment of the hydrodynamic flow field (HDFF) surrounding the sphere and the application of the numerical approach have conducted through an experiment [1], wherein velocities and pressures at various flow points have calculated for a sphere subjected to actual flow conditions. The experiment has conducted in accordance with the parameters outlined in the methodology section.

A different opinion on the issue related to the experimental evaluation of the HDFF around a sphere has presented in a source [6]. Quoting the author of source [1] in developing the methodology for numerical calculation of the ship's HDFF, the theoretical setup discussed in chapter two was applied. Methodology was built based on the method of Ness & Smith [88], established for bodies moving in an infinite ideal fluid, and further developed mathematical apparatus accounting for the influence of water boundaries and pressure from wave motions.

The accuracy of the model is also verified by calculating the velocities and pressures at points in the fluid

flow, for a clouded sphere, of an infinite ideal fluid. The theoretical computation was implemented with the help of the program "SFERA", with the problem setup shown in Fig. 1, source [1].

where into Fig. 1 from source [1]:

V_∞ - flow velocity of flowing sphere

Z_t - distance from x axis to the line A-A (per z axis)

D - diameter of sphere – 320 mm

When estimating the numerically obtained values of the velocities and pressures around the sphere with the experiment, the induced velocities, and pressures around the sphere from infinite flow to an ideal fluid are determined at 25 points on the line A-A equidistant to the x axis, [1]. The pressures at the points obtained by the realized numerical approach and comparison with experimental ones were calculated when flowing the sphere from flow with velocities in infinity.

$$V_\infty = 2m/s; V_\infty = 1.5m/s; V_\infty = 1m/s;$$
$$V_\infty = 0.5m/s$$

The pressure coefficient for the points on A-A is determined by expression, [1]:

$$C_p = 1 - \left(\frac{V}{V_\infty}\right)^2 = 1 - \frac{9}{4}sin^2\,\alpha, \text{ (1)}$$

a hydrodynamic pressure for the same points is determined by the following expression [1]:

$$p - p_0 = \frac{\rho V_\infty^2}{2}\left[1 - \left(\frac{V}{V_\infty}\right)^2\right] = \frac{\rho V_\infty^2}{2}c_p \text{ (2)}$$

Building on [1], this numerical problem also incorporates insights from [7], [8], [9].

II. METHODS

A. Numerical Model

Geometry and dimensions of the object- sphere. The geometry of the constructed numerical 3D model of the streamlined sphere in the ANSYS Fluent environment is shown in Figure 2.
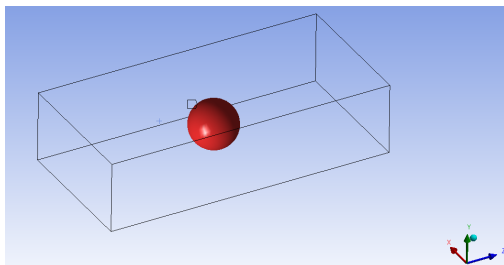
Fig. 2. The geometry of the constructed 3D model of the streamlined sphere in ANSYS Workbench environment.

The computational area (CA) of the real flow model around a streamlined sphere realized in ANSYS Fluent is constructed with the following computational dimensions shown in Fig. 3:

$R = 160mm$ - radius of a sphere

$L6 = 250mm$ - height from the center of the sphere to the free surface

$L7 = 480mm$ - height of computational area (CA)

$L8 = 460mm$ - distance from the center of the sphere to the edges of the wall of the computational area relative to the x axis.

$L9 = 920mm$ - distance from the center of a sphere to the inlet and outlet of computational area relative to z axis
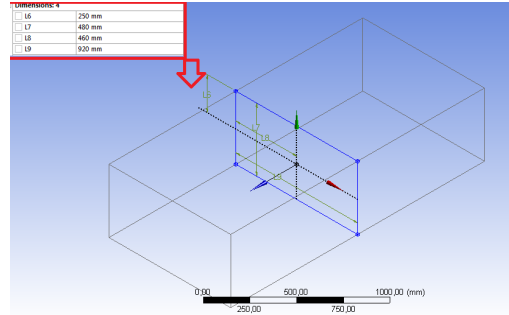
Fig. 3. Dimensions of created computational domain around the sphere.

B. Numerical Mesh

The idea of estimating hydrodynamic flow field (HDFF) in a streamlined area using numerical methods such as ANSYS Fluent is based on the analytical and experimental approach presented in the source [1], [5]. The numerical model of the flow around the sphere uses as an idea the method proposed in source, [2], [4]. In the present study, the geometry of the streamlined sphere was modeled using the CAD software package ANSYS Workbench. The numerical simulation of the flow around a sphere is realized in ANSYS Fluent environment.

One of the main steps in developing the numerical model of the streamlined sphere is the construction of an appropriate computational mesh around the sphere. Proper estimation of hydrodynamic flow field (HDFF) of the flow around the sphere and obtaining the values of the pressure and the velocity field around it includes appropriate and accurate numerical mesh. The type of computational mesh constructed around the streamlined sphere, as well as the number of cells and nodes are shown in Fig. 4. A quarter shape of cell elements was used to accurately consider the characteristics of the real flow. The density of the computational mesh in this study are extremely important to accurately approximate and solve the equation of the fluid particle's motion, as well as Navier Stokes equations in each cell of the fluid volume describing the actual flow of water around a moving sphere.
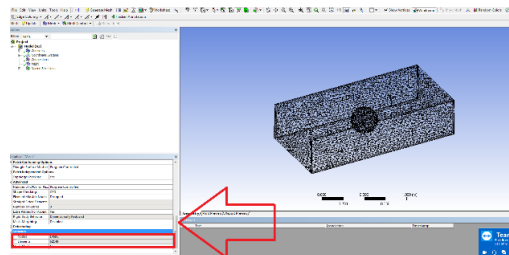
Fig. 4. Numerical model of the streamlined sphere with constructed computational mesh.

C. Boundary Conditions and set input data

Firstly, the geometry of the sphere and the constructed fluid volume limiting the flow around it are implemented using the CAD program ANSYS Workbench, [2], [3], [4].

The computational domain around the sphere is drawn with corresponding dimensions first 2D then through the function "extrude" is obtained the 3D shape of the fluid volume limiting the flow field around the sphere. According to what is stated in source [1] and the above formulation of the problem, the sphere should be placed in the center of fluid volume, after which the boundary conditions should be applied, as shown in Figure 5. The set boundary conditions, which are required by the fact that a flow around the sphere is real flow are described mathematically as follow:

Inlet: Input velocity in all four cases, as follows: $V = 0,5; 1; 1.5; 2 m/s$
Outlet: pressure that changes
Sphere: wall
Bottom (Inlet Bottom): wall.
Free surface: Pressure of 1 atm

The free surface is set as a boundary condition, i.e. it expresses the contact of the water from the fluid volume with the air, [3]. The constructed geometry of the fluid volume around streamlined sphere is in accordance with the conducted experiment and the experimental formulation of the problem set it the source [1], which was used for the comparative analysis with the obtained numerical results.
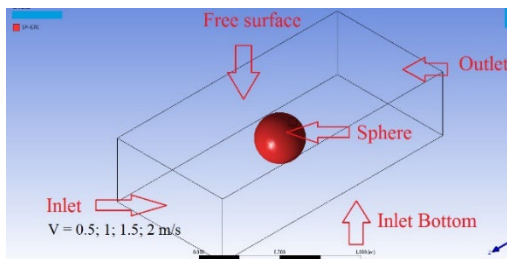
Fig. 5. Fluid domain with set boundary conditions in ANSYS Fluent environment.

The solution process, i.e. calculation of the parameters of flow around the moving sphere streamlined with real flow – water is calculated by four numerical simulations realized with ANSYS Fluent at set velocity range. A turbulence model was used to calculate the real flow around the sphere.

III. RESULTS AND DISCUSSION

A. Pressure field around the sphere

The realized numerical simulation of the flowing the sphere with real liquid by means of ANSYS Fluent makes it possible to obtain the results of the values of the total and static pressure at flow points around streamlined sphere. The nature of the total pressure field curves around the sphere is shown in Fig. 7a, Fig. 7c, Fig. 7e and Fig. 7g for the four cases of the streamlined sphere i.e. RS 11, v=0,5 m/s; RS 21, v=1 m/s, RS 31, v=1,5 m/s and for sphere RS 41, v=2 m/s. The type of static pressure curves around the sphere are shown in Fig. 7b), Fig. 7d), Fig. 7f) and Fig. 7h) again for the four cases of the streamlined sphere i.e. RS 11, v=0,5 m/s; RS 21, v=1m/s, RS 31, v=1,5 m/s and for sphere RS 41, v=2 m/s.

Velocities and velocity field around streamlined sphere. The values of the numerically calculated velocities at flow points around the sphere, as well as the velocity field around it are shown at Fig. 6a – Fig 6c for three cases of the streamlined sphere: RS 21, v=1 m/s, RS 31, v=1,5 m/s and for sphere RS 41, v=2 m/s in figures respectively:
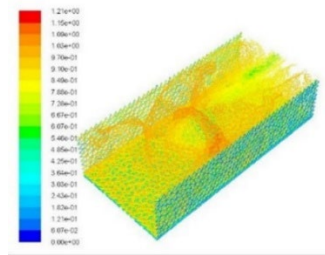
Fig. 6a. Velocities and velocity field of the liquid around the sphere RS 21 $V = 1 m/s$
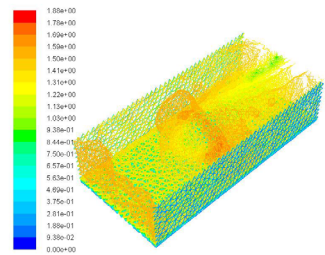
Fig. 6b. Velocities and velocity field of the liquid around the sphere RS 31, v=1,5 m/s.
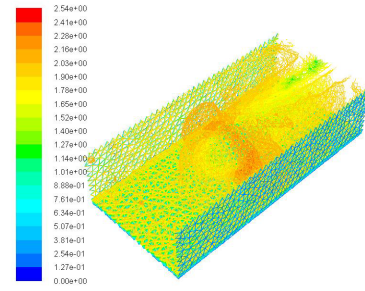
Fig. 6c. Velocities and velocity filed of the liquid around the sphere RS 41, v=2m/s.

B. Pressure values at flow points around the streamlined sphere obtained by a real experiment.

The data on the values of the pressure at points of the flow, when the sphere moves in real liquid, according to the source [1], are given in Fig. 8.
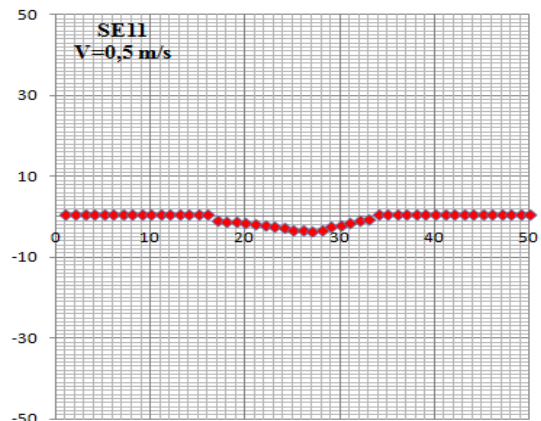
Fig. 8a. Statistical characteristics of the results obtained for the pressure by a real experiment around the sphere SE11, v=0,5 m/s.
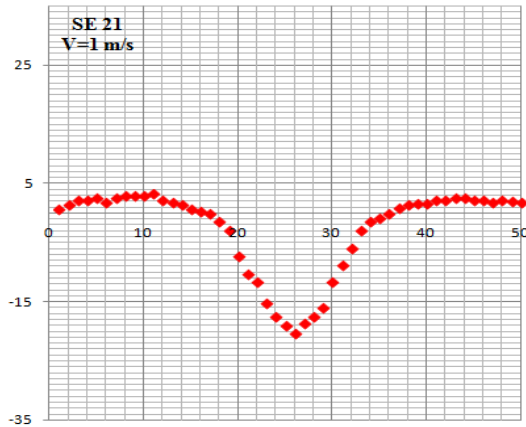
Fig. 8b. Statistical characteristics of the results obtained for the pressure by a real experiment around the sphere SE21, v=1 m/s.
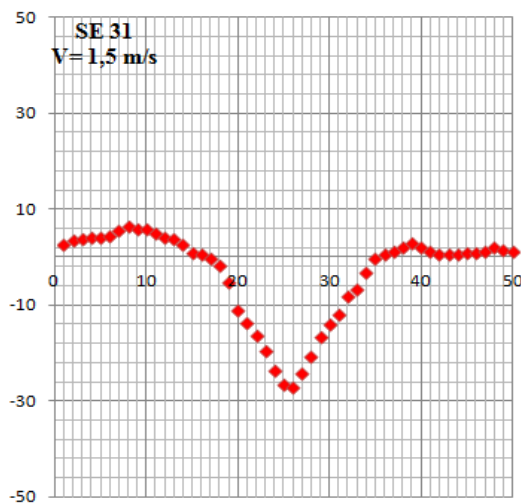
Fig. 8c. Statistical characteristics of the results obtained for the pressure by a real experiment around the sphere SE31, $V = 1,5 m/s$.
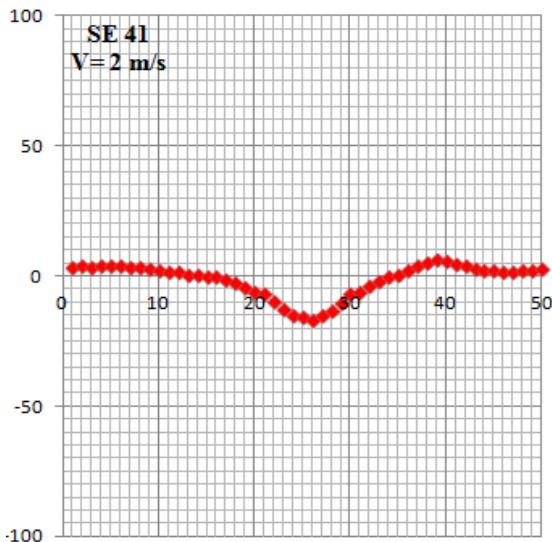
Fig. 8d Statistical characteristics of the results obtained for the pressure by a real experiment around the sphere SE41, v=2m/s.

IV. CONCLUSION

This study investigated the adequacy of a proposed numerical model for calculating pressure and velocity fields around a sphere in real fluid flow. The calculated pressure field using the model (Fig. 7a-h) exhibited good qualitative agreement with experimental data (Fig. 8a-d) from [1]. This agreement suggests the model effectively captures the essential features of the pressure field around a streamlined sphere. However, minor discrepancies were observed in static pressure (Fig. 7b, d, f, h). These discrepancies are attributed to discretization errors arising from the coarseness of the computational mesh used in the simulations.

To achieve higher accuracy in future studies, refining the computational mesh is recommended, particularly near the sphere boundary. This refinement should involve a denser cell distribution and the incorporation of a well-defined boundary layer with at least ten rows of cells within the computational domain. Implementing these refinements will likely minimize discretization errors and lead to more quantitatively accurate results.

V. ACKNOWLEDGEMENTS
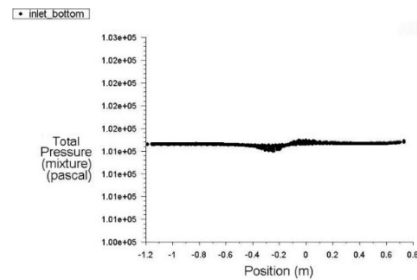
Fig. 7a. Total pressure - p_t for sphere RS 11, v=0,5 m/s.
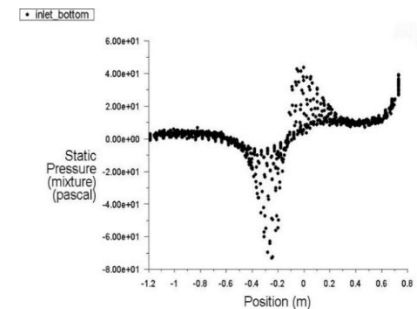
Fig. 7b. Static pressure - p for sphere RS 11, v=0,5m/s.
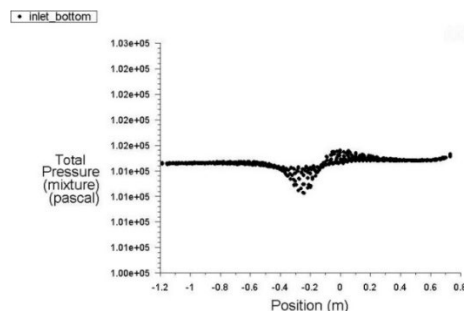
Fig. 7c. Total pressure - p_t for sphere RS 21, v=1 m/s.
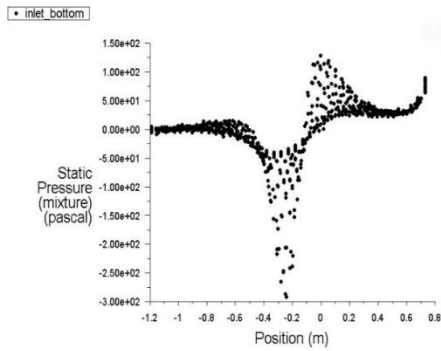
Fig. 7d. Static pressure - p for sphere RS 21, v=1 m/s.
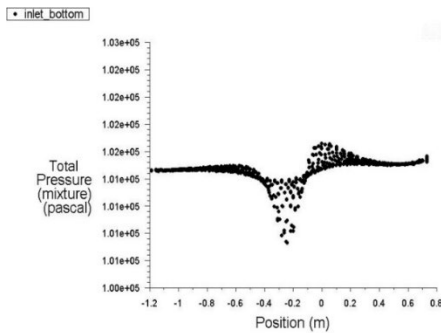
Fig. 7e. Total pressure - p_t for sphere RS 31, v=1,5 m/s.
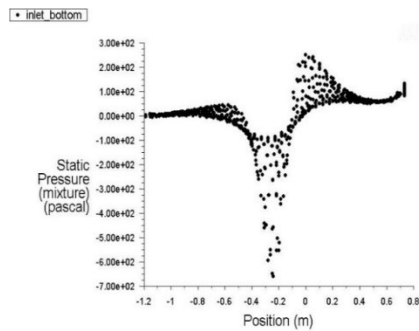
Fig. 7f. Static pressure - p for sphere RS 31, v=1.5 m/s.
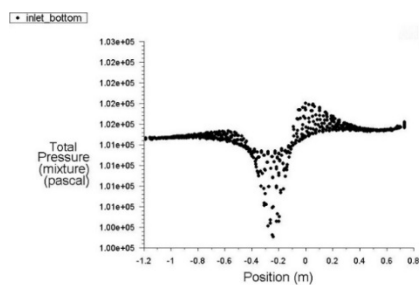
Fig. 7g. Total pressure - p_t for sphere RS 41, v=2 m/s.
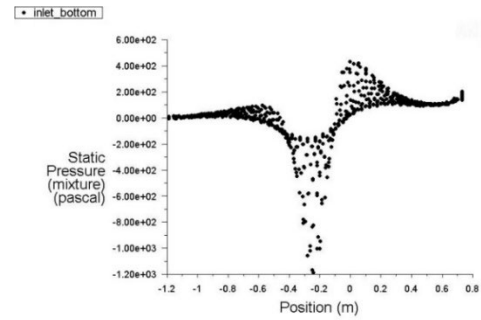
Fig. 7h. Static pressure - p for sphere RS 41, v=2m/s.

REFERENCES

[1] M. Marinov, Investigation and Control of the Hydrodynamic Field (HDF) of Ships – Dissertation, Nikola Vaptsarov Naval Academy, Varna, 1999.

[2] P. Mehta, Flow over a sphere - tutorial using Ansys Fluent, 2014. [Online]. Available: https://www.youtube.com/watch?v=8QgmO92AL70&t=23s [Accessed: Jan. 12, 2024].

[3] Cornell University. FLUENT - Turbulent Flow Past a Sphere - Problem Specification. B Simulation Wiki. 2009. [Online]. Available: https://confluence.cornell.edu/display/SIMULATION/FLUENT+-+Turbulent+Flow+Past+a+Sphere+-+Problem+Specification [Accessed: Jan. 12, 2024].

[4] J. Blazek, Computational Fluid Dynamics: Principles and Applications, 1st Edition. May 11, 2001. eBook ISBN: 9780080545547, Chapter 5: "Simulation of Viscous Flows." 2001.

[5] A. W. Date, Introduction to Computational Fluid Dynamics. Cambridge University Press, 8.08.2005., Chapter 9: "External Flow Simulations." 2005.

[6] J. S. Olafsen and P. M. Chaikin, Publisher: Cambridge University Press. Experimental and Computational Techniques in Soft Condensed Matter Physics, Chapter 10: "Simulating Fluid Flow.", 2010.

[7] K.Shyy, A. Udaykumar, T. K. Sengupta, Computational Fluid Dynamics Study on the Flow around a Sphere at Low Reynolds Numbers., Physics of Fluids, Vol. 9, Issue 11, 1997, pp. 3634-3641.

[8] B. Kandasamy, S. Mittal, Numerical Study of the Flow around a Sphere at Low Reynolds Numbers. International Journal for Numerical Methods in Fluids, Vol. 46, Issue 10, 2004, pp. 1073-1093.

[9] C.Tropea, M.Porfiri, H. H. Fernholz, A Comparative Study of the Flow around a Sphere at Low Reynolds Numbers, Experiments in Fluids, Vol. 45, 2008, pp. 99-107.

Using advanced fluid flow simulation of centrifugal pump for the purpose of education of maritime professionals

line 1: 1st Cvetelina Velkova
line 2: *Department of Mechatroncis*
line 3: *Naval Academy N.Vaptsarov,*
Varna, Bulgaria
line 4: Varna, Bulgaria
line 5: cvvelkova@nvna.eu

Abstract. **The purpose of the study is to suggest the advanced fluid flow simulation of centrifugal pump that will be implemented in training of maritime specialists. It has been developed numerical simulation using full-cloud CAE simulation software. The study describes how to use rotating zones to run incompressible fluid flow simulation on a centrifugal pump component of turbo equipment. The complexity of this use case results from the requirement of modeling a rotating region. Simulations including spinning regions necessitate additional processes for meshing and modeling the flow, which are discussed in this current study. The main value of that study is that here the task like modeling of the flow behavior of any complex turbo machinery like centrifugal pump is extremely difficult and all this is overcome by clarifying incompressible flow field around Centrifugal pump. Another main advantage of this study is that the results obtained to clarify the flow behavior through the centrifugal pump are applied in the training of students in the disciplines of marine machinery and mechanisms and hydraulics. With the results obtained in this way, which are implemented in the teaching methodology, a visual example is given to the future specialists of ship mechanics by clarifying a practical problem in a complex turbomachinery element such as the centrifugal pump using the methods of modern computing programs.**

Keywords: centrifugal pump, flow simulation, CAE, education, training simulation

I. Introduction

According to source [2] centrifugal pumps are one of the most prevalent components found in fluid systems.

Understanding the head and flow relationships for a centrifugal pump is necessary to comprehend how a fluid system with a centrifugal pump works. A centrifugal pump, according to source [1,] is a mechanical device that moves a fluid by transferring rotational energy from one or more driven rotors known as impellers.

When fluid enters a centrifugal pump, it is instantly directed to the low-pressure area at the centre or eye of the impeller. As they rotate, the impeller and blading impart momentum to the incoming fluid. A momentum transfer to a moving fluid raises its velocity. A fluid's kinetic energy increases as its velocity increases. Fluid with high kinetic energy is driven out of the impeller area and into the volute.

The volute is a region with a rising cross-sectional area designed to transfer fluid kinetic energy into fluid pressure. This energy conversion mechanism is the same as that for subsonic flow through a nozzle's diverging portion. The general energy equation, the continuity equation, and the equation connecting the internal attributes of a system are used to mathematically analyse the flow through the volute. The important parameters influencing energy conversion are the expanding cross-sectional area of the volute, the increased system back pressure at the volute discharge, and the incompressible, subsonic flow of the fluid. The fluid flow in the volute is analogous to subsonic flow in a pipe because both characteristics are interconnected.

The impeller is the most critical component of a centrifugal pump, according to [1]. It consists of a series of curved vanes. These are often sandwiched between two discs (an enclosed impeller). For fluids containing entrained particulates, an open or semi-open impeller (supported by a single disc) is ideal. Fluid enters the impeller via its axis (the 'eye') and escapes via the

circumferential between the vanes. The impeller is attached to a motor through a drive shaft and turns rapidly on the opposite side of the eye (usually 500-5000rpm). The spinning motion of the impeller vanes accelerates the fluid out of the pump casing.

There are two types of pump casings: volute and diffuser. Both designs aim to transform fluid flow into a pressure-controlled discharge, as shown in [1].

In a volute casing, the impeller is offset, resulting in a curved funnel with increasing cross-sectional area approaching the pump output. Because of this design, the fluid pressure rises towards the outflow, as seen in Fig. 1, [1].
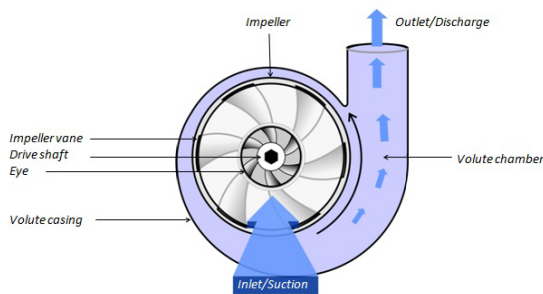
Fig. 1 Volute case design, [1]

In this study is suggesting the advanced fluid flow simulation of centrifugal pump that will be implementing in training of maritime specialists. We expect to obtain results to be a good visual example in the training of the future specialists of ship machinery and mechanisms to clarify a practical problem in a complex turbomachinery element such as the centrifugal pump using the methods of modern computing programs.

According to [2] a centrifugal pump typically produces a relatively low pressure increase in the fluid. Across a centrifugal pump with a single stage impeller, this pressure increase can range from a few dozen to several hundred psid. PSID (Pounds Force Per Square Inch Differential) is the same as P. It is the pressure difference between a pump's suction and discharge in this context. PSID can also refer to a pressure drop across a system component (strainers, filters, heat exchangers, valves, demineralizers, etc.). When a centrifugal pump is running at a constant speed, an increase in the system back pressure on the flowing stream reduces the magnitude of volumetric flow rate that the pump can maintain [2].

The relationship between the volumetric flow rate ($\dot{V}$) that a centrifugal pump can maintain and the pressure differential across the pump (Pump) is analyzed using various physical properties of the pump and the system fluid. The pump efficiency, the power supplied to the pump, the rotational speed, the diameter of the impeller and blading, the fluid density, and the fluid viscosity are all variables that design engineers consider when determining this relationship. The graph in Figure 7 in source [2] depicts the outcome of this complex analysis for a typical centrifugal pump operating at a single speed.

According to [2,] cavitation can be a significant problem for centrifugal pumps. Some pumps can be engineered to have very little cavitation. Most centrifugal

pumps are harmed by impeller erosion, vibration, or another cavitation-related problem and cannot survive extended cavitation. Cavitation can be avoided during pump operation by monitoring the pump's net positive suction head. The net positive suction head (NPSH) of a pump is the difference between the suction pressure and the saturation pressure of the fluid being pumped. [2] The NPSH value is used to calculate how close a fluid is to saturation. The net positive suction head available for a pump can be calculated using Equation 3-19 in source [2]. NPSH is measured in feet of water. Cavitation can be avoided by keeping the available NPSH higher than the NPSH required by the pump manufacturer, [2].

We can use source [1] to answer the question, "What are the limitations of a centrifugal pump?" According to [1,] the efficient operation of a centrifugal pump is dependent on the impeller's consistent, high-speed rotation. With high viscosity feeds, centrifugal pumps become progressively inefficient: there is greater resistance, and a higher pressure is required to maintain a specific flow rate. Centrifugal pumps are thus well adapted to low pressure, high-capacity pumping applications of liquids ranging in viscosity from 0.1 to 200 cP. Unlike a positive displacement pump, a centrifugal pump cannot create suction while it is dry; it must first be primed with the pushed fluid. Centrifugal pumps are consequently unsuitable for any application with an intermittent power supply. Furthermore, a centrifugal pump provides variable flow as the input pressure changes, whereas a positive displacement pump is insensitive to changing pressures and delivers a constant output. In applications requiring accurate dosage, a positive displacement pump is therefore chosen [1].

The applications of centrifugal pumps are presented in tabular form in source [1]. According to [1,] centrifugal pumps are commonly used to pump water, solvents, organics, oils, acids, bases, and any 'thin' liquid in industrial, agricultural, and home applications. In fact, a centrifugal pump design exists that is suitable for practically any application requiring low viscosity fluids.

II. Centrifugal Pump- Problem Specification

Figure 2 shows the imported centrifugal pump into Sim Scale.
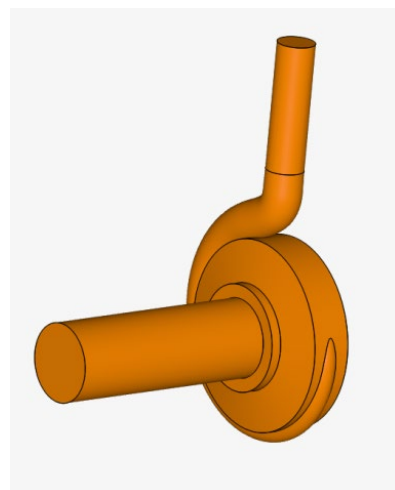
Fig. 2 Geometry of centrifugal pump

The study deals with conducting incompressible fluid flow simulation through centrifugal pump using rotating zone. The geometry presented in Fig. 2 contains the flow region, as well as a volume representing the rotating zone. The steps to make the original geometry CFD ready are given at source [5], [6].

After importing the geometry for this study, it is ready for CFD simulation using Sim Scale.

A.   Numerical model of Centrifugal pump

The developed numerical model of centrifugal pump under this study is based on the relevant models of Sim Scale web, [3].

B. Steady state incompressible fluid flow simulation

Citing [3] k-omega SST turbulence model is commonly used in turbo machinery applications. Within the pump blades, the flow experiences separation, which is effectively captured by k-omega SST turbulence model.

C. Assigning the material and boundary conditions.
Using [3] Fig. 3 shows an overview of the boundary conditions.

Citing [3] velocity inlet and pressure outlet is a very common combination used in CFD simulations as it often results in good stability. This combination permits flow to adjust aiming to assure mass continuity.
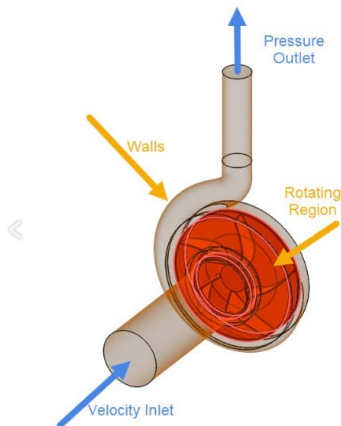
Fig. 3 Overview of the boundary conditions for centrifugal pump simulation, [3].

In the study the performed CFD simulation uses water as a material. After making the proper settings for the velocity inlet, a volumetric flow rate of '8.5e-3 m^3/s' enters the domain through the inlet. In the pressure outlet we must be sure that the gauge pressure is set to 'Mean value=0'. Next boundary condition that is assigned is wall, and all solid walls should receive a no-slip condition.

After assigning all boundary conditions it has been created a rotating zone. The rotating zone was created according to x axis. All entities within this rotating zone are rotating at 350 rad/s. According to [3] MRF Rotating zones are chosen in this simulation because we are running a steady-state simulation. If we were calculating a transient problem, we would need to choose AMI Rotating Zone.

D. Assigning the material and boundary conditions.
Using [3] Fig. 3 shows an overview of the boundary conditions.
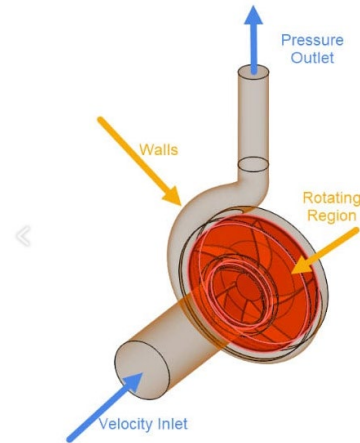
Fig. 3 Overview of the boundary conditions for centrifugal pump simulation, [3].

Citing [3] velocity inlet and pressure outlet is a very common combination used in CFD simulations as it often results in good stability. This combination permits flow to adjust aiming to assure mass continuity.

In the study the performed CFD simulation uses water as a material. After making the proper settings for the velocity inlet, a volumetric flow rate of '8.5e-3 m^3/s' enters the domain through the inlet. In the pressure outlet we must be sure that the gauge pressure is set to 'Mean value=0'. Next boundary condition that is assigned is wall, and all solid walls should receive a no-slip condition.

After assigning all boundary conditions it has been created a rotating zone. The rotating zone was created according to x axis. All entities within this rotating zone are rotating at 350 rad/s. According to [3] MRF Rotating zones are chosen in this simulation because we are running a steady-state simulation. If we were calculating a transient problem, we would need to choose AMI Rotating Zone.

E. Numerical and simulation control.

Using the algorithm [3] under the Simulation control setting it must be chosen 'Potential flow initialization' which enhances the stability for velocity-driven flows, especially in early iterations. The maximum runtime was 30000 seconds, and the writing interval is 600 iterations.

F. Data control

Citing [3] outcome control allows you to see the convergence behavior during the calculation process at specified points in the model. As a result, it is a crucial indication for assessing the quality and dependability of the outcomes.
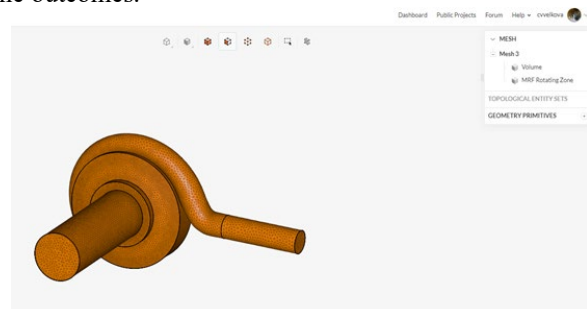
Fig. 4 View of mesh geometry around Centrifugal pump.

In this investigation, the global simulation settings were left at their default, while local refinement was applied to the regions of interest. As stated in [3,] defining cell zones is required if we want to apply a specific property, such as a rotating motion, to a subset of cells. When Physics-based meshing is enabled, the conventional Mesher automatically produces the required cell zones. Because physics-based meshing is used in this case study, the algorithm will handle cell zone definition.

For this study, it was made mesh refinement. Citing [3] the maximum edge length should be '7e-4' meters, applied to the Local element size refinement topological entity set. With this refinement we have better control over the cell size in the regions of interest.

The 'Force and Moments' control to the impeller was chosen for the simulation under this study. In addition, an 'Area average' for the inlet and another for the outlet were produced.

G. Mesh

According to [3,] the Standard algorithm is recommended for creating the mesh, which is a solid choice in general because it is quite automated and produces decent results for most complex geometries, such as the centrifugal pump in our instance. Figure 4 depicts the geometry of a centrifugal pump with a produced mesh.

Citing [3] MRF rotating zones are chosen in this simulation because we are running a steady-state simulation. If we are calculating a transient problem, we would need to choose AMI Rotating zone.

III. RESULTS AND ANALYSIS

Convergence is crucial for the fluid flow simulation. As the iterations go on, key parameters are expected to stop changing. At this point, the simulation is considered converged. For the flow simulation through centrifugal pump the key parameters for convergence that must be monitored are the velocity at the outlet, the pressure at the inlet, and forces onto the impeller. Fig. 5 shows velocity at the outlet.
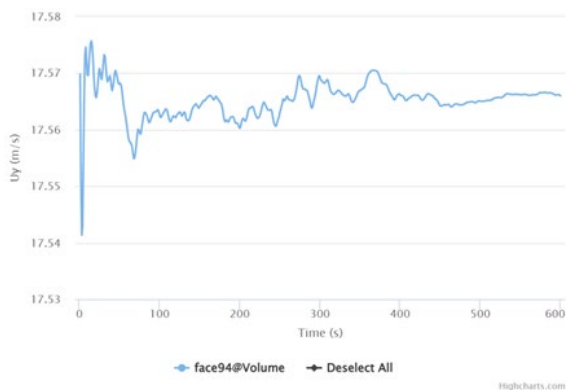
Fig. 5 Velocity at the outlet control.

From Fig. 5 we can notice that after 600 iterations the results become stable. Also, we must make sure to check the convergence plots to see residual levels. Smaller residuals indicate a more tightly converged solution.

Citing [3] Sim Scale has a built-in post-processing environment, which can be accessed by clicking on 'Solution Fields' or 'Post-process results. First, the simulation gives the opportunity to visualize the pressure. Fig. 6 shows the pressure visualization on the blades, and the bottom.
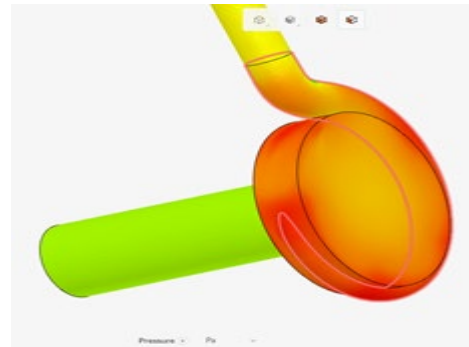
Fig. 6 The pressure visualization on the impeller from centrifugal pump.

The surface of the impeller reveals a high distribution on the edge towards the exit of the pump, near the exit of the fluid.

To get a better understanding of what is going on inside the pump, as a result it can be proceeded to add a 'Cutting Plane' filter. Fig. 7 shows the cutting plane normal to X-axis that shows the behavior of the flow when exiting the model.
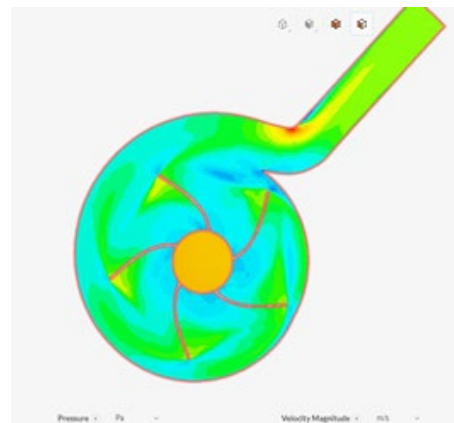
Fig. 7 Cutting plane filter for velocity magnitude

Fig. 8 shows the velocity contours with velocity vectors plotted. It can be observed that in areas where the fluid accelerates, such as the tips of the blades, and the entrance to the outlet, the vectors are also enlarged.

From Fig. 8 we can conclude that near the edges of the blades, the acceleration of the flow can be distinguished due to the representation with a warmer color compared to its surroundings.

To obtain the additional information we can look at other configurations for the cutting plane, for instance, we can change the orientation to Y axis as is shown in Fig. 9.

With the configuration given in Fig. 9 you can observe the flow pattern around the blades from a different perspective.
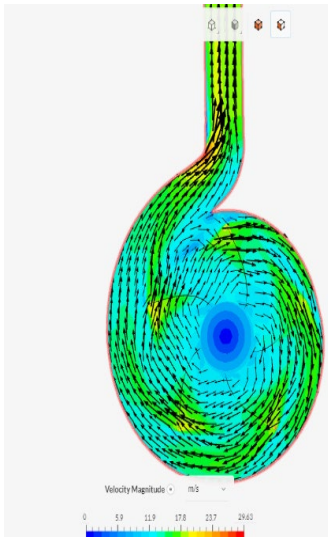
Fig. 8 Velocity contours with velocity vectors.
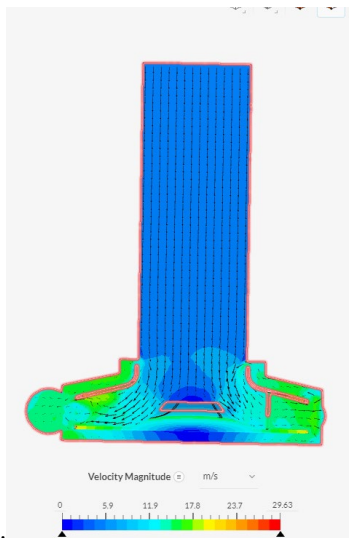
Fig. 9 Velocity vectors to Y axis

IV. CONCLUSIONS

Centrifugal pump was performed for the purpose of education of maritime students. All calculations were made with CAE software Sim Scale. It was used $k-\varepsilon$ turbulence model for flow simulation around Centrifugal pump. The flow domain has been modeled, meshed, and solved, and post-processing visualization options have been used for better understanding, investigation, and evaluation of the flow field around the pump.

The analysis is used to investigate the flow behavior around Centrifugal pump and to be applied as a tool part of educational training of the students. Pressure distribution and velocity magnitude are displayed. Using the analysis, it is getting velocity at the outlet and pressure of the pump.

The results of this study's efforts to clarify the behaviour of the flow via the centrifugal pump are used to instruct students in the fields of hydraulics and marine machinery and mechanisms. This is another major benefit of the study. By using the outcomes of this research, which are incorporated into the teaching methodology, future ship mechanic specialists are given a visual example by clarifying a practical issue in a complex turbomachinery component like the centrifugal pump using the techniques of contemporary computing programs.

Furthermore, this investigation is a guideline for obtaining quick and correct results for flow filed around Centrifugal pump.

Furthermore, the validity of the obtained results is supported by the fact that the study was carried out according to a well-established methodology approach, [3] that predicts certain flow characteristics around the centrifugal pump. The study's results match those expected from the used approach. Such conformation strengthens the reliability of the analysis and makes it suitable for educational purposes. It provides students of hydraulics and marine machinery and mechanisms with a real example for understanding complex flows into the turbomachinery.

REFERENCES

[1] Michael Smith Engineers Ltd. (2023). Useful information on centrifugal pumps. Retrieved from https://www.michael-smith-engineers.co.uk/resources/useful-info/centrifugal-pumps

[2] DOE Fundamentals Handbook:Thermodynamics, Heat Transfer, and Fluid Flow.DOE-HDBK-1012/3-92,U.S. Department of Energy, June 1992,https://engineeringlibrary.org/reference/centrifugal-pumps-fluid-flow-doe-handbook

[3] SimScale. (2022, August 30). Advanced Tutorial: Fluid Flow Simulation through a Centrifugal Pump. B SimScale Docs.
URL: https://www.simscale.com/docs/tutorials/

[4] Rana, M. S., Upadhyay, S. H., Harsha, S. P. (2014). "CFD Analysis of Centrifugal Pump: A Review." International Journal of Research in Advent Technology, 2(7), July 2014.

[5] Harikrishnan, T., Sankaranarayanasamy, K. (2014). "Numerical Investigation of the Performance Characteristics of a Centrifugal Pump Using CFD." International Journal of Mechanical Engineering and Robotics Research, 3(3), July 2014.

[6] Gautam, M., Deshpande, S. M., Rana, M. S. (2013). "Computational Fluid Dynamics Analysis of a Centrifugal Pump." International Journal of Engineering and Innovative Technology, 3(2), August 2013.

[7] Lobanoff, V. S., Ross, R. R. (1992). Centrifugal Pumps: Design and Application.

[8] Tu, J., Yeoh, G. H., Liu, C.,Butterworth-Heinemann, 2012 г. Computational Fluid Dynamics: A Practical Approach.

[9] Durran, D. R., Springer (2010). Numerical Methods for Fluid Dynamics: With Applications to Geophysics.

Mathematical model equation of the energy willow cutting unloading process from the slot hopper automated planter

Serhii Yermakov
Educational and Scientific Laboratory "DAK GPS",
Higher educational institution
«Podillia State University»,
Kamianets-Podilskyi,Ukraine
dakgps@pdatu.edu.ua

Taras Hutsol
Department of Mechanics and Agroecosystems Engineering
Polissia Natoinal University
Zhytomyr, Ukraine
wte.inter@gmail.com

Iryna Mushenyk
Department of Physics, Labor Safety and Environmental Engineering
Higher educational institution
«Podillia State University»,
Kamianets-Podilskyi,Ukraine

Stepan Zamojskij
Department of Agricultural Engineering and Systems Engineering
Higher educational institution
«Podillia State University»,
Kamianets-Podilskyi,Ukraine

Oleksandr Hovorov
Department of Tractors, Automobiles and Energy Vehicles
Higher educational institution
«Podillia State University»,
Kamianets-Podilskyi,Ukraine

Abstract. **This work is a logical continuation of the authors' cycle of works devoted to construction of a mathematical model of the unloading process of cuttings from a slotted hopper. The purpose of the paper is a theoretical justification of the movement of an array of cuttings during gravity unloading. The article proposes consideration of the process of unloading the energy willow cuttings from the point of view of hydrodynamic multiphase systems. It is suggested to consider the set of cuttings as a pseudo-fluid consisting of two phases: discrete (cuttings) and continuous (air). Each of these phases can be considered as a continuous environment. Under such conditions, the task is reduced to consideration of the cuttings' discharge as the movement of a viscous non-contacting pseudo-liquid. Under such assumptions, the velocity field of the set of cuttings can be characterized by the Navier-Stokes equation, the solution of which will allow forming of an algorithm for building a mathematical model of the motion of such pseudo-fluid and moving to the calculation equations of the motion with initial and boundary conditions.**

Keywords: unloading of cuttings, energy willow, mathematical model, Navier–Stokes equation, Laplace transform, calculation equations.

I. Introduction

Recently, in the field of energy, more and more attention is paid to renewable energy sources. One of the most promising trends from the point of view of increasing volumes is biomass energy. Particularly, there is a trend towards increasing popularity of fuels from bioenergy crops, for which fast and productive fuels are needed. The most widespread in Ukraine, energy willow is propagated vegetatively by cuttings 20-25 cm long and 5-20 mm in diameter [1-3]. Today, the planting of such material is carried out by planters, in which the planting material is fed exclusively by hand, which significantly limits the possibilities of increasing the efficiency of the units. The theoretical study of the movement of cuttings during gravity unloading and the implementation of the obtained results in practice can help to create a planting machine [4-6].

In accordance with the scientific direction that is being developed at the Higher Educational Institution "Podillia State University", "Justification of the work process and parameters of the cuttings supply mechanism of the machine for planting energy willow" (state registration number 0119U100945), an automated system of supply and selection of planting material of woody energy crops is being developed.

Analysis of recent research and publications.

Many works have dealt with the issues of improving the unloading process of materials, but, despite the significant successes in this field, the dynamic processes of unloading loose homogeneous materials have not been

studied enough. Thus, currently the main characteristics are considerably investigated and physical and mechanical properties of bulk materials, which to one degree or another affect the process of crypt formation, are considered. General directions of research in the field of uninterrupted functioning of hopper devices and the improvement of crypt breaking equipment for bulk cargoes with a wide range of physical and mechanical properties are reflected [7-17].

Numerous studies of the crypt formation process made it possible to establish only some dependencies that explain the essence of this process. The degree of influence of a huge number of different interrelated factors on crypt formation is difficult to assess practically and predict theoretically: it is a geometry of the hopper and outlet opening, and the physical and mechanical properties of materials, and the conditions of loading, storage, and release. Precisely, due to the difficulties in ensuring uniform continuous movement, which excludes the process of crypt formation, until now there is no universal feeding device that would work effectively with any loose material, and the variety of material that requires unloaded contributes to further searches for justifications movement of one or another material.

It is also difficult to overestimate the scientific and practical importance of studies of the mechanism of movement of loose materials under the influence of their own weight, since the physical and mechanical properties of these materials and the patterns of their termination have a decisive influence on the design of hoppers, as well as discharge devices and devices that stimulate discharge.

It should be emphasized that today there is no single theory of discharge of loose materials and crypt formation processes in the hopper.

The problem is even more complicated when it is necessary to ensure a uniform and continuous discharge of material in which one dimension (length) significantly exceeds the other two dimensions. Plant cuttings are an example of such material.

When creating an automatic planter for such material, the task of fast and accurate feeding of cuttings occurred, which led us to search for ways to justify the movement of cuttings during unloading from the storage tank [18-20].

Therefore, the study of this issue will continue to be relevant. The authors of this work made a significant contribution to the development of this issue in their previous works. One of the first steps in this direction was the construction of a mathematical model of the process of gravitational discharge of rod-like materials from slotted hoppers [21-23].

The authors also worked out general principles for building a mathematical model of the process of unloading cuttings from a hopper, defined boundary conditions and characteristics of their movement [23, 25].

The main assumptions about the nature of the movement of the stem-air mixture, which was presented in the form of a two-phase pseudo-liquid, were considered and substantiated. Thanks to this, some components of the equations could be neglected, and the existing equations of motion could be significantly simplified.

In previous studies, based on the assumptions made about the nature of the movement of a two-phase fluid, simplified equations were obtained [21,22]:

$$\frac{\partial \vec{u}}{\partial \bar{t}} = -\gamma \vec{\nabla} \rho + \bar{v} \Delta \vec{u} + \Phi(\vec{u}_1 - \vec{u}) - \overline{g}\overline{e}_2 \qquad (1)$$

$$\frac{\partial \vec{u}_1}{\partial \bar{t}} = -0.5 \frac{\delta}{1-\delta} \frac{\partial}{\partial \bar{t}} (\vec{u}_1 - \vec{u}) - \Phi_1 \int_0^{\bar{t}} \frac{\partial}{\partial \bar{t}} (\vec{u}_1 - \vec{u})(\bar{t} - \bar{\tau})^{-\frac{1}{2}} d\bar{\tau} - \Phi_2(\vec{u}_1 - \vec{u}) - \overline{g}\overline{e}_2 \qquad (2)$$

$$\text{div}\,\vec{u} = 0, \quad \text{div}\,\vec{u}_1 = 0 \qquad (3)$$

Equations (1) - (3) became the basis for describing the process of unloaded cuttings from the hopper. It is necessary to add initial and boundary conditions to these equations, which in the new notation have taken the form:

Initial conditions:

$$\vec{u}\big|_{\bar{t}=0} = \vec{u}_1\big|_{\bar{t}=0} = 0$$
$$\rho\big|_{\bar{t}=0} = 0 \qquad (4)$$

Boundary conditions:

at $\bar{x}_2 = h(\bar{t})/L$, $\quad -\rho + \dfrac{2\mu V_0}{L}\dfrac{\partial u_2}{\partial \bar{x}_2} = 0 \qquad (5)$

where h - the thickness of the layer of cuttings

$$\frac{\partial u_1}{\partial \bar{x}_2} + \frac{\partial u_2}{\partial \bar{x}_{12}} = 0, \qquad (6)$$

$$\dot{h} = V_0 T u_2, \qquad (7)$$

a $\bar{x}_2 = -\text{tg}\,\alpha(\bar{x}_1 + b/2L) \quad -\text{ctg}\,\alpha h_0/L - b/2L < \bar{x}_1 < b/2L$

$$\sin \alpha u_1 + \cos \alpha u_2 = \frac{A\omega}{V_0}\sin 2\pi \bar{t}, \qquad (8)$$

$$\cos 2\alpha\left(\frac{\partial u_1}{\partial \bar{x}_1} + \frac{\partial u_2}{\partial \bar{x}_2}\right) + 2\sin 2\alpha \frac{\partial u_1}{\partial \bar{x}_1} = \frac{gL\cos^2 \alpha h(\bar{t})}{2\nu V_0}, \qquad (9)$$

at $\bar{x}_2 = \text{tg}\,\beta(\bar{x}_1 - b/2L) \quad b/2L < \bar{x}_1 < b/2L + \dfrac{\text{ctg}\beta h_0}{L}$

$$\cos 2\beta\left(\frac{\partial u_1}{\partial \bar{x}_2} + \frac{\partial u_2}{\partial \bar{x}_1}\right) - 2\sin 2\beta \frac{\partial u_1}{\partial \bar{x}_1} = \frac{gL\cos^2 \beta h(\bar{t})}{2\nu V_0}. \qquad (10)$$

By applying the Laplace transform to determine the Fourier coefficients, a system of linear algebraic equations for the speed of movement of a pseudo-fluid was obtained (see (11), (12)) [21, 23]

$$U_1 = \overline{A}_{10}e^{-\sqrt{\lambda}\bar{x}_2} + \sum_{n=1}^{\infty}\bar{\lambda}_n e^{-\sqrt{\lambda_n}\bar{x}_2}\left(\overline{B}_{1n}\sin\frac{2\pi n}{M}\bar{x}_1 - \overline{B}_{2n}\cos\frac{2\pi n}{M}\bar{x}_1\right), \qquad (11)$$

$$U_2 = -d/\lambda + \sum_{n=0}^{\infty}e^{-\sqrt{\lambda_n}\bar{x}_2}\left(\overline{B}_{1n}\cos\frac{2\pi n}{M}\bar{x}_1 + \overline{B}_{2n}\sin\frac{2\pi n}{M}\bar{x}_1\right), \qquad (12)$$

where $A_{1n}, A_{2n}, B_{1n}, B_{2n}$ - the quantities that are unknown functions of the variable x_2.

$$\dot{B}_{1n} + \frac{2\pi n}{M} A_{2n} = 0, \quad \dot{B}_{2n} - \frac{2\pi n}{M} A_{1n} = 0.$$

$$\overline{A}_{1n} = -\sqrt{\overline{\lambda}_n}\,\frac{M}{2\pi n}\,\overline{B}_{2n}, \quad \overline{A}_{2n} = \sqrt{\overline{\lambda}_n}\,\frac{M}{2\pi n}\,\overline{B}_{1n}.$$

$$\overline{\lambda}_n = \sqrt{\lambda\left(\frac{M}{2\pi n}\right)^2 + 1}$$

(13)

Formulas (11), (12) provide a general solution to the system of equations of fluid motion. To find values $\overline{B}_{1n}, \overline{B}_{2n}$ it is necessary to use the boundary conditions (5) - (10).

This work is the final part of a cycle of works devoted to the construction of a mathematical model of the process of unloading cuttings from a slotted hopper, therefore its purpose is to derive calculation formulas for the movement of an array of cuttings during their gravitational unloading from a slotted hopper.

II. MATERIAL AND METHODS

The theoretical basis of the research was the work of domestic and foreign scientists, in which scientific methods were developed to justify the process of unloading bulk material from containers, with the development of issues of solving the problems of crypt formation and continuous unloading of material. Based on the analysis of existing solutions for the movement of material during gravity dumping, a model of the movement of cylindrical bodies (cuttings) during free unloading from the hopper was created.

For preliminary studies, the hopper model (Fig. 1) was used as a basis, in which consideration of the process is limited to a two-dimensional model (in the x_1x_2 plane), since it is believed that the movement of cuttings in the hopper does not depend on the x_3 coordinate, due to the presence of walls parallel to the x_1x_2 plane, which limit the movement of cuttings along the x_3 axis.
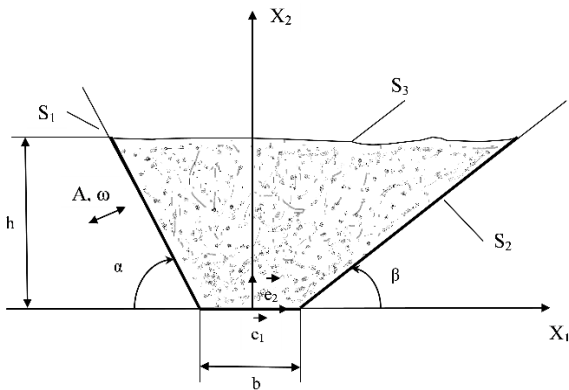
Fig. 1. Calculation diagram of a hopper with cuttings: S_1 and S_2 surfaces describ-ing the boundaries of the hopper walls; S_3 – free surface of the hopper boundaries; α and β - angles to the horizontal plane of the two half-planes describing the bunker model; h - thickness of the layer of cuttings; b –width of the unloading window; A, ω - amplitude and circular speed of harmonic oscillations parallel to the axis x_2; e_1, e_2, e_3 – unit vectors of the Cartesian coordinate system.

At the same time, based on the analysis of existing solutions, a number of assumptions were made, which allowed to consider the gravitationally unloaded cuttings from the point of view of hydrodynamic multiphase systems.

According to this approach, the set of cuttings is considered as a fluid consisting of two phases: a discrete phase formed by the cuttings and a continuous phase - a gaseous medium (air). Each of these phases is considered as a continuous environment, which allowed us to consider the discharge as the movement of a viscous incompressible fluid. The velocity field of such a pseudo-fluid must satisfy the Navier-Stokes equation.

III. RESULTS AND DISCUSSION

As noted in the authors' previous studies the system of linear algebraic equations was obtained for determination of the Fourier coefficients of the Laplace transformation of the speed of movement of the pseudo-fluid (see (11), (12)) [26,27].

In the future, we will limit ourselves to the case of a symmetrical hopper in order to obtain calculation formulas for the velocity of fluid movement. Within the framework of the adopted model of the hopper, this means that for the angles α and β the equality $\alpha = \beta$ is fulfilled. This restriction, on one hand, does not deny the commonality of the previously presented results, and on the other hand, it allows obtaining a solution to problem (1) - (3), (4) - (10) in closed analytical form.

So, let $\alpha = \beta$, then the system of linear algebraic equations takes the form:

$$\overline{B}_0 \frac{1-e^{-\sqrt{\lambda}\,h_0}}{\sqrt{\lambda}}\cos\alpha + \overline{B}_1\left(\cos\alpha\Phi_c - \overline{\lambda}_1\sin\alpha\Phi_s\right) - \overline{B}_2\left(\overline{\lambda}_1\sin\alpha\Phi_c + \cos\alpha\Phi_s\right) =$$
$$\overline{h}_0\,\mathrm{ctg}\,\alpha\left(\overline{N}_3 - \overline{d}\right)$$

(14)

$$\cos 2\alpha \frac{1-e^{-\sqrt{\lambda}\,\overline{h}_0}}{\mathrm{tg}\,\alpha}\overline{B}_0 - \overline{B}_1 G_c + \overline{B}_2 G_s = -f\,\overline{N}\,\overline{h}_0\,\mathrm{ctg}\,\alpha$$

(15)

$$\cos 2\alpha \frac{1-e^{-\sqrt{\lambda}\,\overline{h}_0}}{\mathrm{tg}\,\alpha}\overline{B}_0 + \overline{B}_1 G_c + \overline{B}_2 G_s = -f\,\overline{N}\,\overline{h}_0\,\mathrm{ctg}\,\alpha$$

(16)

Here

$$\overline{N} = \frac{ga\cos^2\alpha\overline{h}}{\nu A\omega}$$

(17)

$$\Phi_s = \frac{1}{\lambda_1 tg^2\alpha + \frac{4\pi^2}{M^2}}\left[\sqrt{\lambda_1}\,tg\,\alpha\sin\frac{\pi\overline{b}}{M} + \frac{2\pi}{M}\left(\cos\frac{\pi\overline{b}}{M} + e^{-\sqrt{\lambda_1}\,\overline{h}_0}\right)\right]$$

(18)

$$\Phi_c = \frac{1}{\lambda_1 tg^2\alpha + \frac{4\pi^2}{M^2}}\left[\sqrt{\lambda_1}\,tg\,\alpha\left(\cos\frac{\pi\overline{b}}{M} + e^{-\sqrt{\lambda_1}\,\overline{h}_0}\right) - \frac{2\pi}{M}\sin\frac{\pi\overline{b}}{M}\right],$$

(19)

$$G_c = \frac{2\pi}{M}\left(1 + \frac{\lambda_1 M^2}{4\pi^2}\right)\cos 2\alpha\,\Phi_s + 2\sqrt{\lambda_1}\sin 2\alpha\,\Phi_c$$

(20)

$$G_s = 2\sqrt{\lambda_1} \sin 2\alpha \, \Phi_s - \frac{2\pi}{M}\left(1 + \frac{\lambda_1 M^2}{4\pi^2}\right)\cos 2\alpha \, \Phi_c \qquad (21)$$

Let's get the solution of this system of equations. It follows from (15) and (16).

$$\overline{B}_1 = 0 \qquad (22)$$

$$\overline{B}_0 = -\frac{b_2 G_s \, \mathrm{tg}\,\alpha + f\overline{N}\overline{h}_0}{\cos 2\alpha\left(1 - e^{-\sqrt{\overline{\lambda}}\,\overline{h}_0}\right)} \qquad (23)$$

Substituting (22) and (23) into (14), finally have:

$$\overline{B}_0 = \frac{\sqrt{\lambda}\,\overline{h}_0}{1 - e^{-\sqrt{\lambda}\,\overline{h}_0}}\,\mathrm{ctg}\,\alpha\left[\begin{array}{c}\overline{N}_3 - \overline{d} - \\ -\dfrac{\left(\overline{\lambda}_1 \sin\alpha\,\Phi_c + \cos\alpha\Phi_s\right)\left(\sqrt{\lambda}\cos 2\alpha\,\mathrm{ctg}\,\alpha\left(\overline{N}_3 - \overline{d}\right) + f\overline{N}\right)}{G_s + \sqrt{\lambda}\,\mathrm{ctg}\,\alpha\cos 2\alpha\left(\overline{\lambda}_1 \sin\alpha\Phi_c + \cos\alpha\Phi_s\right)}\end{array}\right] \qquad (24)$$

$$\overline{B}_2 = -\frac{\overline{h}_0\,\mathrm{ctg}\,\alpha\left(\sqrt{\lambda}\cos 2\alpha\,\mathrm{ctg}\,\alpha\left(\overline{N}_3 - \overline{d}\right) + f\overline{N}\right)}{G_s + \sqrt{\lambda}\,\mathrm{ctg}\,\alpha\cos 2\alpha\left(\overline{\lambda}_1 \sin\alpha\Phi_c + \cos\alpha\Phi_s\right)}. \qquad (25)$$

Formulas (22), (24), (25) provide a solution to the system of equations (14) - (16).

Next, using (22), (24) and (25), we obtain the following formulas for the Laplace transform U_1 and U_2 of the speed of movement of a pseudo fluid:

$$U_1 = \overline{h}_0\,\mathrm{ctg}\,\alpha\left[\begin{array}{c}\dfrac{\sqrt{\lambda}}{1 - e^{-\sqrt{\lambda}\,\overline{x}_2}}\left(\dfrac{2\pi}{q^2 + 4\pi^2} + \dfrac{d}{\lambda} - D_1 D_2\right)e^{-\sqrt{\lambda}\,\overline{x}_2} + \\ + D_2\dfrac{\sqrt{\lambda_1} M}{2\pi}e^{-\sqrt{\lambda_1}\,\overline{x}_2}\cos\dfrac{2\pi}{M}\overline{x}_1\end{array}\right] \qquad (26)$$

$$U_2 - \frac{d}{\lambda} - \overline{h}_0\,\mathrm{ctg}\,\alpha\, D_2 e^{-\sqrt{\lambda_1}\,\overline{x}_2}\sin\frac{2\pi}{M}\overline{x}_1 \qquad (27)$$

$$D_1 = \sqrt{\lambda_1}\,\frac{M}{2\pi}\sin\alpha\,\Phi_c + \cos\alpha\,\Phi_s \qquad (28)$$

$$D_2 = \frac{\sqrt{\lambda}\cos 2\alpha\,\mathrm{ctg}\,\alpha\left(\dfrac{2\pi}{q^2 + 4\pi^2} + \dfrac{d}{\lambda}\right) + f\overline{N}}{G_s + \sqrt{\lambda}\,\mathrm{ctg}\,\alpha\cos 2\alpha\, D_1}. \qquad (29)$$

These formulas can be simplified, taking into account the fact that the value $\frac{2\pi}{M} \ll 1$, if $\alpha \neq \frac{\pi}{2}$ and $\overline{h}_0 = \frac{h_0}{2\alpha} \gg 1$.
In this approximation, we have:

$$D_1 \approx \sqrt{\lambda}\,\frac{M}{2\pi}\sin\alpha\,\Phi_c \qquad (30)$$

$$G_s \approx -\frac{\lambda M}{2\pi}\cos 2\alpha\,\Phi_c \qquad (31)$$

$$\Phi_c \approx \frac{\mathrm{ctg}\,\alpha}{\sqrt{\lambda}}\cos\frac{\pi\overline{b}}{M} \qquad (32)$$

Substitute (30)–(32) into (29) and (26), (27) and, after performing the necessary transformations, we have:

$$U_2 \approx -\frac{d}{\lambda} + \frac{2\pi\overline{h}_0}{M(1 - \cos\alpha)\cos\dfrac{\pi\overline{b}}{M}}\left(\mathrm{ctg}\,\alpha D + \frac{f\overline{N}}{\sqrt{\lambda_1}\cos 2\alpha}\right)e^{-\sqrt{\lambda_1}\,\overline{x}_2}\sin\frac{2\pi}{M}\overline{x}_1 \qquad (33)$$

$$U_1 \approx \overline{h}_0\,\mathrm{ctg}\,\alpha\left[\begin{array}{c}\dfrac{\sqrt{\lambda}}{1 - e^{-\sqrt{\lambda}\,\overline{h}_0}}\left(D\left(1 + \mathrm{ctg}\dfrac{\alpha}{2}\mathrm{ctg}\,\alpha\right) + \dfrac{f\overline{N}\mathrm{ctg}\dfrac{\alpha}{2}}{\sqrt{\lambda_1}\cos 2\alpha}\right)e^{-\sqrt{\lambda}\,\overline{x}_2} - \\ -\dfrac{\sqrt{\lambda_1}}{(1 - \cos\alpha)\cos\dfrac{\pi\overline{b}}{M}}\left(D + \dfrac{f\overline{N}}{\sqrt{\lambda_1}\cos 2\alpha\mathrm{ctg}\,\alpha}\right)e^{-\sqrt{\lambda_1}\,\overline{x}_2}\cos\dfrac{2\pi}{M}\overline{x}_1\end{array}\right]. \qquad (34)$$

$$D = \frac{2\pi}{q^2 + 4\pi^2} + \frac{d}{\lambda}, \qquad \overline{N} = \frac{ga\cos^2\alpha\,\overline{h}}{\nu A\omega}.$$

Formulas (33), (34) give an approximate value of the functions U_1 and U_2.

In order to use (33), (34) to solve the original problem, it is sufficient to apply the inverse transformation to the Laplace transform [26]

$$u_1 = \frac{1}{2\pi i}\int_{\overline{a} - i\infty}^{\overline{a} + i\infty} U_1 e^{q\overline{t}}\,dq, \quad u_2 = \frac{1}{2\pi i}\int_{\overline{a} - i\infty}^{\overline{a} + i\infty} U_2 e^{q\overline{t}}\,dq \qquad (35)$$

$$\overline{a} > 0.$$

The next step is to calculate the integrals (35). For this purpose, we examine the functions U_1 and U_2 as a function - a parameter of the Laplace transform. As follows from (33) and (34), this function depends on $\sqrt{q}$. Therefore, bearing in mind that q can take a complex value, one of the branches of the analytical function $\sqrt{q}$ should be singled out. To do this, in the complex plane of the variable q, we will make a cut along the negative real semiaxis ($\mathrm{Re}\,q < 0$, $\lim q < 0$). In such a complex plane, we select a branch $\sqrt{q}$ for which $\mathrm{Re}\sqrt{q} \geq 0$ and $-\pi < \arg q \leq \pi$. It is easy to see that the functions U_1 and U_2 are analytic functions of the complex variable q excluding the above cut and the points $q = 0$, $q = \pm i2\pi$. Moreover, the points $q = \pm i2\pi$ are special points of the pole type, and the point $q = 0$ is a branching point of the algebraic type. In addition, the functions U_1 and U_2 tend to zero. Such properties of the functions U_1 and U_2 guarantee the applicability of the remainder theorem [26] and allow the calculation of the integral (35) to be replaced by the calculation of the remainders at points $q = \pm i2\pi$ and integrals of these functions over a circle with an infinitesimally small radius and centered at the branching point $q = 0$. Residuals can be calculated using the formula [25, 26].

$$\mathrm{res}\,U_{1,2}(\pm i2\pi) = \lim_{q \to \pm i2\pi}\left(q \pm i2\pi\right)U_{1,2}(q) \qquad (36)$$

Thus, based on the above, we get

$$u_1(x_1, x_2, t) = \mathrm{res}\left(U_1(2\pi i)e^{i\omega t}\right) + \mathrm{res}\left(U_1(-2\pi i)e^{-i\omega t}\right) - \lim_{\varepsilon \to 0}\int_{C_\varepsilon} U_1 e^{\frac{qt\omega}{2\pi}}\,dq \qquad (37)$$

$$u_2(x_1, x_2, t) = \mathrm{res}\left(U_2(2\pi i)e^{i\omega t}\right) + \mathrm{res}\left(U_2(-2\pi i)e^{-i\omega t}\right) - \lim_{\varepsilon \to 0}\int_{C_\varepsilon} U_2 e^{\frac{qt\omega}{2\pi}}\,dq \qquad (38)$$

Here - denotes an excess, - a circle of radius ε centered at a point $q = 0$.

Using formula (36), we get

$$u_{11} = res\left(U_1(2\pi i)e^{i\omega t}\right) + res\left(U_1(-2\pi i)e^{-i\omega t}\right) =$$
$$= \frac{\sqrt{\frac{\omega}{2v}}h_0 \operatorname{ctg}\alpha\left(1 + \operatorname{ctg}\alpha\operatorname{ctg}\frac{\alpha}{2}\right)\left[\cos\gamma - \sin\gamma - e^{-\gamma}(\cos(\gamma-\bar{\gamma}) - \sin(\gamma-\bar{\gamma}))\right]}{1 + e^{-2\bar{\gamma}} - 2\cos\bar{\gamma}e^{-\bar{\gamma}}}e^{-\bar{\gamma}\frac{x_2}{h_0}} -$$
$$- \frac{\sqrt{\frac{\omega}{2v}}h_0 \operatorname{ctg}\alpha(\cos\gamma - \sin\gamma)}{(1-\cos\alpha)\cos\frac{\pi b}{\overline{M}}}e^{-\bar{\gamma}\frac{x_2}{h_0}}\cos\frac{2\pi x_1}{M} \tag{39}$$

$$u_{21} = res\left(U_2(2\pi i)e^{i\omega t}\right) + res\left(U_2(-2\pi i)e^{-i\omega t}\right) =$$
$$= \frac{2\pi h_0 \operatorname{ctg}\alpha\cos\gamma}{(b + 2h_0 \operatorname{ctg}\alpha)(1-\cos\alpha)\cos\frac{\pi b}{\overline{M}}}e^{-\bar{\gamma}\frac{x_2}{h_0}}\sin\frac{2\pi x_1}{M} \tag{40}$$

In formulas (39), (40), dimensionless variables $\bar{t}, \bar{x}_1, \bar{x}_2$ are replaced by dimensional t, x_1, x_2 variables. The value $\overline{M} = b + h_0 \operatorname{ctg}\alpha$, b is the width of the unloaded window,

h_0 - the distance from the free border of the layer of cuttings to the plane of the unloaded window at the moment of time $t=0$.

Value $\gamma = \omega t - \sqrt{\frac{\omega}{2v}}x_2$, $\bar{\gamma} = \sqrt{\frac{\omega}{2v}}h_0$

Let's calculate the integrals in (37), (38). For this, we will assume that the distance from the border of the free surface of the cuttings to the plane of the unloading window changes over time according to a linear law

$$h(t) = ct + h_0 \tag{41}$$

where c – is some constant to be determined.
Then the Laplace transform of this function

$$\bar{h}(q) = \frac{c}{q^2} + \frac{h_0}{q} \tag{42}$$

Substitute (42) into (36) and (33) into (34). Having made the necessary transformations, we have

$$u_{12} = \lim_{\varepsilon \to 0}\int_{c_\varepsilon}U_1 e^{\frac{q t \omega}{2\pi}}dq = \frac{\operatorname{ctg}\alpha\,g}{A\omega}\times\begin{bmatrix}\left(1 + \operatorname{ctg}\alpha\operatorname{ctg}\frac{\alpha}{2}\right)\frac{2\bar{\rho}_1(1-\delta)}{\omega\bar{\rho}\delta} - \frac{\overline{M}f\operatorname{ctg}\frac{\alpha}{2}\sin 2\alpha}{4\pi\cos^2\alpha\,v}\times \\ \times(\bar{c} + h_0)e^{-\frac{2\pi}{\overline{M}}x_2} + \\ \frac{4\pi h_0\bar{\rho}_1(1-\delta)}{(1-\cos\alpha)\overline{M}\cos\frac{\pi b}{\overline{M}}\bar{\rho}\omega\delta} + \\ + \frac{h_0\operatorname{tg}2\alpha\,f}{4(1-\cos\alpha)v}(\overline{C} + h_0)\end{bmatrix}e^{\frac{2\pi}{\overline{M}}x_2}\cos\frac{2\pi}{\overline{M}}x_1 \tag{43}$$

$$u_{22} = \lim_{\varepsilon \to 0}\int_{c_\varepsilon}U_2 e^{\frac{q t \omega}{2\pi}}dq = \frac{2g\bar{\rho}_1(1-\delta)}{A\omega\bar{\rho}\delta}\left(1 - \frac{2\pi h_0 \operatorname{ctg}\alpha}{(1-\cos\alpha)\overline{M}\cos\frac{\pi b}{\overline{M}}}e^{-\frac{2\pi}{\overline{M}}x_2}\sin\frac{2\pi}{\overline{M}}x_1\right) -$$
$$- \frac{h_0 fg\cos^2\alpha}{(1-\cos\alpha)\cos\frac{\pi b}{\overline{M}}\cos 2\alpha vA\omega}(\overline{C} + h_0)e^{-\frac{2\pi}{\overline{M}}x_2}\sin\frac{2\pi}{\overline{M}}x_1, \tag{44}$$

$$\overline{C} = 2ca/\pi.$$

Finally, we have the following calculation formulas for the components of the speed of movement of the discrete phase (set of cuttings) of the fluid

$$u_1 = u_{11} - u_{12} \tag{45}$$

$$u_2 = u_{21} - u_{22} \tag{46}$$

where values u_{11}, u_{12}, u_{21}, u_{22} are determined by formulas (39), (40) and (43), (44).

As follows from (43), (44), the values u_{12} and u_{22} do not depend on the temporal variable t but depend on the spatial variables x_1 and x_2. The values u_{11} and u_{21} depend on the time variable according to the harmonic law in accordance with the vibrational oscillations that affect one of the walls of the hopper. In addition, these values depend on the physico-mechanical and geometric parameters of the cuttings (average density, the radius of the circle in area coincides with the cross-sectional area of the cuttings, the coefficient of dry friction between the cuttings), the parameters of the hopper (the angle of inclination of the walls, the width of the unloading window, the coefficient of friction around the walls of the hopper), amplitude and frequency of harmonic vibrations, kinematic coefficient of viscosity and air density.

In addition to the specified parameters, the speed components u_1 and u_2 implicitly depend on the function $h(t)$ (see 41). As follows from the boundary condition, this function must satisfy a nonlinear differential equation of the first order

$$\dot{h} = A\omega u_2\left(x_1, h(t), t\right) \tag{47}$$

The solution of this equation, in the general case, can be found only by numerical methods with the help of a computer. However, if we assume that the function $h(t)$ depends on time according to a linear law (see 41)

$$h(t) = ct + h_0,$$

Then you can define a constant c.

Indeed, let's put in (47) $x_1 = 0$. Then, taking into account (40) and (44), we have

$$c = -\frac{2g\bar{p}_1(1-\delta)}{\omega\bar{p}\delta} \tag{48}$$

This constant should be substituted in (39), (40) and (43), (44). This completes the construction of a mathematical model of the process of unloaded cuttings from the hopper.

IV. CONCLUSIONS

To date, planters of woody energy crops are known exclusively with manual laying of planting material. Therefore, development of automation systems for this process will contribute to the possibility of rapid expansion of areas under energy plantations.

The simplest way to move the material when it is unloaded, is its movement under the influence of gravitational forces. The theoretical foundations of such a movement do not have a single approach, and the specifics of the material for planting energy willow create additional difficulties for the development of a mathematical model of this process. Building a mathematical model of the movement of energy willow cuttings will allow automating the planting process.

Accepting several assumptions, it is proposed to consider gravitationally unloaded cuttings from the point of view of hydrodynamic multiphase systems. According to this approach, the collection of cuttings is considered as an incompressible fluid consisting of two phases: discrete, formed by the cuttings, and a continuous phase (gaseous - the medium between the cuttings). And by applying the Laplace transformation to determine the Fourier coefficients, the system of linear algebraic equations of the motion speed of the pseudo-fluid is obtained (see (12), (13)), which give a general solution to the system of equations of motion of such a pseudo-fluid with the outline of initial and boundary conditions.

In order to obtain calculation formulas for the speed of fluid movement, we limited ourselves to the case of a symmetric hopper, which allowed us to obtain a solution to problem (1) - (3), (4) - (10) in a closed analytical form.

Formulas (33), (34) give an approximate value of the functions U_1 and U_2 with a relative error of less than 5%, which is sufficient for practical calculations. In order to obtain the solution of the original problem with the help of (33), (34), it is sufficient to apply the inverse transformation to the Laplace transform [26, 27].

Thus, the calculation formulas for the components of the speed of movement of the discrete phase (set of cuttings) of the fluid (45) and (46) were finally obtained, the individual components of which $u_{11}, u_{12}, u_{21}, u_{22}$ are determined by formulas (39), (40) and (43), (44).

This mathematical model describes the movement of cuttings of energy tree crops when unloading a slotted hopper, which creates opportunities for designing mechanisms for automatic unloading of such material, which in turn will allow to propose the design of automatic planters.

REFERENCES

[1] M.V. Roik, V.M. Sinchenko, Y.D. Fuchylo. Energety`chna verba: texnologiya vy`roshhuvannya ta vy`kory`stannya [Energy willow: cultivation technology and usage]., Vinnitsa: LLC "Nilan-LTD", 2015 (in Ukrainian)

[2] J. Frączek, K.. Mudryk. Jakości sadzonek wierzby energetycznej w aspekcie sadzenia mechanicznego [The quality of energy willow seedlings in terms of mechanical planting]. Inżynieria Rolnicza, 6 (66), 2005 (in Polish)

[3] S. Yermakov, T. Hutsol, S. Slobodian, S.Komarnitskyi, M. Tysh,. Possibility of using automation tools for planting of the energy willow cuttings. Renewable Energy Sources: Engineering, Technology, Innovation. 2018, pp. 419–429. https://doi.org/10.1007/978-3-030-13888-2_42

[4] R.N. Mynko. Problema svodoobrazovanyia v emkostiakh bunkernoho tipa v uslovyiakh dlitelnoho khraneniya [The problem of arch formation in bunker-type tanks under long-term storage conditions]. Yaroslavskyi pedahohycheskyi vestnyk, 3(1). 2017.(in Russian)

[5] V.S. Loveikin, L.S. Shymko, V.V. Yaroshenko. Ohliad doslidzhen vytoku sypkykh materialiv [Review of research on the leakage of bulk materials]. Kon-struiuvannia, vyrobnytstvo ta ekspluatatsiia silskohospodarskykh mashyn [Design, manufacture and operation of agricultural machinery], 40(1), 2010, pp.324–333. (in Ukrainian).

[6] U. Nedilska, A. Rud, O. Kucher, O. Dumanskyi. Bioenergetic evaluation of miscanthus giant roductivity in the conditions of the western forest-steppe of Ukraine for use as a solid. Engineering for rural development. Jelgava, 2023, pp.1017-1025.

[7] G.A. Geniev. Dinamika plasticheskoj i sypuchej sred. [Dynamics of plastic and granular media]. Moskva. 1972 (in Russian)

[8] Y.V. Horiushynskyi. Emkosty dlia sypuchikh gruzov v transportno-hruzovykh sistemakh [Tanks for bulk cargo in transport and cargo systems]. Samara: SamHAPS. 2003 (in Russian)

[9] L.V. Gjachev. Osnovy teorii bunkerov [Fundamentals of hopper theory]. Novosibirsk: Izd-vo Novosibirskogo universiteta. 1992 (in Russian)

[10] I.S. Aranson, L.S. Tsimring. Patterns and collective behavior in granular media: Theoretical concepts. Reviews of modern physics, 78(2), 2006, pp.641-692.

[11] A.M. Dalskiy. Spravochnik tehnologa-mashinostroitelya [Reference book of machine technologist-builder]. Moskow: Mashinostroenie. 2001. (in Russian).

[12] V.N. Dolgunin, V.Ya. Borschev. Bystryie gravitatsionnyie techeniya zern-istyih materialov: tehnika izmereniya, zakonomernosti, tehnologicheskoe prime-nenie [Rapid gravitational flows of grainy materials: technique of measuring, con-formity to law, technological application]. Moskow: Mashinostroenie. 2005. (in Russian).

[13] M. Korchak, T. Hutsol, L. Burko, W. Tulej. Features of weediness of the field by root residues of corn Vide. Tehnologija. Resursi - Environment, Technology, Resources, V. 1, 2021. pp. 122–126

[14] A. Samadani, A. Pradham, A. Kudrolli. Size segregation of granular matter in silo discharges. Phys Rev E 1999. 7203-9.

[15] V.V. Sokolovskiy. Statika syipuchey sredyi [Statics of friable environment]. Moskow, Nauka. 1990 (in Russian).

[16] R.M. Nedderman. Statics and kinematics of granular materials. Cambridge: Cambridge University Press; 1992.

[17] G.R. Power. Modelling granular flow in caving mines: large scale physical modelling and full scale experiments. PhD thesis, The University of Queensland, Brisbane; 2004.

[18] S. Yermakov, K. Mudryk, T. Hutsol. The analysis of stochastic processes in unloadingthe energywillow cuttings from the hopper. Environment. Technology. Resources. Rezekne, Latvia. Vol. III. 2019, pp. 249-252, https://doi:10.17770/etr2019vol3.4159.

[19] S. Yermakov, T. Hutsol, I. Gerasymchuk, , Fedirko, P., Dubik, V. (2023). Study of the Unloading and Selection Process of Energy Willow Cuttings for the Creation a Planting Machine. Environment. Technologies. Resources. Proceedings of the International Scientific and Practical Conference, 3, 271-275. https://doi.org/10.17770/etr2023vol3.7199

[20] S. Yermakov, A. Rud, M. Vusatyi The Distribution Of Cash Expenses For The Creation Of Bioenergy Willow Plantations In Ukraine. Vide. Tehnologija. Resursi - Environment. Technologies. Resources. V.1. Rezekne, Latvia. 2023. Pp. 74-80 https://doi.org/10.17770/etr2023vol1.7191

[21] V. Ivanyshyn, S. Yermakov , T. Ishchenko. Calculation algorithm for the dynamic coefficient of vibro-viscosity and other properties of energy willow cuttings movement in terms of their unloading from the tanker. Renewable Energy Sources, vol. 154, E3S Web of Conferences. 2020, pp. 04005, https://doi:10.1051/e3sconf/202015404005 .

[22] S.V. Yermakov, T.D. Hutsol. Features of the heterogeneous rood-like mate-rials outflow (by example of energy willow cutting). Technological and methodo-logical aspects of agri-food engineering in young scientist research. 2018. Pp.55–68.

[23] S. Yermakov, T. Hutsol, O. Ovcharuk, I. Kolosiuk. Mathematic simulation of cutting unloading from the bunker. Independent journal of management & produc-tion. Special Edition PDATU, 10, 758–777; 2019. 2236-269X. https://doi.org/10.14807/IJMP.V10I7.909.

[24] S. Yermakov. Application of the Laplace transform to calculate the velocity of a two-phase fluid modulated by the movement of cuttings of an energy willow (Salix Viminalis). Teka. Quarterly journal of agri-food industry. 2. 2019. 71–78.

[25] V. Maksimenko, V. Kuzmenko, L. Shymko, V. Achkevych. Justification of accelerator parameters of feeding harvester unloading channel. Engineering for Rural Development, 20, 2021. Pp.1534–1540

[26] M.A. Lavrentev. Metody i teorii funktsiy kompleksnogo peremennogo [Meth-ods of the theory of functions of a complex variable]. Moskow: Izdatelstvo flziko-matematicheskoy lit. 1958. (in Russian).

[27] N.N. Bogolyubov. Asimptoticheskie metodyi v teorii nelineynyih kolebaniy [Asymptotic methods in the theory of nonlinear oscillations]. Moskow: Nauka. 1974

Justification of the parameters and development of the design of the mechanism of automated selection and supply of cuttings in energy culture plants

Serhii Yermakov
Educational and Scientific Laboratory "DAK GPS",
Higher educational institution
«Podillia State University»,
Kamianets-Podilskyi, Ukraine
dakgps@pdatu.edu.ua

Pavlo Potapskyi
Faculty of Energy and Information Technologies,
Higher educational institution
«Podillia State University»,
Kamianets-Podilskyi, Ukraine

Oksana Bialkovska
Innovation and International Affairs
Higher Educational Institution
"Podillia State University"
Kamianets-Podilskyi, Ukraine

Mykola Volynkin
Faculty of Engineering and Technology
Higher Educational Institution
"Podillia State University"
Kamianets-Podilskyi, Ukraine

Viktor Duhanets
Faculty of Engineering and Technology
Higher Educational Institution
"Podillia State University"
Kamianets-Podilskyi, Ukraine

Abstract. **An important field of bioenergy development is the use of biomass energy, which requires significant amounts of raw materials grown in the fields. One of the prospective sources of such raw materials is the planting of fast-growing wood species capable of restoring the above-ground part after cutting in a short period of time. The article sets out the task of developing approaches and constructive solutions regarding the possibilities of creating highly productiveaggregates for planting such woody energy crops as willow, poplar, and others that are propagated by cuttings. The analysis of the current state of development of this issue revealed that one of the factors inhibiting the process is the insufficient level of developments and their implementation in the field of automation of the technological process of planting. In most technical solutions, the use of the labor of the planter is included, which makes the process as a whole dependent on human capabilities and other related factors.The work is intended to solve the empirical task of developing an automated planter for plants planted with lignified cuttings.To develop an automated system that would provide uninterrupted and uniform supply of cuttings to the coulter of the planter, a two-factor experiment was conducted on a developed laboratory stand simulating a slotted hopper. As a result of research, it was found that the optimal width of the unloading window of the feeder should be at least 80 mm, and the optimal angles of inclination of the slotted hopper walls should be at least 40°. These parameters will provide complete and continuous unloading of cuttings both in the absence of external forces acting on them (oscillations, vibrations, etc.) and with them. Taking into account the analysis of existing technical solutions and the results of a laboratory experiment, a number of solutions were synthesized, which were used in the development of a new construction of the cuttings unloading mechanism. The developed construction of the mechanism of automated dosing, selection and supply of cuttings for the planter of energy willow is protected by a patent and embodied in a single-row design and tested in field conditions. Such a planting machine allows to plant without the support of a planter, whose functions are reduced to periodically loading the slotted hopper with cuttings previously oriented in one direction.**

Keywords: energy crops, energy willow, automatic feeder, planting machine, cuttings, feeder, piecemeal selection.

I. Introduction

The intensive development of the world energy creates demand for ever greater volumes of energy production, and considering the modern realities of environmental sustainability and the desire of countries for energy

independence, more and more attention is paid to the development of alternative energy sources. According to various estimates, by 2050, almost 40% of energy needs will be covered by renewable energy sources, in particular, about 30% - by bioenergy [1]. The main priority of bioenergy development for many countries is the use of different highly productive bioenergy crops. One of the perspective directions is the cultivation of energy raw materials on plantations of fast-growing wood species, in particular, willows, poplars and other crops capable of easy restoration of the above-ground part after its cutting. European countries, which began to actively implement the cultivation of energy raw materials by plantation methods at the beginning of the 18th century, demonstrate the best experience in these issues. The impetus for the development of this direction was the aggravation of the world energy crisis.

In Ukraine, in recent years, this trend has become particularly widespread, so the issue of quickly setting up plantations of energy plants, especially various varieties of willows, on an industrial scale has become urgent.

For growing willow on large plantations, a number of special machines for growing and harvesting energy willow have been developed [2]-[4]. Work technology with this crop has a number of its characteristics, so it is not rare that some aspects remain insufficiently studied. In particular, the issue of automated planting of energy willow remains problematic, because propagation takes place by cuttings, which are usually planted manually by planters, which not only limits the productivity of the aggregate, but also cannot guarantee high quality work. Some attempts to automate the process were implemented through the creation of aggregate whose raw material for planting is long rods. The laying of the rod in them is still carried out manually, but then such a machine cuts the willow rod on the cutting directly during planting and works them into the soil with its compaction around the cutting, which provides a high percentage of rooting [5], [6]. An example of such a machine is the Energy Planter planter of the Danish company Egedal. The advantages of this technology are that the human factor is significantly reduced, the quality of the planting material improves (it is cut immediately before planting), the possibility of parallel driving appears during care and harvesting, and, accordingly, there is less damage to rooted seedlings at the same time [7], [8]. However, such a machine is quite expensive for the Ukrainian consumer and does not give the opportunity to completely do without a planter and requires carefully prepared long straight rods.

In most cases, simpler machines are used, where the planting material is energy willow cuttings 20...25 cm long and 0.7...1.4 cm in diameter [8], [9]. Usually, the laying of material in such machines is manual, but the task of our research is the development of such an automatic machine, which would provide uninterrupted, piecemeal delivery of cuttings from a certain massif and thereby free up the place of a planter.

Nowadays, work on improving the process of planting plants continues. There are many works analyzing both the theoretical aspects of automation [10]-[12], and the automation of a specific type of plant [13] and even before the implementation of robotics into the planting process [14]-[16]. However, each specific type of plant requires a separate approach. In particular, energy willow or poplar needs to take into account the characteristics of lignified cuttings as planting material.

The authors of the project dealt with issues of automation of the process of planting energy willow cuttings in the Educational and Scientific Laboratory "DAK GPS" of the Higher Educational Institution "Podillia State University", where within the framework of the scientific topic "Agrobiomass of Ukraine as the energy potential of Central and Eastern Europe" for more than five years scientific work was conducted [17]-[21]. In particular, a preliminary analysis of the existing tools for automating the planting of cuttings was conducted. The works [22], [23] highlight the main approaches and strategies of advanced practices for improving the productivity of garden aggregates. Besides solutions that are directly related to the planting of energy willow and poplar, where the work of a planter is mainly used for piecemeal planting of cuttings, technical solutions to solve this problem in seedling planting and forestry were also analyzed [24]. The technological processes on the way of the cuttings getting to the planting site are structured and the main factors that need to be improved are singled out. Thus, the main obstacle in further increasing the productivity of planters is the limitation of human possibilities in supplying cuttings - 40–60 pcs·min^{-1} [10], which is appropriate to the speed of forward movement of the machine 0.8...2.1 km·h^{-1}. In these conditions, it is important to change the operator's work with means of automation, therefore, it is urgent to search for perspective technological processes and structures of working bodies for the automated supply of cuttings in machines for planting energy wood crops, which can be structurally displayed in the diagram of Fig. 1.
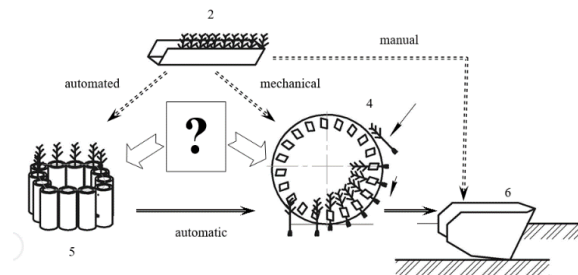
Fig. 1. Structural and logical scheme of operations of the process of planting cuttings of energy willow:1 – containers with seedlings; 2 – planting devices; 3 – coulters or furrow-forming equipment; 4 – accumulators of planting material; 5 – cuttings supply mechanism.

In Fig. 1, a question mark highlights the position that is responsible for supplying the cuttings from containers with seedlings to the planting site. In modern machines for planting energy willow, this process is performed exclusively manually [27].

Having analyzed various constructions, we came to the conclusion that in order to increase the productivity of planters, it is necessary to improve the process of supplying cuttings from containers to the planting device. It is also necessary to use intermediate stockpiles of cuttings, which creates a buffer that compensates for the discrepancy between the productivity of the planting apparatus and human capabilities. But this only partially

solves the issue of increasing productivity and reducing the share of manual labor.

The creation of mechanisms for the automated supply of cuttings to the planting device or directly to the planting site is an important scientific task on the way to increasing the productivity of planting machines.

II. MATERIALS AND METHODS

The paper sets an empirical task to develop an automated planter for plants planted with lignified cuttings. A number of theoretical and practical research activities were carried out to develop a mechanism that would ensure uninterrupted and uniform supply of cuttings to the coulter of the planter. Previous studies established that when designing the mechanism for supplying cuttings, the process of individual selection and movement can be divided into three functional zones: dosing (bunker + unloading window); compensating (mechanism for cutting off excess cuttings); transporting (transporters, drums, rolling boards). It was found that the issue of primary dosing of cuttings is the least researched, since this material is not typical for most technological processes, so it is worth focusing on the parameters of the bunker in more detail.

A mathematical model of a two-slope bunker with an adjustable unloading window and wall inclination angles was developed, and a formula for the movement of the cuttings array was derived according to this mathematical model [26].

For the practical verification of some parameters, a laboratory stand (Fig. 2) was developed and a study was conducted to identify patterns of cuttings discharge [25] and some of its parameters. The stand consists of two inclined walls with an adjustable position in the horizontal plane and installation angles. These walls are placed between vertical planes, the front of which is transparent for observing the unloading process. In this way, we obtained a typical slotted bunker, which makes it possible to determine the main parameters of the movement of the mass of cuttings during unloading.

Fig. 2. Laboratory stand for research the parameters of a slotted bunker

Empirical research on the laboratory bench was carried out according to the matrices of the two-factor experiment, as a result of which the optimal angles of inclination of the walls of the slotted hopper, the rational width of the unloading window was discovered, which will ensure full and uninterrupted unloading of cuttings in the absence of external forces (oscillations, vibrations, etc.) and with them. During the experiment, at each stage, the corresponding parameters α, β were set, which formed the width of the window b. With the closed unloading

window, the space between the walls of the bunker was filled with cuttings. When the walls were opened, unloading took place. If it stopped due to crypt formation, the experiment was repeated with an increased value of b. In this way, the minimum width of the unloading window was determined, at which the complete unloading of the hopper will be possible at the given values of α and β.

Based on the preliminary theoretical data, as well as the parameters obtained as a result of laboratory research, a number of solutions were synthesized, which were used in the development of a new design of the cuttings unloading mechanism.

III. RESULTS AND DISCUSSION

A. Laboratory research of the parameters of the dosing device

For the design of the cuttings feeding machine, the primary task is to ensure uniform and continuous unloading of a limited array of cuttings, from which they will later be individually selected and sent to the coulter. It was established that the main problem of delays and interruptions of movement when unloading cuttings from the bunker by gravity method is crypt formation. The cuttings in the vault (each of them) are kept from falling by normal reactions and corresponding frictional forces of adjacent cuttings.

Cuttings that occupy extreme positions are held by normal reactions and frictional forces of the sloping board and adjacent cuttings. Previous researches have established the main reasons for the formation of vaults and delays during unloading [25], [26]. It has also been established that there are bunker parameters at which all cuttings will leave the container. These parameters are primarily expressed by the width of the unloading window and the angles of inclination of the walls.

In order to test the hypothesis that there are such parameters of a bunker with passive walls at which crypt formation will not occur (will not affect the unloading process) and to research the parameters α, β and b, the following assumptions were made:

o   The humidity of the cuttings does not significantly affect the character of the crypt formation and the width of the minimum opening for the full unloading of the cuttings.

o   The angles α and β must be greater than the coefficient of friction of the cutting material against the hopper wall (for our research α and β>=40°.

o   Variants of type α=40°, β=90° i α=90°, β=40° arespecular («mirrors») the measurements on them should be the same.

o   The angle of inclination of one of the walls β can theoretically be more than 90°, by a maximum of 90°- α. Thus, we will take α=40...90° β=40...140°.

o   An important parameter of the bunker is the opening angle of the walls δ. Which is formed by two walls δ = 90 - (α + β).
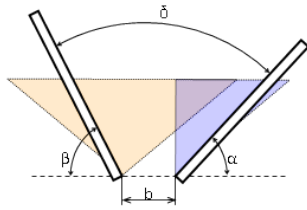
Fig. 3. Scheme for justification the magnitude of the angles α, β, and δ in the experiment.

As a result of the conducted research, it was established that the cuttings are unloaded according to the rules of normal (non-hydraulic) outflow of bulk material (Fig. 4a,b), i.e., first a pillar falls out above the hole, and then the layers move from the side. As research has shown (Fig. 4c, d), cuttings that are placed on a wall that is placed at a smaller angle (α or β) are the last to fall out.
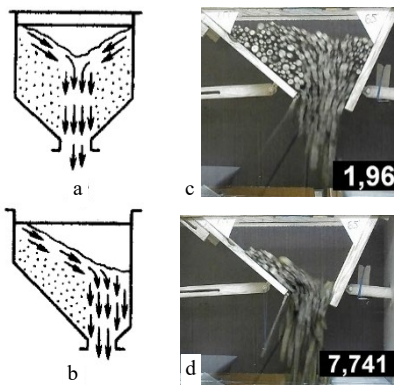
Fig. 4. The nature of cuttings unloading from a slotted hopper: a) the classic scheme of normal unloading from a double-sloped hopper, b) the same from a single-sloped hopper; c) formation of a dynamic flow during the experiment; d) completion of the unloading of cuttings from the hopper.

According to the results of the experiment were created different interpretations of the minimum width dependence of the unloading window b on the angles of inclination of the hopper walls (α and β).

It is convenient to choose the optimal width of the unloading window according to the bar chart, which takes into account the angle of inclination of one of the walls (α or β) and the angle of inclination of the walls (δ). We will have the diagram of Fig. 5.
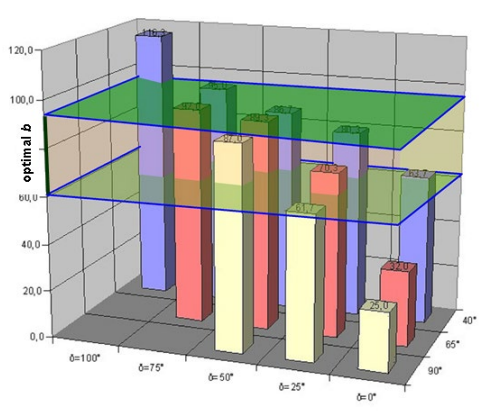
Fig. 5. Bar chart of the size of the width of the unloading window depending on the angle of inclination of the walls δ.

Figure 5 shows that the theoretically acceptable, minimum permissible value of the width of the unloading window b is 61-95 mm. However, as a result of research, it was observed that at critically small values of the window width, the cuttings are unloaded unevenly due to "temporary" crypt formation and its destruction. The movement of the flow becomes intermittent, and during unloading, as a result of the destruction of "temporary" vaults and micro vaults, the cuttings fly out disorderly (at different angles). When the value of the width of the unloading window b increases, this effect decreases, the movement of cuttings is smoother, the flow of cuttings is more uniform, and delays in the short-term formation of micro vaults and their destruction are reduced. Note that in a dynamic flow, emerging crypt formations self-destruct more easily, so it is important that the flow of cuttings "accelerate". It was also noticed that the unloading of cuttings is not affected by a slight (up to 20°) deviation of individual cuttings from the direction of the rows. During the researches, they were self-aligned while moving to the unloading window. That is, when unloading without vaults (large b), the unloaded material managed to be collected in an ordered array, composed of parallel rod-like elements, which could be considered as described in the mathematical model [26], [27].

Thus, to ensure a more uniform and smooth unloading of the cuttings flow, it is worth taking the width of the unloading window with a margin of the minimum permissible. When constructing the bunker, we will take the minimum value of the bunker to be 80 mm. Such a gap will provide with a margin (minimum permissible - 61.5 mm) unloading with a one-sided hopper with an angle of inclination of 25°) and angles of inclination of the walls to the horizon α and β more than 40°.

B. Development of a dosing mechanism, individual selection and feeding of cuttings into the coulter.

On the basis of laboratory researches, it was found that by choosing the rational parameters of the slotted hopper, it is possible to achieve a complete discharge from it of rod-like materials with an imperfect shape (cuttings). These parameters were laid down in the mechanism of automated selection and supply of cuttings from the slotted hopper [33].

The basis of the development was the task of increasing the reliability and reducing labor costs for the process of planting cuttings, due to the development of an automatic machine for feeding them into the coulter, which ensures the possibility of obtaining uniform unloading of the hopper and uninterrupted individual delivery of planting material to the planting site.

To solve the problem, the design of an automatic machine for feeding cuttings into the opener is offered, in which the storage capacity is a slotted hopper formed with the help of two inclined walls. The walls of the hopper create a narrowing, forming an unloading window at the bottom (Fig. 6). The hopper is made so that the cuttings are located in it between two vertical parallel walls, the distance between which corresponds to the placement of the cuttings across the gap. The working elements of the machine are a drum with cells, a stop and a guide funnel (Fig. 6).
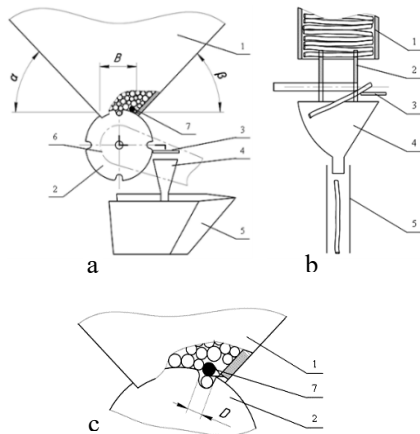
Fig. 6. Construction scheme of the machine for feeding cuttings into the coulter: a. side view of the automatic planter (with partial cuts); b – cross-section of the mechanism in the machine; c - scheme of operation of the cuttings separator; 1 – slotted hopper, 2. drum with cells, 3. stop, 4. guide funnel, 5 – coulter, 6 – flexible transmission (chain), 7 – cleaner.

The slotted hopper is filled with a layer of cuttings, which, under the influence of gravity, tend to advance to the unloading window. Narrowing of the layer of cuttings before their individual selection is carried out by narrowing the hopper in the lower part, until the edges form the walls of the unloading window. The width of the hopper corresponds to the placement of the cuttings transversely with a gap for their free movement. The angle of inclination of the sloping walls of the bunker α and β should be at least 40°, which will ensure the free rise of cuttings under the action of gravitational forces. To avoid the possibility of crypt formations, the width of the unloading window of bunker B, for cuttings with a diameter of 10...18 mm, should be at least 8 cm. The drum is made in the form of two disks with cells. The disks are placed at a distance of 0.3...0.5 of the length of the planting material, which allows cuttings to be accepted even with defects in shape. The cells are made in such a way as to ensure the retention of one cutting in them and the free emergence of others (Fig. 6c). Their width and depth should be 1.3...1.8 diameters of the cuttings, and the shape should ensure a smooth exit. A spring-loaded cleaner is installed on the front wall of the hopper for the free descent of excess cuttings. The diameter of the cleaner should correspond to the average diameter of the cuttings and have sufficient amplitude to enter the cells of the drum at least 1/3 of the depth. At the point where planting material falls from the cells of the drum, a stop is installed on one side, which ensures a change in the horizontal position in one direction. A guide funnel is installed under the stop, which finally orients the cuttings in a vertical position. The watering can at the bottom ends with a planting pipe from which the planting material enters the gap prepared by the coulter.
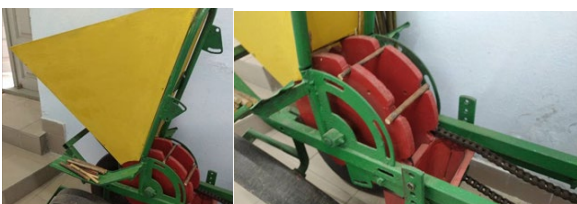
Fig. 7. General view of a field installation equipped with an automatic machine for feeding cuttings into the coulter

Before starting the operation of the machine equipped with this automatic device for feeding cuttings into the coulter, planting material is loaded into the slotted hopper so that its upper parts are on the side of the stop. The cuttings in the hopper continue to maintain their orientation, gradually moving towards the unloading window of the hopper under the influence of gravitational forces. When the aggregate moves, a drum with cells is activated by means of a flexible (chain) transmission. Cuttings that fall to the bottom of the cell are fixed there, and others are removed due to the shape of the back wall of the cell and the spring-loaded cleaner. When the drum rotates, the cuttings that got into its cells are taken out from under the hopper and fall out of the cell in a certain position, meeting the upper part with a stop, due to which their position changes from horizontal to inclined only in a certain direction and the cutting continues to move in the lower part forward. In the directional watering can, the planting material finally acquires a vertical position and enters the coulter, into the gap made by it, after which its position is fixed by wrapping or rolling means. The size of the step of planting cuttings can be adjusted by changing the gear ratio of the flexible transmission of the drive or the number of cells on the drum.

IV. Conclusions

In the conditions of the growing need for rapid expansion of the areas of energy crop plantations, there is a problem with the existing technical park for these purposes. In particular, increasing the productivity of planters inhibits the use of planters' labor for laying planting material. The development of a mechanism for individual selection and feeding of cuttings of energy willow to the opener will significantly increase the efficiency of planting both in terms of the quality of work and in terms of increasing the productivity of the aggregate. This paper proposes a solution to this problem, for which:

1. It has been experimentally proven that to ensure full gravity unloading of the hopper with a uniform and uniform flow of cuttings, it is necessary that the width of the unloading window be at least 80 mm, and the angle of inclination to the horizon (α or β) of at least one of the inclined walls should be more than 40°.

2. The developed design of the machine for feeding energy willow cuttings into the opener allows for the smooth individual selection of previously oriented energy willow cuttings from the slotted hopper and feeding them into the opener.

3. The automated system for supplying cuttings consists of a slotted hopper, a drum with cells, a flexible transmission of the drum drive, a guide funnel to the coulter. This design is protected by a patent of Ukraine.

4. The presented solution makes it possible to automate the process during the movement of the unit along the furrow, and accordingly, the need for a for an employee who would accompany the planter throughout the technological process, disappears.

The results obtained in the work can further serve to clarify and improve the machines that work with piece-by-piece selection of rod-like materials.

REFERENCES

[1] V. Sinchenko, Ya. Fuchylo, M. Humentyk, Koryhuvannia dlia verby (Adjustments for willow). The Ukrainian Farmer. 2015

[2] D.H. Voitiuk, Silskohospodarski mashyny: osnovy teorii ta rozrakhunku. [Agricultural machines: basics of theory and calculation.] D.H. Voitiuk, S.S. Yatsun, M.Ia. Dovzhyk. Sumy: VTD Universytetska knyha. 2008. 543p.

[3] P.M. Zaika, Teoriia silskohospodarskykh mashyn. T.1 Mashyny ta znariaddia dlia obrobitku gruntu. [Theory of agricultural machines. T.1 (4.1). Machines and tools for soil cultivation]. Kharkiv: Oko. 2011. 444p.

[4] Willowpedia. Retrieved: https://www.youtube.com/user/Willow pedia. Access: 20.10.2023.

[5] M. Manzone, P. Balsari, Planters performance during a very Short Rotation Coppice planting. Biomass and Bioenergy. Vol.67, 2014. pp.188-192, https://doi.org/10.1016/j.biombioe.2014.04.029

[6] N. Talagai, M.V. Marcu, G. Zimbalatti, A.R. Proto, Productivity in partly mechanized planting operations of willow short rotation coppice. Biomass and Bioenergy. Vol. 138, 2020. 105609. https://doi.org/10.1016/j.biombioe.2020.105609

[7] V. Kravchuk, M. Novokhatskyi, M. Kozhushko, V. Dumych, Na shliakhu do stvorennia plantatsii enerhetychnykh kultur (On the way to creating energy plantations). Tekhnika i tekhnolohii APK № 2 (41). 2013

[8] M.V. Roik, V.M. Sinchenko, Y.D. Fuchylo, Energety`chna verba: texnologiya vy`roshhuvannya ta vy`kory`stannya (Energy willow: cultivation technology and usage). LLC "Nilan-LTD", Vinnitsa. 2015. 340p.

[9] J. Frączek, K. Mudryk, Jakości sadzonek wierzby energetycznej w aspekcie sadzenia mechanicznego. Inżynieria Rolnicza, 6 (66), 2005. pp.159-167.

[10] I.M. Bartenev, Avtomatizaciya processa posadki rasteniy (Automation of the planting process). Scientific journal of the KubSAU 75(01), 2012. pp. 384-396.

[11] Y. Miwa, Automation of plant tissue culture process. In Automation in biotechnology: a collection of contributions presented at the Fourth Toyota Conference, Aichi, Japan, Amsterdam: Elsevier. 1991

[12] D.T. Galle, Development of an automated precision planter for establishment of Miscanthus giganteus. Purdue University. ProQuest Dissertations Publishing, 2012. 10156261.

[13] K.Abhijit, S. M. Mathur, B. B. Gaikwad, Automation in Transplanting: A Smart Way of Vegetable Cultivation. Current Science 115, no. 10: 2018. pp.1884–92. https://www.jstor.org/stable/ 26978519.

[14] L.J. Kutz, J.B. Craven, Evaluation of photoelectric sensors for robotic transplantation. Applied Engineering in Agriculture, 10 (1), 1994. pp.115-121.

[15] K. Liu, G. Cheng and Z. Kong, Beidou agricultural machinery automatic driving software design, 2019 IEEE 4th Advanced Information Technology, Electronic and Automation Control Conference (IAEAC), 2019. pp. 1770-1775, https://doi.org/10.1109/IAEAC47372.2019.8997712

[16] H. Mao, L. Han, J. Hu, F. Kumi, Development of a pincette-type pick-up device for automatic transplanting of greenhouse seedlings. Applied engineering in agriculture, 30(4), 2014. pp. 547-556.

[17] U. Nedilska, S. Yermakov, A. Rud, O. Kucher, O. Dumanskyi, Bioenergetic evaluation of miscanthus giant productivity in the conditions of the western forest-steppe of Ukraine for use as a solid. Engineering for rural development. Jelgava, 2023, pp.1017—1025 https://doi.org/1025.10.22616/ERDev.2023.22.TF207

[18] S. Yermakov, Rud A., Vusatyi M. The Distribution Of Cash Expenses For The Creation Of Bioenergy Willow Plantations In Ukraine. Vide. Tehnologija. Resursi - Environment. Technologies. Resources. V.1. Rezekne, Latvia. 2023. pp. 74-80 https://doi.org/10.17770/etr2023vol1.7191

[19] S. Yermakov, T. Hutsol, A. Rozkosz, S. Glowacki, S. Slobodian (2021). Evaluation Of Effective Parameters Of Biomass Heat Treatment In Processing For Solid Fuel. Engineering For Rural Development. 2021. https://doi.org/10.22616/ERDev.2021.20.TF241.

[20] S. Yermakov, L. Tkach, P. Potapskyi, S. Oleksiyko, A. Olenyuk Architecture and Construction students' perception of "Technical Drawing" and "Descriptive Geometry" discipline content. Vide. Tehnologija. Resursi - Environment. Technologies. Resources. V.2. Rezekne, Latvia. 2023. pp. 209-213 https://doi.org/10.17770/etr2023vol2.7207

[21] V. Devin, S. Yermakov, O. Gorbovy, V. Pidlisnyj, A. Semenov Research on Working Bodies of Hammer Crushers Employing the Finite Element Method. Vide. Tehnologija. Resursi - Environment. Technologies. Resources. V.3. Rezekne, Latvia. 2023. pp. 65-68 https://doi.org/10.17770/etr2023vol3.7197

[22] K. Ericsson, H. Rosenqvist, E. Ganko, M. Pisarek, L. Nilsson, An agro-economic analysis of willow cultivation in Poland. Biomass and Bioenergy. Vol.30, Issue 1, 2006. pp. 16-27 https://doi.org/10.1016/j.biombioe.2005.09.002

[23] S. Edelfeldt, T. Verwijst, A. Lundkvist, J. Forkman, Effects of mechanical planting on establishment and early growth of willow. Biomass and Bioenergy. Vol. 55, 2013. pp. 234-242. https://doi.org/10.1016/j.biombioe.2013.02.018

[24] I.M. Zyma, T.T. Maliutin, Mekhanizatsiia lisohospodarskykh robit (Mechanization of forestry works). Kyiv: INKOS. 2006. 488p.

[25] S. Yermakov, T. Hutsol, I. Garasymchuk, P. Fedirko, V. Dubik, Study of the Unloading and Selection Process of Energy Willow Cuttings for the Creation a Planting Machine. Vide. Tehnologija. Resursi - Environment. Technologies. Resources. V.3. Rezekne, Latvia. 2023. pp. 271-275 https://doi.org/10.17770/etr2023vol3.7199

[26] S. Yermakov, K. Mudryk and T. Hutsol, The analysis of stochastic processes in unloadingthe energywillow cuttings from the hopper. Environment. Technology. Resources. Rezekne, Latvia. Proceedings of the 12th International Scientific and Practical Conference. Volume III. 2019. pp. 249-252, https://doi:10.17770/etr2019vol3.4159

[27] V. Ivanyshyn, S. Yermakov, T., Ishchenko, K. Mudryk, T. Hutsol, Calculation algorithm for the dynamic coefficient of vibroviscosity and other properties of energy willow cuttings movement in terms of their unloading from the tanker. E3S Web of Conferences, 2020. 154, 04005. https://doi.org/10.1051/e3sconf/202015404005

[28] G. Aijun, L. Xiaoyu, H. Jialin, Z. Zhilong, Z. Ji, C. Jun, Design and experiment of automatic directing garlic planter[J]. Transactions of the Chinese Society of Agricultural Engineering (Transactions of the CSAE), 2018, 34(11), pp. 17-25. https://doi.org/10.11975/j.issn.1002-6819.2018.11.003

[29] A. Tryhuba, T. Hutsol, S. Glowacki. Forecasting Quantitative Risk Indicators of Investors in Projects of Biohydrogen Production from Agricultural Raw Materials. Processes 2021, 9, 258. https://doi.org/10.3390/pr9020258

[30] I. Appavoo, A. Marionneau, M. Berducat, B. Merckx, N. Olivier, A high yield automatic tree planting machine. 5th International Conference on Machine Control & Guidance MCG 2016, Vichy, France. 5 p.

[31] T. Buchholz, T.A. Volk, Improving the Profitability of Willow Crops—Identifying Opportunities with a Crop Budget Model. Bioenerg. Res. 4, 2011. pp.85–95. https://doi.org/10.1007/s12155-010-9103-5

[32] C. Bush, T.A. Volk, H. Eisenbies Planting rates and delays during the establishment of willow biomass crops. Biomass and Bioenergy. Vol.83, 2015. pp.290-296 https://doi.org/10.1016/j.biombioe.2015.10.008

[33] V.V. Ivanyshyn, S.V. Yermakov, T.D. Hutsol, L.M. Mykhailova, O.V. Kucher Avtomat podachi zhyvtsiv enerhetychnoi verby u soshnyk [Automatic feeding of energy willow cuttings into the coulter]. Patent Ukrainy № 152256. 11.01.2023.

Facilitation of the 3D Scanning Process of Industrial Sites using a Self-Moving Autonomous Robotic System

Mihail Zagorski
Technical University of Sofia,
Faculty of industrial technology;
"AI and CAD systems Lab",
R&D&I Consortium, Sofia Tech Park
Sofia, Bulgaria
mihail.zagorski.tu@gmail.com

Radoslav Miltchev
Technical University of Sofia,
Faculty of industrial technology;
"AI and CAD systems Lab",
R&D&I Consortium, Sofia Tech Park
Sofia, Bulgaria
rmiltchev@tu-sofia.bg

Abstract. **The present paper aims to examine how industrial sites can be more easily 3D scanned by integrating a self-moving autonomous robotic system and a large scale scanning technique. A case study is developed where an Unitree Go 1 Edu quadruped robot and a Trimble X7 3D laser scanning system are combined to illustrate the successful integration. For the full integration of the 3D scanner and the robot, several components are designed, using CAD software, and produced via Rapid Prototyping technologies. In the case study, different 3D scanning regimes are also tested. The case study showcases how the industrial 3D scanning process can be aided and potential ideas for the integration of 3D scanning technologies with quadruped robots are further discussed in the paper.**

Keywords: 3D scanner, industrial, quadruped robot, autonomous robotic system

I. INTRODUCTION

Self-moving autonomous systems of the quadruped robot type have undergone an extremely rapid development in the last few decades [1], correspondingly leading to the creation of various so called "robot dog" platforms [2]. These types of robots find increasingly wider applications in some areas, such as: surveying and mapping of hard-to-reach terrains [3], providing autonomous monitoring and guarding of objects [4], tactical actions, conducting rescue operations, lifting heavy loads [5,6], carrying-out manipulations in dangerous environments – for example, areas with an increased content of toxic gases or radioactive environment [7], etc.

Long range industrial-grade 3D scanners are key instruments in design and development of construction sites. By providing accurate and detailed measurements, the so-called scan to BIM (building information modeling) process can help to identify potential problems early on, avoid costly mistakes, and ensure that projects are completed on time and within budget [8,9].

Often the construction sites are large and their area exceeds the working range of the scanner. One of the main challenges in such cases is that the 3D scanning process cannot be fully automated – the scanner should be moved manually to another location after each scan is finished. Integrating the scanning system to a self-moving robot can help automate the process and to facilitate the operator's work. There are similar existing solutions on the market, but they are tied to specific equipment manufacturers and are expensive [10,11].

The present paper aims to examine how a quadruped robot Unitree Go 1 Edu and a Trimble X7 3D scanning system can be integrated together for facilitation of the 3D scanning process of industrial sites. In the case study, different 3D scanning regimes are also tested.

II. MATERIALS AND METHODS

Unitree Go 1 Edu quadruped robot is aimed in particular at higher education and professionals, for developing applications in fields ranging from service robotics to autonomous surveillance. Some of the important specifications of the robot are presented in Table 1 [12].

TABLE 1 SPECIFICATIONS OF UNITREE GO 1 EDU

Maximum speed	17 km/h
Maximum load capacity	10 kg
Weight	12 kg
Length	60 cm
Battery Life	20 min – up to 2.5 h (depending on application and battery capacity)

The quadruped robot is shown in Fig. 1.

Fig. 1.   Unitree Go 1 Edu quadruped robot.

Trimble X7 is a high-speed 3D laser scanning system allowing for scan and BIM data to be referenced, registered and refined in the field. Some of the important specifications of the 3D scanner are presented in Table 2 [13].

TABLE 2 SPECIFICATIONS OF TRIMBLE X7

Laser Wavelength	1550 nm, invisible
Scanning Speed	Up to 500 kHz
Scanning range	0.6 – 80.0 m
Accuracy	2.4 mm @ 10 m, 3.5 mm @ 20 m, 6.0 mm @ 40 m
Weight	5.8 kg
Size	Width = 178 mm, Height = 353 mm Depth = 170 mm
Controller	Trimble T10 Tablet with Trimble FieldLink over WiFi or Cable
Integrated Calibration System	Full auto-calibration of range and angular systems in 25 seconds with no user interaction or targets

The 3D scanning system is shown in Fig. 2.

Fig. 2.   Trimble X7 3D laser scanning system.

The scanning system has several work modes. The scan modes with the corresponding parameters, according to the measuring system specification, are presented in Table 3.

One of the main challenges regarding the integration of the two systems is the mounting of the 3D scanner on the back of the quadruped dog. The construction of the fastening device should be as light as possible, while ensuring a secure attachment of the scanning system. For this reason an adapter plate is developed in a CAD environment. It is shown in Fig. 3.

TABLE 3 SCAN MODES OF TRIMBLE X7

Scan Mode	Duration (min:sec)	Spacing (mm) @ 10 m	Spacing (mm) @ 35 m	Spacing (mm) @ 50 m	Number of points (MPTS)
Standard	1:35	11	40	57	12
	3:43	5	18	26	58
	6:39	4	12	18	125
High sensitivity	3:33	9	33	47	17
	6:54	6	21	30	42
	15:40	4	13	19	109
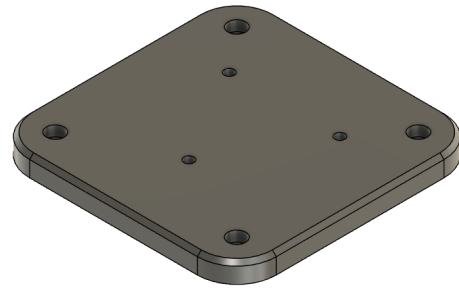
Fig. 3.   Adapter plate in CAD environment.

The constructed adapter plate allows attachment to pre-placed V-slot 2020 aluminum profiles on the back of the robot by means of four bolts and four T-nuts. It is 3D printed using FDM/FFF Rapid Prototyping technology. The process parameters are shown in Table 4.

TABLE 4 PARAMETERS OF 3D PRINTING PROCESS

Material	PETG
Nozzle temperature	240°C
Platform temperature	75°C
Nozzle diameter	1 mm
Layer height	0.4 mm
Number of top layers	3
Number of bottom layers	3
Infill	Grid
Infill density	20%
Number of walls	2
Printing speed	45 mm/s
Wall speed	25 mm/s
Top/bottom speed	25 mm/s
Cooling	20%

The placement of the part in the working area of the printer and a visualization of the internal layers in Ultimaker Cura slicer are shown in Fig. 4. The approximate time to print the part is 2 hours and 7 minutes, and the required material is 80 g.
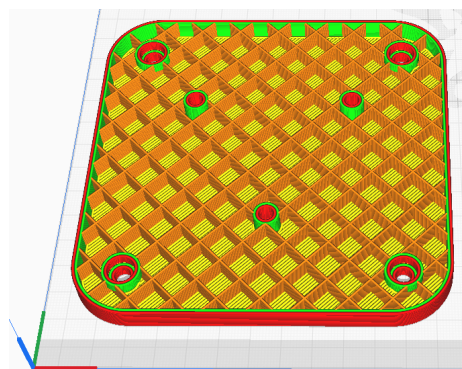
Fig. 4.   Adapter plate in Ultimaker Cura slicer.

III. RESULTS AND DISCUSSION

After the assembling of the fastening device is done the scanner is mounted to the adapter plate using three bolts and is then installed on the back of the robot dog. The final result is shown in Fig. 5.

Fig. 5. Trimble X7 mounted on the back of Unitree Go 1 Edu using the constructed fastening device.

The total weight of the mounting jig including the two V-slot aluminum profiles, the adapter plate and the bolts is around 600 g. The total mass of the load including the 3D scanner and the fastening device is around 6.7 kg which is in the extended load capacity range of the robot dog. One of the main problems is that the 3D scanning system shifts the mass center of the system upwards, which inevitably leads to instability in dynamic conditions. For this reason, it is necessary to operate the robotic system carefully - to move without sudden accelerations and at a relatively low speed.

Two different industrial premises are scanned with the system. The first one is scanned at one location without moving the scanner using the high sensitivity scan mode. The resulting point cloud is shown in Fig. 6.
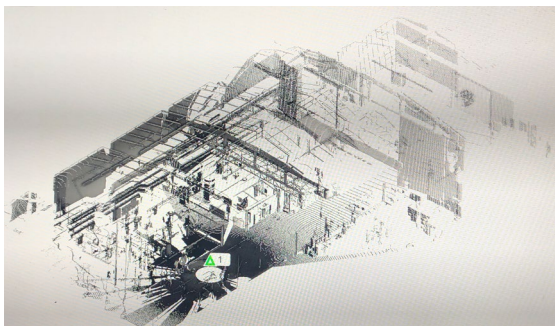
Fig. 6. Point cloud of the first industrial premise.

A black-and-white photography is also taken. Various measurements from the point cloud can be made and can be visualized on the photo, as shown in Fig. 7. The total time for the scan is around four minutes.

Fig. 7. Visualization of a measurement on the photo of the first premise.

The second industrial premise is scanned at two different locations – the robot dog is moved between the scans. The fastest standard scan mode is chosen – the full process takes around seven minutes, including the relocation of the system. The point cloud is shown in Fig. 8 – the scanning points are clearly visible.

Fig. 8. Point cloud of the second industrial premise.

The black-and-white photography of the premise with a measurement is shown in Fig. 9.

Fig. 9. Visualization of a measurement on the photo of the second premise.

The increase of the spacing between the points with increasing distance from the scanner is clearly seen on both of the 3D scans. Nevertheless, the density of the point cloud of the second premise is greater, although the scans are taken in the standard mode.

IV. CONCLUSIONS

The case study shows that scanning of an industrial site at different locations increases the density of the point cloud even when faster scan modes are chosen. The robotic system with the integrated scanner could be used for various industrial sites including but not limited to:

- Construction sites;
- Industrial sites and infrastructure;
- Plants and factories;
- Tunnels;
- Storage tanks;
- Warehouses;
- Mines;
- Large sites in the energy sector, such as thermal power plants, hydroelectric power plants, nuclear power plants, etc.;

The main disadvantage of the system is related to the dependence on batteries. The 4500 mAh battery of the robot dog is limited to around 30 minutes of active work with load. A bigger battery would be more suitable for larger sites [14].

REFERENCES

[1] M. Silva and J. T. Machado, "A Historical Perspective of Legged Robots," Journal of Vibration and Control, Vol. 13, 2007, pp. 1447 – 1486.

[2] Z. Yuhai, R. Wang, F. Huashan and Y. Chen, "Analysis and research of quadruped robot's legs: A comprehensive review," International Journal of Advanced Robotic Systems, Vol. 58, 2019.

[3] D. Bellicoso, M. Bjelonic, L. Wellhausen, K. Holtmann, F. Günther, M. Tranzatto, P. Fankhauser and M. Hutter, "Advances in RealWorld Applications for Legged Robots," Journal of Field Robotics, 2018.

[4] S. Halder, K. Afsari, J. Serdakowski, S. DeVito, M. Ensafi amd W. Thabet, "Real-Time and Remote Construction Progress Monitoring with a Quadruped Robot Using Augmented Reality," Buildings, Vol. 12, 2022.

[5] N. Hu, S. Li, D. Huang and F. Gao, "Modeling and Optimal Control of Rescue Quadruped Robot with High Payload," Proceedings of ASIAN MMS 2016 and CCMMS 2016, Guangzhou, 2016.

[6] "Could robotics help slash inefficiencies in the construction industry?", Feb. 22, 2023. [Online]. Available: https://www.prnewswire.com/news-releases/faro-launches-trek-the-automated-3d-laser-scanning-integration-with-boston-dynamics-spot-mobile-robot-301106739.html/. [Accessed: Feb. 7, 2024].

[7] Y. Jang, W. Seol, K. Lee, K. Kim and S. Kim, "Development of quadruped robot for inspection of underground pipelines in nuclear power plants," Electronics Letters, Vol. 58, 2021.

[8] "Complete Guide on 3D Laser Scanning for Construction | Benefits of Laser Scanning | Process of Scan to BIM," Aug. 17, 2023. [Online]. Available: https://www.linkedin.com/pulse/how-3d-laser-scanning-save-time-money-construction-benefits/. [Accessed: Feb. 7, 2024].

[9] I. Skrzypczak, G. Oleniacz, A. Lesniak, K. Zima, M. Mrówczyńska and J. K. Kazak, "Scan-to-BIM method in construction: assessment of the 3D buildings model accuracy in terms inventory measurements," Building Research and Information, Vol. 50, 2022.

[10] "FARO® Launches Trek, the Automated 3D Laser Scanning Integration with Boston Dynamics Spot® Mobile Robot, Aug. 5, 2020. [Online]. Available: https://www.prnewswire.com/news-releases/faro-launches-trek-the-automated-3d-laser-scanning-integration-with-boston-dynamics-spot-mobile-robot-301106739.html/. [Accessed: Feb. 7, 2024].

[11] "This $75,000 Boston Dynamics robot 'dog' is for sale—take a look," Jun. 22, 2020. [Online]. Available: https://www.cnbc.com/2020/06/22/75000-boston-dynamics-robot-dog-for-sale-take-a-look.html/. [Accessed: Feb. 7, 2024].

[12] "Go1 quadruped robot Edu," [Online]. Available: https://www.generationrobots.com/en/403919-go-1-quadruped-robot.html. [Accessed: Feb. 7, 2024].

[13] "Datasheet - Trimble X7 3D Laser Scanner," Jul. 6, 2023. [Online]. Available: https://www.generationrobots.com/en/403919-go-1-quadruped-robot.html. [Accessed: Feb. 7, 2024].

[14] "Unitree Go1 Battery," [Online]. Available: https://shop.unitree.com/products/unitree-go1-battery. [Accessed: Feb. 23, 2024].

Computer Modeling and Simulation of Mechanisms using Free and Open-source Software

Mihail Zagorski
Technical University of Sofia,
Faculty of industrial technology;
"AI and CAD systems Lab",
R&D&I Consortium,
Sofia Tech Park
Sofia, Bulgaria
mihail.zagorski.tu@gmail.com

Radoslav Miltchev
Technical University of Sofia,
Faculty of industrial technology;
"AI and CAD systems Lab",
R&D&I Consortium,
Sofia Tech Park
Sofia, Bulgaria
rmiltchev@tu-sofia.bg

Mario Semkov
Technical University of Sofia,
Faculty of industrial technology;
Lab. "CAD/CAM/CAE in Industry",
Sofia, Bulgaria
msemkov@3clab.com

Abstract. **The present paper aims to examine how free and open-source software (FOSS) can be applied in the processes of computer modeling and simulations of mechanisms. Successful examples of the application of free software for CAD (computer-aided design) and simulation of mechanisms are presented and discussed. A case study is used to exemplify how engineering tasks, related to position function determination, first transfer function and output link's velocity of a four-bar linkage, can be resolved with the help of an open-source scientific programming language – GNU Octave. Recommendations about the applicability of free open-source software in mechanism analysis are provided.**

Keywords: open-source software, GNU Octave, four-bar linkage, CAD software

I. INTRODUCTION

Free and open-source software (FOSS) is software for which the owner of the copyright of the source code grants the rights to study, modify and distribute the software to anyone and for any purpose (or software with an open-source license for short) [1,2]. Open-source software can also be developed in a cooperative public manner [3]. This type of free software is the most common example of open-source development and is often compared to user-generated content (technical definition) or open content movements (legal definition) [4]. GNU (General Public License) is the project within which the free software concept originated. Richard Stallman, the founder of the project, views GNU as a "technical means to a social end" [5]. Relatedly, Lawrence Lessig states in his introduction to the second edition of Stallman's book "Free Software, Free Society" that in it Stallman has written about "the social aspects of software and how Free Software can create community and social justice" [6].

The open-source model, or collaborative development from many independent sources, generates a much more diverse scope in terms of code design and structure than development by a single firm, allowing it to survive over a long period of time [7]. A report by the Standish Group (from 2008) says that the adoption and use of the open-source software model has resulted in savings of $60 billion per year to users [8]. Various companies are benefiting from different open-source solutions. A research estimates that in 2018 FOSS had at least 260 000 contributors in the EU (around 8% of all employees in software development sector). They produced a volume of software code equivalent to the full-time work of 16 000 developers. For the same year the economic impact of open source software stands between $77.8 billion and $113.7 billion [9].

Free and open-source software has several key advantages and disadvantages compared to paid solutions.

The main advantages of FOSS are the following [10]:

- The software is available for use and modification for any purpose, including educational and professional, completely free and unlimited;
- Some open-source solutions require less computing resources than paid alternatives, often because of the lack of graphical user interface;
- A large database of training materials for working with the software is available;
- There is a large community of users;
- The software provides flexibility and freedom for the user.

The main disadvantages of open-source software are the following [11]:

- The software often has a limited graphical interface, which makes its use more difficult than that of the paid alternatives;
- Usually its use is related to writing commands/code in a given programming language;
- Due to the possibility of anyone working on the software code, there is a risk of "bugs" and unexpected results;
- Some open-source solutions are not compatible with Windows and/or MacOS, so the user needs a dedicated machine or a virtual machine with a specific version of Linux;
- FOSS typically lacks dedicated technical support;
- A dedicated technical support team is often non-existing.

Industrial CAD (computer-aided design) and CAE (computer-aided engineering) solutions for mechanical design and simulation are often very expensive. Open-source solutions are existent and some of them could be a good alternative compared to paid software, especially for scientific researches and education.

The present paper aims to examine different free softwares for computer modeling and simulations of mechanisms. Successful examples of the applications of such solutions are presented and discussed. Case study is used to exemplify how engineering tasks, related to several important parameters of a four-bar linkage, can be resolved with the help of an open-source scientific programming language - GNU Octave.

II. MATERIALS AND METHODS

A. MBDyn

MBDyn is the first and one of the few full-featured free general purpose Multibody Dynamics analysis software, released under GNU's GPL 2.1. It has been developed at the Dipartimento di Scienze e Tecnologie Aerospaziali (formerly Dipartimento di Ingegneria Aerospaziale) of the University "Politecnico di Milano", Italy. MBDyn simulates the behavior of heterogeneous mechanical, aeroservoelastic systems based on first principles equations. The software is being actively developed and used in the aerospace, wind energy, automotive and mechatronic fields (industrial robots, parallel robots, micro aerial vehicles) for the analysis and simulation of the dynamics of complex systems [12].

MBDyn is structured in terms of statements. Statements are logically divided in blocks. Each block is opened by a begin statement and it is closed by an end statement:

```
begin: data;
      # global simulation data
      problem: initial value;
end: data

begin: initial value;
# problem-dependent data
end: initial value;

begin: control data;
# global model data
end: control data;
```

```
begin: nodes;
# nodes
end: nodes;

begin: drivers;
# drivers
end: drivers;

begin: elements;
# elements
end: elements;
```

B. Integration of MBDyn to other softwares

MBDyn can be integrated to Blender, FreeCAD (Dynamics Workbench) and MATLAB through add-ons in order to be used for model preparation and visualization.

FreeCAD is an open-source software, which is fully compatible with Python, a widely used free and open-source programming language [13]. FreeCAD is a platform which can be used not only for 3D modelling, but also for various analysis and simulations when the proper add-ons are installed. It has a steep learning curve but provides a completely free alternative to various CAD, CAM and CAE solutions.

Dynamics Workbench project aims at integrating FreeCAD and MBDyn. The objective is to use FreeCAD as pre-post processor for MBDyn, simplifying the process of successfully simulating multibody-dynamics systems and post-processing the simulation results [14]. An exemplary application of Dynamics Workbench is shown in Fig. 1.
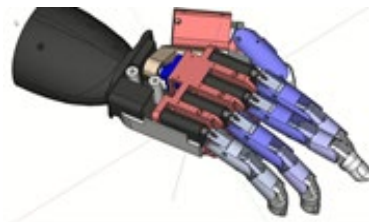
Fig. 1 An exemplary application of Dynamics Workbench.

Blendyn is another interesting project which aims to integrate MBDyn physics to Blender graphics – a so-called graphical post-processor [15]. Blendyn is built as an add-on of Blender which allow user to visualise MBDyn output datas with 3D animations. Blendyn was first implemented in 2017 [16]. ATTILA model, an example of a real-life application of Blendyn, is shown in Fig .2 [17].
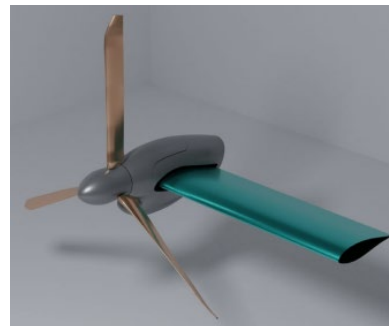
Fig. 2 Semispan Wing ATTILA Tiltrotor Model.

Another example of an integration between MBDyn and engineering software is MBS3D: an easy-to-use open-source general-purpose program for dynamic simulation

of multibody systems. It is entirely programmed as plain-text in MATLAB and uses a very efficient and tested mathematical semi-recursive formulation. It covers open-chain and closed-loop systems [18].

MBDyn Analysis can be implemented in MATLAB Graphics, as shown in Fig. 3 [19].
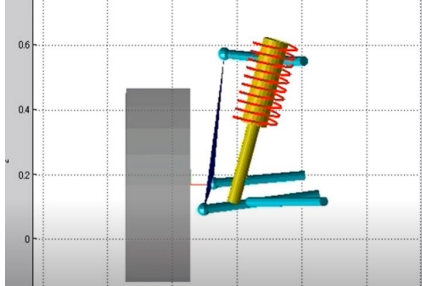
Fig. 3 Double Wishbone Suspension simulation using MBDyn Analysis and MATLAB Graphics.

C. OpenFOAM

OpenFOAM (Open Field Operation And Manipulation) is a C++ toolbox for the development of customized numerical solvers, and pre-/post-processing utilities for the solution of continuum mechanics problems, most prominently including computational fluid dynamics (CFD) [20]. OpenFOAM's finite volume method uses a co-located methodology on an unstructured polyhedral grid with arbitrary grid elements [21]. An exemplary application of the toolbox is shown in Fig. 4 [22].
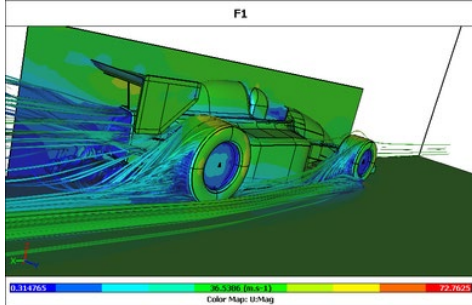
Fig. 4 Flow simulation using OpenFOAM and ParaView for visualization.

D. Linkage

Linkage is a free computer-aided design program for Microsoft Windows used for prototyping of mechanical linkages. The mechanism is edited and animated in the same window allowing for quick analysis and modification while working on a design. It is developed by David Rector – Developer, Designer, and Software Engineer [23].

E. GNU Octave

GNU Octave is a scientific programming language for scientific computing and numerical computation. Octave helps in solving linear and nonlinear problems numerically, and for performing other numerical experiments using a language that is mostly compatible with MATLAB. As part of the GNU Project, it is free software under the terms of the GNU General Public License [24].

III. RESULTS AND DISCUSSION

A case study is developed to exemplify how engineering tasks, related to position function determination, first transfer function and output link's velocity of a four-bar linkage, can be resolved with the help of an open-source scientific programming language - GNU Octave. Linkage is used for visualisation.

A. Visualisation with Linkage

The kinematic scheme of a four-bar linkage – crank-rocker mechanism, is shown in Fig. 5.
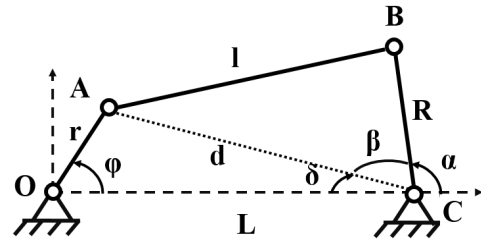
Fig. 5 Kinematic scheme of a crank-rocker mechanism.

The visualisation of the designed mechanism in Linkage is shown in Fig. 6.
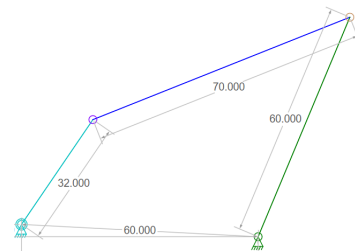
Fig. 6 Visualisation of the designed four-bar mechanism in Linkage.

The dimensions of the different links are as follows:

- Crank (OA = r) = 0.032 m;
- Intermediate link (AB = l) = 0.07 m;
- Rocker (BC = R) = 0.06 m;
- Fixed link (OC = L) = 0.06 m.

B. Calculations and visualizations with Octave

The rocker oscillates between two limiting angles (α or *alpha*). The angle between the input link and the fixed link is φ or *phi*. The position function of the angle of the output link with respect to the angle of the input link can be calculated in Octave using trigonometric functions with the following code:

```
%input data
r = 0.032;
l = 0.07;
R = 0.06;
L = 0.06;
%defining the angle of the input link
phi = 0:pi/180:2*pi;
%defining the diagonal
d = sqrt(L.^2 + r.^2 - 2.*L.*r.*cos(phi));
%position function alpha = phi(alpha)
alpha = pi - acos((R.^2 + d.^2 -
l.^2)./(2.*R.*d)) - asin(r.*sin(phi)./d);
%radians to degrees
phideg = rad2deg(phi);
alphadeg = rad2deg(alpha);
```

```
%plot of the position function alpha(phi)
plot(phi_deg,alpha_deg,'k');
xlabel('phi',"fontsize",20);
ylabel('alpha', "fontsize", 20);
xlim([0 360]);
set(gca,'XTick',0:30:360);
grid on;
```

The resulting diagram is shown in Fig. 7.
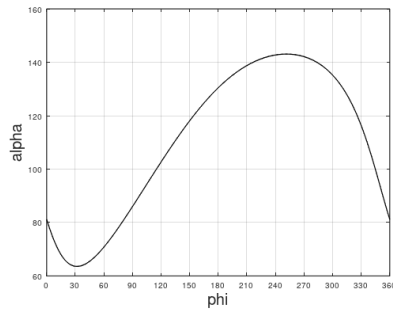
Fig. 7 Position function of the mechanism.

The first transfer function of the mechanism can be calculated by differentiating the position function with the help of the following code:

```
%first transfer function
aDiff = diff(alpha_deg)./diff(phi_deg);

%plot of the first transfer function
plot(aDiff,'k');
xlabel("phi", "fontsize", 20);
ylabel("a'", "fontsize", 20);
set(gca,'XTick',0:30:360);
xlim([0 360]);
```

The resulting diagram is shown in Fig. 8.
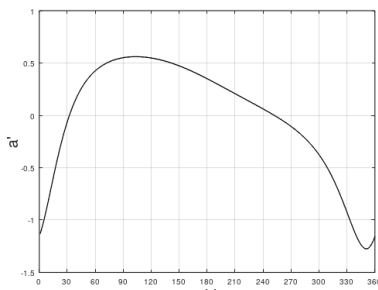
Fig. 8 First transfer function of the mechanism.

The velocity of the output link can be calculated by multiplying the first transfer function by the angular velocity of the input link:

```
%first transfer function
w = 500; %angular velocity of the output link
v = aDiff*w;
plot(v,'k');
xlabel('phi',"fontsize",20);
ylabel("v", "fontsize", 20);
set(gca,'XTick',0:30:360);
xlim([0 360]);
grid on;%plot of the first transfer function
```

The resulting diagram is shown in Fig. 9.
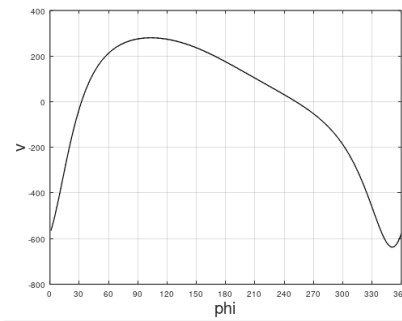
Fig. 9 Velocity of the output link.

The present case study shows some of the advantages of using free and open-source software for engineering tasks. However, there are also disadvantages related to FOSS. For example most of the software is not equipped with user-friendly GUI (Graphical User Interface) and it requires additional add-ons and/or libraries for visualization.

IV. CONCLUSIONS

The software reviewed in the paper can be used for solving of various engineering tasks including but not limited to:

- Simulation of different mechanisms and machines using multibody dynamics simulation software;
- Visualization and computation of various theoretical problems;
- Various tasks including computational fluid dynamics, for example in the field of energetics, for optimization of geometries etc.
- Education and scientific researches.

The licenses for paid engineering software can be worth tens of thousands of dollars. However, paid solutions often provide a better user interface, they are usually much easier to get up and running with substantially less time spent and have better compatibility with other products – hardware or software.

The choice of suitable software – paid, free or open-source, cannot always be considered unambiguously. It is for this reason that the engineer must be familiar with the various software products and select the right one for solving the specific engineering problem.

REFERENCES

[1] R. Stallman, "The Free Software Movement and the GNU/Linux Operating System", 22nd IEEE International Conference on Software Maintenance, 2006.

[2] "License information," [Online]. Available: https://www.debian.org/legal/licenses/. [Accessed: Feb. 19, 2024].

[3] "Cooperatives Europe developing open source software," Nov. 25, 2019. [Online]. Available: https://coopseurope.coop/news_article/coopseurope-developing-open-source-software/. [Accessed: Feb. 19, 2024].

[4] M. Santos, "The "so-called" UGC: an updated definition of user-generated content in the age of social media," Online Information Review, Vol. 46, 2022.

[5] J. Simpson, "Expanding Human Capabilities Through the Adoption and Utilization of Free, Libre, and Open Source Software", University of the Incarnate Word, 2014.

[6] R. Stallman, "Free software, free society : selected essays of Richard M. Stallman", GNU Press, 2002. [E-book] Available: www.gnupress.org.

[7] D. A. Tamburri, F. Palomba, A. Serebrenik and A. Zaidman, "Discovering community patterns in open-source: a systematic approach and its evaluation," Empirical Software Engineering, Vol. 24, 2019, pp. 1369 – 1417.

[8] R. Rothwell, "Creating wealth with free software," Free Software Magazine, 2008.

[9] "How much are open-source developers really worth? Hundreds of billions of dollars, say economists," Feb 8, 2021. [Online]. Available: https://www.zdnet.com/article/how-much-are-open-source-developers-really-worth-hundreds-of-billions-of-dollars-say-economists/. [Accessed: Feb. 20, 2024].

[10] H. Hamidovic, A. Buljubasic, M. Djulic, E. Sejic, "BENEFITS AND RISKS OF FOSS STRATEGIES", Conference: DIEC 2022, 2022.

[11] M. Heron, V. Hanson and I. Ricketts, "Open Source and Accessibility: Advantages and Limitations", Journal of Interaction Science, Vol. 1, 2013.

[12] P. Masarati, M. Morandini and P. Mantegazza, "An Efficient Formulation for General-Purpose Multibody/Multiphysics Analysis", Journal of Computational and Nonlinear Dynamics, Vol. 9, 2014.

[13] F. Machando, N. Malpica and S. Borromeo, "Parametric CAD modeling for open source scientific hardware: Comparing OpenSCAD and FreeCAD Python scripts", PLOS ONE, Vol. 14, 2019.

[14] "FreeCAD-MBDyn dynamics workbench," [Online]. Available: https://gitlab.com/josegegas/freecad-mbdyn-dynamics-workbench. [Accessed: Feb. 20, 2024].

[15] "Blendyn," [Online]. Available: https://github.com/zanoni-mbdyn/blendyn. [Accessed: Feb. 20, 2024].

[16] "Blendyn Development," [Online]. Available: https://github.com/BryanGsep/Blendyn-Development/blob/main/README.md. [Accessed: Feb. 20, 2024].

[17] A. Cocco, S. Mazzetti. P. Masarati, S. Hoff and B. Timmerman, "Numerical Whirl–Flutter analysis of a tiltrotor semi-span wind tunnel model", CEAS Aeronautical Journal, Vol. 13, 2022, pp. 923 – 938.

[18] C. Caccia and P. Masarati, "Coupling multi-body and fluid dynamics analisys with preCICE and MBDyn", 9th edition of the International Conference on Computational Methods for Coupled Problems in Science and Engineering, 2021.

[19] "MBDyn Tutorial," [Online]. Available: https://www.sky-engin.jp/en/MBDynTutorial/. [Accessed: Feb. 20, 2024].

[20] H. Medina, A. Beechook, J. Saul, S. Porter, S. Alexandrova and S. Benjamin, "Open source Computational Fluid Dynamics using OpenFOAM," Light Aircraft Design: Methods and Tools 2015, London, 2015.

[21] H. Jasak,, "OpenFOAM: Open source CFD in research and industry", International Journal of Naval Architecture and Ocean Engineering, Vol. 2, 2009, pp. 89 – 94.

[22] "OpenFOAM+ParaView_flow_simulation.png," [Online]. Available: https://upload.wikimedia.org/wikipedia/en/e/e9/OpenFOAM%2BParaView_flow_simulation.png. [Accessed: Feb. 22, 2024].

[23] "Linkage Mechanism Designer and Simulator," [Online]. Available: https://blog.rectorsquid.com/linkage-mechanism-designer-and-simulator/. [Accessed: Feb. 22, 2024].

[24] J. Eaton, "GNU Octave and reproducible research", Journal of Process Control, Vol. 22, 2012, pp. 1433 – 1438.

III
LASER TECHNOLOGIES

Laser radiation made hydrophobic surface on stainless steel for food industry, a review

Arturs Abolins
Faculty of engineering
Rezekne Academy of Technologies
Rezekne, Latvia
artur.abolinsh@inbox.lv

Abstract. **Main requirement in food processing industry is providing a food safety through all the production cycle. One of many procedures that guarantee food safety is cleanliness of surfaces that are in contact with food or its raw materials. Surface cleanliness could be achieved in different ways, either by regular washing with clean water and detergents or by creating surfaces, that repel water or other residues. It is important, because remaining water with residues create conditions for growth of unwanted microflora.**

As classic, or active, cleaning method of washing with clean water and detergents require a lot of resources and energy. But nowadays more and more self cleaning, passive, methods are used, such as hydrophobic surfaces. These surfaces are made with in different ways, where most common are water reppeling coatings, for example – wax. But there are other methods, such as laser radiation treatment, that can create hydrophobic surface on required material, such as stainless steel, which is most common used material in food processing.

There are studies that show effectivnes of laser radiation created hydrophobic surface for water repelling, but unfortunately, there are no researches found, that could provide information of such surface interaction with milk. As milk by itself is water emulsion with different nutrients, its most favourable environment for microbiological growth. By examining and analyzing different scientific articles, that are linked to topic of hydrophobic surface usage in food industry, it was concluded, that laser radiation made hydrophobic surfaces on stainless steel could have large potential. Especially in dairy industry, where such surface treatment could decrease risks of microflora growth and save resources and energy that are required for active washing process.

Keywords: Hydrophobic surface, laser treatment, milk, stainless steel .

I. INTRODUCTION

Food is the basis of human health and longevity, where the main role is played by its quality and safety. Throughout human history, various methods have been discovered and tested to improve the quality and safety of products, which are ultimately successfully applied in practice. At one time, such revolutionary processes as pasteurization and sterilization are now a given. With the advent of new materials and types of packaging, the quality and safety of products became even better, where we also should not forget about the development of the concept and requirements of hygiene. This is one of the reasons why modern human is able to live a longer life than his ancient ancestors [1].

Nowadays, food processing and hygiene technologies are developing further, but there is still a kind of stagnation of innovations or revolutionary ideas, since the basic technologies and processes almost fully satisfy modern needs. The main vector of development at the moment is related to environmental protection, saving energy and materials, as well as the movement for a healthier lifestyle and alternative food products. This movement creates new challenges for science and industry, since some basic technologies of food production and hygiene cannot fully solve them, and sometimes even go against them [2], [3].

Of the many potential directions in the development of food safety and quality, the use of various types of surfaces that repel water or oil shows promise. One of the most famous examples are anti-stick surfaces for frying pans and waffle irons. These surfaces actually help save cooking oil and detergents for cleaning burnt marks. Another example is the wax coating on paper cups and cardboard tetra packs, which prevent the liquid product from wetting the packaging. Thus, for the transportation and storage of liquid products, more environmentally friendly and lightweight types of packaging can be used [4].

But still, these properties are obtained by applying one material to another, which in turn creates a potential threat of foreign substances or particles entering food products. As a solution to this problem, new methods of obtaining repellent surfaces are being developed, for example, laser processing, where the structure of the base material performs the necessary functions. In this case, such surfaces may be suitable for the dairy industry, where the

issue of food safety and hygiene is at a special level, since milk is one of the most favourable environments for the development of microflora, and also, milk is very sensitive to contaminants that can negatively affect on its organoleptic properties [5].

II. HYDROPHOBIC SURFACES IN FOOD INDUSTRY

Main risk factor in dairy processing is biofilm creation on stainless steel surfaces. This biofilm is created by bacteria and milk residue, that could be resistant to most cleaning protocols and thermal processing. Also, biofilm decrease heat transfer, where even 0,05 mm thick biofilm layer results in 30% heat transfer decrease. Finally, it's proven that biofilm also can cause surface corrosion. All these milk biofilm effects not only increase risk of dairy product contamination and quality loss, but also could lead to ineffective work of equipment or even damage it. Considering these factors, solutions of removing or at least minimizing biofilm effects for dairy industry are needed. In that case, article authors have conducted experiment, where 4 different materials where applied on stainless steel AISI 316, such as: Ni-P-PTFE, AMC-18, Dursan, Lectrofluor-641. Ni-P-PTFE coating showed most promising results, due to high resistance to biofilm formation and other residue attachment. Comparing to control example (clean AISI 316), new coating decreased surface roughness by 43% and increased contact angle by 2-3 times, showing that Ni-P-PTFE coated example is more hydrophobic. Unfortunately, these tests were condemned only under limited lab conditions, and there were no further researches found, that could show Ni-P-PTFE coating durability in real life conditions and its interaction with milk itself [6].

There is other method that helps to prevent dairy product contamination with biofilm forming bacteria, by using superhydriphobic wax surfaces. Tests have proven that even under similar conditions as in dairy factory, where continuous flow of milk and cleaning fluids are present, biofilm development was cut up to 99%. Also, paraffin/fluorinated wax coating has shown no negative effects on milk quality, in comparison to other technologies, that were available up to 2019 [7].

As a solution to minimize bacterial cross contamination where leafy vegetables were in contact with stainless steel surfaces, nickel- nanodiamond nanocomposite film was created on AISI 304 stainless steel. This coating has shown good superhydrophobic properties with static water contact angle of 156.3 ± 1.9° and durability to cleaning process [8].

Quite a number of articles where found where food safe hydrophobic coatings were used for packaging in order to minimize liquid food waste. It is very important problem nowadays not only due to waste of products as a resource, but food residue itself creates good environment for pathogenic bacteria and fungus evolving and spreading. Also, dirty used package usually is not properly recycled, as it requires resources and energy for cleaning [9]. In most cases, natural wax and ethanol solutions were sprayed on most common used types of packaging. Insect waxes such as Shellac and Beeswax were proven as a robust coating on paper packaging, where 145° contact angle was achieved [10]. Mixture of beeswax and coffee lignin creates coating with more than

150° contact angle and stability to long time heating and flushing [11]. Microcrystalline or paraffin wax coating gives 158° contact angle, is resistant to pressure washing and corrosive water based solutions. Can be applied on substrates as PET, PE and glass where shows great anti adhesive properties to products such as: honey, cola and dairy products [12]. Food grade candelilla and rice bran wax shows similar contact angle and resistance results. It also can be applied on materials such as: aluminium foil, paper, PTFE, PP and glass [13]. Also soybean wax coating has similar properties, with 159° contact angle, but it starts to lose its superhydrophobic properties if it is hated above 50°C, that makes it unsuitable for use with heated liquid products [14].

Other non biological coatings were tested too, such as paraffin wax combined with clay minerals or multiwalled carbon nanotubes. If paraffin-clay performs similarly to other bio-wax coatings [15], multiwalled carbon nanotubes have even better properties, where contact angle is 167°. Coating is extremely durable, resisting intensive water jetting, immersion in corrosive liquids and temperatures up to 390°C, which is far more extreme conditions, that are commonly used in liquid food production, but unfortunately, it is not known if such coating is safe for health in long term [16].

Overall, more and more hydrophobic coatings are used not only for food packaging, but for food itself, creating eatable protective coating. Most of these coatings are made from bio-wax for paper packaging, which in some cases is a good alternative to PS and PP packaging. Except minimisation of food waste and protecting materials from wetting, hydrophobic surfaces have proven its effectiveness against microflora growth and corrosion of metals. Other, non natural coatings are developed too, but not all are usable due to costliness, technological complicity or food safety concerns. Use of laser texturing for creating hydrophobic surface on main material, without using any coatings, is quite promising [17].

III. HYDROPHOBIC SURFACES CREATED BY LASER RADIATION

Laser technologies have opened wide spectrum of possibilities, that in some cases were not possible before. In case of laser texturing, process, where laser beam creates precise surface texture by melting or evaporating top layer of processed material in programmed pattern, makes possible to create surfaces with different properties. Creation and examination of hydrophobic surfaces on different materials using laser radiation is quite popular for many researchers nowadays, where stainless steel is commonly used due its wide usage. As laser texturing is only a surface modification process, it does not require high power laser sources [18], [19], [20], [21].

Using 800nm Regenerative/Multi-pass Ti: sapphire laser system with 130fs pulse duration and 1kHz repetition rate it is possible to create hydrophobic surface on stainless steel with 166.3° contact angle and 4.2° sliding angle. Increasing laser fluencies (from 0,1 to 2,5 J/cm^2), contact angle also increased (from 150 to 166.3°) [22]. In other case, a 1032 nm femtosecond laser with

310 fs pulses, 5 W average power output and a circular polarisation for texture creation was used. Main goal was to achieve large area surface treatment with single step process with high speed (1 m/s) and pulse frequency (500 kHz) [23]. Similar research authors experimented with different laser fluencies (from 178 to 1143 J/cm^2) achieving surface with 164° ± 5° contact angle that saves its hydrophobic properties for 30 days after treatment [24]. Finally, another femtosecond laser was used in other one research, where authors used achieved 156° contact angle on AISI 304 stainless steel [25].

Nd:YAG laser with wavelengths of 532 nm and 1064 nm also could be used for stainless steel microtexturing. Even more, a comparative research was made for creating superhydrophobic surfaces in different medias. Since air or inert gas media is most commonly used, water media provides better heat sinking due to its high heat capacity, makes possible to control generated temperature gradients and most important – redeposition of ablated particles is prevented [26].

Nanosecond lasers could be used for stainless steel texturing too. For example, 1064 nm nanosecond fiber laser with 20 kHz pulse rate, 100 ns pulse duration and 1mJ pulse energy was used to create surface with maximum contact angle of 153.3°. It was achieved by creation of microstructured surface pitch of 110 μm with 14 W laser power [27]. Very detailed review article theoretically proves effectiveness of superhydrophobic surface creation on stainless steel with different wavelength nanosecond lasers [28].

Regardless of stainless steel high resistance to corrosion, under some circumstances it still can deteriorate. As hydrophobic surfaces repel water, this factor by itself is a good way to minimize possibility of corrosion process. Several researches have been made to create hydrophobic surfaces on different metals by laser treatment, in order to fight with corrosion. In all cases, research authors have achieved good results to create self cleaning superhydrophobic surfaces on stainless steel using different laser types [29], [30], [31], [32].

From microbiological point of view, it is proven, that laser made hydrophobic surface on stainless steel can reduce growth of most common bacteria by 99.8% for *E. coli* and 79,1% for *S.aureus*. Antibacterial effect is achieved due to hydrophobic surface that repels water with residues, that is the main media for bacterial growth [33].

In most cases researchers focused their attention only to surface ability to repel water, but there are different kind of oils, fats, alcohols or their mixtures, that in some situations have to be repelled too. To achieve this effect, an omniphobic surface have to be created. Quite noticeable is article, where authors managed to create superomnyphobic surfaces on different kind of materials, including stainless steel 304, 316 and 340, that repels both water and n-hexadecane. Use of 10.2 μm CO2 laser engraver, proves, that such surfaces could be created even with much simpler equipment. Unfortunately this surface has shown poor mechanical durability, but still can be used in cases, where solid particles are not present [34]. Other way of creating superomnyphobic surface on stainless steel was made by using nanosecond laser on AISI 304 stainless steel and treating surface with aqueous solution of perfluorooctanoic acid, superomnyphobic surface was created, that repels different substances such as: water, hexadecane, peanut oil and glycerol (with contact angles 165.77°, 152.83°, 155.24° and 155.09°). This surface has self cleaning effect and good wear resistance, that is guaranteed up to two months under natural conditions [35].

TABLE I. COMPARISON OF DIFFERENT LASER SOURCES FOR ACHIEVING SUPERHYDROPHOBIC SURFACE ON STAINLESS STEEL.

Laser type	Wavelength | spot size	Power density or pulse power	Pulse | rate | scan speed	Water contact angle	Source nr.
NIR Ytterbium Fiber Laser system	1060 nm | 30 μm	n/a	n/a | n/a | 5000 mm/s	>150°	[32]
YLP-ST20E fiber laser	1061 nm | 50 μm	7643 W/mm2	100 ns | 20 kHz | n/a	>150°	[29]
Nd:YAG laser	1064 nm | n/a	31 J/cm2	95 ns | 1 kHz | n/a	153°	[37]
Nanosecond pulsed fiber laser	1064 nm | 15 um	1 mJ	100 ns | 20 kHz | n/a	153.2°	[27]
Yb:YAG DLIP laser setup	1030 nm | 60 μm	0.05 & 0.1 J/cm2	8 ps | 100 kHz | 100 mm/s	154 ± 3°	[33]
UV nanosecond laser	n/a | 30.0 μm	8.14 J/cm2	n/a | n/a | 20 mm/s	160 ± 5°	[31]
Regenerative/Multi-pass Ti: sapphire laser	800nm | LIPSS - 0.5 μm	0.08 & 0.2 J/cm2	130 fs | 1 kHz | n/a	166.3°	[22]
Nd:YAG pulsed laser (LPKF, OK DP10)	1064 nm | n/a	86.45 J/cm2	40 ns | 25 kHz | n/a	168 ± 3.0°	[36]
CO$_2$ laser engraver	10.2 μm | n/a	120 W	n/a | n/a | 20 mm/s	168°	[34]

IV.CONCLUSIONS

Main inspiration of self cleaning or "lotus effect" comes from nature, where plants and animals have developed ability to repel water for various survival reasons. That is why, idea of self cleaning, water repelling surface is always actual for human daily life. From this research of current situation in field of using hydrophobic surfaces in food industry, it is clear, that a lot methods exist for achieving water or other substance repelling effect on most of materials. Laser texturing on stainless steel, most common used material in food processing, provides promising results for future researches and implementation of new technologies. This surface treatment could be done by large variety of laser sources and their work parameters, but the key for achieving superhydrophobic effect is a texture of surface itself. It would be desirable to create a template of an "almost perfect" 3 dimensional texture map of the surface, that provides best superhydrophobic effect.

As most researches were carried out to create water repelling surface, our aim for future researches is to create milk repelling surface on stainless steel, by using available laser setups in order to find new ways making dairy industry more safe and efficient.

REFERENCES

[1] K.W. Alt, A.A.-Ahmad, J.P. Woelber. Nutrition and Health in Human Evolution–Past to Present. Nutrients. September 2022; 14(17): 3594.

[2] E.Radu, A.Dima, E.M. Dobrota, A.M. Badea, D.Ø.Madsen, C.Dobrin, S.Stanciu. Global trends and research hotspots on HACCP and modern quality management systems in the food industry. Heliyon. Volume 9, Issue 7, July 2023, e18232.

[3] A.Amorim, V.L.Silva, P.J.A. Sobral. Food Processing: An overview on links between safety, security, supply chains, and NOVA classification. Cleaner and Circular Bioeconomy. Volume 5, August 2023, 100047.

[4] G.G.Vacas, F.Comino, O.R.Alabanda. Evaluation of the effectiveness and durability of commercial non-stick coatings. Journal of Food Engineering. Volume 370, June 2024, 111959.

[5] Shreya Saha a, Reshab Majumder a, Pavel Rout b, Shamim Hossain. Unveiling the significance of psychrotrophic bacteria in milk and milk product spoilage – A review. The Microbe. Volume 2, March 2024, 100034.

[6] S.Jindal, S.Anand, K.Huang, J.Goddard, L.Metzger, J.Amamcharla. Evaluation of modified stainless steel surfaces targeted to reduce biofilm formation by common milk sporeformers. Journal of Dairy Science Vol. 99 No. 12, 2016. pp.9502–9513.

[7] I. Ostrov, I. Polishchuk, M. Shemesh, B. Pokroy, Superhydrophobic Wax Coatings for Prevention of Biofilm Establishment in Dairy Food. ACS Applied Bio Materials. 2019, 2, 11, pp. 4932–4940.

[8] W.DeFlorio, S. Liu, Y. Arcot, B.Ulugun, X. Wang, Y. Min, L. Cisneros-Zevallos, M. Akbulut. Durable superhydrophobic coatings for stainless-steel: An effective defense against Escherichia coli and Listeria fouling in the post-harvest environment. Volume 173, Part 1, November 2023, 113227.

[9] M.Ruzi, N.Celik, M.s.Onses. Superhydrophobic coatings for food packaging applications: A review. Food Packaging and Shelf Life. Volume 32, June 2022, 100823.

[10] A.Ahuja, V.K.Rastogi. Spray coating of edible insect waxes for liquid food packaging. Applied Surface Science. Volume 624, 1 July 2023, 157150.

[11] Y.Zhang, J.Bi, S.Wang, Q.Cao, Y.Li, J.Zhou, B.Zhu. Functional food packaging for reducing residual liquid food: Thermo-resistant edible super-hydrophobic coating from coffee and beeswax. Journal of Colloid and Interface Science. Volume 533, January 2019, pp. 742-749.

[12] X.Zhao, T.Hu, J.Zhang. Superhydrophobic coatings with high repellency to daily consumed liquid foods based on food grade waxes. Journal of Colloid and Interface Science. Volume 515, April 2018, pp. 255-263.

[13] B.-Y. Liu, C.-H. Xue, Q.-F. An, S.-T. Jia, M.-M. Xu. Fabrication of superhydrophobic coatings with edible materials for super-repelling non-Newtonian liquid foods. Chemical Engineering Journal Volume 371, September 2019, pp. 833-841.

[14] T.Shen, S. Fan, Y.Li, G.Xu, W.Fan. Preparation of Edible Non-wettable Coating with Soybean Wax for Repelling Liquid Foods with Little Residue. School of Chemistry and Chemical Engineering, Henan Institute of Science and Technology, Xinxiang, Henan 453003, China. 2020, 13(15), 3308.

[15] W.Ding, J.Wei, J.Zhang. Stable food grade wax/attapulgite superhydrophobic coatings for anti-adhesion of liquid foods. Journal of Colloid and Interface Science. Volume 650, Part A, November 2023, pp. 865-874.

[16] X.Zhao, B.Yu, J.Zhang. Transparent and durable superhydrophobic coatings for anti-bioadhesion. Journal of Colloid and Interface Science. Volume 501, September 2017, pp. 222-230.

[17] M.M. Frota, A.L.A.Mattos, K.W.E. Miranda, H.N. Cheng, A.Biswas, M.S.R. Bastos. Superhydrophobic systems in food science and technology: Concepts, trends, challenges, and technological innovations. Applied Food Research. Volume 2, Issue 2, December 2022, 100213.

[18] D.-M. Chun, C.-V. Ngo, K.-M. Lee. Fast fabrication of superhydrophobic metallic surface using nanosecond laser texturing and low-temperature annealing. CIRP Annals. Volume 65, Issue 1, 2016, pp. 519-522.

[19] E.Skoulas, A.Manousaki, C.Fotakis, E.Stratakis. Biomimetic surface structuring using cylindrical vector femtosecond laser beams. Scientific Reports volume 7, March 2017, 45114.

[20] A.F.Obilor, M.Pacella, A.Wilson, V.V.Silberschmidt. Micro texturing of polymer surfaces using lasers: a review. The International Journal of Advanced Manufacturing Technology. 2022, 120, pp. 103–135.

[21] A.Riveiro, P.Pou, J.del Val, R.Comesaña, F.Arias-González, F.Lusquiños, M.Boutinguiza, F.Quintero, A.Badaoui, J.Pou. Laser texturing to control the wettability of materials. Procedia CIRP. Volume 94, 2020, pp. 879-884.

[22] B.Wu, M. Zhou, J. Li, X. Ye, G. Li, L. Cai. Superhydrophobic surfaces fabricated by microstructuring of stainless steel using a femtosecond laser. Applied Surface Science. Volume 256, Issue 1, October 2009, pp. 61-66.

[23] J.M.Romano, A.G.Giron, P.Penchev, S.Dimov. Triangular laser-induced submicron textures for functionalising stainless steel surfaces. Applied Surface Science. Volume 440, May 2018, pp. 162-169.

[24] C.Sciancalepore, L.Gemini, L.Romoli, F.Bondioli. Study of the wettability behavior of stainless steel surfaces after ultrafast laser texturing. Surface and Coatings Technology. Volume 352, October 2018, pp. 370-377.

[25] M.M. Calderon, A.Rodríguez, A.D.Ponte, M.C.M.Miñana, M.G. Aranzadi, S.M.Olaizola. Femtosecond laser fabrication of highly hydrophobic stainless steel surface with hierarchical structures fabricated by combining ordered microstructures and LIPSS. Applied Surface Science. Volume 374, June 2016, pp. 81-89.

[26] S.Razi, K.Madanipour, M. Mollabashi. Laser surface texturing of 316L stainless steel in air and water: A method for increasing hydrophilicity via direct creation of microstructures. Optics & Laser Technology Volume 80, June 2016, pp. 237-246.

[27] Y.Cai, W.Chang, X.Luo, A.M.L.Sousa, K.H.A. Lau, Y.Qin. Superhydrophobic structures on 316L stainless steel surfaces machined by nanosecond pulsed laser. Precision Engineering. Volume 52, April 2018, pp. 266-275.

[28] Z.Liu, T.Niu, Y.Lei, Y.Luo. Metal surface wettability modification by nanosecond laser surface texturing: A review. Biosurface and Biotribology. Volume8, Issue2. June 2022. pp. 95-120.

[29] Y.Wan, X.Wang, C.Zhang, J. Xu. Durable self-cleaning hydrophobic surface of hollow cylindrical stainless steel with controllable adhesion prepared by nanosecond laser. Vacuum. Volume 205, November 2022, 111422.

[30] L.Zhang, N.Lin, J.Zou, X.Lin, Z.Liu, S.Yuan, Y.Yu, Z.Wang, Q.Zeng, W.Chen, L.Tian, L.Qin, R.Xie, B.Li, Z.Wang, B.Tang, Y.Wu. Super-hydrophobicity and corrosion resistance of laser

surface textured AISI 304 stainless steel decorated with Hexadecyltrimethoxysilane (HDTMS). Optics & Laser Technology. Volume 127, July 2020, 106146.

[31] Y.Lu, Y.Guan, Y.Li, L.Yang, M.Wang, Y.Wang. Nanosecond laser fabrication of superhydrophobic surface on 316L stainless steel and corrosion protection application.Colloids and Surfaces A: Physicochemical and Engineering Aspects. Volume 604, November 2020, 125259.

[32] C.-L. Chang, M.-T.Hsu, H.-K. Lin, K. Chuang, J. Huang. Effects of metal film coatings on surface properties of laser-textured stainless steel. Surface and Coatings Technology. Volume 461, May 2023, 129446.

[33] A.Peter, A.H.A. Lutey, S.Faas, L.Romoli, V.Onuseit, T.Graf. Direct laser interference patterning of stainless steel by ultrashort pulses for antibacterial surfaces. Optics & Laser Technology. Volume 123, March 2020, 105954.

[34] A.Pendurthi, S.Movafaghi, W.Wang, S.Shadman, A.P Yalin , A.K Kota. Fabrication of Nanostructured Omniphobic and Superomniphobic Surfaces with Inexpensive CO2 Laser Engraver. ACS Applied Materials & Interfaces. July 2017. 9(31).

[35] W.Ma, M.Zhao, J.Zhao, Z.Guo, Y.Cui, H.Li. Preparation of superamphiphobic stainless steel surface by laser and perfluorooctanoic acid treatment. Optics & Laser Technology. Volume 154, October 2022, 108321.

[36] U.Trdan, M.Hočevar, P.Gregorčič. Transition from superhydrophilic to superhydrophobic state of laser textured stainless steel surface and its effect on corrosion resistance. Corrosion Science. Volume 123, July 2017, pp 21-26.

[37] P.Gregorčič, B.Šetina Batič, M.Hočevar. Controlling the stainless steel surface wettability by nanosecond direct laser texturing at high fluences. Applied Physics A, Volume 123, Issue 12, article id.766, 2017. pp. 8.

Investigation of laser texturing on the surface of anodized aluminium

Ļubova Denisova
Faculty of Engineering
Rezekne Academy of Technologies
Rezekne, Latvia
ld15036@edu.rta.lv

Antons Pacejs
Faculty of Engineering
Rezekne Academy of Technologies
Rezekne, Latvia
antons.pacejs@rta.lv

Emil Yankov
Faculty of Engineering
Rezekne Academy of Technologies
Rezekne, Latvia
emil.yankov@rta.lv

Lyubomir Lazov
Faculty of Engineering
Rezekne Academy of Technologies
Rezekne, Latvia
lyubomir.lazov@rta.lv

Abstract. **This study examines the texturing of anodized aluminium using a Rofin PowerLine F 20 Varia nanosecond Yb doped fiber laser. It explores how varying laser parameters like scanning speed, hatching step, laser power, and frequency impact the surface's wetting properties, particularly the contact angle with a water droplet. The research aims to understand the influence of these parameters on the aluminium's surface, offering insights into the laser micromachining process and its industrial and material science applications. This study examines the texturing of anodized aluminium using a Rofin PowerLine F 20 Varia nanosecond Yb doped fiber laser. It explores how varying laser parameters like scanning speed, hatching step, laser power, and frequency impact the surface's wetting properties, particularly the contact angle with a water droplet. The research aims to understand the influence of these parameters on the aluminium's surface, offering insights into the laser micromachining process and its industrial and material science applications.**

This study investigates the texturing of anodized aluminium using a Rofin PowerLine F20 Varia nanosecond fiber laser. It investigates how different laser parameters such as scan speed, hatching step, laser power and frequency affect the surface wetting properties, especially the contact angle of a water droplet. The research aims to understand the influence of these parameters on the aluminium surface, offering insights into the laser micromachining process and its applications in industry and materials science.

Keywords: nanosecond laser, laser texturing, fiber laser, roughness, wettability.

I. INTRODUCTION

Aluminium stands out as the most abundant metal in the earth's crust, and he are one of the most widely used metal structural materials. Anodized aluminium exceptional chemical, electrical, thermal, and mechanical properties make it indispensable across numerous industries, ranging from aerospace to consumer electronics. Through anodising aluminium can develop a transparent coating with hardness akin to sapphire, contingent upon the coating thickness and anodising procedure employed. In recent years, the exploration of surface treatment techniques has garnered significant attention to further enhance aluminium performance characteristics. Additionally, it examines the role of laser marking as a complementary method for achieving precise surface modifications [1] - [4].

The strengths of various laser marking techniques, and their suitability for industrial use, have been amply analysed and reported by many researchers over the years. The vast expertise accumulated to-date makes it possible to understand the influence of various material properties and processing parameters on the quality [5].

In general, laser marking involves the targeted removal or melting of material from a surface using a high-powered, focused laser beam, resulting in localized heating and various modifications to the material, such as melting, vaporization, decomposition, or chemical alteration [6].

Laser technology offers an efficient approach for creating micro/nano structures directly onto various materials while ensuring precise control over their size.

Researchers are actively investigating hydrophobic metal structures crafted using nanosecond laser techniques. Laser machining at micro and nano scales enables the fabrication of surfaces with robust hydrophobic or hydrophilic features, presenting promising applications across environmental, medical, agricultural. Recent focus has been on surface wettability, particularly super-hydrophilic and super-hydrophobic characteristics. The terms hydrophilic and hydrophobic have been extensively used in literature to describe water behaviour on solid surfaces, typically measured through water droplet contact angles (CA). Surface roughness and energy significantly influence wettability, with roughness being a primary determinant. According to the Cassie-Baxter model, incomplete wetting on rough surfaces is attributed to entrapped air pockets, resulting in higher contact angles compared to smoother surfaces. Surfaces are categorized as hydrophilic, when the CA is less than 90 and hydrophobic, when the CA is greater than 90°. Superhydrophobic surface is when the CA is greater than 150° [7] - [12].

Numerous studies revealed that laser-textured surfaces are usually hydrophilic shortly after laser treatment, then turn superhydrophobic after storage in an ambient atmosphere [13].

Prior to implementing the laser method for various industrial products, it is crucial to optimize the technological procedures. This involves performing a combination of numerical simulations and practical experiments to pinpoint the optimal operational parameters for laser marking [14].

The main objective of this study is to investigate the laser marking techniques on the aluminium anode surface, in particular delving into the effects of various parameters on the surface structure and hydrophilicity. By fine-tuning the laser processing parameters, we can generate different micro/nano structures, thus influencing the hydrophilic properties of the surface.

II. MATERIALS AND METHODS

2.1 Material

Anodized aluminum is a material that has undergone an anodizing process in which the aluminum surface is covered with an oxide layer, increasing its resistance to corrosion and improving other physical and chemical characteristics. Anodized aluminum is widely used in various industries and elsewhere where high resistance to corrosion and mechanical wear is required.

In the experimental investigation used anodized aluminum plates measuring 50 mm x 50 mm x 1.1 mm. To ensure the integrity of our results, surface samples underwent a thorough cleaning process with $C_5H_{12}O$ to eliminate any contaminants that could impact the experimental outcomes.

2.2 Experimental set-up

For the marking of the anodized aluminium samples are used the nanosecond Fiber laser Rofin PowerLine F 20 Varia, see in Fig. 1.

A fiber laser was equipped with an f-theta lens having a focal length of 184 mm, which yielded a spot size of 40 µm at the focal point. The technical specifications of the Rofin PowerLine F20 laser system are presented in Table 1.

Fig. 1. Fiber laser Rofin PowerLine F20 [15].

A fiber laser was equipped with an f-theta lens having a focal length of 184 mm, which yielded a spot size of 40 µm at the focal point. The technical specifications of the Rofin PowerLine F20 laser system are presented in Table 1.

TABLE 1. LASER SYSTEM ROFIN POWERLINE F 20 TEHNICAL SPECIFICATIONS

Laser type	Fiber laser
Wavelength	1064 nm
Power	0…19.7 W
Pulse duration	4, 8, 14, 20, 30, 50, 100, 200 ns
Pulse repetition frequency	2…1000 kHz
Scan speed	1…20000 mm/s
Line step	0,001…120 mm
Focus shift	-10…10 mm
Beam quality	<1,5 M^2

With the assistance of a digital microscope, the layer of deionized water applied by a dispenser onto the processed square of anodized aluminium sample was measured. The digital microscope is shown in Fig 2.

Fig. 2. Microscope Dino-Lite AM7115MZT EDGE [16].

The technical parameters of the digital microscope are presented in Table 2.

TABLE 2. TEHNICAL SPECIFICATION OF DINO-LITE EDGE AM7115MZT

Light/ LED type	White
Number of LEDs	8
Resolution	5 mega pixels (2592x1944)
Magnification	10-220x
Dimensions	10.5cm (height) x 3.2cm (diameters)
Operating system	Windows

Before measuring the contact angle, the samples of anodized aluminium were cleaned with C5H7OH, to remove all dirt.

Using a microscope Dino Capture 2.0 software and pulling down a tangent line between the sides of the drop, similar to what was indicated above in Fig. 4 was measured wettability angle. The controlled dose of the drop is 10 μl, which is administered manually, according to standard D7334-08.

Schematic view of experimental set-up could be observed in Fig.3.
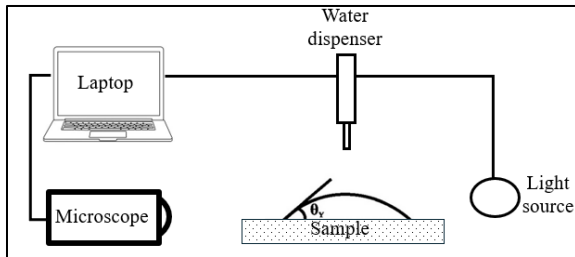
Fig. 3. Schematic view of experimental set-up of wettability measurement.

Example of made wettability measurements could be observed in Fig. 4.
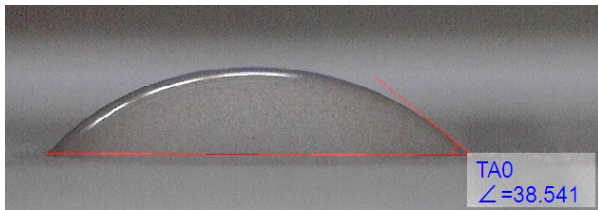
Fig. 4. Anodized aluminium with laser measurement of market surface wetting, where the contact angle of the water drop is 38,5°.

2.3 Methodology

The experiment was done in laser technologies research center.

The experiment began with the use of the Visual Laser Marker software to generate a matrix with 6 columns and 6 rows. Subsequently, the software was configured to set laser parameters accordingly. Following this setup, the matrix was then marked onto an anodized aluminium plate. As a result, two matrices were created, each featuring different laser processing parameters.

In the first matrix, the constant parameters were the average power (P), frequency (v), pulse duration (τ) and different - scanning speed (v) and raster step (Δx). In the second matrix, the constant parameters were the raster step (Δx), scanning speed (v), pulse duration (τ) and different - average power (P) and frequency (v).

The matrix parameters are presented in Table 3.

TABLE 3. LASER MARKING PARAMETERS FOR ANODIZED ALUMINIUM SAMPLE

Matrix	1	2
Power	3.2 W	0.1 - 2.5 W
Frequency	20 kHz	2 – 25 kHz
Pulse duration	14 ns	8 ns
Scanning speed	25–150 mm/s	100 mm/s
Raster step	5 -30 μm	10 μm

General view of an exemplary experimental first matrix given in Fig. 5.
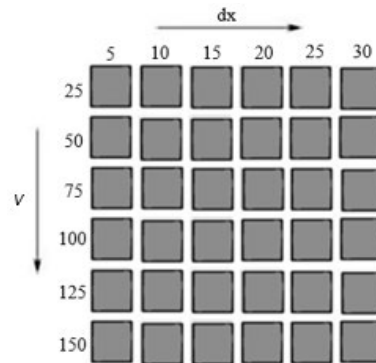
Fig. 5. General view of an exemplary experimental first matrix used in the researches.

General view of an exemplary experimental second matrix given in Fig. 6.
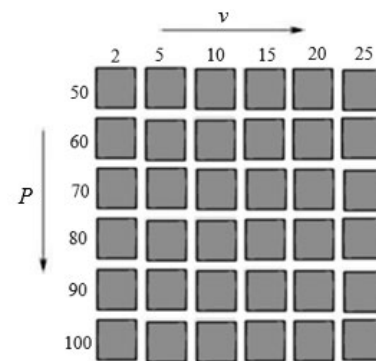
Fig. 6. General view of an exemplary experimental second matrix used in the researches.

The average power of the Rofin Powerline Varia F20 laser varies depending on the frequency and pulse length used in the treatment process. This is confirmed by both the laser system manual and measurements made with the OPHIR F150A-BB-26 power measurement sensor.

Fig. 7 show how the average laser power changes with different frequencies and pulse widths at different power factors (%) entered in the laser system software with an 8 ns pulse duration [17].
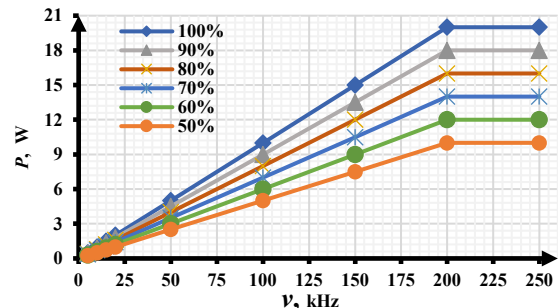
Fig. 7. Average power dependence of impulse width and frequency at different laser system software power factors [17].

Pulse overlap (k_{ov}) is parameter in laser processing, which determines the pulse overlap in percent within single laser scanning path. It can be calculated by using formula (1).

$$k_{ov} = \left(1 - \frac{v}{v \times d} \right) \times 100 \ \% \qquad (1)$$

where: v – scanning speed (mm/s),

v – laser frequency (kHz),

d – laser point diameter (mm).

Line overlap (k_{soc}) is parameter in laser processing, which determines the line overlap in percent within a single laser scanning path. It can be calculated by using formula (2).

$$k_{soc} = \left(1 - \frac{\Delta x}{d}\right) \times 100\ \%$$ (2)

where: Δx – distance between scanning lines (mm),

d – laser point diameter (mm).

Laser point diameter for aluminium is 0,04 mm.

III. RESULTS AND DISCUSSION

How different parameters affect the hydrophobicity and hydrophilicity of marked anodised aluminium is shown in Fig. 8 to Fig. 15.
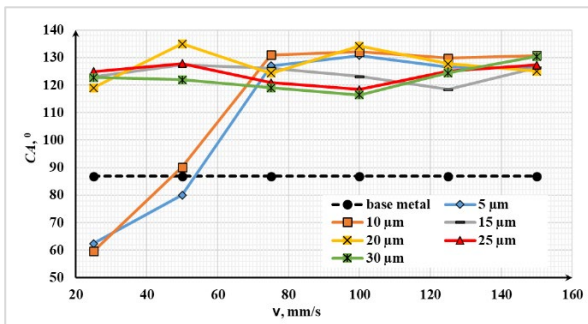
Fig. 8. Contact angle dependence on the scanning speed.

Analysing the graph in Fig. 8, can see that a hydrophilic surface can be obtained with a scanning speed of 25 mm/s and raster step of 5 µm, 10 µm, as well as with a scanning speed of 50 mm/s and a raster step of 5 µm, because the contact angle is less than 90 degrees.

With for the others scanning speed and raster step, hydrophobic surfaces can be obtained, because the contact angle of water is greater than 90 degrees.

In the first matrix an untreated anodized aluminium surface is hydrophilic. When marking anodized aluminium with scanning speed 50 mm/s and raster step 10 µm, the surface structure changes from hydrophilic to hydrophobic.

By changing the laser scanning speed and raster step, a superhydrophobic surface cannot be obtained.

The largest contact angle 135 degrees, formed with scanning speed 150 mm/s and raster step 20 µm.
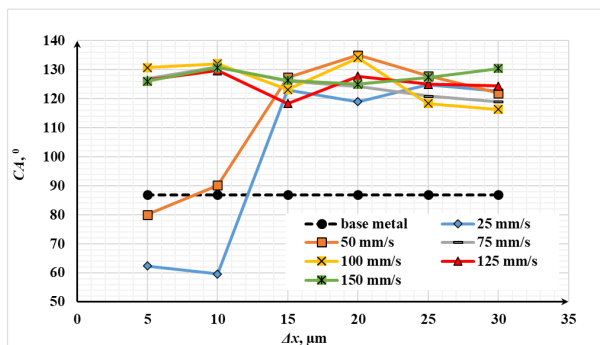
Fig. 9. Contact angle dependence on the raster step.

From Fig. 9 can see, the contact angle decreases with increasing scanning speed for all raster step values. This suggests that higher scanning speeds lead to a more wetted surface. The effect of scanning speed is more pronounced at smaller raster steps. This means that the difference in contact angle between different scanning speeds is larger at smaller raster steps.

There is a general trend of decreasing contact angle with increasing raster step for all scanning speeds. This suggests that larger raster steps lead to a more wetted surface.

Increasing the raster step, the contact angle is increased, and the line overlap (k_{soc}) is reduced, because the distance between the scanning points affects the laser deflection and the line arrangement on the surface of the material.

The smallest contact angle 60 degrees, formed with raster step 10 µm scanning speed 25 mm/s.

In the first matrix, the line overlap increases as the raster step increases, which means the lines are projected wider, and as a result, the overlap between them is reduced.
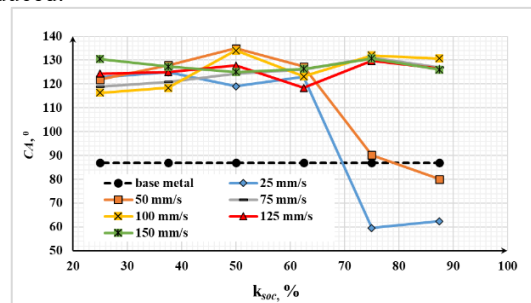
Fig. 10. Contact angle dependence on line overlap and scanning speed.

Fig. 10 show, the increasing the line overlap coefficient, the surface changes from hydrophobic to hydrophilic. At high scanning speed from 75 mm/s to 125 mm/s, the line overlap ratio indicates little change in hydrophobicity.

The smallest contact angle is 62 degrees, formed with a scanning speed of 25 mm/s and a line overlap coefficient of 75 percent.
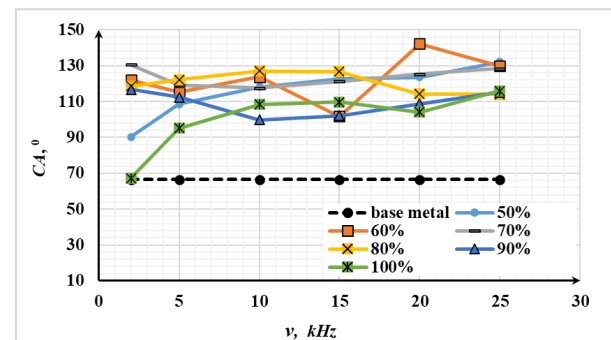
Fig. 11. Contact angle dependence on the frequency.

Based on the graph data in Fig. 11, it is evident that the formation of a hydrophobic surface on the second matrix occurs at all laser power setting and frequency, but only with laser power 100% and 2 kHz frequency are hydrophilic surface.

At the frequency from 2 to 25 kHz and laser power 50%, the water contact angle increases, but using others

laser powers the contact angle both increases and decreases as the frequency changes.

The largest contact angle 142 degrees, formed with frequency 20 kHz and laser power 60%.
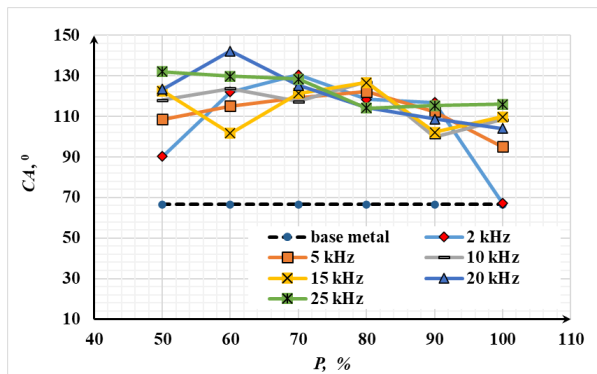
Fig. 12. Contact angle dependence on the average power.

From the analysis of the experimental wettability in Fig. 12, it can be observed that:

- The smallest contact angle 67 degree is formed with a power 100% and frequency 2 kHz.
- The untreated anode aluminium sample used in the experiment in the second matrix also forms a hydrophilic surface.
- Increasing the laser power from 50% to 80% and using frequency 5 kHz, the contact angle increases because each laser pulse has a longer duration on the surface, which leads to a deeper treatment of the material. This in turn can lead to deeper changes in surface structure and properties that can affect the contact angle.

Increasing the laser power and using hight frequency 25 kHz, the contact angle decreases, because a higher frequency means more laser pulses are being applied per unit time. This can result in more frequent interactions between the laser beam and the material's surface.

In the second matrix, the overlap of pulses (k_{ov}) increases as the frequency increases, which means that several pulses are sent to the surface close to each other.
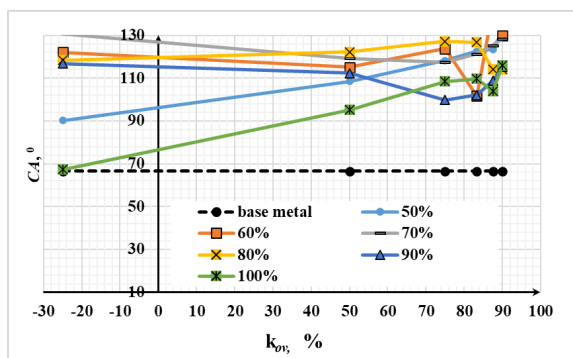
Fig. 13. Contact angle dependence on pulse overlap and power.

The increasing pulse overlap coefficient increases the contact angle, as can be seen in Fig. 13.

Hydrophobicity and hydrophilicity also can be influenced by roughness marking. Roughness can be different parameter:

- R_a - average roughness indicating the surface's average irregularity.

- R_q - root mean square providing information about the overall surface roughness, including all variations in the surface profile.
- R_z - maximum surface texture indicating the largest difference between the highest and lowest points in the surface profile.
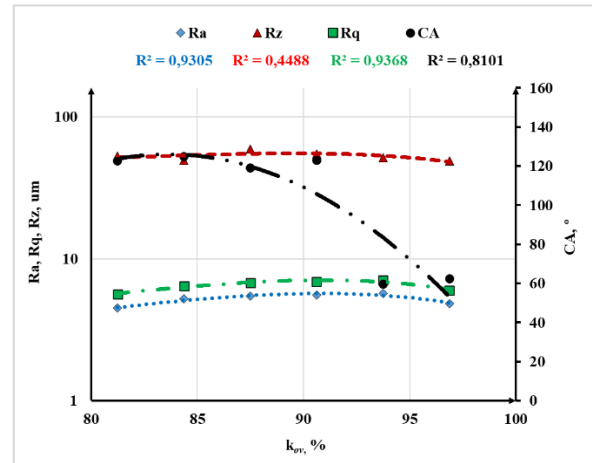
Fig. 14. Contact angle dependence on roughness for the first matrix on scanning speed 25 mm/s.

Wettability analyses trendline show that the contact angle generally increases with increasing roughness. Analyzing the Fig. 14 can see that hydrophobic surfaces repel water and cause larger contact angles, while hydrophilic surfaces attract water and cause smaller contact angles. Less roughness creates a hydrophilic character because they repel water better than a rough surface.
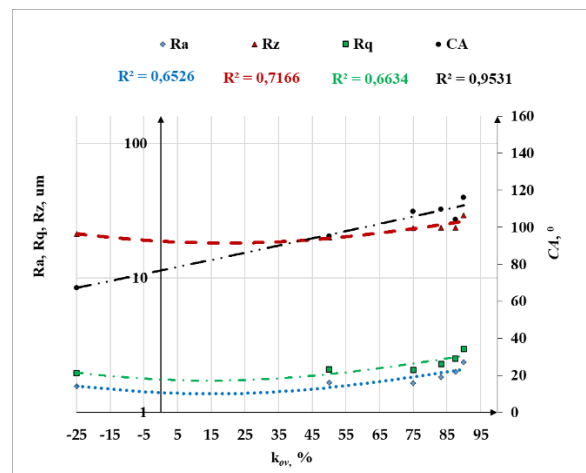
Fig. 15. Contact angle dependence on roughness for the second matrix on laser power 100 %.

Analysing the second matrix for the change in wettability from pulse overlap shows that there is a "-" sign at the beginning of the pulse overlap because the laser pulses are sent to the material with a long enough delay between them that they do not occur in an overlapping state. This situation arises because a low laser frequency of 2 kHz has been chosen.

When the pulse overlap is with the "-" sign, which means the laser pulses are not overlapped, it creates smooth surface with minimal roughness of 1.56 nm, which can be seen on the Fig. 15, and its formation a hydrophilic surface which promoting the spread of

liquids across the surface. This results in a surface forms a small contact angle - 67 degrees.

Anodized aluminium samples surface wettability is changes over time, which can be seen on the Fig. 16.
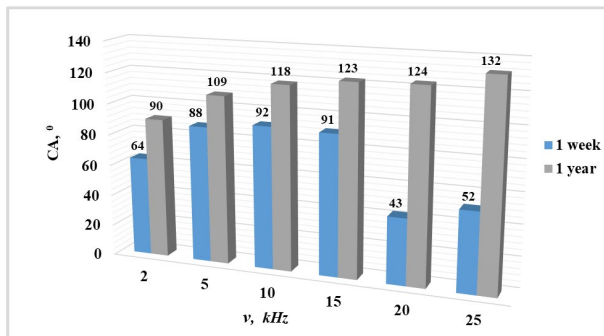
Fig. 16. Contact angle dependence on over time at laser power 50 %.

Studying the graph show it can be observed that the wettability of the anodized aluminium surface increases over time. Due to oxidation, carbon, oxygen content absorption from ambient environment [13].

The surfaces with higher average surface roughness exhibit significantly lower contact angles immediately after laser treatment compared to those with smoother surfaces. Furthermore, over time, the contact angles on surfaces with higher roughness increase at a faster rate than those with lower roughness.

IV. CONCLUSIONS

The analysis of various parameters' effects on the hydrophobicity and hydrophilicity of marked anodized aluminium reveals several significant trends.

- Specific combinations of scanning speed and raster step yield hydrophilic surfaces, characterized by contact angles less than 90 degrees. Conversely, other combinations produce hydrophobic surfaces, exhibiting contact angles greater than 90 degrees. Notably, altering these parameters can induce a transition from hydrophilic to hydrophobic surface characteristics.
- The water contact angle increases with increasing frequency, using laser power 50%, suggesting possible material-specific interactions. Change laser power and frequency the formation of a hydrophilic surface occurs exclusively at specific laser power and frequency setting.
- Higher pulse overlap leads to decreased contact angles, indicating a more uniform energy distribution and greater cumulative heating effects. In addition, the lack of pulse overlap, and high laser power create a hydrophilic surface due to minimal surface roughness.
- Roughness parameters Ra, Rq, and Rz significantly impact wetting behaviour, with lower roughness generally associated with hydrophilic and small contact angles.
- The wettability of the anodized aluminium surface gradually increases over time, transitioning from initially hydrophilic to eventually hydrophobic behaviour.

In conclusion, the manipulation of laser processing parameters allows for precise control over surface characteristics, impacting the wetting behaviour of marked aluminium surfaces. The formation of hydrophobic or hydrophilic surfaces is dependent on a combination of factors, including scanning speed, raster step, laser power, frequency, pulse overlap, and surface roughness.

Understanding these relationships enables tailored surface engineering for desired wetting properties.

Hydrophobic and hydrophilic surfaces are essential to many industries, where they are used to improve product performance, durability, and safety, and to promote innovation and technology development.

REFERENCES

[1] M. Gedvilas, B. Voisiat and G. Račiukaitis, "Grayscale Marking of Anodized Aluminium Plate by Using Picosecond Laser and Galvanometer Scanner", Journal of Laser Micro/Nanoengineering, vol. 9, no. 3, p. 267-270, November 2014. [Abstract]. Available: ProQuest http://dx.doi.org/10.2961/jlmn.2014.03.0017 [Accessed February 5, 2024].

[2] AAC, "What is Anodizing?". [Online]. Available: https://www.anodizing.org/page/what-is-anodizing. [Accessed: February 5, 2024].

[3] J. Penide, F. Quintero, A. Riveiro, A. Fernandez, J.del Val, R. Comesana, F. Lusquinos and J. Pou, "High contrast laser marking of alumina", Applied Surface Science, vol. 336, p. 118-128, May 2015. [Abstract]. Available: ProQuest https://doi.org/10.1016/j.apsusc.2014.10.004 [Accessed February 5, 2024].

[4] D. Zhemchuzhnikova, J. Zollinger, "Microstructure formation in 6061 aluminum alloy during nano-second pulsed laser processing', Journal of Materials Processing Technology, vol. 314, May 2023. [Abstract]. Available: ProQuest https://doi.org/10.1016/j.jmatprotec.2023.117898 [Accessed February 15, 2024].

[5] X. S. Li, W. P. He, L. Lei, J. Wang, G. F. Guo, T. Y. Zhang, T. Yue, "Laser direct marking applied to rasterizing miniature Data Matrix Code on aluminum alloy", Optics Laser Technology, vol. 77, p. 31-39, March 2016. [Abstract]. Available: ProQuest https://doi.org/10.1016/j.optlastec.2015.08.020 [Accessed February 15, 2024].

[6] D. Austin, L. Beagle, C. Muratore and N. R. Glavin, "Laser processing of nanomaterials: From controlling chemistry to manipulating structure at the atomic scale", Hybrid Atomic-Scale Interface Design for Materials Functionality, p. 179-208, January 2021. [Abstract]. Available: ProQuest https://doi.org/10.1016/B978-0-12-819117-0.00008-5 [Accessed February 20, 2024].

[7] J. Guo, X. Ma, Xiaolei, X. Si, Z. Yang, "Effect of Nanosecond Laser Treatment Parameters on Surface Wettability Behaviour of Pure Aluminium", IOP Conference Series: Materials Science and Engineering, p. 538, June 2019. [Abstract]. Available: ProQuest https://iopscience.iop.org/article/10.1088/1757-899X/538/1/012021/pdf [Accessed February 22, 2024].

[8] J. T. Cardoso, A. I. Aguilar-Morales, S. Alamri, D. Huerta-Murillo, F. Cordovilla, A. F. Lasagni, J. L. Ocana, "Superhydrophobicity on hierarchical periodic surface structures fabricated via direct laser writing and direct laser interference patterning on an aluminium alloy", Optics and Lasers in Engineering, vol. 111, p. 193-200, December 2018, [Abstract]. Available: ProQuest https://doi.org/10.1016/j.optlaseng.2018.08.005 [Accessed February 22, 2024].

[9] J. Zhao, J. Guo, P. Shrotriya, Y. Wang, Y. Han, Y. Dong, S. Yang, "A rapid one-step nanosecond laser process for fabrication of super-hydrophilic aluminum surface", Optics Laser Technology, vol. 117, p. 134-141, September 2019. [Abstract]. Available: ProQuest https://doi.org/10.1016/j.optlastec.2019.04.015 [Accessed February 22, 2024].

[10] Y. Cai, W. Chang, X. Luo, A. M. L. Sausa, K. H. A. Lau, Y. Qin, "Superhydrophobic structures on 316L stainless steel surfaces machined by nanosecond pulsed laser", Precision Engineering, vol. 52, p. 266-275, April 2018. [Abstract]. Available: ProQuest https://doi.org/10.1016/j.precisioneng.2018.01.004 [Accessed February 23, 2024].

[11] A. Pacejs, E. Yankov, I. Adijans., E. Terumnieks, L. Lazov, "Modification of Aluminum 1050 and 2219 Alloys Using CuBr Nanosecond Laser for Hydrophobic and Hydrophilic Properties", Engineering Proceedings, vol. 56(1), p. 326, December 2023. [Abstract]. Available: ProQuest https://doi.org/10.3390/ASEC2023-16582 [Accessed February 23, 2024].

[12] J. Drelich, E. Chibowski, D. D. Meng, K. Terpilowski, "Hydrophilic and superhydrophilic surfaces and materials", Soft Matter, Issue 21, 2011. [Abstract]. Available: ProQuest https://doi.org/10.1039/C1SM 05849E [Accessed February 24, 2024].

[13] A. O. Ijaola, E. A. Bamidele, C. J. Akisin , I. T. Bello , A. T. Oyatobo, A. Abdulkareem, P. K. Farayibi, E. Asmatulu, "Wettability Transition for Laser Textured Surfaces: A Comprehensive. Surfaces and Interfaces", vol. 21, December 2020. [Abstract]. Available: ProQuest https://doi.org/10.1016/j.surfin.2020.100802 [Accessed February 24, 2024].

[14] L. Lazov, E. Teirumnieks, T. Karadzhov, N. Angelov, "Influence of power density and frequency of the process of laser marking of steel products", Infrared Physics Technology, vol. 116, August 2021. [Abstract]. Available: ProQuest https://doi.org/10.1016/j.infrared.2021.103783 [Accessed February 25, 2024].

[15] Indimart.com, "Powerline". [Online]. Available: https://m.indiamart.com/proddetail/powerline-3593583130.html [Accessed: February 25, 2024].

[16] Dino-Lite Europe, "AM7115MZT" https://www.dino-lite.eu/en/products/microscopes/universal/am7115mzt-edge [Accessed: February 25, 2024].

[17] L. Denisova, A. Pacejs, E. Yankov, L. Lazov, "Analysing the influence of technological parameters on the process of laser marking of surface of anodised aluminium samples", 2023, Proceedings of the 14th International Scientific and Practical Conference, vol. 3, p. 289-296.

Investigation Of Laser Marking On Chromium-Nickel Samples

Nikolay Todorov Dolchinkov
Vasil Levski National Military University, Veliko Tarnovo, Bulgaria
Veliko Tarnovo, Bulgaria
n_dolchinkov@abv.bg

Milen Krasimirov Tortorikov
Vasil Levski National Military University, Veliko Tarnovo, Bulgaria
Veliko Tarnovo, Bulgaria
milen_tortorikov@abv.bg

Abstract. **In the present century, laser marking on various materials is increasingly used. Very good results are achieved when working on resistant materials and as in our experiment with chrome-nickel samples.**
Chrome-nickel is used in the production of a number of details and products, especially in the military-industrial complex. Experiments were performed on thin chromium-nickel samples and the variation of marking quality with variation of laser speed and power and material roughness was investigated. The results obtained have been analysed and this will enable both the use of the obtained results and the continuation of research. These studies were carried out at the Laser Centre of the Rezekne Academy of Technology during an Erasmus internship.

Keywords: chrome-nickel, laser, marking, power, roughness, speed.

I. INTRODUCTION

Joint research in the field of laser technologies between the Rezekne Academy of Technology, as a leading partner, and the National Military University "Vasyl Levski" has been starting since 2018. The partnership between educational institutions is even older, with the first cooperation framework agreements and Erasmus contracts being signed more than 10 years ago [1], [2], [3]. There is a regular exchange of students and teachers between the two educational institutions and joint research projects are developed and research is mainly in the field of laser technology.

Teachers, cadets and students from the military educational institution from Bulgaria have also repeatedly visited the Latvian university. Under the guidance of Prof. Lazov, cadets and students from the National University of Applied Sciences carried out research and data processing from the creation of experimental and theoretical studies of different types of materials at the laser centre in Rezekne.

Marking is an essential part of the production cycle that provides the necessary information about the product and serves as a marketing tool to attract the attention of the consumer to the specified product. Despite the fact that different markings are applied to the types of products, permanent markings that do not lose their qualities over time and are difficult to manipulate are optional [4], [5], [6]. A variety of techniques can be used to create a permanent mark, including etching, electrochemical etching, engraving, dot etching, and laser marking. In the dynamic wide stage of our development, laser marking is widely used in various sections of the production line for a variety of applications to create high-quality permanent prints. The laser marking method is effective, non-contact and applies to both metallic and non-metallic surfaces, and it is also applicable to non-traditional materials. In addition, it requires no additional additives or solvents and produces no waste; thus, it is sustainable for the environment and does not pollute it [1], [7], [8].

II. MATERIALS AND METHODS

Setting and parameters of the laser procedure Stainless steel contains chromium in its composition, which provides chemical stability and high heat resistance of the alloy and makes it suitable for use in the laser process. In this study, 2 mm thick chromium-nickel steel plates with initial roughness $Rz = 8.42$ μm, reflectivity R ($\lambda=1.06$ μm) = 0.75, thermal diffusivity a = 3×10^{-6} are used. m2/s, thermal conductivity k = 37 W/mK, melting point = 1800 °C and boiling point = 3145 °C. At the initial stage, the surfaces were cleaned with acetone to avoid any contamination or stains. A nanosecond pulse ytterbium fibber laser supplied by IPG Photonics Corporation

$<\tau<200$ ns at a repetition rate of 1.6 was selected as the source of laser radiation with a wavelength of $1055<\lambda<1075$ nm generating pulses of 4 seconds duration $<f<1000$ kHz. The configuration of the laser processing system developed for scribing and marking purposes is presented in Fig. 1 and consists of 1) IPG Photonics nanosecond fibber laser, 2) fibber optic transfer, 3) SCANLAB scanning system, 4) 100 mm objective, 5) Neff-Wiesel linear drive for vertical movement, 6) XY coordinate stage, 7) Koll morgen ACD servo drives [9].
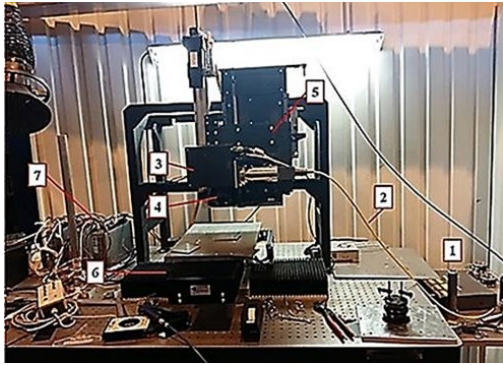
Fig. 1: The configuration of the laser processing system

A fibber pulsed ytterbium laser was emitted and fed into a collimating system via an optical fibber to form a parallel beam output. A dual-axis galvanometer scanning system (hurry SCAN II 14 digital scanning head from SCANLAB corp.) was installed to move along the X and Y axes. A focusing lens with a focal distance 100 mm [10], [11], [12]. Additional horizontal movements and vertical movements can be performed using a multi-axis linear motor coordinate stage, which allows the extension of the working space to 250×250 mm. Laser radiation parameters and scan speed can be changed using the developed lab VIEW code. Also, all vertical and horizontal movements can be controlled by the same code.

Product coatings and markings must withstand various environmental conditions and must not change during the period of use of the product [1], [9]. In this study, environmental testing was performed in a chamber based on several different operating conditions. For more complete results, the experiments are conducted under temperature and humidity conditions that are rarely obtained in real conditions, such as a combination of extremely low or high temperatures (-40, -20, 40, 100 °C) with high humidity (70 %, 90%). In this way, the stability of the samples under normal conditions is guaranteed for an extended period. At the same time, this compensates for the short duration of the test exposure (24 hours) compared to the actual operating time. The first test was conducted under ambient conditions with a temperature of -20 °C and a humidity of 70%. The result shows no change in colors or materials after 24 hours in the environmental test chamber. Optical microscope analyses did not reveal any damage or defects in the oxide layers.

III. Results and Discussion

The process of colour laser marking on chrome-nickel steel involves successive melting and hardening of the material, resulting in oxidation and intruding of the surface of the material. The final surface and oxide film formation is the result of repeated pulsed laser operation,

which varies depending on the heat of the laser and the overlap value of the laser pulses [13]. The result of the relief and colour of the surface is affected by almost all parameters of the laser source. In this study, the dependence of the micro hardness of a series of samples on scan speed, laser power, pulse duration, and laser pulse frequency is investigated. The study of the dependence of the obtained colour on the relief of the surface is not the purpose of this study, the purpose of the study was to obtain a qualitative and stable marking on chrome-nickel steel [4], [13].

Due to the impossibility of presenting the entire study due to its large volume, we will emphasize some basic data and graphs that were obtained after measuring the obtained results and analysing them.
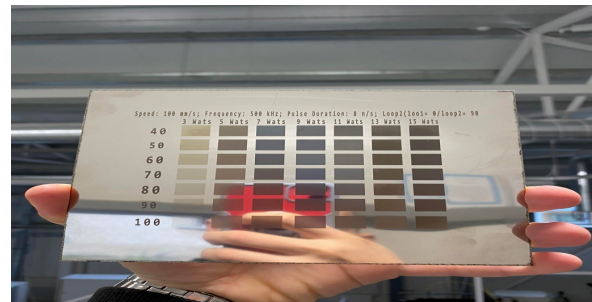
Fig. 2. Sample 1 study matrix

In fig. 2 shows the results obtained for measuring the microhardness of the surface of sample #1. Measurements were made at a constant speed of 100 m/s. of the laser beam and at a laser radiation frequency of 500 kHz. During the measurement, a matrix of 7x7 fields was made, with the variables being the laser power and the marking step. The results of the conducted research are shown in table 1.

TABLE 1 MEASUREMENT OF MICROHARDNESS OF CHROMIUM-NICKEL STEEL, SPECIMEN 1

Speed: 100m/s ; Frequency: 500 kHz; Pulse duration: 8n/s; Loop1-90° Loop2 0°							
Power ,W	3	5	7	9	11	13	15
40	173,5	182,2	187,4	193,2	188,5	204,8	205,6
50	170	182,4	186,7	190,5	194,7	212,5	223,5
60	171,9	173,9	182,7	174,8	186,7	209,9	214,1
70	167,5	184,9	181,9	195,3	189,1	210,8	227,9
80	170,3	178,9	189,5	185,3	181,9	234,4	248,4
90	172,3	174	187,6	183,7	196,1	223,1	205,5
100	169,7	187,7	185,8	186,2	187,5	194,5	198,3

The obtained results are also shown in graph 3. It can be clearly seen that at low powers (up to 11 Watts) the change is close to linear with increase. After 11 watts, there is a sharp change in the picture and no dependence of the micro hardness on the power or on the step of the laser beam can be determined.
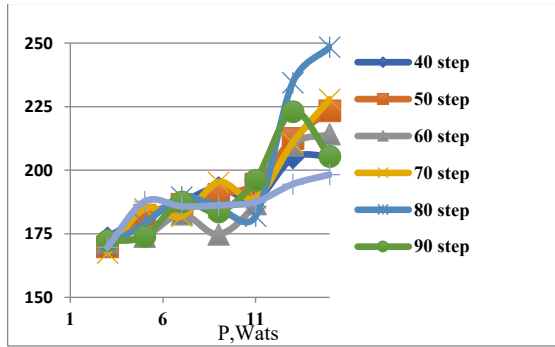
Fig. 3. Dependence of Micro hardness on the power and step of the laser beam for sample 1

Measurements were made on 12 samples, and the results up to 11 watts had a related growth rate, and after 11 watts there was a wear and tear of the indicators and no definite pattern of change could be captured. This means that in order to obtain good indicators of the laser marking of chrome-nickel steel, the laser equipment must work at a low power. The best data was obtained on sample 2 and the graph of the obtained results is shown in fig. 4.
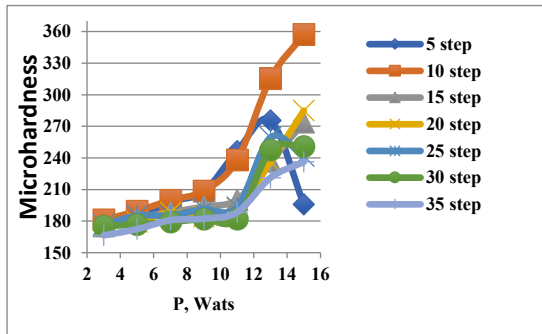
Fig.4 Dependence of the microhardness on the power and step of the laser beam of sample 2

From fig. 4 it is clearly seen that at smaller steps (5, 10) the microhardness is higher and at larger power values it already leaves the zone of linearity of the dependence and there are sharp changes. At larger steps, there is a change in the dependence, as the microhardness increases sharply.
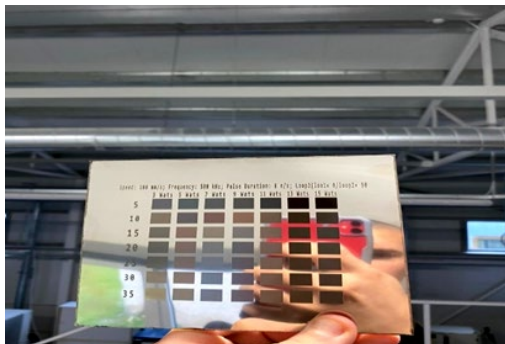
Fig.5. Sample 2

Figure 5 shows the visually obtained results for marking chrome-nickel steel on sample 2, where the best relationships were obtained. Due to the volume of the report, the remaining samples are not presented, but the authors can further analyse the results and present them in a subsequent report.

In parallel with these studies, studies were also made of the achieved marking quality and the micro roughness of the resulting machined surface. Plates of the same chromium-nickel steel samples and the same laser were used, the variables here being speed, power and step of the laser beam. The matrix that was developed and the quality of the images obtained are shown in Fig. 5.
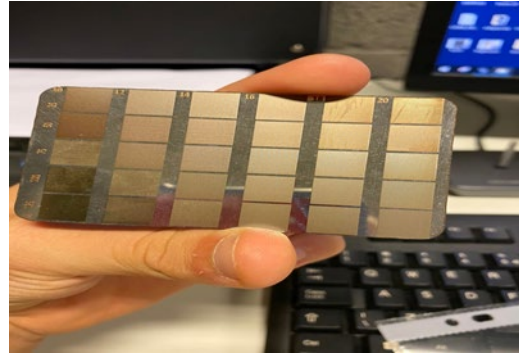
Fig. 6. Plate with a matrix from the quality studies of the roughness of the marking

Accordingly, the obtained results were processed and graphs of the dependences of the 12 measurements made were built. In fig. 7 shows the resulting graph of sample 4.
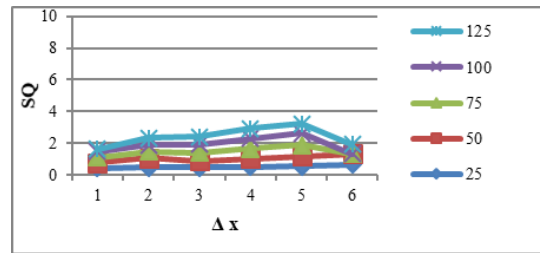
Fig. 7. Graph of the dependence of SQ on the variation of x and the step of the laser beam

What is characteristic of this study is that up to 5 Watts the change is linear and smoothly increasing, and then there is a sharp change and the larger the step, the more SQ decreases. For larger powers, no measurement was made because the results obtained have no practical significance [5], [14], [15], [16].

As the next research that was done was measuring the roughness of the obtained marking depending on the speed of the laser beam and its power. Here too, 12 chrome-nickel steel dies were made and interesting results were obtained. Table 2 shows the obtained numerical values, and fig. 7 the dependence of the roughness on the power and step of the laser beam is plotted.

TABLE 2. DEPENDENCE OF THE ROUGHNESS ON THE POWER AND STEP OF THE LASER BEAM

	P, W	10	12	14	16	18	20
v, mm/s	25	0,389	0,431	0,482	0,535	0,615	0,715
	50	0,307	0,351	0,404	0,461	0,543	0,645
	75	0,231	0,278	0,335	0,395	0,48	0,585
	100	0,161	0,209	0,267	0,328	0,414	0,529
	125	0,101	0,152	0,213	0,277	0,365	0,482
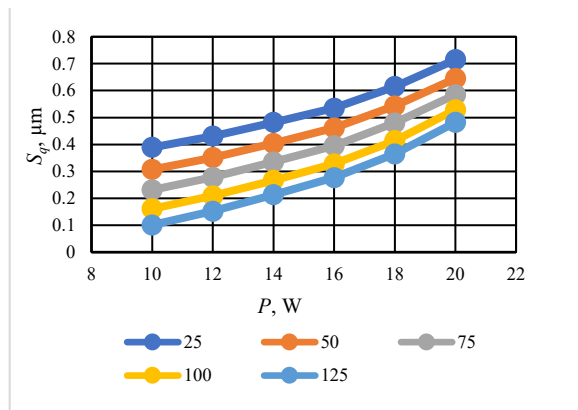
Fig. 8. Graph of the dependence of SQ on the variation of x and the step of the laser beam

From the last 2 measurements, the results of only one sample are shown, due to the limited volume of the report. The results obtained from the comprehensive research, which was carried out within 2 months, are many and could not be presented in such a small volume [7].

IV. CONCLUSIONS

The laser processing system developed for the purpose of this research work is based on a nanosecond ytterbium fibre laser on a multi-axis work piece platform and a vertical movement capability of the laser scanning head. In the preliminary phase, the scanning system was calibrated and the specifications of the laser beam at the focal point were determined. To find the appropriate power density value, the distribution of the laser spot on the surface is measured. The dependence of the resulting colours on laser processing parameters, including scan speed, pulse duration, emission power, and pulse repetition rate, was investigated.

Based on the analysis, 12 blanks were prepared for the three trials, and a suitable matrix was developed for each trial. Each blank from the first study consists of 49 squares with different indicators of power and course of the laser beam and dimensions 8×15 mm. The obtained oxide films were examined using optical microscopy and scanning electron microscope (SEM). The surface topology was established using atomic force microscopy (AFM).

In a similar way, the samples for the second and third experiments were prepared, and here the number of fields was 30. The results confirm that the created samples have appropriate consistency, brightness and cover approximately all spectral regions.

In the joint work of the representatives of the Vasil Levski National Military University and the Rezekne Academy of Technology, the algorithms for working and conducting the research to find the optimal parameters for marking different color spectra on chrome-nickel steel were initially compiled. The research was carried out during a practice at the Academy in Rezekne and the obtained matrices were examined with the equipment available in the laser center. The obtained results contributed to finding the optimal mode for marking on this material and obtaining the best quality surface marking. The results obtained so far will be developed in further experiments.

The obtained results are the basis for further research on the marking of chromium-nickel steel, taking into account the operating conditions of the resulting surface. Based on the obtained results, the most suitable speeds and beam travel were selected to obtain an excellent marking with good indicators on the resulting surface. Marking with a laser beam power higher than 11 Watts was excluded from further research, and depending on the desired result, a corresponding step of the laser beam was also selected.

REFERENCES

[1] N.Dolchinkov, C.Tolev, T. Petrov, E. Dimitrov, G. Petrov, Features of Color Laser Marking on Metals, 14th International Scienfic and Practical conference Environment. Technology. Resources. Vide. Tehnologija. Resursi, 2023, ISSN 1691-5402,3, pp. 297–305

[2] N.Dolchinkov, Marking and Cutting of Non-metallic Products with CO2 Laser, IOP Publishing Ltd. Journal of Physics: Conference Series, Volume 2224, 2021 2nd International Symposium on Automation, Information and Computing (ISAIC 2021) 03/12/2021 - 06/12/2021 Online ISSN: 1742-6596, Print ISSN: 1742-6588, pp 1-8

[3] N.Dolchinkov, Practical research of marking and cutting of textiles with increased resistance, using CO2 laser, Journal of Physics: Conference Series, Volume 1681, 2020, 1681 012014 IOP Publishing The 6th International Conference on Chemical Materials and Process 2-4 July 2020, Warsaw, Poland, doi:10.1088/1742-6596/1681/1/012014 Online ISSN: 1742-6596 Print ISSN: 1742-6588

[4] N.Dolchinkov, Y. Shterev, St. Lilianova, D. Boganova, M. Peneva, L. Linkov, D. Nedialkov, Exploring the possibility of laser cutting with CO2 laser on felt in the range from 1W to 26W power, International scientific journal: Industry 4.0 Issue 1/2019, ISBN 2534-8582, стр. 29-31.

[5] L.Lazov, N.Angelov, The 50th anniversary of laser, Technical University of Gabrovo, Bulgaria, 2010.

[6] S. Sharaf, R. Nofal, E. Sakr, Effects of Co2 Laser Cutting Technique on Bending Properties of Cotton and Cotton Blended Fabrics, International Design Journal, Vol. 14 No. 2, (March 2024) pp 297-312

[7] L.Lazo, H. Deneva, E. Teirumnieka, Study of Auxiliary Gas Pressure on Laser Cutting Technology, Environment. Technology. Resources, Rezekne, Latvia Proceedings of the 11th International Scientific and Practical Conference. Volume III, 159-162

[8] L.Lazov, E. Teirumnieks, Application of laser technology in the army, Proceedings of International Scientific Conference "Defense Technologies", Faculty of Artillery, Air Defense and Communication and Information Systems, Shumen, Bulgaria, 2018

[9] M. Zoghi, A. J. Dehkordi, CW CO2 laser cutting of multiple-layer blended fabric, Optik, Volume 287, 2023, 171168, ISSN 0030-4026, https://doi.org/10.1016/j.ijleo.2023.171168.

[10] Y.Shterev, N. Dolchinkov, St. Lilianova, D. Boganova, M. Peneva, L. Linkov, D. Nedialkov, Examining the possibility Of marking and engraving of textiel using CO2 laser, International journal for science Machines, Technologies, Materials 12/2018 стр 491-493

[11] Y.Shterev, N. Dolchinkov, St. Lilianova, D. Boganova, M. Peneva, L. Linkov, D. Nedialkov, Laser marking and cutting of plexiglas with CO2 , International journal for science Machines, Technologies, Materials 4/2018 стр 494-496.

[12] L.Lazov, N.Angelov N., Scanning the contrast in function of velocity in laser marking of samples of steel, International Scientific Conference, Gabrovo, 2010.

[13] Lazov L., Dolchinkov N. T., Shterev Y., Boganova D., Peneva M, Study of laser cutting and marking on the filt with the help of a CO2-laser, 12th International Scienfic and Practical conference Environment. Technology. Resources. ISBN 1691-5402, Vol 3, 20-22.06.2019, Rezekne, Latvia, p. 143-147, DOI.org/10.17770/ETR2019VOL3.4202;

[14] L.Lazov, N.T.Dolchinkov, Y.Shterev, St.Lilianova, A.Pacejs, Use of CO2 laser for marking and clearing of textile materials for manufacture of military equipment, 12th International Scienfic and Practical conference Environment. Technology. Resources. Vol 3, 20-22.06.2019 г. Rezekne, Latvia, ISBN 1691-5402, стр. 32-36;

[15] L. Lazov, N.T. Dolchinkov, Y.Shterev, L. Linkov, D. Nedialkov, Study of cutting and labeling of polymethylmethacrylate using a CO2 laser, 12th International Scienfic and Practical conference Environment. Technology. Resources. ISBN 1691-5402, Vol 3, 20-22.06.2019 г. Резекне, Латвия, стр. 37-40.

[16] N.Padarev, L. Lazov, M. Yovchev, L. Linkov, The Change of Contrast is Investigation of 75 Steel Samples Laser Marked with Different Modes, Environment. Technology. Resources. Rezekne, Latvia Proceedings of the 14th International Scientific and Practical Conference. Volume 3, pp 334-338, Print ISSN 1691-5402 Online ISSN 2256-070X Published by Rezekne Academy of Technologies, 2023

Numerical Modeling of Laser Transmission Welding: State of the Art

Ivo Draganov
Faculty of Mechanical and Manufacturing Engineering
University of Ruse
Ruse, Bulgaria
iivanov@uni-ruse.bg

Lyubomir Lazov
Faculty of Engineering
Rezekne Academy of Technologies (RTA)
Rezekne, Latvia
lyubomir.lazov@rta.lv

Abstract. **This work presents the current state of the numerical modeling of laser transmission welding. A review of publications with a similar theme was made and some aspects that remained outside the focus of the authors were highlighted. Laser transmission welding is a technological process, the physical description of which requires the consideration of several physical laws, which are discussed here. Works were reviewed in which the numerical model is based on: the law of conservation of energy, Fourier's law of heat transfer, Lambert-Beer's law of light propagation, Newton's law of convective heat transfer, Stefan-Boltzmann's law of radiant heat transfer, the Navier-Stokes equation for a fluid, the laws of mechanics for a deformable solid along with the criteria for plasticity. Since their joint solution in analytical form is not possible, the authors' approach is to single out one or several of the laws and use numerical methods to solve the differential equations that describe them. In this work, the use of several numerical methods is considered, and the finite element method is most often used for the discretization of space. The programs used by the authors for the numerical modeling of laser transmission welding are mentioned. The results obtained for the temperature field, heat affected zone and weld pool dimensions, voids, material degradation, residual stresses and weld pool flow rate are discussed. Particular attention is paid to the issues of calibration, verification and validation of numerical models. Some conclusions and directions are highlighted, emphasizing not so much the physical interpretation of the obtained results, but the essence of numerical modeling.**

Keywords: laser transmission welding (LTW), numerical modeling, simulation, temperature, HAZ, thermal degradation, flow, stress.

I. INTRODUCTION

Laser transmission welding (LTW) was proposed in the 1980s. It represents a laser impact on two details placed on top of each other, the upper one being transparent and the lower one being opaque [1], [2]. The transparent part transmits the laser beam, and the opaque part absorbs it, generating heat that melts the parts. After cooling, a joint is obtained.

The formation of welded joints with suitable mechanical properties requires the correct determination of the required amount of heat in the welding zone. Overheating results in stress cracking and the formation of bubbles [3]. The parts do not connect well if the heating is insufficient.

Determining the appropriate welding parameters can be done experimentally or through calculations. The numerical simulations are a very convenient and frequently used tool for calculations. Reliable experimental determination of temperature is difficult. The use of thermocouples is accompanied by an impact of the laser beam on them. The use of thermal cameras also does not offer great accuracy because most laser-transparent polymers are infrared-opaque. The use of numerical simulations leads to a reduction in process setup time and cost. The mass adoption of computer aided design (CAD) systems and numerical simulation with computer-aided engineering (CAE) modules enables the successful simulation of LTW. In recent years, a large number of collectives have been working in this direction [4].

In this work, the various aspects of numerical modeling of LTW are considered.

II. LITERATURE REVIEW

Publications that review the progress of the LTW numerical simulations focus on the essence of the method, treating its physical and technological side. They consider different techniques, materials to be welded, process parameters (wavelength, impact duration, power, speed, etc.), results obtained (temperature fields, stresses, strains, voids, etc.) and their interrelationship.

The issue of numerical modeling of LTW is usually considered in the context of the physical side of the process. Hu et al. [4] review the simulation of temperature

field, stress, melt flow field and thermal degradation, citing 90 literature sources. They offer a flowchart that describes the simulation process, depending on the chosen physico-mathematical model. Also, in their work they present the different models of heat input, the influence of absorbers, process optimization techniques and the obtained results. The issues of calibration, verification and validation are commented on but not clearly highlighted. They pay little attention to the characteristics of the numerical models themselves, focusing more on the physical interpretation of the results.

A. Physico-mathematical models

The heating of the parts is due to the absorption of electromagnetic waves from the laser beam in the opaque material. The law of Lambert-Beer is used to model the absorption in LTW [5]:

$$I(z) = I_0 e^{-kz} \tag{1}$$

where $I(z)$ is the laser pawer density along the direction of the part thickness, I_0 is the laser power density on the top surface of opaque part, k is the absorption coefficient, and z is the depth along the direction of part thickness.

Absorption in transparent material is most often assumed to be zero [5].

The authors use different physico-mathematical models to describe the LTW process. The model in which the process is described by the Fourier law of heat conduction [6] – [9] placed in the law of conservation of energy has received the greatest spread:

$$\text{div}(\boldsymbol{\lambda} \cdot \text{grad}(T)) + Q = V\rho\dot{U} \tag{2}$$

where $\boldsymbol{\lambda}$ is the tensor of material properties, which are functions of the temperature T, Q is the heat quantity in the studied volume, and U is the specific enthalpy.

LTW is accompanied by the occurrence of temperature deformations and their corresponding stresses. The resulting stresses in the welding process can exceed the strength limit of a material. Even at lower values, residual stresses occurring after cooling would reduce the overall load-carrying capacity of the joint. For these reasons, a number of authors determined the stress and strain state in the welded parts. This necessitates solving the thermo-mechanical problem. The algorithm for numerical modeling of LTW is given in [7].

According to the source, strain can be divided into temperature - $\boldsymbol{\varepsilon}^{th}$, elastic - $\boldsymbol{\varepsilon}^{el}$, plastic - $\boldsymbol{\varepsilon}^{pl}$, creep - $\boldsymbol{\varepsilon}^{cr}$ and swelling - $\boldsymbol{\varepsilon}^{sw}$ parts:

$$\boldsymbol{\varepsilon} = \boldsymbol{\varepsilon}^{el} + \boldsymbol{\varepsilon}^{pl} + \boldsymbol{\varepsilon}^{th} + \boldsymbol{\varepsilon}^{cr} + \boldsymbol{\varepsilon}^{sw}. \tag{3}$$

The temperature strains depend on the temperature amplitude. To consider this setup, it is necessary to solve the transient problem.

According to the mode of occurrence, the strains can be divided into elastic and plastic. For elastic strains, Hooke's generalized law applies, which relates them linearly to stress:

$$\boldsymbol{\varepsilon} = \mathbf{S}\boldsymbol{\sigma}. \tag{4}$$

where $\mathbf{S}$ is fourth order tensor of the compliance and $\boldsymbol{\sigma}$ is the stress tensor.

The assessment of the plastic properties of the welded parts is done by applying one of the criteria for the plasticity. In [7] they use the Von Mises criterion. Another possibility is to use the Drucker-Prager criterion [10].

Polymers are viscoplastic materials. Viscoplasticity is a time-dependent mechanical behaviour of materials in which the evolution of plastic strains depends on the loading rate. This property can be described by Perzyna model [7]:

$$\sigma = \left[1 + \left(\frac{\dot{\varepsilon}^{pl}}{\gamma}\right)^m\right]\sigma_0 \tag{5}$$

where σ and σ_0 are the dynamic and static yield stress of the material, $\dot{\varepsilon}^{pl}$ is the equivalent plastic strain rate, and m and γ are the strain rate hardening and material viscosity parameters, respectively.

LTW is accompanied by the formation of a liquid phase. The continuum formulation is based on the mass, momentum and energy conservation laws [3], [11], respectively:

$$\frac{\partial\rho}{\partial t} + \text{grad}(\rho\mathbf{v}) = 0, \tag{6}$$

$$\frac{\partial(\rho\mathbf{v})}{\partial t} + \text{grad}(\rho\mathbf{vv}) = -\text{grad}P + \\ + \text{grad}(\mu.\text{grad}(\mathbf{v})) + \rho\mathbf{g}\beta_T(T - T_r) - \frac{\mu}{K}\mathbf{v}, \tag{7}$$

$$\text{grad}(\lambda\text{grad}T) = c\left(\frac{\partial T}{\partial t} + \text{grad}(T\mathbf{v})\right) - \tilde{Q}, \tag{8}$$

where ρ is the material density, $\mathbf{v}$ is the velocity vector, μ is the dynamic viscosity, $\mathbf{g}$ is the acceleration of gravity, β_T is the volume expansion coefficient, T_r is reference temperature, K is porous medium permeability, c is effective heat capacity, and $\tilde{Q}$ are volumetric heat sources.

The porous medium permeability can be expressed by Caman-Kozeny equation [12]:

$$K = K_0 \frac{(1-f_s)^3}{f_s^2}, \tag{9}$$

$$K_0 = \frac{d_0^2}{180}, \tag{10}$$

where d_0 is an average solid particle diameter, f_s is assumed with linear approximation between solidus – T_S, and liquidus – T_L, temperature:

$$f_s = \begin{cases} 1 & \text{for} & T < T_S \\ \frac{T_L - T}{T_L - T_S} & \text{for} & T_S \le T \le T_L \\ 0 & \text{for} & T > T_L \end{cases} \tag{11}$$

B. Initial and boundary conditions

The most important boundary condition is the laser beam, which will be discussed in the next subsection.

The initial conditions depend on the chosen physico-mathematical model. Solving the heat problem requires

setting the initial temperature, which is most often room temperature in the range of 20° to 27° C [13], [14]. The solution of the mechanical problem is carried out assuming that there are no strains and stresses at the beginning of the process.

The boundary conditions for solving the heat problem are convective and radiative heat exchange. Some authors ignore them [15], [16], and others consider their joint influence by setting the heat transfer coefficient (HTC) [8], [17]. The authors in [13] consider only radiation heat transfer, using the Ray Tracing method, an optical method to compute the optical propagation of laser beams. Liu et al. ignore radiative heat transfer and consider only convection [5].

Certain authors consider the contact between the welded parts as not ideal and study the influence of its imperfections. Liu et al. [5] took this fact into account and found that it resulted in a different width of the weld pool in the lower and upper parts. According to [18] Thermal Contact Conductance – TCC, can be determined by the equation

$$TCC = \frac{\Delta T}{q} \qquad (12)$$

where q is the heat flux caused by temperature difference - ΔT.

Welded parts most often have different roughness in different directions. Wang et al. use a model to account for this difference [11].

In the mechanical task, the fastening of the welded parts [10] or clamping force (pressure) is set [11], [19].

The boundary conditions in the numerical modeling of the liquid phase are the boundaries of the weld pool. They depend on the melting point [3], [20].

Very often, authors consider symmetric joints and account for this in numerical models [7], [17], [21]. This leads to a reduction in computational time, as demonstrated in [5].

C.   Laser beam modeling

Aden [15] model the laser beam using the "Henyey-Greenstein phase function" - p:

$$p(\mu) = \frac{1}{2} \frac{1-g^2}{(1+g^2-2g\mu)^{3/2}}, \qquad (13)$$

$$\mu = \cos(\theta), -\pi < \theta < \pi, \qquad (14)$$

where θ is the scattering angle and a random variable, g gives the degree of anisotropy.

LTW is performed by impulses. Most often, authors ignore this and use a quasi-simultaneous heat source. For this purpose, the linear energy is used [21]:

$$E = \frac{P}{v}n, \qquad (15)$$

where P is the laser power, v is the feed rate and n is the number of repeats.

Pulse train modeling is computationally intensive, as it requires solving the problem with a large number of increments. Chen et al. [22] model laser welding as a sequence of three pulses.

The laser beam can be modeled as moving [8], [16] or as stationary [6], [17]. Nguyen et al. [21] define the Peclet number, which gives a qualitative estimate of the temperature distribution in the body, which depends on the speed of the laser beam. They use the equation

$$Pé = \frac{vw_0}{a}, \qquad (16)$$

where w_0 is the beam diameter and a is the thermal diffusivity.

The efficiency of the laser is determined by the dependence [5]:

$$\eta = \frac{P_A}{P_E}, \qquad (17)$$

where P_A is the laser output power, and P_E represents the nominal laser power.

There are different patterns of heat flow distribution in the absorbent part. They can be divided into two main types volumetric and surface heat source model. The choice depends on the thickness of the welded parts. In both cases, a Gaussian distribution is most often used, which for surface cases has the form [11]:

$$q = \eta_t \frac{P_A}{\pi R^2} \exp\left(-\left(\frac{r^2}{R^2}\right)\right), \qquad (18)$$

where R is the radius of spot on the upper surface of absorption specimen, r is the distance from each point on the upper surface of the absorbed specimen to the center of the laser spot, η_t the transmittance of the transparent specimen, P_A is the laser power.

Chen et al. [23] define the volumetric heat source by dependence:

$$q(x,y,z,t) = \frac{9Q}{\pi H R_0^2 \left(1-\frac{1}{e^3}\right)}.$$
$$.\exp\left(-\frac{9}{R_0^2 \log\left(\frac{H}{z}\right)}\left((x-vt)^2 + y^2\right)\right), \qquad (19)$$

where, H is the thickness of heat source, R_0 is the diameter of laser spot, v is welding speed, Q_1 is the laser energy absorbed by laser-transparent part.

Other heat flux distribution functions are M-shape beam [15], which is described with a polynomial function:

$$I_M \begin{cases} I_{MO} \sum_{n=0}^{3} a_n \left(\frac{r}{R}\right)^{2n}, 0 \le r \le R \\ 0, \; r > R \end{cases},$$
$$I_{MO} = \frac{P}{\pi R^2 \sum_{n=0}^{3} \frac{a_n}{n+1}}, \qquad (20)$$

where R is the beam radius, a_n are the polynomial coefficients.

It is possible to use Goldak's double ellipsoid [10]. Some authors use a combination of volume and surface heat source.

D. Material models

The modeling of the heat distribution is possible with linear and nonlinear material properties. Wang et al. used material model with constant conduction and specific thermal capacity [17]. Moust of the authors used nonlinear relation between thermal properties and temperature [24]. Ali et al. used nonlinear specific thermal capacity and constant conductivity [8].

Phase transitions give rise to a large gradient in specific heat capacity. This necessitates the use of latent heat to reduce the non-linearity in the task [5].

When solving the thermo-mechanical problem, the non-linear mechanical properties of the material are taken into account [7].

Liquid phase in the weld pool is assumed as laminar, Newtonian and incompressible [3].

Modeling of plastic deformations in LTW is possible using material ductility criteria. In [7] they use the von Mises criterion. Another possibility is to use the Drucker-Prager criterion [10].

E. Numerical and computer models

Potente et al. propose an analytical model for the temperature field in welded parts [25]. They compare the obtained results with experimental data.

Taha et al. [26] determine the temperature field by the control volume technique (CVT). In this method, the calculation domain is divided into numerous non-overlapping control volumes surrounding each grid point, where the temperature is calculated. The differential equations are integrated over each control volume based on some assumed profile to yield a linear algebraic equation for the concerned grid point. They give details of the mesh and compare the results with experimental data.

Xu et al. used the volume of fluid method (VOF) [20] to solve the fluid flow problem. To solve the same problem, Chen et al [22] used computational fluid dynamics (CFD) and finite volume method (FVM), combined with pressure implicit operator splitting (PISO) algorithm.

The main part of the authors aims to determine the temperature field by solving equation (2) using the finite element method. The most commonly used programs are ANSYS [5] [7], [17], COMSOL [8], [15], [16], [21], [27] and ABAQUS [6], [9], [28]. They allow the implementation of appropriate fixed and moving functions for the heat flow. All these programs are suitable for solving the thermo-mechanical problem.

Solving the fluid mechanics problem is done using ANSYS Fluent [11], [22]. Thise program implement FVM.

Aden modeled the propagation of the laser beam through the details using the program ZEMAX [15].

Most authors model the welding of two prismatic parts or representative volumes of such a shape, but there are exceptions. Xu et al. [20] modeled a sandwich structure consisting of two plates and ribs.

The number of nodes and time steps make it possible to determine the amount of computational work, and from there to judge the computation time.

It is possible to model LTW in 2D [29], but at present it is mostly solved transient 3D problem. This raises the question of proper time discretization. Very often, this issue is not considered in details, assuming a priori that the presented solution satisfies the requirement of independence of the results of the time increment. Some authors pay attention to this issue. Chen et al. [22] give information on the about the time increment.

The discretization of the space is carried out with the type of finite elements depending on the type of problem being solved and the specific program for implementing the numerical method. Most often, the authors use finite elements with a hexahedral shape, but triangular prisms [8], [28] and tetrahedron [23] are also used. The simulation of LTW by solving the heat problem is performed using SOLID 70 in ANSYS [17], [7] and type DC3D8 in ABAQUS [28]. Deformation problem requires SOLID45 in ANSYS [7] and C3D8T in ABAQUS [10]. Liu et al. [5] use CONTA173 and TARGE170 contact elements.

The discretization of space is performed using the local mesh refinement technique. This allows to reduce the amount of computational work. Often the authors do not explicitly comment on the issue of the number of finite elements used, but put a figure from which to determine them. Some authors pay special attention to this issue. Asséko et al. [27] used 2250 elements, [24] - 391762, [23] - 770000. There is a tendency to increase the number of used elements, which is related to the development of computing technology. A limitation for the elements used is the calculation time, which is mostly not commented on. Chen et al. [24] give the calculation time, which is 2.8 minutes per set of parameters.

The setting of the laser beam is carried out through special built-in functions in the used program or through subroutines that were created by the authors.

F. Results

The obtained results depend on the type of the solved task. The most important feature of LTW is the temperature field. They are a measure of the quality of the weld joint. Determination of the temperature field allows to determine the shape and dimensions of the weld pool and heat affected zone (HAZ) [6], [21]. By solving the fluid problem, the flow rate in the bath and the resulting gaps or bubbles can be determined [3], [20]. The latter model bubbles by removing material above a certain temperature. The change of the temperature field in the welding process serves to determine the temperature deformation [7], [11]. It is divided into elastic and plastic [7]. The strain field serves to determine the stresses during welding and the residual stresses [7]. Table 1 gives

a summary of the type of problems solved, the required inputs and the results obtained.

TABLE 1 PROBLEM AND RESULTS

Type of the problem	Input variables	Results
Laser beam propagation	Laser rays	Rays of radiation, temperature field
Heat propagation	Heat flux from the laser beam	Temperature field, welding pool, HAZ, maximum temperature
Thermo-mechanical	Heat flus from the laser beam, clamping force, fixing	Temperature field, strains, stresses, residual stress
Fluid	Heat flux from the laser beam	Temperature field, velocity of the fluid flow, gaps, bubbles and key holes

E. Calibration, verification and validation

Most often, the authors use the numerical models to study the influence of the physical parameters and the main focus falls on obtaining results that match as well as possible the obtained experimental data in the specific welding conditions.

The calibration is the process of the determination of appropriate parameters of the model to bring the simulation results closer to the experimental ones. Model parameters can be divided into two main groups: parameters that are from the physical world (physical parameters) and parameters that derive from the mathematical description, numerical model, or programming algorithm (model parameters). The first group of parameters includes: geometric dimensions, material density, thermal conductivity, specific heat capacity, gap between details, emissivity, transmittance, reflectivity, melting temperature, absorption coefficient, latent heat, heat convection coefficient, initial temperature, liquid dynamic viscosity, glass transition temperature, decomposition temperature, thermal expansion coefficient, heat deflection temperature, compressive strength, modulus of elasticity, Poisson's ratio, tensile strength, flexural strength, elongation at break and laser parameters. The laser parameters are power, laser efficiency, laser wavelength, frequency, laser beam spot shape and dimensions, energy density, and travel speed. The second group of parameters includes the time step, number of finite elements, number of nodes, correction coefficients of the energy density and shape of the laser beam and all approximating parameters in the material models. Model parameters can be divided into those that have no physical meaning and the solution should not depend on them, and those that affect the physical parameters. The latter are used for calibration. The results obtained are temperature field, maximum temperature, pool shape and size, HAZ shape and size, stressed and strain state, equivalent stresses, residual stresses, flow rate, laser beam propagation.

LTW modeling is accompanied by idealizations that lead to unacceptable differences in the results of simulations and experiments. One possible approach to reconcile the differences is by using some of the model parameters as calibrations. This should be clearly defined, and it is necessary to highlight the scope of the solution. This issue is greatly underestimated by most authors and often remains outside the discussion. However, some authors comment on it. Labiase et al. [30] calibrate a thermo-mechanical numerical model using an overall error function:

$$E_{TOT} = \sum_{i=1}^{N} \left(\frac{F_{EXP}(i) - F_{MOD}(i, C_1, C_2, C_n)}{F_{EXP}(i)} \right) \quad (21)$$

where F_{EXP} is the experimental strength, F_{MOD} is the computed strength, C_i are control point, and N is the number of calibration cases.

In another work of the same team [9], they performed calibration on emissivity and absorption coefficient. Xu et al. [31] vary with volumetric heat source and use the geometry of the keyhole as a criterian to calibrate the thermal model. Wang et al. [32] calibrate a thermomechanical model using two release coefficients that are involved in the residual stress formulas.

Obtaining reliable results at numerical modeling of LTW requires the steps of verification and validation. The first one is an assessment of the accuracy of the solution to a computational model by comparison with known solutions. The second is the assessment of the accuracy of a computational simulation by comparison with experimental data.

The verification process is greatly underestimated in LTW modeling. Some authors mention it without emphasizing it [5]. Most often, the authors proceed to the validation stage without verifying the numerical model, using their own experimental data for this purpose.

III. CONCLUSIONS

There has been significant progress in the ability to solve individual physics problems, most often with results for the temperature field. The joint solution of problems with several physical laws is still very limited, with the greatest experience in the thermo-mechanical problem.

Numerical models of LTW for structures with complex configuration are very rare.

Most often, the description of numerical models of LTW is incomplete, especially in its part with time and space discretization and computational performance.

The calibration of numerical models is done in different ways, but the most authors do not describe this stage. Few authors discuss the issue of model verification. The main emphasis is on validation.

ACKNOWLEDGMENTS

REFERENCES

[1] F.G. Bachmann and U. Russek, "Laser welding of polymers using high power diode lasers," Proc. SPIE, pp. 505–518, 2002, https://doi.org/10.1117/12.470660

[2] E. Haberstroh, W. M. Hoffmann, R. Poprawe, and S. Fahri, "Applications of laser transmission processes for the joining," Microsyst. Technol., pp. 632–639, 2006, https://doi.org/10.1007/s00542-008-0675-3

Y. Ai, K. Zheng, Y. Shin, and B. Wu, "Analysis of weld geometry and liquid flow in laser transmission welding between polyethylene terephthalate (PET) and Ti6Al4V based on numerical simulation," Optics & Laser Technology, vol. 103, pp. 99-108, 2018, https://doi.org/10.1016/j.optlastec.2018.01.022

S. Hu, F. Li, and P. Zuo, "Numerical Simulation of Laser Transmission Welding—A Review on Temperature Field, Stress Field, Melt Flow Field, and Thermal Degradation," Polymers 2023, vol. 15, 2125, https://doi.org/10.3390/polym15092125

H. Liu; W. Liu, D. Meng, and X. Wang, "Simulation and experimental study of laser transmission welding considering the influence of interfacial contact status," Mater. Des., vol. 92, pp, 246–260, 2016, https://doi.org/10.1016/j.matdes.2015.12.049

C. Hopmann and S. Kreimeier, "Modelling the Heating Process in Simultaneous Laser Transmission Welding of Semicrystalline Polymers," Hindawi Publishing Corporation Journal of Polymers, vol. 2016, pp. 1-11, 2016, https://doi.org/10.1155/2016/3824065

[3] B. Acherjee, A. S. Kuar, S. Mitra, and D. Misra, "Modeling of laser transmission contour welding process using FEA and DoE," Optics & Laser Technology, vol. 44, no. 5, pp. 1281–1289, 2012, https://doi.org/10.1016/j.optlastec.2011.12.049

[4] M.M. Ali, F. Dave, R. Sherlock, A. McIlhagger, and D. Tormey, "Simulated Effect of Carbon Black on High Speed Laser Transmission Welding of Polypropylene With Low Line Energy," Front. Mater., vol. 8, 737689, 2021, https://doi.org/10.3389/fmats.2021.737689

F. Lambiase, S. Genna, and R. Kant, "Optimization of laser-assisted joining through an integrated experimental-simulation approach," Int. J. Adv. Manuf. Technol. vol. 97, pp. 2655–2666, 2018, https://doi.org/10.1007/s00170-018-2113-8

[5] I. Draganov, "Numerical simulation of laser beam welding applied to polymers," Proceedings of University of Ruse – 2020, vol. 59, pp. 11-17, 2020.

[6] C.Y. Wang; M. H. Jiang, C. D. Wang, H. H. Liu, D. Zhao, and Z. L. Chen, "Modeling three-dimensional rough surface and simulation of temperature and flow field in laser transmission welding," J. Adv. Join. Process., vol. 1, 100021, 2020, https://doi.org/10.1016/j.jajp.2020.100021

[7] L. Han and F.W. Liou, "Numerical investigation of the influence of laser beam mode on melt pool," Int. J. Heat Mass Transf., vol.47, 4385–402, 2004, https://doi.org/10.1016/j.ijheatmasstransfer.2004.04.036

[8] A. Asseko, B. Cosson, M. Deleglise, F. Schmidt, Y. Le Maoult, et al., "Analytical and numerical modeling of light scattering in composite transmission laser welding process," International Journal of Material Forming, 8 (1), pp.127-135, 2015, https://doi.org/10.1007/s12289-013-1154-7

[9] B. Acherjee, "3-D FE heat transfer simulation of quasi-simultaneous laser transmission welding of thermoplastics," J. Braz. Soc. Mech. Sci. Eng., vol. 41, 466, 2019, https://doi.org/10.1007/s40430-019-1969-3

M. Aden, "Influence of the Laser-Beam Distribution on the Seam Dimensions for Laser-Transmission Welding: A Simulative Approach," Lasers Manuf. Mater. Process., vol. 3, pp. 100–110, 2016, https://doi.org/10.1007/s40516-016-0023-x

M. Brosda, P. Nguyen, A. Olowinsky, and A. Gillner, "Analysis of the interaction process during laser transmission welding of multilayer polymer films with adapted laser wavelength by numerical simulation and thermography," J. Laser Appl., vol. 32, 022060, 2020, https://doi.org/10.2351/7.0000113

[10] X. Wang, H. Chen, H. Liu, P. Li, Z. Yan, C. Huang, Z. Zhao, and Y. Gu, "Simulation and optimization of continuous laser transmission welding between PET and titanium through FEM, RSM, GA and experiments," Opt. Lasers Eng. vol., 51, 1, 2013

https://doi.org/10.1016/j.optlaseng.2013.04.021

[11] J. Zheng, Y. Li, L. Wang, and H. Tan, "An improved thermal contact resistance model for pressed contacts and its application analysis of bonded joints", Cryogenics, vol. 61, pp. 133–142, 2014, https://doi.org/10.1016/j.cryogenics.2013.11.002

[12] C. Wang, H. Liu, Z. Chen, D. Zhao, and C. Wang, "A new finite element model accounting for thermal contact conductance in laser transmission welding of thermoplastics," Infrared Phys. Technol., vol. 112, 103598, 2021, https://doi.org/10.1016/j.infrared.2020.103598

[13] K. Xu; H. Cui, and F. Li, "Connection Mechanism of Molten Pool during Laser Transmission Welding of T-Joint with Minor Gap Presence," Materials, vol. 11, 1823, 2018, https://doi.org/10.3390/ma11101823

[14] N.P. Nguyen; S. Behrens, M. Brosda, A. Olowinsky, and A. Gillner, "Modelling and thermal simulation of absorber-free quasisimultaneous laser welding of transparent plastics," Weld. World, vol. 64, pp. 1939–1946, 2020, https://doi.org/10.1007/s40194-020-00973-5

J. Chen, B. Kong , Q. Wang, Z. Qi, and Y. Wei, "Morphology, mechanical property, and molten pool dynamics in spot modulated-PLBW of Ti6Al4V alloy sheets with air gap condition," Science and Technology of Welding and Joining, vol. 28(8), pp. 775-783, 2023, https://doi.org/10.1080/13621718.2023.2227810

Z. Chen, Y. Huang, F. Han, and D. Tang, "Numerical and experimental investigation on laser transmission welding of fiberglassdoped PP and ABS," J. Manuf. Process., vol. 31, pp. 1–8, 2018, https://doi.org/10.1016/j.jmapro.2017.10.013

[15] M. Chen, G. Zak, and P. J. Bates, "3D Finite Element Modelling of Contour Laser Transmission Welding of Polycarbonate," Weld. World, vol. 53, pp. 188–197, 2009, https://doi.org/10.1007/BF03266731

[16] H. Potente, J. Korte, and F. Becker, "Laser transmission welding of thermoplastics: analysis of the heating phase," j. Reinf. Plast. Comp. pp. 914–920, 1999, https://doi.org/10.1177/073168449901801005

[17] Z.A. Taha, G. G. Roy, K. I. Hajim, and I. Manna "Mathematical modeling of laser-assisted transmission lap welding of polymers," Scr. Mater., vol. 60, pp. 663–666, 2009, https://doi.org/10.1016/j.scriptamat.2008.12.041

[18] A.C. Asséko, B. Cosson, F. Schmidt, Y. Le Maoult, R. Gilblas, and E. Lafranche, "Laser transmission welding of composites— Part B: Experimental validation of numerical model," Infrared Phys. Technol., vol. 73, pp. 304–311 2015, https://doi.org/10.1016/j.infrared.2015.10.005

T. Mahmood, A. Mian, M. R. Amin, G. Auner, R. Witte, H. Herfurth, and G. Newaz, "Finite element modeling of transmission laser microjoining process." J. Mater. Process. Technol., vol. 186, pp. 37–44, 2007, https://doi.org/10.1016/j.jmatprotec.2006.11.225

[19] L. S. Mayboudi, A. M. Birk, G. Zak, and P. J. Bates, "A two-dimensional thermal finite element model of laser transmission welding for T joint," J. Laser Appl., vol. 18, pp. 192–198, 2006, https://doi.org/10.2351/1.2227007

[20] F. Lambiase, S. Genna, and R. Kant, "A procedure for calibration and validation of FE modelling of laser-assisted metal to polymer direct joining," Opt. Laser Technol., vol. 98, pp. 363–372, 2018, https://doi.org/10.1016/j.optlastec.2017.08.016

G. X. Xu, C. S. Wu, G. L. Qin, et al., "Adaptive volumetric heat source models for laser beam and laser + pulsed GMAW hybrid welding processes," Int. J. Adv. Manuf. Technol., vol. 57, pp. 245–255, 2011, https://doi.org/10.1007/s00170-011-3274-x

[21] W. Chuanyang, X. Yu, M. Jiang, Z. Xing, and C. Wang, "Numerical and experimental investigation into the evolution and distribution of residual stress in laser transmission welding of PC/Cu/PC," Optics & Laser Technology, vol. 136, 106786, 2021, https://doi.org/10.1016/j.optlastec.2020.106786

Determination of preliminary operating intervals of the power density for laser technological processes on copper samples

Risham Singh Ghalot
Faculty of Engineering
Rezekne Academy of Technology
Rezekne, Latvia
singhrisham93@gmail.com

Lyubomir Lazov
Faculty of Engineering
Rezekne Academy of Technology
Rezekne, Latvia
Lyubomir.lazov@rta.lv

Nikolay Angelov
Department of Mathematics,
Informatics and Natural Sciences
Technical University of Gabrovo
Gabrovo, Bulgaria
Angelov.np@abv.bg

Edmunds Teirumnieks
Faculty of Engineering
Rezekne Academy of Technology
Rezekne, Latvia
edmunds.teirumnieks@rta.lv

Abstract. **The report investigates the role of power density of melting and evaporation and speed to realize several laser technological processes on copper samples for a fibre laser and a CuBr laser. A methodology has been developed to determine preliminary operating intervals of power density for different speeds for the laser marking, laser ablation and laser texturing processes. From theoretical calculations, graphics of the dependences of the critical power density of melting and evaporation on the speed were drawn. Areas where oxidation, melting or evaporation occur were defined. Comparing the theoretical results and the obtained experimental results shows a very good convergence between them for both laser sources.**

Keywords: Laser density, Laser power, Laser surface texturing, Laser manufacturing - modelling and simulation on technology processes.

I. INTRODUCTION

In the domain of laser material processing, laser surface treatment technologies show substantial potential for growth in the forthcoming years [1]. Therefore, there is a necessity for a comprehensive understanding of the physicochemical and phase changes that occur during the interaction between laser beam and various material types. Presently, laser surface treatment stands as a focal point of cutting-edge scientific research due to its application in diverse sectors such as aeronautics, mechanical engineering, medicine, and other pivotal domains shaping modern economic development worldwide [2] [3].

Laser surface treatment technologies offer a broad spectrum of opportunities to achieve innovative surface properties. The modification of the surface layer is dictated by laser processing parameters and the optical and thermal properties of materials [4] [5].These factors collectively influence the resulting temperature profile within the processing zone, thereby instigating alterations in the material's properties (including mechanical, corrosion resistance, tribological, antibacterial, etc.) in both depth and radial directions [6] [7] [8]. The achieved modifications of the surface properties of the layer are largely determined by the settings of the parameters of the laser source, such as: wavelength of the laser beam, continuous wave (CW) or pulsed mode of operation, pulse length, peak power, shape of the pulse, repetition rate, beam energy distribution in its cross section, including focal spot size and depth of focus [9] .

The application of different laser technologies also leads to different effects on the modified surface properties. Thus, for example, in addition to the power density and the energy density in the processing area, the scanning speed or the laser interaction time have a strong influence on the modification of a metal surface [10] [11] [12]. All these specific features determine the number of advantages of laser surface treatment over conventional treatment methods, such as local heating of the surface without changing the properties of the substrate material, precision, and high speed of work and low cost [13] [14].

The use of copper in several industries, such as mechanical engineering, electronics, aircraft construction and aeronautics, is increasing as copper-based components are used in personal computers, cellular telephones, and the expansion of telecommunications [15] [3]. Modern laser processing of copper has its inherent problems due to its high reflectivity and very high thermal conductivity, and today it faces several challenges [2].

The surface critical density of laser power in the context of melting and vaporization of metals is a significant parameter in laser material processing. It represents the threshold at which the incident laser power density is sufficient to induce phase changes in the material [16] [17] [18] [19].

Determining this critical density is essential for several reasons. Knowing the threshold power density for melting or vaporization optimizes laser processing parameters. It enables precise control of the energy input required for specific material transformations, ensuring efficient and accurate processing. Understanding critical power density prevents excessive energy input, reducing the risk of unintended material damage or property alterations. It contributes to achieving consistent, high-quality results in laser material processing, ensuring reproducibility and uniformity in treated material properties like surface morphology, hardness, and microstructure. Accurate determination of critical power density aids in cost efficiency, minimizing energy and material wastage by precisely directing the energy needed for desired material changes. Moreover, it is a critical parameter in research and development efforts aimed at exploring new applications and improving laser-based manufacturing techniques, informing the development of novel processes and applications. In essence, determining the surface critical laser power density in metal melting and vaporization is fundamental for precision control, quality assurance, cost-effectiveness, and advancing laser material processing technologies [20] [21] [22] [23].

This work develops a numerical surface heat treatment method to analyse various phase changes on the surface of copper samples. The phase state of the melting and evaporation surface is analysed, and the surface morphology of Cu samples is investigated concerning key laser processing parameters, including power density, processing speed. Numerical calculations are compared with our experimental studies by varying the above process parameters.

II. Theoretical Aspects and Methodology

A. Theoretical Aspects

The power density q_s and the speed 'v' are the main parameters determining the temperature T in the impact zone for laser technological processes such as laser marking, laser engraving, laser ablation, laser texturing, laser cutting, laser welding, laser sintering, etc. There is a relationship and interdependence between these three quantities. And such a theoretical relationship between the critical melting and evaporation power density and the processing rate has been obtained by several other authors.

Under some simplifying assumptions (independence of thermophysical and optical parameters from temperature) for the critical power density of melting q_{scm} the expression is obtained

$$q_{scm} = \frac{(1+s)k(T_m-T_0)}{2A}\sqrt{\frac{\pi v}{ad}}, \qquad (1)$$

where k is coefficient of thermal conductivity, T_m – melting point, T_0 – initial temperature (environmental temperature), A – absorbed laser energy, a – coefficient of thermal diffusivity, d - diameter of work spot, the parameter s is determined by the formula.

$$s = \frac{L_m}{c(T_m-T_0)}, \qquad (2)$$

L_m is latent heat of melting, c – specific heat capacity.

For the critical power density of vaporization q_{scv} under the same simplifying assumptions, it is used the expression:

$$q_{scv} = \frac{(1+s')k(T_v-T_0)}{2A}\sqrt{\frac{\pi v}{ad}} \qquad (3)$$

where T_v is vaporization temperature, The parameter s' is determined by the formula:

$$s' = \frac{L_m+L_v}{c(T_v-T_0)}, \qquad (4)$$

L_v is latent heat of evaporation.

It should be noted that each specific laser system used for a given technological process has a maximum power density q_{smax} of the laser radiation with which to affect the processed area. It is given with the expression:

$$q_{smax} = \frac{4P_{max}}{\pi d^2} \qquad (5)$$

where P_{max} is the maximum power of the laser.

To achieve the goals, work is being done in two directions:

B. Steps in Determining Preliminary Power Density Operating Intervals

The following sequence is used to determine the preliminary laser power density operating intervals for **oxidation, melting**, and **evaporation** laser texturing:

1) Determination of the maximum power density q_{smax} for the used laser system fibre laser ($\lambda = 1,06$ μm) and CuBr laser ($\lambda = 511\&578$ μm).

Each laser has a certain maximum power of its radiation, which is associated with its manufacture and is of a constructive nature. When it is built into a specific technological system, its maximum power density can also be determined, which is of a constructive nature. It has a constant value and does not depend on the speed with which the laser beam moves, and other factors related to the technological process, i.e. it is the design maximum density of the power of the laser radiation. The maximum power density q_{smax} for the laser system is determined by formula (5), which is required for the preliminary operating intervals of the power density of evaporation q_{scv}.

2) Calculation of critical melting power density q_{scm} for different speeds v.

Calculations of the critical melting power density for different speeds for the two lasers (fibre laser and CuBr laser) are performed using expressions (1) and (2). The speed v varies from 10 mm/s to 100 mm/s in 10 mm/s increments. The selected laser impact speeds 'v' is suitable for the technological process laser texturing of metals (including Cu). Graphics of the dependence of the melting power density on the speed are drawn from the obtained results.

3) Calculation of critical power density of vaporization q_{scv} for different speeds v.

Calculations of the critical power density of vaporization q_{scv} for different speeds for the two lasers are performed using expressions (3) and (4). The speed v varies from 10 mm/s to 100 mm/s in 10 mm/s increments. They draw graphs of the dependence of the power density of evaporation q_{scv} on the speed 'v'.

These two power densities (q_{scm} and q_{scv}) are technological in nature and depend on the speed v of the laser beam.

4) Determination of power density q_s intervals during marking by **oxidation**, by **melting** and by **evaporation** of the selected laser and material.

When determining the preliminary operating intervals of the power density q_s for different speeds 'v', the following requirements are observed:

- For laser texturing by **oxidation** - the power density q_s is less than the critical melting power density q_{scm} for the respective speed 'v'.

- For laser texturing by **melting** - the power density q_s is between the critical melting q_{scm} power density and the critical evaporation power density q_{scv} for the respective speed 'v'.

- For laser texturing by **vaporization** – the power density is between the critical vapor power density q_{scv} for the respective speed 'v' and the maximum power density q_{smax} of the laser system.

Graphical dependences for each laser are being given on a separate coordinate system. Three areas of laser texturing are defined on the graphic field: area 1 – by oxidation; area 2 – by melting; area 3 – by evaporation.

B. *Experimental studies on fibre laser and copper bromide laser copper wafers and comparison of experimental data with calculation results*

Laser technological experiments of copper are performed with both lasers at different power densities q_s and speeds 'v'. The treated areas (squares) are photographed with a metallographic microscope, and it is determined whether there is surface oxidation, melting or evaporation in the affected area. A comparison is made with the location of the specific processed zone in the formed areas (it is marked with a black dot) and the actual obtained way of texturing. Design matrices for performing experimental studies on the influence of speed 'v' and power 'P' (respectively power density 'q_s')

are presented in Figure 1. They are suitable for the technological processes of laser marking, laser ablation and laser texturing. Experiments are conducted using a raster method. The treated fields are 10 mm squares, and the experiments are conducted according to the designed matrices (see Figure 1). To investigate the influence of speed at 3 constant powers, the test field consists of 6 rows of 8 squares for impact with both types of lasers.

Experimental results are drawn as black dots on the graphical images for both types of lasers. The experimental results are compared with the theoretical ones.
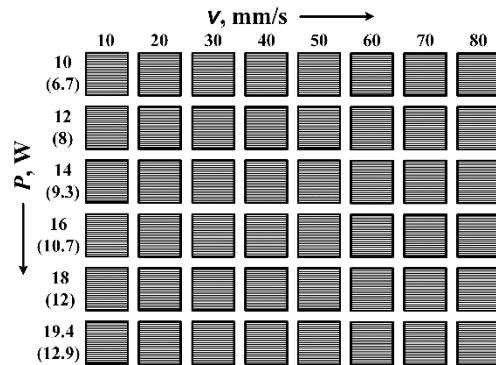
Fig. 1. Design matrix for experimental studies on the influence of speed and power in impact with fibre laser and CuBr laser on copper plates (data in brackets are for CuBr laser)

III. RESULTS AND DISCUSSION

According to the established methodology, research was carried out in two directions:

A.Determination of preliminary operating intervals of power density for laser marking and texturing by oxidation, laser marking and laser marking by melting, laser ablation and laser texturing by evaporation.

In order to study the dependence of the critical power density of melting q_{scm} and evaporation q_{scv} on the speed v of laser impact on copper samples, the following steps were taken. According to the methodology presented above, the values of the critical density power of melting q_{scm} (see formulas 1 and 2) and evaporation q_{scv} (see formulas 3 and 4) were calculated for copper samples for the different speeds v. Formulas (1) and (3) are derived for lasers operating in continuous mode. Due to the high frequency $v = 20$ kHz of the lasers, it can be assumed that the lasers work in CW mode. In the experiments performed with both lasers, the pulse overlaps k_{ovr} coefficient varied from 86.7% to 98.5%.

The necessary data for copper characteristics are taken from Table 2. The calculations refer to a fibre laser and a CuBr laser. From the obtained values of the quantities, graphics of the dependence of the critical density power of melting q_{scm} and evaporation q_{scv} on the speed for copper samples were drawn.

The graphics that apply to a fibre laser are presented in Fig. 2. It follows from their analysis:

- A non-linear increase in both the critical power density of melting and the critical power density of evaporation is observed as the speed increases.

- In the speed v interval from 10 mm/s to 100 mm/s, the critical power density q_{scm} of melting changes from 0.24×10^{10} W/m^2 to 0.76×10^{10} W/m^2.
- In the speed v interval from 10 mm/s to 100 mm/s, the critical power density q_{scv} of evaporation changes from 2.32×10^{10} W/m^2 to 7.35×10^{10} W/m^2.

Fig. 2. Graphics of critical power density versus speed v for a fibre laser: blue colour - of melting q_{scm}, orange colour - of evaporation $q_{scv.}$ Legend: area 1 – by oxidation; area 2 – by melting; area 3 – by evaporation.

The same graphical dependencies are given in Fig. 3, but for a CuBr laser. The blue coloured graphic is for the critical power density of melting and the orange-coloured graphic is for the critical power density of evaporation. The following conclusions can be done from them:

- With an increase in speed, a non-linear increase of the two critical power densities is again observed for the entire studied interval of speed.
- In the speed interval from 10 mm/s to 100 mm/s, the critical power density q_{scm} of melting changes from 0.16×10^{10} W/m^2 to 0.51×10^{10} W/m^2.
- In the speed interval from 10 mm/s to 100 mm/s, the critical power density q_{scv} of evaporation changes from 1.54×10^{10} W/m^2 to 4.90×10^{10} W/m^2.
- The critical power density of melting and evaporation of a CuBr laser is about 33% less than that of a fibre laser. It is explained by the greater absorption capacity of copper for the radiation of the CuBr laser compared to the fibre laser.
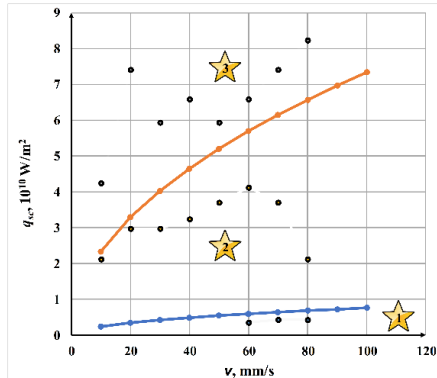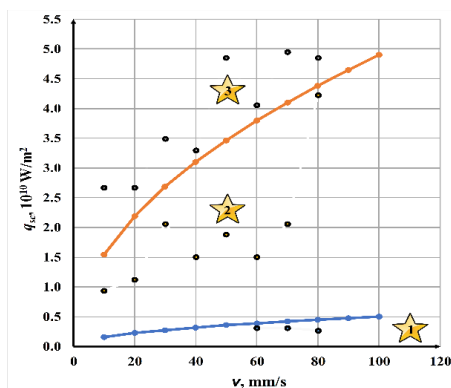

Fig. 3. Graphics of critical power density versus speed for a CuBr laser: blue colour - of melting q_{scm}, orange colour - of evaporation $q_{scv.}$ Legend: area 1 – by oxidation; area 2 – by melting; area 3 – by evaporation.

To determine the preliminary operating intervals of the power density, it is necessary to determine the maximum power density of the two lasers. According to

formula (5), the following values are obtained: $q_{smax} = 10.1 \times 10^{10}$ W/m^2 for the fibre laser and $q_{smax} = 6.37 \times 10^{10}$ W/m^2 for the CuBr laser. The preliminary operating intervals of the power density for oxidation, melting and vaporization at different rates for fibre laser and CuBr laser, respectively, are given in Tables 1 and 2. The selected speeds are used in the industry for the relevant laser technological processes.

TABLE 1: PRELIMINARY OPERATING INTERVALS OF THE POWER DENSITY FOR COPPER SAMPLES AND FIBRE LASER.

Marking Method	Oxidation	Melting	Evaporation
v, mm/s		q_s, 10^{10} W/m^2	
10	< 0.240	0.240 - 2.32	2.32 - 9.90
20	< 0.339	0.339 - 3.28	3.28 - 9.90
30	< 0.416	0.416 - 4.03	4.03 - 9.90
40	< 0.480	0.480 - 4.65	4.65 - 9.90
50	< 0.537	0.537 - 5.20	5.20 - 9.90
60	< 0.558	0.558 - 5.69	5.69 - 9.90
70	< 0.635	0.635 - 6.15	6.15 - 9.90
80	< 0.679	0.679 - 6.57	6.57 - 9.90
90	< 0.720	0.720 - 6.97	6.97 - 9.90
100	< 0.759	0.759 - 7.35	7.35 - 9.90

TABLE 2. PRELIMINARY OPERATING INTERVALS OF THE POWER DENSITY FOR COPPER SAMPLES AND CUBR LASER.

Marking Method	Oxidation	Melting	Evaporation
v, mm/s		q_s, 10^{10} W/m^2	
10	< 0.160	0.160 - 1.55	1.55 - 6.37
20	< 0.226	0.226 - 2.19	2.19 - 6.37
30	< 0.277	0.277 - 2.88	2.68 - 6.37
40	< 0.320	0.320 - 3.10	3.10 - 6.37
50	< 0.358	0.358 - 3.46	3.46 - 6.37
60	< 0.392	0.392 - 3.79	3.79 - 6.37
70	< 0.423	0.423 - 4.10	4.10 - 6.37
80	< 0.453	0.453 - 4.38	4.38 - 6.37
90	< 0.480	0.480 - 4.65	4.65 - 6.37
100	< 0.506	0.506 - 4.90	4.90 - 6.37

A. Comparison of experimental results for laser marking and laser ablation of copper plates with theoretically obtained results

According to the plan in the methodology, experimental studies were carried out with a fibre laser and a CuBr laser on copper samples. The experiments are for the technological processes of laser marking, laser ablation and laser texturing. A raster way for marking and ablation was applied to 3 copper plates (two plates with fibre laser and one plate with CuBr laser). Obtained experimental results are placed in Figures 2 and 3 with black dots with certain power densities and speeds.

- **Results for fibre laser**

Photographs of the impact zones taken with a laser microscope are given in Fig. 4. Fig. 4a is for laser impact with a fibre laser at power density $q_s = 0.42 \times 10^{10}$ W/m^2 and velocity v = 80 mm/s. Oxidation can be observed on

the treated area. The experimental result is plotted in the first zone, which shows agreement between theory and experiment. Figures 4b is at the power density $q_s = 2.12 \times 10^{10}$ W/m^2 and velocity v = 80 mm/s, and Figure 4c is at the power density $q_s = 3.24 \times 10^{10}$ W/m^2 and velocity v = 40 mm/s. The two results are in area 2 of Fig. 2, which corresponds to melting. From the photographs, melting from laser processing can be observed, which shows a good agreement between the theoretical and experimental results. Laser marking by evaporation, laser ablation and laser texturing was obtained in Fig. 4d. The channels obtained because of the laser processing are clearly outlined. The values $q_s = 8.24 \times 10^{10}$ W/m^2 and v = 80 mm/s locate the treated area in zone 3, corresponding to evaporation. For all the pictures shown in Figure 4, good agreement between theory and experiment is obtained.
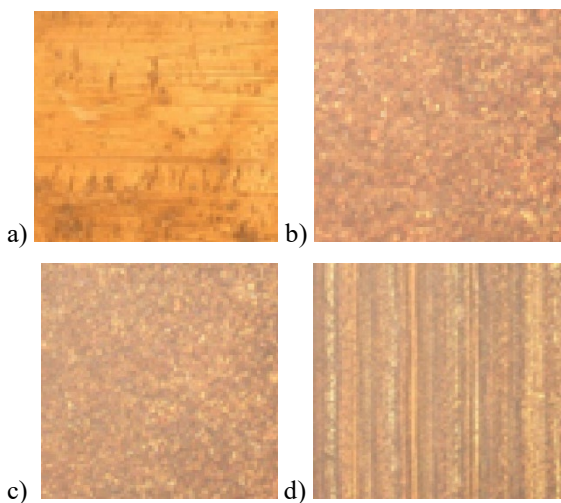

Fig. 4. Areas of impact with a fibre laser: a) oxidation; b) & c) melting; d) evaporation.

- **Results for CuBr laser**

Photographs of the impact zones, also taken with a laser microscope, are presented in Fig. 5. In Fig. 5a laser marking by oxidation is obtained, in Figures 5b and 5c we have laser marking by melting, and in Fig. 5d is obtained laser marking by evaporation, laser ablation and laser texturing. When considering the power densities and velocities, these experimental results are in the correct areas of Fig. 3. Good agreement is again obtained between the theoretical and experimental results. It should be noted that the placement of the black dot in Fig. 5c is close to the plot of the dependence of the critical density of the melting power on the speed. This explains the obtaining of poorly formed channels, which are observed in the photograph.

In the experiments performed with both lasers, the pulse overlap coefficient varied from 86.7% to 98.5%. The pulse energy of the CuBr laser (350 µJ) is much higher than that of the fibre laser (20 µJ), which helps to enable the processes with CuBr laser at lower power densities.
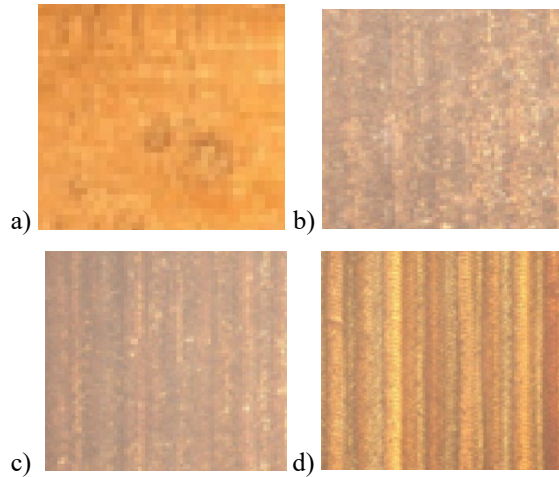
Fig. 5. Areas of impact with a CuBr laser: a) oxidation; b) & c) melting; d) evaporation.

IV. CONCLUSION

In the present work, the following results were achieved when investigating the role of power density for the processes of laser marking, laser ablation and laser texturing of copper samples:

- Preliminary operating intervals of oxidation, melting and vaporization power density for copper samples using a fibre laser have been determined.

- Preliminary operating intervals of oxidation, melting and vaporization power densities for copper samples using a CuBr laser have been determined.

- A good correlation was obtained when comparing experimental results for laser marking, laser ablation and laser texturing of copper wafers with theoretically obtained results.

The preliminary working intervals contribute to increasing the efficiency when conducting the real experiments, because indicate to the researcher in which power density interval they should conduct research for the certain laser process, in the case of laser marking, laser texturing or laser ablation. The resulting operating intervals serve as a basis for optimizing laser processing parameters, ultimately improving the capabilities and applications of laser technology in the production of copper products. Research can also continue for the role of other fundamental quantities such as speed, frequency, pulse duration, pulse energy together with power density on these technological processes with both types of lasers.

REFERENCES

[1] S. Arulvel, R. Dsilva, A. Jain and et.al., "Laser processing techniques for surface property enhancement: Focus on material advancement," *Surfaces and Interfaces,* vol. 42, no. A, November 2023.

[2] J. Helinka and Z. Weltsch, "Analysis of Laser Treated Copper Surfaces," *Periodica Polytechnica Transportation Engineering,* vol. 40, no. 2, pp. 140 - 145, October 2017.

[3] L. Jin, K. Jiang, H. Ren, J. Liu and et.al., "A Review of Laser Cladding on Copper and Copper Alloys," *International Journal of ELECTROCHEMICAL SCIENCE,* vol. 17, 2022.

[4] A. Atanasov and A. Lengerov, "Analysis of the methods for laser marking in mechanical engineering," in *AIP Conference Proceedings*, 2024.

[5] A. A. Siddiqui and A.K. Dubey, "Laser Surface Treatment," IntechOpen, 2020.

[6] T. Mioković, V. Schulze, O. Vöhringer, and D. Löhe, "Influence of cyclic temperature changes on the microstructure of AISI 4140 after laser surface hardening," *Acta Materialia,* vol. 55, no. 2, pp. 589-599, 2007.

[7] A.K. Mondal, S. Kumar, C. Blawert, and Narendra B. Dahotre, "Effect of laser surface treatment on corrosion and wear resistance of ACM720 Mg alloy," *Surface and Coatings Technology,* vol. 202, no. 14, pp. 3187-3198, 2008.

[8] A. Petkova, O. Ganzulenko, S. Gorbatyuk and et.al., "Rationale for Choice of the Laser Marking Modes for Corrosion-Resistant Metals and Alloys," *Metallurgist,* vol. 67, p. 738–748, 2023.

[9] F.O. Olsen and L. Alting, "Pulsed Laser Materials Processing, Nd-YAG versus CO2 Lasers," *CIRP Annals - Manufacturing Technology.,* vol. 44, no. 1, pp. 141-145, 1995.

[10] X. Li and Y. Guan, "Theoretical fundamentals of short pulse laser–metal interaction: A review," *Nanotechnology and Precision Engineering,* vol. 3, no. 3, pp. 105-125, 2020.

[11] M. Xei, F. Li, S. Zhou, L. Lu and et.al., "Effect of laser energy density on microstructure and properties Cu–Fe–P immiscible alloys fabricated by laser selective melting: heterogeneous and high strength and magnetic," *Journal of Materials Research and Technology,* vol. 26, pp. 2759-2769, 2023.

[12] Y. Huang, R. Han, H. Zhang, and C. Zhao, "The effect of laser power and scanning speed on forming structure in selective laser melting process," *Materials Research Express,* vol. 9, no. 5, 2022.

[13] M. Kalyon and B.S. Yilbas, "Laser pulse heating: a formulation of desired temperature at the surface," *Optics and Lasers in Engineering,* vol. 39, no. 1, pp. 109-119, 2003.

[14] L. Dobrzański, A. Dobrzańska-Danikiewicz, T. Tański, E. Jonda and et.al., "Laser Surface Treatment in Manufacturing," in *Handbook of Manufacturing Engineering and Technology*, 2015.

[15] P. Stefanov, N. Minkovski, I. Balchev and et.al., "XPS studies of short pulse laser interaction with copper," *Applied Surface Science.,* vol. 253, pp. 1046-1050, 2006.

[16] G. Zhang, J. Chen, M. Zheng, Z. Yan and et.al., "Element Vaporization of Ti-6Al-4V Alloy during Selective Laser Melting," *Metals,* vol. 10, no. 4, p. 435, 2020.

[17] Y. Zhang and A. Faghri, "Vaporization, melting and heat conduction in the laser drilling process," *International Journal of Heat and Mass Transfer,* vol. 42, pp. 1775-1790, 1999.

[18] C. Zhao, B. Shi, S. Chen, D. Du and et.al., "Laser melting modes in metal powder bed fusion additive manufacturing," *Reviews of Modern Physics,* vol. 94, 2022.

[19] M. Ridolfi, P. Folgarait and A. DiSchino, "Modelling Selective Laser Melting of Metallic Powders," *Metallurgist,* vol. 64, pp. 588-600, 2020.

[20] L. Lazov, N. Petrov and E. Teirumnieks, "Method for preliminary estimation of the critical power density in laser technological processes," in *Environment Technology Resources Proceedings of the International Scientific and Practical Conference*, 2019.

[21] M. Naumova, I. Morozova, A. Zarapin and et.al., "Copper Alloy Marking by Altering its Surface Topology Using Laser Heat Treatment," *Metallurgist,* vol. 62, p. 464–469, 2018.

[22] J. Li, Z. Kuai, Z. Li, B. Liu and et.al., "Effects of Process Parameters on the Relative Density and Properties of CuCrZr Alloy Produced by Selective Laser Melting," *Metals,* vol. 12, no. 5, 2022.

[23] M. G. Naumova, I. G. Morozova, A. Y. Zarapin and P. V. Borisov, "Copper alloy marking by altering its surface topology using laser heat treatment," *Metallurgist,* vol. 62, no. 5-6, 2018.

Investigation of Laser Texturing Parameters and their Impact on Glue Adhesion Properties on the Surface of Birch Plywood

Artis Stanislavs Gusts
Faculty of Engineering
Rezekne Academy of Technologies
Rezekne, Latvia
artisgusts@inbox.lv

Imants Adijāns
Faculty of Engineering
Rezekne Academy of Technologies
Rezekne, Latvia
imants.adijans@rta.lv

Abstract. **Laser technologies are wide-ranging applications in various fields such as manufacturing, medicine, research, entertainment, and more. They are used in processes, such as, for cutting, welding, marking, engraving, surgery, spectroscopy, and many other purposes, owing to their precision, versatility and etc. Birch plywood is a type of manufactured wood product made from thin layers of birch veneer bonded together with special glue under high pressure and heat. It is known for its strength, stability, and visual look, making it a popular material in woodworking, furniture making, construction, and other applications. This study investigates the effect of laser textured treatment on the adhesion properties of birch plywood surface using PVA wood glue. A SUNTOP ST-CC9060 CO_2 laser with a wavelength of 10640 nm was used to texture birch plywood samples with different power and speed parameters, including untreated samples (base). Dino-Lite Edge AM7115MZT digital microscope, and an OLYMPUS LEXT OLS5000 laser microscope were used to measure the samples. The depth and width of the treated area were measured for these samples and graphs were created to analyze the results. Material testing machine Zwick / Roell Z150 was used for tensile and shear analysis of the processed samples. These results show that laser-treated samples have an effect on glue adhesion compared to untreated samples. The study provides valuable insight into the optimization of laser processing parameters in adhesion, and also shows the potential of this type of adhesion to improve the quality of the adhesion properties of laser-treated birch plywood.**

Keywords: Adhesion, birch plywood, CO_2 laser, laser texturing, tensile shear strength.

I. INTRODUCTION

In the 1960s the laser was discovered soon after and is popular in industry especially in material processing such as cutting of engineering structures due to its high-power density and accuracy [1], [2].

Laser texturing is an effective method for the fabrication of surface structures in a single-step process for a large range of applications [3], [4]. Surface functionalities in the field of tribology, wettability etc. introduced by well-defined surface structures strongly depend on the surface texture homogeneity and quality [5]. Laser sources are used in various technological processes such as marking, engraving, cutting, texturing, hardening, welding etc. The process of laser processing is complicated, and it depends on the following groups of factors: laser source parameters, technological process parameters, structure, and physical, chemical properties of the processed material [6], [7].

Wood is one of the most popular and valuable renewable materials. Development of wood-based advanced products comprises an important, exciting, and interesting area of research. Birch plywood has superior mechanical properties compared to plywood made from most softwood species, making it suitable for structural and decorative use. Plywood is also more environmentally friendly, economical and requires less effort than metal plates [8], [9], [10].

Adhesion is the tendency of dissimilar particles or surfaces to bond to one another. The internal forces between molecules that are responsible for adhesion are chemical bonding, dispersive bonding, and diffusive bonding. These intermolecular forces can make cumulative bonding and bring certain emergent mechanical effects [11].

There are several researchers who have investigated laser marking, engraving, and cutting processes on various wood materials, such as birch plywood, pine wood, spruce wood, beech wood, MDF wood etc. [12] – [20]. However, no information is found about the laser treatment of the birch plywood surface and the adhesion of the wood glue.

II. MATERIALS AND METHODS

A. Birch plywood

In the research used a 50 × 50 × 6 (length × width × thickness) laser treated Baltic birch plywood INT FSC B/BB samples. INT means glue intended for interior work, not moisture resistant. FSC is certificate, FSC Latvia | Forest Stewardship Council and B/BB is surface quality of material [21], [22].

Birch plywood (betula spp.) is a hardwood plywood that is widely known for its panel strength, grain texture, durability, and ease of finishing [23]. Baltic birch plywood is composed exclusively of birch veneer (thin sheets of birch wood) compressed and bonded together. Each layer of birch veneer is the same thickness, resulting in a more consistent, void-free, stable, and aesthetically attractive sheet of plywood [24].

B. Equipment

CO_2 laser machine (SUNTOP ST-CC9060) was used for laser texturing of birch plywood samples with a wavelength of 10640 nm (see in Figure 1).

Fig. 1. SUNTOP ST-CC9060 CO_2 laser machine.

The technical specifications of the SUNTOP ST-CC9060 laser machine are showed in Table 1.

TABLE 1. SUNTOP ST-CC9060 LASER MACHINE TECHNICAL SPECIFICATIONS

Laser type	CO_2 laser
Operation mode	CW
Wavelength	10640 nm
Maximum output power	100 W
Workspace (Cutting area)	900 x 600 mm
Precision	0,02 mm
Scan speed	0 – 1000 mm/s
Laser Safety Class	4
Cooling system	Water cooling
Total power	1500 W

For measuring the depth and width of the laser treated samples, we used a Dino-Lite Edge AM7115MZT digital microscope (shown in Figure 2).

Fig. 2. Dino-Lite Edge AM7115MZT digital microscope.

The technical specifications of the digital microscope Dino-Lite Edge AM7115MZT are shown in Table 2.

TABLE 2. DINO-LITE EDGE AM7115MZT MICROSCOPE TECHNICAL SPECIFICATIONS

Operating System	Windows
Resolution	2592 × 1944 pixels
Magnification	20x~220x
Unit Dimension	10.5cm (H) x 3.2cm (D)

The structure changes of the textured birch plywood samples were explored using the Olympus LEXT OLS5000 3D Measuring Laser Microscope, as shown in Figure 3.

Fig. 3. Olympus LEXT OLS5000 3D Measuring Laser Microscope.

These measured sample structures were carried out using 5x magnification with measured area 2580 × 2580 µm ± 5 µm.

For measuring samples for tensile and shear mechanical properties using a Zwick/Roell Z150 testing machine, which is shown in Figure 4.

Fig. 4. Zwick / Roell Z150 material testing machine [25]

C. Methodology

In this experiment, birch plywood samples with dimensions of $50 \times 50 \times 6$ mm (length × width × thickness) were laser textured using three different power densities q_s and five different scanning speeds v. The power densities used for texturing were 0.93, 4.20, 6.71 ($\cdot\ 10^5$) W/cm^2, as listed in Table 4. Each set of parameters was used to texture lines in all sample dimension, with a step Δx of 1 and 0,5 mm between each line. The depth h [mm] and width b [mm] of the textured lines were measured, and graphs were constructed as a function of the laser parameters. Figure 5 shows the texturing schematics of birch plywood samples.
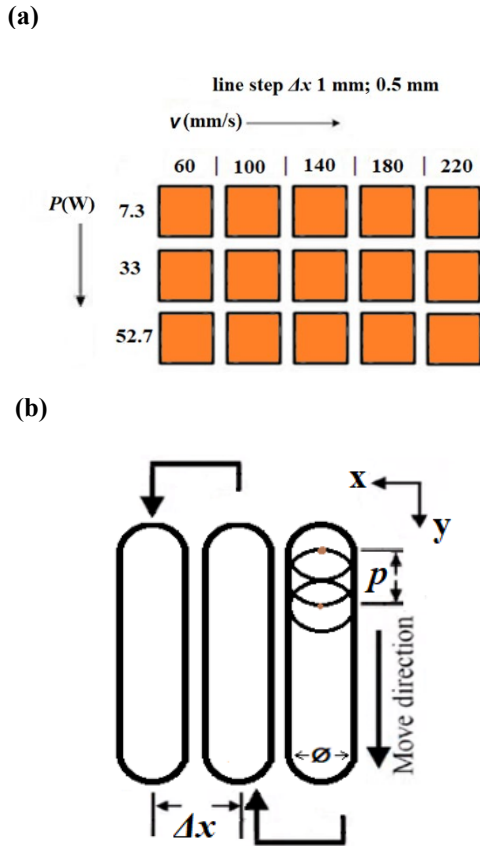
(a)

(b)

Fig. 5.   Laser texturing schematics of birch plywood samples (a), (b).

After laser processing, these samples are glued together by placing one surface of the sample of the processed parameter on the surface of the other sample of the same parameters, in a perpendicular direction. PVA wood glue is used for gluing the samples. Using a professional-mini digital scale with an accuracy of ± 0.01 gram, 0.15 - 0.18 g/mm^2 PVA wood glue was applied to the surface of each sample in an area of 20×50 mm (length × width). Glue is applied to the samples, making sure that the entire sample is correctly glued without leaving marks or gaps. A weight of 1.7 kg was applied to these glued samples for about 20 minutes and then these samples were dried in a dry and clean room for 24 hours. At the time of gluing, the room temperature was 23.8 degrees Celsius, and the relative humidity was 21%.

The power output of the laser was measured using an OPHIR F150A-BB-26 laser power meter before starting the experiment. The recorded power values can be found in Table 3.

TABLE 3. AVERAGE LASER POWER DEPENDENCE ON RESONATOR PUMP COEFFICIENT (KP, %)

κP, %	10	20	30
P, W	7,3	33	52,7

The power density q_s [W/cm^2] was calculated using formula (1):

$$q_s = \frac{P}{S} \qquad (1)$$

where P [W] is the power and S [cm^2] is the cross-sectional area of the laser beam on the surface of the material to be textured, as given in formula (2):

$$S = \pi \frac{d^2}{4} \qquad (2)$$

where d [cm] being the diameter of the laser beam ($d = 0.01$ cm). The calculated power density values in W/cm^2, corresponding to the measured power values in W, which is shown in Table 3, are presented in Table 4.

TABLE 4. CALCULATED LASER POWER DENSITY VALUES FOR THE CO$_2$ LASER MACHINE

P, W	7.3	33	52.7
$q_s \times 10^5$, W/cm^2	0.93	4.20	6.71

To measure the surface structure of textured and tested birch plywood samples used Olympus LEXT OLS5000 3D Measuring Laser Microscope, measurements are shown in Figure 6.

(a)   **(b)**

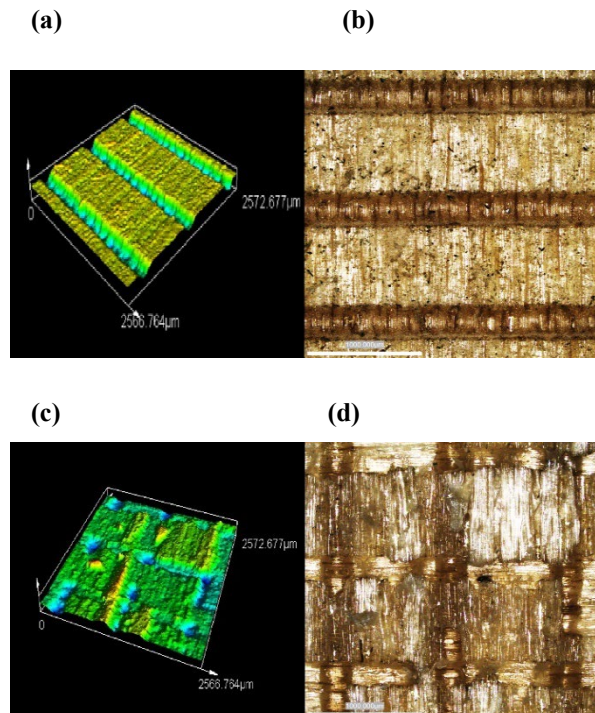**(c)**   **(d)**

Fig. 6.   Effect of laser textured birch plywood structure on the surface: (a) 3D laser scanning microscope image, (b) 2D laser scanning microscope image, (c) 3D laser scanning microscope image after adhesion test, (d) 2D laser scanning microscope image after adhesion test.

Figure 6 shows the effect of laser textured birch plywood samples structures on the surface. In case (a), (b) $q_s = 0.93 \cdot 10^5$ W/cm^2 and v = 100 mm/s and Δx = 1 mm. In case (c), (d) $q_s = 0.93 \cdot 10^5$ W/cm^2 and v = 140 mm/s , and Δx = 0.5 mm.

Texture depth measurement on one of the samples using digital microscope Dino - Lite Edge AM7115MZT is shown in Fig. 6 and width measurement is shown in Fig. 7.
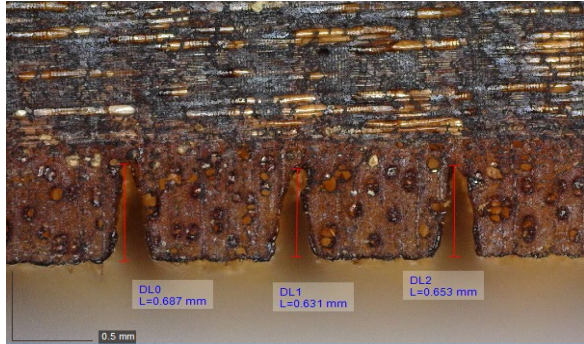

Fig. 7.   Measurement of depth on a birch plywood sample with magnification x100.

Figure 7 shows a laser textured sample with three cuts obtained using a laser power density $q_s = 6.71 \cdot 10^5$ W/cm^2 and scan speed *v* = 220 mm/s and line step Δx = 1 mm. Depth of these cuts are measured and average depth h = 0.622 mm. Total number of measurements of cuts for each power density and scan speed parameter sample is 5.
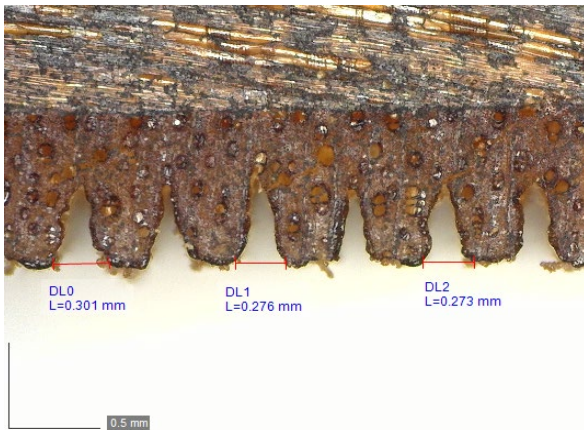

Fig. 8.   Measurement of width on a birch plywood sample with magnification x100.

Figure 8 shows a laser textured sample with six cuts obtained using a laser power density $q_s = 4.20 \cdot 10^5$ W/cm^2 and scan speed v = 220 mm/s with line step Δx = 0.5 mm. Width of these cuts are measured and average width b = 0.293 mm. Total number of measurements of cuts for each power density and scan speed parameter sample is 5.

III.   Results and discussions

The study results are shown in graphs that show the impact of laser power density and scan speed on the depth and width of laser textured lines. Also, the mechanical properties of the glue adhesion of laser textured surfaces, as tensile strength was shown in graphs (Fig. 13. and Fig.

14). The graphs illustrate the relation between line depth and width and maximal tensile strength as a function of energy density and scanning speed for birch plywood samples. Figures 9 and 10 shows dependence of the line depth h on the scan speed v at power density q_s for birch plywood samples with two different line steps Δx 1 mm, Δx 0.5 mm.

Fig. 9.   Dependence of the line depth h on the scan speed v at three different power density q_s for birch plywood samples with line step Δx 1 mm.

As can see in figure 9, the depth on birch plywood sample with $\Delta x = 1$ mm is bigger at scan speed 60 mm/s, and lesser at scan speed v = 220 mm/s. The maximum line depth value is 1.964 mm at power density $q_s = 6.71 \cdot 10^5$ W/cm^2, but minimum line depth value is 0.110 mm at power density $0.93 \cdot 10^5$ W/cm^2.

Fig. 10.   Dependence of the line depth h on the scan speed v at three different power density q_s for birch plywood samples with line step Δx 0.5 mm.

In figure 10, the depth on birch plywood sample with line step 0.5 mm is bigger at scan speed 60 mm/s, and lesser at scan speed 220 mm/s. The maximum line depth value is 1.900 mm at power density $q_s = 6.71 \cdot 10^5$ W/cm^2, but minimum line depth value is 0.109 mm at power density $0.93 \cdot 10^5$ W/cm^2.

From these graphs are showed that there is a linear regularity that increasing the power density q_s increases the depth of the line, increasing the scanning speed *v* decreases the line depth h.

Figures 11 and 12 show the dependence of the line width b on scan speed *v* at three power densities $q_s = 0.93 \cdot 10^5$ W/cm^2, $4.20 \cdot 10^5$ W/cm^2 and $6.71 \cdot 10^5$ W/cm^2 for birch plywood samples with line step Δx = 1 mm (Fig. 11), Δx 0.5 mm (Fig.12).

Fig. 11.   Dependence of the line width *b* on the scan speed *v* at three different power density q_s for birch plywood samples with line step *Δx* 1 mm.
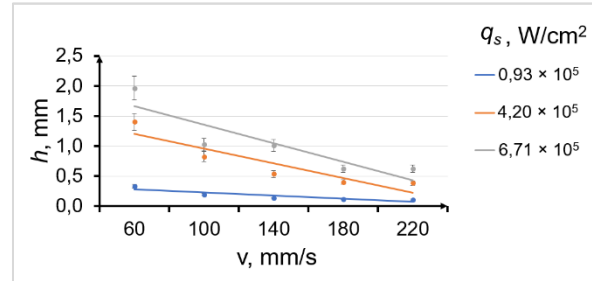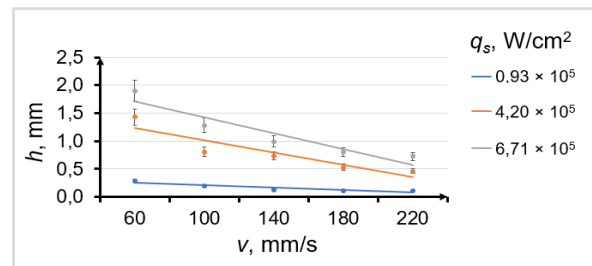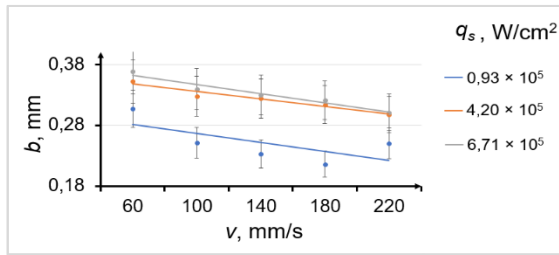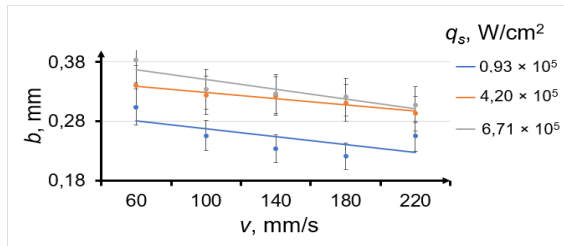

Fig. 12.   Dependence of the line width *b* on the scan speed *v* at three different power density q_S for birch plywood samples with line step *Δx* 0.5 mm.

The graphs on Figures 11 and 12 represent dependence of the line width b with two different line steps *Δx*. The line width at scan speed v = 60 mm/s and power density $0.93 \cdot 10^5$ W/cm^2 is 0.307 mm for birch plywood with line step *Δx* = 1 mm, and 0.304 mm for birch plywood with line step *Δx* = 0.5 mm. Average line width *b* at scan speed v = 220 mm/s and power density $6.71 \cdot 10^5$ W/cm^2 is 0.301 mm for birch plywood with line step *Δx* = 1 mm, and 0.308 mm for birch plywood with line step *Δx* = 0.5 mm. From these graphs are showed that there is a regularity that increasing the power density q_s increases the depth of the line, increasing the scanning speed v decreases the line depth *h*.

It can be seen from these graphs that the changes of line width with power density and scan speed are linear and small, the line width being slightly smaller at lower power density and larger at higher power density.

Figure 13 show the dependence of the maximal tensile strength F_{max} on scan speed *v* at three power densities q_s for birch plywood samples with line step *Δx* = 1 mm. These treated samples are compared to untreated (base) samples.

The average maximum tensile strength F_{max} value for untreated (base) samples is 3598 N. Number of measurements of tensile strength tests for base samples is 5.
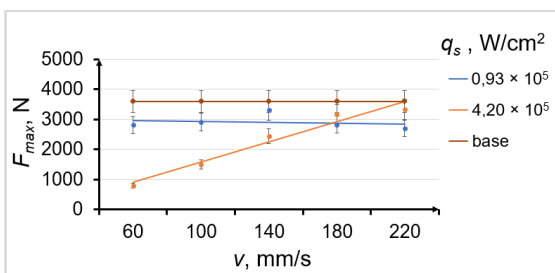
Fig. 13.   Dependence of the maximal tensile strength F_{max} on the scan speed *v* at three different power density q_s for birch plywood samples with line step *Δx* 1 mm.

In Figure 13, the maximum tensile strength value F_{max} for textured samples is 3338 N at power density $4.20 \cdot 10^5$ W/cm^2, and scan speed 220 mm/s but minimum line depth value is 805 N at power density $4.20 \cdot 10^5$ W/cm^2 and scan speed 60 mm/s.

Figure 14 represent the dependence of the maximal tensile strength F_{max} on scan speed *v* at two power densities for birch plywood samples with line step *Δx* 0.5 mm which is compared to untreated (base) samples.
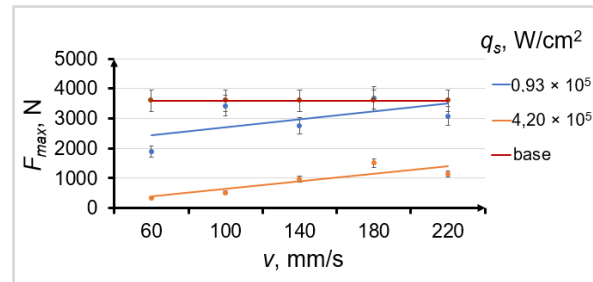
Fig. 14.   Dependence of the maximal tensile strength F_{max} on the scan speed v at two different power density q_S for birch plywood samples with line step *Δx* 0.5 mm.

In Figure 14, the maximum tensile strength value F_{max} for textured samples is 3690 N at power density $0.93 \cdot 10^5$ W/cm^2, and scan speed 180 mm/s but tensile strength value is 349 N at power density $4.20 \cdot 10^5$ W/cm^2 and scan speed 60 mm/s. These graphs result also are changing linearly (Fig 13. and Fig. 14.)

IV. CONCLUSION

In this study are investigated the laser texturing process the effects of power density and scan speed on the depth and width of textured lines at different line steps on birch plywood samples, which is shown in figures 9. – 12. The results showed that the depth of textured lines is affected by both power density and scan speed, with higher power densities and lower scan speeds leading to deeper lines. Also, studies of the mechanical properties of the glue adhesion of laser textured surfaces, as tensile strength, were carried out. These results are shown in figures 13., 14. The results show that the adhesion remains higher as the scanning speed increases and decreases power density. Line step also affects the adhesive properties of the glue, as was shown in the results. The textured glued samples were compared to untreated glued samples. It was concluded that samples with a power density of $0.93 \cdot 10^5$ W/cm^2 and a scanning speed of 180 mm/s and a line step of 0.5 mm have better adhesion than untreated samples. Other textured samples have similar or smaller adhesion comparing untreated (base) samples.

The results of this study could have a real and significant impact on the use of laser processing in the woodworking industry, especially in the production of decorative or functional wooden items such as panels.

In further research could investigate the effect of laser parameters such as power density and scan speed on the bonded surface in a sample of untreated birch plywood. As well as to further investigate the effect of laser treatment with other parameters of power density, scan speed and

line step. In addition, more detailed analyzes could be performed to investigate the microstructural changes that occur in the glued surface of birch plywood during the laser texturing process, as well as the effect of different types of power density and scan speed parameters on texturing and adhesive results.

REFERENCES

[1] H. A. Eltawahni, N. S. Rossini, M. Dassisti, K. Alrashed, T. A. Aldaham, K. Y. Benyounis and A. G. Olabi, "Evalaution and optimization of laser cutting parameters for plywood materials, " Optics and Lasers in Engineering, vol. 51(9), pp. 1029–1043, Sep. 2013.

[2] L. Lazov, E. Teirumnieks, N. Angelov, E. Teirumnieka, "Methodology for automatic determination of contrast of laser marking for different materials," Environment, Technology, Resources, vol. III, pp. 134–136, June 2019.

[3] A. Y. Vorobyev and C. Guo, "Direct femtosecond laser surface nano/microstructuring and its applications," Laser & Photonics Reviews, vol. 7(3), pp. 385–407, May 2013.

[4] L. Lazov, E. Teirumnieks, T. Karadzhov, and N. Angelov, "Influence of power density and frequency of the process of laser marking of steel products," Infrared Physics & Technology, vol. 116, 103783, Aug. 2021.

[5] A. I. Aguilar-Morales, S. Alamri, T. Kunze and A. F. Lasagni, "Influence of processing parameters on surface texture homogeneity using Direct Laser Interference Patterning," Optics & Laser Technology, vol. 107, pp. 216–227, Nov. 2018.

[6] L. Lazov, H. Deneva and P. Narica, "Factors influencing the color laser marking," Environment, Technology, Resources, vol. 1, pp. 102–107, June 2015.

[7] N. Angelov, E. Teirumnieks and L. Lazov, "Influence of pulse duration on the process of laser marking of CT80 carbon tool steel products," Laser Physics, vol. 31(4), 045601, Apr. 2021.

[8] P. Narica, L. Lazov, A. Teilans, P. Grabusts, E. Teirumnieks and P. Cacivkins, "Method for color laser marking process optimization with the use of genetic algorithms," Environment, Technology, Resources, vol. 2, pp. 101–106, June 2017.

[9] Md. Nazrul Islam, Atanu Kumar Das, Md Morsaline Billah, Khandkar-Siddikur Rahman, Salim Hiziroglu, Nobuaki Hattori, David A. Agar, and Magnus Rudolfsson, "Multifaceted Laser Applications for Wood – A Review from Properties Analysis to Advanced Products Manufacturing," Lasers in Manufacturing and Materials Processing, vol. 10(16), pp 1-26, Feb. 2023.

[10] Y. Wang, T. Wang, R. Crocetti, M. Schweigler and M. Wålinder, "Embedment behavior of dowel-type fasteners in birch plywood: Influence of load-to-face grain angle, test set-up, fastener diameter, and acetylation," Construction and Building Materials, vol. 384, 131440, June 2023.

[11] O. Ülker, Wood Adhesives and Bonding Theory. Adhesives - Applications and Properties, Chapter 11, pp. 271-288, Nov. 2016. Available: https://www.doi.org/10.5772/65759 [Accessed January 17, 2024]

[12] J. Kúdela, I. Kubovský, and M. Andrejko, "Surface Properties of Beech Wood after CO_2 Laser Engraving," Coatings, 10(1): 77, Jan. 2020.

[13] S. M. Hasan, K. A. Hubeatir, and Abd. Sh. Dhuha, "Effect of CO_2 laser parameters on redwood engraving process complemented by Taguchi method," Materials Today: Proceedings, vol. 42, pp. 2566–2572, 2021.

[14] Juan Carlos Hernández-Castañeda, H. Kursad Sezer and Lin Li, "The effect of moisture content in fibre laser cutting of pine wood," Optics and Lasers in Engineering, vol. 49(9-10), pp. 1139–1152, Sept. – Oct. 2011.

[15] X. Guo, M. Deng, Y. Hu, Y. Wang, and T. Ye, "Morphology, mechanism, and kerf variation during CO_2 laser cutting pine wood," Journal of Manufacturing Processes, vol. 68, pp. 13–22, Aug. 2021.

[16] M. Gaff, F. Razaei, A. Sikora, Š. Hýsek, M. Sedlecký, G. Ditommaso, … and K. Řipa, "Interactions of monitored factors upon tensile glue shear strength on laser cut wood," Composite Structures, vol. 234, 111679, Feb. 2020.

[17] I. Kubovský, L. Kristak, J. Suja, M. Gajtanska, R. Igaz, I. Ružiak, and R. Réh, "Optimization of Parameters for the Cutting of Wood-Based Materials by a CO_2 Laser," Applied Sciences, vol. 10(22):8113, Nov. 2020.

[18] H. A. Eltawahni, A. G. Olabi and K. Y. Benyounis, "Investigating the CO_2 laser cutting parameters of MDF wood composite material," Optics & Laser Technology, vol. 43(3), pp. 648–659, Apr. 2011.

[19] J. Kúdela, M. Andrejko and I. Kubovský, "The Effect of CO_2 Laser Engraving on the Surface Structure and Properties of Spruce Wood," Coatings 2023, vol. 13(12), Nov. 2023.

[20] L. Lazov, P. Narica, J. Valiniks, A. Pacejs, H. Deneva, and D. Klavins, "Optimization of CO_2 Laser Parameters for Wood Cutting," Environment. Technology. Resources, vol. 3, pp. 168-173, June 2017.

[21] "Visu_veidu_produktu_virsmu_isais_skaidrojums.pdf" [Online]. Available: https://www.finieris.lv/docs/E-veikals/Visu_veidu_produktu_virsmu_isais_skaidrojums.pdf [Accessed January 18, 2024].

[22] "FSC.pdf" [Online]. Available: https://www.finieris.lv/docs/Produkti/sertifikati/FSC.pdf [Accessed January 18, 2024].

[23] Birch Plywood | Birch Plywood Construction [Online]. Available: https://www.patriottimber.com/ [Accessed January 19, 2024].

[24] All About Baltic Birch Plywood - Forests Plywood [Online]. Available: https://forestplywood.com/ [Accessed January 19, 2024].

[25] AllroundLine floor-standing testing machine | ZwickRoell, [Online]. Available: https://www.zwickroell.com/products/static-materials-testing-machines/universal-testing-machines-for-static-applications/allroundline/ [Accessed January 25, 2024].

Influence of Technological Parameters on Laser Marking Process of Copper Surfaces

Vitālijs Jurčs
Faculty of Engineering
Rezekne Academy of Technologies
Rēzekne, Latvia
vj17017@edu.rta.lv

Emil Yankov
Faculty of Engineering
Rezekne Academy of Technologies
Rēzekne, Latvia
Emil.yankov@rta.lv

Nikolay Angelov
Department of MINS
Technical University of Gabrovo
Gabrovo, Bulgaria
angelov_np@abv.bg

Antons Pacejs
Faculty of Engineering
Rezekne Academy of Technologies
Rēzekne, Latvia
Antons.pacejs@rta.lv

Imants Adijāns
Faculty of Engineering
Rezekne Academy of Technologies
Rēzekne, Latvia
Imants.adijans@rta.lv

Abstract. **Laser marking technology today is a key part of the production of many products and devices used in our daily lives. At the same time, for specific types of products, the process must be optimized depending on the material used, laser system and marking method. Copper is such a metal that has a number of applications in the military industry, electrical engineering, electronics, household, etc. The scientific report investigates the influence of the technological parameters speed, raster step and number of repetitions on the contrast and roughness of marking for copper samples. A fiber laser technology system was used to perform the experiments, and the roughness measurements were performed with an OLS 5000 laser microscope. A wide range of marking speeds from 10 mm/s to 1500 mm/s was selected, where the contrast and roughness behavior of the marking is tracked for different raster steps in both single marking and double marking. It was found that as the speed increased, the contrast and roughness decreased. Also, with double marking, the contrast and roughness values are higher than with single marking. The velocity intervals in which the contrast has positive values and those in which it has negative values are established. The regularity was obtained that increasing the step of the raster leads to a decrease in contrast and an increase in roughness.**

Keywords:- Copper, Laser marking, Contrast, Roughness, Speed, Raster step

I. INTRODUCTION

One of the early applications of lasers was the marking of various mechanical and electronic components. One of the well-known and practical methods in modifying the surface of a material is Laser Surface Modification[1]. Today, laser marking has found its place in a wide range of specific industrial applications [2], [3], [4]. This is due to the fact that every single product cannot appear on the market without having its identification (logo, serial number, etc. alphanumeric information). In laser marking technology, a process of interaction of a laser beam with the surface of the material is implemented in order to change it or cause melting and evaporation, creating a certain informational design on the surface [5], [6]. This process enables precise marking on a variety of materials, from metals to plastics, without direct contact [7]. Today, we can say that laser marking has become an essential tool in multiple industries, thanks to advances in technology and its flexibility [8].

The use of fiber lasers and Nd:YAG lasers has become common practice, providing effective processing alternatives to traditional marking methods. The new systems can adapt to different geometries, expanding the possibilities for 2D and 3D laser marking [9]. Laser marking technology is critical for embedding unique data such as QR codes on products. This is how traceability is realized through all stages of production, and also from the manufacturer and warehouses to the end user[10].

Copper is an engineering material with excellent thermal and electrical properties that has wide applications in mechanical engineering, electronics, the defense sector and computer technology.[11] Copper materials used in these industry sectors, such as 3D integrated circuits (ICs) and electrical contact material, face severe corrosion and poor mechanical properties. Laser marking of surfaces on metal substrates is an effective method of protection against corrosion as well [12]. Many superhydrophobic films produced on a copper substrate do improve its corrosion resistance. However, they often further reduce

the mechanical strength of the surface. Common strategies for realizing laser marking do not reduce the mechanical strength of the substrate [13].

This work develops an experimental method for laser marking on the surface of copper samples, with the focus of research on the influence of the technological parameters speed, raster step and number of repetitions on the contrast and roughness of copper sample marking.

II. MATERIAL AND METHODS

A. Material

Physically, the copper surface has its own values of absorption of light radiation. The copper light spectrum that is mostly absorbed is in the blue-green region, that is, at wavelengths from 450 nm to 570 nm of the radiation spectrum. The coefficient of surface reflection is $R=1-A$, that is higher for copper shown in Table 1[14].

TABLE 1: REFLECTANCE OF VARIOUS MATERIALS COMPARED TO COPPER'S REFLECTIVITY.

Material (Symbol)	Iron (Fe)	Copper (Cu)	Aluminium (Al)	Gold (Au)
reflectivity (R)	0.63	0.91	0.93	0.98

B. Anticipating Value

Materials contrast measurements theoretically could be defined as variation of spectral brightness of the laser processed and un-processed are of the surface. Contrast variable k_x^* is determined in relative values on percentages on defined reference scale.[15] Reference number N_f is determined for the image of the surface around the untouched area around matrix. And from the processed area, a N_x value is obtained. The contrast k_x^* is determined by linear interpolation from the expression (1).

$$k_x^* = \frac{N_f - N_x}{N_f} \times 100\% \qquad (1)$$

where:

N_f – The measured value of an untreated area (unmarked area).

N_x – Measured value in the laser-treated area (marked area).

C. Laser Source for Processing

For study processing was used Rofin powerline laser system, which is diode pumped Ytterbium (Yb) fibre laser operating at impulse mode. In table 2 listed important parameters of laser system, that were used for surface treatment in experiments.
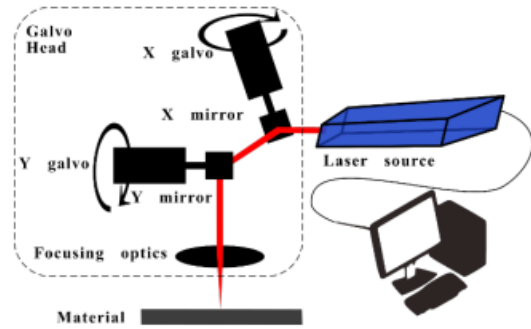
Figure 1: Schematic view of Rofin powerline laser system

TABLE 1: PARAMETERS OF USED LASER SYSTEM

Symbol	Name	Values range	Units
v	Scan speed	1 — 20000	mm/s
P	Average power	0 — 19,7	W
v	Impulse frequency	20 — 1000	kHz
τ	Impulse length	4 - 200	ns
λ	Wavelength	1064	nm
d	Focal spot size	40	μm
	Working area	120 x 120	mm^2

D. Measurement device

"Lext" 3D Laser Measuring Microscope OLS 5000 was used for measurements of laser processing impact on the materials surface. In this case after laser processing, we measured the width and depth of laser beam influence on the material.

Figure 2: Photography of Lext" 3D Laser Measuring Microscope OLS 5000

Measurements were made using MPLFNN10XLEXT lens with x20 objective, and summary 451x zoom, numerical aperture (N.A. 0.6, working distance of 1mm, focusing spot diameter at 0.4 μm, measured field range at 640 μm x 640 μm and following technical data was given from manufacturer:

- Z measurement pitch: 2 μm;
- Z axis measurement accuracy: 0.15+L/20 μm;
- X and Y axis resolution: +/- 1.5%.
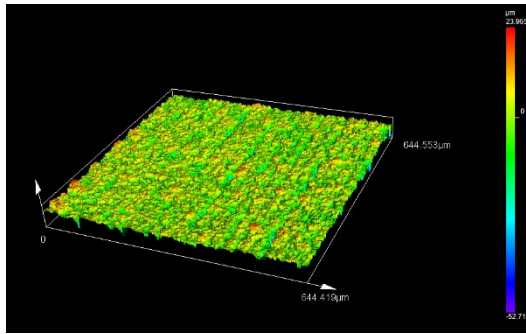
Figure 3. 3D surface field model of roughness.

E. Methodology

The study process was carried out on three polished copper plates with fibre laser of processed field 180 mm x 100 mm x 0.8 mm. According to processing steps was labelled as sample 1 and sample 2. On first steps was tested laser processing parameters that was studied in other papers according to copper surface treatment.

Plates was prepared by laser cutting and cleared with C_3H_7OH and blown with a stream of dry air to remove all debris that may affect the following measurements. Marked samples were stored in individual sealed air-tight bags.

The texturing parameters of the plates are shown below:

The processing of a copper sample 1 is carried out with the values of the parameters in Table 3. The processing speed (v, mm/s) and the raster pitch ($Δx$, μm) are changed, and the other parameters are kept constant. The designed matrix from Fig. 4 is realized. The size of each square is 5 mm x 5 mm with a distance between adjacent squares of 2 mm. Number of marking repetitions is 1 (one-time raster marking).

TABLE 2: LASER PARAMETERS FOR MARKING OF SAMPLE 1

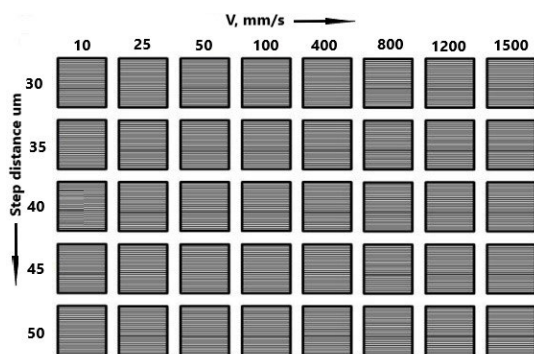| Parameter	Value
Pulse Duration ($τ$)	100 ns
Raster Step ($Δx$)	30, 35, 40, 45 and 50 μm
Speed (v)	10, 25, 50, 100, 400, 800, 1200, and 1500 mm/s
Power (P)	10 W
Frequency (v)	20 kHz
Focal Length (F)	184 mm

Figure 4: The designed matrix for performing the experiments on sample 1 and sample 2

The processing of a copper sample 2 is carried out with the same values of the parameters in Table 3. Number of marking repetitions is 2 (double raster marking with angles 0º and 90º). The designed matrix from Fig. 4 is realezed. The size of each square is 5 mm x 5 mm with a distance between adjacent squares of 2 mm.

III. RESULTS AND DISCUSSIONS

The machined samples of copper plates presented in Fig. 5 and fig. 6 were examined under a laser microscope to analyze surface changes, texture formation and several other analytical results. To measure surface contrast, plates were scanned with a scanner and formatted in .tif format. The required format image of each textured sample square was analysed with Adobe Photoshop CS4 for the N_f and N_x values to be determined. Areas and plaques not marked were removed from the study and the analysis was narrowed. Scanned photos and their graphic images follow below.

The experimental matrix of Fig. 5 is obtained for different values of the speed (horizontal) and the raster pitch (vertical). The specific values of these two quantities are presented in Table 3. A one-time raster marking was done. The dependence of the contrast of the mark on the speed for three raster steps is given in Fig. 7 as Fig. 7a is for speeds from 10 mm/s to 100 mm/s, and Fig. 7b is for speeds from 100 mm/s to 1500 mm/s. Analysis of the graphs shows that:

- **For interval of speed from 10 mm/s to 100 mm/s**

the contrast changes from 61.8 % to 7.50 % for a raster step of 30 μm;
the contrast is changed from 56.5 % to 5.50 % for a raster step of 40 μm;
the contrast changes from 52.8 % to 3.50 % for a raster step of 50 μm;

- In this interval, the marked images are darker than the unmarked surface and the contrast has positive values. The power density of laser radiation is above the critical power density of melting, and the process is laser marking by melting;

- **For interval of speed from 400 mm/s to 1500 mm/s**

the contrast changes from -14.0 % to -21.5 % for a raster step of 30 μm;
the contrast changes from -17.5 % to -25.0 % for a raster step of 40 μm;
the contrast changes from -21.0 % to -28.5 % for a raster step of 50 μm;

- In this interval, the marked images are lighter than the unmarked surface and the contrast has negative values. The power density of laser radiation is below the critical power density of melting, and the process is laser marking by oxidation.
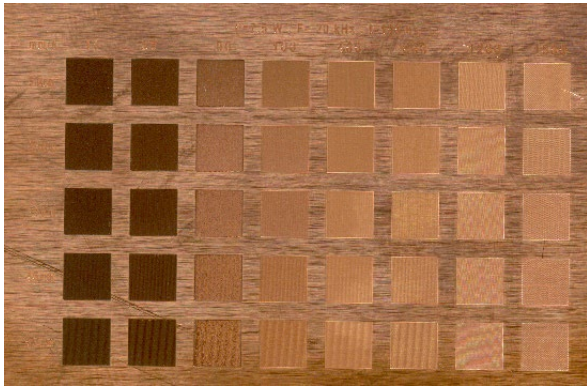
Figure 5: The experimental matrix with one-time marking
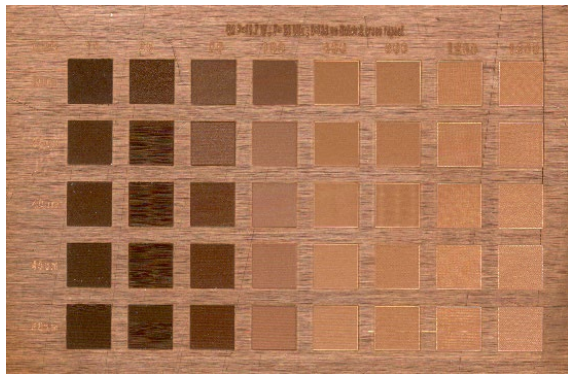
Figure 6: The experimental matrix with double marking
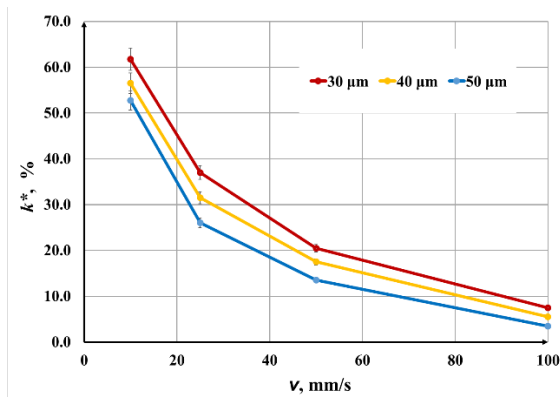
Figure 7a: Graphics of the dependence of the contrast on the speed from 10 mm/s to 100 mm/s for three powers for one-time marking
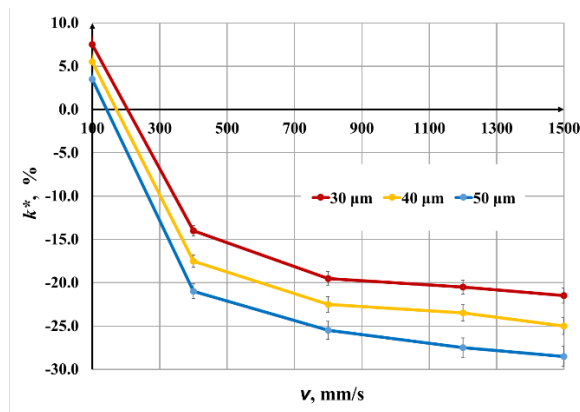
Figure 7b: Graphics of the dependence of the contrast on the speed from 100 mm/s to 1500 mm/s for three powers for one-time marking

The experimental matrix in Fig. 6 is again for different values of speed (horizontal) and raster pitch (vertical), which are the same as for the experimental matrix in Fig. 5.

The difference is that in this case cross-marking is applied twice (at angles 0º and 90º). The velocity dependence of the mark contrast for three raster steps is shown in Fig.8 with Fig.8a for speeds from 10 mm/s to 100 mm/s and Fig.8b for speeds from 100 mm/s. s to 1500 mm/s. From the analysis of the drawn graphs it follows:

- As the speed increases, a non-linear decrease in contrast is observed for the three investigated raster pitches.
- As the raster pitch increases, a decrease in contrast is observed;
- **For interval of speed from 10 mm/s to 100 mm/s**

the contrast changes from 66.8 % to 14.5 % for a raster step of 30 µm;

the contrast is changed from 62.5 % to 10.5 % for a raster step of 40 µm;

the contrast changes from 59.8 % to 8.50 % for a raster step of 50 µm;

- The obtained contrast values for double marking are about 12% higher than for one-time marking;
- In this interval, the marked images are darker than the unmarked surface and the contrast has positive values. Raster marking by melting is realized;
- **For interval of speed from 400 mm/s to 1500 mm/s**

the contrast varies from -9.0 % to -19.5 % for a raster step of 30 µm;

the contrast changes from -11.5 % to -21.5 % for a raster step of 40 µm;

the contrast changes from -14.0 % to -24.5 % for a raster step of 50 µm;

- In this interval, the marked images are lighter than the unmarked surface and the contrast has negative values. The process that has been carried out is laser marking by oxidation.

Figure 8a: Graphics of the dependence of the contrast on the speed from 10 mm/s to 100 mm/s for three powers for double marking
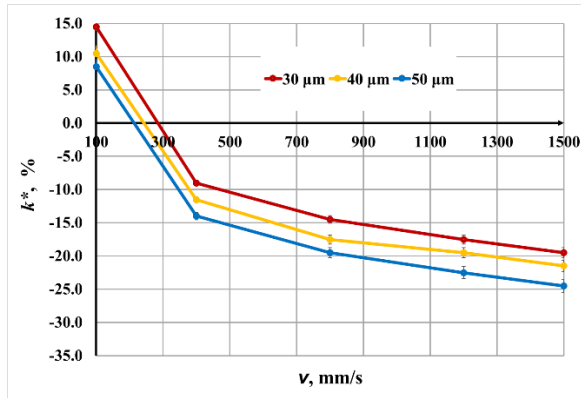
Figure 8a: Graphics of the dependence of the contrast on the speed from 100 mm/s to 1500 mm/s for three powers for double marking

A microscopic image of an unmarked area is given in Fig. 9a. In Fig. 9b is a microscopic image of a one-time raster marked area with parameters speed v = 1500 mm/s and step Δx = 30 μm. The parameters held constant are given in Table 3. The process of laser marking by oxidation has been realised, because the power density of the laser radiation is below critical for this speed.
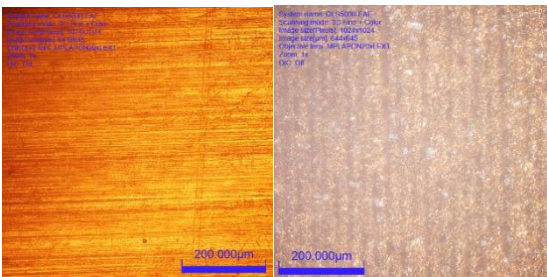
Figure 9: Laser microscope image of a) unmarked surface, b) one-time raster marked square.

The dependence of the roughness on the speed for three raster pitches for one-time marking is presented in Fig. 10. In Fig. 10a shows this dependence in the speed interval from 10 mm/s to 100 mm/s, and in Fig. 10b – from 100 mm/s to 1500 mm/s. These patterns follow the analysis of the graphics:

•   Low speed processing surface roughness values are drastically higher that processing at high speeds.

•   As the speed increases from 10 mm/s to 25 mm/s, the roughness increases sharply, at a speed of 25 mm/s the roughness becomes maximum;

•   At speeds from 25 mm/s to 100 mm/s, the roughness decreases sharply, and at speeds from 100 mm/s to 400 mm/s, the decrease in roughness is smoother. In the interval from 400 mm/s to 1500 mm/s the roughness does not change (see Fig. 10b);

•   About 50% lower roughness difference is obtained at raster pitch 30 μm versus 50 μm.
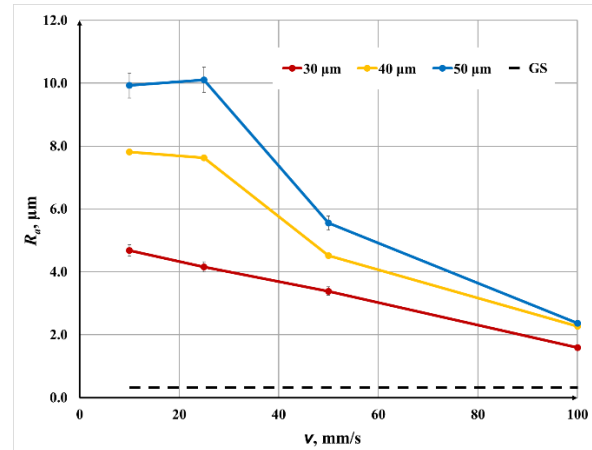
Figure 10a: Graphics of the dependence of the roughness on the speed from 10 mm/s to 100 mm/s for three raster steps for one-time marking
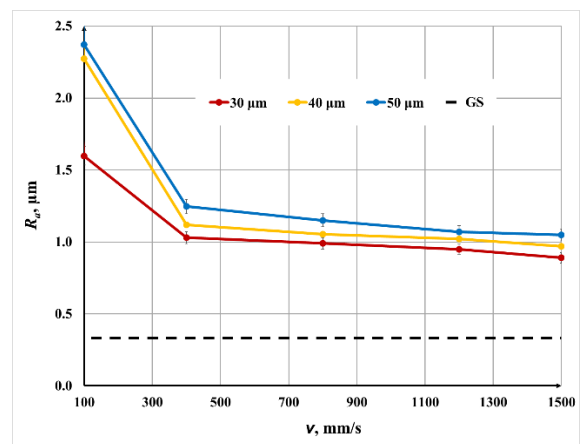
Figure 10b: Graphics of the dependence of the roughness on the speed from 100 mm/s to 1500 mm/s for three raster steps for one-time marking

The dependence of the roughness on the speed for three raster pitches for double marking (with angles 0° and 90°) is shown in Fig. 10. In Fig. 10a gives this dependence in the speed interval from 10 mm/s to 100 mm/s, and in Fig. 10b – from 100 mm/s to 1500 mm/s. These patterns follow the analysis of the graphics:

•   Again as with single marking, for a speed of 10 mm/s to 25 mm/s the roughness increases sharply, for a speed of 25 mm/s to 400 mm/s the roughness decreases, and for a speed of 400 mm/s to 1500 mm/s the roughness does not change.

•   As the raster pitch increases, the roughness increases;

•   When comparing the roughness for double marking compared to one-time marking, it can be seen that double marking roughness is significantly greater than that of one-time marking, all other parameters being equal. It is 40-90% greater in the speed interval from 25 mm/s to 100 mm/s.
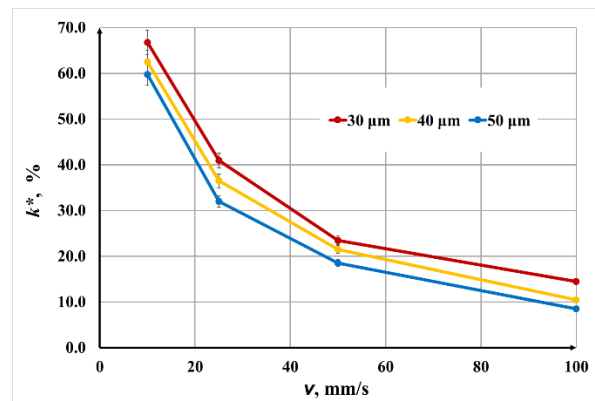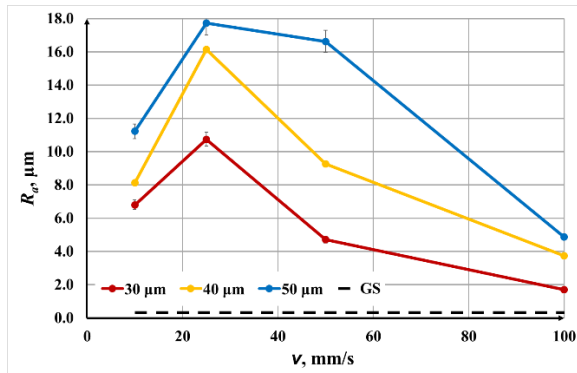
Figure 11a: Graphics of the dependence of the roughness on the speed from 10 mm/s to 100 mm/s for three raster steps for double marking
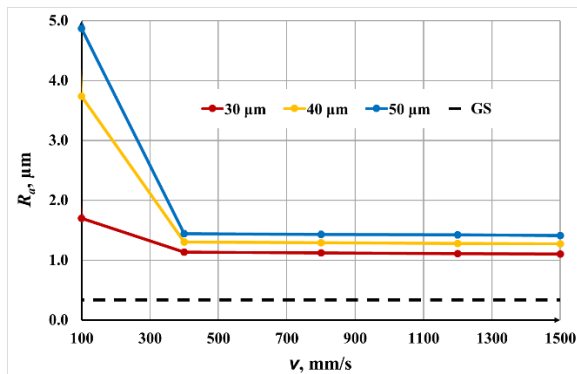
Figure 11b: Graphics of the dependence of the roughness on the speed from 100 mm/s to 1500 mm/s for three raster steps for double marking

IV. Conclusions

In the scientific report, the influence of speed, raster step and number of repetitions on the contrast and roughness of the marking was investigated, and some regularities were established:

- with increasing speed, a non-linear decrease in contrast is observed for the three investigated raster steps. In the speed range from 10 mm/s to 100 mm/s the contrast is positive (darker marking than unmarked areas) and in the speed range from 400 mm/s to 1500 mm/s the contrast is marking (lighter marking from the unmarked areas);
- as the raster step increases, the contrast decreases, with the contrast for the 30 μm raster step being about 10% higher than the contrast for the 40 μm raster step and about 15% higher than the contrast for the 50 μm raster step;
- with double marking, the regularities are the same, but with higher contrast values;
- in one-time and double marking for speeds from 10 mm/s to 25 mm/s the roughness grows and for a speed of 25 mm/s it reaches a maximum, and in from 25 mm/s to 400 mm/s the roughness decreases. For speeds from 400 mm/s to 1500 mm/s, the roughness hardly changes;
- As the raster step increases, the roughness increases for both one-time and double marking.

The quality of the marking strongly depends on the contrast and roughness of the marked surface, which must be within certain limits for its perception (visually and with readers and obtaining a marker with a certain colour or instances of this colour. Therefore, it is necessary to establish the influence of other parameters on contrast and roughness such as effective energy, pulse energy, pulse power and overlap coefficients (pulsed and scanning). Such studies would contribute to a more complete definition of the limits of the technological parameters necessary to achieve a high quality of the resulting marking.

References

[1]. A Q Zaifuddin1 , M H Aiman1, M M Quazi1 , Mahadzir Ishak1 ,T Ariga "Effect of Laser Surface Modification (LSM) on laser energy absorption for laser brazing" Materials Science and Engineering 788 (2020) 012013, doi:10.1088/1757-899X/788/1/012013

[2]. Narica P., Lazov L., Teilans A., Grabusts P., Teirumnieks E., Cacivkins P., Method for color laser marking process optimization with the use of genetic algorithms, (2017) Vide. Tehnologija. Resursi - Environment, Technology, Resources, 2, pp. 101 - 106, DOI: 10.17770/etr2017vol2.2607

[3]. Lazov L., Teirumnieks E., Karadzhov T., Angelov N., Influence of power density and frequency of the process of laser marking of steel products, Infrared Physics and Technology, 116, art. no. 103783, (2021), DOI: 10.1016/j.infrared.2021.103783

[4]. Teirumnieks E., et. al., Methodology for automatic determination of contrast of laser marking for different materials, Vide. Tehnologija. Resursi - Environment, Technology, Resources, 3, pp. 134 - 136, (2019), DOI: 10.17770/etr2019vol3.4143

[5]. Deneva H., Narica P.,et.al., Factors influencing the color laser marking, (2015) Vide. Tehnologija. Resursi - Environment, Technology, Resources, 1, pp. 102 - 107, DOI: 10.17770/etr2015vol1.223

[6]. Angelov, N., et. al., Influence of pulse duration on the process of laser marking of CT80 carbon tool steel products, Journal, Laser Physics, 31(4):045601, DOI:10.1088/1555-6611/abe5af

[7]. Todorov D.N., Shterev I.J., Nikolaeva P.M., Angelova B.D., Study of laser cutting and marking on the filt with the help of a CO_2-laser, Vide. Tehnologija. Resursi - Environment, Technology, Resources, 3, pp. 143 - 147, (2019), DOI: 10.17770/etr2019vol3.4202

[8]. Balchev I., Atanasov A.,et.al., Investigation of the influence of the scanning speed and step in laser marking and engraving of aluminum, (2021) Journal of Physics: Conference Series, 1859 (1), art. no. 012002, DOI: 10.1088/1742-6596/1859/1/012002

[9]. Lazov L., Teirumnieka E., Angelov N., Yankov E., Modification of the roughness of 304 stainless steel by laser surface texturing (LST), (2023) Laser Physics, 33 (4), art. no. 046001, DOI: 10.1088/1555-6611/acbb76

[10]. Lazov L.K., Petrov N.A., Investigation of the impact of the number of repetitions and the defocus on the contrast of laser marking for products made of tool steel, Metallofizika i Noveishie Tekhnologii, 34 (7), pp. 1003 - 1011,(2012)

[11]. M.R. Akbarpour, F. Gazani, H. M. Mirabad, I. Khezri "Recent advances in processing, and mechanical, thermal and electrical properties of Cu-SiC metal matrix composites prepared by powder metallurgy", Progress in Materials ScienceVolume 140, December 2023. 101191. https://doi.org/10.1016/j.pmatsci.2023.101191

[12]. Risham Singh Ghalot, et al., Investigation of the Change in Roughness and Microhardness during Laser Surface Texturing of Copper Samples by Changing the Process Parameters, 2023, Coatings, 13(11):1970, DOI:10.3390/coatings13111970

[13]. L. Lazov and N. Angelov, "OPTIMISATION OF THE PROCESS OF LASER MARKING OF PRODUCTS MADE OF TOOL STEEL," Contemporary Materials, vol. III, no. 1, pp. 189-193, 2012.

[14]. Gachot C, Rosenkranz A, Hsu S, Costa H. A critical assessment of surface texturing for friction and wear improvement. Wear 2017; 372:21–41. https://doi.org/10.1016/j.wear.2016.11.020.

[15]. Smith, John K. "Why Copper Is Reddish in Colour: Comparing Copper, Silver, and Gold." *Journal of Materials Science*, vol. 15, no. 3, 2020, pp. 102-115. DOI: 10.1234/jms.2020.01234

Investigation Fiber Laser Effects on Titanium Gr2: Color marking and Surface Roughness

Jēkabs Lapa
Rezekne Academy of Technologies
Faculty of engineering
Rēzekne, Latvia
jekabs.lapa@gmail.com

Imants Adijāns
Rezekne Academy of Technologies
Faculty of engineering
Rēzekne, Latvia
imants.adijans@rta.lv

Emil Yankov
Rezekne Academy of Technologies
Faculty of engineering
Rēzekne, Latvia
emil.yankov@rta.lv

Lyubomir Lazov
Rezekne Academy of Technologies
Faculty of engineering
Rēzekne, Latvia
lyubomir.lazov@rta.lv

Ritvars Rēvalds
Rezekne Academy of Technologies
Faculty of engineering
Rēzekne, Latvia
ritvars.revalds@rta.lv

Abstract. **In this subsequent investigation, we expand upon our initial research by delving into the laser engraving and marking of Grade 2 Titanium (Ti Gr 2) using frequencies of 300 kHz and 700 kHz. Building upon our preliminary experiments involving 100 kHz and 500 kHz, we utilized the Rofin PowerLine F 20 Varia fiber laser to mark Grade 2 titanium within a 6x6 matrix, with each square measuring 5x5 mm. Our meticulous adjustments to the laser marking parameters — encompassing speed (100-1100 mm/s), power (8-18 W), and the introduction of new frequencies (300 kHz and 700 kHz) — allowed us to scrutinize their impact on surface roughness and contrast. Employing advanced techniques, including a laser scanning microscope and Adobe Photoshop software, our analysis unveiled explicit connections among contrast, roughness, frequency, scanning speed, and power. These findings not only extend the scope of our previous experiments but also illuminate subtleties specific to the 300 kHz and 700 kHz frequencies. The insights derived from this study furnish crucial information on the optimal laser marking parameters for Grade 2 titanium, thereby augmenting its efficacy and durability across a diverse array of applications. Moreover, this research contributes to the progressive comprehension of color variations in laser-engraved titanium Grade 2, particularly within the 300 kHz and 700 kHz frequency range.**

Keywords: Fiber laser, laser color marking, laser texturing, titanium Gr2.

I. INTRODUCTION

In the ever-evolving landscape of materials processing, lasers have emerged as transformative tools, revolutionizing traditional methodologies over the past two decades. Known for their precision, heightened productivity, and cost efficiency, lasers have become integral across various industries. Laser processing, encompassing activities from marking and texturing to welding, stands at the forefront of material transformation, impacting metals and nonmetals alike.

Laser applications have witnessed a surge in popularity [1], finding diverse applications in marking [2], texturing [3], welding, and material treatment across both metallic and non-metallic substrates [4], [5]. When juxtaposing laser-induced marking and texturing against alternative techniques such as pattern marking systems, abrasive etching [6], and others, the distinctive advantages of laser methodologies [7] become readily apparent. These include exceptional swiftness in marking, unmatched precision, and the elimination of the need for subsequent post-treatment steps. Currently, a wealth of academic explorations and research pursuits dive into the expansive domain of laser processing, encompassing a diverse spectrum of materials like titanium [8].

Particularly notable is the scientific quest to unveil new hues on titanium surfaces [9], through the interplay of laser irradiation and infrared temperature measurements. The process of transforming the color of titanium with a laser involves the intentional development of oxidation layers or structures on the material's surface [10]. This purposeful manipulation induces thin-layer diffraction, culminating in a noticeable transformation of color [11].

Several investigations have delved into the realm of laser color marking on metals [12]. The pursuit of desired colors necessitates meticulous control over the thickness of the thin film oxide layer. Recent

advancements underscore the capability of nanosecond fiber lasers to generate oxide layers on titanium surfaces within ambient atmospheric conditions [13], leading to dynamic color transformations. These breakthroughs significantly contribute to the evolving landscape of material processing methodologies. The significance of textured surfaces extends notably to the maritime industry, where enhanced durability against environmental stressors is crucial. Additionally, these textured surfaces find applications in the aviation sector [14], contributing to the development of heat-resistant coatings for spacecraft during atmospheric re-entry [15]. This versatility further expands their utility in aviation and maritime contexts, where the benefits of texturing are leveraged to optimize performance and ensure long-term colorfastness and resilience.

The objective of this investigation is to unveil the intricate dynamics governing the impact of power, frequency, and scanning speed, key parameters associated with a pulsed (ns) fiber laser with a wavelength of 1064 nm, on the outcomes of laser marking and texturing processes [16] applied to Grade 2 titanium. The findings contribute valuable insights to the evolving landscape of laser materials processing [17], further enhancing our understanding of optimal conditions for these surface modification techniques and their used laser parameters to achieve the desired color and texture changes.

II. MATERIALS AND METHODS

A. Sample Characteristics

This study focused on an experimental examination involving a titanium Grade 2 sheet specimen, characterized by its chemical composition: Ti (titanium) concentration ≥98.9%, Fe (iron) content ≤0.30%, O (oxygen) levels ≤0.25%, C (carbon) presence ≤ 0.080%, N (nitrogen) trace amounts ≤0.030%, and H (hydrogen) minimal content ≤ 0.015%. The physical dimensions of the specimen measured 100x100x1 mm. Prior to the commencement of the experiments, the sample surfaces underwent a meticulous purification process utilizing (C_3H_7OH) to eliminate any contaminants or potential blemishes.

B. Laser setup

The laser experimentation utilized the Rofin PowerLine F-20 Varia pulsed fiber laser system, as illustrated in Figure 1. Operating at a wavelength of 1064 nm, the laser demonstrated a maximum power of 19 W, and its pulse duration could be adjusted. The focusing mechanism employed a 160 mm lens, resulting in a 40 μm spot size. Laser control was facilitated through a computer-managed Galvano scanner, offering a scan field of 120x120 mm.

Fig. 1. Fiber laser Rofin PowerLine F-20 Varia.

Specification for Rofin PowerLine F-20 Varia laser is shown in Table I.

TABLE I. PARAMETERS OF ROFIN POWERLINE F-20 VARIA

Parameter	Magnitude, Unit
Wavelength (λ)	1064 nm
Max. Power (P)	19 W
Max. Pulse Energy (E)	1 mJ
Scan Speed (v)	1 mm/s to 20000 mm/s
Pulse Width (τ)	4 ns to 200 ns
Repetition Rate (F)	20 kHz to 1000 kHz

C. Microscope setup

To scrutinize the surface characteristics and alterations in the titanium Grade 2 (Ti Gr2) samples, an Olympus LEXT OLS5000 3D Measuring Laser Microscope was employed, as depicted in Figure 2. The microscope operated at a magnification of x451, ensuring a measurement precision of 0.4 μm. Additional specifications comprised a numerical aperture (N.A.) of 0.6, a working distance (W.D.) of 1 mm, a focal depth of 1.8 μm, a focusing spot diameter of 0.82 μm, covering a measurement area of 640 X 640 μm.

Fig. 1. Olympus LEXT OLS5000 3D Measuring Laser Microscope.

D. Scanner

Marked titanium Gr2 plates were scanned using an HP Scanjet G3010 scanner with a scanning area of 216 X 297 mm and a color depth of 48-bit. The scanning parameters were set to a resolution of 2400 DPI, brightness of 100, contrast of 80, and the file format used was .tif.

E. Experimental Method

Laser marking was performed on a Ti Gr 2 sample measuring 100x100x1 mm using a fiber laser. To ensure a clean surface for marking, the sample underwent thorough cleaning with isopropyl alcohol 99.8% (IPA) to eliminate any potential contaminants. The sample was marked with two matrices, each consisting of 6 rows and 6 columns, resulting in a total of 72 markings. Different combinations of speed, power, and frequency parameters were used for marking, while maintaining a constant pulse duration of 4 ns. The experiments were conducted in ambient conditions without the use of any assist gases. The marking of the Ti Gr 2 plate involved variations in three key parameters: power (P) in watts, scanning speed (v) in mm/s, and frequency (F) in kHz. Figure 3 illustrates the marking schematics of the Ti Gr 2 samples.

The marking process in the current experiment involved two matrices, each defined by specific parameters shown in Table II. For marking the first matrix, a frequency of 300 kHz was used. For marking the second matrix, a frequency of 700 kHz was used. This adaptation aims to explore the laser marking process comprehensively, particularly focusing on the effects under the influence of different frequency settings with constant pulse duration.

TABLE II. FIBER LASER MARKING PARAMETERS FOR TI GR 2 SHEET SAMPLE AT 300 KHZ AND 700 KHZ

Parameter	Magnitude, Unit
Pulse Duration (τ)	4 ns
Output Power (P)	8/10/12/14/16/18 W
Scanning Speed (v)	100/300/500/700/900/1100 mm/s
Square Size	5×5 mm
Frequency (F)	300 kHz and 700 kHz

Equation (1) was used to convert the laser power from % to W.

$$P(W) = \frac{19 * P(\%)}{100\%} \qquad (1)$$

Here, $P(W)$ = laser power in W, and $P(\%)$ = signifies laser power in %. The resulting power values in watts, corresponding to the power percentages, are presented in Table III.

TABLE III. POWER CONVERSION CHART

P (%)	41.7	52.1	62.5	72.9	83.3	93.8
P (W)	8	10	12	14	16	18

To compute the contrast factor, denoted as k_x, a percentage value is employed [18]. The determination of k_x involves assessing the volume N_f, of the unmarked region [19]. Conversely, the N_x value pertaining to the laser-marked region is directly derived from the marked area. The formula utilized for the calculation of k_x is expressed in Equation (2):

$$K_x = \frac{N_F - N_X}{N_F} \times 100\% \qquad (2)$$

To depict the distinction between two measured colors within the CIE color uniform space, the CIE color difference L* a* b* formula [19], is applied. The overall color difference, N_x, [20] between two points in the three-dimensional color space is articulated using Equation (3):

$$N_x = \sqrt{(\Delta L_x)^2 + (\Delta a_x)^2 + (\Delta b_x)^2} \qquad (3)$$

Similarly, the total color difference N_f is expressed using Equation (4):

$$N_f = \sqrt{(\Delta L_f)^2 + (\Delta a_f)^2 + (\Delta b_f)^2} \qquad (4)$$

In these equations, ΔL, Δa, and Δb represents differences in brightness, color along one axis, and color along another axis, respectively [20]. These differences are derived from the marked areas L, a, and b using the Adobe Photoshop color tool. The L channel pertains to variations in lightness or darkness within the color spectrum.

To avoid negative contrast values, an absolute value ($|k_x|$) is applied to each calculated contrast value.

III. RESULTS AND DISCUSSIONS

The laser treatment of Titanium Grade 2 resulted in changes in contrast (color marking) and surface roughness compared to untreated material. The obtained results for the marked samples of Titanium Grade 2 can be observed in Figures 3 to 10, where the data from the conducted experiment are depicted at frequencies of 300 kHz and 700 kHz.

In Figure 3, a sample of Titanium Grade 2 plate subjected to laser treatment with a frequency of 300 kHz is depicted. As a result of this laser interaction, the pattern matrix manifested with colors, thereby creating an intriguing comparison with the matrix created using a frequency of 700 kHz, visualized in Figure 7.

Upon closer examination of the color change, various phenomena and their correlations can be observed. This color dynamics encompass transitions from green to blue, red to violet, graphite gray to gray, white to yellowish, and beige to blue. These variations in color produce a unique visual effect, providing insight into the laser impact on the surface structure of Titanium Grade 2 and the approximate color shifts it induces.
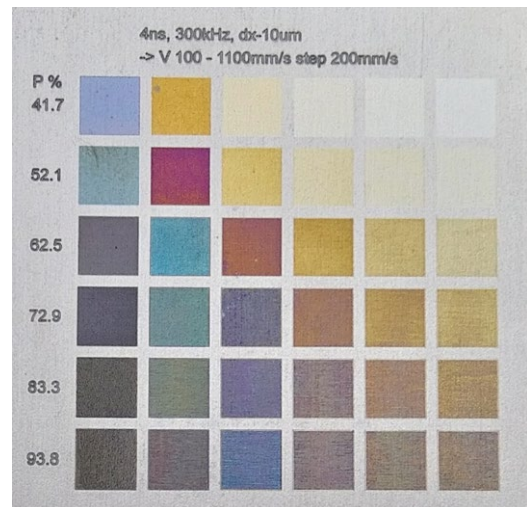
Fig. 3. Laser marked Ti Gr 2 samples with 300 kHz.

In Figure 4, surface changes are visualized by performing treatment at a frequency of 300 kHz, maintaining a constant pulse duration of 4 ns, and altering scanning speeds and laser power. The obtained absolute contrast values, calculated by considering the percentage difference between the marked and unmarked areas, provide information about the alteration in visual perception, where the contrast value N_f of the unmarked area remains constant at 75.
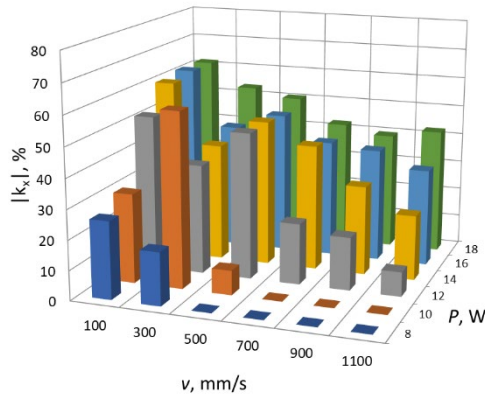
Fig. 4. Exploring the influence of scan speed, frequency (300 kHz), and power variation on the absolute contrast values in Ti Gr2 laser marking.

Delving into the laser-marked surface alterations, the scrutiny of acquired outcomes unveils a perceptible association between the established matrix and the graphical portrayal of contrast values, evident in Figures 3 and 4. Notably, the amplification in power values corresponds to a proportional surge in the absolute contrast value $|k_x|$ (%), while a simultaneous decline in $|k_x|$ values transpires with the escalation of speed values from 100 mm/s to 1100 mm/s.

A detailed examination of both visual representations highlights consistent patterns among the parameters. Adjusting power values from 8 W to 18 W at a scanning speed of 100 mm/s produces darker tones, whereas an augmentation in speed results in lighter hues. The zenith of contrast $|k_x|$ absolute values is reached at the lowest speed of 100 mm/s and the highest power of 18 W, culminating in a specific $|k_x|$ absolute value of 61.3%. Conversely, the nadir of $|k_x|$ absolute value, 1.37%, is discerned at 10 W power and a scanning speed of 700 mm/s. With an increase in scanning speed, lighter color tones emerge, appearing approximately at $|k_x|$ % values within the range of 30-50%. This phenomenon is also evident in Figure 3, specifically in the central section of the matrix, where shades of red, green, and blue begin to surface. These tones become noticeable at 10 W power and 300 mm/s scanning speed, as well as at 12-14 W power and 300-500 mm/s scanning speed.

Ti Gr 2 material surface roughness, obtained through laser marking/treatment, was analyzed using the R_q parameter. Roughness R_q of the non-marked Ti surface (Base) was measured to be 0.8 µm. In Figure 5, the surface roughness of Ti Gr 2 is depicted under consistent conditions, with a 4 ns pulse duration, 10 µm marking step, 300 kHz frequency, and scanning speeds ranging from 100 to 1100 mm/s.

Fig. 5. Surface roughness (R_q) dependence from scanning speed for Ti Gr 2 marked samples at 300 kHz laser frequency, 4 ns pulse duration, and 10 µm marking step.

At a laser power of 8 W, R_q parameter varied from 0.70 µm, achieved at a scanning speed of 100 mm/s, to the highest roughness value of 0.96 µm at a scanning speed of 300 mm/s. When comparing these results to the processing zone of 18 W power, significant differences were observed. At a scanning speed of 100 mm/s, the roughness value reached 9.5 µm, while the lowest roughness value at a scanning speed of 1100 mm/s was recorded at 0.73 µm. In Figure 5, we observe an increase in roughness only at speeds of 100 mm/s and power levels of 18 W and 14 W.

Figure 6 shows how roughness varies with laser power. At power 14 W, 16 W and 18 W and speed 100 mm/s, the roughness increases and reaches a maximum of 10.5 µm at 16 W and 100 mm/s. At all other combinations of power and speed, the roughness changes minimally and remains practically the same as the unmarked titanium surface (Base).

Fig. 6. Surface roughness (R_q) dependence from power for Ti Gr 2 marked samples at 300 kHz laser frequency, 4 ns pulse duration, and 10 µm marking step.

In Figure 7, the generated matrix for the Ti Gr2 sample is observed at a frequency of 700 kHz. This sample displays more vivid colors, including violet, yellow, various shades of gray, blue, and green. These distinct color tones notably contrast with the matrix tones observed at a frequency of 300 kHz, although certain areas also demonstrate a few similarities.
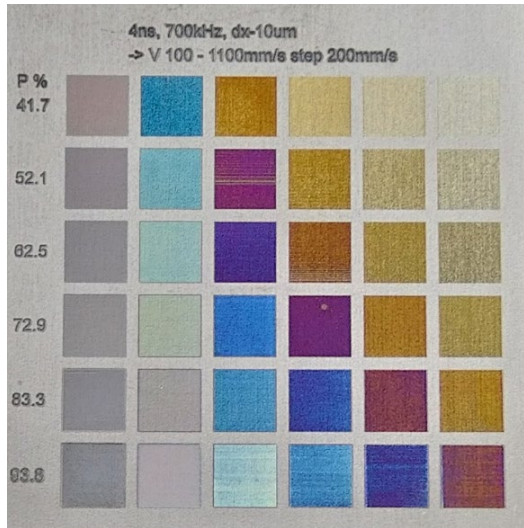
Fig. 7. Laser marked Ti Gr 2 samples with 700 kHz.

Reviewing the obtained contrast values %, at 700 kHz matrix processing, the highest contrast value is observed at 12 W power and a scanning speed of 500 mm/s, reaching a contrast value of 73.9% $|k_x|$ (see fig. 8.). Conversely, the lowest contrast value, 8.22%, was observed at 8 W power and a scanning speed of 1100 mm/s, where the color tone almost matches the sample color tone.
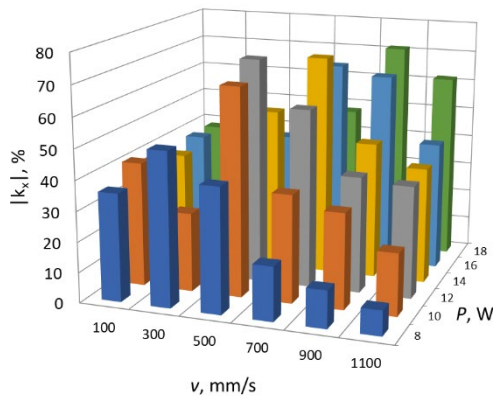
Fig. 8. Exploring the influence of scan speed, frequency (700 kHz), and power variation on the absolute contrast values in Ti Gr2 laser marking.

In Figure 9, the surface roughness of Ti Gr 2 is depicted under consistent conditions, with a 4 ns pulse duration, 10 μm marking step, 700 kHz frequency, and scanning speeds ranging from 100 to 1100 mm/s.
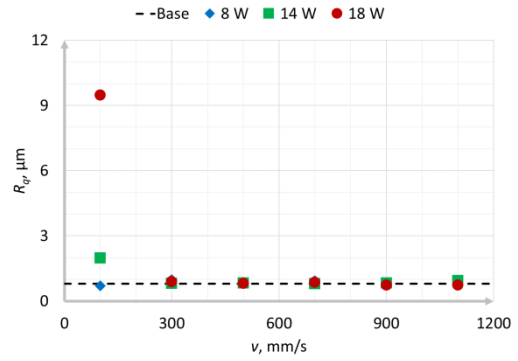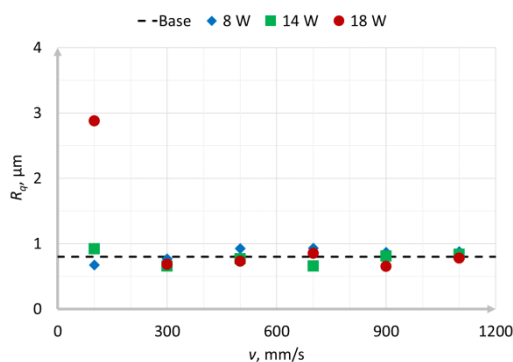

Fig. 9. Surface roughness (R_q) dependence from scanning speed for Ti Gr 2 marked samples at 700 kHz laser frequency, 4 ns pulse duration, and 10 μm marking step.

Similar roughness characteristics are observed at a frequency of 700 kHz. The study demonstrates that the behavior of the treated surface at 700 kHz frequency is identical to that at 300 kHz frequency. At 8 W power, a slight increase in roughness is observed, starting from 0.67 μm and increasing to 0.88 μm proportionally with the scanning speed. However, analyzing the marking at 18 W power reveals roughness value patterns like those at 300 kHz marking but with some differences. Similar to 300 kHz, the highest roughness value starts at a scanning speed of 100 mm/s with a roughness value of 2.9 μm, and as the scanning speed increases, the roughness value decreases to 0.8 μm. In Figure 9, we observe an increase in roughness only at speeds of 100 mm/s and power levels of 18 W.

Figure 10 shows how roughness varies with laser power. At power 18 W and speed 100 mm/s, the roughness increases and reaches a maximum of 2.9 μm. At all other combinations of power and speed, the roughness changes minimally and remains practically the same as the unmarked titanium surface.
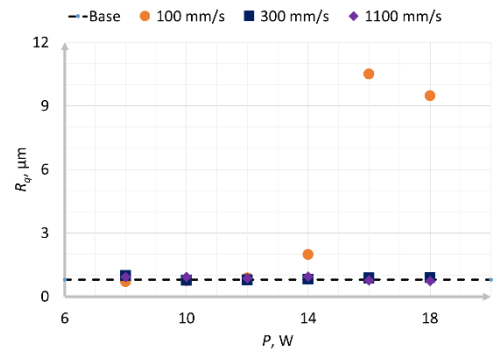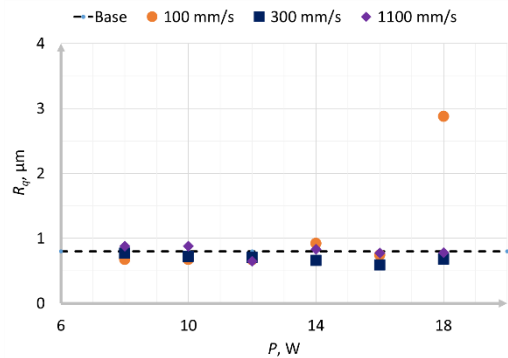

Fig. 10. Surface roughness (R_q) dependence from power for Ti Gr 2 marked samples at 700 kHz laser frequency, 4 ns pulse duration, and 10 μm marking step.

Figure 11 shows a surface with high roughness and a dark color tone, as seen in the first column of the matrix at 93.8% power (18 W), as shown in Figure 3. Analyzing the collected data leads to the observation that rougher surfaces tend to display darker tones. However, scrutinizing the data reveals that this assertion does not consistently align with the obtained results, as evidenced by the case at 300 kHz, where the color tone in the first row at 72.9% power (14 W) is darker than at 93.8% (18 W). In this instance, the roughness value is 2.0 μm, while the measurement at maximum power is 9.5 μm. Uncovering correlations suggests that higher powers and lower scanning speeds result in darker tones and larger roughness. However, the color tone itself is not always a shade of black. It is conceivable that there is a relationship between roughness and color tones, but further experiments are needed to elucidate this connection.
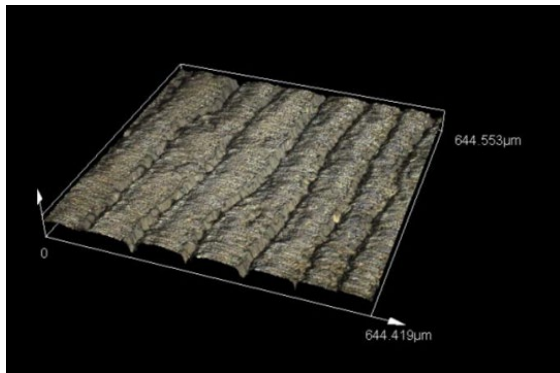
Fig. 11. Surface Roughness Analysis of Ti Gr 2 Markings at 300 kHz: 3D Laser Scanning Microscope Image (x451 Magnification) Showing R_q = 9.5 µm.

Based on our findings, the comparison of contrast values and colors revealed that at a frequency of 700 kHz, the roughest marking reached 2.9 µm, as depicted in Figure 12. Figures 11 and 12 illustrates how the roughness values change while maintaining identical parameters but with a different frequency. It appears that as the frequency increases to 700 kHz, the manifestation of roughness improves.
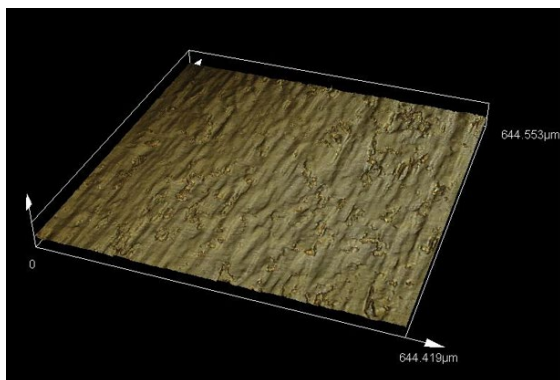
Fig. 12. Surface Roughness Analysis of Ti Gr 2 Markings at 700 kHz: 3D Laser Scanning Microscope Image (x451 Magnification) Showing R_q = 2.9 µm.

In Figure 13, the most pronounced colors are captured under the Olympus LEXT laser microscope.
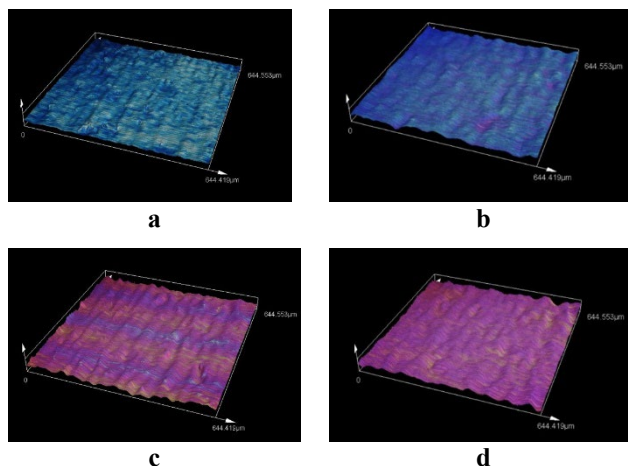
Fig. 13. Color and Roughness Variation on Ti Gr 2 Surface Following Laser Treatment with Specific Parameters.
Δx = 10 µm; τ = 4 ns; F = 700 kHz.
a: P = 10 W; v =300 mm/s. **b**: P = 8 W; v =300 mm/s.
c: P = 10 W; v =500 mm/s. **d**: P = 14 W; v =700 mm/s.

This image illustrates the formation and transition of colors, providing insights into both their structure and the details of the color spectrum. Although the color shades differ significantly, the structure and roughness of the Ti surface remains practically unchanged.

IV. CONCLUSION

In this study, we continued our investigation into laser marking treatments for Titanium Grade 2 (Ti Gr 2), focusing on frequencies of 300 kHz and 700 kHz. Our objective was to enhance the global color coding for Ti Gr 2 materials and analyze surface roughness. The data obtained lays the groundwork for achieving desired outcomes across various laser parameters. These findings have significant implications for advancing laser-material interactions and optimizing laser marking processes, particularly for Ti Gr 2, which is widely used in aerospace, medical, and automotive industries. Exploring different frequencies has provided valuable insights into tailoring color spectrum and surface texture, refining laser marking techniques. Further experimentation guided by these insights can enhance control over laser processing of Ti Gr 2, facilitating the production of high-quality components in critical sectors. Our investigation revealed that at 300 kHz, color dynamics and surface roughness are influenced by power and scanning speed, with adjustments in laser parameters showing potential for enhancing desired outcomes. Similarly, at 700 kHz, vivid color tones and similar roughness characteristics were observed, suggesting potential applications in various industries. Future research should explore specific factors influencing observed phenomena within defined frequency ranges, and further investigations into additional frequencies are anticipated to deepen our understanding of Ti Gr 2 laser processing.

REFERENCES

[1] Romaniuk, R. S., Gajda, J. (April 2013). "Laser Technology and Applications 2012." *International Journal of Electronics and Telecommunications*, 59(2), 195-202.

[2] Gao, W., Xue, Y., Li, G., Chang, C., Li, B., Hou, Z., Li, K., Wang, J. (2018). "Investigations on the Laser Color Marking of TC4." *International Journal of Electronics and Optoelectronics*, https://doi.org/10.1016/j.ijleo.2018.12.113

[3] Pou, P., Riveiro, A., del Val, J., Comesaña, R., Penide, J., Arias-González, F., Soto, R., Lusquiños, F., Pou, J. (2017). Laser surface texturing of Titanium for bioengineering applications. *Procedia Manufacturing, 13, 102-107.* https://doi.org/10.1016/j.promfg.2017.09.102

[4] Nath, A. (2014). Laser Drilling of Metallic and Nonmetallic Substrates. In: *Laser Precision Microfabrication*. DOI: 10.1016/B978-0-08-096532-1.00904-3.

[5] Subramonian, S., Kasim, M. S., Ali, M. A. M., Anand, T. J. S., & citi. (2015). Micro Drilling of Silicon Wafer by Industrial CO_2 Laser. *International Journal of Mechanical and Materials Engineering, 10(1), 1-7.* DOI: 10.1186/s40712-015-0029-8.

[6] Kumar, A., & Kumar, H. (2021). Analysis of material removal of Inconel 718 cylinder using magnetic abrasive finishing process assisted with chemical etching. *Materials Today: Proceedings.* DOI: 10.1016/j.matpr.2021.09.304.

[7] Hristov, V. N., Lazov, L., Petrov, N. A., Yankov, E. H. (2023). Influence of basic parameters of the laser marking process on stainless steel samples. *Environment Technology Resources Proceedings of the International Scientific and Practical*

Conference, 3, 311-315. DOI: 10.17770/etr2023vol3.7216.

[8] Melo-Fonseca, F., Guimarães, B., Gasik, M., Silva, F. S., & Miranda, G. (2022). Experimental analysis and predictive modelling of Ti6Al4V laser surface texturing for biomedical applications. *Surface Innovations*. DOI: 10.1016/j.surfin.2022.102466.

[9] Henriksen, N. G., Poulios, K., Somers, M. A. J., & Christiansen, T. L. (2023). Impact of laser marking on microstructure and fatigue life of medical grade titanium. *Materials Science and Engineering: A*, 145020. DOI: 10.1016/j.msea.2023.145020.

[10] Awasthi, A., Kumar, D., & Marla, D. (2023). Understanding the role of oxide layers on color generation and surface characteristics in nanosecond laser color marking of stainless steel. *Optics and Laser Technology*. DOI: 10.1016/j.optlastec.2023.110469.

[11] Gräf, S., Kunz, C., Undisz, A., Wonneberger, R., Rettenmayr, M., & Müller, F. A. (2019). Mechano-responsive colour change of laser-induced periodic surface structures. *Applied Surface Science*. DOI: 10.1016/j.apsusc.2018.12.051.

[12] Geng, Y., Li, J., & Lu, C. (2022). Experimental and numerical investigations on color stability of laser color marking. *Optics and Lasers in Engineering*. DOI: 10.1016/j.optlaseng.2022.107225.

[13] Li, Z., Xu, J., Zhang, D., Xu, Z., Su, X., Jin, Y., Shan, D., Chen, Y., & Guo, B. (2022). Nanosecond pulsed laser cleaning of titanium alloy oxide films: Modeling and experiments. *Journal of Manufacturing Processes*. DOI: 10.1016/j.jmapro.2022.08.033.

[14] Boyer, R.R. (1996). An overview on the use of titanium in the aerospace industry. *Materials Science and Engineering: A,* 213(1-2), 103-114. DOI: 10.1016/0921-5093(96)10233-1.

[15] Monogarov, K.A., Pivkina, A.N., Grishin, L.I., Frolov, Yu. V., & Dilhan, D. (2016). Uncontrolled re-entry of satellite parts after finishing their mission in LEO: Titanium alloy degradation by thermite reaction energy. *Acta Astronautica*. DOI: 10.1016/j.actaastro.2016.10.031.

[16] Arun, A., Lakshmanan, P., Parthiban, K., Kumanan, G., & Arunkumar, L. (2022). Experimental study on laser surface texturing and wear characterization of titanium alloy. *Materials Today*: Proceedings. DOI:10.1016/j.matpr.2022.03.621.

[17] Morales, M., Munoz-Martin, D., Marquez, A., Lauzurica, S., & Molpeceres, C. (2018). Laser-Induced Forward Transfer Techniques and Applications. In: *Advances in Laser Materials Processing,* Chapter 13, 339-379. DOI: 10.1016/B978-0-08-101252-9.00013-3.

[18] L. Lyubomir, N. Pavels un D. Hristina, «Laser Marking Methods» *Technology. Resources, (2015), Volume I, 108-115,* pp. 109-112., 2015.

[19] K. McLAREN, XIII—The Development of the CIE 1976 (L* a* b*) Uniform Colour Space and Colour-difference Formula, vol. 92, Journal of the Society of Dyers and Colourists, 1976, pp. 338-341.

[20] A. J. Arkadiusz, S. Bogusz, K. E. Paweł un A. M. Krzysztof, «The influence of process parameters on the laser-induced coloring» *Applied Physics A volume 115, pages1003–1013 (2014),* March 2013.

[21] Lapa, J., Adijans, I., Yankov, E. H., Revalds, R. (2023). "Investigation of Laser Marking and Texturing of Titanium Gr 2 with Fiber Laser." *Environment Technology Resources Proceedings of the International Scientific and Practical Conference*, 3, 321-327. DOI: 10.17770/etr2023vol3.7251.

Methods for Measurement of Pulse Parameters of Fiber Lasers

Lyubomir Lazov
Rezekne Academy of Technology
Rezekne, Latvia
lyubomir.lazov@rta.lv

Tsanko Karadzhov
Technical University of Gabrovo
Gabrovo, Bulgaria
karadjov_st@abv.bg

Edmunds Teirumnieks
Rezekne Academy of Technology
Rezekne, Latvia
edmunds.teirumnieks@rta.lv

Antons Pacejs
Rezekne Academy of Technology
Rezekne, Latvia
antons.pacejs@rta.lv

Conyu Conev
National Military University
Artillery, AD and CIS Faculty
Shumen, Bulgaria
coni19@abv.bg

Abstract. **Fiber lasers play an increasingly pivotal role in numerous scientific and industrial domains, spanning from optical communications to medicine. Their utilization across various technological realms continues to surge, prompting the demand for novel physical methods and principles to precisely measure laser pulse parameters during technological investigations. This article provides an overview of contemporary techniques and approaches employed in measuring the parameters of laser pulses generated by fiber laser systems, with a focus on accurately determining pulse frequency and duration. Special attention is paid to the specific measurement of the relationships between frequency, average power, pulse energy and pulse power for a 20W fiber laser source used for laser color marking on stainless steel.**

Keywords: Frequency, Pulse duration, Fiber laser, Color marking, Measurement, Laser technology, Pulsed parameters.

I. INTRODUCTION

On the need for accurate pulse characterization of nanofiber lasers for various industrial and medical applications

Accurate characterization of nanofiber laser pulses is crucial for optimizing productivity, increasing process efficiency, ensuring safety, advancing research, and facilitating standardization across various industrial and medical applications (Figure 1). By precisely controlling pulse parameters, industries and researchers can unlock the full potential of nanofiber lasers for a wide range of practical applications. Accurate pulse characterization allows researchers and engineers to precisely control parameters such as pulse duration, repetition rate, and output energy. This optimization ensures that the laser's performance is tailored to the specific requirements of

various applications, including industrial processes such as micromachining and medical procedures such as laser surgery.

Understanding the characteristics of nanofiber laser pulses enables industries to improve the efficiency of manufacturing processes [1], [2], [3], [4], [5]. For example, in laser material processing applications such as welding or cutting, precise control over pulse parameters can minimize heat-affected areas and reduce processing time, resulting in higher productivity and lower expenses.

In modern communications, the use of optical lasers with nanosecond pulses facilitates high-speed data transmission [6]. By modulating the intensity and timing of nanosecond pulses, information can be encoded and transmitted through optical fibers at ultrafast speeds, enabling efficient communication over long distances with minimal signal degradation [7].

Accurate pulse characterization is crucial for ensuring the safety and reliability of laser systems, especially in medical applications. By precisely controlling parameters such as pulse energy and smoothness, medical professionals can minimize the risk of tissue damage and ensure optimal treatment outcomes for patients. Additionally, nanosecond pulse lasers are used in imaging techniques such as optical coherence tomography (OCT) for high-resolution imaging of biological tissues [8], [9], [10].

Nanosecond pulse fiber lasers are also valuable tools in biomedical research for studying cellular and molecular processes. Their ability to deliver high-energy pulses in a controlled manner allows researchers to manipulate and study biological samples at the nanoscale, facilitating advancements in areas such as cell biology, neuroscience,

and drug discovery [11]. Characterization of nanofiber laser pulses provides researchers with a better understanding of the fundamental physical processes involved in laser-material interactions.

This knowledge is essential for developing new laser technologies and advancing scientific understanding in areas such as photonics, materials science, and biomedicine.
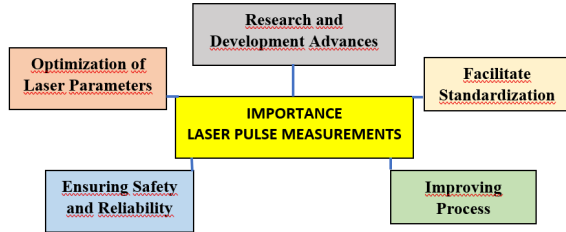

Fig. 1. Accurate characterization of laser pulses is important for various applications in industry, medicine, and research.

Nanosecond pulse fiber lasers are used in spectroscopic techniques for material analysis [12]. By interacting with materials at the nanoscale, nanosecond pulse lasers can induce specific optical and chemical changes, providing valuable information about material properties, composition, and structure. This information is crucial for various industrial and scientific applications, including materials science, nanotechnology, and environmental monitoring [13].

Standardized methods for pulse characterization allow consistency and comparability across different laser systems and applications. This facilitates collaboration between researchers and industries, accelerates the adoption of technologies, and ensures that performance metrics are meaningful and universally understood.

II. General content

A. Types of fiber lasers

Due to the specificity of its constriction, such as the flexibility of the fiber material used as the active medium, as well as the fiber structure and cavity configuration, there are also many different types of fiber lasers. The fiber core is doped with a different type of active dopant material, usually rare earth elements, and the laser generation is propagated and amplified in the thus doped medium/core. The inner shell and core together direct the pump light, which provides the energy needed for amplification in the core (Figure 2).
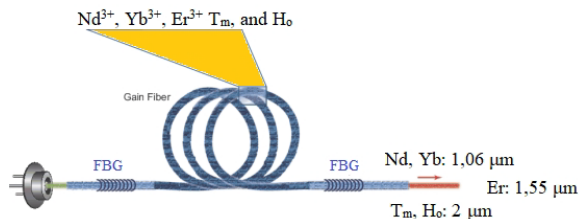
Fig. 2. Varieties of fiber lasers according dopant material.

In fiber laser, there are several widely used ion dopants, such as Nd^{3+}, Yb^{3+}, Er^{3+} Tm, Ho. Nd- or Yb-doped fiber laser emits laser in 1.06 μm wavelength region which is widely used in laser process and laser weapon [14], [15], [16] . Er-doped fiber laser emits laser in 1.55   μm wavelength region which is suitable for optical communication and optical sensing [17], [18]. Tm- or Ho-doped fiber laser emits laser in 2 μm wavelength region which is eye-safe and widely used in special laser communication, atmosphere sensing, and medical application [19], [20].
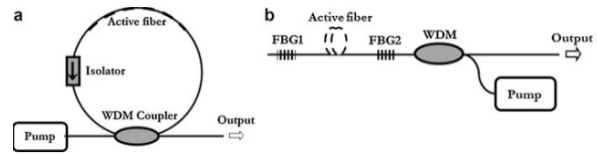
Fig. 3. Ring cavity and linear cavity fiber laser. (a) Ring laser, (b) Linear cavity laser

According to the cavity configuration used, fiber lasers can be classified into ring cavity fiber laser and linear cavity fiber laser [21]. Ring cavity fiber laser (Fig. 2a) usually utilizes an optical coupler and connects its two ends together with a gain optical fiber so that the optical feedback is formed. It is a traveling wave cavity laser and has a relatively long cavity resulting in a small longitudinal mode gap. Usually the separate component is needed in the ring cavity to achieve single-frequency operation [22]. Linear cavity fiber laser (Fig. 2b) usually utilizes the fiber gratings as reflectors replacing the traditional optic reflectors. Since fiber Bragg grating (FBG) can be written in the passive fiber or active fiber directly, the linear cavity fiber laser can be very composite. By adjusting the bandwidth and reflectivity of the FBGs and the cavity length, single-frequency operation is easily obtained in a short-cavity fiber laser. Both distributed Bragg reflector fiber laser (DBR-FL) [23] and distributed feedback fiber laser (DFB-FL) [24] belong to this linear cavity fiber laser.

The fiber lasers can operate in different modes and wavelengths. Because of all these differences, the precise measurement of the characteristics of the pulses generated by the lasers is essential for the wide applications of this type of laser.

B. The relation between the frequency and the duration of the pulses with the energy characteristics of the laser generation.

The pulse-following frequency *v* in laser systems, which refers to the rate at which successive laser pulses are emitted (see Figure 4), as well as the duration of each individual pulse play a significant role in determining the overall output energy P_{avg} characteristics of the laser system, which in turn affects the various aspects of laser-material interaction and processing results [25].

Pulse energy refers to the total amount of optical energy contained within a single laser pulse. It is a crucial parameter in applications such as laser material processing, where the amount of energy deposited per pulse influences material removal, ablation, or modification. The relationship between the average laser output power P_{avg}, frequency *v* and the laser pulse energy *E* is defined by the following relationship

$$E = \frac{P_{avg}}{v}, [J] \qquad (1)$$
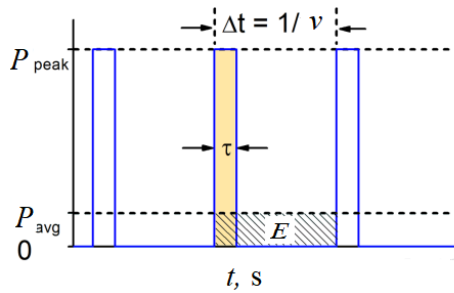
Fig. 4. The graph of the parameters of the laser pulse and the energy characteristics of the laser

Peak power P_{peak}, which is the maximum instantaneous power achieved within a laser pulse, is also affected by pulse frequency v and duration τ

$$P_{peak} = \frac{P_{avg}}{v.\tau}, [kW] \qquad (2)$$

This characteristic has an important role for processes such as laser cutting, ablation, etc., where a high power density is required for the effective implementation of the specific technological process.

Pulse duration τ refers to the length of time that an individual laser pulse interacts with matter. It determines the time range of the laser pulse and plays a crucial role in processes such as laser machining, where a shorter pulse duration can result in less heat-affected areas and finer resolution. The pulse duration τ is inversely proportional to the spectral bandwidth Δf of the pulse via the uncertainty principle in physics

$$\Delta\tau.\Delta f \geq \frac{1}{2} \qquad (3)$$

The uncertainty principle in physics - the product of the time width $\Delta\tau$ and the spectral width Δf of the pulse is a constant quatity.

These relationships and equations help characterize the temporal and energetic properties of laser pulses and are essential for understanding and optimizing laser systems for various applications. Together, they play a critical role in determining the performance, efficiency and suitability of laser systems for various applications [27].

C. Laser pulse measurement methods

This diagram effectively maps out the hierarchy and relationships between different aspects of laser pulse measurement, highlighting the importance of various techniques and tools used in the field. The diagram provides an organized overview of the methods and tools used to measure laser pulse characteristics.

Laser pulse measurements are the central concept, from which all other measurements branch out. They involve a comprehensive assessment of laser pulse characteristics. Duration Measurement: This technique assesses the length of time a laser pulse last. The Autocorrelator determines the width of a pulse by measuring how it interferes with a delayed copy of itself. FROG is a more advanced technique that provides a complete characterization of the pulse.

Two common methods are the Autocorrelator and FROG (Frequency-Resolved Optical Gating). The method provides a detailed temporal and spectral characterization

of a laser pulse. SPIDER (Spectral Phase Interferometry for Direct Electric-field Reconstruction) offers an even more detailed view of the pulse's temporal shape and phase.
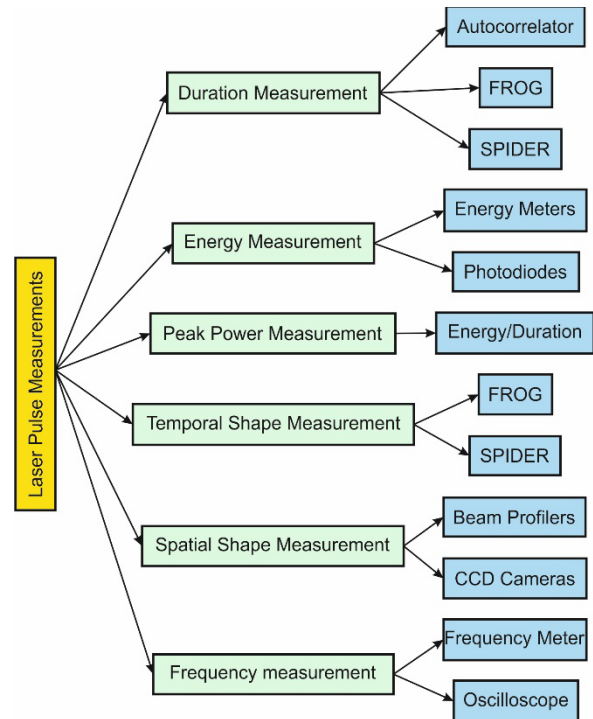
Fig. 5. Laser pulse measurement methods

Energy measurement quantifies the total energy delivered by a pulse. It is divided into two methods. Energy meters measure the energy of laser pulses, while photodiodes indirectly measure the pulse's energy by converting light into electrical current. Peak power measurement calculates the maximum power of a pulse by dividing its total energy by its duration.

Temporal shape measurement is also used, which is divided into two methods FROG and SPIDER. This method investigates the distribution of a pulse's energy across its beam profile. Beam profilers are devices used to capture the two-dimensional spatial intensity profile of a laser beam. CCD cameras, or charge-coupled devices, can image the spatial distribution of laser pulses.

This diagram clearly illustrates the hierarchy and relationships between different aspects of laser pulse measurement, emphasizing the significance of various techniques and tools used in the field.

Based on the methods discussed above, a Laser pulse parameters measurement system has been developed [30].

D. Laser pulse parameters measurement system
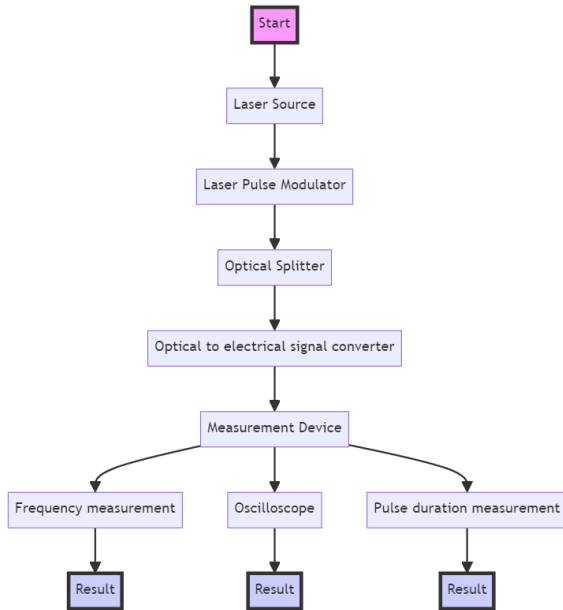
Fig. 6. Block diagram illustrating the laser pulse parameters measurement system.

The system starts with a laser source that generates the laser pulses to be measured [31]. The pulses are then fed into a laser pulse modulator, which adjusts their properties, such as amplitude, frequency, or duration, to ensure they are in the correct form for measurement. Finally, the pulses are directed to an optical splitter. After modulation, the laser pulses pass through an optical splitter which divides the incoming beam into separate paths. One path is sent to the measurement device and the other to a reference or another part of the system. One of these paths goes to an optical-to-electrical signal converter that transforms the optical signal into an electrical one. Measurement devices, such as oscilloscopes and frequency counters, typically operate with electrical signals [32].

Further on describes the measurement devices used to measure various laser pulse parameters. The optical-to-electrical converter feeds the electrical signal into these devices. One of the important parameters that is measured is the frequency of the laser pulses. The measurement of frequency is done using an oscilloscope. Frequency is critical in applications like spectroscopy or laser cutting. An oscilloscope visually displays the waveform of laser pulses, providing information about pulse shape, peak power, and fluctuations over time. The result is a measurement of the time duration of each laser pulse. Pulse duration measurement is crucial for applications where the interaction time between the laser and material is important, such as in materials processing or medical surgeries. Finally, the measurements are collected, and the results can take the form of digital data, printed reports, or visual displays on the measurement devices.

Each step is critical for accurately determining the parameters of laser pulses, which is essential for scientific, industrial, and medical applications. The measurement of pulse repetition rate and pulse duration of laser pulses requires specific instrumentation and techniques tailored to the characteristics of the laser system. For the measurement of pulse repetition rates an optical frequency counter. The counter detects successive pulses and calculates their

frequency based on the time interval between them. Another approach is to use a fast photodiode detector coupled to an oscilloscope to detect each laser pulse and measure the time interval between successive pulses, allowing the repetition rate to be calculated. A photodetector and a frequency counter can also be used. The photodetector converts the optical pulses into electrical signals. These signals are then fed to a frequency meter or frequency counter to determine the repetition rate.

Pulse Duration – Autocorrelation Technique. To measure pulse durations in the femtosecond to picosecond range, an autocorrelation technique can be used. This involves splitting the laser pulse into two beams, delaying one beam relative to the other, and then measuring the interference pattern generated when the beams are recombined. The width of the interference pattern provides information about the pulse duration. Second Harmonic Generation (SHG): SHG involves doubling the frequency of a laser pulse using a nonlinear crystal. The pulse duration can be determined by varying the relative delay between the fundamental and second harmonic pulses and analyzing the shape of the generated SHG signal. Frequency-Resolved Optical Gating (FROG) is a more advanced technique that measures the spectral and temporal characteristics of the laser pulse simultaneously [28]. The pulse duration can be accurately determined by analyzing the spectrogram obtained from FROG measurements [29].

Measuring the pulse shape, also known as the temporal profile or temporal waveform of a laser pulse, is essential for characterizing its temporal characteristics accurately. There are several methods for measuring the pulse form, each with its own advantages and limitations. Here are some common techniques as photodiode and Oscilloscope. This is a straightforward method where a fast photodiode is used to convert the optical pulse into an electrical signal. The electrical signal is then captured by an oscilloscope, which displays the waveform. This method is relatively simple and provides real-time visualization of the pulse shape. However, it may not be suitable for measuring very short pulses or complex pulse shapes.

Autocorrelation – Autocorrelation is a technique used to measure the similarity between a pulse and a time-delayed copy of itself. In second-order autocorrelation, the pulse is split into two beams. One of the beams is delayed using an adjustable delay line. The delayed and not delayed pulses are then overlapped and sent through a nonlinear crystal. This generates a signal proportional to the autocorrelation function. The pulse shape can be reconstructed by scanning the delay and measuring the resulting signal. This method is commonly used to measure ultrafast laser pulses with femtosecond or picosecond durations.

Frequency-Resolved Optical Gating (FROG) is a more advanced technique that measures both the spectral and temporal characteristics of a pulse simultaneously. It involves sending the pulse through a nonlinear medium and measuring the resulting spectral interference pattern. By analyzing the spectrogram obtained from FROG measurements, the pulse shape can be reconstructed with high accuracy. FROG is particularly useful for measuring complex pulse shapes and ultrashort pulses with femtosecond or sub-femtosecond durations.

For the measurements as a converter of laser pulses into electrical pulses was used High Speed Photodiode Detector.

Fig. 7. High Speed Photodiode Detector for Pulse Laser

He is designed specifically for pulse lasers with a rising edge less than 500 ps. It operates within a wavelength response range of 300 nm to 1100 nm and features a silicon-based detector with a photosensitive diameter of less than 0.5mm. This device is capable of detecting femtosecond, picosecond, nanosecond laser pulses, as well as quasi-continuous and continuous laser or non-laser light sources with high precision. It offers a measurement frequency greater than 1GHz, a rising edge below 300ps, and a falling edge below 500ps, with an output voltage range of 0-12V. The detector requires a power supply voltage of 9 to 24VDC and includes an internal output impedance of 1m ohm, recommending parallel connection with resistors for optimal response speed depending on the pulse width of the laser being detected. This device is versatile, supporting both free space and optical fiber inputs, and is designed to balance bandwidth and output voltage efficiently.

E. Experimental measurements of laser pulses

To measure the frequency of laser pulses according to the algorithm in Fig. 6, a converter with a high-speed photodiode detector, for instance, can be utilized (refer to Fig. 7). This type of converter is suitable for pulsed lasers with a rising edge of less than 500 ps, operating in the wavelength range from 300 nm to 1100 nm. It is capable of detecting femtosecond, picosecond, and nanosecond laser pulses, as well as quasi-continuous and continuous laser or non-laser light sources with high accuracy, even measuring frequencies exceeding 1 GHz.

For the specific scientific study of the laser color marking process using a 20 W fiber laser source "Rofin Power Line F 20" with a wavelength of 1064 nm, calibration measurements of the output laser pulse were conducted. Based on the device and algorithm described in the preceding point, measurements were performed to determine the dependencies between the frequency and the average power of the laser source, the pulse power, and the energy: $P = P(v)$; $P_p = P_p(v)$; and $E_p = E_p(v)$. A PRONTO-50-W5 meter with a range of up to 50 W was employed to measure power, while an E8SP-B-MT-IDR-D0 meter with an RS-232 output, capable of measuring pulse energy up to 0.93 mJ, was used. Both measuring devices encompass a very wide spectral range, including the wavelength of the laser source under study ($\lambda = 1064$ nm). Additionally, the duration τ of the laser pulse from 4 ns to 200 ns was measured during the study (see figure 8).
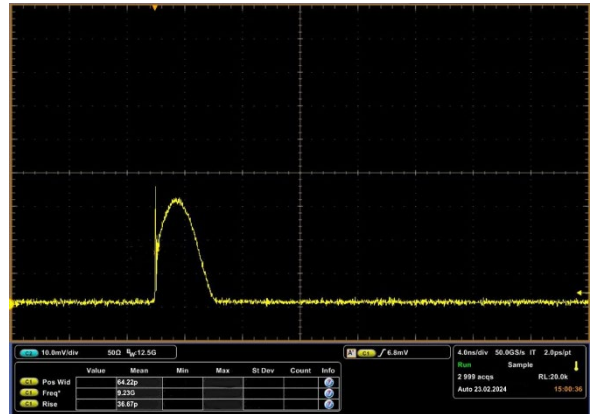
Fig. 8. Oscillogram of laser pulse - 4 ns measured with high speed photodiode detector

The calibration results of the above parameters are presented in Figure 9, Figure 10 and Figure 11.
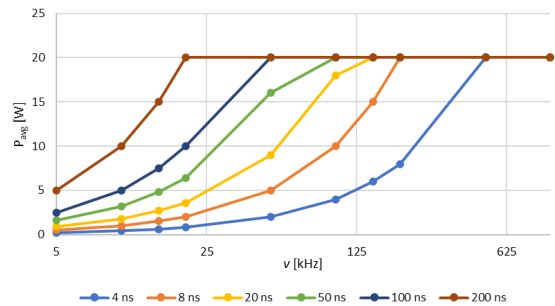
Fig. 9. Functional dependence of average power P_{avg} on pulse frequency v. The pulse duration is constant in the $4 \div 200$ ns range.

After analyzing the graphs and studying the characteristics of the laser pulse for the laser color marking process, the following conclusions can be drawn.

The peak power of each focused laser pulse decreases with increasing pulse frequency.
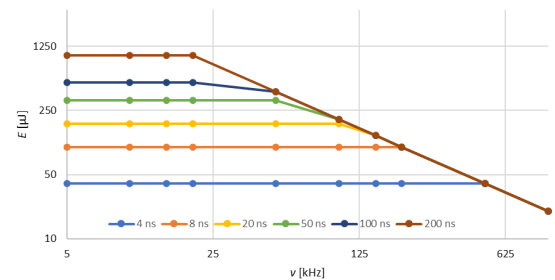
Fig. 10. Functional dependence of impulse energy E on pulse frequency v. The pulse duration is constant in the $4 \div 200$ ns range.
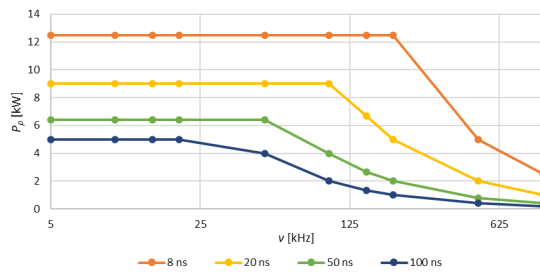
Fig. 11. Functional dependence of peak power P_P on pulse frequency v. The pulse duration is constant in the $8 \div 100$ ns range.

Since the purpose of laser color marking in the processing zone is to heat it only to the oxidation temperature of the surface and not to vaporize it, lower peak powers (Pp) and higher pulse frequencies are more suitable because they tend to heat the surface of the laser impact without reaching the melting point and vaporization.

By lengthening or shortening the pulse width, as observed in the graphs, the amount of heat on the surface of the part can also be controlled. Making small changes in pulse frequency and pulse width allows for the variation of the thickness of the oxide layer in the laser-affected zone, and these discrete changes in oxide thickness lead to certain color differences.

III. Conclusion

In conclusion, this article emphasizes the crucial importance of precise laser pulse measurement in improving the efficiency of fiber lasers in various applications in industry, medicine, and research. It discusses the complexities of fiber laser technology, including the different types of fiber lasers, their modes of operation, and the significance of dopant materials. The paper emphasizes the importance of pulse parameters, such as pulse duration, frequency, and energy characteristics, to optimize laser-material interaction. It describes advanced measurement techniques, including Autocorrelation, FROG, and SPIDER, and provides insights into their applications and advantages for comprehensive pulse characterization. This work contributes significantly to the advancement of the field by presenting a systematic approach to measuring laser pulse parameters. The theoretical material is also supported by experimental evidence. This enables the development of more efficient, reliable, and precise laser systems, fostering innovation in applications that depend on the precise control of laser pulses.

Overall, the analysis provides valuable insights into the relationship between pulse parameters and the laser color marking process. However, there are several areas where the analysis could be improved or expanded:

Quantitative Analysis: While the analysis describes trends observed in the graphs, it could benefit from more quantitative analysis. For example, providing specific numerical values or equations that relate pulse frequency, peak power, and pulse width to surface heating and oxide layer thickness would enhance the clarity and rigor of the conclusions.

Experimental Validation: It would strengthen the analysis to include experimental validation of the conclusions drawn. Conducting experiments to confirm the effects of varying pulse parameters on surface heating, oxide layer thickness, and resulting color differences would provide empirical support for the conclusions.

Discussion of Limitations: Addressing potential limitations or confounding factors in the analysis would enhance its credibility. For example, factors such as material composition, surface roughness, and ambient conditions could influence the effectiveness of pulse parameters in achieving desired color outcomes.

Consideration of Other Factors: While the analysis focuses on pulse frequency and pulse width, it may be beneficial to consider other factors that could impact the laser color marking process. Factors such as laser power, scanning speed, and substrate properties could also play significant roles and should be discussed if relevant.

Future Research Directions: The analysis could conclude with suggestions for future research directions or areas for further investigation. Identifying unanswered questions or areas where additional research could provide deeper insights into the laser color marking process would add value to the analysis.

By addressing these aspects, the analysis would be strengthened and provide a more comprehensive understanding of the relationship between pulse parameters and the laser color marking process.

IV. Reference

[1] M. Khorasani, at.al., On the role of process parameters on meltpool temperature and tensile properties of stainless steel 316L produced by powder bed fusion, *Journal of Materials Research and Technology*, Volume 12, 2021, p. 2438-2452, ISSN 2238-7854, doi.org/10.1016/j.jmrt.2021.04.043.

[2] Q. Wang, F. Wang, C. Cai, at.al., The essential role of the microstructure and composition in the corrosion resistance of laser-decontaminated surfaces, *Optics & Laser Technology*, Volume 152, 2022, 108111, ISSN 0030-3992,doi.org/10.1016/j.optlastec.2022.108111.

[3] W. Pacquentin, N. Caron, R. Oltra, Effect of microstructure and chemical composition on localized corrosion resistance of a AISI 304L stainless steel after nanopulsed-laser surface melting, *Applied Surface Science*, Volume 356, 2015, Pages 561-573, ISSN 0169-4332, https://doi.org/10.1016/j.apsusc.2015.08.015.

[4] M. Stafe, at.al., Nanopulsed ablation rate of metals dependence on laser fluence and wavelength in atmospheric air, *U.P.B. Sci. Bull., Series A*, Vol. 70, Iss. 4, 2008, ISSN 1223-7027

[5] Zhu, Q., Sun, W., Yoo, Y., Zhang, X., Hunter, N., Mao, A., ... & Lu, Y. (2023). Enhance corrosion resistance of 304 stainless steel using nanosecond pulsed laser surface processing. *Surfaces and Interfaces*, 42, 103479.

[6] Kim, H., Lee, W. J., Farrell, A. C., Balgarkashi, A., & Huffaker, D. L. (2017). Telecom-wavelength bottom-up nanobeam lasers on silicon-on-insulator. *Nano letters,* 17(9), 5244-5250.

[7] Gupta, S., Engin, D., Puffenberger, K., Litvinovich, S., Kimpel, F., & Utano, R. (2013, September). Fiber laser systems for space lasercom and remote sensing. In Nanophotonics and Macrophotonics for Space Environments VII (Vol. 8876, pp. 105-113). SPIE.

[8] Cusumano, A., Falsini, B., Giardina, E., Cascella, R., Sebastiani, J., & Marshall, J. (2019). Doyne honeycomb retinal dystrophy–Functional improvement following subthreshold nanopulse laser treatment: A case report. Journal of Medical Case Reports, 13, 1-5.

[9] Kim, I., Martins, R. J., Jang, J., Badloe, T., Khadir, S., Jung, H. Y., ... & Rho, J. (2021). Nanophotonics for light detection and ranging technology. *Nature nanotechnology*, 16(5), 508-524.

[10] Chhablani, J., Roh, Y. J., Jobling, A. I., Fletcher, E. L., Lek, J. J., Bansal, P., ... & Luttrull, J. K. (2018). Restorative retinal laser therapy: Present state and future directions. Survey of ophthalmology, 63(3), 307-328.

[11] Vaiano, P., Carotenuto, B., Pisco, M., Ricciardi, A., Quero, G., Consales, M., ... & Cusano, A. (2016). Lab on Fiber Technology for biological sensing applications. *Laser & Photonics Reviews*, 10(6), 922-961.

[12] Zhang, L., Tang, Y., & Tong, L. (2020). Micro-/nanofiber optics: Merging photonics and material science on nanoscale for advanced sensing technology. Iscience, 23(1).

[13] Georgi Iliev, Hristov H. "Modelling and Simulation of Electropneumatic Positioning System Including the Length of Pneumatic Lines" ENVIRONMENT. TECHNOLOGY. RESOURCES 14th International Scientific and Practical Conference. June 15-16, 2023, Rezekne Academy of Technologies, Rezekne, Latvia, Page 106-111 ISSN 1691-5402 Online IS. DOI 10.17770/etr2023vol3.7186

[14] Otto, H.-J., Stutzki, F., Modsching, N., Jauregui, C., Limpert, J., and Tünnermann, A. (2014). 2 kW Average Power from a Pulsed Yb-Doped Rod-type Fiber Amplifier. *Opt. Lett.* 39, 6446–6449. doi:10.1364/OL.39.006446

[15] Wei, H., Chen, K., Yang, Y., and Li, J. (2016). All-solid Very Large Mode Area Ytterbium-Doped Silica Microstructured Fiber Based on Accurate Control on Cladding index. *Opt. Express* 24, 8978–8987. doi:10.1364/OE.24.008978

[16] Wang, L., He, D., Feng, S., Yu, C., Hu, L., Qiu, J., et al. (2014). Yb/Er Co-doped Phosphate All-Solid Single-Mode Photonic crystal Fiber. *Sci. Rep.* 4, 6139. doi:10.1038/srep06139

[17] Lv, Y., Lou, S., Tang, Z., Liu, X., and Wang, X. (2020). Tunable C-Band and L-Band Multi-Wavelength Erbium-Doped Fiber Ring Laser Based on a Triple-Core Photonic crystal Fiber with Polarization-dependent Loss. *Opt. Laser Tech*. 128, 106269. doi:10.1016/j.optlastec.2020.106269

[18] Elahi, P., Kalaycıoğlu, H., Li, H., Akçaalan, Ö., and Ilday, F. Ö. (2017). 175 Fs-Long Pulses from a High-Power Single-Mode Er-Doped Fiber Laser at 1550 Nm. *Opt. Commun.* 403, 381–384. doi:10.1016/j.optcom.2017.07.072

[19] Stutzki, F., Gaida, C., Gebhardt, M., Jansen, F., Jauregui, C., Limpert, J., et al. (2015). Tm-based Fiber-Laser System with More Than 200 MW Peak Power. *Opt. Lett*. 40, 9–12. doi:10.1364/OL.40.000009

[20] Lee, E., Sun, B., Sun, B., Luo, J., Singh, S., Choudhury, D., et al. (2020). Compact Pulsed Thulium-Doped Fiber Laser for Topographical Patterning of Hydrogels. *Opto-Electronic Adv*. 3, 190039. doi:10.29026/oea.2020.190039

[21] S. Ali, K. A. S. Al-Khateeb and B. Bouzid, "Comparison of the effect structure on Ring and Linear Cavity Lasers of Er-Doped Optical Fibers," 2008 International Conference on Computer and Communication Engineering, Kuala Lumpur, Malaysia, 2008, pp. 546-549, doi: 10.1109/ICCCE.2008.4580663.

[22] Luna Zhang, Fengping Yan, Ting Feng, Wenguo Han, Yan Bai, Zhuoya Bai, Dan Cheng, Hong Zhou, Yuping Suo, Wavelength-tunable thulium-doped fiber laser with sampled fiber Bragg gratings, *Optics & Laser Technology*, Volume 120, 2019, https://doi.org/10.1016/j.optlastec.2019.105707

[23] Pulov D., P. Tsvyatkov "Optical Systems for Reducing the Divergence of Laser Beams", in. Proceedings of the 14th International Scientific and Practical Conference Environment. Technology. Resources. Rezekne, Latvia, Volume 3, 339-343, 2023, Online ISSN 2256-070X. DOI: 10.17770/etr2023vol3.7217

[24] Kokalarov, M., B. Sakakushev, S. Parvanov (2021). Generalized Methodology for Application of the Photogrammetric Method for Measurement in Heavy Engineering XXXI International Scientific Symposium Metrology and Metrology Assurance, , IV.3., doi: 10.1109/MMA52675.2021.9610966

[25] G. Račiukaitis, M. Brikas, P. Gecys, B. Voisiat, M. Gedvilas, et al., Use of high repetition rate and high power lasers in microfabrication: how to keep the efficiency high? *JLMN J. Laser Micro/Nanoeng*., 4 (2009), pp. 186-191

[26] Schille, J., Schneider, L. & Loeschner, U. Process optimization in high-average-power ultrashort pulse laser microfabrication: how laser process parameters influence efficiency, throughput and quality. Appl. Phys. A 120, 847–855 (2015). https://doi.org/10.1007/s00339-015-9352-4

[27] J. Finger, C. Kalupka, M. Reininghaus, High power ultra-short pulse laser ablation of IN718 using high repetition rates, Journal of Materials Processing Technology, Volume 226, 2015, 221-22, https://doi.org/10.1016/j.jmatprotec.2015.07.014.

[28] D.J. Kane; R. Trebino. Characterization of arbitrary femtosecond pulses using frequency-resolved optical gating. IEEE Journal of Quantum Electronics (Volume: 29, Issue: 2, February 1993), DOI: 10.1109/3.199311.

[29] Zhang, H., Fu, M., Chen, X., Qi, J., Yi, W., Zhang, Y., Zhang, Y., Xu, Y., Li, X. Highly precise timing alignment of multi-wavelength interleaved cavity-less pulse sources with FROG (2023) Optics Express, 31 (26), pp. 44515-44522. DOI: 10.1364/OE.505879

[30] Dichev, D., I. Zhelezarov, R. Dicheva, D. Diakov, H. Nikolova, G. Cvetanov. Algorithm for estimation and correction of dynamic errors. 30th International Scientific Symposium "Metrology and Metrology Assurance 2020", September, 2020, Sozopol, Bulgaria. DOI: 10.1109/MMA49863.2020.9254261

[31] Dichev, D., Koev, H., Bakalova, T., Louda, P. A Gyro-Free System for Measuring the Parameters of Moving Objects. Measurement Science Review, volume 14, issue 5, 2014, pp. 263-269. DOI: 10.2478/msr-2014-0036

[32] Yamada, R., Yamamoto, etc., Correction: Derivation of 1.064 μm normal albedos on the C-type asteroid Ryugu from laser pulse intensity measurement of the Hayabusa2 LIDAR (Earth, Planets and Space, (2022), 74, 1, (166), 10.1186/s40623-022-01717-z) (2024) Earth, Planets and Space, 76 (1), art. no. 17, DOI: 10.1186/s40623-023-01949-7

[33] https://www.gentec-eo.com/

Investigation of the optimization process of laser surface marking on polyamide samples

Anželika Litavnieka
Rezekne Academy of Technologies
Faculty of Engineering
Rēzekne, Latvia
litavnieka12@gmail.com

Imants Adijāns
Rezekne Academy of Technologies
Faculty of Engineering
Rēzekne, Latvia
line 5: imants.adijans@rta.lv

Emil Yankov
Rezekne Academy of Technologies
Faculty of Engineering
Rēzekne, Latvia
line 5: emil.yankov@rta.lv

Lyubomir Lazov
Rezekne Academy of Technologies
Faculty of Engineering
Rēzekne, Latvia
lyubomir.lazov@rta.lv

Artis Bikovs
Rezekne Academy of Technologies
Faculty of Engineering
Rēzekne, Latvia
ab21336@edu.rta.lv

Abstract. **Give Thermoplastic laser marking technology is becoming increasingly popular in the electronics industry. Using marking codes requires more information to store, which requires the marking to be of good contrast and durability over time. The main goal of the research was to achieve high-quality marking on polyamide surfaces. A nanosecond fiber laser was used to laser mark polyamide samples. An experimental marking matrix of 8 columns and 6 rows was developed, respectively varying the marking step, scanning speed, marking repeats. The dimensions of the marked squares are 10×10 mm. Surface changes and marking quality were examined using a laser scanning microscope. Markings with good contrast were found, as well as marking modes with partial and full melting modes. Roughness and contrast were measured for the optimal marking modes. Graphical dependences are constructed for the effect of roughness and contrast on propagation speed and distance in laser marking. For the study, the average laser power was fixed. During the experiment, it was found that laser marking on polyamide can lead to different shades of gray and yellow, and the surface after laser treatment has become rougher.**

Keywords: fiber laser, laser marking, polyamide, roughness, contrast.

I. Introduction

Currently, lasers are increasingly used, especially in industry and in various industries, and laser marking on thermoplastics is especially in demand [1], [2], [3]. One of the most common thermoplastics is polyamide, which has many advantages over other polymers: good hardness, chemical resistance, corrosion and wear resistance [4]. Thermoplastics can be marked with: ablation, bleaching or darkening (thermal), carbonization, color marking, engraving, foaming and melting [5]. But laser marking on materials such as polyamide is based on laser heating of the processed material, and the heating is below the melting temperature or the initial point of thermal decomposition [6]. However, polyamide cannot be marked; problems can arise both with direct printing and with laser marking [7], [8].

Therefore, the author Li in his study added glass fiber to polyamide in order to obtain a good marking. The marking mechanism was a combination of carbonization with microbubbles. The results of Li's study were as follows: the optimal formulation was achieved with a combination of medium dye loading [9]. Authors Estella Neiss and Li used the same laser, Nd:YAG, in their experiments. However, Estella's technology was direct marking without additives. The average laser power was fixed at 5.5 W for all experiments, but the pulse repetition frequency rate (20-60 kHz) and scanning speed varied from 200-600 mm/s. The results of the study showed that the quality of the marking depends on the speed and frequency, and as a result, various shades of gray and white with a slightly rough surface can be obtained. Knowing the energy density and area, it is possible to estimate the duration of exposure required for marking. The reference energy density for polyamide is 0.18 to 0.55 J/mm2. In the second part of the study by Estella and others, 2 lasers were compared: Nd:YAG (pulse repetition frequency 10 kHz, pulse duration 1 ms, average power 30 W) and fiber laser (pulse repetition

frequency 20 kHz, average power 20 W). The results showed that the duration of exposure is the same, although these two lasers show very different characteristics [10]. But the authors of McKee and others believe that more successful marking parameters with a solid-state YAG laser are: an average power of about 20 W and a pulse repetition rate of 20,000 pulses per second [11]. Jia and others conducted their research based on a nanosecond pulsed laser. An analysis of the results showed that the best processing quality on polyamide can be obtained when the energy density of a single laser pulse is 25 J/cm^2, the pulse repetition frequency is 30 kHz [12]. When marking on polyamide, different lasers can be used, however, it is mentioned that high-energy lasers are used for marking the surface of materials [13]. Author Lawrence and others used a 60W CO_2 laser. Four patterns were applied on the surface of polyamide samples: with a step of 50 μm and 100 μm. For each circuit, laser power 7W and scanning speed 600mm/s. The results of the study were similar to those of the author Estella Neiss, as the laser-treated polyamide samples were significantly rougher than the original sample. But the author Lawrence found that the surface pattern was sharper along one hatching axis than the other [14]. Scott also noted that polyamides are one of the most difficult polymers for laser marking. But he achieved good contrast using a fiber laser with a short pulse in the range from 20 ns to 50 ns [15]. Hofmann and others used 5 different lasers in their work and came to the conclusion that providing an energy density of about 0.9-1 J/cm2 is sufficient for marking white polymers, but due to the uneven intensity of the beam along the profile, areas with strong and weak color are obtained. Overexposure is usually recognized by a light gray tint that shows a foamy structure under the microscope. Also, the authors noticed an interesting fact that samples of seemingly the same color and the same polymer composition react differently under the same exposure conditions, some give clear traces, and some do not react at all [16]. Recently, there has been a lot of interest in the use of laser marking and texturing in various fields of industry [17], [18], [19] and [20].

The above research and analysis by various authors show that achieving high quality marking on polyamide is a multi-factorial task. The main objective of the present study is to emphasize the influence of two factors having a significant role in the laser marking process, namely; changing the marking step and scanning speed.

II. MATERIALS AND METHODS

2.1. Substrates. Scientific study on marking on polyamide 12 plates. Melt temperature 185.6 °C – 186.5 °C, melting enthalpy ΔH$_m$- 110.7 J/g – 120.2 J/g and crystallization point T$_c$ 155.3 °C – 156.3 °C. Plate dimensions: height 79 mm, width 100 mm and thickness 3 mm. The polyamide samples were laser marked with a planned matrix of 8 columns and 6 rows. The size of one square is 10×10 mm with a distance of 1 mm between them. The samples were not processed and marked in a warm air environment. They are marked as delivered.

2.2. Laser Marking Setup. All experiments were carried out using fiber laser Rofin-Sinar Powerline F-20 (Fig. 1.). This is a fiber optic laser operating at a wavelength of 1064 nm. When marking on a sample of polyamide was fixed: the average output power P (W), constant pulse duration τ (ns) and pulse repetition rate v (Hz) shown in Table 1. The laser system is equipped with a galvanometer that allows the beam to be deflected. The laser beam was focused on the target through an L-Theta lens with a focal length of 184 mm. The beam diameter at the focus was 40 μm. A fan and a temperature controller were used to stabilize the substrate temperature.
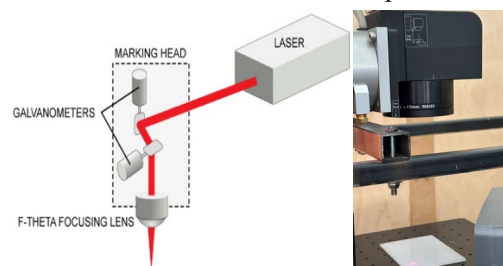
Fig.1. Fiber laser system Rofin Powerline F-20 Varia.

TABLE 1 LASER SYSTEM PARAMETRS

Wavelenght (λ), nm	1064
Output Power (P), W	0.1 to 19.7
Pulse Duration (τ), ns	4, 8, 14, 20, 30, 50, 100 and 200
Pulse Repetition (v), kHz	2 to 1000

2.3. Surface characterization methods. Two matrices were scanned using an HP Scanjet G3010 scanner. Color format, file type: TIF, resolution 2400 DPI. The Adobe Photoshop program was used to measure the contrast of each square of the matrix. To calculate the contrast in percentage, the formula (1) was used:

$$K = \frac{N_f - N_x}{N_f} \times 100\% \qquad (1)$$

Where N_f is the contrast of the material before processing, N_x is the contrast of the material after processing. Surface changes and marking quality of each matrix were examined using an Olympus OLS5000 3D laser scanning microscope Fig. 2. Microscope parameters: increase x113, area 2566 x 2572 μm, objective 5x, step 25, pitch 20 μm.
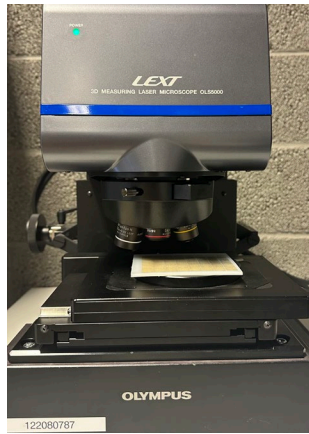
Fig.2. Laser scanning microscope Olympus OLS5000 3D.

2.4. Laser treatment. Two samples were made for the marking study on polyamide. By varying the scanning speed and step between marking lines, various surface roughness can be obtained. But by changing only the scan speed and marking step, the results were not positive. Thus was added an important parameter repetitions. Therefore, for the first matrix, six scanning speeds ν (mm/s) – one step 100 mm/s and 8 different marking steps *Δx* (μm)- one step 5 μm and 4 repetitions for each square were chosen shown in Table 2.

TABLE 2. FIRST MATRIX LASES SYSTEM PARAMETERS

Scanning Speed (ν), mm/s	100, 200, 300, 400, 500, 600
Marking Step (Δ**x**), μm	10, 15, 20, 25, 30, 35, 40, 45
Repetitions,	4
Pulse Duration (τ), ns	200
Pulse Repetition (ν), kHz	20

For the first and second matrix, was used the same pulse repetition frequency ν =2 kHz, pulse duration τ = 200 ns, power P =19.7 W, area size 10x10 mm, angle step of 45° and start angle of 90° were used. For the second matrix was changed repetitions and marking step shown in Table 3. A scanning speed was fixed. The results of laser processing can be seen on Fig.3.a and Fig.3.b.

TABLE 3. SECOND MATRIX LASES SYSTEM PARAMETERS

Repetitions	2, 4, 6, 8, 10, 12
Marking Step *Δx*, μm	10, 15, 20, 25, 30, 35, 40, 45
Scanning Speed (ν), mm/s	100
Pulse Duration (τ), ns	200
Pulse Repetition (ν)	2 kHz
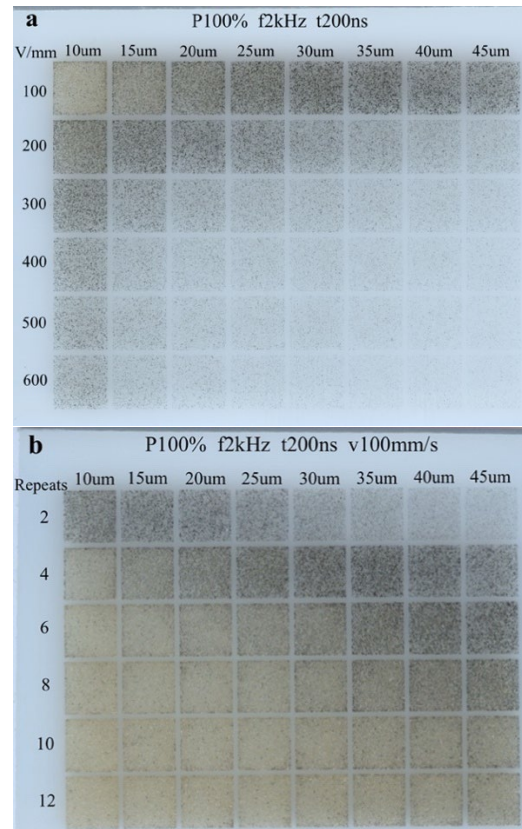
Fig.3. Laser marking of polyamide samples with a fiber laser a) first matrix: scanning speed 100 mm/s - 600 mm/s and marking step 10 μm - 45 μm b) second matrix: repeats 2-12 and marking step 10 μm -45 μm.

III. RESULTS AND DISCUSSION

To measure the experimental results, two different analyzes were performed for each matrix: a contrast analysis and a roughness analysis. If look at figure 3 (a), at first glance, the highest contrast appears at scanning speed ν = 100 mm/s.
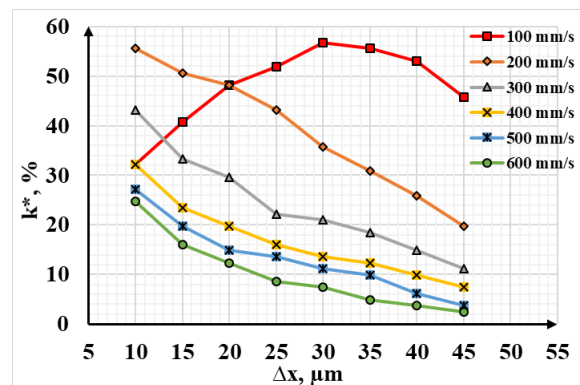
Fig.4. Contrast changes of marking at first polyamide sample depending the scanning speed and marking step.

The results of the first matrix, where the scanning speed and marking step were changed, showed that the highest contrast is observed at a scanning speed *ν* = 100 mm/s and a marking step Δ*x* = 30 μm Fig. 4. But if seen at other speeds, can see that the more marking step and scanning speed, the lower marking contrast becomes. This is confirmed by trend lines, which indicate that the contrast is getting smaller.

The graph highlights the results at 2 repetitions, which show that by changing the marking step, the contrast sharply decreases. But if look at repetitions from 4 to 12 increasing the marking step, the contrast increases. This is confirmed by the trend lines that go up.
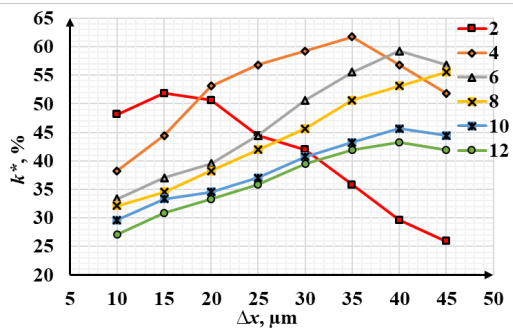
Fig.5. Contrasting marking changes on the second polyamide sample depending the marking step and repetitions.

The texture of the markings on the polyamide surface were analyzed using a laser microscope. Figure 6 shows examples of images obtained using a microscope of the first matrix with a marking step $\Delta x = 10$ µm and a scanning speed $v = 100$, 200, and 400 mm/s. As can be seen in the figure, the roughness of the raw material is different from the roughness of the material processed by the laser beam, and this is affected by different scanning speeds. The most roughness changes are appears at the smallest scanning speeds $v = 100$ and 200 mm/s, increasing the speed the roughness of the polyamide becomes less.
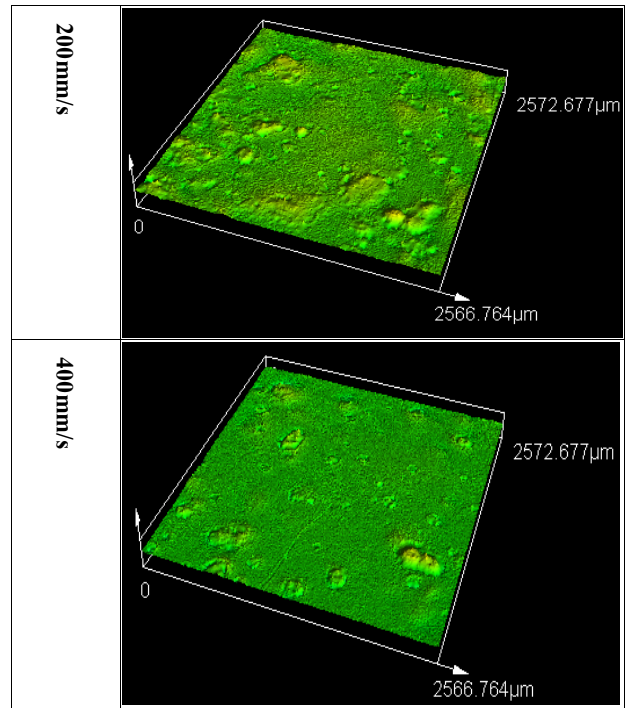
Fig.6. 3D image of the first matrix, first column scanning speed from 100 to 600 mm/s, marking step 10 µm.

If emphasize on at one of the lines of the first matrix Fig. 3(a), you can see that the roughness becomes smaller. This is confirmed by the graph in Fig. 7. At scanning speeds $v = 100$, 200, 300, 400, 500 and 600 mm/s, the roughness decreased with an increase in the marking step. The greatest changes in the surface roughness of polyamide were observed at a scanning speed $v = 100$ mm/s and marking step $\Delta x = 15$ µm.
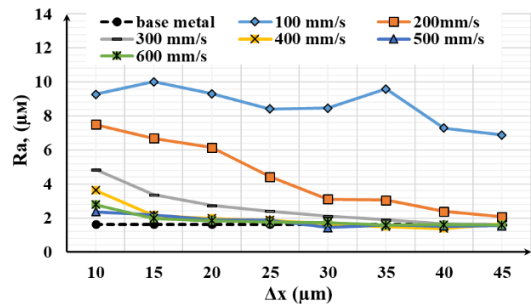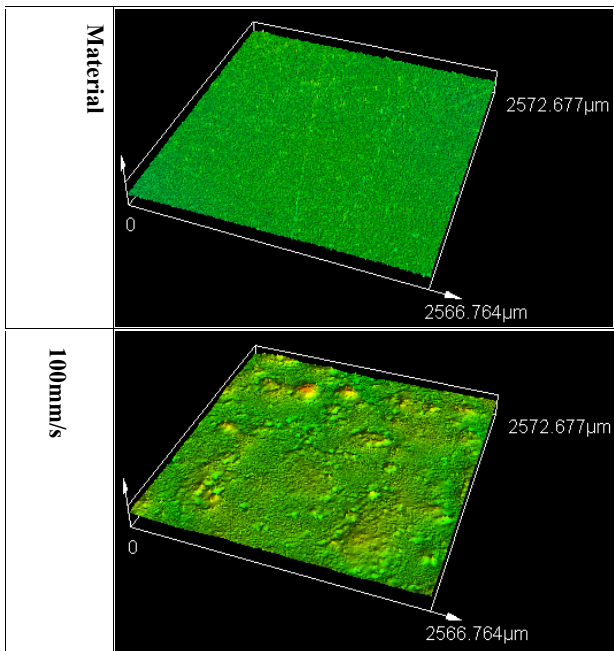
Fig.7. Change in the surface roughness of the first polyamide matrix with a change in scanning speed and marking step.

Fig.8 shows examples images for second matrix using microscope with a marking step $\Delta x = 10$ µm and repetitions 2, 4 and 12. Based on the results, can be seen that repetitions also affect the surface roughness. But can see that the largest changes in roughness are precisely with 4 repetitions. At 12 repetitions, the changes in roughness are not as significant as at 2 and 4. The rest of the repetitions are approximately the same at first glance.

Fig.9. Change in the surface roughness of the second polyamide matrix with a change in the marking step and repetitions.

IV. Conclusion

This scientific publication describes the features of the process of marking polyamide with a laser. Material such as polyamide is difficult to mark, this was confirmed by the first unsuccessful attempts, in which only the scanning speed and marking step were changed. By adding a parameter such as repetitions, the results improved. A fiber laser source with a wavelength of 1064 nm was used in the experiments. The results showed that by varying the scanning speed, marking pitch and repetition, high contrast markings and a rough surface can be achieved. The greatest contrast was found at 2 and 4 repetitions, scanning speed of 100 mm/s. The highest roughness was obtained with the following parameters: 12 repetitions, scanning speed 100 mm/s, and marking step 45 µm. However, in the first matrix, with 4 repetitions, increasing the scanning speed and marking step reduced the roughness. These results confirm that scanning speed, repetition, and marking pitch affect marking. It has also been found that different shades of gray and yellow can be obtained by laser marking polyamide. In the future, it would be interesting to carry out such experiments with smaller marking steps or, for example, using a CO_2 laser and different colors of polyamide.

Fig.8. 3D image of the second matrix, first column scanning speed from 100 to 600 mm/s, marking step 10 µm.

But if we compare all the results of changing the roughness at different marking steps and repetitions, then we can see that with repetitions 2 and 4, with an increase in the marking step, the roughness decreases. With repetitions 6, 8, 10 and 12, with an increase in the marking step, the roughness increases. With 2 repetitions, by increasing the marking step, the roughness decreases. The greatest roughness was found with a 12-fold repetition and a marking step $\Delta x = 45$ µm, the smallest changes in roughness - with a 2-fold repetition and a marking step $\Delta x = 45$ µm (Fig. 9).

References

[1] L. Lazov, H. Deneva, P. Narica, "Laser marking methods," Environment. Technology. Resources. Proceedings of the International Scientific and Practical Conference, vol. 1, p.108-115, 2015. [Accessed January 10, 2023], http://dx.doi.org/10.17770/etr2015vol1.221

[2] I. Balchev, L. Lazov, et al., Investigation of the influence of the scanning speed and step in laser marking and engraving of aluminum, 2021, J. Phys., Conf. Ser., 1859 012002, https://doi.org/10.1088/1742-6596/1859/1/012002

[3] L. Lazov, N. Angelov, Influence of some technological parameters on the contrast of laser marking on the fly. Laser Phys., 2012, 22, 1755–1758 . https://doi.org/10.1134/S1054660X12110084

[4] R. M. Boom, "Membrane Formation by Immersion Precipitation: The Role of a Polymerıc Additive, "Proefschrift Enschede. Netherlands. ISBN 90-9005223-2, 1992.

[5] E. Bitay, "ELaser markability of PVC coated automotive electric cables," Express Polymer Letters, vol. 13, p. 379-389, 2019. [Accessed January 12, 2023], https://doi.org/10.3144/expresspolymlett.2019.31

[6] I. D. Savu, S. V. Savu, N. A. Sirbu, "Heat affected zones in polymer laser marking."J Therm Anal Calorim, vol.115, p.1427–1437, 2014. [Accessed February 25, 2023], https://doi.org/10.1007/s10973-013-3443-2

[7] S. Y Li, X. R. Dang, Y. Zhang, "Recent progress of laser marking on plastics, " China Plastics technology Industrialization Symposium, p366-374, 2009. [Accessed January 9, 2023].

[8] A. Burgess, K. Feng, "Color laser marking: a new marking and decorating alternative for olefins". Coloring Technology for Plastics, p301–307, 1999. [Accessed January 25, 2023], https://doi.org/10.1016/B978-188420778-5.50039-5

[9] H. W. Li, "Preparation of laser markable polyamide compounds. Journal of Physics: Conference Series, 1765, 2021. [Accessed January 9, 2023], https://doi.org/10.1088/1742-6596/1765/1/012003

[10] E. Neiss, M. Flury, J. Fontaine, "Diffractive optical elements for laser marking applications," Optical Sensors, vol. 7003, p. 1-8, 2008. [Accessed January 9, 2023], https://doi.org/10.1117/12.779944

[11] T. J. McKee, L. Toth, W. Sauerer, "Customized Decorating of Plastic Parts with Gray Scale and Multi-Color Images Using Lasers," Coloring Technology for Plastics, p.295–300, 1999. [Acessed March 13, 2023], https://doi.org/10.1016/B978-188420778-5.50038-3

[12] Z. Jia, K. Zhao, W. Liu, J. Ma, L. Wang,"Nanosecond pulsed laser processing circuits on the copper clad polyimide," International Journal of Machining and Machinability of Materials, vol.15, p.157-173, 2014. [Accessed March 16, 2023], https://doi.org/10.1504/IJMMM.2014.060547

[13] Z. Cao , G. Lu, H. Gao, Z. Xue, K. Luo, K. Wang, M. Luo, "Preparation and laser marking properties of poly (propylene)/molybdenum sulfide composite materials." ACS omega, vol.6(13), p.9129-9140, 2021, [Accessed February 25, 2023], https://pubs.acs.org/doi/abs/10.1021/acsomega.1c00255

[14] D. G. Waugh, J. Lawrence, P. Shukla, C. Chan, I. Hussain, H. C Man, G. C. Smith, "Laser surface treatment of polyamide and NiTi alloy and the effects on mesenchymal stem cell response," Industrial Laser Applications Symposium, 2015. [Accessed January 9, 2023], https://doi.org/10.1117/12.2182432

[15] S. R. Sabreen, "Fiber laser marking on nylon (polyamide) plastics," April 2021. [Online]. Available: https://plasticsdecorating.com/articles/2021/fiber-laser-marking-on-nylon-polyamide-plastics/ [Acessed March 13, 2023]

[16] M. Hofmann, F. Breitenfellner, N. Buhler, R. C. Sykes, H. Gugger, "High Contrast and intact Surface - a Challenge in Laser Marking of Plastics," Lasers in Motion for Industrial Applications, vol. 744, p. 156-180, 1987. [Acessed March 13, 2023], https://doi.org/10.1117/12.966970

[17] T. W. Ng and S. C. Yeo, "Aesthetic laser marking assessment," Optics & Laser Technology, vol. 32 no. 3, p. 187–191, 2000. [Accessed January 9, 2023], https://doi.org/10.1016/S0030-3992(00)00040-2

[18] Risham Singh Ghalot, L. Lazov, et al., Investigation of the Change in Roughness and Microhardness during Laser Surface Texturing of Copper Samples by Changing the Process Parameters, 2023, Coatings, 13(11):1970, https://doi.org/10.3390/coatings13111970

[19] L. Lazov, et al., Modification of the roughness of 304 stainless steel by laser surface texturing (LST), Laser Physics, 2023, Volume 33, Number 4, https://doi.org/10.1088/1555-6611/acbb76

[20] N.Angelov, Investigation the Influence of the Number of Repetition and Volumetric Energy Density on Laser Marking of Products, Contemporary Materials, V−2, pp. 251-253, 2014, https://doi.org/110.7251/COMEN1402250A

Laser surface marking on engineering thermoplastic: polyamide

Anzelika Litavnieka
Rezekne Academy of Technologies
Faculty of Engineering
Rēzekne, Latvia
litavnieka12@gmail.com

Imants Adijāns
Rezekne Academy of Technologies
Faculty of Engineering
Rēzekne, Latvia
imants.adijans@rta.lv

Abstract. **Its style sheet. Marking on polyamide is an important process because this type of material is widely used in many industrial sectors. Also, laser marking is a popular and easily automated method. But materials like polyamide have several properties, such as white color, that make laser marking a complicated process. White color has low laser absorption, so good marking results are difficult to achieve. Different types and parameters of the laser system are used for marking polyamide. To improve the marking results on polyamide, auxiliary materials are often used, which are applied to the polyamide surface. However, the most promising ranges of marking parameters without incorporating auxiliaries on the polyamide surface are still unknown. Successful marking on polyamide requires a deep study of parameters and various conditions.**

Keywords: laser marking, polyamide, laser parametrs, laser sources.

I. INTRODUCTION

Research into the impact of laser radiation on materials has been ongoing since the invention of lasers. As technology continues to advance, lasers are widely used for processing various materials [1]. Laser marking is an area of significant interest in laser technology due to its widespread application. Currently, plastics, glass, metals and polymers are the primary focus of scientific investigation concerning the interaction between radiation and materials. There are various models and mechanisms that attempt to explain this interaction, but a comprehensive framework for selecting parameters and explaining material behavior under specific conditions is still lacking [2]. The analysis also seeks to identify the best speed and power levels to use for a specific ablation zone geometry when marking and engraving products, catering to different user needs. Laser marking and engraving has evolved as an appealing method for labeling plastic and polymers consumer goods, offering a fast and cost-effective way to create various identification products such as barcodes, security information, and codes with flexibility in design [2], [3].

Laser marking is a surface modification technique that changes the surface's optical properties, structural characteristics, and melting or evaporation in the impact zone Fig. 1.

Fig. 1. Different physical processes by interaction of laser beam with the substrate [1]

The aim of this study is to reveal the different possibilities for laser marking of polyamide and how different processing parameters respond to laser irradiation.

II. EFFECTS OF LASER IRRADIATION ON POLYAMIDE PROPERTIES

Some of the most commonly observed effects and changes in surface properties are related to: a) Surface modification; b) Changes in chemical structure; c) Coloring; d) Thermal properties; e) Modification of the microstructure; f) Improved adhesion:

a) Surface modification often results in changes in surface roughness, wettability and adhesion properties. For example, the surface can become more hydrophilic or

hydrophobic depending on the laser parameters and polymer composition. That is, the laser impact on the surface of polyamide materials leads to significant changes in morphology.

b) Laser interaction with polyamide molecules can cause chemical changes in them. This often results in chain scission, cross-linking, or the formation of new chemical groups. These changes, in turn, lead to a change in the polymer's mechanical properties, such as tensile strength, elongation at break, and impact resistance.

c) Depending on the laser parameters and the composition of the polyamide, laser irradiation can cause changes in the color of the material. This is often due to the formation of chromophoric groups or changes in the molecular structure of the polymer, leading to changes in the absorption and reflection properties of light.

d) The interaction of laser radiation with polyamide materials can affect their thermal characteristics. It caused changes in the crystallinity, melting point and thermal stability of the polymer.

e) Laser interaction with polyamide can affect the mechanical, optical and barrier properties of the material. This effect is a result of microstructural changes in the polyamide matrix. This includes changes in the orientation of polymer chains, crystal structure and morphology.

f) Laser surface treatment can improve the adhesion of polyamide materials to other substrates or coatings. By modifying surface chemistry and morphology, laser irradiation can promote bonding with adhesives, paints, or other functional coatings, improving overall material performance in a variety of applications.

Based on literature reports, three thermal models that describe the interaction of laser radiation with a material have been identified [3-4].

III. FOR SOME SPECIFIC EXAMPLES OF THE INTERACTION OF LASER RADIATION WITH MATERIAL

For example, when using long pulses (less than 1 ms), the material can be removed through photothermal ablation or evaporation caused by heat, resulting in the destruction of chemical bonds without significant heat input in some instances. Other example, shorter pulses (less than 1 ns) still maintain thermal equilibrium but mainly lead to evaporation. The heating and cooling processes follow specific mathematical functions, and plasma formation leads to gradual crater formation. Or ultra short pulses (less than 1 ps) lead to non-thermal equilibrium, causing direct evaporation and the Coulomb effect. This process removes material without significantly heating nearby areas, and traditional thermal concepts do not apply. Each case has distinct patterns to be considered when processing materials [6-9]. Laser technology offers various methods for marking polymers, such as carbonization, ablation, discoloration, melting. These processes induce changes in the molecular structure, particularly in the position of carbon within the polymer. Under specific wavelengths of laser radiation, the material undergoes energy-induced local alterations in its structure and properties. The selected impact area aims to be minimal yet detectable by the necessary

technical equipment for marking. Utilizing wavelengths, typically within the UV range, the irradiated material undergoes alterations in its optical properties, particularly its transmission coefficient. Even translucent materials with ideal microstructures and no impurities exhibit fundamental light absorption. Upon light absorption in the UV and visible spectrum, the electron shells of molecules become excited, transitioning the molecule from a lower energy state to a higher one. The excitation energy of the electron shell exceeds the energy of its vibrations [6]. As has already been mentioned different techniques such as ablation, oxidation, melting, carbonization, and foaming, as well as effects like discoloration, flowering, and dehydration, can be identified as the primary methods for marking plastic products. For example, some authors used thermoplastic marking Nd:YAG laser-direct marking without additives in their experiments using a fixed mean laser power of 5.5 W, a pulse repetition frequency speed of 20-60 kHz, and a scanning speed of 200-600 mm/s. As a result, various shades of gray and white arose with a slightly rough surface. In another study comparing two lasers: Nd:YAG with a fiber laser found that the duration of exposure for these lasers was similar despite the different laser properties. In addition, already using the solid-state YAG laser, the average power was about 20 W and the pulse repetition rate at 20,000 pulses per second. 60 W power was applied using CO_2 laser. When using fiber lasers for marking, experiments were performed with a short pulse range of 20 ns to 50 ns. While different lasers can be used to label thermoplasts, it is noted that high-energy lasers are commonly used for this purpose. In another article, used fiber lasers with 19.7 W average power, had the following parameters: scanning speed from 100 mm/s to 600 mm/s and marking step from 10 to 45 μm with repetitions from 2 to 12. The results showed that the best contrast was achieved at the marking step of 30-45 μm and the scanning speed of 100 mm/s, markings with gray and yellowish tone were created [10-15]. In polymer production, adding marks at the final stage holds significant value. Many polymer items bear markings for diverse reasons, including adorning or customizing objects, imprinting serial numbers or barcodes for identification, ensuring quality control, and etching logos or product names, serving practical and aesthetic purposes. Typically, the needs involve rapid writing, direct application on the finished product to bypass additional time-consuming and costly measures, as well as limited use of toxic or hazardous substances, ideally relying on uncomplicated and adaptable equipment [16].

IV. LASER MARKING SYSTEMS FOR POLYAMIDE

Laser marking refers to the use of a laser beam to mark or label items and materials. This can involve several methods, including removing material, adding color, annealing, and creating a foaming effect.

Laser marking involves a multifaceted technological procedure, requiring the careful selection of an appropriate laser. When assessing the optimal choice for a particular laser marking system, several important factors must be considered: the mechanism for delivering laser radiation, laser specifications, ease of operation, manufacturer recommendations, service guarantee and

maintenance, as well as cost. It's important to note that the specifications of lasers canvary significantly between different types [17]. Various laser systems can be used in the process of marking - see table 1.

TABLE 1 CLASSIFICATION OF LASER MARKING SYSTEMS TYPES FOR POLYMER/POLYAMIDE MATERIALS [18]

Laser Marking System Type	Description
CO2 Laser Marking Systems	Utilize a carbon dioxide laser to mark polymer materials. CO2 lasers are suitable for marking a wide range of polymers, including polyamides. They typically operate in the infrared wavelength range and are known for their high power and precision. CO2 lasers can produce high-quality marks with minimal thermal damage to the surrounding material.
Fiber Laser Marking Systems	Employ a fiber laser source to mark polymer materials. Fiber lasers offer high beam quality, excellent focusability, and efficient energy conversion. They are capable of producing fine, high-contrast marks on polyamide surfaces. Fiber lasers are particularly suitable for marking applications that require high-speed processing and precision.
Diode-Pumped Solid-State (DPSS) Laser Marking Systems	Use a diode-pumped solid-state laser to mark polymer materials. DPSS lasers offer a compact and efficient laser solution with high beam quality and reliability. They are often used for marking polymers due to their versatility, precision, and ability to produce permanent marks with minimal heat-affected zones.
UV Laser Marking Systems	Employ ultraviolet (UV) lasers to mark polymer materials. UV lasers operate at shorter wavelengths compared to other laser types, allowing for precise and high-resolution marking on polyamide surfaces. UV laser marking systems are suitable for applications requiring fine details, such as micro-marking or marking on sensitive materials.
Green Laser Marking Systems	Utilize green lasers to mark polymer materials. Green lasers offer a compromise between the infrared CO2 lasers and UV lasers, providing good beam quality and absorption characteristics for marking polyamides. Green laser marking systems are suitable for a wide range of marking applications, including high-contrast marking and color change marking on polymer.
Hybrid Laser Marking Systems	Combine multiple laser sources or wavelengths within a single marking system. Hybrid laser marking systems offer versatility and flexibility, allowing users to switch between different laser types or wavelengths depending on the specific marking requirements of polyamide materials. They can accommodate a wide range of marking applications, from surface engraving to color marking and barcode printing.

Practical considerations play a role in selecting the right laser, but the most critical factor is its wavelength. Lasers are available across a range of wavelengths.

Common lasers for marking include the following: CO_2 gas laser (used for thermosetting polymers), xenon chloride (XeCl) excimer gas laser with a 308 nm wavelength, Nd:YAG solid-state laser, ytterbium fiber laser with a wavelength of 1060 nm, frequency-doubled Nd:YVO4, 532 nm wavelength (visible, green), frequency-tripled Nd:YVO4 or Nd:YAG solid-state laser with a 355 nm wavelength (UV). UV lasers have gained rapid popularity lately. [17-19].

The use of lasers to mark polymers has become increasingly popular in the past ten years. This method is quick, affordable, and adaptable, enabling the creation of permanent and durable marks. The process involves directing a laser (typically a focused Nd-YAG pulsed laser emitting at 1064 nm) onto the polymer's surface to achieve the marking [16]. The main aim of laser marking is to alter the visual contrast. This can be achieved in two ways: by changing the color or by changing the reflections. Virtually all types of lasers can be utilized for marking. Small spots of this kind are commonly employed in machine-readable systems. The use of such a small spot diameter for eye-readable codes is feasible if multiple lines are used to increase the width. However, adding more lines also increases the resulting marking time. To reduce processing time and increase the spot size, special long-focus lenses or telescopes are utilized. The type of image being marked, its design and quality, the type of item, operational requirements, and the material being used should determine the type of laser and the laser beam positioning systems to be employed. Typically is employed wiht galvano mirrors systems Fig. 2. [20].
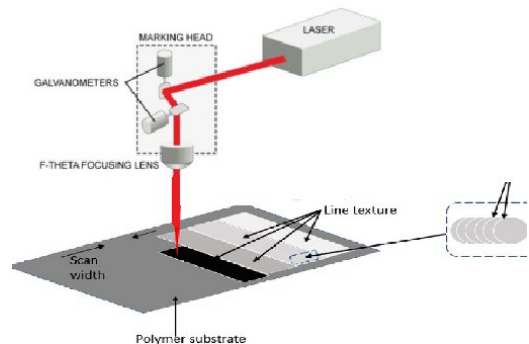
Fig. 2. Laser marking schematic image [20]

The focal length is crucial in deciding the size of the focused area, marking field, minimum line width, and power density on the workpiece. The combination of the scanner and the marking software dictates the scanning speed. Control systems and software for various laser marking setups vary significantly. The control system may involve workpiece feeding, beam activation/deactivation control, and interfaces for computers, laser sources, stages, and protection/alarm systems. The marking software should be simple to integrate into the consumer system and offer user-friendly interaction [17]. The characteristics of laser marking on materials, like surface texture, contrast in marking, and the coloration of the surface, are interconnected with the operational settings of the laser beam. This includes factors such as the speed of scanning, electrical current, the size of the beam spot, and the width of the line. These parameters

can be adjusted conveniently to ensure that the material's surface receives adequate localized heat from the laser while minimizing any undesired damage. Nevertheless, many plastics either have a light color, are transparent to laser beams, or exhibit minimal surface alterations following laser exposure [21].

V. MATERIAL POLYAMIDE

Thermoplastics are the main polymers used for marking, engraving, and welding processes (Figure 2). In etching, the laser beam eliminates a portion of the original material. This leaves a noticeable indentation. During ablation, the laser eliminates a layer of coating, revealing the underlying base material in the mark. Through annealing and color transformation processes, the laser heats the workpiece, changing its color while maintaining a smooth surface. In foaming, reactions in the plastic material cause the formation of gas bubbles, resulting in a raised or textured mark [22].

Polymers are actively used in a number of engineering applications, therefore the study of laser marking processes on these materials is extremely important. One of the three most important groups of factors affecting laser marking processes are the properties of polymers. Structurally, they are mainly made up of linear, branched or cross-linked chains, and the forces of attraction between the polymer chains determine the characteristic properties of the polymer Fig. 3. [18]

Fig. 3. Polymer classification (adopted from [18])

Understanding the material behavior during marking requires continuous information about the physical properties under specific sets of marking parameters. Obtaining such information is challenging because the material's structure (amorphous, partially crystalline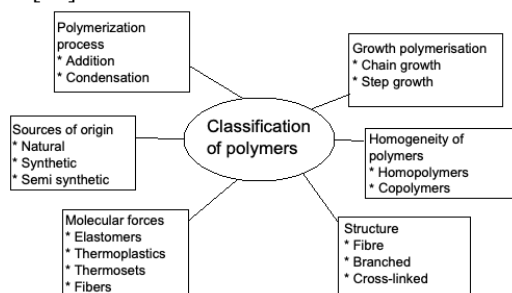, or fully crystalline) depends on the heating-cooling cycles. Additionally, the temperature range during marking can lead changes in structure through heating and cooling [23]. Depending on the characteristics of the polymer and the intensity of the laser, various processes can occur. The marking occurs as a result of the polymer surface undergoing carbonization at high laser power. At lower power levels, foaming or melting may be observed. Most commonly used polymers are suitable for this marking method. However, for an effective process, the polymer must have strong absorption at the laser wavelength. Materials such as inherently possess some level of photosensitivity at 1064 nm and can be easily carbonized at high temperatures, allowing them to be marked without the use of additives. Nevertheless, even for these

polymers, additives are typically included to enhance the required photosensitivity for achieving a writing speed suitable for practical applications. Certain polymers are transparent in the near-infrared range (1000–1100 nm). In such cases, additives are necessary [24-25]. Increasingly, thermoplasts are added to the marking paint, pigments. Inorganic pigments, such as color effect pigments, are often added to plastic resins as additives for laser marking applications. The well-distributed pigment particles within the plastic resin matrix absorb the incoming laser radiation and transfer the resulting heat to the surrounding polymer molecules of the resin. High pulse power and short interaction time are commonly used for laser beam marking. This thermal influence leads to carbonized black marking or light marking (foaming) depending on the polymer type. Due to their specific dispersion as particles, inorganic pigments are held in place by the macromolecular structure, hindering migration, unlike organic dyes [26]. When choosing a laser marking system for a specific application and material, for example polyamide, several factors need to be taken into account, including power density, thermal properties such as thermal conductivity, heat capacity, melting point, and heat of vaporization, as well as reflectivity, including material factors, wavelength, and temperature [29].

TABLE 2 CLASSIFICATION PHYSICAL PROPERTIES OF POLYMERS INFLUENCED BY LASER IRRADIATION DURING LSM[29]

Polymer	Glass-transition temp, T_g (°C)	Melting point (°C)	Ultimate tensile strength (MPa)	Yield tensile strength (MPa)	Thermal conductivity (W/mK)	Specific heat capacity
PTFE	-97	330	33.6	11.6	0.27	1.4
PP (isostatic)	+100	160	13.8-460	12-43	0.11-0.44	1.92
PS	90-95	240	44.9	43.9	0.14	2.1
PMMA (atactic)	+105	270	75.0	75.4	0.2085	1.46
Nylon 6,6	+57	250	73.1	45-63.6	0.26	2.2
LDPE	-20	110	11	10.8	0.3	2.2
HDPE	-90	120-140	30.5-35	26-33	0.48	1.9
PP (atactic)	-18	160	36.8	30.7	0.11	2.0
PC	+150	288-316	64	62	0.2	1.2
PE	+69	260	51.8		0.05	1.87
PVC	+87	100-260	1.38	55	0.190	0.84-1.17
PSU	+190	332-371	72	74.9	0.22	1.2
PEEK	+140	+340	110	98.8	0.25	2
PVDF	-37.6	160	42.8	44-48	0.19	1.5

High molecular weight polyamides have become incredibly important in practical applications, particularly in the production of nylon fibers. One of the most commonly used polyamides in this context is the one created through the condensation of hexamethylene

diamine and adipic acid, known as "66 polymer". In the abbreviated naming system for polyamides created from diamines and dibasic acids, two numbers are used to signify the number of carbon atoms in the diamine and dibasic acid, respectively. For instance, the polymer created from hexamethylene diamine and sebacic acid ($HOOC(CH_2)_8COOH$) is named "6,10". The focus is on the high tensile strength of the fibers, which closely resemble natural silk, and the high melting points of the polyamides in comparison to polyethylene (for example, 66 nylon melts at 250°C, but while polyethylene melts at 115°C). It is presumed that these characteristics are somehow linked to forces between the polar groups in the molecules. It's expected that there are hydrogen bonds between the C=O groups of one molecule and the NH groups of its neighboring molecules. Furthermore, polyamides are of interest due to their connection to proteins: the grouping -CO-NH- is present in both types of substances [27]. But there are other types of polyamide. For instance, one part is polylaurolactam, a material with a high molecular weight. It is known as polyamide 12 (PA 12) and is used in various industrial applications. The other part in each belongs to a group of segmented polymers with the following chemical structure Fig. 4.
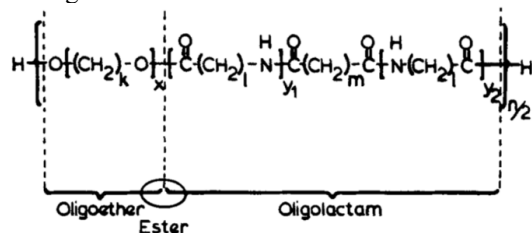

Fig.4. Chemical structure of polyamide (PA12) [27]

A single unit of the structure is made up of a relatively short chain of a type of nylon. This component has the ability to form crystals and is known as the hard section due to its high melting point. The other component comprises a short chain of tetrahydrofuran molecules (with an average molecular weight of 1000 g/mole). This part is considered the soft section because it has a low glass transition temperature and contains a low level of crystalline structure. The hard and soft sections are connected together through an ester linkage facilitated by a dicarboxylic acid [28], [29].

VI. CONCLUSIONS

Today, various lasers are used to label plastics. They can include fiber lasers, solid state lasers, and gas lasers. However, in most cases, 1064 nm fiber lasers are used for marking thermoplastics. The main parameters affecting the results of the natural marking process are contrast, the structure of the material, and the color of the material. These parameters depend on the settings of the laser system. When marking, it is important to know not only the parameters of the laser system but also the physical characteristics of the labeled material. For example, a thermoplastic material like polyamide has a white color, which complicates the marking process. A "gold

standard" for polyamide labeling has still not been found, as dyes are often used in the labeling process to facilitate it. However, these additives can alter the physical structures and properties of polyamide.

REFERENCES

[1] L. Lazov, Lyubomir, H. Deneva, P. Narica, "Laser Marking Methods", Environment. Technology. Resources. Proceedings of the International Scientific and Practical Conference. 1., 2015,.108. https://doi.org/10.17770/etr2015vol1.221

[2] L. Lazov, E. Teirumnieks, T. Karadzhov, N. Angelov, "Influence of power density and frequency of the process of laser marking of steel products," Infrared Physics & Technology 116, 103783, 10, 2021 https://doi.org/10.1016/j.infrared.2021.103783

[3] S.V. Gulak, A. I. Cherkashin, I. Balashov, V.Zarytskyi, Y.S. Kurskoy, Y.V. Zhdanova, "Laser marking system for plastic products" 2019 IEEE 8th International Conference on Advanced Optoelectronics and Lasers, 2019. https://doi.org/10.1109/caol46282.2019.9019422

[4] L. Lazov, A. Snikeris, I. Balchev, E. Teirumnieks, "Laser marking and engraving of household and industrial plastic products," Journal of Physics: Conference Series, vol. 1859, p.1-8, 2021, https://doi.org/10.1088/1742-6596/1859/1/012016

[5] M.F. Koldunov, A.A. Manenkov, I.L. Pokotilo, "Efficiency of various mechanisms of the laser damage in transparent solids", Quantum electron, 2002, vol. 32, No.7, pp. 623–628.

[6] N. Angelov, L.Lazov, et al, Influence of pulse duration on the process of laser marking of CT80 carbon tool steel products, Laser Phys., 2021, 31 045601, DOI: 10.1088/1555-6611/abe5af

[7] A.S. Gnatenko, Yu.P. Machekhin, Yu.S. Kurskoy, V.P. Obozna, "Providing mode locking in fiber laser", J. Nano- Electron. Phys., vol.10, 2018.

[8] J. Bosman, "Processes and strategies for solid state Q-switch laser marking of polymers", Velden, The Netherlands, p.243-244, 2007.

[9] A.S. Gnatenko, Y.P. Machechin, "Generation mode stability of a fiber ring laser", Telecommunications and Radio Engineering, vol. 74, no.7, p. 641-648, 2015.

[10] T. J. McKee, L. Toth, W. Sauerer, (1999). "Customized Decorating of Plastic Parts with Gray Scale and Multi-Color Images Using Lasers," Coloring Technology for Plastics, p.295–300, 1999. https://doi.org/10.1016/B978-188420778-5.50038-3

[11] Z. Jia, K. Zhao, W. Liu, J. Ma, L. Wang,"Nanosecond pulsed laser processing circuits on the copper clad polyimide," International Journal of Machining and Machinability of Materials, vol.15, p.157-173, 2014. , https://doi.org/10.1504/IJMMM.2014.060547

[12] E. Neiss, M. Flury, J. Fontaine, "Diffractive optical elements for laser marking applications," Optical Sensors, vol. 7003, p. 1-8, 2008. https://doi.org/10.1117/12.779944

[13] D.G.Waugh,J.Lawrence,P.Shukla,C.Chan,I.Hussain,H. C Man, G. C. Smith, "Laser surface treatment of polyamide and NiTi alloy and the effects on mesenchymal stem cell response," Industrial Laser Applications Symposium, 2015, https://doi.org/10.1117/12.2182432

[14] Z.Cao,G.Lu,H.Gao,Z.Xue,K.Luo,K.Wang,M.Luo, "Preparation and laser marking properties of poly (propylene)/molybdenum sulfide composite materials," ACS omega,vol.6,p.9129-9140,2021., https://pubs.acs.org/doi/abs/10.1021/acsomega.1c00255

[15] L Lazov, E Teirumnieks, N Angelov, E Teirumnieka, "Methodology for automatic determination of contrast of laser marking for different materials", ENVIRONMENT. TECHNOLOGIES. RESOURCES., Proceedings of the International, 7, 2019, DOI: 10.17770/etr2019vol3.4143

[16] P. Chang, A. Bruntz, L. Vidal, P. Vetter, P. Roudot, L. Bua, … O. Soppera, "Laser Polymer Tattooing: A Versatile Method for Permanent Marking on Polymer Surfaces, "Macromolecular Materials and Engineering, p.1-9, 2019. , https://doi.org/10.1002/mame.201900402

[17] P. Narica, L. Lazov, A. Teilans, P. Grabusts, E. Teirumnieks, P. Cacivkins, "Method for color laser marking process optimization with the use of genetic algorithms", ENVIRONMENT.

TECHNOLOGIES. RESOURCES. Proceedings of the International, 2017, DOI: 10.17770/etr2017vol2.2607

[18] N.S. Mustafa, et al., Ch CH Reviewing of general polymer types, properties and application in medical field. Int J Sci Res(IJSR),2016,5(8):212e221. https://doi.org/10.21275/art20167 72

[19] E.Bitay, "Laser markability of PVC coated automotive electric cables," eXPRESS Polymer Letters, vol.13, p.379-389, 2019. , https://doi.org/10.3144/expresspolymlett.2019.31

[20] R.M. Harris, "Coloring technology for Plastics, Plastics Design Library", p.333-334, 1999.

[21] W. Zhong, Z. Cao, P. Qiu, D. Wu,C. Liu, H. Li, H. Zhu, "Laser-Marking Mechanism of Thermoplastic Polyurethane/Bi2O3 Composites," ACS Applied Materials & Interfaces, vol.7,p. 24142–24149, 2015. [Accessed February 19, 2024], https://doi.org/10.1021/acsami.5b07406

[22] L.Sobotova, M. Badida, "Laser marking as environment technology" Open Engineering, vol. 7, p.303-316, 2017, https://doi.org/10.1515/eng-2017-0030

[23] I.D. Savu, S.V. Savu, N.A. Sirbu, "Heat affected zones in polymer laser marking", J Therm Anal Calorim, vol.115, p.1427–1437, 2014., https://doi.org/10.1007/s10973-013-3443-2

[24] C. Shan Wang, J. Yueh Shieh, "Synthesis and flame retardancy of phosphorus containing polycarbonate," Journal of Polymer Research, vol.6, p.149–154, 1999. , https://doi.org/10.1007/s10965-006-0082-3

[25] A.P Ranade, A. Hiltner, E. Baer, D.G. Bland, "Structure-Property Relationships in Coextruded Foam/Film Microlayers, "Journal of Cellular Plastics, vol.40, p.497–507, 2014. https://doi.org/10.1177/0021955x04048425

[26] R. Wissemborski, R. Klein, "Welding and Marking of Plastics with Lasers," Laser Technik Journal, vol.7(5), p.19–22, 2010. https://doi.org/doi:10.1002/latj.201090070

[27] C.W. Bunn, E.V. Garner, "The Crystal Structures of Two Polyamides ('Nylons')," Proceedings of the Royal Society A: Mathematical, Physical and Engineering Sciences, vol.189, p. 39–68, 1947., https://doi.org/10.1098/rspa.1947.0028

[28] A.F. Obilor, et al., "Micro-texturing of polymer surfaces using lasers: a review". Int J Adv Manuf Technol 120, 103–135 (2022). https://doi.org/10.1007/s00170-022-08731-1

[29] G. Goldbach, M. Kita, K. Meyer, K.P Richter, "Structure and properties of polyamide 12 alloys, " In: Springer, J. (eds) Polymers as Colloid Systems. Progress in Colloid & Polymer cience,vol.72,p.82-96,1985. https://doi.org/10.1007/BFb011 4480

Study of Adhesion of Physical Vapor Deposition Coatings on Functional Textile with Laser Post-processing

Silvija Mežinska
Engineering faculty
Rezekne Academy of Technologies
Rezekne, Latvia
Silvija.Mezinska@rta.lv

Antons Pacejs
Engineering faculty
Rezekne Academy of Technologies
Rezekne, Latvia
Antons.Pacejs@rta.lv

Imants Adijāns
Engineering faculty
Rezekne Academy of Technologies
Rezekne, Latvia
Imants.Adijans@rta.lv

Edgars Zaicevs
Engineering faculty
Rezekne Academy of Technologies
Rezekne, Latvia
Edgars.Zaicevs@rta.lv

Lyubomir Lazov
Engineering faculty
Rezekne Academy of Technologies
Rezekne, Latvia
Lyubomir.Lazov@rta.lv

Abstract. **Functional textile are one of the most critical fields in the textile industry and textile materials science. In recent years, advanced technologies in textile processing have become relevant in order to improve its usability. In the production of various types of functional textile, one of the methods is the modification of textile surfaces. To improve the properties of the textile surface, magnetron vacuum sputtering and laser post-processing technologies can be used, which in general gives the material new or improved properties and functionalities. In this study, mixed fiber fabrics containing polyester, protal and cotton fibers are used to determine how laser post-treatment of the metalized fabrics impact the adhesive properties between fabric and deposited metal. The following materials were used for magnetron vacuum sputtering for functional textile coatings: Cu, Al, Ti, Ag. Individually or by combining these metals, it is possible to assign the textile such properties as: electromagnetic, UV and IR radiation shielding; antistatic, antibacterial, hydrophilic and hydrophobic properties, as well as increasing wear resistance. In this study a 100 W continuous wave CO_2 laser with a wavelength of 10.6 µm is used for post-treatment of magnetron vacuum sputtered modified textile surfaces. The study's conclusions point towards a tailored approach in determining linear energy densities that bolster adhesion for each metal-textile combination, which is essential for the development of durable and functional advanced textile. The patterns noted in the adhesion strengths, influenced by different energy densities and metal types, highlight the intricate relationship between the thermal impact of laser treatment and the inherent characteristics of the metals deposited. Some metals demonstrated improved adhesion at lower energy densities. However, a general trend emerged showing a reduction in the strength of adhesion as the energy density increased, especially when surpassing certain energy levels.**

Keywords: **functional textile, laser post-processing technologies, magnetron vacuum sputtering, peel-off tape adhesion test.**

I. Introduction

Functional textiles are one of the most important fields in textile industry and textile materials science. They include breathable, heat and cold-resistant materials, ultra-strong fabrics (e.g. as reinforcement for composites), new flame retardant fabrics (e.g. intumescent materials), optimization of textile fabrics for acoustic properties, etc. Functional textiles became more and more important materials for various applications and interest in them grew year by year [1].The purpose and perception of textile materials are changing, from simple protection to clothing with new functionalities and added value [2].

"Functional clothing" can be defined as "a general term that includes all types of clothing or sets of clothing that are specifically designed to provide the user with predetermined performance or functionality in addition to normal functions" [3]. This type of garment can be made using a high-performance fiber, a new finish, or a significant modification of a traditional material. Clothing must perform some specific functions, which

may be protecting a person from a hazardous work environment [4].

Magnetron sputtering technology is a promising method for the surface modification of textiles. The use of magnetron sputtering technology can impart textiles anti-static, antibacterial, anti-ultraviolet, electromagnetic shielding, electrical conductivity and other single or composite properties [5]. The magnetron sputtering method has the advantages of controllable film thickness, high purity, high speed and low temperature, favorable adhesion, easy operation, and environmental friendliness, etc. [6,7].

Lasers are utilized for processing various materials, including textiles [8,9,10]. Utilizing lasers for heat treatment in experiments with metal-coated textiles is critically important due to lasers' unique ability to deliver precise, controllable, and localized heat [11]. This precision is crucial for ensuring consistent quality and integrity of the coatings without damaging the underlying textile substrate. Lasers enable fine-tuning of heat application, allowing researchers to systematically study the effects of various treatment parameters on material properties [12]. This level of control is unmatched by traditional heat treatment methods and is essential for developing advanced materials with specific characteristics.

The aim of this study is to examine the effects of CO_2 laser post-processing on the adhesion properties of physical vapor deposition (PVD) coatings on functional textiles. Tasks:

1. Investigate the adhesion strength of metals (Cu, Al, Ti, Ag) when coated on textile fabrics using magnetron sputtering and subsequently heat treated with a CO_2 laser.
2. Analyze the impact of varying laser linear energy densities on the adhesion properties of the metalized textiles.
3. Conduct comparative analyses using peel-off tape adhesion tests to quantify the adhesive strength and evaluate the effectiveness of laser post-processing in enhancing the functional properties of the textiles.

I. MATERIALS AND METHODS

A. Fabrics

Mixed-fiber fabrics, composed of polyester and cotton fibers, are chosen for this study because they combine the durability of synthetic materials with the comfort of natural fibers. Polyester provides resistance to wear and lower water absorption, while cotton offers high breathability and comfort. By combining these two fibers, a material suitable for various usage needs is obtained, for example, can be used for work clothes and casual uniforms. The most important blend in the industry which is still in use, as the optimum performance fabric from KLOPMAN International, blend of 65% polyester / 35% cotton [13,14]. For comparison, a third fabric sample is used which has a different fiber composition and fire-retardant properties. The third fabric sample contains Protex Q fiber which is "the only modacrylic which has been specifically designed for PPE use and is Oeko-tex Class 1 compliant and REACH ready" [15]. In the research, samples of two different types of fabric weave (twill and

derived canvas weave (rip stop)) with slightly different surface densities of 220 g/m² ±5% and 250 g/m² ±5% were selected. Characteristics of fabrics can be observed in Table 1.

TABLE 1 CHARACTERISTICS OF SELECTED FABRICS

Fabrics	A	B	C
Fiber composition	65% Polyester, 35% Cotton	65% Polyester, 35% Cotton	55% Protal, 44% Cotton, Antistatic 1%
Weave	Twill 2x1 Z	Rip stop	Twill 2x1 Z
Weight g/m²±5%	220	250	250
Finish	Crease Resist		

B. Sputtering process

The magnetron sputtering is carried out by SIDRABE Magnetron Sputtering System: Vacuum Deposition System for R&D purpose SAF M. The machine is equipped with 2 magnetrons for simultaneous coating of 2 metals (1 magnetron is used for a given process) and a rotating base for uniform coating of the material to be coated over the entire sample area shown in Fig.1.
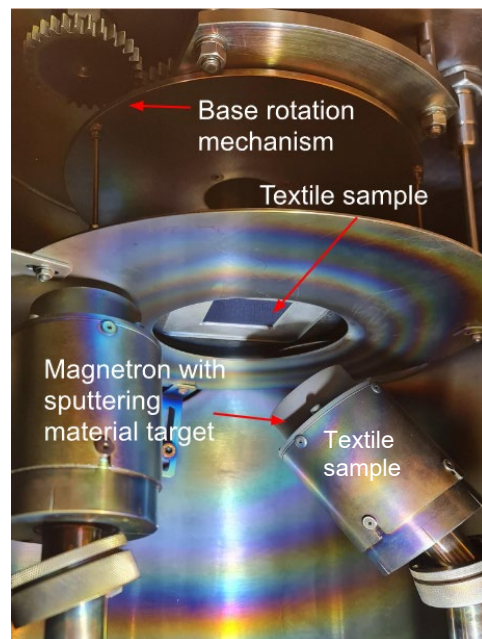

Fig. 1. Magnetron sputtering machine set-up.

Textile samples with a sputtered area of 48mm x 48mm for each material have been prepared for laser processing.

C. Magnetron sputtering

The target materials for sputtering were selected such metals as copper (Cu), titanium (Ti), silver (Ag), aluminum (Al), because of findings of other authors

which such metal sputtering can give the base material: hydrophobicity, EMF shielding, IR shielding etc. [16,17,18,19]. The sputtering parameters used can be observed in Table 2.

TABLE 2 MAGNETRON PARAMETERS USED IN THE SPUTTERING PROCESS

Material (CAS Number of the elements)	Al (7429-90-5)	Ag (7440-22-4)	Cu (7440-50-8)	Ti (7440-32-6)
Deposition time, s	120	150	150	270
Pulse duration, μs	1,2	1,5	2	1,5
Pulse frequency, kHz	320	250	20	250
Power (used as setpoint), W	300	250	250	250
Coating Thickness, μm	50	60	80	85

Sputtered metal properties such as heat capacity, melting temperatures and heat conductivity could be observed in Table 3.

TABLE 3 DEPOSITED METAL MATERIAL PHYSICAL PROPERTIES

Material	Al	Ag	Cu	Ti
Heat conductivity, W/m*K	247	430	398	17
Melting temperature, °C	660	962	1084	1668
Heat capacity, J/g ° C	0.90	0.237	0.385	0.523

From available resources the reflectance coefficients of a choosed sputtered metals for a CO_2 laser wavelength are 0.91 for Ti [20] while Al, Ag and Cu have reflective coefficients of approximately 0.97 [21].

D. Laser system

In the process of heat treatment of a metal-coated fabric, authors utilized a carbon dioxide (CO_2) gas laser. Specifically, a Suntop ST-CC9060 continuous wave CO_2 laser system, which operates at a wavelength of 10.6 micrometers which corresponds to an infrared spectrum and can reach a maximum average power of 100 W. This laser system, equipped with 2 axis CNC-controlled beam steering, was employed to scan the textile samples. Principal scheme of an experimental set up of laser processing could be observed in Fig. 2.

Laser scanning path was controlled via computer with a principal scheme demonstrated in Fig.3. Should be noted that the laser treatment corresponds to the "Laser on" area.
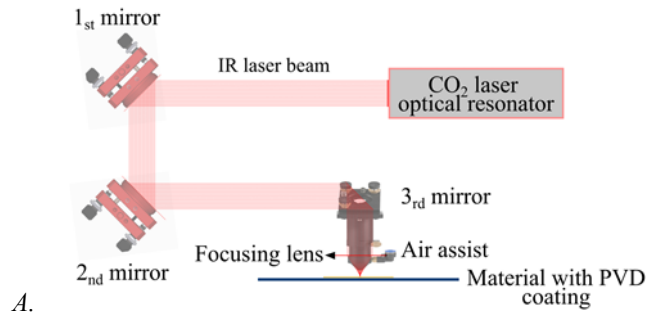
Fig. 2. Experimental set-up of carbon dioxide laser heat treatment of physical vapor deposited (PVD) coating on textile.
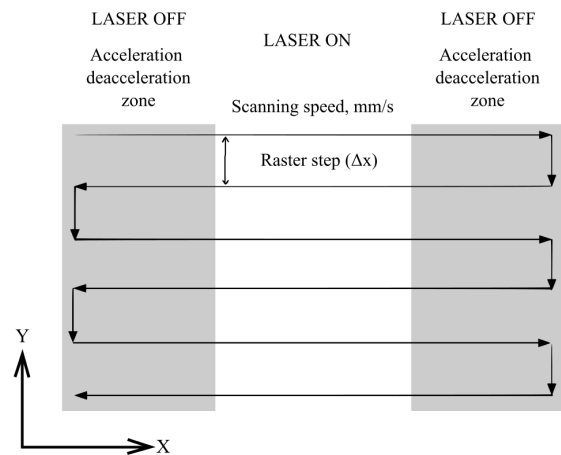
Fig. 3. Laser scanning path scheme

E. Laser processing

The laser scanning speed (*v*) remained constant at 100 mm/s for all laser-processed samples. The raster step was consistent at 100 μm across all samples, while the linear energy density (*E*) varied with values of 2.5 J/m, 5.1 J/m, and 7.1 J/m. Beam was focused on the samples with a focal point of approximately 80 micrometers and air assisted gas to the treatment area with pressure of 12 PSI and 90 liter per minute flow has been provided via nozzle.

F. Peel-off tape adhesion test

To assess the bond strength between the metallic coating and its base material e.g. fabric, we performed a 90-degree peel of test. This involved the use of 3M 610 permanent adhesive tape as described in reference [22]. Post-separation, the surface of the adhesive tape that was in contact with the metallized fabrics both laser treated and untreated was examined using confocal laser scanning microscope Olympus OLS5000, after the image software was used for analyzing the particles stuck to the tape via thresholding image by color and utilizing "particle count" tool whereas the summary results "%Area" was used to plot a graphs.

II. RESULTS AND DISCUSSIONS

The impact of CO_2 laser treatment on the adhesion of sputtered metals to textile substrates was investigated

using peel-off tape adhesion tests. These tests quantified adhesive strength by measuring the percentage of metal remaining on the tape post laser treatment, with a higher percentage indicating weaker adhesion. Our analysis, depicted in Figures 4, 5, and 6, correlates average energy density (E, J/m) delivered to the metalized fabric with adhesive strength (Area, %), corresponding to fabrics A, B, and C described in Section 2 of this paper.

It should be noted that the "0" on the horizontal axis of the graphs indicates the percentage of the deposited coating area that peeled off of the fabric-metal combination without laser treatment applied.
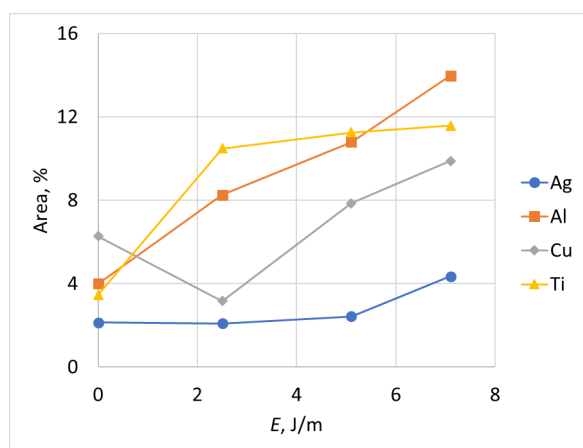

Fig.4. Peeled off adhesion test results of deposited metals on Fabric A dependent on laser linear energy density.

Across Al, Cu, Ag, and Ti, a general trend emerged: adhesion strength decreased with increasing linear energy density from 0 to 7.1 J/m. Contrary to expectations, no direct positive correlation was observed between delivered energy density and adhesive strength. Al exhibited a substantial increase in the percentage of metal remaining on the tape for fabric A, up to 3.5 times, fabric B up to 9.8 times, and fabric C up to 2.1 times, at an energy density of 7.1 J/m. Ag demonstrated enhanced adhesion over the range of linear energy densities, outperforming other metals, and did not exhibit the pronounced decline observed in Al.
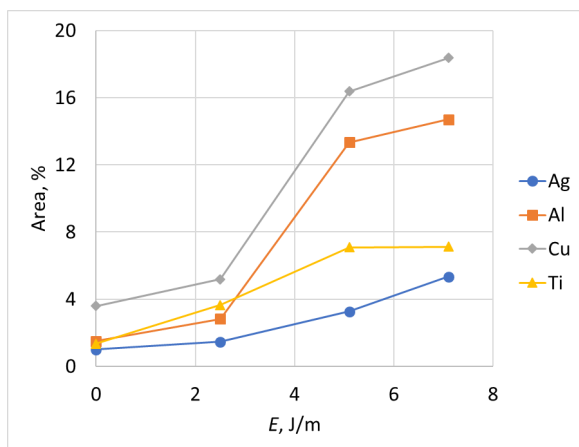

Fig.5. Peeled off adhesion test results of deposited metals on Fabric B dependent on laser linear energy density.

Cu showed increased adhesion at lower linear energy densities, almost 2 times for fabric A and almost 1.5 times for fabric C, but experienced a subsequent decrease as energy levels rose, similar to Al. Ti showed increased adhesion almost 1.9 times at lower linear energy density of 2.5 J/m for fabric C, but experienced a decrease at higher energy levels similar to other metals.
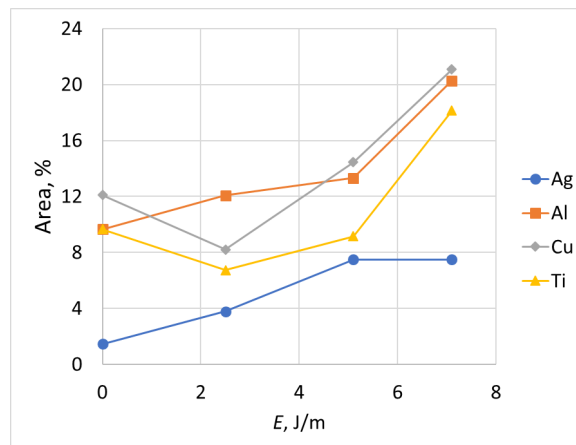
Fig.6. Peeled off adhesion test results of deposited metals on Fabric C dependent on laser linear energy density.

The reflective coefficient was hypothesized to be pivotal due to its influence on a metal's energy absorption at the laser's wavelength. However, an intricate balance is required as increased absorption beyond a certain threshold can induce thermal damage, reducing adhesive strength. The observed trends underscore the complex interplay between laser-induced thermal effects and the intrinsic properties of deposited metal layers. Overall, optimizing laser parameters is crucial to enhance adhesion without causing damage, emphasizing the need for further research in this area. Additionally, the differences in adhesion performance may also reflect variations in textile characteristics, sputtering conditions, and specific treatment procedures, highlighting the nuanced nature of sputtered metal-textile interactions and neednes for further research.

III. CONCLUSION

Our investigation into the adhesion characteristics of sputtered metals on functional textiles reveals a distinct dependency on laser linear energy density for each metal-textile combination.

For Fabric A, optimal adhesion for Ag and Cu is observed at 2.5 J/m, resulting in approximately 2% and 3% peel-off areas, respectively. Al and Ti exhibit decreasing adhesion percentages with increasing energy density.

Fabric B shows similar trends, with Ag peaking at 2.5 J/m with approximately 1.5% peel-off area. Al and Cu show increasing peel-off area percentages with rising energy density, while Ti displays better adhesion compared to Al and Cu.

Fabric C demonstrates increased peel-off area for Al and Ag with higher linear energy, whereas Cu and Ti exhibit smaller peel-off areas at a lower energy density of approximately 2.5 J/m.

These findings underscore the importance of identifying precise laser parameters values to optimize metal adhesion to textiles, crucial for composite material longevity and functionality. Future research should focus on determining exact energy thresholds and exploring the impact of laser parameters such as speed, raster step, focal spot, laser wavelength, repetition rate as well as impulse width on the metal-textile interface in an all-encompassing manner.

Overall, further studies could include better understanding via investigation of thermal treatment post metallized textile and impact on the textile fibers, as well as impact of different post sputtering treatment sources such as short and ultrashort impulse lasers as well as CAP plasma treatment.

IV. ACKNOWLEDGMENT

REFERENCES

[1] P. Kiekens, E. Van der Burght, E. Kny, T. Uyar, R. Milašius, Functional textiles – from research and development to innovations and industrial uptake. AUTEX Research Journal, Vol. 14, No 4, December 2014. DOI: 10.2478/aut-2014-0031 © AUTEX

[2] A. Ojstršek, O. Plohl, S. Gorgieva, M. Kurečič, U. Jančič, S. Hribernik, D. Fakin, Metallisation of Textiles and Protection of Conductive Layers: An Overview of Application Techniques. Sensors 2021, 21, 3508. https://doi.org/ 10.3390/s21103508

[3] D. Gupta, Functional clothing—Definition and classification. Indian Journal of Fiber and Textile Research. 2011; 36(4):321-326

[4] N. Pan, G. Sun, Functional Textiles for Improved Performance, Protection and Health. Sawston, United Kingdom: Elsevier; Copyright © 2011 Woodhead Publishing Limited.

[5] Xue-Qiang Tan, Jian-Yong Liu, Jia-Rong Niu, Jia-Yin Liu, Jun-Ying Tian. Recent Progress in Magnetron Sputtering Technology used on fabrics. 2018. DOI:10.3390/ma11101953

[6] Mei-Lin Huang, Ying-Zhu Wu, Zhi-Kai Liu, Sheng-Guo Lu. Metallic coloration and multifunctional preparation on fabrics via nitriding reactive sputtering with copper and titanium targets, Vacuum, Volume 202, August 2022. https://doi.org/10.1016/j.vacuum. 2022.111177

[7] L. Surdu, E. Visileanu, A. Ardeleanu, C. Mitran, I. Răzvan Rădulescu, C. Stancu, I. Sandulache, B. Mitu, Research regarding the cover factor of magnetron sputtering plasma coated fabrics, January 2019. DOI: 10.35530/IT.070.02.1618

[8] E. Korzeniewska, J. Gocławski, J. Sekulska-Nalewajko, M. Walczak, B. Wilbik-Hałgas, Changes in Fabric Surface Pilling under Laser Ablation. MDPI, October 2020. https://doi.org/10.3390/s20205832

[9] Y. P. Angelova, Factors influencing the laser treatment of textile materials: An overview. Journal of Engineered Fibers and Fabrics, September 2020. https://doi.org/10.1177/1558925020952803

[10] T. Atwee, N. Elshafei, H. Y. Mostafa, F. Bassynouni, Surface Treatments using CO_2 Lasers on a Variety of Synthetic Textiles. J Mater sci Appl 6: 1-9, March 2022. DOI:10.17303/jmsa.2022.6.103

[11] J. Bonse, S. Gräf, Ten Open Questions about Laser-Induced Periodic Surface Structures. Nanomaterials 2021, *11*(12), 3326; https://doi.org/10.3390/nano11123326

[12] M. Sabri Salim, T. K. Naseer Sabri, M. Ibrahim Noaman, N. Noaman Israa, H. Akram Israa Latif, Effect of laser processing parameters on the efficiency of material: a review in industrial application field., International Journal of Engineering & Technology, 2019. DOI: 10.14419/ijet.v8i4.29729

[13] POLYCOTTON FABRIC [Online]. Available: https://www.klopman.com/polyester-cotton#fabric/23712 [Accessed: Febr. 02, 2024].

[14] M. Vančo, J. Krmela, F. Pešlová., The Use of PVD Coating on Natural Textile FibersProcedia Engineering, Volume 136, 2016, Pages 341-345. https://doi.org/10.1016/j.proeng.2016.01.220

[15] What is Protal? [Online]. Available: https://www.protal.co.uk [Accessed: Febr. 02, 2024].

[16] Sheng Qiu, Hao Jia, Shou-xiang Jiang, Fabrication and characterization of thermal management fabric with heating and cooling modes through magnetron sputtering. Materials Letters, Volume 300, 1 October 2021, 130217. https://doi.org/10.1016/j.matlet.2021.130217

[17] Xiao Zhang, Shouxiang Jiang, Ming Cai, Hongmei Zhao, Fukui Pan, Dagang Miao, Xin Ning. Magnetron sputtering deposition of Ag/Ag2O bilayer films for highly efficient color generation on fabrics. Ceramics International, Volume 46, Issue 9, 15 June 2020, Pages 13342-13349. https://doi.org/10.1016/j.ceramint.2020.02.113

[18] B. Subramanian, K. Anu Priya, S. Thanka Rajan, P. Dhandapani, M. Jayachandran, Antimicrobial activity of sputtered nanocrystalline CuO impregnated fabrics. Materials Letters, Volume 128, 1 August 2014, Pages 1-4. https://doi.org/10.1016/j.matlet.2014.04.056

[19] S. Shahidi, M. Ghoranneviss, B. Moazzenchi, A. Anvari, A. Rashidi, Aluminum coatings on cotton fabrics with low temperature plasma of argon and oxygen. Surface and Coatings Technology, Volume 201, Issues 9–11, 26 February 2007, Pages 5646-5650. https://doi.org/10.1016/j.surfcoat.2006.07.105.

[20] E. Linden, P. Vitruk, SuperPulse 10.6um CO_2 laser-assisted, closed flap treatment of peri-implantitis. Implant Practice-US. 8. 30-34, 2015.

[21] S. Katayama, Handbook of Laser Welding Technologies; Woodhead Publishing: Cambridge, UK, 2013.

[22] A. E. Karnoukhov, Y. A. Timoshina, E. F. Voznesensky, V. A. Sysoev, I. V. Krasina, & N. V. Tikhonova, Study of the adhesion of metal coatings on synthetic textile materials. *Journal of Physics: Conference Series*, *1954*(1). 2021. https://doi.org/10.1088/1742-6596/1954/1/012016

Modeling the Influence of Grain Morphology on the Laser Engraving Processes

Roussi Minev
Department of Materials Science and Technology,
"Angel Kanchev" University of Ruse, Bulgaria
e-mail: rus@uni-ruse.bg

Veselin Hristov
Department of Materials Science and Technology,
"Angel Kanchev" University of Ruse, Bulgaria
e-mail: vhristov@uni-ruse.bg

Danail Gospodinov
Department of Materials Science and Technology,
"Angel Kanchev" University of Ruse, Bulgaria
e-mail: dgospodinov@uni-ruse.bg

Emil Yankov
Department of Materials Science and Technology,
"Angel Kanchev" University of Ruse, Bulgaria
e-mail: eyankov@uni-ruse.bg

Mariana Ilieva
Department of Materials Science and Technology,
"Angel Kanchev" University of Ruse, Bulgaria
e-mail: mdilieva@uni-ruse.bg

Abstract. **The study describes the Monte Carlo modelling of the ablation depth during the laser marking process. The effect of grain size on the resulting roughness is studied. The results were validated by experiments with model samples of pure iron with different grain sizes. The influence of the laser power, speed and raster distance were also studied and commented.**

Keywords: Engraving, Grains morphology, Laser ablation

I. INTRODUCTION

The pulse fibre laser system are successfully used to engrave metal surfaces for the purpose of creating labels, protection signs, engineering coding. They are also used to prepare different type of micro and mezzo micro fluidic channels for MNT tooling and other type of surface structuring (e.g. for designing specific tribological characteristics) [1]-[3]. In all cases the surface roughness and integrity is of paramount importance.

The surface characteristics (roughness and surface integrity in general) of the laser processed materials depend on the technological parameters such as raster pitch and scanning speed but it is also supposed to depend on [4]-[8] the material morphology - the size of the grains in first place. The last issue is not very well studied and with regards to the particular materials different and controversial results are reported. The grain size of a metallic sample can affect the laser ablation depth through a number of mechanisms [9]-[12]:

- Small grain sizes can lead to reduced thermal conductivity in the material, which can cause the material to heat up more quickly during laser ablation. This can result in increased melting and vaporization of the material, leading to higher ablation depths.

- Absorption of laser energy by a material can be affected by its grain size. In some cases, smaller grain sizes may result in increased absorption of laser energy, which can lead to increased melting and vaporization and therefore deeper ablation.

- If small grain sizes lead to rougher surfaces they can scatter laser energy and reduce the effective energy density at the surface of the material. This can result in an opposite effect - shallower ablation depths.

- Grain size can also affect the mechanical and physical properties of a material (hardness, strength, and ductility). These properties are a function of the internal stresses of 3rd order (stresses that are introduced in the crystal lattice and are balanced out within the crystal grain). These stresses and the corresponding increase of the phase internal energy may influence how the material responds to laser ablation, and can therefore affect the ablation depth.

In general the relationship between grain size and laser ablation depth can be complex and depend on many factors, including the specifics of the material, laser parameters, and experimental conditions. Therefore, it's important to characterize the material properties and optimize the laser parameters for each specific case to achieve the desired ablation depth.

The aim of this research is to create a digital model (using the Monte Carlo method) for studying the influence of the grain size morphology on the surface roughness of the sample.

Validation of the model was carried out with a 1064 nm nanosecond fibre laser PL F 20 (10W, pulse duration 30 ns, pulse frequency 20 kHz and spot size 30 µm), raster pitch in the range of 20 to 80 µm and the scanning speed of 75 to 200 mm/s. The conducted experiments analyse the influence of the parameters on the roughness and penetration depth in low carbon iron alloy (0.04%C; 0,12%Si; 0,16%Mn; <0,01%P; <0,01%S; 0,05%Cr; 0,09%Ni; 0,16%Cu). This material was chosen for its nearly single α-Fe phase content and the ease of modelling the grain size structure by applying different heat treatments.

II. MATERIALS AND METHODS

Since the distribution of grains in the material according to their size is statistically determined, but random for a given sample or section, it can be simulated using random numbers generated by a computer program. In EXCEL this could be done using the RANDBETWEEN function. If we have data about grain size distribution and the ablation depth of grains of different sizes then using a tabular model in EXCEL [13] and the VLOOKUP function we can create a link between them (Fig.1). So on each randomly generated grain size we can assign corresponding ablation depth. In this way a model of a profile of the surface of the material is obtained similar to the diagram taken by a contact profilometer or surface roughness tester.
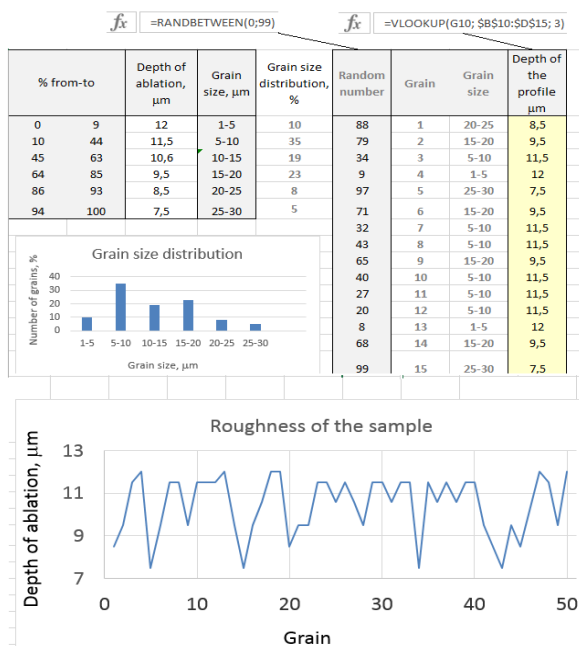

Fig. 1. The model and surface profile of a sample.

For obtaining the data of ablation depth the steel samples were heat treated to produce different and relatively uniform size of the grains [14] [15]. The samples were heated in electrical furnace for 5 hours to 1000 ºC and cooled with different speeds (using hot and cold oil, water, air with and without ventilation, cooling with the furnace, etc.). This way model samples were produced with average grain size from 13 to 37 µm (Fig. 2). This samples were treated with the laser with scan speeds 75, 100, 125, 150, 175, 200 mm/s and the depth of ablation and roughness were measured using LEXT OLS5000 laser microscope. The apparatus allows simultaneous 2D and 3D measurement and observation of the deep-focus field. The microscope works according to ISO/TC 213 and ISO 2517 surface roughness measurement standards.
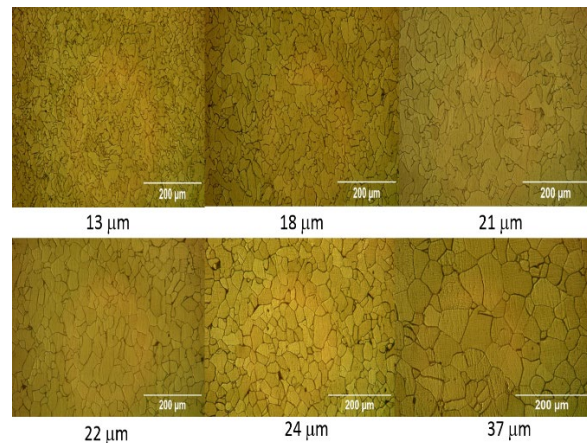
Fig. 2. Grain morphology after the heat treatment.

III. RESULTS AND DISCUSSIONS

The geometrical and technological parameters (Fig. 3) of the laser ablation process (laser beam spot, speed of scanning, step of scanning, grain size) are supposed to be of main importance to the final result - the roughness of the material surface and its exploitation characteristics.

Depending on the purpose of the product, the requirements for roughness are different and often contradictory. In engraving greater roughness can have a positive effect on contrast and resolution but in micro-features production and surface structuring (e.g. for MEMS tooling, microfluidic channels, etc.) - lower roughness improves product quality.
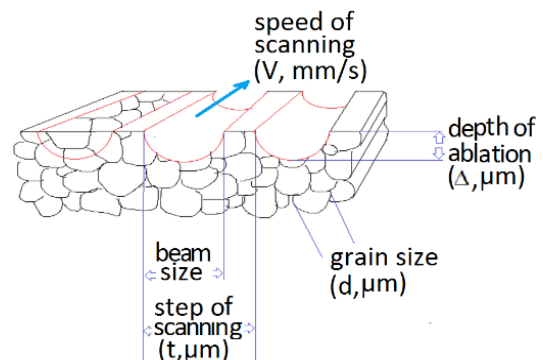
Fig. 3. Parameters of the laser ablation process.

Scanning speed

Decreasing the scan speed leads to an increase in the depth of ablation for all grain size samples and consequently to higher sample roughness. The reason is the increase of the linear density of the applied laser energy. This result illustrates a possible way to achieve better contrast but at the expense of increasing the engraving time. At the same time, as can be seen from Fig. 4 decreasing the scan rate leads to an increase in the influence of the grain size on the depth of the profile (the points of the graph corresponding to low scan rates - e.g. 75 mm/s are tree times more spread out compared to the points corresponding to the 200 mm/s).

Fig. 4. The influence of the scanning speed on the roughness of the samples.

Scanning step

When the scan step is decreased the surface roughness is decreased (Fig. 5) due to the increase in the surface density of the applied laser energy when the laser beam spots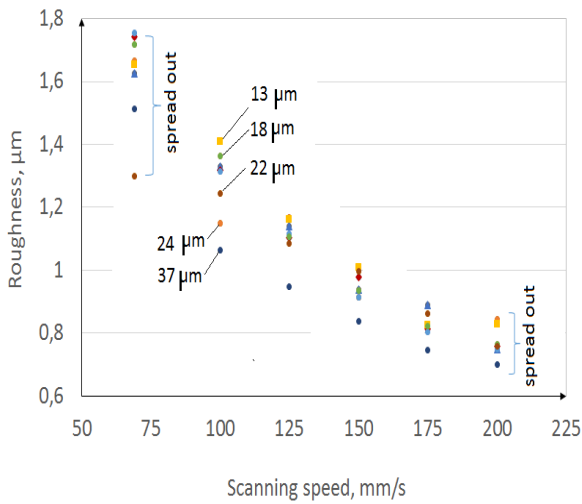 overlap or are close to each other. This means that we will have the effect of flattening the surface profile. This illustrates the way the surface smoothness could be improved but this effect will be at an expense of increase the technological time. If the higher contrast is desirable than the scan step should be increased with caution since the rather sparse lines will affect the contrast of the picture.
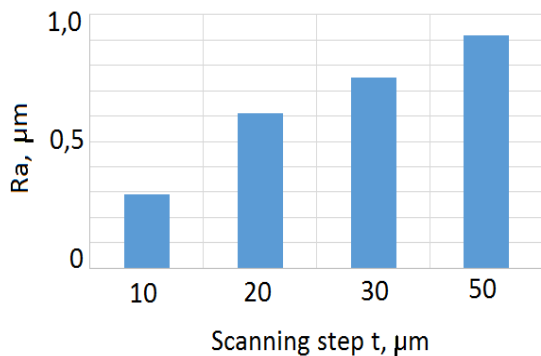
Fig. 5. The influence of the scanning step (t, μm) on the roughness of the samples (data for the scanning speed 150 mm/s).

Grain size

Our experiments with the low carbon steel model samples reviled that the larger the grain size of the metal the lover depth of ablation on the sample (Fig. 6). This could be explained by the assumption that larger grains (which corresponds to less volume of grain boundaries that would hinder the energy transfer) facilitates more intensive dissipation of the energy and require more laser energy on the material surface for the processes of deeper ablation to take place. Therefore they tend to have lover depth of ablation while the smaller grains "lock" more energy in smaller volume within the grain boundaries which act as a heat transfer brier.

At the same time the material with small grains having a reduced thermal conductivity which can cause the material to heat up more quickly during laser ablation. This can result in increased melting and vaporization of the material, leading to higher ablation depths (Fig. 7).

It should be emphasized that this outcome is associated with the studied material (α-Fe) and laser parameters described in previous section that could predetermine particular material removal mechanisms. This aspects may differ in other circumstances and other energy sources such as e-beam, magnetron field, etc. and are not subject of this study.
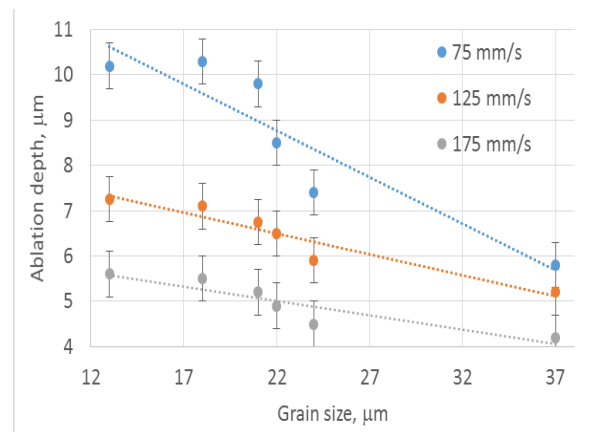
Fig.6. The influence of the grain size on the ablation depth of the samples.
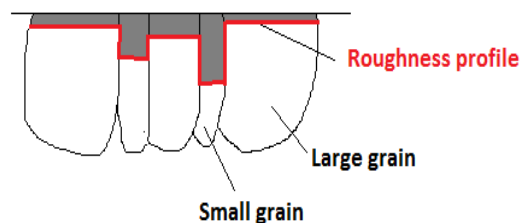
Fig. 7. Small v/s large grain ablation depth.

Modelling

To design the model representing the surface profile and the corresponding roughness calculation, we need initial experimental data on the influence of grain size on the actual ablation depth. This was done on the samples with different grain sizes obtained after the respective heat treatment described in the previous section. Laser processing was performed with 50 μm steps and 20 μm

beam diameter to ensure minimal overlap and mutual influence of the neighbouring scanned areas. Thus the data presented on Fig. 8 was obtained and used to calculate mathematical model applicable at different scan speeds.

A linear regression analyses (with average correlation coefficient = 0.9) was performed for the data obtained at 75, 125 and 175 mm/s scanning speed. The general appearance of the formula is as follows:

$$\Delta \, [\mu m] = k \cdot d \, [\mu m] + b \,, \qquad (1)$$

where Δ - depth of ablation, d - average grain size, k, b - proportionality factor and free term.

Table 1 shows the values of the above parameters for different scan speed.

TABLE 1 PARAMETERS OF THE EQUATION

Scanning speed, v	k	b	Ra, μm model	Ra, μm experiment
75 μm/s	-0,2	13,3	0,55	0,60
125 μm/s	-0,1	8,5	0,37	0,41
175 μm/s	-0,06	6,4	0,28	0,30

This equations was then used to assign the ablation depth in respect of the grain size and to model by Monte Carlo method (as described in previous section) the surface profile of a low carbon steel with real grain size distribution (shown on the EXCEL model snapshot on Fig.1) after laser engraving. In this way, roughness profiles were generated (Fig. 9) and the corresponding mean roughness's at different scan speeds were calculated (Table 1). The results were compared (as a validation experiment) with actual measured samples, and it turned out that they differ from them by no more than 10%.

Fig. 9. Modelling the sample profile.

IV. CONCLUSIONS

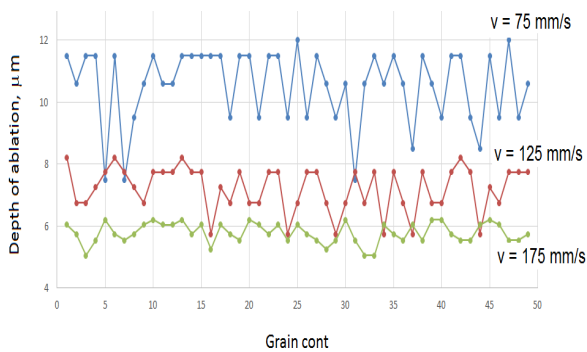It has been revealed that the scan speed and the step of scanning influence the depth of ablation and surface roughness (due to the change of density of the applied laser energy). The roughness increases by 100% when changing the scan speed from 75 to 200 mm/s and decreases by 50% when change the step of scanning from 10 to 50 μm.

The larger grains require more laser energy for the processes of ablation to take place. Therefore they tend to have lover depth of ablation while the smaller grains "lock" more energy within the grain boundaries and tend to have deeper ablation.

A Monte Carlo Model of the surface profile predicts the surface roughness of the samples depending of the grain size morphology. The model predicts the Ra value for the iron sample with 10% credibility.

V. ACKNOWLEDGMENTS

REFERENCES

[1] M. Q. Chau, "An Overview Study On The Laser Technology and Applications in the Mechanical and Machine Manufacturing Industry", Journal of Mechanical Engineering Research and Developments (JMERD) 42(5), 2019 pp.16-20

[2] N. Angelov, L.Lazov, et al, Influence of pulse duration on the process of laser marking of CT80 carbon tool steel products, Laser Phys., 2021, 31 045601 DOI: 10.1088/1555-6611/abe5af

[3] J. Kusinski er al., "Laser modification of the materials surface layer - a review paper", Technical Sciences, Vol. 60, No. 4, 2012, DOI: 10.2478/v10175-012-0083-9

[4] L. Lazov, Edmunds Teirumnieks, Tsanko Karadzhov, Nikolay Angelov, Influence of power density and frequency of the process of laser marking of steel products, Infrared Physics & Technology, 2021,Volume 116, 103783, https://doi.org/10.1016/j.infrared.2021.103783.

[5] A. Temmler et al., "Influence of laser polishing on surface roughness and microstructural properties of the remelted surface boundary layer of tool steel H11", Materials and Design 192, 2020, DOI:10.1016/j.matdes.2020.108689

[6] Y. Ahmed et al, "Laser surface texturing and characterization of austenitic stainless steel for the improvement of its surface properties", The Int. Journal of Advanced Manufacturing Technology, 2021, v.115. pp. 1795–1808

[7] M. Švantner et al., "Thermal effects of laser marking on microstructure and corrosion properties of stainless steel", Optical Society of America Vol. 55, No. 34, Applied Optics, 2016, DOI:10.1364/AO.55.000D35

[8] M. Pandey, B. Doloi, "Parametric analysis on fiber laser marking characteristics for generation of square shaped marked surface on stainless steel 304", Materials Today: Proceedings, 56, 2022), pp. 1908–1913

[9] S. Shin et al., "Wavelength selection for femtosecond laser processing of materials: Comparison of ablation efficiency and surface quality", Optics & Laser Technology, 2024, v.171, DOI: 10.1016/j.optlastec.2023.110428

[10] C. Chen et al., "Towards obtaining high-quality surfaces with nano metric finish by femtosecond laser ablation: A case study on coppers", Optics & Laser Technology, 2022, 155(15), DOI:10.1016/j.optlastec.2022.108382

[11] X. Xiang et al., "Study of Nanosecond Laser Ablation on Aluminum and Stainless Steel Targets", Chinese Journal of Lasers, 2016, 43(2), DOI:10.3788/CJL201643.0203005

[12] Jun-Jie Zhang et al., "Nanosecond Pulsed Laser Ablation on Stainless Steel - Combining Finite Element Modeling and Experimental Work", Adv. Eng. Materials, 2019, v.21, issue8, doi.org/10.1002/adem.201900193

[13] Karajewski L.J. et al., "Operations management - processes and supply chains", textbook, Pearson, 2010, pp.177-193

[14] Lazov, L., Angelov, N. Influence of some technological parameters on the contrast of laser marking on the fly. Laser Phys., 2012, 22, 1755–1758 . https://doi.org/10.1134/S1054660X12110084

[15] L. Lazov, et al., Modification of the roughness of 304 stainless steel by laser surface texturing (LST), Laser Physics, 2023, Volume 33, Number 4, DOI:10.1088/1555-6611/acbb76

The impact of CO₂ laser power and scanning speed on various wood and thermowood samples

Dzintars Rāviņš
Faculty of Engineering
Rezekne Academy of Technologies
Rezekne, Latvia
dzintars.rav@gmail.com

Imants Adijāns
Faculty of Engineering
Rezekne Academy of Technologies
Rezekne, Latvia
imants.adijans@rta.lv

Emil Yankov
Faculty of Engineering
Rezekne Academy of Technologies
Rezekne, Latvia
emil.yankov@rta.lv

Vladislavs Bakakins
Faculty of Engineering
Rezekne Academy of Technologies
Rezekne, Latvia
vb21121@edu.rta.lv

Abstract. **In this study, the impact of CO_2 laser engraving and scanning on various types of wood before and after thermal treatment is investigated. An infrared CO_2 laser with a wavelength of 10640 nm is used in the study for engraving various wood samples before and after thermal treatment at a specific processing temperature of 214°C. All samples had a similar moisture content - approximately 8%. The engraving depth and width were measured for each wood sample. The findings reveal that thermal pre-treatment exert a discernible influence on the efficacy of laser engraving, and the engraving depth is notably influenced by the particular wood species involved. Consequently, the study offers a platform for assessing the optimization of laser engraving parameters applicable to different wood types and thermally modified wood, thereby facilitating the enhancement of product quality through judicious parameter selection.**

Keywords: CO_2 laser, laser engraving wood, laser processing parameters, wood thermally modified.

I. INTRODUCTION

Laser technologies are widely used in various industries and offer many advantages as they can offer a precise and efficient way to process materials and perform various functions. Here are some industries where laser technology is common: manufacturing and engineering, metalworking, materials processing, electronics, optics, science, medicine, military industry and much more [1], [2], [3]. Laser engraving and marking technologies are used to create precise and aesthetic graphic designs on various wood materials [4].

A popular decorative and construction material is wood. Wood is a natural material that comes from the trunk and branches of trees. It has been used in many industries including construction, furniture, interior design and more. Here are some examples of how wood is used decoratively and in construction - furniture, floors and carpets, doors and windows, wood trim, walls and roofs, decorative elements. Wood is an attractive material due to its natural beauty, and many people choose it to introduce elements of their homes and interior design. In addition, wood is a sustainable material if its management takes place in a responsible manner, thus contributing to environmental protection [5].

Heat treatment of wood is a process in which wood is treated at high temperatures in order to change its properties or improve its resistance to various physical influencing factors. This type of treatment is carried out to obtain better properties of wood products, such as wooden structures or finishing materials [6], [7].

The laser processing technology is considered a very modern and effective way to process wood and perform material processing operations by adjusting the correct parameters. This technology uses laser beams to cut, engrave, mark, or otherwise process materials. To optimize the pruning process based on processing time, knowing the linear energy density, when cutting a tree [8]. Lasers can have different wavelengths and intensities and are used for various purposes depending on the requirements [9]. Considering that different lasers, such

as those with wavelengths of 1.06 μm and 10.6 μm, interact differently with materials [10].

The aim of this study is to investigate the laser ablation process using infrared laser radiation at a wavelength of 10.6 μm (CO$_2$ laser) on various wood and thermally modified wood samples.

II. MATERIALS AND METHODS

A. Thermowood

In this study, ten types of wood materials were used (Ukrainian ash, Latvian spruce, alder, birch, maple, pine and beech, New Zealand pine Taeda and Radiata, Finnish pine) that were thermally processed by drying the wood at high temperatures, without using any chemical substances, heating it up to 214°C [11]. Processing wood affects various thermally treated wood physico-mechanical properties, increases resistance to brown rot fungi decay and compressive strength, reduces moisture adsorption, and improves hygroscopic hysteresis [12], [13]. Various weather conditions indicate that thermally treated wood is more resistant to photodegradation than untreated reference wood [14], [15], [16]. Thermowood is indeed a notable construction material with a series of unique properties that contribute to its popularity and versatility, including natural beauty and aesthetic appeal, versatility, environmental sustainability, carbon sequestration, energy efficiency, positive microclimate, durability, and ease of construction [17].

The experiment utilized wood material samples that underwent thermal treatment at 214°C, with a processing duration of 36 hours in a cycle, where the peak thermal treatment period itself lasts 2 hours. All samples used in the experiment were equally treated in a single thermal process.

Fig. 1. Ten wood samples both before and after thermal treatment.

As seen in Fig. 1, ten types of wood samples, thermally untreated and after thermo-treatment, include Ukrainian ash, Latvian spruce, alder, birch, maple, pine, and beech, New Zealand pines (Taeda and Radiata), and Finnish pine. All samples, before and after thermo-treatment, were measured with the digital moisture meter HT632, and the moisture content was determined to be 8%.

B. Equipment

The CO$_2$ laser system used in the experiment (SUNTOP ST-CC9060) with a wavelength of 10640 nm. (see Fig. 2).

Fig. 2. SUNTOP ST-CC9060 CO$_2$ laser system.

Technical specifications of the SUNTOP ST-CC 9060 laser system in Table 1.

TABLE 1. LASER SYSTEM SUNTOP ST-CC9060 TECHNICAL SPECIFICATIONS

CO$_2$ laser, CW mode	Laser type
4	Laser Safety Class
10640 nm	Wavelength
100 W	Maximum output power
0,02 mm	Precision
0 – 1000 mm/s	Scan speed
dxf, plt, bmp	Data formats used
Water cooling	Cooling system
1500 W	Total power

The digital microscope Dino-Lite Edge AM7115MZT was used for measuring engraving width and depth (shown in Figure 3).

Fig. 3. Digital Mikroskope Dino-Lite Edge AM7115MZT.

Technical specifications of the digital microscope Dino-Lite Edge AM7115MZT are provided in Table 2.

TABLE 2. DINO-LITE EDGE AM7115MZT MICROSCOPE TECHNICAL SPECIFICATIONS

2592 × 1944 pixels	Resolution
Windows	Operating System
20x~220x	Magnification Range
USB 2.0	Connectivity
8 (FLC)	LEDs

C. METHODOLOGY

In this experiment, ten types of wood samples were used (Ukrainian ash, Latvian spruce, alder, birch, maple,

pine, and beech, New Zealand pine Taeda and Radiata, Finnish pine) with dimensions of 15 x 60-70 x 200 mm, engraved with a laser using various power densities q_S and scanning speeds v. The power densities used for engraving are 0.71, 3.83, 6.52, and 8.31 ($\times 10^5$) W/cm², as indicated in Table 4. For each set of parameters, five lines were engraved with a distance of 2 mm between each line and a length of 50 mm. The depth h [mm] and width d [mm] of each engraved line were measured, and graphs were constructed as a function of laser parameters.

Before conducting the experiment, the laser power was measured using the OPHIR F150A-BB-26 laser power meter. Power values used for the experiments are shown in Table 3.

TABLE 3. POWER VALUES USED FOR THE EXPERIMENTS

P, W	5.6	30.1	51.2	65.2

The power density q_S [W/cm²] was calculated using formula (1):

$$q = \frac{P}{S} \tag{1}$$

where P [W] is the power and S [cm²] is the cross-sectional area of the laser beam on the surface of the material to be engraved, as given in formula (2):

$$S = \pi \frac{d^2}{4} \tag{2}$$

where d [cm] is the diameter of the laser beam (d = 0,01 cm). The values of power density calculated in W/cm², corresponding to the measured power values in W (shown in Table 3), are presented in Table 4.

TABLE 4. CALCULATED POWER DENSITY VALUES FOR THE CO_2 LASER SYSTEM

P, W	5.6	30.1	51.2	65.2
$q_S \times 10^5$, W/cm²	0.71	3.83	6.52	8.31

To create a laser cutting workflow, an engraving parameter matrix was established using the RDWorksV8 program (see Fig. 4), which supports drawing points, lines (horizontal/vertical), and applicable formats such as DXF, PLT, and AI, facilitating engraving and cutting operations.
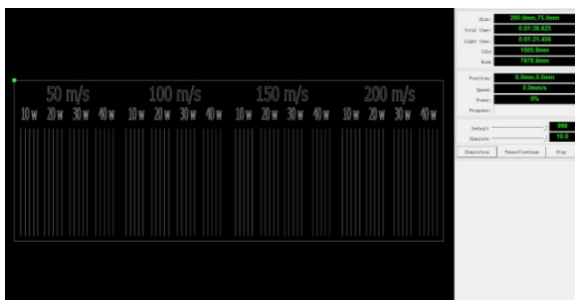
Fig. 4. Line engraving matrix in the RDWorksV8 program.

All twenty wood samples, including ten natural wood samples and ten thermally modified wood samples, were engraved according to the visible matrix (see Fig. 4) using the RDWorksV8 program (see Fig. 5).

Fig. 5. Photograph of a thermally treated radiata wood sample engraved according to the created matrix.

To measure the engraved line depth more accurately, all twenty wood samples were cross-cut through the center of the engraved line using a precise woodworking panel saw, Altendorf F45.

Fig. 6 and Fig. 7 shows depth and width measurement samples are shown respectively, where measurements were taken with the digital microscope Dino-Lite Edge AM7115MZT.
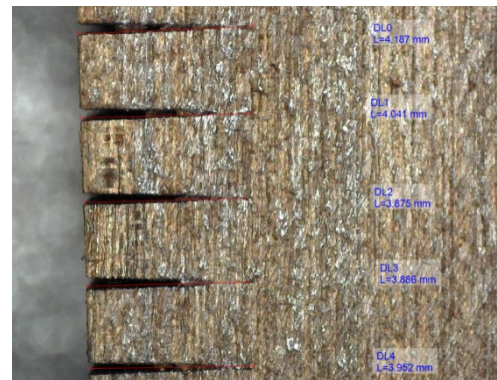
Fig. 6. Measurement of engraving depth in maple wood sample at 214°C thermal treatment and magnification x32.

Fig. 6 shows a thermally treated maple sample at 214°C temperature is shown with five cuts, obtained using a power density q_S = 8.31 × 10^5 W/cm² and scanning speed v = 50 mm/s. The average depth of the cut is calculated as h = 3,99 mm.
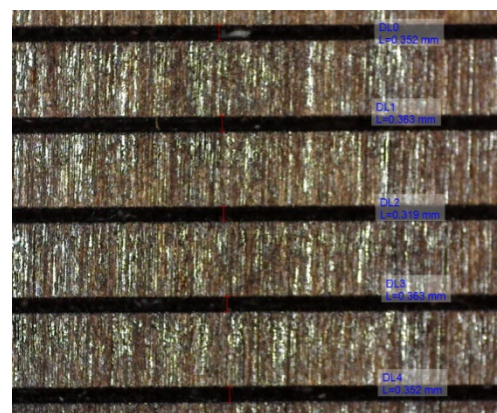
Fig. 7. Measurement of line width in a maple wood sample at a thermal treatment temperature of 214°C and at a magnification of x32.

Fig. 7 shows a thermally treated maple sample processed at a temperature of 214°C with five cuts, obtained using a power density q_S = 8.31 × 10^5 W/cm²

and a scanning speed v = 50 mm/s. The cut width was measured, and the average width calculated is d = 0,35 mm.

III. RESULTS AND DISCUSSION

The research findings are presented in graphs illustrating the influence of laser power density and scanning speed on the width and depth of laser-engraved lines. The graphs depict relationships between line width and depth as functions of power density and scanning speed for various pre- and post-processed thermally modified wood samples at a specified temperature.

Table 5 and table 6 shows the relationships between line width (d) and two power densities (q_S= $0.71 \cdot 10^5$ W/cm² and q_S= $8.31 \cdot 10^5$ W/cm²) at two scanning speeds (50 mm/s and 200 mm/s) for ten wood samples subjected to thermal treatment at 214°C.

Calculation of the percentage change in width Δd as a function of untreated (base) wood and thermally modified wood, obtained using equation (3).

$$\Delta d = \left(\frac{d_{max}}{d_{min}} - 1\right) \times 100\% \qquad (3)$$

TABLE 5. WIDTH CHANGES Δd IN PERCENT OF TEN THERMAL WOOD SAMPLES COMPARED WITH UNTREATED WOOD SAMPLES AT MIN POWER DENSITY q_S = $0.71 \cdot 10^5$ W/cm² AND MAX SCAN SPEED V = 200 mm/s

Wood	base d, mm	214°C d, mm	Δd, %
Ash UA	0,21	0,21	0
Spruce LV	0,21	0,21	0
Alder LV	0,22	0,22	0
Birch LV	0,22	0,23	4,55
Maple LV	0,22	0,22	0
Beech LV	0,22	0,23	4,55
Taeda NZ	0,23	0,23	0
Radiata NZ	0,23	0,23	0
Pine LV	0,20	0,21	4,35
Pine FIN	0,22	0,22	5

At a high scanning speed of 200 mm/s, the average line width is 0,218 mm for all baseline wood samples, and for thermally treated wood at 214°C, it is 0,22 mm. This indicates a difference of Δd = 0,92 %. At a lower scanning speed of 50 mm/s, the average line width is 0,32 mm for baseline wood, and for thermally treated wood at 214°C, it is 0,331 mm, resulting in a difference of Δd = 3,44 %. Tables 5 and 6 reveal that line width variations are minor, including both non-thermally treated and thermowood samples. The variations are dependent on power density, with the line width being slightly larger at higher power density and slightly smaller at lower power density.

TABLE 6. WIDTH CHANGES Δd IN PERCENT OF TEN THERMAL WOOD SAMPLES COMPARED WITH UNTREATED WOOD SAMPLES AT MAX POWER DENSITY q_S = $8.31 \cdot 10^5$ W/cm² AND MIN SCAN SPEED V = 50 mm/s

Wood	base d, mm	214°C d, mm	Δd, %
Ash UA	0,32	0,32	0
Spruce LV	0,32	0,32	0
Alder LV	0,31	0,32	3,23
Birch LV	0,30	0,30	0
Maple LV	0,31	0,33	6,45
Beech LV	0,32	0,33	3,13
Taeda NZ	0,29	0,31	6,9
Radiata NZ	0,36	0,37	2,78
Pine LV	0,36	0,37	2,78
Pine FIN	0,31	0,34	9,68

Fig. 8 shows the dependence of the line depth h on the power density (q_S) at two scanning speeds (v) 50 mm/s and 200 mm/s for a sample of natural maple.
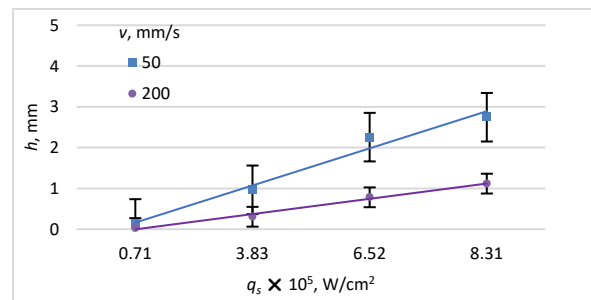
Fig. 8. The dependence of line depth (h) on power density (q_S) at two different scanning speeds (v) for a natural maple sample.

Fig. 9 shows the dependence of line depth (h) on power density (q_S) for two scanning speeds, 50 mm/s and 200 mm/s, for a maple thermowood sample that has undergone thermal treatment at 214°C.
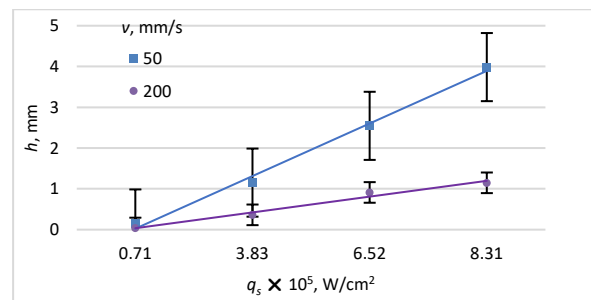
Fig. 9. The dependence of line depth (h) on power density (q_S) at two different scanning speeds (v) for a maple thermowood sample that has been thermally treated at 214°C.

In Fig. 8 and Fig. 9, it is observed that the line depth is significantly smaller at low power density and much greater at high power density. The maximum depth for untreated wood is 2,75 mm and for thermally treated wood it is 3,99 mm, achieved at a power density of $8.31 \cdot 10^5$ W/cm² and a scanning speed of 50 mm/s for a maple thermowood sample treated at 214°C. The minimum depth, less than 0,15 mm, is attained at a power

density of $0.71 \cdot 10^5$ W/cm^2 and a scanning speed of 200 mm/s for both samples. Diagrams for other pre- and post-processing samples show similar trends within this range. The line depth for all samples exhibits an increase close to linear.

The depth change rate tg $h(q_s)$ [$\frac{mm}{W \times cm^2}$] depending on the power density is calculated using equation (4).

$$tg\ h(qs) = \frac{\Delta h}{\Delta qs} \qquad (4)$$

Where $\Delta h = h_{max} - h_{min}$ is the difference between maximum depth and minimum depth, and $\Delta q_s = q_{s\ max} - q_{s\ min}$ is the difference between maximum power density and minimum power density. The calculated results of the depth change rate are shown in Table 7.

TABLE 7. RATE OF CHANGE OF DEPTH tg $h(q_s)$ DEPENDING ON POWER DENSITY

tg $h(q_s)$, $\frac{mm}{W \times cm^2}$	v, mm/s	
	50	200
base	0,35	0,143
214°C	0,505	0,146

The two graphs below illustrate the dependence of line depth (h) on scanning speed (v) at the lowest power density $q_S = 0.71 \cdot 10^5$ W/cm^2 (see Fig. 10) and the highest power density $q_S = 8.31 \cdot 10^5$ W/cm^2 (see Fig. 11) for samples of natural maple and thermally modified maple. The samples were subjected to thermal treatment at 214°C temperature.
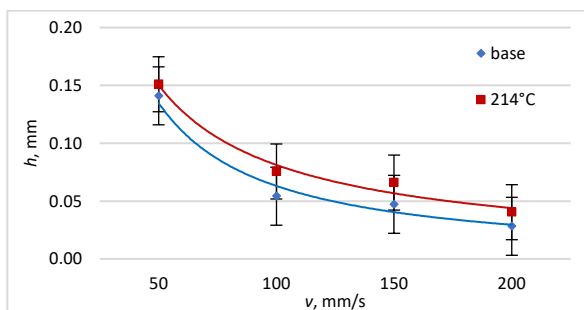

Fig. 10. The dependence of line depth (h) on scanning speed (v) at a specific power density. $q_S = 0.71 \cdot 10^5$ W/cm^2.
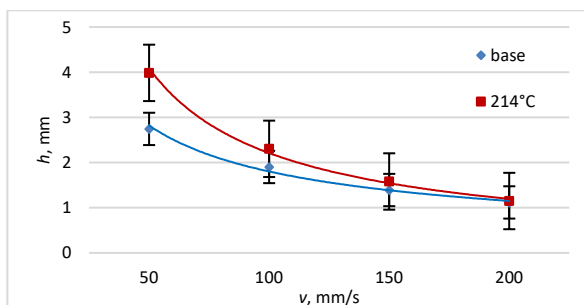

Fig. 11. The dependence of line depth (h) on scanning speed (v) at a specific power density. $q_S = 8.31 \cdot 10^5$ W/cm^2.

The depth is greater at a low scanning speed of 50 mm/s and smaller at a high scanning speed of 200 mm/s. The maximum depth is achieved at a power density of $8.31 \cdot 10^5$ W/cm^2 for a maple thermowood sample,

reaching 3.99 mm, treated at 214°C. The minimum depth is 0,15 mm at a power density of $0.71 \cdot 10^5$ W/cm^2 for a natural maple sample. The reduction in line depth in the graphs is nonlinear.

The rate of change of depth, tg $h(v)$ [s^{-1}], is calculated based on the scanning speed using the equation (5).

$$tg\ h(v) = \frac{\Delta h}{\Delta v} \qquad (5)$$

Where $\Delta v = v_{max} - v_{min}$ is the difference between maximum and minimum scan speed. The calculated results of the depth change rate are shown in Table 8.

TABLE 8. RATE OF CHANGE OF DEPTH tg $h(v)$, DEPENDING ON SCANNING SPEED.

tg $h(v)$, s^{-1}	q_s ✗ 10^5, W/cm^2	
	0.71	8.31
base	0,001	0,011
214°C	0,001	0,019

Calculate the percentage change in depth, denoted (Δh), based on heat-treated maple wood using equation (6).

$$\Delta h = \left(\frac{h_{max}}{h_{min}} - 1 \right) \times 100\% \qquad (6)$$

In Table 9, the calculated depth changes in percentage are presented for ten different wood samples, with thermowood samples compared to untreated wood samples. Depth measurements are conducted on lines engraved at maximum power density ($q_s = 8.31 \times 10^5$ W/cm^2) and minimum scanning speed ($v = 50$ mm/s).

TABLE 9. THE PERCENTAGE VARIATIONS IN DEPTH, DENOTED AS Δh, AMONG TEN THERMALLY TREATED SAMPLES AND UNTREATED SAMPLES, OBSERVED AT THE MAXIMUM POWER DENSITY $q_S = 8.31 \times 10^5$ W/cm^2 AND THE MINIMUM SCANNING SPEED $v = 50$ mm/s.

Wood	base h, mm	214°C h, mm	Δh, %
Ash UA	2,35	2,4	2,13
Spruce LV	4,94	5,55	12,35
Alder LV	4,34	4,67	7,6
Birch LV	3,57	3,72	4,2
Maple LV	2,8	3,99	42,5
Beech LV	3,34	3,41	2,1
Taeda NZ	3,98	4,88	22,61
Radiata NZ	4,16	5,19	24,76
Pine LV	4,08	4,47	9,56
Pine FIN	4,16	4,46	7,21

IV. CONCLUSION

This research employed a laser engraving process to examine the influence of power density and scanning speed on the depth and width of etched lines. The outcomes revealed that both power density and scan speed significantly impact the depth of etched lines, with

higher power density and lower scan speed resulting in greater depths, while line width variations are minor.

The calculation of the depth change rate was performed separately for power density and scanning speed, and the outcomes are presented in Tables 7 and 8, respectively. Additionally, Table 9 illustrates the percentage variation in depth among ten distinct wood samples (Ukrainian ash, Latvian spruce, alder, birch, maple, pine, and beech, New Zealand pine Taeda and Radiata, Finnish pine) when comparing heat-treated and untreated samples at maximum power density and minimum scanning speed.

The implications of this study hold significance for the application of laser engraving in the woodworking industry, especially in the creation of decorative or functional wooden items. By comprehending the factors influencing the depth of etched lines, manufacturers can optimize their laser engraving procedures to attain desired outcomes.

Subsequent investigations could explore the effects of other laser parameters, such as pulse duration and spot size, on the depth of etched lines. Furthermore, more detailed analyses could delve into the microstructural changes occurring in wood during the laser engraving process, along with exploring the impact of various wood types on engraving results.

REFERENCES

[1] L.Lazov, K.Tsanko, '' Methods for Measuring Laser Power'', 2021 Proceedings of the 13th International Scientific and Practical Conf. 3 173-180

[2] D. Klavins, L. Lazov, A. Pacejs, R. Revalds, E. Zaicevs '' Research of Laser Marking and Engraving on Brass Alloy 260'', 2019 Proceedings of the 12th International Scientific and Practical Conference. Volume III, 119-123

[3] L.Lazov, N.Angelov, Teirumnieks E, Teirumnieka E, ''Preliminary Numerical Analysis for the Role of Speed onto Laser Technological Processes'', 2019 Proceedings of the 12th International Scientific and Practical Conf. 3 137-142

[4] Laser engraving machine for wood, [Online]. Available: https://www.gweikecloud.com/?gad_source=1&gclid=CjwKCAiA 1fqrBhA1EiwAMU5m_w71hI5vOoh5dM6MUYUdjjU12uxNKm lgB6nDRD3OWkecAeeghonBqhoCqmgQAvD_BwE/. [Accessed February 23, 2024].

[5] The most common types of wood in construction, [Online]. Available: https://www.indeed.com/career-advice/career-development/types-of-wood-in-construction. [Accessed February 28, 2024].

[6] Thermally modified wood, [Online]. Available: https://thermory.com/blog-and-news/a-closer-look-at-wood-as-a-building-material/. [Accessed February 10, 2024].

[7] Published press release "Thermal industry,,, SIA "Ošukalns,, [Online]. Available: https://www.osukalns.lv. [Accessed February 16, 2023], https://www.la.lv/zimols-owood-ar-osukalna-identitati

[8] L. Lazov, Edmunds Teirumnieks, Tsanko Karadzhov, Nikolay Angelov, Influence of power density and frequency of the process of laser marking of steel products, Infrared Physics & Technology, 2021,Volume 116, 103783, https://doi.org/10.1016/j.infrared.2021.103783.

[9] L. Lazov, P. Narica, J. Valiniks, A. Pacejs, H. Deneva, D. Klavins, '' Optimization of CO₂ Laser Parameters for Wood Cutting'', 2017 Proceedings of the 11th International Scientific and Practical Conference. Volume III, 168-173

[10] L. Lazov, et al., Modification of the roughness of 304 stainless steel by laser surface texturing (LST), Laser Physics, 2023, Volume 33, Number 4, DOI:10.1088/1555-6611/acbb76

[11] Hüseyin Pelit, ''Influence of Densification on Mechanical Properties of Thermally Pretreated Spruce and Poplar Wood'', Pelit & Yorulmaz (2019). "Modification of wood," BioResources 14(4), 9739-9754

[12] Yonggun P, Jun-Ho P, Sang-Yun Y, Hyunwoo C, Hyunbin K, Yeonjung H, Yoon-Seong C, Kyoungjung K, Hwanmyeong Y, ''Evaluation of Physico-mechanical Properties and Durability of Larix kaempferi Wood Heat-treated by Superheated Steam'', Journal of the Korean Wood Science and Technology · September 2016, 44(5): 776~784

[13] Cristian A.Chávez, Nelson O.Moraga, Carlos H.Salinas, Roberto C.Cabrales, Rubén A.Ananías, ''Modeling unsteady heat and mass transfer with prediction of mechanical stresses in wood drying'', [Online]. Available: https://doi.org/10.1016/j.icheatmasstransfer.2021.105230. [Accessed February 14, 2024].

[14] M. Nuopponen, H. Wikberg, T. Vuorinen, S.L. Maunu, S. Jamsa, P. Viitaniemi, ''Heat-treated softwood exposed to weathering'', J. Appl. Polym. Sci. 91 (2004) 2128–2134, https://doi.org/10.1002/app.13351.

[15] E.D. Tomak, D. Ustaomer, M.A. Ermeydan, S. Yildiz, ''An investigation of surface properties of thermally modified wood during natural weathering for 48 months'', Measurement 127 (2018) 187–197, https://doi.org/10.1016/j

[16] Iveta Č., Martin Z., František K., Tereza T., ''Impact of Thermal Loading on Selected Chemical and Morphological Properties of Spruce ThermoWood'', Čabalová et al. (2019). "Spruce ThermoWood," BioResources 14(1), 387-400

[17] Dennis J., Ed S., Jukka Ala-V., Nils B., Duncan M., ''THE INTERNATIONAL RESEARCH GROUP ON WOOD PROTECTION'', Paper prepared for the 37th Annual Meeting Tromsø, Norway 18-22 June 2006

Obtaining a promising laser induced surface nanostructure of titanium alloy for biocompatibility

Edmunds Sprudzs
Faculty of Engineering
Rezekne Academy of Technologies
Rezekne, Latvia
sprudzs.edmunds@gmail.com

Lyubomir Lazov
Faculty of Engineering
Rezekne Academy of Technologies
Rēzekne, Latvia
lyubomir.lazov@rta.lv

Emil Yankov
Faculty of Engineering
Rezekne Academy of Technologies
Rezekne,Latvija
emil.yankov@rta.lv

Imants Adijans
Faculty of Engineering
Rezekne Academy of Technologies
Rēzekne, Latvia
imants.adijans@rta.lv

Abstract. Biocompatibility of materials is of paramount importance in many areas of research, engineering, medical and consumer grade product development. Biocompatibility of surfaces can be understood as resistance of the surface to harmful bacteria colonisation and subsequent biofilm creation. Traditionally, such surfaces are created by coating the base material with a different material that offers the necessary biocompatibility features. This is often not desirable, as it introduces different surface chemistry, has different physical properties than the base material, and in many cases, does not provide a lasting solution. Modification of the surface of the base material would be preferrable. In the last decade, laser ablation of surfaces to create microscale and nanoscale patterns that improve biocompatibility has been at the forefront of research in this field. This research paper provides insight into current understanding of bactericidal surface topologies and demonstrates an example of obtaining a potentially bactericidal surface of grade V titanium alloy with an industrial grade nanosecond laser.

Keywords: Biocompatibility, Nanotextures, Laser.

I. INTRODUCTION

Nanotechnology has been advancing rapidly in the last few decades. This has fostered development of surface enhancement techniques that can dramatically change surface properties and interaction with the environment. These include drag reducing, water repellent and antibacterial coatings [1], self-cleaning surfaces [2], anti-icing coatings [3] and many others.

There are two ways to alter surface properties - by changing surface chemistry or by creating physical structures on existing surfaces. Sometimes the two methods are combined to obtain a surface with desired properties.

Materials with improved antibacterial properties can have great impact on how industries like medicine, food production, processing and storage develop. Bacteria and other microorganisms attach to the surface of material and form complex multi-layered habitats protected by biofilms [4]. These structures are only partly susceptible to antibiotics, as these usually reach only the first layer with subsequent layers developing antibiotic resistance capabilities. Antimicrobial-resistant infection related deaths are expected to reach 10 million by 2050, so surfaces that prevent ab initio formation of bacteria are of high interest [5].

It has been established that micro- and nano-modifications of surfaces induce changes in cell shape and adhesion to materials [6]. Such changes include, but are not limited to changes in cell morphology, orientation, activity, behaviour, and phenotypic expression. For an example, for dental implants, preliminary research shows, that by optimising biomaterials to improve osteogenic cell proliferation, infection risks can be reduced by 60-90% without using any antibiotics [7]. The phenomenon of inducing a desired cell reaction with adequate surface structure is known as "contact guidance" and it has been observed in several cell types interacting with anisotropically patterned substrates [8]. Another term - mechano-bactericidal effect – has been used to describe capacity of nano-scale structures to physically impede and deactivate bacterial cells [9].

Several examples of this mechano-bactericidal effect are known and have been studied in nature. Wings of cicada [9] – [11] and dragonflies [12], [13] as well as feet of a gecko [14] have all been observed to show such properties. Further, it has been demonstrated that modified surfaces of materials, such as black silicon (bSi) and hydrothermally

etched titanium show bactericidal properties comparable to that of their natural inspiration [15], [16].

A finite element model (FEM) to describe the mechanics of surface nanospikes rupturing bacterial cells has been developed recently by a group of scientists in Australia. An array of nanospikes with hemispherical end radius of 0.03 μm, height of 0.2 μm and centre to centre distance of 0.2 μm was used for the model and magnitude of stress and strain leading to the creep deformation of the cell wall was predicted (Fig. 1) [17].

Fig. 1. Contour plot of the cell on nanospikes, elastic strain

energy density (MPa) [17].
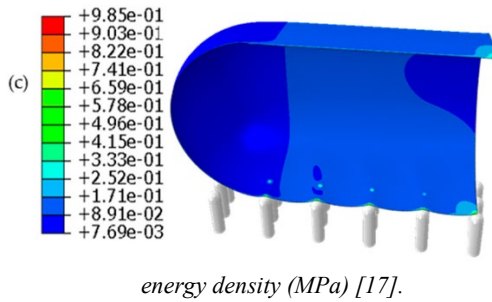
A practical demonstration of similar nanostructures to those derived theoretically and thus, applicability of the model referred to above has been verified on chemically etched titanium. The surface texture shown in Fig. 2 demonstrated strong bactericidal properties against *Pseudomonas aeruginosa* and *Staphylococcus aureus* cells [18].

Fig. 2. Optical profilometry images of HTE-Ti surface along with height profiles [18].

In the current study, grade V titanium alloy surface was processed with a nanosecond laser to obtain surface nanotextures like those showing strong bactericidal properties present in nature, obtained with other surface modification technique, and those predicted mathematically.

II. MATERIALS AND METHODS

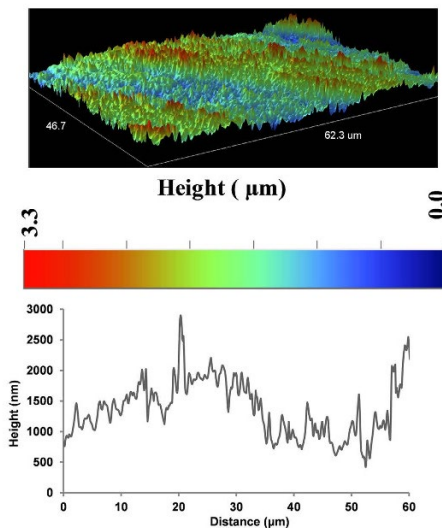Medical grade V titanium alloy (Gr.5, Ti6-Al-4V) was selected for experiments. A sheet of 2 mm thickness was cut into 60 mm x 60 mm squares for convenient positioning under the laser for processing and under the microscope for result evaluation. No surface processing or treatment was applied prior to laser processing.

Rofin PowerLine F20 Varia dual-galvanometer laser was used for processing the samples. This is an ytterbium laser with a wavelength of 1064 nm and a pulse length down to 4 ns. The key parameters of the machine are summarized in the table below [19].

TABLE 1. ROFIN POWERLINE F20 VARIA SPECIFICATION

Parameter	Value
Operating Mode	Pulsed laser
Wavelength	1064 nm
Output Power	0-19.7 W
Pulse Energy	1 mJ
Pulse Width	4, 8, 14, 20, 30, 50, 100, 200 ns
Repetition Rate	20 to 1000 kHz

Working principle of the test setup is provided in Fig. 3 [20], where a test sample is placed on the test bed and two precision mirror galvanometers direct the laser beam through an F-theta lens as set up by the user in software.

Distance between the lens and the surface of the
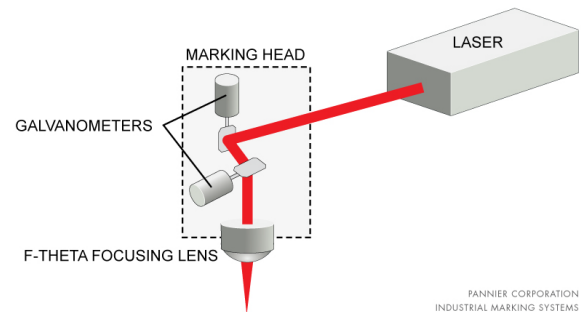
Fig. 3. Dual-Galvanometer laser operating principle and test setup [20].

sample can be adjusted with micrometre resolution to focus or defocus the laser beam. The focal distance of the current lens is 184 mm and laser spot size is 40 μm at this focal point. No assist gas was used, and all experiments were conducted at room temperature of about 20C.

Samples were analysed with Olympus LEXT OLS5000 3D Measuring Laser Microscope to assert the created nanostructures for compatibility with the desired topology visually as well as surface roughness was established and documented. When this analysis revealed a promising sample, additional spatial measurements were made to confirm the dimensions of surface elements and their distribution. This sample was also inspected with scanning electron microscopy (SEM) to compare the image of the structure to that of other authors.

While the exact spatial dimensions of elements and their distribution of antibacterial surfaces vary, all are in nanometre or a few micrometres scale [21]. Given the laser spot size of 40 μm, direct machining of those surface topologies is not possible with the equipment available. Thus, a strategy to produce such structures indirectly had to be found. While sources exist describing successfully creating this type of surface topology with femtosecond lasers, no documented examples were found in literature for nanosecond lasers.

Without a clear starting point, approach of matrices of

Fig. 4. A matrix of 32 test samples.

32 rectangles with size of 3 mm x 1 mm was chosen, were two factors of pulse width, laser power, repetition rate, scanning speed, scanni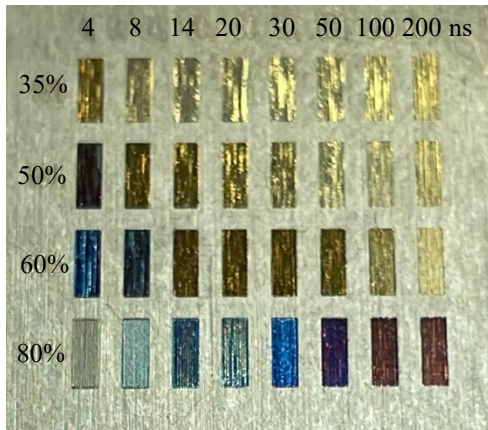ng line step or angle would be altered with the remaining factors fixed. For illustration, one such matrix with varying pulse width and laser power is provided in Fig. 4. At first, cross-hatching at 90-degree angle and combined 90-degree and 45-degree angle was
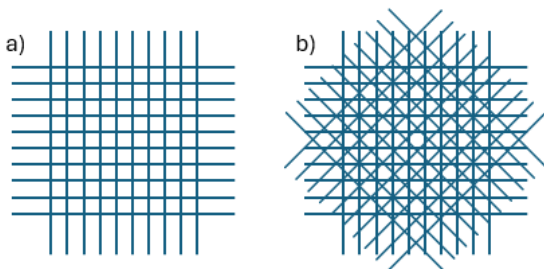

Fig. 6. Schematic representation of hatched laser scanning patterns: a)90-degree angle, b) 90-degree and 45-degree angle.

attempted using the entire range of laser power settings and pulse widths at a constant scanning speed of 100 mm/s (Fig. 5).

This approach did not produce the desired results. Surfaces with large, melted areas at higher energy density levels and surfaces with no visible topology change at lower energy density levels were obtained. However, sporadic appearance of desired surface structures was noticed along the scanning lines of some samples. One such example is provided in Fig. 6.
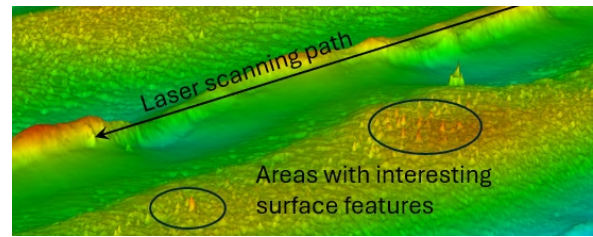

Fig. 7. Interesting surface structures along the laser path.

Measurements of those features were made Fig. 6 to discover they closely resemble some of the bactericidal structures found in nature discussed earlier in this paper. Rz roughness was established at close to 0.7 μm with many such features being 1 μm or closer apart. Given the chaotic nature of these features, several measurements were made to establish the scale, but visual inspection remained a key method for confirmation of suitability of the surface structure of the sample.
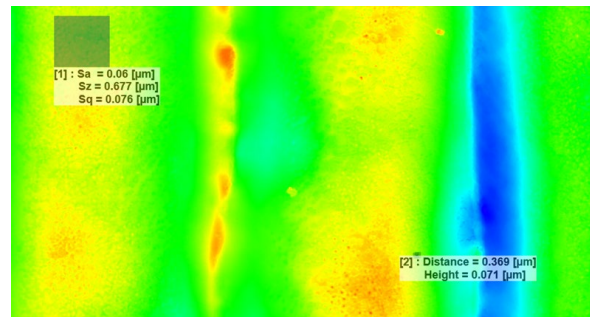
Fig. 5. Surface roughness and distance between features.

With this discovery, the cross-hatching strategy was dropped, and further experiments conducted in an attempt to compose the entire sample area from these "along-the-scan-line" structures. After a series of experiments, it was established that the pulse length of 4 ns was giving the most consistent features with highest structure peaks and minimum distance between features. The scanning speed was kept constant at 100 mm/s and 80% laser power setting used. Through iteration, it was established that the distance between the scanning lines of 1 μm, produced the most consistent surface structure with predominantly desirable features. Additional data and images covering the entire experiment are omitted here due to the limited number of pages available for this publication and are available on request from authors.

Effective laser radiation energy can be used to assess and compare the effect of laser processing, even when factors like pulse width, scanning speed, power and frequency differ. It is a useful measure to help put a novel approach with a different type of laser into perspective and help other researchers speed up their efforts for similar research. Laser radiation absorbed per mm² was calculated according to (1)

$$E_{eff} = \frac{APf}{v^2}, \qquad (1)$$

where A is the absorption coefficient of the material, P is the average power of the laser, f is the repetition rate and v is the laser scanning speed, respectively. While some

debate exists between scientists, it seems fair to use a constant absorption coefficient [22] of a median value of 0.4 for the given titanium alloy [23].

III. RESULTS AND DISCUSSION

The result of the study is a surface sample that is ready for the next step – investigation of its bactericidal properties.

It was found, that surface topology with random nanospikes with centre to centre distance between 0.1 μm and 1 μm and Rz roughness of 0.15 to 0.70, i.e. those, with spatial profile closely resembling that of bactericidal surfaces found in nature [9] – [14], obtained experimentally [15], [16], and those shown in mathematical model [17] are formed at E_{Eff} close to 0.30 J/mm² with a pulse width of 4 ns. A Micrograph of the sample is provided in Fig. 8.

Fig. 9. A micrograph of the surface of the sample.

A closeup for better visualization is provided in Fig. 9. Surface roughness to assess the depth of the features and feature peak-to-peak measurements are provided in Fig. 10.
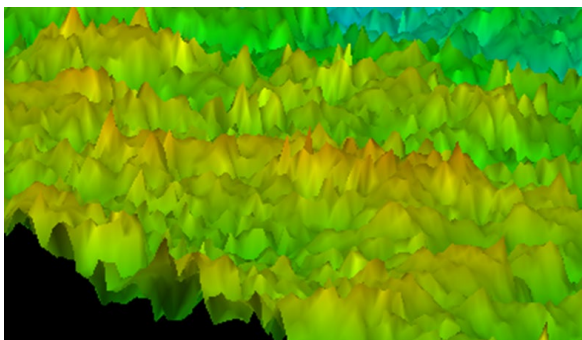
Fig. 10. A closeup of the surface topology of the sample.

Fig. 8. Sample measurements: (a) Surface roughness measurement, (b) feature peak-to-peak- distance measurement.

Image of the sample at a magnification of 100x is provided in fig10.
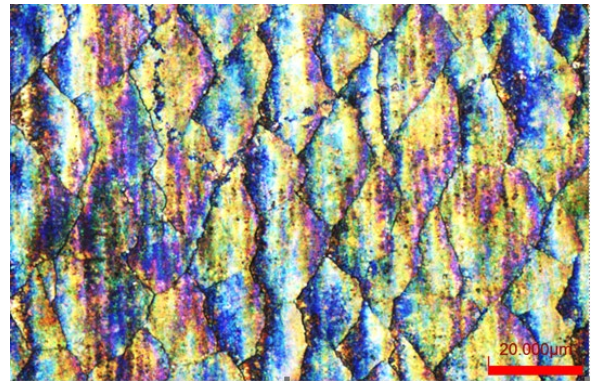
Fig. 12. 100x image of the sample.
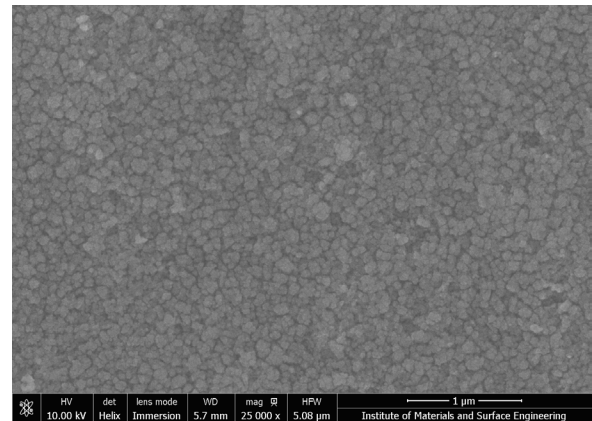
Fig. 11. SEM image of the sample.

SEM investigation of the achieved topology was conducted for further reference and is provided in Fig. 12.

IV. CONCLUSIONS

This study attempted and successfully produced surface topology structures on titanium grade V alloy that based on current state of the art shall exhibit bactericidal properties. The work described in this study is the first step of a multi-step journey and provides promising grounds for further research of laser induced surface nanostructures with industrial grade nanosecond lasers as opposed to

much more complex and lab-constrained femtosecond lasers. The next step is to conduct anti-bacterial experiments to confirm reduced rates of gram-negative and gram-positive bacterial development and biofilm formation. More experiments with the resulting energy densities close to the E_{eff}, pulse width and scanning pattern already identified shall be conducted to finetune the surface structure response of the material and to increase the processing speed. Stereoscopic SEM imaging shall be performed to both, confirm the already established spatial dimensions of surface nanotexture profile as well as establish the effective spike hemispherical end radius and try to reduce it during future experiments. X-ray diffractometer could be used to perform analysis of the surface texture to better understand the processes governing the formation of the required nanospikes.

REFERENCES

[1] Samaha, M. A., Tafreshi, H. V., & Gad-el-Hak, M. (2012). Superhydrophobic surfaces: From the Lotus Leaf to the submarine. Comptes Rendus Mécanique, 340(1-2), 18–34. https://doi.org/10.1016/j.crme.2011.11.002.

[2] Zhang, X., Liu, X., Laakso, J., Levänen, E., & Mäntylä, T. (2012). Easy-to-clean property and durability of superhydrophobic flaky γ-alumina coating on stainless steel in field test at a paper machine. Applied Surface Science, 258(7), 3102–3108. https://doi.org/10.1016/j.apsusc.2011.11.045.

[3] Wang, F., Li, C., Lv, Y., Lv, F., & Du, Y. (2010). Ice accretion on superhydrophobic aluminum surfaces under low-temperature conditions. Cold Regions Science and Technology, 62(1), 29–33. https://doi.org/10.1016/j.coldregions.2010.02.005.

[4] Donlan, R. M. (2002). Biofilms: Microbial life on surfaces. Emerging Infectious Diseases, 8(9), 881–890. https://doi.org/10.3201/eid0809.020063.

[5] Tripathy, A., Sen, P., Su, B., & Briscoe, W. H. (2017). Natural and bioinspired nanostructured bactericidal surfaces. Advances in Colloid and Interface Science, 248, 85–104. https://doi.org/10.1016/j.cis.2017.07.030.

[6] Curtis, A., & Wilkinson, C. (1997). Topographical control of cells. Biomaterials, 18(24), 1573–1583. https://doi.org/10.1016/s0142-9612(97)00144-0.

[7] Gasik, M., Braem, A., Chaudhari, A., Duyck, J., & Vleugels, J. (2015). Titanium implants with modified surfaces: Meta-analysis of in vivo osteointegration. Materials Science and Engineering: C, 49, 152–158. https://doi.org/10.1016/j.msec.2014.12.074.

[8] Meyle, J., Gültig, K., Brich, M., Hämmerle, H., & Nisch, W. (1994). Contact guidance of fibroblasts on biomaterial surfaces. Journal of Materials Science: Materials in Medicine, 5(6-7), 463–466. https://doi.org/10.1007/bf00058984.

[9] Linklater D.P., S. Juodkazis, E.P. Ivanova, Nanofabrication of mechanobactericidal surfaces, Nanoscale 9 (43) (2017) 16564-16585. https://doi.org/10.1039/c7nr05881k.

[10] Ivanova E.P., et al., Natural bactericidal surfaces: mechanical rupture of Pseudomonas aeruginosa cells by cicada wings, Small 8 (16) (2012) 2489-2494. https://doi.org/10.1002/smll.201200528.

[11] Kelleher S.M., et al., Cicada wing surface topography: an investigation into the bactericidal properties of nanostructural features, ACS Appl. Mater. Interfaces 8 (24) (2016) 14966-14974. https://doi.org/10.1021/acsami.5b08309.

[12] Bandara C.D., et al., Bactericidal effects of natural nanotopography of dragonfly wing on Escherichia coli, ACS https://doi.org/10.1021/acsami.6b13666.

[13] Mainwaring D.E., et al., The nature of inherent bactericidal activity: insights from the nanotopology of three species of dragonfly, Nanoscale 8 (12) (2016) 6527-6534. https://doi.org/10.1039/c5nr08542j.

[14] Li X., et al., The nanotipped hairs of gecko skin and biotemplated replicas impair and/or kill pathogenic bacteria with high efficiency, Nanoscale 8 (45) (2016) 18860-18869. https://doi.org/10.1039/c6nr05046h.

[15] Ivanova E.P., et al., Bactericidal activity of black silicon, Nat. Commun. 4 (2013) 2838. https://doi.org/10.1038/ncomms3838.

[16] Hayles A., et al., Hydrothermally etched titanium: a review on a promising mechano-bactericidal surface for implant applications, Mater. Today Chem. 22 (2021), 100622, https://doi.org/10.1016/j.mtchem.2021.100622.

[17] Islam, M., et al., Finite Element Modeling of a Gram-Negative Bacterial Cell and Nanospike Array for Cell Rupture Mechanism Study. (2023) Molecules. 28. 2184. 10.3390/molecules28052184.

[18] Bhadra, C.M., et al., Antibacterial titanium nano-patterned arrays inspired by dragonfly wings. Sci. Rep. 2015, 5, 16817, https://doi.org/10.1038/srep16817.

[19] Rofin. (2015). FIBER LASERS PowerLine F Series for Marking and Micro Processing. Bergkirchen, Germany; Rofin.

[20] Pannier Corporation. (2021, November 29). Comparison: Galvanometer vs. flatbed laser marking. Pannier Corporation. Retrieved January 18, 2023, from https://www.pannier.com/laser/flatbed-vsgalvo-lasers/.

[21] Larrañaga-Altuna, M., Zabala, A., Llavori, I., Pearce, O., Nguyen, D. T., Caro, J., Mescheder, H., Endrino, J. L., Goel, G., Ayre, W. N., Seenivasagam, R. K., Tripathy, D. K., Armstrong, J., & Goel, S. (2021). Bactericidal surfaces: An emerging 21st-century ultra-precision manufacturing and materials puzzle. Applied Physics Reviews, 8(2), 021303. https://doi.org/10.1063/5.0028844

[22] J. Yang, S. Sun, M. Brandt, W. Yan, Experimental investigation and 3D finite element prediction of the heat affected zone during laser assisted machining of Ti6Al4V alloy. J. Mater. Process. Technol., 210 (15) (2010), pp. 2215-2222, https://doi.org/10.1016/j.jmatprotec.2010.08.007.

[23] M. Keller, A. Chaudhary, S. Kelly, S. Medieros, Absorption coefficient characterization in Ti-6Al-4V laser additive manufacturing, Proceedings of ICALEO (2006), p. 1204, https://doi.org/10.2351/1.5060759.

Methodology and Model for the Study of Relative Accuracy Deviation in Laser Cutting of C 235 steel

Nikolay Tonchev Tonchev
Bulgaria University of Transport
„Technique and construction technologies in transport" Faculty
Sofia, Bulgaria
tontchev@vtu.bg

Victor Boykov Georgiev
Bulgaria University of Transport
„Technique and construction technologies in transport" Faculty
Sofia, Bulgaria
viktor_georgiev@vtu.bg

Nikolay Todorov Dolchinkov
„V. Levski" NMU
Faculty of Security and Defence
Veliko Tarnovo, Bulgaria
n_dolchinkov@abv.bg

Nikolay Iliyanov Padarev
„V. Levski" NMU
Faculty of Security and Defence
Veliko Tarnovo, Bulgaria
nipadarev@gmail.com

Emil Yankov
University of Ruse „A. Kanchev"
Departments of Materials Science and Technology
Ruse, Bulgaria
eyankov@uni-ruse.bg

Abstract. **The paper presents an analysis using the design methodology based on the response of investigated quantities in the optimization of laser cutting parameters in terms of dimensional accuracy for C235 steel samples. The input factors, such as cutting speed, power, and carbon dioxide pressure, on the quality cut, expressed by the relative deviation from accuracy, are examined. The paper proposes an algorithm and a regression model to optimize the deviation from the dimensions between a model and a cut contour, by minimizing the error of this deviation. Based on the conducted experiment and research results, a generalized methodology was created. It can be used after a planned experiment to determine the accuracy of any contours of a test material of a specific thickness.**

Keywords: Laser cutting, laser cutting modes for C235 steel, modelling, multifactorial analysis.

I. Introduction

Laser beam machining (LBM) as an effective tool for material removal, is establishing laser treatment more and more as a technology in the industry. Precisely as an effective alternative to some conventional machining processes, LBM has attracted the attention of researchers to conduct extensive experimental and numerical research [1], [2]. Laser cutting is no exception in this direction, which is a non-contact, production-flexible and highly productive technique, allowing relatively accurate profiling of a wide range of sheet materials [3]. To obtain a high-quality result of laser cutting, an optimization process [4, 5, 6, 7] is usually started, which justifies the quality obtained and the costs incurred in terms of time and finances. Therefore, there is great motivation in modelling and optimizing this unconventional machining process. Modelling and optimization are performed based on related experiments. The experimental data formulate the relationship between the quality characteristic and the input parameters through the model and the response surface. The experiments were made using DOE (Design of Experiments) and the results were confirmed by analysis of variance.

In the references cited in this research, the DOE method such as the response surface method has been shown to be useful for deriving accurate mathematical models. Developing an accurate model between the input and output variables of the LBM process is difficult and complex due to the non-linear behaviour of the process under different conditions. There is no general formula or formulation in the general case. Each thickness or material, and laser equipment in the case of LBM, requires its own experiments. In them, the input variables are the system, material, and process parameters, and the output variables are the quality characteristics of the laser-processed part, including geometric characteristics, metallurgical characteristics, surface roughness, and material removal rate.

Algorithms for laser parameter optimization for laser cutting without irregularities are found in the references

[8], which, however, are not related to the accuracy of the product between the set and the obtained contour. The cited algorithm involves designing experiments with only one factor at a time. The influence of more than one process parameter on the cut quality was discussed in [9], where the laser cut quality was analysed by notch geometry and surface roughness.

For the precise implementation of the technology, guaranteed accuracy is required. Unfortunately, the science team didn't find specific research in this regard. For this reason, it was necessary to apply the design methodology based on the response of the examined quantity when optimizing the parameters of laser cutting in terms of the accuracy of dimensions for C235 samples.

II. MATERIALS AND METHODS

The purpose of the research is to create an algorithm and regression model to optimize the deviation from the dimensions between the model and the cut contour by minimizing the error of this deviation. Based on the conducted experiment and the results of the research, a generalized methodology is created. Using the methodology, it is necessary to analyse the accuracy deviation depending on the parameters of the technological mode. The goal of the research is the most widely rolled steel C235. It's chemical composition is show in Table 1.

TABLE 1. CHEMICAL COMPOSITION OF 235 STEEL

C	Si	Mn	Ni	S	P	Cr	N	Cu
≤0,22	≤0,05	≤0,60	≤0,30	≤0,040	≤0,040	≤0,30	≤0,012	≤0,30

TABLE 2. TECHNOLOGICAL PARAMETERS FOR CUTTING BLACK STEEL WITH A THICKNESS OF 3 MM

Type of mode	Speed, mm/min	Focus Off-set	Gas Pressure, Bar	Laser Power [W]	Frequency [kHz]
Fast	3000	3.7	0.5	2500	5
Medium	2400	3.7	0.4	2300	5
Small	2600	3.7	0.6	1700	5

In The equipment we used is Fiber Laser Durma HD-F 4020/4KW, with general purpose for cutting sheet material with a thickness of sheet steel up to 20 mm, chrome-nickel steel up to 10 mm and rolled aluminum sheet up to 12 mm with sheet sizes up to 4064x2032. It is a dynamic laser machine characterized by intelligent cutting heads for its operations. The laser head has an integrated sensor system monitoring the cutting process and providing relevant information to the operator. In this way, it became possible to implement the technological modes provided for the implementation of the research goals. Each type of sheet metal contains three cutting technologies according to what contour is being cut. Fig. 1 shows the sample with pre-cut different contours for a 3 mm sheet of C 235 steel samples. The sheet steel cutting process takes place at a speed of 3000 mm/min in Fast mode (in which the outer contour of the square is cut, Fig. 1) and a beam power of 2500W. With techno medium mode, at a speed of 2400 mm/min, the inner four squares and the circle are cut at a power of 2300 W. With the techno small mode, at a speed of 2600 mm/min at a power of 1700 W, the four small circles are cut. Table 2 shows the cutting modes of the three contours. These modes

helped to plan the experiment with the modes shown in Table 3.

After the cut contour with the corresponding mode, the difference between the set and received values can be determined. That can be done by measuring the actual diagonals after cutting for each process mode and on their basis determining the relative deviation from each diagonal. After determining the relative deviation from accuracy for the two diagonals, the deviation from accuracy for the overall shape of the product can be determined. The formulas for these transformations are shown in the methodology algorithm, Fig. 2.

Fig. 1. Pre-cut experimental contours on the basis of which the plan of the experiment was formed

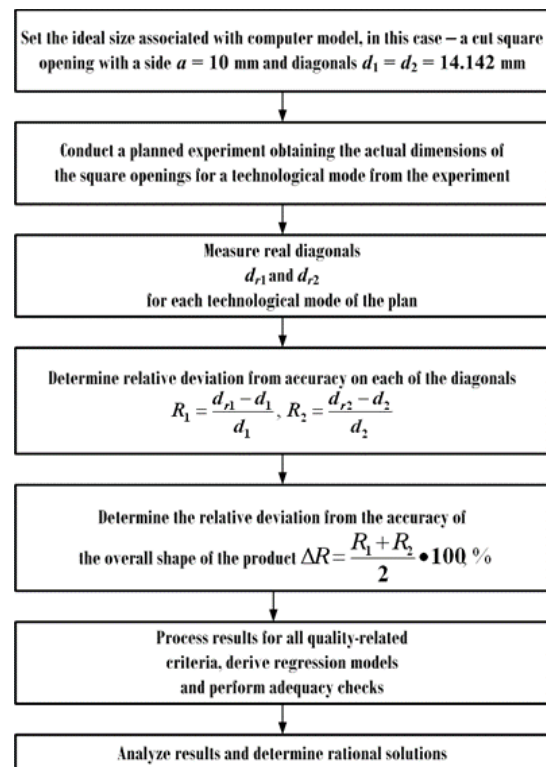Fig. 2. Methodology for determining the relative deviation from the shape of the dimensions during cutting

The one described in Fig. 2 methodology can be successfully modified for 3D printing [10], where again there is a problem with a difference between set and received.

III. RESULTS AND DISCUSSION

Based on the preliminary experiments described in Table 1, an experiment is planned, which is as below:

TABLE 3. PLANNED EXPERIMENT TO DERIVE A MODEL FOR THE MODEL FOR THE RELATIVE DEVIATION FROM ACCURACY

№	V, mm/min	P, W	N, bar	Relative deviation from accuracy, ΔR %
1	2400	1700	0,4	9.21
2	3000	1700	0,4	9.31
3	2400	2500	0,4	9.10
4	3000	2500	0,4	9.85
5	2400	1700	0,6	10.0
6	3000	1700	0,6	9.21
7	2400	2500	0,6	10.1
8	3000	2500	0,6	9.52
9	3000	2100	0,5	9.62
10	2400	2100	0,5	9.31
11	2700	2500	0,5	9.46
12	2700	1700	0,5	9.42
13	2700	2100	0,6	9.62
14	2700	2100	0,4	9.31

In Table 3, for each cut contour, a value for the relative deviation from the accuracy ΔR, % was obtained, for which a regression model was derived according to standard methodology [11].

The model of relative deviation from accuracy ΔR, % in laser cutting has the form:

$\Delta R = 9.41593 - 0.023609 \times X_1 + 0.107756 \times X_2 + 0.162448 \times X_3 + 0.0719866 \times X_1^2 + 0.156836 \times X_1 \times X_2 - 0.337385 \times X_1 \times X_2 + 0.03429 \times X_2^2 + 0.0487461 \times X_3^2$

An adequacy check was made for the model, the results of which are:

− Multiple regression coefficient R = 0.9517;

− Fisher test:

F calculated 6.0078 > F tabulated 4.8183 ($\alpha = 0.05$, 8, 5).

As a result of the verification, it can be determined that the model is adequate and can be used for prediction.

DEFMOT [12, 13] identifies the goals of using experiments for the research indicator and specifies the practical considerations that drive the design. The conducted physical experiment helps to make decisions, to implement and discuss concepts that serve as a basis for all conclusions.

A common three-factor representation is shown in Fig.3. However, it violates the "local embedded in the global" principle, a principle adopted by our team in the analysis of multifactorial processes. The image in Fig.4 is a solution to the graphical representation used by DEFMOT. The advantage of implementing this principle is its essential importance in the development of the decision support system. [14] - [18]

Fig.3 shows the organization of information when deciding with the DEFMOT system.

More useful for the decision-maker in the analysis of the corresponding response surface may be the image of a contour diagram with lines at a constant level, in which

the value of the examined quantity is already set with a given color in a certain interval.

The regression model analysis with the DEFMOT system is shown in Fig. 4, where the response surface, the relative deviation from the accuracy ΔR, %, is depicted on the three-dimensional scale by projecting the corresponding color. The values in the interval [0 – 33.33 %] correspond to the technological modes associated with the smallest deviation from the desired dimensions.
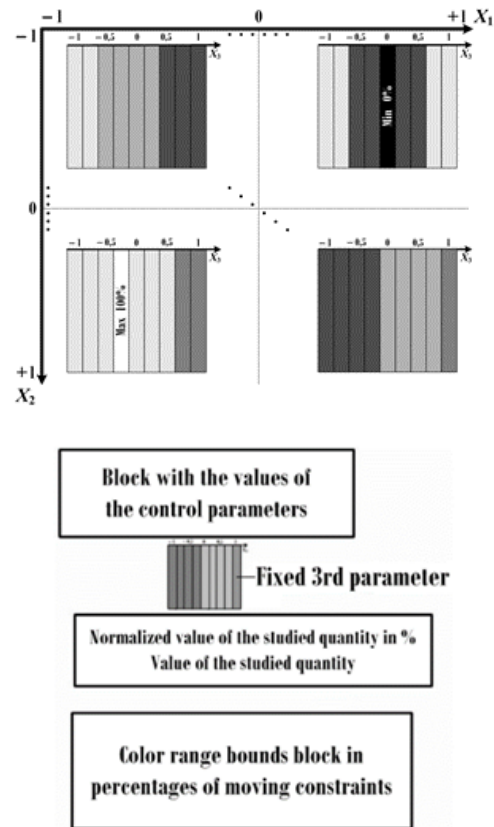
Fig. 3. The organization of information when deciding with the Defmot system.

On Fig. 3 there is the complex influence of all three parameters. As proof of this, the following can be commented: the more accurate modes at the smallest pressure of the attesting gas at low speed – regardless of the power, and at the maximal gas pressures, the speed is maximal; the power changes from lowest to medium for the interval.
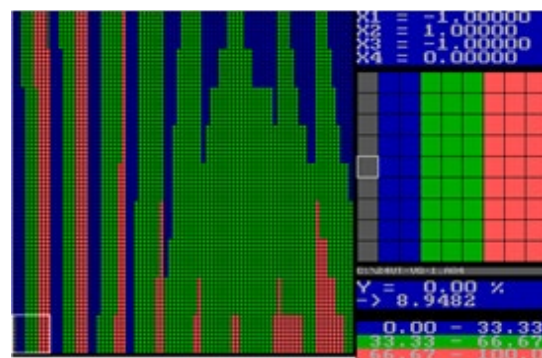
Fig. 4. Graphic interpretation of relative deviation from accuracy ΔR, %

The conclusion made is fundamental to the interpretation of the regression model and it fully fulfills the set goal.

IV. CONCLUSIONS

The research presents an analysis through the design methodology based on the response of the examined quantities when optimizing the laser cutting parameters in terms of dimensional accuracy for C-235 steel samples. Input factors such as cutting speed, power, and carbon dioxide pressure on cut quality, expressed as relative deviation from accuracy, were examined. It was found that the more accurate modes at the smallest test gas pressure required a small speed regardless of the power, and at the maximal gas pressures, they were associated with the maximal speed, and the power changed from the lowest to the average of the interval. To be able to draw this conclusion it was necessary to create an algorithm and a regression model to optimize the deviation from the dimensions between the model and the cut contour by minimizing the error of this deviation. For the implementation of the algorithm, it was necessary to conduct an experiment and to summarize the results of the research at the level of methodology. This methodology can be used after a planned experiment to determine the accuracy of any contours of a test material of a specific thickness.

## V. ACKNOWLEDGMENTS

REFERENCES

[1] L. Lazov, et.al., Numerical modeling and simulation for laser beam welding of ultrafine-grained aluminium, Laser Physics, 2021, 31(6), 6. 10.1088/1555-6611/abf5d3

[2] L. Lazov, E. Teirumnieks, T. Karadzhov, N. Angelov, Influence of power density and frequency of the process of laser marking of steel products, Infrared Physics & Technology, 2021,Volume 116, 103783, https://doi.org/10.1016/j.infrared.2021.103783 .

[3] H.A. Eltawahni, M. Hagino, K.Y. Benyounis, T. Inoue, A.G. Olabi, Effect of CO_2 laser cutting process parameters on edge quality and operating cost of AISI316L, Optics & Laser Technology, Volume 44, Issue 4, 2012, pp. 1068-1082, ISSN 0030-3992, https://doi.org/10.1016/j.optlastec.2011.10.008 .

[4] K. Huehnlein, K. Tschirpke, R. Hellmann, Optimization of laser cutting processes using design of experiments,Physics Procedia,Volume 5, Part B, 2010, pp. 243-252,ISSN 1875-3892, https://doi.org/10.1016/j.phpro.2010.08.050 .

[5] A.K. Dubey, V. Yadava, Robust parameter design and multi-objective optimization of laser beam cutting for aluminium alloy sheet. Int J Adv Manuf Technol 38, 268–277 (2008), DOI 10.1007/s00170-007-1105-x.

[6] Avanish Kumar Dubey, Vinod Yadava, Multi-objective optimisation of laser beam cutting process, Optics & Laser Technology, Volume 40, Issue 3, 2008, Pages 562-570, https://doi.org/10.1016/j.optlastec.2007.09.002 .

[7] D. Kondayya, Gopala Krishna, A. An integrated evolutionary approach for modelling and optimization of laser beam cutting process. Int J Adv Manuf Technol 65, 259–274 (2013), DOI 10.1007/s00170-012-4165-5.

[8] B. Adelmann, R. Hellmann, Fast Laser Cutting Optimization Algorithm, Physics Procedia, Volume 12, Part A, 2011, Pages 591-598, ISSN 1875-3892, https://doi.org/10.1016/j.phpro.2011.03.075 .

[9] S. Genna, E.Menna, G.Rubino, V.Tagliaferri, Experimental Investigation of Industrial Laser Cutting: The Effect of the Material Selection and the Process Parameters on the Kerf Quality. Applied Sciences. 2020, 10(14):4956, https://doi.org/10.3390/app10144956 .

[10] I.Vuchkov, L. Boyadjieva, Quality Improvement with Design of Experiments. A Response Surface Approach, 2001, https://link.springer.com/book/10.1007/978-94-009-0009-7 .

[11] N.Tontchev, 2014. Materials Science, Effective Solutions and Technological Variants. 1st ed. LAP LAMBERT Academic Publishing. https://www.perlego.com/book/3343664/materials-science-effective-solutions-and-technological-variants-numerical-approaches-to-identification-of-effective-solutions-pdf.

[12] N.Tontchev, G. Gaydarov, N. Hristov, "Analyses and applications using the computational approach "DEFMOT", Sofia, 2022, 167 p. (in Bulgarian)

[13] Л. Бузов, Миневски, И., Морфологичен модел на опасностите в ковашко-пресовото производство, Четвърта научна конференция – „Пожарна и аварийна безопасност", МВР-Академия гр.София -2007, с. 108-110, ISBN 978-954-348-012-8

[14] L. Lazov, et al., Modification of the roughness of 304 stainless steel by laser surface texturing (LST), Laser Physics, 2023, Volume 33, Number 4, DOI:10.1088/1555-6611/acbb76

[15] R. S. Ghalot, L. Lazov, et al., Investigation of the Change in Roughness and Microhardness during Laser Surface Texturing of Copper Samples by Changing the Process Parameters, 2023, Coatings, 13(11):1970, DOI:10.3390/coatings13111970

[16] L. Lazov, et.al., Numerical modeling and simulation for laser beam welding of ultrafine-grained aluminium, Laser Physics, 2021, 31(6), 6. doi:101088/1555-6611/abf5d3

[17] L. Lazov, N. Petrov, Investigation of the Impact of the Number of Repetitions and the Defocus on the Contrast of Laser Marking for Products Made of Tool Steel, METALLOFIZIKA I NOVEISHIE TEKHNOLOGII, 2012, 34(7):1003-1011

[18] I. Balchev, L. Lazov, et al., Investigation of the influence of the scanning speed and step in laser marking and engraving of aluminum, 2021, J. Phys., Conf. Ser., 1859 012002, DOI: 10.1088/1742-6596/1859/1/012002

Multi-criteria Research of Geometric, Mechanical, Energetic and Temporal Indicators Depending on Laser Hardening Parameters

Nikolay Tontchev
Faculty Transport management
University of Transport
Sofia, Bulgaria
tontchev@vtu.bg

Normunds Teirumnieks
Faculty Transport management
University of Transport
Sofia, Bulgaria
normunds.teirumnieks@gmail.com

Emil Yankov
Materials Science and Technology
University of Ruse "A. Kanchev"
Ruse, Bulgaria
eyankov@uni-ruse.bg

Valentin Gaydarov
Faculty Transport management
University of Transport
Sofia, Bulgaria
v_gaydarov@yahoo.com

Abstract. **In the paper, using experimental data, models for geometric, mechanical, energetic, and temporal indicators of surface laser hardening are derived. A single-criteria and multi-criteria research was performed using DEFMOT. On this basis, three compromise solutions were obtained, which were rated in terms of performance and energy intensity. From them, a mode for the most rational use is recommended. It consists of V = 3.5 mm/s; P = 1450 W; FPP = 60 mm. The controlled indicators calculated according to the models are specified for it.**

Keywords: surface laser, hardening process, energy intensity, multi-criteria research, optimization models,

I. INTRODUCTION

In the paper, using experimental data of laser hardening of AISI 4130 steel published by authors Mahmoud Moradi, Mojtaba Karami Moghadam [1]. The solution of modern technical problems is associated with the removal of a given technical or physical contradiction of the factors describing the problem [2 - 7]. In the field of surface laser hardening, multi-criteria problems are defined with criteria depending on the technological parameters of the equipment used. For the composed multi-criteria tasks in laser surface strengthening, the DEFMOT approach can be useful, facilitating the Decision Maker (DM) in the analyses he/she makes. The approved software can be defined as a multifunctional tool, with the help of which the desired solution is reached. In control theory, independent variables are defined as input factors varying within a certain range, and dependent variables are defined as output parameters.

The method, which is built into the software, is extremely suitable for systems where these two groups of parameters are not optimized. Optimization of the system (object) process can be done for several output parameters with pre-set requirements for them. The software determines all efficient combinations of the input factors that fulfill the desired preferences for the output parameters. This approach was founded by the authors of the present paper and is described in detail in the monographs [8, 9]. When applying it, sustainable effective solutions are obtained with a sufficiently large number of the examined goal functions to determine the input data of non-optimized or undetermined technological processes. If acceptable energy-saving solutions are determined for the obtained effective solutions in terms of a complex of mechanical, energetic, temporal indicators and other investigated parameters, this is defined as innovation by all rules. The latter involves the convergence of laser surface-structured materials together with decision-supporting systems (DSS) so that the proposed technological modes of structuring are proven, as reliable as possible and less energy intensive.

In laser hardening of steels, the surface of the workpiece is heat treated by a laser beam that heats the workpiece locally while the rest of the workpiece acts as a heat sink with respect to the core of the workpiece. The movement of the laser along the surface creates the hardened traces. The complex of properties of a hard wear-resistant surface and a soft and tough core, resistant to brittle failure and impact cracks, is useful in a number

of elements and details of machine and instrument construction. Surface strengthening techniques include coatings, diffusion methods, and hardening processes. Hardening processes can be performed by flame, induction heating, electron beams and laser beams. Laser hardening of steel offers significant advantages over conventional hardening processes.

Efficient technological modes bring benefits to the production process. To discover these modes, however, it is necessary that the process under consideration be fully defined in terms of the set objectives. This seemingly elementary formulation of the problem inevitably becomes more complicated when examining real problems, characterized by more than two governing factors that simultaneously affect the various investigated quality indicators. Modern means of automating engineering work create good conditions for intelligently solving such problems.

The surface integrity during processing is summarized in [10], [11], which describes the main advances in the research of contact strength after chemical heat treatment. Tribological issues, and in particular those related to wear resistance, need to be identified before the process of designing treatment modes when it comes to thermal treatment. Similar research is described in the monograph [12], [13], where the relationship between the goal parameters and the technological factors of the modes for processing are defined.

The brief overview of this research can determine the characteristics of the chosen topic, which is associated with complexity and nonlinearity, in properties of materials in depth of the examined surfaces. These new surface conditions are formed by a desired set of properties, which is determined by solving multicriteria problems [14]. The latter guarantee certain benefits of the research, most often expressed in increased longevity (extended life) of contact products [15]. All this is related to the resource for production, characterization and applications in the field of hard coatings and wear-resistant surfaces. This review would be more targeted if a methodology could be analytically or numerically created to establish the influence of different modes equally affecting an entire class of steels. In this way, the particular influence of one or another alloying element as a concentration and in combination with other elements will be ignored.

II. MATERIALS AND METHODS

In [1], a planned DOE research of laser surface hardening of AISI 4130 carbon steel performed with a high-power diode laser was conducted. In this paper, the authors of the DEFMOT computational methodology use data from the research [1] to demonstrate the advantages of the methodology in process identification. This adaptation is necessary because in the future they intend to examine the same steel with a fiber laser with which the present results will be compared. The schematic diagram of the parameters of the laser hardening process is shown in Fig.1.

In Fig.1 and in Table 1 the input parameters of the technological process are indicated. They are, respectively, the scanning speed X_1 (mm/s), the laser power X_2 (W) and the position of the focal plane X_3 (mm). These quantities are parameters controlling the surface hardening process. These variables significantly influence the cross-sectional geometry of the hardened zone (width Y_1 and length Y_2 of the hardened zone (mm), entrance angle of the quench bath Y_3 (°)), average microhardness of the hardened layer Y_4 (HV), percentage of soft phase (the ferrite phase) Y_7 (%), the power density Y_5 (W/mm^2), the duration of the process between two cycles Y_6 (s).The structure of manuscripts:
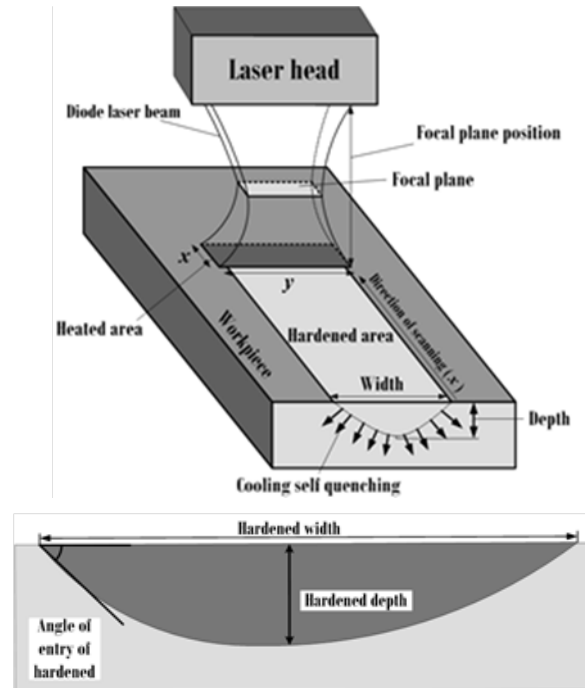
Fig. 1. Schematic of the surface laser hardening process.

TABLE 1 RANGE OF VARIATION OF INPUT PARAMETERS OF THE TECHNOLOGICAL PROCESS OF SURFACE LASER HARDENING

Independent process parameters with design levels	Variable, Symbol		
	Scanning speed V [mm/s]	Laser power P [W]	Focal plane position FPP [mm]
Zero level – [0]	5	1400	70
Amendment step – S	2	100	10
Lower level – [–1]	3	1300	60
Upper level – [+1]	7	1500	80

III. RESULTS AND DISCUSSION

A) RESULTS OF THE SINGLE-CRITERIA

The change of the interval of variation, as a range of change of the values of the technological input parameters is indicated in Table 1, and Table 2 shows the results of the experimental research defined in [1]. The authors of this research wish to perform a side-by-side comparison between a diode laser and a fiber laser, applying their proprietary methodology. That is why the experimental data from [1] were used as the basis for the research. The aim of the research is to determine the effective solutions

for a diode laser of geometric, mechanical, energetic and temporal indicators depending on the parameters of the surface laser hardening. The obtained results are part of a comprehensive analysis for research on carbon steel AISI 4130. The approach can define one or more sets of process parameters to be experimentally tested in specifying the technology for the test item. The desired complex of properties depends on one or several certain combinations of technological parameters. This set of properties will be determined using the author's DEFMOT approach.

One of the main directions for the creation of highly efficient competitive products is the formation, at the stage of their design, of such a set/combination of their parameters and characteristics, which ensure the satisfaction of a set of conflicting requirements for the different operative modes during work. With this task, our approach will be applied for the first time to the simultaneous optimization of geometric, mechanical and indirectly economic metrics. Increasingly, there is a significant reorientation of the research and design parts of the work from physical CAE simulation of products and their modes of operation to the use of models for optimization purposes. Such approaches, along with their inherent tools, have procedures for optimizing the parameters (static properties) of simulated systems based on nonlinear programming methods and the mathematical theory of experimental design. The formation of characteristics of the developed engineering products (dynamic properties) with the help of such tools is not provided in the existing virtual modeling systems, which reduces their instrumental potential. At the same time, it is possible to solve specific problems with the calculation of characteristics when setting fixed values for the parameters of the simulated product.

Classical regression analysis is based on processing the results of active experiments, as described in Table 2. At the same time, in connection with the engineering problem, the researcher draws up an experimental plan, choosing experimental points based, for example, on intuition or own experience. After running the experiment, using a standard statistical procedure described in [16], adequate models are derived. After checking the adequacy of the models, the specific results of the identification are determined.

Geometrical criteria are defined in Table 3, and mechanical, energetic and temporal criteria are defined in Table 4, and on this basis the features of the considered proposal are reflected. In this case, it is about the defined statistical models of a qualitative and quantitative kind.

The derivation of the models in this case is done with the use of our own DSTAT system, which automatically performs the adequacy check.

Fig.2 shows the indicator of the entry angle of the stiffened zone, which is directly proportional to the depth of the stiffened zone. These two indicators, together with the width of the bath, are directly related to the efficiency of the technological operation.

TABLE 2 NUMERICAL VALUES OF THE EXPERIMENTAL DATA FOR THE RELATIONSHIP BETWEEN ALL PARAMETERS [1]

№	Scanning speed		Laser power		Focal plane position		h	b	α	HV	qs	τ
	V, [mm/s]	X_1, kod	P, [W]	X_2, kod	FPP, [mm]	X_3, kod	Y_1, [mm]	Y_2, [mm]	Y_3, [o]	Y_4, [/]	Y_5, [W/mm²]	Y_5, [s]
1	4	-0,5	1500	0,5	65	-0,5	0.94	9.30	10.82	586.0	59.2	0.64
2	7	1	1400	0	70	0	0.22	8.86	3.04	342.0	32.7	0.50
3	5	0	1400	0	70	0	0.47	8.82	5.95	489.0	32.7	0.70
4	5	0	1400	0	70	0	0.44	9.84	5.89	480.0	32.7	0.70
5	5	0	1400	0	60	-1	1.22	9.78	13.02	577.0	117.0	0.30
6	5	0	1400	0	80	1	0.30	9.97	4.29	370.0	15.70	1.13
7	6	0,5	1300	-0,5	75	0,5	0.27	8.73	4.06	338.0	20.20	0.80
8	6	0,5	1300	-0,5	65	-0,5	0.42	9.03	7.02	424.0	51.30	0.40
9	4	-0,5	1300	-0,5	75	0,5	0.39	9.24	5.24	386.0	20.20	1.16
10	4	-0,5	1300	-0,5	65	-0,5	0.52	9.10	6.78	549.0	51.30	0.60
11	6	0,5	1500	0,5	65	-0,5	0.50	9.27	6.57	544.0	59.20	0.40
12	5	0	1400	0	70	0	0.43	9.85	5.70	400.0	32.70	0.70
13	5	0	1600	1	70	0	0.52	10.10	6.47	342.0	37.40	0.70
14	6	0,5	1500	0,5	75	0,5	0.34	9.24	4.47	350.0	23.30	0.80
15	3	-1	1400	0	70	0	0.48	9.27	6.02	496.0	32.70	1.20
16	5	0	1200	-1	70	0	0.23	8.58	3.72	330.0	28.10	0.70
17	5	0	1500	0,5	75	0,5	0.62	9.86	8.21	474.0	23.30	1.16

TABLE 3 COEFFICIENTS OF THE REGRESSION MODELS OF THE GEOMETRIC PARAMETERS OF THE STIFFENED ZONE

	Depth	Width	Angle
b_0	0.461304	9.72522	6.06130
$b_1 \times x_1$	-0.18250	-0.281250	-1.8125
$b_2 \times x_2$	0.17250	0.576250	1.55875
$b_3 \times x_3$	-0.2750	0.0937496	-3.32875
$b_{11} \times x_1^2$	-0.0893477	-0.777393	-1.2095
$b_{12} \times x_1 \times x_2$	-0.250	-0.0349984	-3.52500
$b_{13} \times x_1 \times x_3$	0.0700001	-0.5150	-0.4550
$b_{22} \times x_2^2$	-0.0643477	-0.552394	-0.644348
$B_{23} \times x_2 \times x_3$	-0.10	0 .345001	-0.104999
$b_{33} \times x_3^2$	0.220652	-0.0173925	2.90565
R =0 .9634 F = 10.0370 F (a=0.05, 9, 7)= 3.6767		`R= 0.9140 F= 3.9481 F(a=0.05, 9,7)=3.6767	R= 0 .9649 F - 10.5036 F= (a=0.05, 9, 7) = 3.6767

TABLE 4 COEFFICIENTS OF THE REGRESSION MODELSOF THE MECHANICAL, ENERGY AND TIME INDICATORS

|	hardnes	% Ferit	Dentisity	Time iteraction
b_0	474.217	-0.494783	45.7632	0.701579
**$b_1 \times x_1$	-61.6250	9.520	$-0.953674 \times 10^{-06}$	-0.640000
$b_2 \times x_2$	77.1250	-7.470	10.1500	0 .00999
$b_3 \times x_3$	-111.375	7.180	-84.1500	0.8850
$b_{11} \times x_1^2$	-7.89126	25.3104	-54.2369	0 .601580
$b_{12} \times x_1x_2$	-51.5000	-	-	-0.0799999
$b_{13} \times x_1x_3$	-65.5000	19.040	-	-0.560
$b_{22} \times x_2^2$	4.10874	17.9704	-54.0369	-
R =0.9222 F - 4.4206 F -(a=0.05, 9, 7) = 3.6767		R= 0.8633 F =3.7631 F (a=0.05, 7,9) = 3.2927	R .9061 F =7.6479 F -(a=0.05, 6,10)=3.2172	R = 0.9972 F= 177.0720 F -(a=0.05, 8, 8) = 3.4381
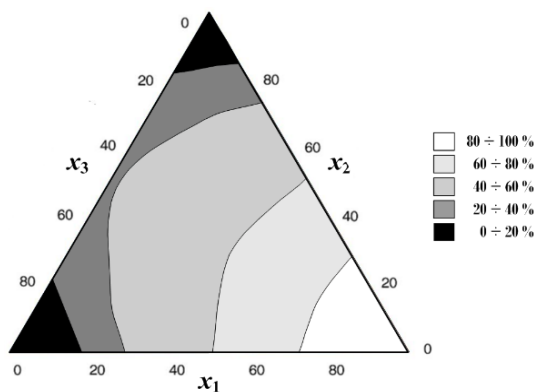
Fig. 2.   A standard three-variable representation of constant-level lines.
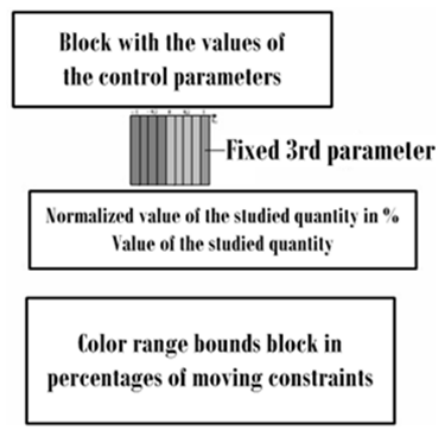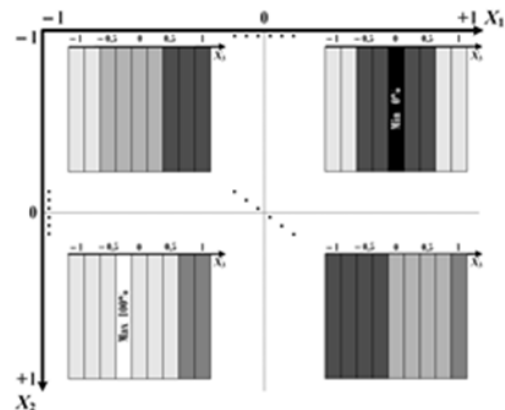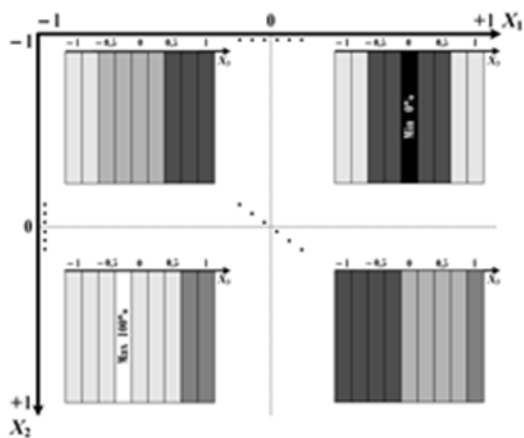

Fig. 3.   A three-factor representation using on the principle of - local embedded in the global.

The model of the examined indicator is obtained using the results of experiments. The task of planning an experiment is to establish the minimal number of experiments required.

B) OPTIMIZATION WITH DEFMOT

DEFMOT identifies the goals of using experiments for the research indicator and specifies the practical considerations that drive the design. The conducted physical experiment helps to make decisions, to implement and discuss concepts that serve as a basis for all conclusions.

Fig. 4.   The organization of information when deciding with the DEFMOT system.

In the field of materials science, the above outlined topic is used both in the synthesis and modeling, and to specify the modes in their processing [10].

A common three-factor representation is shown in Fig.4. However, it violates the "local embedded in the global" principle, a principle adopted by our team in the analysis of multifactorial processes. The image in Fig.5 is a solution to the graphical representation used by DEFMOT. The advantage of implementing this principle is its essential importance in the development of the decision support system.

Fig.4 shows the organization of information when deciding with the DEFMOT system. More useful for the decision-maker in the analysis of the corresponding response surface may be the image of a contour diagram with lines at a constant level (Fig.2 and Fig.3), in which the value of the examined quantity is already set with a given color in a certain interval.

The analysis can be performed for several iterations of the moving constraints (Fig.5 and Fig.6 – as the different input angle images are constructed). Initially, these constraints can be located around the minimum and the influences determined and then judged as to whether they are confirmed when the moving constraints are located around the maximum.
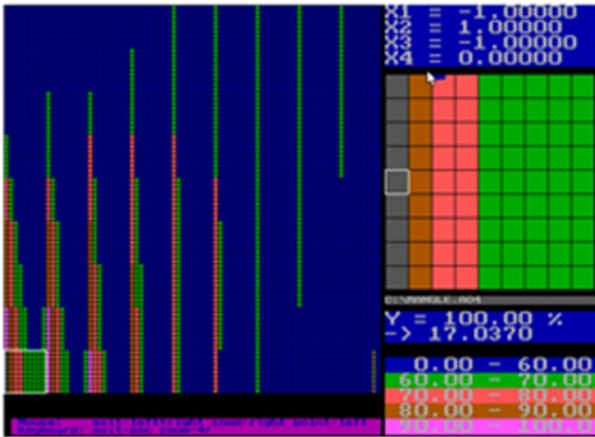
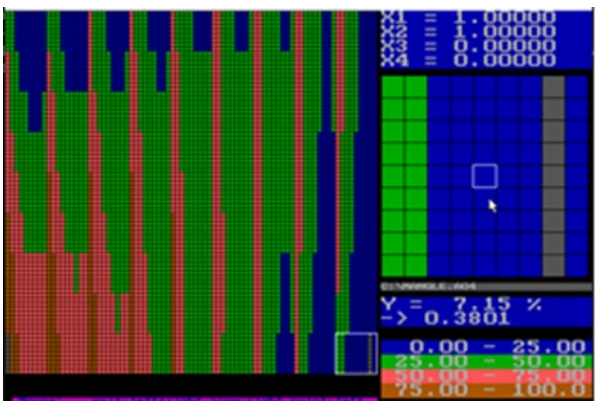Fig. 5.   Input parameters of the maximal angle

Fig. 6.   Input parameters of the minimal angle

The results of the experiment are used to obtain the mathematical model of the examined process. A mathematical model is a system of mathematical dependencies that describe the investigated process.
When planning an experiment, a mathematical model is often understood as an equation that relates an optimization parameter to factors. The criterion equation is also called the response function.

The results of the one-criterion optimization based on the data shown in Fig. 6 – Fig. 10 are shown in Table 5.
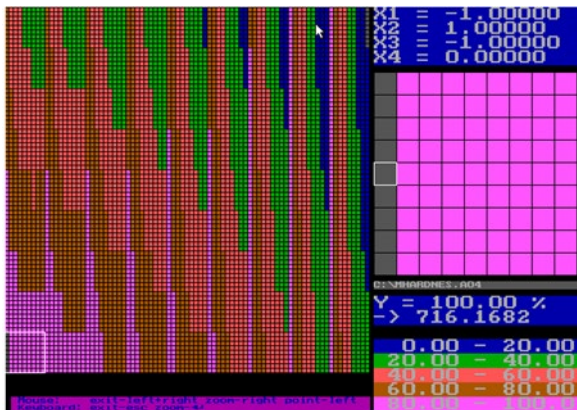
Fig. 7.   Input parameters of the maximum hardness
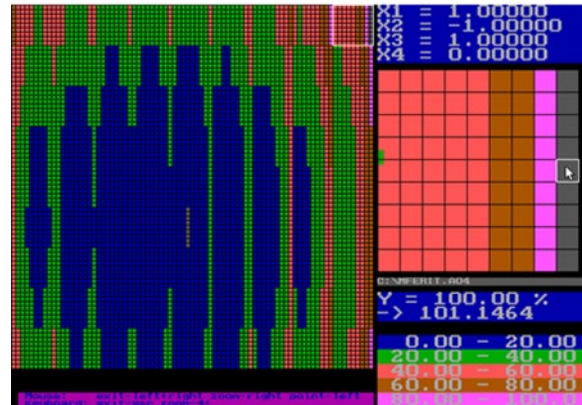
Fig. 8.   Input parameters of the maximum hardness

Fig. 9.   Input parameters of the maximum power density
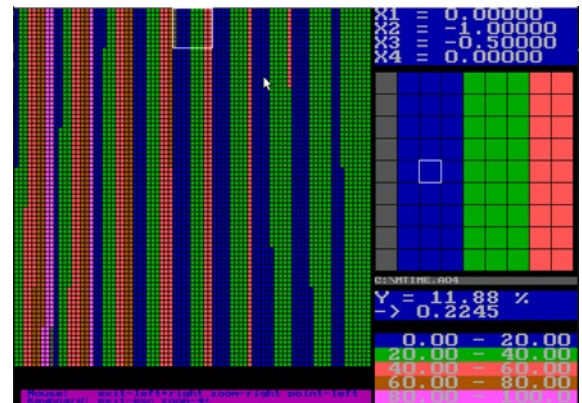
Fig. 10. . Input parameters of the minimum time of one cycle during laser hardening

The indicated in Table 5 results are due to the research of each model separately from Table 3 and Table 4. Despite some differences in the values between the experimental research and the model-derived values, the results can be accepted due to the adequacy of the models. Apart from this, the DEFMOT system works with a normalized percentage – an approach that smooths out the observed inaccuracies. This normalized percentage will play an important role in the next section on multi-criteria optimization

TABLE 5 RESULTS OF THE SINGLE-CRITERIA OPTIMIZATION OF THE CONTROLLED INDICATORS OF THE STUDY OF SURFACE LASER HARDENING

Examined values	Min	A combination in which the relevant extremum occurs			Max	A combination in which the relevant extremum occurs		
		$[X_1]$ V, (mm/s)	$[X_2]$ P, (W)	$[X_3]$ FPP, (mm)		$[X_1]$ V, (mm/s)	$[X_2]$ P, (W)	$[X_3]$ FPP, (mm)
Angle	0.38	[1] 7	[1] 1500	[0] 70	17.03	[-1] 3	[1] 1500	[-1] 60
Hardness	216	[1] 7	[-1] 1300	[1] 80	716.1	[-1] 3	[1] 1500	[-1] 60
Ferit [%]	1.89	[0] 5	[0] 1400	[0.25] 72	101	[1] 7	[-1] 1300	[1] 80
Denticity	0.68	[1] 7	[1] 1500	[-0.5] 65	133.8	[0] 5	[0.25] 1425	[-1] 60
Time iteractio n	0.2	[0] 5	[-1] 1300	[-0.5] 65	3.45	[-1] 3	[1] 1500	[1] 80

C) Results of the Multi-Criteria Optimization with DEFMOT

If necessary, include parts or entire texts of your programs following the "Programs and Codes" style or using "New Courier" font. Try to fit such texts in one column.
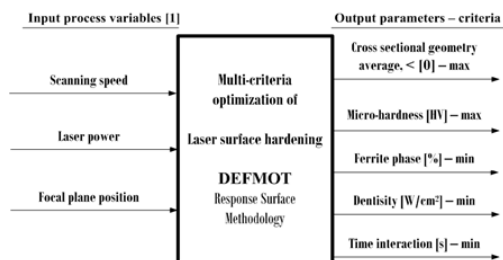

Fig. 11. Statement of the problem for the multi-criteria research

The results of this research are shown in Table 6 based on the derived equations in Table 3 and Table 4, after setting the identifiers of the criteria from Fig.11.

From the analysis of the results indicated in Table 6, decisions (1) and (2) stand out. In terms of performance, both modes are suitable for industrial application. However, the authors recommend mode (1) because not only is the stiffness higher, but of the two modes, mode (1) is less energy intensive. This mode is with V = 3.5 mm/s; P = 1450 W; FPP = 60 mm. The specific values of the controlled indicators are as follows: width – 9.40 mm; entrance angle to the strengthened zone – 15.5 º; average microhardness – 685 HV; percentage of ferrite in the

strengthening zone – 33.35 %; power density – 91 W/mm², time between two cycles – 0.38 s. Mode (3) is the least energy-intensive, but from the one cited in Table 6, the indicators have the most unsatisfactory characteristics. Solution (4) is ranked third among all compromise solutions in applicability. Only with it the interaction time is the greatest. However, the latter is compensated by the low power density value.

TABLE 6 RESULTS OF FOUR COMPROMISE SOLUTIONS WITH CALCULATIONS FOR ALL CONTROLLED INDICATORS OF THE SURFACE LASER HARDENING PROCESS

Parameters Values	Combinations of the solution complex from the multi-criteria optimization determined by DEFMOT			
	$[X_1]$ = -0.75 $[X_2]$ = 0.75 $[X_3]$ = -1	$[X_1]$ = -0.25 $[X_2]$ = 0.5 $[X_3]$ = -1	$[X_1]$ = 1 $[X_2]$ = -1 $[X_3]$ = -0.75	$[X_1]$ = -0.5 $[X_2]$ = 1 $[X_3]$ = 0.
Solution	(1)	(2)	(3)	(4)
Angle – max	[91.65] %	[81.30] %	[53.56] %	[57.24] %
Width – max	[78.51] %	[93.23] %	[17.90] %	[89.11] %
Hardnes – max	[93.84] %	[88.08] %	[69.82] %	[78.79] %
Ferrite [%] – min	[34.34] %	[13.83] %	[49.13] %	[13.23] %
Denticity – min	[85.2] %	[97.86] %	[45.5] %	[49.74] %
Time iteraction – min	[16.37] %	[10.88] %	[18.41] %	[39.05] %

Conclusion

After deriving models of the geometric, mechanical, energetic and temporal indicators for surface laser hardening, multi-criteria research was conducted. Based on it, three compromise solutions were obtained, which were rated according to performance and energy consumption. It is determined by the values V = 3.5 mm/s; P = 1450 W; FPP = 60 mm. The controlled indicators calculated according to the models are specified for it.

Acknowledgment:

REFERENCES

[1] M. Moradi, M. Karami Moghadam, High power diode laser surface hardening of AISI 4130; statistical modelling and optimization, Optics & Laser Technology, Vol. 111,2019, pp. 554-570, https://doi.org/10.1016/j.optlastec.2018.10.043

[2] M.Miloš, G. Petrović, D. Petković, J. Antucheviciene, D.Marinković. 2022. "Application of a Robust Decision-Making Rule for Comprehensive Assessment of Laser Cutting Conditions and Performance" Machines 10, no. 2, DOI: 10.3390/machines10020153.

[3] N. Angelov, L.Lazov, et al, Influence of pulse duration on the process of laser marking of CT80 carbon tool steel products, Laser Phys, 2021, 31 045601 DOI: 10.1088/1555-6611/abe5af.

[4] L. Lazov, E. Teirumnieks, T. Karadzhov, N. Angelov, Influence of power density and frequency of the process of laser marking of steel products, *Infrared Physics & Technology*, 2021,Volume 116, 103783, https://doi.org/10.1016/j.infrared.2021.103783.

Environment. Technology. Resources. Rezekne, Latvia

Proceedings of the 15th International Scientific and Practical Conference. Volume III, 449-455

[5] L. Lazov, et al., Modification of the roughness of 304 stainless steel by laser surface texturing (LST), Laser Physics, 2023, Volume 33, Number 4, DOI:10.1088/1555-6611/acbb76.

[6] R. S. Ghalot, L. Lazov, et al., Investigation of the Change in Roughness and Microhardness during Laser Surface Texturing of Copper Samples by Changing the Process Parameters, 2023, Coatings, 13(11):1970, DOI:10.3390/coatings13111970

[7] I. Balchev, L. Lazov, et al., Investigation of the influence of the scanning speed and step in laser marking and engraving of aluminum, 2021, J. Phys., Conf. Ser., 1859 012002, DOI: 10.1088/1742-6596/1859/1/012002.

[8] N.Tontchev, „Materials science, Effective solutions, and technological variants", Lambert, Academic Publishing, 2014, 142 p., https://www.semanticscholar.org/paper/Materials-Science%2C-Effective-Solutions-and-Variants-Nikolay/e5904f3bc8c5ddd127daf5e6f798d1d931cae7a3.

[9] N.Tontchev, V. Gaydarov, N. Hristov, "Analyses and applications using the computational approach "DEFMOT", Sofia, 2022, 167 p. (in Bulgarian).

[10] G.Bozzolo, R.D.Noebe , P.B.Abel P.B. (eds), Applied computational materials modeling. Theory, simulation and experiment, Springer Science, 507 pp (2007), https://link.springer.com/book/10.1007/978-0-387-34565-9.

[11] D.J.Paulo, Surface Integrity in Machining Springer, 2010, pp. 222, https://link.springer.com/book/10.1007/978-1-84882-874-2.

[12] A.P.Zumbilev, I.A. Zumbilev, Ionic nitriding and carbonitriding of steels, 2020, pp. 325, ISBN: 978-619-236-187-7 (in Bulgarian), https://e-university.tu-sofia.bg/e-publ/search-det.php?id=6805.

[13] L.Lazov, N. Padarev, M. Yovchev, L.I. Linkov, THE CHANGE OF CONTRAST IS INVESTIGATION OF 75 STEEL SAMPLES LASER MARKED WITH DIFFERENT MODES. ENVIRONMENT. TECHNOLOGIES. RESOURCES. Proceedings of the International Scientific and Practical Conference, 2023, DOI:10.17770/etr2023vol3.7264.

[14] O.Abdelkhalik, Engineering Systems Optimization, Boca Raton: CRC Press, 2021, pp. 230, .

[15] R.B.Statnikov, J.B.Matusov, Multicriteria Optimization and Engineering, Springer, 1995, pp. 250, https://link.springer.com/book/10.1007/978-1-4615-2089-4.

[16] I.Vuchkov, L.Boyadjieva, Quality Improvement with Design of Experiments. A Response Surface Approach, 2001, https://link.springer.com/book/10.1007/978-94-009-0009-7.

Modeling the Hardening of Carbon Steels After Quenching and Tempering

Nikolay Tonchev
Bulgaria University of Transport
„Technique and construction
technologies in transport" Faculty
Sofia, Bulgaria
tontchev@vtu.bg

Normunds Teirumnieks
Bulgaria University of Transport
„Technique and construction
technologies in transport" Faculty
Sofia, Bulgaria
normunds.teirumnieks@gmail.com

Emil Yankov
University of Ruse „A. Kanchev"
Departments of Materials Science
and Technology
Ruse, Bulgaria
eyankov@uni-ruse.bg

Abstract. **In the paper, after an overview and defined tasks, a methodology is applied and a model is derived for establishing the dependence of hardness on carbon content, hardness after hardening and tempering temperature after hardening for the entire range of carbon steels from structural to tool steels. The research was based on eight steels and four tempering temperatures formed in a total of 32 combinations. First, one-dimensional dependences of hardness change on carbon content were derived for each annealing temperature, then accuracy was improved with a three-control parameter model. The derived model was examined and its theoretical maximum was corrected. The difference between the theoretical and the real logical maxima amounts to 17.44%. For all specified extremes, the heat treatment modes are defined.**

Keywords: hardness, quenching, tempering, matematic modes, carbon steel, multifactorial analysis.

I. INTRODUCTION

Clarification and evaluation of the possibilities of different types of strengthening have always interested researchers not only because of the significant application of this effect, but also because of the complexity of the processes taking place in it. Whether superficial or volumetric, hardening is primarily evaluated by hardness. Modeling the hardness of steels depending on the chemical composition, from the point of view of the physics of metals, is generally a difficult to formulate and unsolved task. The problem is that mechanical hardness at the atomic level is based on electrostatics and elastic shear, which can be generalized only for single-phase annealed alloys, and consequently only semi-empirical dependences can be obtained. Such an approach is used in [1], [2], [3], [4], [5], [6], [7] and [8] where, after adaptation, the interaction between dislocations and alloying elements is included. This interaction has been applied to eight two-component and three three-component alloys. In the cited research, a discrepancy between two of the main equations was found, and it was necessary to correct them with certain coefficients.

Simulation of the hardness is done because of the cooling rate during hardening of the steels. In such studies, the change in the temperature field is simulated by analyzing the phase transformation kinetics and modifying the hardness calculation model: [9], [10], [11]. In the cited research, when comparing the simulation results and the experimentally measured values, a good match between them was found. Very often, simulations are related to approximation from stiffness data, which can also be done by modeling with artificial neural networks with multilayer topology. An example of this is [12] where the relationship between phase composition and hardness of high entropy alloys (HEA) is investigated. Chemical composition was used as a set of input characteristics. In prediction, the neural network was trained with 775 experimental samples with a prediction accuracy of 93.4%. Despite the unprecedentedly large data set, for stiffness the model showed an average regression value of 0.88, and most of the predicted values that these authors indicate [13], are within the margin of error of 20%. Again by artificial neural network in [14] a prediction of the effect of chemical composition and tensile properties on both the impact strength and hardness of microalloyed steels intended for pipe manufacture was made. Such research requires, as noted, a larger number of observations, in the case of 104. Nevertheless, the role of the individual alloying elements is addressed implicitly, only through a single variable – "carbon equivalent based on the Ito-Bessyo equation (CEPcm)", as well as the "yield strength (YS)", the tensile properties. "ultimate tensile strength (UTS)" and "elongation (El)" are considered together as input parameters of the networks, while Vickers microhardness

with applied load and Charpy impact energy are taken as outputs of the constructed models. Such generalizations will require the need for additional calculations with certain approximations. Without implicit forms for the properties and additional calculations, using a Russian database, six numerical author approaches are developed in [15], where, in addition to artificial neural networks and a carbon equivalent approach for small databases, a polynomial regression approximation is also applied. The research is done for seven control parameters of low-alloy steels with grain sorbite structure. This approach is also known as "Design of alloys". The amount and combinations of the alloy composition in this case offer the opportunity to specify properties-oriented compositions and modes of strengthening technologies. The research [16], [17] are also devoted to similar questions.

II. METHODOLOGY OF THE EXPERIMENT

Based on the overview, regardless of the variety of applied methods, the following more important conclusions can be drawn:

2.1. There is constant development in the field of mechanical properties of carbon steel, but almost all approaches used have been through experimental processes that are summarized with applied modeling. For it, it is always necessary to have pre-collected experimental data which, as a sample, are related to the approach to be applied.

2.2. The approach (from empirical, automated to the use of artificial intelligence) and the sample are related to the research object and this significantly affects the accuracy of the obtained decision.

2.3. A limited number of investigations have been devoted to the polynomial regression approximation, for which there is no research on modeling the hardness of the quenching mode after quenching (alloy quenched and tempered steel) considering the change of hardness after quenching and the chemical composition of the steel, expressed by the carbon content.

2.4. In widely available tools such as Excel and in the literature, solutions to assist the researcher in making decisions with more than 2 control parameters are absent. Based on the conclusions drawn, the purpose and tasks of the research were formulated.

In the available literature, the change of the hardening after quenching and tempering (quenched and tempered steel) depending on the carbon content has been numerically confirmed, Table 1. This trend for seven carbon compositions (8 steels) and 4 tempering temperatures is plotted in Fig. 1.

TABLE 1. NATURAL AND CODED INPUT AND OUTPUT PARAMETERS FROM THE TASK STATEMENT

№	X_1 [%] – carbon content in the steel	X_1 [/] – encoded value	X_2 [/] – HRC after quenching	X_2 [/] – encoded value	X_3 [°C] – temperature at tempered	X_3 [/] – encoded value	HRC [/] – after quenched and tempered
1	0,31	-1,00	44	-1	180	-1	42
2	0,36	-0,89	48,5	-0,53846	180	-1	47
3	0,46	-0,66	52,5	-0,12821	180	-1	50,5
4	0,695	-0,13	62	0,846154	180	-1	61
5	0,795	0,10	63,5	1	180	-1	62
6	0,795	0,10	63,5	1	180	-1	62
7	0,995	0,55	63,5	1	180	-1	62
8	1,195	1,00	63,5	1	180	-1	61
9	0,31	-1,00	44	-1	300	-0,25	36
10	0,36	-0,89	48,5	-0,53846	300	-0,25	41
11	0,46	-0,66	52,5	-0,12821	300	-0,25	45
12	0,695	-0,13	62	0,846154	300	-0,25	54
13	0,795	0,10	63,5	1	300	-0,25	54
14	0,795	0,10	63,5	1	300	-0,25	54
15	0,995	0,55	63,5	1	300	-0,25	54,5
16	1,195	1,00	63,5	1	300	-0,25	53
17	0,31	-1,00	44	-1	400	0,375	30
18	0,36	-0,89	48,5	-0,53846	400	0,375	34
19	0,46	-0,66	52,5	-0,12821	400	0,375	40
20	0,695	-0,13	62	0,846154	400	0,375	48
21	0,795	0,10	63,5	1	400	0,375	48
22	0,795	0,10	63,5	1	400	0,375	48
23	0,995	0,55	63,5	1	400	0,375	48,5
24	1,195	1,00	63,5	1	400	0,375	48
25	0,31	-1,00	44	-1	500	1	22
26	0,36	-0,89	48,5	-0,53846	500	1	26
27	0,46	-0,66	52,5	-0,12821	500	1	31
28	0,695	-0,13	62	0,846154	500	1	42
29	0,795	0,10	63,5	1	500	1	41,5
30	0,795	0,10	63,5	1	500	1	41,5
31	0,995	0,55	63,5	1	500	1	42,5
32	1,195	1,00	63,5	1	500	1	43

III.   ANALYSIS OF RESULTS

From the visualization of the data, all postulates known from the theory are confirmed:

- The carbon content has a significant influence on the hardening and the tendency to increase the hardening is maintained as a similarity among the investigated tempering temperatures.

- As the tempering temperature increases, the hardening decreases, and at 180 °C tempering it is negligible, applied to remove internal stresses for tools, while at 500 °C tempering it is applied to improve the grain structure, increasing the strength of blow.

- Based on the experimental data presented in Fig. 1 using the widely spread Excel, relationships predicting the unexamined carbon content at a specific retort temperature are derived. The results of this modeling are presented in Table 2
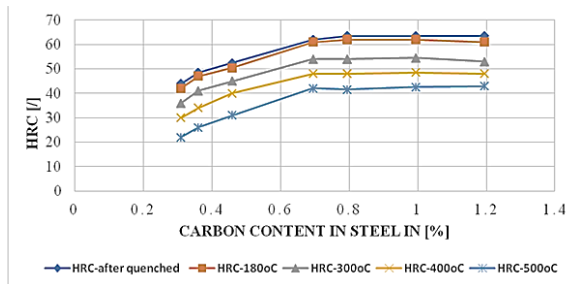

Fig. 1.   Effect of carbon content and annealing temperature on hardening

TABLE 2. HARDNESS PATTERNS AS A FUNCTION OF CARBON CONTENT AND TEMPERING TEMPERATURE

№	Speed, mm/ min	Hardness model as a function of carbon content	Correlation coefficient
1	Heating in the range 860 – 760 °C and quenching while cooling in water	$y = -44,813 \times X^2 + 87,888 \times X + 21,83$	R² = 0,9904
2	Tempering and quenching at 180 °C	$y = -49,202 \times X^2 + 93,996 \times X + 18,388$	R² = 0,9886
31	Tempering and quenching at 300 °C	$y = -46,132 \times X^2 + 86,689 \times X + 14,741$	R² = 0,9848
4	Tempering and quenching at 400 °C	$y = -44,671 \times X^2 + 85,446 \times X + 8,8962$	R² = 0,9815
5	Tempering and quenching at 500 °C	$y = -45,045 \times X^2 + 89,816 \times X - 0,8252$	R² = 0,9828

Models from the polynomial regression approximation of hardness from the carbon state are plotted in natural units, along the abscissa axis in Fig. 1; the peculiarity of these models is the relatively low coefficient of multiple correlation for the models describing the return. Sufficient experimental data are available through which the accuracy of the modeling can be improved. One of these possibilities is by using the coded values from Table 1.

The disadvantage of this kind of representation is the low dimensionality of the modeling; for this reason, it does not comprehensively cover all examined indicators that are controlled. To overcome this shortcoming, the aim of the research is formulated: by means of modeling, the influence of the change in composition and the tempering temperature on the hardening of carbon steels after hardening heat treatment can be identified. Quenching and tempering (Q&T alloy quenched and tempered steel) is a combined heat treatment process to achieve maximal hardness with a certain strength and ductility. The goal of the research is to develop a mathematical model for the quenching and tempering process for the entire range of carbon steels – both structural and tool..

The results of the experiment are used to obtain the mathematical model of the examined process. A mathematical model is a system of mathematical relationships that describe the process or phenomenon under research. When planning an experiment, a mathematical model is often understood as an equation that relates an optimization parameter to factors. This equation is also called the response function. For the data from Table 1, in coded form, the model for the hardness depending on the carbon content of the steel X_1, the hardness after quenching X_2 and the tempering temperature X_3 is derived.

$$\begin{aligned} HRC = {} & 47.9658 + 6.80107 \times X_1 + 2.60967 \times X_2 \\ & - 9.54842 \times X_3 - 0.149884 \times X_1{}^2 - 7.06309 \times X_1 \times X_2 \\ & + 0.850104 \times X_1 \times X_3 + 1.79414 \times X_2{}^2 \\ & - 0.448902 \times X_2 \times X_3 - 0.598823 \times X_3{}^2 \end{aligned} \quad (1)$$

Polynomial regression analysis was used as the algorithm to express the model, and the programming language – Authoring Decision Support System was used to interpret the model results. The model data, which are the predicted stiffness values, were validated using an F-test combined with mean, correlation coefficient, and standard error analyses. The finding of improvement in accuracy at coded values for which the model was derived actually occurred with all control parameters considered together. The multiple correlation coefficient for the resulting model increased to $R^2 = 0.9977$. The adequacy of the model is also proven by Fisher's test, where the calculated value in this test is extremely much larger: $538.3673 \gg 2.3419_{(a=0.05, 9.22)}$ than the one determined in the table.

Analysis of the mutual influence of a set of three, four or more controlled parameters is difficult and requires an "advisor" developed as a system that takes into account:

- The exact complex interaction between parameters such as value and normalized percentage of the maximum. The interaction is visualized and can be justified iteratively by refining color intervals.

- A friendly oriented system, initially working with colors and upon reaching the desired solution for a maximum or minimum, the values of the control parameters and the investigated quantities are specified [18].

- The system is successfully applied to determine a complex of properties of a contradictory nature.

Using the cited decision support system, the following extremes of model (1) were obtained. Table 3 shows the minimal and maximal stiffness, as well as the values of the control parameters at which these values occur.

TABLE 3. MAXIMA AND MINIMA OF MODEL-DETERMINED STIFFNESS

№	HRC	X1 C [%]	X2 HRC after quenching	X3 T [°C]
1	Minimum – 22.6 [0 %]	0.31	44	500
2	Theoretical maximum – 68,51 – [100 %]	1.195	44	180
3	Real logical maximum – 61.1 –[82,56 %]	1.195	63.5	180

Based on the analysis, it was found that the theoretical maximum is unrealistic and it is 17.44 % greater than the actual logical one.

IV. CONCLUSION

Through the means of modeling in a new way, it has been proven that tool steels are always tempered at low temperatures in the range of 150 – 200 °C. This is proven by the derived model in which, after analysis, it was necessary to adjust its theoretical maximum. The difference between the theoretical and the real logical maxima amounts to 17.44 %. The analysis was performed by means of a system applied in varying the parameters of a technological process of retort for seven steels in order to identify the parameters of the process thickness.

IV. ACKNOWLEDGMENT

REFERENCES

[1] Daryl G Clerc, Mechanical hardness and elastic stiffness of alloys: semiempirical models1 Contribution of NIST—an agency of the U.S. Government. Not Subject to Copyright in the United States1, Journal of Physics and Chemistry of Solids, Volume 60, Issue 1, 1999, Pages 83-102, ISSN 0022-3697

[2] Dolchinkov N., Optimizing energy efficiency in the conditions of a global energy crisis, Optimizing Energy Efficiency During a Global Energy Crisis, 2023, ISBN13: 9798369304006 EISBN13: 9798369304013, DOI: 10.4018/979-8-3693-0400-6 pp. 1–9

[3] Dolchinkov N., Loktionov, O.A., Korolev, I.V., Karaivanova-Dolchinkova, B.E., Influence of Electromagnetic Waves on the Human Body, 2021 Sixth Junior Conference on Lighting (Lighting), 2021, pp. 1-5, doi: 10.1109/Lighting49406.2021.9599072, Electronic ISBN:978-1-6654-3792-9, CD:978-1-6654-3791-2

[4] Loktionov, O.A., Fedotova, E.V., Kondrateva, O.E., Dolchinkov, N.T., Kuznetsov, N.S. Actual and design wind loads for overhead transmission lines in the Central European part of Russia, IOP Conference Series: Earth and Environmental ScienceThis link is disabled., 2023, 1281(1), 012050

[5] Dolchinkov N., Pavlov, M.P., Influence of meteorological elements in accidents in enterprises with radioactive elements or dangerous chemical substances in Bulgaria, 14th International Scienfic and Practical conference Environment. Technology. Resources. Vide. Tehnologija. Resursi, 2023, ISSN 1691-5402, 1, pp. 49–54

[6] Dolchinkov N., Results and Analysis of Achieved Joint Research and Activities Between Rezekne Academy of Technology and Vasil Levski National Military University, 14th International Scienfic and Practical conference Environment. Technology. Resources. Vide. Tehnologija. Resursi, 2023, ISSN 1691-5402, 3, pp. 90–93

[7] Lazov, N. Padarev, Laser Safety in Army Education, Revista, Vol. XXVIII, Nr. 1 (109), ED. Academiei Forţelor Terestre „Nicolae Bălcescu" Sibiu, Romania 2023, ISSN 2247-840X, ISSN-L = 1582-6384, pp. 61–68, DOI: 10.2478/raft-2023-0009

[8] N. Padarev, Lyubomir Lazov, Milko Yovchev, Lyubomir Linkov, The Change of Contrast is Investigation of 75 Steel Samples Laser Marked with Different Modes. Environment. Technology. Resources. Rezekne, Latvia. Proceedings of the 14th International Scientific and Practical Conference. Volume 3, 334-338, Print ISSN 1691-5402. Online ISSN 2256-070X. Published by Rezekne Academy of Technologies, 2023 https://doi.org/10.17770/etr2023vol3.7264

[9] Zhang, X., Tang, Jy. & Zhang, Xr. An optimized hardness model for carburizing-quenching of low carbon alloy steel. J. Cent. Southern Univ. 24, 9–16 (2017). https://doi.org/10.1007/s11771-017-3403-2

[10] Xiaohu Deng, Dongying Ju, Modeling and Simulation of Quenching and Tempering Process in steels, Physics Procedia, Volume 50, 2013, Pages 368-374, ISSN 1875-3892

[11] Smoljan, B., Iljkić, D. & Totten, G.E. Mathematical Modeling and Simulation of Hardness of Quenched and Tempered Steel. Metall Mater Trans B 46, 2666–2673 (2015). https://doi.org/10.1007/s11663-015-0451-6

[12] Mahmoud Bakr, Junaidi Syarif, Ibrahim Abaker Targio Hashem, Prediction of phase and hardness of HEAs based on constituent elements using machine learning models, Materials Today Communications, Vol. 31, 2022

[13] N.S. Reddy, J. Krishnaiah, Seong-Gu Hong, Jae Sang Lee, Modeling medium carbon steels by using artificial neural networks, Materials Science and Engineering: A, Volume 508, Issues 1–2, 2009, Pages 93-105, ISSN 0921- 5093

[14] Faizabadi, M.J., Khalaj, G., Pouraliakbar, H. et al. Predictions of toughness and hardness by using chemical composition and tensile properties in microalloyed line pipe steels. Neural Comput & Appl 25, 1993–1999 (2014). https://doi.org/10.1007/s00521-014-1687-9

[15] Tontchev, N., Materials science, Effective solutions, and technological variants, Lambert,Academic Publishing, 2014, 142

[16] Martin Walbrühl, David Linder, John Ågren, Annika Borgenstam, A new hardness model for materials design in cemented carbides, International Journal of Refractory Metals and Hard Materials, Volume 75, 2018, Pages 94-100

[17] S.G. Borisade, O.O. Ajibola, A.O. Adebayo, A. Oyetunji, Development of mathematical models for the prediction of mechanical properties of low carbon steel (LCS), Materials Today: Proceedings,Volume 38, Part 2, 2021, Pages 1133-1139

[18] Tontchev, N., Gaydarov, V., N. Hristov, N., Analyzes and applications through thecomputational approach DEFMOT, Sofia, 2022, 167 p. (in Bulgarian),

Investigation of the effect of laser power, speed and frequency on surface roughness and color marking on AISI 304

Gatis Tutins
Faculty of Engineering
Rezekne Academy of Technologies
Rēzekne, Latvia
gt17005@edu.rta.lv

Imants Adijans
Faculty of Engineering
Rezekne Academy of Technologies
Rēzekne, Latvia
imants.adijans@rta.lv

Emil Yankov
Faculty of Engineering
Rezekne Academy of Technologies
Rezekne, Latvia
emil.yankov@rta.lv

Artis Bikovs
Faculty of Engineering
Rezekne Academy of Technologies
Rēzekne, Latvia
ab21336@edu.rta.lv

Abstract. **Austenitic steels are widely used in machine and tool making, and many of the products produced are marked with ink or impact marking systems. This study aims to investigate contrast color marking methods using advanced, environmentally friendly fiber laser systems.**

We developed marking matrices with 14 columns and 6 rows, each square measuring 5x5 mm. We investigated the effect of scanning speed, laser power and frequency on color marking and surface roughness. Our results showed that increasing the scanning speed leads to a decrease roughness, resulting in different colored markings. As the average power increased, the marking changed to different colors. At low frequencies of 50 kHz, the color marking was observed with a lower contrast saturation, while increasing the frequency to 300 kHz resulted in a more homogeneous and contrast with brighter and more saturated colors. These results provide valuable information for improving color marking techniques using laser systems in the manufacturing industry.

Keywords: AISI 304, Fiber laser, Laser color marking, LIPSS, Surface roughness.

I. INTRODUCTION

Today, laser technology is increasingly preferred in industrial production for marking products, due to its undeniable advantages over traditional methods [1], [2], [3]. Modern manufacturers strive to adopt laser technology as a reliable technique for marking their products [4].

In the field of surface modification of materials, the quest for precision and flexibility has led to the widespread adoption of fiber laser technology. With their compact design, high efficiency, and exceptional beam quality, 20 W optical lasers have become powerful tools for numerous industrial applications. Among the various materials subjected to laser processing, stainless steel AISI 304 stands out as a prime candidate, valued for its durability, corrosion resistance, and aesthetic appearance. Numerous studies have been conducted on laser color marking [5], [6], [7], [8], [9].

Some interesting research in this area is worth noting; for example, Veiko [10] proposed an original palette development method in the nanosecond pulse duration laser coloring process. The authors [11] in their study analyzed the laser color marking process of AISI 304 steel samples by examining 15 different colors. The influence of the gas environment on the composition and color of the nanosecond laser-modified surface was demonstrated by Luo et al. [12]. In [13], Lazov et al. studied laser marking on the fly of the product.

While the aforementioned studies investigated laser color marking with nanofiber lasers, the authors in [14] [15] [16] focused on investigating the process using a femtosecond laser. On stainless steel, they achieved

iridescent metallic shades of different colors when viewed from different angles, demonstrating good reproducibility of results. Adams et al. [17] investigated the growth of interference oxide films on the surface of 304L stainless steel.

Despite the successes achieved, further research is needed to achieve high reproducibility of different colors in marking, thus expanding its widespread use in the industry.

This paper seeks to explore the potential of 20 W optical lasers for color marking on AISI 304 stainless steel, delving into the subtleties of laser parameters, surface interactions, and practical applications affecting contrast and roughness in the machining zone. From understanding the role of laser parameters such as power, speed, and frequency to exploring innovative techniques to achieve precise and durable color markings. By elucidating the basic principles and showing examples from real experiments, we aim to provide insights for the industry to use the full potential of fiber laser technology for color marking on AISI 304.

II. MATERIAL, LASER SYSTEM AND METHODOLOGY

A. Material.

The research was conducted on samples made of a commonly used type of stainless steel AISI 304 (chemical composition: *(LEAX measurements)* C = 0.017 %, Si = 0.37 %, Mn = 1.79 %, P = 0.028 %, S = 0.010 %, Cr = 18.1 %, Ni = 8.0 %, Mo = 0.40 %, Cu = 0.34 %, N = 0.06 %,) with dimensions of 43 mm × 93 mm and thicknesses of 3 mm. Samples were marked on fiber laser with different laser parameters. The samples were marked in the atmospheric air and room temperature.

B. Laser Marking System.

Experiments were made using a Rofin PowerLine F 20, shown in Figure 1, laser specification shown in (Table 1). A pulsed fiber laser is used. The laser system has good positioning accuracy and a high degree of repeatability.

Fig. 1. Rofin powerline f 20 marking fibre laser system

TABLE 1. CHARACTERISTICS OF THE LASER SYSTEM

Characteristic	Value
Wavelength	1064 nm
Output power (pulsed)	19 W
Max. Pulse Energy	1 mJ
Pulse Width	4 – 200 ns
Repetition Rate	20 to 1000 kHz
Efficiency	30 %

C. Microscope setup.

The marked stainless steel AISI 304 samples structure change was examined under microscope LEXT 3D MEASURING LASER MICROSCOPE OLS5000 shown in Figure 2. With set parameters at objective at 20X, measure pitch was 0.40 μm, measure field 645 μm x 645 μm. Witch was used to measure the laser marking samples of AISI 304 plates.
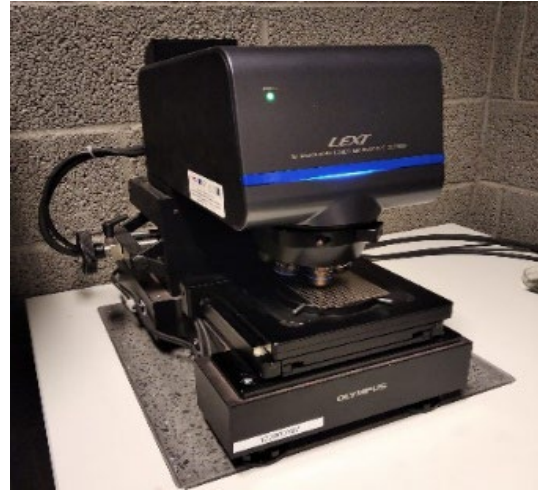

Fig. 1. Lext 3D measuring laser microscope OLS5000

D. Methodology.

In order to fulfill the objective of the scientific report, it was necessary to perform at least 2 marking processes with different laser parameters. The samples were treated from grease and contaminants of the sample surface with technical spirt.

By performing such an operation, we understand what changes occur when the parameters of the lasers are changed, and we can evaluate the results.

During the experiments, two stainless steel samples were used. The following constant parameters were set on sample 1: raster step Δx was set as 10 μm, pulse duration was 4 ns, frequency – 400 kHz. Also, there was set of variable parameters, these parameters are shown in Fig. 3.
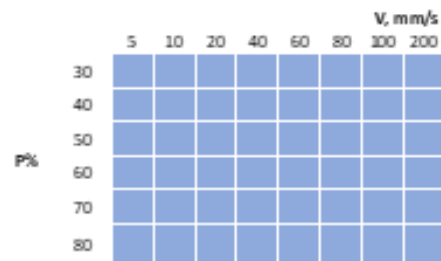

Fig.3. Scheme for laser marking of stainless steel sample 1.

On sample 2, raster step Δx was set same as on the sample 1, 10 μm, pulse duration was 4ns, and laser power P was 12,8 W. And during changes on constant parameters we also change variable parameters, these parameters is shown in Fig. 4.
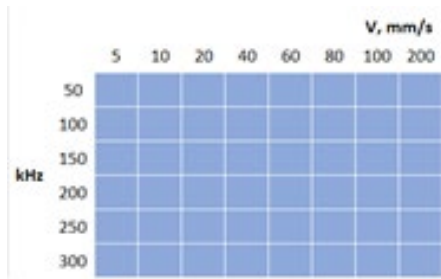
Fig.4. Scheme for laser marking of stainless steel sample 2.

The experiment began with the scheme test method. Through the combination of parameters, a square area of 5 mm × 5 mm was created on the surface of the sample, with an interval of 1.5 mm between the rows and columns. The entire stainless-steel plate contained 48 areas (squares), as shown in Fig. 5.

Roughness Measurement Methods. Roughness measurements and the resulting microstructure were examined with an Olympus model "OLS5100-EAF" laser microscope (Fig. 2). The obtained microstructural images were carried out using a 10× objective, magnification 227×, as the examined area for each measurement 1280 µm ×1280 µm with a measurement accuracy of ± 2.0 µm. From the obtained 3D images with the laser system of the microscope, the roughness Ra for the entire examined area 1280 µm ×1280 µm were measured. The obtained values are plotted in tables and graphical dependences of changes in roughness depending on speed and step during surface laser processing are shown. The built dependencies are presented in the results.

III. RESULTS AND DISCUSSION

A. Results of surface roughness measurement.

After raster marking was carried out on the first sample according to the above methodology, a textured surface was obtained on the squares. A general view of the obtained picture on the sample is presented in Fig. 5. Average line roughness (R_a) measurements were taken. Average surface roughness on untreated surface was $R_a = 0.695$ µm.

In Fig. 6 shows the marked square with the largest roughness (2.33 µm) with technological parameters power $P = 9.6$ W and speed $v = 5$ mm/s. In fig. 6a shows the 2D image of the marked square, and in fig. 6b – the 3D image.

Fig. 5. Raster marked sample of stainless steel at different speeds and powers
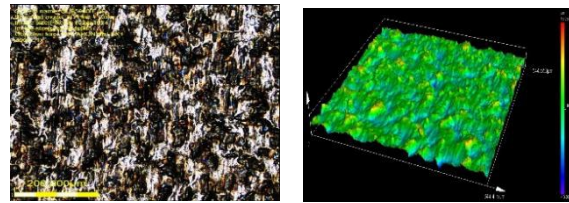

a)   b)
Fig 6. Marked square with biggest roughness R_a for the first sample

Smallest roughness (0.70 µm) on marked surface was with parameters $P = 4.8$ W and $v = 200$ mm/s as shown in Fig. 7. As we can see that surfaces also visually looks different, and colours also has been different. In Fig. 6a we observe brown colour and in Fig. 7a its grey.

At a speed of 200 mm/s, the roughness of the machined surface approaches that of the untreated surface (0.695 µm) for all studied powers.
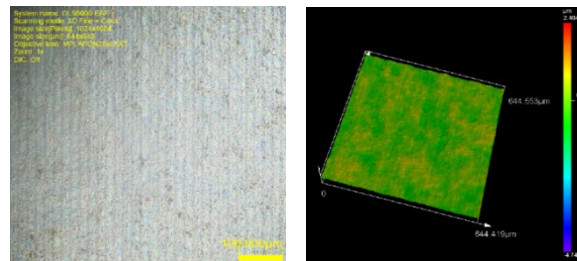

a)   b)
Fig 7. Marked square with smallest roughness R_a for the first sample

The experimental dependence of the roughness on the velocity for three powers for the studied sample is presented in Fig. 8. The following dependencies are observed:

- As speed increases, roughness decreases for all three powers. In the interval from 5 mm/s to 100 mm/s, the curves are significantly steeper than those in the interval from 100 mm/s to 200 mm/s;

- For power 4.8 W, the roughness changes from 2.33 µm to 0.64 µm, and in the interval from 100 mm/s to 200 mm/s it is almost constant and is close to that of the untreated surface;

- For power 6.4 W, the roughness changes from 1.82 µm to 0.80 µm;

- For a power of 9.6 W, the roughness changes from 0.97 µm to 0.70 µm;

- In the interval of 5 mm/s to 100 mm/s, the roughness change rate at 9.6 W is 15% greater than that at 6.4 W and 85% greater than that at 4.8 W.
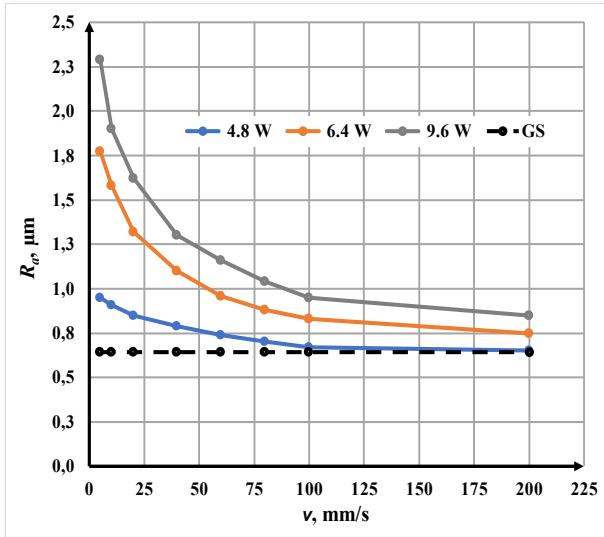
Fig 8. Dependence of the roughness R_a on the speed v during laser marking of a sample of stainless steel for powers P: blue color - 4.8 W, orange color - 6.4 W, gray color - 9.6 W and GS – ground (untreated) surface.

On the second sample (see Fig. 9) raster marking of squares with different speeds and frequencies was performed. The speed was varied in the interval from 10 mm/s to 200 mm/s.
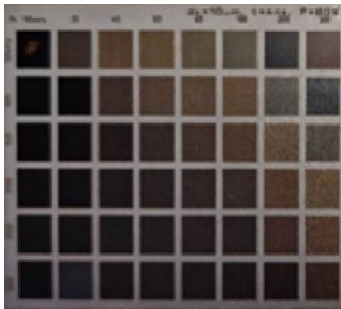

Fig. 9. Raster marked sample of stainless steel at different speeds and frequencies

Biggest roughenss R_a on the sample was on laser parameters frequency $v = 50$ kHz and speed $v = 10$ mm/s (see Fig. 10, Fig. 10a – 2D image, Fig. 10b – 3D image).
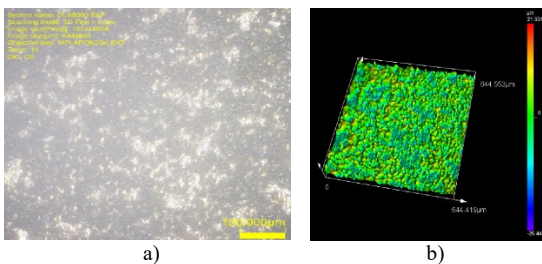

a)   b)
Fig 10. Marked square with biggest roughness R_a

Smallest roughness on marked surface was with parameters frequency $v = 250$ kHz and speed $v = 200$ mm/s as shown in Fig. 11.

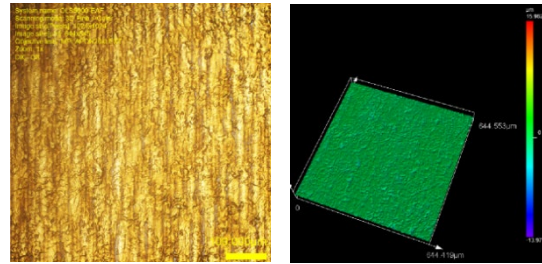a)   b)
Fig 11. Marked square with smallest roughness R_a for the second sample

The dependence of the roughness on the speed for three frequencies for the second sample is presented in Fig. 12. From the obtained graphs it follows:

- As the speed increases, a nonlinear decrease in roughness is observed for the entire speed interval for all three frequencies;

- For a frequency of 50 kHz, the roughness is about 25 % greater than that for a frequency of 150 kHz and about 63 % greater than that for a frequency of 250 kHz;

- Again as with the graphs in Figs. 7, the curves in the interval from 10 mm/s to 100 mm/s are significantly steeper than those in the range from 100 mm/s to 200 mm/s.
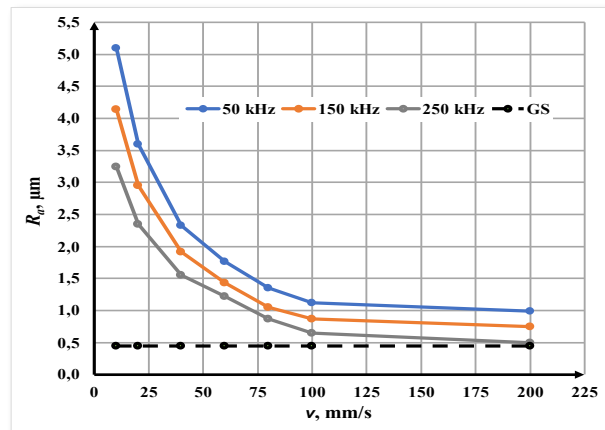

Fig 12. Dependence of the roughness R_a on the speed v during laser marking of a sample of stainless steel for frequencies v: blue color – 50 kHz, orange color – 150 kHz, gray color – 250 kHz and GS – ground (untreated) surface.

IV.   CONCLUSIONS

The quality of the marking is determined by a number of criteria, the most important of which are contrast, clarity, necessary roughness, wear resistance, etc. The influence of speed, power and frequency on the roughness of the marking was analyzed and the following regularities were established:

- It was found that with increasing speed, a non-linear decrease in roughness was observed for the three powers studied;
- With increasing power, an increase in roughness is observed as the roughness at 9.6 W is 15% greater than that at 6.4 W and 85% greater than that at 4.8 W;
- A decrease in roughness with increasing speed is observed for the three investigated frequencies;
- As the frequency increases, the roughness decreases as for a frequency of 50 kHz it is 25 % greater than that for 150 kHz and about 63 % greater than for 250 kHz;
- Two ways of laser marking (by melting and oxidation) were analyzed, in which color marking is obtained.

Research can also continue with the influence of step, number of repetitions and duration of pulses on the roughness of the marked areas. This will help to obtain the complex influence of more important parameters on the roughness of the marking.

REFERENCES

[1]. Lazov, L., Deneva, H., Narica, P., Factors influencing the color laser marking, Vide. Tehnologija. Resursi - Environment, Technology, Resources, 2015, 1, pp. 102–107, DOI: 10.17770/etr2015vol1.223

[2]. Angelov, N., Teirumnieks, E., Lazov, L., Influence of pulse duration on the process of laser marking of CT80 carbon tool steel products, Laser Physics, 2021, 31(4), 045601, DOI: 10.1088/1555-6611/abe5afC.

[3]. Leone, S. Genna, G. Caprino, I. De Iorio, AISI 304 stainless steel marking by a Q-switched diode pumped Nd:YAG laser, Journal of Materials Processing Technology, V 210, 10, 2010, p. 1297-1303, https://doi.org/10.1016/j.jmatprotec.2010.03.018.

[4]. M. Pandey, B. Doloi, Parametric analysis on fiber laser marking characteristics for generation of square shaped marked surface on stainless steel 304, Materials Today: Proceedings, Volume 56, Part 4, 2022, p 1908-1913, https://doi.org/10.1016/j.matpr.2021.11.169.

[5]. L.Lazov, E. Teirumnieks, N. Angelov, E. Yankov, Modification of the roughness of 304 stainless steel by laser surface texturing (LST), Laser Physics, 2023, 33 046001

DOI 10.1088/1555-6611/acbb76

[6]. B. Krawczyk, P.Cook, et al.,Atmospheric chloride-induced stress corrosion cracking of laser engraved type 316L stainless steel, Corrosion Science,2018, Volume 142,p. 93-101, DOI:org/10.1016/j.corsci.2018.07.016.

[7]. L. Lazov, E. Teirumnieks, T. Karadzhov, N. Angelov, Influence of power density and frequency of the process of laser marking of steel products, Infrared Physics and Technology, 2021, 116, 103783, DOI: 10.1016/j.infrared.2021.103783

[8]. E.H. Amara, F. Haïd, A. Noukaz, "Experimental investigations on fiber laser color marking of steels," Appl. Surf. Sci., vol. 351, pp. 1–12, Oct. 2015, https://doi.org/10.1016/j.apsusc.2015.05.095.

[9]. Narica, P., Lazov, L., Teilans, A., ...Teirumnieks, E., Cacivkins, P., Method for color laser marking process optimization with the use of genetic algorithms, Vide. Tehnologija. Resursi - Environment, Technology, Resources, 2017, 2, pp. 101–106 DOI:10.17770/etr2017 vol2.2607

[10].V. Veiko, G. Odintsova, at. Al., Development of complete color palette based on spectrophotometric measurements of steel oxidation results for enhancement of color laser marking technology,Materials & Design,Volume 89,2016, p. 684-688, https://doi.org/10.1016/j.matdes. 2015.10.030.

[11].H. Roozbahani et al., Laser color marking: repeatability, stability and resistance against mechanical, chemical and environmental effects, IEEE Access, 2020, DOI: 10.1109/ACCESS.2020.3040744

[12].F. Luo, W. Ong, Y. Guan, F. Li, S. Sun, G.C. Lim, M. Hong, "Study of micro/nanostructures formed by a nanosecond laser in gaseous environments for stainless steel surface coloring," Appl. Surf. Sci., vol. 328, pp. 405–409, Feb. 2015

[13].Lazov, L., Angelov, N. Influence of some technological parameters on the contrast of laser marking on the fly. Laser Phys. 22, 1755–1758 (2012). https://doi.org/10.1134/S1054660X12110084

[14].Livakas N, Skoulas E, Stratakis E. Omnidirectional iridescence via cylindrically-polarized femtosecond laser processing. Opto-Electron Adv 3, 190035 (2020). doi: 10.29026/oea.2020.190035

[15].W. Shi, A. Schulzgen, R. Amezcua, X. Zhu, S. Alam, "Fiber lasers and their applications: Introduction," J. Opt. Soc. Am. B, vol. 34, Mar. 2017, https://doi: 10.1364/JOSAB.34.00FLA1

[16]. W. Shi, A. Schulzgen, R. Amezcua, X. Zhu, S. Alam, "Fiber lasers and their applications: Introduction," J. Opt. Soc. Am. B, vol. 34, Mar. 2017, https://doi: 10.1364/JOSAB.34.00FLA1.

[17]. D. P. Adams, V.C. Hodges, D.A. Hirschfeld, M.A. Rodriguez, J.P. McDonald, P.G. Kotula, "Nanosecond pulsed laser irradiation of stainless steel 304L: Oxide growth and effects on underlying metal, Surf. and Coat. Technol., vol. 222, p. 1–8, 2013, DOI: org/10.1016/j.surfcoat.2012.12.044

Professor, leading researcher Dr.habil.geol. Gotfrīds Noviks
(15/09/1935 – 07/03/2024)

Professor Gotfrīds Noviks worked at Rezekne Academy of Technologies (RTA) since the establishment of the education institution. A lot of work was devoted to further development of the Academy. Professor Noviks was the scientist: habilitated doctor of geology, vice-rector of the Science and Studies Department, head of the Department of Natural and Engineering Sciences, creator of environmental engineering study programs and program director at the bachelor's, master's and doctoral levels. He prepared more than 320 scientific publications, obtained 25 authorship certificates, participated in more than 100 scientific conferences, led scientific projects and research groups. Professor was the initiator of the scientific conference "Environment. Technology. Resources" where the scientists and researchers from foreign countries and Latvia have been participating for many years. Professor's pedagogical experience lasted for almost 60 years. He was also the author of many textbooks which are still used in many countries of the world. Professor Noviks was the founder of rock physics, the author of the first textbook "Fundamentals of Rock Physics" which was the first one in this field in the former Soviet Union. He was the member of the International Water Federation (WEF) from 1995, the member of the ecological committee and ecological education committee from 1996, the member of the New York Academy of Sciences.

Gotfrīds Noviks was born in Ludza, graduated from Viļani Secondary School, later from Leningrad Institute of Mining, where he studied geology. In the scientific field, he worked at the Moscow Mining Institute in Russia, then at the Kabul Polytechnic Institute in Afghanistan for a short period. Afterwards he decided to return to Latvia, responding to an invitation to work in Rezekne. In 1994, Professor Noviks started to work at Rezekne Higher Education Institute (now Rezekne Academy of Technologies).

He worked at the Rezekne Academy of Technologies, led the scientific work, as well as enjoyed the hobbies that brought a lot of joy and inspiration for him. Gotfrīds Noviks once admitted that his hobby was kayak trips on rivers. His idea of ecological expeditions for 1st-year students of the environmental engineering still lives on. The first expedition was organized in 1997. Professor told that he liked reading books, cooking; he was interested in photography, enjoyed the nature with forests, rivers, and mountains as well.